Université Nice Sophia Antipolis

Habilitation à Diriger des Recherches

présentée par

Benoit CARRY

The small bodies of our solar system: 02∞

soutenue le 6 Juin 2018 à 14h devant le jury:

Philippe	Bendjoya	Président
Alberto	Cellino	Rapporteur
Guy	Libourel	Rapporteur
Mirel	Birlan	Rapporteur
Agnès	Fienga	Examinatrice
Philippe	Rousselot	Examinateur
Paolo	Tanga	Examinateur

Laboratoire Lagrange UMR 7293, Observatoire de la Côte d'Azur
benoit.carry@oca.eu

Résumé

Les petits corps du système solaire sont les restes des planétésimaux qui se sont accrétés pour former les planètes telluriques et les coeurs des géantes gazeuses. Leurs compositions et propriétés physiques, et comment celles-ci sont réparties dans le système solaire, portent la marque des processus qui ont eu lieu dans le disque protoplanétaire et de l'évolution dynamique de notre système planétaire.

Ce manuscrit décrit comment j'ai diversifié mes activités de recherche depuis le début de mon doctorat en 2006 jusqu'à 2018: de l'étude détaillée des plus gros astéroïdes par imagerie et spectro-imagerie à haute résolution angulaire à l'usage massif d'archives et de grands relevés pour caractériser les différentes populations de petits corps; de la modélisation 3-D à la minéralogie de surface.

D'abord, je décris les propriétés physiques et de surface de (1) Cérès et (4) Vesta, cibles de la mission Dawn de la NASA. De l'analyse d'images obtenues par optique adaptative, j'ai déterminé la taille et l'orientation de Cérès, plus tard confirmée par Dawn. J'en ai étudié les propriétés spectrales, révélant une surface très homogène, avec seulement des variations d'albédo correspondant aux principales structures imagées par Dawn, tel le cratère Occator et son puit central brillant. Étudiant le cycle de l'eau de Cérès, j'ai participé à la détection de vapeur d'eau avec l'observatoire spatial Herschel de l'agence spatiale européenne, et relié son émission au cratère Occator.

Je décris ensuite l'algorithme de modèlisation 3-D multi-données KOALA, et comment nos prédictions sur l'astéroïde (21) Lutetia ont été validées par les images prises lors son survol par la sonde Rosetta de l'ESA. Une reconstruction précise de la forme 3-D est cruciale pour déterminer le volume, et donc la densité, propriété fondamentale pour comprendre la structure interne de ces corps. J'illustre ceci sur les différents astéroïdes que j'ai étudiés, et comment je me suis concentré sur les systèmes binaires, où l'interaction gravitationnelle entre les composantes fournit la masse. Ensuite, je résume nos connaissances sur l'intérieur des petits corps à partir de mon analyse statistique des déterminations de taille et masse, donc densité, que j'ai compilées.

En suivant le fil rouge tracé par les systèmes binaires, je présente ensuite mes travaux sur les objets de Kuiper. Depuis l'étude de la dynamique du système triple de l'étrange Haumea, à sa famille dynamique étudiée par photométrie à large bande, à sa composition de surface riche en glace d'eau par spectroscopie. Tirant parti de l'optique adaptative, je montre comment j'ai obtenu les spectres proche infrarouge d'objets lointains, et étudié leur composition de surface, incluant celle de Charon, satellite de Pluton et cible de la mission New Horizons de la NASA.

Finalement, je décris comment j'ai généralisé l'utilisation de la photométrie pour étudier la distribution de la matière dans le système solaire interne, en utilisant le grand échantillon fourni par le Sloan Digital Sky Survey: de la ré-écriture de la structure compositionnelle de la ceinture principale d'astéroïde à l'étude des régions sources et du processus de vieillissement des surfaces des objets géocroiseurs. Je conclu par une étude prospective de l'utilisation de la photométrie infrarouge par la mission Euclid de l'ESA pour améliorer notre compréhension de la composition des petits corps.

Abstract

The small bodies of our solar system are the leftovers of the material that accreted to form the terrestrial planets and the core of the giant planets. Their compositions and physical properties, and how they distribute throughout the Solar System, still record the prints of the processes that took place in the protoplanetary disk and of the subsequent dynamical evolution of our planetary system.

This manuscript describes how I diversified my research activities from the start of my PhD in 2006 to 2018: from the detailed study of the largest asteroids using high-angular-resolution imaging and spectro-imaging on large ground-based telescopes to a massive use of archives and surveys to characterize the different populations of small bodies; from 3-D shape modeling to surface mineralogy.

First, I describe the physical and surface properties of (1) Ceres and (4) Vesta, targets of the NASA Dawn mission. From the analysis of adaptive-optics images, I determined the size and spin orientation of Ceres, which were later confirmed by the NASA Dawn. I studied its spectral properties, revealing a very homogeneous surface, with only a few albedo markings corresponding to the major features imaged by Dawn, such as the Occator crater with its central bright pit. Studying the water regime of Ceres, I participated to the detection of water vapour with the ESA Herschel space observatory, and linked its emission to the Occator crater.

Then I describe the multidata 3-D shape modeling algorithm KOALA, and how our predictions on asteroid (21) Lutetia were validated by the images taken during the flyby of the asteroid by the ESA Rosetta mission. Accurate reconstruction of the 3-D shape is key in determining the volume of asteroids, and study their density, which is perhaps the most fundamental property to understand their internal structure. I illustrate this on different asteroids I studied, and how I focused on binary systems in which mutual gravitational interaction provides their mass. I then summarize our knowledge on asteroid interiors from my statistical analysis of the diameter and mass estimates, hence density, I compiled.

Using the dynamical study of binaries as a guideline, I then present my work on Kuiper belt objects. From the dynamics of the peculiar Haumea triple system, to its dynamical family, characterized by broad-band photometry, to its water ice-rich surface by spectroscopy. Taking advantage of adaptive-optics, I show how I also acquired near-infared spectra of others remote objects, and studied their surface composition, incluing Charon, satellite of Pluto and target of the NASA New Horizon mission.

Finally, I describe how I generalized the use of photometry, taking advantage of the large sample of the Sloan Digital Sky Survey, to study the distribution of material in the inner solar system: from a rewriting of the compositional structure of the main belt to the study of the source regions and space weathering among near-Earth asteroids. I conclude with a prospective on the use of ESA Euclid near-infared photometry to increase our understanding of the composition of small bodies.

Acknowledgments

Done! I have finished the writing of this manuscript for the *Habilitation à Diriger les Recherches*, and it feels strange to go back to writing acknowledgments like 9 years ago, when I had finalized the manuscript for my PhD. Many things have happened in these years: one year of ATER (teaching assistant) post-doc at Paris 7 Denis-Diderot University in Paris, two years as Research Fellow at ESA in Madrid, my recruitment as *Astronome Adjoint* by the CNAP in 2012, my *prise de fonction* at the IMCCE in Paris on January the 1st, 2013, and my transfert to the TOP team, Lagrange laboratory, Observatoire de la Côte d'Azur in July 2015, and the SF2A 2017 Young Researcher Prize this year. Not to count my first daughter Anaël in 2009, and the twins David and Maelys in 2014. Wow!

I feel extremely fortunate to have a permanent position in research in astronomy. Becoming an astrophysicist was a dream that begun when I saw the total solar eclipse in August 1999, and it luckily became true. I am infinitely grateful to all those who helped me and made this happen. All the colleagues, friends, and relatives, especially my wife Clara, who have supported me in this long-but-luckily-short-for-me quest of becoming an astronomer.

So let's start where my PhD's acknowledgments end: 2009. I would like to thanks those in Paris, Nice, and Madrid with who I collaborated during my post-doc years, who encouraged me and helped me applying for the permanent position. Among many, I have a special thought for Nicolas Altobelli, Jérôme Berthier, Marco Delbo, Francesca DeMeo, Daniel Hestroffer, Michaël Küppers, Marcello Fulchignoni, William Merline, Paolo Tanga, Frédéric Vachier, and Pierre Vernazza, with who I discussed longly the process of recruitment, from laughing to enraging.

From my years at IMCCE, I learned what it meant to be on the other side: participating to the life of a laboratory, councils, discussions on young bright post-doc for recruitment. I also tasted for the first time the benefit of the permanent position: designing and running research projects on long timescale, and not running for publication. All the efforts to study binary asteroids we started in 2013 only came to fruition with the first article of my PhD student Myriam Pajuelo this year, but what results! I am glad we spent years thinking about and working on the algorithms and codes to produce high quality results.

I also discovered the pleasure and disappointment of the *tâches de service*, that are at the core of the CNAP corps. I really appreciate doing this service for the community and I am proud of some developments I made for the Virtual Observatory ephemerides services at IMCCE, and for the ESA Gaia short-term pipeline for asteroids, even if these tasks often interfere with research plans. And for these years, including the enjoyable teaching weeks at the *Observatoire de Haute Provence*, I am grateful to have met and interacted with Jérôme Berthier, Mirel Birlan, François Colas, Francesca DeMeo, Siegfried Eggl, Valéry Lainey, Lucie Maquet, Enrique Solano, William Thuillot, Frédéric Vachier, and Jérémie Vaubaillon.

I moved to the TOP team in Nice knowing the entire team from all their great articles, but without knowing any personally with the exception of Marco Delbo and Paolo Tanga from our scientific interactions and our common implication in Gaia. I have discovered great colleagues and friends. These past two years have been extremely dense in discussions and new ideas, interactions with great minds. I must also thank the restaurant at the observatory in its social role: I quickly met many persons from the other teams and laboratories, from which I also learned and even started collaborations. They endorsed me for the SF2A Prize, encouraged me to write this manuscript, supported the new development toward Euclid... I really would like to thanks all researchers, engineers, and administratives of the OCA for the productive and healthy work environment they have developed.

The Mont Gros and Nice are two small families for me since I moved here: large enough to offer a lot, small enough to enjoy and to know everyone. These past two years have been amazing, let's hope for many more! Hopefully without forgetting too many of them, a big big thank to Ph!l Bendjoya, Aurélien Crida, Patrick Delaverny, Clémence Durst, Agnès Fienga, Laurent Galuccio, Paul Girard, Sylvie Goletto, Tristan Guillot, Vanessa Hill, Seth Jacobson, Eric Lagadec, Michiel Lambrechts, Guy Libourel, Sophie Maurogordato, Alexis Matter, Nicolas Mauclert, Morby, Héloïse Méheut, Patrick Michel, François Mignard, Rose Pinto, Christophe Ordenovic, Alejandra Recio-Blanco, Jean-Pierre Rivet, Sophie Rousset, Delphine Saissi, Delphine Sastron, F**R**ederica Spoto, Philipe Stee, Frédéric Thévenin, Paolo Tanga, Fabrice Ubaldi, et bien sûr Khaled le chef, Karima, Nadia et Dominique!

I also would like to thank all the members of my defense committee, in alphabetical order, Philippe Bendjoya, Mirel Birlan, Alberto Cellino, Agnès Fienga, Guy Libourel, Philippe Rousselot, and Paolo Tanga, to have accepted to read the present manuscript and attend the defense. And last but not least, my profound thanks to Mirel Birlan, who co-supervised the PhD of Myriam Pajuelo with me between 2014 and 2017, which was the first PhD student I ever supervised. I learned from his patience and advises on how to guide a student through the process of becoming a doctor. Merci co-dir!

Let's play (music) together

I always work listening to music. All those who shared my office can testify that either I have speakers playing psychelic or progressive rock, or I am listening to even weirders brands of music such as Zheul or Space Rock, ... with my headphones.

Because I love music (mainly from the 1960s and 70s) and because well-known music help me concentrating as it hides the noises around. Writing this manuscript for the *Habilitation à Diriger les Recherches* did not contravene with this habit. I listened to tons of music while writing these lines.

So I would like to share this passion, and I have hidden 20 references to songs and bands in the text. Some should be easy to find, others may require more work. Rewards for the first to find each item!

#	Page	Band	Record
1			
2			
3			
4			
5			
6			
7			
8			
9			
10			
11			
12			
13			
14			
15			
16			
17			
18			
19			
20			

Contents

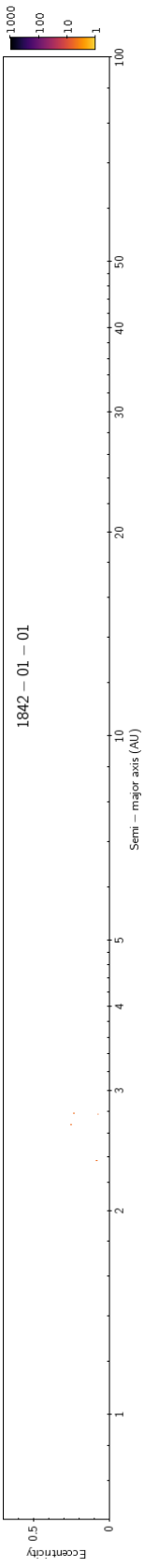

Chapter I

A Golden Age for the study of small bodies

The small bodies of our solar system are the remnants of the building blocks that accreted to form the terrestrial planets and the cores of the giant planets. What remains today is only a small fraction of the material available in the proto-planetary nebula: the asteroid belt accounts for only 4% of the mass of the Moon! Yet, their distributions in the orbital elements space, composition, size, still record the prints of the dynamical events that shaped our solar system. As such, the study of small bodies must be statistical. Since a couple of decades, the wide-spread usage of Charge Coupled Device (CCD) cameras, even amongst amateur astronomers, and the ever-growing computing power, have open the era of statistical studies of small bodies.

Contents

I.1 A brief history of small body research

I.1.a Remnants of planet formation

Asteroids, or more generally the small bodies of our solar system, are the leftovers of the material that accreted to form both the terrestrial planets in the inner solar system and the core of the giant planets in the outer solar system. By understanding their compositions and how they distribute throughout the solar system, we have access to many informations on the accretion processes that took place in the dust and gas disk around the young Sun, and on the subsequent evolution of our planetary system.

Most of the asteroids we see today are the products of collisions which occured (much) later than the earliest stages of our History, and the picture we see nowadays must not be taken at face value. Hence the need to combine detailed census of current populations with numerical simulations. Since my earliest works, I have been observing these bodies, one by one in dedicated programs or harvesting them in public archives, to build a reference vision of how the Solar System Objects (SSOs) are? What are they made of? And how do they distribute in the solar system?

If asteroids were my first targets of interest, I worked on almost all SSO populations, from Near-Earth Asteroids (NEAs) to Kuiper-Belt Objects (KBOs), although the closest I have been to study a comet was ironically an active asteroid (P/2010A2, Snodgrass et al., 2010, see the full text in Appendix B.5.a). In the following, I consider the following populations of SSOs, defined by their orbital elements (Fig. I.1, Table I.1):

- the Near-Earth Asteroid (NEA), including the Aten, Apollo, Amor, and Atira classes, which orbits cross that of terrestrial planets;
- the Mars-crosser Asteroid (MCA), a transitory population between the asteroid main belt and the near-Earth space;
- the Main-Belt Asteroid (MBA), in the principal reservoir of asteroids in the Solar System, between Mars and Jupiter, split into Hungarian, Inner Main-Belt (IMB), Middle Main-Belt (MMB), Outer Main-Belt (OMB), Cybele, and Hilda;
- the Jupiter trojans (Trojans), orbiting the Sun at the Lagrange L4 and L5 points of the Sun-Jupiter system;
- the Centaurs, which orbits cross that of giant planets;
- the Kuiper-Belt Object (KBO), further than Neptune, divided into Detached, Resonant, and Scattered-Disk Objects (SDO), and Inner, Main, and Outer Classical Belt (ICB, MCB, OCB);
- the comets, from the outskirts of the solar system, on highly eccentric orbits, and showing activities at short heliocentric distances.

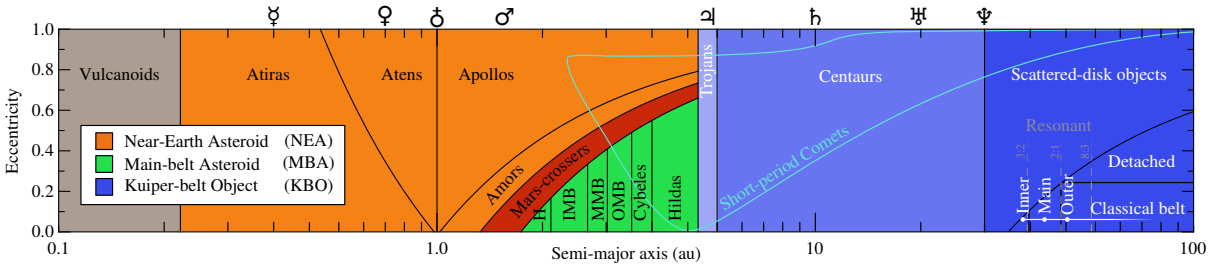

Figure I.1: The different classes of SSOs used throughout the chapters. H stands for Hungarias, and IMB, MMB, and OMB for inner, middle, and outer belt respectively. CREDITS: Carry (2018)

I.1.b From discovery to dynamics

The study of small bodies started even before they were recognized as such. The first orbital study of a SSO dates from 1705, when E. Halley linked together three comet apparitions (in 1531, 1607, and 1682).

Class	Semi-major axis (au)		Eccentricity		Perihelion (au)		Aphelion (au)	
	min.	max.	min.	max.	min.	max.	min.	max.
NEA	–	–	–	–	–	1.300	–	–
Atira	–	a_E	–	–	–	–	–	q_E
Aten	–	a_E	–	–	–	–	q_E	–
Apollo	a_E	4.600	–	–	–	Q_E	–	–
Amor	a_E	4.600	–	–	Q_E	1.300	–	–
MC	1.300	4.600	–	–	1.300	Q_M	–	–
MBA	Q_M	4.600	–	–	Q_M	–	–	–
Hungaria	–	$J_{4:1}$	–	–	Q_M	–	–	–
IMB	$J_{4:1}$	$J_{3:1}$	–	–	Q_M	–	–	–
MMB	$J_{3:1}$	$J_{5:2}$	–	–	Q_M	–	–	–
OMB	$J_{5:2}$	$J_{2:1}$	–	–	Q_M	–	–	–
Cybele	$J_{2:1}$	$J_{5:3}$	–	–	Q_M	–	–	–
Hilda	$J_{5:3}$	4.600	–	–	Q_M	–	–	–
Trojan	4.600	5.500	–	–	–	–	–	–
Centaur	5.500	a_N	–	–	–	–	–	–
KBO	a_N	–	–	–	–	–	–	–
SDO	a_N	–	–	–	–	37.037	–	–
Detached	a_N	–	0.24	–	37.037	–	–	–
ICB	37.037	$N_{2:3}$	–	0.24	37.037	–	–	–
MCB	$N_{2:3}$	$N_{1:2}$	–	0.24	37.037	–	–	–
OCB	$N_{1:2}$	–	–	0.24	37.037	–	–	–

Table I.1: The definition of all the dynamical populations used in this work, as function of their semi-major axis, eccentricity, perihelion, and aphelion (using the definitions in Gladman et al., 2008; Carry et al., 2016). The numerical value of the semi-major axes a, perihelion q, aphelion Q, and mean-motion resonances (Indices $_{i:j}$) are for the Earth a_E, q_E, and Q_E at 1.0, 0.983, and 1.017 Astronomical Unit (au); for Mars Q_M at 1.666 au; for Jupiter $J_{4:1}$, $J_{3:1}$, $J_{5:2}$, $J_{2:1}$, and $J_{5:3}$ at 2.06, 2.5, 2.87, 3.27, 3.7 au; and for Neptune a_N, $N_{2:3}$, and $N_{1:2}$ at 30.07, 47.7, and 39.4 au. The somewhat arbitrary limit of 37.037 au corresponds to the innermost perihelion accessible to detached KBOs (semi-major axis of $N_{1:2}$ and eccentricity of 0.24).

He computed the orbit of a single comet responsible for those apparitions, and successfully predicted its return for 1758 (Halley, 1705), using the recently published law of gravity (Newton, 1687). After such a demonstration of the prediction capabilities of Newton's physics, many astronomers in Europe went on a comet hunt in the years following the return of Halley's comet. Ironically, the next major discovery in the solar system (the first planet since ancient times!) was realized by W. Herschel in 1781, during its survey for double stars.

Yet, asteroid science official kick-off was the discovery of Ceres by G. Piazzi in 1801. Here again, the discovery was made by an astronomer working on a survey of stars, searching for parallaxes, albeit a group of European astronomers were actively searching for a *planet* with a semi-major axis of 2.8 au, following the Titius-Bode numerological pseudo-law. When more objects were discovered, their planetary status was challenged, and W. Herschel cornered the term of *asteroids* to design this new population. Was he extremely visionary and understood that a whole population was hidden behind Ceres? Or did he wanted to be the only one who discovered a true, genuine, planet?

For almost a century, all the discovered asteroids had an orbit between Mars and Jupiter, in what has been dubbed since then the main asteroid belt. The discovery of (433) Eros in 1898 changed the game, its orbit crossing that of Mars. It was the first NEA. In the outer solar system, the counterpart of the main belt was discovered as soon as 1930, when C. Tombaugh found Pluto in photographic plates taken at the Lowell observatory. Yet, it was only after the discovery of 1992 QB1 by Jewitt and Luu (1993) that the existence of a belt of minor bodies further than Neptune, independently predicted by Edgeworth (1949) and Kuiper (1951), was recognized. The same process that declassified Ceres from a planet to an asteroid converted Pluto into a dwarf planet (Binzel, 2006). Amusingly, if the status of Pluto as a KBO and not a planet had been recognized right away in 1930, it would be numbered (1164) Pluto, instead of

(134340) Pluto, being discovered after asteroid (1163) Saga on 1930, January the 20th. History repeats, Ceres was born as a planet, then classified as "not even a star" (asteroid). Pluto logically followed the same fate. Will we call the first Oort cloud object a planet? The ninth planet[1]?

For decades, asteroid studies followed the general trend of astrophysics, and focused on dynamical aspects. This started with the discovery of gaps by Kirkwood (1869) and of dynamical families (Hirayama, 1918). The work of these authors is remarkable, especially considering the low number statistics available to them (Fig. I.2, and the evolution of the figures of the distribution of SSOs in semi-major axis *vs* eccentricity in the margin). The study of these gaps revealed to be a cornerstone of SSOs evolution, as they are the main process to inject Main-Belt Asteroids (MBAs) into the NEA space (e.g., Wetherill, 1979; Wisdom, 1983; Michel et al., 2000; Morbidelli et al., 2002; Bottke et al., 2005; Greenstreet et al., 2012; Granvik et al., 2016). The families provided an elegant way to study surface aging processes, the dynamic spread of the family providing its age from the catastrophic disruption or cratering impact of a parent body (e.g., Willman et al., 2008; Vernazza et al., 2009; Spoto et al., 2015).

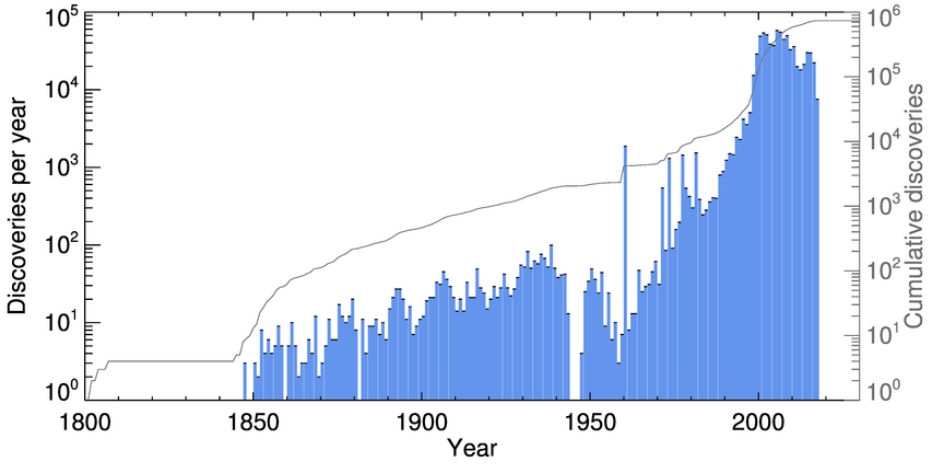

Figure I.2: The number of asteroid discoveries per year since 1801.

The numerical simulations of SSO motion in the solar system were used early on to study the dynamical evolution of the solar system (e.g., Ruzmaikina et al., 1989; Petit et al., 1997; O'Brien et al., 2007), which acme is the framework offered by the Nice model (Gomes et al., 2005; Tsiganis et al., 2005; Morbidelli et al., 2005). Since 2005, the Nice model s have seen significant refinements, including the study of the earliest stages of planetary migration in the gas disk (the Grand Tack, Walsh et al., 2011), an extension of the main belt to Mars (the E-belt, Bottke et al., 2012), the possibility to have accreted and lost a fifth or even a sixth giant planet (Nesvorný and Morbidelli, 2012), and the origin of giant planet irregular satellites (Nesvorný et al., 2007, 2014; Bottke et al., 2010).

I.1.c From colors to surface composition

The first studies of surface composition, by visible colors, showed a great dichotomy in the main belt, with redder objects predominating in the inner belt, while bluer objects were most often found in the outer belt (Fischer, 1941; Wood and Kuiper, 1963; Chapman et al., 1971, 1975). This broad description of asteroid surfaces in terms of blue/red aspect is still used nowadays to describe their reflectance spectra. Following the earliest works, a decade of broad-band filter photometry in the visible lead to a major milestone, with the spectral classification of about 600 asteroids and the description of their distribution in the main belt, setting of the landscape for almost two decades (Gradie and Tedesco, 1982; Gradie et al., 1989).

In the 1980s, the taxonomy of asteroids was refined in a major way, by including the albedo derived from the InfraRed Astronomical Satellite (IRAS) mid-infrared measurements (Zellner et al., 1985; Tedesco

[1]Haven't you heard about the ninth planet? See Batygin and Brown (2016) and Fienga et al. (2016)

et al., 1989; Bell et al., 1989). Yet, the spectral description remained limited to visible wavelengths only, and based on photometry. The availability of 4 m class telescopes offered the collective power to move to low-resolution spectroscopy (resolving power of a few hundreds). By the 1990s, dedicated spectroscopic surveys using consistent observing protocol, standard stars, and data reduction techniques led to a massive sample of hundreds of reflectance spectra of asteroids in the visible (SMASS, SMASSII, S^3OS^2, see Xu et al., 1995; Bus and Binzel, 2002b,a; Lazzaro et al., 2004). The intersection between the albedo determinations from IRAS and those surveys being very small, the albedo was unfortunately no longer used in the emerging taxonomy (Bus and Binzel, 2002a). This mostly impacted the former E, M, and P taxonomic classes, all merged into the X complex of Bus taxonomy. The latest improvement has been a redefinition of the taxonomy, based on a longer wavelength range, including both visible and near-infrared (0.4 to 2.4 μm), in currently used Bus-DeMeo taxonomy (DeMeo et al., 2009a).

In parallel to the efforts to build a large sample in the visible and near-infrared, several authors investigated the region around 3 μm in which hydrated silicates can present very strong absorption bands (e.g., Jones et al., 1990; Sato et al., 1997; Rivkin et al., 2000). However, the much lower solar flux and intrinsic lower reflectance of asteroid surface at these wavelengths, combined with the poor atmospheric transmission precluded large samples to be observed. As such, studies concentrated on Ceres, and some of the largest outer belt and Trojan asteroids (Milliken and Rivkin, 2009; Takir and Emery, 2012; Takir et al., 2015) . From space, attempts of mineralogical characterization were conducted with the Infrared Space Observatory (ISO) and the Spitzer space telescope (e.g., Dotto et al., 2000, 2002; Emery et al., 2006) followed by ground-based observations (e.g. Lim et al., 2005). The difficulty to prepare laboratory samples mimicking the packing of asteroid regolith was however making mineralogical interpretation a challenge (Vernazza et al., 2010). A solution has been recently proposed, in which the samples are diluted in optically transparent material at mid-infrared wavelength to account for the loose packing of asteroid regolith (e.g., KBr, see Vernazza et al., 2012).

The history of KBO taxonomy has been following the same trends, and is currently based in visible and near-infrared colors (Fulchignoni et al., 2008). The faintness of KBOs precluded large spectroscopic survey such as those existing for asteroids. Nevertheless, the surface composition of the largest has been studied with medium to high resolution spectroscopy, and a variety of ices were discovered (e.g., Trujillo et al., 2007; Delsanti et al., 2010).

I.1.d From point-like sources to worlds

Small bodies are... small (physically) and far, hence they are **really** small (angularly). Even the largest, Ceres, only sustains an angular diameter of $\approx 0.6''$ at opposition. To angularly resolve their apparent disk, an angular resolution of at least $0.1''$ is thus required, and for most, an angular resolution at the level of 1 mas is closer to what is needed. To achieve 20 to 100 mas resolution, allowing the study of the few hundred largest asteroids, a 1–2 m telescope in space operating in the visible, or 4+ m ground-based telescopes equipped with Adaptive-optics (AO) systems and observing in the near-infrared are required (operating AO in the visible is not technically feasible yet, due to the very high density of actuators required in the deformable mirror). It was therefore impossible to image asteroids before the advent of the Hubble Space Telescope (HST) and AO in late 1980s (e.g., Saint-Pé et al., 1993b,a; Thomas et al., 1997b). What provided practical observing capabilities were however the 8–10 m class telescopes, such as the W. M. Keck, the Very Large Telescope (VLT), the Gemini, and the Subaru. This started in the 2000s, and I had the chance to participate to this adventure (Chapter III), almost from the beginning.

Nevertheless, astronomers are always creative and impatient and found alternative solutions long before we could directly image asteroids. When an asteroid pass between the Earth and a star, it casts its shadow on Earth. Provided several stations are located on the shadow paths and record the timing of disappearance and reappearance of the star, the silhouette of the asteroid, that is a projection of its 3-D shape on the plane of the sky, can be measured. The first asteroid occultation ever recorded was by (3) Juno in 1953, and since then 3224 have been recorded (Dunham et al., 2017). If occultations were a simple way to measure the overall dimension, the formalism to determine spin and ellipsoid shape from occultations was derived in the 1980s (Drummond and Cocke, 1989; Magnusson et al., 1989).

Because we cannot choose when or where our favorite target asteroid will occult a bright star, determination of asteroid diameters with this technique was backed-up with radiometry, i.e., photometry

in the thermal infrared. These measurements provide the diameter of an asteroid, as the flux follows a black-body distribution at the temperature of the surface, in equilibrium with the incoming sunlight. Radiometry started over four decades ago (e.g., Morrison, 1974) and the recent National Aeronautics and Space Administration (NASA) Wide-field Infrared Survey Explorer (WISE) mission brought it to its acme, with the determination of the diameter of over 150,000 asteroids (Masiero et al., 2011, 2012; Grav et al., 2011, 2012; Grav et al., 2012; Mainzer et al., 2011, 2012, 2014; Bauer et al., 2013).

In parallel with these studies of asteroid dimensions, lightcurves were gathered. Indeed, the temporal variations of an asteroid magnitude are due to changes in its projected area on the plane of the sky. Hence, by acquiring lightcurves, one get easily access to its rotation period, and indirectly to the spin-vector coordinates and 3-D shape, although the last two points require multiple lightcurves over a wide range of Sun-target-observer geometries. Study of asteroid rotation started early (e.g., Gehrels, 1967; Schober, 1981) and ellipsoidal shapes derived in the 1980s (Cellino et al., 1989), but the complete mathematical arsenal to determine period, spin, and convex 3-D shape only appeared in the early 2000s (Kaasalainen and Torppa, 2001; Kaasalainen et al., 2001, 2002a), with an amazing success: the number of known shapes sky-rocketed in a couple of years for virtually zero to about a hundred (Kaasalainen et al., 2002b; Torppa et al., 2003). Over the last decade, this sample grew slowly, up to about a thousand, mostly thanks to the use of photometry sparse in time (with measurements separated by more than a rotation period) and the constant dedication of amateur astronomers (e.g., Kaasalainen, 2004; Ďurech et al., 2009; Hanuš et al., 2016). The possibility to combine lightcurves and stellar occultations overcame the major limitation of the lightcurve inversion approach of Kaasalainen and Torppa (2001): the lack of dimension of the shape models (Ďurech et al., 2009).

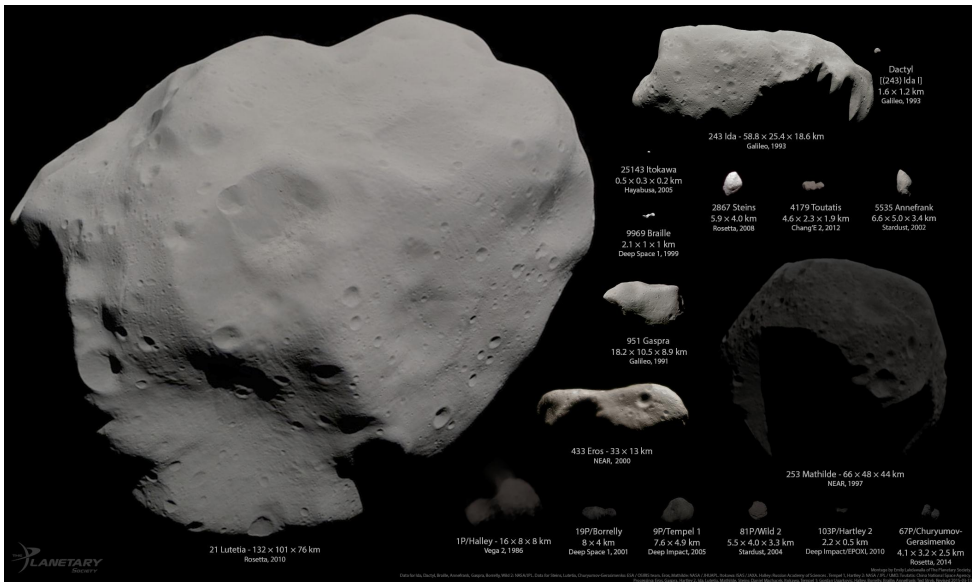

Figure I.3: Illustration of the diversity of size, shape, albedo of asteroids and comets visited by space missions, to scale. Only Ceres, Vesta, and Pluto are missing from the montage. Credits: E. Lakdawalla (The Planetary Society)

Yet, the real breakthrough was the flyby and orbit of asteroids by space missions. The details of the surfaces, shape, cratering totally changed our conception of asteroids, from their internal structure, to surface processes, by revealing a great diversity (Fig. I.3). For instance, when the NASA Galileo space probe encountered the asteroid (243) Ida and discovered its tiny moon Dactil (Chapman, 1996; Chapman et al., 1995), it put an end to a long-running discussion on the existence of satellites of asteroids (Weidenschilling et al., 1989), and opened a new branch of asteroid science (see Chapter III). The discovery by the NASA NEAR Shoemaker mission of craters as large as the asteroid (253) Mathilde were a shock (no pun intended): how could an asteroid survive such acataclysmic events? The presence of large voids, the essence of rubble-pile, were somehow confirmed, and compaction instead of excavation proposed (Housen et al., 1999). When the same mission reached and orbited (433) Eros, it determined its mass,

hence density. Although compatible with the surface material, it also hinted at cracks/voids in the interior (Veverka et al., 2000). It also revealed that asteroids were more active than thought, with regolith motion.

These first encounters were followed by the first sample return, by the Japan Aerospace Exploration Agencya (JAXA) Hayabusa mission from the NEA (25143) イトカワ. This was a major step in mineralogy of asteroids, as it confirmed the link between Ordinary Chondrite (OC) meteorites and S-type asteroids (Binzel et al., 2001; Nakamura et al., 2011). This (again) put an end to a long-running discussion on the parent bodies of OCs and space weathering processes. Space exploration has that: it sets references for remote sensing studies. Then, the European Space Agency (ESA) mission Rosetta on its way to the 67P hard-to-pronounce Churyumov–Gerasimenko comet encountered asteroids (2867) Šteins and (21) Lutetia, opening the controversial idea of partial differentiation (Elkins-Tanton et al., 2011; Vernazza et al., 2011). Finally, the NASA Dawn and New Horizon missions are currently providing a wealth of data on the dwarf planets Ceres (Chapter II, Russell et al., 2012, 2015, 2016) and Pluto (Stern et al., 2015).

Our understanding of asteroid physical properties has thus dramatically improved over the last two decades. However, the data sets we used, either space mission, lightcurves, or stellar occultations, remained strongly limited in number, and the geometrical and physical properties of asteroids are the least known of all (Fig. I.4).

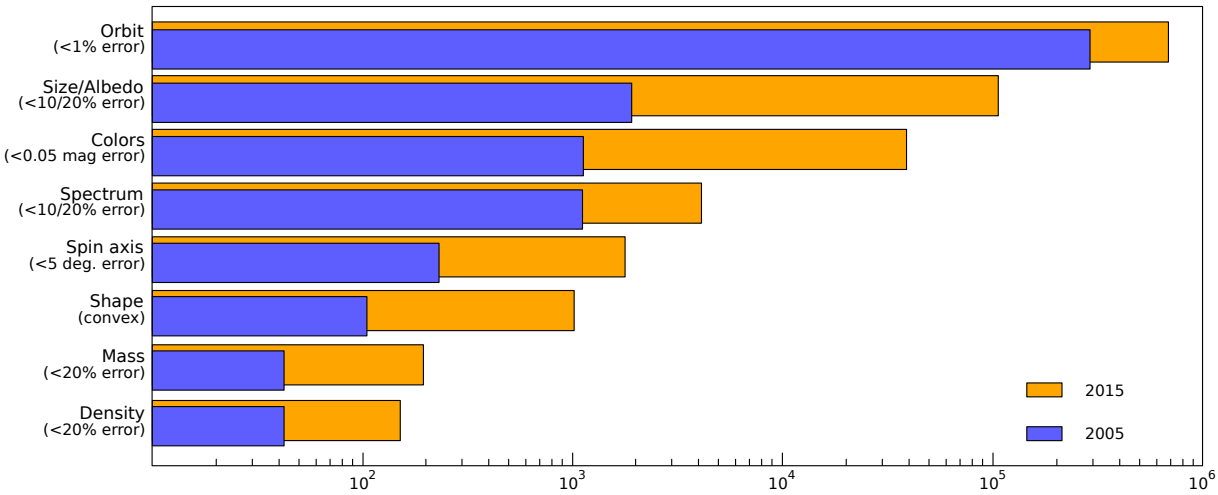

Figure I.4: Order of magnitude estimates of the number of determination of orbit, dimensions, colors, spectra, etc of asteroids. By far, we know much less on their physical properties (multiplicity, shape, orientation), than gross surface properties or dynamical properties. CREDITS: M. Marsset & B. Carry

I.2 In-a-Gadda-da-Data

An improved capability of observation has always led to major advance in astrophysics. We can think for instance of the refractor, used by Galileo, which led to the discovery of Jupiter satellites or lunar craters. Without the set of very accurate instruments at Uraniborg, Tycho Brahe would never had derived his stellar catalog. Or the telescope, reflecting instead of refracting light, proposed by Newton, which allowed to build large instruments. More recently, the photographic plates were the game changer of the XIX century. This is how ~~(1164)~~ (134340) Pluto was discovered, and how Charlois discovered 99 asteroids (or even 100 if we include Eros that he spot on the same night as Witt) when only 500 were known! Even closer, electronic detectors have again changed the game. Discovery rate exploded when the CCDs became installed at the telescopes (Fig. I.2), colors and lightcurves followed, even more when amateur astronomers could afford them. Only electronic detectors could open other wavelength ranges than the visible, such as the near-infrared and the wealth of diagnostic features for ices, or the mid-infrared for radiometry.

It is obvious that technology development played a major role in getting more data. This wealth of data is crucial for SSOs: we can think about Kirkwood's gaps, or dynamical families, or colors and

taxonomy. Minor classes and small scale details can be studied thoroughly with big data sets only. These developments led to the design of major sky surveys, covering large fraction of the celestial sphere: 2-, 3-, and even 4-π steradians. These surveys have each a different main goal, from mapping of the Milky Way (e.g., Gaia), the distant universe (e.g., Sloan Digital Sky Survey (SDSS), Euclid), or exoplanets (e.g., SuperWASP, Kepler) to give recent examples. Yet, they all share a common issue: some vermins lay streaks on their images. This is how we had our most recent change of pace in the observation of small bodies: with near-infrared colors for several thousands of asteroids in the Two Micron All-Sky Survey (2MASS) (Sykes et al., 2000) recently pushed up to 40,000 with the VISTA Hermisphere Survey (VHS) (Popescu et al., 2016), visible colors for almost half a million[2] of asteroid with the SDSS (e.g., Ivezić et al., 2001), and about 150,000 albedo and diameters of asteroids with WISE (e.g., Masiero et al., 2011).

In few cases, the team/consortium running a survey releases catalogs of SSO sightings. This was the case for SDSS for instance, and it may be the best way to take full advantage of the survey capabilities. But this is unfortunately seldom the case. Any asteroid data from Visible and Infrared Survey Telescope for Astronomy (VISTA), or Kepler, SuperWASP, *etc* must be dug from archives usually not moving-object-friendly. If asteroid observations could be easily extracted from the archives of large facilities such as VLT Survey Telescope (VST), Dark Energy Survey (DES), or VISTA, the sample of asteroid with known taxonomy would dramatically improve. For lightcurves, SuperWASP, K2, and the upcoming PLAnetary Transits and Oscillations of stars (PLATO), or Transiting Exoplanet Survey Satellite (TESS) could totally change the landscape. We expect a revolution, almost as important as photographic plate or CCD, in a near future, with the release of Gaia data for SSOs, quickly followed by the Large Synoptic Survey Telescope (LSST) and Euclid (Chapter V).

This is why it is such a Golden Age for Solar System study: we have the technology to fly to our targets (planets, satellites, or minor bodies) and set stringent references for numerous studies, based on robust statistics coming from observations by large surveys.

I.3 My own trajectory in the search for space

I really feel extremely lucky to work on small bodies, at that stage of their study. We have seen a tremendous increase of sample size over the last two decades, the computing power has allowed major steps forward in explaining planet formation and planetary system evolutions. We even have the resolving power to image small bodies from the Earth! But next decade promises even more. Millions of asteroids and tens of thousands of NEAs, KBOs, comets with the LSST. Extremely accurate orbits with Gaia, a stellar catalog unbelievably precise in astrometry and photometry, complete to V$\sim$20.7. Wow!

My own trajectory, since my first step in planetary science in 2005 during an internship at European Southern Observatory (ESO) Chile, has somehow followed the same path as the history of SSOs study: from the study of a couple of objects (Chapter II), to a larger sample (Chapter III), including new populations (KBOs in Chapter IV, and NEAs and Mars-crosser Asteroids (MCAs) in Chapter V). It is quite logical: we need a few references to understand the whole. From scratch to a vast understanding. From zero to infinity. We need some tangible solid rock to build on, both as single researcher and as a community.

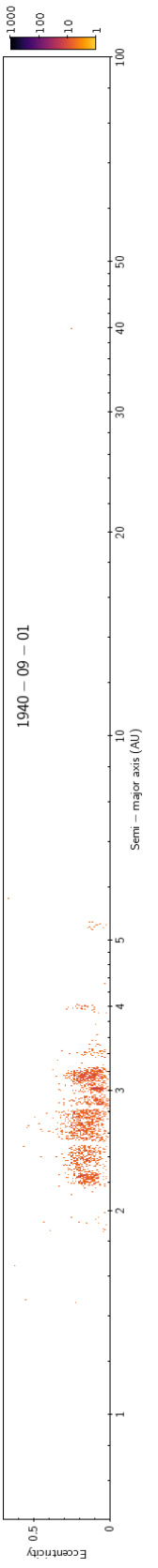

[2] 470,000 moving objects were detected in SDSS images, of which only 250,000 were identified and corresponded to 100,000 unique asteroids

Chapter II

Ceres and Vesta, targets of the NASA Dawn mission

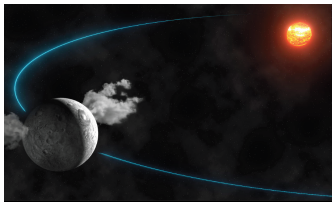

The two largest asteroids in the main belt have been among the first asteroids I studied, being large enough for disk-resolved studies, and being targets of the NASA Dawn mission. They represent the last remnants of the growing embryos that formed the terrestrial planets. Using (1) Ceres as an example, I present the high-angular resolution imaging observations, and how we can use them to the constrain asteroid physical properties (II.1). To obtain both spectral and spatial information, integral-field spectroscopy can be used, and I illustrate its use to determine the variability of surface composition of both (1) Ceres and (4) Vesta (II.2). Finally, I present our quest for water at Ceres, and its implications on the presence of water in the inner solar system. (II.3).

Contents

II.1 Physical properties and first near-infrared mapping of Ceres

The ~~planet~~ ~~asteroid~~ dwarf-planet (1) Ceres is, apart from the first asteroid[1] to have been discovered, the most massive body between Mars and Jupiter. Ceres sticks out of the swarm of minor planets. It is twice as large as the second largest asteroids, Pallas and Vesta, with a diameter of almost 1000 km. It represents roughly a forth of the total mass of the main belt (Carry, 2012; Kuchynka and Folkner, 2013), and yet, its composition remained largely unknown, with the noticeable exception of reports on the potential presence of water ice at its surface (e.g., Lebofsky, 1978). Let's have a closer look!

II.1.a High-angular resolution imaging

The visible and near-infrared spectrum of Ceres was not presenting much contrast, nor identified absorption bands, with the exception of the 3 μm region (e.g., Feierberg et al., 1980; King et al., 1992; Vernazza et al., 2005). At the same time, its optical lightcurve, presenting a single minimum and maximum was linked to albedo variation at its surface rather than to its shape. The idea thus emerged that by looking at its resolved apparent disk, one could get access to patches of identified minerals.

Given its angular diameter of about 0.6″ at opposition, only space-born telescopes or large ground-based facilities equipped with AO can provide the angular resolution required to image its disk. This of course applies to all the minor bodies of the solar system. The state of the art in high angular resolution imaging of asteroids before I started in the field can be summarized as HST imaging of the largest asteroids (Ceres and Vesta, see Thomas et al., 1997a, 2005) and of multiple systems (Storrs et al., 1999, 2005), some early AO experiment by Saint-Pé et al. (1993b,a), extensive multiplicity searches (e.g., Merline et al., 1999, 2002; Marchis et al., 2005, 2006), and a few studies of the triaxial shape of asteroids (e.g., Drummond et al., 1998; Conrad et al., 2007).

The pressure factor on large telescopes was of course a limitation for AO imaging of asteroids, but mostly, it is tough to achieve. Asteroids present apparent disks which angular size is close to the diffraction limit of even the largest telescopes on Earth or in space. Even with AO support, or from the HST, the images still require huge post-processing efforts to either measure the size and shape of the asteroid, or to identify a small satellite in its close vicinity.

I have dedicated a significant fraction of my time as a researcher to build a suite of tools to handle images from AO observations. I refer to my PhD (Carry, 2009) for a description of the basic data reduction steps. The key ingredients for studying asteroids are then:

- the measure of the 2-D profile of a target from its deconvolved image, which triggered the development of the multidata shape inversion algorithm Knitted Occultations, Adaptive-optics, and Lightcurve Analysis (KOALA) with Mikko Kaasalainen (Chapter III);
- the projection of images onto a 3-D shape model to map a surface (Sections II.1.b and II.2); and
- the subtraction of the diffuse halo around a target to search for satellites (Section III.2).

II.1.b The surface, spin-axis, size, and shape of Ceres

When 10 m class telescopes became available, my former PhD supervisor C. Dumas got telescope time on the W. M. Keck to image (1) Ceres, soon after the selection of the NASA Dawn mission (2002). I think this is the best imaging data set on an asteroid ever (Fig. II.1). I was very lucky to inherit it to start my career. I will not describe the data processing, this information is available in Carry et al. (2008), provided in the Appendix B.1.a. I only focus here on a few results.

The spin-axis coordinates I derived implied a very low obliquity (about 4°). The seasonal variations on Ceres should thus be tied with its heliocentric distance, which ranges from 2.55 to 2.98 AU, and not with the direction of its spin-axis. This was going against A'Hearn and Feldman (1992) who explained a detection, followed by a non-detection, of water vapor around Ceres, based on seasons being different in the northern and southern hemisphere of Ceres. I will come back to the detection of water vapor at Ceres later (Section II.3).

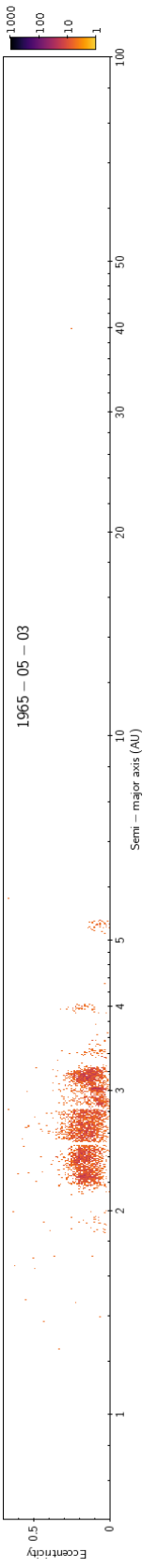

[1] nevermind

The shape of Ceres seemed well-approximated by an oblate spheroid. This was expected from its optical lightcurve and had been already determined from HST imaging (Thomas et al., 2005). The dimensions I derived were nevertheless in clear disagreement with those from Thomas et al. (2005). This had strong implications of the potential differentiation of Ceres (e.g., Zolotov, 2009). This started an argument with the team behind these observations, which encompassed not only Ceres, but also (2) Pallas that I studied after (Chapter III). Because this argument against AO studies of asteroids regularly popped out during years, I steered a revision of my original study, by compiling a decade of AO images of Ceres. We published our results in Drummond et al. (2014). With the additional publication of the dimensions of Ceres from in-orbit Dawn imaging by Russell et al. (2016), the conclusion is clear (Table II.1): the method I have developed to analyze AO images is solid and provide accurate measurements.

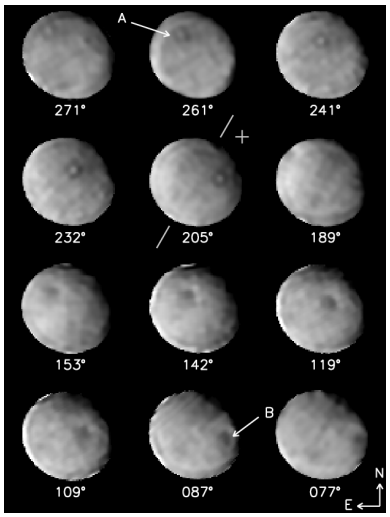

Figure II.1: Images of Ceres obtained at Keck from Carry et al. (2008).

Table II.1: Spin-vector coordinates (R.A., Dec.) and triaxial radii ($a > b > c$) of Ceres.

Ref.	R.A. (°)	Dec. (°)	a (km)	b (km)	c (km)	D (km)
1	291 ± 5	59 ± 5	487.3 ± 1.8	487.3 ± 1.8	454.7 ± 1.6	475.9 ± 3.0
2	288 ± 5	66 ± 5	479.7 ± 2.3	479.7 ± 2.3	444.4 ± 2.1	467.3 ± 3.9
3	287 ± 3	64 ± 3	483.5 ± 5.0	483.5 ± 5.0	446.0 ± 5.0	467.3 ± 8.7
4	291.42 ± 0.01	66.76 ± 0.02	483.1 ± 0.2	481.0 ± 0.2	445.3 ± 0.2	469.7 ± 0.2

References: 1: Thomas et al. (2005), 2: Carry et al. (2008), 3: Drummond et al. (2014), and 4: Russell et al. (2016).

Using the spin-vector coordinates and shape model of Ceres (an oblate spheroid), I mapped the images onto its surface, looking for patches with characteristic colors. The maps I derived with the near-infrared J, H, and K band filters revealed a wealth of structures, at both large and small scales, and confirmed similar work in the visible (Li et al., 2006). However, the interpretation was limited by the broad wavelength interval sampled by each filter. Were these features craters? Basins? Places with different surface composition or regolith properties? This high-angular resolution mapping showed the way, the next move was to obtain disk-resolved spectroscopy.

II.2 First disk-resolved spectroscopy of (1) Ceres and (4) Vesta

My early work on the surface of Ceres motivated the acquisition of disk-resolved spectra. This nicely followed the technological developments, with the availability of AO-fed Integral-Field Unit (IFU) spectrographs on large telescopes after 2005.

II.2.a Ménage à trois: Spectroscopy, integral field, and adaptive optics

I quickly mentioned in previous section the fact that AO observations of asteroids are complex, but when trying to sum the advantages of AO imaging and spectroscopy in an IFU, you eventually multiply their complexity. An IFU spectrometer such as Spectrograph for INtegral Field Observations in the Near Infrared (SINFONI) at the ESO VLT is equipped with an image slicer, which splits the incoming field of view, sends it to a diffraction grating, and the spectra are folded again, and recorded on the detector. The spectro-image cube is reconstructed a posteriori, based on extensive field distortion and wavelength reference data acquired as day-time calibrations.

The observations of Vesta were the very first on any asteroid, being acquired during the Science Verification phase of SINFONI. As a result the calibration plan was not fully defined, resulting in a data reduction nightmare. I conducted the observation of Ceres during my PhD at ESO, as part of a larger program aiming at understanding the composition and volatile content of Ceres (Section II.3).

II.2.b On the surface of (1) Ceres and (4) Vesta

The results of the IFU observations of (1) Ceres and (4) Vesta were presented in Carry et al. (2010c) and Carry et al. (2012c), and I only provide a short summary here below.

The surface of Ceres presented in Fig. II.2 is amazingly homogeneous! Given the wealth of albedo features discovered in both the visible (Li et al., 2006) and the near infrared (Carry et al., 2008), some spectral contrast was expected. The observation had been taken under spectacular observing conditions (the stars did not twinkle below an airmass of about 2!), and SINFONI AO module provided a very good strehl ratio, hence a spatial resolution of only 75 km at Ceres surface. The high Signal to Noise Ratio (SNR) of the spectra allowed to set a stringent upper limit of 1% to any absorption band in the ranges 1.17–1.32 μm and 1.45–2.35 μm. This implies that if patches of different compositions were present, they should be very limited in area. This is indeed what NASA Dawn reported (de Sanctis et al., 2015, 2016; Combe et al., 2016; Ammannito et al., 2016)

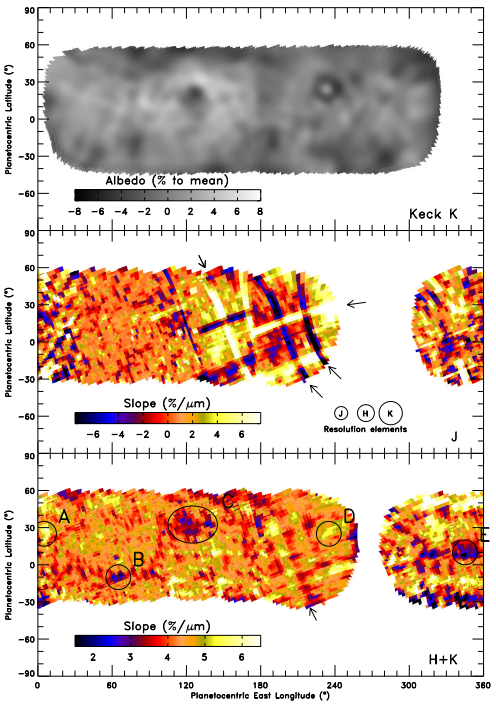

Figure II.2: **Top**: Albedo map from Keck (II.1.b). **Middle**: Spectral slope in J band. **Bottem**: Spectral slope in H+K band. Arrows indicate probable artifacts, and five major features are labeled A to E. CREDITS: Carry et al. (2012c)

The case of Vesta was simply the opposite: the observing conditions were poor, resulting in a spatial resolution close to an entire hemisphere, i.e., barely better than with disk-integrated slit spectroscopy, and yet, we detected strong variations across the surface. This surface heterogeneity had been known for years from disk-integrated rotation-resolved spectra (e.g., Gaffey, 1997; Vernazza et al., 2005). Our main result was an apparent anti-correlation between the near-infrared spectral slope, measured on SINFONI data, and the optical albedo, obtained from HST observations (Binzel et al., 1997). Such an anti-correlation was expected (as predicted by Vernazza et al., 2006) on pyroxenes, olivines, or olivines/pyroxenes mixtures (typical of Q-, S-, A-, and V-types asteroids) under the bombardment of solar wind ions, called *space weathering* (Chapman, 2004; Strazzulla et al., 2005; Brunetto et al., 2006; Fulvio et al., 2012). The observable effect of space weathering on the visible and near-infrared spectrum of such compositions is an overall reddening and darkening, i.e., an increase of the spectral slope combined with a decrease of the visual albedo.

However, the very high spatial resolution observations of Vesta conducted by the NASA Dawn mission did not confirm this preliminary result. The question of the non-weathered surface of Vesta hence remained un-answered. Indeed, most *Vestoids*, the members of its dynamical family originating from a large impact a Gyr ago (Binzel and Xu, 1993; Thomas et al., 1997a) present clear signs of space weathering (Carry et al., 2010c) while Vesta does not.

II.3 Detection of water vapor at (1) Ceres

Ceres and Vesta are the two brightest asteroids as seen from the Earth. As such, they have been the targets of most "first studies", (including my own IFU observations presented here above, Section II.2).

Vesta was the first asteroid linked with a meteorite (McCord et al., 1970), while Ceres composition remained elusive. The first absorption band reported at Ceres attracted much attention, however, as Lebofsky (1978) attributed it to hydration products.

Presence of a polar water ice cap was even suggested by A'Hearn and Feldman (1992) after their (marginal) detection of the OH radical, product of the photo-dissociation of H_2O, at one of Ceres poles with the NASA/ESA International Ultraviolet Explorer (IUE) telescope. The presence of water at the surface was however challenged, the 3 μm band being alternatively interpreted as a signature of water ice, or hydrated minerals only (e.g., Feierberg et al., 1980; King et al., 1992; Vernazza et al., 2005). The keystone being that the report by A'Hearn and Feldman (1992) had not been confirmed nor revoked.

II.3.a Non-detection of OH with UVES at ESO VLT

This was the starting point to our program at ESO VLT to a) search for ice-rich patches with SINFONI (Section II.2, Carry et al., 2012c) and b) search for OH signature with the Ultraviolet and Visual Echelle Spectrograph (UVES). The main difficulty was of course sensitivity. Even if we were using an 8 m telescope compared to the 45 cm aperture of IUE, the atmosphere contains water vapor[citation needed], which can also be photo-dissociated. The Earth atmosphere hence produces its own OH spectral signature.

We thus went through a carefully planning of observations, aiming at time windows where Ceres would be bright enough, and with a radial velocity to shift intrinsic OH lines from the O lines from Earth atmosphere. While computing ephemerides for the team I somehow got the vocation for support, which later motivated me for the Corps National des Astronomes et Physiciens (CNAP), which I luckily joined in 2012.

After several delays from the original plan, the observations were carried out in 2007 and 2009, and after an extensive analysis to assess the detection limit (which resulted ten times more sensitive than that of A'Hearn and Feldman, 1992), we put a stringent limit on the amount of water vapor around Ceres (Rousselot et al., 2011).

II.3.b H_2O detection from space with ESA Herschel

A couple of years later, while Research Fellow at the European Space Astronomy Center (ESAC) of the ESA, we had the opportunity to use the ESA space telescope Herschel to attempt (yes, again) the detection of water around Ceres. There were two main motivations for this:

a. From space with Herschel observing in the far infrared, we could directly search for H_2O instead of its product OH, and

b. The (delayed) UVES observations had been taken further from the Sun than those by A'Hearn and Feldman (1992).

If Ceres had an activity driven by sublimation, like comets, its heliocentric distance was expected to be the trigger of the activity. Observations close to perihelion were thus still required.

After a non detection in November 2011, we had a positive detection in October 2012. But the water was surprisingly seen in absorption, meaning it was not extended, and its displayed an unexpected strong polarization. To discard instrumental effects on what could be a major report, we immediately requested additional Directory Discretionary Time (DDT) observations. Those were carried out a week later, and confirmed the first detection.

The depth of the absorption band was, however, clearly presenting variability on short timescales. Using the Virtual Observatory (VO) tool `Miriade`[2] (Berthier et al., 2009) to predict which albedo markings (Carry et al., 2008) were visible during the Herschel observations, we managed to localized the source of the water vapor: a round-shaped feature (feature D in Fig. II.2, now called Occator). Our observations thus set a final point to a 20-years-long discussion on the water regime of Ceres by showing the presence of geyser-like emission at its surface, close to perihelion (Fig. II.3, and Küppers et al., 2014, available in Appendix B.5.c). Hence Ceres should formally have a cometary designation like Dr. 133P/Elst–Pizarro and Mr. (7968) Elst–Pizarro.

[2] http://vo.imcce.fr/webservices/miriade/

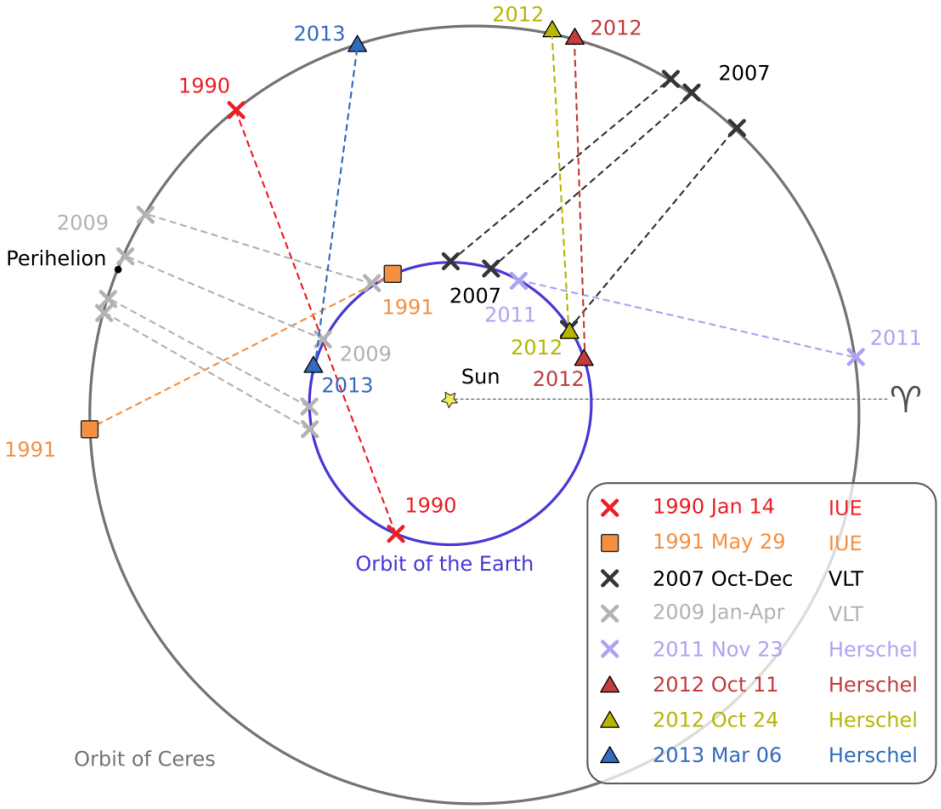

Figure II.3: Schematic view of the relative positions of the Earth and Ceres during the detections (square and triangles) and non-detections (crosses) of water vapor or its photo-dissociation product OH.

The presence and stability over the age of the solar system of water well within the ice line was challenging the early idea that the asteroid belt was dry. Other reports have confirmed this view, such as the active asteroids (Hsieh and Jewitt, 2006; Jewitt et al., 2015), and water ice on Themis (Campins et al., 2010) and Cybele (Licandro et al., 2011). This opened a new door to the question of the origin of Earth's water. Indeed, studies of the deuterium to hydrogen ratio (D/H) in comets provided a puzzling view, in which both Oort cloud comets and Jupiter-family comets were found enhanced in Deuterium compared to Earth oceans (Bockelée-Morvan et al., 2015; Altwegg et al., 2015), while some Carbonaceous Chondrites (CCs) matched. The detection of water at present days in the main belt offered an alternative to comet for water delivery, as well as a new paradigm on the presence of volatiles in the solar system as a whole.

Chapter III

Physical properties of asteroids: 3-D shape, multiplicity & density

The physical properties are the least known of all SSO properties (Fig. I.4). The subject of my PhD was to study them taking advantage of large ground-based telescopes equipped with AO cameras. Since my PhD, I have diversified the observing techniques, which led to the development of a multi-data inversion technique and the study of many objects (III.1). In parallel, I started the study of binary systems to determine their mass (III.2), and produced an extensive statistical study of the density of small bodies (III.3).

Contents

III.1 Occultations, Adaptive-optics & Lightcurves Analysis

The physical properties are the least known of all SSO properties (Fig. I.4). The subject of my PhD was to study them taking advantage of large ground-based telescopes equipped with AO cameras.

III.1.a From genesis to revelation

Optical lightcurves had been used for decades to study the rotation period of asteroids (e.g., Schober, 1981), their spin coordinates (e.g., Lagerkvist et al., 1995), and overall shape (Cellino et al., 1989). A comprehensive and robust method had even been developed in the early 2000s to determine the 3-D shape of asteroid with lightcurves (Kaasalainen and Torppa, 2001; Kaasalainen et al., 2001). In parallel, stellar occultations had also been used to estimate the diameter of asteroids (Wasserman et al., 1979), and even their tri-axial shape in the case of multiple recorded events (Drummond and Cocke, 1989).

These data were publicly available for many objects, and potentially easy to obtain for many more, calling for a algorithm capable of taking them into account with the disk-resolved images from AO cameras. Kaasalainen and Lamberg (2006) had recently shown how to combine disk-resolved and disk-integrated data, so I contacted Mikko Kaasalainen. Using the 2-D profiles I was extracting from the AO images, he quickly designed what we promoted as the Knitted Occultations, Adaptive-optics, and Lightcurve Analysis (KOALA) inversion technique (Carry et al., 2010a; Kaasalainen, 2011).

From the original code by Mikko, Josef Ďurech and I produced a version taking properly into account the geometry of stellar occultations. Joined by Marco Delbò, we then started a version using mid-infrared photometry to constrain the surface properties (Ďurech et al., 2012, 2017), which proved very helpful to determine the spin axis orientation of (162173) Ryugu, the target of the JAXA mission Hayabusa-2 (Müller et al., 2017). The most recent developments have been in the hands of Matti Viikinkoski, and the algorithm, re-dubbed All Data Asteroid Modeling (ADAM), can now uses radar echoes, mid-infrared photometry, AO images, optical lightcurves, and stellar occultations (Viikinkoski et al., 2015a). We recently summarized the landscape of 3-D shape modeling of asteroids in a chapter of the *Asteroids IV* book (Ďurech et al., 2015), reproduced in the Appendix B.1.d.

III.1.b Validation by the ESA Rosetta flyby of (21) Lutetia

A crucial aspect of the development of this new multi-data framework was to assess its reliability. For instance, although the lightcurve inversion by Kaasalainen and Torppa (2001) could only produce *convex* shape models, generally without size determination, the results it produced were useful, being successfully validated both in the lab (Kaasalainen et al., 2005) and on sky (Kaasalainen et al., 2002a). Conversely, because the shape of (25143) イトカワ was clearly different from that predicted by the modeling of radar echoes (Ostro et al., 2005), suspicions raised on that technique; thankfully cleared up after the flyby of Toutatis by Chang'E (Huang et al., 2013). The upcoming flyby of (21) Lutetia by the ESA Rosetta mission on its way to the comet 67P offered the possibility to validate our tool (or to go back to square one).

Using AO disk-resolved images from the ESO VLT NACO camera in 2007 and W. M. Keck NIRC2 in 2008/2009, we determined the sidereal rotation period, spin-vector coordinates, diameter, and 3-D shape of Lutetia (Drummond et al., 2010; Carry et al., 2010b). Owing to unfavorable observing geometry, in which all AO images had been obtained at very high sub-Earth point latitudes (i.e., *pole on*), the dimensions along the rotation axis were loosely constrained. Yet, this solution with KOALA led to thorough discussions before the flyby, as it implied that only one hemisphere would be observed (Carry et al., 2010b).

While Rosetta flew next to (21) Lutetia, I was in Madrid, searching a flat for my soon-to-start Research Fellowship at the ESAC. I was anxiously following ESA broadcast event covering the flyby, when the first images by the OSIRIS camera were released, and they were amazing (Sierks et al., 2011, available in the Appendix B.5.b)! The overall shape seemed similar to what we had predicted. Over the following months, I extensively compared the images taken by OSIRIS with the predictions from the KOALA model, and assessed the reliability and precision of the results (Fig. III.1): the orientation of the spin axis was accurate to two degrees, and the diameter to a couple of percent. More, the local topographic

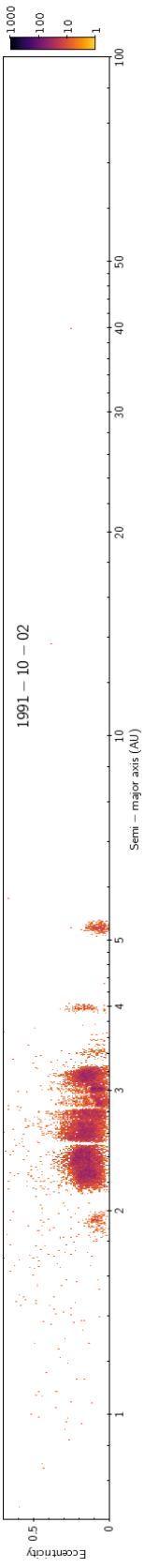

deviations between the KOALA model and the flyby images were of 2 km root mean square (RMS) only (Carry et al., 2012a, available in the Appendix B.1.b).

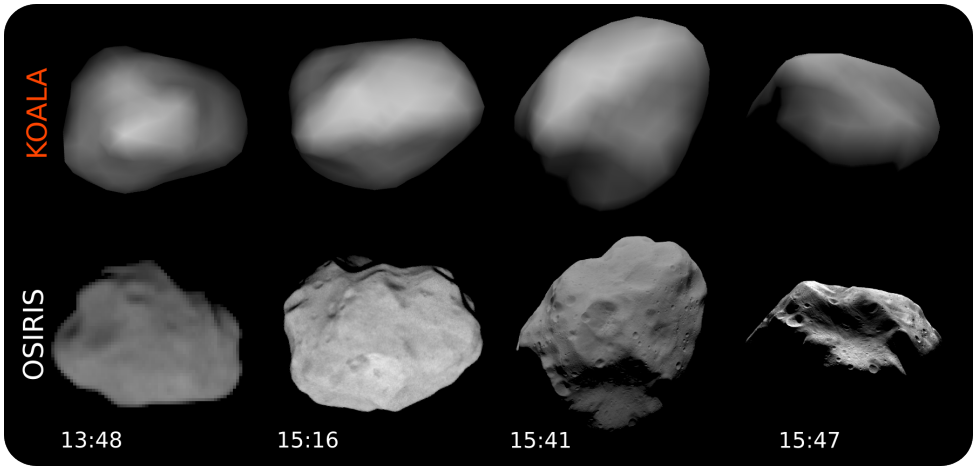

Figure III.1: Comparison of the KOALA pre-flyby shape model of (21) Lutetia (top, Carry et al., 2010b) with the images from the OSIRIS camera on-board ESA Rosetta taken during the fly-by of the asteroid (Sierks et al., 2011), validating the algorithm.

III.1.c 1 (Ceres), 2 (Pallas), 3 (Juno) ... many!

The spacecraft rendezvous with (1) Ceres and (21) Lutetia have demonstrated the validity of the multi-data approach to asteroid 3-D shape modeling, and especially of the reliability of AO images.

Over the last years, I have led and been involved in many studies (Fig. III.2) of asteroids spin and 3-D shape based on the combination of lightcurves, disk-resolved images, and stellar occultations, such as

- (2) Pallas (Carry et al., 2010a), for which KOALA was developed, showing structural differences between Ceres and Pallas, the later being much denser, and irregular.
- (52) Europa (Merline et al., 2013a), revealing the presence of two large flat facets, reminiscent of the large craters seen on (253) Mathilde (Veverka et al., 1997), hinting at a low cohesive strength among its *amigos* C-type asteroids.
- (87) Sylvia (Berthier et al., 2014), showing evidence of a non-homogeneous distribution of mass inside Sylvia, by comparing its dynamical quadrupole J_2 from the orbit of its satellites to that determined from its shape model.
- (3) Juno (Viikinkoski et al., 2015b), including images from the Science Verification programs of both the second generation extreme-AO SPHERE camera, and of the Atacama Large Millimeter/Submillimeter Array (ALMA) interferometer. It illustrated how the resolution of the models could be pushed thanks to the improved angular resolution of the instruments.
- (234) Barbara (Tanga et al., 2015), assessing the non-binarity of this very peculiar object, first reported by Delbo et al. (2009). The "two solid rocks two solid blocks" suspected behavior from interferometry was indeed due to highly irregular shape with large concavities.
- (107) Camilla with my PhD student (Pajuelo et al., 2018a), in which we thoughtfully digged and analyzed 15 years of data from all large ground-based telescopes equipped with AO cameras, revealing the likely presence of ice in its interior.
- (6) Hebe (Marsset et al., 2017, available in Appendix B.1.c), taking advantage of the angular resolution of SPHERE, with data also acquired during its Science Verification program, to map its topography, compute the maximum volume excavated by impacts, and assess the origin of H-type ordinary chondrites.

Figure III.2: Portrait de famille...

- And many more to come, as we are currently running a Large Program (PI Vernazza) at ESO VLT with SPHERE to image 35 asteroids during the next two years. The spectacular angular resolution provided by this camera compared with first-generation AO cameras, and even to space missions in their approach phase (Fig. III.3), will allow to detect and characterize large craters and basins on these bodies.

In the meanwhile, I worked with the amateur community, regularly interacting with amateur astronomers in meetings, encouraging them to observe lightcurves of asteroids, and suggesting targets (Mousis et al., 2014). Taking their observations together with historical lightcurves, we modeled the spin and 3-D shape of several hundred asteroids, allowing to study the strength of the Yarkovsky–O'Keefe–Radzie (YORP) thermal recoil effect from the distribution of spin obliquities (Hanuš et al., 2013), and improve density estimates of asteroids with known masses (Hanuš et al., 2016).

III.2 Is there any binary out there?

For decades, the question "*Do asteroids have satellite?*" remained unanswered (Weidenschilling et al., 1989). Early searches, by direct imaging, stellar occultations, or lightcurves did not provide evidences for them, and suspicion raised on their existance, until the NASA mission Galileo on its way to Jupiter discovered the small satellite Dactyl around (243) Ida (Chapman et al., 1995). Then, the availability of AO camera on ground-based telescopes quickly led to the first discovery from the ground (Merline et al., 1999). Simultaneously, first discoveries occurred by detecting mutual eclipses in optical lightcurves and a secondary echo in radar pulses (Pravec et al., 1997; Margot et al., 2000). As such, the early 2000s were an era rich in discoveries with these techniques. Starting my PhD in 2006, I was lucky to participate to this adventure.

III.2.a Discovery of satellites by adaptive-optics imaging

Since 2006, I actively participated to searches of satellites of asteroids, in a group led by W. Merline (SwRI), using the AO cameras on the Gemini and W. M. Keck telescopes. We were targeting asteroids

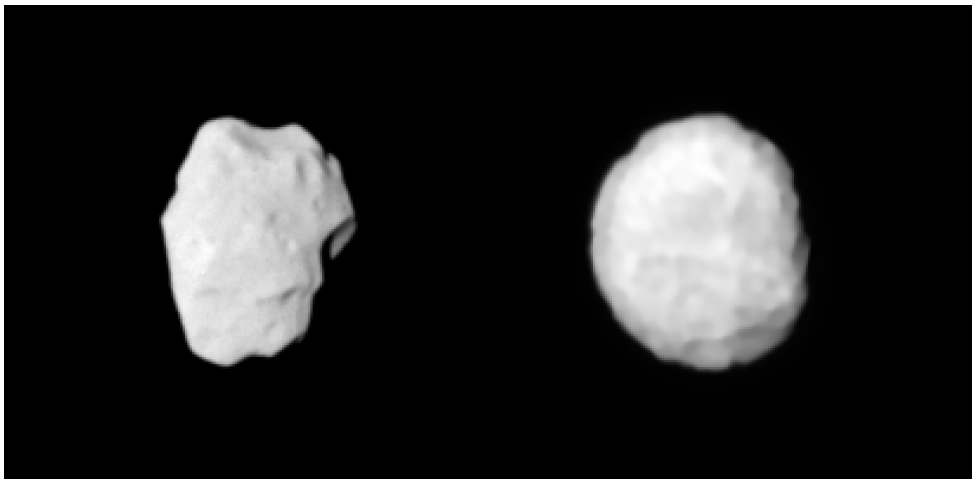

Figure III.3: Asteroids (21) Lutetia (left) imaged by OSIRIS at a distance of 71,000 km and (7) Iris (right) imaged by VLT SPHERE at a distance of 1,346,000 km. The new imaging capacities are opening tremendous prospects.

with suspected binarity from their lightcurves (e.g. Pravec et al., 2006), and large main-belt asteroids. The activities of this group decreased strongly after 2013, but since I was focusing on the density of asteroids (Section III.3 below), I naturally worked at characterizing binary systems. This is how I contributed to the discovery the satellites of

- (41) Daphne, which is likely the binary asteroid system with the most extreme mass ratio (Conrad et al., 2008). The work was reported in my PhD dissertation (Carry, 2009), and has been used by others authors (e.g. Matter et al., 2011; Viikinkoski et al., 2015a), although its hasn't been published yet (waiting for a co-author from *Arles*).
- (107) Camilla (Marsset et al., 2016), on an inner orbit compared with its already known satellite (Storrs et al., 2001; Marchis et al., 2008; Pajuelo et al., 2018a).
- (317) Roxane (yes, a single "n", but don't call the police for that misspelling), which is the first E-type asteroid known to be a binary (Merline et al., 2009).
- (2577) Litva, on a very loosely bound orbit (Merline et al., 2013b), much farther than its already-known first satellite (Pravec et al., 2012).
- (35107) 1991 VH. This corresponds to the first image of a satellite of a NEA (Merline et al., 2008). Indeed, the satellite had already been suspected from optical lightcurves (Pravec et al., 1997).

III.2.b Characterization of binary systems

Once a definitive answer was provided to Weidenschilling's question and we knew that "*Asteroids do have satellites*" (Merline et al., 2002), it instantaneously brought many more questions: What were the mechanisms for their formation? Were they stable over long time scales? How did they evolve? Questions for which a statistical description of their orbital, physical, and surface properties was required.

This is how we studied the near-infrared spectrum of the satellite of (379) Huenna, confirming its spectral similarity with its host asteroid (DeMeo et al., 2011). We recently repeated a similar study, on the satellite of (107) Camilla (Pajuelo et al., 2015, 2018a), and again, the spectra of the two components of the system are similar. This is indeed what has been reported for asteroids (22) Kalliope (Laver et al., 2009), (90) Antiope (Marchis et al., 2011), and (130) Elektra (Yang et al., 2016). The spectral similarity implies similar compositions, and favor a formation mechanism of these small satellites by impact excavation on their large host asteroids, rather than capture (see our review chapter in Asteroids IV: Margot et al., 2015, available in the Appendix B.2.d).

The first binary for which I studied the orbit is (41) Daphne, following its discovery in 2008 by our group (see above). The properties of this system have been described in my PhD dissertation (Carry,

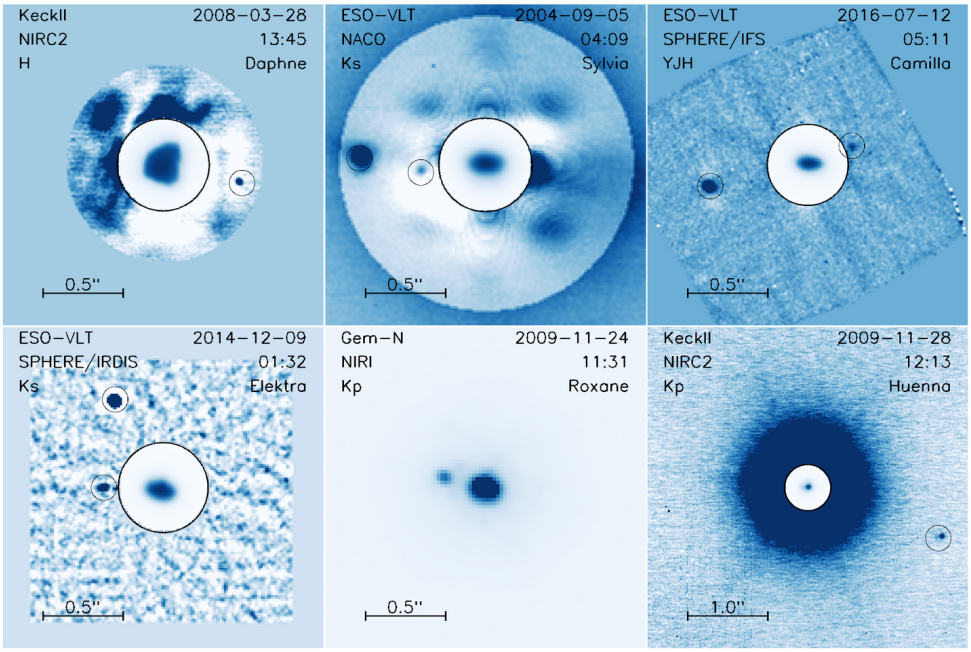

Figure III.4: Examples of AO images of binary asteroids. On each image, the central circle of a diameter of 0.28″ shows the central body, while the external regions have been processed to reveal the satellite (position highlighted by small circles).

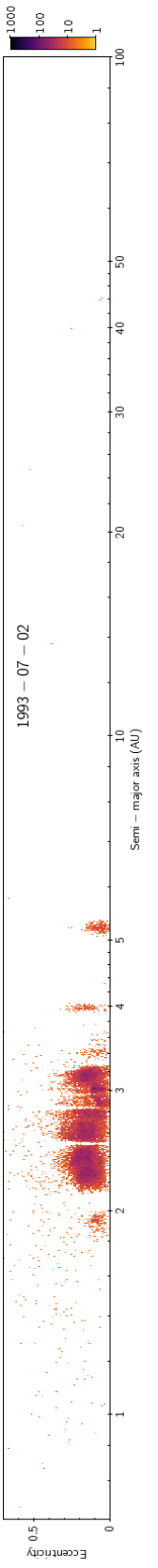

2009), but the publication got stalled (partly because the satellite dodged further observations). The prediction of the occultation of a bright star by (87) Sylvia fortunately provided a new start to my activity on binaries. We determined the orbit of its satellites Romulus and Remus, allowing the prediction of the occultation of the star by Romulus, which was successfully observed, confirming the results of our method and providing a direct measurement of Romulus' size (Berthier et al., 2014, available in the Appendix B.2.a).

Over the years, we analyzed AO images from archives of large ground-based telescope of asteroids (45) Eugenia, (93) Minerva, (107) Camilla, (130) Elektra, (283) Emma, (702) Alauda, and KBOs (90482) Orcus, and (136108) Haumea for the same purpose: predicting the occultation of star by their satellite. Prediction for all these satellites are available through the ephemerides service `Miriade`[1] (Berthier et al., 2009) and we are publishing these orbits in peer-reviewed journals (e.g., Dumas et al., 2011; Carry et al., 2011; Gourgeot et al., 2016; Pajuelo et al., 2018a).

In parallel, with my PhD student Myriam Pajuelo and Mirel Birlan we initiated a survey dedicated to determine the taxonomic class of binary asteroids. Indeed, the current theory of formation of small binary is that they suffer a fission induced by over-critic rotation, which is reached by YORP spin-up (see, e.g., Walsh and Jacobson, 2015). Hence, different cohesion or internal structure would lead to different incidence of binaries among taxonomic classes. We thus acquired SDSS photometry (Section V.1) at Pic du Midi, and near-infrared spectroscopy at the InfraRed Telescope Facility (IRTF). The survey is still on-going, but we already spectrally classified 24 binaries, corresponding roughly to a quarter of those without known taxonomy. There is apparently an over-representation of Q-types among binaries (with respect to S-types), which is naturally explained by the resurfacing events that must following the spin-up fission (Pajuelo et al., 2017, 2018b).

III.2.c Pushing further the angular resolution via interferometry

After the first discoveries of satellites of asteroids in the 2000s via AO and HST imaging, most discoveries were realized by lightcurves and radar echoes. This is due to a significant fraction of *small* asteroids being

[1] http://vo.imcce.fr/webservices/miriade/

binaries ($\approx 15 \pm 3\%$, see Margot et al., 2015), which cannot be angularly resolved by 10 m-class telescopes (see Fig. III.5), compared to the low fraction of large asteroids with satellites (couple of percent).

The properties of these systems have led to the following explanation regarding their formation:

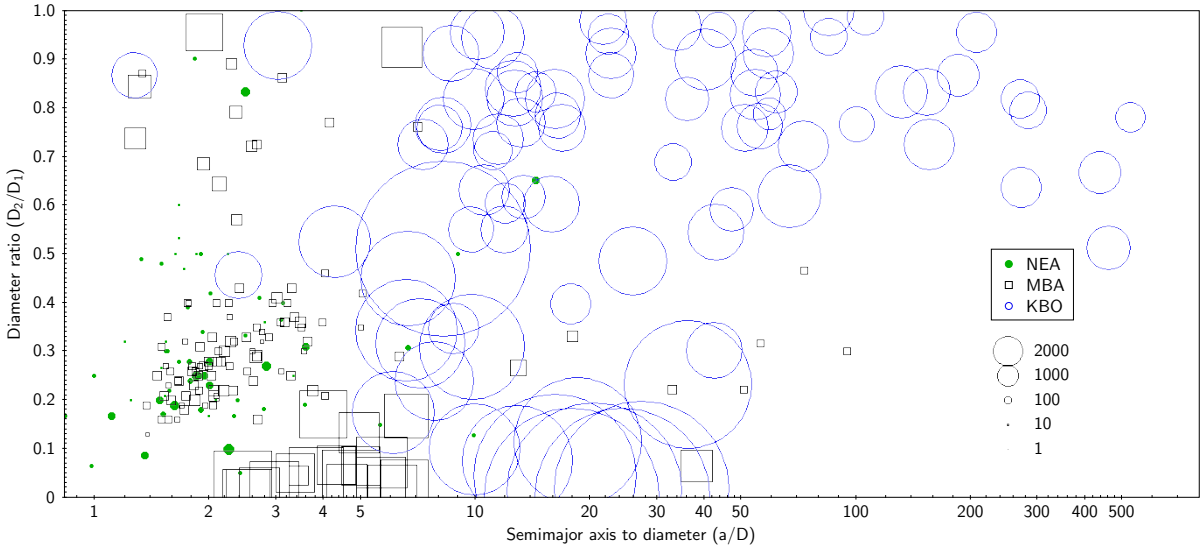

Figure III.5: The great diversity of binary systems among SSOs. Satellites are found around all dynamical classes, from NEAs to MBAs to KBOs, and diameters, from a 100 m to 2500 km, from dramatically different to near-equal size ratios.

large asteroids harboring small satellites are the outcome of violent collisions, excavating material which re-accumulated in orbit (e.g., Durda et al., 2004). The small binary systems, however, form by rotation fission induced by YORP spin-up, and can later on evolve as pairs of asteroids (Walsh et al., 2008; Pravec et al., 2010; Walsh and Jacobson, 2015).

I led a pilot study to use optical interferometry to angularly resolve small binary systems, following the pioneering works by Delbo et al. (2009) and Matter et al. (2011, 2013). The angular resolution of a telescope is at the best limited by the diffraction (but generally limited by the seeing without AO), and can be approximated by λ/D, with λ the wavelength and D the diameter of the aperture. By studying the interference fringes resulting from the combination of the light from two telescopes separated by a distance B (the baseline), the best angular resolution achievable is λ/B and can thus be much higher than the resolution of a single telescope.

We thus conducted a suite of multi-technique observations, including optical lightcurves over many epochs, near-infrared spectroscopy, and interferometry in the thermal infrared (Fig. III.6) to characterize the small main-belt binary asteroid (939) Isberga (Carry et al., 2015, available in the Appendix B.2.c). We performed the interferometric measurements using the VLT MID-infrared Interferometer (MIDI) instrument. If the study was successful and we could determine the surface composition, mutual orbit, size, mass, and density of Isberga, the observations remained extremely challenging, at the edge of current capabilities of optical interferometers. The method we developed is however general, applicable to others suites of instruments, and the ALMA interferometer seems particularly promising.

III.3 Density of small bodies

Following my works on the physical properties of asteroids, I was invited in 2011 to give a talk at a workshop on *Solar System Science before and after Gaia* in Pisa (Carry, 2011). In what should have been a quick attempt to update a figure from the very good work by Consolmagno et al. (2008), I realized that there are things known, and things unknown, and in between are the doors. The meeting in Pisa was my door from 02∞ on asteroid densities.

Searching for mass, volume, and density estimates of minor planets spread in many articles, I built a

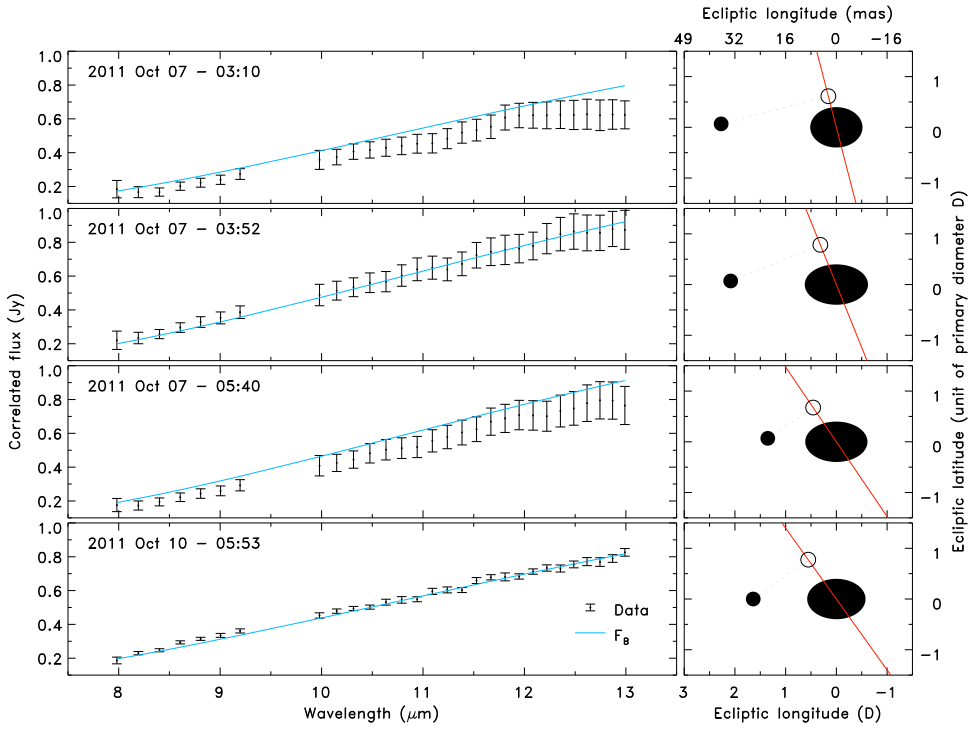

Figure III.6: **Left**: Correlated flux of Isberga observed with MIDI over four epochs. The best-fit solution of binary model (F_B) is also plotted as a solid blue line. **Right**: Corresponding geometry of the system on the plane of the sky. The red line represents the projected VLT interferometer baseline, the black ellipse Isberga, the black disk its satellite, and the black circle the projection of the satellite on the baseline.
CREDITS: Carry et al. (2015)

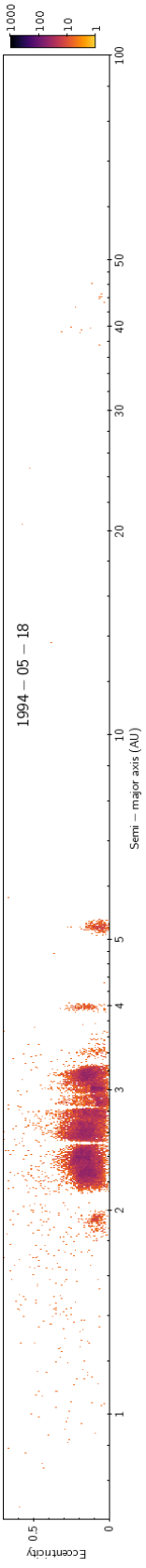

comprehensive catalog for 287 objects (Carry, 2012, available in Appendix B.3.a), jumping an order of magnitude from the 20-ish objects listed by Consolmagno et al. (2008)! This allowed to study the level of accuracy and biases affecting the methods used to determine these quantities. From a strict selection of best-estimates, I determined the average density of each taxonomic class. Furthermore, by comparing these density with that of the most-likely meteorite analogs, I derived the macroporosity (i.e., amount of voids) within these bodies (see also our chapter in *Asteroids IV*, Scheeres et al., 2015, for an update, available in the Appendix B.3.b).

Dwarf-planets apparently have no macroporosity, while smaller bodies (<400 km) can have large voids. This trend is apparently correlated with size: C and S-complex asteroids, and KBOs, tend to have larger density with increasing diameter. S-complex asteroids are more dense on average than those in the C-complex that in turn have a larger macroporosity, although both complexes partly overlap. Within the C-complex asteroids, B-types stand out in albedo, reflectance spectra, and density, indicating a unique composition and structure. Asteroids in the X-complex span a wide range of densities, suggesting that many compositions are included in the complex. Comets and TNOs have high macroporosity and low density, supporting the current models of internal structures made of icy aggregates (Fig. III.7).

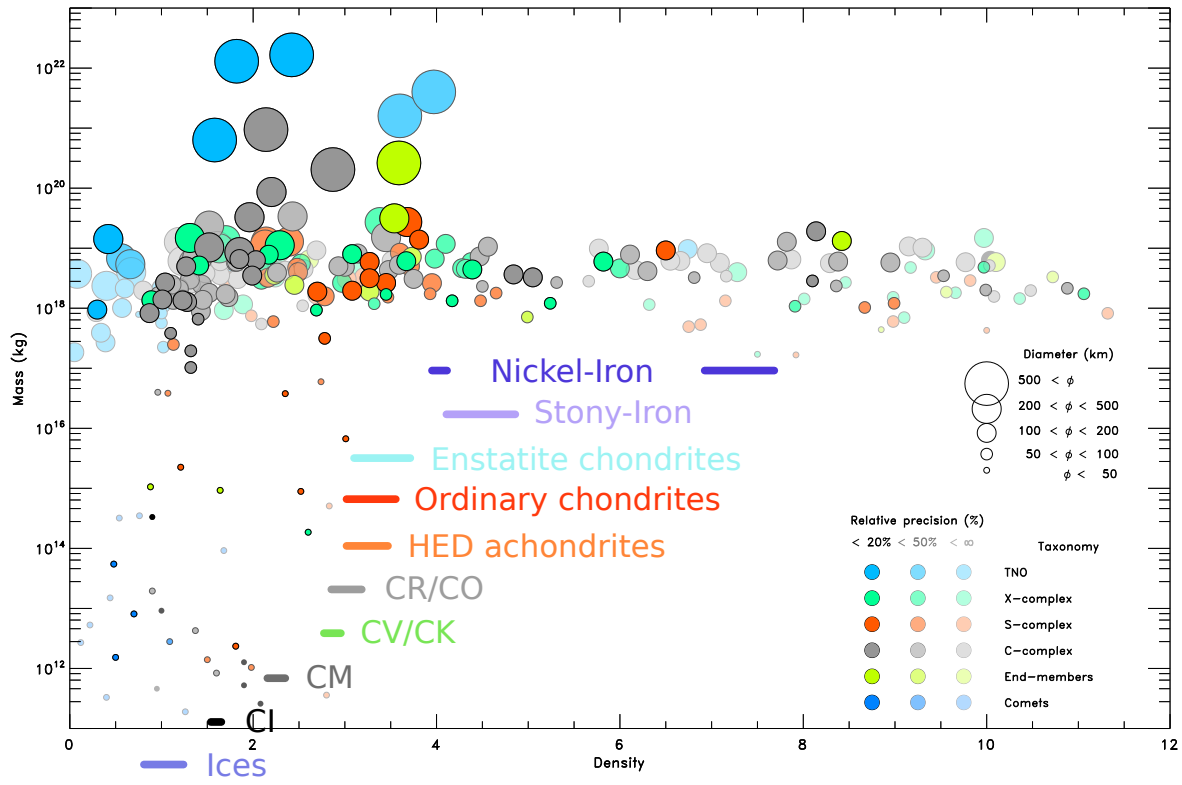

Figure III.7: Density of small bodies according to their mass. Small bodies are divided into six categories: KBOs (light blue), comets (blue), and asteroids (all dynamic class together) divided into four taxonomic groups: S-complex in red, C-complex in grey, X-complex in green, and end-members in yellow. Asteroids which taxonomy is unknown are plotted in black. The size of the symbols is a function of the object diameters, and the three different levels of contrast correspond to three cuts of relative accuracy: <20%, <50%, and regardless to the precision ($< \infty$). The density of the different class of meteorites is also drawn, at arbitrary masses.
CREDITS: Carry (2012)

Chapter IV

The Kuiper Belt
~~2000 light years~~ 30 AU
From Home

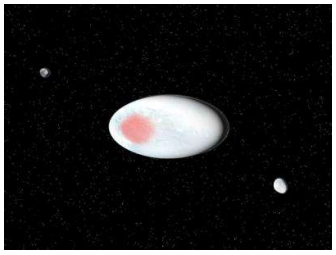

Although my prime targets of interest are the asteroids, their cold cousins the remote KBOs also track of the history of our solar system. Starting from my expertize with AO observations, I participated to several studies of KBO multiple systems (IV.1), including (136108) Haumea, which properties are still puzzling the community, in particular its family, the only one ever detected in the Kuiper Belt (IV.2). Finally, I was also involved in the study of the surface composition of these icy bodies (IV.3), again taking advantage of AO instruments.

Contents

IV.1 Pushing adaptive optics to faint end: Haumea and Orcus

There are many interests in using Adaptive-optics instruments as the improved angular resolution provides more details and a better SNR on the flux measurements. However, AO correction relies on point-like astronomical sources, called Natural Guide Star (NGS), to analyze the wavefront and correct it from the deformations introduced by the atmospheric turbulence. The typical timescale of the atmospheric turbulence is of a couple of milli-seconds only (in the near-infrared in good observing sites), and the analysis of the wavefront corresponds to splitting it in sub-pupil, each equivalent to smaller aperture telescopes, hence the need for bright sources to achieve sufficient SNR in each sub-pupil.

This is why AO, although providing amazing results, is not installed on every instrument: on a 10 m telescope, AO is limited to NGS brighter than V ≈14–15 at most, and V ≈10–13 for extreme AO instruments such as SPHERE (Section III.1.c). The fraction of the celestial sphere accessible to these instruments is therefore limited to a couple of percent only. The upcoming generation of 30+ m telescopes such as the Thirty Meter Telescope (TMT) or European Extremely Large Telescope (ELT) will not change the situation, their sub-pupil for AO wavefront sensing being of similar size as current 10 m telescopes, their potential NGS will be of the same magnitudes.

IV.1.a How can we observe faint targets with adaptive optics?

The question is therefore how could we still use AO even if the scientific target is fainter than V ≈14–15? This question raised in the context of the study of the multiplicity of KBOs, for which the angular resolution must be enhanced from seeing-limited, and of their surface composition, for which a decent SNR was challenging to achieve in spectroscopy.

A solution consists in casting a laser beam from the telescope to excite molecules in the high atmosphere, creating an artificial star usable for AO, called the Laser Guide Star (LGS). A real astronomical source is still required to probe the lowest orders of the atmospheric turbulence, which cannot be probed with the LGS, but the constraints on its magnitude are much relaxed, and these so-called Tip-Tilt Star (TTS) can be as faint as V ≈ 17–17.5 at VLT. A laser facility was installed at VLT in 2005, and I was fortunate to witness its premiere operations, and work on Science Verification data on (136108) Haumea (Section IV.1.b below).

Another solution exploits the fact that moving objects... move! By searching for close encounters on the plane of the sky between a SSO and a bright star, one can take advantage of the bright NGS to observe the close-by SSO. The opposite is also possible: using bright asteroids as NGS for deep sky targets without close-by stars. This solution requires less technology, but it more challenging to perform, in particular owing to the time-critical aspects (Section IV.1.c below).

IV.1.b The strange dwarf-planet (136108) Haumea

The dwarf planet (136 108) Haumea (dubbed Santa upon its discovery during Christmas 2003) is among the largest objects found in the Kuiper Belt (Rabinowitz et al., 2006; Stansberry et al., 2008), together with ~~(1164)~~ Pluto, Eris and Makemake. Since its discovery late 2003 (Santos-Sanz et al., 2005), it attracted a lot of attention, following the discovery of its highly unusual characteristics:

1. It has a very elongated shape (Rabinowitz et al., 2006; Lellouch et al., 2010).
2. It is a fast rotator ($P_{rot} \sim 3.9$ h, Rabinowitz et al., 2006).
3. It has two non-coplanar satellites (Brown et al., 2006; Ragozzine and Brown, 2009).
4. It is the largest member of a dynamical family (Brown et al., 2007; Ragozzine and Brown, 2007), whose velocity dispersion is surprisingly small (Schlichting and Sari, 2009; Leinhardt et al., 2010).
5. Its surface composition is dominated by water ice (Tegler et al., 2007; Trujillo et al., 2007; Merlin et al., 2007; Pinilla-Alonso et al., 2009), yet it has a high density of 2.5-3.3 g cm^{-3} (Rabinowitz et al., 2006), implying there is rock bottom.
6. It surface presents hemispherical colour heterogeneity, with a dark red "spot" on one side (Lacerda et al., 2008; Lacerda, 2009).

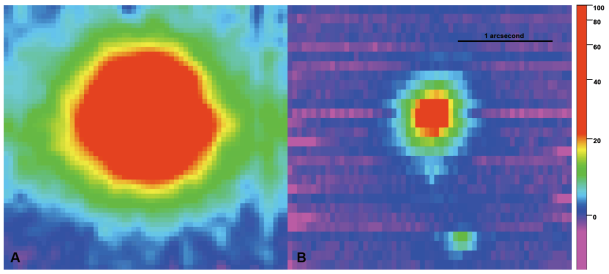

Figure IV.1: Illustration of AO correction with LGS. **Left:** SINFONI reconstructed images of Haumea obtained in seeing-limited observations. **Right:** SINFONI reconstructed images of Haumea obtained with LGS-AO under similar atmospheric conditions. The spatial and intensity (in ADU) scales are similar. The improved contrast and spatial resolution with AO correction makes possible the detection of the two faint satellites. CREDITS: Dumas et al. (2011)

The IFU spectrograph SINFONI, supported by the LGS facility, at VLT offered the possibility to study both the surface composition and the dynamics of this system. Haumea itself was thus used as a TTS during the Science Verification program of the LGS in 2007 illustrating the feasibility of the approach (Fig. IV.1).

Using the astrometry of the satellites already published by Ragozzine and Brown (2009) together with the additional SINFONI epoch, we refined the orbital parameters of the satellites and confirmed the predicted mutual eclipsing events to take place (Fabrycky et al., 2008), confirming the high density of Haumea.

Furthermore, we investigated the amount of heating that tides between Haumea and its satellites could generate. Indeed, the water ice on the surface of Haumea, and also of its large satellite Hi'iaka as we showed (Section IV.3), was in a crystalline form. Because its structure was expected to be broken by solar ions over time, a heat source was required to bring its/their surface(s) to a temperature of at least 80–90 K to crystallize the ice again (Schmitt et al., 1988). We showed that the energy generated by the tides could be responsible for the heating, although only under specific circumstances (Dumas et al., 2011, see the full text in the Appendix B.4.a).

IV.1.c Stars can be useful: (90482) Orcus & Vanth

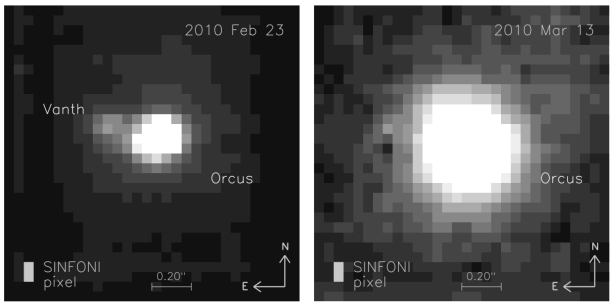

Figure IV.2: Illustration of AO capabilities on faint targets such as (90482) Orcus. **Left**: Using a NGS during a close encounter on the plane of the sky. **Right**: Using the LGS, in a case no TTS is available.
CREDITS: Carry et al. (2011)

Following the success of the first observations of KBOs with LGS, I was involved in a suite of observing programs to image and obtain near-infrared spectra of binary systems (Hestroffer and VLT/TNB Team, 2010). The observations mainly followed the protocol used for Haumea described above, but we also actively searched for close encounters between KBOs and bright stars (V ≈10–13).

On 2010 February 23 UT, (90482) Orcus had a particularly favorable encounter with the star UCAC2 29643541 (R = 11.6) at an angular separation of only 4″. The AO thus used the star as NGS and worked

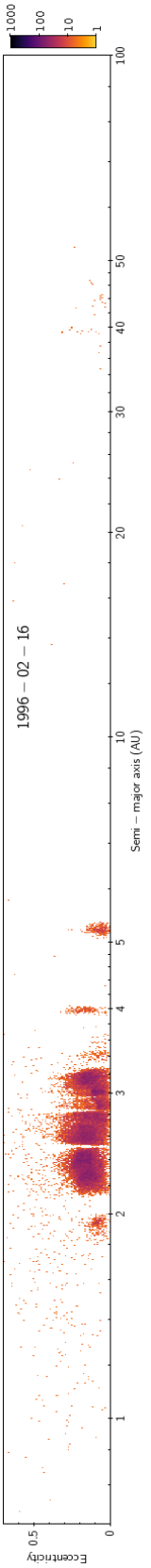

smoothly, while we acquired the spectro-images with SINFONI on Orcus, 8 magnitudes fainter. The interest of these close encounters is depicted in Fig. IV.2, showing our observations compared to some LGS-without-TTS observations we performed two weeks later.

As we did for Haumea, we measured the position of Vanth, the satellite of Orcus, and combined it with the positions reported by Brown et al. (2010). We confirmed the nearly-circular orbit of Vanth, hinting at circularization by tides, and refined all orbital parameters, crucial for the planning of stellar occultations (Section III.2). Using the revised diameter of Orcus by Lim et al. (2010), we derived a density of $2.3 \pm 0.8\,\mathrm{kg.m^{-3}}$, implying the presence of a silicate core below the icy surface (Carry et al., 2011, available in the Appendix B.4.b).

IV.2 The dynamical family of (136108) Haumea

IV.2.a Families are not frequent in the Kuiper Belt

As describe above, the dwarf-planet Haumea presents many outstanding characteristics. Maybe the most striking was the discovery by Brown et al. (2007) of a dynamical family associated with it. The initial list of candidate members, and the corresponding low ejection velocity of 150 m/s was indeed totally unexpected (Ragozzine and Brown, 2007).

If dynamical families are common in the asteroid belt (e.g., Nesvorný et al., 2015; Spoto et al., 2015), it is deemed very hard to identify any in the Kuiper Belt, in which relative velocity between objects is of a few hundred meters only (Marcus et al., 2011). Large KBOs have high escape velocity (e.g., 1 km/s for [ ][1] Pluto), meaning family formation by collisions are expected to spread over the entire belt quickly, making their identification almost impossible. Conversely, small KBOs could have tight families, but their members are so faint that they haven't been discovered yet.

A simple workaround to explain the cluster of objects around Haumea would be a recent collision, but owing to the extremely low density of objects in the Kuiper Belt, the collision between two large bodies is utterly unlikely at present days (Levison et al., 2008). A characterization of the family was therefore required to understand its formation. During my PhD at ESO in Chile, we set up a photometric survey of these bodies with C. Snodgrass, Research Fellow at ESO at that time.

IV.2.b Photometry of candidate members

The first step was to identify genuine family members from the background population. Thankfully, the spectral properties of Haumea, high albedo and almost pure water ice, provided easy selection criteria.

The task was nevertheless challenging. Haumea, the progenitor of the family, is a dwarf-planet with a diameter of about 1500 km (Rabinowitz et al., 2006) and yet only sustains an apparent magnitude of about 17.5 in V. The *chips of the block* are therefore very faint (V ≈22-24). Acquiring visible and near-infrared spectra would be a telescope-time consuming project.

We thus selected a suite of broad- and narrow-band filters, with EFOSC2 on the New Technology Telescope (NTT) in the visible and with Hawk-I on the VLT in the near-infrared, that would allow the identification of water ice on the targets, without requiring spectral resolving power. Because we were not aiming at a fine characterization of the surface compounds, this approach of classification using broad-band photometry was very productive.

We observed 28 candidate members and rejected 17 of them, either from the very red color in the visible, or absence of water ice absorption at 1.5 μm (Fig. IV.3). The 11 confirmed members represent only a third of the original candidates. We showed that confirmed members were clustered in a small region in the orbital elements space, thus confirming a very low ejection velocity of 150 m/s (Fig. IV.3), Snodgrass et al., 2010, see the full text reproduced in Appendix B.4.c).

IV.2.c Properties of family members

Together with the visible and near-infrared colors, we acquired time series. Combining our measurements with literature, we built a sample of 8 confirmed family members for which the rotation period and

[1] should have been 1164 but it's 134340, but clearly **not** 9

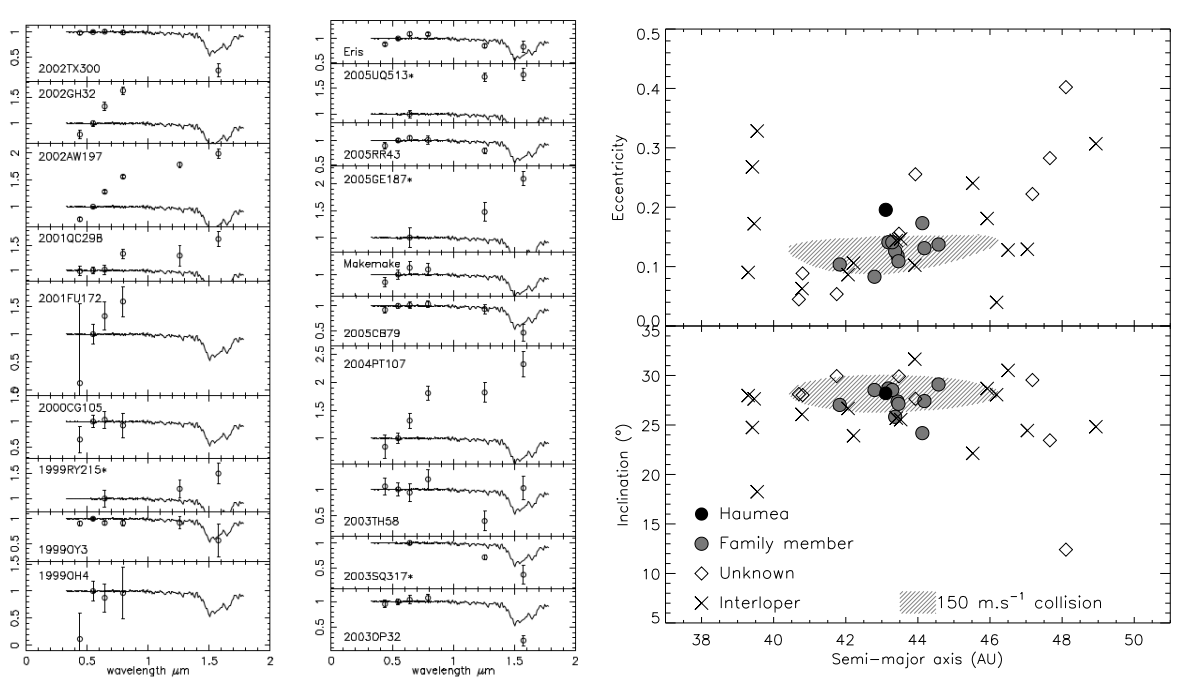

Figure IV.3: **Left:** Examples of photometry of candidate members of the family of Haumea, compared with the reflectance spectrum of Haumea, allowing easy identification of genuine family members. **Right:** Orbital distribution of the family, trimmed from the list of 35 candidates by Ragozzine and Brown (2007) to 11 genuine members. Credits: Snodgrass et al. (2010) and Carry et al. (2012b)

lightcurve amplitude were known. These parameters can be used to estimate the density of the bodies by two methods: by either balancing gravitational and centrifugal forces for an assumed strengthless body, as applied to asteroids (Pravec et al., 2002) and comets (Snodgrass et al., 2006), or by assuming a fluid equilibrium shape (i.e., a Jacobi ellipsoid), which may be more appropriate for large icy bodies such as KBOs (Lacerda and Jewitt, 2007). Fig. IV.4 compares these confirmed family members with all other KBOs taken from the compilation of Duffard et al. (2009).

The distribution of the family members is striking. Seven of the eight fall into the long-period (low-density) area of Fig. IV.4, implying a density lower than 0.64 g.cm^{-3}. The only exception has a large lightcurve amplitude which implies that it is likely to be a contact binary (and therefore the Jacobi ellipsoid model does not hold, Lacerda and Jewitt, 2007). Using 2-D Kolmogorov-Smirnov test, we found a high probability (96%) that members of Haumea's family were presenting different rotation properties than the other 64 KBOs considered. Their low density suggests they are made of pure water ice, and they originate from the outer shell of Haumea which was ripped out during the event(s) that formed the family.

The survey we conducted provided a solid observational basis to discriminate models of the formation of Haumea's family. The more convincing may be the *graze and merge* impact model proposed by Leinhardt et al. (2010), in which Haumea suffers a very oblique collision during which the impactor rips Haumea outer shell, spins it up, and continues its trajectory. The impactor merges with Haumea shortly after. The other models of spin-up and fission (Ortiz et al., 2012) or cataclysmic disruption of a large moon (Schlichting and Sari, 2009) fail to explain either the low-velocity of the family or the short rotation period of Haumea (Carry et al., 2012b, available in Appendix B.4.d).

IV.3 On the ices of KBOs

The determination of the composition of airless bodies of the solar system is challenging. Contrarily to compound in their gas state, presenting very narrow absorption or emission lines at wavelengths

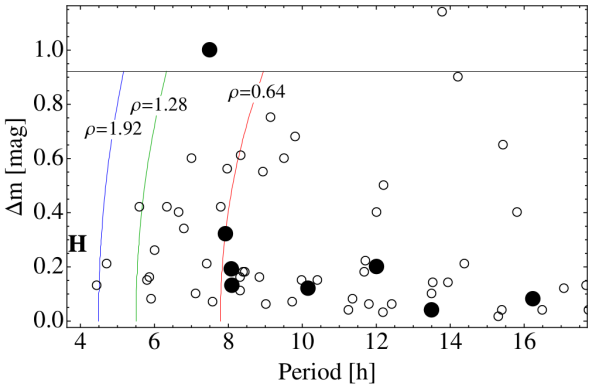

Figure IV.4: Lightcurve amplitude (Δm) as a function of the rotation period (in hours) for KBOs. Filled and open circles stand for confirmed family members and background population. The letter H shows the position of Haumea. Vertical blue, red, and green curves are the limit for stability, assuming the objects are in hydrostatic equilibrium, i.e., stable objects left of a line are denser than the number in the label (in g.cm^{-3}). Objects above the black line ($\delta m \approx 0.9$ mag) are likely contact binaries. CREDITS: Carry et al. (2012b)

predicted by quantum mechanics, solid silicates and ices tend to present very broad absorption bands. This is particularly dramatic for asteroids, for which only a third of the 26 classes have bands successfully corresponding to identified minerals, mainly olivines and pyroxenes. For KBOs, covered by ices, much more compounds have been identified (e.g. Brown et al., 1998; Delsanti et al., 2010; Trujillo et al., 2011). The spectral analysis will find the mixture of compounds that best fits the observed spectra. The process hence consists in choosing the icy compound end-members, feed them to the minimization function, and let it go.

IV.3.a Crystalline water ice on (136108) Haumea

My first experience with studying the surface of a KBO was a by-product of my involvement in the study of Haumea's triple system (Section IV.1.b). We extracted the near-infrared spectrum of Haumea, and of its brightest satellite Hi'iaka on the SINFONI spectro-cubes (Fig. IV.5).

These spectra clearly revealed the presence of water ice, as already reported (Barkume et al., 2006; Trujillo et al., 2007). The high SNR allowed to quantify the amount of crystalline and amorphous ice, and triggered our study of the tides regime within the system described earlier.

Following the report by Lacerda (2009) of the presence of a dark and red spot on the surface of Haumea, we coached Florian Gourgeot, the new PhD student of my former supervisor Christophe Dumas, to conduct followup observations of Haumea, again with SINFONI, to study the spectral properties of surface over Haumea's rotation.

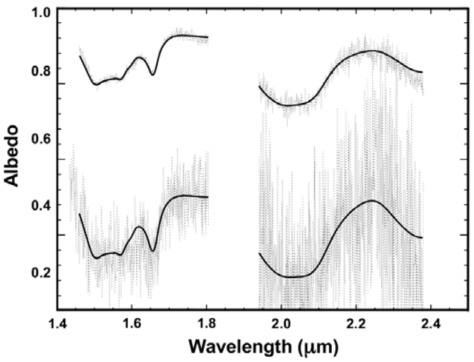

Figure IV.5: Spectra of Haumea (top, offset by +1) and its satellite Hi'iaka (bottom). The solid line represent the spectral model. CREDITS: Dumas et al. (2011)

Albeit we suffered terrible atmospheric conditions (it was not a sweet night, see the Weather Report[2]) that precluded observations over the entire rotation, the short time window of observation luckily corresponded to a rotation phase different from our first observations in 2007.

The darker region with a higher spectral slope in the visible also presented a steeper spectral slope in the near-infrared, compared to the rest of Haumea's surface. We, however, did not detect significant differences in the water composition, but the higher content of amorphous carbon needed to fit the spec-

[2] http://archive.eso.org/wdb/wdb/asm/historical_ambient_paranal/form

trum corresponding to the dark region still points to a slightly different compositions (Gourgeot et al., 2016).

IV.3.b Methane ice on (90482) Orcus

Like Haumea, the near-infrared spectrum of Orcus is dominated by water ice in crystalline form (e.g. de Bergh et al., 2005). Moreover, Trujillo et al. (2007) Barucci et al. (2008), and Delsanti et al. (2010) detected a weak absorption band around 2.2 μm that might be associated with either methane (CH_4) or ammonia (NH_3). Both methane and ammonia are expected to be destroyed by solar irradiation on short timescales (e.g. Strazzulla and Palumbo, 1998). Ammonia's presence, if confirmed, would thus require an active process to resupply the surface with ammonia, such as impact gardening or, more favorably, cryovolcanism (Cook et al., 2007).

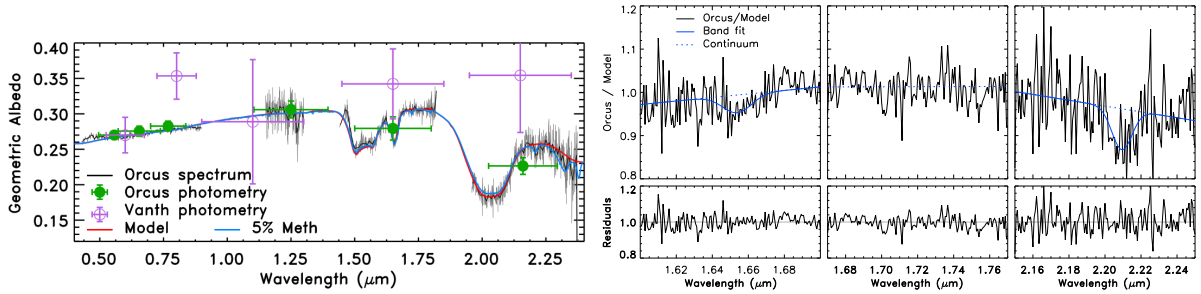

Figure IV.6: **Left:** Orcus spectrum together with the visible data from DeMeo et al. (2009b). The two models (red and blue) differ by the presence of 5% of methane. Purple circle represent the colors of Vanth (V, I, and J bands from Brown et al., 2010). **Right:** Search for subtle absorptions at wavelength corresponding to the major bands of methane from Quirico and Schmitt (1997). Two absorptions at 1.65 and 2.20 μm are detected. CREDITS: Carry et al. (2011)

We thus took advantage of a very favorable close encounter between Orcus and a bright star (described in Section IV.1.c) to observe it with SINFONI at the ESO VLT. We first modeled the spectrum of Orcus with a mixture of water ice (amorphous and crystalline) and tholins, with success (Fig. IV.6). We then searched for minor absorption bands in the spectrum. We clearly detected a band a 2.2 μm, possibly linked with methane or ammonia. The fact that no band was detected around 1.72 μm indicates that methane alone cannot account for the depth of the 2.2 μm band. Ammonia or hydrated ammonium could explain this band, with strong implications on cryovolcanism: ammonia lower the melting temperature of water ice and hence favors such mechanism (Carry et al., 2011).

IV.3.c Spectral variability of Charon, satellite of (134340) Pluto

Charon is the largest moon of Pluto. With a contrast of 3 magnitudes and a small angular separation of less than an arcsecond, early studies of its surface relied on mutual eclipse events (e.g. Buie et al., 1987). The angular resolution provided by the space telescope and AO on large ground-based telescopes allowed the study of Charon outside of eclipses, and near-infrared spectral data have revealed its surface to be rich in crystalline water ice and ammonia hydrates (e.g. Brown and Calvin, 2000; Cook et al., 2007).

The different studies suggested compositional variations across the surface of Charon (Buie and Fink, 1987; Buie and Grundy, 2000), especially between the trailing and leading hemisphere (see Dumas et al., 2001, for instance). We thus compiled published spectra of Charon over the 2 micron region from the literature, and observed it in K-band using SINFONI on the VLT, CorMASS on the 6.5 Magellan telescope, and the Near-InfraRed Imager (NIRI) on the Gemini North telescope.

Using the same set of tools we had used to detect faint bands in the spectrum of Orcus (see above), we analyzed the center, depth, and area of the 2.21 μm absorption band as its strength is dependent on the state of the ammonia hydrate ice, concentration in H_2O, grain size, temperature and exposure to radiation. We detected some variability of the band center and band depth among spectra taken at

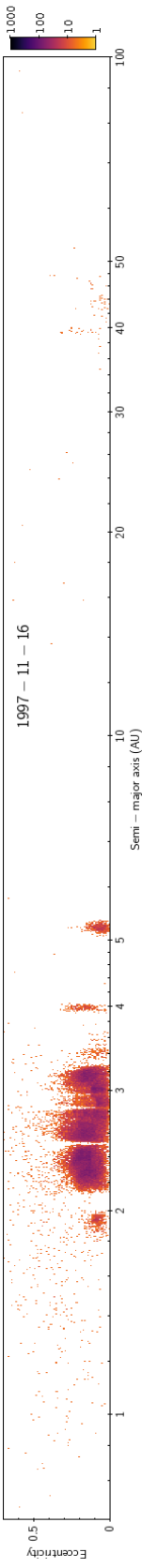

different epochs, corresponding to different longitudes on Charon (Fig. IV.7, DeMeo et al., 2015). This could indicate variability in the grain size or concentration of ammonia hydrate across Charon's surface.

The main conclusion was however that ammonia is ubiquitous over the entire surface of Charon. Since it is dissociated on ≈20 Myr timescales (Cook et al., 2007), its presence everywhere on Charon's surface requires a means of replenishment, such as slow diffusion from sub-surface layers through cracks or fresh craters (such as the Organa crater, Grundy et al., 2016). These results have been confirmed by the data taken during the New Horizons flyby and complementary data from Keck telescope (Holler et al., 2017).

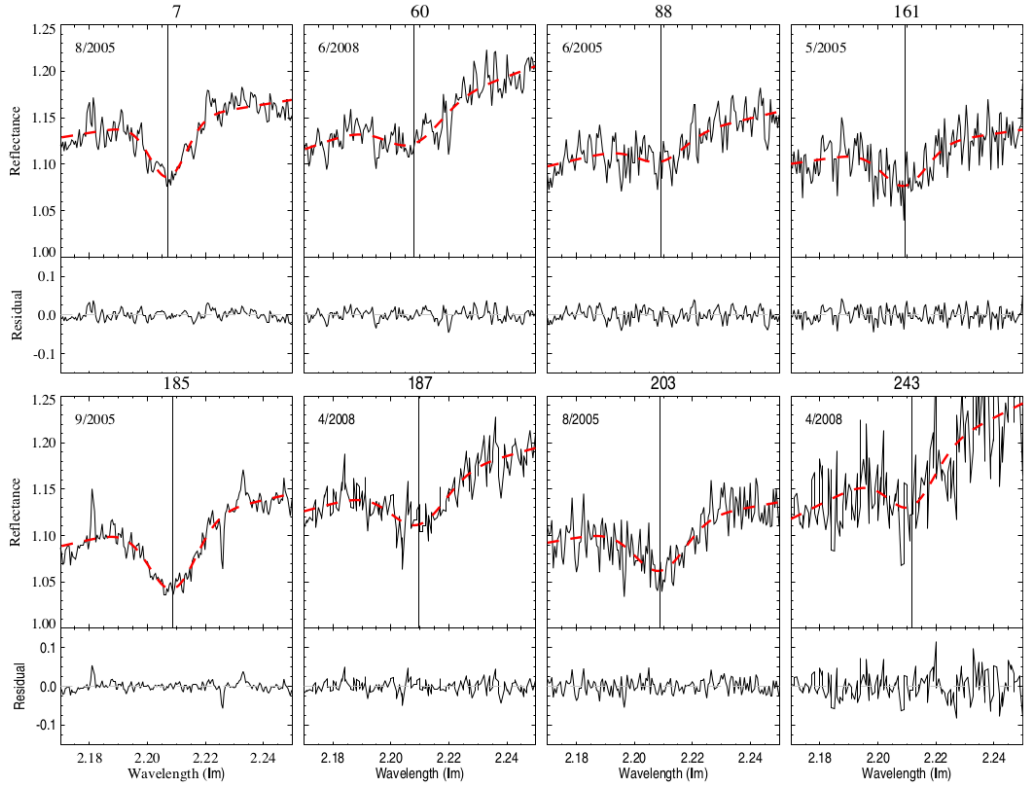

Figure IV.7: Reflectance of Charon in the 2.2 μm spectral region from 2005 to 2008. The measured spectra are in black with gaussian fits drawn as a red, dashed line. The vertical line marks the position of the band center. The bottom panel of each plot shows the residual of the gaussian subtracted from the data. The observation date and longitude at which each spectrum was taken are marked at the top of each plot. Differences in the characteristics of the band are visually apparent. Credits: DeMeo et al. (2015)

Chapter V

A Boom in Asteroid Data from All-Sky Surveys

In previous chapters, I have described different studies I did on individual targets (e.g., III), or limited groups (e.g., IV.2). These steps are required to build references, on which larger samples can be interpreted. To me, the study of Haumea's family (IV.2) by broad-band photometry was key to orient my research activities toward large samples of SSOs, such as the Moving Object Catalog (MOC) of the SDSS (V.1). We pushed even further the mining of SDSS data to recover the fast moving NEAs missing in the MOC (V.2).
I am currently expending this line of investigation (V.3), waiting impatiently at the release of Gaia data (V.3.a), hunting asteroid lightcurve in exoplanet surveys by the transit method (V.3.b), and setting a Working Group for Solar System Objects within the consortium of the ESA dark matter explorer Euclid (V.3.c).

Contents

V.1 Compositional mapping of the asteroid belt

While acquiring the colors of KBOs to assess their membership to the family of Haumea (Section IV.2), I realized how efficient was broad-band photometry to achieve rough spectral classification, in a relatively small amount of telescope time, compared to spectroscopy (which provides much more information on the composition).

V.1.a The Sloan Digital Sky Survey

This is how Francesca DeMeo and I started to design a simple spectral classification tool, with the aim of selecting "interesting" targets for spectroscopic followup observations. We decided to use the visible photometry taken over four filters (g, r, i, z, from 0.5 to 1.0 μm) by the SDSS, an imaging and spectroscopy survey dedicated to observing galaxies and quasars (Ivezić et al., 2001). The survey also observed serendipitously over 400,000 SSOs, of which over 100,000 are unique objects linked to known asteroids, listed in the MOC.

This dataset has already been used by the community, to study the effects of space weathering (Nesvorný et al., 2005), the size distribution of asteroid families (Parker et al., 2008), the composition of Hildas and Trojans (Roig et al., 2008; Gil-Hutton and Brunini, 2008). Yet, these studies had concentrated on the broad spectral complexes (C, X, and S) and peculiar V-types. We had the intuition that this amazing dataset could be used to class objects with a finer scheme (as Carvano et al., 2010, published little later).

V.1.b A color-based taxonomy compatible with spectroscopy

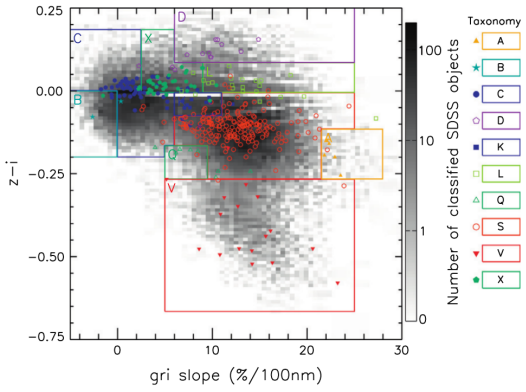

Figure V.1: Boundaries used to classify SDSS data into taxonomic classes. The colored points are the spectra from DeMeo et al. (2009a). The MOC is plotted in the background to show the dispersion of the SDSS data. CREDITS: DeMeo and Carry (2013)

We designed our classification from SDSS data to maximize the taxonomic detail contained in the dataset and at the same time to keep the class definitions as consistent as possible with previous spectral taxonomies, based on higher spectral resolution and larger wavelength coverage (mainly Bus and Binzel, 2002a; DeMeo et al., 2009a).

The classification scheme was fairly simple. We first converted the SDSS photometry into reflectance, by subtracting the colors of the Sun. Then, we used the 370 asteroids that defined the taxonomy by DeMeo et al. (2009a) to define *ad hoc* boundaries between each class in a 2-D space (Fig. V.1), made of the spectral slope (computed over the g-r-i filters) and the depth of the 1 micron band (taken as z-i). As such, the scheme mimicked the first taxonomies from the 1970s (Chapman et al., 1971; Chapman and Salisbury, 1973; McCord and Chapman, 1975), while being consistent with the latest developments.

V.1.c The distribution of compositions in the inner solar system

We thus determined the taxonomic class of 100,000 asteroids (DeMeo and Carry, 2013, full text available in the Appendix B.6.a). We had realized by then that the SDSS dataset could be used for much more that target selection. The concomitant publication of estimates of the density of each taxonomic class (Carry, 2012) and of the diameter of 150,000 asteroids (Masiero et al., 2011) opened new perspectives.

For the first time, we were able to characterize the distribution of material in the main belt by mass (i.e., the true amount of material) rather than by number of asteroids. It provided a dramatic improvement over previous studies: an analysis of the belt by numbers would undeniably by biased toward families and against the largest bodies: Ceres alone encompasses as much material as one *billion* of 1 km diameter asteroids!

Assessing the different biases at play within the SDSS observations, we selected a smaller sample of 35,000 asteroids limited to bodies larger than 5 km in diameter, deemed unbiased. We then extrapolated the fraction of each classes to the whole population, and studied how the different spectral classes were distributed.

Here is what we found (Fig. V.2, DeMeo and Carry, 2014, full details in the article reproduced in the

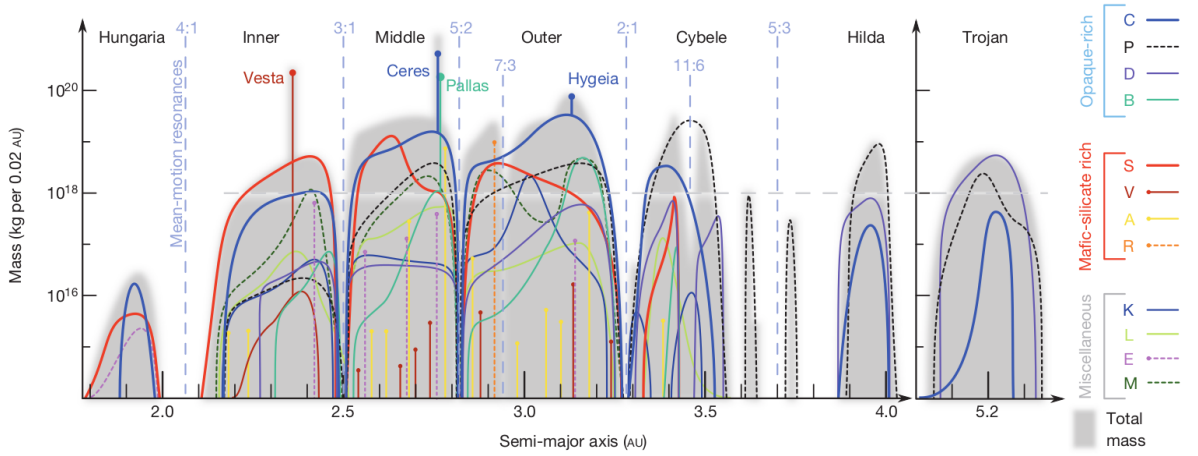

Figure V.2: The compositional mass distribution in the asteroid belt and Trojan space. The grey background is the total mass within each 0.02 AU bin. Each colour represents a taxonomic class of asteroid. The horizontal line at 10^{18} kg is the limit of the work from Gradie and Tedesco (1982). The upper portion of the plot remains consistent with that work, but the data from SDSS revealed immense detail at the lower mass range.
CREDITS: DeMeo and Carry (2014)

Appendix B.6.b). The rarer asteroid types, such as the crust (V-types) and mantle (A-types) remnants of fully heated and melted bodies, are seen in all regions of the main belt (we confirmed this later on, with two spectral surveys, see DeMeo et al., 2014a, 2016). Asteroids that look compositionally Trojan-like (D-types) are detected in the inner belt, where they were not predicted to exist by dynamical models (e.g. Levison et al., 2009). Their presence so close to the Sun demanded an explanation for how they arrived there and whether they were really linked to the Trojan asteroids at all (the recent dynamic simulations by Vokrouhlický et al., 2016, suggest they are of similar origin).

The Hungaria region is typically associated with its eponymous and brightest member, (434) Hungaria, and similarly high-albedo asteroids (E-types). Despite this, most of the mass of this region is contained within a few S-types and C-types asteroids The relative mass contribution of each asteroid class changes as a function of size in each region of the main belt. Most dramatic is the increase of C-types as size decreases in the inner belt. Although C-types are notoriously rare in the inner belt at large sizes , where they comprise only 6% of the total mass, half of the mass is made of C-types at the smallest sizes.

V.2 Spectral properties of NEAs and MCs

V.2.a Harvesting asteroids with the public

The SDSS was an amazing survey, and the wealth of data on asteroids, cataloged in the MOC was the foundation of more than 40 articles in the community. Nevertheless, there were some limitations in the identification process, affecting its completeness. For instance, objects moving faster than 0.5 deg/day have been classified as separate objects by the automatic process that generated the MOC.

We thus set up a citizen science project, designed and implemented by Enrique Solano at the Spanish Virtual Observatory (SVO), taking advantage of VO tools to

1. retrieve all the fields of view of the SDSS,
2. compute ephemerides for all NEAs and MCAs for the time period of the observations;

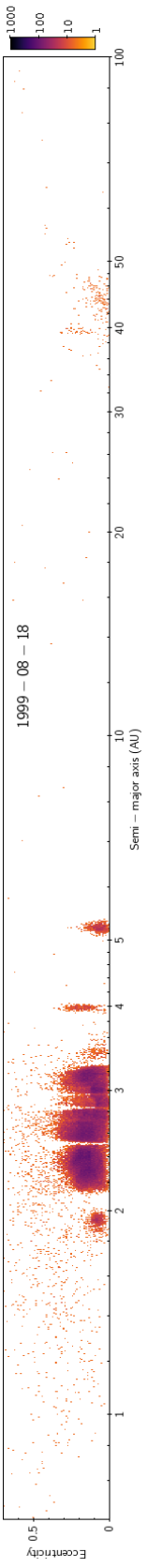

3. search whenever they were present within the field of view, with an apparent magnitude lower than 22 (the limiting magnitude of the SDSS images).

For each candidate NEA/MCA in a field of view, the object was proposed to the public via a suite of Internet Web pages[1]. With only a few clicks, users can download images, which are opened in Aladin[2] (Bonnarel et al., 2000) for visual inspection. The astrometry measured by users was then collected and sent to the Minor Planet Center (MPC).

We released the service in July 2011. Since then, 3,582 users have registered into the system, measuring 415,288 positions of 1,690 NEAs and 3,017 MCAs. We are still running this citizen science project, in which we have added the UKIRT Infrared Deep Sky Survey (UKIDSS), the VISTA Hermisphere Survey (VHS), and all optical surveys from the VLT Survey Telescope (VST).

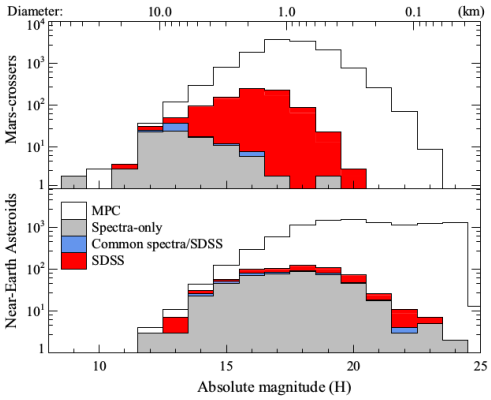

Figure V.3: Known taxonomy of NEA and MCA vs absolute magnitude. CREDITS: Carry et al. (2016)

We then applied the classification scheme I had developed with F. DeMeo (DeMeo and Carry, 2013) to this sample of 206 NEAs and 776 MCAs, increasing the number of known taxonomy for these populations by 40% and 663% (Fig. V.3, Carry et al., 2016, available in the Appendix B.6.c).

V.2.b On the source regions of NEAs

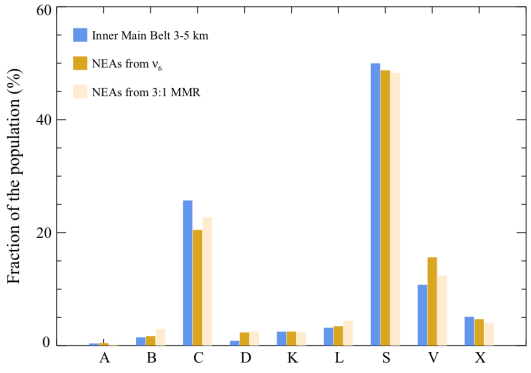

Figure V.4: Relative fractions of taxonomic classes for small asteroids in the inner belt (from DeMeo and Carry, 2013) compared with predicted fractions from NEAs observations.
CREDITS: Carry et al. (2016)

The population of NEAs erodes on short timescale (<10 My) by planetary collisions and dynamical ejections and new objects must be injected in the NEA space to explain the current population. Since decades (Wetherill, 1979; Wisdom, 1983), the resonances between the asteroids and Jupiter were identified as the mechanism pumping the eccentricity of MBAs and placing them on planet-crossing orbits. Later, the secular resonance ν_6 and 3:1 mean-motion resonance with Jupiter were found the most effective (see Morbidelli et al., 2002, for a review). This was confirmed by the spectral match between the OCs meteorites (80% of all meteorite falls), the dominant class of NEAs the S-type asteroids (about 65%, Binzel et al., 2004), and the family of Flora (Vernazza et al., 2008).

Dynamical models were built to predict the source regions of NEAs (e.g., Bottke et al., 2002; Greenstreet et al., 2012). Thanks to our recent publication of the distribution of compositions of MBAs down to a diameter of 5 km (DeMeo and Carry, 2014), we were able for the first time to compare the distribution of taxonomic classes between NEA and asteroids in their potential source regions of similar diameters (recent development of these dynamical models have shown that the effectiveness of the source regions was size-dependent, Granvik et al., 2016). For that, for each asteroid in our large sample of 982 NEAs and MCAs (Fig. V.3), we computed its probability to originate from each source region using the model by Greenstreet et al. (2012), and assigned to each source region the corresponding probability to be made of bodies belonging to the asteroid taxonomic class. The comparison between these prediction and the population of asteroids in the inner main-belt is striking (Fig.V.4), validates the results of the dynamical models, and confirms that ν_6 and 3:1 resonances are the main sources of NEAs (Carry et al., 2016).

[1] http://www.laeff.cab.inta-csic.es/projects/near/main/index.php
[2] http://aladin.u-strasbg.fr/

V.2.c Space weathering and planetary encounters

The availability of such a large sample of spectral properties for NEAs of different orbits and size allowed to study another particularity: the high fraction of Q-type asteroids among NEAs. These asteroids are spectrally similar to the most common meteorites, logically called Ordinary Chondrite (OC), made of olivine and pyroxene assemblages. Under the constant bombardment of solar wind ions, their spectra becomes redder and their surface darker (i.e., the albedo decreases) due to enrichment of nano-sized iron on the upper side of surface grains. This process changing OC spectra into S-type spectra is called *space weathering*.

This effect had been suspected for long to explain the apparent mismatch between the most common meteorites and the dominant type of asteroids in the inner belt, but harshly debated. Definitive observational evidences came only late, with ions irradiation of meteorites (e.g., Strazzulla et al., 2005; Brunetto et al., 2006, 2015), and study of asteroid families of different ages (e.g., Vernazza et al., 2009). The sample return from the S-type (25143) イトカワ by the JAXA mission Hayabusa said "This is the end" to the debate (Binzel et al., 2001; Nakamura et al., 2011).

The space weathering is now well-understood on surfaces made mainly of olivine and pyroxene (i.e., from the S-complex, plus A- and V-types, Brunetto et al., 2007; Fulvio et al., 2012), and the typical timescale to change a Q-type surface into a S-type seems very short, at about 1 My (Vernazza et al., 2009). The presence of Q-types among NEAs thus required a process to refresh the surfaces. Based on an original suggestion by Nesvorný et al. (2005), several studies explored the effect on planetary encounters on asteroid surfaces. Binzel et al. (2010), followed by Nesvorný et al. (2010) and DeMeo et al. (2014b), found that all the Q-types NEAs had low Minimum Orbital Insertion Distance (MOID) with the Earth, Venus, and/or Mars in the past 500,000 years. Although a large majority of S-types also had a low MOID at some point in their past, these authors argued that MOID measures the distance between orbits but not between bodies. Using this argument and the statistics of MOID, they derived a distance threshold at which the effect of the planetary encounters would be strong enough to resurface an asteroid: between 5 to 16 planetary radii.

The process that would resurface the asteroid was not given much attention, although the velocity and duration of the encounter, the object's shape, internal structure, surface gravity, local slopes, rotation rate and orientation, and the nature of the pre-existing regolith and its cohesion, were all listed as possible parameters dictating the distance at which an encounter can resurface the asteroid.

We thus built a simple model, describing all the forces acting on a grain at the surface of the asteroid during a planetary encounter: the tidal forces due to the planetary encounter, the centrifugal pseudo force due to the asteroid's rotation, the repulsive electrostatic force that originates from the electric charging of surface particles, the displacement force acting when the asteroid's rotation state changes (librational transport, Yu et al., 2014), the self-gravity of the asteroid, the cohesion between surface particles, and the solar radiation pressure. We used this model to determine the minimum distance to the planet required to resurface an asteroid, in two limiting conditions: favorable (hereafter *easy*) and unfavorable (hereafter *hard*) for resurfacing. We found that this distance is a strong function of the asteroid rotation period, and very small overall: between 2 and 5 planet radii only (Carry et al., 2016).

We then performed backward dynamical integration of all 46 Q- and 519 S-type asteroids of our sample, for 500,000 years, keeping record of encounters with all planetary bodies: Mercury, Venus, the Earth, Mars and the four most massive asteroids (Ceres, Pallas, Vesta, Hygeia, Carry, 2012). We showed that the populations of Q- and S- are indeed different in their encounters with Venus and the Earth but not with Mars (Fig. V.5). Hence, if planetary encounters can explain the high fraction of Q-types among NEAs, they cannot for MCA.

We thus explored the possibility that the observed distribution of Q-types is due to a selection effect: Q-types could be found more abundant among NEAs because we probe this population to smaller sizes than other asteroid populations. By comparing similar size-range, we indeed found a similar fraction of Q- and S-types among NEAs and MCAs (Carry et al., 2016). Recent simulation of resurfacing through YORP spin-up and regolith motion performed by the PhD student K. Graves seems in better agreement with observations, and predict many Q-types to exist in the main belt (Graves et al., 2016, 2018).

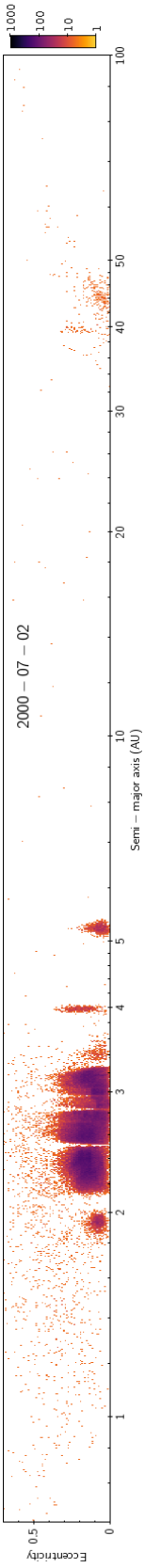

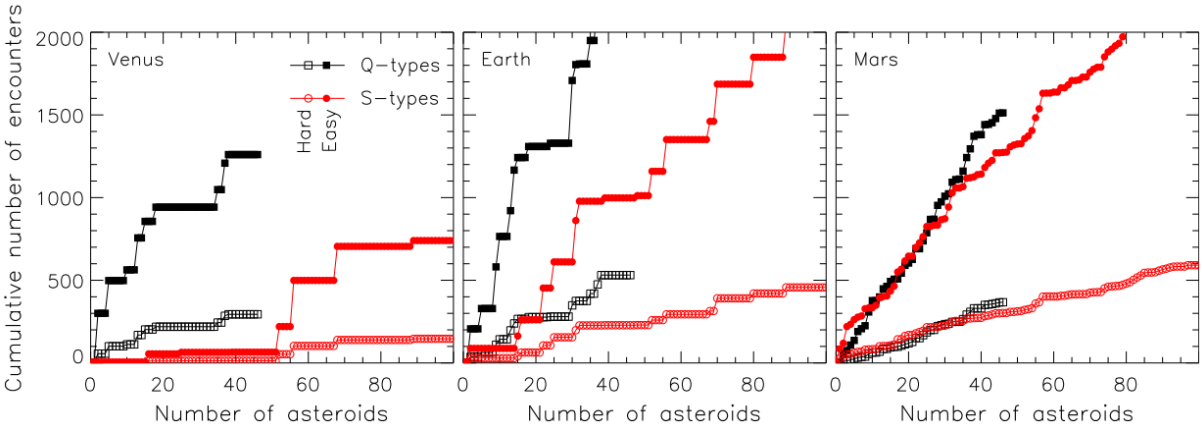

Figure V.5: Number of planetary encounters for the Q- and S-type asteroids (in black squares and red circles), for the easy and hard resurfacing cases. CREDITS: Carry et al. (2016)

V.3 Current and future surveys

V.3.a Observations of asteroids by the great Gaia in the sky

Gaia is current ESA astrometric mission, successor of the successful Hipparcos mission in the 1990s. Gaia is as much a revolution in astronomy as was the invention of photographic plates or the CCDs. Gaia is repeatedly observing the entire celestial sphere down to V=20.7, and its final catalog will contain about 2 billions star positions with micro-arcsecond precision (μas!!), magnitudes at the milli-magnitude level, proper motions, parallaxes, stellar parameters, radial velocity, ... etc (Gaia Collaboration et al., 2016).

With Gaia, our understanding of the Milky Way, and of the sky will change forever: almost any star brighter than V=20.7 becoming an astrometric and photometric reference star! The wide range of legacy science allowed by Gaia is also incredible, from reference frame, to general relativity, including exoplanets, variable stars, quasars...

During its continuous scan of the sky, Gaia is observing about 300,000 asteroids, 60 times each. Owing to Gaia specifications, the potential for orbit determination, surface characterization, and shape modeling is tremendous (Zappala and Cellino, 2002; Mignard et al., 2007; Cellino et al., 2007; Mouret et al., 2007; Tanga and Delbo, 2007; Delbo et al., 2012; Spoto et al., 2017). Since I was recruited as CNAP astronomer in 2012, I have been involved in Gaia Data Processing and Analysis Consortium (DPAC), in charge of dissemination of call-for-observations for SSOs discovered by Gaia (Tanga et al., 2016, available in Appendix B.7.a).

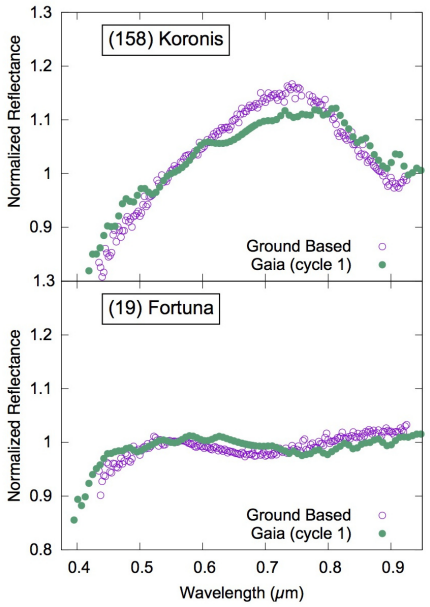

Figure V.6: Asteroid reflectance from Gaia compared with ground-based spectra. CREDITS: ESA/Gaia/DPAC/CU4+CU5/M. Delbo

Although I am not working directly on the tools that will produce the catalogs of SSOs observations and properties, being part of such an amazing mission is stupendous. Especially after my studies of asteroids taxonomy from SDSS (Section V.1 above), I am impatiently waiting for Gaia color-photometry data (Fig. V.6, Delbo et al., 2012), at a higher spectral resolution and with a better photometric accuracy, to confirm and expand our study of taxonomic distribution among asteroids.

V.3.b Lightcurves of asteroids in exoplanet surveys

As mentionned in Section III.1.c, building a solid statistically relevant sample of rotation period, spin-axis orientation, and 3-D shape of asteroids allows to study fine effects, such as the YORP effect. However, after half a century of targeted lightcurve observations of asteroids, "only" a thousand shape models were determined.

This limitation has several origins: first, the lightcurve inversion method by Kaasalainen and Torppa (2001) requires many lightcurves, taken under different Sun-Target-Observer geometries. Second, the community slowly dropped lightcurve observations of asteroids in the 1990s (but amateur astronomers have been extremely active in that respect). As such, there was not enough data to study more asteroids.

The work-around developed by Kaasalainen (2004), and extensively exploited by "Big" Josef Durech and his former PhD student "Little" Josef Hanus (e.g. Ďurech et al., 2009; Hanuš and Ďurech, 2012; Hanuš et al., 2016) was to use photometry sparse in time (with measurements separated by more than a rotation period) produced by astrometric surveys. Such data could indeed be considered as a very poorly sampled many-years-long lightcurve, still holding crucial information on the period, spin, and shape of the target.

The photometric quality of these data set is however generally limited (0.10–0.15 mag, Hanuš et al., 2011), and often affected by zonal biases. This is again an area which will greatly benefit from Gaia stellar catalog and SSO observations, and the spin and tri-axial ellipsoid solution is expected for 300,000 asteroids (Cellino et al., 2007). Nevertheless, from sparse photometry only, several issues raise:

1. the rotation period can remain ambiguous,
2. the 3-D description remains crude, and
3. the lightcurve inversion is CPU intensive.

Lightcurves dense in time, even a single one, can remove period ambiguity, and restrict the interval of period search, greatly optimizing the process. So in an era rich in sparse photometry from Gaia, LSST, the real challenge is to find the treasure box full of dense lightcurves, such as the recent exploitation of the Palomar Transient Factory (PTF) by Chang et al. (2015) and Waszczak et al. (2015).

Since a long while I was considering using images from exoplanet characterization surveys by the transit method. To find exoplanets, all these surveys require large fields of view, observed frequently, and monitored for many days, weeks, even months. Recently, this idea came to fruition in two large projects.

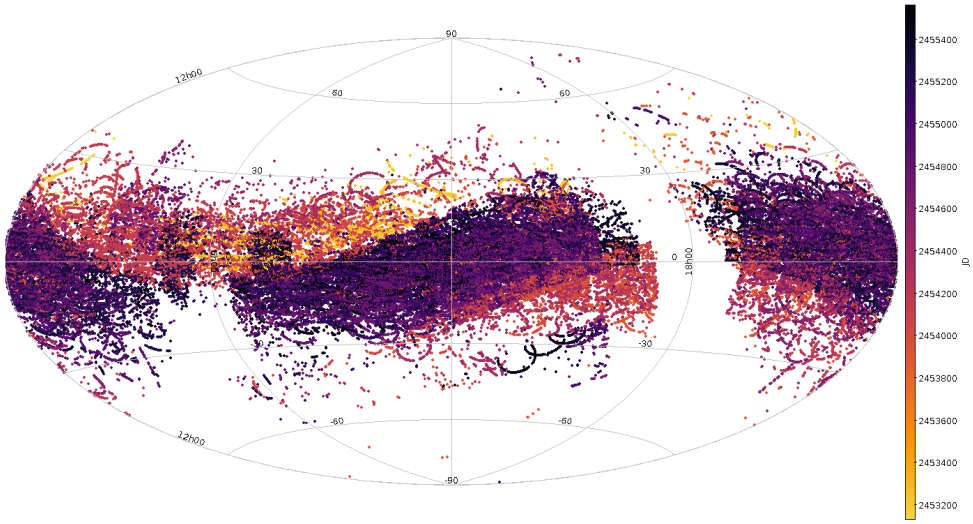

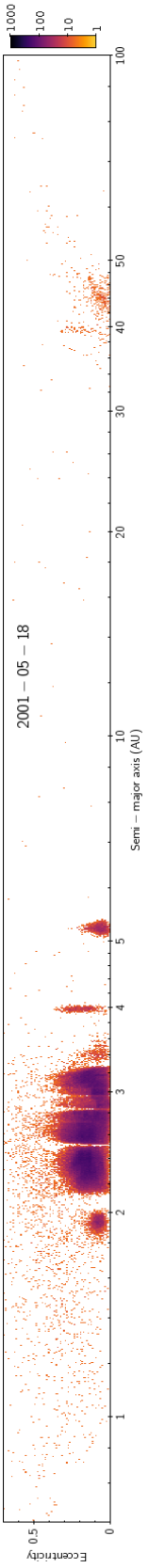

Figure V.7: Distribution of asteroid detection in 2004-2010 by SuperWASP in ecliptic coordinates, color-coded by date. Credits: Data from Parley et al. (2005).

SuperWASP: SuperWASP is a UK project to detect and characterize exoplanets by measuring the dimming of their host stars during transits. It is composed of two telescopes, in Canary Island and South Africa, each covering 7.8×7.8 square degrees. Even if its limiting magnitude is around V=14–15, it is a gold mine for lightcurves of large and primordial asteroids.

Together with Colin Snodgrass and Simon Green, we are co-supervising a PhD student, Jonathon Grice, who is retrieving the asteroids from the junk sources table of the SuperWASP source extraction, by cross-matching with ephemerides (following the early developments by Parley et al., 2005). The photometry of these SSOs is then cleaned from outliers due to, e.g., mis-association with nearby stars (Grice et al., 2017). Then, the lightcurves are used to determine the rotation period and spin-axis coordinates and reconstruct the 3-D shape of the asteroids (e.g., Marsset et al., 2017). The amount of data is tremendous: we listed over 900 asteroids with lightcurves taken in more than 40 nights (Fig. V.7)!

Kepler/K2: Kepler is a NASA space mission designed for the same purpose as SuperWASP, but with an amazing 116 square degrees field of view, a 30 min cadence, and a precision of a few hundreds ppm down to $V \approx 15$, allowing the detection of much fainter targets. Given these characteristics, Kepler could have been an incredible source of data (even if the entire field of view is not downloaded to Earth, but only small windows around each targeted star). However, its original pointing was far from the ecliptic, and no observation of SSOs was likely. Thankfully (*sic*), two reaction wheels broke and the mission had to be re-designed, and in its K2 extension, the spacecraft points in the ecliptic plane.

We thus designed a suite of tools to compute all the epochs in which SSOs were inside the small windows around targeted stars, and developed a simple photometric extraction tool to test our system (Berthier et al., 2016). These preliminary results are amazing: short lightcurves of 2–4 h for thousands and thousands of asteroids are available (Fig. V.8). The main challenge is now to measure accurately the photometry and clean it from the short-term variability introduced to K2 pointing drift.

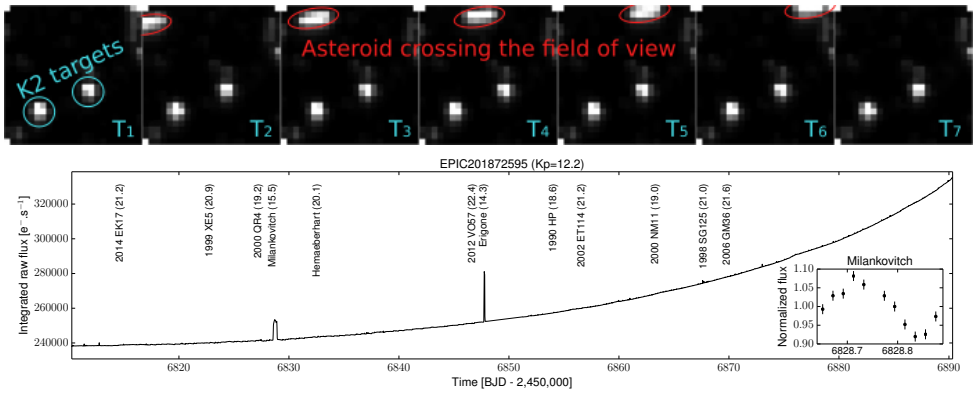

Figure V.8: **Top:** Crossing of a stellar window by an asteroid. **Bottom:** Example of a K2 raw lightcurve. The increase in flux along the campaign is a systematic effect. The predicted transits of known SSOs are indicated together with their expected V magnitude. The transit of two bright SSOs, (1605) Milankovitch and (163) Erigone, are clearly visible. The fainter SSOs also imprint a significant increase in the observed flux as they pass into the target imagette. The inset in the bottom right is a zoom on the transit of (1605) Milankovitch

V.3.c Solar System Science with ESA Euclid

The large sample of asteroid colors from SDSS (Ivezić et al., 2001) and albedo from WISE (Masiero et al., 2011) have changed our approach of asteroid taxonomy forever. As a community, we were not used yet to large data set, but now we have entered the era of big data. Upcoming surveys such as Gaia or LSST promise even larger data sets, including multi-epoch positions, photometry, and low-resolution spectroscopy (Mignard et al., 2007; LSST Science Collaboration et al., 2009).

These surveys will all operate in the visible. This is a major issue for spectral classification of asteroids, as several classes are degenerated over visible wavelengths, and only near-infrared can discriminate them (Fig. V.9). This is why the extension of the Bus taxonomy in the near-infrared by DeMeo et al.

(2009a) was so well-received by the community.

Seeking for a large data set of near-infrared colors of asteroids to complete the aforementioned surveys, I initiated a data mining effort of the VHS with Enrique Solano and my PhD student Myriam Pajuelo, based on our experience with SDSS (Section V.2 above). Soon after we started, Popescu et al. (2016) published a catalog of the colors of 39,000 SSOs present in VHS, so we concentrated on developing a taxonomic scheme for these data. This work is part of M. Pajuelo's PhD thesis, in which she developed the classification tool and determined the taxonomy of the 10,000 asteroids with accurate colors (article in preparation).

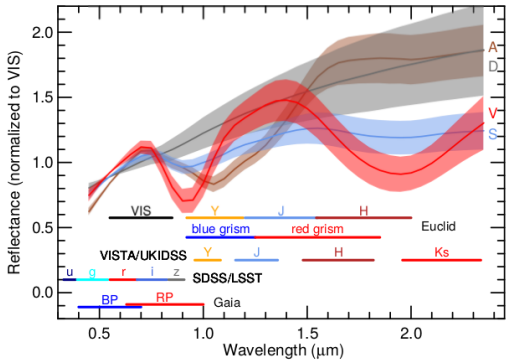

Figure V.9: Examples of asteroids classes (A, L, S, and V) which are degenerated over visible wavelength range. Horizontal bars represent the spectral coverage of large surveys: Gaia, SDSS, LSST, and Euclid. CREDITS: Carry (2018)

Her work showed the strength of near-infrared colors for SSOs spectral classification. Over the last year, I have thus been studying the potential of Euclid, the ESA wide-field space mission dedicated to the study of dark energy and dark matter through a mapping of weak gravitational lensing (Laureijs et al., 2011), for solar system science. Euclid will be equipped with 1.2 m-aperture Korsch telescope, and two instruments: a VISible imaging camera (VIS) and a Near Infrared Spectrometer and Photometer (NISP) (Cropper et al., 2014; Maciaszek et al., 2014). The mission design combines a large field of view (0.57 deg^2) with high angular resolution (pixel scales of 0.1″ and 0.3″ for VIS and NISP, corresponding to the diffraction limit at 0.6 and 1.7 μm).

Scheduled for a launch in 2020 and operating during six years from the Sun-Earth Lagrange L2 point, Euclid will carry out an imaging and spectroscopic survey of the extra-galactic sky of 15,000 deg^2 (the *Wide Survey*), avoiding galactic latitudes smaller than 30° and ecliptic latitudes below 15° (Fig. V.10), totaling 35,000 pointings. A second survey, two magnitudes deeper and located at very high ecliptic latitudes, will cover 40 deg^2 spread in three areas (the *Deep Survey*). Additionally, 7,000 observations of 1,200 calibration fields, mainly located at -10° and +10° of galactic latitude, will be acquired over the course of the mission to monitor the stability of the telescope Point-Spread Fonction (PSF), and assess the mission photometric and spectroscopic accuracy.

Euclid imaging detection limits are required at $m_{AB} = 24.5$ ($10\,\sigma$ on a 1″ extended source) with VIS,

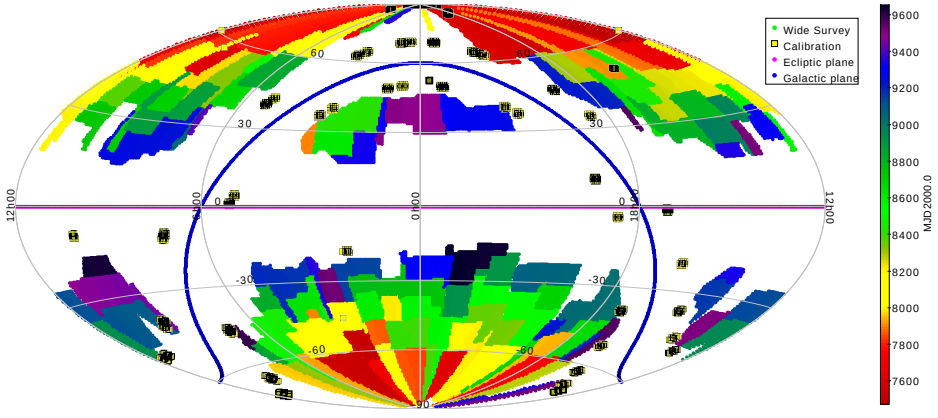

Figure V.10: Expected coverage of the Euclid *Wide survey* (called the reference survey), color-coded by observing epoch, in an Aitoff projection of ecliptic coordinates. The horizontal gap corresponds to the ecliptic plane (cyan line), and the circular gap to the galactic plane (deep blue line). The black squares filled with yellow are the calibration fields, repeatedly observed over the six years of the mission.

and $m_{AB} = 24$ ($5\,\sigma$ point source) in the Y, J, and H filters with NISP. Spectroscopic requirements are to cover the same near-infrared wavelength range at a resolving power of 380 and to detect at $3.5\,\sigma$ an

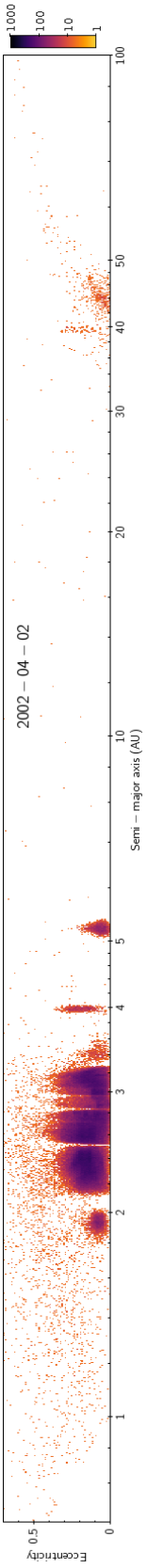

emission line at 3.10^{-16} erg.cm^{-1}.s^{-1} (on a 1″ extended source). The NISP grisms provide a continuum sensitivity to $m_{AB} \approx 21$. To achieve these goals, the following survey operations were designed:

1. The observations will consist in a step-and-stare tiling mode, in which both instruments target the common 0.57 deg^2 field of view before the telescope slews to other coordinates.
2. Each tile will be visited only once, with the exception of the *Deep Survey* in which each tile will be pointed 40 times, and the calibration fields, observed 5 times each on average.
3. The filling pattern of the survey will follow lines of ecliptic longitude at quadrature. Current survey planning foresees a narrow distribution of solar elongation of $\Psi = 91.0 \pm 1.5°$ only, the range of solar elongation available to the telescope being limited to 87°–110°.
4. The observation of each tile will be sub-divided in four observing blocks, differing only by small jitters ($100'' \times 50''$). These small pointing offsets will allow to fill the gaps between the detectors composing each instrument focal plane, resulting in 95% of the sky covered by three blocks, and 50% by four.
5. In each block, near-infrared slitless spectra will be obtained with NISP simultaneously to a visible image with VIS, with an integration time of 565 s. This integration time implies a saturation limit of V≈17 for a point-like source. Then, three NISP images will be taken with the Y, J, and H near-infrared filters, with integration time of 121, 116, and 81 s respectively.

All these characteristics make Euclid a potential prime data set for legacy science. In particular, the access to the near-infrared sky, about 7 magnitudes fainter than DENIS and 2MASS (Epchtein et al., 1994; Skrutskie et al., 2006) surveys, and 2–3 magnitudes fainter than current ESO VISTA VHS (McMahon et al., 2013), makes Euclid appealing for surface characterization of SSOs.

To estimate the number of SSOs that could be detected by Euclid, the first step was to build the cumulative size distribution of each population, extrapolating them to smaller size using latest published models (Jewitt et al., 2000; Gladman et al., 2009; Snodgrass et al., 2011; Bauer et al., 2013; Harris and D'Abramo, 2015; Granvik et al., 2016; Volk et al., 2016; Shankman et al., 2016; Petit et al., 2016, Fig. V.11). The second step to compute the range of absolute magnitudes accessible to Euclid for each population by determining the probability density function of the (H-V) index for each population, taking into account the dispersion of orbital elements, the non-uniformity of Keplerian motion, and the geometry of Euclid observations at a low solar elongation. The last step was to compute the fraction of SSOs present within the limit of Euclid surveys. Overall, some 150,000 SSOs should be observed by Euclid (Carry, 2018, see the full text in Appendix B.6.d for all the details).

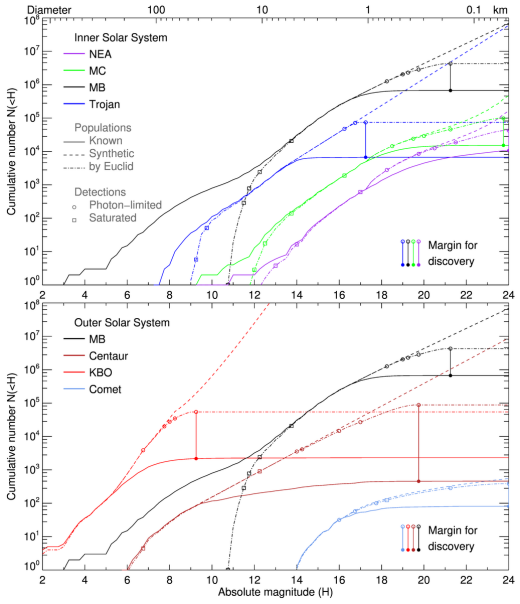

Figure V.11: Cumulative size distribution of each SSO population, for current census (solid lines), synthetic populations (dashed lines), and observable by Euclid (dot-dashed lines).
CREDITS: Carry (2018)

To estimate the potential of Euclid photometry for spectral classification of SSOs, I ran simulations based on the 371 spectra of asteroids from DeMeo et al. (2009a), and 29 KBOs compiled by Hong and Merlin (2016). For each spectral class and combination of filter, the average color, dispersion, and co-variance was computed to define a straightforward taxonomic scheme based on distance to class center. Although simplistic, it allows to estimate Euclid capabilities by applying the classification scheme to the same sample (Fig. V.12). The leverage provided by the long wavelength coverage allows to easily identify several classes: A, B, D, V, Q, and T. The main classes in the asteroid belt, the C, S, and X (DeMeo and Carry, 2014), are more clumped, and our capabilities to properly classify them will also depend on the exact throughput of Euclid optical path. For KBOs, their spectral

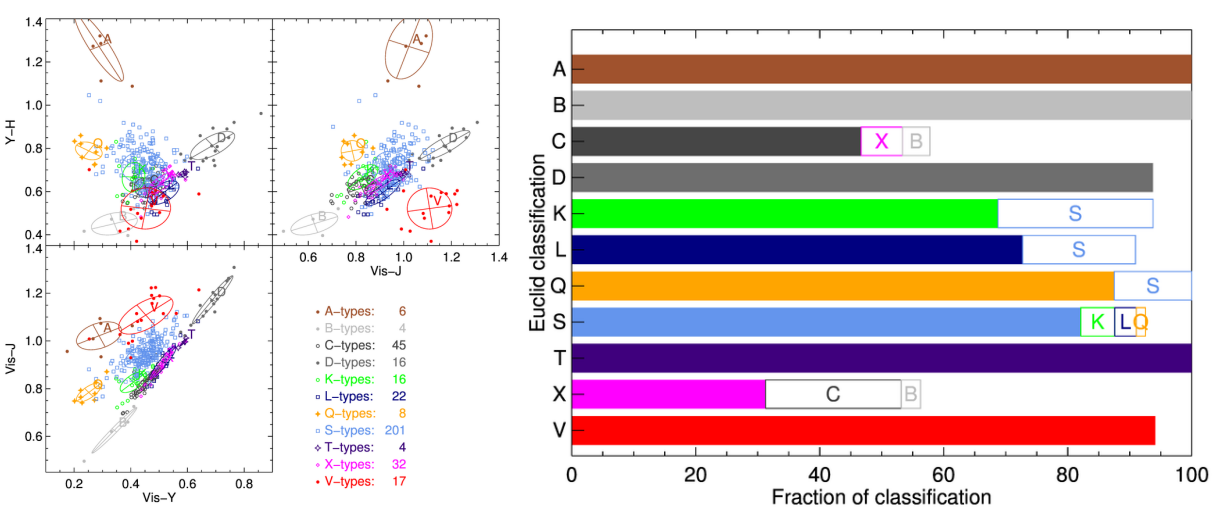

Figure V.12: **Left:** Result of the classification of the asteroids from DeMeo et al. (2009a), presented in three filter combinations. Several extreme classes, like A, B, D, V, and T, can be easily sorted out. **Right:** Percentage of correct (solid bar) and compatible (open bar) classifications. CREDITS: Carry (2018)

behavior from the blue-ish BB to the extremely red RR will place them in these graphs along a line going along the C, T, and D-types. Identifying the different KBO spectral classes should therefore be possible with Euclid set of filters.

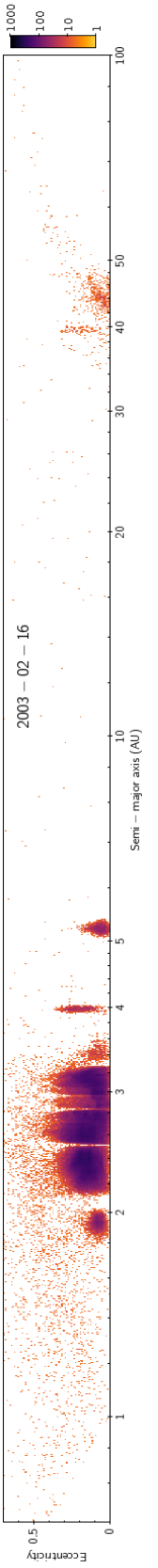

Chapter VI

Conclusions and perspectives

Starting a decade ago by studying a couple of the largest asteroids in the Main Belt with Adaptive-optics (AO), my research activities have grown toward statistical studies. Based on the experience and understanding gained on a handful of thoroughly studied targets (Ceres, Vesta, Lutetia), subsequently visited by spacecrafts, I was involved in and led multiple studies of the physical properties of asteroids: period, spin, 3-D shape, size, density, and multiplicity. These studies ascertained the non-isotropic distribution of spin-vectors on the celestial sphere, highlighting the major role played by the YORP effect on the orientation of small asteroids. The combined access to 3-D shape, gravitational field, and density revealed heterogeneous internal structures, from differentiated asteroids to cracked and porous rubble-piles. Consistently, bodies larger than 100-200 km were found compact, contrarily to the smaller objects, results of eons of collisions.

In parallel, I developed an extensive activity of surface characterization, from a few spectroscopic studies to massive taxonomic classifications using broad-band colors. Originally studying remote KBOs, I aimed closer and closer, from MBAs to finally MCAs and NEAs. The resulting map describing how asteroid compositions distribute in the main belt not only has summarized decades of spectroscopic surveys, but also extended our knowledge toward a new and smaller size range. This allowed to challenge the source regions of NEAs determined dynamically by comparing the distribution of composition among NEAs with these source regions, confirming the inner belt as a main provider of NEAs, and hence meteorites.

This last decade has been rich in increasing statistics. The prospects for increasing our understanding of the physical and surface properties for large numbers of SSOs are even more appealing.

Since April 2017, we are running a large program at ESO VLT (PI P. Vernazza) to image 35 large MBAs with the second-generation extreme-AO SPHERE camera. The spectacular angular resolution provided by this camera compared with first-generation AO cameras will allow to detect and characterize large craters and basins on these bodies. In parallel, I am steering a re-analysis of the high-angular-resolution and high-contrast images of binary asteroids present in the archives of large ground-based telescope. Dedicated and homogeneous processing of all these data provide large observing data set to constrain the orbit of these systems.

Based on our recent results on (107) Camilla, this allows to predict the position of the satellites around their host asteroid to a few mas only. This opens the possibility to predict and record stellar occultations by satellite of asteroids, whose small physical and angular size prohibits direct imaging. These challenging observations are now possible, thanks to the dramatic improvement of both stars and SSOs astrometry resulting of the ESA Gaia mission, as illustrated by the recent successful observations of stellar occultations by (10,199) Chariklo. There is therefore a huge potential for stellar occultations to study the size, 3-D shape, and multiplicity of SSOs, and we are currently dreaming of a dedicated network of robotic telescopes to that purpose.

Following our initial use of interferometers MIDI and ALMA, there are great prospects for using ALMA to *image* angularly small binary systems, and MATISSE, the new mid-infrared interferometric instrument for the Very Large Telescope Interferometer (VLTI), to study thermal and physical properties

of large asteroids. Further in time, the ESO 39 m ELT will provide the angular resolution needed to image smaller MBAs, in particular binary systems, and outer solar system dwarf-planets. I am involved in the consoritum of MICADO, the first-light AO-fed high-angular resolution camera.

Because 3-D shape reconstruction relies strongly on disk-integrated photometry, either for lightcurve-only or multidata inversion, I am focusing on harvesting lightcuves from archives. The very large surveys by Gaia and the LSST will produce many photometric measurements sparse in time for each SSO. Shape modeling will be possible from these datasets. However, the addition of a single lightcurve generally restricts the volume of the parameter space to be searched, and discriminates between ambiguous solutions. This is why I am interested in surveys to characterize exoplanets by detection of their transit in front of their host stars. Our current analysis of SuperWASP has shown that such surveys can be goldmines of asteroid lightcurves, and I plan to extract SSO signature from RoPACS, K2, and TESS in the future.

Prospect on SSO surface characterization are maybe even more promising. Gaia and the LSST are expected to deliver low-resolution spectra for several 10^5 asteroids, and broad-band colors for several *millions*! Completed with Euclid near-infrared photometry, these data sets will allow to classify spectral diversity in the entire solar system. Based on my experience with SDSS and VISTA data, I am setting up tools to use data from all these sources, and study the distribution of material. There are still many open questions that these large samples will allow to answer: how does composition distribute in the outer solar system? Are they any other dynamical families than Haumea's? Are there variations of compositions with inclination? What was the size distribution of the asteroid belt before dynamical families? How does space weathering affect different compositions?

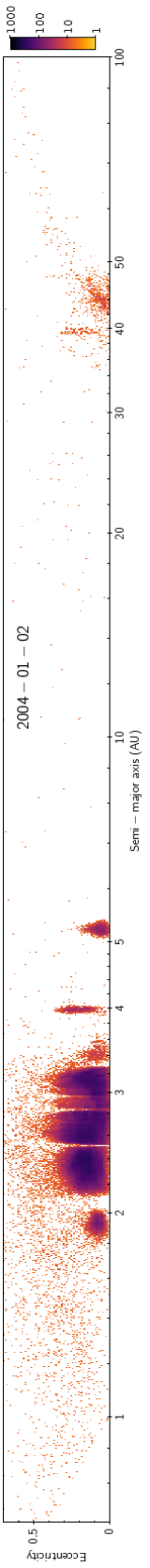

Bibliography

A'Hearn, M. F. and Feldman, P. D. (1992). Water vaporization on Ceres. Icarus, 98:54–60.

Altwegg, K., Balsiger, H., Bar-Nun, A., Berthelier, J. J., Bieler, A., Bochsler, P., Briois, C., Calmonte, U., Combi, M., De Keyser, J., Eberhardt, P., Fiethe, B., Fuselier, S., Gasc, S., Gombosi, T. I., Hansen, K. C., Hässig, M., Jäckel, A., Kopp, E., Korth, A., LeRoy, L., Mall, U., Marty, B., Mousis, O., Neefs, E., Owen, T., Rème, H., Rubin, M., Sémon, T., Tzou, C.-Y., Waite, H., and Wurz, P. (2015). 67P/Churyumov-Gerasimenko, a Jupiter family comet with a high D/H ratio. Science, 347(27):1261952.

Ammannito, E., DeSanctis, M. C., Ciarniello, M., Frigeri, A., Carrozzo, F. G., Combe, J.-P., Ehlmann, B. L., Marchi, S., McSween, H. Y., Raponi, A., Toplis, M. J., Tosi, F., Castillo-Rogez, J. C., Capaccioni, F., Capria, M. T., Fonte, S., Giardino, M., Jaumann, R., Longobardo, A., Joy, S. P., Magni, G., McCord, T. B., McFadden, L. A., Palomba, E., Pieters, C. M., Polanskey, C. A., Rayman, M. D., Raymond, C. A., Schenk, P. M., Zambon, F., and Russell, C. T. (2016). Distribution of phyllosilicates on the surface of ceres. Science, 353:aaf4279.

Barkume, K. M., Brown, M. E., and Schaller, E. L. (2006). Water Ice on the Satellite of Kuiper Belt Object 2003 EL_{61}. ApJ, 640:L87–L89.

Barucci, M. A., Merlin, F., Guilbert, A., de Bergh, C., Alvarez-Candal, A., Hainaut, O. R., Doressoundiram, A., Dumas, C., Owen, T., and Coradini, A. (2008). Surface composition and temperature of the TNO Orcus. A&A, 479:L13–L16.

Batygin, K. and Brown, M. E. (2016). Evidence for a Distant Giant Planet in the Solar System. AJ, 151:22.

Bauer, J. M., Grav, T., Blauvelt, E., Mainzer, A. K., Masiero, J. R., Stevenson, R., Kramer, E., Fernández, Y. R., Lisse, C. M., Cutri, R. M., Weissman, P. R., Dailey, J. W., Masci, F. J., Walker, R., Waszczak, A., Nugent, C. R., Meech, K. J., Lucas, A., Pearman, G., Wilkins, A., Watkins, J., Kulkarni, S., Wright, E. L., WISE Team, and PTF Team (2013). Centaurs and Scattered Disk Objects in the Thermal Infrared: Analysis of WISE/NEOWISE Observations. ApJ, 773:22.

Bell, J. F., Davis, D. R., Hartmann, W. K., and Gaffey, M. J. (1989). Asteroids - The big picture. Asteroids II, pages 921–945.

Berthier, J., Carry, B., Vachier, F., Eggl, S., and Santerne, A. (2016). Prediction of transits of Solar system objects in Kepler/K2 images: an extension of the Virtual Observatory service SkyBoT. MNRAS, 458:3394–3398.

Berthier, J., Hestroffer, D., Carry, B., Vachier, F., Lainey, V., Emelyanov, N. V., Thuillot, W., Arlot, J.-E., and Ephemerides Service, I. (2009). Miriade: A Service for Solar Sytem Ojects Ephemerides in the VO Framework. In European Planetary Science Congress 2009, page 676.

Berthier, J., Vachier, F., Marchis, F., Ďurech, J., and Carry, B. (2014). Physical and dynamical properties of the main belt triple Asteroid (87) Sylvia. Icarus, 239:118–130.

Binzel, R. P. (2006). Definition of a planet: Prague 2006 IAU resolutions. Minor Planet Bulletin, 33:106–107.

Binzel, R. P., Gaffey, M. J., Thomas, P. C., Zellner, B. H., Storrs, A. D., and Wells, E. N. (1997). Geologic Mapping of Vesta from 1994 Hubble Space Telescope Images. Icarus, 128:95–103.

Binzel, R. P., Morbidelli, A., Merouane, S., DeMeo, F., Birlan, M., Vernazza, P., Thomas, C. A., Rivkin, A. S., Bus, S. J., and Tokunaga, A. T. (2010). Earth encounters as the origin of fresh surfaces on near-Earth asteroids. Nature, 463:331–334.

Binzel, R. P., Rivkin, A. S., Bus, S. J., Sunshine, J. M., and Burbine, T. H. (2001). MUSES-C target asteroid (25143) 1998 SF36: A reddened ordinary chondrite. Meteoritics and Planetary Science, 36:1167–1172.

Binzel, R. P., Rivkin, A. S., Stuart, J. S., Harris, A. W., Bus, S. J., and Burbine, T. H. (2004). Observed spectral properties of near-Earth objects: results for population distribution, source regions, and space weathering processes. Icarus, 170:259–294.

Binzel, R. P. and Xu, S. (1993). Chips off of Asteroid 4 Vesta: Evidence for the parent body of basaltic achondrite meteorites. Science, 260(5105):186–191.

Bockelée-Morvan, D., Debout, V., Erard, S., Leyrat, C., Capaccioni, F., Filacchione, G., Fougere, N., Drossart, P., Arnold, G., Combi, M., Schmitt, B., Crovisier, J., de Sanctis, M.-C., Encrenaz, T., Kührt, E., Palomba, E., Taylor, F. W., Tosi, F., Piccioni, G., Fink, U., Tozzi, G., Barucci, A., Biver, N., Capria, M.-T., Combes, M., Ip, W., Blecka, M., Henry, F., Jacquinod, S., Reess, J.-M., Semery, A., and Tiphene, D. (2015). First observations of H_2O and CO_2 vapor in comet 67P/Churyumov-Gerasimenko made by VIRTIS onboard Rosetta. A&A, 583:A6.

Bonnarel, F., Fernique, P., Bienaymé, O., Egret, D., Genova, F., Louys, M., Ochsenbein, F., Wenger, M., and Bartlett, J. G. (2000). The ALADIN interactive sky atlas. A reference tool for identification of astronomical sources. Astronomy & Astrophysics Supplement, 143:33–40.

Bottke, W. F., Durda, D. D., Nesvorný, D., Jedicke, R., Morbidelli, A., Vokrouhlický, D., and Levison, H. (2005). The fossilized size distribution of the main asteroid belt. Icarus, 175:111–140.

Bottke, W. F., Morbidelli, A., Jedicke, R., Petit, J.-M., Levison, H. F., Michel, P., and Metcalfe, T. S. (2002). Debiased Orbital and Absolute Magnitude Distribution of the Near-Earth Objects. Icarus, 156:399–433.

Bottke, W. F., Nesvorný, D., Vokrouhlický, D., and Morbidelli, A. (2010). The Irregular Satellites: The Most Collisionally Evolved Populations in the Solar System. AJ, 139:994–1014.

Bottke, W. F., Vokrouhlický, D., Minton, D., Nesvorný, D., Morbidelli, A., Brasser, R., Simonson, B., and Levison, H. F. (2012). An Archaean heavy bombardment from a destabilized extension of the asteroid belt. Nature, 485:78–81.

Brown, M. E., Barkume, K. M., Ragozzine, D., and Schaller, E. L. (2007). A collisional family of icy objects in the Kuiper Belt. Nature, 446:294–296.

Brown, M. E. and Calvin, W. M. (2000). Evidence for crystalline water and ammonia ices on pluto's satellite charon. Science, 287:107–109.

Brown, M. E., Ragozzine, D., Stansberry, J., and Fraser, W. C. (2010). The Size, Density, and Formation of the Orcus-Vanth System in the Kuiper Belt. AJ, 139:2700–2705.

Brown, M. E., van Dam, M. A., Bouchez, A. H., Le Mignant, D., Campbell, R. D., Chin, J. C. Y., Conrad, A. R., Hartman, S. K., Johansson, E. M., Lafon, R. E., Rabinowitz, D. L., Stomski Jr., P. J., Summers, D. M., Trujillo, C. A., and Wizinowich, P. L. (2006). Satellites of the Largest Kuiper Belt Objects. ApJ, 639:43–46.

Brown, R. H., Cruikshank, D. P., Pendleton, Y., and Veeder, G. J. (1998). Identification of Water Ice on the Centaur 1997 CU26. Science, 280:1430–1432.

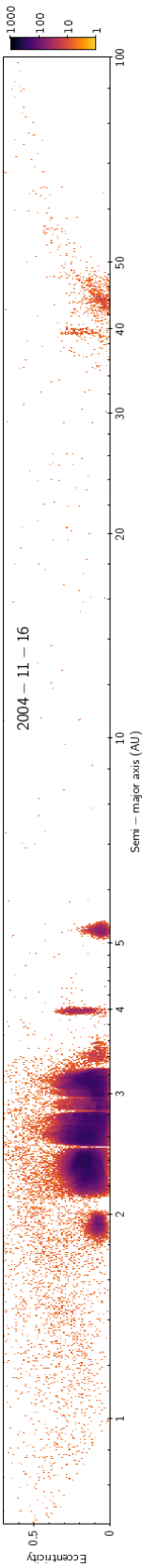

Brunetto, R., de León, J., and Licandro, J. (2007). Testing space weathering models on A-type asteroid (1951) Lick. A&A, 472:653–656.

Brunetto, R., Loeffler, M. J., Nesvorný, D., Sasaki, S., and Strazzulla, G. (2015). Asteroid Surface Alteration by Space Weathering Processes, pages 597–616.

Brunetto, R., Vernazza, P., Marchi, S., Birlan, M., Fulchignoni, M., Orofino, V., and Strazzulla, G. (2006). Modeling asteroid surfaces from observations and irradiation experiments: The case of 832 Karin. Icarus, 184:327–337.

Buie, M. W., Cruikshank, D. P., Lebofsky, L. A., and Tedesco, E. F. (1987). Water frost on charon. Nature, 329:522.

Buie, M. W. and Fink, U. (1987). Methane absorption variations in the spectrum of pluto. Icarus, 70:483–498.

Buie, M. W. and Grundy, W. M. (2000). The distribution and physical state of h $_2$o on charon. Icarus, 148:324–339.

Bus, S. J. and Binzel, R. P. (2002a). Phase II of the Small Main-Belt Asteroid Spectroscopic Survey: A Feature-Based Taxonomy. Icarus, 158:146–177.

Bus, S. J. and Binzel, R. P. (2002b). Phase II of the Small Main-Belt Asteroid Spectroscopic Survey: The Observations. Icarus, 158:106–145.

Campins, H., Hargrove, K., Pinilla-Alonso, N., Howell, E. S., Kelley, M. S., Licandro, J., Mothé-Diniz, T., Fernández, Y., and Ziffer, J. (2010). Water ice and organics on the surface of the asteroid 24 themis. Nature, 464:1320–1321.

Carry, B. (2009). Asteroids physical properties from high angular-resolution imaging. PhD thesis, Observatoire de Paris.

Carry, B. (2011). Shape models and densities of asteroids in the post-gaia era. In GREAT Workshop on Solar System Science before and after Gaia.

Carry, B. (2012). Density of asteroids. Planet. Space Sci., 73:98–118.

Carry, B. (2018). Solar system science with ESA Euclid. A&A, 609:A113.

Carry, B. and Berthier, J. (2016). A Simpler Procedure for Specifying Solar System Objects in Phase 2. The Messenger, 163:12–13.

Carry, B., Dumas, C., Fulchignoni, M., Merline, W. J., Berthier, J., Hestroffer, D., Fusco, T., and Tamblyn, P. (2008). Near-Infrared Mapping and Physical Properties of the Dwarf-Planet Ceres. A&A, 478(4):235–244.

Carry, B., Dumas, C., Kaasalainen, M., Berthier, J., Merline, W. J., Erard, S., Conrad, A. R., Drummond, J. D., Hestroffer, D., Fulchignoni, M., and Fusco, T. (2010a). Physical properties of (2) Pallas. Icarus, 205:460–472.

Carry, B., Hestroffer, D., DeMeo, F. E., Thirouin, A., Berthier, J., Lacerda, P., Sicardy, B., Doressoundiram, A., Dumas, C., Farrelly, D., and Müller, T. G. (2011). Integral-field spectroscopy of (90482) Orcus-Vanth. A&A, 534:A115.

Carry, B., Kaasalainen, M., Leyrat, C., Merline, W. J., Drummond, J. D., Conrad, A. R., Weaver, H. A., Tamblyn, P. M., Chapman, C. R., Dumas, C., Colas, F., Christou, J. C., Dotto, E., Perna, D., Fornasier, S., Bernasconi, L., Behrend, R., Vachier, F., Kryszczynska, A., Polinska, M., Fulchignoni, M., Roy, R., Naves, R., Poncy, R., and Wiggins, P. (2010b). Physical properties of the ESA Rosetta target asteroid (21) Lutetia. II. Shape and flyby geometry. A&A, 523:A94.

Carry, B., Kaasalainen, M., Merline, W. J., Müller, T. G., Jorda, L., Drummond, J. D., Berthier, J., O'Rourke, L., Ďurech, J., Küppers, M., Conrad, A. R., Dumas, C., Sierks, H., and the OSIRIS TeamPSS (2012a). Koala shape modeling technique validated at (21) lutetia by esa rosetta mission. Planet. Space Sci., 66:200–212.

Carry, B., Matter, A., Scheirich, P., Pravec, P., Molnar, L., Mottola, S., Carbognani, A., Jehin, E., Marciniak, A., Binzel, R. P., DeMeo, F., Birlan, M., Delbo, M., Barbotin, E., Behrend, R., Bonnardeau, M., Colas, F., Farissier, P., Fauvaud, M., Fauvaud, S., Gillier, C., Gillon, M., Hellmich, S., Hirsch, R., Leroy, A., Manfroid, J., Montier, J., Morelle, E., Richard, F., Sobkowiak, K., Strajnic, J., and Vachier, F. (2015). The small binary asteroid (939) Isberga. Icarus, 248:516–525.

Carry, B., Snodgrass, C., Lacerda, P., Hainaut, O., and Dumas, C. (2012b). Characterisation of candidate members of (136108) Haumea's family. II. Follow-up observations. A&A, 544:A137.

Carry, B., Solano, E., Eggl, S., and DeMeo, F. (2016). Spectral properties of near-Earth and Mars-crossing asteroids using Sloan photometry. Icarus, 268:340–354.

Carry, B., Vernazza, P., Dumas, C., and Fulchignoni, M. (2010c). First disk-resolved spectroscopy of (4) Vesta. Icarus, 205:473–482.

Carry, B., Vernazza, P., Dumas, C., Merline, W. J., Mousis, O., Rousselot, P., Jehin, E., Manfroid, J., Fulchignoni, M., and Zucconi, J.-M. (2012c). The remarkable surface homogeneity of the dawn mission target (1) ceres. Icarus, 217:20–26.

Carvano, J. M., Hasselmann, H., Lazzaro, D., and Mothé-Diniz, T. (2010). SDSS-based taxonomic classification and orbital distribution of main belt asteroids. A&A, 510:A43.

Cellino, A., Tanga, P., Dell'Oro, A., and Hestroffer, D. (2007). Asteroid science with Gaia: Sizes, spin properties, overall shapes and taxonomy. Advances in Space Research, 40:202–208.

Cellino, A., Zappala, V., and Farinella, P. (1989). Asteroid shapes and lightcurve morphology. Icarus, 78:298–310.

Chang, C.-K., Ip, W.-H., Lin, H.-W., Cheng, Y.-C., Ngeow, C.-C., Yang, T.-C., Waszczak, A., Kulkarni, S. R., Levitan, D., Sesar, B., Laher, R., Surace, J., and Prince, T. A. (2015). Asteroid spin-rate study using the intermediate palomar transient factory. ApJ, 219:27.

Chapman, C. R. (1996). S-Type Asteroids, Ordinary Chondrites, and Space Weathering: The Evidence from Galileo's Fly-bys of Gaspra and Ida. Meteoritics and Planetary Science, 31:699–725.

Chapman, C. R. (2004). Space Weathering of Asteroid Surfaces. Annual Review of Earth and Planetary Sciences, 32:539–567.

Chapman, C. R., Johnson, T. V., and McCord, T. B. (1971). A Review of Spectrophotometric Studies of Asteroids. NASA Special Publication, 267:51.

Chapman, C. R., Morrison, D., and Zellner, B. H. (1975). Surface properties of asteroids - A synthesis of polarimetry, radiometry, and spectrophotometry. Icarus, 25:104–130.

Chapman, C. R. and Salisbury, J. W. (1973). Comparisons of meteorite and asteroid spectral reflectivities. Icarus, 19:507–522.

Chapman, C. R., Veverka, J., Thomas, P. C., Klaasen, K., Belton, M. J. S., Harch, A., McEwen, A., Johnson, T. V., Helfenstein, P., Davies, M. E., Merline, W. J., and Denk, T. (1995). Discovery and physical properties of Dactyl, a satellite of asteroid 243 Ida. Nature, 374:783–785.

Combe, J.-P., McCord, T. B., Tosi, F., Ammannito, E., Carrozzo, F. G., De Sanctis, M. C., Raponi, A., Byrne, S., Landis, M. E., Hughson, K. H. G., Raymond, C. A., and Russell, C. T. (2016). Detection of local h_2o exposed at the surface of ceres. Science, 353:aaf3010.

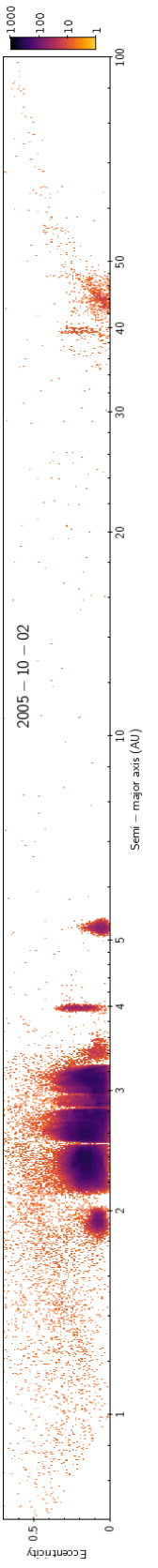

Conrad, A. R., Dumas, C., Merline, W. J., Drummond, J. D., Campbell, R. D., Goodrich, R. W., Le Mignant, D., Chaffee, F. H., Fusco, T., Kwok, S. H., and Knight, R. I. (2007). Direct measurement of the size, shape, and pole of 511 Davida with Keck AO in a single night. Icarus, 191(2):616–627.

Conrad, A. R., Keck Observatory, W. M., Merline, W. J., Drummond, J. D., Tamblyn, P. M., Dumas, C., Carry, B., Campbell, R. D., Goodrich, R. W., Owen, W. M., and Chapman, C. R. (2008). S/2008 (41) 1. IAU Circular, 8930:2–2.

Consolmagno, G., Britt, D., and Macke, R. (2008). The significance of meteorite density and porosity. Chemie der Erde / Geochemistry, 68:1–29.

Cook, J. C., Desch, S. J., Roush, T. L., Trujillo, C. A., and Geballe, T. R. (2007). Near-Infrared Spectroscopy of Charon: Possible Evidence for Cryovolcanism on Kuiper Belt Objects. ApJ, 663:1406–1419.

Cropper, M., Pottinger, S., Niemi, S.-M., Denniston, J., Cole, R., Szafraniec, M., Mellier, Y., Berthé, M., Martignac, J., Cara, C., di Giorgio, A. M., Sciortino, A., Paltani, S., Genolet, L., Fourmand, J.-J., Charra, M., Guttridge, P., Winter, B., Endicott, J., Holland, A., Gow, J., Murray, N., Hall, D., Amiaux, J., Laureijs, R., Racca, G., Salvignol, J.-C., Short, A., Lorenzo Alvarez, J., Kitching, T., Hoekstra, H., and Massey, R. (2014). VIS: the visible imager for Euclid. In Space Telescopes and Instrumentation 2014: Optical, Infrared, and Millimeter Wave, volume 9143 of SPIE, page 91430J.

de Bergh, C., Delsanti, A., Tozzi, G. P., Dotto, E., Doressoundiram, A., and Barucci, M. A. (2005). The surface of the transneptunian object 90482 Orcus. A&A, 437:1115–1120.

de Sanctis, M. C., Ammannito, E., Raponi, A., Marchi, S., McCord, T. B., McSween, H. Y., Capaccioni, F., Capria, M. T., Carrozzo, F. G., Ciarniello, M., Longobardo, A., Tosi, F., Fonte, S., Formisano, M., Frigeri, A., Giardino, M., Magni, G., Palomba, E., Turrini, D., Zambon, F., Combe, J.-P., Feldman, W., Jaumann, R., McFadden, L. A., Pieters, C. M., Prettyman, T., Toplis, M., Raymond, C. A., and Russell, C. T. (2015). Ammoniated phyllosilicates with a likely outer Solar System origin on (1) Ceres. Nature, 528:241–244.

de Sanctis, M. C., Raponi, A., Ammannito, E., Ciarniello, M., Toplis, M. J., McSween, H. Y., Castillo-Rogez, J. C., Ehlmann, B. L., Carrozzo, F. G., Marchi, S., Tosi, F., Zambon, F., Capaccioni, F., Capria, M. T., Fonte, S., Formisano, M., Frigeri, A., Giardino, M., Longobardo, A., Magni, G., Palomba, E., McFadden, L. A., Pieters, C. M., Jaumann, R., Schenk, P., Mugnuolo, R., Raymond, C. A., and Russell, C. T. (2016). Bright carbonate deposits as evidence of aqueous alteration on (1) ceres. Nature, 536:54–57.

Delbo, M., Gayon-Markt, J., Busso, G., Brown, A., Galluccio, L., Ordenovic, C., Bendjoya, P., and Tanga, P. (2012). Asteroid spectroscopy with Gaia. Planet. Space Sci., 73:86–94.

Delbo, M., Ligori, S., Matter, A., Cellino, A., and Berthier, J. (2009). First VLTI-MIDI Direct Determinations of Asteroid Sizes. ApJ, 694:1228–1236.

Delsanti, A., Merlin, F., Guilbert-Lepoutre, A., Bauer, J. M., Yang, B., and Meech, K. J. (2010). Methane, ammonia, and their irradiation products at the surface of an intermediate-size KBO?. A portrait of Plutino (90482) Orcus. A&A, 520:A40.

DeMeo, F., Binzel, R. P., Carry, B., Polishook, D., and Moskovitz, N. A. (2014a). Unexpected D-type interlopers in the inner main belt. Icarus, 229:392–399.

DeMeo, F., Binzel, R. P., and Lockhart, M. (2014b). Mars encounters cause fresh surfaces on some near-Earth asteroids. Icarus, 227:112–122.

DeMeo, F., Binzel, R. P., Slivan, S. M., and Bus, S. J. (2009a). An extension of the Bus asteroid taxonomy into the near-infrared. Icarus, 202:160–180.

DeMeo, F. and Carry, B. (2013). The taxonomic distribution of asteroids from multi-filter all-sky photometric surveys. Icarus, 226:723–741.

DeMeo, F. and Carry, B. (2014). Solar System evolution from compositional mapping of the asteroid belt. Nature, 505:629–634.

DeMeo, F., Carry, B., Polishook, D., Binzel, R., Burt, B., and Moskovitz, N. (2016). A search for differentiated fragments within asteroid families. In AAS/Division for Planetary Sciences Meeting Abstracts, volume 48 of AAS/Division for Planetary Sciences Meeting Abstracts, page 510.04.

DeMeo, F., Dumas, C., Cook, J. C., Carry, B., Merlin, F., Verbiscer, A. J., and Binzel, R. P. (2015). Spectral variability of Charon's 2.21-μm feature. Icarus, 246:213–219.

DeMeo, F. E., Carry, B., Marchis, F., Birlan, M., Binzel, R. P., Bus, S. J., Descamps, P., Nedelcu, A., Busch, M., and Bouy, H. (2011). A spectral comparison of (379) Huenna and its satellite. Icarus, 212:677–681.

DeMeo, F. E., Fornasier, S., Barucci, M. A., Perna, D., Protopapa, S., Alvarez-Candal, A., Delsanti, A., Doressoundiram, A., Merlin, F., and de Bergh, C. (2009b). Visible and near-infrared colors of Transneptunian objects and Centaurs from the second ESO large program. A&A, 493:283–290.

Dotto, E., Barucci, M. A., Müller, T. G., Brucato, J. R., Fulchignoni, M., Mennella, V., and Colangeli, L. (2002). ISO observations of low and moderate albedo asteroids. PHT-P and PHT-S results. A&A, 393:1065–1072.

Dotto, E., Müller, T. G., Barucci, M. A., Encrenaz, T., Knacke, R. F., Lellouch, E., Doressoundiram, A., Crovisier, J., Brucato, J. R., Colangeli, L., and Mennella, V. (2000). ISO results on bright Main Belt asteroids: PHT-S observations. A&A, 358:1133–1141.

Drummond, J. D., Carry, B., Merline, W. J., Dumas, C., Hammel, H., Erard, S., Conrad, A., Tamblyn, P., and Chapman, C. R. (2014). Dwarf planet Ceres: Ellipsoid dimensions and rotational pole from Keck and VLT adaptive optics images. Icarus, 236:28–37.

Drummond, J. D. and Cocke, W. J. (1989). Triaxial ellipsoid dimensions and rotational pole of 2 Pallas from two stellar occultations. Icarus, 78:323–329.

Drummond, J. D., Conrad, A., Merline, W. J., Carry, B., Chapman, C. R., Weaver, H. A., Tamblyn, P. M., Christou, J. C., and Dumas, C. (2010). Physical properties of the ESA Rosetta target asteroid (21) Lutetia. I. The triaxial ellipsoid dimensions, rotational pole, and bulk density. A&A, 523:A93.

Drummond, J. D., Fugate, R. Q., Christou, J. C., and Hege, E. K. (1998). Full Adaptive Optics Images of Asteroids Ceres and Vesta; Rotational Poles and Triaxial Ellipsoid Dimensions. Icarus, 132:80–99.

Duffard, R., Ortiz, J. L., Thirouin, A., Santos-Sanz, P., and Morales, N. (2009). Transneptunian objects and Centaurs from light curves. A&A, 505:1283–1295.

Dumas, C., Carry, B., Hestroffer, D., and Merlin, F. (2011). High-contrast observations of (136108) Haumea. A crystalline water-ice multiple system. A&A, 528:A105.

Dumas, C., Terrile, R. J., Brown, R. H., Schneider, G., and Smith, B. A. (2001). Hubble space telescope nicmos spectroscopy of charon's leading and trailing hemispheres. AJ, 121:1163–1170.

Dunham, D. W., Herald, D., Frappa, E., Hayamizu, T., Talbot, J., and Timerson, B. (2017). Asteroid Occultations. NASA Planetary Data System. EAR-A-3-RDR-OCCULTATIONS-V15.0.

Durda, D. D., Bottke, W. F., Enke, B. L., Merline, W. J., Asphaug, E., Richardson, D. C., and Leinhardt, Z. M. (2004). The formation of asteroid satellites in large impacts: results from numerical simulations. Icarus, 170:243–257.

Edgeworth, K. E. (1949). The origin and evolution of the Solar System. MNRAS, 109:600–609.

Elkins-Tanton, L. T., Weiss, B. P., and Zuber, M. T. (2011). Chondrites as samples of differentiated planetesimals. Earth and Planetary Science Letters, 305:1–10.

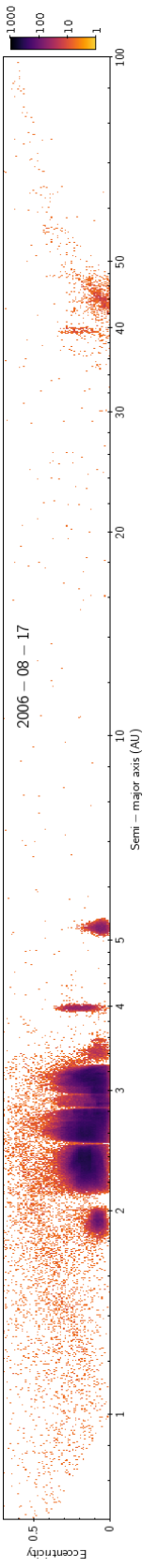

Emery, J. P., Cruikshank, D. P., and van Cleve, J. (2006). Thermal emission spectroscopy (5.2 38 μm) of three Trojan asteroids with the Spitzer Space Telescope: Detection of fine-grained silicates. Icarus, 182:496–512.

Epchtein, N., de Batz, B., Copet, E., Fouque, P., Lacombe, F., Le Bertre, T., Mamon, G., Rouan, D., Tiphene, D., Burton, W. B., Deul, E., Habing, H., Boersenberger, J., Dennefeld, M., Omont, A., Renault, J. C., Rocca-Volmerange, B., Kimeswenger, S., Appenzeller, I., Bender, R., Forveille, T., Garzon, F., Hron, J., Persi, P., Ferrari-Toniolo, M., and Vauglin, I. (1994). DENIS: A Deep Near-Infrared Survey of the southern sky. Astrophysics and Space Science, 217:3–9.

Fabrycky, D. C., Ragozzine, D., Brown, M. E., and Holman, M. J. (2008). Mutual Events of (136108) 2003 EL_61 and S/2005 (136108) 2. IAU Circular, 8949.

Feierberg, M. A., Lebofsky, L. A., and Larson, H. P. (1980). Spectroscopic evidence for aqueous alteration products on the surfaces of low-albedo asteroids. Geochimica et Cosmochimica Acta, 45:971–981.

Fienga, A., Laskar, J., Manche, H., and Gastineau, M. (2016). Constraints on the location of a possible 9th planet derived from the Cassini data. A&A, 587:L8.

Fischer, H. (1941). Farbmessungen an Kleinen Planeten. Astronomische Nachrichten, 272:127.

Fulchignoni, M., Belskaya, I., Barucci, M. A., De Sanctis, M. C., and Doressoundiram, A. (2008). Transneptunian Object Taxonomy. The Solar System Beyond Neptune, pages 181–192.

Fulvio, D., Brunetto, R., Vernazza, P., and Strazzulla, G. (2012). Space weathering of vesta and v-type asteroids: new irradiation experiments on hed meteorites. A&A, 537:L11.

Gaffey, M. J. (1997). Surface Lithologic Heterogeneity of Asteroid 4 Vesta. Icarus, 127:130–157.

Gaia Collaboration, Prusti, T., de Bruijne, J. H. J., Brown, A. G. A., Vallenari, A., Babusiaux, C., Bailer-Jones, C. A. L., Bastian, U., Biermann, M., Evans, D. W., and et al. (2016). The Gaia mission. A&A, 595:A1.

Gehrels, T. (1967). Minor planets. I. The rotation of Vesta. AJ, 72:929.

Gil-Hutton, R. and Brunini, A. (2008). Surface composition of Hilda asteroids from the analysis of the Sloan Digital Sky Survey colors. Icarus, 193:567–571.

Gladman, B., Marsden, B. G., and Vanlaerhoven, C. (2008). Nomenclature in the Outer Solar System, pages 43–57. Univ. Arizona Press.

Gladman, B. J., Davis, D. R., Neese, C., Jedicke, R., Williams, G., Kavelaars, J. J., Petit, J.-M., Scholl, H., Holman, M., Warrington, B., Esquerdo, G., and Tricarico, P. (2009). On the asteroid belt's orbital and size distribution. Icarus, 202:104–118.

Gomes, R., Levison, H. F., Tsiganis, K., and Morbidelli, A. (2005). Origin of the cataclysmic Late Heavy Bombardment period of the terrestrial planets. Nature, 435:466–469.

Gourgeot, F., Carry, B., Dumas, C., Vachier, F., Merlin, F., Lacerda, P., Barucci, M. A., and Berthier, J. (2016). Near-infrared spatially resolved spectroscopy of (136108) Haumea's multiple system. A&A, 593:A19.

Gradie, J. and Tedesco, E. F. (1982). Compositional structure of the asteroid belt. Science, 216:1405–1407.

Gradie, J. C., Chapman, C. R., and Tedesco, E. F. (1989). Distribution of taxonomic classes and the compositional structure of the asteroid belt. Asteroids II, pages 316–335.

Granvik, M., Morbidelli, A., Jedicke, R., Bolin, B., Bottke, W. F., Beshore, E., Vokrouhlický, D., Delbò, M., and Michel, P. (2016). Super-catastrophic disruption of asteroids at small perihelion distances. Nature, 530:303–306.

Grav, T., Mainzer, A. K., Bauer, J., Masiero, J., Spahr, T., McMillan, R. S., Walker, R., Cutri, R., Wright, E., Eisenhardt, P. R., Blauvelt, E., DeBaun, E., Elsbury, D., Gautier, T., Gomillion, S., Hand, E., and Wilkins, A. (2012). WISE/NEOWISE Observations of the Hilda Population: Preliminary Results. ApJ, 744:197.

Grav, T., Mainzer, A. K., Bauer, J., Masiero, J., Spahr, T., McMillan, R. S., Walker, R., Cutri, R., Wright, E., Eisenhardt, P. R. M., Blauvelt, E., DeBaun, E., Elsbury, D., Gautier, IV, T., Gomillion, S., Hand, E., and Wilkins, A. (2011). WISE/NEOWISE Observations of the Jovian Trojans: Preliminary Results. ApJ, 742:40.

Grav, T., Mainzer, A. K., Bauer, J. M., Masiero, J. R., and Nugent, C. R. (2012). WISE/NEOWISE Observations of the Jovian Trojan Population: Taxonomy. ApJ, 759:49.

Graves, K., Minton, D., Hirabayashi, M., DeMeo, F., and Carry, B. (2018). Resurfacing asteroids from yorp spin-up and failure. Icarus, 304:162–171.

Graves, K., Minton, D. A., Hirabayashi, M., Carry, B., and DeMeo, F. E. (2016). Size and perihelion distribution of s and q-type asteroid spectral slopes from the near earth region through the main belt. In AAS/Division for Planetary Sciences Meeting Abstracts, volume 48 of AAS/Division for Planetary Sciences Meeting Abstracts, page 510.09.

Greenstreet, S., Ngo, H., and Gladman, B. (2012). The orbital distribution of Near-Earth Objects inside Earth's orbit. Icarus, 217:355–366.

Grice, J., Snodgrass, C., Green, S., Parley, N., and Carry, B. (2017). The shapes of primordial asteroids. Asteroids, Comets, and Meteors: ACM 2017.

Grundy, W. M., Binzel, R. P., Buratti, B. J., Cook, J. C., Cruikshank, D. P., Dalle Ore, C. M., Earle, A. M., Ennico, K., Howett, C. J. A., Lunsford, A. W., Olkin, C. B., Parker, A. H., Philippe, S., Protopapa, S., Quirico, E., Reuter, D. C., Schmitt, B., Singer, K. N., Verbiscer, A. J., Beyer, R. A., Buie, M. W., Cheng, A. F., Jennings, D. E., Linscott, I. R., Parker, J. W., Schenk, P. M., Spencer, J. R., Stansberry, J. A., Stern, S. A., Throop, H. B., Tsang, C. C. C., Weaver, H. A., Weigle, G. E., and Young, L. A. (2016). Surface compositions across pluto and charon. Science, 351:aad9189.

Halley, E. (1705). Astronomiae cometicae synopsis.

Hanuš, J., Ďurech, J., Brož, M., Warner, B. D., Pilcher, F., Stephens, R., Oey, J., Bernasconi, L., Casulli, S., Behrend, R., Polishook, D., Henych, T., Lehký, M., Yoshida, F., and Ito, T. (2011). A study of asteroid pole-latitude distribution based on an extended set of shape models derived by the lightcurve inversion method. A&A, 530:A134.

Hanuš, J. and Ďurech, J. (2012). The potential of sparse photometric data in asteroid shape modeling. Planet. Space Sci., 73:75–79.

Hanuš, J., Ďurech, J., Brož, M., Marciniak, A., Warner, B. D., Pilcher, F., Stephens, R., Behrend, R., Carry, B., Čapek, D., Antonini, P., Audejean, M., Augustesen, K., Barbotin, E., Baudouin, P., Bayol, A., Bernasconi, L., Borczyk, W., Bosch, J.-G., Brochard, E., Brunetto, L., Casulli, S., Cazenave, A., Charbonnel, S., Christophe, B., Colas, F., Coloma, J., Conjat, M., Cooney, W., Correira, H., Cotrez, V., Coupier, A., Crippa, R., Cristofanelli, M., Dalmas, C., Danavaro, C., Demeautis, C., Droege, T., Durkee, R., Esseiva, N., Esteban, M., Fagas, M., Farroni, G., Fauvaud, M., Fauvaud, S., Del Freo, F., Garcia, L., Geier, S., Godon, C., Grangeon, K., Hamanowa, H., Hamanowa, H., Heck, N., Hellmich, S., Higgins, D., Hirsch, R., Husarik, M., Itkonen, T., Jade, O., Kamiński, K., Kankiewicz, P., Klotz, A., Koff, R. A., Kryszczyńska, A., Kwiatkowski, T., Laffont, A., Leroy, A., Lecacheux, J., Leonie, Y., Leyrat, C., Manzini, F., Martin, A., Masi, G., Matter, D., Michałowski, J., Michałowski, M. J., Michałowski, T., Michelet, J., Michelsen, R., Morelle, E., Mottola, S., Naves, R., Nomen, J., Oey, J., Ogłoza, W., Oksanen, A., Oszkiewicz, D., Pääkkönen, P., Paiella, M., Pallares, H., Paulo, J., Pavic, M., Payet, B., Polińska, M., Polishook, D., Poncy, R., Revaz, Y., Rinner, C., Rocca, M., Roche, A., Romeuf, D., Roy, R., Saguin, H., Salom, P. A., Sanchez, S., Santacana, G., Santana-Ros, T., Sareyan,

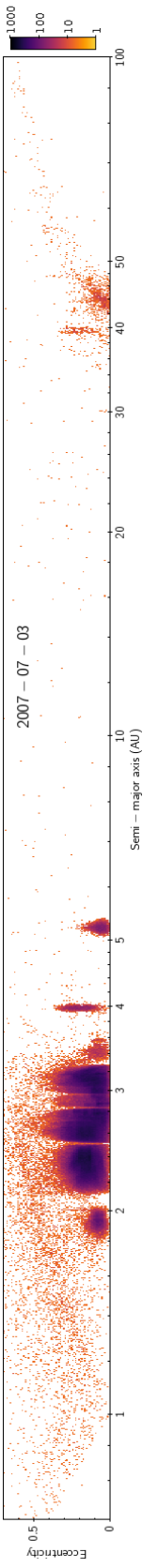

J.-P., Sobkowiak, K., Sposetti, S., Starkey, D., Stoss, R., Strajnic, J., Teng, J.-P., Trégon, B., Vagnozzi, A., Velichko, F. P., Waelchli, N., Wagrez, K., and Wücher, H. (2013). Asteroids' physical models from combined dense and sparse photometry and scaling of the YORP effect by the observed obliquity distribution. A&A, 551:A67.

Hanuš, J., Ďurech, J., Oszkiewicz, D. A., Behrend, R., Carry, B., Delbo, M., Adam, O., Afonina, V., Anquetin, R., Antonini, P., Arnold, L., Audejean, M., Aurard, P., Bachschmidt, M., Baduel, B., Barbotin, E., Barroy, P., Baudouin, P., Berard, L., Berger, N., Bernasconi, L., Bosch, J.-G., Bouley, S., Bozhinova, I., Brinsfield, J., Brunetto, L., Canaud, G., Caron, J., Carrier, F., Casalnuovo, G., Casulli, S., Cerda, M., Chalamet, L., Charbonnel, S., Chinaglia, B., Cikota, A., Colas, F., Coliac, J.-F., Collet, A., Coloma, J., Conjat, M., Conseil, E., Costa, R., Crippa, R., Cristofanelli, M., Damerdji, Y., Debackère, A., Decock, A., Déhais, Q., Déléage, T., Delmelle, S., Demeautis, C., Dróżdż, M., Dubos, G., Dulcamara, T., Dumont, M., Durkee, R., Dymock, R., Escalante del Valle, A., Esseiva, N., Esseiva, R., Esteban, M., Fauchez, T., Fauerbach, M., Fauvaud, M., Fauvaud, S., Forné, E., Fournel, C., Fradet, D., Garlitz, J., Gerteis, O., Gillier, C., Gillon, M., Giraud, R., Godard, J.-P., Goncalves, R., Hamanowa, H., Hamanowa, H., Hay, K., Hellmich, S., Heterier, S., Higgins, D., Hirsch, R., Hodosan, G., Hren, M., Hygate, A., Innocent, N., Jacquinot, H., Jawahar, S., Jehin, E., Jerosimic, L., Klotz, A., Koff, W., Korlevic, P., Kosturkiewicz, E., Krafft, P., Krugly, Y., Kugel, F., Labrevoir, O., Lecacheux, J., Lehký, M., Leroy, A., Lesquerbault, B., Lopez-Gonzales, M. J., Lutz, M., Mallecot, B., Manfroid, J., Manzini, F., Marciniak, A., Martin, A., Modave, B., Montaigut, R., Montier, J., Morelle, E., Morton, B., Mottola, S., Naves, R., Nomen, J., Oey, J., Ogłoza, W., Paiella, M., Pallares, H., Peyrot, A., Pilcher, F., Pirenne, J.-F., Piron, P., Polińska, M., Polotto, M., Poncy, R., Previt, J. P., Reignier, F., Renauld, D., Ricci, D., Richard, F., Rinner, C., Risoldi, V., Robilliard, D., Romeuf, D., Rousseau, G., Roy, R., Ruthroff, J., Salom, P. A., Salvador, L., Sanchez, S., Santana-Ros, T., Scholz, A., Séné, G., Skiff, B., Sobkowiak, K., Sogorb, P., Soldán, F., Spiridakis, A., Splanska, E., Sposetti, S., Starkey, D., Stephens, R., Stiepen, A., Stoss, R., Strajnic, J., Teng, J.-P., Tumolo, G., Vagnozzi, A., Vanoutryve, B., Vugnon, J. M., Warner, B. D., Waucomont, M., Wertz, O., Winiarski, M., and Wolf, M. (2016). New and updated convex shape models of asteroids based on optical data from a large collaboration network. A&A, 586:A108.

Harris, A. W. and D'Abramo, G. (2015). The population of near-Earth asteroids. Icarus, 257:302–312.

Hestroffer, D. and VLT/TNB Team (2010). Orbits of trans-neptunian binaries with the eso vlt. In AAS/Division of Dynamical Astronomy Meeting #41, volume 42 of Bulletin of the American Astronomical Society, page 936.

Hirayama, K. (1918). Groups of asteroids probably of common origin. AJ, 31:185–188.

Holler, B. J., Young, L. A., Buie, M. W., Grundy, W. M., Lyke, J. E., Young, E. F., and Roe, H. G. (2017). Measuring temperature and ammonia hydrate ice on charon in 2015 from keck/osiris spectra. Icarus, 284:394–406.

Hong, M. J. and Merlin, F. (2016). Photométrie et spectroscopie des objets trans-neptuniens. Technical report, LESIA-Observatoire de Paris, CNRS, UPMC Univ Paris 06, Université Denis Diderot, Sorbonne Paris Cité.

Housen, K. R., Holsapple, K. A., and Voss, M. E. (1999). Compaction as the origin of the unusual craters on the asteroid Mathilde. Nature, 402:155–157.

Hsieh, H. H. and Jewitt, D. (2006). A population of comets in the main asteroid belt. Science, 312:561–563.

Huang, J., Ji, J., Ye, P., Wang, X., Yan, J., Meng, L., Wang, S., Li, C., Li, Y., Qiao, D., Zhao, W., Zhao, Y., Zhang, T., Liu, P., Jiang, Y., Rao, W., Li, S., Huang, C., Ip, W.-H., Hu, S., Zhu, M., Yu, L., Zou, Y., Tang, X., Li, J., Zhao, H., Huang, H., Jiang, X., and Bai, J. (2013). The Ginger-shaped Asteroid 4179 Toutatis: New Observations from a Successful Flyby of Chang'e-2. Scientific Reports, 3:3411.

Ivezić, Ž., Tabachnik, S., Rafikov, R., Lupton, R. H., Quinn, T., Hammergren, M., Eyer, L., Chu, J., Armstrong, J. C., Fan, X., Finlator, K., Geballe, T. R., Gunn, J. E., Hennessy, G. S., Knapp, G. R., Leggett, S. K., Munn, J. A., Pier, J. R., Rockosi, C. M., Schneider, D. P., Strauss, M. A., Yanny, B., Brinkmann, J., Csabai, I., Hindsley, R. B., Kent, S., Lamb, D. Q., Margon, B., McKay, T. A., Smith, J. A., Waddel, P., York, D. G., and the SDSS Collaboration (2001). Solar System Objects Observed in the Sloan Digital Sky Survey Commissioning Data. AJ, 122:2749–2784.

Jewitt, D., Hsieh, H., and Agarwal, J. (2015). The Active Asteroids, pages 221–241. Univ. Arizona Press.

Jewitt, D. and Luu, J. (1993). Discovery of the candidate Kuiper belt object 1992 QB1. Nature, 362:730–732.

Jewitt, D. C., Trujillo, C. A., and Luu, J. X. (2000). Population and Size Distribution of Small Jovian Trojan Asteroids. AJ, 120:1140–1147.

Jones, T. D., Lebofsky, L. A., Lewis, J. S., and Marley, M. S. (1990). The composition and Origin of the C,P and D Asteroids: Water as Tracer of Thermal Evolution in the Outer Belt. Icarus, 88:172–193.

Kaasalainen, M. (2004). Physical models of large number of asteroids from calibrated photometry sparse in time. A&A, 422:L39–L42.

Kaasalainen, M. (2011). Maximum compatibility estimates and shape reconstruction with boundary curves and volumes of generalized projections. Inverse Problems and Imaging, 5(1):37–57.

Kaasalainen, M. and Lamberg, L. (2006). Inverse problems of generalized projection operators. Inverse Problems, 22:749–769.

Kaasalainen, M., Mottola, S., and Fulchignoni, M. (2002a). Asteroid Models from Disk-integrated Data. Asteroids III, pages 139–150.

Kaasalainen, M. and Torppa, J. (2001). Optimization Methods for Asteroid Lightcurve Inversion - I. Shape Determination. Icarus, 153:24–36.

Kaasalainen, M., Torppa, J., and Muinonen, K. (2001). Optimization Methods for Asteroid Lightcurve Inversion - II. The Complete Inverse Problem. Icarus, 153:37–51.

Kaasalainen, M., Torppa, J., and Piironen, J. (2002b). Models of Twenty Asteroids from Photometric Data. Icarus, 159:369–395.

Kaasalainen, S., Kaasalainen, M., and Piironen, J. (2005). Ground reference for space remote sensing. Laboratory photometry of an asteroid model. A&A, 440:1177–1182.

King, T. V., Clark, R. N., Calvin, W. M., Sherman, D. M., and Brown, R. H. (1992). Evidence for ammonium-bearing minerals on Ceres. Science, 255:1551–1553.

Kirkwood, D. (1869). On the Nebular Hypothesis, and the Approximate Commensurability of the Planetary Periods. MNRAS, 29:96–102.

Kuchynka, P. and Folkner, W. M. (2013). A new approach to determining asteroid masses from planetary range measurements. Icarus, 222:243–253.

Kuiper, G. P. (1951). On the Origin of the Solar System. Proceedings of the National Academy of Science, 37:1–14.

Küppers, M., O'Rourke, L., Bockelée-Morvan, D., Zakharov, V., Lee, S., von Allmen, P., Carry, B., Teyssier, D., Marston, A., Müller, T., Crovisier, J., Barucci, M. A., and Moreno, R. (2014). Localized sources of water vapour on the dwarf planet (1)Ceres. Nature, 505:525–527.

Lacerda, P. (2009). Time-Resolved Near-Infrared Photometry of Extreme Kuiper Belt Object Haumea. AJ, 137:3404–3413.

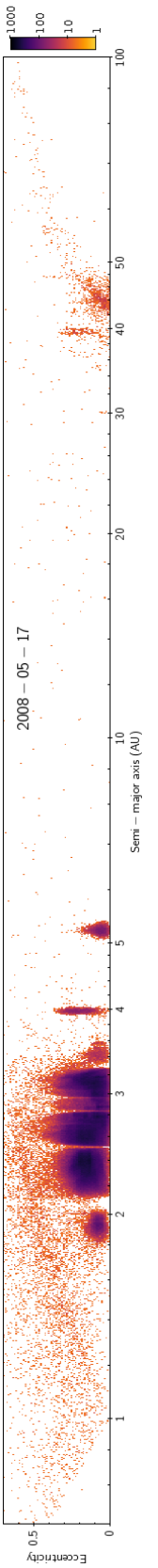

Lacerda, P. and Jewitt, D. C. (2007). Densities of solar system objects from their rotational light curves. AJ, 133:1393–1408.

Lacerda, P., Jewitt, D. C., and Peixinho, N. (2008). High-Precision Photometry of Extreme Kbo 2003 EL_{61}. AJ, 135:1749–1756.

Lagerkvist, C.-I., Erikson, A., Debehogne, H., Festin, L., Magnusson, P., Mottola, S., Oja, T., de Angelis, G., Belskaya, I. N., Dahlgren, M., Gonano-Beurer, M., Lagerros, J. S. V., Lumme, K., and Pohjolainen, S. (1995). Physical studies of asteroids. XXIX. Photometry and analysis of 27 asteroids. A&A, 113:115–129.

Laureijs, R., Amiaux, J., Arduini, S., Augueres, J. ., Brinchmann, J., Cole, R., Cropper, M., Dabin, C., Duvet, L., Ealet, A., and et al. (2011). Euclid Definition Study Report. ArXiv e-prints.

Laver, C., de Pater, I., Marchis, F., Ádámkovics, M., and Wong, M. H. (2009). Component-resolved near-infrared spectra of the (22) kalliope system. Icarus, 204:574–579.

Lazzaro, D., Angeli, C. A., Carvano, J. M., Mothé-Diniz, T., Duffard, R., and Florczak, M. (2004). S^3OS^2: the visible spectroscopic survey of 820 asteroids. Icarus, 172:179–220.

Lebofsky, L. A. (1978). Asteroid 1 Ceres - Evidence for water of hydration. MNRAS, 182:17–21.

Leinhardt, Z. M., Marcus, R. A., and Stewart, S. T. (2010). The Formation of the Collisional Family Around the Dwarf Planet Haumea. ApJ, 714:1789–1799.

Lellouch, E., Kiss, C., Santos-Sanz, P., Müller, T. G., Fornasier, S., Groussin, O., Lacerda, P., Ortiz, J. L., Thirouin, A., Delsanti, A., Duffard, R., Harris, A. W., Henry, F., Lim, T., Moreno, R., Mommert, M., Mueller, M., Protopapa, S., Stansberry, J., Trilling, D., Vilenius, E., Barucci, A., Crovisier, J., Doressoundiram, A., Dotto, E., Gutiérrez, P. J., Hainaut, O. R., Hartogh, P., Hestroffer, D., Horner, J., Jorda, L., Kidger, M., Lara, L. M., Rengel, M., Swinyard, B. M., and Thomas, N. (2010). TNOs are Cool': A survey of the trans-Neptunian region. II. The thermal lightcurve of (136108) Haumea. A&A, 518:L147.

Levison, H. F., Bottke, W. F., Gounelle, M., Morbidelli, A., Nesvorný, D., and Tsiganis, K. (2009). Contamination of the asteroid belt by primordial trans-Neptunian objects. Nature, 460:364–366.

Levison, H. F., Morbidelli, A., Vokrouhlický, D., and Bottke, Jr., W. F. (2008). On a Scattered-Disk Origin for the 2003 EL_{61} Collisional Family - An Example of the Importance of Collisions on the Dynamics of Small Bodies. AJ, 136:1079–1088.

Li, J.-Y., McFadden, L. A., Parker, J. W., Young, E. F., Stern, S. A., Thomas, P. C., Russell, C. T., and Sykes, M. V. (2006). Photometric analysis of 1 Ceres and surface mapping from HST observations. Icarus, 182:143–160.

Licandro, J., Campins, H., Kelley, M., Hargrove, K., Pinilla-Alonso, N., Cruikshank, D., Rivkin, A. S., and Emery, J. (2011). (65) Cybele: detection of small silicate grains, water-ice, and organics. A&A, 525:A34.

Lim, L. F., McConnochie, T. H., Bell, J. F., and Hayward, T. L. (2005). Thermal infrared (8-13 μm) spectra of 29 asteroids: the Cornell Mid-Infrared Asteroid Spectroscopy (MIDAS) Survey. Icarus, 173:385–408.

Lim, T. L., Stansberry, J., Müller, T. G., Mueller, M., Lellouch, E., Kiss, C., Santos-Sanz, P., Vilenius, E., Protopapa, S., Moreno, R., Delsanti, A., Duffard, R., Fornasier, S., Groussin, O., Harris, A. W., Henry, F., Horner, J., Lacerda, P., Mommert, M., Ortiz, J. L., Rengel, M., Thirouin, A., Trilling, D., Barucci, A., Crovisier, J., Doressoundiram, A., Dotto, E., Gutiérrez Buenestado, P. J., Hainaut, O. R., Hartogh, P., Hestroffer, D., Kidger, M., Lara, L. M., Swinyard, B. M., and Thomas, N. (2010). TNOs are Cool: A survey of the trans-Neptunian region . III. Thermophysical properties of 90482 Orcus and 136472 Makemake. A&A, 518:L148.

LSST Science Collaboration, Abell, P. A., Allison, J., Anderson, S. F., Andrew, J. R., Angel, J. R. P., Armus, L., Arnett, D., Asztalos, S. J., Axelrod, T. S., and et al. (2009). LSST Science Book, Version 2.0. ArXiv e-prints.

Maciaszek, T., Ealet, A., Jahnke, K., Prieto, E., Barbier, R., Mellier, Y., Costille, A., Ducret, F., Fabron, C., Gimenez, J.-L., Grange, R., Martin, L., Rossin, C., Pamplona, T., Vola, P., Clémens, J. C., Smadja, G., Amiaux, J., Barrière, J. C., Berthe, M., De Rosa, A., Franceschi, E., Morgante, G., Trifoglio, M., Valenziano, L., Bonoli, C., Bortoletto, F., D'Alessandro, M., Corcione, L., Ligori, S., Garilli, B., Riva, M., Grupp, F., Vogel, C., Hormuth, F., Seidel, G., Wachter, S., Diaz, J. J., Grañena, F., Padilla, C., Toledo, R., Lilje, P. B., Solheim, B. G. B., Toulouse-Aastrup, C., Andersen, M., Holmes, W., Israelsson, U., Seiffert, M., Weber, C., Waczynski, A., Laureijs, R. J., Racca, G., Salvignol, J.-C., and Strada, P. (2014). Euclid near infrared spectrophotometer instrument concept and first test results at the end of phase B. In Space Telescopes and Instrumentation 2014: Optical, Infrared, and Millimeter Wave, volume 9143 of SPIE, page 91430K.

Magnusson, P., Barucci, M. A., Drummond, J. D., Lumme, K., and Ostro, S. J. (1989). Determination of pole orientations and shapes of asteroids. Asteroids II, pages 67–97.

Mainzer, A., Bauer, J., Grav, T., Masiero, J., Cutri, R. M., Wright, E., Nugent, C. R., Stevenson, R., Clyne, E., Cukrov, G., and Masci, F. (2014). The Population of Tiny Near-Earth Objects Observed by NEOWISE. ApJ, 784:110.

Mainzer, A., Grav, T., Bauer, J., Masiero, J., McMillan, R. S., Cutri, R. M., Walker, R., Wright, E., Eisenhardt, P., Tholen, D. J., Spahr, T., Jedicke, R., Denneau, L., DeBaun, E., Elsbury, D., Gautier, T., Gomillion, S., Hand, E., Mo, W., Watkins, J., Wilkins, A., Bryngelson, G. L., Del Pino Molina, A., Desai, S., Gómez Camus, M., Hidalgo, S. L., Konstantopoulos, I., Larsen, J. A., Maleszewski, C., Malkan, M. A., Mauduit, J.-C., Mullan, B. L., Olszewski, E. W., Pforr, J., Saro, A., Scotti, J. V., and Wasserman, L. H. (2011). NEOWISE Observations of Near-Earth Objects: Preliminary Results. ApJ, 743:156.

Mainzer, A., Grav, T., Masiero, J., Bauer, J., Cutri, R. M., McMillan, R. S., Nugent, C. R., Tholen, D., Walker, R., and Wright, E. L. (2012). Physical Parameters of Asteroids Estimated from the WISE 3-Band Data and NEOWISE Post-Cryogenic Survey. ApJ, 760:L12.

Marchis, F., Descamps, P., Baek, M., Harris, A. W., Kaasalainen, M., Berthier, J., Hestroffer, D., and Vachier, F. (2008). Main belt binary asteroidal systems with circular mutual orbits. Icarus, 196(1):97–118.

Marchis, F., Descamps, P., Hestroffer, D., and Berthier, J. (2005). Discovery of the triple asteroidal system 87 Sylvia. Nature, 436:822–824.

Marchis, F., Enriquez, J. E., Emery, J. P., Berthier, J., Descamps, P., and Vachier, F. (2011). The origin of (90) antiope from component-resolved near-infrared spectroscopy. Icarus, 213:252–264.

Marchis, F., Hestroffer, D., Descamps, P., Berthier, J., Bouchez, A. H., Campbell, R. D., Chin, J. C. Y., van Dam, M. A., Hartman, S. K., Johansson, E. M., Lafon, R. E., Le Mignant, D., de Pater, I., Stomski Jr., P. J., Summers, D. M., Vachier, F., Wizinowich, P. L., and Wong, M. H. (2006). A low density of 0.8gcm-3 for the Trojan binary asteroid 617 Patroclus. Nature, 439:565–567.

Marcus, R. A., Ragozzine, D., Murray-Clay, R. A., and Holman, M. J. (2011). Identifying Collisional Families in the Kuiper Belt. ApJ, 733:40.

Margot, J. L., Nolan, M. C., Benner, L. A. M., Ostro, S. J., Jurgens, R. F., Slade, M. A., Giorgini, J. D., and Campbell, D. B. (2000). Satellites of minor planets. IAU Circular, 7503.

Margot, J.-L., Pravec, P., Taylor, P., Carry, B., and Jacobson, S. (2015). Asteroid Systems: Binaries, Triples, and Pairs, pages 355–374. Univ. Arizona Press.

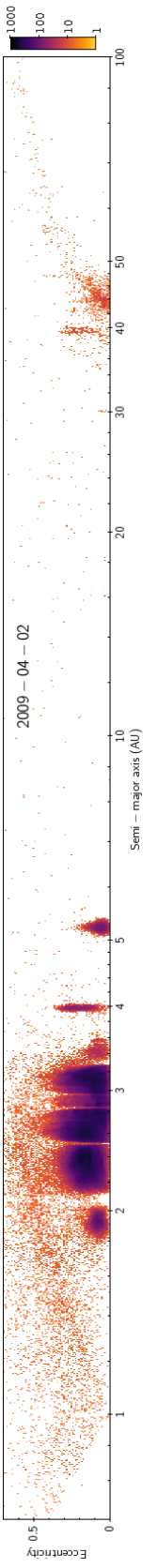

Marsset, M., Carry, B., Dumas, C., Hanuš, J., Viikinkoski, M., Vernazza, P., Müller, T. G., Delbo, M., Jehin, E., Gillon, M., Grice, J., Yang, B., Fusco, T., Berthier, J., Sonnett, S., Kugel, F., Caron, J., and Behrend, R. (2017). 3D shape of asteroid (6) Hebe from VLT/SPHERE imaging: Implications for the origin of ordinary H chondrites. A&A, 604:A64.

Marsset, M., Carry, B., Yang, B., Marchis, F., Vernazza, P., Dumas, C., Berthier, J., and Vachier, F. (2016). S/2016 (107) 1. IAU Circular, 9282.

Masiero, J. R., Mainzer, A. K., Grav, T., Bauer, J. M., Cutri, R. M., Dailey, J., Eisenhardt, P. R. M., McMillan, R. S., Spahr, T. B., Skrutskie, M. F., Tholen, D., Walker, R. G., Wright, E. L., DeBaun, E., Elsbury, D., Gautier, IV, T., Gomillion, S., and Wilkins, A. (2011). Main Belt Asteroids with WISE/NEOWISE. I. Preliminary Albedos and Diameters. ApJ, 741:68.

Masiero, J. R., Mainzer, A. K., Grav, T., Bauer, J. M., Cutri, R. M., Nugent, C., and Cabrera, M. S. (2012). Preliminary Analysis of WISE/NEOWISE 3-Band Cryogenic and Post-cryogenic Observations of Main Belt Asteroids. ApJ, 759:L8.

Matter, A., Delbo, M., Carry, B., and Ligori, S. (2013). Evidence of a metal-rich surface for the asteroid (16) Psyche from interferometric observations in the thermal infrared. Icarus, 226:419–427.

Matter, A., Delbo, M., Ligori, S., Crouzet, N., and Tanga, P. (2011). Determination of physical properties of the asteroid (41) Daphne from interferometric observations in the thermal infrared. Icarus, 215:47–56.

McCord, T. B., Adams, J. B., and Johnson, T. V. (1970). Asteroid vesta: Spectral reflectivity and compositional implications. Science, 168(3938):1445–1447.

McCord, T. B. and Chapman, C. R. (1975). Asteroids - Spectral reflectance and color characteristics. ApJ, 195:553–562.

McMahon, R. G., Banerji, M., Gonzalez, E., Koposov, S. E., Bejar, V. J., Lodieu, N., Rebolo, R., and VHS Collaboration (2013). First Scientific Results from the VISTA Hemisphere Survey (VHS). The Messenger, 154:35–37.

Merlin, F., Guilbert, A., Dumas, C., Barucci, M. A., de Bergh, C., and Vernazza, P. (2007). Properties of the icy surface of the TNO 136108 (2003 EL{61}). A&A, 466:1185–1188.

Merline, W. J., Close, L. M., Dumas, C., Chapman, C. R., Roddier, F., Ménard, F., Slater, D. C., Duvert, G., Shelton, C., and Morgan, T. (1999). Discovery of a moon orbiting the asteroid 45 Eugenia. Nature, 401:565–568.

Merline, W. J., Conrad, A. R., Keck Observatory, W. M., Drummond, J. D., Tamblyn, P. M., Dumas, C., Carry, B., Campbell, R. D., Goodrich, R. W., Chapman, C. R., and Owen, W. M. (2008). S/2008 (35107) 1. IAU Circular, 8977:2.

Merline, W. J., Drummond, J. D., Carry, B., Conrad, A., Tamblyn, P. M., Dumas, C., Kaasalainen, M., Erikson, A., Mottola, S., Ďurech, J., Rousseau, G., Behrend, R., Casalnuovo, G. B., Chinaglia, B., Christou, J. C., Chapman, C. R., and Neyman, C. (2013a). The Resolved Asteroid Program - Size, shape, and pole of (52) Europa. Icarus, 225:794–805.

Merline, W. J., Tamblyn, P. M., Drummond, J. D., Christou, J. C., Conrad, A. R., Keck Observatory, W. M., Carry, B., Chapman, C. R., Dumas, C., Durda, D. D., Owen, W. M., and Enke, B. L. (2009). S/2009 (317) 1. IAU Circular, 9099:2.

Merline, W. J., Tamblyn, P. M., Warner, B. D., Pravec, P., Tamblyn, J. P., Neyman, C., Conrad, A. R., Owen, W. M., Carry, B., Drummond, J. D., Chapman, C. R., Enke, B. L., Grundy, W. M., Veillet, C., Porter, S. B., Arcidiacono, C., Christou, J. C., Durda, D. D., Harris, A. W., Weaver, H. A., Dumas, C., Terrell, D., and Maley, P. (2013b). S/2012 (2577) 1. IAU Circular, 9267.

Merline, W. J., Weidenschilling, S. J., Durda, D. D., Margot, J.-L., Pravec, P., and Storrs, A. D. (2002). Asteroids Do Have Satellites. Asteroids III, pages 289–312.

Michel, P., Migliorini, F., Morbidelli, A., and Zappalà, V. (2000). The Population of Mars-Crossers: Classification and Dynamical Evolution. Icarus, 145:332–347.

Mignard, F., Cellino, A., Muinonen, K., Tanga, P., Delbo, M., Dell'Oro, A., Granvik, M., Hestroffer, D., Mouret, S., Thuillot, W., and Virtanen, J. (2007). The Gaia Mission: Expected Applications to Asteroid Science. Earth Moon and Planets, 101:97–125.

Milliken, R. E. and Rivkin, A. S. (2009). Brucite and carbonate assemblages from altered olivine-rich materials on Ceres. Nature Geoscience, 2:258–261.

Morbidelli, A., Bottke, Jr., W. F., Froeschlé, C., and Michel, P. (2002). Origin and Evolution of Near-Earth Objects. Asteroids III, pages 409–422.

Morbidelli, A., Levison, H. F., Tsiganis, K., and Gomes, R. (2005). Chaotic capture of Jupiter's Trojan asteroids in the early Solar System. Nature, 435:462–465.

Morrison, D. (1974). Radiometric diameters and albedos of 40 asteroids. ApJ, 194:203–212.

Mouret, S., Hestroffer, D., and Mignard, F. (2007). Asteroid masses and improvement with GAIA. A&A, 472:1017–1027.

Mousis, O., Hueso, R., Beaulieu, J.-P., Bouley, S., Carry, B., Colas, F., Klotz, A., Pellier, C., Petit, J.-M., Rousselot, P., Ali-Dib, M., Beisker, W., Birlan, M., Buil, C., Delsanti, A., Frappa, E., Hammel, H. B., Levasseur-Regourd, A. C., Orton, G. S., Sánchez-Lavega, A., Santerne, A., Tanga, P., Vaubaillon, J., Zanda, B., Baratoux, D., Böhm, T., Boudon, V., Bouquet, A., Buzzi, L., Dauvergne, J.-L., Decock, A., Delcroix, M., Drossart, P., Esseiva, N., Fischer, G., Fletcher, L. N., Foglia, S., Gómez-Forrellad, J. M., Guarro-Fló, J., Herald, D., Jehin, E., Kugel, F., Lebreton, J.-P., Lecacheux, J., Leroy, A., Maquet, L., Masi, G., Maury, A., Meyer, F., Pérez-Hoyos, S., Rajpurohit, A. S., Rinner, C., Rogers, J. H., Roques, F., Schmude, R. W., Sicardy, B., Tregon, B., Vanhuysse, M., Wesley, A., and Widemann, T. (2014). Instrumental methods for professional and amateur collaborations in planetary astronomy. Experimental Astronomy, 38:91–191.

Müller, T. G., Ďurech, J., Ishiguro, M., Mueller, M., Krühler, T., Yang, H., Kim, M.-J., O'Rourke, L., Usui, F., Kiss, C., Altieri, B., Carry, B., Choi, Y.-J., Delbo, M., Emery, J. P., Greiner, J., Hasegawa, S., Hora, J. L., Knust, F., Kuroda, D., Osip, D., Rau, A., Rivkin, A., Schady, P., Thomas-Osip, J., Trilling, D., Urakawa, S., Vilenius, E., Weissman, P., and Zeidler, P. (2017). Hayabusa-2 mission target asteroid 162173 Ryugu (1999 JU_3): Searching for the object's spin-axis orientation. A&A, 599:A103.

Nakamura, T., Noguchi, T., Tanaka, M., Zolensky, M. E., Kimura, M., Tsuchiyama, A., Nakato, A., Ogami, T., Ishida, H., Uesugi, M., Yada, T., Shirai, K., Fujimura, A., Okazaki, R., Sandford, S. A., Ishibashi, Y., Abe, M., Okada, T., Ueno, M., Mukai, T., Yoshikawa, M., and Kawaguchi, J. (2011). Itokawa Dust Particles: A Direct Link Between S-Type Asteroids and Ordinary Chondrites. Science, 333:1113–1115.

Nesvorný, D., Bottke, W. F., Vokrouhlický, D., Chapman, C. R., and Rafkin, S. (2010). Do planetary encounters reset surfaces of near Earth asteroids? Icarus, 209:510–519.

Nesvorný, D., Brož, M., and Carruba, V. (2015). Identification and Dynamical Properties of Asteroid Families, pages 297–321.

Nesvorný, D., Jedicke, R., Whiteley, R. J., and Ivezić, Ž. (2005). Evidence for asteroid space weathering from the Sloan Digital Sky Survey. Icarus, 173:132–152.

Nesvorný, D. and Morbidelli, A. (2012). Statistical Study of the Early Solar System's Instability with Four, Five, and Six Giant Planets. AJ, 144:117.

Nesvorný, D., Vokrouhlický, D., and Deienno, R. (2014). Capture of Irregular Satellites at Jupiter. ApJ, 784:22.

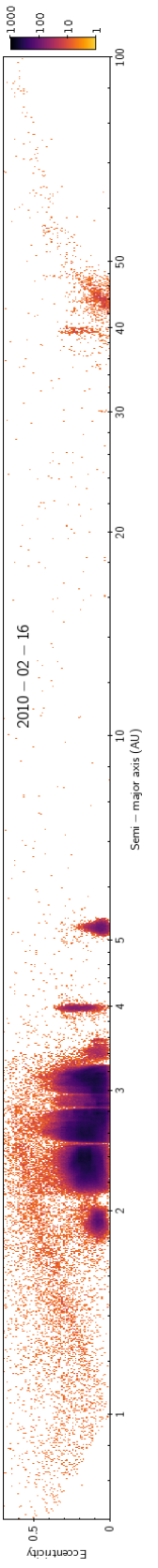

Nesvorný, D., Vokrouhlický, D., and Morbidelli, A. (2007). Capture of Irregular Satellites during Planetary Encounters. AJ, 133:1962–1976.

Newton, I. (1687). Philosophiae Naturalis Principia Mathematica. Auctore Js. Newton.

O'Brien, D. P., Morbidelli, A., and Bottke, W. F. (2007). The primordial excitation and clearing of the asteroid belt - Revisited. Icarus, 191:434–452.

Ortiz, J. L., Thirouin, A., Campo Bagatin, A., Duffard, R., Licandro, J., Richardson, D. C., Santos-Sanz, P., Morales, N., and Benavidez, P. G. (2012). Rotational fission of trans-Neptunian objects: the case of Haumea. MNRAS, 419:2315–2324.

Ostro, S. J., Benner, L. A. M., Magri, C., Giorgini, J. D., Rose, R., Jurgens, R. F., Yeomans, D. K., Hine, A. A., Nolan, M. C., Scheeres, D. J., Broschart, S. B., Kaasalainen, M., and Margot, J. (2005). Radar observations of Itokawa in 2004 and improved shape estimation. Meteoritics and Planetary Science, 40:1563–1574.

Pajuelo, M., Carry, B., Vachier, F., Marsset, M., Berthier, J., Descamps, P., Merline, W. J., Tamblyn, P. M., Grice, J., Conrad, A., Storrs, A., Timerson, B., Dunham, D., Preston, S., Vigan, A., Yang, B., Vernazza, P., Fauvaud, S., Bernasconi, L., Romeuf, D., Behrend, R., Dumas, C., Drummond, J. D., Margot, J.-L., Kervella, P., Marchis, F., and Girard, J. H. (2018a). Physical, spectral, and dynamical properties of asteroid (107) Camilla and its satellites. Icarus, 309:134–161.

Pajuelo, M. V., Birlan, M., Carry, B., Berthier, J., DeMeo, F., and Popescu, M. (2017). Spectral properties of binary asteroids. ACM.

Pajuelo, M. V., Birlan, M., Carry, B., Berthier, J., DeMeo, F., and Popescu, M. (2018b). Spectral properties of binary asteroids. MNRAS, accepted for publication.

Pajuelo, M. V., Carry, B., Vachier, F., Berthier, J., Descamp, P., Merline, W. J., Tamblyn, P. M., Conrad, A., Storrs, A., Margot, J.-L., Marchis, F., Kervella, P., and Girard, J. H. (2015). A refined orbit for the satellite of asteroid (107) Camilla. In AAS/Division for Planetary Sciences Meeting Abstracts, volume 47 of AAS/Division for Planetary Sciences Meeting Abstracts, page 201.05.

Parker, A., Ivezić, Ž., Jurić, M., Lupton, R., Sekora, M. D., and Kowalski, A. (2008). The size distributions of asteroid families in the SDSS Moving Object Catalog 4. Icarus, 198:138–155.

Parley, N. R., McBride, N., Green, S. F., Haswell, C. A., Clarkson, W. I., Christian, D. J., Collier-Cameron, A., Evans, N. A., Fitzsimmons, A., Hellier, C., Hodgkin, S. T., Horne, K., Irwin, J., Kane, S. R., Keenan, F. P., Lister, T. A., Norton, A. J., Osborne, J. P., Pollacco, D., Ryans, R., Skillen, I., Street, R. A., West, R. G., and Wheatley, P. J. (2005). Serendipitous Asteroid Lightcurve Survey Using SuperWASP. Earth Moon and Planets, 97:261–268.

Petit, J.-M., Bannister, M. T., Alexandersen, M., Chen, Y.-T., Gladman, B., Gwyn, S., Kavelaars, J., and Volk, K. (2016). The absolute magnitude distribution of cold classical Kuiper belt objects. In AAS/Division for Planetary Sciences Meeting Abstracts, volume 48 of AAS/Division for Planetary Sciences Meeting Abstracts, page 120.16.

Petit, J.-M., Durda, D. D., Greenberg, R., Hurford, T. A., and Geissler, P. E. (1997). The Long-Term Dynamics of Dactyl's Orbit. Icarus, 130:177–197.

Pinilla-Alonso, N., Brunetto, R., Licandro, J., Gil-Hutton, R., Roush, T. L., and Strazzulla, G. (2009). The surface of (136108) Haumea (2003 EL{61}), the largest carbon-depleted object in the trans-Neptunian belt. A&A, 496:547–556.

Popescu, M., Licandro, J., Morate, D., de León, J., Nedelcu, D. A., Rebolo, R., McMahon, R. G., Gonzalez-Solares, E., and Irwin, M. (2016). Near-infrared colors of minor planets recovered from VISTA-VHS survey (MOVIS). A&A, 591:A115.

Pravec, P., Harris, A. W., and Michalowski, T. (2002). Asteroid Rotations. Asteroids III, pages 113–122.

Pravec, P., Scheirich, P., Kušnirák, P., Šarounová, L., Mottola, S., Hahn, G., Brown, P. G., Esquerdo, G. A., Kaiser, N., Krzeminski, Z., Pray, D. P., Warner, B. D., Harris, A. W., Nolan, M. C., Howell, E. S., Benner, L. A. M., Margot, J.-L., Galád, A., Holliday, W., Hicks, M. D., Krugly, Y. N., Tholen, D. J., Whiteley, R. J., Marchis, F., Degraff, D. R., Grauer, A., Larson, S., Velichko, F. P., Cooney, W. R., Stephens, R., Zhu, J., Kirsch, K., Dyvig, R., Snyder, L., Reddy, V., Moore, S., Gajdoš, Š., Világi, J., Masi, G., Higgins, D., Funkhouser, G., Knight, B., Slivan, S. M., Behrend, R., Grenon, M., Burki, G., Roy, R., Demeautis, C., Matter, D., Waelchli, N., Revaz, Y., Klotz, A., Rieugné, M., Thierry, P., Cotrez, V., Brunetto, L., and Kober, G. (2006). Photometric survey of binary near-Earth asteroids. Icarus, 181:63–93.

Pravec, P., Scheirich, P., Vokrouhlický, D., Harris, A. W., Kušnirák, P., Hornoch, K., Pray, D. P., Higgins, D., Galád, A., Világi, J., Gajdoš, Š., Kornoš, L., Oey, J., Husárik, M., Cooney, W. R., Gross, J., Terrell, D., Durkee, R., Pollock, J., Reichart, D. E., Ivarsen, K., Haislip, J., Lacluyze, A., Krugly, Y. N., Gaftonyuk, N., Stephens, R. D., Dyvig, R., Reddy, V., Chiorny, V., Vaduvescu, O., Longa-Peña, P., Tudorica, A., Warner, B. D., Masi, G., Brinsfield, J., Gonçalves, R., Brown, P., Krzeminski, Z., Gerashchenko, O., Shevchenko, V., Molotov, I., and Marchis, F. (2012). Binary asteroid population. 2. Anisotropic distribution of orbit poles of small, inner main-belt binaries. Icarus, 218:125–143.

Pravec, P., Vokrouhlický, D., Polishook, D., Scheeres, D. J., Harris, A. W., Galád, A., Vaduvescu, O., Pozo, F., Barr, A., Longa, P., Vachier, F., Colas, F., Pray, D. P., Pollock, J., Reichart, D., Ivarsen, K., Haislip, J., Lacluyze, A., Kušnirák, P., Henych, T., Marchis, F., Macomber, B., Jacobson, S. A., Krugly, Y. N., Sergeev, A. V., and Leroy, A. (2010). Formation of asteroid pairs by rotational fission. Nature, 466:1085–1088.

Pravec, P., Wolf, M., and Sarounova, L. (1997). 1991 vh. IAU Circular, 6607.

Quirico, E. and Schmitt, B. (1997). Near-Infrared Spectroscopy of Simple Hydrocarbons and Carbon Oxides Diluted in Solid N_2 and as Pure Ices: Implications for Triton and Pluto. Icarus, 127:354–378.

Rabinowitz, D. L., Barkume, K. M., Brown, M. E., Roe, H. G., Schwartz, M., Tourtellotte, S. W., and Trujillo, C. A. (2006). Photometric Observations Constraining the Size, Shape, and Albedo of 2003 EL61, a Rapidly Rotating, Pluto-sized Object in the Kuiper Belt. ApJ, 639:1238–1251.

Ragozzine, D. and Brown, M. E. (2007). Candidate Members and Age Estimate of the Family of Kuiper Belt Object 2003 EL61. AJ, 134:2160–2167.

Ragozzine, D. and Brown, M. E. (2009). Orbits and Masses of the Satellites of the Dwarf Planet Haumea (2003 EL61). AJ, 137:4766–4776.

Rivkin, A. S., Howell, E. S., Lebofsky, L. A., Clark, B. E., and Britt, D. T. (2000). The nature of M-class asteroids from 3-micron observations. Icarus, 145:351–368.

Roig, F., Ribeiro, A. O., and Gil-Hutton, R. (2008). Taxonomy of asteroid families among the Jupiter Trojans: comparison between spectroscopic data and the Sloan Digital Sky Survey colors. A&A, 483:911–931.

Rousselot, P., Mousis, O., Dumas, C., Jehin, E., Manfroid, J., Carry, B., and Zucconi, J.-M. (2011). A search for water vaporization on Ceres. AJ, 142:A125.

Russell, C. T., McSween, H. Y., Jaumann, R., and Raymond, C. A. (2015). The Dawn Mission to Vesta and Ceres, pages 419–432. Univ. Arizona Press.

Russell, C. T., Raymond, C. A., Ammannito, E., Buczkowski, D. L., De Sanctis, M. C., Hiesinger, H., Jaumann, R., Konopliv, A. S., McSween, H. Y., Nathues, A., Park, R. S., Pieters, C. M., Prettyman, T. H., McCord, T. B., McFadden, L. A., Mottola, S., Zuber, M. T., Joy, S. P., Polanskey, C., Rayman, M. D., Castillo-Rogez, J. C., Chi, P. J., Combe, J. P., Ermakov, A., Fu, R. R., Hoffmann, M., Jia, Y. D., King, S. D., Lawrence, D. J., Li, J.-Y., Marchi, S., Preusker, F., Roatsch, T., Ruesch, O., Schenk, P., Villarreal, M. N., and Yamashita, N. (2016). Dawn arrives at ceres: Exploration of a small, volatile-rich world. Science, 353(6303):1008–1010.

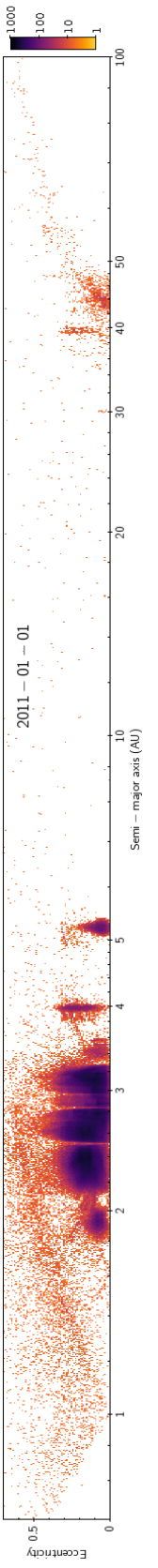

Russell, C. T., Raymond, C. A., Coradini, A., McSween, H. Y., Zuber, M. T., Nathues, A., De Sanctis, M. C., Jaumann, R., Konopliv, A. S., Preusker, F., Asmar, S. W., Park, R. S., Gaskell, R., Keller, H. U., Mottola, S., Roatsch, T., Scully, J. E. C., Smith, D. E., Tricarico, P., Toplis, M. J., Christensen, U. R., Feldman, W. C., Lawrence, D. J., McCoy, T. J., Prettyman, T. H., Reedy, R. C., Sykes, M. E., and Titus, T. N. (2012). Dawn at Vesta: Testing the Protoplanetary Paradigm. Science, 336:684–686.

Ruzmaikina, T. V., Safronov, V. S., and Weidenschilling, S. J. (1989). Radial mixing of material in the asteroidal zone. In Binzel, R. P., Gehrels, T., and Matthews, M. S., editors, Asteroids II, pages 681–700.

Saint-Pé, O., Combes, M., and Rigaut, F. (1993a). Ceres surface properties by high-resolution imaging from earth. Icarus, 105:271–281.

Saint-Pé, O., Combes, M., Rigaut, F., Tomasko, M., and Fulchignoni, M. (1993b). Demonstration of adaptive optics for resolved imagery of solar system objects - Preliminary results on Pallas and Titan. Icarus, 105:263–270.

Santos-Sanz, P., Ortiz, J. L., Aceituno, F. J., Brown, M. E., and Rabinowitz, D. L. (2005). 2003 EL_61, 2003 UB_313, and 2005 FY_9. IAU Circular, 8577:2.

Sato, K., Miyamoto, M., and Zolensky, M. E. (1997). Absorption bands near 3 μm in diffuse reflectance spectra of carbonaceous chondrites: Comparison with asteroids. Meteoritics and Planetary Science, 32:503–507.

Scheeres, D. J., Britt, D., Carry, B., and Holsapple, K. A. (2015). Asteroid Interiors and Morphology, pages 745–766. Univ. Arizona Press.

Schlichting, H. E. and Sari, R. (2009). The Creation of Haumea's Collisional Family. ApJ, 700:1242–1246.

Schmitt, B., Grim, R., and Greenberg, R. (1988). Spectroscopy and physico-chemistry of CO:H_2O and CO_2:H_2O ices. Eslab Symposium on Infrared Spectroscopy in Astronomy.

Schober, H. J. (1981). Rotation period of 234 Barbara, a further slowly spinning asteroid. A&A, 96:302–305.

Shankman, C., Kavelaars, J., Gladman, B. J., Alexandersen, M., Kaib, N., Petit, J.-M., Bannister, M. T., Chen, Y.-T., Gwyn, S., Jakubik, M., and Volk, K. (2016). Ossos. ii. a sharp transition in the absolute magnitude distribution of the kuiper belt's scattering population. AJ, 151:31.

Sierks, H., Lamy, P., Barbieri, C., Koschny, D., Rickman, H., Rodrigo, R., A'Hearn, M. F., Angrilli, F., Barucci, A., Bertaux, J.-L., Bertini, I., Besse, S., Carry, B., Cremonese, G., Da Deppo, V., Davidsson, B., Debei, S., De Cecco, M., De Leon, J., Ferri, F., Fornasier, S., Fulle, M., Hviid, S. F., Gaskell, G. W., Groussin, O., Gutierrez, P. J., Jorda, L., Kaasalainen, M., Keller, H. U., Knollenberg, J., Kramm, J. R., Kührt, E., Küppers, M., Lara, L. M., Lazzarin, M., Leyrat, C., Lopez Moreno, J. L., Magrin, S., Marchi, S., Marzari, F., Massironi, M., Michalik, H., Moissl, R., Naletto, G., Preusker, F., Sabau, L., Sabolo, W., Scholten, F., Snodgrass, C., Thomas, N., Tubiana, C., Vernazza, P., Vincent, J.-B., Wenzel, K.-P., Andert, T., Pätzold, M., and Weiss, B. P. (2011). Images of asteroid (21) Lutetia: A remnant planetesimal from the early Solar System. Science, 334:487–490.

Skrutskie, M. F., Cutri, R. M., Stiening, R., Weinberg, M. D., Schneider, S., Carpenter, J. M., Beichman, C., Capps, R., Chester, T., Elias, J., Huchra, J., Liebert, J., Lonsdale, C., Monet, D. G., Price, S., Seitzer, P., Jarrett, T., Kirkpatrick, J. D., Gizis, J. E., Howard, E., Evans, T., Fowler, J., Fullmer, L., Hurt, R., Light, R., Kopan, E. L., Marsh, K. A., McCallon, H. L., Tam, R., Van Dyk, S., and Wheelock, S. (2006). The Two Micron All Sky Survey (2MASS). AJ, 131:1163–1183.

Snodgrass, C. and Carry, B. (2013). Automatic Removal of Fringes from EFOSC Images. The Messenger, 152:14–16.

Snodgrass, C., Carry, B., Dumas, C., and Hainaut, O. R. (2010). Characterisation of candidate members of (136108) Haumea's family. A&A, 511:A72.

Snodgrass, C., Fitzsimmons, A., Lowry, S. C., and Weissman, P. (2011). The size distribution of Jupiter Family comet nuclei. MNRAS, 414:458–469.

Snodgrass, C., Lowry, S. C., and Fitzsimmons, A. (2006). Photometry of cometary nuclei: rotation rates, colours and a comparison with Kuiper Belt Objects. MNRAS, 373:1590–1602.

Snodgrass, C., Tubiana, C., Vincent, J.-B., Sierks, H., Hviid, S., Moissi, R., Boehnhardt, H., Barbieri, C., Koschny, D., Lamy, P., Rickman, H., Rodrigo, R., Carry, B., Lowry, S. C., Laird, R. J. M., Weissman, P. R., Fitzsimmons, A., Marchi, S., and OSIRIS Team (2010). A collision in 2009 as the origin of the debris trail of asteroid P/2010A2. Nature, 467:814–816.

Solano, E., Rodrigo, C., Pulido, R., and Carry, B. (2014). Precovery of near-Earth asteroids by a citizen-science project of the Spanish Virtual Observatory. Astronomische Nachrichten, 335:142.

Spoto, F., Milani, A., and Knežević, Z. (2015). Asteroid family ages. Icarus, 257:275–289.

Spoto, F., Tanga, P., Bouquillon, S., Desmars, J., Hestroffer, D., Mignard, F., Altmann, M., Herald, D., Marchant, J., Barache, C., Carlucci, T., Lister, T., and Taris, F. (2017). Ground-based astrometry calibrated by Gaia DR1: new perspectives in asteroid orbit determination. A&A, 607:A21.

Stansberry, J., Grundy, W., Brown, M. E., Cruikshank, D. P., Spencer, J. R., Trilling, D., and Margot, J.-L. (2008). Physical Properties of Kuiper Belt and Centaur Objects: Constraints from the Spitzer Space Telescope. The Solar System Beyond Neptune, pages 161–179.

Stern, S. A., Bagenal, F., Ennico, K., Gladstone, G. R., Grundy, W. M., McKinnon, W. B., Moore, J. M., Olkin, C. B., Spencer, J. R., Weaver, H. A., Young, L. A., Andert, T., Andrews, J., Banks, M., Bauer, B., Bauman, J., Barnouin, O. S., Bedini, P., Beisser, K., Beyer, R. A., Bhaskaran, S., Binzel, R. P., Birath, E., Bird, M., Bogan, D. J., Bowman, A., Bray, V. J., Brozovic, M., Bryan, C., Buckley, M. R., Buie, M. W., Buratti, B. J., Bushman, S. S., Calloway, A., Carcich, B., Cheng, A. F., Conard, S., Conrad, C. A., Cook, J. C., Cruikshank, D. P., Custodio, O. S., Dalle Ore, C. M., Deboy, C., Dischner, Z. J. B., Dumont, P., Earle, A. M., Elliott, H. A., Ercol, J., Ernst, C. M., Finley, T., Flanigan, S. H., Fountain, G., Freeze, M. J., Greathouse, T., Green, J. L., Guo, Y., Hahn, M., Hamilton, D. P., Hamilton, S. A., Hanley, J., Harch, A., Hart, H. M., Hersman, C. B., Hill, A., Hill, M. E., Hinson, D. P., Holdridge, M. E., Horanyi, M., Howard, A. D., Howett, C. J. A., Jackman, C., Jacobson, R. A., Jennings, D. E., Kammer, J. A., Kang, H. K., Kaufmann, D. E., Kollmann, P., Krimigis, S. M., Kusnierkiewicz, D., Lauer, T. R., Lee, J. E., Lindstrom, K. L., Linscott, I. R., Lisse, C. M., Lunsford, A. W., Mallder, V. A., Martin, N., McComas, D. J., McNutt, R. L., Mehoke, D., Mehoke, T., Melin, E. D., Mutchler, M., Nelson, D., Nimmo, F., Nunez, J. I., Ocampo, A., Owen, W. M., Paetzold, M., Page, B., Parker, A. H., Parker, J. W., Pelletier, F., Peterson, J., Pinkine, N., Piquette, M., Porter, S. B., Protopapa, S., Redfern, J., Reitsema, H. J., Reuter, D. C., Roberts, J. H., Robbins, S. J., Rogers, G., Rose, D., Runyon, K., Retherford, K. D., Ryschkewitsch, M. G., Schenk, P., Schindhelm, E., Sepan, B., Showalter, M. R., Singer, K. N., Soluri, M., Stanbridge, D., Steffl, A. J., Strobel, D. F., Stryk, T., Summers, M. E., Szalay, J. R., Tapley, M., Taylor, A., Taylor, H., Throop, H. B., Tsang, C. C. C., Tyler, G. L., Umurhan, O. M., Verbiscer, A. J., Versteeg, M. H., Vincent, M., Webbert, R., Weidner, S., Weigle, G. E., White, O. L., Whittenburg, K., Williams, B. G., Williams, K., Williams, S., Woods, W. W., Zangari, A. M., and Zirnstein, E. (2015). The Pluto system: Initial results from its exploration by New Horizons. Science, 350:aad1815.

Storrs, A., Vilas, F., Landis, R., Wells, E., Woods, C., Zellner, B., and Gaffey, M. (2001). S/2001 (107) 1. IAU Circular, 7599:3.

Storrs, A. D., Dunne, C., Conan, J.-M., Mugnier, L. M., Weiss, B. P., and Zellner, B. H. (2005). A closer look at main belt asteroids 1: WF/PC images. Icarus, 173(2):409–416.

Storrs, A. D., Weiss, B. P., Zellner, B. H., Burleson, W., Sichitiu, R., Wells, E. N., Kowal, C., and Tholen, D. J. (1999). Imaging Observations of Asteroids with Hubble Space Telescope. Icarus, 137(2):260–268.

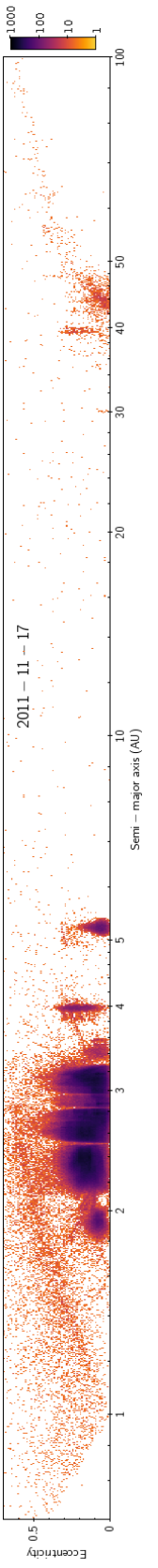

Strazzulla, G., Dotto, E., Binzel, R. P., Brunetto, R., Barucci, M. A., Blanco, A., and Orofino, V. (2005). Spectral alteration of the Meteorite Epinal (H5) induced by heavy ion irradiation: a simulation of space weathering effects on near-Earth asteroids. Icarus, 174:31–35.

Strazzulla, G. and Palumbo, M. E. (1998). Evolution of icy surfaces : an experimental approach. Planet. Space Sci., 46:1339–1348.

Sykes, M. V., Cutri, R. M., Fowler, J. W., Tholen, D. J., Skrutskie, M. F., Price, S., and Tedesco, E. F. (2000). The 2MASS Asteroid and Comet Survey. Icarus, 146:161–175.

Takir, D. and Emery, J. P. (2012). Outer Main Belt asteroids: Identification and distribution of four 3-μm spectral groups. Icarus, 219:641–654.

Takir, D., Emery, J. P., and McSween, H. Y. (2015). Toward an understanding of phyllosilicate mineralogy in the outer main asteroid belt. Icarus, 257:185–193.

Tanga, P., Carry, B., Colas, F., Delbo, M., Matter, A., Hanuš, J., Alí Lagoa, V., Andrei, A. H., Assafin, M., Audejean, M., Behrend, R., Camargo, J. I. B., Carbognani, A., Cedrés Reyes, M., Conjat, M., Cornero, N., Coward, D., Crippa, R., de Ferra Fantin, E., Devogéle, M., Dubos, G., Frappa, E., Gillon, M., Hamanowa, H., Jehin, E., Klotz, A., Kryszczyńska, A., Lecacheux, J., Leroy, A., Manfroid, J., Manzini, F., Maquet, L., Morelle, E., Mottola, S., Polińska, M., Roy, R., Todd, M., Vachier, F., Vera Hernández, C., and Wiggins, P. (2015). The non-convex shape of (234) Barbara, the first Barbarian*. MNRAS, 448:3382–3390.

Tanga, P. and Delbo, M. (2007). Asteroid occultations today and tomorrow: toward the GAIA era. A&A, 474:1015–1022.

Tanga, P., Mignard, F., Dell'Oro, A., Muinonen, K., Pauwels, T., Thuillot, W., Berthier, J., Cellino, A., Hestroffer, D., Petit, J.-M., Carry, B., David, P., Delbo', M., Fedorets, G., Galluccio, L., Granvik, M., Ordenovic, C., and Pentikäinen, H. (2016). The daily processing of asteroid observations by Gaia. Planet. Space Sci., 123:87–94.

Tedesco, E. F., Williams, J. G., Matson, D. L., Veeder, G. J., Gradie, J. C., and Lebofsky, L. A. (1989). Three-parameter asteroid taxonomy classifications. Asteroids II, pages 1151–1161.

Tegler, S. C., Grundy, W. M., Romanishin, W. J., Consolmagno, G. J., Mogren, K., and Vilas, F. (2007). Optical Spectroscopy of the Large Kuiper Belt Objects 136472 (2005 FY9) and 136108 (2003 EL61). AJ, 133:526–530.

Thomas, P. C., Binzel, R. P., Gaffey, M. J., Storrs, A. D., Wells, E. N., and Zellner, B. H. (1997a). Impact excavation on asteroid 4 Vesta: Hubble Space Telescope results. Science, 277:1492–1495.

Thomas, P. C., Binzel, R. P., Gaffey, M. J., Zellner, B. H., Storrs, A. D., and Wells, E. N. (1997b). Vesta: Spin Pole, Size, and Shape from HST Images. Icarus, 128:88–94.

Thomas, P. C., Parker, J. W., McFadden, L. A., Russell, C. T., Stern, S. A., Sykes, M. V., and Young, E. F. (2005). Differentiation of the asteroid Ceres as revealed by its shape. Nature, 437:224–226.

Torppa, J., Kaasalainen, M., Michalowski, T., Kwiatkowski, T., Kryszczyńska, A., Denchev, P., and Kowalski, R. (2003). Shapes and rotational properties of thirty asteroids from photometric data. Icarus, 164:346–383.

Trujillo, C. A., Brown, M. E., Barkume, K. M., Schaller, E. L., and Rabinowitz, D. L. (2007). The Surface of 2003 EL_{61} in the Near-Infrared. ApJ, 655:1172–1178.

Trujillo, C. A., Sheppard, S. S., and Schaller, E. L. (2011). A Photometric System for Detection of Water and Methane Ices on Kuiper Belt Objects. ApJ, 730:105.

Tsiganis, K., Gomes, R., Morbidelli, A., and Levison, H. F. (2005). Origin of the orbital architecture of the giant planets of the Solar System. Nature, 435:459–461.

Ďurech, J., Carry, B., Delbo, M., Kaasalainen, M., and Viikinkoski, M. (2015). Asteroid Models from Multiple Data Sources, pages 183–202. Univ. Arizona Press.

Ďurech, J., Delbo, M., and Carry, B. (2012). Asteroid models derived from thermal infrared data and optical lightcurves. In Asteroids, Comets, Meteors 2012, volume 1667 of LPI Contributions, page 6118.

Ďurech, J., Delbo', M., Carry, B., Hanuš, J., and Alí-Lagoa, V. (2017). Asteroid shapes and thermal properties from combined optical and mid-infrared photometry inversion. A&A, 604:A27.

Ďurech, J., Kaasalainen, M., Warner, B. D., Fauerbach, M., Marks, S. A., Fauvaud, S., Fauvaud, M., Vugnon, J.-M., Pilcher, F., Bernasconi, L., and Behrend, R. (2009). Asteroid models from combined sparse and dense photometric data. A&A, 493:291–297.

Vernazza, P., Binzel, R. P., Rossi, A., Fulchignoni, M., and Birlan, M. (2009). Solar wind as the origin of rapid reddening of asteroid surfaces. Nature, 458:993–995.

Vernazza, P., Binzel, R. P., Thomas, C. A., DeMeo, F. E., Bus, S. J., Rivkin, A. S., and Tokunaga, A. T. (2008). Compositional differences between meteorites and near-Earth asteroids. Nature, 454:858–860.

Vernazza, P., Brunetto, R., Strazzulla, G., Fulchignoni, M., Rochette, P., Meyer-Vernet, N., and Zouganelis, I. (2006). Asteroid colors: a novel tool for magnetic field detection? The case of Vesta. A&A, 451:43–46.

Vernazza, P., Carry, B., Emery, J. P., Hora, J. L., Cruikshank, D. P., Binzel, R. P., Jackson, J., Helbert, J., and Maturilli, A. (2010). Mid-infrared spectral variability for compositionally similar asteroids: Implications for asteroid particle size distributions. Icarus, 207:800–809.

Vernazza, P., Delbo, M., King, P. L., Izawa, M. R. M., Olofsson, J., Lamy, P., Cipriani, F., Binzel, R. P., Marchis, F., Merín, B., and Tamanai, A. (2012). High surface porosity as the origin of emissivity features in asteroid spectra. Icarus, 221:1162–1172.

Vernazza, P., Lamy, P., Groussin, O., Hiroi, T., Jorda, L., King, P. L., Izawa, M. R. M., Marchis, F., Birlan, M., and Brunetto, R. (2011). Asteroid (21) Lutetia as a remnant of Earth's precursor planetesimals. Icarus, 216:650–659.

Vernazza, P., Mothé-Diniz, T., Barucci, M. A., Birlan, M., Carvano, J. M., Strazzulla, G., Fulchignoni, M., and Migliorini, A. (2005). Analysis of near-IR spectra of 1 Ceres and 4 Vesta, targets of the Dawn mission. A&A, 436:1113–1121.

Veverka, J., Robinson, M., Thomas, P., Murchie, S., Bell, J. F., Izenberg, N., Chapman, C., Harch, A., Bell, M., Carcich, B., Cheng, A., Clark, B., Domingue, D., Dunham, D., Farquhar, R., Gaffey, M. J., Hawkins, E., Joseph, J., Kirk, R., Li, H., Lucey, P., Malin, M., Martin, P., McFadden, L., Merline, W. J., Miller, J. K., Owen, W. M., Peterson, C., Prockter, L., Warren, J., Wellnitz, D., Williams, B. G., and Yeomans, D. K. (2000). NEAR at Eros: Imaging and Spectral Results. Science, 289:2088–2097.

Veverka, J., Thomas, P. C., Harch, A., Clark, B. E., Bell, J. F., Carcich, B., Joseph, J., Chapman, C. R., Merline, W. J., Robinson, M. S., Malin, M., McFadden, L. A., Murchie, S. L., Hawkins, S. E., Faquhar, R., Izenberg, N., and Cheng, A. F. (1997). NEAR's Flyby of 253 Mathilde: Images of a C Asteroid. Science, 278:2109–2114.

Viikinkoski, M., Kaasalainen, M., and Durech, J. (2015a). ADAM: a general method for using various data types in asteroid reconstruction. A&A, 576:A8.

Viikinkoski, M., Kaasalainen, M., Ďurech, J., Carry, B., Marsset, M., Fusco, T., Dumas, C., Merline, W. J., Yang, B., Berthier, J., Kervella, P., and Vernazza, P. (2015b). VLT/SPHERE- and ALMA-based shape reconstruction of asteroid (3) Juno. A&A, 581:L3.

Vokrouhlický, D., Bottke, W. F., and Nesvorný, D. (2016). Capture of Trans-Neptunian Planetesimals in the Main Asteroid Belt. AJ, 152:39.

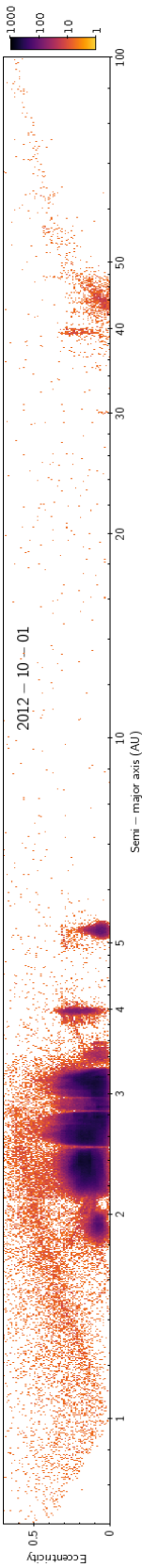

Volk, K., Murray-Clay, R., Gladman, B., Lawler, S., Bannister, M. T., Kavelaars, J. J., Petit, J.-M., Gwyn, S., Alexandersen, M., Chen, Y.-T., Lykawka, P. S., Ip, W., and Lin, H. W. (2016). Ossos iii:resonant trans-neptunian populations: Constraints from the first quarter of the outer solar system origins survey. AJ, 152:23.

Walsh, K. J. and Jacobson, S. A. (2015). Formation and Evolution of Binary Asteroids, pages 375–393.

Walsh, K. J., Morbidelli, A., Raymond, S. N., O'Brien, D. P., and Mandell, A. M. (2011). A low mass for Mars from Jupiter's early gas-driven migration. Nature, 475:206–209.

Walsh, K. J., Richardson, D. C., and Michel, P. (2008). Rotational breakup as the origin of small binary asteroids. Nature, 454:188–191.

Wasserman, L. H., Millis, R. L., Franz, O. G., Bowell, E., White, N. M., Giclas, H. L., Martin, L. J., Elliot, J. L., Dunham, E., Mink, D., Baron, R., Honeycutt, R. K., Henden, A. A., Kephart, J. E., A'Hearn, M. F., Reitsema, H. J., Radick, R., and Taylor, G. E. (1979). The diameter of Pallas from its occultation of SAO 85009. AJ, 84:259–268.

Waszczak, A., Chang, C.-K., Ofek, E. O., Laher, R., Masci, F., Levitan, D., Surace, J., Cheng, Y.-C., Ip, W.-H., Kinoshita, D., Helou, G., Prince, T. A., and Kulkarni, S. (2015). Asteroid light curves from the palomar transient factory survey: Rotation periods and phase functions from sparse photometry. AJ, 150:75.

Weidenschilling, S. J., Paolicchi, P., and Zappala, V. (1989). Do asteroids have satellites? Asteroids II, pages 643–658.

Wetherill, G. W. (1979). Steady state populations of Apollo-Amor objects. Icarus, 37:96–112.

Willman, M., Jedicke, R., Nesvorný, D., Moskovitz, N., Ivezić, Ž., and Fevig, R. (2008). Redetermination of the space weathering rate using spectra of Iannini asteroid family members. Icarus, 195:663–673.

Wisdom, J. (1983). Chaotic behavior and the origin of the 3/1 Kirkwood gap. Icarus, 56:51–74.

Wood, X. H. J. and Kuiper, G. P. (1963). Photometric Studies of Asteroids. ApJ, 137:1279–1286.

Xu, S., Binzel, R. P., Burbine, T. H., and Bus, S. J. (1995). Small Main-belt Asteroid Spectroscopic Survey: Initial results. Icarus, 115:1–35.

Yang, B., Wahhaj, Z., Beauvalet, L., Marchis, F., Dumas, C., Marsset, M., Nielsen, E. L., and Vachier, F. (2016). Extreme ao observations of two triple asteroid systems with sphere. Astrophysical Journal Letter, 820:L35.

Yu, Y., Richardson, D. C., Michel, P., Schwartz, S. R., and Ballouz, R.-L. (2014). Numerical predictions of surface effects during the 2029 close approach of Asteroid 99942 Apophis. Icarus, 242:82–96.

Zappala, V. and Cellino, A. (2002). The impact of GAIA in our knowledge of asteroids. EAS Publications Series, 2:343–349.

Zellner, B., Tholen, D. J., and Tedesco, E. F. (1985). The eight-color asteroid survey - Results for 589 minor planets. Icarus, 61:355–416.

Zolotov, M. Y. (2009). On the composition and differentiation of Ceres. Icarus, 204:183–193.

List of Figures

Let's play (music) together
Solutions!

I list here below the solutions to the musical quizz. Congratulations if you went above 10 references!

#	Page	Band	Record
1	1	Gong	02∞
2	11	Iron Butterfly	In-a-gadda-da-vida
3	12	Hawkwind	In search for space
4	17	Gong	Camembert Electrique
5	20	Genesis	From Genesis to Revelation
6	21	Santana	Amigos
7	21	dIRE sTRAITS	Making Movies
8	22	Pink Floyd	The Wall
9	23	Bizet	Arlésienne
10	23	The Police	Outlandos d'Amour
11	25	Jim Morrison	
12	28	The Rolling Stones	2000 Lightyears From Home
13	29	Robert Wyatt	Rock Bottom
14	30	Led Zeppelin	Stairway to Heaven
15	31	Sigur Rós	[ ]
16	33	Frozen	Let It Go
17	33	Weather Report	Sweetnighter
18	40	The Doors	The end
19	41	Pink Floyd	Dark Side of the Moon
20	69	Serges Gainsbourg	69 Année érotique

The defense committee added another quizz:
What are the solar system bodies named in "*Astronomy Domine*" by Pink Floyd?
Thanks to them to have played the game!

Lime and limpid green
A second scene
A fight between the blue you once knew
Floating down, the sound resounds
Around the icy waters underground
Jupiter and Saturn, Oberon, Miranda and Titania
Neptune, Titan
Stars can frighten
...

Appendix A

Version française abbrégée

Ce chapitre présente une version très abbrégée du présent manuscrit, dans une version française. Partant d'une présentation générale du contexte de mes travaux, je décris ensuite mes activités de recherche par imagerie à haute résolution angulaire (A.2), modélisation 3-D (A.3), et l'étude des systèmes multiples (A.4), aboutissant à l'étude de la densité et structure interne des petits corps (A.5).
Dans un second temps, je décris mon utilisation massive des données de grands relevés pour étudier la distribution des compositions d'astéroïdes dans la ceinture principale (A.6) et dans l'espace géocroiseur et aréocroiseur (A.7), avant d'évoquer mes prospectives de recherche.

Contents

A.1 Introduction

Je suis planétologue et j'étudie les petits corps du système solaire: les astéroïdes, comètes, et objets transneptuniens. Ces corps sont les restes des briques qui se sont agglomérées pour former les planètes telluriques et les coeurs des planètes géantes. Formés dans le disque proto-planétaire, leurs compositions nous renseignent sur leur lieu et âge de formation. Comment ces compositions se distribuent dans le système solaire actuel résulte de l'évolution dynamique de notre système planétaire, et garde en particulier la trace des migrations planétaires. Ainsi, l'étude dynamique, compositionnelle, et physique des petits corps nous fournit de fortes contraintes observationnelles sur les différentes étapes de notre histoire, et sert de socle au développement des modèles d'évolution des systèmes planétaires tel le modèle de Nice.

Depuis l'obtention en 2009 de mon doctorat intitulé "Propriétés physiques des astéroïdes par imagerie à haute résolution angulaire", j'ai grandement diversifié mes activités de recherche, tant sur le plan méthodologique que statistique. Mes travaux de thèse portaient principalement sur l'étude détaillée des propriétés physiques de plusieurs objets par imagerie, en utilisant les grands télescopes au sol équipés d'optique adaptative. Depuis lors, tout en continuant mes travaux sur les propriétés physiques, je me suis également intéressé à la composition des petits corps, et ai travaillé sur des données de grands relevés du ciel, étudiant plusieurs dizaines de milliers d'astéroïdes.

Cette évolution personnelle suit le chemin logique de compréhension de quelques objets de référence pour ensuite interpréter les propriétés d'un grand ensemble d'objets, que j'aime appeler 02∞. Elle suit le chemin suivi par la communauté, avec des études au cas par cas qui ont progressivement évoluées en études statistiques. Ce dernier aspect est tout particulièrement notable depuis les années 2000, et l'arrivée de grands relevés comme le Sloan Digital Sky Survey (SDSS), et la promesse des futurs relevés par les sondes Gaia et Euclid de l'agence spatiale européenne (ESA) et le Large Synoptic Survey Telescope (LSST).

A.2 Cérès et Vesta, astéroïdes cibles de la mission Dawn

Mes premiers objets d'étude ont été les deux astéroïdes les plus grands de la ceinture principale: (1) Cérès et (4) Vesta, tous deux cibles de la mission Dawn de la NASA. C'est en étudiant ces deux corps durant ma thèse que j'ai développé les compétences et les outils d'analyse d'images et spectro-images obtenues par des instruments assistés par optique adaptative. J'ai ainsi pu étudier les variations spectrales à la surface de Vesta (Carry et al., 2010c), et déterminer la forme et la taille de Cérès (Carry et al., 2008), montrant un fort aplatissement aux pôles. Les valeurs de cette étude étaient fortement différentes des estimations publiées alors via des observations avec le Hubble Space Telescope (Thomas et al., 2005).

Ces différences faisant polémiques, j'ai récemment piloté une analyse compréhensive de toutes les images de Cérès disponibles dans les archives des grands télescopes terrestres équipés d'optique adaptative, qui a confirmé mes premiers résultats (Drummond et al., 2014). Les résultats de la sonde Dawn ont finalement validés nos résultats (Russell et al., 2016), montrant la robustesse des techniques que j'ai développées pour analyser les images à haute résolution angulaire.

D'autres part, motivé par les signatures visibles dans les cartes d'albédo (capacité de la matière à réfléchir la lumière) que j'avais réalisées durant ma thèse (Carry et al., 2008), j'ai étudié la surface de Cérès par spectro-imagerie, étudiant la distribution de la pente spectrale à sa surface (Carry et al., 2012c). Ces cartes ont été au coeur de l'interprétation de notre détection de vapeur d'eau autour de Cérès, avec le télescope spatial Herschel (Küppers et al., 2014). En effet, après une détection marginale de OH^- par A'Hearn and Feldman (1992), aucune trace d'eau n'avait été détectée, rendant suspicieuse leur annonce. Même nos efforts au VLT (Rousselot et al., 2011), pourtant dix fois plus sensible que les mesures de A'Hearn and Feldman (1992), ne détectèrent de trace de OH^-.

C'est pourquoi la variabilité prononcée de notre détection directe de H_2O, dans le très proche environnement de Cérès, suscita des interrogations au sein de l'équipe de découverte. Grâce à mon expertise sur la surface de Cérès et sa rotation, j'ai identifié deux marques à la surface dont la visibilité correspondait aux variations d'intensité observées dans nos détections.

A.3 Propriétés physiques des astéroïdes: modélisation 3-D

Comme indiqué ci-dessus, mon doctorat portait sur l'étude des propriétés physiques par imagerie à haute résolution angulaire. Durant celle-ci, grâce à une collaboration avec M. Kaasalainen, un nouvel algorithme multi-données de reconstruction de la forme 3D des petits corps fut développé, et nous l'avons baptisé KOALA (Carry et al., 2010a; Kaasalainen, 2011). Un tel développement était nécessaire pour tirer partie des différentes sources de données disponibles (courbes de lumière, occultations stellaires, images à haute résolution angulaire) et modéliser les formes irrégulières des astéroïdes. Le point de départ de KOALA étant en effet l'étude de l'astéroïde (2) Pallas dont la forme irrégulière très clairement visible sur les images nécessitait une nouvelle méthode pour décrire les propriétés géométriques/physiques des petits corps (Carry et al., 2010a).

Après mon doctorat, j'ai évidement continué à développer et utiliser cet algorithme. La première étape fut de valider les résultats qu'il fournissait. L'occasion fut fournie par le survol de l'astéroïde (21) Lutetia par la sonde Rosetta de l'ESA. Longtemps avant la rencontre, j'avais déterminé la taille, l'orientation, et la forme de Lutetia avec KOALA (Carry et al., 2010b), solution qui avait été utilisée pour la préparation de la rencontre. Une comparaison extensive des images prises par la caméra OSIRIS à bord de Rosetta avec le modèle que j'avais publié montre que KOALA est robuste et fiable. Pour un diamètre de 98 km, les résidus sur la topographie du modèle KOALA n'étaient que de 2 km, et l'orientation correcte à seulement 2 degrés près (Carry et al., 2012a).

Figure A.1: Exemples de modèles 3-D d'astéroïdes.

Fort de cette validation, j'ai mené et participé à de nombreuses études utilisant KOALA pour étudier divers astéroïdes (Fig. A.1), comme

- (52) Europa (Merline et al., 2013a), révélant la présence de larges bassins rappelant ceux de (253) Mathilde (Veverka et al., 1997), suggérant une faible cohésion des astéroïdes de type C;
- (87) Sylvia (Berthier et al., 2014), présentant une distribution de masse non-homogène et apparement différenciée;
- (3) Juno (Viikinkoski et al., 2015b), incluant des données des programmes de validation scientifique de la caméra de nouvelle génératoin SPHERE et de l'interféromètre ALMA, illustrant le gain en résolution apporté par ces nouveaux instruments;
- (234) Barbara (Tanga et al., 2015), déterminant la nature non binaire de cet objet très particulier. La signature de binarité annoncée par Delbo et al. (2009) vue dans les données interférométriques était en réalité due à la forme irrégulière de Barbara;

- (107) Camilla avec mon étudiante en thèse (Pajuelo et al., 2018a), pour lequel nous avons déterrer 15 ans de données dans les archives des grands télescopes au sol, révélant la présence probable de glace dans son intérieur;
- (6) Hebe (Marsset et al., 2017), tirant parti de la résolution angulaire de SPHERE pour cartographier sa topographie, et évaluer l'origine des chondrite ordinaires, les plus communes des météorites.

A.4 Découverte et caractérisation d'astéroïdes multiples

La question de l'existence de satellites d'astéroïdes s'est posée pendant des décennies, jusqu'à la découverte de Dactyl, satellite de (243) Ida, par la sonde Galileo en 1993 sur son chemin vers Jupiter. L'avènement de l'optique adaptative ouvrit ensuite la possibilité d'imager ces systèmes (e.g., Merline et al. 1999). C'est ainsi que je participe depuis des années à des programmes de recherche de satellites. J'ai ainsi co-découvert 4 des 21 satellites d'astéroïde découverts par imagerie directe, et imagé le premier satellite de géocroiseur: (41) Daphne, (107) Camilla, (317) Roxane, (2577) Litva et (35107) 1991 VH (Conrad et al., 2008; Merline et al., 2008, 2009; Merline et al., 2013b; Marsset et al., 2016).

J'ai également caractérisé certains de ces systèmes, tirant partie de mon expérience pour les observations à haute résolution angulaire: (41) Daphne (Carry, 2009), (87) Sylvia (Berthier et al., 2014), (107) Camilla (Pajuelo et al., 2018a), (90482) Orcus (Carry et al., 2011), et (136108) Haumea (Dumas et al., 2011). Pour chacun, seul un traitement rigoureux des images a permis de mesurer les positions relative des satellites autour de leur corps hôtes (Fig. A.2), permettant de déterminer leurs orbites. Celles-ci sont toutes circulaires, et dans le plan équatorial du corps principal. Dans le cas des systèmes triples Sylvia, Camilla, et Haumea, ceci s'applique aux satellites externes, et non aux internes, plus petits, et vraisemblablement perturbés. Ces caractéristiques orbitales, couplées avec la similitude spectrale entre les composantes que nous avons mesurée (Dumas et al., 2011; DeMeo et al., 2011; Carry et al., 2011; Pajuelo et al., 2018a), indiquent que les satellites se sont formés par collision, entraînant une excavation de matériel qui s'est ré-accumulé en orbite.

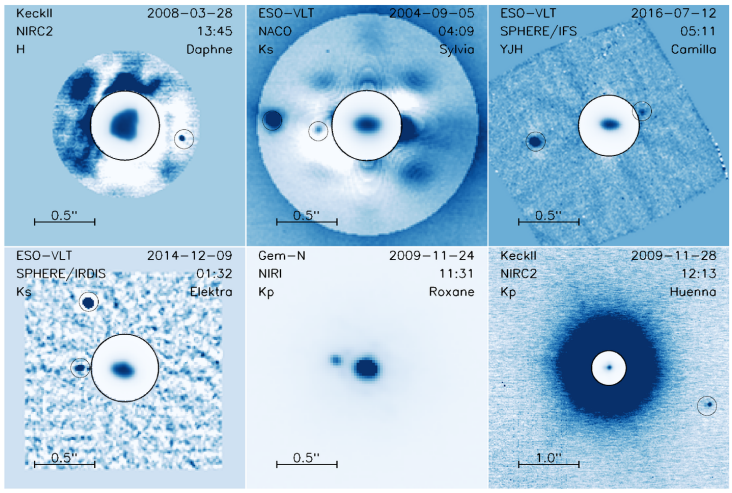

Figure A.2: Exemples d'images de systèmes binaires. Sur chaque image, le cercle au centre d'un diamètre de 0.28″ présente le corps central tandis que la région externe a été traitée pour faire ressortir les satellites (indiqués par les petits cercles).

La résolution angulaire étant *in fine* limitée par la diffraction, j'ai conduit un projet pilote pour caractériser les astéroïdes binaires par interférométrie. Le gain en résolution est en effet drastique, puisque la résolution est limitée par la distance entre les télescopes et non plus leur taille. C'est ainsi que j'ai coordonné une campagne d'observation internationale de (939) Isberga par courbes de lumière tout en l'observant par interférométrie au VLT (Carry et al., 2015). Si l'étude s'est révélée fructueuse, permettant la détermination de l'orbite mutuelle des composantes, leur masse, etc, elle a néanmoins montré les limites des interféromètres actuels.

En parallèle à l'étude de ces systèmes, j'ai mis en place un survey spectroscopique afin de déterminer la composition de tous les astéroïdes binaires connus. En effet, si les petits satellites autour de grands corps comme ceux listés ci-dessus se sont probablement formés par impact, les satellites autour de petits astéroïdes (diamètre inférieur à environ 10 km) partagent tous certaines caractéristiques clefs: rapport de taille d'un tiers, orbite mutuelle et héliocentrique coplanaires, primaire en rotation très rapide proche de la limite critique de désagregation, etc. Leur mécanisme de formation semble ainsi très différent, et du à la fission du corps central suite à sa rotation trop rapide, accélérée par l'effet thermique YORP (voir notre revue: Margot et al., 2015). Mon étudiante en thèse a présenté les premiers résultats cette année avec en particulier un plus grand rapport entre le nombre d'astéroïdes de type Q et de type S que dans la population générale, soutenant l'hypothèse de formation décrite ci-dessus (Pajuelo et al., 2017).

A.5 Densité des petits corps

Un des buts de la détermination de la forme 3-D des astéroïdes et de l'orbites de satellites est la détermination de la densité de ces corps. En effet, cette grandeur est peut être l'information la plus fondamentale sur leur composition et leur structure interne. Compilant les déterminations de masse, volume, et densité provenant de nombreux articles, j'ai ainsi créé un catalogue extensif de 287 objets (Carry, 2012), sautant un ordre de grandeur par rapport à la liste d'une vingtaine d'objets présentée par Consolmagno et al. (2008). Cette base de données m'a permis d'évaluer les degrés de précision et de biais affectant chacune des méthodes utilisées pour mesurer la masse et le volume des petits corps.

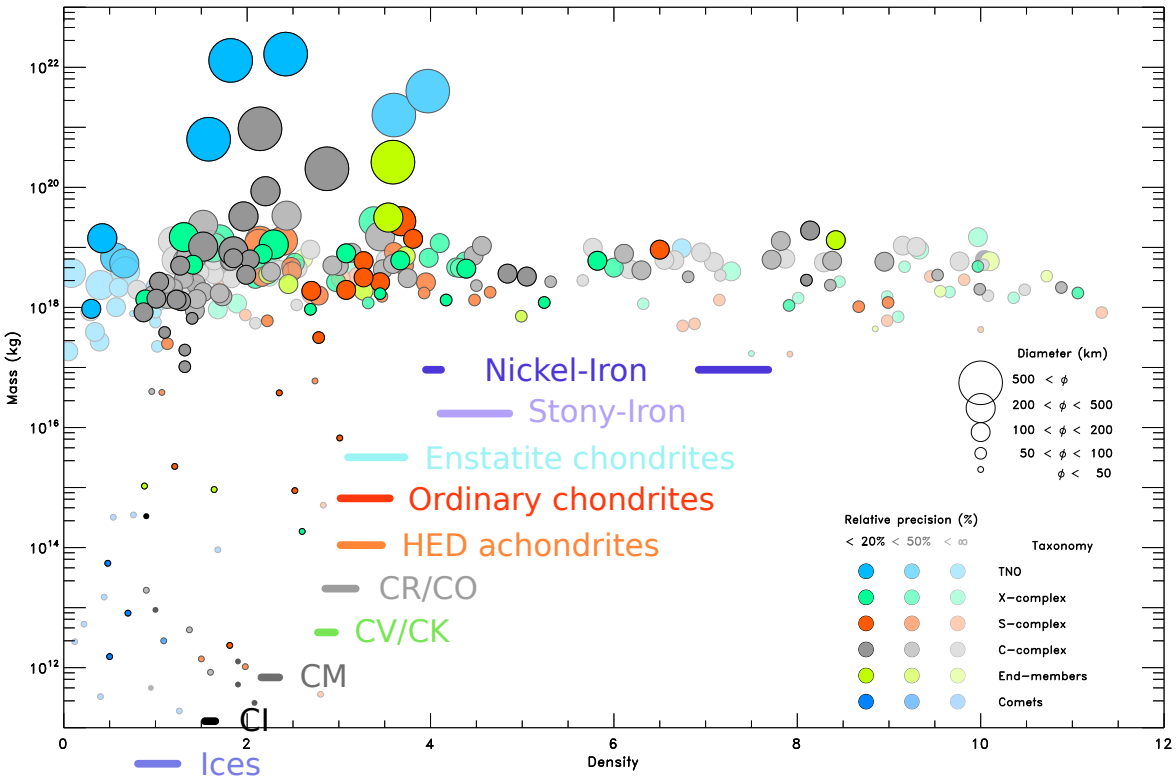

Figure A.3: Diagramme masse-densité des petits corps (Carry, 2012). Les couleurs des disques représentent les types d'objets, leur taille le diamètre des corps, et leur contraste la précision des estimations. La densité des différentes classes de météorites sont également rapportées.

À partir d'une sélection rigoureuse des meilleures estimations, j'ai pu dériver la densité moyenne de chaque classe spectrale, ainsi que la quantité de vide au sein des corps, appelée macroporosité, en comparant la densité des corps avec leurs météorites analogues (voir également notre revue Scheeres et al., 2015, pour une version plus récente). Les planètes naines n'ont apparement pas de macroporosité, mais

celle-ci peut être très importante pour les corps plus petits (<400 km). Cette tendance est corrélée avec la taille, et au sein d'un même groupe compositionnel, la densité augmente avec le diamètre (Fig. A.3). Les différents groupes compositionnels ont des densités en adéquation avec leur météorites analogues, et en particulier, la très faible densités des corps du système solaire externe (objet de Kuiper, comètes) est en accord avec les modèles de structure consistant en des aggrégats de blocs de glace.

A.6 Cartographie compositionnelle des astéroïdes

La spectroscopie dans le visible a été à la base des différentes classifications compositionnelles (appelées taxonomies) des petits corps, et ce depuis les premiers travaux de Chapman et al. (1975) jusqu'à la définition de la taxonomie en usage actuellement, qui inclut le proche infrarouge (DeMeo et al., 2009a). Néanmoins, trois décénnies après l'avènement des CCDs, et malgré des surveys dédiés à la spectroscopie visible et proche-infrarouge des astéroïdes, nous ne disposons que de quelques milliers de spectres visibles et quelques centaines de spectres infrarouges.

Il est toutefois possible d'utiliser les couleurs d'astéroïdes obtenues par imagerie à large bande pour les classer spectralement, car les bandes d'absorption typiques sont très larges et ne requièrent qu'un pouvoir de résolution spectral limité. C'est ainsi qu'avec Francesca DeMeo nous avons décidé d'utiliser les données du Sloan Digital Sky Survey (SDSS) pour étudier la distribution de la composition des petits corps.

Le SDSS est un survey d'imagerie à but cosmologique qui a couvert environ un quart du ciel, de 1999 à 2008, avec cinq filtres visibles. Lors du survey, de nombreux astéroïdes ont été observés par inadvertance, simplement car ils se trouvaient dans le champs de vue du télescope. Un catalogue de ces astéroïdes a été produit par le SDSS, contenant plus de 100,000 objets (470,000 détectés, mais seuls 100,000 identifiés)! Divers auteurs avaient d'ailleurs utilisé ces données pour classer les astéroïdes en quelques grandes classes, étudier la distribution en taille des familles, ou encore le *space weathering* (Nesvorný et al., 2005; Parker et al., 2008; Carvano et al., 2010).

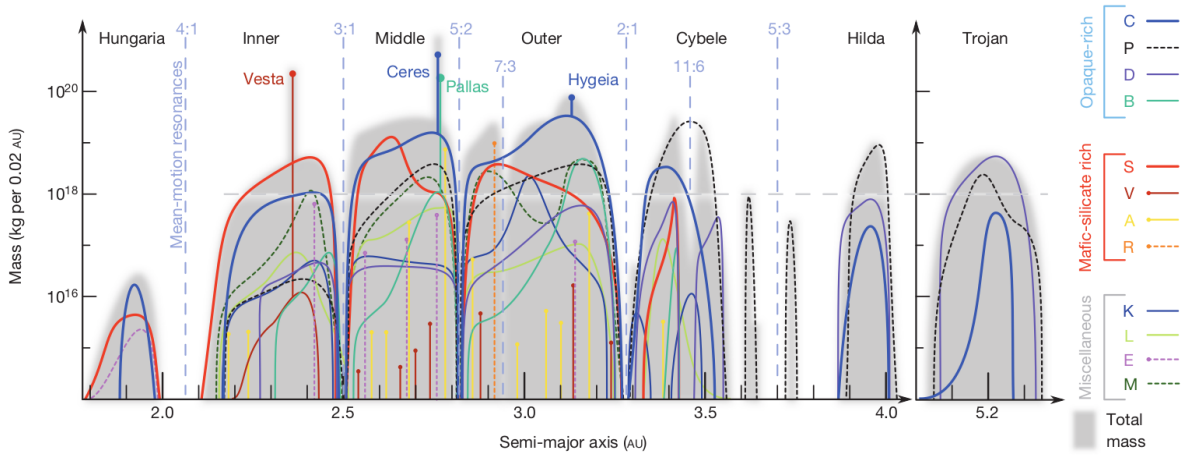

Figure A.4: Distribution en masse des composition d'astéroïde dans le système solaire interne. L'arrière plan en gris représente la masse totale par boîte de 0.02 au. Chaque classe spectrale est représentée par une couleur. La limite horizontale à 10^{18} kg représente la limite des travaux par Gradie and Tedesco (1982). Nos travaux révèlent une complexité inattendue aux plus petites masses (DeMeo and Carry, 2014).

Nous avons donc créé un outils de classement spectral à partir des couleurs du SDSS, déterminant la classe de 100,000 astéroïdes (DeMeo and Carry, 2013). En combinant cet échantillon avec les mesures de diamètre par le satellite WISE (Masiero et al., 2011) et la densité moyenne de chaque classe taxonomique (ci-dessus, et Carry, 2012) nous avons pu reconstruire une carte de la distribution des compositions entre Mars et Jupiter, par masse et non par nombre d'objets (Fig. A.4 DeMeo and Carry, 2014). Ceci est un point critique, en effet, le plus gros astéroïde (1) Cérès représente un quart de la masse totale de

la ceinture d'astéroïde. De même, en étudiant cette répartition par nombre, les familles d'astéroïdes – les fragments de collisions cataclysmiques – biaisent totalement notre vue. Cette étude par masse nous a permis de réécrire 30 ans d'observations, et forme une contrainte observationnelle pour les modèles dynamiques d'évolution du système solaire, type modèle de Nice (Morbidelli et al., 2005).

A.7 Origine des astéroïdes géocroiseurs et aréocroiseurs

Le catalogue d'astéroïdes produit par le SDSS, appelé le MOC, a représenté une source d'information énorme pour notre communauté: plus de 40 articles ont été écrits grâce à lui, dont la description de la structure de la ceinture décrite ci-dessus (DeMeo and Carry, 2014). Néanmoins, le MOC est loin d'être complet, en effet, toutes les sources dont le mouvement apparent était plus rapide que 0.5°/jour ont été filtrées. Ceci implique que les objets géocroiseurs, source des météorites, n'étaient pas catalogués.

Avec Enrique Solano nous avons donc mis en place un projet de science participative dans lequel les internautes peuvent identifier ces objets dans les images SDSS en quelques clicks (Solano et al., 2014). Pour chaque objet potentiellement présent dans une image (identifié à partir du calcul de ses éphémérides), notre système propose les images, et la position prédite. Depuis son ouverture en Juillet 2011, 3500 internautes ont réalisé 415,000 mesures pour 4500 géocroiseurs et aréocroiseurs.

En utilisant ces mesures et l'algorithme de classification spectrale décrit ci-dessus (DeMeo and Carry, 2013), nous avons pu déterminer la composition d'environ 1000 objets, augmentant les échantillons de composition connue pour les géocroiseurs et aréocroiseurs de 40% et 660%! À partir de ces échantillons, nous avons étudié l'origine dynamique de ces corps, et les processus de vieillissement des surface, connus sous le nom de space weathering, et le rôle des rencontres planétaires dans leur rajeunissement (Carry et al., 2016).

A.8 Prospectives

Suivant l'évolution de mes activités de recherche décrite ci-dessus, je suis actuellement deux grands lignes scientifiques, toutes deux basées sur l'analyse à grande échelle de données de grands relevés:

1. En exploitant les observations non-ciblées des astéroïdes dans les surveys d'exoplanètes par la méthode des transits, comme SuperWASP ou Kepler/K2, il est possible d'obtenir les courbes de lumière de milliers d'astéroïdes. Mon étudiant en thèse Jonathon Grice (en co-tutelle avec l'Open University, Londres) s'attèle justement au survey SuperWASP (Grice et al., 2017), et nous avons d'ores et déjà développé les outils nécessaires à l'exploitation des données K2 (Berthier et al., 2016). Dans les années à venir, les sondes TESS de la NASA et PLATO de l'ESA promettent également une moisson de données pour les petits corps.

2. La sonde Gaia de l'ESA va délivrer des spectres basse-résolution dans le visible pour 300,000 astéroïdes (Delbo et al., 2012). Le LSST va également fournir des couleurs dans le visible pour plusieurs millions de petits corps (LSST Science Collaboration et al., 2009), avec les mêmes filtres que le SDSS. Courant 2016, j'ai mis sur pied un groupe de travail européen pour exploiter les données de la sonde Euclid de l'ESA (lancement prévu pour 2020), qui observera 150,000 petits corps dans l'infrarouge, complétant leurs spectres obtenus par Gaia et le LSST (Carry, 2018). Cet extension en longueur d'onde est cruciale car certaines classes spectrales sont dégénérées dans le visible.

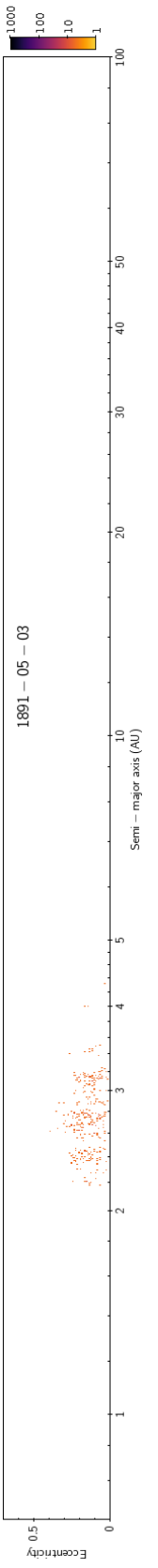

Appendix B

Excerpts from my bibliography

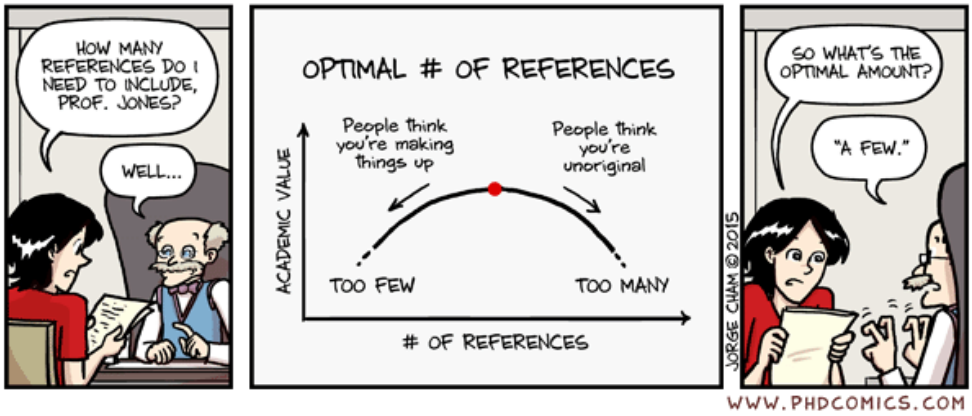

This appendix provides an excerpt of my publication record. I have selected "a few" references to illustrate my work over the past decade. The publications are organized by theme, mainly following the different chapters of the present HDR manuscript.

First, I present four articles representative of my work on high-angular resolution imaging and 3-D shape modeling: my first-ever first-author article (on the physical properties of Ceres, Carry et al., 2008) in Section B.1.a, the validation of the KOALA algorithm by the ESA Rosetta flyby of asteroid Lutetia (Carry et al., 2012a) in Section B.1.b, the modeling of Hebe and its implication on the origin of H chondrites (Marsset et al., 2017) in Section B.1.c, and the review chapter on this subject in *Asteroids IV* I contributed to (Ďurech et al., 2015, , Section B.1.d).

The following three articles focus on binary systems, from minute study of the satellites of Sylvia (Berthier et al., 2014, Section B.2.a) and Camilla (the first article by my PhD student: Pajuelo et al., 2018a, Section B.2.b) with adaptive-optics supported high-contrast imaging, to the use of interferometry in the mid-infrared to directly detect the satellite of small binary asteroids (Carry et al., 2015), in Section B.2.c. I also attach the chapter of *Asteroids IV* reviewing our knowledge on multiple asteroids (Margot et al., 2015, Section B.2.d) of which I am a co-author.

The following article (Carry, 2012, Section B.3.a) and review chapter of *Asteroids IV* (Scheeres et al., 2015, B.3.b) focus on the density of asteroids, and their internal structure. The compilation of all the data required for these studies is a never-ending task. However, the high number of citations to my article shows how such a statistical study was awaited by the community.

Then, two articles illustrate how I used my expertise on adaptive-optics and integral-field spectroscopy on KBOs, from the LGS Science Verification observations of the triple Haumea system (Dumas et al., 2011, Section B.4.a) to the use of background stars for KBO observations like Orcus (Carry et al., 2011, Section B.4.b). The following pair of articles encompasses the photometric survey of the family of Haumea I performed with Colin Snodgrass: Snodgrass et al. (2010) in Section B.4.c and Carry et al. (2012b) in Section B.4.d.

The next three articles were *targets of opportunity*, and I include them here because they are major results, even if they were not planned ahead on my side. It is during an observing run dedicated to the family of Haumea that I observed the outbursting P/2010 A2 which had just been discovered, and we understood later that it had suffered an impact (Snodgrass et al., 2010, Section B.5.a). Based on my pre-flyby determination of the spin-vector coordinates and 3-D shape of Lutetia, I was invited to participate to the analysis of the images taken by the OSIRIS camera during the ESA Rosetta flyby. The ground-based data was in the end crucial: Rosetta imaged only half of Lutetia due to the flyby geometry (Sierks et al., 2011, Section B.5.b). Finally, after participating to a negative search for water vapour around Ceres, I was invited to analyze the H_2O signature detected by ESA Herschel observation owing to my previous studies of the surface marking of Ceres (Küppers et al., 2014, Section B.5.c).

The next section (B.6) shows the new orientation of my research activities, starting by the definition of asteroid taxonomy from SDSS photometry (DeMeo and Carry, 2013, Section B.6.a), leading to the description of the distribution of material in the main belt (DeMeo and Carry, 2014, Section B.6.b) and near-Earth space (Carry et al., 2016, Section B.6.c), to my current development of a Solar System Working Group to use the ESA Euclid mission for planetary sciences (Carry, 2018, Section B.6.d).

Last but not least for a CNAP astronomer, I present articles representative of my work on ESA Gaia (Tanga et al., 2016) in Section B.7.a, and on softwares and services I have released to the community, from image cleaning (Snodgrass and Carry, 2013, Section B.7.b) to ephemerides (Carry and Berthier, 2016, Section B.7.c) and (Berthier et al., 2016, Section B.7.d).

Contents

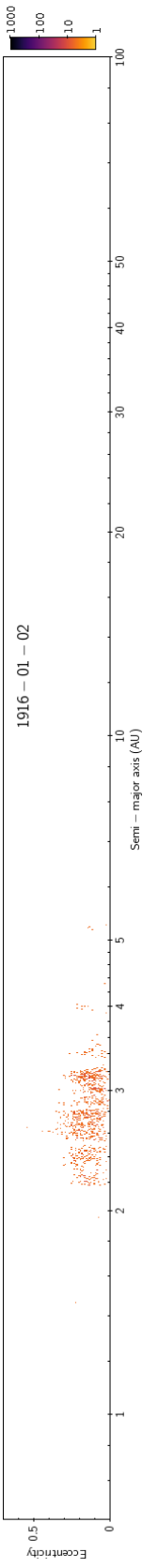

A&A 478, 235–244 (2008)
DOI: 10.1051/0004-6361:20078166

Astronomy & Astrophysics

Near-infrared mapping and physical properties of the dwarf-planet Ceres

B. Carry[1,2], C. Dumas[1,3,⋆], M. Fulchignoni[2], W. J. Merline[4], J. Berthier[5], D. Hestroffer[5], T. Fusco[6], and P. Tamblyn[4]

[1] ESO, Alonso de Córdova 3107, Vitacura, Santiago de Chile, Chile
e-mail: bcarry@eso.org
[2] LESIA, Observatoire de Paris-Meudon, 5 place Jules Janssen, 92190 Meudon Cedex, France
[3] NASA/JPL, MS 183-501, 4800 Oak Grove Drive, Pasadena, CA 91109-8099, USA
[4] SwRI, 1050 Walnut St. # 300, Boulder, CO 80302, USA
[5] IMCCE, Observatoire de Paris, CNRS, 77 Av. Denfert Rochereau, 75014 Paris, France
[6] ONERA, BP 72, 923222 Châtillon Cedex, France

Received 26 June 2007 / Accepted 6 November 2007

ABSTRACT

Aims. We study the physical characteristics (shape, dimensions, spin axis direction, albedo maps, mineralogy) of the dwarf-planet Ceres based on high angular-resolution near-infrared observations.
Methods. We analyze adaptive optics *J*/*H*/*K* imaging observations of Ceres performed at Keck II Observatory in September 2002 with an equivalent spatial resolution of ∼50 km. The spectral behavior of the main geological features present on Ceres is compared with laboratory samples.
Results. Ceres' shape can be described by an oblate spheroid ($a = b = 479.7 \pm 2.3$ km, $c = 444.4 \pm 2.1$ km) with EQJ2000.0 spin vector coordinates $\alpha_0 = 288° \pm 5°$ and $\delta_0 = +66° \pm 5°$. Ceres sidereal period is measured to be $9.074\,10^{+0.000\,10}_{-0.000\,14}$ h. We image surface features with diameters in the 50–180 km range and an albedo contrast of ∼6% with respect to the average Ceres albedo. The spectral behavior of the brightest regions on Ceres is consistent with phyllosilicates and carbonate compounds. Darker isolated regions could be related to the presence of frost.

Key words. minor planets, asteroids – infrared: solar system – techniques: high angular resolution – methods: observational

1. Introduction

Ceres is by far the largest body among the population of main-belt asteroids. Curiously, although it was discovered more than 200 yr ago (Piazzi 1802), significant progress to understand its surface and interior properties has only been made over the last two decades. In particular we have seen a renewal of interest towards Ceres triggered by (i) the availability of sensitive spectro-imaging instrumentation on medium-to-large size telescope, enabling a detailed study of Ceres surface and physical properties (e.g. Mitchell et al. 1996; Drummond et al. 1998; Dotto et al. 2000, and others); and (ii) more recently the selection of the NASA DAWN Discovery mission, which will visit Vesta and Ceres in 2011 and 2015 respectively (Russell et al. 2003). But the main scientific interest drawn by Ceres is that it provides an excellent laboratory to understand how planetoids accreted early in the history of our solar system, and the role of volatiles in planetary formation and evolution. Unlike Vesta, which is dry and shows evidence of the melting phase and planetary differentiation (Keil 2002) seen in larger terrestrial planets like Earth, the "dwarf planet" Ceres (as it should now be named following the IAU guidelines) shows strong signs of water alteration on its surface (Jones et al. 1990). In this respect, Ceres displays stronger similarities with the icy outer satellites of Jupiter than with the dry asteroids that populate the inner region of the Main Belt. A possible scenario is that Ceres formed in a "wet" environment, from the accretion of both rocky planetesimals originally present at this heliocentric distance in the early planetary nebula, and icy planetesimals that migrated inward from the outer regions and whose ices had been preserved (Mousis & Alibert 2005). As a consequence of this "wet" history, the study of Ceres is of paramount importance to understand the process of planetary accretion and formation of the low-albedo primitive asteroids that populate the outer part of the Main Belt.

With a typical angular diameter of 0.6″ at opposition, Ceres can be spatially resolved from the ground using adaptive optics instruments available on medium-to-large telescopes. We carried out a program of multi-band imaging of Ceres from Keck Observatory at high angular-resolution, with the goals of precisely deriving its shape, dimensions, direction of spin axis, and distributions of albedo and color across its surface.

2. Observations and data reduction

2.1. Observations

Our Ceres observations were made with the Keck II telescope on Mauna Kea, Hawaii, on 2002 September 22 and 28 UT, one week before the opposition of Ceres. These observations were obtained under optimal atmospheric conditions with a sub-arcsec seeing at an airmass lower than 1.65 (with half of the data taken with an airmass lower than 1.2). The 2002 opposition occured near Ceres aphelia (Ceres was at a geocentric and heliocentric distance of 1.98 AU and 2.94 AU respectively), its apparent angular diameter was ∼0.66″. The phase angle was of 7° and 5.5° for the two nights, leading to an illuminated fraction of the surface of 99.6% and 99.7% respectively.

⋆ Affiliation at the time the observations were obtained.

Ceres was imaged using NIRC2, the second-generation near-infrared camera (1024 × 1024 InSb Aladdin-3) and the adaptive optics (AO) system installed at the Nasmyth focus of the Keck II telescope (van Dam et al. 2004). The images of Ceres were acquired at 3 near-infrared wavebands J [1.166–1.330 μm], H [1.485–1.781 μm], and K [1.948–2.299 μm], with an image scale of 9.942 ± 0.050 milliarcsec per pixel. Within the Ceres observation sequence we interspersed observations of reference stars, at similar airmass and through the same set of filters, to evaluate the system Point Spread Function (PSF). This calibration was required to perform a posteriori image restoration as described in the next section. No offset to sky was done but the telescope position was dithered between each exposure in order to record simultaneous sky and object frames, while the target (science or calibration) was positioned at three different locations on the detector, separated by nearly 5″ from each other.

2.2. Data reduction

We first reduced the data using the standard procedure for near-infrared images. A bad pixel mask was made by combining the hot and dead pixels found from the dark and flatfield frames. The bad pixels in our calibration and science images were then corrected by replacing their values with the median of the neighboring pixels (7 × 7 pixel box). Our sky frames were obtained from the median of each series of dithered science image, and then subtracted from the corresponding science images to remove the sky and instrumental background. By doing so, the dark current was also removed. Finally, each image was divided by a normalized flatfield to correct the pixel-to-pixel sensitivity differences of the detector.

After these first basic reduction steps, we applied image deconvolution techniques to our set of Ceres data using the MISTRAL algorithm (Fusco 2000; Mugnier et al. 2004). The use of such an algorithm permits to restore the optimal spatial resolution of each image and is particularly well adapted to deconvolve objects with sharp edges, such as asteroids. Image restoration techniques are known to be constrained by the limitations to measure the precise instrumental + atmosphere responses at the exact same time the science observations are made. MISTRAL is a myopic deconvolution method, which estimates both the most probable object, and the PSF, from analysis of science and reference star images. The time needed for the algorithm to converge is largely dependent on the image size. Due to our large number of images to process, we decreased the deconvolution computation time by resizing all our images to a smaller (128 × 128 pixels, but still over 2× the diameter of Ceres) window centered on the object (Ceres or PSF). Comparison tests showed that no deconvolution artifacts were introduced by the use of smaller images. The deconvolved images of Ceres were then compared to identify the few frames (9 in total, that is less than 2.5% of the full set of data) whose outputs were not satisfactory and discard them from our set of data. In the end we obtained 360 images of Ceres with a spatial resolution (Table 1) equivalent to the diffraction limit of a 10 m telescope (given by the angular sampling $\Theta = \lambda/D$, with λ the wavelength and D the telescope diameter). A subset of the restored images is presented in Fig. 1.

3. Ceres global physical properties

3.1. Spin vector coordinates

Measuring the Spin Vector Coordinates (SVC) of Ceres has always been a difficult task. The small amplitude of its lightcurve (~0.04 mag) prevented its determination using classical lightcurve inversion techniques. Until recently, the solutions that were reported for the pole coordinates of Ceres were widely dispersed (spanning a 90° range in the plane of the sky during the 1995 opposition as reported by Parker et al. (2002), based on the compilation of Johnson et al. (1983), Millis et al. (1987), Saint-Pé et al. (1993) and Drummond et al. (1998) pole solutions). This situation changed dramatically with the use of high-contrast direct imaging techniques capable of resolving the disk of Ceres and image fine details on its surface, such as AO observations (e.g. Dumas et al. 2003, and this paper) and HST observations (e.g. Parker et al. 2002; Thomas et al. 2005). The high-quality data obtained at Keck allow us to obtain an independent measurement of the SVC of Ceres, which is compared to the HST results (Thomas et al. 2005). Precise knowledge of the SVC is mandatory to re-project the individual images into Ceres planetocentric referential and establish albedo maps of its surface (see Sect. 4.2).

Table 1. Central wavelength (λ_c) and bandpass width ($\Delta\lambda$) for each filter. The equivalent size (in km) of the theoretical resolution element (Θ) on Ceres and the number of resolution elements across the diameter and over the apparent disk of Ceres are also reported. Ceres covers more than 3200 pixels (projected major- and minor-radius of ~33 and ~31 pixels respectively) on the NIRC2 detector.

Filter	λ_c (μm)	$\Delta\lambda$ (μm)	Θ (km)	Θ Across diameter	Θ Over surface
J	1.248	0.163	37.2	~26	~666
H	1.633	0.296	47.9	~20	~400
K	2.124	0.351	64.6	~15	~228

We performed a control-point method, which consists of following the apparent motion of a surface feature while the asteroid rotates. The path of a rotating feature on the surface of Ceres describes an ellipse if the asteroid is seen under a Sub-Earth Point latitude (SEP_φ) different from 0°, or ±90° (where it describes a line, or a circle respectively). We marked the positions of two main features A and B (Fig. 1) while they rotated respectively over a 93.9° and 87.7° range around Ceres' spin axis (100 and 87 images respectively). All these measurements are shown together on a 3-D representation of Ceres in Fig. 2. The shape of the projected track being determined by the direction of the rotational axis, we were able to measure the north pole angle (p_n) and the SEP_φ at the time of the observations.

In order to compare our solution with other results, we followed the IAU recommendations and calculated the SVC in the J2000.0 equatorial frame: $\alpha_0 = 288° \pm 5°$ and $\delta_0 = +66° \pm 5°$. This result is in agreement with the latest result from HST (Thomas et al. 2005) ($\alpha_0 = 291° \pm 5°$ and $\delta_0 = +59° \pm 5°$).

To directly derive the obliquity of a planetary body, it is also convenient to express the SVC in an ecliptic reference frame. Our measurements give $\lambda_0 = 7°$ and $\beta_0 = +83°$ (with 5° uncertainty), leading to an obliquity for Ceres of about 4°. Such a small obliquity was expected from analysis of lightcurve data (Tedesco et al. 1983) and thermal properties of Ceres regolith (Spencer 1990). Indeed, a larger obliquity would imply stronger variations in the amplitude of Ceres' lightcurves, which have never been reported. As a result, Ceres can only be observed over a small range of Sub-Earth Point latitude (SEP_φ) (–11°, +10°) (computed until 2015), we must wait for the arrival of the DAWN spacecraft to get a direct view of its polar regions.

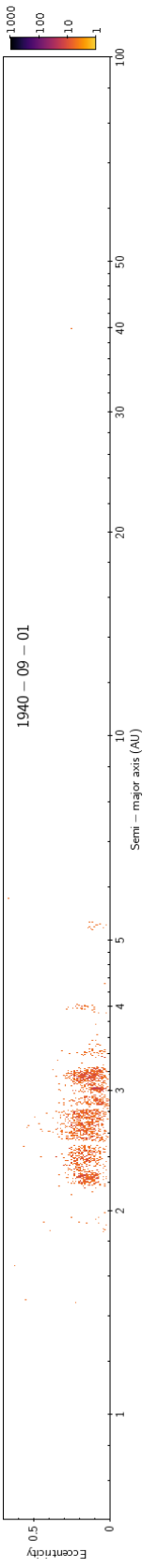

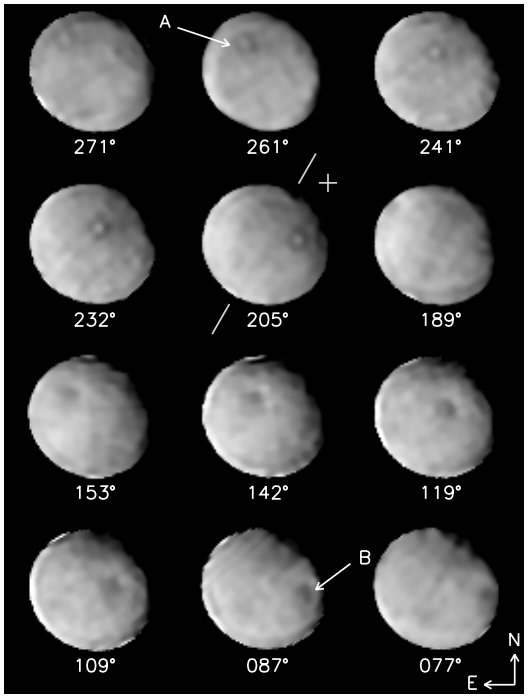

Fig. 1. Selected views of Ceres in K-band during ∼200° of its rotation. The image is oriented with North up and East left. The values of the Sub-Earth Point longitude (SEP$_\lambda$) measured positively from 0 to 360 degrees in a right-hand system (following the IAU recommandation Seidelmann et al. 2005) are indicated below their corresponding images. Our meridian origin is chosen to be the same than Li et al. (2006a). The Ceres spin axis and positive pole are also indicated. The image stretch was chosen to enhance the surface features visible on Ceres at the detriment of the terminator. The two main surface features present on Ceres are indicated with the arrows A and B (see Sect. 3.1) and can be followed during part of their rotation. The brighter spots visible near the limb of Ceres in some of the images are artifacts from the deconvolution (see Sect. 4.2).

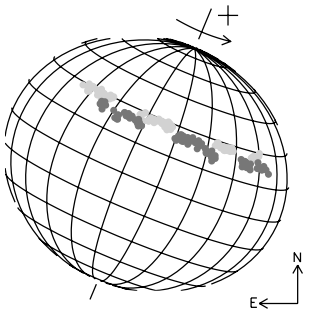

Fig. 2. Apparent motion of the two main features A (bright) and B (dark) over ∼90° of Ceres rotation during the night of the 2002 September 22 UT (SEP$_\varphi \simeq +8°$, $p_n \simeq 338°$). We used the rotational track of these two features to determine the direction of the rotation axis (as described in text).

Table 2. Sub-Earth Point longitude (SEP$_\lambda$) for the three epochs (t_1 and t_2 from Keck, t_3 from HST). Using t_1 as reference, Ceres sidereal phasing with t_2 and t_3 can be obtained by applying a +1.3° and a –98.7° correction taking into account the apparent geometry of the Earth with respect to Ceres.

Epoch	Date (Julian Day)	SEP$_\lambda$ (°)
t_1	2 452 539.894 02	234.6 ± 2
t_2	2 452 545.915 46	261.4 ± 2
t_3	2 453 002.241 28	22.6 ± 5

3.2. Rotational period

We establish a precise and independent measurement of the rotation period of Ceres using images from our two Keck epochs (2002 September 22 and 28 UT), plus one additional processed Hubble ACS/HRC image (*j8p502amq_iof.fit*) from the HST program GO 9748 retrieved from the Small Body Nodes archive (Li et al. 2006b) for the epoch 2003 December 28 UT (Table 2) (Thomas et al. 2005; Li et al. 2006a; Parker et al. 2006). Two main albedo marks visible in all images were used to obtain precise information on Ceres rotational phase at these three epochs (see Table 2). In addition, the period between the Keck and HST observations was sufficiently large to accurately measure the error accumulation on Ceres' period over more than 1000 rotations.

We then used the Eproc ephemeris generator (Berthier 1998) to predict the longitude of the Sub-Earth Point and determine the value of the Ceres sidereal period that minimizes the difference ΔSEP$_\lambda$ between the observed and the computed SEP$_\lambda$. We adopted the pole solution derived in this work as well as the priorly determined Ceres sidereal period of $P_s = 9.075 \pm 10^{-3}$ h (Tedesco et al. 1983) as a best estimate. Table 3 shows the sidereal periods that are in agreement with the Sub-Earth Point longitude (SEP$_\lambda$) at the epochs of the observations.

The value of Ceres sidereal period best matching our observations was found to be $P_s = 9.074\,10^{+0.000\,10}_{-0.000\,14}$ h with a $\sim 10^{-4}$ h resolution. The small ∼0.5 s uncertainty, which come mainly from the error on the mesured longitudes (see Table 2), makes possible to predict Ceres' Sub-Earth Point longitude, SEP$_\lambda$, with an error of only 40° in rotational phase over the next decade. By comparison, the recent study by Chamberlain et al. (2007) compiled 50 yr of lightcurve measurements to derive a period of $P_s = 9.074\,170 \pm 2 \times 10^{-6}$ h.

3.3. Dimensions

Precise measurements of the shape of Ceres allow us to remotely investigate its internal structure and test whether it is a differentiated body (Thomas et al. 2005). We thus performed a Laplacian of Gaussian (LoG) wavelet analysis to 192 images of Ceres to extract its limb contours. Because it is very sensitive to variations of gradient, the LoG permits to precisely detect the inflection points in the flux distribution of our individual deconvolved images of Ceres. We found Ceres to be rotationally symmetric as first reported from a preliminary analysis of the Keck-AO data by Dumas et al. (2003), and later confirmed by Thomas et al. (2005). Analysis of our complete set of contours did not return any deviation from our ellipsoidal model larger than ∼18 km (see Fig. 3). From this model, and our knowledge of the direction of its spin axis, we were able to determine the minor- and major- projected radius of Ceres and correct them from their

Table 3. Sidereal periods of Ceres which are in agreement with our observations, based on $SEP_\lambda(t_1) = 234.6°$. The predicted Sub-Earth Point longitude (SEP_λ) are computed at epochs t_2 and t_3 and are compared with the measurements (difference ΔSEP_λ). We only kept sidereal periods whose predicted $SEP_\lambda(t)$ were inside measurement uncertainties.

Sidereal period (h)	$SEP_\lambda(t_2)$ (°)	ΔSEP_λ (°)	$SEP_\lambda(t_3)$ (°)	ΔSEP_λ (°)
9.066 588	255.1	6.3	17.9	4.7
9.066 685	255.1	6.3	22.6	0.0
9.066 780	255.1	6.3	27.2	–4.6
9.074 000	259.8	1.6	17.8	4.8
9.074 090	259.8	1.6	22.1	0.5
9.074 100	259.8	1.6	22.6	0.0
9.074 110	259.8	1.6	23.1	0.5
9.074 200	259.9	1.6	27.5	–4.9
9.081 526	264.4	–3.0	17.9	4.7
9.081 526	264.5	–3.1	22.6	0.0
9.081 526	264.6	–3.2	27.2	–4.6

Table 4. Ceres sidereal period (P_s), pole direction (α_0, δ_0) and initial rotational phase angle (W_0) at epoch of reference in the J2000.0 equatorial frame.

α_0 (°)	δ_0 (°)	W_0 (°)	P_s (h)	Epoch (JD)
288 ± 5	+66 ± 5	−46 ± 2	9.0741 ± 10^{-4}	2 452 539.894 02

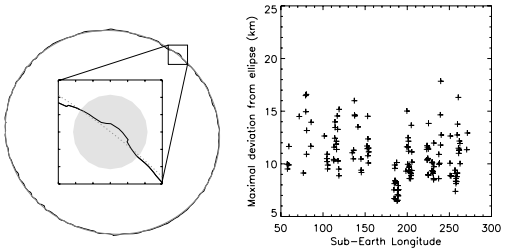

Fig. 3. *Left figure*: extracted limb contour (black) from a *J*-band image of Ceres with its ellipsoidal fit overplotted for comparison (dotted gray). This example shows that deviations from the ellipsoidal model are much smaller than the resolution element (gray disk inside the box) obtained with Keck-AO. *Right figure*: compilation of our deviation measurements as function of the Sub-Earth Point longitude (SEP_λ). No deviations larger than ∼18 km (half a resolution element at *J*-band) are detected.

aspect and phase angles. We found that Ceres is well described by an oblate spheroid whose semi-axes are $a = b = 479.7 \pm 2.3$ km and $c = 444.4 \pm 2.1$ km (1-σ dispersion for the fitted axis). These values are different from HST's by ∼10 km (relative difference of two percent). In comparison, the agreement between our semi-major axis and the determination made from stellar occultation by Millis et al. (1987) is remarkable: 479.6 ± 2.4 km (occultation) vs. 479.7 ± 2.3 km (Keck), while our minor-axis value differ from theirs by ∼6–9 km (Table 5). Whereas Millis et al. (1987) assumed a zero-obliquity at the time of the occultation, our SVC solution gives a SEP_φ of +3.3°. The corrected polar radius from stellar occultation is thus 453.3 ± 4.5 km, which is still different from our measurement by nearly 10 km. It is important to note that during the occultation of 1987, the cords along Ceres orbit were aligned in an East-West direction, whereas the north

Table 5. Semi-major (*a*) and -minor (*c*) axes, and equivalent radius ($R = \sqrt[3]{aac}$) for Ceres derived in this paper (Keck), Thomas et al. (2005) (HST), and Millis et al. (1987) (Occultation). The pixel size of the Keck and HST images are also given for comparison.

Quantity	Imagery		Occultation	
(km)	Keck	HST	Sol. 1	Sol. 2
a	479.7 ± 2.3	487.3 ± 1.8	479.6 ± 2.4	481.6 ± 2.4
c	444.4 ± 2.1	454.7 ± 1.6	453.4 ± 4.5	450.1 ± 2.0
R	467.6 ± 2.2	476.2 ± 1.7	470.7 ± 3.1	470.8 ± 2.3
pixel	14.3 ± 0.7	33.9 × 29.6	...	...

pole position angle was $p_n \sim 339°$. This implies that the estimation of the small radius of Ceres was more loosely constrained than its semi-major axis. In addition, Table 5 provides a comparison between the pixel size of the HST and Keck images, and shows that the coarser sampling of the disk of Ceres as seen by HST could explain the differences in our respective determinations of its size. Our mean radius for Ceres is estimated to be $R = 467.6 \pm 2.2$ km, which is also closer to the determination made from stellar occultation than HST's.

Adopting a mass for Ceres of $M = 9.43 \pm 0.07 \times 10^{20}$ kg (average of most recent measurements, Viateau & Rapaport 1998; Michalak 2000; Kovačević & Kuzmanoski 2007), we find a mean density $\rho = 2\,206 \pm 43$ kg m^{-3}. This value is relatively high for a hydrated G-type asteroid like Ceres, but can be explained by a low porosity (see Britt et al. 2002), and is similar to the density of the icy outer Jovian satellites Ganymede and Callisto. One can assume Ceres to be in hydrostatic equilibrium and inverse the relation between *a*, *c* and J_2 (given by McCord & Sotin 2005) as following

$$J_2 = \left[1 - \frac{c}{a} - \frac{2\pi^2 R^3}{P_s^2 GM}\right]\left[\frac{c}{2a} + \left(\frac{a}{c}\right)^2\right]^{-1}$$

and find $J_2 = 26.7 \times 10^{-3} \pm 1.9 \times 10^{-5}$. By comparison, Thomas et al. (2005) have found $J_2 = 21.7 \times 10^{-3} \pm 8.5 \times 10^{-5}$. If we refer to McCord & Sotin (2005), these two independent estimates of J_2 correspond to their internal models #2 and #3 for Ceres, that is to a differentiated Ceres with a silicate-rich region in its center. The rather large difference between the two J_2 determinations is due to the fact that J_2 is highly dependant on the *a*/*c* ratio which shows large uncertainties depending on the measurement technique used. Lightcurve analysis for a quasi-spherical object is generally little sensitive to this parameter; while measurements made from direct imaging from the Earth distance suffer from lack of sufficient spatial resolution to estimate this parameter with the required precision. Nevertheless, both studies converge towards a differentiated asteroid and gravity field measurement made by DAWN will provide a better understanding of its mass repartition and internal structure.

Conrad et al. (2007) have shown that a detailed study of an asteroid shape, and its departure from a perfect ellipsoid, can be carried out using images deconvolved with MISTRAL. Deviations of Ceres limb measurements from our shape model can thus directly be linked to topography. Figure 3 shows that no features deviating from our shape model by more than 15–18 km can been observed. The highest relief expected on Ceres is calculated to be ∼10–20 km high (see also Johnson & McGetchin 1973, Fig. 1), thus confirming that no significant deviation from an ellipsoid can be detected given the size of our resolution element. Search for relief would require a resolution of at least about 5 km to provide unambiguous detection of a topography.

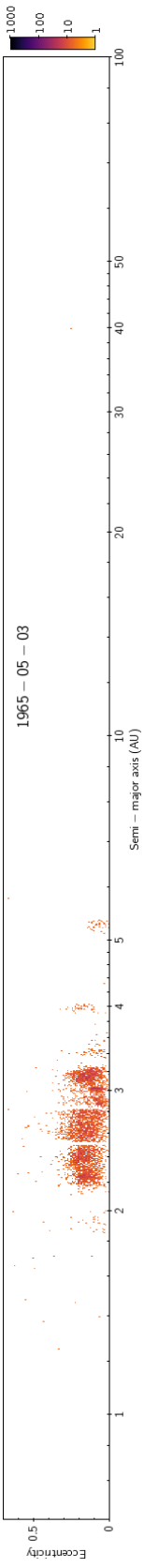

4. Ceres surface composition

4.1. Background

Ceres occupies a particular place in our solar system. It is physically located far enough from the Sun to have been preserved from strong heating during the T Tauri phase of the Sun (Ghosh et al. 2006, and references therein), and has possibly retained some of its primordial elements. Ceres' low amplitude lightcurve (∼0.04 mag) cannot result from its symmetrical shape (Thomas et al. 2005). This shows that its surface, while rather uniform, displays faint albedo features, unlike the igneous asteroid Vesta whose hemispheric albedo variations are among the strongest seen among main belt objects (Gaffey 1997). Similarly, in contrast to Vesta, whose shape is highly irregular due to past collisions (Thomas et al. 1997), Ceres displays a uniform spheroidal shape, deprived of strong surface and topographic features, and its density (see Sect. 3.3) cannot simply be attributed to macroporosity of its internal material (see Britt et al. 2002). All these characteristics point to the presence of volatile elements in the interior of Ceres. Mousis & Alibert (2005) show that Ceres could have accreted from an assemblage of rocky and icy planetesimals, even at such short heliocentric distances. They calculated that icy planetesimals could have drifted from more distant regions of our solar system (up to 15 AU heliocentric) to the actual position of Ceres (2.7 AU) without losing entirely their volatiles. This idea supports the model of Fanale & Salvail (1989) in which the C/G-type objects accreted from anhydrous minerals, organics and water ice. The recent discovery of comets orbiting among the main-belt asteroids, at semi-major axes similar to Ceres' (Hsieh & Jewitt 2006) support the possibility that small bodies can preserve part of their ices within the snow line region, which is defined as the heliocentric distance for which the temperature equals the condensation temperature of water (∼5 AU).

Other studies supporting a wet history for Ceres come from meteorites. Although no meteorites have been convincingly linked to Ceres (Feierberg et al. 1980; Jones et al. 1990; Sato et al. 1997), the C-type asteroids (whom G-type is a subclass) display a low albedo, and are thought to be the source of the Carbonaceous Chondrites (CC) meteorites. It has been shown that water ice could be stable inside CC meteorites over 4.5 Gyr (Fanale & Salvail 1989, and references therein), thus supporting the possibility that the Main Belt has likely experienced a hydrated stage in its history (at least its outermost part). Moreover, spectral studies of Ceres reveal a strong 3.07 μm absorption band characteristic of hydrated minerals (Jones et al. 1990; Sato et al. 1997). This particular band has been the center of interest of many studies: In the early 80's, Feierberg et al. (1980) and Lebofsky et al. (1981) associated it with the signature of water frost on Ceres surface and predicted the possible existence of a polar cap. A decade later, King et al. (1992) fitted the 3 μm absorption with saponite, which is an ammonium-bearing phyllosilicate whose presence in CV and CI meteorites have been suggested by Zolensky & McSween Jr. (1988). Later, Vernazza et al. (2005) found that crystalline water ice mixed with ion-irradiated asphaltite could reproduce a better fit to this feature. Recently, Rivkin et al. (2006) reviewed this past work and found that an hydrated iron-bearing phyllosilicate identified as cronstedtite, plus a few percent of carbonates could also fit adequately the near-infrared spectrum of Ceres. This recent interpretation could be supported by the detection in the mid-infrared range of emission features attributed to carbonates (from Cohen et al. 1998). In addition, iron-bearing minerals have also been invoked by Feierberg et al. (1980) and Vilas & Gaffey (1989) to explain other spectral features present in the visible and near-infrared spectra of Ceres: 0.4 μm cutoff, 0.60 μm and 0.67 μm weak absorption bands and 1 μm shallow band (see also Vilas & McFadden 1992). Given the radical different interpretations of the 3.07 μm band reported over the past decade, it is quite impossible to conclude on its exact nature. A persistent conclusion though, consists to support the presence of hydrated minerals, or residues from aqueous alteration, in the regolith material.

As discussed above, surface water ice is not stable at distances smaller than 5 AU and is expected to sublimate if exposed directly to solar radiation (Fanale & Salvail 1989). Indeed, water ice migrating from the mantle region could possibly reach the surface but will escape on very short time-scale (Nazzario et al. 2003). As a result, direct detection of water ice vaporization from Ceres surface might be possible from the surroundings of a fresh impact crater, or from cracks in the sub-surface layers. Water escaping from Ceres polar region has possibly been detected in the early 90's (A'Hearn & Feldman 1992), although this 2-σ detection could never be unambiguously confirmed. Another supporting element comes from the relaxed shape of Ceres, which could be explained by the presence of large amount of ice in its interior (McCord & Sotin 2005). The measurements of J_2 obtained from HST and Keck both clearly support a model of a differentiated Ceres with a volatile-rich mantle, rather than a homogeneous interior model (see Sect. 3.3).

4.2. Near-infrared maps

To better represent the distribution and spatial extent of the features observed on the surface of Ceres (albedo, geological marks), we projected our high-angular resolution images into maps. The following sections are used to describe in details the various steps involved in the process of map projection, and the subsequent analysis of Ceres surface properties.

Geometry: Any projection of an ellipsoidal shape onto a plane introduces deformations (Greeley & Batson 1990). We attempted to minimize these effects by choosing the cylindrical equidistant projection, which maps the surface of the asteroid onto a cylinder tangent to its equator and conserves the distances along the meridians. As a result, this projection minimizes the deformations of Ceres' equatorial area, which is seen at highest resolution thanks to its small obliquity. Higher planetocentric latitudes suffer stronger deformations after projection, but the impact is mitigated since these regions correspond to areas imaged tangentially, at a lower equivalent spatial resolution.

Region of interest: We produced albedo maps of Ceres using the pixels located within an ellipsoidal Region Of Interest (ROI) centered on the image, and whose semi-axes were equal to 80% of the corresponding projected semi-axes on Ceres. The ROI corresponds to 64% of the projected surface for each image (see Fig. 6). Ignoring the pixels near the edge of Ceres was based on several considerations:

1- Although all images used to produce the maps were carefully cleaned before deconvolution (including from correlated noise), some of them still presented artifacts after restoration of their optimal resolution, particularly near discontinuities such as the limb and terminator.
2- It appeared difficult in a few cases to restore optimally both the contour of the object and the surface details, even if

MISTRAL is optimized to minimize the "ringing" effect introduced by the deconvolution of sharp edge objects.

3- Finally, the resolution per pixel being highest at the center of the disk of Ceres, the use of the pixels located near the edge would strongly degrade the optimal resolution of our final product.

Phase angle correction: As seen on Fig. 1, a phase angle of just a few degrees at near-infrared wavelengths produces a strong gradient of luminosity across the disk of Ceres. This effect had to be corrected prior to combine our individual images onto single maps. Several diffusion laws were investigated to model it, such as adopting a simple linear gradient, or using more complete models such as provided by the Lambert, Lommel-Seelinger, Minnaert and Hakpe laws (including single-scattering and multiple-scattering effects) (see Hapke 1993). The linear gradient was adopted since it provided the best fit to Ceres surface (residuals produced were nearly twice smaller than in the case of the Hapke model).

Projection: The main difficulty to project an image of Ceres into its planetocentric referential (defined by its planetocentric longitude (λ) and latitude (φ) as recommended by the IAU, Seidelmann et al. 2005), resides in the accurate determination of its geometrical center. As the distribution of Ceres gravity field is unknown, we made the assumption that its center of mass, which is the center of the planetocentric referential, coincides with its geometrical center. The conversion into planetocentric coordinates was based on our determination of Ceres dimensions (see Sect. 3.3) and the orientation of its spin axis (SVC, see Sect. 3.1), which is defined by the north pole angle (p_n) and by the Sub-Earth Point coordinates (SEP_λ, SEP_φ). We used our value for Ceres rotation period (see Sect. 3.2) and the Eproc ephemeris generator to obtain the SEP_λ, SEP_φ and p_n at the time of each observation. We then projected the images onto half-degree gridded maps to sample all areas of Ceres with sufficient resolution, from the equatorial region, up to the edge of the ROI. This fine grid map helped recover the smallest scale information from our set of 360 images.

Combination of images into maps: No absolute photometric calibration was obtained for our data. We therefore used a near-infrared disk-integrated spectrum of Ceres (R. Binzel, personal communication) normalized to unity at 0.5 μm to calculate the equivalent disk-integrated photometric value for each band, and normalize our albedo maps with respect to each other. Prior to combine the different views into maps for each wavebands, we corrected the intensity variations of the individual projections caused by the differential atmospheric absorption across our wavelength range, as well as the quality of the AO correction. We first projected each image onto the planetocentric referential of Ceres. Then we adjusted the brightness level of spatially adjacent maps by measuring the flux ratio over their overlapping area and applying the corresponding re-normalization coefficient. After correction, the maps could be combined to produce the albedo maps presented in Fig. 4 for each waveband. Each pixel of the final maps (covering a quarter of a square degree) was obtained by combining the corresponding pixels from the individual projections using a gaussian-weighted average function (we chose a gaussian with a standard deviation of 5 pixels). The largest weight (weight value = 1) was attributed to the pixel providing the best spatial resolution, while the pixels with a lower resolution were assigned a lower weight. Table 6 gives the average and maximum number of images used to produce a single pixel of the final maps for each waveband, as well as the percentage of surface coverage of Ceres (~80%). In order to facilitate comparison between our near-infrared data and the UV/Visible (223, 335 and 535 nm) HST maps, we chose to adopt the same reference meridian as Li et al. (2006a).

Maps description: The J-, H- and K-band maps shown in Fig. 4, and covering ~80% of Ceres' surface (see Table 6), are the result of combining 126, 99 and 135 individual projections respectively. We also derived error albedo maps (Fig. 5) by measuring, for each pixel, the intensity dispersion across the individual views. The theoretical size of the resolution elements for the J-, H- and K-band are 36.8 km, 47.4 km and 62.9 km respectively (corresponding to 4.4°, 5.6° and 7.5° at the equator). The major features have diameters of ~180 km (A and B) but smaller features can be seen in all three maps down to ~50 km scale. Although the theoretical resolution is highest in J-band, Fig. 4 shows that the final resolution is nearly equivalent across our three bands (i.e. ~60 km at equator). The degradation of the H- and J-band resolution is due to a more variable PSF at these wavelengths, which is supported by the larger photometric error (Fig. 5) derived for these bands. The amplitude of the albedo variation is within ±6% around the mean surface value for each band. The error maps show that the albedo maps (Fig. 4) display an increasing error with decreasing wavelength: the 1-σ uncertainty is smaller than 1% in the equatorial area in K band while it is estimated to be ~2% in J-band. The shape of the error distribution around 60° longitude reveal that the linear oblique features seen in J- and H-band are noise and should be ignored from our analysis. The K-band map displays the lowest noise level, due to the highest Strehl ratio delivered by the AO system at these wavelengths and should be considered as the most accurate of the three.

Some of the main albedo features in our near-infared maps can also be seen in the UV/Visible HST maps published by Li et al. (2006a), like the large bright area around (125°, +20°) and the dark spot at (130°, –24°). The fact that these features are visible in all wavelengths suggests that they are geological features like basins or impact craters. However the UV/Visible and near-infrared maps show also discrepancies: the bright feature at (115°, –30°) visible in the UV/Visible maps is not present in our maps, nor the dark feature located around (45°, +10°). Whereas all the discrepancies cannot be linked to surface properties (the dark annulus of the "A" feature (234°, +23°) is not visible in the UV/Visible map due to its size which is comparable to the resolution element provided by the HST), such variations in their spectral behavior suggest compositional differences between these regions. The next section will provide a discussion on possible composition and geological origin.

4.3. 3-D model

We re-projected our multicolor maps of Ceres onto its 3D shape model. Such model is used to check the distribution of albedo features present in our final maps against the features seen in our original images after deconvolution (see Fig. 6). This model can also be used to predict[1] what Ceres surface would look like at any epochs, which will certainly be useful when preparing any future ground-based, or space based observations of Ceres.

[1] http://www.imcce.fr/page.php?nav=en/ephemerides/formulaire/form_ephephys.php

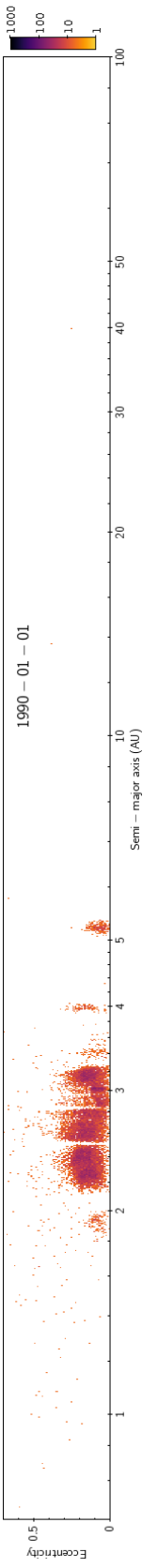

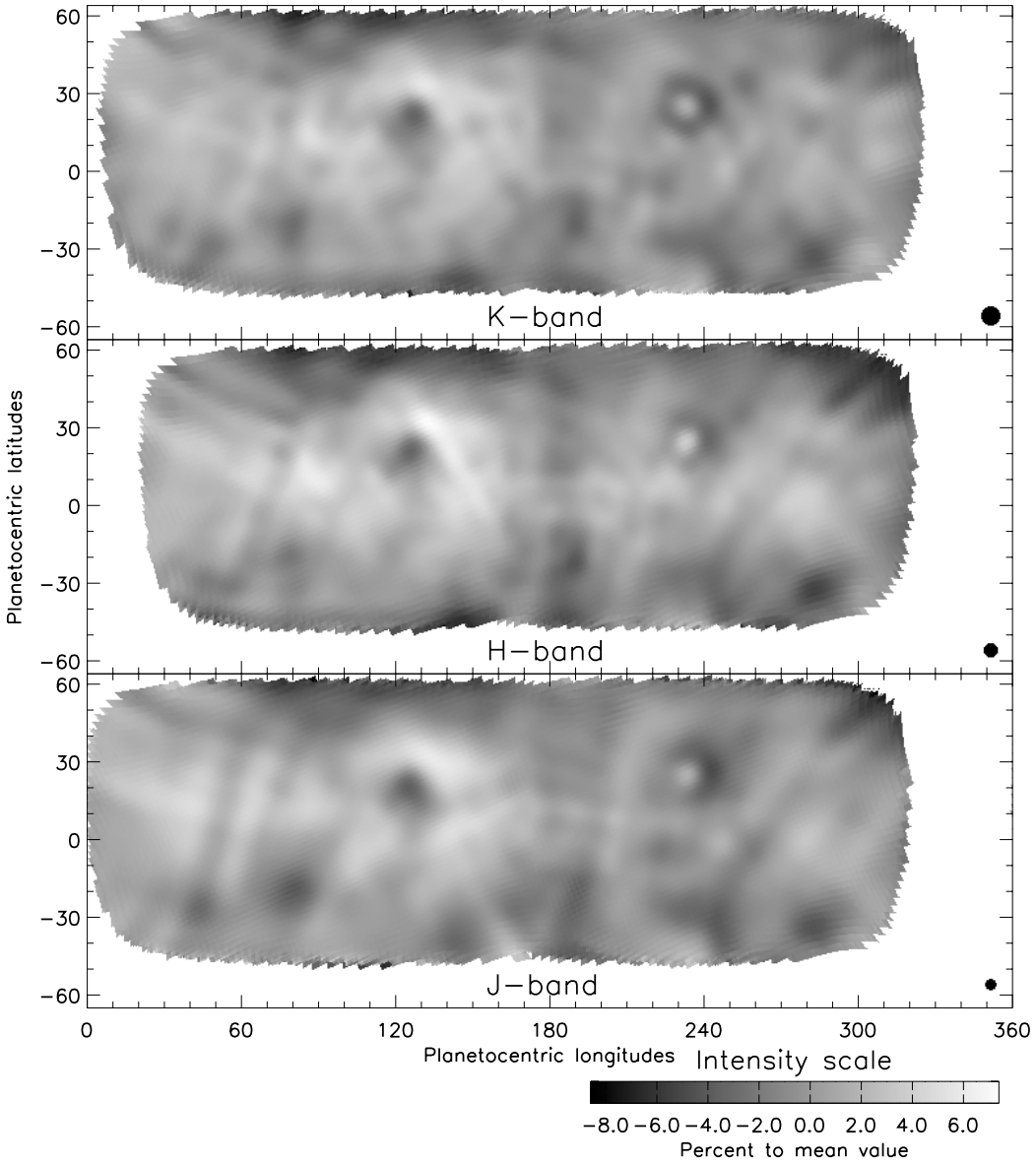

Fig. 4. *J*-, *H*- and *K*- band maps of Ceres covering ~80% of Ceres' surface. The areas in white are *terra incognita* due to the limited ROI and rotational phases not imaged from Keck (see text). The theoretical resolution elements Θ at *J/H/K* bands are shown at the bottom-right corners. Albedo variations are within ±6% around the mean surface value for each map. We estimate the errors to be 2.5% maximum (see Fig. 5). The color scale is common for the three filters. Several round shaped features are visible including a dark feature with a bright center spot at ~(234°, +23°) (named "A") and a dark region at ~(125°, +20°) named "Piazzi" by Parker et al. (2002) (here "B"). Two other dark features are visible in the Southern hemisphere at ~(80°, –20°) and ~(285°, –35°) as well as other smaller features elsewhere (see Fig. 7). Any feature or albedo distribution present in the three maps has a very low probablity to be an artifact, with the exception of the diagonal stripes seen across the surface in *H*- and *J*-band (see text and Fig. 5). One hemisphere (0° to 180°) appears to be brighter (1%) than the other at these wavelengths. A dark region running North/South is located at the boundary between the two hemispheres and is present in all maps.

Table 6. Average and maximum number of images used to produce a single pixel of the final *J*/*H*/*K* bands maps, and their corresponding surface coverage.

Filter	Average images (# per pixel)	Maximum images (# per pixel)	Coverage (% total surface)
J	16	63	81.8
H	14	54	74.2
K	19	72	80.0

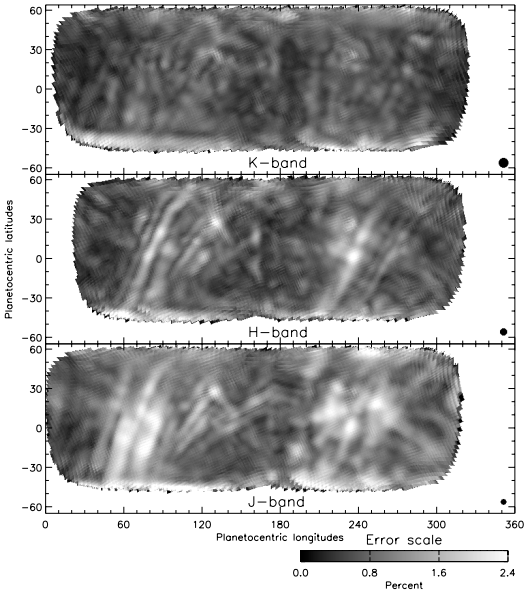

Fig. 5. 1-σ deviation map expressed in percent with respect to the map mean value for each filter. The error is greater in *J*-band than in *K*-band as it could be expected from the lower strehl ratio at smaller wavelengths. The error also grows with latitude, which is due to the nearly equatorial view of Ceres as seen from an Earth observer.

4.4. Three-band spectra

We investigate the nature of the major features seen in our maps by reporting their relative brightness variation at *J*-, *H*- and *K*-bands. We selected 10 type of area (6 bright and 4 dark, noted b_i and d_i respectively) and show in Fig. 7 their photometric measurements normalized to Ceres integrated spectrum. The photometric value obtained for each band is the result of averaging the photometric measurements over an area equivalent to a resolution element. We estimate the error on the relative photometry as $\sqrt{\sum \sigma_i^2}$, where σ_i is the standard deviation for each pixel as read in the error map (Fig. 5). The results are shown in Fig. 7 with their 3-σ error bars.

Whereas spectral variation with the rotational phase of Ceres has never been reported, our data show differences of spectral behavior across the surface. The analysis of Fig. 7 reveals a clear trend of the bright features (left) to display a higher *H*-band albedo (with respect to *J*- and *K*-band) than the rest of Ceres' surface. On the contrary, the dark features (right) do not display a similar trend. This may indicate a common origin for the bright features, whereas the dark regions may be the result of various surface processes, or represent different level of surface aging.

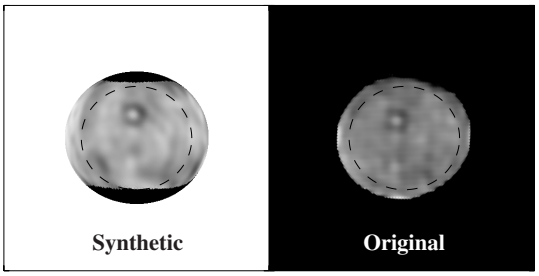

Fig. 6. Comparison between a synthetic view of Ceres (*left*) and a single deconvolved image (*right*). The overplotted dotted ellipse corresponds to the ROI limit (80% of projected axis). The synthetic view appears "smoother" than the original view because it is the result of the weighted average of several deconvolved images. The main albedo features are seen in both the synthetic and the original views, while other features did not resist the weighted average of several images, which acted as a filter to remove artifacts present in a single frame.

We then compare the 3-band spectra to those of various laboratory compounds. We used the ASTER[2] and RELAB[3] spectral libraries, to obtain the equivalent near-infrared spectra of various compounds predicted to be present on Ceres. We show in Fig. 8 their broad band photometric values, normalized to Ceres disk-integrated spectrum, each mineral being mixed with a dark neutral compound, using the mixing ratios given in Table 7. Due to the low spectral resolution provided by our broad band imagery, it is not possible to identify unequivocally the compounds present on the surface of Ceres. We thus based our study to the comparison between the possible surface compounds proposed by Rivkin et al. (2006), who showed that carbonates like Siderite, Dolomite or Calcite mixed with phyllosilicates provide an excellent fit to the 3 μm region of Ceres. Carbonates could also explain the mid-infrared spectral emission features detected by Cohen et al. (1998). We also included an orthopyroxene (Enstatite), a clinopyroxene (Augite) and Olivine, the most abundant elements in the Solar System. A water ice frost spectrum is also reported.

Although the compositional information returned at such a low spectral resolution should be considered with caution, we can use the comparison between the spectral behavior measured on the surface and that of the laboratory samples to constrain and discuss the possible surface composition of Ceres. There are similarities between the spectral behavior of the bright features seen in Fig. 7 (left) and that of phyllosilicates and carbonates in Fig. 8. The Calcite and Montmorillonite "spectra" display the same shape as the majority of the bright features. For instance, the Montmorillonite reproduces quite well the behavior of the b_4 feature as well as the bright region b_2 surrounding d_3. On the other hand, the spectral behavior of the Siderite (a iron-rich Calcite), Cronstedtite (an iron-bearing phyllosilicate), or Augite (a clinopyroxene) only match the spectrum of a small percentage of Ceres surface, and for small mixing ratios show that all of them might be minor compounds of the regions discussed in this section. Igneous rocks like pyroxenes and olivine are not expected to be present on the surface of primitive

[2] http://speclib.jpl.nasa.gov
[3] http://www.planetary.brown.edu/relab/

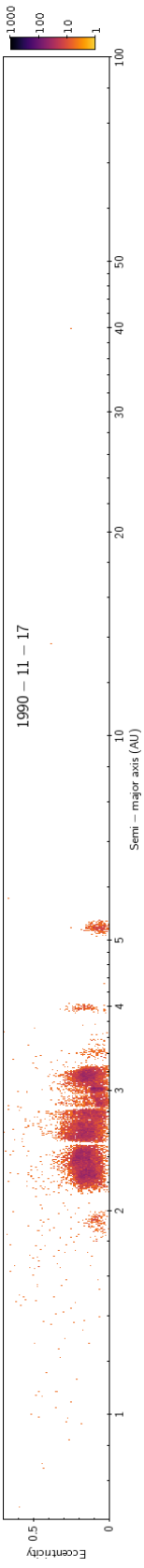

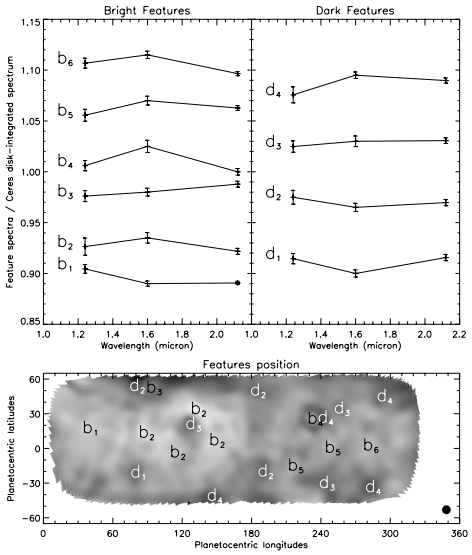

Fig. 7. Three-band spectra of selected surface features normalized to Ceres disk-integrated spectrum. The *left* (and *right*) *panels* show the photometric points obtained for the bright and dark features respectively. All spectra are shifted vertically by 0.045 (bright) or 0.065 (dark) to improve clarity. The letters positioned left of each spectrum are used to locate the corresponding features on the map. The *K*-band resolution element is shown at the bottom-right corner.

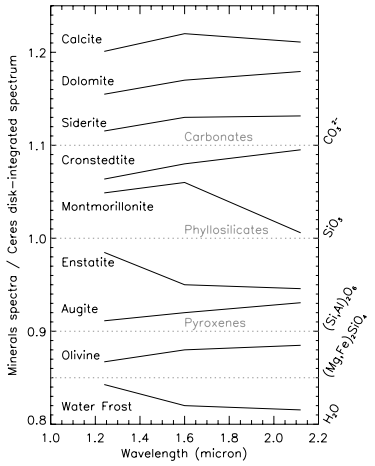

Fig. 8. Three-band spectra of selected carbonates [CO_3^{2-}], phyllosilicates [SiO_3], pyroxenes [$(Si,Al)_2O_6$], olivine [$(Mg,Fe)_2SiO_4$], and water ice frost [H_2O] normalized to Ceres disk-integrated spectrum. Error bars are negligible.

asteroids; these compounds are likely minor components of the regions discussed in this section if present at all.

The interpretation of the dark features is more complex. Indeed, the lower *H*-band value that characterizes half of the dark features (d_1, d_2) does not match the behavior seen in phyllosilicates and carbonates, which are the major compounds predicted to be present over Ceres (see Sect. 4.1). Such a drop in *H*-band matches better the behavior of Enstatite, but its high density of ~3200 kg m^{-3} and the mid-infrared mismatch between Ceres and Enstatite spectra makes its presence unprobable. Another possible matching compound is water ice (Fig. 8). Water ice is not expected to be found in a stable form over Ceres, but "dirty" ice, i.e. ice or frost mixed with other minerals, could be present and reproduce the more elevated *K*-band point seen in the "spectra" of these features. Another point to consider is the relatively high planetocentric latitude of these dark features. None of them is found in the equatorial region, most being located above 30–40° latitude. If dirty ice exists on the surface or sub-surface layers of Ceres (McCord & Sotin 2005; Mousis & Alibert 2005), it would be expected to be more stable at higher latitudes, where surface temperature is lower. Nevertheless, we cannot ascertain from these data alone that ice is present on Ceres. Higher spectral resolution, coupled with the high-contrast and spatial resolution provided by adaptive optics, is required to investigate in detail the composition of the main features seen on its surface. The limits of such a broad-band analysis in constraining the composition of the main features is illustrated by the bright feature b_1, which appears to match quite well the behavior expected for water frost, but it is located at low latitude and differ in reflectivity from the dark features discussed above.

Table 7. Grain size and mixing ratio for the selected compounds. The last column indicates the sample reference in the spectral libraries (*a*: ASTER and *r*: RELAB).

Component	Grain size (μm)	Mixing ratio (%)	Sample No.
Calcite [a]	0–45	100	C-3A
Dolomite [a]	0–45	50	C-5A
Siderite [a]	0–45	4	C-9A
Crondstedtite [r]	0–45	5	CR-EAC-021
Montmorillonite [a]	0–45	50	PS-2D
Enstatite [a]	0–45	30	IN-10B
Augite [a]	0–45	2	IN-15A
Olivine [r]	0–50	5	DD-MDD-013
Water Frost [a]	~10	2	FROST.SNW

The two main observed features A (b_4, d_4) and B (d_3 and the surrounding region b_2), were referenced as #5 and #2 by Li et al. (2006a). These two features are remarkable because whereas they sustain large physical dimensions ($\oslash_A$ ~ 180 km and $\oslash_B$ ~ 350 km), their spectral behavior appears to be homogeneous over such large area, which might point to a same composition and/or resurfacing history. The external annulus of the B feature (b_2) shows the same uniformity. This annulus shape is reminiscent of a large cratering event. The bright central regions of feature A resembles the central peak seen in craters originating from high energetic impact, which would then be subject to different aging processes than the lower altitude neighboring areas. At smaller physical scale, similar differences of albedo have been reported on asteroid 25 143 Itokawa between the central part and surrounding areas of small craters, this time via grain sorting (Miyamoto et al. 2007).

In summary, our AO study permits to map the albedo variations over the surface of Ceres down to a 40–60 km scale and investigate whether these variations correspond to changes in the composition. Also, the high-spatial resolution capabilities returned by AO make possible to search for areas of distinctive signature (e.g. icy rich spots), which would remain undetected otherwise in disk-averaged studies of Ceres. A dusty regolith a

few centimeters thick (Webster et al. 1988), created by the impact of micrometeorites and possibly larger bodies, has been proposed (Witteborn et al. 1999; Lim et al. 2005) as a possible explanation for the shallow spectral signatures in the visible and near-infrared spectrum of Ceres and its small albedo constrast. But some small areas visible in our high-angular resolution images of Ceres could correspond to places on the surface where the regolith material has been cleared by "recent" endogenic or exogenic activity to expose more pristine material from the subsurface layers.

References

A'Hearn, M. F., & Feldman, P. D. 1992, Icarus, 98, 54
Berthier, J. 1998, Notes scientifique et techniques du Bureau des longitudes, S061
Britt, D. T., Yeomans, D. K., House, K., & Consolmagno, G. 2002, Asteroid Density, Porosity, and Structure, ed. W. F. Bottke, A. Cellino, P. Paolicchi, & R. P. Binzel (University of Arizona Press), 485
Chamberlain, M. A., Sykes, M. V., & Esquerdo, G. A. 2007, Icarus, 188, 451
Cohen, M., Witteborn, F. C., Roush, T., Bregman, J. D., & Wooden, D. H. 1998, Astron. J., 115, 1671
Conrad, A., Dumas, C., Merline, W. J., et al. 2007, Icarus
Dotto, E., Müller, T. G., Barucci, M. A., et al. 2000, A&A, 358, 1133
Drummond, J. D., Fugate, R. Q., Christou, J. C., & Hege, E. K. 1998, Icarus, 132, 80
Dumas, C., Merline, W. J., Binzel, R. P., et al. 2003, in BAAS, 956
Fanale, F. P., & Salvail, J. R. 1989, Icarus, 82, 97
Feierberg, M. A., Lebofsky, L. A., & Larson, H. P. 1980, Geoch. Cosmochim. Acta, 45, 971
Fusco, T. 2000, Ph.D. Thesis, Université de Nice Sophia-Antipolis
Gaffey, M. J. 1997, Icarus, 127, 130
Ghosh, A., Weidenschilling, S. J., McSween Jr., H. Y., & Rubin, A. 2006, Asteroidal Heating and Thermal Stratification of the Asteroid Belt, Meteorites and the Early Solar System II, ed. D. S. Lauretta, & H. Y. McSween Jr (University of Arizona Press), 555
Greeley, R., & Batson, R. M. 1990, Planetary Mapping (Cambridge University Press)
Hapke, B. 1993, Theory of reflectance and emittance spectroscopy (Cambridge University Press)
Hsieh, H. H., & Jewitt, D. 2006, Science, 312, 561
Johnson, P. E., Kemp, J. C., Lebofsky, M. J., & Rieke, G. H. 1983, Icarus, 56, 381
Johnson, T. V., & McGetchin, T. R. 1973, Icarus, 18, 612
Jones, T. D., Lebofsky, L. A., Lewis, J. S., & Marley, M. S. 1990, Icarus, 88, 172
Keil, K. 2002, Geological History of Asteroid 4 Vesta: The Smallest Terrestrial Planet, Asteroids III, ed. W. F. Bottke, A. Cellino, P. Paolicchi, & R. P. Binzel (University of Arizona Press), 573
King, T. V., Clark, R. N., Calvin, W. M., Sherman, D. M., & Brown, R. H. 1992, Science, 255, 1551
Kovačević, A., & Kuzmanoski, M. 2007, Earth Moon and Planets, 100, 117
Lebofsky, L. A., Feierberg, M. A., Tokunaga, A. T., Larson, H. P., & Johnson, J. R. 1981, Icarus, 48, 453
Li, J.-Y., McFadden, L. A., Parker, J. W., et al. 2006a, Icarus, 182, 143
Li, J.-Y., Young, E. F., Thomas, P. C., et al. 2006b, HST Images, Albedo Maps, and Shape of 1 Ceres, eAR-A-HSTACS-5-CERESHST-V1.0., NASA Planetary Data System
Lim, L. F., McConnochie, T. H., Bell, J. F., & Hayward, T. L. 2005, Icarus, 173, 385
McCord, T. B., & Sotin, C. 2005, J. Geophys. Res. (Planets), 110, 5009
Michalak, G. 2000, A&A, 360, 363
Millis, R. L., Wasserman, L. H., Franz, O. G., et al. 1987, Icarus, 72, 507
Mitchell, D. L., Ostro, S. J., Hudson, R. S., et al. 1996, Icarus, 124, 113
Miyamoto, H., Yano, H., Scheeres, D. J., et al. 2007, Science, 316, 1011
Mousis, O., & Alibert, Y. 2005, MNRAS, 358, 188
Mugnier, L. M., Fusco, T., & Conan, J.-M. 2004, J. Opt. Soc. Am. A, 21, 1841
Nazzario, R., Hyde, T. W., & Barge, L. 2003, Adv. Space Res., 31, 2591
Parker, J. W., McFadden, L. A., Russell, C. T., et al. 2006, Adv. Space Res., 38, 2039
Parker, J. W., Stern, S. A., Thomas, P. C., et al. 2002, Astron. J., 123, 549
Piazzi, G. 1802, Nella Stamperia Reale, 65
Rivkin, A. S., Volquardsen, E. L., & Clark, B. E. 2006, Icarus, 185, 563
Russell, C. T., Coradini, A., Christensen, U., et al. 2003, Plan. Space Sci., 52, 465
Saint-Pé, O., Combes, M., Rigaut, F., Tomasko, M., & Fulchignoni, M. 1993, Icarus, 105, 263
Sato, K., Miyamoto, M., & Zolensky, M. E. 1997, Meteorit. Plan. Sci., 32, 503
Seidelmann, P. K., Archinal, B. A., A'Hearn, M. F., et al. 2005, Celest. Mech. Dyn. Astron., 91, 203
Spencer, J. R. 1990, Icarus, 83, 27
Tedesco, E. F., Taylor, R. C., Drummond, J. D., et al. 1983, Icarus, 54, 23
Thomas, P. C., Binzel, R. P., Gaffey, M. J., et al. 1997, Science, 277, 1492
Thomas, P. C., Parker, J. W., McFadden, L. A., et al. 2005, Nature, 437, 224
van Dam, M. A., Le Mignant, D., & Macintosh, B. 2004, Appl. Opt., 43, 5458
Vernazza, P., Mothé-Diniz, T., Barucci, M. A., et al. 2005, A&A, 436, 1113
Viateau, B., & Rapaport, M. 1998, A&A, 334, 729
Vilas, F., & Gaffey, M. J. 1989, Science, 246, 790
Vilas, F., & McFadden, L. A. 1992, Icarus, 100, 85
Webster, W. J., Johnston, K. J., Hobbs, R. W., et al. 1988, AJ, 95, 1263
Witteborn, F. C., Cohen, M., Bregman, J. D., et al. 1999, AJ, 117, 2552
Zolensky, M., & McSween Jr., H. Y. 1988, Aqueous Alteration, Meteorites and the Early Solar System ed. J. F. Kerridge, & M. S. Matthews (University of Arizona Press), 114

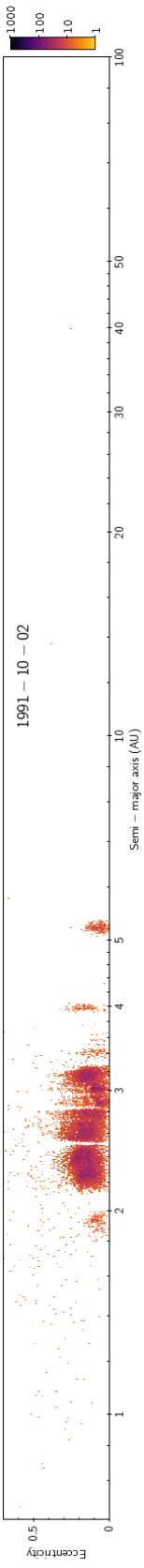

Planetary and Space Science 66 (2012) 200–212

Contents lists available at SciVerse ScienceDirect

Planetary and Space Science

journal homepage: www.elsevier.com/locate/pss

Shape modeling technique KOALA validated by ESA Rosetta at (21) Lutetia

B. Carry [a,*], M. Kaasalainen [b], W.J. Merline [c], T.G. Müller [d], L. Jorda [e], J.D. Drummond [f], J. Berthier [g], L. O'Rourke [a], J. Ďurech [h], M. Küppers [a], A. Conrad [i], P. Tamblyn [c], C. Dumas [j], H. Sierks [k], The OSIRIS Team[1]

[a] European Space Astronomy Centre, ESA, P.O. Box 78, 28691 Villanueva de la Cañada Madrid, Spain
[b] Tampere University of Technology, P.O. Box 553, 33101 Tampere, Finland
[c] Southwest Research Institute, 1050 Walnut St. #300, Boulder, CO 80302, USA
[d] Max-Planck-Institut für extraterrestrische Physik (MPE), Giessenbachstrasse, 85748 Garching, Germany
[e] Laboratoire d'Astrophysique de Marseille, Université de Provence, Marseille, France
[f] Starfire Optical Range, Directed Energy Directorate, Air Force Research Laboratory, Kirtland AFB, NM 87117-577, USA
[g] Institut de Mécanique Céleste et de Calcul des Éphémérides, Observatoire de Paris, UMR8028 CNRS, 77 av. Denfert-Rochereau 75014 Paris, France
[h] Astronomical Institute, Faculty of Mathematics and Physics, Charles University in Prague, V Holešovičkách 2, 18000 Prague, Czech Republic
[i] Max Planck Institute für Astronomy (MPA), Königstuhl 17, 69117 Heidelberg, Germany
[j] European Southern Observatory, Alonso de Córdova 3107, Vitacura, Casilla 19001, Santiago de Chile, Chile
[k] Max-Planck-Institut für Sonnensystemforschung (MPS), Max-Planck-Strasse 2, 37191 Katlenburg-Lindau, Germany

ARTICLE INFO

Article history:
Received 20 June 2011
Received in revised form
2 November 2011
Accepted 22 December 2011
Available online 30 December 2011

Keywords:
Asteroid
(21) Lutetia
Disk-resolved imaging
KOALA
Rosetta

ABSTRACT

We present here a comparison of our results from ground-based observations of asteroid (21) Lutetia with imaging data acquired during the flyby of the asteroid by the ESA Rosetta mission. This flyby provided a unique opportunity to evaluate and calibrate our method of determination of size, 3-D shape, and spin of an asteroid from ground-based observations. Knowledge of certain observable physical properties of small bodies (e.g., size, spin, 3-D shape, and density) have far-reaching implications in furthering our understanding of these objects, such as composition, internal structure, and the effects of non-gravitational forces. We review the different observing techniques used to determine the above physical properties of asteroids and present our 3-D shape-modeling technique KOALA – Knitted Occultation, Adaptive-optics, and Lightcurve Analysis – which is based on multi-dataset inversion. We compare the results we obtained with KOALA, prior to the flyby, on asteroid (21) Lutetia with the high-spatial resolution images of the asteroid taken with the OSIRIS camera on-board the ESA Rosetta spacecraft, during its encounter with Lutetia on 2010 July 10. The spin axis determined with KOALA was found to be accurate to within 2°, while the KOALA diameter determinations were within 2% of the Rosetta-derived values. The 3-D shape of the KOALA model is also confirmed by the spectacular visual agreement between both 3-D shape models (KOALA pre- and OSIRIS post-flyby). We found a typical deviation of only 2 km at local scales between the profiles from KOALA predictions and OSIRIS images, resulting in a volume uncertainty provided by KOALA better than 10%. Radiometric techniques for the interpretation of thermal infrared data also benefit greatly from the KOALA shape model: the absolute size and geometric albedo can be derived with high accuracy, and thermal properties, for example the thermal inertia, can be determined unambiguously. The corresponding Lutetia analysis leads to a geometric albedo of 0.19 ± 0.01 and a thermal inertia below $40\,J\,m^{-2}\,s^{-0.5}\,K^{-1}$, both in excellent agreement with the Rosetta findings. We consider this to be a validation of the KOALA method. Because space exploration will remain limited to only a few objects, KOALA stands as a powerful technique to study a much larger set of small bodies using Earth-based observations.

1. Remote-sensing shape modeling

Perhaps the most striking observable of any asteroid is its shape. In 1993, spacecraft exploration revealed for the first time the stunning non-spherical shape of asteroid (951) Gaspra when NASA's Galileo spacecraft made the first of its two asteroid encounters, on its way to Jupiter. Asteroids had remained point-sources in the sky since the discovery of (1) Ceres in 1801 by Piazzi, almost two

* Corresponding author. Tel.: +34 91 81 31 233.
E-mail address: benoit.carry@esa.int (B. Carry).
[1] M. A'Hearn, F. Angrilli, C. Barbieri, A. Barucci, J.-L. Bertaux, G. Cremonese, V. Da Deppo, B. Davidsson, S. Debei, M. De Cecco, S. Fornasier, M. Fulle, O. Groussin, P. Gutiérrez, W.-H. Ip, S. Hviid, H.U. Keller, D. Koschny, J. Knollenberg, J.R. Kramm, E. Kuehrt, P. Lamy, L.M. Lara, M. Lazzarin, J.J. López-Moreno, F. Marzari, H. Michalik, G. Naletto, H. Rickman, R. Rodrigo, L. Sabau, N. Thomas, K.-P. Wenzel.

0032-0633/$ - see front matter © 2011 Elsevier Ltd. All rights reserved.
doi:10.1016/j.pss.2011.12.018

centuries before. Only the advent of space exploration and large Earth-based telescopes (*e.g.*, Arecibo and Goldstone radio telescopes, space-based-optical – HST, or ground-based near-IR, equipped with adaptive optics – Palomar, Lick, CFHT, Keck, ESO VLT, and Gemini) allowed their apparent disks to be spatially resolved, and their irregular shapes to be imaged. The past decade has seen a revolution in our understanding of the physical properties (*e.g.*, size, 3-D shape, and spin axis) of asteroids. This revolution has come about thanks to improved observing facilities and, of equal importance, from improved methods of analysis.

Determination of the physical properties for a statistically relevant set of asteroids has many implications for our understanding of these remnants of solar-system formation and, in turn, can be expected to improve our understanding of the history and evolution of the Solar System. For instance, the distribution of spin axes of the larger asteroids (diameter larger than $\sim$100 km) on the celestial sphere is not expected to be isotropic. Numerical hydrocode simulations have predicted a slight excess in prograde rotators, due to the gas-pebble interaction in the protoplanetary disk (Johansen and Lacerda, 2010). Similarly, the spin state of *small* asteroids (diameter not larger than few kilometers) is dominated by the non-gravitational YORP effect (Hanuš et al., 2011). Statistical knowledge of spin coordinates, how they are distributed within and among asteroid families of different ages, will provide strong constraints on the effectiveness of YORP (Slivan et al., 2003).

Reconstruction of the 3-D shape (including the size) is required to estimate the volume of an asteroid, which in turn is used to derive its density, possibly the property most fundamental to our understanding of an asteroid (Britt et al., 2002). Observations of the surface of an asteroid, such as colors, spectra, or phase effects, can provide clues to the surface composition of the asteroid. This may or may not be related to the bulk composition of the body (*e.g.*, Elkins-Tanton et al., 2011). Masses for asteroids can be determined from a spacecraft flyby, from the orbital motion of a natural moon, or even from the perturbations of asteroids on other bodies, such as Mars (Hilton, 2002). In most cases, however, the uncertainty in the density is dominated by the uncertainty in the volume, rather than the uncertainty in the mass (Merline et al., 2002). Precise reconstruction of the 3-D shape is therefore of high importance for all asteroids for which a mass has been, or will be, estimated (*e.g.*, Hilton, 2002; Mouret et al., 2007; Baer et al., 2011).

From the comparison of an asteroid's density with the densities of its most-likely constituents, we can constrain the macroporosity (large-scale voids) in its interior, probably produced by impacts over its history (Britt et al., 2002). These impacts could have partially disrupted the body, producing large-scale fractures, or even totally disrupted the body, with subsequent re-accumulation of the resulting fragments, leading to a "rubble-pile" structure.

Evidence of gigantic, but less than totally disruptive, impacts can be seen by high-resolution imaging and also inferred from our shape-modeling of asteroids. The huge impact craters evident in the images of C-type asteroid (253) Mathilde (Veverka et al., 1997) are thought to be about as large as could be sustainable by a body without disruption. There have been suggestions that these craters were created by compaction of low-density target material, rather than explosive ejection typical of hard-rock impacts (Housen et al., 1999). Already, our ground-based adaptive-optics imaging has shown what appear to be facets or depression-like features, similar to those seen on Mathilde, in some other large C-type asteroids (*e.g.*, (511) Davida in Conrad et al., 2007). Alternatively, some of our other images of C-type asteroids, such as (52) Europa, appear to bear no evidence of giant impacts (Merline et al., personal communication). Evaluation of the prevalence of such large impact events can give us insight into the size and frequency of these impact events over time, and thus into the history of the impacting population.

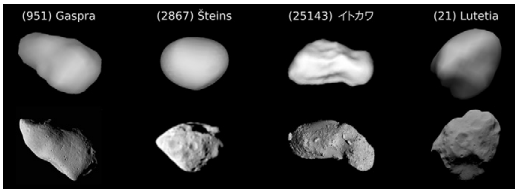

Fig. 1. Comparison of four shape models, derived using ground-based observations, with high-spatial-resolution images obtained in situ by spacecraft (left-to-right): (951) Gaspra lightcurve inversion model from Kaasalainen et al. (2002a), image from NASA Galileo; (2867) Šteins lightcurve inversion model from Lamy et al. (2008a,b), image from ESA Rosetta; (25143) Itokawa radar delay-Doppler model from Ostro et al. (2005), image from JAXA Hayabusa; and (21) Lutetia KOALA model from Carry et al. (2010b) and Drummond et al. (2010), image from ESA Rosetta.

We summarize below the most common of the many observing techniques used to derive size, 3-D shape, and spin-vector coordinates and highlight some of their advantages and drawbacks. Then, in Section 2, we describe our KOALA multi-data shape-modeling algorithm. In Section 3, we present a comparison of the results produced by KOALA (from Earth-based observations) with those derived from the ESA Rosetta flyby of asteroid (21) Lutetia. In Section 4, we use our KOALA model in conjunction with mid-infrared data and a thermophysical model to derive the thermal properties of Lutetia and compare the results with those derived using thermal observations from the Rosetta spacecraft (Gulkis et al., 2012) and from the ground, making use of the shape model from the flyby (O'Rourke et al., 2012). We assess the accuracy of the KOALA shape-modeling method in Section 5.

1.1. Optical lightcurve

Historically, spin properties and triaxial-ellipsoid shapes have been studied largely through observations of rotationally induced variability in disk-integrated brightness (lightcurves). Indeed, the object's shape, its rotational state (period and spin-vector coordinates), and the scattering properties of its surface can be determined from the analysis of its lightcurves over time (as the viewing/illumination geometry changes).

For about a decade, starting with the lightcurve inversion algorithm presented by Kaasalainen and Torppa (2001) and Kaasalainen et al. (2001), lightcurves also have been used extensively to derive 3-D shape models of asteroids (see the examples for asteroids Gaspra and Šteins in Fig. 1). The 3-D shape models and spin properties of more than 200 asteroids already have been derived (these are accessible from DAMIT,[2] see Ďurech et al., 2010). These shape models are, however, limited to dimensionless, *convex* shapes, with limited spatial resolution. Recently, Ďurech et al. (2011) have shown that the size of these models can be set by using other types of input data (*e.g.*, stellar occultation profiles, see Section 1.2). The intrinsic *convex* nature of the models precludes accurate determination of the volume, and hence density, of the objects, however.

Because lightcurve observations require neither large telescope aperture nor specialized instrumentation, they are, and will remain, a major source of information on small bodies. Thousands of lightcurves, for hundreds of asteroids,[3] have been accumulated during the last half century. Amateur astronomers

[2] DAMIT: http://astro.troja.mff.cuni.cz/projects/asteroids3D/web.php.

[3] The Asteroid Photometry Catalogue (APC) or the Asteroid Lightcurve Database (Warner et al., 2009, LCDB) list more than 6000 lightcurves for about 700 asteroids: APC: http://asteroid.astro.helsinki.fi/apc and LCDB: http://www.minorplanet.info/lightcurvedatabase.html.

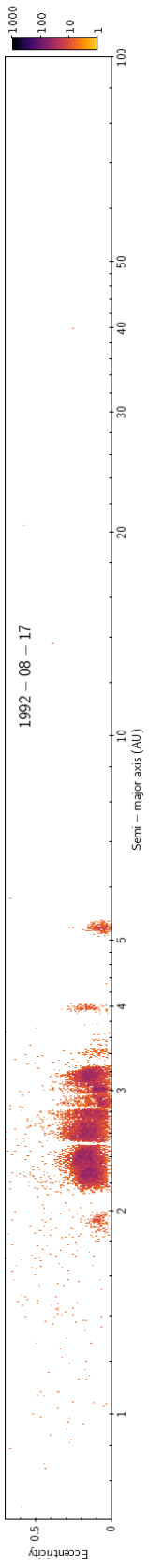

contribute significantly to this ever-growing database of lightcurves[4] (*e.g.*, Behrend et al., 2006; Ďurech et al., 2007).

Sparse photometry (*i.e.*, when the typical separation between measurements is larger than the rotation period, as opposed to historical lightcurves, which are dense in time) can also be used to reconstruct 3-D models (see Kaasalainen, 2004). Hanuš et al. (2011) have used a combination of sparse photometry, together with dense lightcurves, to derive about 100 new shape models, using measurements extracted from large all-sky surveys (such as USNO, Catalina, Siding Spring, and Hipparcos). Knowledge of the absolute photometry (as opposed to relative photometric measurements, as in a dense lightcurve) is, however, required to make these sparse measurements useful to 3-D shape modeling (see Hanuš et al., 2011, for a detailed discussion). From the upcoming PanSTARRS and Gaia surveys we can expect hundreds of thousands of objects to be modeled using this method (Ďurech et al., 2005).

1.2. Stellar occultation

Occultations occur when a solar-system object passes between a star and Earth, causing the asteroid's shadow to cross some portion of Earth as a track. Because the star is very far relative to the Earth–asteroid separation, the shadow cast by the asteroid is effectively parallel. Thus, the width of the shadow track (perpendicular to the track) gives the maximum width of the asteroid in the cross-track direction. It is usually not possible to get a high density of observers stationed across the track, and thus this dimension may not be so well established. But along the track, the size of the asteroid, as an along-track chord on the asteroid, corresponding to the position of the observer within the shadow, is given by the length of time of the blink-out event. With many observers, many along-track events can be recorded and the blink-out intervals are converted to chord lengths at the asteroid by using the asteroid's known speed (see Millis and Dunham, 1989, for a review).

One advantage of stellar occultations is that very small minor planets can be probed (provided one accounts properly for diffraction effects). Even stellar occultations by small trans-Neptunian objects (TNOs) of a few kilometers diameter can be recorded (see Roques et al., 2009). Finally, stellar occultations provide a powerful means for studying thin atmospheres and/or exospheres (*e.g.*, Sicardy et al., 2003).

In theory, three occultation events (each recorded by enough observers to secure a unique apparent-ellipse to be fit on the chords) provide enough constraints to determine the triaxial dimensions (ellipsoid) and spin-vector coordinates of an asteroid (Drummond and Cocke, 1989; Dunham et al., 1990). The number of chords that result from an event will often be larger with brighter occulted stars. This is because many more observers can be fielded if the required telescope aperture is modest. In practice, however, occultations of bright stars by any given asteroid occur rather infrequently. This difficulty in obtaining sufficient chords, plus the noise level often encountered (especially the systematic errors coming from imperfect knowledge of asteroid and star astrometry, combined with observer timing errors), strongly limit our ability to construct 3-D shape models and derive spin properties from occultations alone. Nevertheless, stellar occultations are an efficient way to provide additional size/shape information, particularly for shape models that otherwise lack a scale, such as those from lightcurves alone (see 1.1 and Ďurech et al., 2011).

With the availability of low-cost GPS positioning equipment and CCD cameras (the majority of measurements are made by amateur astronomers), the accuracy of occultation timings has improved greatly over the last decade. From this improved precision, together with the refinement of the orbits of small bodies expected to result from Gaia/PanSTARRS (allowing an extremely precise prediction of the occultation track on Earth, see Tanga and Delbo, 2007), we can expect that stellar occultations will become ever more useful in the determination of certain physical properties of asteroids, especially for objects having small angular diameters.

1.3. Thermal radiometry

The amount of thermal emission from an asteroid is mainly a function of its physical diameter and surface albedo, and, to a lesser extent, the physical properties of its surface (*e.g.*, thermal inertia, roughness). Main-belt asteroids are among the brightest sources in the sky in the mid-infrared (5–20 μm), so infrared satellites (IRAS, ISO, AKARI, Spitzer, Herschel, and WISE) have been able to acquire observations of a vast number of these objects (see Mainzer et al., 2011, for instance).

Estimates for size and albedo are model-dependent, however, and several thermal models co-exist, from the simple Standard Thermal Model (STM) of non-rotating spheres of Lebofsky et al. (1986) to the detailed Thermophysical Model (TPM) of Lagerros (1996, 1997), having a complete description of 3-D shape and surface properties. Unfortunately, the systematic uncertainties involved when applying those models (resulting from their respective assumptions and approximations) are not always properly taken into account in estimating error bars, and results often differ from one determination to another by more than the quoted uncertainties (see Table 3 in Delbo and Tanga, 2009, illustrating the issue). For instance, it now seems that the database of 2228 diameters (Tedesco et al., 2002) estimated using the overly simple STM with IRAS data may be biased by a few percents (see the re-analysis of IRAS data by Ryan and Woodward, 2010).

The radiometric technique to derive sizes and albedos from thermal infrared data benefits greatly from the availability of 3-D shape models. For example, the absolute size of (25143) Itokawa derived by Müller et al. (2005), based on a 3-D shape model implementation in a TPM code, agreed to within 2% of the final in situ result from the Hayabusa mission (Fujiwara et al., 2006). In general, mid-infrared observations are highly valuable for scaling dimensionless shape models (similar to the situation with stellar occultations, as mentioned in Section 1.2) and mid-infrared data are available for several thousand asteroids. These data even allow determination of the most likely spin-axis solutions in cases where lightcurve inversion techniques lead to more than one possible shape and spin-axis solution (see, *e.g.*, Müller et al., 2011, for a recent example). In cases where the shape-model already comes with size information (or alternatively, if many thermal observations are available for a given target), it is possible to derive the thermal inertia, indicative of the surface characteristics: *e.g.*, bare rock, ice, boulders, dust regolith (see, for instance Müller et al., 2005; Delbo et al., 2007, among many others).

In some particular cases of extensively observed asteroids, the thermal radiometry can also provide hints on the 3-D shape, through the measure of the apparent projected cross-section of the asteroid on the plane of the sky at each epoch. By comparing the predicted with observed thermal fluxes of Lutetia under many geometries, O'Rourke et al. (2012) have shown that adding a hill/plateau, whose size remains within the quoted 3-D shape uncertainty, could explain the discrepancies observed for a certain observing geometry.

1.4. Radar delay-Doppler echoes

Radar observations consist in transmitting a radio signal toward the target and recording the echo. The distribution of

[4] About 2300 lightcurves for more than 1700 asteroids have been acquired by the CdR group: http://obswww.unige.ch/~behrend/page_cou.html.

the echo power in delay time and Doppler frequency is related to the spin state and 3-D shape of the target (see the reviews by Ostro, 1989; Ostro et al., 2002). The time and frequency precision currently achievable (Arecibo, Goldstone) allow the study of very small objects, the main limit of radar observations being the distance of the target (echo power scales inversely with distance to the fourth power). This is why most radar studies have concentrated on Near-Earth Objects (NEOs), while dedicated observations of Main-Belt Asteroids (MBAs) have been more limited (see Ostro et al., 2002).

The difficulty in constructing 3-D shapes from a series of delay-Doppler "*images*" is due to the absence of a direct, one-to-one, link between each region of the surface with a pixel in delay-Doppler space. Indeed, all points situated at the same range from the observer, and moving at the same radial velocity (possibly spread over the apparent disk) will contribute to a single delay-Doppler pixel. So delay-Doppler images are many-to-one maps of the shape as highlighted by Ostro et al. (2002): there is no *a priori* way to determine how many regions will contribute to a single pixel, which strongly contrasts with the one-to-one mapping ("WYSIWYG") achieved in disk-resolved imaging.

Radar echoes remain, however, the best way to determine the physical properties of NEOs (*e.g.*, the very small NEO Itokawa in Fig. 1). For instance, the possible migration of the regolith at the surface of a fast-rotating asteroid triggered by YORP spin-up (Walsh et al., 2008) was suggested by the detailed 3-D shape of the NEO (66391) 1999 KW_4 (Ostro et al., 2006).

1.5. Disk-resolved imaging

Since the 1990s, with the advent of the Hubble Space Telescope and large ground-based telescopes equipped with adaptive optics (AO: Lick, CFHT, Keck, ESO VLT, and Gemini), we have access to the angular resolution required to resolve the apparent disk of asteroids (*e.g.*, Saint-Pé et al. 1993a,b; Drummond et al., 1998; Parker et al., 2002, 2006).

From a time-series of disk-resolved images, spin-vector coordinates can be derived (using previous knowledge of the rotation period) by analyzing the changes in the apparent shape of the asteroid profile (see for instance Thomas et al., 1997b; Drummond and Christou, 2008), or by following the apparent path taken by an albedo patch on the surface during the rotation (*e.g.*, Thomas et al., 2005; Carry et al., 2008). Triaxial shapes (ellipsoids) can also be derived (see Drummond et al., 2009a; Schmidt et al., 2009, for instance), and topography (such as the presence of facets or craters) studied from profile deviations to the ellipsoid (*e.g.*, Thomas et al., 1997a; Conrad et al., 2007). With sufficient spatial resolution, imaging of the asteroid disk can allow construction of albedo maps of the surface, allowing the study of composition heterogeneity or localized space weathering effects (*e.g.*, Binzel et al., 1997; Li et al., 2006, 2010; Carry et al., 2008, 2010a). In the case of asteroids visited by spacecraft, high spatial-resolution and precise photometry can be used to derive precise shape and digital terrain models by using stereophotoclinometric techniques (see examples in Gaskell et al., 2008).

The size and 3-D shape resulting from disk-resolved images are of great value, being obtained in a direct manner (as compared to an indirect determination of the shape from lightcurve inversion, for instance). The best angular resolution[5] of current Earth-based telescopes is about 0.04″. Due to systematics, however, we have found that our ability to accurately measure sizes degrades rapidly below about 0.10″, based on simulations and observations of the moons of Saturn and other objects (Carry, 2009; Drummond et al., 2009b). The sample of asteroids observable (*i.e.*, having angular sizes that get above about 0.10″) is therefore limited to about 200 (over a given 10-year span).

1.6. Interferometry

Apart from building larger telescopes, one efficient way to improve the angular resolution is to combine light beams from separated telescopes and to observe the resulting interference (fringes). In such a mode, each telescope aperture plays the role of a sample aperture within a virtual telescope whose extent is the largest distance between the two telescopes (the spatial resolution Θ is still given by the equation in Footnote 5, except that $\mathcal{D}$ is now the *distance* between the apertures). For instance, with telescopes separated by about 80 m, the VLTI provides an order-of-magnitude improvement in angular resolution over a single telescope of the VLT (8 m aperture).

This improvement in the resolution, however, occurs at the price of a loss in complete spatial information, because the virtual aperture is under-sampled. The very high angular-resolution is limited, at a given instant, to a single line on the plane of the sky, which is given by the baseline linking the two apertures. Along that baseline, the signal is directly related to the Fourier transform of the flux distribution on the plane of the sky. To expand the coverage in the spatial-frequency domain, and thus to allow the construction of 2-D images of the target, one must increase the number of projected baselines. This is commonly achieved by either adding multiple physical baselines (*i.e.*, adding more telescopes) and/or by making observations throughout the night, as the Earth's rotation causes a progression of the position angle of the baseline on the sky. However, because asteroids typically complete their rotation in only a few hours, the method using multiple telescopes is more effective at providing higher spatial sampling. Below we describe another promising technique to effectively increase the number of baselines, by using a Fizeau design.

For objects with no *a priori* information, the overall dimensions and spin properties can be determined under the assumption that the shape is well-described by a triaxial ellipsoid (Li et al., 2011). For example, the two orthogonal directions of the Fine Guidance Sensor (FGS) on-board HST have been used to study binarity and measure the size of several MBAs (Tanga et al., 2001, 2003; Hestroffer et al., 2002). The fringes of interference, however, also contain information on the apparent shape, and can be used in combination with other data to derive 3-D shape models. For instance, Kaasalainen and Lamberg (2006) used FGS data in combination with optical lightcurves to refine the 3-D shape model of (15) Eunomia from Kaasalainen et al. (2002b).

Interferometry in the mid-infrared has been used recently also, with promising results. In this wavelength regime, the signal is linked to the distribution of temperature (*i.e.*, *emitted* light) on the surface of the target (as opposed to the reflected light seen at visible wavelengths). Delbo et al. (2006, 2009) have combined thermal infrared TPM models (see Section 1.3) with interferometry, allowing the size of 3-D shape models to be set (similar to stellar occultation and thermal-infrared-only, see Sections 1.2 and 1.3 and Matter et al., 2011).

The current limitation of interferometry is set by the sensitivity of available facilities and is driven largely by the integration time, which is usually short. Because the light beams from the two apertures traverse different paths in the atmosphere, their wavefronts encounter different turbulence-dominated perturbations, leading to a shift in their phase. Delay lines are used to "slow down" one beam with respect to the other, and to match their phase. The technical difficulties in maintaining coherence in

[5] Limited by the diffraction, which acts as a low-pass filter with a cutoff frequency approximated by $\Theta = \lambda/\mathcal{D}$ (radian), λ being the wavelength and $\mathcal{D}$ the diameter of the telescope aperture.

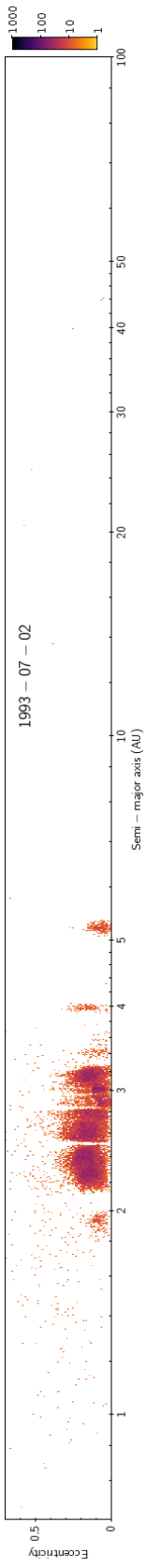

this process limits the integration time to few hundredths or thousandths of a second. A new generation of instruments (like PRIMA at VLT) with fringe-tracking systems will overcome this limitation in the near future, allowing fainter sources to be targeted.

An interesting compromise between co-axial interferometers and traditional, filled aperture, telescopes can be found in Fizeau-type instruments such as LINC-NIRVANA, being built for the Large Binocular Telescope (LBT, see Hill et al., 2010), in which improved coverage of the spatial-frequency plane (commonly called uv-plane, with u and v standing for the two orthogonal unit directions) can be achieved in less telescope time. This design (Fizeau *vs.* pupil-plane interferometer like the VLTI) allows instantaneous filling of the uv-plane up to the frequency set by the 8 m apertures (Fizeau interferometers are true imaging devices and produce direct images of the plane of the sky), with an additional filling along one dimension up to the frequencies corresponding to the maximal baseline (22.7 m for LBT). Two or three epochs, with different position angles of the baseline on the plane of the sky, will be enough to fill the uv-plane up to the maximal extent of the telescope (achievable for transiting asteroids, especially with high elevation, when the position angle evolves quickly). For this purpose, therefore, the LBT is equivalent to a 22.7 m telescope with a mask, corresponding to the configuration of component apertures, placed in the entrance pupil.

The opening of interferometric studies to longer wavelengths also has great potential, with the use of millimeter and sub-millimeter arrays, where there are fewer technological limitations than in the optical range. Future facilities such as ALMA, with 50 antennas (translating into 1225 baselines *vs.* only two baselines for MIDI at the VLTI, see Delbo et al., 2009), will allow dense spatial coverage, together with an angular resolution of few milli-arcseconds. Simulations have shown that several hundreds of MBAs and TNOs will be observable with ALMA (see Busch, 2009; Moullet et al., 2011). Interferometry at thermal wavelengths (mid-infrared to millimeter), in combination with other techniques (*e.g.*, lightcurves, see Section 1.1), will thus allow the derivation of 3-D shape models, together with thermal properties, for many asteroids of small apparent diameter.

2. The KOALA algorithm

With advantages and drawbacks of each observing technique in mind, we have developed a multi-data inversion algorithm: Knitted Occultation, Adaptive-optics, and Lightcurve Analysis (KOALA), that makes simultaneous use of data from three distinct observation types[6] to determine the physical properties of asteroids (Carry et al., 2010a; Kaasalainen, 2011). KOALA takes advantage of the direct measure of the apparent size and shape of asteroids on the plane of the sky provided by the timings of stellar occultations and disk-resolved images, and of the indirect constraints on spin and 3-D shape given by lightcurves. We quickly summarize below how the inversion works (see Kaasalainen, 2011, for a comprehensive description of the algorithm). KOALA is a step-iterative minimization algorithm, solving for the spin parameters (spin-vector coordinates λ, β, and sidereal period $\mathcal{P}$), 3-D shape (given by a set of $\mathcal{N}$ coefficients of spherical harmonics, including the overall size), phase function (defined as a three-parameter model, see Kaasalainen and Torppa, 2001; Kaasalainen et al., 2001), and scattering law (generally taken as a combination of the Lommel–Seeliger and Lambert diffusion laws, following Kaasalainen and Torppa, 2001, although other models such as Hapke can be used).

From a set of estimated parameters (determined from light-curve-only inversion or analysis of the disk-resolved images, for instance), a trial solution is created, with associated synthetic datasets (*i.e.*, simulated lightcurves, disk-resolved images, and occultation profiles). KOALA then follows a Levenberg–Marquardt minimization scheme to determine the set of parameters that best fit all the datasets simultaneously, by comparing at each step the synthetic data with real measurements. The iteration stops when the residuals between the simulated and measured datasets reach an acceptable level (*i.e.*, the level of the intrinsic noise of the measurements).

As a safeguard, the resolution (*i.e.*, $\mathcal{N}$) is set to the lowest possible value for which a fit to the data can be achieved. We also introduced several regularizations: (a) a non-convexity ("smoothness") term, that avoids spurious features (unrealistic topography) at small scales, unconstrained by the data; and (b) an inertia tensor regularization for principal-axis rotators, that forces the asteroid spin-axis to remain aligned, within a few degrees, with the largest moment of inertia. The relative weights of the different data types and also of the regularizations are determined using the maximum compatibility estimate of Kaasalainen (2011), instead of being subjective.

3. KOALA and Rosetta-flyby shape model

On 2010 July 10, the ESA Rosetta spacecraft made a close flyby of the main-belt asteroid (21) Lutetia. In support of the mission, we had combined optical lightcurves with disk-resolved images, from ground-based AO. We produced a full 3-D shape model of Lutetia, using KOALA, months before the encounter (see Drummond et al., 2010; Carry et al., 2010b and Fig. 1). This flyby provided a rare opportunity to test and calibrate KOALA with close-up spacecraft imaging.

The closest approach (CA) occurred at 3170 km from the asteroid at a relative speed of 15 km/s. The narrow angle camera (NAC) of the OSIRIS instrument on-board Rosetta (Keller et al., 2007) returned a total of 202 images during the flyby, which spanned about 9 h. The NAC image scale ranged from 5000 to 60 m/pix, reaching its minimum value at CA. These very high spatial-resolution images have been used to produce detailed 3-D shape models of Lutetia, using stereophotoclinometry (Sierks et al., 2011), and stereophotogrammetry (Preusker et al., 2012). We only consider here the model from Sierks et al. (2011), these two models being similar enough at the medium-to-large scale for our purpose.

Lutetia's spin axis is tilted such that its pole is nearly in its orbital plane (obliquity of 96°, see Carry et al., 2010b; Sierks et al., 2011). At the time of the Rosetta flyby, the southern hemisphere was in seasonal shadow, and observations at optical/near-infrared wavelengths were not possible south of $-40°$ latitude. The detailed 3-D shape model derived from flyby images by stereo-photoclinometry (Sierks et al., 2011) therefore does not cover a large fraction of the asteroid's southern hemisphere (see Fig. 2), the southernmost portion of the shape model being determined using the KOALA algorithm together with the ground-based data from Carry et al. (2010b). Almost all of the AO images that entered into the KOALA solution, even though from multiple epochs, were taken looking at either high southerly or high northerly sub-Earth latitudes (see Carry et al., 2010b; Drummond et al., 2010). For both the ground-based KOALA and the flyby analyses, therefore, the shortest (c) dimension (Table 1) is not well constrained and represents the largest contribution to the uncertainty in the volume estimates.

[6] We categorize dense (*i.e.*, lightcurves) and sparse photometry together to form a single data type.

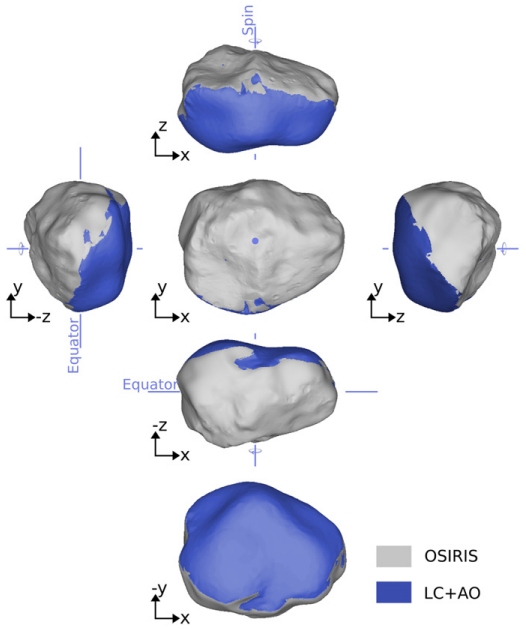

Fig. 2. Lutetia 3-D shape model from Sierks et al. (2011), displayed in a net layout. Regions imaged by OSIRIS are displayed in gray. The part of the shape model that is based on ground-based data only (lightcurves and images: LC+AO) is plotted in blue. (For interpretation of the references to color in this figure legend, the reader is referred to the web version of this article.)

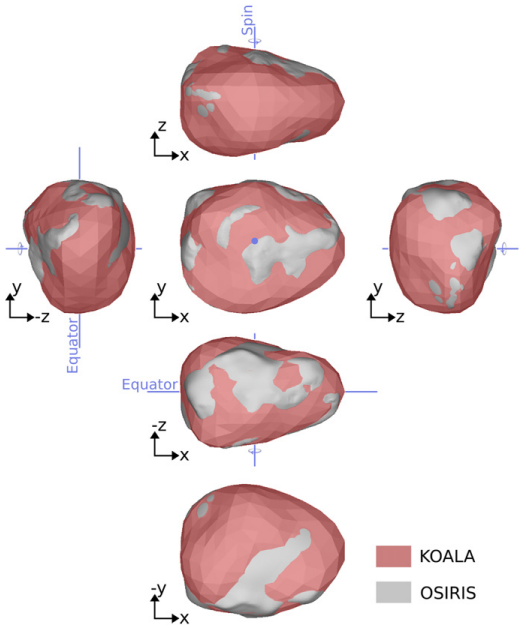

Fig. 3. Similar plot as Fig. 2, showing the agreement between the pre-flyby KOALA (reddish, Carry et al., 2010b) and post-flyby (grayish, Sierks et al., 2011) shape models of (21) Lutetia. The radii of the KOALA model are larger in red regions, and those of the OSIRIS model in gray regions. The amalgam of gray and red colors illustrates the spectacular agreement between the results from the Rosetta flyby and our KOALA model obtained before the flyby. The dominance of red hues, however, highlights the relatively lower sensitivity to concavities of the KOALA model with respect to the OSIRIS 3-D shape. Shown in this comparison is the original KOALA model of Carry et al. (2010b), with a c-dimension of 80 km (overall size $124 \times 101 \times 80$ km), rather than the modified KOALA ("hybrid") estimate of Drummond et al. (2010), having a c-dimension of 93 km and shown in Table 1. This is a more realistic comparison for the figure because much of the southern hemisphere of the OSIRIS model (Fig. 2) is based on the data that entered into the original KOALA model. (For interpretation of the references to color in this figure legend, the reader is referred to the web version of this article.)

Table 1
Comparison of the dimensions and spin-vector coordinates of (21) Lutetia derived from OSIRIS images during the ESA Rosetta flyby (Sierks et al., 2011) with those derived by KOALA (Drummond et al., 2010; Carry et al., 2010b) prior to the flyby. Volume-equivalent diameter (d) and triaxial diameters ($a > b > c$) are reported in km, and spin-vector coordinates in degree (longitude λ, latitude β in the ECJ2000 reference frame, with σ the angular radius of the uncertainty circle).

	Diameters (km)				Spin axis (°)		
	d	a	b	c	λ	β	$\pm\sigma$
KOALA	105	124 ± 5	101 ± 4	93 ± 13	52	-6	± 5
OSIRIS	98	121 ± 1	101 ± 1	75 ± 13	52.2	-7.8	± 0.4

We first present (Section 3.1) an overall comparison of our size and spin estimates (based on ground-based techniques) with those derived from the analysis of the very high spatial-resolution images acquired by OSIRIS (Sierks et al., 2011). We then directly compare the predicted shape profiles, based on KOALA, with those images (Section 3.2), seeking to calibrate our method.

3.1. Overall comparison

In this section, we present a comparison of the spin-vector coordinates and dimensions derived from the flyby with the pre-flyby values from KOALA (Table 1). Because southerly latitudes were not visible during the flyby and the c-dimension in the OSIRIS model comes from a combination of OSIRIS imaging and KOALA model information, the OSIRIS c-dimension is not wholly independent. But the spin-vector coordinates and equatorial dimensions (a, b) from the OSIRIS analysis can be used as "ground-truth" to calibrate our KOALA method.

First, the spin-vector coordinates agree to within 2°,[7] well inside the 5° uncertainty quoted for KOALA. Then, equatorial dimensions (a and b) are within 3 km of the flyby estimates, again well within the uncertainties reported for each dimension using KOALA. The larger difference between the estimates of the short (c) axis results from the expansion of the KOALA c dimension from its original 80 km to 93 km, based on the analysis by Drummond et al. (2010). Indeed, the best-fit solution for all the AO images (including an additional observation taken with a more equatorial geometry, presented by Drummond et al., 2010 and not used by Carry et al., 2010b owing to calibration issues, see Carry et al., 2010b for details) pointed toward a larger c dimension (supported by independent considerations on the amplitude of lightcurves by Belskaya et al., 2010). The volume-equivalent diameter is, therefore, larger (105 *vs.* 98 km) for the KOALA model than for the flyby-derived model by Sierks et al. (2011). Disk-resolved images

[7] The coordinates obtained with KOALA are 1.2° and 1.8° from the spin-vector solutions derived by F. Preusker ($\lambda = 52.6°$, $\beta = -7.1°$, pers. communication) and by Sierks et al. (2011), respectively, using the OSIRIS images.

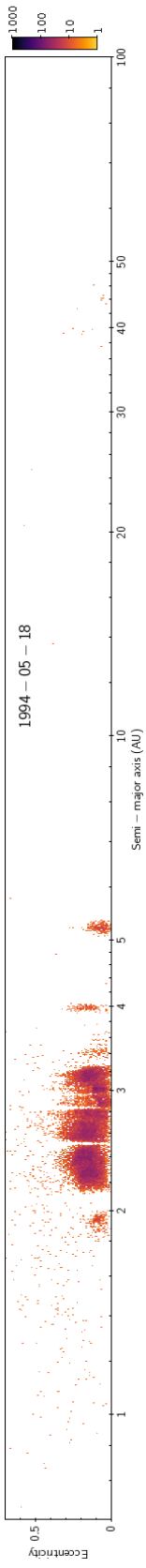

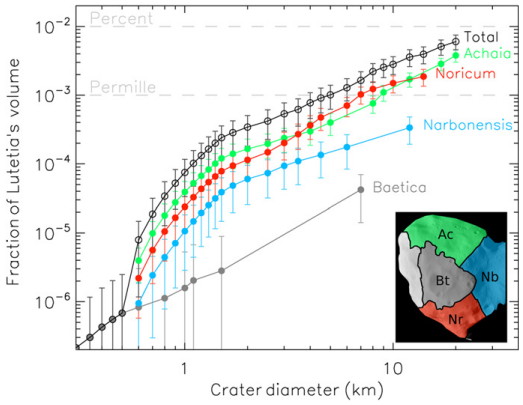

Fig. 4. Cumulative distribution of the volume encompassed by craters as function of their diameter, for four geomorphological units of Lutetia: Achaia (Ac), Baetica (Bt), Narbonensis (Nb), and Noricum (Nr) (see the insert, adapted from Fig. 1 by Sierks et al., 2011, and also Thomas et al., 2012 for the definition of these units).

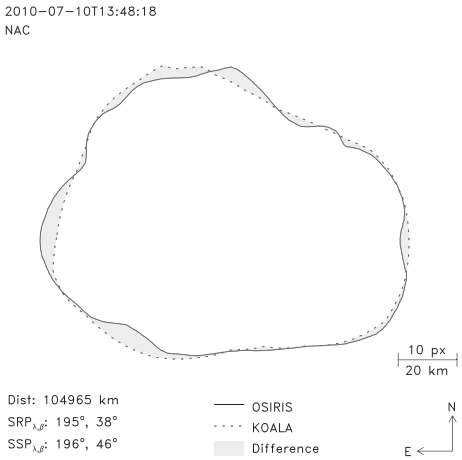

Fig. 5. Example of a profile comparison, as measured on the OSIRIS NAC detector plane (solid line) and simulated from the KOALA model (dotted line), taken at 13:48:18 UT (CA—1 h57 m). The light gray area represents the difference in projected area on the plane of the sky between the prediction and the observation. We report the Rosetta–Lutetia distance, the coordinates of the sub-Rosetta point (SRP) and subsolar point (SSP), and a scale for angular (OSIRIS NAC pixels) and physical dimension.

of Lutetia taken with low sub-observer latitudes are required to confirm its c dimension, and to set tighter constraints on its volume.

The depth of large-scale concavities was slightly underestimated by KOALA (Fig. 3); estimating the depth of a concavity from profiles only is problematical because the concavity is hidden behind its rim. With stereophotoclinometry, it is possible to sense depths. In addition, while KOALA is sensitive to large-scale concavities, the necessarily limited resolution when imaging from a distance of 200 million km means that it is less sensitive to small-to-medium-scale concavities. We evaluated the influence of craters on the volume of Lutetia. For that, we used the crater size distribution measured by Marchi et al. (2012), and estimated their volume as that of a spherical cap (V_{crat}), using the average depth-to-diameter ratio measured by Vincent et al. (2012):

$$V_{\mathrm{crat}} = \frac{\pi}{6} d\left(\frac{3}{4}D^2 + d^2\right) \quad (1)$$

where d is the depth of the crater and D its diameter. We present in Fig. 4 the cumulative distribution of the volume encompassed by craters, counted on four geomorphological units (see Thomas et al., 2012, for a detailed definition of the units), against their diameter. The vast majority of the volume is due to the handful of craters with diameters between 10 and 20 km. The total influence of these craters on the volume of Lutetia is $0.6 \pm 0.1\%$, *i.e.*, the volume of Lutetia would be 0.6% larger if these craters were not included in the 3-D shape model. Extrapolating this value, by considering the area covered by these unit to the whole surface of Lutetia, make the total[8] influence of craters to be $2.4 \pm 0.6\%$.

Proper modeling of the craters in the 3-D shape model (from high-resolution flyby images, Sierks et al., 2011) is therefore crucial, given the level of accuracy reached elsewhere on the surface. For Earth-based observations, however, this will remain a minor source of uncertainty: depending on the methods, the volume accuracy ranges from few percent to few tens of percent (see Section 1). We discuss in the next (Section 3.2) the influence of these craters on the volume accuracy that can be reached using KOALA.

3.2. Detailed analysis

We push further the calibration of the KOALA method by comparing comprehensively the KOALA shape model predictions with the very high-spatial-resolution images provided by OSIRIS NAC. In the absence of a complete 3-D shape model, based on an entirely independent dataset, it is difficult to fully calibrate the volume estimate provided by KOALA. For each OSIRIS image, we extracted the profile of the apparent disk of Lutetia, composed of its limb and its terminator. We produced synthetic views of the KOALA shape model under the same geometry (*i.e.*, as seen from Rosetta, see Fig. 5): phase angle, subsolar point (SSP) and sub-Rosetta point (SRP) coordinates, using the Miriade[9] VO ephemeris generator.[10]

We estimate the fit of KOALA predictions to OSIRIS data by computing the difference between the projected areas on the plane of the sky. The relative accuracy of the volume determination ($\delta V/V$) can then be determined as follows:

$$\frac{\delta V}{V} = \frac{3}{2}\frac{\mathcal{A}_O - \mathcal{A}_K}{\mathcal{A}_O} \quad (2)$$

where $\mathcal{A}_K$ and $\mathcal{A}_O$ are the areas of the KOALA prediction and on OSIRIS frame, respectively. Negative and positive δV, respectively, indicate an overestimate or underestimate of the volume by the KOALA model. We discarded from the current analysis the images taken close to CA, which have substantial phase angle (above 10°), where local topography (*e.g.*, crater rims) produce large projected shadows, increasing the uncertainty in the prediction of the terminator position on the surface of Lutetia.

[8] Because the shape of the southern hemisphere is poorly constrained, and the number of craters there unknown, this extrapolated value is only a rough estimate.

[9] http://vo.imcce.fr/webservices/miriade/

[10] We used Rosetta flight kernel ORHR _____ 00122.BSP.

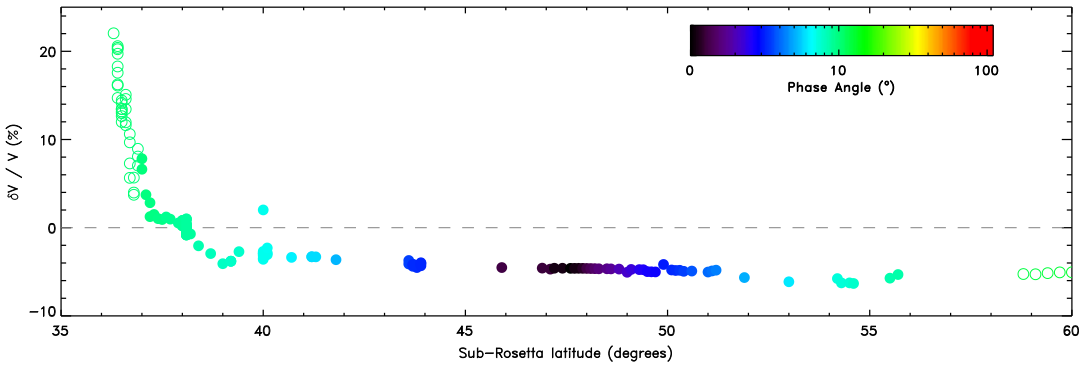

Fig. 6. Difference in volume estimated (Eq. (2)) from the difference in projected area between the profiles of Lutetia extracted from the OSIRIS images and the prediction from the KOALA model (Carry et al., 2010b). The symbols are color-coded as a function of the phase angle. Filled symbols correspond to images where the phase angle was smaller than 10°. (For interpretation of the references to color in this figure legend, the reader is referred to the web version of this article.)

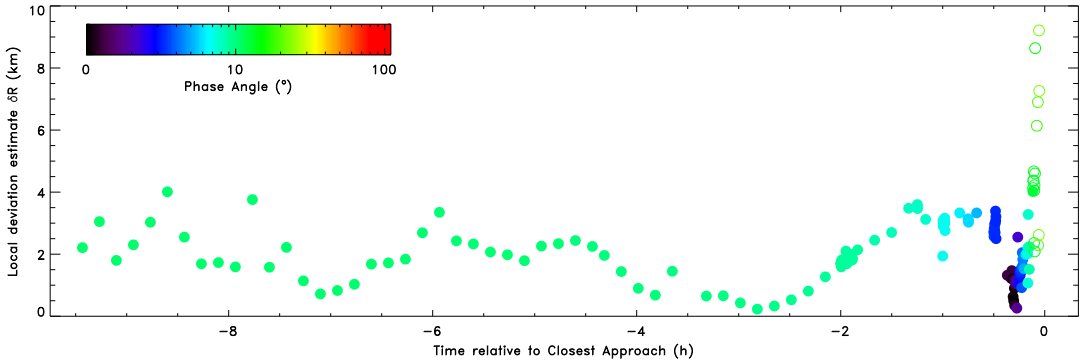

Fig. 7. Estimate of the local deviation (δR) between the profiles of Lutetia extracted from the OSIRIS images and the prediction from the KOALA model (Carry et al., 2010b). The symbols are color-coded as a function of the phase angle. Filled symbols correspond to images where the phase angle was smaller than 10° (see text). (For interpretation of the references to color in this figure legend, the reader is referred to the web version of this article.)

From this detailed analysis, we confirm the results from the overall comparison presented in Section 3.1: the volume was slightly overestimated with KOALA, relative to the results derived from the flyby. But, as visible in Fig. 6, the difference between the KOALA predictions and the OSIRIS images is almost constant, at about −5%, for all images taken with phase angle smaller than ∼10°. The largest deviations, still within the uncertainty reported using KOALA, are found for sub-Rosetta latitudes lower than about 40°, *i.e.*, for geometries that had not been observed from Earth with AO. Owing to the restricted geometries of ground-based AO imaging observations to date (always close to "pole-on", see Drummond et al., 2010; Carry et al., 2010b), the differences between KOALA predictions and OSIRIS frames may be related to two distinct factors: one "inherent" to KOALA (which is the one we seek to evaluate), and another related to the observing geometry. Unfortunately, there is no easy way to distinguish between these two effects. We thus estimate that the inherent uncertainty in the KOALA volume is about 5% (Fig. 6). This uncertainty can increase, however, due to unfavorable observing geometries, such as we have for the present case of Lutetia.

In addition to calibrating the volume estimate, we assess the accuracy of the KOALA 3-D shape determination. From the direct comparison of both models (pre- and post-flyby, in Fig. 3), we can already qualitatively assert that KOALA allows accurate 3-D shape determination. However, many different shapes can result in similar volume, and also in similar overall triaxial-ellipsoid dimensions (which are accurate to a couple of km, see Section 3.1). We therefore apply the following criterion (δR, see Eq. (3)) to estimate the *local* deviation of the KOALA model to the real shape of Lutetia, and therefore calibrate quantitatively the KOALA 3-D shape determination:

$$\delta R = \frac{1}{N}\sum_{i}^{N}\frac{(\mathcal{O}_i - \mathcal{K}_i)^2}{\mathcal{O}_i} \qquad (3)$$

where $\mathcal{O}_i$ and $\mathcal{K}_i$, respectively, are the OSIRIS and KOALA profile radii of the ith point (out of N describing the OSIRIS profile), measured from an arbitrary center.

We present in Fig. 7 the estimate of the local deviation of the KOALA predictions to the apparent shape of Lutetia measured on the OSIRIS NAC images, as a function of the time relative to CA. The deviations are limited to about 4 km at maximum, and are about 2 km on average (confirmed by the independent analysis of Preusker et al., 2012). The typical accuracy in the elevation of each vertex is therefore close to 2 km. This is consistent with the overall comparison presented in Section 3.1, but we show here that not only the overall sizes are accurate to about 2 km, but that this accuracy is maintained at local scales.

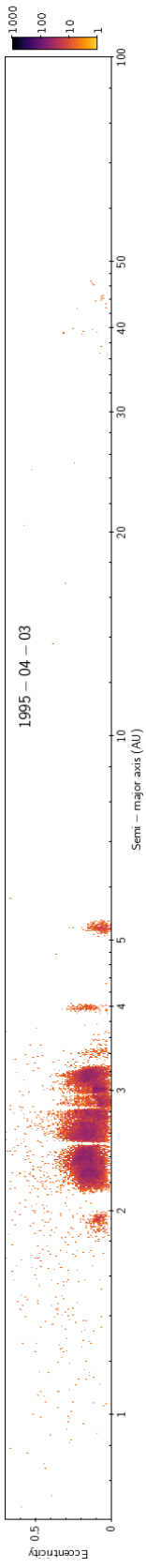

The *apparent* absence of craters in the KOALA model[11] (compared to 3-D shape models derived from flyby, *e.g.*, Sierks et al., 2011; Preusker et al., 2012) has therefore little influence on the volume estimate and its accuracy. The largest craters seen on Lutetia have a diameter of about 20 km and a depth of about 2–3 km (see Fig. 4 and Marchi et al., 2012; Vincent et al., 2012), corresponding to the typical accuracy on elevation, and are therefore already included in the uncertainty envelop around the KOALA shape model.

From this detailed comparison of OSIRIS frames with KOALA predictions, we assert that the KOALA model performed extraordinarily well, especially given two limiting factors related to the observing geometries of the ground-based observations. First, for the imaging observations, Lutetia had an angular diameter of about 0.1″, close to the angular resolution for which we currently can extract useful shape information from ground-based telescopes with AO. Second, for the oppositions in 2007 and 2008, Lutetia was positioned at diametrically opposite apparent ecliptic coordinates from Earth, and because of the high obliquity, we observed Lutetia close to North-pole-on and then close to South-pole-on, and we were not able to achieve a good equatorial view, resulting in a poorly determined *c*-axis (Drummond et al., 2010; Carry et al., 2010b). We expect to improve that in upcoming observations.

We have determined that the difference between the KOALA shape model and the *real* topography of Lutetia to be 2 km, on average. Considering Lutetia's volume-equivalent diameter (98 km, see Table 1), this translates into a relative precision on the radii of about 5%. We can therefore expect a conservative upper limit of 15% for the accuracy that can be achieved on volume estimates made by KOALA (including possible systematic effects), although it appears that the measured uncertainty (Fig. 6) is closer to 5%. These estimates of the accuracy achievable with KOALA are close to our previously estimated uncertainty: Although formal uncertainties for our shape-fitting algorithms are closer to 1 or 2 km, we had estimated that our size measurements were affected by systematic errors at the level of 1–3% (from simulations and observations of Saturn's moons, see Carry, 2009; Drummond et al., 2009b).

4. KOALA and thermal radiometry

As a supplementary investigation of the capabilities of KOALA for the study of a large sample of asteroids from ground-based observations, we analyze here the thermal properties of (21) Lutetia, using only ground-based information: the KOALA 3-D shape model (Drummond et al., 2010; Carry et al., 2010b), and 104 individual thermal measurements (O'Rourke et al., 2012, and reference therein), disregarding any information provided by the flyby of the asteroid by Rosetta. We then compare our results with those derived from the thermal infrared observations acquired by the MIRO instrument during Rosetta flyby (Gulkis et al., 2012). We also comment on the results obtained by O'Rourke et al. (2012) with the same dataset, but using the 3-D shape model derived from Rosetta imaging (Sierks et al., 2011).

Many observations at thermal wavelengths are available: Lutetia was observed multiple times by several infrared survey missions, like IRAS in 1983, or Akari in 2006/2007, but it was also targeted by different observing campaigns from ground: IRTF, ESO-TIMMI2, and from space: Spitzer, Herschel (see O'Rourke et al., 2012, for details on the observing circumstances).

First, we use the spin-vector coordinates provided by KOALA to determine the corresponding (lightcurve averaged) cross-sections for all observations that were used to derive the absolute magnitude of Lutetia: $H=7.25\pm0.01$ mag (Bowell et al., 1989; Belskaya et al., 2010). All observations were taken with sub-observer latitude between -70° and -85°, close to pole-on geometry, when the apparent average diameter of Lutetia was around 110–111 km (compared to its volume-equivalent diameter of 98 km, Sierks et al., 2011). The absolute magnitude of Lutetia was therefore slightly overestimated. We can still use it to determine the geometric visual albedo p_V via the relation: $\log p_V = 6.2559 - 2\log d - 0.4H$ (Pravec and Harris, 2007, and references therein), providing d is the average apparent diameter of Lutetia at the time of the observations. The combination of the KOALA shape model with the published absolute H magnitude leads to $p_V=0.19\pm0.01$, in excellent agreement with the value derived during Rosetta flyby (0.19 ± 0.01, see Sierks et al., 2011 and Table 2). Second, the knowledge of the 3-D shape allows us to correct this bias on the actual H magnitude of Lutetia: Published absolute magnitudes are typically derived from a limited number of latitudes of the sub-observer point, and represent therefore an approximation only to the *real* absolute magnitude. Using the knowledge of the 3-D shape model with an absolute size scale and the geometric albedo (see above), one can determine the proper geometry-independent H-mag. Such an H-mag can then be considered a general, object-related property rather than an observed quantity valid only for certain geometries. Indeed, the absolute magnitude is intended to be a general, object-related property, rather than an observed quantity valid only for certain geometries (Bowell et al., 1989). The geometry-independent H-mag for Lutetia, based on the KOALA shape model and the geometric visual albedo of $p_V=0.19$, is therefore $H_V=7.42\pm0.03$.

Table 2
Albedo (p_V), and thermal inertia (Γ, in SI units: J m^{-2} s$^{-0.5}$ K^{-1}) derived using MIRO on-board Rosetta (Gulkis et al., 2012), ground-based data in combination with the shape model derived from Rosetta flyby (O'Rourke et al., 2012), and ground-based data in combination with the KOALA shape model (present study).

p_V	Γ (SI)	References
Assumed	20	Gulkis et al. (2012)
0.20 ± 0.01	5	O'Rourke et al. (2012)
0.19 ± 0.01	<40	This work

We use this refined H-mag to proceed with radiometric analysis via a TPM code (Lagerros, 1996, 1997, see Section 1.3). This model considers a 1-D heat conduction into the surface, based on realistic surface conditions of illumination provided by the KOALA shape model (see O'Rourke et al., 2012, for details on such computations). As a complementary check of the techniques, we first determine the radiometric size and geometric albedo of Lutetia, regardless of the size information provided by the KOALA shape model (following the method by Müller et al., 2011). The calculation is based on the general thermal properties derived for large main-belt asteroids (Müller and Lagerros, 2002), a wavelength-dependent emissivity model, a default thermal inertia Γ of 15 J m^{-2} s$^{-0.5}$ K^{-1}, and a default roughness implementation with 60% of the surface covered by craters and an RMS of the surface slopes of 0.7 (see, *e.g.*, Lagerros, 1996, 1997, for definitions of these quantities). This leads to a radiometric volume-equivalent diameter (based on a dimensionless version of the KOALA 3-D shape model) of 99.8 ± 4.6 km and a geometric albedo p_V of 0.198 ± 0.017 (weighted mean values and standard deviations from the analysis of the 104 individual thermal measurements). These values are in agreement with the pre-flyby estimates (diameter of 98.3 ± 5.9 km and geometric albedo p_V of 0.208 ± 0.025) by Mueller et al. (2006), using the lightcurve inversion model by Torppa et al. (2003). This demonstrates the

[11] Although the model does not show round, crater-like, features, KOALA allows modeling of concavities, that can be large impact craters.

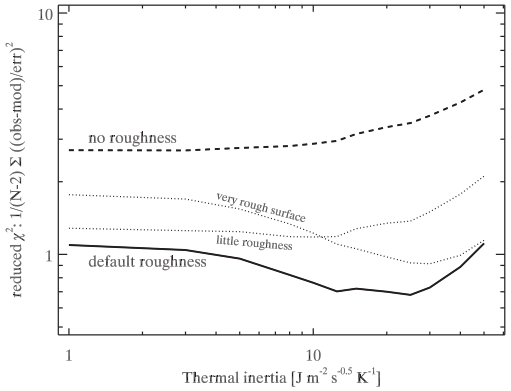

Fig. 8. Thermal inertia determination using the KOALA shape model and ground-based observations. We use four values of surface roughness (default roughness means 60% of the surface is covered by craters and the RMS of the surface slopes is 0.7; see detail in O'Rourke et al., 2012) for thermal inertia ranging from very low to moderate (1–100 J m^{-2} s$^{-0.5}$ K^{-1}).

value of combining thermal data with spin and 3-D shape models to derive accurately the diameters and albedos of asteroids.

Finally, we constrain the thermal inertia of Lutetia by comparing the TPM predictions (using the KOALA 3-D shape model, including its size estimate) for a range of thermal inertias with the 104 observed thermal measurements. This allows us to find the most probable thermal inertia to explain all data simultaneously, *i.e.*, to match the before/after opposition observations as well as the observations taken at the short-wavelength Wien part of the spectral energy distribution (SED) and the long-wavelength Rayleigh-Jeans part of the SED. Thermal data also cover the entire rotation of Lutetia and a significant range of sub-Earth latitudes (see the listing of observations in O'Rourke et al., 2012). Thermal inertias in the range 5–40 J m^{-2} s$^{-0.5}$ K^{-1} produce the lowest χ^2-values (see Fig. 8), indicating the presence of fine-grained regolith (Brown and Matson, 1987). These values are close to the measured values by Rosetta in agreement with the values measured by Rosetta (20 J m^{-2} s$^{-0.5}$ K^{-1}, see Gulkis et al., 2012 and Table 2). The χ^2-analysis also shows that one has to add substantial roughness on the surface to explain the thermal measurements. The KOALA 3-D shape model without any small-scale roughness cannot provide acceptable χ^2-values.

The prediction made using the combination of the KOALA and TPM models provides a good fit to all 104 measurements of Lutetia in the thermal infrared. There is a discrepancy, however, for a given observing geometry that could be solved by the addition of a plateau/hill to the 3-D shape model, whose size remains within the quoted 3-D shape uncertainty as discussed by O'Rourke et al. (2012).

From this detailed comparison of ground-based with flyby results, KOALA has been shown to be a powerful technique for the study of asteroids from the ground, not only for size/shape/spin, but now also for thermal properties. The validated (see Section 3) 3-D shape models, determined using KOALA, allow the study of the surface properties (*e.g.*, albedo and thermal inertia) in great detail, and the results are consistent with those derived from the flyby.

5. Concluding remarks: the future of KOALA

The flyby of (21) Lutetia by ESA Rosetta provided a spectacular demonstration of the capabilities of the KOALA algorithm. Spin-vector coordinates were found to be accurate within 2°, 3-D shape modeling to better than 2 km (local topography), and dimensions to 2%. Volume estimates provided by KOALA are seen to be accurate to better than 10%. The thermal properties (albedo and thermal inertia) of Lutetia determined using a thermophysical model in conjunction with the KOALA shape model agree with the Rosetta-flyby-derived values, within the quoted uncertainties. These levels of accuracy on the spin and 3-D shape/size are typical for large main-belt asteroids, and not specific to Lutetia. Although it was extensively observed from the ground, being a spacecraft target, the number of lightcurves was similar to that of other large main-belt asteroids and the geometry of imaging observations was not particularly favorable (*i.e.*, mostly close to "pole-on").

This ability of KOALA to determine the volume of main-belt asteroids of size ~100 km with an accuracy of about 10% opens the possibility for study of a larger set of small bodies using Earth-based observations. For instance, it can be expected to help efforts to better understand the densities of asteroids belonging to different taxonomic classes (DeMeo et al., 2009). This will be assisted by mass estimates from about 150–200 asteroids that will be determined from gravitational deflections observed by the upcoming ESA Gaia astrometry mission (Mouret et al., 2007), and the ever-growing number of known binary asteroids. During the first stages of the encounter of Rosetta with its main target, comet 67P/Churyumov-Gerasimenko in 2014, we also plan to use a KOALA-style analysis of the first, low-resolution, resolved images to quickly produce a shape/size model. This will support the mission science until a full high-resolution model can be derived.

The present implementation of KOALA allows the combined use of optical lightcurves (including sparse photometry), profiles from disk-resolved images, and chords from stellar occultations. We continue the development of KOALA toward the use of more data modes (*e.g.*, interferometry, thermal radiometry) to increase the number of possible targets, and to set better constraints on targets observable only with certain techniques. Using different wavelength ranges, in particular in the thermal infrared, opens the possibility of deriving additional physical properties, like albedo or thermal inertia. We also plan to incorporate additional cross-checks and constraints on the inversion, such as rigorous attention to differences in the spatial resolution of input images, to improve the confidence on the non-convex features and details.

Acknowledgments

We would like to thank the OSIRIS Team for use of the OSIRIS images. OSIRIS was built by a consortium of the Max-Planck-Institut für Sonnensystemforschung, Lindau, Germany, the Laboratoire d'Astrophysique de Marseille, France, the Centro Interdipartimentale Studi e Attivita' Spaziali, University of Padova, Italy, the Instituto de Astrofisica de Andalucia, Granada, Spain, the Research and Scientific Support Department of the European Space Agency (ESA/ESTEC), Noordwijk, The Netherlands, the Instituto Nacional de Tecnica Aerospacial, Madrid, Spain, the Institut für Datentechnik und Kommunikationsnetze der Technischen Universitat, Braunschweig and the Department of Astronomy and Space Physics of Uppsala University, Sweden. The support of the national funding agencies DLR, CNES, ASI, MEC, NASA, and SNSB is gratefully acknowledged. We thank the Rosetta Science Operations Center and the Rosetta Mission Operations Center for the successful flyby of (21) Lutetia. We would like to thank F. Preusker, S. Marchi, and J.-B. Vincent for providing their results ahead of publication. Herschel is an ESA space observatory with science instruments provided by European-led Principal Investigator consortia and with important participation from NASA. The thermal analysis is also based on observations

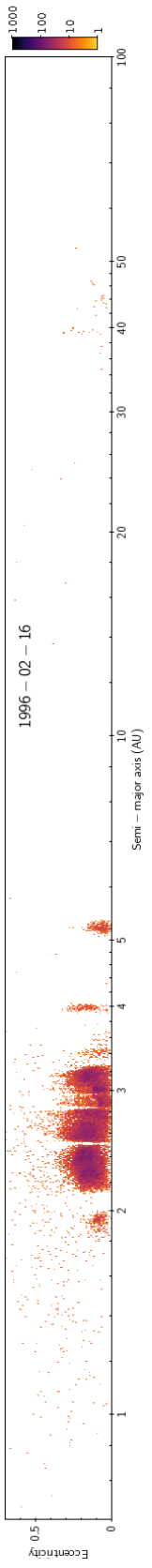

collected at the European Southern Observatory, Chile: 079.C-0006. The KOALA shape model discussed here was based on imaging observations realized at the 079.C-0493, and the W.M. Keck Observatory, which is operated as a scientific partnership among the California Institute of Technology, the University of California, and the National Aeronautics and Space Administration. The Observatory was made possible by the generous financial support of the W.M. Keck Foundation. We also thank our collaborators on Team Keck, the Keck science staff, for making possible some of these observations, and for observing time granted at Gemini Observatory under NOAO time allocation. This work was supported, in part, by the NASA Planetary Astronomy and NSF Planetary Astronomy Programs (Merline PI), and the work of J. Ďurech was supported by the Grant GACR 209/10/0537 of the Czech Science Foundation. This research used Miriade VO tool (Berthier et al., 2008) developed at IMCCE, and NASA's Astrophysics Data System. Thanks to all the developers!

References

Baer, J., Chesley, S.R., Matson, R.D., 2011. Astrometric masses of 26 asteroids and observations on asteroid porosity. Astronomical Journal 141, 143–155.

Behrend, R., Bernasconi, L., Roy, R., Klotz, A., Colas, F., Antonini, P., Aoun, R., Augustesen, K., Barbotin, E., Berger, N., Berrouachdi, H., Brochard, E., Cazenave, A., Cavadore, C., Coloma, J., Cotrez, V., Deconihout, S., Demeautis, C., Dorseuil, J., Dubos, G., Durkee, R., Frappa, E., Hormuth, F., Itkonen, T., Jacques, C., Kurtze, L., Laffont, A., Lavayssière, M., Lecacheux, J., Leroy, A., Manzini, F., Masi, G., Matter, D., Michelsen, R., Nomen, J., Oksanen, A., Pääkkönen, P., Peyrot, A., Pimentel, E., Pray, D.P., Rinner, C., Sanchez, S., Sonnenberg, K., Sposetti, S., Starkey, D., Stoss, R., Teng, J.P., Vignand, M., Waelchli, N., 2006. Four new binary minor planets: four new binary minor planets: (854) Frostia, (1089) Tama, (1313) Berna, (4492) Debussy. Astronomy and Astrophysics 446, 1177–1184.

Belskaya, I.N., Fornasier, S., Krugly, Y.N., Shevchenko, V.G., Gaftonyuk, N.M., Barucci, M.A., Fulchignoni, M., Gil-Hutton, R.G., 2010. Puzzling asteroid 21 Lutetia: our knowledge prior to the Rosetta fly-by. Astronomy and Astrophysics 515, A29.

Berthier, J., Hestroffer, D., Carry, B., Ďurech, J., Tanga, P., Delbo, M., Vachier, F., 2008. A service of position and physical ephemerides computation dedicated to the small bodies of the solar system. LPI Contributions 1405, 8374.

Binzel, R.P., Gaffey, M.J., Thomas, P.C., Zellner, B.H., Storrs, A.D., Wells, E.N., 1997. Geologic mapping of vesta from 1994 hubble space telescope images. Icarus 128, 95–103.

Bowell, E., Hapke, B., Domingue, D., Lumme, K., Peltoniemi, J., Harris, A.W., 1989. Application of photometric models to asteroids. In: Asteroids II, pp. 524–556.

Britt, D.T., Yeomans, D.K., Housen, K.R., Consolmagno, G.J., 2002. Asteroid density, porosity, and structure. In: Asteroids III, pp. 485–500.

Brown, R.H., Matson, D.L., 1987. Thermal effects of insolation propagation into the regoliths of airless bodies. Icarus 72, 84–94.

Busch, M.W., 2009. ALMA and asteroid science. Icarus 200, 347–349.

Carry, B., 2009. Asteroids Physical Properties from High Angular-Resolution Imaging. Ph.D. Thesis. Observatoire de Paris.

Carry, B., Dumas, C., Fulchignoni, M., Merline, W.J., Berthier, J., Hestroffer, D., Fusco, T., Tamblyn, P., 2008. Near-infrared mapping and physical properties of the dwarf-planet Ceres. Astronomy and Astrophysics 478, 235–244.

Carry, B., Dumas, C., Kaasalainen, M., Berthier, J., Merline, W.J., Erard, S., Conrad, A.R., Drummond, J.D., Hestroffer, D., Fulchignoni, M., Fusco, T., 2010a. Physical properties of (2) Pallas. Icarus 205, 460–472.

Carry, B., Kaasalainen, M., Leyrat, C., Merline, W.J., Drummond, J.D., Conrad, A.R., Weaver, H.A., Tamblyn, P.M., Chapman, C.R., Dumas, C., Colas, F., Christou, J.C., Dotto, E., Perna, D., Fornasier, S., Bernasconi, L., Behrend, R., Vachier, F., Kryszczynska, A., Polinska, M., Fulchignoni, M., Roy, R., Naves, R., Poncy, R., Wiggins, P., 2010b. Physical properties of the ESA Rosetta target asteroid (21) Lutetia II. Shape and flyby geometry. Astronomy and Astrophysics 523, A94.

Conrad, A.R., Dumas, C., Merline, W.J., Drummond, J.D., Campbell, R.D., Goodrich, R.W., Le Mignant, D., Chaffee, F.H., Fusco, T., Kwok, S.H., Knight, R.I., 2007. Direct measurement of the size, shape, and pole of 511 Davida with Keck AO in a single night. Icarus 191, 616–627.

Delbo, M., Dell'Oro, A., Harris, A.W., Mottola, S., Mueller, M., 2007. Thermal inertia of near-Earth asteroids and implications for the magnitude of the Yarkovsky effect. Icarus 190, 236–249.

Delbo, M., Gai, M., Lattanzi, M.G., Ligori, S., Loreggia, D., Saba, L., Cellino, A., Gandolfi, D., Licchelli, D., Blanco, C., Cigna, M., Wittkowski, M., 2006. MIDI observations of 1459 Magnya: first attempt of interferometric observations of asteroids with the VLTI. Icarus 181, 618–622.

Delbo, M., Ligori, S., Matter, A., Cellino, A., Berthier, J., 2009. First VLTI-MIDI direct determinations of asteroid sizes. Astrophysical Journal 694, 1228–1236.

Delbo, M., Tanga, P., 2009. Thermal inertia of main belt asteroids smaller than 100 km from IRAS data. Planetary and Space Science 57, 259–265.

DeMeo, F.E., Binzel, R.P., Slivan, S.M., Bus, S.J., 2009. An extension of the bus asteroid taxonomy into the near-infrared. Icarus 202, 160–180.

Drummond, J.D., Christou, J.C., 2008. Triaxial ellipsoid dimensions and rotational poles of seven asteroids from Lick Observatory adaptive optics images, and of ceres. Icarus 197, 480–496.

Drummond, J.D., Christou, J.C., Nelson, J., 2009a. Triaxial ellipsoid dimensions and poles of asteroids from AO observations at the Keck-II telescope. Icarus 202, 147–159.

Drummond, J.D., Cocke, W.J., 1989. Triaxial ellipsoid dimensions and rotational pole of 2 Pallas from two stellar occultations. Icarus 78, 323–329.

Drummond, J.D., Conrad, A., Merline, W., Carry, B., 2009. The dimensions and pole of asteroid (21) Lutetia from adaptive optics images. In: AAS/Division for Planetary Sciences Meeting Abstracts #41, p. 59.07.

Drummond, J.D., Conrad, A., Merline, W.J., Carry, B., Chapman, C.R., Weaver, H.A., Tamblyn, P.M., Christou, J.C., Dumas, C., 2010. Physical properties of the ESA Rosetta target asteroid (21) Lutetia I. The triaxial ellipsoid dimensions, rotational pole, and bulk density. Astronomy and Astrophysics 523, A93.

Drummond, J.D., Fugate, R.Q., Christou, J.C., Hege, E.K., 1998. Full adaptive optics images of asteroids ceres and vesta; rotational poles and triaxial ellipsoid dimensions. Icarus 132, 80–99.

Dunham, D.W., Dunham, J.B., Binzel, R.P., Evans, D.S., Freuh, M., Henry, G.W., A'Hearn, M.F., Schnurr, R.G., Betts, R., Haynes, H., Orcutt, R., Bowell, E., Wasserman, L.H., Nye, R.A., Giclas, H.L., Chapman, C.R., Dietz, R.D., Moncivais, C., Douglas, W.T., Parker, D.C., Beish, J.D., Martin, J.O., Monger, D.R., Hubbard, W.B., Reitsema, H.J., Klemola, A.R., Lee, P.D., McNamara, B.R., Maley, P.D., Manly, P., Markworth, N.L., Nolthenius, R., Oswalt, T.D., Smith, J.A., Strother, E.F., Povenmire, H.R., Purrington, R.D., Trenary, C., Schneider, G.H., Schuster, W.J., Moreno, M.A., Guichard, J., Sanchez, G.R., Taylor, G.E., 1990. The size and shape of (2) Pallas from the 1983 occultation of 1 Vulpeculae. Astronomical Journal 99, 1636–1662.

Ďurech, J., Grav, T., Jedicke, R., Denneau, L., Kaasalainen, M., 2005. Asteroid models from the Pan-STARRS photometry. Earth Moon and Planets 97, 179–187.

Ďurech, J., Kaasalainen, M., Herald, D., Dunham, D., Timerson, B., Hanuš, J., Frappa, E., Talbot, J., Hayamizu, T., Warner, B.D., Pilcher, F., Galád, A., 2011. Combining asteroid models derived by lightcurve inversion with asteroidal occultation silhouettes. Icarus 214, 652–670.

Ďurech, J., Kaasalainen, M., Marciniak, A., Allen, W.H., Behrend, R., Bembrick, C., Bennett, T., Bernasconi, L., Berthier, J., Bolt, G., Boroumand, S., Crespo da Silva, L.D., Crippa, R., Crow, M., Durkee, R., Dymock, R., Fagas, M., Fauerbach, M., Fauvaud, S., Frey, M., Gonçalves, R., Hirsch, R., Jardine, D., Kamiński, K., Koff, R., Kwiatkowski, T., López, A., Manzini, F., Michałowski, T., Pacheco, R., Pan, M., Pilcher, F., Poncy, R., Pray, D.P., Pych, W., Roy, R., Santacana, G., Slivan, S.M., Sposetti, S., Stephens, R., Warner, B.D., Wolf, M., 2007. Physical models of ten asteroids from an observers' collaboration network. Astronomy and Astrophysics 465, 331–337.

Ďurech, J., Sidorin, V., Kaasalainen, M., 2010. DAMIT: a database of asteroid models. Astronomy and Astrophysics 513, A46.

Elkins-Tanton, L.T., Weiss, B.P., Zuber, M.T., 2011. Chondrites as samples of differentiated planetesimals. Earth and Planetary Science Letters 305, 1–10.

Fujiwara, A., Kawaguchi, J., Yeomans, D.K., Abe, M., Mukai, T., Okada, T., Saito, J., Yano, H., Yoshikawa, M., Scheeres, D.J., Barnouin-Jha, O.S., Cheng, A.F., Demura, H., Gaskell, G.W., Hirata, N., Ikeda, H., Kominato, T., Miyamoto, H., Nakamura, R., Sasaki, S., Uesugi, K., 2006. The rubble-pile asteroid Itokawa as observed by Hayabusa. Science 312, 1330–1334.

Gaskell, R.W., Barnouin-Jha, O.S., Scheeres, D.J., Konopliv, A.S., Mukai, T., Abe, S., Saito, J., Ishiguro, M., Kubota, T., Hashimoto, T., Kawaguchi, J., Yoshikawa, M., Shirakawa, K., Kominato, T., Hirata, N., Demura, H., 2008. Characterizing and navigating small bodies with imaging data. Meteoritics and Planetary Science 43, 1049–1061.

Gulkis, S., Frerking, M., Crovisier, J., Beaudin, G., Hartogh, P., Encrenaz, P., Koch, T., Kahn, C., Salinas, Y., Nowicki, R., Irigoyen, R., Janssen, M., Stek, P., Hofstadter, M., Allen, M., Backus, C., Kamp, L., Jarchow, C., Steinmetz, E., Deschamps, A., Krieg, J., Gheudin, M., Bockelée-Morvan, D., Biver, N., Encrenaz, T., Despois, D., Ip, W.H., Lellouch, E., Mann, I., Muhleman, D., Rauer, H., Schloerb, P., Spilker, T., 2012. Continuum and spectroscopic observations of asteroid (21) Lutetia at millimeter and submillimeter wavelengths with the MIRO instrument on the Rosetta Spacecraft. Planetary and Space Science 66, 31–42.

Hanuš, J., Ďurech, J., Brož, M., Warner, B.D., Pilcher, F., Stephens, R., Oey, J., Bernasconi, L., Casulli, S., Behrend, R., Polishook, D., Henych, T., Lehký, M., Yoshida, F., Ito, T., 2011. A study of asteroid pole-latitude distribution based on an extended set of shape models derived by the lightcurve inversion method. Astronomy and Astrophysics 530, A134.

Hestroffer, D., Tanga, P., Cellino, A., Guglielmetti, F., 2002. Asteroids observations with the Hubble space telescope I. Observing strategy, and data analysis and modeling process. Astronomy and Astrophysics 391, 1123–1132.

Hill, J.M., Green, R.F., Ashby, D.S., Brynnel, J.G., Cushing, N.J., Little, J., Slagle, J.H., Wagner, R.M., 2010. The large binocular telescope. In: SPIE, vol. 7733.

Hilton, J.L., 2002. Asteroid masses and densities. In: Asteroids III, pp. 103–112.

Housen, K.R., Holsapple, K.A., Voss, M.E., 1999. Compaction as the origin of the unusual craters on the asteroid Mathilde. Nature 402, 155–157.

Johansen, A., Lacerda, P., 2010. Prograde rotation of protoplanets by accretion of pebbles in a gaseous environment. Monthly Notices of the Royal Astronomical Society 404, 475–485.

Kaasalainen, M., 2004. Physical models of large number of asteroids from calibrated photometry sparse in time. Astronomy and Astrophysics 422, L39–L42.

Kaasalainen, M., 2011. Maximum compatibility estimates and shape reconstruction with boundary curves and volumes of generalized projections. Inverse Problems and Imaging 5, 37–57.

Kaasalainen, M., Lamberg, L., 2006. Inverse problems of generalized projection operators. Inverse Problems 22, 749–769.

Kaasalainen, M., Mottola, S., Fulchignoni, M., 2002a. Asteroid models from disk-integrated data. In: Asteroids III, pp. 139–150.

Kaasalainen, M., Torppa, J., 2001. Optimization methods for asteroid lightcurve inversion—I. Shape determination. Icarus 153, 24–36.

Kaasalainen, M., Torppa, J., Muinonen, K., 2001. Optimization methods for asteroid lightcurve inversion—II. The complete inverse problem. Icarus 153, 37–51.

Kaasalainen, M., Torppa, J., Piironen, J., 2002b. Models of twenty asteroids from photometric data. Icarus 159, 369–395.

Keller, H.U., Barbieri, C., Lamy, P.L., Rickman, H., Rodrigo, R., Wenzel, K.P., Sierks, H., A'Hearn, M.F., Angrilli, F., Angulo, M., Bailey, M.E., Barthol, P., Barucci, M.A., Bertaux, J.L., Bianchini, G., Boit, J.L., Brown, V., Burns, J.A., Büttner, I., Castro, J.M., Cremonese, G., Curdt, W., da Deppo, V., Debei, S., de Cecco, M., Dohlen, K., Fornasier, S., Fulle, M., Germerott, D., Gliem, F., Guizzo, G.P., Hviid, S.F., Ip, W.H., Jorda, L., Koschny, D., Kramm, J.R., Kührt, E., Küppers, M., Lara, L.M., Llebaria, A., López, A., López-Jimenez, A., López-Moreno, J., Meller, R., Michalik, H., Michelena, M.D., Müller, R., Naletto, G., Origné, A., Parzianello, G., Pertile, M., Quintana, C., Ragazzoni, R., Ramous, P., Reiche, K.U., Reina, M., Rodríguez, J., Rousset, G., Sabau, L., Sanz, A., Sivan, J.P., Stöckner, K., Tabero, J., Telljohann, U., Thomas, N., Timon, V., Tomasch, G., Wittrock, T., Zaccariotto, M., 2007. OSIRIS—The scientific camera system onboard Rosetta. Space Science Reviews 128, 433–506.

Lagerros, J.S.V., 1996. Thermal physics of asteroids I. Effects of shape, heat conduction and beaming. Astronomy and Astrophysics 310, 1011–1020.

Lagerros, J.S.V., 1997. Thermal physics of asteroids III. Irregular shapes and albedo variegations. Astronomy and Astrophysics 325, 1226–1236.

Lamy, P.L., Jorda, L., Fornasier, S., Groussin, O., Barucci, M.A., Carvano, J.M., Dotto, E., Fulchignoni, M., Toth, I., 2008a. Asteroid 2867 Steins III. Spitzer space telescope observations, size determination, and thermal properties. Astronomy and Astrophysics 487, 1187–1193.

Lamy, P.L., Kaasalainen, M., Lowry, S.C., Weissman, P., Barucci, M.A., Carvano, J.M., Choi, Y., Colas, F., Faury, G., Fornasier, S., Groussin, O., Hicks, M.D., Jorda, L., Kryszczynska, A., Larson, S., Toth, I., Warner, B.D., 2008b. Asteroid 2867 Steins II. Multi-telescope visible observations, shape reconstruction, and rotational state. Astronomy and Astrophysics 487, 1179–1185.

Lebofsky, L.A., Sykes, M.V., Tedesco, E.F., Veeder, G.J., Matson, D.L., Brown, R.H., Gradie, J.C., Feierberg, M.A., Rudy, R.J., 1986. A refined 'standard' thermal model for asteroids based on observations of 1 Ceres and 2 Pallas. Icarus 68, 239–251.

Li, J., Kuchner, M.J., Allen, R.J., Sheppard, S.S., 2011. Measuring the sizes, shapes, surface features and rotations of Solar System objects with interferometry. Icarus 211, 1007–1021.

Li, J., McFadden, L.A., Thomas, P.C., Mutchler, M.J., Parker, J.W., Young, E.F., Russell, C.T., Sykes, M.V., Schmidt, B.E., 2010. Photometric mapping of Asteroid (4) Vesta's southern hemisphere with Hubble Space Telescope. Icarus 208, 238–251.

Li, J.Y., McFadden, L.A., Parker, J.W., Young, E.F., Stern, S.A., Thomas, P.C., Russell, C.T., Sykes, M.V., 2006. Photometric analysis of 1 Ceres and surface mapping from HST observations. Icarus 182, 143–160.

Mainzer, A., Bauer, J.M., Grav, T., Masiero, J., Cutri, R.M., Dailey, J., Eisenhardt, P., McMillan, R.S., Wright, E., Walker, R.G., Jedicke, R., Spahr, T., Tholen, D.J., Alles, R., Beck, R., Brandenburg, H., Conrow, T., Evans, T., Fowler, J., Jarrett, T., Marsh, K., Masci, F., McCallon, H., Wheelock, S., Wittman, M., Wyatt, P., DeBaun, E., Elliott, G., Elsbury, D., Gautier, T., Gomillion, S., Leisawitz, D., Maleszewski, C., Micheli, M., Wilkins, A., 2011. Preliminary results from NEOWISE: an enhancement to the wide-field infrared survey explorer for solar system science. Astrophysical Journal 731, 53–66.

Marchi, S., Massironi, M., Vincent, J., Morbidelli, A., Mottola, S., Marzari, F., Küppers, M., Besse, S., Thomas, N., Barbieri, C., Naletto, G., Sierks, H., 2012. The cratering history of asteroid (21) Lutetia. Planetary and Space Science 66, 87–95.

Matter, A., Delbo, M., Ligori, S., Crouzet, N., Tanga, P., 2011. Determination of physical properties of the asteroid (41) Daphne from interferometric observations in the thermal infrared. Icarus 215, 47–56.

Merline, W.J., Drummond, J.D., Conrad, A.R., Carry, B., Dumas, C. The resolved asteroid program I: (52) Europa. Personal communication.

Merline, W.J., Weidenschilling, S.J., Durda, D.D., Margot, J.L., Pravec, P., Storrs, A.D., 2002. Asteroids do have satellites. In: Asteroids III, pp. 289–312.

Millis, R.L., Dunham, D.W., 1989. Precise measurement of asteroid sizes and shapes from occultations. In: Asteroids II, pp. 148–170.

Moullet, A., Lellouch, E., Moreno, R., Gurwell, M., 2011. Physical studies of centaurs and trans-Neptunian objects with the Atacama large millimeter array. Icarus 213, 382–392.

Mouret, S., Hestroffer, D., Mignard, F., 2007. Asteroid masses and improvement with GAIA. Astronomy and Astrophysics 472, 1017–1027.

Mueller, M., Harris, A.W., Bus, S.J., Hora, J.L., Kassis, M., Adams, J.D., 2006. The size and albedo of Rosetta fly-by target 21 Lutetia from new IRTF measurements and thermal modeling. Astronomy and Astrophysics 447, 1153–1158.

Müller, T.G., Ďurech, J., Hasegawa, S., Abe, M., Kawakami, K., Kasuga, T., Kinoshita, D., Kuroda, D., Urakawa, S., Okumura, S., Sarugaku, Y., Miyasaka, S., Takagi, Y., Weissman, P.R., Choi, Y.J., Larson, S., Yanagisawa, K., Nagayama, S., 2011. Thermo-physical properties of 162173 (1999 JU3), a potential flyby and rendezvous target for interplanetary missions. Astronomy and Astrophysics 525, A145.

Müller, T.G., Lagerros, J.S.V., 2002. Asteroids as calibration standards in the thermal infrared for space observatories. Astronomy and Astrophysics 381, 324–339.

Müller, T.G., Sekiguchi, T., Kaasalainen, M., Abe, M., Hasegawa, S., 2005. Thermal infrared observations of the Hayabusa spacecraft target asteroid 25143 Itokawa. Astronomy and Astrophysics 443, 347–355.

O'Rourke, L., Müller, T.G., Valtchanov, I., Altieri, B., Gonzlez-Garcia, B., Bhattacharya, B., Carry, B., 2012. Thermal shape properties of asteroid (21) Lutetia from Herschel observations around the Rosetta Flyby. Planetary and Space Science 66, 192–199.

Ostro, S.J., 1989. Radar observations of asteroids. In: Asteroids II, pp. 192–212.

Ostro, S.J., Benner, L.A.M., Magri, C., Giorgini, J.D., Rose, R., Jurgens, R.F., Yeomans, D.K., Hine, A.A., Nolan, M.C., Scheeres, D.J., Broschart, S.B., Kaasalainen, M., Margot, J., 2005. Radar observations of Itokawa in 2004 and improved shape estimation. Meteoritics and Planetary Science 40, 1563–1574.

Ostro, S.J., Hudson, R.S., Benner, L.A.M., Giorgini, J.D., Magri, C., Margot, J.L., Nolan, M.C., 2002. Asteroid radar astronomy. In: Asteroids III, pp. 151–168.

Ostro, S.J., Margot, J.L., Benner, L.A.M., Giorgini, J.D., Scheeres, D.J., Fahnestock, E.G., Broschart, S.B., Bellerose, J., Nolan, M.C., Magri, C., Pravec, P., Scheirich, P., Rose, R., Jurgens, R.F., 2006. De Jong, 2006. Radar imaging of binary near-earth asteroid (66391) 1999 KW4. Science 314, 1276–1280.

Parker, J.W., McFadden, L.A., Russell, C.T., Stern, S.A., Sykes, M.V., Thomas, P.C., Young, E.F., 2006. Ceres: High-resolution imaging with HST and the determination of physical properties. Advances in Space Research 38, 2039–2042.

Parker, J.W., Stern, S.A., Thomas, P.C., Festou, M.C., Merline, W.J., Young, E.F., Binzel, R.P., Lebofsky, L.A., 2002. Analysis of the first disk-resolved images of Ceres from ultraviolet observations with the Hubble Space Telescope. The Astronomical Journal 123, 549–557.

Pravec, P., Harris, A.W., 2007. Binary asteroid population. 1. Angular momentum content. Icarus 190, 250–259.

Preusker, F., Scholten, F., Knollenberg, J., Khrt, E., Matz, K.D., Mottola, S., Roatsch, T., Thomas, N., 2012. The northern hemisphere of asteroid 21 Lutetia topography and orthoimages from Rosetta OSIRIS NAC image data. Planetary and Space Science 66, 54–63.

Roques, F., Boissel, Y., Doressoundiram, A., Sicardy, B., Widemann, T., 2009. Exploration of the outer solar system by stellar occultations. Earth Moon and Planets 105, 201–208.

Ryan, E.L., Woodward, C.E., 2010. Rectified asteroid albedos and diameters from IRAS and MSX photometry catalogs. Astronomical Journal 140, 933–943. 1006.4362.

Saint-Pé, O., Combes, M., Rigaut, F., 1993a. Ceres surface properties by high-resolution imaging from earth. Icarus 105, 271–281.

Saint-Pé, O., Combes, M., Rigaut, F., Tomasko, M., Fulchignoni, M., 1993b. Demonstration of adaptive optics for resolved imagery of solar system objects—preliminary results on Pallas and Titan. Icarus 105, 263–270.

Schmidt, B.E., Thomas, P.C., Bauer, J.M., Li, J., McFadden, L.A., Mutchler, M.J., Radcliffe, S.C., Rivkin, A.S., Russell, C.T., Parker, J.W., Stern, S.A., 2009. The shape and surface variation of 2 Pallas from the Hubble Space Telescope. Science 326, 275–278.

Sicardy, B., Widemann, T., Lellouch, E., Veillet, C., Cuillandre, J., Colas, F., Roques, F., Beisker, W., Kretlow, M., Lagrange, A., Gendron, E., Lacombe, F., Lecacheux, J., Birnbaum, C., Fienga, A., Leyrat, C., Maury, A., Raynaud, E., Renner, S., Schultheis, M., Brooks, K., Delsanti, A., Hainaut, O.R., Gilmozzi, R., Lidman, C., Spyromilio, J., Rapaport, M., Rosenzweig, P., Naranjo, O., Porras, L., Díaz, F., Calderón, H., Carrillo, S., Carvajal, A., Recalde, E., Cavero, L.G., Montalvo, C., Barría, D., Campos, R., Duffard, R., Levato, H., 2003. Large changes in Pluto's atmosphere as revealed by recent stellar occultations. Nature 424, 168–170.

Sierks, H., Lamy, P., Barbieri, C., Koschny, D., Rickman, H., Rodrigo, R., A'Hearn, M.F., Angrilli, F., Barucci, A., Bertaux, J.L., Bertini, I., Besse, S., Carry, B., Cremonese, G., Da Deppo, V., Davidsson, B., Debei, S., De Cecco, M., De Leon, J., Ferri, F., Fornasier, S., Fulle, M., Hviid, S.F., Gaskell, G.W., Groussin, O., Gutierrez, P.J., Jorda, L., Kaasalainen, M., Keller, H.U., Knollenberg, J., Kramm, J.R., Kührt, E., Küppers, M., Lara, L.M., Lazzarin, M., Leyrat, C., Lopez Moreno, J.L., Magrin, S., Marchi, S., Marzari, F., Massironi, M., Michalik, H., Moissl, R., Naletto, G., Preusker, F., Sabau, L., Sabolo, W., Scholten, F., Snodgrass, C., Thomas, N., Tubiana, C., Vernazza, P., Vincent, J.B., Wenzel, K.P., Andert, T., Pätzold, M., Weiss, B.P., 2011. Images of asteroid (21) Lutetia: a remnant planetesimal from the early Solar System. Science 334, 487–490.

Slivan, S.M., Binzel, R.P., Crespo da Silva, L.D., Kaasalainen, M., Lyndaker, M.M., Krčo, M., 2003. Spin vectors in the Koronis family: comprehensive results from two independent analyses of 213 rotation lightcurves. Icarus 162, 285–307.

Tanga, P., Delbo, M., 2007. Asteroid occultations today and tomorrow: toward the GAIA era. Astronomy and Astrophysics 474, 1015–1022.

Tanga, P., Hestroffer, D., Berthier, J., Cellino, A., Lattanzi, M.G., di Martino, M., Zappalá, V., 2001. HST/FGS observations of the asteroid (216) Kleopatra. Icarus 153, 451–454.

Tanga, P., Hestroffer, D., Cellino, A., 2003. Asteroid observations with the hubble space telescope. II. Duplicity search and size measurements for 6 asteroids. Astronomy and Astrophysics 401, 733–741.

Tedesco, E.F., Noah, P.V., Noah, M.C., Price, S.D., 2002. The supplemental IRAS minor planet survey. Astronomical Journal 123, 1056–1085.

Thomas, N., Barbieri, C., Keller, H.U., Lamy, P., Rickman, H., Rodrigo, R., Sierks, H., Wenzel, K.P., Cremonese, G., Jorda, L., Marzari, F., Massironi, M., Preusker, F., Scholten, F., Stephan, K., Barucci, A., Besse, S., Fornasier, S., Groussin, O., Hviid, S.F., Koschny, D., Kührt, E., Küppers, M., Marchi, S., Martelleto, E., Moissl, R., Snodgrass, C., Tubiana, C., Vincent, J.B., 2012. The geomorphology of 21

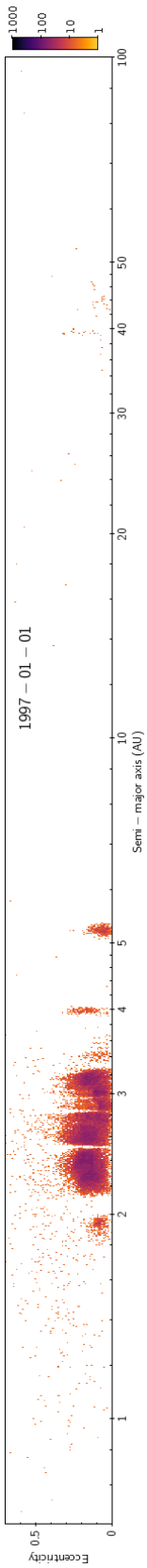

Lutetia: Results from the OSIRIS imaging system onboard ESAs Rosetta spacecraft. Planetary and Space Science 66, 96–124.
Thomas, P.C., Binzel, R.P., Gaffey, M.J., Storrs, A.D., Wells, E.N., Zellner, B.H., 1997a. Impact excavation on asteroid 4 Vesta: Hubble Space Telescope results. Science 277, 1492–1495.
Thomas, P.C., Binzel, R.P., Gaffey, M.J., Zellner, B.H., Storrs, A.D., Wells, E.N., 1997b. Vesta: spin pole, size, and shape from HST images. Icarus 128, 88–94.
Thomas, P.C., Parker, J.W., McFadden, L.A., Russell, C.T., Stern, S.A., Sykes, M.V., Young, E.F., 2005. Differentiation of the asteroid Ceres as revealed by its shape. Nature 437, 224–226.
Torppa, J., Kaasalainen, M., Michalowski, T., Kwiatkowski, T., Kryszczyńska, A., Denchev, P., Kowalski, R., 2003. Shapes and rotational properties of thirty asteroids from photometric data. Icarus 164, 346–383.
Veverka, J., Thomas, P.C., Harch, A., Clark, B.E., Bell, J.F., Carcich, B., Joseph, J., Chapman, C.R., Merline, W.J., Robinson, M.S., Malin, M., McFadden, L.A., Murchie, S.L., Hawkins, S.E., Faquhar, R., Izenberg, N., Cheng, A.F., 1997. NEARs Flyby of 253 Mathilde: images of a C asteroid. Science 278, 2109–2114.
Vincent, J.B., Besse, S., Marchi, S., Sierks, H., Massironi, M., the OSIRIS Team., 2012. Physical properties of craters on asteroid (21) Lutetia. Planetary and Space Science 66, 79–86.
Walsh, K.J., Richardson, D.C., Michel, P., 2008. Rotational breakup as the origin of small binary asteroids. Nature 454, 188–191.
Warner, B.D., Harris, A.W., Pravec, P., 2009. The asteroid lightcurve database. Icarus 202, 134–146.

A&A 604, A64 (2017)
DOI: 10.1051/0004-6361/201731021

Astronomy & Astrophysics

3D shape of asteroid (6) Hebe from VLT/SPHERE imaging: Implications for the origin of ordinary H chondrites⋆

M. Marsset[1], B. Carry[2,3], C. Dumas[4], J. Hanuš[5], M. Viikinkoski[6], P. Vernazza[7], T. G. Müller[8], M. Delbo[2], E. Jehin[9], M. Gillon[9], J. Grice[2,10], B. Yang[11], T. Fusco[7,12], J. Berthier[3], S. Sonnett[13], F. Kugel[14], J. Caron[14], and R. Behrend[14]

[1] Astrophysics Research Centre, Queen's University Belfast, BT7 1NN, UK
e-mail: michael.marsset@qub.ac.uk
[2] Université Côte d'Azur, Observatoire de la Côte d'Azur, 06304 Lagrange, CNRS, France
[3] IMCCE, Observatoire de Paris, PSL Research University, CNRS, Sorbonne Universités, UPMC Univ Paris 06, Univ. Lille, France
[4] TMT Observatory, 100 W. Walnut Street, Suite 300, Pasadena, CA 91124, USA
[5] Astronomical Institute, Faculty of Mathematics and Physics, Charles University, V Holešovičkách 2, 18000 Prague, Czech Republic
[6] Department of Mathematics, Tampere University of Technology, PO Box 553, 33101 Tampere, Finland
[7] Aix Marseille Univ, CNRS, LAM, Laboratoire d'Astrophysique de Marseille, 13013 Marseille, France
[8] Max-Planck-Institut für extraterrestrische Physik, Giessenbachstrasse, 85748 Garching, Germany
[9] Space sciences, Technologies and Astrophysics Research Institute, Université de Liège, Allée du 6 Août 17, 4000 Liège, Belgium
[10] Open University, School of Physical Sciences, The Open University, MK7 6AA, UK
[11] European Southern Observatory (ESO), Alonso de Córdova 3107, 1900 Casilla Vitacura, Santiago, Chile
[12] ONERA – the French Aerospace Lab, 92322 Châtillon, France
[13] Planetary Science Institute, 1700 East Fort Lowell, Suite 106, Tucson, AZ 85719, USA
[14] CdR & CdL Group: Lightcurves of Minor Planets and Variable Stars, Observatoire de Genève, 1290 Sauverny, Switzerland

Received 22 April 2017 / Accepted 19 May 2017

ABSTRACT

Context. The high-angular-resolution capability of the new-generation ground-based adaptive-optics camera SPHERE at ESO VLT allows us to assess, for the very first time, the cratering record of medium-sized (D ~ 100–200 km) asteroids from the ground, opening the prospect of a new era of investigation of the asteroid belt's collisional history.
Aims. We investigate here the collisional history of asteroid (6) Hebe and challenge the idea that Hebe may be the parent body of ordinary H chondrites, the most common type of meteorites found on Earth (~34% of the falls).
Methods. We observed Hebe with SPHERE as part of the science verification of the instrument. Combined with earlier adaptive-optics images and optical light curves, we model the spin and three-dimensional (3D) shape of Hebe and check the consistency of the derived model against available stellar occultations and thermal measurements.
Results. Our 3D shape model fits the images with sub-pixel residuals and the light curves to 0.02 mag. The rotation period (7.274 47 h), spin (ECJ2000 λ, β of 343°, +47°), and volume-equivalent diameter (193 ± 6 km) are consistent with previous determinations and thermophysical modeling. Hebe's inferred density is 3.48 ± 0.64 g cm^{-3}, in agreement with an intact interior based on its H-chondrite composition. Using the 3D shape model to derive the volume of the largest depression (likely impact crater), it appears that the latter is significantly smaller than the total volume of close-by S-type H-chondrite-like asteroid families.
Conclusions. Our results imply that (6) Hebe is not the most likely source of H chondrites. Over the coming years, our team will collect similar high-precision shape measurements with VLT/SPHERE for ~40 asteroids covering the main compositional classes, thus providing an unprecedented dataset to investigate the origin and collisional evolution of the asteroid belt.

Key words. minor planets, asteroids: individual: (6) Hebe – meteorites, meteors, meteoroids – techniques: high angular resolution

1. Introduction

Disk-resolved imaging is a powerful tool to investigate the origin and collisional history of asteroids. This has been remarkably illustrated by fly-by and rendezvous space missions (Belton et al. 1992, 1996; Zuber et al. 2000; Fujiwara et al. 2006; Sierks et al. 2011; Russell et al. 2012, 2016), as well as observations from the Earth (e.g., Carry et al. 2008, 2010b; Merline et al. 2013). In the late nineties, observations of (4) Vesta with the *Hubble* Space Telescope (HST) led to the discovery of the now-called "Rheasilvia basin" and allowed for establishment of the origin of the Vestoids and HED meteorites found on Earth (Thomas et al. 1997; Binzel et al. 1997). Specifically, it was demonstrated that the basin-forming event on Vesta excavated enough material to account for the family of small asteroids with spectral properties similar to Vesta. HST observations thus confirmed the origin of these bodies as fragments from Vesta, as previously suspected based on spectroscopic measurements (Binzel & Xu 1993). Recently, the Rheasilvia basin was revealed in much greater detail by the Dawn mission, which unveiled two overlapping giant impact features (Schenk et al. 2012).

In the 2000's, a new generation of ground-based imagers with high-angular-resolution capability, such as NIRC2 (Wizinowich et al. 2000; van Dam et al. 2004) on

⋆ Based on observations made with ESO Telescopes at the La Silla Paranal Observatory under programme ID 60.A-9379 and 086.C-0785.

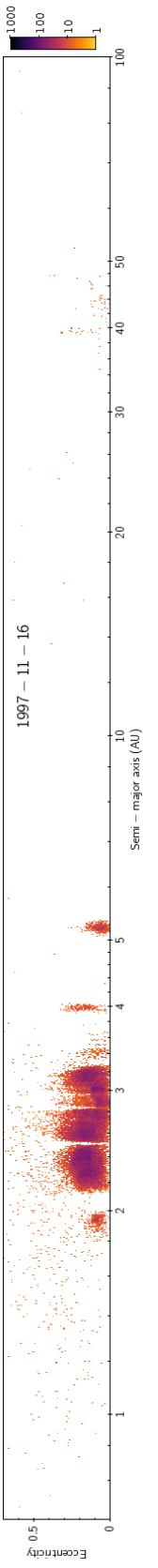

the W. M. Keck II telescope and NACO (Lenzen et al. 2003; Rousset et al. 2003) on the European Southern Observatory (ESO) Very Large Telescope (VLT), made disk-resolved imaging achievable from the ground for a larger number of medium-sized (~100–200-km in diameter) asteroids. In turn, these observations triggered the development of methods for modeling the tridimensional shape of these objects by combining the images with optical light curves (see, e.g., Carry et al. 2010a, 2012; Kaasalainen et al. 2011; Viikinkoski et al. 2015a). These models were subsequently validated by in-situ measurements performed by the ESA Rosetta mission during the fly-by of asteroid (21) Lutetia (Sierks et al. 2011; Carry et al. 2010b, 2012; O'Rourke et al. 2012).

More recently, the newly commissioned VLT/SpectroPolarimetric High-contrast Exoplanet Research instrument (SPHERE) and its very high performance adaptive optics system (Beuzit et al. 2008) demonstrated its ability to reveal in even greater detail the surface of medium-sized asteroids by resolving their largest (D > 30 km) craters (Viikinkoski et al. 2015b; Hanuš et al. 2017). This remarkable achievement opens the prospect of a new era of exploration of the asteroid belt and its collisional history.

Here, we use VLT/SPHERE to investigate the shape and topography of asteroid (6) Hebe, a large main-belt asteroid (D ~ 180–200 km; e.g., Tedesco et al. 2004; Masiero et al. 2011) that has long received particular attention from the community of asteroid spectroscopists, meteoricists, and dynamicists. Indeed, Hebe's spectral properties and close proximity to orbital resonances in the asteroid belt make it a possible main source of ordinary H chondrites (i.e., ~34% of the meteorite falls, Hutchison 2004; Farinella et al. 1993; Migliorini et al. 1997; Gaffey & Gilbert 1998; Bottke et al. 2010). It was further proposed that Hebe could be the parent body of an ancient asteroid family (Gaffey & Fieber-Beyer 2013). The idea of H chondrites mainly originating from Hebe, however, was recently weakened by the discovery of a large number of asteroids (including several asteroid families) with similar spectral properties (hence composition, Vernazza et al. 2014). Here, we challenge this hypothesis by studying the three-dimensional shape and topography of Hebe derived from disk-resolved observations. We observed Hebe throughout its rotation in order to derive its shape, and to characterize the largest craters at its surface. When combined with previous adaptive-optics (AO) images and light curves (both from the literature and from recent optical observations by our team), these new observations allow us to derive a reliable shape model and an estimate of Hebe's density based on its astrometric mass (i.e., the mass derived from the study of planetary ephemeris and orbital deflections). Finally, we analyse Hebe's topography by means of an elevation map and discuss the implications for the origin of H chondrites.

2. Observations and data pre-processing

We observed (6) Hebe close to its opposition date while it was orientated "equator-on" (from its spin solution derived below), that is, with an ideal viewing geometry exposing its whole surface as it rotated. Observations were acquired at four different epochs between December 8–12, 2014, such that the variation of the sub-Earth point longitude was 90 ± 30° between each epoch.

Observations were performed with the recently commissioned second-generation SPHERE instrument, mounted at the ESO VLT (Fusco et al. 2006; Beuzit et al. 2008), during the science verification of the instrument[1]. We used IRDIS broad-band classical imaging in Y (filter central wavelength = 1.043 μm, width = 0.140 μm) in the pupil-tracking mode, where the pupil remains fixed while the field orientation varies during the observations, to achieve the best point-spread function (PSF) stability. Each observational sequence consisted in a series of ten images with 2 s exposure time during which Hebe was used as a natural guide star for AO corrections. Observations were performed under average seeing conditions (0.9–1.1″) and clear sky transparency, at an airmass of ~1.1.

Sky backgrounds were acquired along our observations for data-reduction purposes. At the end of each sequence, we observed the nearby star HD 26086 under the exact same AO configuration as the asteroid to estimate the instrument PSF for deconvolution purposes. Finally, standard calibrations, which include detector flat-fields and darks, were acquired in the morning as part of the instrument calibration plan.

Data pre-processing of the IRDIS data made use of the preliminary release (v0.14.0-2) of the SPHERE data reduction and handling (DRH) software (Pavlov et al. 2008), as well as additional tools written in the interactive data language (IDL), in order to perform background subtraction, flat-fielding and bad-pixel correction. The pre-processed images were then aligned one with respect to the others using the IDL ML_SHIFTFINDER maximum likelihood function, and averaged to maximise the signal to noise ratio of the asteroid. Finally, the optimal angular resolution of each image (λ/D = 0.026″, corresponding to a projected distance of 22 km) was restored with Mistral, a myopic deconvolution algorithm optimised for images with sharp boundaries (Fusco et al. 2002; Mugnier et al. 2004), using the stellar PSF acquired on the same night as our asteroid data.

3. Additional data

3.1. Disk-resolved images

To reconstruct the 3D shape of (6) Hebe, we compiled available images obtained with the earlier-generation AO instruments NIRC2 (Wizinowich et al. 2000; van Dam et al. 2004) on the W. M. Keck II telescope and NACO (Lenzen et al. 2003; Rousset et al. 2003) on the ESO VLT. Each of these images, as well as the corresponding calibration files and stellar PSF, were retrieved from the Canadian Astronomy Data Center[2] (Gwyn et al. 2012) or directly from the observatory's database. Data processing and Mistral deconvolution of these images were performed following the same method as for our SPHERE images. Only a subset of the 25 different epochs listed in Table 1 had been published (Hanuš et al. 2013).

3.2. Optical light curves

We used 38 light curves obtained in the years 1953–1993 and available in the Database of Asteroid Models from Inversion Techniques (DAMIT[3], Durech et al. 2010) that were used by Torppa et al. (2003) to derive the pole orientation and convex shape of (6) Hebe from light curve inversion (Kaasalainen & Torppa 2001; Kaasalainen 2001). We also retrieved 16 light curves observed by the amateurs F. Kugel

[1] Observations obtained under ESO programme ID 60.A-9379 (P.I. C. Dumas).
[2] http://www.cadc-ccda.hia-iha.nrc-cnrc.gc.ca/
[3] http://astro.troja.mff.cuni.cz/projects/asteroids3D

Table 1. Date, mid-observing time (UTC), heliocentric distance (Δ) and range to observer (r), phase angle (α), apparent size (Θ), longitude (λ) and latitude (β) of the subsolar and subobserver points (SSP, SEP).

	Date	UTC	Instrument	Δ (AU)	r (AU)	α (°)	Θ ($''$)	SEP_λ (°)	SEP_β (°)	SSP_λ (°)	SSP_β (°)
1	2002-05-07	14:08:54	Keck/NIRC2[1]	2.52	1.88	20.5	0.131	66.1	–34.4	53.3	–17.4
2	2002-05-08	13:55:01	Keck/NIRC2[1]	2.52	1.86	20.4	0.119	329.8	–34.5	317.2	–17.5
3	2002-09-27	06:29:51	Keck/NIRC2[2]	2.21	1.91	27.0	0.098	162.5	–19.4	187.2	–35.4
4	2007-12-15	14:15:39	Keck/NIRC2[3]	2.47	1.86	20.8	0.149	14.2	32.9	356.2	19.6
5	2007-12-15	14:30:31	Keck/NIRC2[3]	2.47	1.86	20.8	0.145	1.9	32.9	343.9	19.6
6	2007-12-15	14:44:49	Keck/NIRC2[3]	2.47	1.86	20.8	0.145	350.1	32.9	332.1	19.6
7	2007-12-15	15:00:54	Keck/NIRC2[3]	2.47	1.86	20.8	0.138	336.8	32.9	318.9	19.6
8	2007-12-15	15:27:39	Keck/NIRC2[3]	2.47	1.86	20.8	0.143	314.8	32.9	296.8	19.6
9	2007-12-15	16:26:58	Keck/NIRC2[3]	2.47	1.86	20.8	0.151	265.9	32.9	247.9	19.6
10	2009-06-07	10:52:24	Keck/NIRC2[2]	2.81	2.01	15.1	0.129	43.1	8.0	57.9	4.9
11	2010-06-28	13:08:00	Keck/NIRC2[4]	2.06	1.62	28.9	0.168	258.8	–39.3	221.2	–39.0
12	2010-08-26	12:47:10	Keck/NIRC2[3]	1.98	1.05	16.1	0.260	48.5	–27.4	30.6	–31.2
13	2010-08-26	13:04:26	Keck/NIRC2[3]	1.98	1.05	16.1	0.260	34.3	–27.4	16.3	–31.2
14	2010-08-26	13:59:47	Keck/NIRC2[3]	1.98	1.05	16.1	0.265	348.6	–27.4	330.7	–31.2
15	2010-08-26	14:38:00	Keck/NIRC2[3]	1.98	1.05	16.1	0.270	317.1	–27.4	299.2	–31.2
16	2010-11-29	07:10:28	Keck/NIRC2[4]	1.94	1.39	28.9	0.189	160.9	–22.9	191.5	–18.5
17	2010-12-13	01:18:16	VLT/NACO[5]	1.94	1.52	30.0	0.153	28.9	–23.2	59.6	–15.3
18	2010-12-13	02:40:24	VLT/NACO[5]	1.94	1.53	30.0	0.171	321.1	–23.2	351.8	–15.3
19	2010-12-14	00:41:59	VLT/NACO[5]	1.94	1.53	30.0	0.171	311.5	–23.2	342.2	–15.1
20	2010-12-14	01:38:22	VLT/NACO[5]	1.94	1.54	30.0	0.158	265.0	–23.2	295.7	–15.1
21	2010-12-14	02:14:10	VLT/NACO[5]	1.94	1.54	30.0	0.167	235.5	–23.2	266.2	–15.0
22	2014-12-08	00:53:28	VLT/SPHERE[6]	2.03	1.15	17.0	0.216	208.7	3.4	225.7	2.8
23	2014-12-09	01:04:54	VLT/SPHERE[6]	2.03	1.16	17.2	0.211	91.6	3.2	108.9	3.0
24	2014-12-10	01:59:38	VLT/SPHERE[6]	2.03	1.17	17.5	0.221	298.8	3.0	316.4	3.2
25	2014-12-12	04:14:08	VLT/SPHERE[6]	2.04	1.18	18.1	0.221	332.6	2.6	350.7	3.7

Notes. PIs of these observations were [(1)] J.-L. Margot; [(2)] W. J. Merline; [(3)] W. M. Keck engineering team; [(4)] F. Marchis; [(5)] B. Carry; and [(6)] C. Dumas.

and J. Caron, from the *Courbe de Rotation group*[4], and 84 light curves from the data archive of the SuperWASP survey (Pollacco et al. 2006) for the period 2006–2009. This survey aims at finding and characterizing exoplanets by observation of their transit in front of their host star. Its large field of view and cadence provides a goldmine for asteroid light curves (Grice et al. 2017). Finally, four light curves were acquired by our group during April 2016 with the 60 cm TRAPPIST telescope (Jehin et al. 2011).

3.3. Stellar occultations

We retrieved the five stellar occultations listed by Dunham et al. (2016) and publicly available on the Planetary Data System (PDS)[5] for (6) Hebe. We convert the disappearance and reappearance timings of the occulted stars into segments (called chords) on the plane of the sky, using the location of the observers on Earth and the apparent motion of Hebe following the recipes by Berthier (1999). Of the five events, only two had more than one positive chord (that is a recorded blink event) and could be used to constrain the 3D shape (1977-03-05 – also presented in Taylor & Dunham 1978 – and 2008-02-20).

[4] http://obswww.unige.ch/~behrend/page_cou.html
[5] http://sbn.psi.edu/pds/resource/occ.html

3.4. Mid-infrared thermal measurements

Finally, we compiled available mid-infrared thermal measurements to 1) validate, independently of the AO images, the size of our 3D-shape model and; 2) derive the thermal properties of the surface of Hebe through thermophysical modeling of the infrared flux. Specifically, we used a total of 103 thermal data points from IRAS (12, 25, 60, 100 μm, Tedesco et al. 2002), AKARI-IRC (9, 18 μm, Usui et al. 2011), ISO-ISOPHOT (25 μm, Lagerros et al. 1999), and *Herschel*-PACS (70, 100, 160 μm, Müller et al., in prep.).

4. 3D shape, volume, and density

Recent algorithms such as KOALA (Carry et al. 2010a, 2012; Kaasalainen et al. 2011) and ADAM (Viikinkoski et al. 2015a) allow simultaneous derivation of the spin, 3D shape, and size of an asteroid (see, e.g., Merline et al. 2013; Tanga et al. 2015; Viikinkoski et al. 2015b; Hanuš et al. 2017). This combined multi-data approach has been validated by comparing the 3D shape model of (21) Lutetia by Carry et al. (2010b) with the images returned by the ESA Rosetta mission during its fly-by of the asteroid (see Sierks et al. 2011; Carry et al. 2012).

Here, we reconstruct the spin and shape of (6) Hebe with ADAM, which iteratively improves the solution by minimizing the residuals between the Fourier transformed images and a projected polyhedral model. This method allows the use of AO images directly without requiring the extraction of boundary contours. Boundary contours are therefore used here only as a means

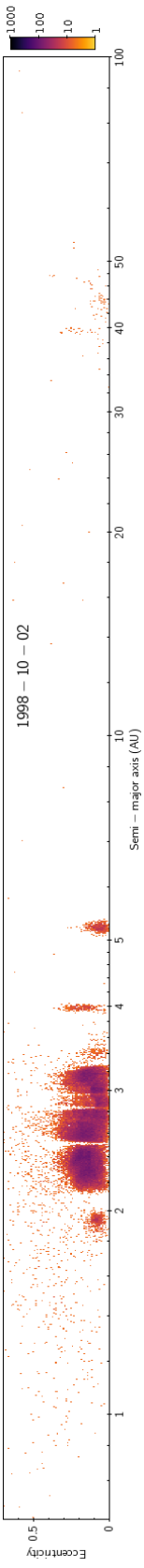

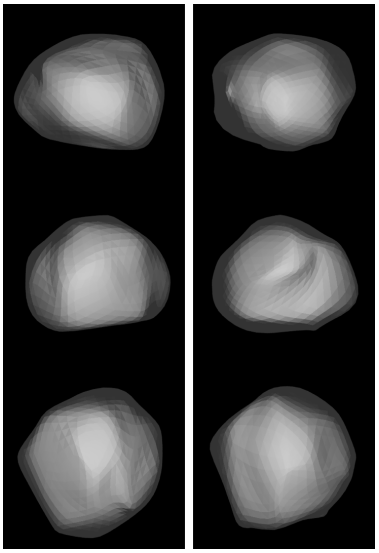

Fig. 1. 3D-shape model of (6) Hebe reconstructed from light curves and all resolved images (*left*), and from light curves and SPHERE images only (*right*). Viewing directions are two equator-on views rotated by 90° and a pole-on view.

to measure the pixel root mean square (RMS) residuals between the location of the asteroid silhouette on the observed and modeled images. ADAM offers two different shape supports: subdivision surfaces and octanoids based on spherical harmonics. Here, we use the subdivision surfaces parametrisation which offers more local control on the model than global representations (see Viikinkoski et al. 2015a).

Two different models depicted in Fig. 1 were obtained; the first one using the light curves combined to the full AO sample, and the second one using the light curves and the SPHERE images only. Comparison of the SPHERE-based model with our SPHERE images, earlier AO images, subsets of optical light curves and stellar occultations are presented in Figs. 2–5, respectively.

The two models nicely fit all data, the RMS residuals between the observations and the predictions by the model being only 0.6 pixels for the location of the asteroid contours, 0.02 mag for the light curves, and 5 km for the stellar occultation of 2008 (the occultation of 1977 has very large uncertainties on its timings). The 3D shape models are close to an oblate spheroid, and have a volume-equivalent diameter of 196 ± 6 km (all AO) and 193 ± 6 km (SPHERE-based; Table 2). Spin-vector coordinates (λ, β in ECJ2000) are close to earlier estimates based on light-curve inversion ((339°, +45°), Torppa et al. 2003) and on a combination of light curves and AO images ((345°, +42°), Hanuš et al. 2013).

The main difference between the two shape models comes from the presence of some surface features in the SPHERE-based model that are lacking in the model obtained using the full dataset of AO images. This is due to the lower resolution of earlier AO images that do not address some of the small-scale surface features revealed by the SPHERE images.

There are 12 diameter estimates for Hebe in the literature (Table A.1, Fig. A.1). Rejecting values that do not fall within

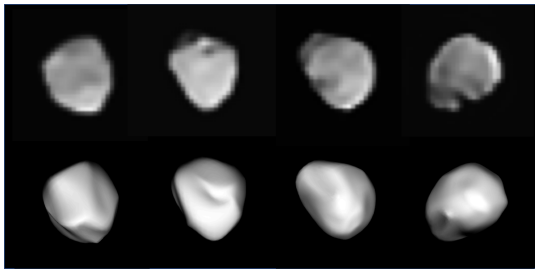

Fig. 2. Deconvolved SPHERE images of Hebe obtained between 8 and 12 December 2014 (top) and corresponding projection of the model (bottom). Orientation of the four images with respect to the north is 15.2°, 12.8°, –5.3° and –89.6° , respectively.

Table 2. Period, spin (ECJ2000 longitude λ, latitude β and initial Julian date T_0), and dimensions (volume-equivalent diameter D, volume V, and tri-axial ellipsoid diameters a, b, c along principal axes of inertia) of Hebe derived with ADAM.

Parameter	Value (all AO)	Value (SPHERE-only)	Unc.	Unit
Period	7.274467	7.274465	5×10^{-5}	hour
λ	341.7	343.2	3	deg.
β	+49.9	+46.8	4	deg.
T_0	2434569.00	2434569.00		
D	196	193	6	km
V	3.95×10^6	3.75×10^6	1.2×10^5	km^3
a	218.4	213.4	6.0	km
b	206.2	200.2	6.0	km
c	172.1	172.6	6.0	km
a/b	1.06	1.07	0.04	
b/c	1.20	1.16	0.05	

one standard deviation of the average value of the full dataset gives an average equivalent-volume sphere diameter of 191.5 ± 8.3 km, in very good agreement with the values of 193±6 km and 196 ± 6 km derived here (also supported by the thermophysical analysis presented in the following section). In the following, we use the value of the diameter obtained from our SPHERE-based model, which is more precise due to the higher angular resolution of the SPHERE images with respect to the NIRC2 and NACO images. A main advantage of using a diameter obtained from a full 3D shape modeling resides in the uncertainty on the derived volume V, which is close to $\delta V/V \approx \delta D/D$, as opposed to a $\delta V/V \approx 3\delta D/D$ in the spherical assumption used in most aforementioned estimates (see Kaasalainen & Viikinkoski 2012 for details).

Combining this diameter with an average mass of 1.31 ± 0.24×10^{19} kg computed from 16 estimates gathered from the literature (Table A.2, Fig. A.2), provides a bulk density of 3.48 ± 0.64 g cm^{-3}, in perfect agreement with the average grain density of ordinary H chondrites (3.42±0.18 g cm^{-3}; Consolmagno et al. 2008). The derived density therefore suggests a null internal porosity, consistent with an intact internal structure. Hebe hence appears to reside in the volumetric and structural transitional region between the compact and gravity-shaped dwarf planets, and the medium-sized asteroids (~10–100 km in diameter) with fractured interior (Carry 2012; Scheeres et al. 2015). However,

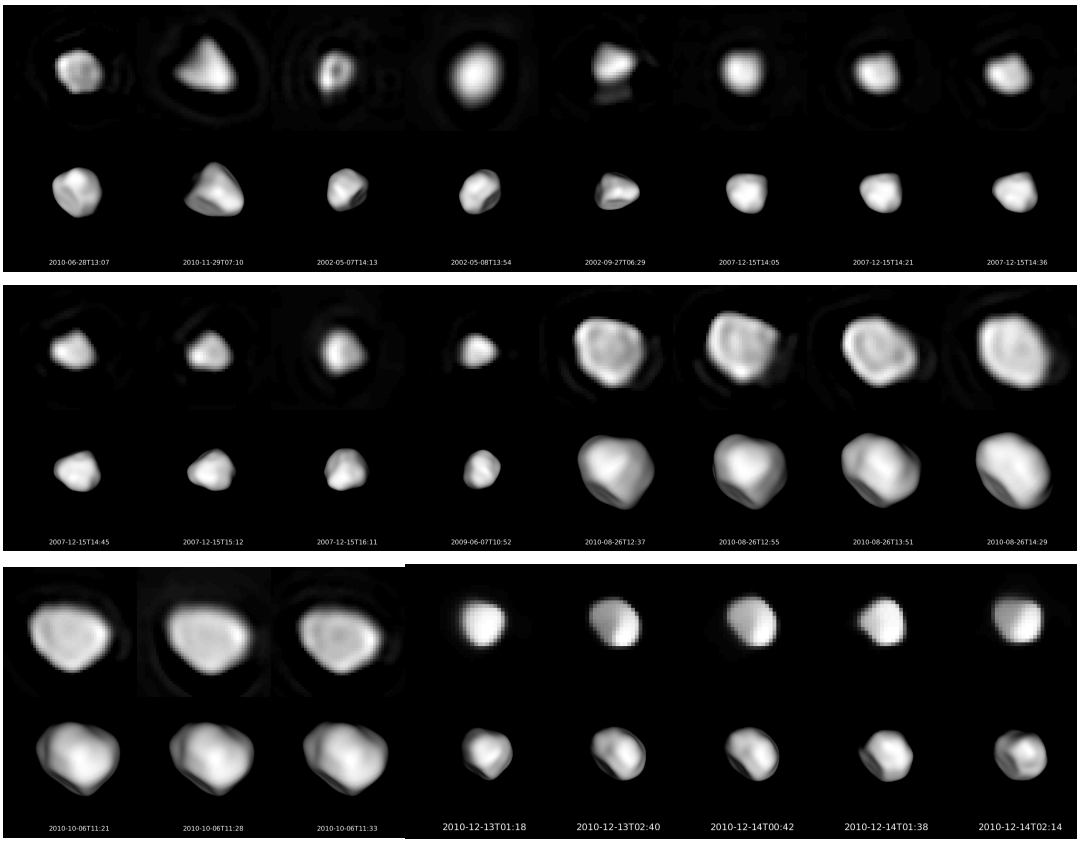

Fig. 3. Previous AO images of Hebe obtained with Keck/NIRC2 and VLT/NACO (*top of the three rows*) and corresponding projection of the model (*bottom*). Each image is $0.8'' \times 0.8''$ in size.

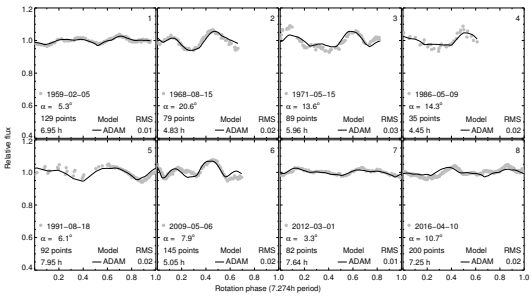

Fig. 4. Comparison of the synthetic light curves (solid line) from the shape model with a selection of light curves (gray points).

due to the current large mass uncertainty that dominates the uncertainty of the bulk density, the possibility of higher internal porosity cannot be ruled out. We expect the *Gaia* mission to trigger higher-precision mass estimates in the near future (Mignard et al. 2007; Mouret et al. 2007) that will help refine the density measurement of Hebe.

5. Thermal parameters and regolith grain size

A thermophysical model (TPM; Müller & Lagerros 1998; Müller et al. 1999) was also used to provide an independent size measurement for Hebe and to derive its thermal surface properties. The TPM uses as input our 3D shape model with unscaled diameter. The procedure is described in detail in Appendix B.

Using absolute magnitude $H = 5.71$ and magnitude slope $G = 0.27$ from the Asteroid Photometric Catalogue (Lagerkvist & Magnusson 2011), the TPM provides a solution for diameter and albedo of $(D, p_v) = (198^{+4}_{-2}\,\mathrm{km}, 0.24 \pm 0.01)$, in good agreement with the size of our 3D-shape model and previous albedo measurements from IRAS ($p_v = 0.27 \pm 0.01$; Tedesco et al. 2002), WISE ($p_v = 0.24 \pm 0.04$; Masiero et al. 2014) and AKARI ($p_v = 0.24 \pm 0.01$; Usui et al. 2011). Best-fitting solutions are found for significant surface roughness (in agreement with Lagerros et al. 1999), and thermal inertia Γ values ranging from 15 to 90 $\mathrm{J\,m^{-2}\,s^{-0.5}\,K^{-1}}$, with a preference for $\Gamma \approx 50\ \mathrm{J\,m^{-2}\,s^{-0.5}\,K^{-1}}$. Interestingly, we note that the best-fitting solution for Γ drops from $\sim$60 $\mathrm{J\,m^{-2}\,s^{-0.5}\,K^{-1}}$ when only considering thermal measurements acquired at $r < 2.1$ AU, to $\sim$40 $\mathrm{J\,m^{-2}\,s^{-0.5}\,K^{-1}}$ for data taken at $r > 2.6$ AU. While this might be indicative of changing thermal inertia with

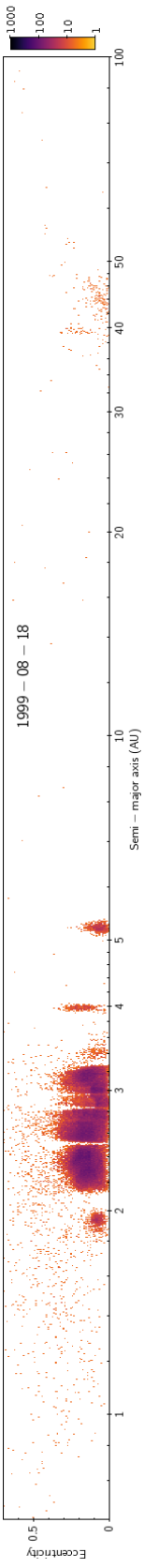

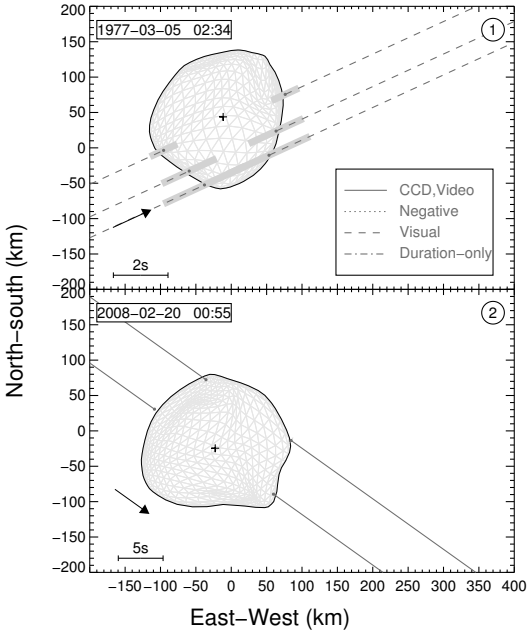

Fig. 5. Comparison of the shape model with the chords from the occultation of 1977 and 2008.

temperature, this result should be taken with extreme caution, as the TPM probably overfits the data due to the large error bars on the thermal measurements (see Appendix B).

From the thermal inertia value derived here, one can further derive the grain size of the surface regolith of Hebe (Gundlach & Blum 2013). Assuming values of heat capacity and material density typical of H5 ordinary chondrites (Opeil et al. 2010) and estimated surface temperature of 230 K and 180 K at 1.94 and 2.87 AU respectively, we find that the typical grain size of Hebe is about 0.2–0.3 mm (see Annexe B for more details).

6. Topography

Hebe's topography was investigated by generating an elevation map of its surface with respect to a volume-equivalent ellipsoid best-fitting our 3D-shape model, following the method by Thomas (1999). This map shown in Figure 6 allows the identification of several low-topographic and concave regions possibly created by impacts (the two shape models depicted in Fig. 1 produce slightly different but consistent topographic maps). Specifically, five large depressions (numbered 1 to 5 on the elevation map) are found at the surface of Hebe, at (29°, 43°), (93°, –42°), (190°, 35°), (289°, –13°), and near the south pole. Estimated dimensions (diameter D and maximum depth below the average surface d) are D_1 = 92–105 km, d_1 = 13 km; D_2 = 85–117 km, d_2 = 12 km; D_3 = 68–83 km, d_3 = 11 km; D_4 = 75–127 km, d_4 = 18 km; and D_5 = 42–52 km, d_5 = 7 km, respectively.

Assuming that the volume of a crater relates approximately to the volume of ejecta produced by the impact – which is most likely very optimistic because 1) a significant fraction of impact crater volume comes from compression (Melosh 1989) and; 2) at least a fraction of the ejecta must have re-accumulated on the surface of the body (e.g., Marchi et al. 2015), one can further estimate the volume of a hypothetical family derived from an impact on Hebe. The largest depression on Hebe roughly accounts for a volume of 10^5 km^3, corresponding to a body with an equivalent diameter of ~58 km.

For comparison, the five known S-type families spectrally analogous to Hebe (therefore to H chondrites; Vernazza et al. 2014) and located close to the main-belt 3:1 and 5:2 mean-motion resonances, namely Agnia (located at semi-major axis a = 2.78 AU and eccentricity e = 0.09), Koronis (a = 2.87 AU, e = 0.05), Maria (a = 2.55 AU, e = 0.06), Massalia (a = 2.41 AU, e = 0.14) and Merxia (a = 2.75 AU, e = 0.13) encompass a total volume of respectively ~2.4×10^4 km^3, 5.6×10^5 km^3, 3.6×10^5 km^3, 5.7×10^4 km^3 and 1.8×10^4 km^3 when the larger member of each family is removed. Family membership was determined using Nesvorný (2015)'s hierarchical clustering method (HCM)-based classification[6] and rejecting possible interlopers that do not fit the "V-shape" criterion as defined in Nesvorný et al. (2015). The diameter of each asteroid identified as a family member was retrieved from the WISE/NEOWISE database (Masiero et al. 2011) when available, or estimated from its absolute H magnitude otherwise, assuming an albedo equal to that of the largest member of its family (respectively 0.152, 0.213, 0.282, 0.241 and 0.213 for (847) Agnia, (158) Koronis, (170) Maria, (20) Massalia and (808) Merxia; https://mp3c.oca.eu). We note that these values should be considered as lower limits as those families certainly include smaller members beyond the detection limit.

We therefore find that the volume of material corresponding to the largest depression on Hebe is of the order of some H-chondrite-like S-type families, and ~4–6 times smaller than the largest ones. Therefore, although we cannot firmly exclude Hebe as the main (or unique) source of H chondrites, it appears that such a hypothesis is not the most likely one. This is further strengthened by the following two arguments. First, it seems improbable that the volume excavated from Hebe's largest depression, which we find to be roughly 10 to 30 times smaller than the volume of the Rheasilvia basin on Vesta (Schenk et al. 2012), would contribute to ~34% of the meteorite falls, when HED meteorites only represent ~6% of the falls (Hutchison 2004). We note, however, that the low number of HED meteorites may also relate to the relatively old age (Schenk et al. 2012) of the Vesta family (Heck et al. 2017). Second, the current lack of observational evidence for a Hebe-derived family indicates that such a family, if it ever existed, must be very ancient and dispersed. Yet, there is growing evidence from laboratory experiments that the current meteorite flux must be dominated by fragments from recent asteroid breakups (Heck et al. 2017). In the case of H chondrites, this is well supported by their cosmic ray exposure ages (Marti & Graf 1992; Eugster et al. 2006). It therefore appears that a recent – yet to be identified – collision suffered by another H-chondrite-like asteroid is the most likely source of the vast majority of H chondrites.

7. Conclusion and outlook

We have reconstructed the spin and tridimensional shape of (6) Hebe from combined AO images and optical light curves, and checked the consistency of the derived model against available stellar occultations and thermal measurements. Whereas the irregular shape of Hebe suggests it was moulded by impacts, its density appears indicative of a compact interior. Hebe thus

[6] http://sbn.psi.edu/pds/resource/nesvornyfam.html

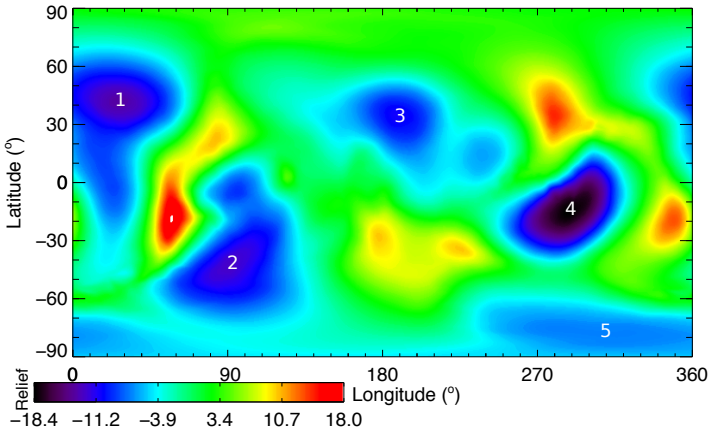

Fig. 6. Elevation map (in km) of (6) Hebe, with respect to a volume-equivalent ellipsoid best fitting our 3D-shape model. The five major depressions are identified by numbers.

seems to reside in the structural regime in transition between round-shaped dwarf planets shaped by gravity, and medium-sized asteroids with fractured interiors (i.e., significant fractions of macro-porosity; Carry 2012). This however needs to be confirmed by future mass measurements (e.g., from *Gaia* high-precision astrometric measurements) that will help improve the current mass uncertainty that dominates the uncertainty on density.

The high angular resolution of SPHERE further allowed us to identify several concave regions at the surface of Hebe possibly indicative of impact craters. We find the volume of the largest depression to be roughly five times smaller than the volume of the largest S-type H-chondrite-like families located close to orbital resonances in the asteroid belt. Furthermore, this volume is more than an order of magnitude smaller than the volume of the Rheasilvia basin on Vesta (Schenk et al. 2012) from which HED meteorites (∼6% of the falls) originate. Our results therefore imply that (6) Hebe is not the most likely source of ordinary H chondrites (∼34% of the falls).

Finally, this work has demonstrated the potential of SPHERE to bring important constraints on the origin and collisional history of the main asteroid belt. Over the next two years, our team will collect – via a large program on VLT/SPHERE (run ID: 199.C-0074, PI: Pierre Vernazza) – similar volume, shape, and topographic measurements for a significant number (∼40) of $D \geq 100$ km asteroids sampling the four major compositional classes (S, Ch/Cgh, B/C and P/D).

Acknowledgements. Based on observations made with ESO Telescopes at the La Silla Paranal Observatory under programme ID 60.A-9379. The asteroid diameters and albedos based on NEOWISE observations were obtained from the Planetary Data System (PDS). Some of the data presented herein were obtained at the W.M. Keck Observatory, which is operated as a scientific partnership among the California Institute of Technology, the University of California and the National Aeronautics and Space Administration. The Observatory was made possible by the generous financial support of the W.M. Keck Foundation. This research has made use of the Keck Observatory Archive (KOA), which is operated by the W. M. Keck Observatory and the NASA Exoplanet Science Institute (NExScI), under contract with the National Aeronautics and Space Administration. The authors wish to recognize and acknowledge the very significant cultural role and reverence that the summit of Mauna Kea has always had within the indigenous Hawaiian community. We are most fortunate to have the opportunity to conduct observations from this mountain. This research used the MP^{3}C service developed, maintained, and hosted at the Lagrange laboratory, Observatoire de la Côte d'Azur (Delbo et al. 2017). Photometry of 6 Hebe was identified and extracted from WASP data with the help of Neil Parley (Open University, now IEA Reading). The WASP project is currently funded and operated by Warwick University and Keele University, and was originally set up by Queen's University Belfast, the Universities of Keele, St. Andrews and Leicester, the Open University, the Isaac Newton Group, the Instituto de Astrofisica de Canarias, the South African Astronomical Observatory and by STFC. The WASP project is currently funded and operated by Warwick University and Keele University, and was originally set up by Queen's University Belfast, the Universities of Keele, St. Andrews and Leicester, the Open University, the Isaac Newton Group, the Instituto de Astrofisica de Canarias, the South African Astronomical Observatory and by STFC. TRAPPIST-South is a project funded by the Belgian Funds (National) de la Recherche Scientifique (F.R.S.-FNRS) under grant FRFC 2.5.594.09.F, with the participation of the Swiss National Science Foundation (FNS/SNSF). E.J. and M.G. are F.R.S.-FNRS research associates. Based on observations with ISO, an ESA project with instruments funded by ESA Member States and with the participation of ISAS and NASA. *Herschel* is an ESA space observatory with science instruments provided by European-led Principal Investigator consortia and with important participation from NASA. *Herschel* fluxes of Hebe where extracted by Csaba Kiss (Konkoly Observatory, Research Centre for Astronomy and Earth Sciences, Hungarian Academy of Sciences, H-1121 Budapest, Konkoly Thege Miklós út 15–17, Hungary). TM received funding from the European Union's Horizon 2020 Research and Innovation Programme, under Grant Agreement No. 687378.

References

Baer, J., & Chesley, S. R. 2008, Celest. Mech. Dyn. Astron., 100, 27
Baer, J., Chesley, S. R., & Matson, R. D. 2011, AJ, 141, 143
Belton, M. J. S., Veverka, J., Thomas, P., et al. 1992, Science, 257, 1647
Belton, M. J. S., Chapman, C. R., Klaasen, K. P., et al. 1996, Icarus, 120, 1
Berthier, J. 1999, Notes scientifiques et techniques du Bureau des longitudes, S064
Beuzit, J.-L., Feldt, M., Dohlen, K., et al. 2008, Ground-based and Airborne Instrumentation for Astronomy II, Proc. SPIE, 7014, 701418
Binzel, R. P., & Xu, S. 1993, Science, 260, 186
Binzel, R. P., Gaffey, M. J., Thomas, P. C., et al. 1997, Icarus, 128, 95
Bottke, W., Vokrouhlický, D., Nesvorný, D., & Shrbeny, L. 2010, BAAS, 42, 1051
Carry, B. 2012, Planet. Space Sci., 73, 98
Carry, B., Dumas, C., Fulchignoni, M., et al. 2008, A&A, 478, 235
Carry, B., Dumas, C., Kaasalainen, M., et al. 2010a, Icarus, 205, 460
Carry, B., Kaasalainen, M., Leyrat, C., et al. 2010b, A&A, 523, A94
Carry, B., Kaasalainen, M., Merline, W. J., et al. 2012, Planet. Space Sci., 66, 200
Consolmagno, G., Britt, D., & Macke, R. 2008, Chemie der Erde/Geochemistry, 68, 1

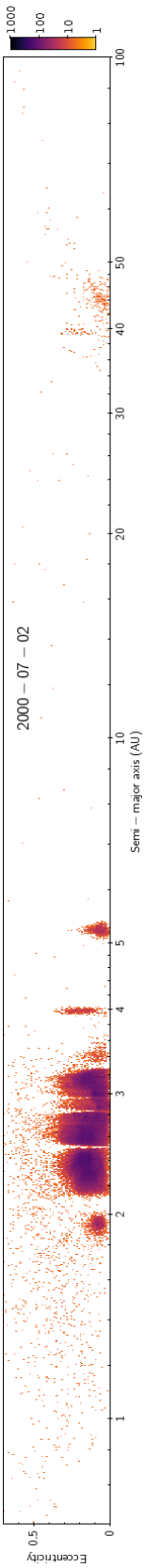

Delbo, M., Tanga, P., Carry, B., Ordenovic, C., & Bottein, P. 2017, The minor planet physical properties catalogue, Int. Conf. Asteroids, Comets, and Meteors: ACM 2017

Dunham, D. W., & Mallen, G. 1979, Rev. Mex. Astron. Astrofis., 4, 205

Dunham, D. W., Herald, D., Frappa, E., et al. 2016, NASA Planetary Data System, 243

Durech, J., Sidorin, V., & Kaasalainen, M. 2010, A&A, 513, A46

Durech, J., Kaasalainen, M., Herald, D., et al. 2011, Icarus, 214, 652

Eugster, O., Herzog, G. F., Marti, K., & Caffee, M. W. 2006, in Meteorites and the Early Solar System II (Tucson: University of Arizona Press), 829

Farinella, P., Gonczi, R., Froeschle, C., & Froeschlé, C. 1993, Icarus, 101, 174

Fienga, A., Laskar, J., Morley, T., et al. 2009, A&A, 507, 1675

Fienga, A., Laskar, J., Kuchynka, P., et al. 2011, Celest. Mech. Dyn. Astron., 111, 363

Fienga, A., Manche, H., Laskar, J., Gastineau, M., & Verma, A. 2013, ArXiv e-prints [arXiv:1301.1510]

Fienga, A., Manche, H., Laskar, J., Gastineau, M., & Verma, A. 2014, ArXiv e-prints [arXiv:1405.0484]

Folkner, W. M., Williams, J. G., & Boggs, D. H. 2009, Interplanetary Network Progress Report, 178, 1

Fujiwara, A., Kawaguchi, J., Yeomans, D. K., et al. 2006, Science, 312, 1330

Fusco, T., Mugnier, L. M., Conan, J.-M., et al. 2002, in Astronomical Telescopes and Instrumentation, eds. P. L. Wizinowich, & D. Bonaccini (SPIE), 1065

Fusco, T., Rousset, G., Sauvage, J. F., et al. 2006, Optics Express, 14, 7515

Gaffey, M. J., & Fieber-Beyer, S. K. 2013, Meteor. Planet. Sci. Suppl., 76

Gaffey, M. J., & Gilbert, S. L. 1998, Meteor. Planet. Sci., 33, 1281

Goffin, E. 2014, A&A, 565, A56

Grice, J., Snodgrass, C., Green, S., Parley, N., & Carry, B. 2017, The shapes of primordial asteroids, Int. Conf. Asteroids, Comets, and Meteors: ACM 2017

Gundlach, B., & Blum, J. 2013, Icarus, 223, 479

Gwyn, S. D. J., Hill, N., & Kavelaars, J. J. 2012, PASP, 124, 579

Hanuš, J., Marchis, F., & Durech, J. 2013, Icarus, 226, 1045

Hanuš, J., Marchis, F., Viikinkoski, M., Yang, B., & Kaasalainen, M. 2017, A&A, 599, A36

Heck, P. R., Schmitz, B., Bottke, W. F., et al. 2017, Nat. Astron., 1, 0035

Hutchison, R. 2004, Meteorites, Cambridge Planetary Science (Cambridge University Press)

Jehin, E., Gillon, M., Queloz, D., et al. 2011, The Messenger, 145, 2

Kaasalainen, M. 2001, Icarus, 153, 37

Kaasalainen, M., & Torppa, J. 2001, Icarus, 153, 24

Kaasalainen, M., & Viikinkoski, M. 2012, A&A, 543, A97

Kaasalainen, M., Viikinkoski, M., Carry, B., et al. 2011, EPSC-DPS Joint Meeting 2011, 416

Kochetova, O. M. 2004, Sol. Syst. Res., 38, 66

Kochetova, O. M., & Chernetenko, Y. A. 2014, Sol. Syst. Res., 48, 295

Konopliv, A. S., Asmar, S. W., Folkner, W. M., et al. 2011, Icarus, 211, 401

Kuchynka, P., & Folkner, W. M. 2013, Icarus, 222, 243

Lagerkvist, C. I., & Magnusson, P. 2011, NASA Planetary Data System, 162

Lagerros, J. S. V., Müller, T. G., Klaas, U., & Erikson, A. 1999, Icarus, 142, 454

Lenzen, R., Hartung, M., Brandner, W., et al. 2003, Instrument design and Performance for optical/Infrared Ground-based Telescopes, Proc. SPIE, 4841, 944

Marchi, S., Chapman, C. R., Barnouin, O. S., Richardson, J. E., & Vincent, J. B. 2015, in Asteroids IV (University of Arizona Press)

Marti, K., & Graf, T. 1992, Ann. Rev. Earth Planet. Sci., 20, 221

Masiero, J. R., Mainzer, A. K., Grav, T., et al. 2011, ApJ, 741, 68

Masiero, J. R., Grav, T., Mainzer, A. K., et al. 2014, ApJ, 791, 121

Melosh, H. J. 1989, Oxford Monographs on Geology and Geophysics (Oxford University Press), 11

Merline, W. J., Drummond, J. D., Carry, B., et al. 2013, Icarus, 225, 794

Michalak, G. 2001, A&A, 374, 703

Migliorini, F., Manara, A., Scaltriti, F., et al. 1997, Icarus, 128, 104

Mignard, F., Cellino, A., Muinonen, K., et al. 2007, Earth Moon Planets, 101, 97

Morrison, D. 1974, ApJ, 194, 203

Morrison, D. 1977, Icarus, 31, 185

Mouret, S., Hestroffer, D., & Mignard, F. 2007, A&A, 472, 1017

Mugnier, L. M., Fusco, T., & Conan, J.-M. 2004, J. Opt. Soc. Am. A, 21, 1841

Müller, T. G., & Lagerros, J. S. V. 1998, A&A, 338, 340

Müller, T. G., Lagerros, J. S. V., Burgdorf, M., et al. 1999, Asteroids, Comets, and Meteors: ACM 2002, 427, 141

Nesvorný, D. 2015, NASA Planetary Data System, 234

Nesvorný, D., Brož, M., & Carruba, V. 2015, in Asteroids IV, eds. P. Michel et al., 297

Opeil, C. P., Consolmagno, G. J., & Britt, D. T. 2010, Icarus, 208, 449

O'Rourke, L., Müller, T., Valtchanov, I., et al. 2012, Planet. Space Sci., 66, 192

Pavlov, A., Möller-Nilsson, O., Feldt, M., et al. 2008, in Advanced Software and Control for Astronomy II, Proc. SPIE, 7019, 701939

Pitjeva, E. V. 2013, Sol. Syst. Res., 47, 386

Pollacco, D. L., Skillen, I., Collier Cameron, A., et al. 2006, PASP, 118, 1407

Rousset, G., Lacombe, F., Puget, P., et al. 2003, Adaptive optical system Technologies II, Proc. SPIE, 4839, 140

Russell, C. T., Raymond, C. A., Coradini, A., et al. 2012, Science, 336, 684

Russell, C. T., Raymond, C. A., Ammannito, E., et al. 2016, Science, 353, 1008

Ryan, E. L., & Woodward, C. E. 2010, AJ, 140, 933

Scheeres, D. J., Britt, D., Carry, B., & Holsapple, K. A. 2015, in Asteroid Interiors and Morphology, eds. P. Michel, F. E. DeMeo, & W. F. Bottke (University of Arizona Press), 745

Schenk, P., O'Brien, D. P., Marchi, S., et al. 2012, Science, 336, 694

Sierks, H., Lamy, P., Barbieri, C., et al. 2011, Science, 334, 487

Tanga, P., Carry, B., Colas, F., et al. 2015, MNRAS, 448, 3382

Taylor, G. E., & Dunham, D. W. 1978, Icarus, 34, 89

Tedesco, E. F., Noah, P. V., Noah, M., & Price, S. D. 2002, AJ, 123, 1056

Tedesco, E. F., Noah, P. V., Noah, M., & Price, S. D. 2004, NASA Planetary Data System, 12

Thomas, P. 1999, Icarus, 142, 89

Thomas, P. C., Binzel, R. P., Gaffey, M. J., et al. 1997, Science, 277, 1492

Torppa, J., Kaasalainen, M., Michalowski, T., et al. 2003, Icarus, 164, 346

Usui, F., Kuroda, D., Müller, T. G., et al. 2011, PASJ, 63, 1117

van Dam, M. A., Le Mignant, D., & Macintosh, B. A. 2004, Appl. Opt., 43, 5458

Vernazza, P., Zanda, B., Binzel, R. P., et al. 2014, ApJ, 791, 120

Viikinkoski, M., Kaasalainen, M., & Durech, J. 2015a, A&A, 576, A8

Viikinkoski, M., Kaasalainen, M., Durech, J., et al. 2015b, A&A, 581, L3

Wizinowich, P. L., Acton, D. S., Lai, O., et al. 2000, Adaptive Optical Systems Technology, Proc. SPIE, 4007, 2

Zielenbach, W. 2011, AJ, 142, 120

Zuber, M. T., Smith, D. E., Cheng, A. F., et al. 2000, Science, 289, 2097

Asteroid Models from Multiple Data Sources

Josef Ďurech
Astronomical Institute, Faculty of Mathematics and Physics, Charles University in Prague

Benoît Carry
Institut de Mécanique Céleste et de Calcul des Éphémérides

Marco Delbo
Laboratoire Lagrange, UNS-CNRS-Observatoire de la Côte d'Azur

Mikko Kaasalainen
Tampere University of Technology

Matti Viikinkoski
Tampere University of Technology

In the past decade, hundreds of asteroid shape models have been derived using the lightcurve inversion method. At the same time, a new framework of 3-D shape modeling based on the combined analysis of widely different data sources such as optical lightcurves, disk-resolved images, stellar occultation timings, mid-infrared thermal radiometry, optical interferometry, and radar delay-Doppler data, has been developed. This multi-data approach allows the determination of most of the physical and surface properties of asteroids in a single, coherent inversion, with spectacular results. We review the main results of asteroid lightcurve inversion and also recent advances in multi-data modeling. We show that models based on remote sensing data were confirmed by spacecraft encounters with asteroids, and we discuss how the multiplication of highly detailed 3-D models will help to refine our general knowledge of the asteroid population. The physical and surface properties of asteroids, i.e., their spin, 3-D shape, density, thermal inertia, surface roughness, are among the least known of all asteroid properties. Apart for the albedo and diameter, we have access to the whole picture for only a few hundreds of asteroids. These quantities are nevertheless very important to understand as they affect the non-gravitational Yarkovsky effect responsible for meteorite delivery to Earth, or the bulk composition and internal structure of asteroids.

1. INTRODUCTION

The determination of asteroid physical properties is an essential part of the complex process of revealing the nature of the asteroid population. In many cases, this process starts with obtaining observational data, continues with creating a model of the asteroid (i.e., its size, 3-D shape, and spin state, in the first approximation), and ends with interpreting new facts based on the model or a set of these. In this sense, modeling is a crucial mid-step between observations and theory. Results based on individual well-studied asteroids can be generalized to other members of the population. On the other hand, a statistically large sample of asteroids with known properties can reveal physical effects that play an important role for the whole population.

In this chapter, we will build on the content of the *Asteroids III* chapter by *Kaasalainen et al.* (2002a) about asteroid models reconstructed from *disk-integrated* photometry. Although visual photometry still remains the most important data source of the modeling, the main progress in this field since *Asteroids III* has been the addition of *complementary data sources*. Many of these data sources are *disk-resolved*, thus containing much more information than disk-integrated data. This shift in paradigm – using photometry not alone but simultaneously with complementary data – was mentioned in the last paragraph of the *Asteroids III* chapter as "*perhaps the most interesting future prospect*", and we are now at this stage. In the following, we will review all data types suitable for inversion, their sources, uncertainties, and how they can be used in modeling.

When describing the methods of data inversion and the results obtained by these methods, it is also important to emphasize caveats, ambiguities, and possible sources of errors. Although the description of what can be obtained from different data sources is exciting, the knowledge of what cannot, i.e., what are limitations of our data sets, is of the same importance. Omitting this may lead to over interpretation of results.

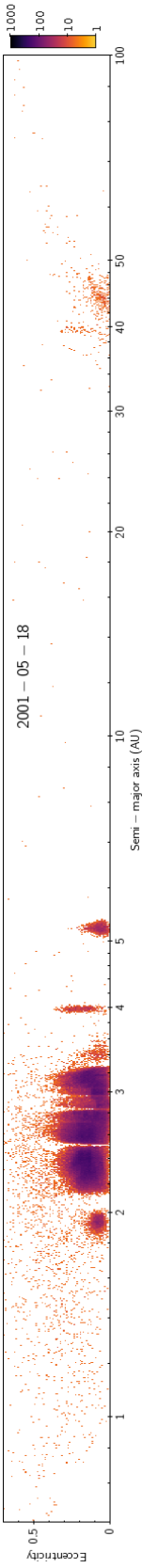

This chapter is structured as follows. First we review the main principles of the multimodal inverse problem in Sect. 2. Then, in Sect. 3, we discuss each data type and their contribution to model characteristics and details, and we describe some extensions of the predominant model. In Sect. 4, we discuss the main results based on lightcurve inversion and multimodal asteroid reconstruction. We conclude with prospects for the future in Sect. 5.

2. THEORETICAL ASPECTS OF INVERSION AND DATA FUSION

Asteroid physical model reconstruction from multimodal data is, by its nature, a mathematical inverse problem. It is ill-posed; i.e., the uniqueness and stability properties of the solution are usually not very good unless the data are supported by a number of prior constraints. Furthermore, it is not sufficient just to fit some model to the data numerically and try to probe the solution space with some scheme. Although there are more approaches to the problem of asteroid shape reconstruction, they are usually dealing with only one data type and we mention them in the next section. Here, we describe the problem in a general way in the framework of *generalized projections*: our data are various 1-D or 2-D projection types of a 3-D model, and understanding the fundamental mathematical properties of the inverse projection mapping is essential. This includes a number of theorems on uniqueness, information content, and stability properties (*Kaasalainen and Lamberg*, 2006; *Kaasalainen*, 2011; *Viikinkoski and Kaasalainen*, 2014).

Let the projection point ξ_0 in the image plane (plane-of-sky or range-Doppler) of the point $\mathbf{x}_0$ on the body be mapped by the matrix A: $\xi_0 = A\mathbf{x}_0$. Define the set $\mathcal{I}(\xi)$ for any ξ as

$$\mathcal{I}(\xi) = \{\mathbf{x} | g(\xi, \mathbf{x}; R, t)\, h(\mathbf{x}; M, R, t) = 1\}, \qquad (1)$$

where we have explicitly shown the time t and the adjustable parameters: M for the shape and R for the rotation. The projection point function $g(\xi, \mathbf{x}) = 1$ if $A(R, t)\mathbf{x} = \xi$, and $g = 0$ otherwise. The ray-tracing function $h = 1$ if $\mathbf{x}$ is visible (for occultation, thermal, and radar data), or visible and illuminated (for disk-resolved imaging and photometry in the optical); otherwise $h = 0$. The set $\mathcal{I}(\xi)$ is numerable and finite. The number of elements in $\mathcal{I}(\xi)$ is at most one for plane-of-sky projections (each point on the projection corresponds to at most one point of the asteroid's surface); for range-Doppler, it can be more (more points on asteroid's surface can have the same distance to the observer and the same relative radial velocity). Generalized projections, i.e., all the data modes presented in Sect. 3, can now be presented as scalar values $p(\xi)$ in the image field Ω:

$$p(\xi; t) = \int_\Omega f(\xi, \eta) \sum_{\mathbf{x} \in \mathcal{I}(\eta)} S(\mathbf{x}; M, R, L, t)\, \mathrm{d}\eta, \qquad (2)$$

where L denotes the luminosity parameters (for scattering or thermal properties), and the luminosity function is denoted by S. The function f is the point-spread, pixellation, or other transfer function of the image field. For interferometry, it is typically the Fourier transform kernel. In fact, the reconstruction process works efficiently by taking the Fourier transform of any image type rather than using the original pixels (*Viikinkoski and Kaasalainen*, 2014). For lightcurves, $f = 1$ (and ξ is irrelevant, $p(\xi)$ is constant). The surface albedo is usually assumed to be constant, although its variegation can be included in S by the parameters L if there are high-quality disk-resolved data. In the case of lightcurves only, we can get an indication of non-uniform albedo and compensate for this with a (non-unique) spot model (*Kaasalainen et al.*, 2001).

The multimodal inverse problem can be expressed as follows. Let us choose as goodness-of-fit measures some functions δ_i, $i = 1, \ldots, n$, of n data modalities. Typically, δ is the usual χ^2-fit form between p_{model} and p_{obs}. Our task is to construct a joint δ_{tot} with weighting for each data mode:

$$\delta_{\mathrm{tot}}(P, D) = \delta_1(P, D_1) + \sum_{i=2}^{n} \lambda_{i-1} \delta_i(P, D_i), \quad D = \{D_i\}, \qquad (3)$$

where D_i denotes the data from the source i, λ_{i-1} is the weight of the source i, and $P = \{M, R, L\}$ is the set of model parameter values. The best-fit result is obtained by minimizing δ_{tot} with nonlinear techniques, typically Levenberg-Marquardt for efficient convergence. Regularization functions $r(P)$ can be added to the sum; these constrain, for instance, the smoothness of the surface to suppress large variations at small scales, the deviation from principal-axis rotation to force the model to rotate around the shortest inertia axis (assuming uniform density), or the gravitational slope, etc. (*Kaasalainen and Viikinkoski*, 2012).

The modality (and regularization) weights λ_i are determined using the maximum compatibility estimate (MCE) principle (*Kaasalainen*, 2011; *Kaasalainen and Viikinkoski*, 2012). This yields well-defined unique values that are, in essence, the best compromise between the different data sets that often tend to draw the solution in different directions. Moreover, MCE values of weighting parameters are objective, not dependent on users choice, although their values are usually close to those determined subjectively based on experience. Plotting various choices of weights typically results in an L-shaped curve shown in Fig. 1; the best solution is at the corner of the curve. In this way, the reconstruction from complementary data sources is possible even if no single data mode is sufficient for modeling alone.

For practical computations, the surface is rendered as a polyhedron, and S and h are computed accordingly with ray-tracing (*Kaasalainen et al.*, 2001). Rather than using each vertex as a free parameter, the surface can be represented in a more compact form with spherical harmonics series (for starlike or octantoid; i.e., generalized starlike, shapes) or subdivision control points (*Kaasalainen and Viikinkoski*, 2012; *Viikinkoski et al.*, 2015). These *shape supports* are essential for convergence: they

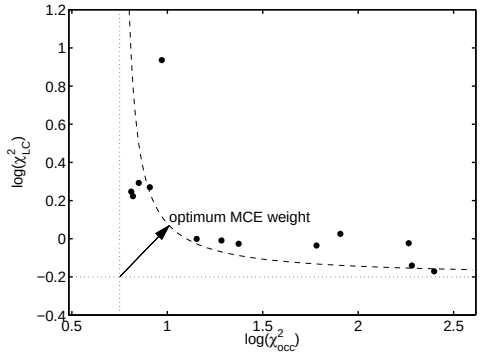

Fig. 1.— The level of fit for lightcurves and occultation data for different weighting between the two data types. The optimum weight is around the "corner" of the L-curve. Each dot corresponds to an inversion with a different weight λ.

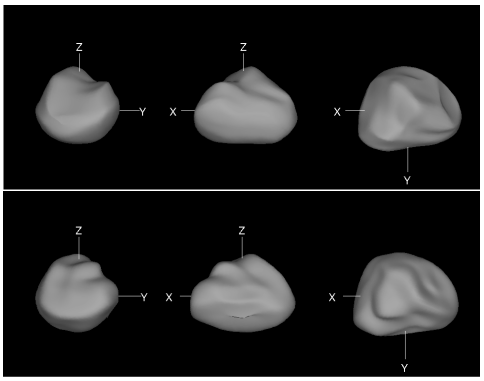

Fig. 2.— Model of (41) Daphne reconstructed from lightcurves and adaptive-optics images using subdivision surfaces (top) and octantoids (bottom). The general shape remains stable, even if small-scale features slightly change.

allow flexible modifications of the surface with a moderate number of parameters while not getting stuck in local minima or over-emphasizing the role of regularization functions when searching for the best-fit solution. Each shape support has its own characteristic way of representing global and local features. For example, the octantoid parametrization

$$\mathbf{x}(\theta,\varphi) = \begin{cases} x(\theta,\varphi) = & e^{a(\theta,\varphi)} \sin\theta\cos\varphi, \\ y(\theta,\varphi) = & e^{a(\theta,\varphi)+b(\theta,\varphi)} \sin\theta\sin\varphi, \\ z(\theta,\varphi) = & e^{a(\theta,\varphi)+c(\theta,\varphi)} \cos\theta, \end{cases} \tag{4}$$

where a, b, and c are linear combinations of the (real) spherical harmonic functions $Y_l^m(\theta,\varphi)$, with coefficients $\{a_{lm}\}$, $\{b_{lm}\}$, and $\{c_{lm}\}$, respectively, is easy to regularize globally while retaining the ability to produce local details. The coordinates (θ,φ), $0 \le \theta \le \pi$, $0 \le \varphi < 2\pi$, parametrize the surface on the unit sphere S^2 but do not represent any physical directions such as polar coordinates.

This inverse problem is a typical example of a case where model and systematic errors dominate over random measurement errors. Thus the stability and error estimation of the solution are best examined by using different model types (Fig. 2). In the case of shape, for example, the reliability of the features on the solution can be checked by comparing the results obtained with two or more shape supports (starlike, octantoid, subdivision; *Viikinkoski et al.*, 2015). This yields better estimates than, e.g., Markov chain Monte Carlo sequences that only investigate random error effects within a single model type.

A particular feature of the model reconstruction from disk-resolved data is that the result is dominated by the target image boundaries rather than the pixel brightness distribution within the target image. This is because the information is contained in the pixel contrast which is the largest on the boundary (occultations are special cases of this as they are samples of the boundary contour). This is very advantageous when considering the effect of model errors in luminosity properties (scattering or thermal models): it is sufficient to have a reasonable model, and the result is not sensitive to the parameters L. Thus, for example, Atacama Large Millimeter Array data can be used for efficient reconstruction even with a very approximate semianalytical Fourier-series thermal model – more detailed models have hardly any effect on the shape solution (Sect. 3.5, *Viikinkoski and Kaasalainen*, 2014; *Viikinkoski et al.*, 2015).

3. DATA AND MODELING

We describe all data types that can be used, the way of collecting the data, their accuracy, typical number of asteroids for which the data exist, and expectations for the future. We also discuss a typical result of inversion – what is the resolution of the model and how many targets can be modeled (Table 1).

3.1. Photometry

Disk-integrated photometry is, and will always be, the most abundant source of data, because it is available for essentially every single known asteroid. Because asteroid brightness periodically changes with its rotation, frequency analysis of asteroid lightcurves provides asteroid rotation periods – the basic physical property derivable from time-resolved photometry. The regularly updated Asteroid Lightcurve Database of *Warner et al.* (2009) available at *http://www.minorplanet.info/lightcurvedatabase.html* now contains rotation periods and other physical parameters for almost 7000 objects, for about half of them their rotation period is secure and unambiguous. The role of amateur astronomers in this field is traditionally strong, getting even

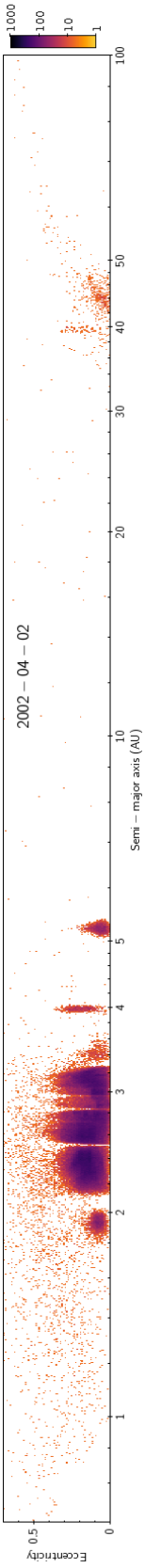

stronger with increasing level of their technical and software equipment. Hundreds of asteroid lightcurves are published quarterly in the Minor Planet Bulletin; most of them are then archived in the Asteroid Light Curve Database at the Minor Planet Center site (*http://mpc.cfa.harvard.edu//light_curve2/light_curve.php*) in the ALCDEF standard (*Warner et al.,* 2011). The efficiency of lightcurve production can be increased by dedicated wide-field photometric surveys (*Masiero et al.*, 2009; *Polishook et al.*, 2012, for example), although the period determination from undersampled lightcurves is often ambiguous (*Harris et al.*, 2012).

For period determination, a single lightcurve covering the full rotation is sufficient. However, a set of such lightcurves observed at different geometries (asteroid illuminated and seen from various directions) is needed to reconstruct the shape and spin state of an asteroid. The *lightcurve inversion* method of *Kaasalainen and Torppa* (2001); *Kaasalainen et al.* (2001) was already reviewed in *Asteroids III* (*Kaasalainen et al.*, 2002a). Since then, the method has been widely used and hundreds of asteroid models have been derived. They are publicly available at the Database of Asteroid Models from Inversion Techniques (DAMIT, *http://astro.troja.mff.cuni.cz/projects/asteroids3D*). The reliability of the method was proved by comparing its results with independent data such as laboratory asteroid model (*Kaasalainen et al.,* 2005), adaptive-optics images (*Marchis et al.,* 2006), stellar occultations (*Ďurech et al.,* 2011), or spacecraft images of asteroids (2867) Šteins (*Keller et al.*, 2010) and (433) Eros (*Kaasalainen et al.*, 2002a).

From disk-integrated photometry alone, only a global shape without any small-scale details can be derived. Because the reflectivity of the surface is not known, the models are not scaled and the information about the size has to come from complementary data. To avoid overinterpretation and artifacts of the modeling, the shapes are usually represented by a *convex* model. This allows to work not in the obvious radius parameter space but in the Gaussian image space (describing a convex body by the curvature of its surface). This is less intuitive but it makes the inverse problem less vulnerable to errors of data and model because of the Minkowski stability (*Lamberg and Kaasalainen,* 2001) – even if the areas of individual surface facets may change significantly for slightly different data sets, the global convex shape changes very little.

From the practical point of view, we are interested in finding a *unique solution* of the inverse problem. To guarantee this, observations covering a sufficiently wide range of viewing and illumination geometries are needed. For a typical main-belt asteroid, it means observations during several apparitions. For a close-approaching near-Earth asteroid, several months could be sufficient. For more distant objects, we can in principle observe changing lightcurve amplitude because of changing aspect, this would anyway take many decades. Nevertheless, trans-Neptunian objects (TNOs) and Centaurs can be never observed from Earth at geometry significantly different from opposition, which is not sufficient to reconstruct a unique convex model (*Russell,* 1906). If the lightcurves observed in various filters are different, there is some spectral/color variegation over the surface, and a crude color map can be reconstructed (*Nathues et al.*, 2005).

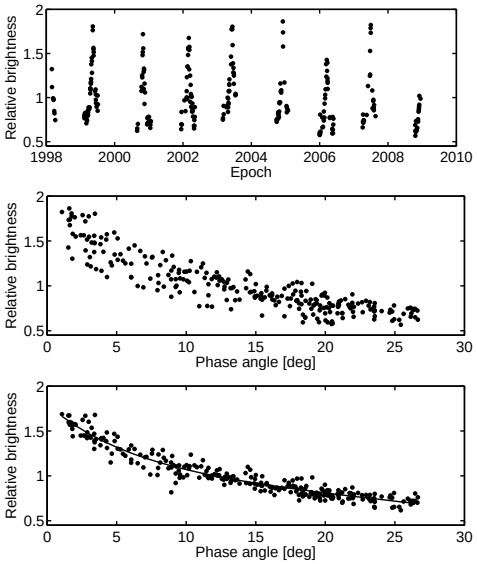

Fig. 3.— Sparse-in-time photometry of (21) Lutetia obtained at US Naval Observatory plotted as a function of time (top) and phase angle (middle). The brightness was reduced to the unit distance from Earth and Sun. The scatter in the phase plot is caused by the intrinsic noise of the data and the rotational and aspect effects. The bottom panel shows residuals for the best-fit model (Fig. 6) plotted over the phase curve (solid curve).

A typical outcome of lightcurve inversion is a convex shape model that describes the global characteristics of the real asteroid. It is also easy to obtain nonconvex versions with the general inversion procedures (see Sect. 2), but then one should produce several solutions with various model types and parameters, and be very cautious about the results (*Viikinkoski et al.,* 2015). In general, disk-integrated photometry contains very little information about nonconvexities unless they are very pronounced or observed at very high phase angles where shadowing effects play an important role (*Ďurech and Kaasalainen,* 2003). Nonconvex models seldom fit lightcurves better than convex ones simply because the latter typically already fit the data down to noise level. This sets the resolution limit of photometry (see the discussion in *Kaasalainen et al.*, 2001, 2002a; *Viikinkoski et al.*, 2015, and references therein).

The relative accuracy of the sidereal rotation period de-

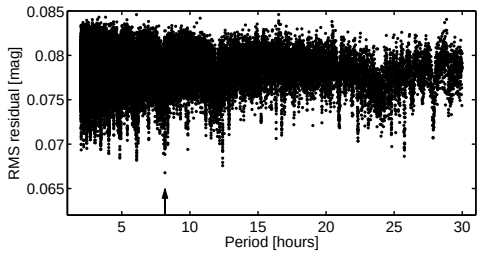

Fig. 4.— Period search for (21) Lutetia. Each point represents a local minimum in the parameter space to which the optimization algorithm converged. The lowest RMS residual (arrow) corresponds to the best-fit model shown in Fig. 6.

termined from lightcurves is of the order of 10^{-5} or better, depending mainly on the time span of observations. The direction of the spin axis can be determined with an accuracy from a couple of degrees for the models based on many decades of observations with many dense lightcurves, to more than twenty degrees for models based on limited and noisy data. For asteroids orbiting in the ecliptic plane, the geometry for an Earth-based observer is limited to that plane. Then the disk-integrated brightness of a body with surface described by radius vector (x, y, z) and pole direction (λ, β) in ecliptic coordinates is the same as for a body $(x, y, -z)$ with the spin axis direction $(\lambda + 180°, \beta)$ (*Kaasalainen and Lamberg*, 2006). That is why for a typical main-belt asteroid, there are usually two equally good mirror shape solutions with about the same pole latitude and pole longitude difference of about 180°. This ambiguity can be removed with disk-resolved plane-of-sky projections (e.g., images, stellar occultations, see Sect. 3.2, 3.4).

Apart from "classical" lightcurves where the sampling of brightness variations is dense with respect to the rotation period, there are also data that are *sparse in time*. Such data sets typically consist of only a single to a few brightness measurements per night. Provided the whole sparse data set is internally calibrated, it can be used the same way as a standard lightcurve that would be extremely long and very sparsely sampled (*Kaasalainen*, 2004). These data are routinely provided by all-sky astrometric surveys with various – usually poor – photometric quality. Current surveys provide data of accuracy scarcely better than 0.1 mag. Given a typical lightcurve amplitude of 0.3 mag, the signal is often drowned in noise and systematic errors. This leads to many physically acceptable models fitting the data to the noise level (*Ďurech et al.*, 2005). However, the total amount of data is huge and it has been shown that at least for some asteroids, models can be successfully derived from these data or from their combination with dense lightcurves (*Ďurech et al.*, 2009; *Hanuš et al.*, 2011).

As an example, we show sparse photometry for asteroid (21) Lutetia from US Naval Observatory (260 points covering ten years) in Fig. 3 and the period search results in Fig. 4. The best-fit model based on this data set has the same rotation period and a similar spin axis direction as the models based on much larger and multiple data sets (Fig. 6).

When using noisy sparse data or only a limited number of data points, a simple shape model of a triaxial ellipsoid is usually sufficient to model the data and to derive the correct period and spin vector orientation (*Cellino et al.*, 2009; *Cellino and Dell'Oro*, 2012; *Carbognani et al.*, 2012). The advantage of this approach is that the shape is described by only two parameters (axes ratios) and the scanning of the period parameter space is much faster than with general shapes.

The on-going (Pan-STARRS, Catalina, Gaia) and future (ATLAS, LSST) surveys will provide new data every night for essentially every known asteroid. Using this data for automated lightcurve inversion with well-mastered treatment of systematic effects, recognition of the best-fit models, definition of uniqueness of the solution etc., is the main challenge for the future lightcurve inversion.

3.2. Remote sensing disk-resolved images

The most direct way to obtain information on the shape of an asteroid is to take pictures of it. The apparent shape as visible on the plane of the sky is delimited by the limb and the terminator, and multiple views obtained while the target rotates can fully characterize its 3-D shape. To resolve the small angular diameter ($< 0.5''$) sustained by asteroids, large facilities are, however, required.

In the 1980s, speckle imaging or speckle interferometry provided "*the first glimpses of an asteroid's surface*" (i.e., (4) Vesta by *Drummond et al.*, 1988). This technique is based on the analysis of the speckle pattern in the images of astronomical sources obtained through large telescopes at high magnification power and very short integration time. The aim is to overcome the blurring effects due to the astronomical seeing and to attain diffraction-limited resolution images. Speckle interferometry has been commonly used to study the size, shapes, and surface features of the largest asteroids (*Drummond et al.*, 1985, 1988; *Ragazzoni et al.*, 2000; *Cellino et al.*, 2003). With the launch of the Hubble Space Telescope (HST) in orbit and the first light of the large (10-m class) ground-based telescopes equipped with adaptive-optics fed cameras (e.g., W. M. Keck, European Southern Observatory (ESO) Very Large Telescope (VLT), Geminis, Subaru), the importance of speckle interferometry has decreased.

The critical issue in direct imaging is of course the angular resolution. Any image is the result of the convolution of the object on the plane of the sky with the instrument response, the point spread function (PSF). In space, the PSF is stable and corresponds to the diffraction pattern of the telescope. From the ground, the atmospheric turbulence constantly deforms the PSF and blurs the images, hence the need of real-time correction of the PSF by adaptive optics (AO). The technical challenges of sending a large telescope in space and of building deformable

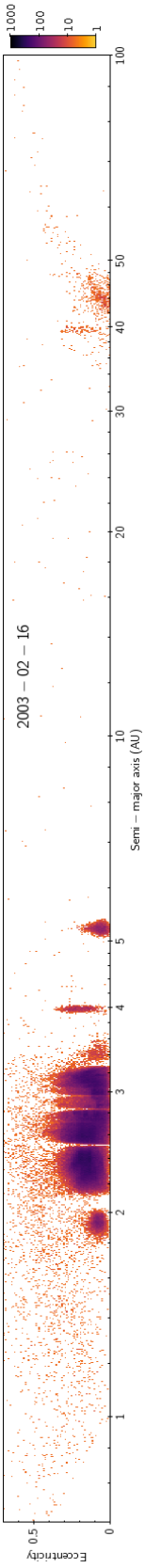

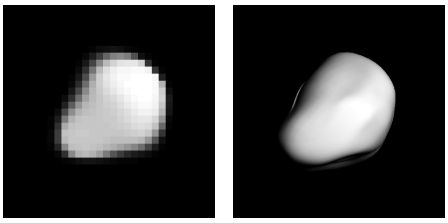

Fig. 5.— Deconvoluted adaptive optics image (left) of asteroid (41) Daphne, and the corresponding image of the reconstructed model (right, projection of the the octantoid model from Fig. 2). The model is shown under artificial illumination that enhances its 3-D shape and is different from the simple light-scattering model used for the inversion. The AO image has resolution of 10 mas/pixel. The model was reconstructed from 14 AO images obtained with ESO VLT and several lightcurves.

mirrors, explain why the first disk-resolved images in the 1990s were still limited in resolution and only the largest asteroids (1) Ceres, (2) Pallas, and (4) Vesta have been imaged. In the decade since *Asteroids III*, numerous studies have been based on direct imaging of asteroids (e.g., *Thomas et al.*, 2005; *Carry et al.*, 2008; *Descamps et al.*, 2008; *Schmidt et al.*, 2009; *Marchis et al.*, 2013).

Both from space or with adaptive optics on the ground, however, the contrast and angular resolution can be improved by deconvolution of the image by the PSF. This is particularly true for images acquired from the ground with residuals from non-perfect AO correction. Deconvolution is an ill-posed problem, but robust algorithms adapted to planetary images are available (*Conan et al.*, 2000; *Mugnier et al.*, 2004; *Hom et al.*, 2007) and have been validated on sky (*Witasse et al.*, 2006). It is nevertheless the most critical part of the post-processing, as an incorrect deconvolution can introduce a systematic error on the apparent size. An example of an AO image and the reconstructed shape model for asteroid (41) Daphne is shown in Fig. 5

Current facilities deliver an angular resolution of about 30 to 50 milliarcseconds (mas), depending on the wavelength. The apparent shape can therefore be measured for asteroids with an apparent diameter larger than $\approx$80–100 mas, i.e., a couple of hundred targets. Simulations and observations of known targets such as the satellites of Saturn (*Marchis et al.*, 2006; *Drummond et al.*, 2009; *Carry*, 2009) have shown that a precision of a few mas can be derived on the 2-D profile on the plane of the sky, corresponding to only a few kilometers for main-belt asteroids. With upcoming large telescopes (30+ m, such as the Thirty Meter Telescope or the European Extremely Large Telescope), the angular resolution will be improved by a factor 3–4, providing more than 500 targets. Second generation instruments with extreme AO foreseen on these telescopes should allow the observation of about 7000 asteroids, with sizes of only a few kilometers (*Merline et al.*, 2013).

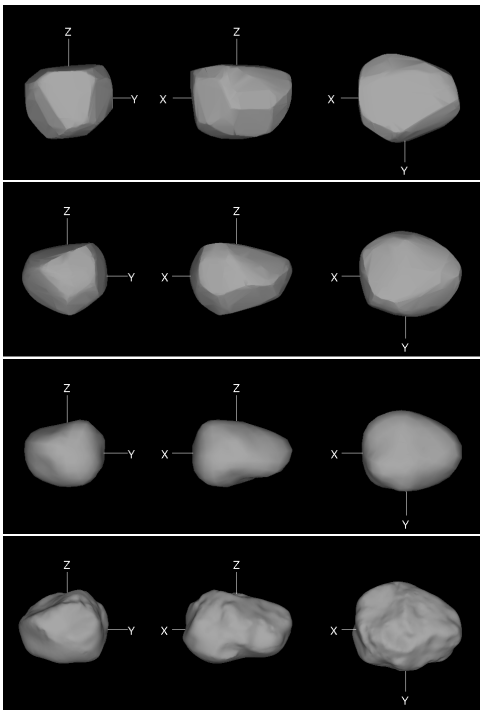

Fig. 6.— Different shape models for (21) Lutetia derived from different sets of data. The level of detail increases with more data from top to bottom: sparse photometry (Sect. 3.1), dense lightcurves (*Torppa et al.*, 2003), lightcurves and AO (*Carry et al.*, 2010b), Rosetta flyby (*Sierks et al.*, 2011).

Using disk-resolved images, giant craters have been discovered (*Thomas et al.*, 1997; *Conrad et al.*, 2007), ambiguity in spin solutions have been solved (*Marchis et al.*, 2006; *Carry et al.*, 2010a), albedo maps have been constructed (*Li et al.*, 2006; *Carry et al.*, 2008), convex 3-D shape models from lightcurves have been set to scale (*Hanuš et al.*, 2013a), and full 3-D shape models determined (*Carry et al.*, 2010b; *Descamps et al.*, 2011).

3.3. Flybys

Asteroid imaging and mapping *in situ* is essentially an extreme example of disk-resolved images. The modeling in such cases is more a cartographic than an inverse problem as the data are abundant, directly usable (containing identification points on the surface, etc.), and high-resolution (there is no ill-posedness). However, asteroid *flybys*, during which roughly a half of the target is likely to remain unseen (not visible and illuminated), pose a special problem: how to see the dark side? The principle here is to use the high-resolution map of the seen side,

constructed with a number of methods of photoclinometry, photogrammetry, and image fitting (*Preusker et al.*, 2012; *Gaskell et al.*, 2008; *Jorda et al.*, 2012), as a constraint in the otherwise same multi-mode inverse problem as with ground-based observations. The procedure is described in *Kaasalainen and Viikinkoski* (2012); with it, the reconstruction of the dark side, such as those of (2867) Šteins (*Keller et al.*, 2010) or (21) Lutetia (*Sierks et al.*, 2011, see also Fig. 6), is more detailed than from, e.g., lightcurves alone. This is because half of the target is accurately reconstructed, with practically no error margin: therefore the fluctuation margin of the dark side is considerably smaller as well.

3.4. Stellar occultations

The observation of a stellar occultation consists in recording the duration of the disappearance of a star behind the asteroid. Knowing the apparent motion of the asteroid on the plane of the sky, obtained from its ephemeris, this duration can be converted in a physical length on the disk of the asteroid, called a chord. Provided several observers record the same event from different locations on Earth, the 2-D profile of the asteroid is drawn on the plane of the sky (*Millis and Dunham*, 1989). The main difference with disk-resolved imaging resides in the profile, made by only the limb for occultations, and limb+terminator for imaging. In fine, both techniques provide the 2-D profile of the target as projected on the plane of the sky at the epoch of observations (Fig. 7).

Disk-resolved imaging and stellar occultation are, however, radically different in term of facilities, data processing, potential targets, reproducibility, and achievable precision. For stellar occultations, the properties of the occulted star matter generally more than the actual target: the asteroid. If the occulted star is bright enough, its occultation, even by a very small asteroid, can be detected with small aperture telescopes. This is of course the main advantage of stellar occultations, where the apparent size and shape of potentially any asteroid can be measured. Moreover, this technique can be successfully used also for distant TNOs, which have angular sizes too small to be resolved by imaging (*Sicardy et al.*, 2011). In practice, however, a given asteroid will only seldom occult bright stars. Measurements are thus hard, if not impossible, to reproduce.

Stellar occultations are nevertheless extremely valuable. The accuracy of the timing is dictated by time-series photometry, and can therefore be extremely precise. An uncertainty of 50 ms in timings converts into only a 300 m uncertainty in the length of the chord, typical for a main-belt asteroid (at 1.5 au from Earth with an apparent motion of 10″/h). The main source of uncertainty is, however, the absolute timing of each chord, required to align them on the plane of the sky. Most of historical occultations were recorded by naked eye, and suffered from this. Since a decade ago, thanks to the availability of low-cost positioning and timing systems (e.g., GPS), stellar occultations are being more and more valuable.

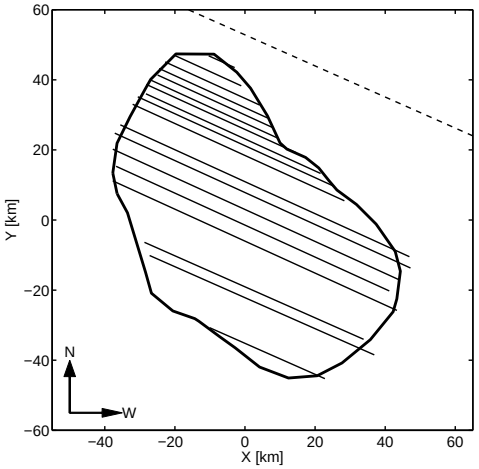

Fig. 7.— An example of a well-covered occultation that provides almost an "image" of the projected asteroid (135) Hertha (*Timerson et al.*, 2009). The model of Hertha based on its lightcurves and occultation data is over plotted. The dashed line is a negative observation constraining the northern part of the model's projection. Formal timing uncertainties are between 0.02 and 0.2 s, corresponding to 0.12–1.2 km in the projection, which is below the resolution of the model. The RMS of the fit is 1.9 km.

The main contributors to the field are currently amateur astronomers: for a given event, observers have to move to set themselves on the predicted occultation path on Earth. Small aperture (< 20 cm) mobile stations are therefore ideal for recording stellar occultations. Because of the uncertainties of the star and asteroid positions on sky, there is generally an uncertainty of a few tens of kilometers in the location of the occultation path on Earth, requiring observers to spread over large area to cover the event. This usually prohibits dense coverage of the asteroid profile. When only a couple of chords are available, the event provides only limited information on the size, if any on the shape. Current occultation predictions of sufficient accuracy concern only stars in the Hipparcos catalogue and large (at least tens of kilometers) asteroids. With the upcoming publication of the ESA Gaia stellar catalog, and update of asteroid orbits, this position uncertainty is expected to drop significantly and future occultations will be easier to predict, hence observe (*Tanga and Delbo*, 2007).

Overall, stellar occultations can provide precise measurements of the size and shape of an asteroid, as projected on the plane of the sky. However, events are rare for a given target. Occultations are therefore very valuable in combined data sets, as for instance, to set scale to otherwise dimensionless 3-D shape models (e.g., *Ďurech et al.*, 2011; *Hanuš et al.*, 2011). From almost 2500 occultations com-

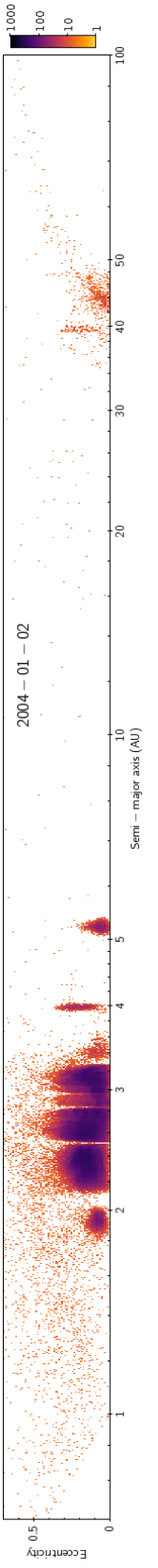

piled by *Dunham et al.* (2014), there are about 160 "good" ones that allow a reliable determination of asteroid's size and about 40 "excellent" ones that show details in asteroid's profile.

3.5. Interferometry

Another technique to overcome the limitations of small angular sizes of asteroids, in order to measure their sizes, shapes, and possible presence of satellites, is interferometry. An astronomical interferometer combines coherently (i.e., conserving the phase information) the light from two or more apertures of the same telescope or of distinct telescopes spaced by a distance B. The spatial resolution (in radians) is of the order of λ/B where λ is the wavelength.

In the following, we give a basic introduction to interferometry of asteroids. Further details can be found in the following works: *Jankov* (2010) and *Matter et al.* (2013) for a broad introduction to astronomical optical interferometry, methods and instrumentation; *Delbo et al.* (2009) for a description of the techniques, and the models for deriving the size and basic shape proprieties of asteroids from the ESO Very Large Telescope Interferometer (VLTI) MID-infrared Interferometric instrument (MIDI) data; *Carry et al.* (2015) for an extension of the technique of *Delbo et al.* (2009) to the determination of the sizes and the separation of binary asteroids; *Matter et al.* (2011) for a description and the extension of a thermophysical model to the analysis of interferometric data of asteroids with the aim of obtaining surface properties such as the thermal inertia.

Interferometers measure the coherence function of the source, also called the interferometric visibility, which is given by the ratio between the correlated and the total flux. The correlated flux is the amount of flux in the interferometric fringes. More precisely the correlated flux is the Fourier transform of the brightness distribution of the source measured on the interferometer's baseline projected on the plane of the sky (see *Delbo et al.*, 2009, for example, and references therein).

The Fine Guidance Sensors (FGS) aboard the Hubble Space Telescope (HST) are optical white-light shearing interferometers (*Nelan et al.*, 1998) that combine the light from distinct apertures of the HST primary mirror and have been used to measure the size and basic shape properties of asteroids (*Hestroffer et al.*, 2002; *Tanga et al.*, 2003). HST/FGS data have clearly demonstrated the bi-lobed nature of some bodies such as (216) Kleopatra (*Tanga et al.*, 2001) and (624) Hektor (*Tanga et al.*, 2003), but were not able to detect the presence of the little moons orbiting these asteroids (*Descamps et al.*, 2011; *Marchis et al.*, 2014), due to the large magnitude difference between the asteroids and their respective moons. Despite the impressive angular resolution of a few mas, corresponding to a few kilometers at a distance of 1.2–1.5 au, a clear limitation of HST/FGS asteroid studies is the bright limiting magnitude of the instrument of about $V \sim 13$–14 mag (*Tanga et al.*, 2003). A recapitulation of the HST/FGS asteroids results can be found in *Dotto et al.* (2002).

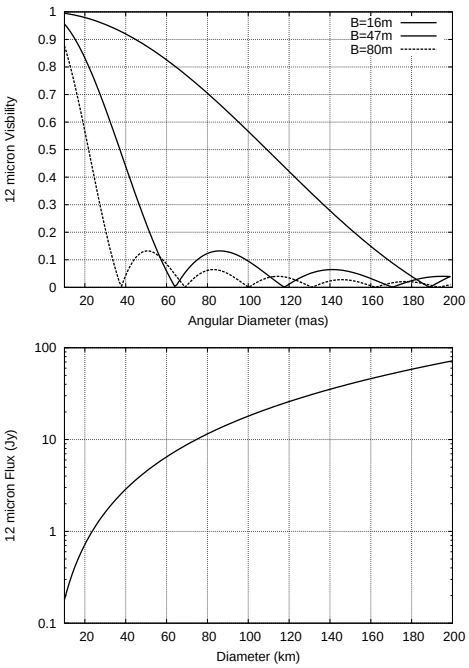

Fig. 8.— Visibility and total flux for an asteroid at 2.5 au from Sun and 1.5 au from Earth as a function of its diameter for different values of the baseline. The MIDI limiting correlated flux (flux times visibility) is 0.5–1 Jy and 10–20 Jy for the UTs and the ATs respectively. Similar limiting fluxes are expected for MATISSE. See text for further details.

Ground-based interferometry is limited to observation of bright targets because of the requirement to take exposures shorter than the atmospheric coherence time of a few milliseconds. The limiting magnitudes of ground-based long-baseline interferometers and the intrinsic low surface brightness of asteroids, have prevented the use of these instruments for the studies of small solar system bodies until the availability of the VLTI.

Interferometry in the mid-infrared was proven to be also very sensitive to the global shape of asteroids and also to their surface characteristics (*Matter et al.*, 2011, 2013). In particular, since observations are typically carried out in the thermal infrared (8–13 μm), MIDI data are sensitive to the surface temperature distribution, which is strongly affected by the value of the thermal inertia (*Delbo et al.*, this volume).

Figure 8 shows the visibility and the total flux as a function of the angular diameter of an asteroid at 2.5 au from Sun and at 1.5 au from Earth, where 1 mas roughly corre-

sponds to 1 km on the asteroid. Note that main-belt asteroids smaller than ~ 20 km cannot be easily observed with MIDI at the VLTI. There are about thousand known asteroids with diameter above 20 km, implying that interferometry is potentially an interesting technique for shape modelling. On the other hand, as interferometry in the thermal infrared is sensitive to the spatial distribution of the temperature on the asteroid surface, this technique can be used to determine thermophysical properties of asteroids when the body shapes are known as demonstrated by *Matter et al.* (2011, 2013).

Each VLTI baseline can be used with MIDI only one at the time. MIDI will likely be decommissioned in the near future to be substituted after 2016 by the Multi AperTure mid-Infrared SpectroScopic Experiment (MATISSE). This instrument will combine up to four Unit Telescopes (UTs) or Auxiliary Telescopes (ATs), allowing six simultaneous baselines. This feature will enable us to measure the spatial distribution of the infrared flux along different directions. MATISSE will also measure closure phase relations and thus offer an efficient capability for image reconstruction. In addition to the N band, the MATISSE will also operate in the L and M bands. Unfortunately, MATISSE is not expected to be more sensitive than MIDI.

Another second generation instrument at the VLTI, GRAVITY, that will combine the light from all four UTs, will offer further improvements in spatial resolution compared to MIDI and MATISSE (though with more a more stringent $V \lesssim 11$ limiting magnitude). It will provide near-infrared adaptive-optics assisted precision narrow-angle (about $4''$) astrometry at the $10\,\mu$as level in the K band ($2.2\,\mu$m). Both the reference star and the science object have to lie within the $\sim 4''$ field of view. In imaging mode, GRAVITY can achieve a resolution of ~ 3 mas in the near-IR (*Eisenhauer et al.*, 2008). The imaging mode can be interesting to precisely measure the sizes and the orbits of the satellites of large asteroids, the latter with $V \lesssim 11$ mag.

AMBER is the current near-infrared focal instrument of the VLTI. It operates in the J, H, and, K bands (i.e., from 1.0 to $2.4\,\mu$m). The AMBER limiting magnitude for asteroid observations is $V \sim 9$ mag. There is only a handful of asteroids brighter than this limit. These bodies are also the largest ones with angular extensions generally >100 mas, implying a very low visibility in the J-H-K with the UTs baselines. Although the photometric flux of these few asteroids is such that $H < 7.5$ mag, their correlated magnitudes due to the low visibilities are much higher than 7.5 mag, preventing their fringe detection and tracking in the near-IR.

However, one of the most interesting instruments for asteroid ground based interferometry is the Large Binocular Telescope Interferometer (LBTI). It consists of two 8.4-m telescopes mounted side by side in a single mount, with a 14.4-m center-to-center spacing. This configuration offers a unique capability for interferometry of a Fizeau beam combination. This offers a wide field of view ($\sim$10–$20''$) and low thermal background. For example, the LINC-NIRVANA instrument can – in principle – be able to resolve binary asteroids whose components are separated $>$ 20 mas. This will allow splitting many binary asteroids.

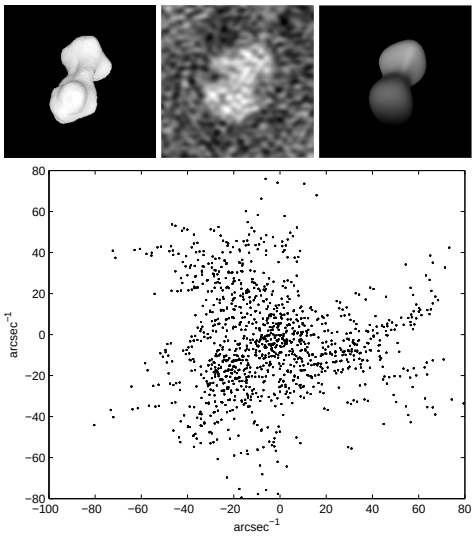

Fig. 9.— Simulated infrared flux from an asteroid (left, a radar shape model of Kleopatra by *Ostro et al.*, 2000) and a "dirty image" (center) with atmospheric noise, obtained by transforming the incompletely sampled frequency plane (bottom, 6000 points, 50 antennas). The smallest resolvable detail is approximately 10 mas. Provided enough observations at different geometries are available (here eight observation runs were used), a shape model (right) can be constructed directly from the raw interferometric data.

Another important source of interferometric data in the near future is the Atacama Large Millimeter Array (ALMA). It will provide resolution ~ 5 mas at 0.3 mm and a dense mesh of baselines, thus enabling "imaging" of hundreds of asteroids in the main belt (*Busch*, 2009). A useful feature of the multimodal inversion is that the raw ALMA (and any other interferometric) data can be used directly as the original Fourier transform: there is no need to reconstruct the image estimate. What is more, the reconstruction of the overall shape is insensitive to inaccuracies and uncertainties in the thermal model used because the model is determined mainly by the boundary of the projection, the distribution of brightness inside the boundary is much less important (*Viikinkoski and Kaasalainen*, 2014; *Viikinkoski et al.*, 2015). An example of inversion of simulated ALMA data is shown in Fig. 9

Long-baseline interferometry can also represent a novel approach to determine the masses and the densities of asteroids in a range of sizes and distances never studied before. In particular, modern interferometers such as the VLTI, LBTI and the Magdalena Ridge Observatory Interferometer

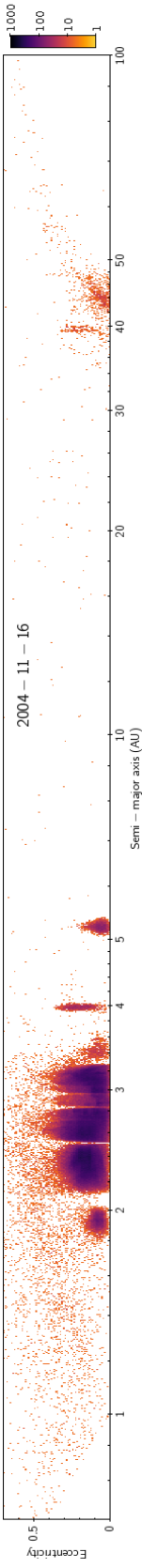

can spatially resolve binary asteroids discovered by photometric lightcurves in the main belt (*Carry et al.*, 2015). The separation of the components of these systems is too narrow for traditional observational techniques such as AO at 10-m class telescopes.

3.6. Direct size measurement with ESA Gaia

The ESA Gaia mission, whose operations started in 2014, will provide accurate astrometry and photometry of asteroids. Photometric data can be used the same way as sparse photometry from ground-based observatories (Sect. 3.1). The potential of Gaia-like data was demonstrated by *Cellino et al.* (2009) on data from the Hipparcos satellite. Apart from disk-integrated brightness, Gaia will provide also direct measurements of asteroid sizes, in a way much similar to the interferometry. Being designed as an astrometry mission at the μas level, the PSF of Gaia is accurately known and stable. Deviations of the PSF from that of a point-like source can thus be measured and used to estimate the apparent size of asteroids.

Owing to the amount of sources observed by Gaia, the satellite does not download images to Earth, but only 1-D flux profiles, corresponding to small 2-D windows centered on targets, stacked along one direction, similar to interferometry in that respect. Interpretation of this 1-D profile relies therefore on the *a priori* knowledge of the 2-D flux distribution on the plane of the sky. In the creation of Gaia catalog, this will be done iteratively, starting from simple spheres at zero phase angle to finally use the spin and tri-axial ellipsoid solutions determined otherwise from Gaia photometry (*Mignard et al.*, 2007; *Cellino et al.*, 2007).

These measurements represent a great opportunity for multi-data inversion algorithms: the measurement of the extension is direct, but clearly requires a realistic description of the projected shape on the plane of the sky. Considering Gaia specifications and observing geometry, *Mignard et al.* (2007) have estimated the fraction of asteroids for which 1-D dimension will be measured with a precision better than 10%. This fraction is highly dependent on diameter, and 20% of asteroids between 20–30 km will be measured at least once, while all asteroids larger than $\sim$ 80 km will be measured repeatedly.

3.7. Disk-integrated radiometry

Measurements of asteroids emission in the thermal infrared – in general at wavelengths between 4–5 and 20–30 μm – are mostly used to determine the sizes of these bodies (*Mainzer et al.*, this volume; *Delbo et al.*, this volume; *Delbo and Harris*, 2002; *Harris and Lagerros*, 2002). Ground based telescopes can only observe in specific windows of the electromagnetic spectrum where the atmosphere is relatively transparent: i.e., the L, M, N, and Q bands at 3, 5, 10, and 20 μm, respectively. However, such observations are strongly affected by the variability of the transparency of the atmosphere and its thermal background. The background also receives contribution from the telescope and the optics. Hence, the thermal infrared observation of asteroids from the ground is limited to relatively bright asteroids ($V \lesssim 18$ mag with 10-m class telescopes). Absolute calibration of the flux is rarely better than 5–10%. On the other hand, in space the instrument calibration is usually stable and there is no need to reduce the thermal background from the atmosphere. As a consequence, space based telescopes such as Spitzer can observe much fainter and smaller asteroids (*Mommert et al.*, 2014), with uncertainties in the calibration that can reach $\sim$ 1% error. Also, from space the range of the observational wavelength is limited only by the detector technology, typically $\sim$ 3.5–50 μm. At longer wavelengths, the telescope optics require cooling and the observation of faint objects is confronted with the background from solar system dust cloud and infrared cirrus.

In the *Asteroids III* era, the main source of thermal infrared observations of asteroids has been the IRAS Minor Planet Survey that collected observations of more than 2200 asteroids (*Tedesco et al.*, 2002). Since then, the NASA Wide-field Infrared Survey Explorer (WISE) has observed more than 130,000 main-belt asteroids (*Mainzer et al.*, this volume; *Masiero et al.*, 2012, 2011), about 500 near-Earth asteroids (*Mainzer et al.*, 2011, 2012b,a), about 1100 Hilda asteroids (*Grav et al.*, 2012a), and almost 2000 Jupiter-Trojan asteroids (*Grav et al.*, 2012b, 2011) in four infrared wavelengths at 3.4, 4.6, 12, and 22 μm; the AKARI space telescope observed more than 5000 asteroids during its mission (*Usui et al.*, 2011, 2013; *Hasegawa et al.*, 2013); the Spitzer space telescope observed hundreds of asteroids (e.g., *Emery et al.*, 2006; *Trilling et al.*, 2010; *Licandro et al.*, 2012, among others); the Herschel Space Observatory, that, due to its longer wavelengths, spanning 55–671 μm, was primarily used to observe trans-Neptunian objects (*Müller et al.*, 2010). For a review about all these missions and their results see *Mainzer et al.*, this volume.

The thermal infrared spectrum of asteroids carries information about their size and surface properties, such as the thermal inertia, roughness and emissivity. These properties are typically derived by interpreting thermal infrared data by means of thermal models (*Mainzer et al.*, this volume; *Delbo et al.*, this volume; *Delbo and Harris*, 2002; *Harris and Lagerros*, 2002). The "simple" thermal models that assume a spherical shape, a Lambertian emission of the surface, and a simplified calculation of the surface temperature distribution are used when we lack knowledge of the asteroid global shape, spin vector and rotation period, which is the majority of the cases. Widely used are, for example, the Near-Earth Asteroid Thermal Model (NEATM, *Harris*, 1998; *Delbo and Harris*, 2002; *Harris and Lagerros*, 2002), or the Standard Thermal Model (STM, *Lebofsky et al.*, 1986; *Harris and Lagerros*, 2002; *Delbo and Harris*, 2002).

However, in order to derive the thermal inertia of an asteroid from measurements of its thermal infrared emission, more sophisticated models, called thermophysical models (TPMs), are needed (*Spencer*, 1990; *Spencer et al.*, 1989;

Lagerros, 1996, 1997, 1998; *Rozitis and Green*, 2011; *Mueller*, 2007; *Delbo*, 2004). Such models are used to calculate the temperature distribution over the body's surface as a function of different parameters, including the thermal inertia. In these models, the asteroid shape is usually fixed and is modeled as a mesh of planar facets. The temperature of each facet is determined by numerically solving the one-dimensional heat diffusion equation using assumed values of the thermal inertia, with the boundary condition given by the time-dependent solar energy absorbed at the surface of the facet (see *Delbo et al.*, this volume, for a review). This latter quantity is calculated from the heliocentric distance of the asteroid, the value assumed for the albedo, and the solar incident angle. Macroscopic surface roughness is usually modelled by adding hemispherical section craters of variable opening angle and variable surface density to each facet. Shadowing and multiple reflections of incident solar and thermally emitted radiation inside craters are taken into account as described by *Spencer* (1990); *Emery et al.* (1998); *Rozitis and Green* (2011) and *Lagerros* (1998). Heat conduction is also accounted for within craters (*Spencer et al.*, 1989; *Spencer*, 1990; *Lagerros*, 1996; *Delbo*, 2004). Surface roughness can be adjusted by changing the opening angle of the craters, the density of the crater distribution, or a combination of both (*Mueller*, 2007). The total observable thermal emission is calculated by summing the contributions from each facet visible to the observer. Model parameters are adjusted until the best agreement with observational data is obtained, i.e., the least-squares residual of the fit is minimized, thereby constraining the physical properties (albedo, size, macroscopic roughness, and thermal inertia) of the asteroid.

From the point of view of multi-data inversion however, the optimization of thermophysical parameters as described above is a two-step process – first, the spin and shape model is derived from one data type (photometry, radar,...), then this model is fixed and used for deriving thermophysical parameters from another data type (thermal infrared). This approach lacks the possibility to weight the two data types with respect to each other. Moreover, the thermophysical parameters can be very sensitive to small modifications of the input shape and spin, so various modifications of the shape should be tested to see how stable the solution is (*Hanuš et al.*, 2015). Ideally, one should model shape and spin parameters together with thermal parameters. This multi-data approach using lightcurves and thermal infrared data simultaneously was successfully tested by *Ďurech et al.* (2012); *Ďurech et al.* (2014) and in principle it can be used also to data that are sparse in time.

3.8. Radar

Radar observations that measure the distribution of echo power in time delay and Doppler frequency (so-called range-Doppler or delay-Doppler measurements) are discussed in detail in *Ostro et al.* (2002) and in *Benner et al.* (this volume). The delay-Doppler projection is many-to-one mapping of a 3-D surface of the target into a 2-D "image". Each pixel on the image represents a bin containing integrated echo power from surface elements that have the same distance from the radar and the same relative speed (due to the rotation of the asteroid). From the point of view of inversion, images in the range-Doppler plane are generalized projections that can automatically be handled with the general procedure discussed in Sect. 2 and in detail in *Viikinkoski and Kaasalainen* (2014) and *Viikinkoski et al.* (2015). In this approach, the multi-mode reconstruction is tuned to produce models with intermediate scale resolution ($\sim$1/10 of the diameter) since these are computationally inexpensive (can be obtained in a few minutes with a laptop), and data sources other than radar do not contain more detailed information. An example of radar range-Doppler data of asteroid 2000 ET_{70} is shown in Fig. 10 and the corresponding reconstructed shape model in Fig. 11. If detailed radar data are available, such model can then be further refined (*Naidu et al.*, 2013) with the radar techniques described by *Benner et al.* (this volume).

Due to the steep decrease of echo power with the distance to the object (the fourth power of the distance), asteroids achievable by current radar facilities Arecibo and Goldstone are only close-approaching near-Earth asteroids or the largest members of the main belt. A number of exam-

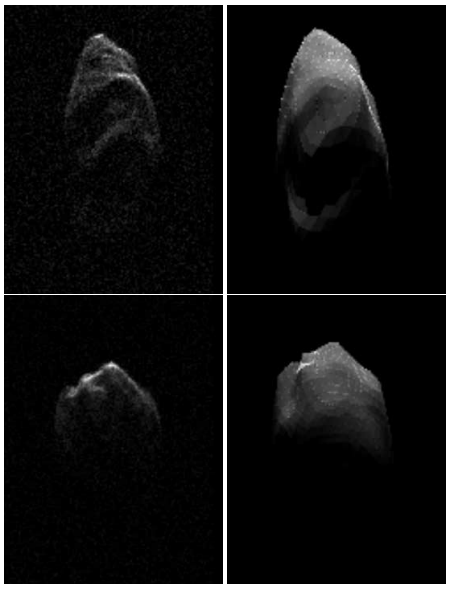

Fig. 10.— Example range-Doppler radar images (left) of asteroid 2000 ET_{70} observed at Arecibo observatory (*Naidu et al.*, 2013). Range and frequency resolutions are 15 m and 0.075 Hz, respectively. Range increases towards the bottom, Doppler frequency increases to the right. The simulated images (right) correspond to the reconstructed shape model in Fig. 11.

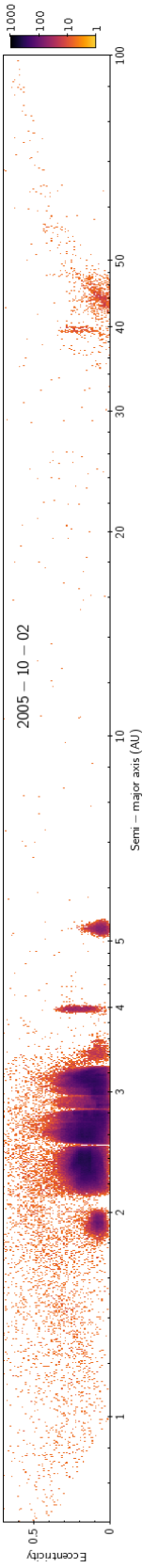

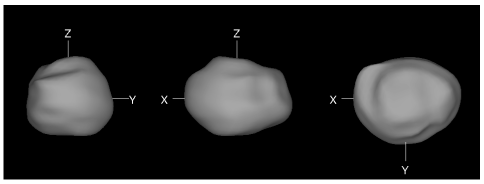

Fig. 11.— Shape model of the asteroid 2000 ET_{70} reconstructed from Arecibo and Goldstone delay-Doppler radar images with ADAM (Sect. 3.11).

ples of what can be reconstructed from radar data is given by *Benner et al.* (this volume).

3.9. Asteroid interior

We briefly discuss here the interesting possibility of peer into an asteroid. This is somewhat separate from the remote-sensing framework as the data can only be obtained in situ; on the other hand, such data can be acquired with the future space missions. The most practical option is to plant radio transmitters/receivers on the surface of a kilometer-sized asteroid and measure low-frequency (~ 100 MHz) signals between these and an orbiter when they pass through the interior of the target.

The most robust observables are simply signal travel-time data (*Pursiainen and Kaasalainen*, 2013). These allow an efficient formulation of the inverse problem via the refraction index and are relatively insensitive to noise and model error. Nevertheless, they suffice to give a coarse-scale picture of the general distribution of permittivity inside the asteroid, as well as the locations and sizes of large anomalies (sudden low- or high-density regions such as voids or heavier minerals). This approach has also been robustly tested in laboratory conditions (*Pursiainen and Kaasalainen*, 2014b). A more refined possibility is to measure changes in the pulse profile, although this is more prone to errors (*Pursiainen and Kaasalainen*, 2014a). The interior of the asteroid is practically impossible to model accurately in three dimension since it is supposed to have a number of cracks, voids, discontinuities etc., all refracting and reflecting the radio waves in complicated ways. Thus a very robust scheme is essential for extracting the available information with stability. Regardless of the data type, one or two transmitters on the surface are not sufficient for a unique solution. A tetrahedral configuration of four transmitters would be ideal, but this places heavy demands on the payload design.

3.10. Extension of the model

So far, we assumed that the asteroid can be described as a solid single body with constant spin vector, i.e., rotating along the axis with the maximum moment of inertia with a constant rotation rate. Although this model represents a typical asteroid, there are other configurations that can be also treated with an extension of the simple model.

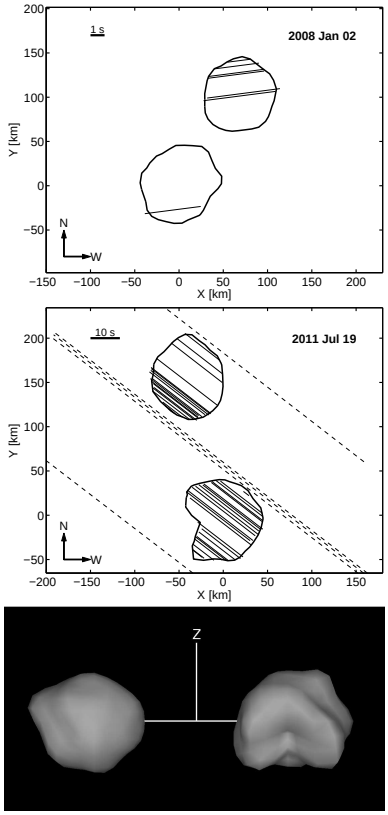

Fig. 12.— Shape model of (90) Antiope seen form its equator (bottom) reconstructed from lightcurves and two occultations observed in 2008 and 2011 (top and middle). The model silhouette is projected on the plane of the sky, the solid lines are positive chords, the dashed ones are negative observations.

3.10.1. Binaries

Binary asteroids form a significant part of the population of small asteroids. *Pravec et al.* (2006) estimated that the fraction of binaries is 15% for the near-Earth population and a similar fraction is assumed for the main-belt population in the same size range (*Margot et al.*, this volume). The formation, dynamics, and physical properties of binary and multiple asteroid systems are discussed in detail in other chapters of this volume (*Walsh et al.*, *Margot et al.*). In general, modeling of such systems is more complex because the dynamics has to be taken into account. However, in some cases described below, the technique used for modeling single asteroids can be used also for multiple systems or at least their primary components.

For binary (or multiple) systems where the primary com-

ponent is much larger than the satellite, the photometric signal from the satellite can be neglected and the primary can be modeled as a single body. For such systems, the shape of the primary and the constraints on its gravitational quadrupole J_2 from the orbit analysis of the secondary can be used to investigate the distribution of the density (*Berthier et al.*, 2014; *Takahashi and Scheeres*, 2014).

For systems with comparable sizes, the problem becomes complicated when the system is asynchronous, i.e., when the rotation period of the primary is different from the orbital period of the secondary. Such systems are usually modeled as two ellipsoids (*Scheirich and Pravec*, 2009), although more general models were created from radar observation (1999 KW_4, for example, see *Ostro et al.*, 2006).

Fully synchronous binaries can be approximated by single bodies if the separation of their components is not large. Even a convex model can provide a good fit to the lightcurves (*Ďurech and Kaasalainen*, 2003). Such model does not represent the true configuration of the system, of course, but it provides the correct rotation period and direction of the orbital plane.

When the separation of components is larger, the system has to be modeled as two-component. However, from the modeling point of view, it is just a moderate modification of the nonconvex problem, where the system is described by only one rotation/orbital period and orientation of the normal of the orbital plane (parallel to the spins of the bodies). If the model is based on lightcurves only, the spin and period parameters can be reconstructed accurately, but the uncertainty in shapes is large. As has been shown by *Marchis et al.* (2014) on (624) Hektor, the distinction between a highly nonconvex single body, two bodies in contact, or two bodies orbiting each other is difficult to make.

An example of reconstruction of a doubly synchronous binary system (90) Antiope from lightcurves and occultations is shown in Fig. 12, where the model is shown together with the silhouettes from occultations. Tens of chords observed during the occultation in 2011 (*Colas et al.*, 2012) portray the two components to details unattainable by any other observational technique and the large set of lightcurves observed over many apparitions constrains the rotational parameters. A similar model can be obtained also by using lightcurves separately to create a scale-free model that is then scaled by occultation data (the Shaping Asteroids with Genetic Evolution algorithm, *Bartczak et al.*, 2014). However, this two-step approach lacks the advantages of simultaneous inversion where the two data types can be weighted with respect to each other.

3.10.2. YORP effect

As described in detail by *Vokrouhlický et al.* (this volume), rotation state of small asteroids is affected by the anisotropic recoil of scattered sunlight and thermal radiation, which causes a net torque called the Yarkovsky-O'Keefe-Radzievskii-Paddack (YORP) effect. This effect secularly changes the obliquity of the spin vector and the rotation period. Whereas the former is too small to be measured with current data, the latter has been measured on several asteroids (see Table 3 in *Vokrouhlický et al.*, this volume). If the change of the rotation period is larger than the uncertainty of the period, the change can be traced from apparition to apparition as was the case for (54509) YORP (*Lowry et al.*, 2007). In other cases, the effect was much smaller and it revealed itself by the discrepancy between the data and the model assuming the period to be constant (*Kaasalainen et al.*, 2007; *Ďurech et al.*, 2008, 2012; *Lowry et al.*, 2014).

The YORP effect is easy to include into the model. We assume that the rotation rate ω changes linearly in time t as $\mathrm{d}\omega/\mathrm{d}t = v$. Then the parameter v is another free parameter of the modeling. Because the shift in the rotation phase increases quadratically in time as $\phi = \omega t + 1/2 v t^2$, even small changes $\mathrm{d}\omega/\mathrm{d}t$ of the order 10^{-8} rad/d^{-2} can be detected with data sets covering tens of years.

In principle, the measured value of v can be compared with the theoretical value computed from the spin state, shape, size, and the thermal parameters of the surface with the density as a free parameter. However, due to sensitivity of YORP on small scale details of the shape that are far below the resolution of the model (*Statler*, 2009; *Kaasalainen and Nortunen*, 2013), and the problem of transverse heat diffusion (*Golubov and Krugly*, 2012; *Golubov et al.*, 2014; *Ševeček et al.*, 2015), this can hardly be more than a rough comparison.

Because the YORP effect scales as inverse of the square of the size of asteroid, it becomes more important for small bodies, where it might be necessary to include it into the modeling if the data cover a wider span of time. YORP is assumed to play an important role in many dynamical processes – the distribution of rotation periods and spin obliquities of small asteroids (*Pravec et al.*, 2008; *Hanuš et al.*, 2013b) or the creation of asteroid binaries and asteroid pairs (*Pravec et al.*, 2010), for example. It is important to have more asteroids with YORP detection. Better statistics of values of period change will help to constrain theories of YORP evolution of small asteroids.

3.10.3. Excited rotation

Asteroids rotating in the relaxed mode are fully described by the spin axis direction, rotation rate, and the initial orientation. However, some asteroids are in an excited rotation state, which can be described as a rotating free top. More parameters are needed to describe this tumbling motion (*Kaasalainen*, 2001). The reason why some asteroids are in this state can be (i) primordial, (ii) collisional excitation (*Henych and Pravec*, 2013), or (iii) end state of YORP-driven spin down. The approach to the modeling is in principle the same as for asteroids in principal axis rotation, only the orientation for a given time is given by solving differential equations. From lightcurves, models of asteroids 2008 TC_3 (*Scheirich et al.*, 2010) and (99942) Apophis (*Pravec et al.*, 2014) have been derived. A model of aster-

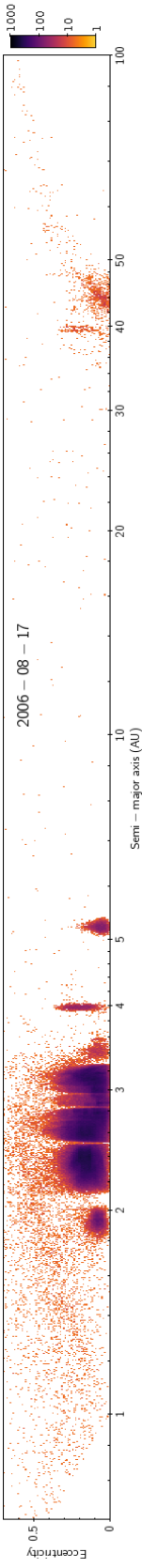

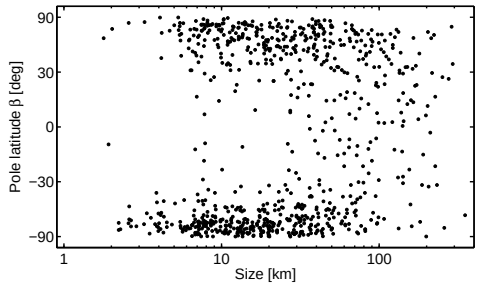

Fig. 13.— Distribution of pole ecliptic latitude β with respect to the size of the asteroid for $\sim$ 800 asteroids. The the scale on the vertical axis is linear in $\sin\beta$, which makes the vertical distribution of points in this plot uniform for an isotropic distribution of spin vectors.

oid (4179) Toutatis (*Hudson et al.*, 2003) was derived from radar data and lightcurves. This model was later compared with the fly-by images of Chang'E-2 mission – the general shape was in agreement, although there were some minor discrepancies (*Zou et al.*, 2014).

3.11. Procedures: Convexinv, KOALA, and ADAM

Software for the inverse problems is available at DAMIT (*http://astro.troja.mff.cuni.cz/projects/asteroids3D*). `Convexinv` is a procedure for lightcurve inversion, while ADAM (All-Data Asteroid Modeling) is a collection of functions from which one can tailor an inversion procedure for any data sources (*Viikinkoski et al.*, 2015). An earlier version of this is called KOALA (Knitted Occultation, Adaptive optics and Lightcurve Analysis, *Carry et al.*, 2012); this is based on lightcurves and silhouette contours obtainable from images and occultations (*Kaasalainen*, 2011; *Kaasalainen and Viikinkoski*, 2012). KOALA is especially suitable for lightcurve and occultation data, while ADAM allows the use of any images (camera, radar, or interferometry) with or without lightcurves without having to process them to extract contours or other information. Both KOALA and ADAM can be used for lightcurves only but, as discussed earlier, this is not reliable. Any resulting shape should only be taken in the global sense (as a more realistic-looking rendering of a convex solution), and the details or nonconvex features are seldom likely to be real (*Viikinkoski et al.*, 2015).

4. WHAT HAVE WE LEARNED FROM 3-D SHAPES?

The purpose of modeling methods described in previous sections is to reveal new facts about the nature of asteroids. The approach is made on two fronts: The first strategy is to use the most abundant data sources (photometry in visual and thermal IR) to produce many low-resolution models that will be a statistically significant sample of the whole asteroid population from which conclusions about the physical properties can be drawn. The second approach is to concentrate on selected targets, obtain as many different data types as possible, create detailed models of these asteroids, and extrapolate the obtained results to the whole class of similar objects. We describe in this section new research areas that directly benefit from availability of spin solutions and 3-D shape models.

4.1. Spin-axis distribution and evolution

One of the main results of the lightcurve inversion is the increasing sample of asteroids with known orientation of the spin axis. For main belt asteroids, the long-known lack of asteroids with poles close to the ecliptic (*Kryszczyńska et al.*, 2007) was confirmed and it was shown that it is more pronounced for smaller asteroids (*Hanuš et al.*, 2011). In Fig. 13, we plot the distribution of pole latitudes for $\sim$800 asteroid models with respect to their size (an updated version of Fig. 5 in *Hanuš et al.*, 2011). The size-dependent structure can be explained by the YORP effect that is more effective on smaller asteroids ($\lesssim$30 km) and pushes them into extreme values of obliquity (0° or 180°). This corresponds to the clustering of pole latitudes towards values of $\pm$90°. Although there are observation and modeling biases that affect the distribution of poles in the sample of available models, their effect is only marginal compared to the strong anisotropy seen in Fig. 13 (*Hanuš et al.*, 2011). The spin-axis orientation of even smaller asteroids ($\lesssim$5 km) is still not known due to the lack of models. For the largest asteroids ($\gtrsim$60 km), there is a statistically significant increase of prograde rotators (98 prograde vs. 63 retrograde in Fig. 13), probably of primordial origin (*Johansen and Lacerda*, 2010).

A different approach to the problem of spin-axis distribution was used by *Bowell et al.* (2014). They analyzed variations of the mean brightness with the ecliptic longitude, from which they estimated ecliptic longitudes of spin axis for about 350,000 asteroids and revealed a clearly non-uniform distribution. However, the explanation of the cause for this non-uniformity is still missing.

With increasing sample of models, it is also possible to study the distribution of spin axes of members of collisional families. Results of *Hanuš et al.* (2013a) agree with theoretical expectations: if the spread in proper semimajor axis increases with decreasing size due to the Yarkovsky effect (*Nesvorný at al.*, *Vokrouhlický et al.*, this volume), asteroids closer to Sun than the center of the family should rotate retrograde, those farther should rotate prograde. This behavior is shown in Fig. 14 for Flora family.

4.2. A pre-requisite in many cases

Unlike most astronomical objects, the viewing geometry of asteroids continuously changes due to their motion relative to observer. As a corollary, knowing their rotation period and spin-vector coordinates is crucial to interpret projected size measurements, and to tie together observations.

As already described in Sect. 3, the spin and 3-D shape

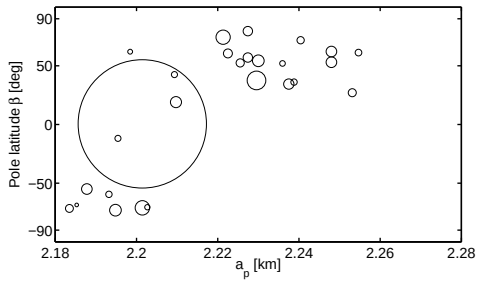

Fig. 14.— Distribution of pole ecliptic latitude β with respect to the proper semimajor axis $a_{\rm p}$ of the Flora family members. The relative size of each circle corresponds to the size of the asteroid.

are required to interpret thermal infrared radiometry, stellar occultations, or apparent sizes measured by Gaia without biases. Similarly, there have been long running discussions to explain inconsistent spectral measurements of asteroids, that can be easily solved once the spin properties (period and orientation) are known: see, for instance, the discussion on (832) Karin by *Sasaki et al.* (2004), *Vernazza et al.* (2007), and *Chapman et al.* (2007), or on (21) Lutetia by *Barucci et al.* (2012).

4.3. Density, composition, and internal structure

Density is one of the most fundamental properties to constrain the composition of asteroids and investigate their internal structure (*Scheeres et al.*, this volume). With the exception of binary asteroids with observable mutual eclipses (*Margot et al.*, this volume), both mass and volume are required to determine the density of an asteroid. Estimating the mass of an asteroid by measuring its gravitational influence on other objects is a challenge because of the relative low mass of asteroids compared to other planetary objects. The number of mass determinations thus limits the number of density estimates. Although there are diameter, hence volume, estimates for all asteroids with a mass determination, the uncertainty in volume generally dominates the balance on density uncertainty (*Carry*, 2012).

In this respect, 3-D shape models are required to determine accurate volume. The level of potential biases increases with stronger assumptions on the shape, and accuracy accounting for systematics improves from sphere, to ellipsoid, to convex hull, to the real shape. In the decade since *Asteroids III*, the number of density estimates has increased from 20 to 300 objects (*Britt et al.*, 2002; *Carry*, 2012). Among these, the most reliable are derived from binary systems for which the volume of the primary was determined after shape modeling (e.g., *Ostro et al.*, 2006; *Shepard et al.*, 2006; *Descamps et al.*, 2009, 2011; *Fang et al.*, 2011; *Marchis et al.*, 2013).

A detailed description on the density of asteroids and their internal structure can be found in *Scheeres et al.* (this volume), from under-dense asteroids, hosting large voids, to over-dense asteroids, likely differentiated. In the context of this chapter, it is important to highlight than only density estimates more precise than 10–20% can be used to discriminate between different analogue meteorites and can provide insights on the internal structure. Such accuracy can only be achieved with volume known to 5–10% or better, which means that a proper description of the 3-D shape is needed.

4.4. Determination of surface properties by means of TPMs

The spin state and shape model of an asteroid is input information for the TPMs. While in the *Asteroids III* era, shape and spin information were available only for a handful of asteroids, preventing application of TPMs to a large number of these bodies, this situation has drastically changed in the last few years. Physical properties (such as the value of the surface thermal inertia) of about 60 asteroids are now available thanks to the application of TPMs (see *Delbo et al.*, this volume). A remarkable improvement in this field is also represented by the availability of high quality thermal infrared data as those produced but the WISE and the Spitzer space telescopes. In the next few years we expect the number of asteroids with known thermal inertia values to grow thanks to the availability of more shape and spin state models.

4.5. Surface re-arrangement

From the spin, 3-D shape, and density, the local gravity at the surface can be computed. Unsuspected physics has been unveiled with the modeling of the near-Earth asteroid (66391) 1999 KW_4 by *Ostro et al.* (2006). Some small asteroids present an equatorial bulge, presumably generated by regolith migration toward lower gravity regions. This process can even form binary systems if the asteroids spin fast enough (*Walsh et al.*, 2008; *Harris et al.*, 2009).

4.6. Cratering events

An evident outcome of shape modeling is the capability to detect large impact craters and basins. Aside from the spacecraft encounters, the first detection was the large impact basin on Vesta, progenitor of the Vestoids (*Binzel and Xu*, 1993), detected with the HST (*Thomas et al.*, 1997) and confirmed by NASA Dawn spacecraft (*Russell et al.*, 2012). Another case is the recent impact suffered by asteroids (596) Scheila, detected by the presence of a dust tail (*Bodewits et al.*, 2011). Lightcurves obtained before and after the impact, under similar geometries are different, revealing different surface properties (*Bodewits et al.*, 2014).

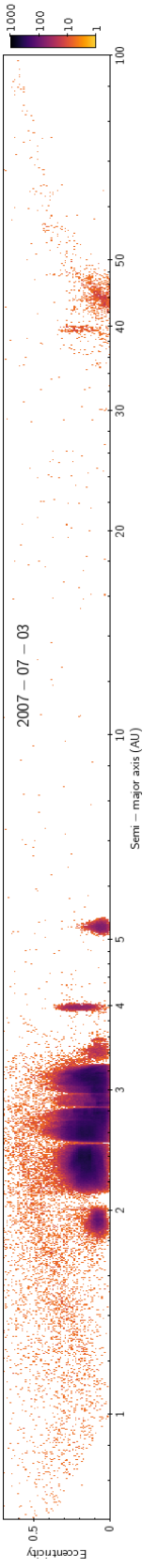

TABLE 1
A LIST OF OBSERVATION TECHNIQUES AND DERIVABLE PHYSICAL PROPERTIES.

Technique	Period	Spin	Size	Shape	Thermal Inertia	Number of models		
						Asteroids III	Asteroids IV	Asteroids V
Photometry	X	X		X		30	500	10^4
Images		X	X	X		5	50	10^2
Occultation		X	X	X		5*	50	10^2
Radar	X	X	X	X		10	30	10^2
Radiometry			X		X	10*	20	10^4
Interferometry		X	X	X		5†	< 10	10^2
Fly-by	X	X	X	X	X	6	10	< 15

The "X" mark indicates which physical properties are derivable from which technique. The number of models available at the time of *Asteroids III* book (Asteroids III) and now (Asteroids IV) is only approximate. The Asteroids V column is an order-of-magnitude estimate for the next decade.

*Ellipsoidal models.

†HST/FGS.

4.7. Mass distribution

Because some asteroids are less or more dense than their most-likely constituents, the question of the mass distribution (denser material or voids) in their interior can be asked. This question is intrinsically tied with the study of the gravity field around the asteroid. The latter has been measured during spacecraft encounters (see *Miller et al.*, 2002, for instance), but studies from Earth-bound observations have recently appeared. By comparing the spherical harmonics of the gravity field as determined from the orbit of a natural satellite, with the expected coefficients resulting from the 3-D shape model, the hypothesis of homogeneous mass distribution can be tested (*Vachier et al.*, 2012; *Berthier et al.*, 2014; *Takahashi and Scheeres*, 2014).

5. FUTURE

In the decade since *Asteroids III*, where the principles of lightcurve inversion based on dense-in-time series were presented (*Kaasalainen et al.*, 2002b), the number of models has seen a tenfold increase – from a few tens to a few hundreds (Table 1). The increasing availability of sparse-in-time photometry, and its appropriate handling in the inversion, coupled with a dramatic increase of computer time (thanks to projects like Asteroids@Home) have made this possible. Upcoming all-sky surveys such as Pan-STARRS, LSST, and Gaia are expected to produce enormous data sets and there is little doubt that thousands of models will be derived in the next decade. Our knowledge on non-gravitational effects such as YORP and Yarkovsky will directly benefit from this larger sample.

With the large number of data and models, new challenges will arise – how to extract scientifically interesting information from a large set of models of asteroids? With big data flows, the processing has to be automated, with effective data processing. The obvious search for correlations has to be done with care because of large biases in the set of models. Although the importance of detailed models of individual well-studied asteroids will be important, the main shift in paradigm and probably the main source of interesting findings will be in tens of thousands of asteroid models derived from photometry in optical and thermal infrared wavelengths. Only a few years ago, only photometry in the visible was available for a large number of asteroids. The situation drastically changed with WISE catalog of thermal fluxes for 150,000 asteroids. Automatized procedures capable of dealing with photometry in the visible and thermal infrared will yield not only 3-D shape and spin state for thousands of asteroids, but also their diameter, albedo, and thermal inertia of their surface. The later being crucial in interpreting asteroid mineralogy once coupled with spectroscopy (*Reddy et al.*, this volume). Understanding of observational and modeling biases will be crucial for correct interpretation of the results. Connecting spin and shape distribution of asteroids with their orbital and spin evolution will hopefully lead to a clear picture of the evolution of the main asteroid belt. The ultimate goal here is the connection of models of evolution of the main belt with spin-axis evolution and current distribution of asteroid physical properties.

Another approach that is complementary to modeling individual objects, is modeling distribution functions of parameters of interest. With any inversion technique and photometric data quality, the number of models will be always much lower than the number of known asteroids just because it takes time to collect enough data at different geometries. So instead of aiming to create unique models for a statistically significant sample of the (sub)populations

with known observational and modeling bias, one can use other observables than the time–brightness pairs. With this approach, there is almost no "wasting" of data because essentially all photometric points are used in the statistical approach. The aim is to model characteristics of a given asteroid population as a whole when there are not enough data to model individual members. One of the observables can be, for example, the mean brightness over one apparition (*Bowell et al.*, 2014) and its dispersion that correlates with lightcurve amplitude. If there are not enough data points to estimate mean brightness and its variance, the statistics of scatter of individual pairs of observations can be used (*Szabó and Kiss*, 2008). If the data come in pairs of observations separated by a constant time interval (like with Pan-STARRS), the rotation period can be estimated (*Ďurech et al.*, 2007).

Another challenge for next decade resides in the derivation of a large sample of higher-resolution models, based on multiple data sources. Building inversion techniques capable of handling different data sources had been highlighted in *Asteroids III* as the next step, and this became reality over the past few years. The models based on multiple data sources are more realistic, more reliable, more precise than the independent analysis of individual data sets. If practical issues of merging data sets arise, mathematical solution have been exposed, and algorithms and software are ready and freely available. The current sample of models derived by such methods is nevertheless still limited. If the multi data analysis is more efficient than the independent analysis of the individual data sets, the practical problem of data sharing arises. Although the tools to invert multiple data sources are ready and freely available, the data are still hard to get and harder to share. To maximize the scientific output, it is necessary to combine all available data sources.

The other observing techniques (i.e., disk-resolved imaging, stellar occultations, Gaia size measurements, or radar echoes) will never provide data for more than a few thousands asteroids. The apparent sizes by Gaia will however be measured with a high precision, and will concern a decent sized sample. Because the data will be made public, they should be used on a regular basis for modeling. The number and quality of profiles derived from stellar occultations have always been restricted due to the intrinsic complexity of prediction, and cost of equipment. The parallel availability of low-cost telescopes and cameras, together with the publication of Gaia stellar catalog and asteroid orbits, will open a new age for stellar occultations. Any mass-production procedure of asteroid models should therefore be able to deal not only with photometry (visible and infrared) but also with stellar occultations.

Finally, if the bulk of asteroids are single objects, rotating along their shortest axis, a small fraction will either be in tumbling state, or have satellites. Automatic modeling procedures should be able to detect such cases, triggering detailed analysis of these peculiar targets.

The rising interest of private companies for near-Earth objects as mining resources will inevitably lead to further development of analysis of remote-sensing data, building dedicated ground-based or space telescopes, and eventually moving from asteroids surface into their interiors.

Acknowledgments. The work of JĎ was supported by the grant GACR P209/10/0537 of the Czech Science Foundation. MD acknowledges support from the grant ANR-11-BS56-008 SHOCKS of the French National Research Agency.

REFERENCES

Bartczak P., Michałowski T., Santana-Ros T., et al. (2014). A new non-convex model of the binary asteroid 90 Antiope obtained with the SAGE modelling technique. *Mon. Not. R. Astron. Soc.*, *443*, 1802–1809.

Barucci M. A., Belskaya I. N., Fornasier S., et al. (2012). Overview of Lutetia's surface composition. *Planet. Space Sci.*, *66*, 23–30.

Berthier J., Vachier F., Marchis F., et al. (2014). Physical and dynamical properties of the main belt triple Asteroid (87) Sylvia. *Icarus*, *239*, 118–130.

Binzel R. P. and Xu S. (1993). Chips off of Asteroid 4 Vesta: Evidence for the parent body of basaltic achondrite meteorites. *Science*, *260*, 186–191.

Bodewits D., Kelley M. S., Li J.-Y., et al. (2011). Collisional excavation of asteroid (596) Scheila. *Astrophys. J. Lett.*, *733*, L3.

Bodewits D., Vincent J.-B., and Kelley M. S. P. (2014). Scheila's scar: Direct evidence of impact surface alteration on a primitive asteroid. *Icarus*, *229*, 190–195.

Bowell E., Oszkiewicz D. A., Wasserman L. H., et al. (2014). Asteroid spin-axis longitudes from the Lowell Observatory database. *Meteoritics and Planetary Science*, *49*, 95–102.

Britt D. T., Yeomans D. K., Housen K. R., et al. (2002). Asteroid Density, Porosity, and Structure. In *Asteroids III* (Bottke W. F., Cellino A., Paolicchi P., et al., editors), pp. 485–500. University of Arizona Press, Tucson.

Busch M. W. (2009). ALMA and asteroid science. *Icarus*, *200*, 347–349.

Carbognani A., Tanga P., Cellino A., et al. (2012). The representation of asteroid shapes: A test for the inversion of Gaia photometry. *Planet. Space Sci.*, *73*, 80–85.

Carry B. (2009). *Asteroids physical properties from high angular-resolution imaging*. PhD thesis, Observatoire de Paris.

Carry B. (2012). Density of asteroids. *Planet. Space Sci.*, *73*, 98–118.

Carry B., Dumas C., Fulchignoni M., et al. (2008). Near-infrared mapping and physical properties of the dwarf-planet Ceres. *Astron. Astrophys.*, *478*, 235–244.

Carry B., Dumas C., Kaasalainen M., et al. (2010a). Physical properties of (2) Pallas. *Icarus*, *205*, 460–472.

Carry B., Kaasalainen M., Leyrat C., et al. (2010b). Physical properties of the ESA Rosetta target asteroid (21) Lutetia. II. Shape and flyby geometry. *Astron. Astrophys.*, *523*, A94.

Carry B., Kaasalainen M., Merline W. J., et al. (2012). Shape modeling technique KOALA validated by ESA Rosetta at (21) Lutetia. *Planet. Space Sci.*, *66*, 200–212.

Carry B., Matter A., Scheirich P., et al. (2015). The small binary asteroid (939) Isberga. *Icarus*, *248*, 516–525.

Cellino A. and Dell'Oro A. (2012). The derivation of asteroid physical properties from Gaia observations. *Planet. Space Sci.*, *73*, 52–55.

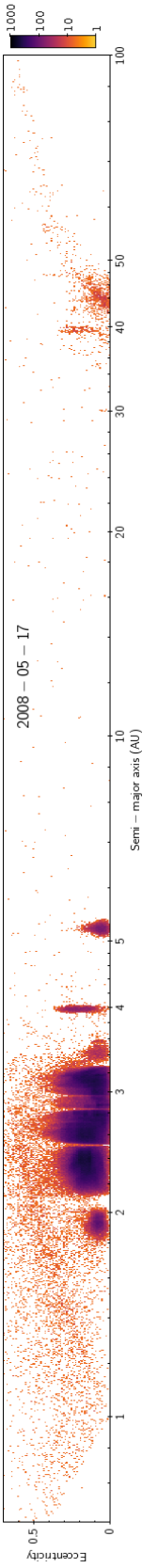

Cellino A., Diolaiti E., Ragazzoni R., et al. (2003). Speckle interferometry observations of asteroids at TNG. *Icarus*, *162*, 278–284.

Cellino A., Hestroffer D., Tanga P., et al. (2009). Genetic inversion of sparse disk-integrated photometric data of asteroids: application to Hipparcos data. *Astron. Astrophys.*, *506*, 935–954.

Cellino A., Tanga P., Dell'Oro A., et al. (2007). Asteroid science with Gaia: Sizes, spin properties, overall shapes and taxonomy. *Advances in Space Research*, *40*, 202–208.

Chapman C. R., Enke B., Merline W. J., et al. (2007). Young Asteroid 832 Karin shows no rotational spectral variations. *Icarus*, *191*, 323–329.

Colas F., Berthier J., Vachier F., et al. (2012). Shape and size of (90) Antiope derived from an exceptional stellar occultation on July 19, 2011. *LPI Contributions*, *1667*, 6427.

Conan J.-M., Fusco T., Mugnier L. M., et al. (2000). MISTRAL: Myopic deconvolution method applied to ADONIS and to simulated VLT-NAOS images. *The Messenger*, *99*, 38–45.

Conrad A. R., Dumas C., Merline W. J., et al. (2007). Direct measurement of the size, shape, and pole of 511 Davida with Keck AO in a single night. *Icarus*, *191*, 616–627.

Delbo M. (2004). The nature of near-Earth asteroids from the study of their thermal infrared emission. *PhD thesis*, pp. 1–210.

Delbo M. and Harris A. W. (2002). Physical properties of near-Earth asteroids from thermal infrared observations and thermal modeling. *Meteoritics & Planetary Science*, *37*, 1929–1936.

Delbo M., Ligori S., Matter A., et al. (2009). First VLTI-MIDI direct determinations of asteroid sizes. *Astrophys. J.*, *694*, 1228–1236.

Descamps P., Marchis F., Berthier J., et al. (2011). Triplicity and physical characteristics of Asteroid (216) Kleopatra. *Icarus*, *211*, 1022–1033.

Descamps P., Marchis F., Pollock J., et al. (2008). New determination of the size and bulk density of the binary Asteroid 22 Kalliope from observations of mutual eclipses. *Icarus*, *196*, 578–600.

Descamps P., Marchis F., Ďurech J., et al. (2009). New insights on the binary asteroid 121 Hermione. *Icarus*, *203*, 88–101.

Dotto E., Barucci M. A., Müller T. G., et al. (2002). Observations from orbiting platforms. In *Asteroids III* (Bottke W. F., Cellino A., Paolicchi P., et al., editors), pp. 219–234. University of Arizona Press, Tucson.

Drummond J., Eckart A., and Hege E. K. (1988). Speckle interferometry of asteroids. IV - Reconstructed images of 4 Vesta. *Icarus*, *73*, 1–14.

Drummond J. D., Cocke W. J., Hege E. K., et al. (1985). Speckle interferometry of asteroids. I - 433 Eros. *Icarus*, *61*, 132–151.

Drummond J. D., Conrad A., Merline W., et al. (2009). The dimensions and pole of asteroid (21) Lutetia from adaptive optics images. *AAS/Division for Planetary Sciences Meeting Abstracts*, *41*, # 59.07.

Dunham D. W., Herald D., Frappa E., et al. (2014). Asteroid Occultations V12.0. *NASA Planetary Data System*, *216*.

Ďurech J. and Kaasalainen M. (2003). Photometric signatures of highly nonconvex and binary asteroids. *Astron. Astrophys.*, *404*, 709–714.

Ďurech J., Grav T., Jedicke R., et al. (2005). Asteroid models from the Pan-STARRS photometry. *Earth, Moon, and Planets*, *97*, 179–187.

Ďurech J., Scheirich P., Kaasalainen M., et al. (2007). Physical models of asteroid from sparse photometric data. In *Near Earth Objects, our Celestial Neighbors: Opportunity and Risk* (Milani A., Valsecchi G. B., and Vokrouhlický D., editors), p. 191. Cambridge University Press, Cambridge.

Ďurech J., Vokrouhlický D., Kaasalainen M., et al. (2008). Detection of the YORP effect in asteroid (1620) Geographos. *Astron. Astrophys.*, *489*, L25–L28.

Ďurech J., Kaasalainen M., Warner B. D., et al. (2009). Asteroid models from combined sparse and dense photometric data. *Astron. Astrophys.*, *493*, 291–297.

Ďurech J., Kaasalainen M., Herald D., et al. (2011). Combining asteroid models derived by lightcurve inversion with asteroidal occultation silhouettes. *Icarus*, *214*, 652–670.

Ďurech J., Delbo M., and Carry B. (2012). Asteroid models derived from thermal infrared data and optical lightcurves. *LPI Contributions*, *1667*, 6118.

Ďurech J., Vokrouhlický D., Baransky A. R., et al. (2012). Analysis of the rotation period of asteroids (1865) Cerberus, (2100) Ra-Shalom, and (3103) Eger – search for the YORP effect. *Astron. Astrophys.*, *547*, A10.

Ďurech J., Hanuš J., Delbo M., et al. (2014). Physical properties of asteroids derived from a novel approach to modeling of optical lightcurves and WISE thermal infrared data. In *AAS/Division for Planetary Sciences Meeting Abstracts*, volume 46 of *AAS/Division for Planetary Sciences Meeting Abstracts*, p. #509.11.

Eisenhauer F., Perrin G., Brandner W., et al. (2008). GRAVITY: getting to the event horizon of Sgr A*. In *Society of Photo-Optical Instrumentation Engineers (SPIE) Conference Series*, volume 7013.

Emery J. P., Cruikshank D. P., and Van Cleve J. (2006). Thermal emission spectroscopy (5.2–38 μm) of three Trojan asteroids with the Spitzer Space Telescope: Detection of fine-grained silicates. *Icarus*, *182*, 496–512.

Emery J. P., Sprague A. L., Witteborn F. C., et al. (1998). Mercury: Thermal modeling and mid-infrared (5–12 μm) observations. *Icarus*, *136*, 104–123.

Fang J., Margot J.-L., Brozovic M., et al. (2011). Orbits of near-Earth asteroid triples 2001 SN263 and 1994 CC: Properties, origin, and evolution. *Astron. J.*, *141*, 154–169.

Gaskell R. W., Barnouin-Jha O. S., Scheeres D. J., et al. (2008). Characterizing and navigating small bodies with imaging data. *Meteoritics and Planetary Science*, *43*, 1049–1061.

Golubov O. and Krugly Y. N. (2012). Tangential component of the YORP effect. *Astrophys. J. Lett.*, *752*, L11.

Golubov O., Scheeres D. J., and Krugly Y. N. (2014). A three-dimensional model of tangential YORP. *Astrophys. J.*, *794*, 22.

Grav T., Mainzer A. K., Bauer J., et al. (2012a). WISE/NEOWISE observations of the Hilda population: Preliminary results. *Astrophys. J.*, *744*, 197.

Grav T., Mainzer A. K., Bauer J., et al. (2011). WISE/NEOWISE observations of the Jovian Trojans: Preliminary results. *Astrophys. J.*, *742*, 40.

Grav T., Mainzer A. K., Bauer J. M., et al. (2012b). WISE/NEOWISE observations of the Jovian Trojan population: Taxonomy. *Astrophys. J.*, *759*, 49.

Hanuš J., Delbo M., Ďurech J., et al. (2015). Thermophysical modeling of asteroids from WISE thermal data – Significance of the shape model and the pole orientation uncertainties. *Icarus, submitted*, *0*, 0.

Hanuš J., Marchis F., and Ďurech J. (2013a). Sizes of main-belt asteroids by combining shape models and Keck adaptive optics observations. *Icarus*, *226*, 1045–1057.

Hanuš J., Ďurech J., Brož M., et al. (2013b). Asteroids' physical models from combined dense and sparse photometry and scaling of the YORP effect by the observed obliquity distribution. *Astron. Astrophys.*, *551*, A67.

Hanuš J., Ďurech J., Brož M., et al. (2011). A study of asteroid pole-latitude distribution based on an extended set of shape models derived by the lightcurve inversion method. *Astron. Astrophys.*, *530*, A134.

Harris A. W. (1998). A thermal model for near-Earth asteroids. *Icarus*, *131*, 291–301.

Harris A. W., Fahnestock E. G., and Pravec P. (2009). On the shapes and spins of "rubble pile" asteroids. *Icarus*, *199*, 310–318.

Harris A. W. and Lagerros J. S. V. (2002). Asteroids in the thermal infrared. In *Asteroids III* (Bottke W. F., Cellino A., Paolicchi P., et al., editors), pp. 139–150. University of Arizona Press, Tucson.

Harris A. W., Pravec P., and Warner B. D. (2012). Looking a gift horse in the mouth: Evaluation of wide-field asteroid photometric surveys. *LPI Contributions*, *1667*, 6069.

Hasegawa S., Müller T. G., Kuroda D., et al. (2013). The asteroid catalog using AKARI IRC slow-scan observations. *PASJ*, *65*, 34.

Henych T. and Pravec P. (2013). Asteroid rotation excitation by subcatastrophic impacts. *Mon. Not. R. Astron. Soc.*, *432*, 1623–1631.

Hestroffer D., Tanga P., Cellino A., et al. (2002). Asteroids observations with the Hubble Space Telescope. I. Observing strategy, and data analysis and modeling process. *Astron. Astrophys.*, *391*, 1123–1132.

Hom E. F. Y., Marchis F., Lee T. K., et al. (2007). AIDA: an adaptive image deconvolution algorithm with application to multi-frame and three-dimensional data. *Journal of the Optical Society of America A*, *24*, 1580–1600.

Hudson R. S., Ostro S. J., and Scheeres D. J. (2003). High-resolution model of Asteroid 4179 Toutatis. *Icarus*, *161*, 346–355.

Jankov S. (2010). Astronomical optical interferometry. I. Methods and instrumentation. *Serbian Astronomical Journal*, *181*, 1–17.

Johansen A. and Lacerda P. (2010). Prograde rotation of protoplanets by accretion of pebbles in a gaseous environment. *Mon. Not. R. Astron. Soc.*, *404*, 475–485.

Jorda L., Lamy P. L., Gaskell R. W., et al. (2012). Asteroid (2867) Steins: Shape, topography and global physical properties from OSIRIS observations. *Icarus*, *221*, 1089–1100.

Kaasalainen M. (2001). Interpretation of lightcurves of precessing asteroids. *Astron. Astrophys.*, *376*, 302–309.

Kaasalainen M. (2004). Physical models of large number of asteroids from calibrated photometry sparse in time. *Astron. Astrophys.*, *422*, L39–L42.

Kaasalainen M. (2011). Maximum compatibility estimates and shape reconstruction with boundary curves and volumes of generalized projections. *Inverse Problems and Imaging*, *5*, 37–57.

Kaasalainen M. and Lamberg L. (2006). Inverse problems of generalized projection operators. *Inverse Problems*, *22*, 749–769.

Kaasalainen M., Mottola S., and Fulchignomi M. (2002a). Asteroid models from disk-integrated data. In *Asteroids III* (Bottke W. F., Cellino A., Paolicchi P., et al., editors), pp. 139–150. University of Arizona Press, Tucson.

Kaasalainen M. and Nortunen H. (2013). Compact YORP formulation and stability analysis. *Astron. Astrophys.*, *558*, A104.

Kaasalainen M. and Torppa J. (2001). Optimization methods for asteroid lightcurve inversion. I. Shape determination. *Icarus*, *153*, 24–36.

Kaasalainen M., Torppa J., and Muinonen K. (2001). Optimization methods for asteroid lightcurve inversion. II. The complete inverse problem. *Icarus*, *153*, 37–51.

Kaasalainen M., Torppa J., and Piironen J. (2002b). Models of twenty asteroids from photometric data. *Icarus*, *159*, 369–395.

Kaasalainen M., Ďurech J., Warner B. D., et al. (2007). Acceleration of the rotation of asteroid 1862 Apollo by radiation torques. *Nature*, *446*, 420–422.

Kaasalainen M. and Viikinkoski M. (2012). Shape reconstruction of irregular bodies with multiple complementary data sources. *Astron. Astrophys.*, *543*, A97.

Kaasalainen S., Kaasalainen M., and Piironen J. (2005). Ground reference for space remote sensing. Laboratory photometry of an asteroid model. *Astron. Astrophys.*, *440*, 1177–1182.

Keller H. U., Barbieri C., Koschny D., et al. (2010). E-Type asteroid (2867) Steins as imaged by OSIRIS on board Rosetta. *Science*, *327*, 190–193.

Kryszczyńska A., La Spina A., Paolicchi P., et al. (2007). New findings on asteroid spin-vector distributions. *Icarus*, *192*, 223–237.

Lagerros J. S. V. (1996). Thermal physics of asteroids. I. Effects of shape, heat conduction and beaming. *Astron. Astrophys.*, *310*, 1011–1020.

Lagerros J. S. V. (1997). Thermal physics of asteroids. III. Irregular shapes and albedo variegations. *Astron. Astrophys.*, *325*, 1226–1236.

Lagerros J. S. V. (1998). Thermal physics of asteroids. IV. Thermal infrared beaming. *Astron. Astrophys.*, *332*, 1123–1132.

Lamberg L. and Kaasalainen M. (2001). Numerical solution of the Minkowski problem. *J. Comp. Appl. Math.*, *137*, 213–227.

Lebofsky L. A., Sykes M. V., Tedesco E. F., et al. (1986). A refined 'standard' thermal model for asteroids based on observations of 1 Ceres and 2 Pallas. *Icarus*, *68*, 239–251.

Li J.-Y., McFadden L. A., Parker J. W., et al. (2006). Photometric analysis of 1 Ceres and surface mapping from HST observations. *Icarus*, *182*, 143–160.

Licandro J., Hargrove K., Kelley M., et al. (2012). 5-14 μm Spitzer spectra of Themis family asteroids. *Astron. Astrophys.*, *537*, A73.

Lowry S. C., Fitzsimmons A., Pravec P., et al. (2007). Direct detection of the asteroidal YORP effect. *Science*, *316*, 272–274.

Lowry S. C., Weissman P. R., Duddy S. R., et al. (2014). The internal structure of asteroid (25143) Itokawa as revealed by detection of YORP spin-up. *Astron. Astrophys.*, *562*, A48.

Mainzer A., Grav T., Bauer J., et al. (2011). NEOWISE Observations of Near-Earth Objects: Preliminary Results. *Astrophys. J.*, *743*, 156.

Mainzer A., Grav T., Masiero J., et al. (2012a). Physical parameters of asteroids estimated from the WISE 3-band data and NEOWISE post-cryogenic survey. *Astrophys. J. Lett.*, *760*, L12.

Mainzer A., Grav T., Masiero J., et al. (2012b). Characterizing subpopulations within the near-Earth objects with NEOWISE: Preliminary results. *Astrophys. J.*, *752*, 110.

Marchis F., Ďurech J., Castillo-Rogez J., et al. (2014). The puzzling mutual orbit of the binary Trojan asteroid (624) Hektor. *Astrophys. J. Lett.*, *783*, L37.

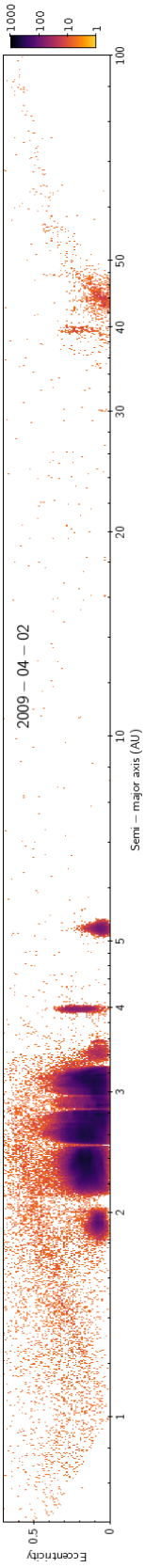

Marchis F., Kaasalainen M., Hom E. F. Y., et al. (2006). Shape, size and multiplicity of main-belt asteroids. *Icarus*, *185*, 39–63.

Marchis F., Vachier F., Ďurech J., et al. (2013). Characteristics and large bulk density of the C-type main-belt triple asteroid (93) Minerva. *Icarus*, *224*, 178–191.

Masiero J., Jedicke R., Ďurech J., et al. (2009). The thousand asteroid light curve survey. *Icarus*, *204*, 145–171.

Masiero J. R., Mainzer A. K., Grav T., et al. (2011). Main belt asteroids with WISE/NEOWISE. I. Preliminary albedos and diameters. *Astrophys. J.*, *741*, 68.

Masiero J. R., Mainzer A. K., Grav T., et al. (2012). Preliminary analysis of WISE/NEOWISE 3-band cryogenic and post-cryogenic observations of main belt asteroids. *Astrophys. J. Lett.*, *759*, L8.

Matter A., Delbo M., Carry B., et al. (2013). Evidence of a metal-rich surface for the asteroid (16) Psyche from interferometric observations in the thermal infrared. *Icarus*, *226*, 419–427.

Matter A., Delbo M., Ligori S., et al. (2011). Determination of physical properties of the asteroid (41) Daphne from interferometric observations in the thermal infrared. *Icarus*, *215*, 47–56.

Merline W. J., Drummond J. D., Carry B., et al. (2013). The Resolved Asteroid Program - Size, shape, and pole of (52) Europa. *Icarus*, *225*, 794–805.

Mignard F., Cellino A., Muinonen K., et al. (2007). The Gaia mission: Expected applications to asteroid science. *Earth Moon and Planets*, *101*, 97–125.

Miller J. K., Konopliv A. S., Antreasian P. G., et al. (2002). Determination of shape, gravity, and rotational state of asteroid 433 Eros. *Icarus*, *155*, 3–17.

Millis R. L. and Dunham D. W. (1989). Precise measurement of asteroid sizes and shapes from occultations. In *Asteroids II* (Binzel R. P., Gehrels T., and Matthews M. S., editors), pp. 148–170.

Mommert M., Farnocchia D., Hora J. L., et al. (2014). Physical properties of near-Earth asteroid 2011 MD. *Astrophys. J. Lett.*, *789*, L22.

Mueller M. (2007). Surface properties of asteroids from mid-infrared observations and thermophysical modeling. *PhD thesis on arXiv.org*, p. 3993.

Mugnier L. M., Fusco T., and Conan J.-M. (2004). MISTRAL: a myopic edge-preserving image restoration method, with application to astronomical adaptive-optics-corrected long-exposure images. *Journal of the Optical Society of America A*, *21*, 1841–1854.

Müller T. G., Lellouch E., Stansberry J., et al. (2010). "TNOs are Cool": A survey of the trans-Neptunian region. I. Results from the Herschel science demonstration phase (SDP). *Astron. Astrophys.*, *518*, L146.

Naidu S. P., Margot J.-L., Busch M. W., et al. (2013). Radar imaging and physical characterization of near-Earth Asteroid (162421) 2000 ET70. *Icarus*, *226*, 323–335.

Nathues A., Mottola S., Kaasalainen M., et al. (2005). Spectral study of the Eunomia asteroid family. I. Eunomia. *Icarus*, *175*, 452–463.

Nelan E. P., Lupie O. L., McArthur B., et al. (1998). Fine guidance sensors aboard the Hubble Space Telescope: the scientific capabilities of these interferometers. In *Astronomical Interferometry* (Reasenberg R. D., editor), volume 3350 of *Society of Photo-Optical Instrumentation Engineers (SPIE) Conference Series*, pp. 237–247.

Ostro S. J., Hudson R. S., Nolan M. C., et al. (2000). Radar observations of asteroid 216 Kleopatra. *Science*, *288*, 836–839.

Ostro S. J., Margot J.-L., Benner L. A. M., et al. (2006). Radar imaging of binary near-Earth asteroid (66391) 1999 KW4. *Science*, *314*, 1276–1280.

Ostro S. J., Rosema K. D., Campbell D. B., et al. (2002). Note: Radar observations of asteroid 1862 Apollo. *Icarus*, *156*, 580–583.

Polishook D., Ofek E. O., Waszczak A., et al. (2012). Asteroid rotation periods from the Palomar Transient Factory survey. *Mon. Not. R. Astron. Soc.*, *421*, 2094–2108.

Pravec P., Harris A. W., Vokrouhlický D., et al. (2008). Spin rate distribution of small asteroids. *Icarus*, *197*, 497–504.

Pravec P., Scheirich P., Kušnirák P., et al. (2006). Photometric survey of binary near-Earth asteroids. *Icarus*, *181*, 63–93.

Pravec P., Scheirich P., Ďurech J., et al. (2014). The tumbling spin state of (99942) Apophis. *Icarus*, *233*, 48–60.

Pravec P., Vokrouhlický D., Polishook D., et al. (2010). Formation of asteroid pairs by rotational fission. *Nature*, *466*, 1085–1088.

Preusker F., Scholten F., Knollenberg J., et al. (2012). The northern hemisphere of asteroid (21) Lutetia – topography and orthoimages from Rosetta OSIRIS NAC image data. *Planet. Space Sci.*, *66*, 54–63.

Pursiainen S. and Kaasalainen M. (2013). Iterative alternating sequential (IAS) method for radio tomography of asteroids in 3D. *Planet. Space Sci.*, *82*, 84–98.

Pursiainen S. and Kaasalainen M. (2014a). Detection of anomalies in radio tomography of asteroids: Source count and forward errors. *Planet. Space Sci.*, *99*, 36–37.

Pursiainen S. and Kaasalainen M. (2014b). Sparse source travel-time tomography of a laboratory target: accuracy and robustness of anomaly detection. *Inverse Problems*, *30*, 114016.

Ragazzoni R., Baruffolo A., Marchetti E., et al. (2000). Speckle interferometry measurements of the asteroids 10-Hygiea and 15-Eunomia. *Astron. Astrophys.*, *354*, 315–320.

Rozitis B. and Green S. F. (2011). Directional characteristics of thermal-infrared beaming from atmosphereless planetary surfaces - a new thermophysical model. *Mon. Not. R. Astron. Soc.*, *415*, 2042–2062.

Russell C. T., Raymond C. A., Coradini A., et al. (2012). Dawn at Vesta: Testing the protoplanetary paradigm. *Science*, *336*, 684–686.

Russell H. N. (1906). On the light variations of asteroids and satellites. *Astrophys. J.*, *24*, 1–18.

Sasaki T., Sasaki S., Watanabe J.-i., et al. (2004). Mature and fresh surfaces on the newborn asteroid Karin. *Astrophys. J.*, *615*, L161–L164.

Scheirich P., Ďurech J., Pravec P., et al. (2010). The shape and rotation of asteroid 2008 TC_3. *Meteoritics and Planetary Science*, *45*, 1804–1811.

Scheirich P. and Pravec P. (2009). Modeling of lightcurves of binary asteroids. *Icarus*, *200*, 531–547.

Schmidt B. E., Thomas P. C., Bauer J. M., et al. (2009). The shape and surface variation of 2 Pallas from the Hubble Space Telescope. *Science*, *326*, 275–278.

Ševeček P., Brož M., Čapek D., et al. (2015). The thermal emission from boulders on (25143) Itokawa and general implications for the YORP effect. *Mon. Not. R. Astron. Soc.*, *submitted*, *0*, 0–0.

Shepard M. K., Margot J.-L., Magri C., et al. (2006). Radar and infrared observations of binary near-Earth Asteroid 2002 CE26. *Icarus*, *184*, 198–210.

Sicardy B., Ortiz J. L., Assafin M., et al. (2011). A Pluto-like radius and a high albedo for the dwarf planet Eris from an occultation. *Nature*, *478*, 493–496.

Sierks H., Lamy P., Barbieri C., et al. (2011). Images of asteroid 21 Lutetia: A remnant planetesimal from the early solar system. *Science*, *334*, 487–490.

Spencer J. R. (1990). A rough-surface thermophysical model for airless planets. *Icarus*, *83*, 27–38.

Spencer J. R., Lebofsky L. A., and Sykes M. V. (1989). Systematic biases in radiometric diameter determinations. *Icarus*, *78*, 337–354.

Statler T. S. (2009). Extreme sensitivity of the YORP effect to small-scale topography. *Icarus*, *202*, 502–513.

Szabó G. M. and Kiss L. L. (2008). The shape distribution of asteroid families: Evidence for evolution driven by small impacts. *Icarus*, *196*, 135–143.

Takahashi Y. and Scheeres D. J. (2014). Morphology driven density distribution estimation for small bodies. *Icarus*, *233*, 179–193.

Tanga P. and Delbo M. (2007). Asteroid occultations today and tomorrow: toward the GAIA era. *Astron. Astrophys.*, *474*, 1015–1022.

Tanga P., Hestroffer D., Berthier J., et al. (2001). NOTE: HST/FGS Observations of the Asteroid (216) Kleopatra. *Icarus*, *153*, 451–454.

Tanga P., Hestroffer D., Cellino A., et al. (2003). Asteroid observations with the Hubble Space Telescope. II. Duplicity search and size measurements for 6 asteroids. *Astronomy and Astrophysics*, *401*, 733–741.

Tedesco E. F., Noah P. V., Noah M., et al. (2002). The Supplemental IRAS Minor Planet Survey. *The Astronomical Journal*, *123*, 1056–1085.

Thomas P. C., Binzel R. P., Gaffey M. J., et al. (1997). Impact excavation on asteroid 4 Vesta: Hubble Space Telescope results. *Science*, *277*, 1492–1495.

Thomas P. C., Parker J. W., McFadden L. A., et al. (2005). Differentiation of the asteroid Ceres as revealed by its shape. *Nature*, *437*, 224–226.

Timerson B., Ďurech J., Aguirre S., et al. (2009). A trio of well-observed asteroid occultations in 2008. *Minor Planet Bulletin*, *36*, 98–100.

Torppa J., Kaasalainen M., Michalowski T., et al. (2003). Shapes and rotational properties of thirty asteroids from photometric data. *Icarus*, *164*, 346–383.

Trilling D. E., Mueller M., Hora J. L., et al. (2010). ExploreNEOs. I. Description and first results from the warm Spitzer near-Earth object slurvey. *Astron. J.*, *140*, 770–784.

Usui F., Kasuga T., Hasegawa S., et al. (2013). Albedo properties of main belt asteroids based on the all-sky survey of the infrared astronomical satellite AKARI. *Astrophys. J.*, *762*, 56.

Usui F., Kuroda D., Müller T. G., et al. (2011). Asteroid catalog using Akari: AKARI/IRC mid-infrared asteroid survey. *PASJ*, *63*, 1117–1138.

Vachier F., Berthier J., and Marchis F. (2012). Determination of binary asteroid orbits with a genetic-based algorithm. *Astron. Astrophys.*, *543*, A68.

Vernazza P., Rossi A., Birlan M., et al. (2007). 832 Karin: Absence of rotational spectral variations. *Icarus*, *191*, 330–336.

Viikinkoski M. and Kaasalainen M. (2014). Shape reconstruction from images: Pixel fields and Fourier transform. *Inverse Problems and Imaging*, *8*, 885–900.

Viikinkoski M., Kaasalainen M., and Ďurech J. (2015). ADAM: a general method of including any data types in asteroid reconstruction. *Astron. Astrophys., submitted*, *0*, 0.

Walsh K. J., Richardson D. C., and Michel P. (2008). Rotational breakup as the origin of small binary asteroids. *Nature*, *454*, 188–191.

Warner B. D., Harris A. W., and Pravec P. (2009). The asteroid lightcurve database. *Icarus*, *202*, 134–146.

Warner B. D., Stephens R. D., and Harris A. W. (2011). Save the lightcurves. *Minor Planet Bulletin*, *38*, 172–174.

Witasse O., Lebreton J.-P., Bird M. K., et al. (2006). Overview of the coordinated ground-based observations of Titan during the Huygens mission. *Journal of Geophysical Research (Planets)*, *111*, 7–19.

Zou X., Li C., Liu J., et al. (2014). The preliminary analysis of the 4179 Toutatis snapshots of the Chang'E-2 flyby. *Icarus*, *229*, 348–354.

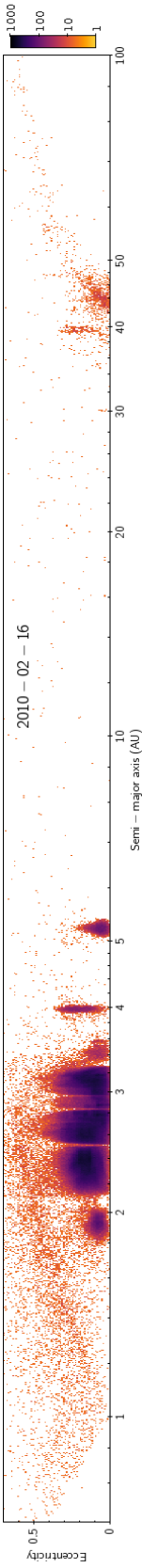

This 2-column preprint was prepared with the AAS LaTeX macros v5.2.

Icarus 239 (2014) 118–130

Contents lists available at ScienceDirect

Icarus

journal homepage: www.elsevier.com/locate/icarus

Physical and dynamical properties of the main belt triple Asteroid (87) Sylvia ☆

J. Berthier [a,*], F. Vachier [b], F. Marchis [b,a], J. Ďurech [c], B. Carry [a]

[a] Observatoire de Paris, CNRS UMR8028, Sorbonne Universités, UPMC Univ Paris 06, IMCCE, 77 Avenue Denfert Rochereau, 75014 Paris, France
[b] Carl Sagan Center, SETI Institute, 189 Bernardo Avenue, Mountain View, CA 94043, USA
[c] Astronomical Institute, Faculty of Mathematics and Physics, Charles University in Prague, V Holešovičkách 2, 18000 Prague, Czech Republic

ARTICLE INFO

Article history:
Received 19 November 2013
Revised 30 April 2014
Accepted 31 May 2014
Available online 12 June 2014

Keywords:
Asteroids
Satellites of asteroids
Adaptive optics
Photometry
Orbit determination
Occultations

ABSTRACT

We present the analysis of high angular resolution observations of the triple Asteroid (87) Sylvia collected with three 8–10 m class telescopes (Keck, VLT, Gemini North) and the Hubble Space Telescope. The moons' mutual orbits were derived individually using a purely Keplerian model. We computed the position of Romulus, the outer moon of the system, at the epoch of a recent stellar occultation which was successfully observed at less than 15 km from our predicted position, within the uncertainty of our model. The occultation data revealed that the Moon, with a surface-area equivalent diameter $D_S = 23.1 \pm 0.7$ km, is strongly elongated (axes ratio of 2.7 ± 0.3), significantly more than single asteroids of similar size in the main-belt. We concluded that its shape is probably affected by the tides from the primary. A new shape model of the primary was calculated combining adaptive-optics observations with this occultation and 40 archived light-curves recorded since 1978. The difference between the $J_2 = 0.024^{+0.016}_{-0.009}$ derived from the 3-D shape model assuming an homogeneous distribution of mass for the volume equivalent diameter $D_V = 273 \pm 10$ km primary and the null J_2 implied by the Keplerian orbits suggests a non-homogeneous mass distribution in the asteroid's interior.

1. Introduction

The minor planet (87) Sylvia is a main belt asteroid discovered in 1866 by Pogson (1866). In the 1990s, frequency analysis of photometric observations hinted that this asteroid could be binary (Prokof'eva and Demchik, 1992; Prokof'eva and Demchik, 1994; Prokof'eva et al., 1995). Its first satellite (S/2001 (87) 1, known as *Romulus*) was discovered in February 2001 by Brown et al. (2001) using the Keck II telescope atop Hawaii's Mauna Kea. Three years later, Marchis et al. (2005b) announced the discovery of a second companion (S/2004 (87) 1, known as *Remus*), using the European Southern Observatory's Very Large Telescope (VLT). Sylvia became the first known triple asteroidal system. Since then, eight others have been discovered and studied (Brown et al., 2005; Bouchez et al., 2006; Ragozzine and Brown, 2009; Brozović et al., 2011; Descamps et al., 2011; Fang et al., 2011; Marchis et al., 2010; Marchis et al., 2013b).

Asteroid (87) Sylvia is the largest member of a collisional family born, at least, several hundreds of million years ago, more probably between 1 and 3.8 Gyr. The age of this family, for which more than 80 members have been identified among current census of asteroids, is commensurable with the evolutionary timescales of Sylvia's satellite system (Vokrouhlický et al., 2010). Various authors estimate that the system is dynamically very stable over a large timescale (at least one million years, see Winter et al. (2009), Vokrouhlický et al. (2010), and Fang et al. (2012)), the satellites being in a deeply stable zone, surrounded by both fast and secular chaotic regions due to mean-motion and evection resonances (Frouard and Compère, 2012).

Observations led to the determination of the dynamical and physical properties of the system. Asteroid (87) Sylvia is classified as a X-type asteroid (Bus and Binzel, 2002) located in the outer main belt ($a \simeq 3.49$ AU, $e \simeq 0.09$, $i \simeq 11°$), within the large Cybele-zone, with a volume-equivalent diameter estimated to 278 ± 11 km, a relatively low density of 1.31 ± 0.15, and a large macro-porosity estimated to $52 \pm 11\%$ (Carry, 2012, and references therein). The two moons, Remus and Romulus, with a diameter respectively estimated to ~7 km and ~18 km (Marchis et al., 2005a, from photometry measurements,) or 9–12 km and

☆ Based on observations collected at the European Southern Observatory, Paranal, Chile (089.C-0944, 087.C-0014, 385.C-0089, 085.C-0480, 077.C-0422, 074.C-0052), at the Gemini North Observatory in Hawaii, and at the W.M. Keck Observatory. The Keck observatory was made possible by the generous financial support of the W.M. Keck Foundation.

* Corresponding author.
E-mail address: berthier@imcce.fr (J. Berthier).

http://dx.doi.org/10.1016/j.icarus.2014.05.046
0019-1035/

5–16 km (derived by Fang et al., 2012, as a free parameter of their dynamical model), orbit at a distance of ~700 km and ~1350 km from the primary. Finally, Fang et al. (2012) estimates dynamically that Sylvia is oblate with a J_2 value in the range 0.0985–0.1.

We report here on new results on the dynamical and physical properties of Sylvia's system based on the analysis of adaptive-optics imaging, light-curves and stellar occultation data (Section 2). We improve Sylvia's 3-D shape model and estimate its overall size (Section 3.1). We estimate the shape and size of the outer satellite Romulus from the analysis of the latest observed stellar occultation (Section 3.2). We improve the determination of orbital parameters for the two satellites, we estimate the mass and density of Sylvia, and we examine its quadrupole term J_2 (Section 4). Finally, we discuss the surprising elongated shape of Romulus revealed by this stellar occultation.

2. Observations and data

2.1. Adaptive-optics observations

We gathered in the VOBAD database (Marchis et al., 2006a) all observations, acquired by our group or already published, from February 2001 to December 2012 recorded in the near-infrared with adaptive-optics (AO) systems available on large ground-based telescopes. We use the ESO Very Large Telescope NACO imaging camera (Lenzen et al., 2003; Rousset et al., 2003) and SINFONI spectro-imaging camera (Eisenhauer et al., 2003), the Gemini North ALTAIR AO system (Herriot et al., 2000) with its camera NIRI (Hodapp et al., 2003), and the NIRC2 camera on the Keck II telescope (Wizinowich et al., 2000; van Dam et al., 2004).

The AO frames were recorded in broad band filters (J, H, or K, from 1 to 2.5 μm) and were all processed in a similar manner. The basic data processing (sky subtraction, bad-pixel removal, and flat-field correction) applied on all these raw data was performed using the recommended eclipse data reduction package (Devillard, 1997). Successive frames taken over a time span of less than 6 min, were combined into one single average image after applying an accurate shift-and-add process through the Jitter pipeline offered in the same package. Data processing with this software on such high signal-to-noise ratio data (>1000) is relatively straightforward. Since these data respect the Shannon's theorem, it is possible to retrieve completely the continuous signal from the knowledge of enough samples. After re-sampling each image to 1/10th of the pixel level, the centroid position on each frame can be accurately measured by a Gaussian fit. The final image is obtained by stacking the set of frames with individual shifts determined from cross-correlation. Once processed, individual images reveal the resolved shape of the primary (angular size ~0.2″), and, sometimes, the unresolved image of the satellites appears. We used a dedicated algorithm (Hanuš et al., 2013a) to extract the contour of the primary and to determine its photocenter, from which we measured the astrometric positions of the satellites by fitting a Moffat-Gauss source profile.

Fig. 1 displays Sylvia's system as seen by VLT/NACO and Keck/NIRC2 instruments after the processing has been applied. Table 1 provides the observing condition at each epoch of image acquisition. Tables 2 and 3 summarize all the astrometric measurements used to fit the orbits of the two satellites of Sylvia. The accuracy on the observing time is the result of the computed mean time of the jittered images, typically 0.2–1 s depending on the observatory where the data were recorded.

2.2. Hubble space telescope data

Storrs et al. (2001) reported the confirmation of the presence of Romulus on Hubble Space Telescope (HST) images collected on February 23, 2001 with the WFPC2 instrument through various filters. We retrieved from the HST archive the three unsaturated observations taken through the F439 filter with an individual exposure time of 3 s. These observations were re-processed using our own pipeline reproducing the HST/WFPC2 cookbook method. The resulting image, shown in Fig. 1, confirmed the detection of Romulus at a position very close to the one reported by Storrs et al. (2001). The second satellite, Remus, is also visible and detected closer to the primary at a distance of 0.34″. The positions of the satellite were derived using the same Moffat-Gauss profile fit than for our AO observations. Interestingly, even though Marchis et al. (2005a) reported the triple nature of (87) Sylvia from observations taken in August 2004 and onward, this February 2001 HST observation was in fact the first detection of the third component of the system. We included these astrometric positions for Romulus and Remus in our analysis, which is particularly useful for Remus since it increases the observational time span by 1264 days (~931 revolutions).

2.3. Light-curve data

We used 40 light-curves observed from 1978 to 1989 published by Harris and Young (1980), Schober and Surdej (1979), Weidenschilling et al. (1987, 1990), Blanco et al. (1989), and Prokof'eva and Demchik (1992). The data were compiled by Lagerkvist et al. (1987) in the Uppsala Asteroid Photometric Catalog, now available through Internet (APC[1] Web site). To this set of dense light-curves we added sparse photometry from US Naval Observatory (IAU code 689), Roque de los Muchachos Observatory, La Palma (950), and Catalina Sky Survey Observatory (703). See the works by Ďurech et al. (2005) and Hanuš et al. (2013b) for details on sparse photometry.

2.4. Stellar occultation data

The observation of a stellar occultation consists in recording the time of immersion and emersion of the star in front of which the asteroid passes, as seen by geographically distributed observers along the occultation path. Each observed occultation point is then projected onto a common plane that passes through the center of the Earth, and lies perpendicular to the direction of the star as seen from the occulting body. Assuming that the relative velocity of the body with respect to the observer is well estimated by the ephemeris, which is a soft assumption, especially for numbered asteroids, one can transform the timings into lengths, and then evaluate the size of the occulting body. We get several segments – the chords – which are directly proportional to the size of the cross-section of the body as seen by observers. With a sufficient number of chords, the silhouette of the body is drawn, and can yield a strong constraint on its 2-D profile in the occultation plane.

The observation of a stellar occultation by an asteroid is one of the few methods which can yield the size and the overall shape of the asteroid without hypothesis on its physical nature. If several independent events of the same occulting body are collected then a 3-D model of the asteroid can even be determined (Drummond and Cocke, 1989). However, due to the low number of well-covered events for a given asteroid, full 3-D reconstruction based on stellar occultations only will always concern a small sample of asteroids. Stellar occultations have however proved to be useful to scale the convex shape models of asteroids derived by light-curve inversion (Ďurech et al., 2011).

Four stellar occultations by Sylvia have been reported in the past 30 years, but only a total of four chords (three for an event,

[1] http://asteroid.astro.helsinki.fi/apc.

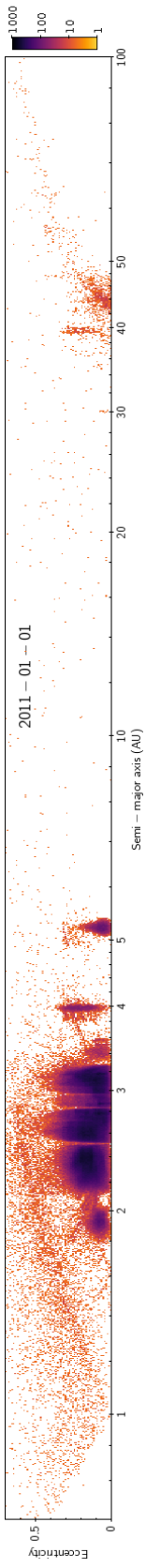

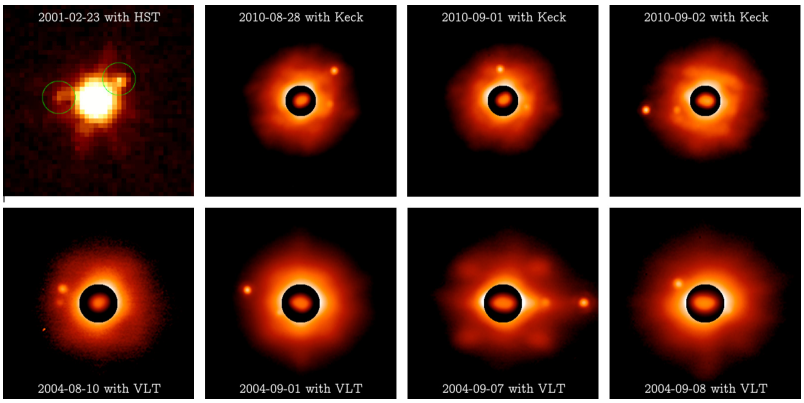

Fig. 1. Sample of observations of the triple Asteroid (87) Sylvia taken with the HST/WFPC2, W.M. Keck AO and VLT/NACO revealing the two satellites and the well resolved primary (angular size ~0.2Prime). The high levels of intensity showing the irregular shape of the primary are shown in the central circle. North is up, and East is left. The plate scale is 40.2 mas for the HST/WFPC2, 9.9 mas for the Keck/NIRC2, and 13.3 mas for the VLT/NACO observations.

one for another, none for the two others) have been collected (Dunham et al., 2012). These occultation data are therefore useless to scale Sylvia's shape model (Kaasalainen et al., 2002). The stellar occultation by Sylvia successfully observed in early 2013 is thus the first opportunity to do so.

On January 6, 2013, about 50 European observers were mobilized to observe the occultation of the TYCHO-2 1856-00745-1 star by (87) Sylvia (Berthier et al., 2013). Among them, 19 observers have recorded a negative event (i.e., no disappearance of the star), and 13 observers have reported a successful observation of the event, providing 16 chords including 4 of the occultation by Romulus. The bad weather forecast on western Europe this night prevented other observers to record the event. Fig. 2 shows the result of the observation of this stellar occultation. Table 4 presents the timings of the event recorded by observers (published on Euraster[2] Web site), and Table 5 lists the observers and the geodetic coordinates of the observing sites.

Stellar occultations by asteroids are usually observed by a group of observers who use different acquisition and timing devices. As a consequence, the accuracy on the measurements differs from one observer to another, and sometimes measurements can disagree owing to systematics in the calibration of the absolute timing reference. A typical example is a chord which is clearly shifted with respect to other chords nearby. The latter can then be used to estimate the offset to apply on the chord to restore its timings. However, it can be tricky to shift the timings of chords, mainly because no evident rule can be found. In such cases it is better to decrease the weight of uncertain chords with respect to accurate ones.

For the January 6, 2013 stellar occultation by Sylvia, we are confident in the absolute timings of the chords as most timing references were insured by GPS or atomic clock time servers (see Table 5). We considered only two chords as discrepant (see column "Offset" of Table 4). The first shows a clear lateness of a few seconds with respect to the three chords immediately next to it (one north, two south). The offset we apply (−3.8 s) sets the chord back in alignment with the three others. The second discrepant chord shows a slight lead on a nearby chord for which the observer can assert the time of the disappearance. The offset we apply (+0.5 s) shift the chord forward in alignment with the latter. As we empirically changed the timings of these two chords, we down-weighted their timings to one thousandth of the weight affected to other chords.

At the mean time of the occultation, January 6, 2013 01:37:06.46 UTC, the computed geocentric orbital velocity of Sylvia is 17.1 km/s. With timing uncertainties lying in the range 0.03–1 s (with a mean value of 0.25 ± 0.3 s), we can expect to measure lengths with a mean accuracy of 4 km (~1.5% of Sylvia's size), which corresponds to ~2 mas at the geocentric distance of Sylvia.

3. Shape and size of the system components

3.1. Shape and size of Sylvia

A convex shape model of Sylvia was previously derived by Kaasalainen et al. (2002). They used 32 light-curves observed in 8 apparitions spanned over 1978–1989, which allowed them to derive a unique model with ECJ2000 pole direction (71°, +66°). As was later shown by Marchis et al. (2006b), this model agreed well with AO observations. It also agrees with the occultation data presented here.

To further improve the fit and to include all data types into the modeling, we used the KOALA algorithm (Carry et al., 2010, 2012). It can simultaneously fit optical light-curves, occultation data and image profiles to give a best-fit 3-D shape model represented by a non-convex polyhedron (Kaasalainen, 2011). Contrary to standard light-curve inversion, where light-curves are fitted by a convex shape model, the best-fit solution is harder to define in case of multiple data sources. Different types of data have to be weighted to compose the total χ^2 as a measure of the goodness of fit (Kaasalainen, 2011). Moreover, given the low number of 2-D profiles available, the non-convex shape solution had to be regularized to suppress unrealistic small-scale fluctuations of the shape. The shape was approximated by a polyhedron described by a spherical harmonics series of the order and degree five or six. This resolution was sufficient to model details of the occultation profile, and still low enough to suppress artificial details that often appeared with higher resolution.

The KOALA algorithm minimizes the total $\chi^2 = \chi^2_{LC} + w_{AO}\chi^2_{AO} + w_{Occ}\chi^2_{Occ}$ that composes the individual contributions from light-curves (LC), adaptive optics profiles (AO), and occultation chords (Occ). Adaptive optics and occultation data are weighted with respect to the light-curves with parameters w_{AO} and w_{Occ},

[2] http://euraster.net/results/2013/.

Table 1
Observational conditions of astrometric positions used for this work. References: (a–c) reanalysis of data collected respectively by Brown et al. (2001), Storrs et al. (2001), and Marchis et al. (2005a); (d) astrometric positions reported in Fang et al. (2012); (e and f) unpublished data acquired respectively by Marchis et al. and Carry et al.; (g) this work.

Date time (UTC)	V (mag)	D_{Earth} (au)	D_{Sun} (au)	Phase (°)	Elong. (°)	AM	Telescope	Ref.
2001-02-19 08:39:46.94	12.41	2.791595	3.755543	3.95	164.84	1.123	Keck/NIRC2	a
2001-02-19 10:03:57.89	12.41	2.791677	3.755554	3.96	164.81	1.014	Keck/NIRC2	a
2001-02-19 10:12:43.20	12.41	2.791686	3.755555	3.96	164.81	1.010	Keck/NIRC2	a
2001-02-20 09:39:27.36	12.41	2.793272	3.755729	4.08	164.33	1.027	Keck/NIRC2	a
2001-02-20 09:46:55.78	12.41	2.793281	3.755730	4.08	164.33	1.021	Keck/NIRC2	a
2001-02-23 13:40:12.58	12.45	2.800411	3.756284	4.58	162.37	-	HST/WFPC2	b
2004-07-25 10:22:17.76	12.14	2.410849	3.218312	12.82	135.39	1.205	VLT/NACO	c
2004-08-10 07:17:16.22	11.89	2.293127	3.217288	8.99	150.30	1.008	VLT/NACO	c
2004-08-29 07:18:19.30	11.64	2.230743	3.216817	5.05	163.73	1.115	VLT/NACO	c
2004-08-29 07:26:17.95	11.64	2.230739	3.216817	5.05	163.73	1.133	VLT/NACO	c
2004-08-29 08:46:08.83	11.64	2.230705	3.216817	5.04	163.75	1.445	VLT/NACO	c
2004-09-01 05:54:55.01	11.63	2.229630	3.216818	4.89	164.26	1.017	VLT/NACO	c
2004-09-01 06:03:55.01	11.63	2.229631	3.216818	4.89	164.26	1.024	VLT/NACO	c
2004-09-01 08:25:31.58	11.63	2.229646	3.216818	4.89	164.27	1.406	VLT/NACO	c
2004-09-03 07:09:06.34	11.63	2.230255	3.216830	4.90	164.22	1.148	VLT/NACO	c
2004-09-04 08:41:35.81	11.64	2.231039	3.216840	4.94	164.07	1.601	VLT/NACO	c
2004-09-05 04:09:27.94	11.64	2.231820	3.216849	4.99	163.89	1.015	VLT/NACO	c
2004-09-05 08:15:20.74	11.64	2.232024	3.216852	5.01	163.85	1.452	VLT/NACO	c
2004-09-06 03:50:04.13	11.65	2.233033	3.216863	5.08	163.61	1.027	VLT/NACO	c
2004-09-07 02:36:23.04	11.65	2.234453	3.216878	5.18	163.28	1.142	VLT/NACO	c
2004-09-07 09:24:57.31	11.65	2.234943	3.216883	5.21	163.17	2.283	VLT/NACO	c
2004-09-08 06:54:52.01	11.66	2.236557	3.216899	5.33	162.78	1.171	VLT/NACO	c
2004-09-11 04:51:29.95	11.69	2.243369	3.216966	5.80	161.20	1.006	VLT/NACO	c
2004-09-13 03:25:24.10	11.72	2.249181	3.217022	6.17	159.92	1.020	VLT/NACO	c
2004-09-13 05:30:10.66	11.72	2.249465	3.217024	6.19	159.86	1.047	VLT/NACO	c
2004-09-14 03:49:52.03	11.73	2.252630	3.217054	6.39	159.19	1.003	VLT/NACO	c
2004-09-14 06:36:31.10	11.73	2.253047	3.217058	6.41	159.10	1.199	VLT/NACO	c
2004-09-14 06:44:34.08	11.73	2.253068	3.217058	6.41	159.10	1.225	VLT/NACO	c
2004-09-15 05:08:21.70	11.75	2.256499	3.217090	6.62	158.39	1.032	VLT/NACO	c
2004-09-15 05:16:22.94	11.75	2.256520	3.217090	6.62	158.39	1.042	VLT/NACO	c
2004-10-19 00:27:06.91	12.30	2.518403	3.219585	14.37	126.79	1.038	VLT/NACO	c
2004-10-20 00:08:28.03	12.31	2.529405	3.219697	14.54	125.85	1.057	VLT/NACO	c
2004-10-25 06:28:30.72	12.39	2.590441	3.220330	15.39	120.89	1.359	Keck/NIRC2	c
2004-11-02 07:34:37.34	12.51	2.690426	3.221417	16.43	113.48	1.428	Gemini/NIRI	c
2005-11-01 13:18:57.31	11.99	2.442235	3.394667	5.81	159.75	1.119	Gemini/NIRI	e
2005-11-06 08:19:53.76	11.90	2.426453	3.398045	4.28	165.18	1.304	Gemini/NIRI	e
2005-11-06 08:31:43.10	11.90	2.426431	3.398051	4.28	165.19	1.254	Gemini/NIRI	e
2005-12-20 10:01:06.82	12.35	2.598025	3.429626	10.23	141.83	1.201	Gemini/NIRI	e
2005-12-20 10:08:25.73	12.35	2.598075	3.429630	10.23	141.82	1.226	Gemini/NIRI	e
2005-12-21 08:42:06.05	12.36	2.607454	3.430311	10.46	140.78	1.041	Gemini/NIRI	e
2005-12-21 08:47:19.68	12.36	2.607491	3.430314	10.46	140.78	1.048	Gemini/NIRI	e
2006-01-01 10:43:07.10	12.56	2.731924	3.438370	12.90	128.79	1.765	Gemini/NIRI	e
2006-01-06 09:14:36.10	12.65	2.794520	3.441971	13.78	123.64	1.295	Gemini/NIRI	e
2006-01-06 09:20:56.26	12.65	2.794578	3.441974	13.78	123.64	1.323	Gemini/NIRI	e
2006-12-12 16:07:33.89	12.73	2.883229	3.670720	10.49	137.29	1.267	Keck/NIRC2	e
2010-07-27 05:23:00.04	11.64	2.259758	3.253753	4.03	166.98	1.027	VLT/SINFONI	e
2010-08-15 08:37:41.66	11.94	2.331035	3.244915	8.95	150.09	1.639	Gemini/NIRI	e
2010-08-25 08:28:46.85	12.10	2.403504	3.240567	11.54	140.07	1.662	Gemini/NIRI	e
2010-08-28 08:22:10.27	12.15	2.429262	3.239301	12.25	137.09	1.671	Gemini/NIRI	e
2010-08-30 05:57:29.00	12.18	2.446480	3.238507	12.68	135.21	1.647	VLT/NCAO	f
2010-09-01 08:27:56.74	12.22	2.466323	3.237635	13.13	133.14	1.717	Gemini/NIRI	e
2010-09-02 06:34:03.36	12.23	2.475252	3.237257	13.33	132.24	1.694	Gemini/NIRI	e
2011-10-07 02:37:58.08	11.68	2.277797	3.251690	4.40	165.53	1.357	VLT/NACO	d
2011-11-06 02:03:15.84	11.99	2.376961	3.266863	8.84	149.55	1.088	VLT/NACO	d
2011-11-08 03:05:36.96	12.03	2.392516	3.267956	9.38	147.45	1.066	VLT/NACO	d
2011-11-10 01:04:56.64	12.06	2.408016	3.268988	9.88	145.48	1.149	VLT/NACO	d
2011-11-15 00:36:51.84	12.15	2.452228	3.271698	11.12	140.34	1.163	VLT/NACO	d
2011-11-16 01:07:06.24	12.17	2.461963	3.272259	11.36	139.28	1.103	VLT/NACO	d
2011-11-20 01:06:14.40	12.24	2.502190	3.274473	12.27	135.18	1.086	VLT/NACO	d
2011-12-15 05:06:34.56	12.65	2.816075	3.289009	16.26	110.50	1.104	Keck/NIRC2	d
2011-12-15 05:29:28.32	12.65	2.816297	3.289018	16.27	110.48	1.087	Keck/NIRC2	d
2011-12-15 06:28:30.72	12.65	2.816873	3.289043	16.27	110.44	1.098	Keck/NIRC2	d
2011-12-16 04:30:17.28	12.66	2.829790	3.289592	16.36	109.59	1.147	Keck/NIRC2	d
2011-12-16 06:01:26.40	12.67	2.830682	3.289630	16.36	109.53	1.084	Keck/NIRC2	d
2011-12-17 06:16:33.60	12.68	2.844990	3.290237	16.45	108.60	1.093	Keck/NIRC2	d
2011-12-18 04:43:58.08	12.69	2.858315	3.290799	16.53	107.74	1.114	Keck/NIRC2	d
2011-12-18 04:53:02.40	12.69	2.858404	3.290803	16.53	107.73	1.104	Keck/NIRC2	d
2013-01-06 01:38:14.18	12.30	2.654901	3.581037	6.01	157.56	1.438	Occ. data	g

respectively. The optimum values of these weights (so called maximum compatibility weights) can be obtained following the approach of Kaasalainen (2011). In our case, the shape of the S surface was 'shallow', thus the optimum weights were not well defined – an order of magnitude range of w_{AO} and w_{Occ} was possible. We varied weights of AO and occultation data with respect to light-curves to see how the models evolved, then we selected only solutions that gave acceptable fits to the data. Thus, instead of one

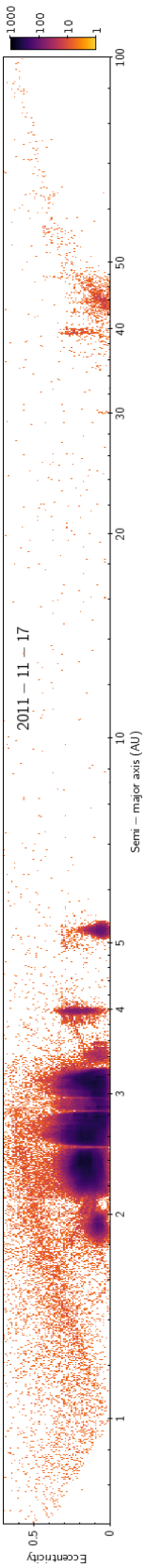

Table 2
List of **Remus** astrometric observations (X_o, Y_o) collected from February 2001 to December 2011. The computed positions (X_c, Y_c) were obtained with the orbital elements published in this paper. The uncertainty σ of astrometric positions is taken as the instrument plate scale. References: c.f. Table 1.

Date time (UTC)	X_o (arcsec)	Y_o (arcsec)	X_c (arcsec)	Y_c (arcsec)	X_{O-C} (arcsec)	Y_{O-C} (arcsec)	σ (mas)	Ref.
2001-02-23T13:40:12.58	0.3448	0.0290	0.3347	0.0341	0.0101	−0.0051	40.2	b
2004-08-10T07:19:16.00	0.3952	0.0136	0.4046	0.0032	−0.0094	0.0104	13.3	c
2004-09-01T05:57:01.00	0.2074	−0.0881	0.2379	−0.0936	−0.0306	0.0054	13.3	c
2004-09-01T06:05:55.00	0.2216	−0.0904	0.2278	−0.0948	−0.0063	0.0044	13.3	c
2004-09-03T07:11:06.00	−0.2199	0.1030	−0.2082	0.0981	−0.0117	0.0049	13.3	c
2004-09-05T04:11:28.00	0.4052	−0.0507	0.4007	−0.0489	0.0045	−0.0018	13.3	c
2004-09-07T02:38:22.00	−0.4350	0.0009	−0.4182	0.0029	−0.0168	−0.0020	13.3	c
2004-09-08T06:56:51.00	−0.2461	−0.0620	−0.2451	−0.0760	−0.0010	0.0141	13.3	c
2004-09-13T03:27:24.00	0.3693	0.0385	0.3786	0.0298	−0.0093	0.0087	13.3	c
2004-09-13T05:32:11.00	0.4086	−0.0136	0.4187	−0.0135	−0.0101	−0.0001	13.3	c
2004-09-14T03:51:51.00	−0.1897	0.1251	−0.1793	0.1050	−0.0105	0.0202	13.3	c
2004-09-15T05:10:21.96	−0.3956	0.0002	−0.4028	−0.0109	0.0073	0.0110	13.3	c
2004-09-15T05:18:22.00	−0.3944	−0.0012	−0.4055	−0.0081	0.0112	0.0069	13.3	c
2010-08-15T08:37:52.00	0.2289	0.1330	0.2249	0.1351	0.0040	−0.0021	13.3	e
2010-08-28T08:23:47.00	−0.3366	−0.0499	−0.3417	−0.0461	0.0052	−0.0038	13.3	e
2010-09-01T08:29:10.00	−0.2675	−0.1232	−0.2695	−0.0989	0.0020	−0.0243	13.3	e
2010-09-02T06:35:15.00	0.3820	−0.1122	0.3555	−0.1057	0.0265	−0.0066	13.3	e
2011-10-07T02:37:58.08	−0.3910	−0.0340	−0.4017	−0.0277	0.0107	−0.0063	13.3	d
2011-11-08T03:05:36.96	0.2180	0.0570	0.2218	0.0283	−0.0038	0.0287	13.3	d
2011-11-10T01:04:56.64	−0.3420	0.0020	−0.3564	−0.0233	0.0144	0.0253	13.3	d
2011-11-16T01:07:06.24	0.3810	0.0180	0.3827	0.0126	−0.0017	0.0054	13.3	d
2011-12-15T05:06:34.56	−0.3410	−0.0110	−0.3346	−0.0097	−0.0064	−0.0013	9.9	d
2011-12-15T05:29:28.32	−0.3420	−0.0150	−0.3347	−0.0121	−0.0073	−0.0029	9.9	d
2011-12-15T06:28:30.72	−0.3250	−0.0120	−0.3266	−0.0179	0.0016	0.0059	9.9	d
2011-12-17T06:16:33.60	0.3480	0.0350	0.3314	0.0116	0.0166	0.0234	9.9	d

best solution, we obtained a set of slightly different models that all fit the data well, each with a slightly different spin, shape, and size. One of these models is shown in Fig. 3, and the fits to the light-curves, image and occultation profiles are shown in Fig. 4. The discrepancy between one AO image contour and the model silhouette comes from an over-estimation of the AO contour due to poor seeing conditions at the time of this observations. The root mean square (RMS) residual of the occultation fit is 2.6 km, which is below the accuracy provided by the timings (see Section 2.4).

To further estimate the uncertainty of our model, we created many clones of the original data set and processed them the same way as the original data. For light-curves, we re-sampled the set with random sampling and replacement – so each new clone consisted of the same light-curves, but some were missing and some were included more times. This approach is similar to the bootstrap method (Press et al., 2007), the difference is that we re-sampled the whole light-curves, not individual measurements, because points within one light-curve cannot be treated as fully independent measurements. By this approach, we can roughly sample the range of possible solutions. For occultation data, we randomly changed the timings using a normal distribution law, with reported uncertainties as standard deviations. Because of the low weight of the AO data in the process, we left them unchanged. The distribution of shapes and spin axis directions then represented the variance of the model given the data and served for a realistic estimation of the model uncertainties. The width of 3σ error intervals reported in Table 6 corresponds to the maximum spread of the relevant parameters across our sample of bootstrap models obtained with different w_{AO} and w_{Occ} weights.

Fig. 5 displays the RMS residuals between synthetic and observed light-curves as function of the spin-vector coordinates (grid interval of 2° on the ECJ2000 celestial sphere). For one of the formally best solutions (based on the total χ^2), the direction of the spin axis (70°, +69°) is almost the same as for the convex model of Kaasalainen et al. (2002), and the 3-D shapes are similar overall. The standard deviation of the pole direction is about 3° in ecliptic longitude and 1° in ecliptic latitude. The volume-equivalent diameter for the best model is $D_V = 273$ km, and $J_2 = 0.024$. The basic physical parameters are listed in Table 6. We also used different resolutions of the model (the degree and order of spherical harmonic expansion used for the shape parametrization) and different weightings between the data to assert the stability of the solution. The plausible shape models cover a range of equivalent diameters from 266 to 280 km and J_2 spans the range 0.015–0.040.

Using our 3-D shape model, we estimated for each image the offset between the center of mass and the photocenter, assuming an uniform density distribution. They span the intervals [−2.3, +1.9] mas in x, and [−0.4, +1.8] mas in y, and are, at least, five time smaller than the uncertainties of the astrometric measurements (see Tables 2 and 3). We have not taken into account these offsets in the astrometric measurements used to fit orbits.

3.2. Shape and size of Romulus

The analysis of the chords of Romulus give us the opportunity to determine its size and, for the first time, to estimate its shape. The distribution of the 4 observed chords is not sufficient to model without ambiguity the profile of the satellite, but they are sufficiently well distributed to estimate its size and biaxial dimensions. The parameters of the ellipsoidal profile (coordinates of the center x_0, y_0, axis radii a, b, and position angle from North of the major axis ψ) are calculated from the set of conics which best fit the n points of coordinates $(x_i, y_i)_n$, which correspond to the coordinates of the extremity of the chords as measured by the observers. We solve the system of linear equations by the linear least-squares method of the Singular Value Decomposition method (Press et al., 2007). Each fitted points is assigned initially a standard deviation calculated as the quadratic mean of the observational uncertainties.

Even if our system is overdetermined ($n = 8$ equations for 5 parameters), the solution can be singular, or numerically very close to singular. In that case, we reduce the system to 3 parameters by fixing the coordinates of the conic center (x_0, y_0). Then we define a grid of values with a given step size, and we solve the equations for each point of the grid, searching for the conics which have $\Delta\chi^2 < 14.2$, the 3-σ confidence region for the normal distribution with 3 degrees of freedom (Press et al., 2007).

Table 3
List of **Romulus** astrometric observations (X_o, Y_o) collected from February 2001 to December 2011. The computed positions (X_c, Y_c) were obtain with the orbital elements published in this paper. The uncertainty σ of astrometric positions is taken as the instrument plate scale. References: c.f. Table 1.

Date time (UTC)	X_o (arcsec)	Y_o (arcsec)	X_c (arcsec)	Y_c (arcsec)	X_{O-C} (arcsec)	Y_{O-C} (arcsec)	σ (mas)	Ref.
2001-02-19T08:41:16.998	0.3401	0.2101	0.3589	0.2108	−0.0189	−0.0007	9.9	a
2001-02-19T10:04:18.001	0.2806	0.2190	0.3017	0.2178	−0.0211	0.0012	9.9	a
2001-02-19T10:13:03.002	0.2815	0.2421	0.2954	0.2185	−0.0139	0.0236	9.9	a
2001-02-20T09:40:55.997	−0.6242	0.0306	−0.6273	0.0337	0.0031	−0.0031	9.9	a
2001-02-20T09:48:26.003	−0.6161	0.0394	−0.6294	0.0317	0.0132	0.0077	9.9	a
2001-02-23T13:40:11.997	−0.2532	0.1957	−0.2688	0.1861	0.0156	0.0096	40.2	b
2004-07-25T10:22:42.003	−0.7657	−0.0070	−0.7530	−0.0084	−0.0128	0.0015	13.3	c
2004-08-10T07:19:16.000	0.3738	0.1392	0.3877	0.1408	−0.0139	−0.0016	13.3	c
2004-08-29T07:20:19.003	0.7728	−0.1082	0.7916	−0.0946	−0.0188	−0.0136	13.3	c
2004-08-29T07:28:17.996	0.7940	−0.1065	0.7890	−0.0963	0.0050	−0.0102	13.3	c
2004-08-29T08:48:08.003	0.7434	−0.1190	0.7584	−0.1132	−0.0150	−0.0058	13.3	c
2004-09-01T05:57:00.996	0.5454	0.1366	0.5514	0.1363	−0.0060	0.0003	13.3	c
2004-09-01T06:05:55.000	0.5545	0.1330	0.5581	0.1346	−0.0036	−0.0016	13.3	c
2004-09-01T08:27:37.995	0.6583	0.1065	0.6552	0.1057	0.0031	0.0007	13.3	c
2004-09-03T07:11:05.999	−0.7498	−0.0610	−0.7497	−0.0599	−0.0001	−0.0011	13.3	c
2004-09-04T08:43:35.999	−0.1603	0.1950	−0.1423	0.2135	−0.0180	−0.0185	13.3	c
2004-09-05T04:11:27.997	0.7851	0.0490	0.7862	0.0433	−0.0012	0.0057	13.3	c
2004-09-05T08:17:20.002	0.8362	−0.0192	0.8363	−0.0191	−0.0001	−0.0002	13.3	c
2004-09-06T03:52:03.999	0.1661	−0.2058	0.1858	−0.2126	−0.0197	0.0068	13.3	c
2004-09-07T02:38:22.004	−0.8307	0.0053	−0.8216	0.0046	−0.0091	0.0007	13.3	c
2004-09-07T09:26:55.999	−0.7914	0.1163	−0.7785	0.1060	−0.0129	0.0104	13.3	c
2004-09-08T06:56:51.002	0.2542	0.1941	0.2694	0.1926	−0.0152	0.0015	13.3	c
2004-09-11T04:53:29.996	−0.6726	0.1650	−0.6542	0.1600	−0.0184	0.0050	13.3	c
2004-09-13T03:27:24.001	0.5571	−0.1980	0.5477	−0.1852	0.0094	−0.0128	13.3	c
2004-09-13T05:32:11.002	0.4478	−0.1852	0.4482	−0.2004	−0.0004	0.0153	13.3	c
2004-09-14T03:51:50.996	−0.7220	−0.0725	−0.7136	−0.0758	−0.0084	0.0033	13.3	c
2004-09-14T06:38:29.999	−0.7710	−0.0361	−0.7811	−0.0330	0.0101	−0.0031	13.3	c
2004-09-14T06:46:34.003	−0.7829	−0.0314	−0.7836	−0.0309	0.0007	−0.0005	13.3	c
2004-09-15T05:18:22.003	−0.2080	0.2215	−0.2048	0.2204	−0.0032	0.0011	13.3	c
2004-10-19T00:29:36.003	0.7423	−0.0400	0.7424	−0.0392	−0.0001	−0.0008	13.3	c
2004-10-20T00:10:57.996	−0.0891	−0.1748	−0.0993	−0.1846	0.0101	0.0098	13.3	c
2004-10-25T06:29:31.001	−0.1298	0.1851	−0.1333	0.1891	0.0034	−0.0040	9.9	c
2004-11-02T07:35:11.999	0.6486	0.0460	0.6243	0.0427	0.0244	0.0033	22.0	c
2005-11-01T13:20:57.001	0.0015	−0.2670	−0.0046	−0.2581	0.0061	−0.0089	22.0	e
2005-11-06T08:20:06.002	0.6840	0.1901	0.6911	0.1814	−0.0071	0.0088	22.0	e
2005-11-06T08:32:42.996	0.6914	0.1739	0.6862	0.1844	0.0051	−0.0105	22.0	e
2005-12-20T10:01:09.001	0.2384	0.2573	0.2450	0.2594	−0.0066	−0.0021	22.0	e
2005-12-20T10:10:25.996	0.2434	0.2434	0.2375	0.2596	0.0059	−0.0162	22.0	e
2005-12-21T08:42:09.002	−0.7005	0.0065	−0.6844	0.0035	−0.0161	0.0030	22.0	e
2005-12-21T08:48:50.002	−0.6704	0.0129	−0.6860	0.0014	0.0156	0.0115	22.0	e
2006-01-01T10:44:37.003	−0.6687	−0.0559	−0.6808	−0.0677	0.0121	0.0118	22.0	e
2006-01-06T09:14:37.996	0.4125	−0.1554	0.4061	−0.1544	0.0063	−0.0009	22.0	e
2006-01-06T09:22:55.997	0.4112	−0.1418	0.4113	−0.1525	−0.0000	0.0106	22.0	e
2006-12-12T16:09:34.001	0.5659	0.1796	0.5353	0.1994	0.0306	−0.0199	9.9	e
2010-07-27T05:23:00.040	0.3900	0.2950	0.3719	0.3024	0.0181	−0.0074	12.5	e
2010-08-15T08:37:51.997	0.6981	−0.2980	0.6827	−0.2803	0.0155	−0.0177	22.0	e
2010-08-25T08:30:23.002	0.4274	0.2690	0.4061	0.2778	0.0213	−0.0089	22.0	e
2010-08-28T08:23:46.996	−0.4167	0.3680	−0.3989	0.3656	−0.0178	0.0024	22.0	e
2010-08-30T05:57:28.998	0.3225	−0.3714	0.3252	−0.3766	−0.0027	0.0052	13.3	f
2010-09-01T08:29:10.003	0.0744	0.3535	0.0584	0.3638	0.0161	−0.0102	22.0	e
2010-09-02T06:35:15.002	0.7748	−0.1153	0.7493	−0.1171	0.0256	0.0018	22.0	e
2011-10-07T02:37:58.002	−0.6980	−0.0720	−0.7047	−0.0615	0.0067	−0.0105	13.3	d
2011-11-06T02:03:15.001	0.3680	−0.0190	0.3771	−0.0250	−0.0091	0.0060	13.3	d
2011-11-08T03:05:36.000	−0.6060	0.0150	−0.6088	0.0054	0.0028	0.0096	13.3	d
2011-11-10T01:04:56.000	0.6430	0.0120	0.6741	0.0015	−0.0311	0.0105	13.3	d
2011-11-15T00:36:51.001	−0.1770	0.0460	−0.1824	0.0373	0.0054	0.0087	13.3	d
2011-11-16T01:07:05.998	−0.6700	−0.0450	−0.6832	−0.0423	0.0132	−0.0027	13.3	d
2011-11-20T01:06:14.002	−0.3550	−0.0350	−0.3609	−0.0527	0.0059	0.0177	13.3	d
2011-12-15T05:06:33.998	−0.5680	−0.0570	−0.5736	−0.0483	0.0056	−0.0087	9.9	d
2011-12-15T05:29:28.000	−0.5680	−0.0630	−0.5644	−0.0495	−0.0036	−0.0135	9.9	d
2011-12-15T06:28:30.002	−0.5390	−0.0460	−0.5387	−0.0523	−0.0003	0.0063	9.9	d
2011-12-16T04:30:17.003	0.3910	−0.0370	0.3829	−0.0392	0.0081	0.0022	9.9	d
2011-12-16T06:01:26.002	0.4460	−0.0160	0.4385	−0.0334	0.0075	0.0174	9.9	d
2011-12-17T06:16:33.003	0.4150	0.0820	0.4080	0.0612	0.0070	0.0208	9.9	d
2011-12-18T04:43:58.002	−0.5280	0.0260	−0.5306	0.0200	0.0026	0.0060	9.9	d
2011-12-18T04:53:02.002	−0.5210	0.0190	−0.5346	0.0193	0.0136	−0.0003	9.9	d
2013-01-06T01:38:14.000	0.5930	−0.1130	0.5898	−0.1041	0.0032	−0.0089	4.5	g

Among the observers, two could have observed the occultation by Romulus, namely M. Bretton and V. Fristot (c.f. Tables 4 and 5). The first one made a naked eye observation and stop too early to observe Romulus event. The analysis of the video acquired by the second confirms that no occultation of Romulus occurred along his path. This result sets a strong upper limit on the size of Romulus, which allows us to reject all the fitted conics which intersect this chord.

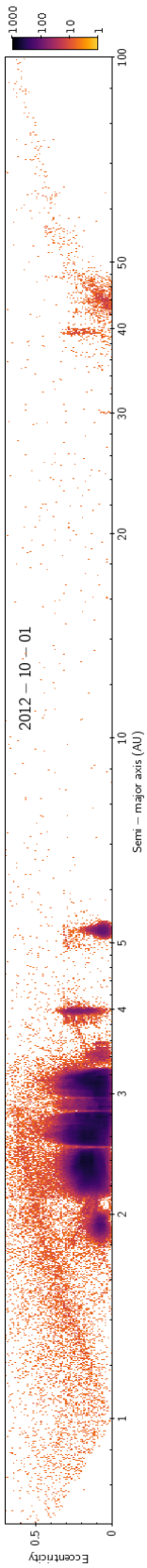

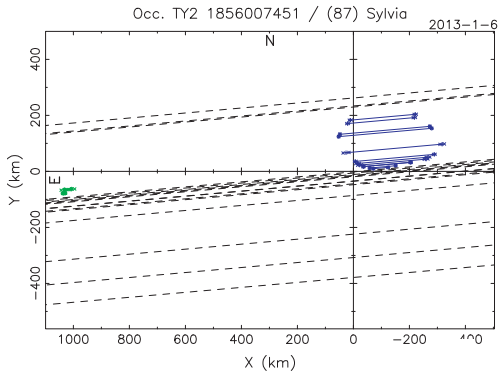

Fig. 2. Observed chords (blue segments) of the January 6, 2013 occultation of TYC2 1856-00745-1 by (87) Sylvia and its satellite Romulus (green leftmost segments). The black dashed lines represent negative observations. (For interpretation of the references to color in this figure legend, the reader is referred to the web version of this article.)

Considering a range of 20 km wide for the coordinates of the conic center, and a grid step size of 10^{-3} km, the best-fit conic profile of Romulus is (Fig. 6):

$a = 19.0$ km ± 1.6 km
$b = 7.0$ km ± 0.4 km
$\psi = 112.4^\circ$ $\pm 13.2^\circ$

with uncertainties at 3-σ. It implies a mean axis ratio $a/b = 2.7 \pm 0.3$, and a surface-area equivalent diameter $D_S = 23.1 \pm 0.7$ km.

This result relies on the reliability of the timings of the two northern chords of Romulus. Even if P. Tanga failed to report accurate absolute timings, he was able to estimate them using the computer clock (synchronized by NTP) used to control the camera, and to measure precisely the duration of events and the delay between the two events (see Table 4). Using the 3-D shape model of Sylvia projected into the occultation plane, we can tie the time of the first disappearance of the star observed by P. Tanga to other timings with an accuracy smaller than 0.2s. In the case we shift Tanga's chords by +0.2 s, the axis ratio of the best-fit profile of Romulus decreases to 2.2, with $a = 18$ km, $b = 8$ km, $D_S = 24$ km, and equivalent uncertainties.

4. Dynamical overview on Sylvia system

Orbital solutions for Sylvia's satellites have been recently published by Fang et al. (2012), and previously by Marchis et al. (2005a) at the occasion of the discovery of the second satellite. We take the opportunity of the successful observation of a stellar occultation by Romulus to test the reliability of its orbital solution, used to predict the event (Berthier et al., 2013), and to improve the orbital parameters of the two satellites.

4.1. Reliability of Romulus orbit

We used our genetic-based algorithm *Genoid-Kepler* (Vachier et al., 2012) to predict the position of Sylvia's satellites for the January 6, 2013 stellar occultation. The dynamics used to model the orbit of the satellites was a pure 2-body Keplerian problem (no mutual perturbation between the two satellites was applied). For Remus, we used 25 astrometric positions (acquired in 2001, 2004, 2010 and 2011) spanning 3948.7 days or 2910.6 revolutions. For Romulus, we used 65 astrometric positions (acquired in 2001, 2004, 2005, 2006, 2010 and 2011) spanning 3953.8 days or 1317.9 revolutions. Tables 1 and 2 detail the observing condition and the astrometric positions used for this work. The best solutions obtained give orbits with a RMS of 12.1 mas for Remus, and 11.2 mas for Romulus.

The successful observation of the occultation by Romulus highlights the reliability of our dynamical model. Fig. 6 shows the goodness of the prediction of Romulus position with respect to Sylvia's center of mass (as defined by the 3-D model). The offset between the observed position of Romulus (e.g., defined by the center of the fitted profile) and its predicted position is $\Delta x = -3.3$ km, $\Delta y = -13.1$ km (x and y are positive toward East and North). This predicted position is located at 13.5 km from the observed position. In the occultation plane, the distance between the fitted profiles of Sylvia and Romulus is 1154.6 km. The geocentric orbital velocity of Sylvia being 17.1 km/s, the occultation by Romulus occurred 67.6 s later than Sylvia event. At this epoch, January 6, 2013 01:38:14.02 UTC, we infer the astrometric position of

Table 4
Timings and uncertainties of the occultation of TYC2 1856-00745-1 by (87) Sylvia on January 6, 2013 (source: *Euraster* Web site).

T [a]	Name	Duration (s)	Disp. Time (h:m:s ± s)	Reap. Time (h:m:s ± s)	Offset (s)
S	A. Carbognani	17.70	01:37:33.30 ± 0.28	01:37:51.00 ± 0.28	−3.8
S	S. Bolzoni	18.20	01:37:29.15 ± 0.30	01:37:47.35 ± 0.20	
S	S. Sposetti, A. Manna	25.34	01:37:26.21 ± 0.03	01:37:51.55 ± 0.04	
S	V. Fristot	21.50	01:37:30.70 ± 0.20	01:37:52.20 ± 0.20	
S	A. Figer	26.20	01:37:22.80 ± 0.60	01:37:49.00 ± 0.80	
S	M. Bretton	18.10	01:37:34.50 ± 0.0 [b]	01:37:52.60 ± 0.0 [b]	
S	J. Lecacheux	4.06	01:37:37.16 ± 0.08	01:37:41.22 ± 0.10	
S	P. Tanga	19.19	00:00:00.00 ± 0.02 [c]	00:00:19.19 ± 0.02 [c]	
S	M. Devogele et al.	12.77	01:37:26.73 ± 0.08	01:37:39.50 ± 0.08	
S	E. Frappa, A. Klotz	12.90	01:37:26.60 ± 0.10	01:37:39.50 ± 0.10	
S	L. Brunetto et al.	7.12	01:37:29.53 ± 0.02	01:37:36.65 ± 0.02	
S	V. Metallinos	24.60	01:36:20.73 ± 0.05	01:36:45.33 ± 0.05	
R	P. Tanga	1.96	00:00:97.10 ± 0.03 [c]	00:00:99.06 ± 0.03 [c]	0.5
R	P. Dubreuil	1.70	01:38:57.60 ± 2.00	01:38:59.30 ± 2.00	
R	M. Devogele et al.	0.56	01:39:00.85 ± 0.08	01:39:01.41 ± 0.08	
R	E. Frappa, A. Klotz	0.48	01:39:00.73 ± 0.08	01:39:01.21 ± 0.08	

[a] Target: S for Sylvia, R for Romulus.
[b] Measurement uncertainty not provided by the observer.
[c] No absolute timing due to technical problem; the only reliable data is the duration of the event, and the delay between the two disappearance times, which is 97.10 ± 0.03 s.

Table 5
Observers of the occultation of TYC2 1856-00745-1 by (87) Sylvia on January 6, 2013 (source: *Euraster* Web site). Method is: ⟨optic⟩, ⟨acquisition⟩, ⟨time source⟩, with abbreviations: L: Refractor, M: Reflector, CCD: CCD or CMOS imaging, VID: video recording, VIS: visual, GPS++: GPS one Pulse Per Second, PHONE: Phone time signal (wired phone), RAD: Radio time signal, RAD+: Intermittent radio controlled clock updated just before event, NTP: Network Time Protocol. Coordinates datum: W = WGS84; Altitude datum: W = WGS84, S = Mean Sea Level.

Name	Method	Longitude (° ′ ″)	Latitude (° ′ ″)	Alt. (m)	Datum
S. Sposetti (CH)	M400, VID	E 09 01 26.5	N 46 13 53.2	260	WS
C. Gualdoni (IT)	M250, VID	E 09 06 01.0	N 45 48 18.0	255	WS
A. Carbognani (IT)	M810, CCD, NTP	E 07 28 42.0	N 45 47 23.5	1678	WS
S. Bolzoni (IT)	M300, VIS, RAD+	E 08 09 59.8	N 45 21 57.0	195	WS
U. Quadri et al. (IT)	M250, CCD	E 10 07 49.5	N 45 19 32.4	63	WS
S. Sposetti, A. Manna (IT)	M200, VID, GPS++	E 07 18 01.3	N 45 07 34.1	585	WS
V. Fristot (FR)	L102, CCD, NTP	E 05 16 35.4	N 44 41 35.5	390	WS
A. Figer (FR)	L68, CCD, PHONE	E 06 40 54.0	N 44 34 24.0	1845	WS
M. Bretton (FR)	M820, VIS, RAD	E 05 30 54.4	N 44 24 29.9	810	WS
J.-L. Penninckx (FR)	M400, VIS	E 04 22 45.8	N 44 07 51.5	245	
C. Peguet (FR)	M350, VIS	E 05 00 09.0	N 44 07 31.8	94	WS
L. Bernasconi (FR)	M500, CCD	E 05 11 11.2	N 44 01 17.5	330	WS
J. Lecacheux (FR)	L130, VID, GPS++	E 06 01 15.3	N 43 58 48.6	720	WS
E. Frappa et al. (FR)	L61, VID	E 05 58 33.4	N 43 56 07.9	460	WS
L. Arnold (FR)	M205, CCD	E 05 42 48.4	N 43 55 00.7	551	WS
E. Frappa (FR)	M203, VID	E 06 00 23.0	N 43 51 51.9	628	WS
G. Brabant (FR)	M200, VID	E 04 54 47.5	N 43 47 48.8	53	WS
P. Tanga (FR)	M356, CCD	E 07 15 47.2	N 43 47 22.2	385	WS
P. Dubreuil (FR)	M203, CCD	E 07 14 30.6	N 43 46 58.5	480	WS
D. Verilhac (FR)	M210, VID	E 04 53 35.1	N 43 46 01.0	115	WS
M. Devogele et al. (FR)	M1000, VID, GPS++	E 06 55 21.8	N 43 45 13.5	1280	WS
E. Frappa, A. Klotz (FR)	M250, CCD, GPS++	E 06 55 25.1	N 43 45 07.3	1270	WS
O. Lecacheux (FR)	L61, VID, GPS++	E 05 30 00.0	N 43 41 31.6	214	WS
R. Poncy (FR)	M400, CCD	E 03 56 24.0	N 43 38 50.0	54	WS
L. Brunetto et al. (FR)	M406, VID, GPS++	E 07 04 18.4	N 43 36 15.7	130	WS
D. Albanese (FR)	M280, CCD	E 06 39 04.9	N 43 29 45.9	43	WS
F. Colas (FR)	M1050, CCD	E 00 08 32.5	N 42 56 10.9	2871	WS
J. Lopez (ES)	M200, VID	E 02 59 50.5	N 42 15 00.2	19	W
C. Perello, A. Selva (ES)	M500, VID	E 02 05 24.6	N 41 33 00.2	224	WS
R. Casas (ES)	M200, VID	E 02 07 14.3	N 41 32 22.1	165	WS
H. Pallares (ES)	M280, VIS	E 04 14 28.1	N 39 49 12.7	19	W
V. Metallinos (GR)	L130, VID, GPS++	E 19 52 23.3	N 39 38 07.4	2	WS

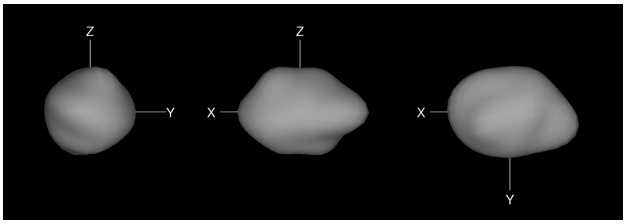

Fig. 3. One of the best-fit models of Sylvia's primary (equatorial, equatorial, and polar view) derived from the combination of light-curve inversion, AO, and occultation data.

Romulus relatively to Sylvia's center of mass: $(x, y) = (590, -113) \pm 1.5$ mas.

4.2. New orbital solutions

We added this astrometric position into *Genoid-Kepler* input dataset, as well as an astrometric position acquired in 2010 with VLT/SINFONI (Marchis et al., 2013a). It increases the time span of data from 3953.8 to 4338.7 days or 1446.2 revolutions. This does not change significantly the dynamical solution of Romulus (RMS = 11.2 mas). Table 7 presents the orbital parameters of Sylvia's satellites obtained with *Genoid-Kepler*, and Fig. 7 displays the residuals (the difference between the observed O and computed C positions of the satellite and the primary) normalized by the positional uncertainty σ. The orbital solutions indicate that the satellites follow a quasi circular orbit, nearly coplanar (very low mutual inclination, lesser than 0°.5), and nearly aligned with the primary equatorial plane (by ∼4°). The average residuals are $dx = -0.4 \pm 11.9$ mas, $dy = 4.7 \pm 11.5$ mas for Remus, and $dx = 0.5 \pm 12.7$ mas, $dy = 0.6 \pm 9.4$ mas for Romulus (uncertainties at 3-σ), matching the level of accuracy of the observations. At the epoch of the occultation, the reliability of the model can be estimated by the difference between the observed and computed positions of Romulus, which are $dx = 0.2$ mas and $dy = -8.9$ mas, or $\Delta x = 1.0$ km and $\Delta y = -13.3$ km in the occultation plane. We inserted these orbital solutions in the Web service Miriade[3] of our Virtual Observatory Solar System portal, allowing everyone to compute the ephemeris of Sylvia's satellites.

The mass of Sylvia can be derived from the best-fit keplerian orbit of the satellites (see Table 7). Assuming the Gaussian gravitational constant and the solar mass, one can easily derive, independently, the mass of Sylvia from the semi-major axis and the orbital period of each satellite (neglecting its own mass). We find

[3] http://vo.imcce.fr/webservices/miriade/.

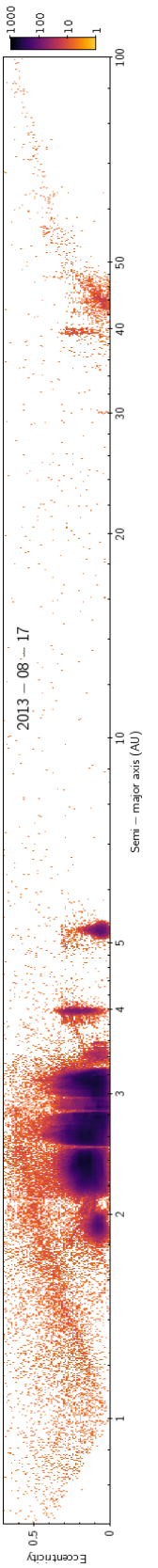

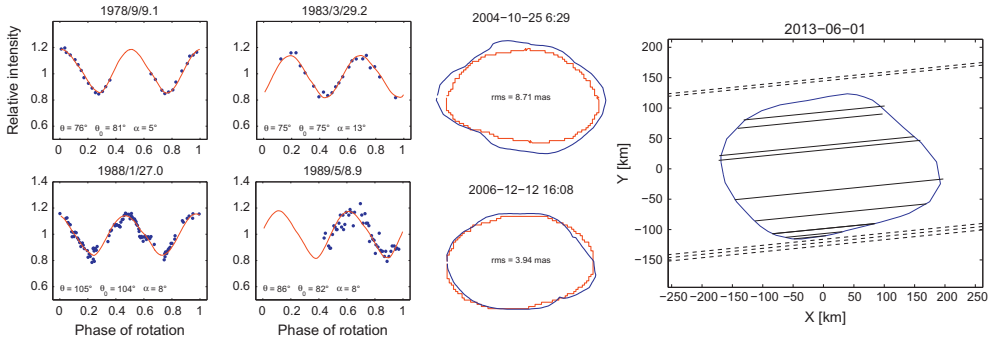

Fig. 4. Result of the fit of Sylvia's 3-D shape compared to a sample of light-curves, image profiles, and occultation chords. The measured light-curves (points) are compared with the model (solid curves). The viewing and illumination geometry is described by the latitudes θ and θ_0 of the sub-Earth and sub-solar point, respectively, and by the solar phase angle α. The observed contours of AO images and the corresponding projections of the model (smooth blue curves) are plotted in the second panel. In the third panel, occultation chords and the model outline are shown. The dashed lines are negative observations. (For interpretation of the references to color in this figure legend, the reader is referred to the web version of this article.)

Table 6
Physical parameters of Sylvia's primary derived using KOALA algorithm.

Parameter	Value	Uncertainty (3-σ)
Spin axis ecliptic J2000 longitude	70°	±9°
Spin axis ecliptic J2000 latitude	69°	±3°
Sidereal rotation period	5.183640 h	$\pm 3 \times 10^{-6}$ h
Volume-equivalent diameter D_V	273 km	±10 km
Quadrupole term J_2	0.024	0.015–0.040
Volume	1.07×10^7 km^3	$\pm 0.09 \times 10^7$ km^3
Surface area	2.47×10^5 km^2	$\pm 0.15 \times 10^5$ km^2
Maximum dimensions along the principal axes		
a	193 km	180–210 km
b	129 km	127–160 km
c	124 km	115–150 km
Dynamically equivalent ellipsoid		
a/c	1.46	1.30–1.75
b/c	1.07	1.02–1.20

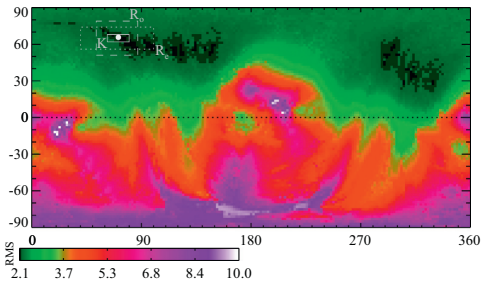

Fig. 5. RMS residuals between the synthetic and observed lightcurves for spin-vector coordinates covering the entire celestial sphere with grid interval of 2°. The white points shows the best-fit spin solution (70°, +69°), and the three rectangles correspond to the 3-σ confidence interval provided by KOALA, the orbital pole of Romulus, and Remus, respectively, outside which spin-vectors coordinates are unlikely.

$M_S = 1.380 \pm 0.151 \times 10^{19}$ kg from Remus, and $M_S = 1.476 \pm 0.128 \times 10^{19}$ kg from Romulus, considering the 1-σ uncertainties of the parameters. It is interesting to note that the two masses are consistent within their uncertainties. The mass derived from

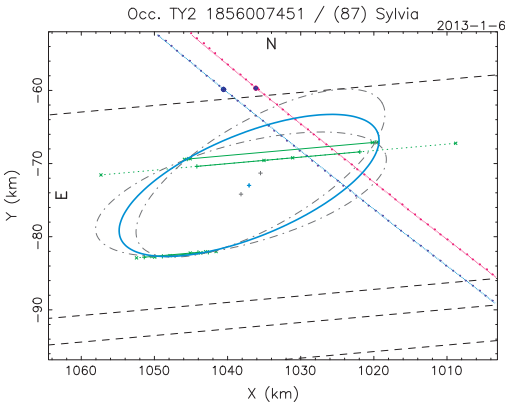

Fig. 6. Romulus conic model fitted on the observed chords (green segments). The (blue) ellipse is the mean model, and the two dashed ellipses are the two extreme solutions at 3-σ. The dashed black lines are negative observations (northern one by V. Fristot). The blue (leftmost) and red lines show the predicted orbit of Romulus projected into the occultation plane, respectively based on the previous and the new orbital models. The two marks on these lines (located at $y \sim -60$ km) enlighten the predicted positions of Romulus at the epoch of occultation. (For interpretation of the references to color in this figure legend, the reader is referred to the web version of this article.)

Romulus orbit is also very similar, by ~0.5%, to that found by Fang et al. (2012), although it has been obtained by the latter by the fit of a fully dynamical three-body model.

From the mass of Sylvia and its volume, defined by its 3-D shape model, we infer its density. We find 1.29 and 1.38 g cm^{-3} from Remus and Romulus data respectively, with an uncertainty of ±0.16 g cm^{-3}, taking into account the 1-σ uncertainties of the parameters. The resulting density of 1.34 ± 0.21 g cm^{-3} is slightly lower, although consistent, with the average density of X-type asteroids of 1.85 ± 0.81 g cm^{-3} (Carry, 2012). The composition and meteorite analogs of X-types is still debated, and proposed analogs encompass CV and CO carbonaceous chondrites, enstatite chondrites, aubrites, mesosiderites, and even iron, stony-iron meteorites (Barucci et al., 2005; Vernazza et al., 2009, 2011; Ockert-Bell et al., 2010; Fornasier et al., 2011), which density

Table 7
Remus and Romulus best-fit orbital elements (EQJ2000) obtained using our *Genoid-Kepler* algorithm (orbital period P, semi-major axis a, eccentricity e, inclination i, longitude of the ascending node Ω, argument of the pericenter ϖ, time of pericenter t_p), and derived parameters (primary mass M, primary density ρ, ecliptic J2000 coordinates of the orbital pole λ_p, β_p). Errors are given at 3-σ.

Element	Remus		Romulus	
P (day)	1.356654	$\pm 5.9 \times 10^{-5}$	3.641191	$\pm 1.98 \times 10^{-4}$
a (km)	684.4	±109.7	1351.7	±151.0
e	0.0	±0.05	0.007	±0.047
i (°)	8.6	±13.5	8.3	±7.7
Ω (°)	93.0	±48.0	93.6	±20.1
ϖ (°)	187.9	±52.1	109.1	±23.6
t_p (JD)	2455594.58824	±0.158	2455596.41837	±0.202
Derived parameters				
M (10^{19} kg)	1.380	±0.669	1.476	±0.497
ρ (g cm^{-3})	1.29	±0.59	1.38	±0.44
λ_p, β_p (°)	70, +65	±30, 9	70, +65	±17, 4

ranges from 2.8 to 7.7 g cm^{-3}. Although we do not have information on the composition of Sylvia, its density, lower than that of its most-likely components, indicates the presence of voids and/or pockets of very low density material (e.g., ices). The macroporosity we derive here ranges from 52% to 82% depending on the density of the analog meteorite.

4.3. Examination of the quadrupole term J_2

We used our *Genoid-ANIS* algorithm (Vachier et al., 2012) to search for a possible influence of an irregular mass distribution, considering the amount of voids determined above. We initialized the problem with $J_2 = 0.024$, the value estimated from the 3-D shape model (see Section 3.1). We search for orbital solutions in the space $0 \leqslant J_2 \leqslant 0.2$, all other parameters being free. The results are shown in Fig. 8. Assuming that the directions of the orbital poles of the satellites must be nearly aligned with the primary pole of rotation (hypothesis justified by the low inclination of orbital planes, see Section 4.2), we discard all solutions for which coordinates of orbital poles are outside the 3-σ confidence interval of the primary spin-vector coordinates (see Section 3.1 and Fig. 5). We find that the best candidate solutions are obtained for $J_2 \to 0$. It means that no significant precession effect of the apsidal and nodal nodes is detected, and that the purely Keplerian orbit is enough to fit the available data to their accuracy.

Winter et al. (2009) showed that Sylvia's system is not stable unless the primary has a minimal amount of oblateness, at least 0.1% of the assumed primary J_2 of 0.17 reported by Marchis et al. (2005a). This oblateness provides a faster stabilizing effect on the satellites' orbits than other gravitational perturbations (e.g., Sun, Jupiter, see also Frouard and Compère (2012)). Our $J_2 \sim 0$ result does not contradict this statement, insofar as we analyze observational data and do not study the long term stability of the system. It shows that the estimation of the quadrupole term J_2 of the gravitational potential of Sylvia is not obvious, even impossible, given the available observational data, especially since a Keplerian model provides the best-fit orbital solution. The discrepancy between our result and those of Fang et al. (2012) (who found a primary J_2 of 0.1), or those of Marchis et al. (2005a), reveals that the estimation of the J_2 term is strongly correlated with the orbit-fitting method. In all cases, very similar orbital solutions are obtained, and the same conclusion applies: Sylvia's system is ancient and in a very stable state.

5. Discussion

5.1. Interior of (87) Sylvia

The difference in J_2 from our dynamical analysis and as derived from the 3-D shape model implies that the assumption of an homogeneous mass distribution is not valid. The $J_2 \sim 0$ determined dynamically indicates a more concentrated mass distribution than the 3-D shape suggests, so that the primary could be differentiated with a dense core. The same result emerged from the analysis of the orbit of the 28 km-diameter satellite of (22) Kalliope, a 166 km-diameter M-type asteroid. Vachier et al. (2012) suggested a differentiated internal structure for the primary of this binary system.

Recent developments (e.g., Ghosh et al., 2003) in thermal modeling of small Solar System bodies showed that large enough (radius >7 km) asteroids that accreted shortly after the Calcium–Aluminum inclusion formation (<2.5 Myr), when ^{26}Al was still abundant, could have been molten internally. As they were cooling off, their internal composition became partially differentiated. Those models showed that these asteroids remained covered with

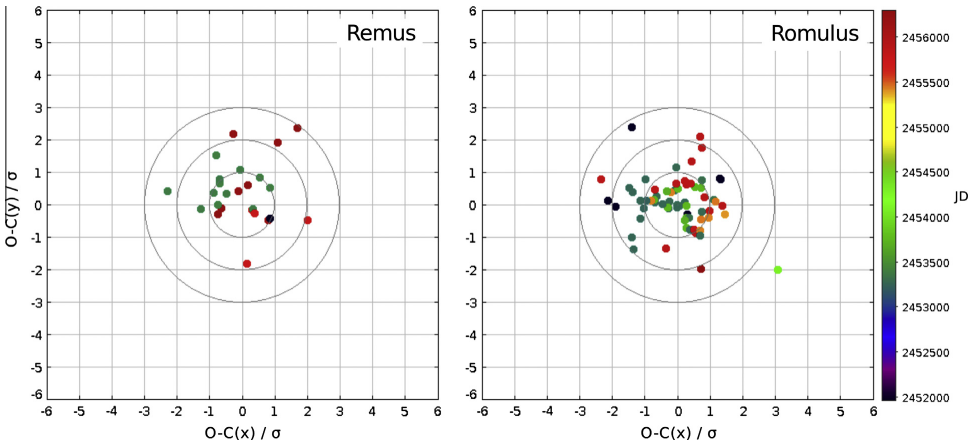

Fig. 7. Mean residuals (observed minus computed satellite – primary positions) normalized by the positional uncertainty σ for Remus and Romulus.

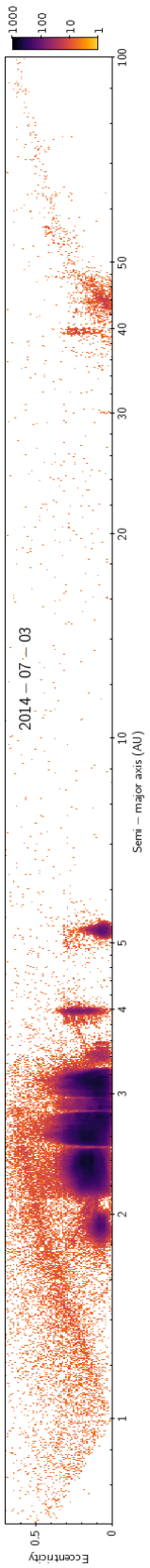

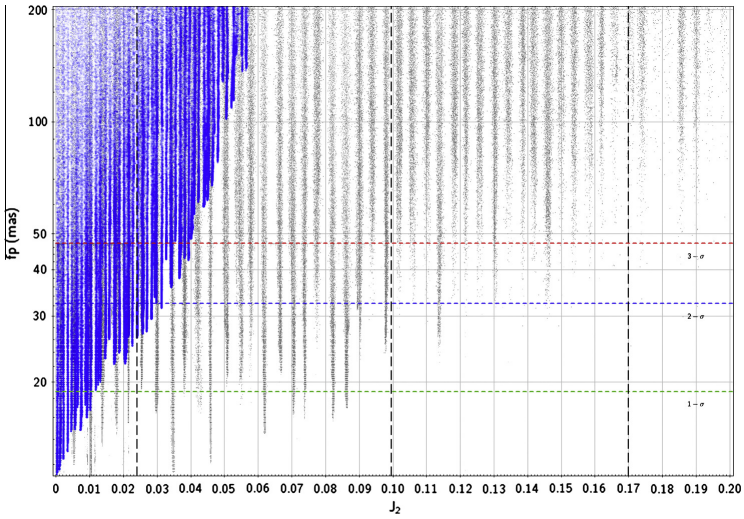

Fig. 8. Result of the examination of the quadrupole term J_2 with *Genoid-ANIS*. The gray dots are all solutions. The (blue) biggest points show the solutions for which the orbital pole covers a range of 20° around the best-fit spin solution of the primary (i.e., rectangles in Fig. 5). The (green, blue, red) horizontal dashed lines correspond, respectively, to 1-σ, 2-σ and 3-σ thresholds. The three vertical lines indicate the J_2 values estimated, from left to right, from the 3-D shape model (see Section 3.1), by Fang et al. (2012) and by Marchis et al. (2005a). The best candidate solutions are obtained for $J_2 \rightarrow 0$. (For interpretation of the references to color in this figure legend, the reader is referred to the web version of this article.)

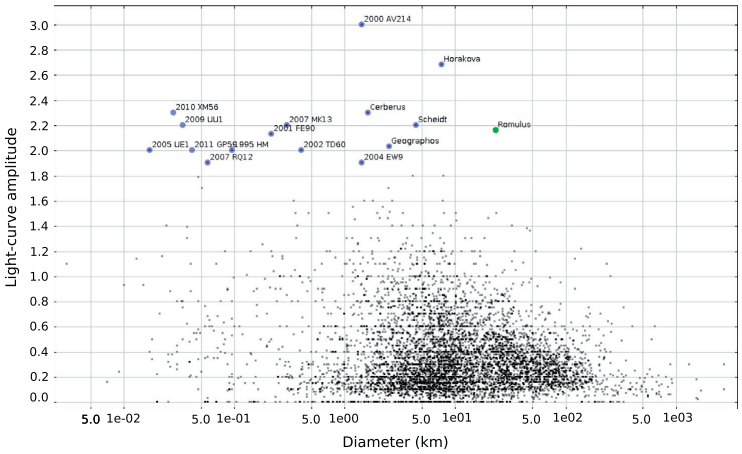

Fig. 9. Distribution of 6160 asteroids based on light-curve amplitude versus diameter (source of data: *Asteroid Lightcurve Database*, Warner et al. (2009)). High amplitude objects are labeled. We added Romulus for comparison, with $D_S = 23.1$ km and an amplitude estimated to 2.16 (corresponding to an axis ratio of 2.7).

a thick (up to tens of kilometers) un-melted relict crust (see a review on this mechanism and a thorough discussion in Weiss and Elkins-Tanton, 2013).

Although we cannot conclude whether or not the internal structure of (87) Sylvia is differentiated, the very low J_2, perturbing the satellite's orbit, hints toward a dense core embedded into an irregularly shaped material. The lower density of the surrounding material may be related to composition or structure, e.g., a large macroporosity generated by fractures.

5.2. Elongated shape of Romulus

The shape and size of Romulus was estimated in Section 3.2 from the chords of an occultation, leading to a surface-area equivalent diameter $D_S = 23.1 \pm 0.7$ km ($H = 12.1$–12.3, assuming the same albedo as the primary of 0.0435, Tedesco et al. (2002)), and an axis ratio $a/b \sim 2.7 \pm 0.3$ (assuming an ellipsoid). This is the second time the shape and size of a satellite of asteroid is measured using this technique. An occultation by Linus, satellite of

Table 8
Selection of stellar occultations by (87) Sylvia scheduled for the next 10 years. Tycho-2 stars; Mean epoch: approximated time of event; m_*: magnitude of the target star; Δm: magnitude drop, Δt: estimated maximum duration of the event, Location: main area of visibility.

Mean epoch (UTC)	Star TYC2	m_* mag	Δm mag	Δt (s)	Location
2016-01-30 07:22	6226 01275	12.1	1.6	8.0	Brazil
2016-06-22 23:54	6815 03609	11.6	0.6	20.5	Chile, Argentina, South Africa, Madagascar
2016-08-16 23:36	6817 01360	12.6	1.1	44.6	Chile, Paraguay, Brazil (South)
2016-11-03 23:17	6854 00301	10.6	1.4	7.2	Chile, Argentina, Brazil (South)
2019-10-15 08:11	1931 01512	9.9	2.0	14.1	Chile, Argentina, Brazil (South), South Africa
2019-10-20 06:08	1932 00479	12.0	1.9	15.8	Spain, France (South), Italy, Greece
2019-10-29 23:45	1932 00469	10.0	1.9	21.0	Spain, France, Italy, Germany, Poland
2023-07-06 08:01	7442 01392	11.9	1.0	22.2	Mexico, USA (East), Canada (East)

the Asteroid (22) Kalliope, gave a similar opportunity (Descamps et al., 2008), but the chords were too close to each other and the shape could only be approximated by a circular fit. In the case of Romulus, the positive and negative chords are sufficiently spread (Fig. 6)) to give a meaningful constraint on its shape. The satellite appears extremely elongated, with the main axis of the silhouette ellipse oriented at $12^\circ \pm 4^\circ$ from the primary.

We searched in the *Asteroid Lightcurve Database* (Warner et al., 2009) containing the light-curves of 6160 small Solar System bodies (including NEAs, TNOs, main-belt and a few comets) those with an amplitude greater than 1.9 (corresponding to a size ratio $\geqslant$2.4) and found 15 asteroids, including 12 NEAs and 3 main-belt asteroids (Fig. 9). They are all significantly smaller than Romulus with a diameter varying from 20 m to 7.5 km. The largest, (44530) Horakova, has a light-curve poorly constrained with a period $P = 160$ h and a maximum light-curve amplitude $\Delta m \sim 2.7$, suggesting that it could be a tidally locked binary. Asteroid (1620) Geographos ($D = 1.6$ km, $\Delta m \sim 2.0$) is smaller but shows the same light-curve amplitude as Romulus. Moreover its shape is well-defined thanks to delay-Doppler radar observations (Ostro et al., 1996). Shape reconstruction from radar gives $a/b = 2.76 \pm 0.18$, similar to Romulus. Bottke et al. (1999) has shown by numerical simulations that tidal disruptions during a close encounter with a planet could produce the elongated shape of Geographos. Similarly, because Romulus is relatively close to the primary ($\sim$10 $\times$ Sylvia's radius), and could be a rubble-pile satellite which formed from fragments of a catastrophic collision on the parent body, its elongated shape may result of the tidal forces from the elongated and spinning primary. Another possibility is that Romulus is a bilobed satellite, relic of its formation by a low-relative speed encounter of two $\sim$10 km fragments of the parent body and captured in the gravitational field of the primary. An accurate modeling of the tidal evolution of the orbit and shape of the satellite could shed light on the internal stress and cohesive forces of the satellite.

6. Conclusion

This work demonstrates once again that the combination of adaptive-optics observations with light-curve photometric observations and stellar occultations is a powerful way to study multiple asteroid system. Similarly to our work on the triple Asteroid (93) Minerva (Marchis et al., 2013b), we derive here the 3-D shape and size of Sylvia's primary and constrain its internal structure. The successful observation of the occultation by Romulus, the outer satellite of the system, provides the first well-constrained estimate of the shape of an asteroid's moon which has an extreme elongation, likely due to the tides due to the primary. A follow-up of the orbits of Sylvia's moons based on additional AO observations, recorded with present AO systems and on the next generation of adaptive optics currently being designed for the Keck telescope (Wizinowich et al., 2010) or set up on new telescopes (e.g., LBTAO, see Esposito et al. (2011)), will help to confirm the absence of precession indicative of a heterogeneous interior for this asteroid.

The analysis of the occultation chords recorded on January 6, 2013 does not reveal the presence of Remus, the inner satellite, because of a poor coverage of the Northern part of the occultation path (Fig. 2), where Remus was predicted to be located. No observer reported occultation events due to the presence of smaller, yet unknown, satellites around Sylvia's primary. From the timing accuracy of recorded light-curves (Table 4), we estimate that observers could have detected other satellites around Sylvia with a diameter larger than 2 km along the occultation chords (Fig. 2). For comparison, the upper limit of detection for the AO observations varies with the distance to the primary and the quality of the AO correction; typically a satellite larger than $\sim$5 km in diameter could have been detected if located at Remus' distance ($\sim$0.3Prime). This is a clear illustration of the usefulness of occultation that help determining the multiplicity of an asteroid, even if it is far, too faint, and/or accompanied with a small Moon undetectable by AO systems. As an example, the observation of an occultation by the Jupiter-trojan Asteroid (911) Agamemnon in 2012 showed a deep brief secondary event that is likely due to a satellite of about 5 km (Timerson et al., 2013). Additional occultations involving (87) Sylvia are predicted in the near future. Table 8 lists a selection of events scheduled for the next 10 years, and their locations. In the future, we will continue to monitor the orbits of the satellites and deliver predictions of the moons' paths at the time of occultations.

Acknowledgments

We are grateful to all the observers for their efforts and for providing their observations (Table 5). We appreciate the help of S. Preston (IOTA) who made available the prediction of the event, to H. Harris (UNSO/Flagstaff) and B. Owen (TMO) for providing last minute astrometric observations of the asteroid, to P. Descamps and *Les Makes* observatory (La Réunion island) for the astrometric measurements of the occulted star, to E. Frappa (Euraster), J. Lecacheux (LESIA/Observatoire de Paris) et al. to have organized the observational campaign and collected the observer reports. The work of F. Marchis was supported by the NASA Grant NNX11AD62G. The work of J. Ďurech was supported by the Grants GACR 209/10/0537 and P209/12/0229 of the Czech Science Foundation. We thank the C2PU team who gave us access to the data collected by the *Omicron* telescope of the *Centre Pédagogique Planète et Univers* (Observatoire de la Côte d'Azur, Calern site), as well as the TAROT observatory team who made available their robotic telescopes to record occultation events.

References

Barucci, M.A. et al., 2005. Asteroid target selection for the new Rosetta mission baseline. 21 Lutetia and 2867 Steins. Astron. Astrophys. 430, 313–317.
Berthier, J., et al., 2013. Detection of a Stellar Occultation by (87) Sylvia I (Romulus). Central Bureau Electronic Telegrams 3398.

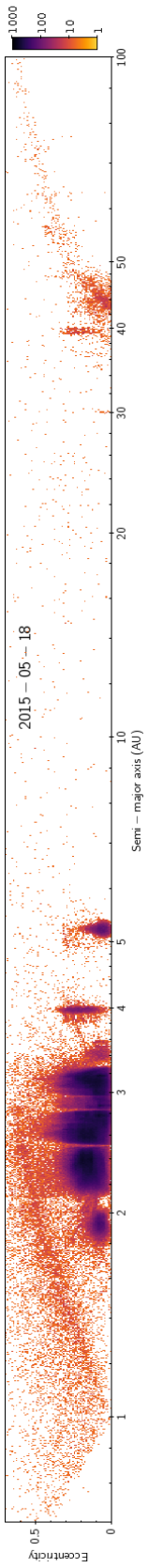

Blanco, C., di Martino, M., Gonano, M., Jaumann, R., Mottola, S., 1989. CCD observations of minor planets. Memorie della Societa Astron. Italiana 60, 195–198.

Bottke Jr., W.F., Richardson, D.C., Michel, P., Love, S.G., 1999. 1620 Geographos and 433 Eros: Shaped by planetary Tides? Astron. J. 117, 1921–1928.

Bouchez, A.H., et al., 2006. Keck laser guide star adaptive optics discovery and characterization of large Kuiper Belt Object satellites. In: American Astronomical Society Meeting Abstracts #207, p. 98.09.

Brown, M.E. et al., 2005. Keck observatory laser guide star adaptive optics discovery and characterization of a satellite to the large Kuiper Belt Object 2003 EL_{61}. Astrophys. J. 632, L45–L48.

Brown, M.E., Margot, J.L., Keck, II, W.M., de Pater, I., Roe, H., 2001. S/2001 (87) 1. Central Bureau Electronic Telegrams 7588.

Brozović, M., Benner, L.A.M., Taylor, P.A., Nolan, M.C., Howell, E.S., Magri, C., Scheeres, D.J., Giorgini, J.D., Pollock, J.T., Pravec, P., Galád, A., Fang, J., Margot, J.L., Busch, M.W., Shepard, M.K., Reichart, D.E., Ivarsen, K.M., Haislip, J.B., Lacluyze, A.P., Jao, J., Slade, M.A., Lawrence, K.J., Hicks, M.D., 2011. Radar and optical observations and physical modeling of triple near-Earth Asteroid (136617) 1994 CC. Icarus 216, 241–256.

Bus, S.J., Binzel, R.P., 2002. Phase II of the small Main-Belt asteroid spectroscopic survey a feature-based taxonomy. Icarus 158, 146–177.

Carry, B., 2012. Density of asteroids. Planet. Space Sci. 73, 98–118.

Carry, B., Dumas, C., Kaasalainen, M., Berthier, J., Merline, W.J., Erard, S., Conrad, A., Drummond, J.D., Hestroffer, D., Fulchignoni, M., Fusco, T., 2010. Physical properties of (2) Pallas. Icarus 205, 460–472.

Carry, B. et al., 2012. Shape modeling technique KOALA validated by ESA Rosetta at (21) Lutetia. Planet. Space Sci. 66, 200–212.

Descamps, P., Marchis, F., Berthier, J., Emery, J.P., Duchêne, G., de Pater, I., Wong, M.H., Lim, L., Hammel, H.B., Vachier, F., Wiggins, P., Teng-Chuen-Yu, J.P., Peyrot, A., Pollock, J., Assafin, M., Vieira-Martins, R., Camargo, J.I.B., Braga-Ribas, F., Macomber, B., 2011. Triplicity and physical characteristics of Asteroid (216) Kleopatra. Icarus 211, 1022–1033.

Descamps, P., Marchis, F., Pollock, J., Berthier, J., Vachier, F., Birlan, M., Kaasalainen, M., Harris, A.W., Wong, M.H., Romanishin, W.J., Cooper, E.M., Kettner, K.A., Wiggins, P., Kryszczynska, A., Polinska, M., Coliac, J.F., Devyatkin, A., Verestchagina, I., Gorshanov, D., 2008. New determination of the size and bulk density of the binary Asteroid 22 Kalliope from observations of mutual eclipses. Icarus 196, 578–600.

Devillard, N., 1997. The eclipse software. Messenger 87, 19–20.

Drummond, J.D., Cocke, W.J., 1989. Triaxial ellipsoid dimensions and rotational pole of 2 Pallas from two stellar occultations. Icarus 78, 323–329.

Dunham, D.W., Herald, D., Frappa, E., Hayamizu, T., Talbot, J., Timerson, B., 2012. Asteroid occultations v10.0. ear-a-3-rdr-occultations-v10.0. NASA Planetary Data System.

Eisenhauer, F., et al., 2003. SINFONI – Integral field spectroscopy at 50 milli-arcsecond resolution with the ESO VLT. In: Iye, M., Moorwood, A.F.M. (Eds.), Society of Photo-Optical Instrumentation Engineers (SPIE) Conference Series, pp. 1548–1561.

Esposito, S., et al., 2011. Large Binocular Telescope Adaptive Optics System: New achievements and perspectives in adaptive optics. In: Society of Photo-Optical Instrumentation Engineers (SPIE) Conference Series.

Fang, J., Margot, J.L., Brozovic, M., Nolan, M.C., Benner, L.A.M., Taylor, P.A., 2011. Orbits of Near-Earth Asteroid triples 2001 SN263 and 1994 CC: Properties, origin, and evolution. Astrophys. J., 154–158.

Fang, J., Margot, J.L., Rojo, P., 2012. Orbits, masses, and evolution of Main Belt triple (87) Sylvia. Astrophys. J. 144, 70–82.

Fornasier, S., Clark, B.E., Dotto, E., 2011. Spectroscopic survey of X-type asteroids. Icarus 214, 131–146.

Frouard, J., Compère, A., 2012. Instability zones for satellites of asteroids: The example of the (87) Sylvia system. Icarus 220, 149–161.

Ghosh, A., Weidenschilling, S.J., McSween Jr., H.Y., 2003. Importance of the accretion process in asteroid thermal evolution: 6 Hebe as an example. Meteorit. Planet. Sci. 38, 711–724.

Hanuš, J., Marchis, F., Ďurech, J., 2013a. Sizes of main-belt asteroids by combining shape models and Keck adaptive optics observations. Icarus 226, 1045–1057.

Hanuš, J. et al., 2013b. Asteroids' physical models from combined dense and sparse photometry and scaling of the YORP effect by the observed obliquity distribution. Astron. Astrophys. 551, A67, 16 pp.

Harris, A.W., Young, J.W., 1980. Asteroid rotation. III – 1978 observations. Icarus 43, 20–32.

Herriot, G., et al., 2000. Progress on Altair: The Gemini North adaptive optics system. In: Wizinowich, P.L. (Ed.), Society of Photo-Optical Instrumentation Engineers (SPIE) Conference Series, pp. 115–125.

Hodapp, K.W. et al., 2003. The Gemini Near-Infrared Imager (NIRI). Publ. Astron. Soc. Pacific 115, 1388–1406.

Kaasalainen, M., 2011. Multimodal inverse problems: Maximum compatibility estimate and shape reconstruction. Inverse Problems Imag. 5, 37–57.

Kaasalainen, M., Torppa, J., Piironen, J., 2002. Models of twenty asteroids from photometric data. Icarus 159, 369–395.

Lagerkvist, C.I., et al., 1987. Asteroid photometric catalogue.

Lenzen, R., et al., 2003. NAOS-CONICA first on sky results in a variety of observing modes. In: Iye, M., Moorwood, A.F.M. (Eds.), Society of Photo-Optical Instrumentation Engineers (SPIE) Conference Series, pp. 944–952.

Marchis, F., et al., 2006a. Large Adaptive Optics Survey of Asteroids (LAOSA): Size, Shape, and Occasionally Density via Multiplicity. LPI Contributions 1325, pp. 57–58.

Marchis, F., Descamps, P., Hestroffer, D., Berthier, J., 2005a. Discovery of the triple asteroidal system 87 Sylvia. Nature 436, 822–824.

Marchis, F., Descamps, P., Hestroffer, D., Berthier, J., Brown, M.E., Margot, J.L., 2005b. Satellites of (87) Sylvia. Cent. Bureau Electronic Telegrams 8582, 1.

Marchis, F., Kaasalainen, M., Hom, E.F.Y., Berthier, J., Enriquez, J., Hestroffer, D., Le Mignant, D., de Pater, I., 2006b. Shape, size and multiplicity of main-belt asteroids. I. Keck Adaptive Optics Survey. Icarus 185, 39–63.

Marchis, F., Lainey, V., Descamps, P., Berthier, J., van Dam, M., de Pater, I., Macomber, B., Baek, M., Le Mignant, D., Hammel, H.B., Showalter, M., Vachier, F., 2010. A dynamical solution of the triple asteroid system (45) Eugenia. Icarus 210, 635–643.

Marchis, F., Ruffio, J.B., Vachier, F., Berthier, J., 2013a. Component-resolved near-infrared spectra of multiple asteroid systems. AGU Fall Meeting Abstracts.

Marchis, F., Vachier, F., Ďurech, J., Enriquez, J.E., Harris, A.W., Dalba, P.A., Berthier, J., Emery, J.P., Bouy, H., Melbourne, J., Stockton, A., Fassnacht, C.D., Dupuy, T.J., Strajnic, J., 2013b. Characteristics and large bulk density of the C-type main-belt triple Asteroid (93) Minerva. Icarus 224, 178–191.

Ockert-Bell, M.E., Clark, B.E., Shepard, M.K., Isaacs, R.A., Cloutis, E.A., Fornasier, S., Bus, S.J., 2010. The composition of M-type asteroids: Synthesis of spectroscopic and radar observations. Icarus 210, 674–692.

Ostro, S.J., Jurgens, R.F., Rosema, K.D., Hudson, R.S., Giorgini, J.D., Winkler, R., Yeomans, D.K., Choate, D., Rose, R., Slade, M.A., Howard, S.D., Scheeres, D.J., Mitchell, D.L., 1996. Radar observations of Asteroid 1620 geographos. Icarus 121, 46–66.

Pogson, N., 1866. Minor planet 87 Sylvia. Mon. Not. R. Astron. Soc. 26, 311–311.

Press, W., Teukolsky, S., Vetterling, W., Flannery, B., 2007. Numerical Recipes: The Art of Scientific Computing.

Prokof'eva, V.V., Demchik, M.I., 1992. Asteroid 87 Sylvia is binary. Astron. Tsirkulyar 1552, 27–28.

Prokof'eva, V.V., Demchik, M.I., 1994. Fourier analysis of simultaneous BVR observations of the asteroid 87 Sylvia and its duplicity. Astron. Lett. 20, 245–252.

Prokof'eva, V.V., Demchik, M.L., Karachkina, L.G., 1995. Photometric evidences for the binary Asteroids 87 Sylvia and 423 Diotima. Astron. Astrophys. Trans. 8, 291–295.

Ragozzine, D., Brown, M.E., 2009. Orbits and masses of the satellites of the dwarf planet Haumea (2003 EL61). Astrophys. J. 137, 4766–4776.

Rousset, G., et al., 2003. NAOS, the first AO system of the VLT: on-sky performance. In: Wizinowich, P.L., Bonaccini, D. (Eds.), Society of Photo-Optical Instrumentation Engineers (SPIE) Conference Series, pp. 140–149.

Schober, H.J., Surdej, J., 1979. UBV photometry of the asteroids 9 Metis, 87 Sylvia and 247 Eukrate during their oppositions in 1978 with respect to lightcurves. Astron. Astrophys. Suppl. 38, 269–274.

Storrs, A., Vilas, F., Landis, R., Wells, E., Woods, C., Zellner, B., Gaffey, M., 2001. S/2001 (87) 1. Cent. Bureau Electronic Telegrams 7590, 3.

Tedesco, E.F., Noah, P.V., Noah, M., Price, S.D., 2002. The supplemental IRAS Minor Planet Survey. Astron. J. 123, 1056–1085.

Timerson, B., et al., 2013. Occultation Evidence for a Satellite of the Trojan Asteroid (911) Agamemnon. ArXiv e-prints.

Ďurech, J., Grav, T., Jedicke, R., Denneau, L., Kaasalainen, M., 2005. Asteroid models from the Pan-STARRS photometry. Earth Moon Planets 97, 179–187.

Ďurech, J., Kaasalainen, M., Herald, D., Dunham, D., Timerson, B., Hanuš, J., Frappa, E., Talbot, J., Hayamizu, T., Warner, B.D., Pilcher, F., Galád, A., 2011. Combining asteroid models derived by lightcurve inversion with asteroidal occultation silhouettes. Icarus 214, 652–670.

Vachier, F., Berthier, J., Marchis, F., 2012. Determination of binary asteroid orbits with a genetic-based algorithm. Astron. Astrophys. 543, A68, 9 pp.

van Dam, M.A., Le Mignant, D., Macintosh, B.A., 2004. Performance of the Keck observatory adaptive-optics system. Appl. Opt. 43, 5458–5467.

Vernazza, P., Brunetto, R., Binzel, R.P., Perron, C., Fulvio, D., Strazzulla, G., Fulchignoni, M., 2009. Plausible parent bodies for enstatite chondrites and mesosiderites: Implications for Lutetia's fly-by. Icarus 202, 477–486.

Vernazza, P., Lamy, P., Groussin, O., Hiroi, T., Jorda, L., King, P.L., Izawa, M.R.M., Marchis, F., Birlan, M., Brunetto, R., 2011. Asteroid (21) Lutetia as a remnant of Earth's precursor planetesimals. Icarus 216, 650–659.

Vokrouhlický, D., Nesvorný, D., Bottke, W.F., Morbidelli, A., 2010. Collisionally born family About 87 Sylvia. Astrophys. J. 139, 2148–2158.

Warner, B.D., Harris, A.W., Pravec, P., 2009. The asteroid lightcurve database. Icarus 202, 134–146.

Weidenschilling, S.J., Chapman, C.R., Davis, D.R., Greenberg, R., Levy, D.H., 1990. Photometric geodesy of main-belt asteroids. III – Additional lightcurves. Icarus 86, 402–447.

Weidenschilling, S.J., Chapman, C.R., Davis, D.R., Greenberg, R., Levy, D.H., Vail, S., 1987. Photometric geodesy of main-belt asteroids. I – Lightcurves of 26 large, rapid rotators. Icarus 70, 191–245.

Weiss, B.P., Elkins-Tanton, L.T., 2013. Differentiated planetesimals and the parent bodies of chondrites. Ann. Rev. Earth Planet. Sci. 41, 529–560.

Winter, O.C. et al., 2009. On the stability of the satellites of Asteroid 87 Sylvia. Mon. Not. R. Astron. Soc. 395, 218–227.

Wizinowich, P., et al., 2010. W.M. Keck Observatory's next-generation adaptive optics facility. In: Society of Photo-Optical Instrumentation Engineers (SPIE) Conference Series.

Wizinowich, P.L., Acton, D.S., Lai, O., Gathright, J., Lupton, W., Stomski, P.J., 2000. Performance of the W.M. Keck Observatory Natural Guide Star Adaptive Optic Facility: the first year at the telescope. In: Wizinowich, P.L. (Ed.), Society of Photo-Optical Instrumentation Engineers (SPIE) Conference Series, pp. 2–13.

Icarus 309 (2018) 134–161

Contents lists available at ScienceDirect

Icarus

journal homepage: www.elsevier.com/locate/icarus

Physical, spectral, and dynamical properties of asteroid (107) Camilla and its satellites☆

M. Pajuelo[a,b,*], B. Carry[a,c], F. Vachier[a], M. Marsset[d], J. Berthier[a], P. Descamps[a], W.J. Merline[e], P.M. Tamblyn[e], J. Grice[c,f], A. Conrad[g], A. Storrs[h], B. Timerson[i], D. Dunham[j], S. Preston[k], A. Vigan[l], B. Yang[m], P. Vernazza[l], S. Fauvaud[n], L. Bernasconi[o], D. Romeuf[o], R. Behrend[o,r], C. Dumas[m,p], J.D. Drummond[q], J.-L. Margot[s], P. Kervella[t,u], F. Marchis[v], J.H. Girard[w]

[a] IMCCE, Observatoire de Paris, PSL Research University, CNRS, Sorbonne Universités, UPMC Univ Paris 06, Univ. Lille, France
[b] Sección Física, Departamento de Ciencias, Pontificia Universidad Católica del Perú, Apartado, Lima 1761, Perú
[c] Université Côte d'Azur, Observatoire de la Côte d'Azur, CNRS, Laboratoire Lagrange, France
[d] Astrophysics Research Centre, Queen's University Belfast, Belfast, County Antrim, BT7 1NN, UK
[e] Southwest Research Institute, Boulder, CO, USA
[f] School of Physical Sciences, The Open University, MK7 6AA, UK
[g] Large Binocular Telescope Observatory, University of Arizona, Tucson, AZ 85721, USA
[h] Towson University, Towson, MD, USA
[i] International Occultation Timing Association (IOTA), 623 Bell Rd., Newark, NY 14513-8805, USA
[j] IOTA, 3719 Kara Ct., Greenbelt, MD 20770-3016, USA
[k] IOTA, 7640 NE 32 nd St., Medina, WA 98039, USA
[l] Aix Marseille Univ, CNRS, LAM, Laboratoire d'Astrophysique de Marseille, Marseille, France
[m] ESO-Chile, Alonso de Córdova 3107, Vitacura, Santiago, RM, Chile
[n] Observatoire du Bois de Bardon, 16110, Taponnat, France
[o] CdR & CdL Group: Lightcurves of Minor Planets and Variable Stars, Switzerland
[p] Thirty-Meter-Telescope, 100 West Walnut St, Suite 300, Pasadena, CA 91124, USA
[q] Leidos, Starfire Optical Range, AFRL/RDS, Kirtland AFB, NM 87117, USA
[r] Geneva Observatory, Sauverny 1290, Switzerland
[s] Department of Earth, Planetary, and Space Sciences, UCLA, Los Angeles, CA 90095, USA
[t] Unidad Mixta Internacional Franco-Chilena de Astronomía, CNRS/INSU UMI 3386 and Departamento de Astronomía, Universidad de Chile, Casilla 36-D, Santiago, Chile
[u] LESIA, Observatoire de Paris, PSL Research University, CNRS, Sorbonne Universités, UPMC Univ. Paris 06, Univ. Paris Diderot, Sorbonne Paris Cité, 5 Place Jules Janssen, Meudon 92195, France
[v] SETI Institute, Carl Sagan Center, 189 Bernado Avenue, Mountain View, CA 94043, USA
[w] Space Telescope Science Institute, 3700 San Martin Drive, Baltimore, MD 21218, USA

ARTICLE INFO

Article history:
Received 25 July 2017
Revised 14 February 2018
Accepted 7 March 2018
Available online 8 March 2018

Keywords:
Asteroids
Composition
Satellites of asteroids
Photometry
Spectroscopy

ABSTRACT

The population of large 100+ km asteroids is thought to be primordial. As such, they are the most direct witnesses of the early history of our Solar System available. Those among them with satellites allow study of the mass, and hence density and internal structure. We study here the dynamical, physical, and spectral properties of the triple asteroid (107) Camilla from lightcurves, stellar occultations, optical spectroscopy, and high-contrast and high-angular-resolution images and spectro-images.

Using 80 positions measured over 15 years, we determine the orbit of its larger satellite, *S/2001 (107) 1*, to be circular, equatorial, and prograde, with root-mean-square residuals of 7.8 mas, corresponding to a sub-pixel accuracy. From 11 positions spread over three epochs only, in 2015 and 2016, we determine a preliminary orbit for the second satellite *S/2016 (107) 1*. We find the orbit to be somewhat eccentric and slightly inclined to the primary's equatorial plane, reminiscent of the properties of inner satellites of other asteroid triple systems. Comparison of the near-infrared spectrum of the larger satellite reveals no significant difference with Camilla. Hence, both dynamical and surface properties argue for a formation of the satellites by excavation from impact and re-accumulation of ejecta in orbit.

We determine the spin and 3-D shape of Camilla. The model fits well each data set: lightcurves, adaptive-optics images, and stellar occultations. We determine Camilla to be larger than reported from modeling of mid-infrared photometry, with a spherical-volume-equivalent diameter of 254 ± 36 km (3σ uncertainty), in agreement with recent results from shape modeling (Hanus et al., 2017, A&A 601). Combining the mass of $(1.12 \pm 0.01) \times 10^{19}$ kg (3σ uncertainty) determined from the dynamics of the satellites and the volume from the 3-D shape model, we determine a density of 1,280 ± 130 kg · m^{-3} (3 σ uncertainty). From this density, and considering Camilla's spectral similarities with (24) Themis and (65) Cybele (for which water ice coating on surface grains was reported), we infer a silicate-to-ice mass ratio of 1–6, with a 10–30% macroporosity.

https://doi.org/10.1016/j.icarus.2018.03.003

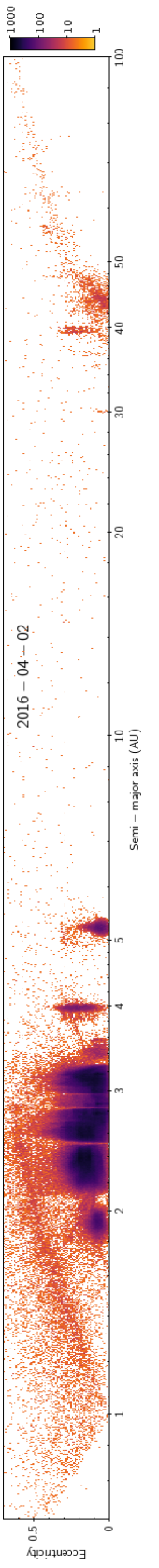

1. Introduction

Main belt asteroids are the remnants of the building blocks that accreted to form terrestrial planets, leftovers of the dynamical events that shaped our planetary system. Among them, large bodies (diameter larger than ≈ 100 km) are deemed primordial (Morbidelli et al., 2009), and contain a relatively pristine record of their initial formation conditions

Decades of photometric and spectroscopic surveys have provided an ever-improving picture of the distribution of material in the inner solar system (e.g. Gradie and Tedesco, 1982; Burbine et al., 1996; 2002; Bus and Binzel, 2002a; Rivkin et al., 2002; 2006; Vernazza et al., 2008; 2010; Vernazza et al., 2014; DeMeo and Carry, 2014), yet these studies have probed the composition of the surface only. As such, they do not necessarily lead us to the original location and time scales for the accretion of these blocks, which are key to understanding the important processes in the disk of gas and dust around the young Sun.

These issues can be addressed by studying the internal structure of asteroids: objects formed far from the Sun are expected to be composed of various mixtures of rock and ice, while objects closer to the Sun are expected to be volatile-free. Depending on their formation time scale, the amount of radiogenic heat varied, leading to complete, partial, or no differentiation. In that respect, density is clearly the most important remotely measurable property that can constrain internal structure (Scheeres et al., 2015).

Determination of density requires measurement of mass and volume, and for that, large asteroids with satellites are prime targets (Merline et al., 1999; 2002; Marchis et al., 2008b; 2008a; Carry et al., 2011; Margot et al., 2015). The study of the orbits of satellites within asteroid binaries or multiple systems is currently the most precise method to estimate the mass of the primary asteroid. If the primary also happen to have an angular diameter large enough to be spatially resolved by large telescopes, this also allows an accurate determination of the primary's volume. In addition, the orbits of the satellites themselves offer a way to probe the gravity field, related to mass distribution inside the asteroid (Berthier et al., 2014; Marchis et al., 2014).

Here we focus on the outer-main-belt asteroid (107) Camilla, orbiting in the Cybele region and discovered on November 17, 1868 from Madras, India by N. R. Pogson. Its first satellite, *S/2001 (107) 1* (hereafter S1), was discovered in March 2001 by Storrs et al. (2001), using the Hubble Space Telescope (HST), and its orbit first studied by Marchis et al. (2008a) using observations from large ground-based telescopes equipped with adaptive-optics (AO) systems. Its second satellite, *S/2016 (107) 1* (hereafter S2), was discovered in 2016 by our team (Marsset et al., 2016), using the European Southern Observatory (ESO) Very Large Telescope (VLT).

Camilla was originally classified as a C-type based on its visible colors and albedo (Tedesco et al., 1989). Later on, both Bus and Binzel (2002a) and Lazzaro et al. (2004) classified it as X, based on visible spectra. More recently, based on a near-infrared spectrum from NASA IRTF Spex, Lindsay et al. (2015) classified Camilla as either Xe or L.

The physical properties of Camilla have been extensively studied, from its rotation period of 4.8 h (e.g., Weidenschilling et al., 1987; di Martino et al., 1987) to its spin and 3D shape model (Torppa et al., 2003; Ďurech et al., 2011; Hanuš et al., 2013; 2017). Its diameter, however, was poorly constrained, with estimates ranging from 185 ± 9 km (Marchis et al., 2006) to 256 ± 12 km (Marchis et al., 2012). More recent studies combining images or stellar occultations with lightcurve-based 3D shape modeling, are yielding diameters in excess of 220 km (see Fig. B.2 and Table B.2 for the exhaustive list of diameter estimates). The mass estimates also spanned a wide range, from $2.25^{+18.00}_{-2.25}$ to $39 \pm 10 \times 10^{18}$kg (Zielenbach, 2011) (see Fig. B.1 and Table B.1 for the exhaustive list of mass estimates). With these large spread of values, deriving an accurate density would require substantial improvements to these parameters.

Gathering all the available disk-resolved and high-contrast images from HST and AO-fed cameras, optical lightcurves, stellar occultations, and visible and near-infrared spectra (Section 2), we present an extensive study of the dynamics of the system (Section 3), of the surface properties of Camilla and its main satellite S1 (Section 4), and of Camilla's spin and 3-D shape (Section 5), all constraining its internal composition and structure (Section 6).

2. Observations

2.1. Optical lightcurves

We gather the 24 lightcurves used by Torppa et al. (2003) to create a convex 3-D shape model of Camilla[1], compiled from the Uppsala Asteroid Photometric Catalog[2] (Lagerkvist and Magnusson, 2011). We also retrieve the three lightcurves reported by Polishook (2009).

In addition to these data, we acquired 29 lightcurves using the 60 cm *André Peyrot* telescope mounted at Les Makes observatory on Réunion Island, operated as a partnership among Les Makes Observatory and the IMCCE, Paris Observatory. We also extracted 63 lightcurves from the data archive of the SuperWASP survey (Pollacco et al., 2006) for the period 2006–2009. This survey aims to find and characterize exoplanets by observations of their transits of the host star. Its large field of view (8° × 8°) provides a goldmine for asteroid lightcurves (Parley et al., 2005; Grice et al., 2017).

A total of 127 lightcurves observed between 1981 and 2016 (Table A.1) are used in this work.

2.2. High-angular-resolution imaging

We compile here all the high-angular-resolution images of Camilla taken with the HST and large ground-based telescopes equipped with AO-fed cameras: Gemini North, ESO VLT, and W. M. Keck, of which only a subset had already been published (Storrs et al., 2001; Marchis et al., 2008a). All of these data sets were acquired by the authors of this paper. The data comprise 62 different epochs, with multiple images each, spanning 15 years, from March 2001 to August 2016.

The images from the VLT were acquired with both the first generation instrument NACO (NAOS-CONICA, Lenzen et al., 2003;

☆ Based on observations obtained at: (1) the Hubble Space Telescope, operated by NASA and ESA; (2) the Gemini Observatory and acquired through the Gemini Observatory Archive, which is operated by the Association of Universities for Research in Astronomy, Inc., under a cooperative agreement with the NSF on behalf of the Gemini partnership: the National Science Foundation (United States), the National Research Council (Canada), CONICYT (Chile), Ministerio de Ciencia, Tecnología e Innovación Productiva (Argentina), and Ministério da Ciência, Tecnologia e Inovação (Brazil); (3) the European Southern Observatory, Paranal, Chile – 071.C-0669 (PI Merline), 073.C-0062 and 074.C-0052(PI Marchis), 087.C-0014(PI Marchis), 088.C-0528 (PI Rojo), 095.C-0217 and 297.C-5034 (PI Marsset) – and (4) the W. M. Keck Observatory, which is operated as a scientific partnership among the California Institute of Technology, the University of California and the National Aeronautics and Space Administration. The Observatory was made possible by the generous financial support of the W. M. Keck Foundation.

* Corresponding author at: IMCCE, Observatoire de Paris, PSL Research University, CNRS, Sorbonne Universités, UPMC Univ Paris 06, Univ. Lille, France.
E-mail address: myriam.pajuelo@obspm.fr (M. Pajuelo).

[1] Available on DAMIT (Ďurech et al., 2010): http://astro.troja.mff.cuni.cz/projects/asteroids3D/

[2] http://asteroid.astro.helsinki.fi/apc/asteroids/

Rousset et al., 2003) and SPHERE (Spectro-Polarimetric High-contrast Exoplanet REsearch, Fusco et al., 2006; Beuzit et al., 2008), the second generation extreme-AO instrument designed for exoplanet detection and characterization. The images taken with SPHERE used its IRDIS differential imaging camera sub-system (InfraRed Dual-band Imager and Spectrograph, Dohlen et al., 2008). Images taken at the Gemini North used NIRI camera (Near InfraRed Imager, Hodapp et al., 2003), fed by the ALTAIR AO system (Herriot et al., 2000). Finally, observations at Keck were acquired with NIRC2 (Near-InfraRed Camera 2, van Dam et al., 2004; Wizinowich et al., 2000). We list in Table A.2 the details of each observation.

The basic data processing (sky subtraction, bad-pixel removal, and flat-field correction) was performed using in-house routines developed in Interactive Data Language (IDL) to reduce AO-imaging data (see Carry et al., 2008, for more details).

2.3. High-angular-resolution spectro-imaging

In 2015 and 2016, we also used the integral-field spectrograph (IFS) of the SPHERE instrument at the ESO VLT, aiming to measure the reflectance spectrum of Camilla's largest satellite S1, and the astrometry of the fainter satellite S2. The observations were made in the IRDIFS_EXT mode (Zurlo et al., 2014), in which both IRDIS (Dohlen et al., 2008) and the IFS (Claudi et al., 2008) data are acquired simultaneously. In this set-up, the IFS covers the wavelength range from 0.95 to 1.65 μm (YJH bands) at a spectral resolving power of $\sim$ 30 in a $1.7'' \times 1.7''$ field of view (FoV), while IRDIS operates in the dual-band imaging mode (DBI, Vigan et al., 2010) with K_{12}, a pair of filters in the K band ($\lambda_{K_1} = 2.110$ μm and $\lambda_{K_2} = 2.251$ μm, $\sim$ 0.1 μm bandwidth), within a $4.5''$ FoV. All observations were performed in the pupil-tracking mode, where the pupil remains fixed while the field orientation varies during the observations. This mode provides the best PSF stability and helps in reducing and subtracting static speckle noise in the images.

For the pre-processing of both the IFS and IRDIS data, we used the preliminary release (v0.14.0–2) of the SPHERE Data Reduction and Handling (DRH) software (Pavlov et al., 2008), as well as additional in-house tools written in IDL, including parts of the public pipeline presented in Vigan et al. (2015). See our recent works on (3) Juno and (6) Hebe for more details (Viikinkoski et al., 2015; Marsset et al., 2017). We used the DRH for the creation of some of the basic calibrations: master sky frames, master flat-field, IRDIFS spectra positions, initial wavelength calibration and flat field. Before creating the data cubes, we used IDL routines to subtract the background from each science frame and correct for the bad pixels identified using the master dark and master flat-field DRH products. This step was introduced as a substitute for the bad pixel correction provided by the DRH. Bad pixels were first identified using a sigma-clipping routine, and then corrected using a bicubic pixel interpolation with the `MASKINTERP` IDL routine. The resulting frames were then injected into the DRH recipe to create the data cubes by interpolating the data spectrally and spatially.

2.4. Stellar occultations

Eleven stellar occultations by Camilla have been observed in the last decade, mostly by amateur astronomers (see Mousis et al., 2014; Dunham et al., 2016a). The timings of disappearance and reappearance of the stars, together with the location of each observing station are compiled by Dunham et al. (2016b), and publicly available on the Planetary Data System (PDS[3]). We converted the disappearance and reappearance timings (Table A.3) of the occulted stars into segments (called chords) on the plane of the sky, using the location of the observers on Earth and the apparent motion of Camilla following the recipes by Berthier (1999). Four stellar occultations had multiple chords; other events had only one or two positive chords, and contributed less to constraining the size and apparent shape of Camilla. In none of these eleven stellar occultations was there any evidence for a companion. We list in Table A.4 the details of the seven events that we used.

[3] http://sbn.psi.edu/pds/resource/occ.html

2.5. Near-infrared spectroscopy

On November 1, 2010, we observed Camilla over 0.8–2.5 μm with the near-infrared spectrograph SpeX (Rayner et al., 2003), on the 3-meter NASA IRTF located on Mauna Kea, Hawaii, using the low resolution Prism mode ($R = 100$). We used the standard *nodding* procedure for the observations, using alternately two separated locations on the slit (e.g., Nedelcu et al., 2007) to estimate the sky background. We used Spextool (SPectral EXtraction TOOL), an IDL-based data reduction package written by Cushing et al. (2004) to reduce SpeX data.

3. Dynamical properties

3.1. Data processing

The main challenges in measuring the position and apparent flux of the satellite of an asteroid results from their sub-arcsecond angular separation and high contrast (several magnitudes), combined with imperfect AO correction. A typical image of a binary asteroid (Fig. 1) displays a central peak (the asteroid itself, angularly resolved or not) encompassed by a halo (its diffused light), within which speckle patterns appear. The faintness of these speckles, produced by interference of the incoming light, make them very similar in appearance to a small moon with a contrast up to several thousands, and they can be misleading. Speckles, however, vary (position and flux) on short timescales, depending on the ambient conditions and AO performances (e.g., seeing, airmass, brightness of the AO reference source). These fluctuations can be used to distinguish genuine satellites from speckles.

As for the direct imaging of exoplanets, it is crucial to substract the halo that surrounds the primary (in a similar way to the digital coronography of Assafin et al., 2008). Because asteroids are also marginally resolved, their light is not fully coherent, and the speckle pattern is not as stable in time, nor simple, as in the case of a star. The tool we developed considers concentric annuli around the center of light of the primary to evaluate its halo. Although the principle is straightforward, great caution was taken in the implementation, especially in the computation of the intersection of the annulus with the pixels to allow the use of annuli with a sub-pixel width. The contribution of each pixel to different annuli is thus solved first, and the median flux of each annulus is computed, and subtracted from each pixel accordingly.

The position and flux of the satellite, relative to the primary, is then measured by fitting a 2-D Gaussian function to the halo-subtracted image. The satellites are distinguished from speckles by comparing different images, taken both close in time and over a range of times. To estimate the uncertainties on the position and apparent flux of both the primary and the satellites, we use different integration apertures for each object. The sizes of the apertures are determined by fitting a 2-D Gaussian to each, with diameters typically being 5 to 150 pixels for the primary, and 3 to 15 pixels for the satellites. The reported positions and apparent magnitudes (Tables A.5 and A.6) are the average of all fits (after removal of outlier values), and the reported uncertainties are the standard deviations.

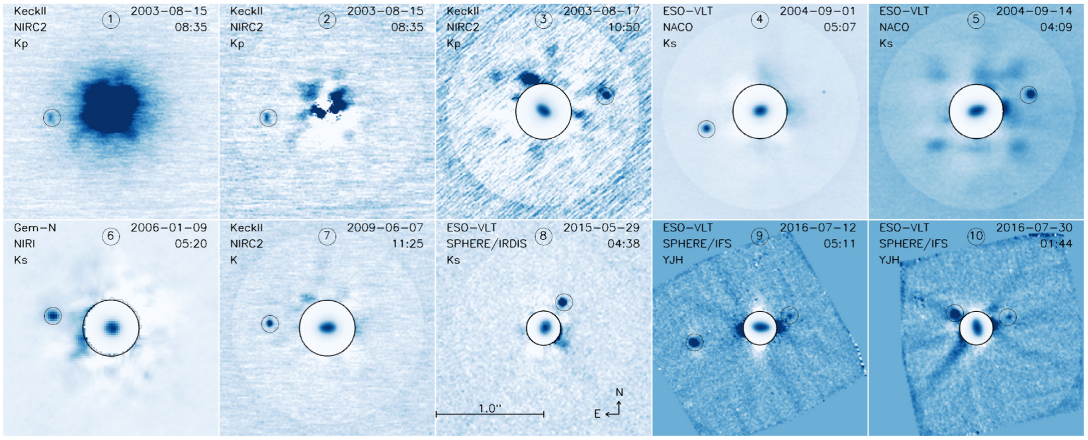

Fig. 1. Examples of AO images from Gemini, Keck, and ESO VLT. The first two panels (1 & 2, August 13, 2003, from Keck) show a typical AO image, before and after halo subtraction: Camilla dominates the background and makes the satellites hard to detect. The remaining panels show halo-subtracted images from different dates, with small circles indicating the positions of the bright satellite S1 and the fainter S2 (frames 9 and 10 only). On these panels, the images before subtraction are also shown in the central circle to highlight the elongated shape of Camilla.

3.2. Orbit determination with `Genoid`

We use our algorithm `Genoid` (GENetic Orbit IDentification, Vachier et al., 2012) to determine the orbit of the satellites. `Genoid` is a genetic-based algorithm that relies on a metaheuristic method to find the best-fit (i.e., minimum χ^2) suite of dynamical parameters (mass, semi-major axis, eccentricity, inclination, longitude of the node, argument of pericenter, and time of passage to pericenter) by refining, generation after generation, a grid of test values (called *individuals*).

The first generation is drawn randomly over a very wide range for each parameter, thus avoiding a miss of the global minimum from inadequate initial conditions. For each individual (i.e., set of dynamical parameters), the χ^2 residuals between the observed and predicted positions is computed as

$$\chi^2 = \sum_{i=1}^{N} \left[\left(\frac{X_{o,i} - X_{c,i}}{\sigma_{x,i}} \right)^2 + \left(\frac{Y_{o,i} - Y_{c,i}}{\sigma_{y,i}} \right)^2 \right] \quad (1)$$

where N is the number of observations, and X_i and Y_i are the relative positions between the satellite and Camilla along the right ascension and declination respectively. The indices o and c stand for observed and computed positions, and σ are the measurement uncertainties.

A new generation of individuals is drawn by mixing randomly the parameters of individuals with the lowest χ^2 from the former generation. This way, the entire parameter space is scanned, with the density of evaluation points increasing toward low χ^2 regions along the process. At each generation, we also use the best individual as initial condition to search for the local minimum by gradient descent. The combination of genetic grid-search and gradient descent thus ensures finding *the* best solution.

We then assess the confidence interval of the dynamical parameters by considering all the individuals providing predictions within 1, 2, and 3σ of the observations. The range spanned by these individuals provide the confidence interval at the corresponding σ level for each parameter.

The reliability of `Genoid` has been assessed during a stellar occultation by (87) Sylvia and its satellites Romulus and Remus on January 6, 2013: `Genoid` had been used to predict the position of Romulus before the event, directing observers to locations specifically to target the satellite. Four different observers detected an occultation by Romulus at only 13.5 km off the predicted track (the cross-track uncertainty was 65 km, Berthier et al., 2014).

3.3. Orbit of S1: S/2001 (107) 1

We measured 80 astrometric positions of the satellite S1 relative to Camilla over a span of 15 years, corresponding to 5642 days or 1520 revolutions. The orbit we derive with `Genoid` fits all 80 observed positions of the satellite with a root mean square (RMS) residual of 7.8 milli-arcseconds (mas) only, which corresponds to a sub-pixel accuracy.

S1 orbits Camilla on a circular, prograde, equatorial orbit, in 3.71 days with a semi-major axis of 1248 km. We detail all the parameters of its orbit in Table 1, with their confidence interval taken at 3σ. The distribution of residuals between the observed and predicted positions, normalized by the uncertainty on the measured positions, are plotted in Fig. 2. The orbit we determine here is qualitatively similar to the one given by Marchis et al. (2008a), while much better constrained: we fit 80 astrometric positions over 15 years with an RMS residual of 7.8 mas, compared to their fit of 23 positions over less than 3 years with an RMS residual of 22 mas. The much longer time span of observations provides a much more stringent constraint on the period (3.712 34 ± 0.000 04 day) of S1, compared to the value of 3.722 ± 0.009 day reported by Marchis et al. (2008a).

As a result, we determine a much more precise mass for Camilla of $(1.12 \pm 0.01) \times 10^{19}$ kg (3σ uncertainty), about 1% of the mass of Ceres (Carry, 2012). We list in Table B.1 the reported values of the mass of Camilla found in the literature. Our mass value agrees well with the average value $(1.10 \pm 0.69) \times 10^{19}$kg we show in Table B.1, although the mass estimates derived from orbital deflection and solar system ephemerides have a large scatter (see Carry, 2012, for a discussion on the precision and bias of mass determination methods). Our determination significantly reduces the uncertainty in the prior value of $(1.12 \pm 0.09) \times 10^{19}$ kg, that also used the orbit of S1 (Marchis et al., 2008a).

Table 1
Orbital elements of the satellites of Camilla, S1 and S2, expressed in EQJ2000, obtained with `Genoid`: orbital period P, semi-major axis a, eccentricity e, inclination i, longitude of the ascending node Ω, argument of pericenter ω, time of pericenter t_p. The number of observations and RMS between predicted and observed positions are also provided. Finally, we report the derived primary mass M, the ecliptic J2000 coordinates of the orbital pole (λ_p, β_p), the equatorial J2000 coordinates of the orbital pole (α_p, δ_p), and the orbital inclination (Λ) with respect to the equator of Camilla. Uncertainties are given at 3-σ.

	S1		S2	
Observing data set				
Number of observations	80		11	
Time span (days)	5642		428	
RMS (mas)	7.8		5.0	
Orbital elements EQJ2000				
P (day)	3.712 34	± 0.000 04	1.376	± 0.016
a (km)	1247.8	± 3.8	643.8	± 3.9
e	0.0	+ 0.013	0.18	$^{+0.23}_{-0.18}$
i (°)	16.0	± 2.3	27.7	± 21.8
Ω (°)	140.1	± 4.9	219.9	± 67.0
ω (°)	98.7	± 6.5	199.4	± 37.6
t_p (JD)	2452835.902	± 0.067	2452835.31589	± 0.174
Derived parameters				
M ($\times$ 10^{19} kg)	1.12	± 0.01		
λ_p, β_p (°)	73, +53	± 2, 2	114, +42	± 44, 18
α_p, δ_p (°)	50, +74	± 5, 2	130, +62	± 67, 22
Λ (°)	4	± 8	32	± 28

3.4. Orbit of S2: S/2016 (107) 1

We measured 11 astrometric positions of the satellite S2 relative to Camilla during 2015 and 2016, corresponding to 428 days or 311 revolutions. These observations correspond to three well-separated epochs: 2015-May-29, 2016-Jul-12, and 2016-Jul-30, providing the minimum needed to constrain the orbit. Thus, although the orbit we determine with `Genoid`fits all 11 observed positions of S2 with an RMS residual of only 5.0 mas and yields reliable values for the major orbital elements, details of all orbital parameters will require further observations.

S2 orbits Camilla in 1.38 days with a semi-major axis of 644 km. We detail all the parameters of its orbit in Table 1 and present the distribution of residuals between the observed and predicted positions in Fig. 3. Unlike S1, its orbit seems neither equatorial nor circular. While cognizant of the larger uncertainties, we favor an orbit inclined to the equator of Camilla by an angle Λ of 32 ± 28° (Fig. 4), and a more eccentric orbit (e=$0.18^{+0.23}_{-0.18}$). Although a circular orbit, co-planar with S1 is marginally within the range of uncertainty, such a solution results in significantly higher residuals. This configuration of an outer satellite on a circular and equatorial orbit with an inner satellite on an inclined and more eccentric orbit has already been reported for other triple systems: (45) Eugenia, (87) Sylvia, and (130) Elektra (Marchis et al., 2010; Fang et al., 2012; Berthier et al., 2014; Yang et al., 2016; Drummond et al., 2016).

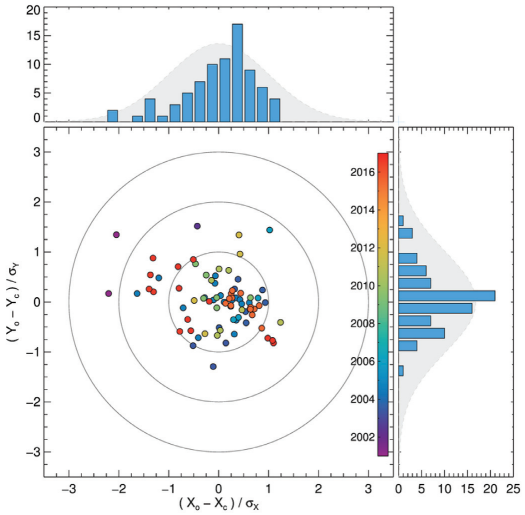

Fig. 2. Distribution of residuals for S1 between the observed (index o) and predicted (index c) positions, normalized by the uncertainty on the measured positions (σ), and color-coded by observing epoch. X stands for right ascension and Y for declination. The three large gray circles represent the 1, 2, and 3 σ limits. The top panel shows the histogram of residuals along X, and the right panel the residuals along Y. The light gray Gaussian in the background has a standard deviation of one.

4. Surface properties

4.1. Data processing

We measured the near-infrared spectra of Camilla and its largest satellite S1 using the SPHERE/IRDIFS data. Telluric features were removed, and the reflectance spectra were obtained by observing the nearby solar type star HD139380.

Similarly to previous sections, the bright halo of Camilla that contaminated the spectrum of the moon was removed. This was achieved by measuring the background at the location of the moon for each pixel as the median value of the area defined as a 40 $\times$ 1-pixel arc centered on Camilla. To estimate the uncertainty and potential bias on photometry introduced by this method, we performed a number of simulations in which we injected fake companions on the 39 spectral images of the spectro-imaging cube, at separation ($\approx$ 300 mas) and random position angles from the primary. The simulated sources were modeled as the PSF, from the calibration star images, scaled in brightness.

The halo from Camilla was then removed from these simulated images using the method described above, and the flux of the simulated companion measured by adjusting a 2D-Gaussian profile. Based on a total statistics of 500 simulated companions, we

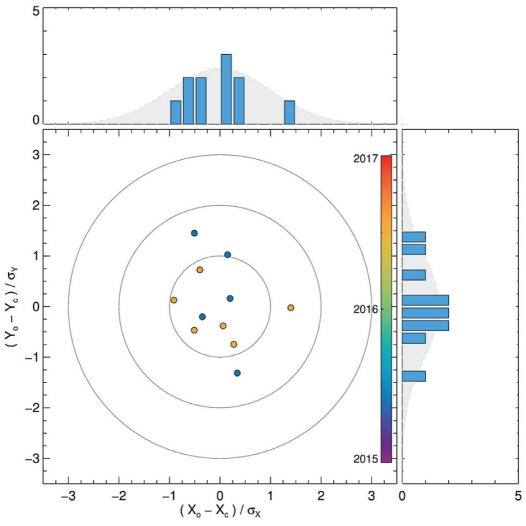

Fig. 3. Similar to Fig. 2, but for S2.

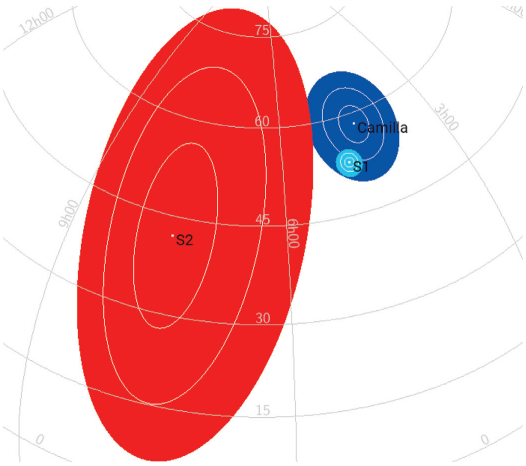

Fig. 4. Coordinates and 1 – 2 – 3 σ contours of Camilla's spin axis (blue) and the orbital poles of S1 (gray) and S2 (red) in ecliptic coordinates. (For interpretation of the references to colour in this figure legend, the reader is referred to the web version of this article.)

find that the median loss of flux at each wavelength is 11 ± 10%. A spectral gradient is also introduced by our technique, but it is smaller than 0.06 ± 0.07% · μm^{-1}. The spectra of Camilla and S1, normalized at 1.1 µm, are shown in Fig. 5.

4.2. Spectrum of Camilla

We combine the near-infrared spectrum we acquired at NASA IRTF (Section 2.5) with the visible spectrum from SMASS (Bus and Binzel, 2002a; 2002b) and analyze them with the M4AST[4] (Modeling for Asteroids, Popescu et al., 2012) suite of Web tools to determine asteroid taxonomic classification, mineralogy, and most-likely meteorite analog. From this longer wavelength range, we found Camilla to be an Xk-type asteroid (using Bus-DeMeo taxonomic scheme, Fig. 5, DeMeo et al., 2009). The low albedo of Camilla (0.059 ± 0.005, taken as the average of the estimates by Morrison and Zellner, 2007; Tedesco et al., 2002; Ryan and Woodward, 2010; Usui et al., 2011; Masiero et al., 2011), hints at a P-type classification, using the Tedesco et al. (1989) scheme.

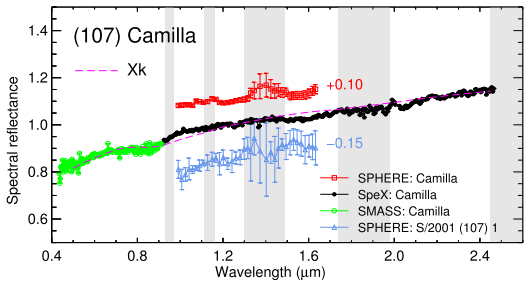

Fig. 5. Visible and near-infrared spectrum of Camilla from IRTF (green and black dots) and SPHERE (red squares, offset by +0.1), and its moon S1 from SPHERE (blue triangles, offset by −0.15). Gray areas represent the wavelength ranges affected by water vapour in the atmosphere. All spectra were normalized to unity at one micron. Overplot to the IRTF spectra is the Bus-DeMeo Xk class. (For interpretation of the references to color in this figure legend, the reader is referred to the web version of this article.)

Although the best spectral match is formally found for an Enstatite Chondrite EH5 meteorite (Queen Alexandra Range, Antarctica origin, maximum size of 10 µm), the low albedo of Camilla argues for a different type of analog material. The composition of P-type asteroids is indeed difficult, if not impossible, to infer from their visible and near-infrared spectra owing to the lack of absorption bands.

Recently, Vernazza et al. (2015) have shown that anhydrous chondritic porous interplanetary dust particules (IDPs) were likely to originate from D- and P-types asteroids, based on spectroscopic observations in the mid-infrared of outer-belt D- and P-type asteroids, including Camilla. The mixture of olivine-rich and pyroxene-rich IDPs they used was compatible with the visible and near-infrared spectrum of Camilla. As such, the surface of Camilla, and more generally of D- and P-types, is very similar to that of comets, as already reported by Emery et al. (2006) from the spectroscopy of Jupiter Trojans in the mid-infrared, revealing the presence of anhydrous silicates.

4.3. Spectrum of S1

As visible in Fig. 5, the spectrum of S1 is similar to that of Camilla. No significant difference in slope nor absorption band can be detected. This implies that the two components are spectraly identical from 0.95 to 1.65 µm, within the precision of our measurements. Such a similarity between the components of multiple systems have already been reported for several other main-belt asteroids: (22) Kalliope (Laver et al., 2009), (90) Antiope (Polishook et al., 2009; Marchis et al., 2011), (130) Elektra (Yang et al., 2016), and (379) Huenna (DeMeo et al., 2011).

Such spectral similarity, together with the main characteristics of the orbit (prograde, equatorial, circular) supports an origin of these satellites, here for S1 in particular, by impact and reaccumulation of material in orbit (see Margot et al., 2015, for a review). Formation by rotational fission is unlikely owing to the rotation period of Camilla (4.84 h).

[4] http://m4ast.imcce.fr/

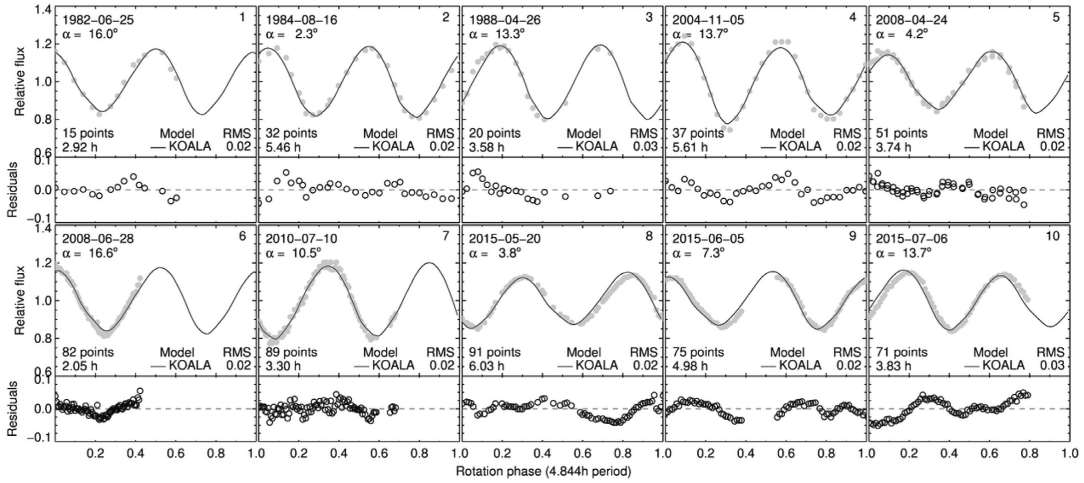

Fig. 6. Examples of optical lightcurves of Camilla. For each epoch, the upper panel presents the observed photometry (grey spheres) compared with synthetic lightcurves generated with the shape model (black lines). The lower panel shows the residuals between the observed and synthetic flux. The observing date, number of points, duration of the lightcurve (in hours), phase angle (α), and RMS residuals between the observations and the synthetic lightcurves are displayed. In most cases, measurement uncertainties are not provided by the observers but can be estimated from the spread of measurements. See Fig. C.1 for the entire data set.

5. Physical properties

5.1. Data processing

We used the optical lightcurves without modification, only converting their heterogeneous formats from many observers to the usual lightcurve inversion format (Ďurech et al., 2010). For the occultation observations, the location of observers, together with their timings of the disappearance and the reappearance of the star, were converted into chords on the plane of the sky, using the recipes from Berthier (1999). Finally, the 2-D profile of the apparent disk of Camilla was measured on the AO images, deconvolved using the `Mistral` algorithm (Fusco, 2000; Mugnier et al., 2004), the reliability of which has been demonstrated elsewhere (Witasse et al., 2006), using the wavelet transform described in Carry et al. (2008, 2010b).

5.2. 3-D Shape modeling with KOALA

We used the multi-data inversion algorithm Knitted Occultation, Adaptive-optics, and Lightcurve Analysis (`KOALA`), which determines the set of rotation period, spin-vector coordinates, and 3-D shape that provide the best fit to all observations simultaneously (Carry et al., 2010a).

The `KOALA` algorithm minimizes the total $\chi^2 = \chi^2_{LC} + w_{AO}\ \chi^2_{AO} + w_{Occ}\ \chi^2_{Occ}$ that is composed of the individual contributions from light curves (LC), profiles from disk-resolved images (AO), and occultation chords (Occ). Adaptive optics and occultation data are weighted with respect to the lightcurves with parameters w_{AO} and w_{Occ}, respectively. Within each type of data, all the epochs are weighted uniformly. The optimum values of these weights can be objectively obtained following the approach of Kaasalainen (2011).

This method has been spectacularly validated by the images taken by the OSIRIS camera on-board the ESA Rosetta mission during its flyby of the asteroid (21) Lutetia (Sierks et al., 2011). Before the encounter, the spin and 3-D shape of Lutetia had been determined with `KOALA`, using lightcurves and AO images (Carry et al., 2010b; Drummond et al., 2010). A comparison of the pre-flyby solution with the OSIRIS images showed that the spin vectorwas accurate to within 2° and the diameter to within 2%. The RMS residual in the surface topography between the `KOALA` predictions and the OSIRIS images was only 2 km, for a 98 km-diameter asteroid (Carry et al., 2012).

5.3. Spin and 3-D shape of Camilla

We used 127 optical lightcurves, 34 profiles from disk-resolved imaging, and 7 stellar occultation events to reconstruct the spin axis and 3-D shape of Camilla. The model fits well the entire data set, with mean residuals of only 0.03 mag for the lightcurves (Figs. 6 and C.1), 0.29 pixel for the images (Fig. 7), and 0.35 s for the stellar occultations (Fig. 8). There are small local departures of the shape model from the stellar occultation chords that can be due to local topography not modeled with our low-resolution shape model.

The rotation period and coordinates of the spin axis (Table 2) agree very well with previous results from lightcurve-only inversion and convex shape modeling (Torppa et al., 2003; Ďurech et al., 2011; Hanuš et al., 2016), as well as models obtained by combining lightcurves and smaller subsets of the present AO data (respectively 3 and 21 epochs, see Hanuš et al., 2013; 2017). The shape of Camilla is far from a sphere, with a strong ellipsoidal elongation along the equator (a/b axes ratio of 1.37 ± 0.12, see Table 2). Departures from the ellipsoid are, however, limited, and mainly consist in two large circular basins, reminiscent of impact craters (Fig. 9).

The spherical-volume-equivalent diameter of Camilla is found to be 254 ± 36 km (3 σ), in excellent agreement with the recent determination by Hanuš et al. (2017) based on a similar data set. Both estimates are high compared to diameter estimates from infrared observations with IRAS, AKARI, or WISE (Tedesco et al., 2004; Ryan and Woodward, 2010; Usui et al., 2011; Masiero et al., 2011, see Table B.2). However, diameter determinations by mid-IR radiometry are based on disk-integrated fluxes. In the case of

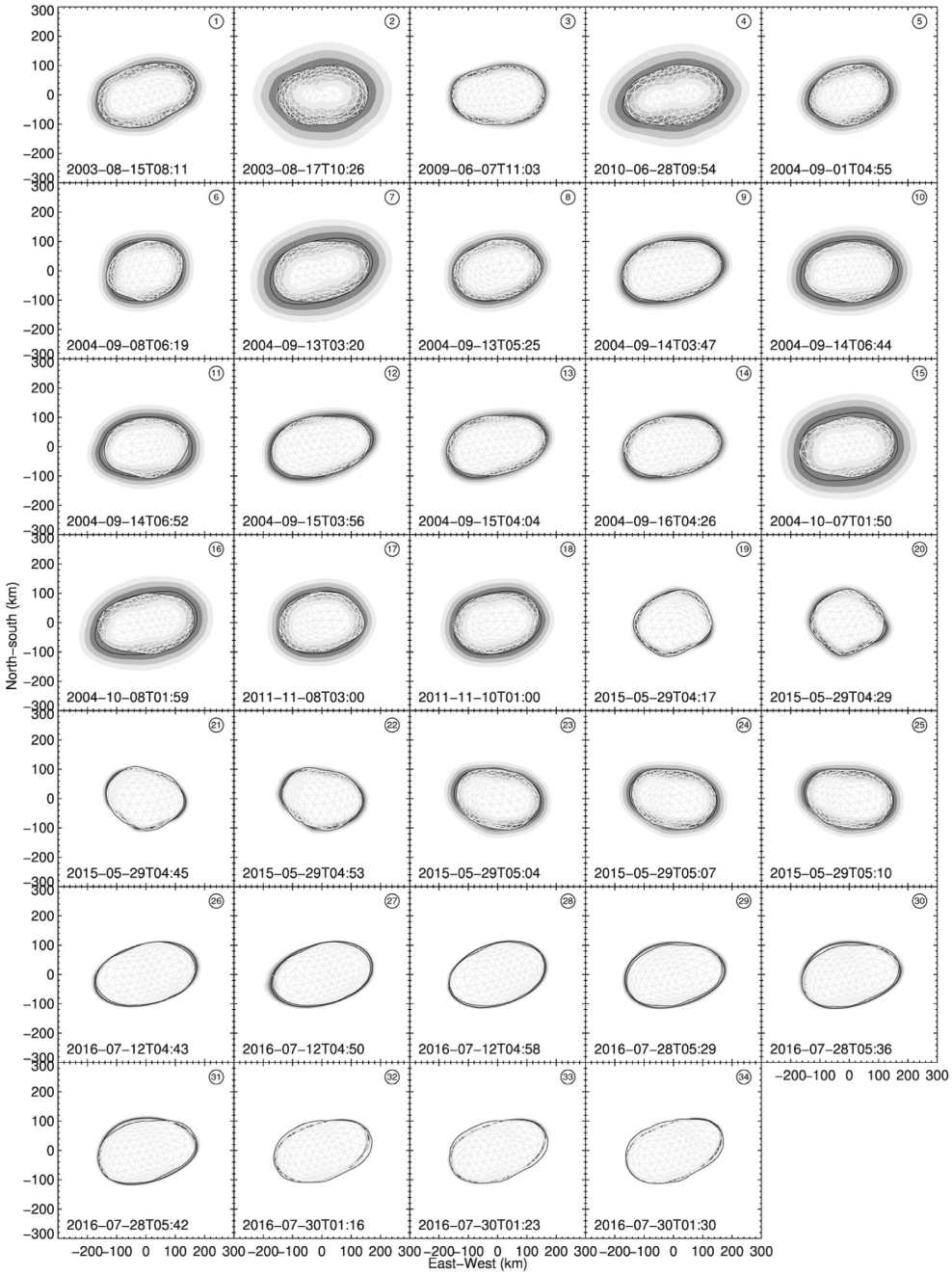

Fig. 7. All 34 profiles of Camilla from disk-resolved images, compared with the projection of the shape model on the plane of the sky. On each panel, corresponding to a different epoch, the grey shaded areas correspond to the 1-2-3σ confidence intervals of each profile, while the shape model is represented by the wired mesh.

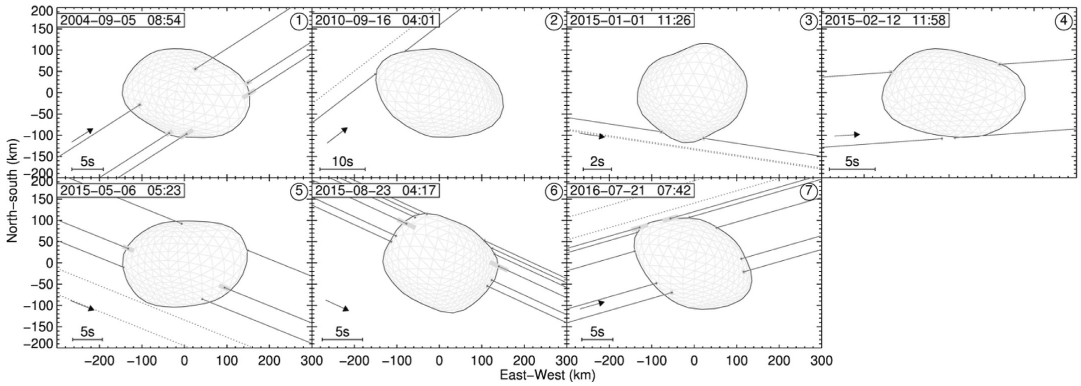

Fig. 8. The seven stellar occultations by Camilla, compared with the shape model projected on the plane of the sky for the times of the occultations. The observer of northern chord in the first occultation, presenting a clear mismatch with the shape model, reported the presence of thin cirrus that may explain the discrepancy.

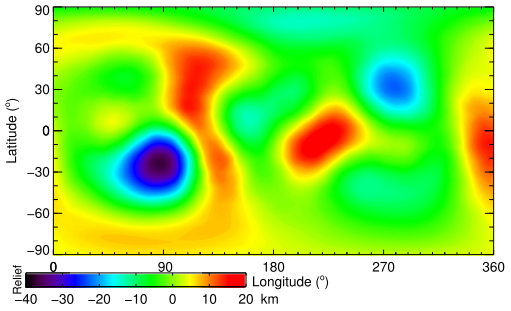

Fig. 9. Topographic map of Camilla, with respect to its reference ellipsoid (Table 2). The main features are the two deep and circular basins located at (87°, −23°) and (278°+33°).

Table 2
Sidereal rotation period, spin-vector coordinates (longitude λ, latitude β in ECJ2000; and right ascension α, declination δ in EQJ2000), spherical-volume-equivalent diameter (D), volume (V), diameters along the principal axis of inertia (a, b, c), and axes ratio of Camilla obtained with KOALA. All uncertainties are reported at 3 σ.

Parameter	Value	Unc.	Unit
Period	4.843927	4.10^{-5}	hour
λ	68.0	9.0	deg.
β	58.3	7.0	deg.
α	35.8	9.0	deg.
δ	76.1	7.0	deg.
T_0	2444636.00		
D	254	36	km
V	$8.55 \cdot 10^6$	$1.21 \cdot 10^6$	km^3
a	340	36	km
b	249	36	km
c	197	36	km
a/b	1.37	0.12	
b/c	1.26	0.12	

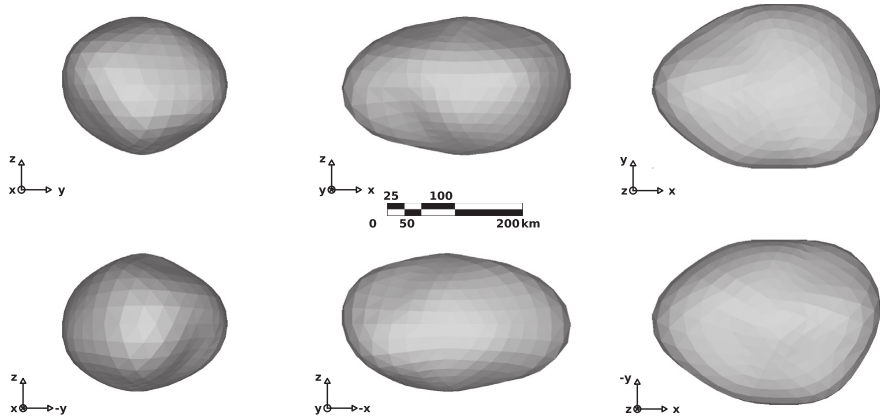

Fig. 10. Views of the shape model along its principal axes (the x,y,z axes in the plot are aligned with the principal moment of inertia of the model).

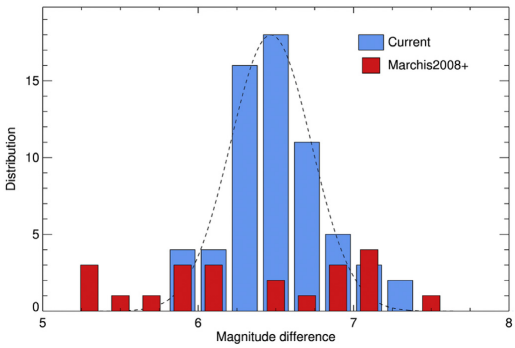

Fig. 11. Distribution of the magnitude differences between Camilla and its largest satellite S1, compared with previous report from Marchis et al. (2008a). The dashed black line represents the normal distribution fit to our results, with a mean and standard deviation of 6.51 ± 0.27.

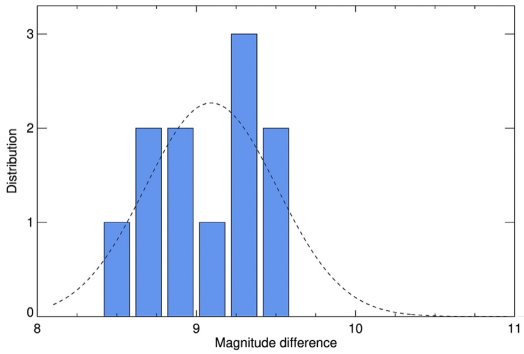

Fig. 12. Distribution of the magnitude differences between Camilla and its second satellite S2. The dashed black line represents the normal distribution fit to our results, with a mean and standard deviation of 9.0 ± 0.3.

highly elongated targets like Camilla, the projected area is often smaller than the average area as shown in Table B.3. Averaging disk-integrated fluxes may thus underestimate the average diameter.

The agreement of the 3-D models by Hanuš et al. (2017) and developed here with lightcurves, disk-resolved images, and stellar occultation timings, providing direct size measurements, indeed argues for Camilla being larger than previously thought. The corresponding volume is 8.5 ± 1.2 · 10^6 km^3. The uncertainty on the volume matches closely that of the diameter ($\delta V/V \approx \delta D/D$) in the case of 3-D shape modeling, as shown by Kaasalainen and Viikinkoski (2012), because it derives from the uncertainty on the radius of each vertex, which are correlated (unlike in the case of scaling a sphere).

5.4. Diameter of S1

We list in Table A.5 and display in Fig. 11 the 65 measured brightness differences with an uncertainty lower than 1 magnitude between Camilla and its largest satellite S1. We found a normal distribution of measurement, as expected from photon noise, and measure an average magnitude difference of $\Delta m = 6.51 \pm 0.27$, similar to the value of 6.31 ± 0.68 reported by Marchis et al. (2008a) on 22 epochs.

Using the diameter of 254 ± 36 km for Camilla (Section 5.3) and assuming S1 has the same albedo as Camilla itself (supported by their spectral similarity, see Section 4.3), this magnitude difference implies a size of 12.7 ± 3.5 km for S1, smaller than previously reported.

5.5. Diameter of S2

We list in Table A.6 and display in Fig. 12 the 11 measured brightness differences between Camilla and its smaller satellite S2. We measure an average magnitude difference of $\Delta m = 9.0 \pm 0.3$ (already reported upon discovery, see Marsset et al., 2016).

Using the diameter of 254 ± 36 km for Camilla (Section 5.3) and assuming S2 has the same albedo as Camilla itself as we did for S1, this magnitude difference implies a size of 4.0 ± 1.2 km for S2.

6. Discussion

6.1. Internal structure

Using the mass derived from the study of the dynamics of the satellites and the volume from the 3-D shape modeling, we infer a density of 1,280 ± 130 kg · m^{-3} (3 σ uncertainty), in agreement with previous reports by Marchis et al. (2008a) and Hanuš et al. (2017). This highlights how critically the density relies on accurate volume estimates: the summary of previous diameter determinations (Table B.2), mainly based on indirect techniques, leads to a density of 1,750 ± 1,400 kg · m^{-3} (3 σ uncertainty, Carry, 2012).

The low density found here is comparable to that of (87) Sylvia, a P-type of similar size, also orbiting in the Cybele region (Berthier et al., 2014), and the D-/P-type Jupiter Trojans (617) Patroclus and (624) Hektor (Mueller et al., 2010; Marchis et al., 2014; Buie et al., 2015). As mentioned above (Section 4.2), the most-likely analog material for this type of asteroids are IDPs (Vernazza et al., 2015). There is no measurement of IDP density in the laboratory. However, a density of 3000 · m^{-3} for the silicate phase was reported by the StarDust mission (Brownlee et al., 2006). Because these silicates are mixed with organic carbonaceous particles (≈ 2200 · m^{-3}), the density of the bulk material is likely of ≈ 2600 · m^{-3} (Greenberg, 2000; Pätzold et al., 2016). A macroporosity of 50 ± 9% would thus be required to explain the density of Camilla, i.e., half of its volume would be occupied by voids. Because the pressure inside Camilla reaches 10^5 Pa less than 15 km from its surface (90% of the radius), it is unlikely that its structure can sustain such large voids. While silicate grains crush at 10^7 Pa, larger structures will not resist pressure significantly smaller, as the compressive strength decreases as the power −1/2 of the size (Lundborg, 1967; Britt et al., 2002).

An alternate explanation to the low density of Camilla may be that it contains large amounts of water ice. An absorption band due to hydration at 3 µm was indeed reported by Takir and Emery (2012), whose shape is similar to those of the nearby (24) Themis and (65) Cybele and interpreted as water frost coating on surface grains (Campins et al., 2010; Licandro et al., 2011). Because water ice sublimates on airless surfaces at the heliocentric distance of Themis, Camilla, and Cybele, the ice on the surface must be replenishment from sub-surface reservoir(s) (Rivkin and Emery, 2010), as it occurs on (1) Ceres (A'Hearn and Feldman, 1992; Rousselot et al., 2011; Küppers et al., 2014; Combe et al., 2016).

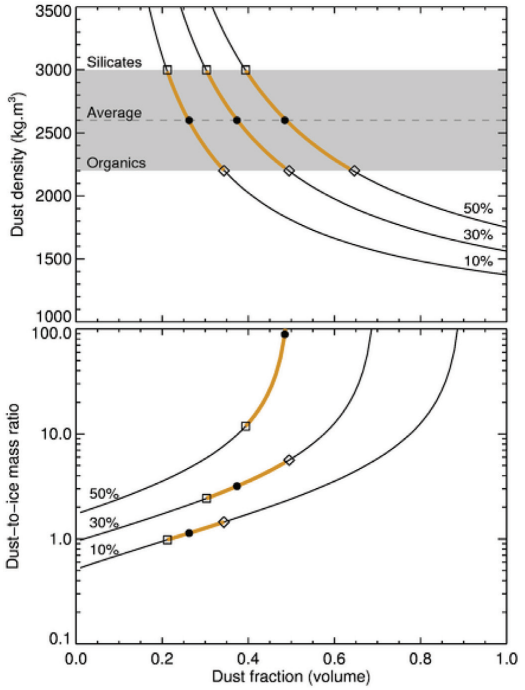

Fig. 13. Top: Dust density as function of its volumetric fraction for different porosities (10, 30, 50%). The expected range from pure organics to pure silicates is represented in shaded gray. Expected range is highlighted in gold. Bottom: Dust-to-ice mass ratios as function of the volumetric fraction of dust.

We thus investigate the possible range of dust-to-ice mass ratios as function of macroporosity in Camilla (Fig. 13). As expected, the porosity decreases with higher ice content and reaches 10–30% for dust-to-ice mass ratios of 1–6. Therefore, the volume occupied by dust, ice, and voids would be 33 ± 10%, 47 ± 19%, and 20 ± 10% respectively, the latter being preferentially found in the outer-most volume of the asteroid body.

To test this, we compute the gravitational potential quadrupole J_2 = 0.042 ± 0.004 of the 3-D shape model (Section 5.3) under the assumption of a homogeneous interior using the method of Dobrovolskis (1996). Because the orbit of S1 fits 80 astrometric positions over 15 years to measurement accuracy under the assumption of a null J_2 (Section 3.3), the mass distribution in Camilla must be more concentrated at the center, with a denser *core*, than suggested by its shape. Similar internal structure has already been suggested for (87) Sylvia and (624) Hektor by Berthier et al. (2014) and Marchis et al. (2014). Considering a core of pure silicate, and an outer shell of porous ice matching the masses above, the core radius would be 87 ± 8 km or 68 ± 7% of the radius of Camilla. Additional observations of S2 to determine precisely its orbit are now required to test further the internal structure of Camilla.

6.2. Future characterization of Camilla triple system

Owing to the large magnitude difference between Camilla and its satellites (6.5 and 9 mag.), constraining the size and orbit of the satellites by photometric observations of mutual event (eclipses and occultations, see, e.g., Scheirich and Pravec, 2009; Carry et al., 2015) is not feasible. Observation of S2 will therefore rely on direct imaging such as presented here, or stellar occultations which can moreover provide a direct measurement of the diameter of the satellites. To this effect, we list in Table D.1 a selection of stellar occultations that will occur in the next three years.

Similarly to our work on (87) Sylvia which led to the observation of a stellar occultation by its satellite Romulus (Berthier et al., 2014), we will continuously update the occultation path of Camilla and of its satellites, for these events. The precision of such predictions will benefit from each successive data release of the ESA Gaia astrometry catalogs (Tanga and Delbo, 2007; Gaia Collaboration et al., 2016; Spoto et al., 2017), that will reduce the uncertainty on the path of Camilla itself to a few kilometers. The uncertainty on the occultation path of the satellites will then mostly derive from the uncertainty on their orbital parameters, and we provide them in Table D.1. The orbit of S2 being little constrained, the uncertainty on its position for upcoming occultations is very large. Initial improvement must thus rely on direct imaging of the system.

7. Summary

In the present study, we have acquired and compiled optical lightcurves, stellar occultations, visible and near-infrared spectra, and high-contrast and high-angular-resolution images and spectro-images from the Hubble Space Telescope and large ground-based telescopes (Keck, Gemini, VLT) equipped with adaptive-optics-fed cameras.

Using 80 positions spanning 15 years, we study the dynamics of the largest satellite, S1, and determine its orbit around Camilla to be circular, equatorial, and prograde. The residuals between our dynamical solution and the observations are 7.8 mas, corresponding to a sub-pixel accuracy. Using 11 positions of the second, smaller, satellite S2 that we discovered in 2015, we determine a preliminary orbit, marginally inclined from that of S1 and more eccentric. Predictions of the relative position of the satellite with respect to Camilla, critical for planning stellar occultations for instance, are available to the community through our VO service `Miriade` [5] (Berthier et al., 2008).

From the visible and near-infrared spectrum of Camilla, we classify it as an Xk-type asteroid, in the Bus-DeMeo taxonomy (DeMeo et al., 2009). Considering its low albedo, it would be classified as a P-type in older taxonomic schemes such as Tedesco's (Tedesco et al., 1989). Using VLT/SPHERE integral-field spectrograph, we measure the near-infrared spectrum of the largest satellite, S1, and compare it with Camilla. No significant differences are found. This, together with its orbital parameters, argue for a formation of the satellite by excavation from impact, re-accumulation of ejecta in orbit, and circularization by tides.

Using optical lightcurves, profiles from disk-resolved imaging, and stellar occultation events, we determine the spin-vector coordinates and 3-D shape of Camilla. The model fits well each data set, and we find a spherical-volume-equivalent diameter of 254 ± 36 km. By combining the mass from the dynamics with the volume of the shape model, we find a density of 1,280 ± 130 kg · m^{-3}. Considering Camilla's most likely analog material are IDPs, this implies a macroporosity of 50 ± 9%, likely too high to be sustained. By considering a mixture of ice and silicate, the macroporosity could be in the range 10–30% for a dust-to-ice mass ratio of 1–6, the denser material being concentrated toward the center as suggested by the dynamics of the system.

[5] http://vo.imcce.fr/

Acknowledgments

Based on observations collected at the European Organisation for Astronomical Research in the Southern Hemisphere under ESO programmes 071.C-0669 (PI Merline), 073.C-0062 & 074.C-0052 (PI Marchis), 088.C-0528 (PI Rojo), 095.C-0217 & 297.C-5034 (PI Marsset).

Some of the data presented herein were obtained at the W.M. Keck Observatory, which is operated as a scientific partnership among the California Institute of Technology, the University of California and the National Aeronautics and Space Administration. The Observatory was made possible by the generous financial support of the W.M. Keck Foundation.

This research has made use of the Keck Observatory Archive (KOA), which is operated by the W. M. Keck Observatory and the NASA Exoplanet Science Institute (NExScI), under contract with the National Aeronautics and Space Administration.

Some of these observations were acquired under grants from the National Science Foundation and NASA to Merline (PI).

The authors wish to recognize and acknowledge the very significant cultural role and reverence that the summit of Mauna Kea has always had within the indigenous Hawaiian community. We are most fortunate to have the opportunity to conduct observations from this mountain.

Based on observations obtained at the Gemini Observatory, which is operated by the Association of Universities for Research in Astronomy, Inc., under a cooperative agreement with the NSF on behalf of the Gemini partnership: the National Science Foundation (United States), the National Research Council (Canada), CONICYT (Chile), Ministerio de Ciencia, Tecnología e Innovación Productiva (Argentina), and Ministério da Ciência, Tecnologia e Inovação (Brazil).

We wish to acknowledge the support of NASA Contract NAS5-26555 and STScI grant GO-05583.01 to Alex Storrs (PI).

Visiting Astronomer at the Infrared Telescope Facility, which is operated by the University of Hawaii under contract NNH14CK55B with the National Aeronautics and Space Administration.

We thank the AGORA association which administrates the 60 cm telescope at Les Makes observatory, under a financial agreement with Paris Observatory. Thanks to A. Peyrot, J.-P. Teng for local support, and A. Klotz for helping with the robotizing.

Thanks to all the amateurs worldwide who regularly observe asteroid lightcurves and stellar occultations. Many co-authors of this study are amateurs who observed Camilla, and provided crucial data.

We thank J. Ďurech for providing his implementation of Dobrovolskis (1996) method.

The authors acknowledge the use of the Virtual Observatory tools `Miriade` [6] (Berthier et al., 2008), `MP3C` [7] (Delbo et al., 2017), `TOPCAT` [8], and `STILTS` [9] (Taylor, 2005). This research used the facilities of the Canadian Astronomy Data Centre operated by the National Research Council of Canada with the support of the Canadian Space Agency (Gwyn et al., 2012).

[6] http://vo.imcce.fr/
[7] https://mp3c.oca.eu
[8] http://www.star.bristol.ac.uk/-pl2X-sim-mbt/topcat/
[9] http://www.star.bristol.ac.uk/-pl2X-sim-mbt/stilts/

Icarus 248 (2015) 516–525

Contents lists available at ScienceDirect

Icarus

journal homepage: www.elsevier.com/locate/icarus

The small binary asteroid (939) Isberga ☆

B. Carry [a,b,*], A. Matter [c,d], P. Scheirich [e], P. Pravec [e], L. Molnar [f], S. Mottola [g], A. Carbognani [m], E. Jehin [k], A. Marciniak [l], R.P. Binzel [i], F.E. DeMeo [i,j], M. Birlan [a], M. Delbo [h], E. Barbotin [o,p], R. Behrend [o,n], M. Bonnardeau [o,p], F. Colas [a], P. Farissier [q], M. Fauvaud [r,s], S. Fauvaud [r,s], C. Gillier [q], M. Gillon [k], S. Hellmich [g], R. Hirsch [l], A. Leroy [o], J. Manfroid [k], J. Montier [o], E. Morelle [o], F. Richard [s], K. Sobkowiak [l], J. Strajnic [o], F. Vachier [a]

[a] IMCCE, Observatoire de Paris, UPMC Paris-06, Université Lille1, UMR8028 CNRS, 77 Av. Denfert Rochereau, 75014 Paris, France
[b] European Space Astronomy Centre, ESA, P.O. Box 78, 28691 Villanueva de la Cañada, Madrid, Spain
[c] Max Planck institut für Radioastronomie, Auf dem Hügel, 69, 53121 Bonn, Germany
[d] UJF-Grenoble 1/CNRS-INSU, Institut de Planétologie et d'Astrophysique de Grenoble (IPAG), UMR 5274, Grenoble F-38041, France
[e] Astronomical Institute, Academy of Sciences of the Czech Republic, Fričova 298, CZ-25165 Ondřejov, Czech Republic
[f] Department of Physics and Astronomy, Calvin College, 3201 Burton SE, Grand Rapids, MI 49546, USA
[g] Deutsches Zentrum für Luft- und Raumfahrt (DLR), 12489 Berlin, Germany
[h] UNS-CNRS-Observatoire de la Côte dAzur, Laboratoire Lagrange, BP 4229 06304 Nice Cedex 04, France
[i] Department of Earth, Atmospheric and Planetary Sciences, MIT, 77 Massachusetts Avenue, Cambridge, MA 02139, USA
[j] Harvard-Smithsonian Center for Astrophysics, 60 Garden Street, MS-16, Cambridge, MA 02138, USA
[k] Institut dAstrophysique et de Géophysique, Universitée de Liège, Allée du 6 août 17, B-4000 Liège, Belgium
[l] Astronomical Observatory Institute, Faculty of Physics, A. Mickiewicz University, Słoneczna 36, 60-286 Poznań, Poland
[m] Astronomical Observatory of the Autonomous Region of the Aosta Valley, Loc. Lignan 39, 11020 Nus (Aosta), Italy
[n] Geneva Observatory, 51 Chemin des Maillettes, CH-1290 Sauverny, Switzerland
[o] CdR & CdL Group: Lightcurves of Minor Planets and Variable Stars, Switzerland
[p] Association des Utilisateurs de Détecteurs Électroniques (AUDE), France
[q] Club d'Astronomie de Lyon Ampère (CALA), Place de la Nation, 69120 Vaulx-en-Velin, France
[r] Observatoire du Bois de Bardon, 16110 Taponnat, France
[s] Association T60, 14 Avenue Edouard Belin, 31400 Toulouse, France

ARTICLE INFO

Article history:
Received 8 April 2014
Revised 10 October 2014
Accepted 2 November 2014
Available online 18 November 2014

Keywords:
Asteroids, dynamics
Satellites of asteroids
Orbit determination

ABSTRACT

In understanding the composition and internal structure of asteroids, their density is perhaps the most diagnostic quantity. We aim here at characterizing the surface composition, mutual orbit, size, mass, and density of the small main-belt binary asteroid (939) Isberga. For that, we conduct a suite of multi-technique observations, including optical lightcurves over many epochs, near-infrared spectroscopy, and interferometry in the thermal infrared. We develop a simple geometric model of binary systems to analyze the interferometric data in combination with the results of the lightcurve modeling. From spectroscopy, we classify Ibserga as a Sq-type asteroid, consistent with the albedo of $0.14^{+0.09}_{-0.06}$ (all uncertainties are reported as 3-σ range) we determine (average albedo of S-types is 0.197 ± 0.153, see Pravec et al. (Pravec et al. [2012]. Icarus 221, 365–387). Lightcurve analysis reveals that the mutual orbit has a period of 26.6304 ± 0.0001 h, is close to circular (eccentricity lower than 0.1), and has pole coordinates within 7° of (225°, +86°) in Ecliptic J2000, implying a low obliquity of $1.5^{+6.0}_{-1.5}$ deg. The combined analysis of lightcurves and interferometric data allows us to determine the dimension of the system and we find volume-equivalent diameters of $12.4^{+2.5}_{-1.2}$ km and $3.6^{+0.7}_{-0.3}$ km for Isberga and its satellite, circling each other on a 33 km wide orbit. Their density is assumed equal and found to be $2.91^{+1.72}_{-2.01}$ g cm^{-3}, lower than that of the associated ordinary chondrite meteorites, suggesting the presence of some macroporosity, but typical of S-types of the same size range (Carry [2012]. Planet. Space Sci. 73, 98–118). The present study is the first direct measurement of the size of a small main-belt binary. Although the interferometric observations of Isberga are at the edge of MIDI capabilities, the method described here is applicable to others suites of instruments (e.g., LBT, ALMA).

☆ Based on observations made with ESO telescopes at the La Silla Paranal Observatory under programme ID: 088.C-0770.

* Corresponding author at: IMCCE, Observatoire de Paris, UPMC Paris-06, Université Lille1, UMR8028 CNRS, 77 Av. Denfert Rochereau, 75014 Paris, France.
E-mail address: bcarry@imcce.fr (B. Carry).

http://dx.doi.org/10.1016/j.icarus.2014.11.002
0019-1035/

1. Introduction

Of the many properties that describe an asteroid, there is perhaps no quantity more fundamental to understand its composition and internal structure than its density. With the exception of the fine-grained dust returned from asteroid (25 143) Itokawa by the Hayabusa spacecraft (Nakamura et al., 2011), our knowledge on the mineralogy of asteroids has been derived from remote-sensing photometry and spectroscopy in the visible and near-infrared, radar polarimetry, and comparison with meteorites studied in the laboratory (e.g., Shepard et al., 2008; Vernazza et al., 2010). These observables, however, tell us about surface composition only, which may or may not be reflective of the bulk composition of the body. The bulk density of meteorites spans a wide range, from the low-density ($\rho \sim 1.6$ g cm^{-3}) primitive CI carbonaceous chondrite to the dense ($\rho \sim 7.4$ g cm^{-3}) Hexahedrite iron meteorites (see, e.g., Consolmagno and Britt, 1998; Consolmagno et al., 2008, for meteorites density measurements). Comparison of asteroid bulk density with meteorite grain density provides a crude, yet useful, tool in the investigation of their bulk composition. This is particularly valuable for taxonomic types devoid of characteristic absorption bands in their spectrum, for which the analog meteorites cannot be ascertained otherwise.

For asteroids with known surface mineralogy and analog meteorite, the density even allows us to make inference on the internal structure of the body. By comparing the grain density of the surface material to the bulk density of the asteroid, we can detect the presence of denser material below the crust, like in the case of (4) Vesta (Russell et al., 2012), or the presence of large voids, called macroporosity, as for the rubble-pile (25 143) Itokawa (Fujiwara et al., 2006). A recent comprehensive analysis of volume and mass determinations of about 300 asteroids has revealed clear differences of density and macroporosity among taxonomic types, together with different trends with size and orbital populations (Carry, 2012). This sample is, however, still limited in number and the precision of the majority of these estimates remains cruder than 50% (1-σ cutoff).

In our quest for asteroid masses, the study of binary systems has been the most productive method (Carry, 2012). Spacecraft encounters provide the most precise mass determination (at the percent level, e.g., Pätzold et al., 2011), but they will always remain limited to a few objects, while studies of orbit deflections during planetary encounters provide numerous mass estimates with limited precision (often above 50% relative accuracy, see Zielenbach, 2011; Kuchynka and Folkner, 2013, for instance). With more than 200 binary systems known, and more discoveries announced almost monthly, the study of mutual orbits can provide numerous mass determinations. For large separation binaries, where the companion can be imaged and tracked along its orbit (e.g., Merline et al., 1999; Marchis et al., 2005; Descamps et al., 2011; Carry et al., 2011; Vachier et al., 2012, among others), the mass can be determined to a high precision, typically about 10–15% (Carry et al., 2012). For the small binaries, detected and studied by the signature of mutual eclipses and occultations in their lightcurves, the density can be indirectly determined without measuring the absolute size nor mass of the objects (e.g., Pravec et al., 2006, 2012b). This, however, requires to assume the same bulk density for both components (e.g., Scheirich and Pravec, 2009), which may be problematic if these small-sized binaries are formed by rotational breakup (Walsh et al., 2008). The accuracy reached with this method can range from a few percent to 100% depending on each system (Carry, 2012).

We present here a suite of observations of the small main-belt binary asteroid (939) Isberga (orbital elements: $a = 2.246$ au, $e = 0.177$, $i = 2.588°$) aiming at determining its surface composition, mutual orbit, mass, diameter, density, and macroporosity. We describe in Section 2 the different methods of observation we use, we present the analysis of the surface composition of Isberga in Section 3 and of the physical properties of the system in Section 4.

2. Observations and data reduction

2.1. Optical lightcurves

The binarity of Isberga was reported by Molnar et al. (2008) from optical lightcurves obtained over 6 nights in 2006 at the Calvin–Rehoboth Observatory. The rotation period of the primary and the orbital period for the satellite were determined to 2.9173 ± 0.0003 h and 26.8 ± 0.1 h. We report observations carried out during 2 nights from the 2008/2009 opposition, 43 nights in 2010, 54 nights in 2011, and 2 nights in 2012. We provide a detailed list of all the lightcurves with ancillary information in Table 1. A subset of the lightcurves is plotted in Fig. 1, showing evidences for mutual events.

As many observers acquired lightcurves of Isberga, we do not go here into the specifics of the data reduction and photometry measurements used by each. Standard procedures were used to reduce the data, including bad pixel removal, bias subtraction, and flat-field correction. Aperture photometry was used to measure the relative flux of Isberga with surrounding stars and build its lightcurves. In lightcurve decomposition, the magnitude scale zero points of individual nights (sessions) were taken as free parameters. Their uncertainties were generally less than 0.01 mag and we checked by experimenting with them that they did not add a significant uncertainty in subsequent modeling of the system, and we did not propagate them there.

2.2. Near-infrared spectroscopy

To constrain the surface mineralogy, we acquired a near-infrared spectrum of Isberga on 2011, August the 22nd, at a phase angle of 28°, as part of the MIT–Hawaii–IRTF joint campaign for NEO reconnaissance (Binzel et al., 2006). Data from this survey are publicly available at `smass.mit.edu`. Observations were taken on the 3-meter NASA Infrared Telescope Facility at the Mauna Kea Observatory. We used the instrument SpeX (Rayner et al., 2003), a near-infrared spectrograph in low resolution mode over 0.8 to 2.5 μm.

Isberga was observed near the meridian (airmass < 1.3) in two different positions, here denoted A and B, on a 0.8 × 15 arcsec^2 slit aligned north–south. Exposure times were 120 s, and we measured 4 A–B pairs. Solar analog stars were observed at similar airmass throughout the night to correct for telluric absorption. We used the same set of solar analogs as the SMASS program (Binzel et al., 2004, 2006) that have been in use for over a decade.

Data reduction and spectral extraction were performed using the Image Reduction and Analysis Facility (IRAF, Tody, 1993) provided by the National Optical Astronomy Observatories (NOAO). Correction in regions with strong telluric absorption was performed in IDL using an atmospheric transmission (ATRAN) model by Lord (1992). More detailed information on the observing and reduction procedures can be found in Rivkin et al. (2004) and DeMeo and Binzel (2008). We present the resulting spectrum of Isberga in Fig. 2.

2.3. Mid-infrared interferometry

Mid-infrared interferometry can provide direct measurements of the angular extension of asteroids (Delbo et al., 2009; Matter et al., 2011, 2013). We used the MID-infrared Interferometric

Table 1
Date, duration ($\mathscr{D}$), phase angle (α), observatory, and observers of each lightcurve used in present study. The observatory code are IAU codes (G98: Calvin–Rehoboth Observatory, 493: Calar Alto 1.2 m telescope, I40: TRAPPIST at La Silla Observatory, J23: Centre Astronomique de La Couyère, 187: Borowiec observatory, 634: Crolles observatory, 586: T60 and T1M at Pic du Midi), except for Far, MBo, StB, and VFa that correspond to the Farigourette, Michel Bonnardeau's (MBCAA), Saint Barthelemy, and Villefagnan observatories.

Date (UT)	$\mathscr{D}$ (h)	α (°)	Obs.	Observers	Date (UT)	$\mathscr{D}$ (h)	α (°)	Obs.	Observers
2006–02–24 – 09:36	5.3	11.7	G98	Molnar et al.	2011–09–06 – 14:24	6.0	23.8	493	Mottola, Hellmich
2006–02–26 – 14:24	6.8	12.5	G98	Molnar et al.	2011–09–07 – 16:48	6.3	23.3	493	Mottola, Hellmich
2006–02–27 – 16:48	6.0	12.9	G98	Molnar et al.	2011–09–19 – 21:36	0.4	18.0	I40	Jehin et al.
2006–02–28 – 19:12	7.0	13.3	G98	Molnar et al.	2011–09–25 – 12:00	6.4	15.1	G98	Molnar et al.
2006–03–03 – 07:12	4.5	14.2	G98	Molnar et al.	2011–09–26 – 14:24	7.5	14.5	G98	Molnar et al.
2006–03–04 – 09:36	5.1	14.6	G98	Molnar et al.	2011–09–27 – 16:48	6.2	13.9	G98	Molnar et al.
2008–12–31 – 02:24	1.3	6.2	G98	Molnar et al.	2011–09–28 – 19:12	1.9	13.3	G98	Molnar et al.
2009–01–01 – 02:24	1.3	6.7	G98	Molnar et al.	2011–10–02 – 04:48	1.5	11.3	I40	Jehin et al.
2010–03–25 – 12:00	5.2	3.6	G98	Molnar et al.	2011–10–07 – 16:48	2.4	8.1	I40	Jehin et al.
2010–03–28 – 19:12	6.6	2.1	G98	Molnar et al.	2011–10–08 – 19:12	3.7	7.4	I40	Jehin et al.
2010–04–03 – 07:12	6.4	1.5	G98	Molnar et al.	2011–10–09 – 21:36	4.2	6.8	I40	Jehin et al.
2010–04–07 – 16:48	6.6	3.3	G98	Molnar et al.	2011–10–19 – 21:36	4.7	2.3	J23	Montier
2010–04–08 – 19:12	6.9	3.8	G98	Molnar et al.	2011–10–20 – 00:00	8.5	2.3	VFa	Barbotin, Behrend
2010–04–09 – 21:36	7.0	4.4	G98	Molnar et al.	2011–10–20 – 00:00	8.3	2.3	VFa	Barbotin, Behrend
2010–04–12 – 04:48	7.0	5.4	G98	Molnar et al.	2011–10–21 – 02:24	7.5	2.4	Far	Morelle, Behrend
2010–04–13 – 07:12	5.7	6.0	G98	Molnar et al.	2011–10–21 – 02:24	2.9	2.4	I40	Jehin et al.
2010–04–14 – 09:36	6.0	6.5	G98	Molnar et al.	2011–10–22 – 04:48	9.3	2.6	VFa	Barbotin, Behrend
2010–04–16 – 14:24	4.6	7.5	G98	Molnar et al.	2011–10–22 – 04:48	1.5	2.6	J23	Montier
2010–04–18 – 19:12	5.9	8.5	G98	Molnar et al.	2011–10–22 – 04:48	5.8	2.6	187	Marciniak et al.
2010–04–18 – 19:12	2.4	8.5	G98	Molnar et al.	2011–10–22 – 04:48	7.4	2.6	MBo	Bonnardeau
2010–04–23 – 07:12	5.0	10.5	G98	Molnar et al.	2011–10–22 – 04:48	5.0	2.6	634	Farissier
2010–04–23 – 07:12	3.8	10.5	G98	Molnar et al.	2011–10–25 – 12:00	1.3	4.1	493	Mottola, Hellmich
2010–05–04 – 09:36	5.0	15.0	G98	Molnar et al.	2011–10–26 – 14:24	8.5	4.7	493	Mottola, Hellmich
2010–05–05 – 12:00	4.8	15.4	G98	Molnar et al.	2011–10–26 – 14:24	2.6	4.7	493	Mottola, Hellmich
2010–05–07 – 16:48	2.2	16.2	G98	Molnar et al.	2011–10–27 – 16:48	4.0	5.3	I40	Jehin et al.
2010–05–08 – 19:12	4.5	16.6	G98	Molnar et al.	2011–10–28 – 19:12	4.4	5.9	StB	Carbognani
2010–05–09 – 21:36	4.8	17.0	G98	Molnar et al.	2011–11–01 – 02:24	4.9	7.7	StB	Carbognani
2010–05–10 – 00:00	4.3	17.0	G98	Molnar et al.	2011–11–01 – 02:24	8.0	7.7	493	Mottola, Hellmich
2010–05–11 – 02:24	0.5	17.3	G98	Molnar et al.	2011–11–15 – 12:00	5.7	15.1	StB	Carbognani
2010–05–15 – 12:00	3.1	18.7	G98	Molnar et al.	2011–11–15 – 12:00	3.9	15.1	Far	Morelle, Behrend
2010–05–16 – 14:24	0.5	19.0	G98	Molnar et al.	2011–11–16 – 14:24	5.8	15.6	StB	Carbognani
2010–05–17 – 16:48	2.1	19.3	G98	Molnar et al.	2011–11–16 – 14:24	7.1	15.6	Far	Morelle, Behrend
2010–05–19 – 21:36	3.7	19.9	G98	Molnar et al.	2011–11–17 – 16:48	8.0	16.1	Far	Morelle, Behrend
2010–05–20 – 00:00	2.7	19.9	G98	Molnar et al.	2011–11–18 – 19:12	6.1	16.6	StB	Carbognani
2010–05–21 – 02:24	0.4	20.2	G98	Molnar et al.	2011–11–20 – 00:00	5.8	17.1	StB	Carbognani
2010–05–28 – 19:12	2.7	21.9	G98	Molnar et al.	2011–11–22 – 04:48	6.6	18.0	StB	Carbognani
2010–05–29 – 21:36	3.2	22.1	G98	Molnar et al.	2011–11–26 – 14:24	8.7	19.6	586	Fauvaud et al.
2010–05–30 – 00:00	1.4	22.1	G98	Molnar et al.	2011–11–27 – 16:48	5.3	20.0	586	Fauvaud et al.
2010–05–31 – 02:24	1.8	22.4	G98	Molnar et al.	2011–12–01 – 02:24	0.9	21.1	I40	Jehin et al.
2010–06–01 – 02:24	2.6	22.5	G98	Molnar et al.	2011–12–03 – 07:12	2.4	21.8	I40	Jehin et al.
2010–06–02 – 04:48	2.3	22.7	G98	Molnar et al.	2011–12–04 – 09:36	1.2	22.1	I40	Jehin et al.
2010–06–03 – 07:12	2.6	22.9	G98	Molnar et al.	2011–12–11 – 02:24	2.0	23.8	I40	Jehin et al.
2010–06–04 – 09:36	2.4	23.1	G98	Molnar et al.	2011–12–18 – 19:12	5.0	25.3	493	Mottola, Hellmich
2010–06–08 – 19:12	2.3	23.7	G98	Molnar et al.	2011–12–19 – 21:36	5.7	25.4	493	Mottola, Hellmich
2011–08–29 – 21:36	4.6	26.4	493	Mottola, Hellmich	2011–12–20 – 00:00	6.1	25.5	493	Mottola, Hellmich
2011–08–30 – 00:00	5.0	26.4	493	Mottola, Hellmich	2011–12–21 – 02:24	5.7	25.6	493	Mottola, Hellmich
2011–08–31 – 02:24	5.7	26.0	493	Mottola, Hellmich	2011–12–22 – 04:48	6.0	25.8	493	Mottola, Hellmich
2011–09–03 – 07:12	4.6	25.0	493	Mottola, Hellmich	2011–12–23 – 07:12	5.1	25.9	493	Mottola, Hellmich
2011–09–04 – 09:36	3.1	24.6	493	Mottola, Hellmich	2012–01–18 – 19:12	4.6	27.4	586	Vachier, Colas, Lecacheux
2011–09–05 – 12:00	6.2	24.2	493	Mottola, Hellmich	2012–01–20 – 00:00	4.0	27.3	586	Vachier, Colas, Lecacheux

instrument (MIDI) of the Very Large Telescope Interferometer (VLTI), combining two of the 8.2 m Unitary Telescopes, UT1 and UT2, with a baseline separation of 57 m, providing a high angular resolution of $\frac{\lambda}{2B} \approx 0.02''$ at $\lambda \approx 10$ μm, corresponding to about 10 km projected at the distance of Isberga at the time of observation.

MIDI records the interference fringes between two beams of incoming light, which gives access to the complex degree of coherence (or complex visibility) between the beams. This complex visibility is the Fourier transform of the object brightness distribution on the plane of the sky, stacked along the baseline direction and sampled at the spatial frequency $\boldsymbol{B}/\lambda$, where $\boldsymbol{B}$ is the baseline vector. In this work, we focused on the correlated flux observable, which is the modulus of the complex visibility.

Fringes on Isberga were acquired at three observing epochs in visitor mode on 2011, October the 6th, and at four observing epochs in service mode on 2011, October the 10th (Table 2), following the observing procedure of Leinert et al. (2004). The fringes were dispersed using the prism of MIDI, which provides a spectral resolving power of $\lambda/\Delta\lambda \approx 30$ at $\lambda = 10$ μm. One correlated flux measurement, dispersed over the N-band (from 8 to 13 μm), was obtained for each observing epoch. Our observations also included a photometric and interferometric calibrator star, HD 15396, to determine the atmospheric and instrumental transfer function. Our calibrator was chosen to be angularly unresolved, and to have a minimum angular separation with the source (≈3°) and a similar airmass (see Table 2).

The correlated flux measurements of (939) Isberga were extracted using the data reduction software package EWS (Expert WorkStation, see Jaffe (2004), for a detailed description). Using the closest calibrator observation in time, calibrated correlated fluxes of (939) Isberga were obtained by multiplying the ratio target/calibration star raw correlated flux counts by the absolutely calibrated infrared flux of the calibrator (see Matter et al. (2011,

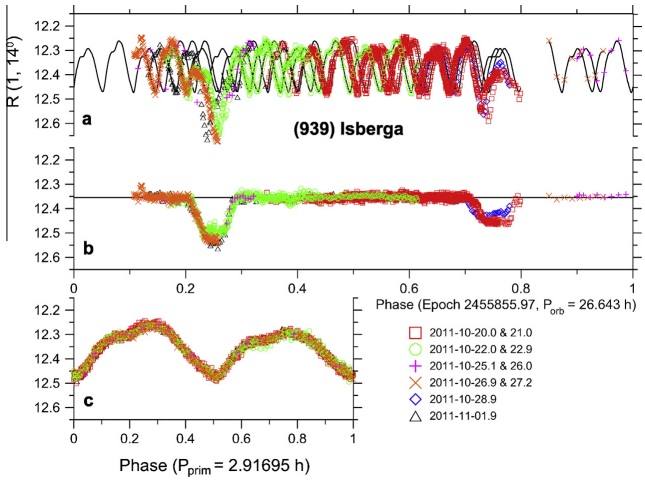

Fig. 1. Lightcurves of Isberga showing the mutual eclipses and photometric variability induced by the primary rotation. (a) All the lightcurves acquired between 2011, October the 20th and 2011, November the 1st folded over the synodic orbital period of 26.643 h. (b) The same as above, with the orbital component of the lightcurve only. (c) The rotation component of the lightcurve only, folded over the rotation period of 2.91695 h.

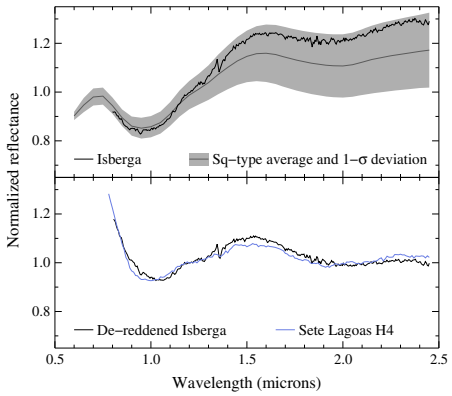

Fig. 2. *Top:* Near-infrared spectrum of Isberga normalized at 1.20 μm compared with the average Bus-DeMeo Sq-type spectrum. *Bottom:* De-reddened spectrum of Isberga (using the space weathering model of Brunetto et al., 2006, see Section 3) compared with the ordinary chondrite H4 Sete Lagoas (RELAB sample ID: MH-JFB-021).

2013), for a complete description of the data reduction and calibration procedure).

Uncertainties on the correlated flux are estimated considering two contributions. First, a short timescale effect (much shorter than typical observations of ≈2 min), dominated by photon noise from the object and thermal background emission. This statistical uncertainty is estimated by splitting a complete exposure, consisting of several thousand of frames and leading to one correlated flux measurement, into five equal parts and by deriving their standard deviation for every spectral channel. Second, the slow variations in the flux transmission of the atmosphere and/or variations of the thermal background can introduce offsets between repeated observations across the night. A rough estimate of this offset-like contribution is obtained by calibrating each correlated flux measurement against all the calibrators of the night, and then computing the standard deviation (see Chesneau, 2007). Such estimate was only possible for the three measurements of 2011, October the 6th where the error bars correspond to the quadratic sum of these two sources of uncertainty.

The four fringe measurements on 2011, October the 10th were acquired over a period of 15 min with only one calibrator observation. Since this is short compared to the estimated rotation and orbital period of Isberga of 2.9 h and 26.8 h respectively, the

Table 2
Projected baseline (length *B* and position angle *PA* counted from north to east), seeing, and airmass for each observation of Isberga and its calibrator (labeled in the last column) using MIDI on the UT1–UT2 baseline of the VLTI.

Object	Date (UT)	*B* (m)	*PA* (°)	Seeing (″)	Airmass	Label
(939) Isberga	2011-10-07 03:09:43	37.4	14.0	0.53	1.60	1
HD 13596	2011-10-07 03:34:14	37.2	13.0	0.70	1.63	Calib
(939) Isberga	2011-10-07 03:51:45	39.7	21.6	0.76	1.43	2
HD 13596	2011-10-07 04:10:16	39.0	19.8	1.09	1.47	Calib
(939) Isberga	2011-10-07 05:40:04	47.5	33.7	0.72	1.30	3
HD 13596	2011-10-07 06:00:29	46.8	33.1	0.84	1.30	Calib
(939) Isberga	2011-10-10 05:44:02	48.9	34.7	0.70	1.31	4
(939) Isberga	2011-10-10 05:54:27	49.6	35.2	0.70	1.33	4
(939) Isberga	2011-10-10 05:57:56	49.8	35.3	0.70	1.33	4
(939) Isberga	2011-10-10 06:01:53	50.0	35.5	0.76	1.34	4
HD 13596	2011-10-10 06:19:44	49.0	35.0	0.79	1.32	Calib

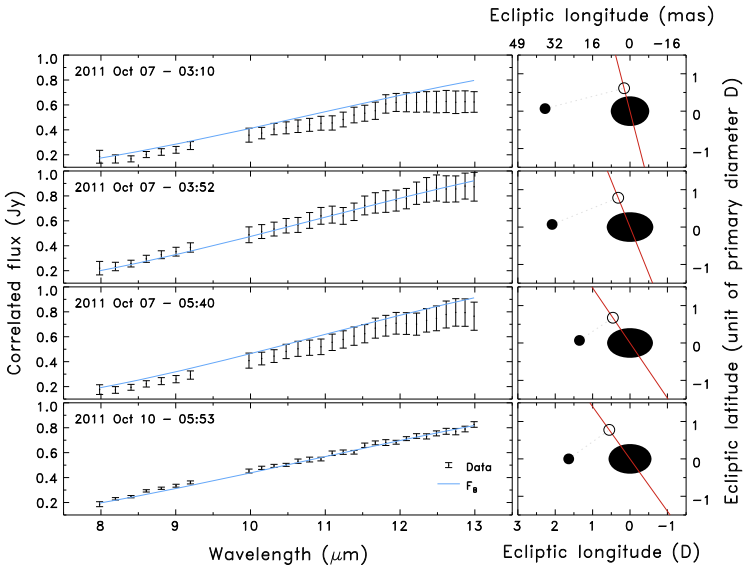

Fig. 3. *Left:* Correlated flux of Isberga observed with MIDI over the four epochs listed in Table 2. The best-fit solution of binary model (F_B) is also plotted as a solid blue line. *Right:* Corresponding geometry of the system on the plane of the sky. The red line represents the projected VLTI baseline, the black ellipse Isberga, the black disk its satellite, and the black circle the projection of the satellite on the baseline. (For interpretation of the references to color in this figure legend, the reader is referred to the web version of this article.)

system apparent geometry, which dominates the data compared to, e.g., putative surface composition heterogeneity, did not change. We thus averaged the four observing epochs to reduce the statistical noise. Assuming that the averaging process also removed the possible offsets affecting the four measurements, the corresponding error bars only include the "averaged" short-term statistical error contribution. Fig. 3 shows the four measurements resulting from the seven initial individual MIDI measurements listed in Table 2.

3. Surface composition

We use the Virtual Observatory (VO) service M4AST[1] (Popescu et al., 2012) to analyze the near-infrared reflectance spectrum of Isberga shown in Fig. 2. It presents two broad absorption bands centered at 0.95 ± 0.01 and 1.91 ± 0.01 μm, tracers of olivine and pyroxene assemblages. We classify Isberga as an S- or Sq-type asteroid (in the classification scheme by DeMeo et al. (2009)), the main class in the inner part of the asteroid belt (DeMeo and Carry, 2013, 2014). We also use M4AST to determine the degree of space weathering presented by Isberga's surface, following the space weathering model by Brunetto et al. (2006), valid for pyroxenes and olivines (see, e.g., Brunetto et al., 2007; Vernazza et al., 2009; Fulvio et al., 2012). In this model, the effect of space weathering is a multiplicative exponential continuum written as $Ke^{(C_S/\lambda)}$. This model is based on many laboratory experiments on ordinary chondrites and mimic the effect of space weathering on lunar-like surfaces (increased spectral slope and decreased albedo, see Sasaki et al., 2001; Chapman, 2004; Strazzulla et al., 2005, among others). Space weathering trends are more subtle and complex for asteroids within the S-complex, owing to the different compositions it encompass (Gaffey et al., 1993; Gaffey, 2010), albeit spectral reddening is consistent.

We determine a reddening strength of $C_S = -0.6$ μm, a value similar to, e.g., (158) Koronis (measured with M4AST on the near-infrared spectrum by Burbine and Binzel (2002) obtained at a phase angle of 19°) and corresponding to significant weathering (responsible for the higher spectral slope of Isberga compared with the average Sq-class of DeMeo et al. (2009) in Fig. 2). The spectrum of Isberga was however obtained at a large phase angle of 28° (Section 2.2), and part of the reddening may be caused by the observing geometry. Spectral observations of Isberga at visible wavelengths

[1] http://m4ast.imcce.fr/.

Table 3
Best-fit values for a circular mutual orbit with 3-σ uncertainties of the parameters described in Section 4.1.

Parameter	Value	Unit
(L_p, B_p)	(225, +86)[a]	deg.
P_{orb}	26.6304 ± 0.0001	h
L_0	354 ± 3	deg.
T_0	2453790.631170	JD
e	$\leqslant 0.10$[b]	
ω	0–360	deg.
$\dot{\omega}$	0–10	deg.
$a/D_{1,C}$	$2.5^{+0.3}_{-0.6}$	
$D_{2,C}/D_{1,C}$	0.29 ± 0.02	
P_{rot}	2.91695 ± 0.00010	h
A_1/C_1	$1.3^{+0.7}_{-0.07}$	
A_2/C_2	1.1[c]	

[a] The 3-σ area is approximately an ellipse of semi-major axes of 8° and 6°, centered on these coordinates, see Fig. 4.
[b] We estimated only an upper limit on the eccentricity from 2011 data.
[c] This is only a formal best-fit value of the elongation of the secondary, a spherical shape is consistent as well.

and small phase angle will help refine its taxonomic classification and state of space weathering.

We determine a visible geometric albedo of $p_V = 0.14^{+0.09}_{-0.06}$ (Section 4.2) which is lower, yet consistent, than the average albedo of asteroids in the S-complex (0.197 ± 0.153, see Pravec et al., 2012a, for values based on WISE mid-infrared surveys) and corresponds to the first quartile of all Bus-DeMeo S-complex asteroids (based on Fig. 6 by Mainzer et al., 2011). We finally search for the best-fit (M4AST χ^2 match) meteorite in the Relab spectral database to Isberga spectrum, corrected from the reddening (either due to the phase angle or space weathering). Ordinary chondrites provide the most-promising candidates, as to be expected from the Sq-type classification, and the best-match is found for the H4 Sete Lagoas (sample MH-JFB-021).

4. Mutual orbit: size, mass, and density

We describe here the different steps that lead to the determination of the geometric properties of the binary Isberga, e.g., component diameter ratio, semi-major axis of the orbit, absolute size.

4.1. Lightcurve analysis and orbit determination

We model the system using the method described in Scheirich and Pravec (2009), modified to allow for precession of the orbit's pericenter. For the modeling, the optical lightcurves were reduced using the technique described in Pravec et al. (2006). In particular, the rotation-induced lightcurve of the primary was fitted using Fourier series and subtracted from the data. The shapes of the components are modeled as ellipsoids, an oblate spheroid for the primary ($A_1 = B_1 > C_1$) and a prolate spheroid for the secondary ($A_2 > B_2 = C_2$), and approximated by polyhedra with triangular facets, orbiting each other on Keplerian orbits. We assume same albedo and density for both components. This assumption is required to translate the unknown mass and diameter ratio of the components into flux ratio (see Scheirich and Pravec, 2009). Depending on the formation scenario, the satellite's density may however be different from that of the primary: under-dense for ejecta re-accumulation or over-dense for ejected boulder (unlikely here given the sizes of Isberga and its satellite). The secondary is moreover assumed to be spin–orbit locked, its long axis aligned with the centers of the two bodies at the pericenter. Finally, spin vectors of both components are assumed to be colinear with mutual orbit pole.

The total brightness of the system as seen by the observer was computed as a sum of contributions from all visible facets, using a ray-tracing code that checks which facets are occulted by or in shadow from the other component. In modeling the eccentric orbit, a precession of the line of apsides was taken into account. A pericenter drift rate depends on primary's oblateness (A_1/C_1, see Murray and Dermott, 1999, Eq. 6.249) that is only poorly estimated from the lightcurves (see Table 3), so we fit the pericenter drift rate as an independent parameter ($\dot{\omega}$). Its initial values were stepped in a range from zero to 30°/day; this range encompasses all possible values for the flattening and other parameters of the system. To reduce a complexity of the modeling, the upper limit on eccentricity is estimated by fitting data from the best-covered apparition (2011) only.

The fitted parameters are the oblateness of the primary, expressed as its equatorial-to-polar semi-major axes ratio, A_1/C_1; an elongation of the secondary, expressed as its equatorial (the largest) to polar (the shortest) semi-major axes ratio, A_2/C_2; a ratio between the mean cross-section equivalent diameters of the components of the binary ($D_{2.C}/D_{1.C}$); the pole coordinates of the mutual orbit in ecliptic frame, L_p and B_p (Epoch J2000); a relative size of the mutual orbit's semi-major axis ($a/D_{1.C}$); the mean length L_0 (i.e., the sum of angular distance from the ascending node and the length of the ascending node) for a given epoch T_0; the sidereal orbit period P_{orb}; and for modeling the eccentric orbit, the eccentricity e; and an argument of pericenter (ω) as well.

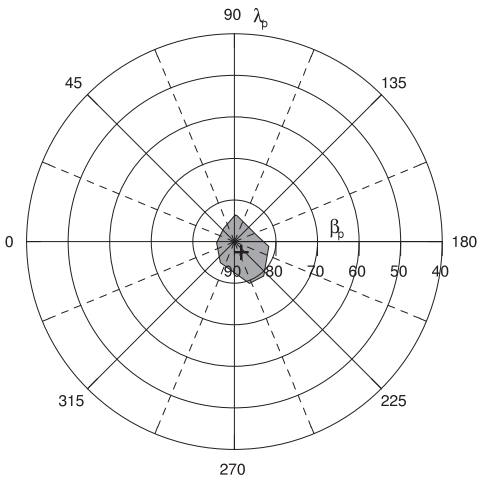

Fig. 4. The 3-σ confidence interval for the pole of the mutual orbit of Isberga (gray area) on an ECJ2000 grid, which can be approximated by an ellipse of semi-major axes of 8°and 6°, respectively. The north pole of the asteroid's heliocentric orbit is marked with the black cross.

We obtain a unique prograde solution of the mutual orbit. The best-fit model parameters are given in Table 3, with uncertainties corresponding to 3-σ confidence level (see Scheirich and Pravec, 2009). The orbital pole coordinates of the system, at a high ecliptic latitude (Fig. 4), implies a small obliquity of $1.5^{+6.0}_{-1.5}$ deg. Mutual events are therefore constantly observable from Earth, although the geometry remains limited to the equatorial region, precluding a detailed modeling of the 3-D shape of the primary. We constrain the equatorial axes (A_1 and B_1) from the amplitude of lightcurves at low phase angle and find $A_1/B_1 = 1.23 \pm 0.02$. The oblateness of the primary A_1/C_1 is, however, loosely constrained, with possible values ranging from 1.2[2] to 2.0. We do not see any evidence[3] for a strong elongation of the satellite (A_2/C_2), even in the long lightcurve observations (6–8 h) that cover a fourth of its rotation period (if it is indeed spin–orbit locked). Examples of the data for the orbital lightcurve component together with the synthetic lightcurve for the best-fit solution are presented in Fig. 5.

4.2. Interferometry analysis and size of the system

To model and interpret the spatial information encoded in the correlated flux, we develop here an extension to the simple model of binary asteroids proposed by Delbo et al. (2009), where the system was described by two uniform disks. Here, we model the primary component of the system by a uniform ellipse, thus taking into account the primary ellipsoid shape and rotation. We denote θ_α and θ_β (with $\theta_\alpha > \theta_\beta$) the apparent major axes of the ellipse representing the primary component, and θ_2 the apparent diameter of the secondary component. The two components are separated by

[2] By definition of the ellipsoid, $A_1 = B_1 > C_1$, A_1/C_1 is thus larger or equal to A_1/B_1.
[3] The elongation of the secondary is indicated by the amplitude of the long-period component of the lightcurves outside mutual events, which is zero or very low here.

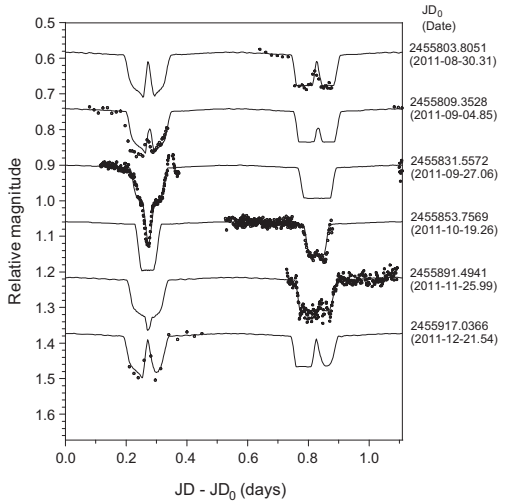

Fig. 5. Selected data of the long-period lightcurve component of Isberga during the 2011 apparition, showing the long term evolution. The observed data are marked as points. The solid curve represents the synthetic lightcurve of the best-fit solution.

the angular distance vector $\mathbf{\Lambda}$. The correlated flux (F_B) produced by such a binary system is:

$$F_B(\lambda) = F_1(\lambda,\theta_\alpha,\theta_\beta)\left[\mathscr{V}_1^2(\lambda)+\mathscr{V}_2^2(\lambda)f_{21}^2+2\mathscr{V}_1(\lambda)\mathscr{V}_2(\lambda)f_{21}\cos\left(\frac{2\pi\boldsymbol{B}}{\lambda}.\mathbf{\Lambda}\right)\right]^{\frac{1}{2}} \quad (1)$$

where $F_1(\lambda,\theta_\alpha,\theta_\beta)$ is the total flux of the first component, $f_{21}=(\theta_2/\sqrt{\theta_\alpha\theta_\beta})^2$ is the flux ratio between the secondary and primary components, $\boldsymbol{B}$ is the baseline vector projected on the plane of the sky, and $\mathscr{V}_i$ are the intrinsic normalized visibilities[4] of each component i, computed as

$$\mathscr{V}_i(\lambda) = 2\frac{J_1\left(\pi\theta_i\frac{B}{\lambda}\right)}{\pi\theta_i\frac{B}{\lambda}} \quad (2)$$

with J_1 the Bessel function of the first kind of order one, and B the length of the projected baseline on the plane of the sky. However, a complexity has to be included in the derivation of the visibility expression for the primary component that we assumed to be elliptic and not circular anymore. An ellipse can be seen as a disk that is compressed along one of its axis, thus becoming the semi-minor axis, and then possibly rotated to define the semi-major axis orientation. Therefore, the link between the visibility of a circularly symmetric brightness distribution (uniform disk) and of its inclined and rotated version (ellipse), is obtained by a proper change in the baseline reference frame. This change takes into account a rotation followed by a compression factor along the proper baseline axis (see Berger and Segransan (2007), for more details). This leads to the concept of *effective baseline*:

$$B_{\text{eff}} = \sqrt{B_{u,\gamma}^2 + B_{v,\gamma}^2\cos\left(\frac{\theta_\alpha}{\theta_\beta}\right)}, \quad (3)$$

[4] The normalized visibility is the ratio between the correlated flux and the total flux.

which is the length of projected baseline expressed in the equatorial reference frame rotated by the angle γ, the position angle, counted from north (v coordinates) to east (u coordinates), of the binary separation vector, with

$$B_{u,\gamma} = B_u\cos(\gamma) - B_v\sin(\gamma) \quad (4)$$
$$B_{v,\gamma} = B_u\sin(\gamma) + B_v\cos(\gamma) \quad (5)$$

In this rotated frame, the object recovers a circularly symmetric shape and the visibility expression of the elliptic brightness distribution is thus obtained by replacing, in Eq. (2), the projected baseline length B (as defined in the initial equatorial reference frame) by the effective baseline length B_{eff}, and θ_i by the longest axis θ_α.

Owing to the low level of the correlated flux of Isberga, we analyze the four epochs together rather than independently, tying all the parameters (4 for each epoch: θ_α, θ_β, θ_2, and Λ) to the effective, i.e., the cross-section equivalent, diameter of Isberga D_C. We use the synthetic lightcurve $m(t)$ of the rotation component (see Section 4.1 and Fig. 1c) to express the apparent major axes of the primary component at each epoch, $\theta_\alpha(t)$ and $\theta_\beta(t)$, as a function of the cross-section equivalent diameter D_C and the primary oblateness A_1/C_1. First, assuming that the system is seen equator-on, which is a minor approximation as the latitude of the sub-Earth point is 4° only, $\theta_\beta(t)$ is constant and equals to the polar dimension C_1. Second, the lightcurve amplitude provides the ratio of equatorial dimensions $A_1/B_1 = 10^{-0.4[m_A-m_B]} = 1.23$, with m_A and m_B the minimum and maximum apparent magnitudes over a rotation. With these definitions, we write the cross-section equivalent diameter as:

$$D_C = \sqrt{\langle\theta_\alpha(t)\theta_\beta(t)\rangle} = \sqrt{\langle\theta_\alpha(t)\rangle C_1}, \quad (6)$$

where $\langle\cdot\rangle$ is the temporal mean over one rotation of the primary. Considering that $\langle\theta_\alpha(t)\rangle = \sqrt{A_1B_1}$, we have:

$$D_C = \sqrt{A_1\cdot 10^{0.2[m_B-m_A]}C_1} = A_1\sqrt{\frac{10^{-0.2[m_B-m_A]}}{A_1/C_1}}. \quad (7)$$

Using $\frac{\theta_\alpha(t)}{A_1} = 10^{-0.4[m(t)-m_A]}$, we find:

$$\theta_\alpha(t) = D_C.\sqrt{A_1/C_1}.10^{0.1[m_B-m_A]}.10^{-0.4[m(t)-m_A]}. \quad (8)$$

With the total flux from the primary $F_1(\lambda,\theta_\alpha,\theta_\beta)$ evaluated using the NEATM (Harris, 1998), the ratio between the component apparent diameters f_{21} computed from their physical size ratio of 0.29 (see above, Section 4.1), and the angular separation Λ provided by the orbital solution, the free parameters are therefore restricted to the effective diameter D_C and the oblateness A_1/C_1 of the primary (see Fig. 3 for a representation of the system configuration at each epoch of observation). All other parameters are determined from these two free parameters. The η parameter is considered constant in our NEATM modeling (using the value of η = 1.211 ± 0.022 from Masiero et al., 2011).

We search for the best-fit solution by comparing the correlated flux of the model ($F_{B,i}$), at each epoch i and for each wavelength j, with the observations (F'_i), for D_C ranging from 5 to 20 km and A_1/C_1 from 1.2 to 2.0. The goodness of fit indicator we use is

$$\chi^2 = \sum_{i=1}^{N_e}\sum_{j=1}^{N_\lambda}\left(\frac{F_{B,i}(\lambda_j) - F'_i(\lambda_j)}{\sigma_{i,j}}\right)^2 \quad (9)$$

where N_e is the number of epochs, N_λ is the number of correlated flux samples at the epoch i, and $\sigma_{i,j}$ is the uncertainty on the measured correlated flux. We computed a grid of models by scanning D_C between 5 and 20 km and A_1/C_1 between 1.2 and 2.0 (see Section 4.1).

As visible in Fig. 6, the χ^2 statistics is highly peaked around 12 km along the D_C direction, while it is flatter along the A_1/C_1

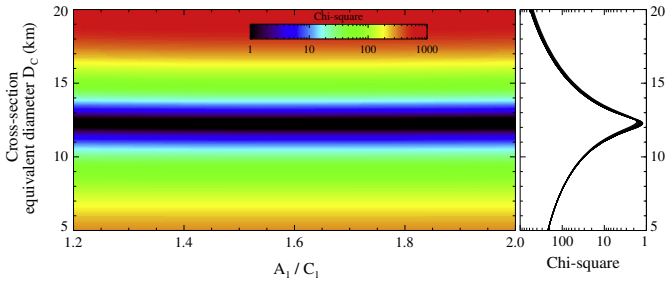

Fig. 6. Goodness of fit for the determination of Isberga effective diameter and oblateness (A_1/C_1).

direction. The best-fit to the data is thus obtained for a diameter $D_C = 12.3 \pm 0.1$ km. Although we cannot estimate accurately the quantitative contribution of the model systematics, we expect them to dominate the uncertainty budget and we adopt a more conservative value of $D_C = 12.3 \pm 1.2$ km, i.e., a 10% relative accuracy for diameter determination. The low contrast of the χ^2 statistics does not convincingly restricts the range of 1.2 to 2.0 derived from lightcurves (Section 4.1), although high oblateness seems to be favored by our modeling, with a formal best-fit value of $A_1/C_1 = 2.00^{+0.00}_{-0.45}$ derived from a Bayesian analysis of the χ^2 statistics.

We present the best-fit model plotted together with the correlated flux and the system geometry in Fig. 3. Our best-fit solution is in best agreement with the fourth averaged measurement. This is expected given the smaller error bars and thus the stronger weight of this measurement in the fit process. Nevertheless, the best-fit model agrees with the other measurements within their error bars. We can however note a slight discrepancy around 12–13 μm for the first correlated flux measurement.

We use this diameter estimate and the absolute magnitude of 12.18 ± 0.27 we determine following the work by Pravec et al. (2012a) and using observations with Trappist (Table 1) to determine an albedo[5] of $0.14^{+0.09}_{-0.06}$. S-type asteroids have higher albedo on average: 0.197 ± 0.153 (Pravec et al., 2012a). Such a value is, however, within the range of possible albedo of S-types.

Masiero et al. (2011) reported a diameter of $D_W = 10.994 \pm 0.067$ km and an albedo of 0.21 ± 0.02 based on a NEATM (Harris, 1998) analysis of WISE mid-infrared radiometry. Taking into account the binarity of Isberga, this converts into a cross-section equivalent diameter for the primary of 10.5 ± 0.1 km, to be compared with our determination. Considering a 5–10% uncertainty on the diameter determined from WISE to encompass possible systematics (see the comparison of diameter estimates from thermal modeling with other methods in Marchis et al., 2006; Carry, 2012), both determinations converge to a ≈11 km surface-equivalent diameter for Isberga. The smaller albedo determined here is due to the larger diameter determination.

4.3. Physical properties of Isberga

The results above restrict the primary oblateness A_1/C_1 between 1.2 and 2.0. Because the density determination from the lightcurve analysis is strongly dependent on this parameter, we fix the oblateness between 1.2 and 2.0 by steps of 0.1 and we determine different density values ranging from $1.89^{+0.85}_{-1.00}$ to $4.03^{+0.60}_{-1.99}$ g cm^{-3} (3-σ confidence interval). Since the ellipsoidal shape approximation tends to overestimate the volumes of the components, the derived bulk densities should be considered as lower limit estimates. Formally, the 3-σ range for the density is therefore $2.91^{+1.72}_{-2.01}$ g cm^{-3}. This level of accuracy corresponds to about 40% relative accuracy at 1-σ level. This crude precision is, however, better than that of 45% of all density determinations (see Fig. 3 in Carry, 2012). This highlights the yet limited knowledge on asteroid interiors.

This density of $2.91^{+1.72}_{-2.01}$ g cm^{-3} is very close to the typical density of S-type asteroids at 2.72 ± 0.54 g cm^{-3} (Carry, 2012). This density is lower than the grain density of the associated H ordinary chondrite meteorites of 3.72 ± 0.12 g cm^{-3} (Consolmagno et al., 2008). The porosity of Isberga is therefore 22^{+54}_{-22}%, and its macroporosity can be estimated to 14^{+66}_{-14}% (using a microporosity of 7.0 ± 4.9% on H chondrites measured by Consolmagno et al. (2008)).

The internal structure of Isberga thus encompasses all possible, from compact to highly porous. Although the presence of some macroporosity is likely, better constrains on Isberga polar oblateness are required to conclude. From the current census of S-type densities, and the linear trend of asteroids to range from large

Table 4
Physical characteristics of the binary (939) Isberga. We list the characteristic of the mutual orbit and for both the primary and the satellite their surface- and volume-equivalent diameter, density, and mass. For the primary, we also report the axes ratios and rotation period. Uncertainties are 3-σ. Values of A_2/B_2 and A_2/C_2 are formal best-fit, but values 1.0 are consistent with the data as well.

Parameter	Value	Unit
Primary		
$D_{1,C}$	12.3 ± 1.2	km
$D_{1,V}$	$12.4^{+2.5}_{-1.2}$	km
ρ_1	$2.91^{+1.72}_{-2.01}$	g cm^{-3}
M_1	$3.52^{+3.90}_{-2.73} \times 10^{15}$	kg
A_1/B_1	1.23 ± 0.02	
A_1/C_1	$1.3^{+0.7}_{-0.03}$	
P_{rot}	2.91695 ± 0.00010	h
Satellite		
$D_{2,C}$	3.6 ± 0.5	km
$D_{2,V}$	$3.6^{+0.7}_{-0.3}$	km
$\rho_2 \equiv \rho_1$	$2.91^{+1.72}_{-2.01}$	g cm^{-3}
M_2	$8.60^{+24.1}_{-7.83} \times 10^{13}$	kg
A_2/B_2	1.1	
A_2/C_2	1.1	
$P_{rot} \equiv P_{orb}$	26.6304 ± 0.0001	h
Mutual orbit		
a	$33.0^{+7.6}_{-1.4}$	km
(λ_p, β_p)	$(225, +86) \pm 7$	deg.
P_{orb}	26.6304 ± 0.0001	h
e	⩽0.10	

[5] We use the widely-used formula between the size D, the visible absolute magnitude H, and the geometric visible albedo p_v : $D(\text{km}) = 1329 p_v^{-1/2} 10^{-H/5}$.

and dense to small and porous (see Fig. 9 in Carry, 2012), it is, however, unlikely that Isberga has a density above ≈ 3 g cm^{-3}. We therefore favor solutions with oblateness below 1.5–1.6.

We finally use this density determination to estimate the mass of Isberga and of its satellite: from the primary volume-equivalent diameter $D_V = \left(\frac{A_1}{C_1}\right)^{-1/6}\left(\frac{A_1}{B_1}\right)^{-1/12} D_C$ (Table 4), we find $M_1 = 3.52^{+3.90}_{-2.73} \times 10^{15}$ kg and $M_2 = 8.60^{+24.1}_{-7.83} \times 10^{13}$ kg, respectively. The size of the Hill sphere associated with these masses is of 2320^{+650}_{-700} and 670^{+330}_{-370} km. The system is therefore extremely compact, the components being separated by only 33 km.

5. Conclusion

We present the first mid-infrared interferometric observations of a small binary asteroid, (939) Isberga. Together with low-resolution spectroscopy in the near infrared and an extensive campaign of lightcurves, we conduct a complete characterization of the surface, orbital, and physical properties of the system. It is composed by a 13 km S-type primary and a 4 km secondary, orbiting each other in 26 h on a nearly-circular orbit of semi-major axis 33 km, deep inside the Hill sphere. The inferred density of $2.91^{+1.72}_{-2.01}$ g cm^{-3} is typical for this composition, but the large uncertainties prevent from concluding on the internal structure. The system has a low obliquity ($1.5^{+6.0}_{-1.5}$ deg.) and mutual eclipses and occultations are always visible from Earth. More lightcurve observations of the system, in particular with absolute photometric reference, will help constrain better the elongation of the secondary and the eccentricity of the mutual orbit.

The low mid-infrared flux of Isberga, at the very edge of VLTI/MIDI capabilities, precludes an independent analysis of these data. The combined analysis of optical lightcurves and mid-infrared visibilities we present here is, however, an efficient way to derive both relative quantities and absolutely scale the system. Among the many small main-belt binaries, all present similar mid-infrared fluxes (given their temperature and apparent angular size), and more sensitive instruments/modes, like the forthcoming VLTI/MATISSE, must be used to better characterize this population of binary systems.

Acknowledgments

We acknowledge support from the Faculty of the European Space Astronomy Centre (ESAC) for the visits of M. Delbo and A. "Momo" Matter. The work by P.S. and P.P. was supported by the Grant Agency of the Czech Republic, Grant P209/12/0229, and by Program RVO 67985815. A. Matter acknowledges financial support from the Centre National d'Études Spatiales (CNES). TRAPPIST is a project funded by the Belgian Fund for Scientific Research (Fonds National de la Recherche Scientifique, F.R.S.-FNRS) E. Jehin and M. Gillon are FNRS Research Associates, and Jean Manfroid is Research Director of the FNRS. Part of the data utilized in this publication were obtained and made available by the MIT-UH-IRTF Joint Campaign for NEO Reconnaissance. The IRTF is operated by the University of Hawaii under Cooperative Agreement No. NCC 5–538 with the National Aeronautics and Space Administration, Office of Space Science, Planetary Astronomy Program. The MIT component of this work is supported by NASA Grant 09-NEOO009–0001, and by the National Science Foundation under Grant Nos. 0506716 and 0907766. F.E.D. acknowledges funding from NASA under Grant No. NNX12AL26G and Hubble Fellowship Grant HST-HF-51319.01-A. Any opinions, findings, and conclusions or recommendations expressed in this material are those of the authors and do not necessarily reflect the views of NASA or the National Science Foundation. This research utilizes spectra acquired by Jeffery F. Bell with the NASA RELAB facility at Brown University.

References

Berger, J.P., Segransan, D., 2007. An introduction to visibility modeling. New Astron. Rev. 51, 576–582.
Binzel, R.P., Rivkin, A.S., Stuart, J.S., Harris, A.W., Bus, S.J., Burbine, T.H., 2004. Observed spectral properties of near-Earth objects: Results for population distribution, source regions, and space weathering processes. Icarus 170, 259–294.
Binzel, R.P., Thomas, C.A., DeMeo, F.E., Tokunaga, A., Rivkin, A.S., Bus, S.J., 2006. The MIT–Hawaii–IRTF joint campaign for NEO spectral reconnaissance. In: Mackwell, S., Stansbery, E. (Eds.), 37th Annual Lunar and Planetary Science Conference. Lunar and Planetary Inst. Technical Report, vol. 37, p. 1491.
Brunetto, R., de León, J., Licandro, J., 2007. Testing space weathering models on A-type Asteroid (1951) Lick. Astron. Astrophys. 472, 653–656.
Brunetto, R., Vernazza, P., Marchi, S., Birlan, M., Fulchignoni, M., Orofino, V., Strazzulla, G., 2006. Modeling asteroid surfaces from observations and irradiation experiments: The case of 832 Karin. Icarus 184, 327–337.
Burbine, T.H., Binzel, R.P., 2002. Small main-belt asteroid spectroscopic survey in the near-infrared. Icarus 159, 468–499.
Carry, B., 2012. Density of asteroids. Planet. Space Sci. 73, 98–118.
Carry, B. et al., 2011. Integral-field spectroscopy of (90482) Orcus–Vanth. Astron. Astrophys. 534, A115.
Carry, B., Vernazza, P., Dumas, C., Merline, W.J., Mousis, O., Rousselot, P., Jehin, E., Manfroid, J., Fulchignoni, M., Zucconi, J.-M., 2012. The remarkable surface homogeneity of the dawn mission target (1) Ceres. Icarus 217, 20–26.
Chapman, C.R., 2004. Space weathering of asteroid surfaces. Annu. Rev. Earth Planet. Sci. 32, 539–567.
Chesneau, O., 2007. MIDI: Obtaining and analysing interferometric data in the mid-infrared. New Astron. Rev. 51, 666–681.
Consolmagno, G.J., Britt, D.T., 1998. The density and porosity of meteorites from the Vatican collection. Meteorit. Planet. Sci. 33, 1231–1241.
Consolmagno, G., Britt, D., Macke, R., 2008. The significance of meteorite density and porosity. Chemie der Erde/Geochemistry 68, 1–29.
Delbo, M., Ligori, S., Matter, A., Cellino, A., Berthier, J., 2009. First VLTI-MIDI direct determinations of asteroid sizes. Astrophys. J. 694, 1228–1236.
DeMeo, F., Binzel, R.P., 2008. Comets in the near-Earth object population. Icarus 194, 436–449.
DeMeo, F., Carry, B., 2013. The taxonomic distribution of asteroids from multi-filter all-sky photometric surveys. Icarus 226, 723–741.
DeMeo, F.E., Carry, B., 2014. Solar System evolution from compositional mapping of the asteroid belt. Nature 505, 629–634.
DeMeo, F.E., Binzel, R.P., Slivan, S.M., Bus, S.J., 2009. An extension of the Bus asteroid taxonomy into the near-infrared. Icarus 202, 160–180.
Descamps, P., Marchis, F., Berthier, J., Emery, J.P., Duchêne, G., de Pater, I., Wong, M.H., Lim, L., Hammel, H.B., Vachier, F., Wiggins, P., Teng-Chuen-Yu, J.-P., Peyrot, A., Pollock, J., Assafin, M., Vieira-Martins, R., Camargo, J.I.B., Braga-Ribas, F., Macomber, B., 2011. Triplicity and physical characteristics of Asteroid (216) Kleopatra. Icarus 211, 1022–1033.
Fujiwara, A. et al., 2006. The rubble-pile Asteroid Itokawa as observed by Hayabusa. Science 312, 1330–1334.
Fulvio, D., Brunetto, R., Vernazza, P., Strazzulla, G., 2012. Space weathering of vesta and v-type asteroids: New irradiation experiments on HED meteorites. Astron. Astrophys. 537, L11.
Gaffey, M.J., 2010. Space weathering and the interpretation of asteroid reflectance spectra. Icarus 209, 564–574.
Gaffey, M.J., Burbine, T.H., Piatek, J.L., Reed, K.L., Chaky, D.A., Bell, J.F., Brown, R.H., 1993. Mineralogical variations within the S-type asteroid class. Icarus 106, 573–602.
Harris, A.W., 1998. A thermal model for near-Earth asteroids. Icarus 131, 291–301.
Jaffe, W.J., 2004. Coherent fringe tracking and visibility estimation for MIDI. In: Traub, W.A. (Ed.), Society of Photo-Optical Instrumentation Engineers (SPIE) Conference Series. Society of Photo-Optical Instrumentation Engineers (SPIE) Conference Series, vol. 5491, p. 715.
Kuchynka, P., Folkner, W.M., 2013. A new approach to determining asteroid masses from planetary range measurements. Icarus 222, 243–253.
Leinert, C. et al., 2004. Mid-infrared sizes of circumstellar disks around Herbig Ae/Be stars measured with MIDI on the VLTI. Astron. Astrophys. 423, 537–548.
Lord, S.D., 1992. A New Software Tool for Computing Earth's Atmospheric Transmission of Near- and Far-infrared Radiation. NASA Tech. Mem. (103957).
Mainzer, A. et al., 2011. NEOWISE studies of spectrophotometrically classified asteroids: Preliminary results. Astrophys. J. 741, 90.
Marchis, F., Descamps, P., Hestroffer, D., Berthier, J., 2005. Discovery of the triple asteroidal system 87 Sylvia. Nature 436, 822–824.
Marchis, F. et al., 2006. Shape, size and multiplicity of main-belt asteroids. Icarus 185 (1), 39–63.
Masiero, J.R. et al., 2011. Main belt asteroids with WISE/NEOWISE. I. Preliminary albedos and diameters. Astrophys. J. 741, 68.
Matter, A., Delbo, M., Ligori, S., Crouzet, N., Tanga, P., 2011. Determination of physical properties of the Asteroid (41) Daphne from interferometric observations in the thermal infrared. Icarus 215, 47–56.

Matter, A., Delbo, M., Carry, B., Ligori, S., 2013. Evidence of a metal-rich surface for the Asteroid (16) Psyche from interferometric observations in the thermal infrared. Icarus 226, 419–427.
Merline, W.J. et al., 1999. Discovery of a Moon orbiting the Asteroid 45 Eugenia. Nature 401, 565–568.
Molnar, L.A., et al., 2008. Lightcurve analysis of a magnitude limited asteroid sample. Minor Planet Bullet. 35, 9–12.
Murray, C.D., Dermott, S.F., 1999. Solar System Dynamics. Cambridge University Press.
Nakamura, T. et al., 2011. Itokawa dust particles: A direct link between S-type asteroids and ordinary chondrites. Science 333, 1113–1115.
Pätzold, M. et al., 2011. Asteroid 21 Lutetia: Low mass, high density. Science 334, 491–492.
Popescu, M., Birlan, M., Nedelcu, D.A., 2012. Modeling of asteroid spectra – M4AST. Astron. Astrophys. 544, A130.
Pravec, P., Scheirich, P., Kušnirák, P., Šarounová, L., Mottola, S., Hahn, G., Brown, P.G., Esquerdo, G.A., Kaiser, N., Krzeminski, Z., Pray, D.P., Warner, B.D., Harris, A.W., Nolan, M.C., Howell, E.S., Benner, L.A.M., Margot, J.-L., Galád, A., Holliday, W., Hicks, M.D., Krugly, Y.N., Tholen, D.J., Whiteley, R.J., Marchis, F., Degraff, D.R., Grauer, A., Larson, S., Velichko, F.P., Cooney, W.R., Stephens, R., Zhu, J., Kirsch, K., Dyvig, R., Snyder, L., Reddy, V., Moore, S., Gajdoš, Š., Világi, J., Masi, G., Higgins, D., Funkhouser, G., Knight, B., Slivan, S.M., Behrend, R., Grenon, M., Burki, G., Roy, R., Demeautis, C., Matter, D., Waelchli, N., Revaz, Y., Klotz, A., Rieugné, M., Thierry, P., Cotrez, V., Brunetto, L., Kober, G., 2006. Photometric survey of binary near-Earth asteroids. Icarus 181, 63–93.
Pravec, P., Harris, A.W., Kušnirák, P., Galád, A., Hornoch, K., 2012a. Absolute magnitudes of asteroids and a revision of asteroid albedo estimates from WISE thermal observations. Icarus 221, 365–387.
Pravec, P., Scheirich, P., Vokrouhlický, D., Harris, A.W., Kušnirák, P., Hornoch, K., Pray, D.P., Higgins, D., Galád, A., Világi, J., Gajdoš, Š., Kornoš, L., Oey, J., Husárik, M., Cooney, W.R., Gross, J., Terrell, D., Durkee, R., Pollock, J., Reichart, D.E., Ivarsen, K., Haislip, J., Lacluyze, A., Krugly, Y.N., Gaftonyuk, N., Stephens, R.D., Dyvig, R., Reddy, V., Chiorny, V., Vaduvescu, O., Longa-Peña, P., Tudorica, A., Warner, B.D., Masi, G., Brinsfield, J., Gonçalves, R., Brown, P., Krzeminski, Z., Gerashchenko, O., Shevchenko, V., Molotov, I., Marchis, F., 2012b. Binary asteroid population. 2. Anisotropic distribution of orbit poles of small, inner main-belt binaries. Icarus 218, 125–143.
Rayner, J.T. et al., 2003. SpeX: A medium-resolution 0.8–5.5 micron spectrograph and imager for the NASA infrared telescope facility. Publicat. Astron. Soc. Pacific 115, 362–382.
Rivkin, A.S., Binzel, R.P., Sunshine, J., Bus, S.J., Burbine, T.H., Saxena, A., 2004. Infrared spectroscopic observations of 69230 Hermes (1937 UB): possible unweathered endmember among ordinary chondrite analogs. Icarus 172, 408–414.
Russell, C.T. et al., 2012. Dawn at Vesta: Testing the protoplanetary paradigm. Science 336, 684–686.
Sasaki, S., Nakamura, K., Hamabe, Y., Kurahashi, E., Hiroi, T., 2001. Production of iron nanoparticles by laser irradiation in a simulation of lunar-like space weathering. Nature 410, 555–557.
Scheirich, P., Pravec, P., 2009. Modeling of lightcurves of binary asteroids. Icarus 200, 531–547.
Shepard, M.K., Clark, B.E., Nolan, M.C., Howell, E.S., Magri, C., Giorgini, J.D., Benner, L.A.M., Ostro, S.J., Harris, A.W., Warner, B.D., Pray, D.P., Pravec, P., Fauerbach, M., Bennett, T., Klotz, A., Behrend, R., Correia, H., Coloma, J., Casulli, S., Rivkin, A.S., 2008. A radar survey of M- and X-class asteroids. Icarus 195, 184–205.
Strazzulla, G., Dotto, E., Binzel, R.P., Brunetto, R., Barucci, M.A., Blanco, A., Orofino, V., 2005. Spectral alteration of the Meteorite Epinal (H5) induced by heavy ion irradiation: A simulation of space weathering effects on near-Earth asteroids. Icarus 174, 31–35.
Tody, D., 1993. IRAF in the nineties. In: Hanisch, R.J., Brissenden, R.J.V., Barnes, J. (Eds.), Astronomical Data Analysis Software and Systems II. Astronomical Society of the Pacific Conference Series, vol. 52, p. 173.
Vachier, F., Berthier, J., Marchis, F., 2012. Determination of binary asteroid orbits with a genetic-based algorithm. Astron. Astrophys. 543, A68.
Vernazza, P., Binzel, R.P., Rossi, A., Fulchignoni, M., Birlan, M., 2009. Solar wind as the origin of rapid reddening of asteroid surfaces. Nature 458, 993–995.
Vernazza, P., Carry, B., Emery, J.P., Hora, J.L., Cruikshank, D.P., Binzel, R.P., Jackson, J., Helbert, J., Maturilli, A., 2010. Mid-infrared spectral variability for compositionally similar asteroids: Implications for asteroid particle size distributions. Icarus 207, 800–809.
Walsh, K.J., Richardson, D.C., Michel, P., 2008. Rotational breakup as the origin of small binary asteroids. Nature 454, 188–191.
Zielenbach, W., 2011. Mass determination studies of 104 large asteroids. Astron. J. 142, 120–128.

Asteroid Systems: Binaries, Triples, and Pairs

Jean-Luc Margot
University of California, Los Angeles

Petr Pravec
Astronomical Institute of the Czech Republic Academy of Sciences

Patrick Taylor
Arecibo Observatory

Benoît Carry
Institut de Mécanique Céleste et de Calcul des Éphémérides

Seth Jacobson
Côte d'Azur Observatory

In the past decade, the number of known binary near-Earth asteroids has more than quadrupled and the number of known large main belt asteroids with satellites has doubled. Half a dozen triple asteroids have been discovered, and the previously unrecognized populations of asteroid pairs and small main belt binaries have been identified. The current observational evidence confirms that small ($\lesssim$20 km) binaries form by rotational fission and establishes that the YORP effect powers the spin-up process. A unifying paradigm based on rotational fission and post-fission dynamics can explain the formation of small binaries, triples, and pairs. Large ($\gtrsim$20 km) binaries with small satellites are most likely created during large collisions.

1. INTRODUCTION

1.1. Motivation

Multiple-asteroid systems are important because they represent a sizable fraction of the asteroid population and because they enable investigations of a number of properties and processes that are often difficult to probe by other means. The binaries, triples, and pairs inform us about a great variety of asteroid attributes, including physical properties, composition, interior structure, formation processes, and evolutionary processes.

Observations of binaries and triples provide the most powerful way of deriving reliable masses and densities for a large number of objects. The density measurements help us understand the composition and internal structure of minor planets. Binary systems offer opportunities to measure thermal and mechanical properties, which are generally poorly known.

The binary and triple systems within near-Earth asteroids (NEAs), main belt asteroids (MBAs), and trans-Neptunian objects (TNOs) exhibit a variety of formation mechanisms (Merline et al. 2002c; Noll et al. 2008). As such, they provide an invaluable window on accretional, collisional, tidal, and radiative processes that are critical in planet formation. The distribution and configurations of the multiple-asteroid systems also provide a rich array of constraints on their environment, their formation, and their evolutionary pathways.

Observations rely primarily on ground-based

telescopes and the Hubble Space Telescope (HST). For an up-to-date list of binaries and triples in the solar system, see Johnston (2014). We describe observational techniques only briefly because this material is available elsewhere (e.g., Merline et al. 2002c). A few emerging techniques will be described in more detail. Likewise, we refer the reader to other texts for an extensive history of the field (e.g., Merline et al. 2002c) and highlight only a few of the developments here.

1.2. History

Early search programs for asteroid satellites were unsuccessful, returning negative or dubious results, such that the authors of the *Asteroids II* review chapter chose the prudent title "Do asteroids have satellites?" (Weidenschilling et al. 1989). The chapter provides an excellent discussion of the physics of several formation mechanisms that were postulated at the time. The perspective changed with the flyby of (243) Ida by the Galileo spacecraft in 1993 and the discovery of its small satellite Dactyl (Chapman et al. 1995; Belton et al. 1995). Ground-based efforts intensified and resulted in the discovery of a satellite around (45) Eugenia by Merline et al. (1999). Several other discoveries followed in rapid succession. The relatively small sizes of the MBA satellites suggested formation in sub-catastrophic or catastrophic collisions (Durda 1996; Doressoundiram et al. 1997).

The discovery of MBA satellites, coupled with analysis of terrestrial doublet craters (Bottke and Melosh 1996a,b) and anomalous lightcurve observations (Pravec and Hahn 1997), suggested the existence of binary asteroids in the near-Earth population as well. The unambiguous detection of five NEA binaries by radar cemented this finding and indicated that NEA satellites form by a spin-up and rotational fission process (Margot et al. 2002). Lightcurve observers reached the same conclusion independently (Pravec and Harris 2007). Both radar and lightcurve observations revealed that, far from being rare, binary asteroids are relatively common (Pravec et al. 1999; Margot et al. 2002; Pravec et al. 2006). By the time the *Asteroids III* review chapter was written, a more decisive title ("Asteroids do have satellites") had become appropriate (Merline et al. 2002c). This review focuses on the developments that followed the publication of *Asteroids III*.

1.3. Terminology

Two- and three-component asteroids that are gravitationally bound will be referred to as *binary asteroids* (or *binaries*) and *triple asteroids* (or *triples*), respectively. (*Triple* is favored over the more directly analogous terms *trinary* and *ternary* because of long-established usage in astronomy). *Asteroid pairs* denote asteroid components that are genetically related but not gravitationally bound. *Paired binaries* or *paired triples* are asteroid pairs where the larger asteroid is itself a binary or triple asteroid. The larger component in binaries, triples, and pairs is referred to as the *primary component* or *primary*. The smaller component in binaries is referred to as the *secondary component* or *secondary*.

There has been some confusion in the literature about the meaning of the word "asynchronous." Here, we adopt the terminology proposed by Margot (2010) and later implemented by Jacobson and Scheeres (2011b) and Fang and Margot (2012c). Binaries with an absence of spin-orbit synchronism are called *asynchronous binaries*. Binaries with a secondary spin period synchronized to the mutual orbit period are called *synchronous binaries*. Binaries with both primary and secondary spin periods synchronized to the mutual orbit period are called *doubly synchronous binaries*. If generalization to systems with more than one satellite is needed, we affix the terms *synchronous* and *asynchronous* to the satellites being considered.

It is useful to present results for *small* and *large* asteroids. We place an approximate dividing line at the size at which objects are substantially affected by the YORP effect during their lifetime. For typical NEAs and MBAs, this dividing line corresponds to a diameter of about 20 km (Jacobson et al. 2014a). We define *very small* asteroids as those with diameters of less than 200 m. This is the approximate size below which many asteroids are observed to spin faster than the disruption

rate of a body with no shear or tensile strength $\omega_d = \sqrt{4\pi\rho G/3}$, where ρ is the density and G is the gravitational constant.

We use two additional acronyms. The YORP effect is a radiation-powered rotational acceleration mechanism for small asteroids (Rubincam 2000). The binary YORP (BYORP) effect is a radiation-powered acceleration mechanism that may expand or contract the orbits of some synchronous asteroids (Ćuk and Burns 2005).

2. OBSERVATIONS

Several observational techniques are available for discovering, detecting, and studying binaries, triples, and pairs, each with its strengths and weaknesses. This section describes recent results and illustrates the complementarity of the observational techniques that characterize individual asteroid systems and entire populations.

2.1 Radar Observations of NEA Systems

Radar has proven to be a powerful method of detecting secondaries to NEAs, enabling the discovery (as of September 2014) of the satellites in 71% of the 49 known multiple-component NEA systems, including 33 of 47 binaries and both undisputed triple systems. Of the 14 binary NEAs discovered via optical lightcurve techniques, 6 have been confirmed with follow-up radar observations during later apparitions. Overall, radar detections suggest that about one in six NEAs larger than 200 m in diameter are multiple-asteroid systems (Margot et al. 2002; Taylor et al. 2012a), though 200 m is not a sharp cutoff. Three binary NEA systems identified by radar have primary components with suggested diameters of 120 m to 180 m: 2003 SS_{84} (Nolan et al. 2003), (363599) 2004 FG_{11} (Taylor et al. 2012c), and 1994 CJ_1 (Taylor et al. 2014). For comparison, the largest primaries of binary NEAs imaged with radar: (5143) Heracles (Taylor et al. 2012b), the possible triple (276049) 2002 CE_{26} (Shepard et al. 2006), and (285263) 1998 QE_2 (Springmann et al. 2014), are more than an order of magnitude larger at $>$3 km in diameter. It is likely that $\sim$8 km diameter (1866) Sisyphus has a secondary based on analysis of frequency-only observations obtained on four separate dates in 1985 (Ostro, pers. comm., 2001).

Radar observations can be used to detect asteroid satellites because of the ability to resolve the components of the system both spatially (along the observer's line of sight) and in terms of frequency (due to Doppler shifts from the rotational and orbital line-of-sight velocities), resulting in a measurable separation between the components in two dimensions. Direct detection of a satellite in frequency-only spectra or radar images typically occurs within one observing session and often within minutes of observation. The bandwidth of the echo of a component scales directly with the diameter and rotation rate. Thus, in a frequency-only experiment, the signal of the smaller, relatively slowly rotating satellite is condensed to a smaller bandwidth that is superimposed upon the broadband signal of the larger, often rapidly rotating, primary (Fig. 1, top). Not all radar-observed binaries present this characteristic spectrum (e.g., where the secondary spins faster than the synchronous rate), but all are readily detected in radar images when the components are also resolved spatially (Fig. 1, bottom). Because the spatial resolution achieved with radar instruments corresponds to an effective angular resolution of better than $\sim$1 milliarcsecond (mas), there is no bias against the detection of satellites orbiting very close to the primary component. Multiple measurements of the range and frequency separations of the components over days of sky motion provide the geometric leverage required to determine the orbit of the secondary around the primary. This can be done for any orbital orientation and yields the total system mass, a property that is difficult to estimate otherwise. Other techniques involve analyzing spacecraft flyby and orbit trajectories (e.g., Yeomans et al. 1999), measuring the Yarkovsky orbital drift in conjunction with thermal properties (e.g., Chesley et al. 2014), or observing the gravitational perturbations resulting from asteroid encounters (e.g., Hilton 2002).

Most binary NEA systems observed to date have a rapidly rotating primary and a smaller

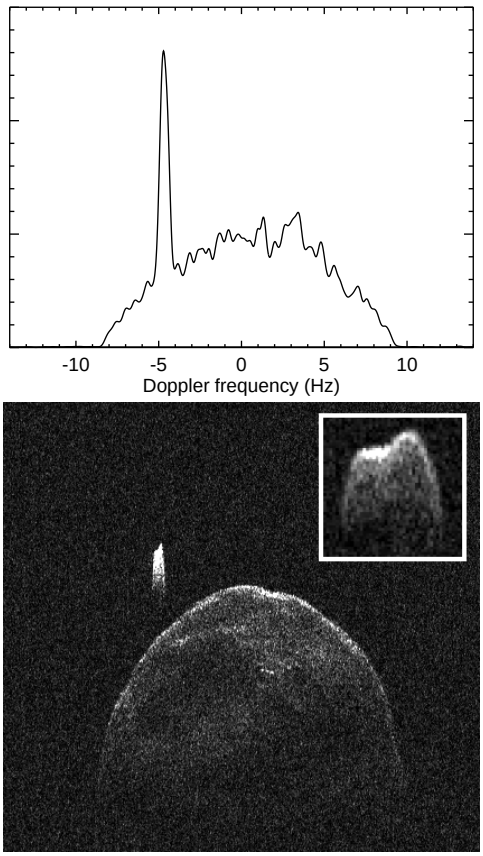

Fig. 1.— Binary near-Earth asteroid (285263) 1998 QE_2 as detected using the Arecibo planetary radar system. In the frequency-only spectrum showing echo power as a function of Doppler frequency (top), the narrowband echo of the tidally locked secondary stands out against the broadband echo of the larger, faster-rotating primary. In the radar image (bottom), the components are spatially resolved (7.5 m/pixel). The vertical axis represents distance from the observer increasing downward. The horizontal axis is Doppler frequency due to the orbital and rotational motion of the components. Note that if one summed the pixel values in each column of the image, the intensity as a function of Doppler frequency would approximate the spectrum above. The secondary is roughly one-fourth the size of the primary (measured in the vertical dimension), though the Doppler breadth of the primary gives the illusion of a greater size disparity. The shape of the secondary (inset) is distinctly nonspherical when viewed with finer frequency resolution.

secondary of order a few tenths the size of the primary (a secondary-to-primary mass ratio of roughly 0.001 to 0.1), whose rotation is synchronized to the mutual orbit period. The majority of primaries rotate in less than 2.8 h, though they range from 2.2593 h for (65803) Didymos (Pravec et al. 2006) to 4.749 h for 1998 QE_2 (P. Pravec, pers. comm., 2013). The known outlier is the nearly equal-mass binary (69230) Hermes, whose components both appear to have 13.894 h periods synchronized to their mutual orbit period (Margot et al. 2006). This doubly synchronous configuration is most likely due to rapid tidal evolution (Taylor and Margot 2011). While the rotations of satellites in NEA binaries tend to be tidally locked to their orbital mean motions with periods typically within a factor of two of 24 h (often resulting in the characteristic appearance shown in Fig. 1), about one in four radar-observed multiple-asteroid systems have an asynchronous satellite (Brozović et al. 2011), all of which rotate faster than their orbital rate. Well-studied examples include (35107) 1991 VH (Naidu et al. 2012), (153958) 2002 AM_{31} (Taylor et al. 2013), (311066) 2004 DC (Taylor et al. 2008), and the outer satellites of both undisputed triple systems (153591) 2001 SN_{263} (Nolan et al. 2008; Fang et al. 2011; Becker et al. 2015) and (136617) 1994 CC (Brozović et al. 2011; Fang et al. 2011). Of the known asynchronous satellites, all have wide component separations ($>$7 primary radii), translating to longer-than-typical orbital periods, and/or eccentric orbits ($>$0.05), that are either remnants of their formation mechanism or products of subsequent dynamical evolution (Fang and Margot 2012c).

The shortest orbital periods detected with radar so far are those of Didymos and 2006 GY_2 with $P_{\rm orb} = 11.90^{+0.03}_{-0.02}$ h and 11.7 ± 0.2 h, respectively (Benner et al. 2010; Brooks 2006). For Didymos, the semi-major axis is $a = 1.18^{+0.04}_{-0.02}$ km, just outside the classical fluid Roche limit of $\sim$1 km for equal-density components. Other systems with satellites orbiting near this limit include 2002 CE_{26} and 2001 SN_{263}. The significance of this limit is unclear, as $\sim$100 m secondaries with a cohesion comparable to comet regolith or sand can likely survive on orbits interior to the Roche

limit (Taylor and Margot 2010, and references therein).

Inversion of a series of radar images can provide a three-dimensional shape model and complete spin-state description given sufficient signal, resolution, and orientational coverage (Hudson 1993; Magri et al. 2007). Shape reconstruction of the larger component of (66391) 1999 KW_4 (Ostro et al. 2006) demonstrated that the canonical shape of an NEA primary has a characteristic circular equatorial bulge, uniformly sloped sides, and polar flattening akin to a spinning top. Such a shape is shared by the primaries of 2004 DC, 1994 CC, 2001 SN_{263}, and (185851) 2000 DP_{107} (Naidu et al. 2015), though some primaries have less pronounced equatorial belts, e.g., 2002 CE_{26} and 1998 QE_2. Some single asteroids have a similar shape, e.g., (101955) Bennu (Nolan et al. 2013) and (341843) 2008 EV_5 (Busch et al. 2011), but do not have satellites, possibly because one has not yet formed or has been lost in the past. Shape model renditions are shown in Benner et al. (this volume). Often the resolution of radar images of the smaller satellites is insufficient for shape inversion, but radar images suggest that the satellites are typically elongated, e.g., 2000 DP_{107}, 1999 KW_4, 2001 SN_{263}, 1991 VH, and 1998 QE_2.

Shapes and volumes obtained from inversion of radar images, combined with the system mass derived from the orbital motion observed in radar images, provide the density of the system (or of the individual components if the mass ratio is measurable from reflex motion). Low densities of order 1 g/cm^3 (Shepard et al. 2006; Becker et al. 2015) to 2 g/cm^3 (Ostro et al. 2006; Brozović et al. 2011) suggest significant internal macroporosity of order 50%, implying a rubble-pile internal structure for the components. At such low densities, the rapid rotation of the primary places particles along the equatorial belt in a near-weightless environment. The combination of rapid rotation, shape, and implied porosity and rubble-pile structure has implications for the formation mechanism of small multiple-asteroid systems (Section 4).

While radar allows for direct, unambiguous detection of asteroid satellites, its range is limited. Because radar requires the transmission and reception of a signal, the strength of the received signal falls as the fourth power of the distance to the target and, thus, is best suited for detecting multiple-component systems passing within ∼0.2 astronomical units (au) of Earth. Satellites in the main asteroid belt simply tend to be too small and too far away to detect with present radar capabilities and require application of different observational techniques.

2.2 Lightcurve Observations of NEA and Small MBA Systems

A photometric lightcurve is a time series of measurements of the total brightness of an asteroid. Detections of binary asteroids by photometric lightcurve observations utilize the fact that the components can obscure or cast a shadow on one another, producing occultations or eclipses, respectively. The attenuations can be used to both reveal and characterize binaries (Fig. 2). The observational, analysis, and modeling techniques were described in Pravec et al. (2006); Scheirich and Pravec (2009); Scheirich et al. (2015).

Early reports (Tedesco 1979; Cellino et al. 1985) of asteroids suspected to be binaries on the basis of anomalous lightcurves (including (15) Eunomia, (39) Laetitia, (43) Ariadne, (44) Nysa, (49) Pales, (61) Danae, (63) Ausonia, (82) Alkmene, (171) Ophelia, and (192) Nausikaa) have remained largely unconfirmed despite extensive follow-up searches. The first serious candidate for detection with this technique was NEA (385186) 1994 AW_1 (Pravec and Hahn 1997), whose binary nature was confirmed by photometric observations in 2008 (Birlan et al. 2010). Since 1997, nearly 100 binaries among near-Earth and small main belt asteroids have been detected with the photometric method. The binary asteroid database constructed by Pravec and Harris (2007) (http://www.asu.cas.cz/∼asteroid/binastdata.htm) includes data for 86 MBA and NEA binaries that were securely detected by photometry and for which basic parameters have been derived, such as the primary spin period, the orbital period, and the primary-to-secondary mean diameter ratio. A

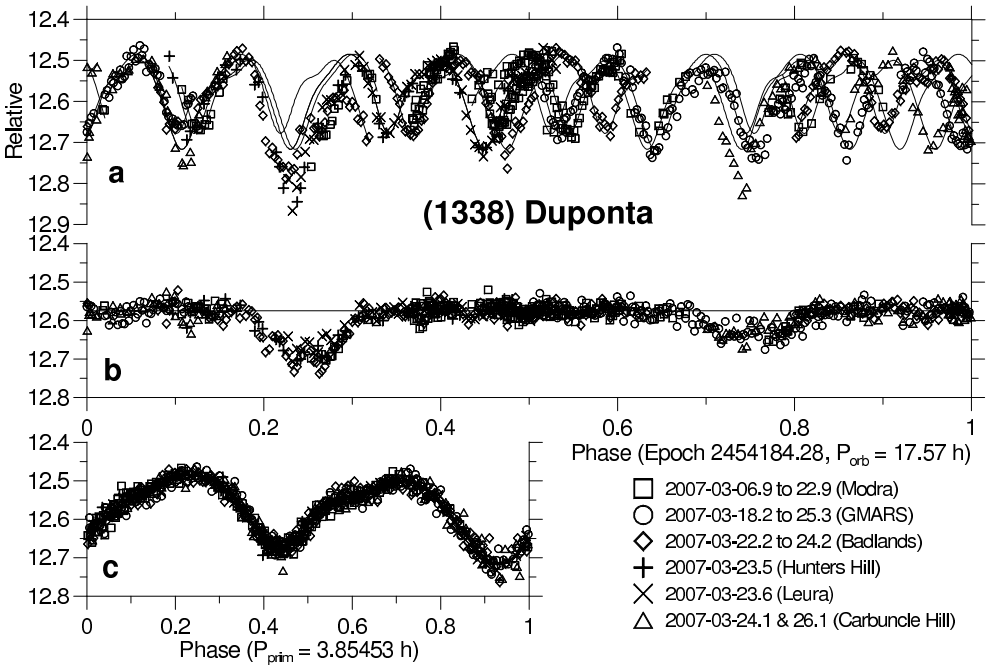

Fig. 2.— Lightcurve data of (1338) Duponta, which has a secondary-to-primary diameter ratio of about 0.24. (a) The original data showing both lightcurve components, folded with the orbit period. (b) The orbital lightcurve component, derived after subtraction of the primary lightcurve component, showing the mutual events between components of the binary system. (c) The primary lightcurve component. Figure from Pravec et al. (2012).

few tens of additional MBAs and NEAs are suspected to be binaries and await confirmation with more detailed observations in the future.

Among the main findings obtained from photometric observations is that binary asteroids are ubiquitous. They have been found among NEAs, Mars-crossers (MCs), and throughout the main belt, both among asteroids that have been identified as family members and among asteroids that have not. Pravec et al. (2006) derived the fraction of binaries among NEAs larger than 300 meters to be 15 ± 4%. A binary fraction among MBAs has not been derived precisely due to less well-characterized observational selection effects, but their photometric discovery rate is similar to the discovery rate of binaries among NEAs. Thus, binaries are suspected to be as frequent among MBAs as they are among NEAs. There appears to be an upper limit on the primary diameter for photometrically detected binaries of about 13 km; the largest detected binary is (939) Isberga with $D_p = 13.4 \pm 1.3$ km (Carry et al. 2015). A lower size limit on the primary diameter D_p is less clear. The smallest detected binary is 2000 UG_{11} with $D_p = 0.26 \pm 0.03$ km (Pravec et al. 2006), but smaller binaries are known to exist (Section 2.1). Their absence in lightcurve data sets may be due in part to a bias against detecting small binaries in the initial surveys.

Another key finding is that small binary asteroids have, with only two or three exceptions, a near-critical angular momentum content (Fig. 3). As shown by Pravec and Harris (2007), their angular momentum is consistent with formation by fission of critically spinning parent bodies of a cohesionless, rubble pile structure. The exceptions

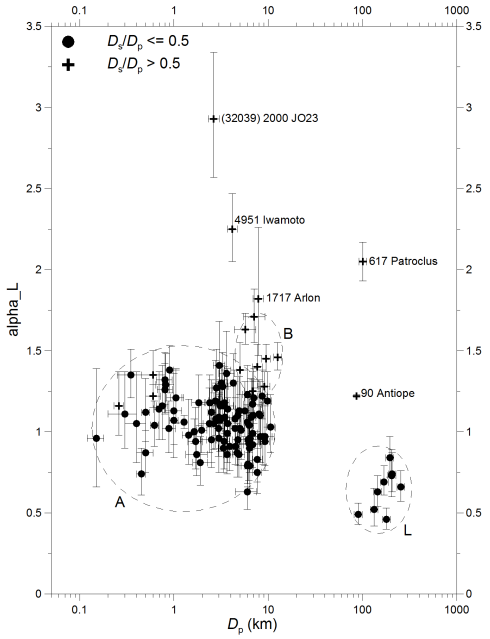

Fig. 3.— Estimated values of the normalized total angular momentum content of binaries versus primary diameter. The quantity α_L is the sum of orbital and spin angular momenta normalized by the angular momentum of an equivalent sphere spinning at the critical disruption spin rate $\omega_d = \sqrt{4\pi\rho G/3}$ where ρ is the density and G is the gravitational constant. In the Darwin notation, $\alpha_L = 1$ corresponds to $J/J' = 0.4$. Group A contains small NEA, MC, and MBA binaries. Group B consists of doubly synchronous small MBAs with nearly equal-size components. Group L represents large MBAs with small satellites (Section 2.5). Two exceptional cases are the doubly synchronous asteroids (90) Antiope and (617) Patroclus (Section 2.5). Figure updated from Pravec and Harris (2007).

are the semi-wide systems (32039) 2000 JO_{23} and (4951) Iwamoto, and possibly also (1717) Arlon, with orbital periods of 117 h to 360 h and supercritical total angular momentum content.

The orbital poles of main belt binaries were found to have a highly anisotropic distribution, concentrating within 30 degrees of the poles of the ecliptic (Pravec et al. 2012). The preferential orientations of the orbital poles suggest that their parent bodies or the primaries were tilted by the YORP effect towards the asymptotic spin states near obliquities 0 and 180 degrees, consistent with observations of single asteroids (Hanuš et al. 2011).

Another significant finding is that there appears to be a lower limit on the separation between components of binary systems of about $a/D_p = 1.5$, corresponding to an orbital period of 11–12 h for typical densities. Lightcurve observations indicate that the orbital period of Didymos is $P_{\rm orb} = 11.91 \pm 0.02$ h (Pravec et al. 2006), consistent with the radar estimate. This suggests an orbit close to the Roche limit for strengthless satellites (but see prior remark about orbits interior to the Roche limit).

Photometric observations of a binary system over multiple apparitions can be used to detect a change in the separation of the components due to the effect on mutual event timing. An extensive set of photometric observations of the synchronous binary (175706) 1996 FG_3 obtained during 1996-2013 places an upper limit on the drift of its semi-major axis that is one order of magnitude less than estimated on the basis of the BYORP theory (Scheirich et al. 2015). This system may be in an equilibrium between BYORP and tidal torques as proposed for synchronous binary asteroids by Jacobson and Scheeres (2011a).

Some data sets strongly suggest the presence of triple asteroids. In these cases, an additional rotational component that does not belong to the primary or the close eclipsing secondary is present in the lightcurve. This additional rotational component does not disappear during mutual events where the eclipsing close secondary is obscured by or in the shadow of the primary. Pravec et al. (2012) identified three such cases: (1830) Pogson, (2006) Polonskaya, and (2577) Litva. The latter has been confirmed by direct imaging observations of the third body (second satellite) on a wide orbit (Merline et al. 2013).

Other data sets reveal the existence of paired binaries/triples. Two such cases have been published: the pair composed of (3749) Balam and 2009 BR_{60} (Vokrouhlický 2009, and references therein) and the pair composed of (8306) Shoko

and 2011 SR_{158} (Pravec et al. 2013). Balam is a confirmed triple, with a distant satellite detected by direct imaging (Merline et al. 2002a) and a close satellite detected by lightcurve observations (Marchis et al. 2008d). Shoko is a suspected triple as well: Using lightcurve observations, Pravec et al. (2013) detected an eclipsing, synchronous close satellite with $P_{\rm orb} = 36.2$ h and a third rotational component attributed to an outer satellite.

While the population of binary NEAs and small MBAs is composed primarily of synchronous systems, and secondarily of asynchronous systems with low secondary-to-primary size ratios ($D_s/D_p < 0.5$), doubly synchronous binaries with nearly equal-size components also exist (Fig. 4). Nine such systems with $D_s/D_p > 0.7$ and orbital periods between 15 h and 118 h have been reliably identified in the main belt (e.g., Behrend et al. 2006; Kryszczyńska et al. 2009, see also the Pravec and Harris binary database described above).

Another important observation is that, with the exception of doubly synchronous systems, all binaries have unelongated, near-spheroidal primary shapes, as evidenced by their low primary amplitudes not exceeding 0.3 mag (when corrected to zero phase angle). This suggests that their primaries may have shapes similar to the top-like shapes that have been observed for 1999 KW_4 (Ostro et al. 2006) and several other binaries by radar.

All the properties revealed by photometric observations indicate that binary systems among NEAs and small MBAs were formed from critically spinning cohesionless parent bodies, with YORP as the predominant spin-up mechanism. This finding is consistent with the fact that the observed 0.2–13 km size range of binaries corresponds to the size range where the spin barrier against asteroid rotations faster than about 2.2 h has been observed (e.g., Pravec et al. 2007).

Although lightcurve observations provide powerful constraints on binaries, there are limitations. Detection of mutual events requires an edge-on geometry and observations at the time of the events, such that some binaries remain undetected (e.g., (69230) Hermes during its 2003 apparition). Small satellites also escape detection because their effect on the lightcurve is not measurable (e.g., satellites with $D_s/D_p \lesssim 0.17$ remain undetected if the minimum detectable relative brightness attenuation is ∼0.03 mag). The probability of mutual event detection is larger at smaller semi-major axes (expressed in units of primary radius) and at larger size ratios, resulting in observational biases (e.g., Pravec et al. 2012). Finally, lightcurve observations yield relative, not absolute, measurements of orbital separations. Detection of small or distant secondaries and direct measurement of orbital separation must instead rely on other observational techniques.

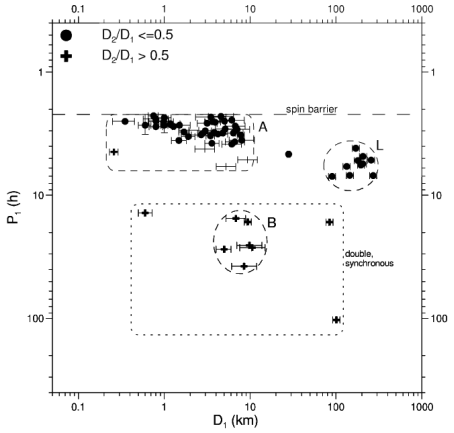

Fig. 4.— Primary rotation period versus primary diameter. Groups A, B, and L are defined in the caption of Fig. 3. Three doubly synchronous asteroids with nearly equal-size components lie isolated in the plot: (69230) Hermes on the left and (90) Antiope and (617) Patroclus on the right of group B. Note that members of group A cluster near the disruption spin limit for strengthless bodies. Figure from Pravec and Harris (2007).

2.3 Lightcurve Observations of Asteroid Pairs

Vokrouhlický and Nesvorný (2008) reported evidence for pairs of MBAs with bodies in each pair having nearly identical heliocentric orbits. Because chance associations can be ruled out,

the asteroids in each pair must be genetically related. Quantifying the difference in orbital parameters is accomplished with a metric d that corresponds roughly to the relative velocity between the bodies at close encounter. Vokrouhlický and Nesvorný (2008) identified 44 asteroid pairs (excluding family members) with a distance between the orbits of their components amounting to $d < 10$ m/s. They showed that, when integrated backwards in time, the orbits converge at a certain moment in the past with a physical distance much less than the radius of the Hill sphere and with a low relative velocity on the order of 1 m/s.

Pravec and Vokrouhlický (2009) developed a method to identify probable asteroid pairs by selecting candidate pairs with a similar distance criterion, then computing the probability that each candidate pair emerged as a result of a coincidence between two unrelated asteroids. They identified 72 probable asteroid pairs, reproducing most of the 44 previously known pairs. Most of the new candidates were later confirmed to be real pairs using backward integrations of their heliocentric orbits.

Vokrouhlický and Nesvorný (2008) proposed a few possible formation mechanisms for the asteroid pairs: collisional disruption, rotational fission, and splitting of unstable asteroid binaries. Pravec et al. (2010) conducted a survey of the rotational properties of asteroid pairs, and they found a strong correlation between the primary rotational periods and the secondary-to-primary mass ratio (Fig. 5). They showed that this correlation fits precisely with the predictions of a model by Scheeres (2007) in which a parent body with zero tensile strength undergoes rotational fission. The model predicts that primaries of low mass ratio pairs ($q \lesssim 0.05$) have not had their spin substantially slowed down in the separation process and should rotate rapidly with frequencies close to the fission spin rate. The observed periods are between 2.4 and 5 h. Primaries of medium mass ratio pairs ($q = 0.05$ to ~ 0.2) have had their spin slowed down according to the model because a substantial amount of angular momentum was taken away by the escaped secondary. This trend

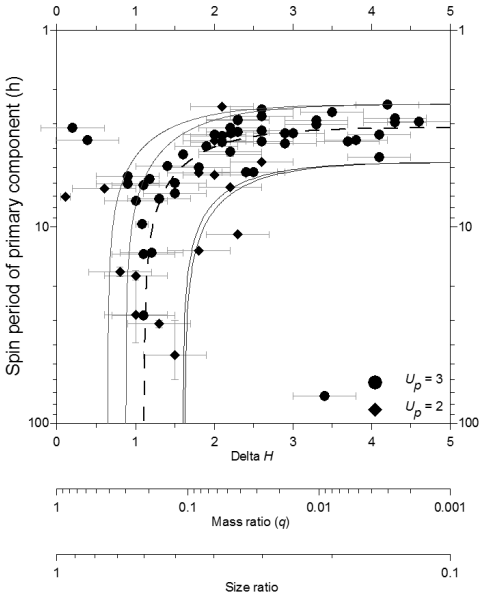

Fig. 5.— Primary rotation periods versus mass ratios of asteroid pairs. The mass ratio values were estimated from the differences between the absolute magnitudes of the pair components, ΔH. Circles are data points with quality code rating $U_p = 3$, meaning a precise period determination. Diamonds are data points with $U_p = 2$, which are somewhat less certain estimates. Error bars are one standard deviation. The data match the predictions (curves) of a model of rotational fission with a few adjustable parameters. In the model, $A_{\rm ini}$ is the binary system's initial orbit semi-major axis, α_L is the normalized total angular momentum of the system (Fig. 3), and a_p, b_p, c_p are the long, intermediate, and short axis of the dynamically equivalent equal mass ellipsoid of the primary. All models shown assume $b_p/c_p = 1.2$. The dashed curve shows the best-fit model with $\alpha_L = 1.0$, $a_p/b_p = 1.4$ and $A_{\rm ini}/b_p = 3$. Solid curves represent upper and lower limiting cases with $\alpha_L = 0.7-1.2$. Figure updated from Pravec et al. (2010).

is observed in the data (Fig. 5). Finally, high mass ratio pairs with $q > 0.2$ should not exist, as the free energy in the proto-binary system formed by rotational fission would be negative and the components would be unable to separate. Observations mostly corroborate this prediction: all 32

pairs in the sample of Pravec et al. (2010) were found to have a mass ratio $\lesssim 0.2$. However, an expanded photometric survey with 64 asteroid pairs observed between 2012 and the date of this writing reveals 3 pairs with high mass ratio ($q > 0.5$). Their formation requires an additional supply of angular momentum. Another important finding by Pravec et al. (2010) is that the primaries of asteroid pairs have lightcurve amplitudes that imply shapes with a broad range of elongations, i.e., unlike the primaries of binaries (Sections 2.1 and 2.2), the primaries of asteroid pairs do not tend to be nearly spheroidal.

2.4 Spectral Observations of Asteroid Pairs

Colorimetric and spectral observations of about 20 asteroid pairs indicate that members of an asteroid pair generally have similar spectra (Duddy et al. 2012; Moskovitz 2012; Duddy et al. 2013; Polishook et al. 2014a; Wolters et al. 2014). In some pairs, the authors observed subtle spectral differences between the components and attributed them to a larger amount of weathered material on the surface of the primary. In two pairs, they observed somewhat more significant spectral differences. For the pair (17198)–(229056), both Duddy et al. (2013) and Wolters et al. (2014) found that the primary is redder, i.e., it has a somewhat higher spectral slope than the secondary in the observed spectral range 0.5–0.9 μm. It is unclear why their spectra differ despite a strong dynamical link between the two asteroids. For the pair (19289)–(278067), Wolters et al. (2014) observed a spectral difference similar to that seen in (17198)–(229056), but Duddy et al. (2013) observed very similar spectra. Cross-validation of the methods or additional observations, perhaps rotationally resolved, are needed to resolve the discrepancy.

2.5 Direct Imaging of MBA and Trojan Systems

Direct imaging of asteroids can reveal the presence of satellites and, following the long tradition of orbit determination of binary stars and planetary satellites, lead to estimates of orbital parameters (Fig. 6). This observing mode remains challenging because the satellites are generally much smaller and fainter than their respective primaries and because most satellites known to date orbit at angular separations below 1 arcsecond. Satellite discoveries have therefore followed the development of adaptive optics (AO), and recent advances have enabled the detection of asteroid satellites that had remained undetected in prior searches.

Instruments must have sufficient contrast and resolving power to detect asteroid satellites with direct imaging. For a 50–100 km diameter asteroid in the main belt orbited by a satellite a few km across, the typical angular separation is generally less than an arcsecond with a contrast of 5 to 10 magnitudes (computed as 2.5 $\log(F_p/F_s)$, where F is the flux and p and s indicate primary and secondary, respectively).

In some situations, direct images can actually resolve the primary. A 50–100 km diameter asteroid at 2 au subtends 34–68 mas while the diffraction limit of a 10 m telescope at a typical imaging wavelength of 1.2 μm is about 30 mas. Although the diffraction limit is not reached, it can be approached with high-performance AO instruments in excellent conditions. With a sequence of disk-resolved images that provide sufficient orientational coverage, it is possible to estimate the 3D shape of the primary. This enables volume and density determinations.

Instruments capable of meeting the contrast and resolution requirements include the Hubble Space Telescope (HST) and large (10 m class) ground-based telescopes equipped with AO. Spacecraft encounters provide an opportunity to detect small satellites at small separations because of proximity to the target and the absence of the point spread function halo that affects ground-based AO instruments.

At the time *Asteroids III* was published, MBA satellite discoveries included one by spacecraft ((243) Ida), one by HST ((107) Camilla), and 6 by ground-based AO instruments. Since then, ground-based AO instruments have been responsible for almost all large MBA satellite discoveries: (121) Hermione (Merline et al. 2002b), (379) Huenna (Margot 2003), (130) Elektra

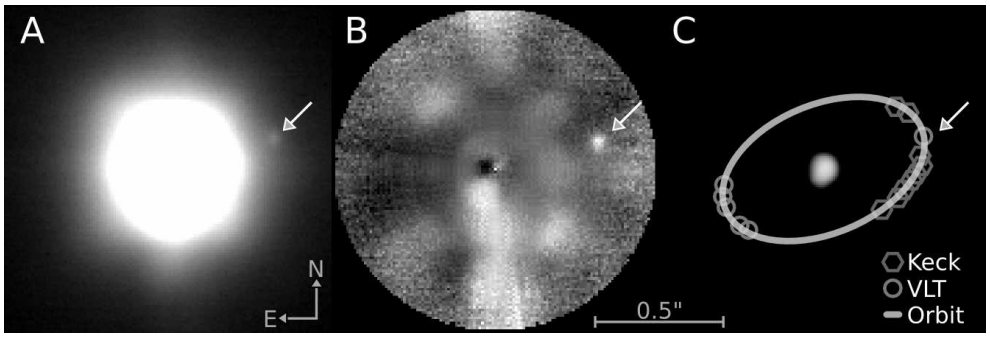

Fig. 6.— Satellite detection by direct imaging with adaptive optics (AO). (a) Image of asteroid (41) Daphne (Vmag=10) obtained with a ground-based AO-fed camera (NACO at ESO VLT, 5 s exposure). (b) Same image after subtraction of the flux from the primary, enabling more accurate measurements of the flux and position of the secondary. (c) Orbit determination. The relative positions of the satellite from VLT/NACO and Keck/NIRC2 images are indicated. Figure adapted from Carry (2009).

(Merline et al. 2003c), a second satellite to (87) Sylvia (Marchis et al. 2005b) and to (45) Eugenia (Marchis et al. 2007), (702) Alauda (Rojo and Margot 2007), (41) Daphne (Conrad et al. 2008), two satellites to (216) Kleopatra (Marchis et al. 2008b) and (93) Minerva (Marchis et al. 2009), and (317) Roxane (Merline et al. 2009). The wide binaries (1509) Esclangona (Merline et al. 2003a) and (4674) Pauling (Merline et al. 2004), which are small asteroids in our classification, have also been identified using AO-fed cameras. HST enabled detections of two additional wide binaries: (22899) 1999 TO_{14} (Merline et al. 2003b) and (17246) 2000 GL_{74} (Tamblyn et al. 2004), both of which are small MBAs. No satellites have been discovered around any of the 7 asteroids recently visited by spacecraft: (4) Vesta, (21) Lutetia, (2867) Šteins, (4179) Toutatis, (5535) Annefrank, (25143) Itokawa, and (132524) APL. The number of known large MBAs with satellites is now 16, which includes the only known large doubly synchronous system, (90) Antiope (Merline et al. 2000; Michałowski et al. 2004; Descamps et al. 2007, 2009). The fraction of large MBAs with satellites is difficult to estimate because of a complex dependence of satellite detectability on primary-to-secondary angular separation and primary-to-secondary flux ratio. However, because several independent programs have surveyed over 300 large MBAs, it is likely that the abundance of binaries in large MBAs is substantially smaller than the $\sim$16% abundance in NEAs and small MBAs.

Properties of large MBA binaries and triples are summarized in Figs. 7 and 8. With the exception of the nearly equal-mass binary (90) Antiope, the known satellites have secondary-to-primary mass ratios between 10^{-6} and 10^{-2}. All have orbital periods between 1 and 5.5 days, except (379) Huenna, whose orbit has a period of $\sim$88 days and an eccentricity of $\sim$0.2 (Marchis et al. 2008c). Many orbits have near-zero eccentricity (e.g., Marchis et al. 2008a), likely the result of tidal damping, but the inner satellites of triples generally have non-zero eccentricities. These eccentricities may have originated when orbits crossed mean motion resonances while tidally expanding (e.g., Fang et al. 2012).

At first glance, large MBA densities appear to cluster in two groups, between 1 and 2 g/cm^3 and above 3 g/cm^3. However, interpretations are limited by the possibility of systematic errors, including overestimates of volumes and underestimates of densities (Pravec and Harris 2007). Because volume uncertainties almost always dominate the error budget for binary asteroid densities (e.g., Merline et al. 2002c; Carry 2012), it is important to assess the realism of uncertainties

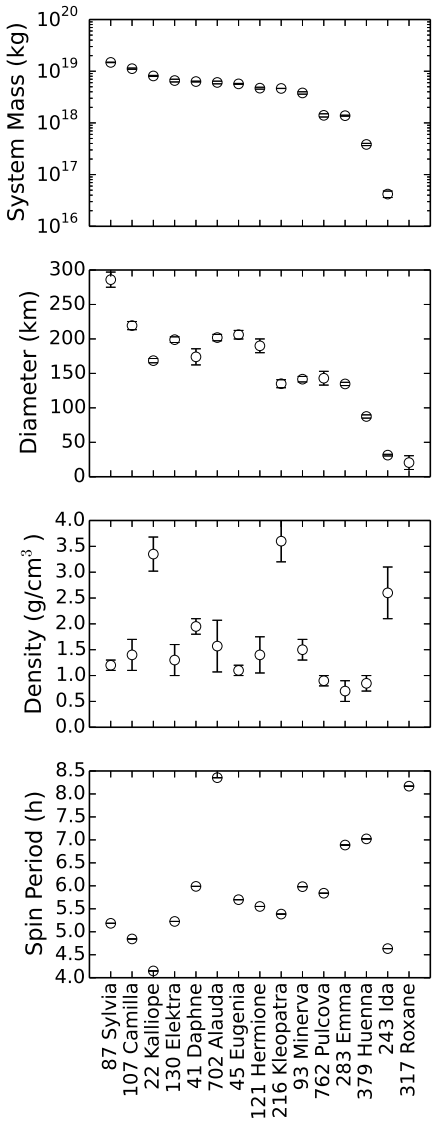

Fig. 7.— Properties of large MBA binaries and triples, excluding the doubly synchronous (90) Antiope. Error bars or upper limits, when available, are shown. Figures 7 and 8 are based on data compiled by Johnston (2014) from references therein.

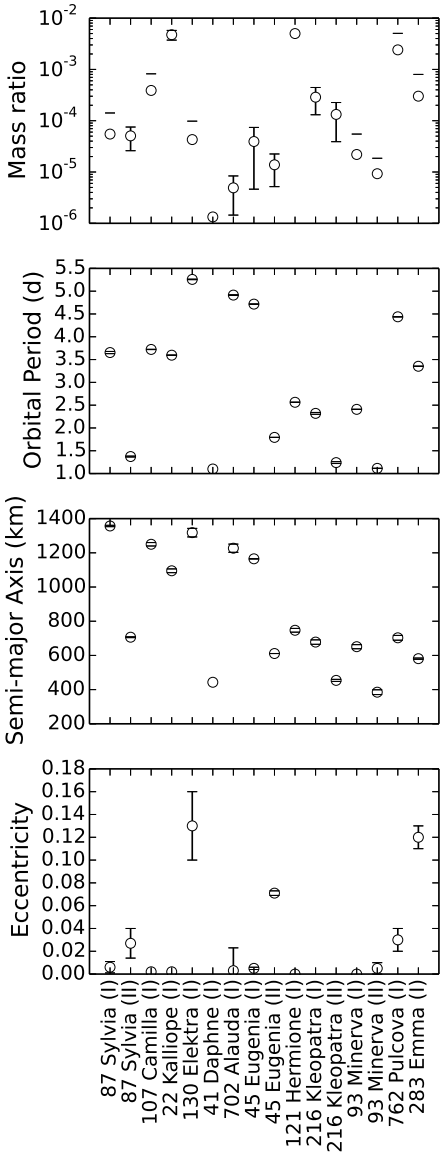

Fig. 8.— Properties of satellites of large MBAs, excluding outliers (90) Antiope and (379) Huenna (see text). Satellites of (243) Ida and (317) Roxane, whose orbits are not well known, are not shown.

associated with volume determinations. Some published density values should be regarded with caution because overconfidence in the fractional uncertainty of volume estimates has led to underestimates of bulk density uncertainties. The platinum standard of an orbiting spacecraft yields densities with $\sim$1% accuracy. The gold standard of radar observations where tens of images with hundreds or thousands of pixels per image are used to reconstruct a detailed 3D shape model yields volumes (and densities) with $\sim$10% accuracy. In contrast, AO images contain at most a few independent resolution cells of the target asteroid. Shape reconstructions based on AO images and/or lightcurve data may not routinely yield volume accuracies at the 10% level, although one analysis reached that level (Carry et al. 2012). In the absence of precise volume information, one might be tempted to infer bulk densities from the theory of fluid equilibrium shapes, but this approach is problematic (Holsapple 2007; Harris et al. 2009).

In the Jupiter trojan population, one satellite to (624) Hektor has been reported (Marchis et al. 2006b) since the discovery of the first trojan satellite to (617) Patroclus (Merline et al. 2001). These are the only trojans confirmed to have satellites in spite of several active search programs. The apparent low abundance of binary trojans is intriguing and, if confirmed, may provide additional support for the idea that Jupiter trojans originated in the trans-Neptunian region (Morbidelli et al. 2005; Levison et al. 2009) where they experienced a different collisional environment than in the main belt of asteroids. (624) Hektor has a satellite in a $\sim$3-day orbit that is eccentric ($\sim$0.3) and inclined ($\sim$50°) with respect to Hektor's equator (Marchis et al. 2014). (617) Patroclus is unusual because it has two components of similar size in a relatively tight ($\sim$680 km) orbit, with a normalized total angular momentum exceeding that available from fission of a single parent body (Marchis et al. 2006a).

In the trans-Neptunian region, 14 and 64 binary systems have been discovered with AO and HST, respectively (Johnston 2014). The apparent larger abundance of binary TNOs in the cold classical belt may be due to a different dynamical environment and formation mechanism (Section 5).

Objects in the trojan and TNO populations are generally too faint for AO observations in natural guide star (NGS) mode, in which the science target is also used to measure the properties of the wavefront and command the deformable mirror. These objects can be observed in appulse when their sky position happens to be within $\lesssim 1$ arcminute of a bright star. The advent of laser guide star (LGS) adaptive optics has been an important development that has freed the observer from finding such chance alignments and has opened up a larger fraction of the sky for observation of faint objects. Even with LGS, however, the availability of a tip-tilt star (Rmag $\lesssim 18$) within $\lesssim 1$ arcminute of the target is still required.

High-resolution and high-contrast imaging capabilities are aggressively sought by instrument builders, in part to enable direct imaging of exoplanets. Cameras equipped with high-performance AO are currently being installed or commissioned on large ground-based telescopes: HiCIAO on Subaru, GPI on Gemini, and SPHERE at the ESO VLT. These instruments will improve the ability to detect faint satellites orbiting close to their respective primaries. However, in most cases, asteroids fall in the faint-end range of these instrument capabilities. The next generation of large telescopes ($\sim$30 m diameter) such as the Thirty Meter Telescope (TMT) and European Extremely Large Telescope (E-ELT) will provide an improvement in sensitivity by a factor of $\sim$10 and in angular resolution by a factor of $\sim$3 compared to current 10 m telescopes. With the anticipated development of AO capabilities at shorter wavelengths, the second generation of instruments at these facilities is expected to provide improvements in angular resolution by a factor of $\sim$5. Such instruments may allow detection of the small MBA binaries that are currently beyond the reach of direct imaging instruments. In many of these systems, the components are separated by only a few mas and the size ratios are larger than in large MBA binaries, resulting in flux ratios closer to unity.

2.6 Spectral Observations of MBA and Trojan Systems

It is generally difficult to separate the light emitted or reflected from the secondary from that of the brighter primary. Nevertheless, such observations can be attempted when the secondary happens to be at a large angular separation from the primary, when the system is undergoing mutual events, or with the help of an integral field spectrograph.

Spectra of (22) Kalliope and its satellite Linus in the 1–2.4 μm region appear to be similar (Laver et al. 2009), which the authors attribute to satellite formation after a major impact on the precursor body. Observations of both components of (90) Antiope in the same spectral region also shows surface reflectances that are similar (Marchis et al. 2011). The spectrum of (379) Huenna is characteristic of C-type asteroids and the secondary does not exhibit a significantly different taxonomic type (DeMeo et al. 2011). Both components of (809) Lundia are consistent with a V-type classification (Birlan et al. 2014).

In the mid-infrared, Spitzer observations of the trojan (617) Patroclus, including during mutual events, provided size estimates for its components and a thermal inertia of 20 ± 15 J s$^{-1/2}$ K^{-1} m^{-2} (Mueller et al. 2010). Spitzer observations combined with photometric results in the visible yielded size and albedo estimates for (624) Hektor (Emery et al. 2006). Spitzer observations of these and other binaries did not resolve the binaries and results typically cannot be compared to observations that place many resolution elements on individual components. One exception is 2000 DP$_{107}$, where analysis of Spitzer data yields a system density of 0.9 ± 0.3 g/cm^3 (Marchis et al. 2012) and the radar results indicate 1.4 ± 0.2 g/cm^3 (Naidu et al. 2015).

2.7 Stellar Occultations of MBA and Trojan Systems

Stellar occultations provide a way of detecting components of a multiple-asteroid system, of placing bounds on component sizes, and of obtaining the relative positions of components on the plane of the sky. A recording of star light as a function of time shows a deep extinction when a target body crosses the line of sight between the observer and the star. This can be interpreted in terms of a *chord* on the apparent disk of the target body projected on the plane of the sky. If several observers are placed across the occultation path on the surface of the Earth, multiple chords can be obtained, and the size and shape of the target projected on the sky can be reconstructed (Fig. 9). When two or more components are present, it is also possible to measure their relative position. While the reliability of this technique was disputed a decade ago due to the lack of digital recordings, the availability of low-cost cameras and global positioning systems has enabled a dramatic improvement in the precision of timing reports. Stellar occultations have become an important observational tool for the study of binary asteroids.

Early reports (e.g., Binzel and van Flandern 1979) of asteroids suspected to be binaries on the basis of occultation data (including (3) Juno, (6) Hebe, (9) Metis, (12) Victoria, (18) Melpomene, (146) Lucina, and (532) Herculina) have remained largely unconfirmed despite extensive follow-up searches. However, it is likely that the outer satellite of (216) Kleopatra was detected during a 1980 occultation (Dunham 1981; Descamps et al. 2011). The detection of a satellite around the trojan (911) Agamemnon has been suggested (Timerson et al. 2013) but not yet confirmed. The occultation technique has also been used to detect rings around the centaur (10199) Chariklo (Braga-Ribas et al. 2014).

One strength of the stellar occultation technique lies in the fact that the observability of the event depends mainly on the brightness of the star and not of the asteroid or satellite. Stellar occultations can thus be used to detect small (km size) satellites, even those that are close to the primary and that would remain undetected in direct imaging.

Another strength of the technique is the potential for high-precision measurements. Stellar occultations are based on time-series photometry. Given a sufficiently high cadence (e.g., 10–30 im-

ages per second), it is possible to obtain a precision of a few mas on the relative position of binary components, which is 5 to 10 times better than with direct imaging with current instrumentation.

Finally, well-sampled stellar occultations allow for recovery of the size and apparent shape of asteroids and their satellites, whereas optical lightcurves and direct imaging observations provide primarily the diameter ratio of the components and more limited shape information. So far, four successful observations of satellite size and shape have been reported: Linus, satellite of (22) Kalliope (Descamps et al. 2008), Romulus, the outer satellite of (87) Sylvia (Berthier et al. 2014), and both components of the equal-size binaries (90) Antiope (Bartczak et al. 2014) and (617) Patroclus (Buie et al. 2014).

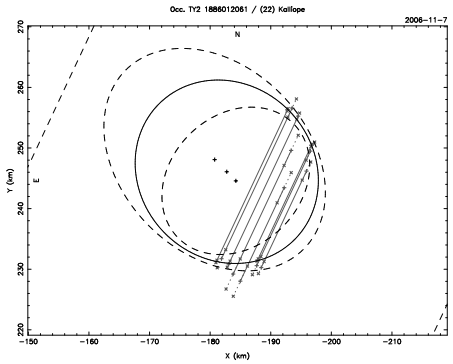

Fig. 9.— The apparent shape of Linus, a satellite of (22) Kalliope (Margot and Brown 2003), detected by stellar occultations. In this analysis, the profile of the satellite (solid curve) fitted to the observed chords (straight lines) yields an equivalent diameter of 30 $\pm$ 6 km. Dashed curves show the corresponding uncertainty of the fitted profile, and dashed lines show negative detections. Figure adapted from Descamps et al. (2008).

Despite all of these strengths, there remains a relatively low number of well-covered stellar occultation events. This is due, in part, to the requirement of successful observations at many stations. Owing to uncertainties on both the star and asteroid positions, the occultation path can shift by several tens or even hundreds of km on Earth compared to the prediction. Observers must therefore spread geographically to cover an event, but the detection of a satellite by several stations requires a fine grid of observers.

The situation is, however, expected to improve dramatically with the availability of the Gaia stellar catalog and better asteroid orbits (Tanga and Delbo 2007). Predictions of the occultation paths (for the center of mass) will be accurate to a few km, and the main source of uncertainty will become the prediction of the relative position of the satellite around the primary.

2.8 Other Observations

There have been several attempts to use ground-based interferometers to measure the angular separation of binary systems (Delbo et al. 2009; Carry et al. 2015). However, asteroid satellites are too faint for current interferometers operating in the visible and near-infrared and at the edge of detection in the mid-infrared. Future instrumentation may allow such observations. There are also prospects for observations with the ALMA sub-millimeter array (Busch 2009).

3. DYNAMICS

In parallel with advances in instrumentation and observing capabilities, the field has seen tremendous developments in understanding the dynamical processes that affect asteroid systems. This has been enabled in large part by the availability of detailed shape models and orbital parameters, by the need to model the dynamics of newly discovered triple systems, and by the desire to understand formation and evolution processes.

A non-exhaustive list of some dynamical problems that have been explored since *Asteroids III* includes the stability of asteroid satellite orbits (Scheeres 2002; Frouard and Compère 2012), the dynamics around triaxial bodies (Scheeres 2009a), the fate of asteroid ejecta (Scheeres 2007), the formation of contact binaries via dynamical evolution (Scheeres 2009a; Taylor and Margot 2011, 2014), the genesis of eccentric and mutually inclined orbits (Fang et al. 2011; Fang

and Margot 2012c), the orbital determination of triple systems using point-mass approximations (Marchis et al. 2010) and full N-body calculations (Fang et al. 2012), the influence of Kozai cycles on binaries (Perets and Naoz 2009; Fang and Margot 2012b), the effects of close planetary encounters on mutual orbits (Fang and Margot 2012a) and spin states (Takahashi et al. 2013), the complex spin-orbit interactions with irregular component shapes (Scheeres et al. 2006), including the libration and irregular rotation of secondaries (Naidu and Margot 2015), the influence of internal structure (Goldreich and Sari 2009), material properties (Taylor and Margot 2011) and nonspherical shapes (Taylor and Margot 2014) on tidal evolution, the possibility of tidal saltation (Harris et al. 2009; Fahnestock and Scheeres 2009), the possibility of significant radiative evolution (Ćuk and Burns 2005; Ćuk 2007; Ćuk and Nesvorný 2010; McMahon and Scheeres 2010a,b), and the possibility of a stable equilibrium between tidal and radiative evolution (Jacobson and Scheeres 2011a).

Several radar data sets provide exquisite constraints for dynamical studies. Reflex motion has been measured for 2000 DP_{107} (Margot et al. 2002; Naidu et al. 2015), 1999 KW_4 (Ostro et al. 2006), and 1991 VH (Naidu et al. 2012), allowing masses of individual components to be determined. Because detailed component shapes are also available, one can fully model the system dynamics and study spin-orbit coupling in detail (Scheeres et al. 2006; Fahnestock and Scheeres 2008; Naidu and Margot 2015). One finding from this work is that even moderately elongated secondaries on mildly eccentric orbits are likely to experience chaotic rotation that substantially affect binary evolution timescales (Fig. 10).

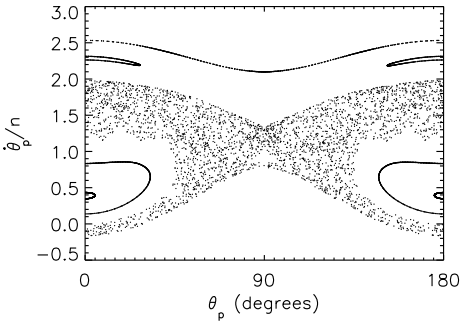

Fig. 10.— Surface of section plot showing the possible rotational regimes of the ∼200 m secondary of 1991 VH (secondary elongation $a/b = 1.5$ and mutual orbit eccentricity $e = 0.05$). The plot shows the angle between the long axis and the line of apsides of the mutual orbit, θ_p, against its time derivative, $\dot{\theta}_p$, normalized by the mean motion, n, at each pericenter passage. Five trajectories are illustrated (from top to bottom: non-resonant quasi-periodic, periodic, chaotic, periodic, periodic). While trapped in the sea of chaos, the secondary experiences torques on its permanent deformation that result in a highly variable spin rate, preventing BYORP-type evolution. Figure from Naidu and Margot (2015).

4. SMALL ASTEROIDS: SYNTHESIS

4.1. Rotational Fission Hypothesis

With the exception of the doubly synchronous binary asteroid systems, the primary asteroids of all small binary systems are rapidly rotating (within a factor of only a few of the critical disruption spin limit for bodies with no shear or tensile strength $\omega_d = \sqrt{4\pi\rho G/3}$). Furthermore, almost all known small binary asteroids have high angular momentum contents (Pravec and Harris 2007). These characteristics are not consistent with formation following a sub-catastrophic impact, capture through a three-body interaction in the near-Earth or main belt, or capture after a catastrophic impact. Instead, they are indicative of formation from a rotational fission event (e.g., Margot et al. 2002; Pravec and Harris 2007). The rotational fission hypothesis posits that a parent asteroid can be torqued to a rotation rate so great that the centrifugal accelerations overpower the gravitational accelerations holding a strengthless asteroid together (Weidenschilling 1980). It is possible that some small asteroids have cohesive or molecular strength in addition

to self-gravity (e.g., Rozitis et al. 2014). In these cases, the centrifugal accelerations must overcome these additional forces in order for the asteroid to fission (Pravec and Harris 2000; Sánchez and Scheeres 2014). At rapid rotation rates, loose surface material can flow from high-latitude regions to the equator along potential gradients (Ostro et al. 2006). It has been shown that rotational acceleration could trigger local slope failures and landslides, which can form the canonical top shape and equatorial bulge seen on primary components in small multiple-asteroid systems (Walsh et al. 2008; Harris et al. 2009).

Bottke et al. (2002) proposed a YORP-induced rotational fission hypothesis. It has since been shown that the YORP effect controls the rotational acceleration of small asteroids (Bottke et al. 2006; Marzari et al. 2011) and naturally explains the period distribution among small asteroids (Pravec et al. 2008; Rossi et al. 2009; Polishook and Brosch 2009). Furthermore, including the YORP-induced rotational fission hypothesis in size-frequency distribution models improves the agreement with observations (Jacobson et al. 2014a). The observed characteristics of the systems described in Sections 2.1-2.3 as well as thermal inertia observations (Delbo et al. 2011) are consistent with a binary formation mechanism that involves spin-up and mass shedding. The YORP-induced rotational fission hypothesis is the leading candidate for explaining the formation of binaries, triples, and pairs among small asteroids.

4.2. Asteroid Pairs

The YORP effect can increase the spin rate of asteroids beyond the critical disruption spin limit, thereby triggering rotational fission. In actuality, there is some uncertainty regarding the spin rate at which disruption occurs—there may be failure and deformation before fission (Walsh et al. 2008; Sánchez and Scheeres 2011; Cotto-Figueroa et al. 2013). The critical disruption spin limit also depends on the detailed shapes, masses, interlocking nature of the interior components and any cohesive forces (Scheeres 2007, 2009b; Sánchez and Scheeres 2014). Despite ignoring these details, simple calculations provide a rotational fission model that can be compared directly and successfully with observations.

If a spherical approximation of each component is made, then the rotational breakup spin rate ω_q necessary for fission as a function of the secondary-to-primary mass ratio q is (Scheeres 2007):

$$\omega_q = \omega_d \sqrt{\frac{1+q}{\left(1+q^{1/3}\right)^3}}. \quad (1)$$

This is the exact solution for two spheres resting on each other with a mass ratio of q and rotating about the axis of maximum moment of inertia.

The spherical component model described above demonstrates the important reality that the larger the mass ratio q of the two future binary members, the slower the required rotation rate necessary to create the binary system. This slower required rotation rate translates into a small initial free energy for the ensuing binary system. The free energy E_f is the energy that is accessible to the different energy reservoirs in the system, including the rotation states of each member and the orbit. It does not include the internal binding energy of each object. The free energy is an important quantity because it determines the boundedness of the system. Bound systems have negative free energy, while unbound systems have positive free energy. An unbound binary system implies that the system is capable of disruption but does not imply that the system will disrupt. For the idealized case of two spheres, the free energy can be expressed as (Scheeres 2007):

$$E_f = \frac{2\pi\rho\omega_d^2 R_p^5}{15} f(q), \quad (2)$$

where R_p is the radius of the primary and $f(q)$ is an algebraic, monotonically decreasing function for $0 < q \leq 1$. For the equation above corresponding to two spheres, the function crosses zero when $q \approx 0.204$. Similar equations can be written for any two component shapes, but $q \sim 0.2$ remains near the binding energy transition point, so the model uses this point as a simple approximation. This crossing point divides bound systems with negative energy and mass ratios $q > 0.2$ and unbound systems with positive energy and

mass ratios $q < 0.2$. Because of this fundamental difference, high mass ratio $q > 0.2$ and low mass ratio $q < 0.2$ binary systems evolve differently (Scheeres 2009a; Jacobson and Scheeres 2011b). Primarily, positive energy low mass ratio systems will chaotically explore orbital phase space until the majority find a disruption trajectory creating an asteroid pair; this evolutionary route is unavailable to high mass ratio systems.

The asteroid pair population provides a natural laboratory to test this relationship (Scheeres 2007; Vokrouhlický and Nesvorný 2008). Pravec et al. (2010) examined many asteroid pair systems and measured the rotation rate of the primary and the absolute magnitude difference between the pair members. These two quantities should follow a simple relationship related to ω_q, although many of the ignored details mentioned at the beginning of this section can move asteroids away from this relationship. Indeed, Pravec et al. (2010) discovered that asteroid pairs do follow this relationship (Fig. 5). Furthermore, they found that the large members of asteroid pairs have a broader range of elongations than the primaries of binary systems, consistent with the findings of Jacobson and Scheeres (2011b) that prolate primaries are less likely to remain in a bound binary system after rotational fission. Thus, there is strong evidence to support the hypothesis that asteroid pairs are the products of rotational fission.

Asteroid pairs continue to be a fertile observational landscape. Since dynamical integrations can derive the "birthdate" of such systems, observers can test ideas regarding space weathering timescales and YORP evolution after fission (Polishook et al. 2014a; Polishook 2014). Along with binary systems, the surfaces of asteroid pairs may provide clues in the future regarding the violence of the rotational fission process (Polishook et al. 2014b).

4.3. Binary and Triple Systems

Jacobson and Scheeres (2011b) showed that after rotational fission there are a number of possible outcomes. Their numerical studies produced the evolutionary flow chart shown in Fig. 11; many of these outcomes were also found by Fang and Margot (2012c). The high and low mass ratio distinction for rotational fission emphasized above plays an important role in distinguishing the two evolutionary pathways. Along the high mass ratio pathway, both binary members tidally synchronize and then evolve according to the BYORP effect.

Along the low mass ratio pathway, the binary system is unbound. Since these systems are chaotic, many are disrupted and become asteroid pairs. During this chaotic binary state, the secondary can often go through rotational fission itself, although this rotational fission is torqued by spin-orbit coupling (Fig. 10) rather than the YORP effect. Loss of material from the secondary stabilizes the remaining orbiting components. The lost mass may reaccrete onto the primary, perhaps contributing to the observed equatorial ridges, or may escape from the system. In these cases, the system undergoes another chaotic binary episode with three possible outcomes: a re-shaped asteroid, an asteroid pair, or a stable binary. These binaries still possess positive free energy such that they may disrupt if disturbed. In other cases, the system retains three components after secondary fission. While the numerical simulations of Jacobson and Scheeres (2011b) did not yield this latter outcome, it is possible that this pathway explains the existence of stable triple systems.

After stabilization of the low mass ratio binary system, the secondary synchronizes due to tides (e.g., Goldreich and Sari 2009), although some satellites may be trapped in a chaotic rotation state for durations that exceed the classic spin synchronization timescales (Naidu and Margot 2015). Then the system evolves according to the BYORP effect and tides. These binary evolutionary processes and their outcomes are discussed in Walsh & Jacobson (this volume). As shown in Fig. 11, these evolutionary paths include each of the binary morphologies identified in this chapter and by other teams (Pravec and Harris 2007; Fang and Margot 2012c). In particular, the formation of wide asynchronous binaries such as (1509) Esclangona, (4674) Pauling, (17246) 2000

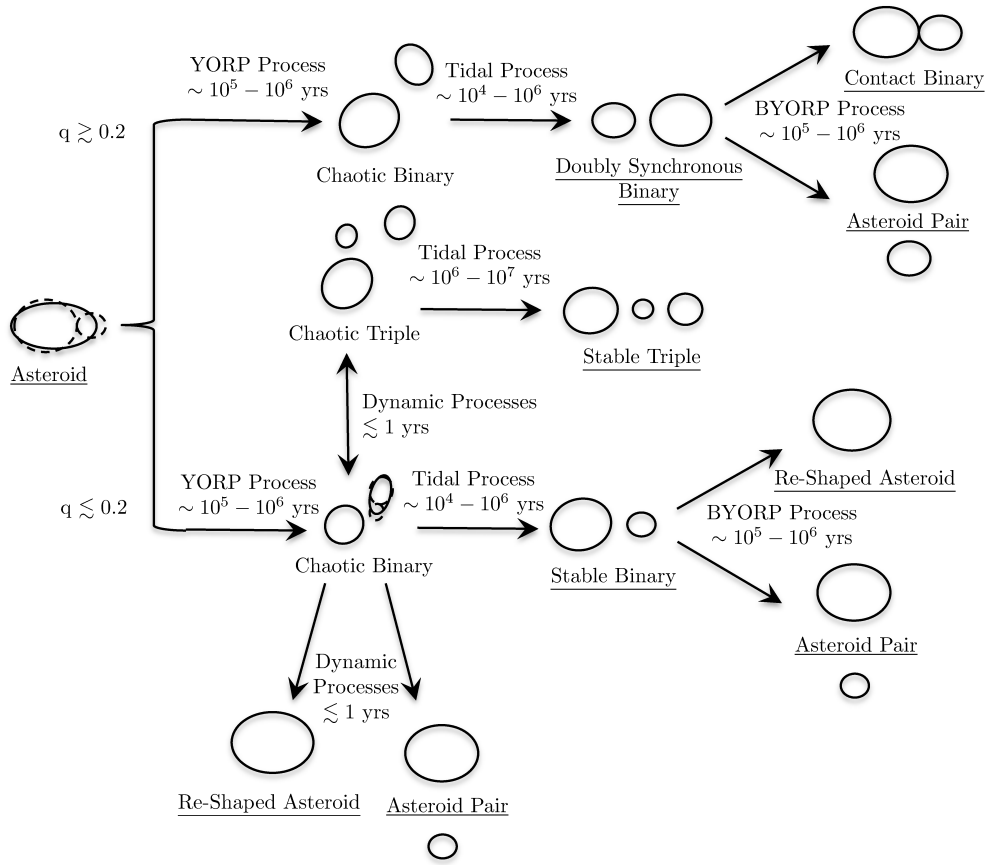

Fig. 11.— Flowchart showing the possible evolutionary paths for an asteroid after it undergoes rotational fission. Each arrow is labeled with the dominant process and an estimated timescale for this process. Underlined states are nominally stable for a YORP effect timescale. Figure from Jacobson and Scheeres (2011b).

GL_{74}, and (22899) 1999 TO_{14} is best explained by a rotational fission mechanism (Polishook et al. 2011) followed by BYORP orbital expansion (Jacobson et al. 2014b).

An alternative formation mechanism for triples such as (153591) 2001 SN_{263} and (136617) 1994 CC is that after creating a stable binary system, the primary undergoes rotational fission a second time. As long as the third component is on a distant enough orbit, then this process may result in a stable triple system (Fang et al. 2011; Fang and Margot 2012c; Jacobson et al. 2014b).

5. LARGE ASTEROIDS: SYNTHESIS

The primaries of most known binary and triple asteroids greater than 20 km have spin periods in the range of 4 h to 7 h (Fig. 7). While these spin rates are not near the disruption spin limit, they are typically faster than the mean spin rates for asteroids of similar sizes. The total angular momentum content, however, is well below that required for rotational fission. The secondary-to-primary mass ratios in these systems range from 10^{-6} to 10^{-2}. These properties are consistent with satel-

lite formation during large collisions (Fig. 12). Durda et al. (2004) have shown in numerical simulations that impacts of 10- to 30-km diameter projectiles striking at impact velocities between 3 kms^{-1} and 7 kms^{-1} can produce satellites that match observed properties. Multiple asteroid systems, e.g., (45) Eugenia (Merline et al. 1999; Marchis et al. 2007) and (87) Sylvia (Margot and Brown 2001; Marchis et al. 2005a) can also plausibly form through collisions.

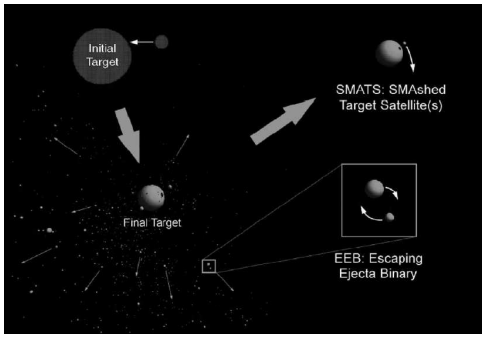

Fig. 12.— Numerical simulations show that binaries can form as a result of large impacts between asteroids. In some scenarios, impact debris can remain gravitationally bound to the target body, forming a satellite (SMATs). This process likely explains the formation of large MBA binaries. In other scenarios, two fragments from the escaping ejecta have sufficiently similar trajectories, such that they become bound to one another (EEBs). Figure from Durda et al. (2004).

There is more uncertainty related to the formation of (90) Antiope and (617) Patroclus, which are both too large to be substantially affected by YORP. Hypotheses for the formation of (90) Antiope include primordial fission due to excessive angular momentum (Pravec and Harris 2007), an improbable low-velocity collision of a large impactor (Weidenschilling et al. 2001), or shrinking of an initially wide binary formed by gravitational collapse (Nesvorný et al. 2010). Gravitational collapse in a gas-rich protoplanetary disk has been invoked to explain the formation of numerous binaries in the trans-Neptunian region. (617) Patroclus may be a primordial TNO that avoided disruption during emplacement in the trojan region (Nesvorný et al. 2010). Wide TNO binaries would not be expected to survive this process, whereas encounter calculations (e.g., Fang and Margot 2012a) show that tight binaries would.

6. CONCLUSIONS

Studies of binaries, triples, and pairs remain a fertile ground for observing processes that are important in planet formation and for measuring quantities that are difficult to obtain by other means. These include masses and densities as well as thermal, mechanical, and interior properties. Binaries or triples have been found in ∼50 NEAs, ∼50 small MBAs, ∼20 large MBAs, and 2 trojans. A unifying paradigm based on rotational fission and post-fission dynamics explains the formation of small binaries, triples, and pairs. Because the sun-powered rotational fission process is unrelenting, and because the production of pairs is a frequent outcome of this process, a substantial fraction of small bodies likely originated in a rotational disruption event. This origin affects the size distribution of asteroids and may explain the presence of single NEAs with equatorial bulges observed with radar. Small satellites of large MBAs are likely formed during large collisions. Advances in instrumentation, observational programs, and analysis techniques hold the promise of exciting findings in the next decade.

REFERENCES

P. Bartczak, T. Michałowski, T. Santana-Ros, and G. Dudziński. A new non-convex model of the binary asteroid 90 Antiope obtained with the SAGE modelling technique. *Mon. Not. R. Astron. Soc.*, 443:1802–1809, 2014.

T. M. Becker, E. S. Howell, M. C. Nolan, C. Magri, P. Pravec, P. A. Taylor, J. Oey, D. Higgins, J. Világi, L. Kornoš, A. Galád, Š. Gajdoš, N. M. Gaftonyuk, Y. N. Krugly, I. E. Molotov, M. D. Hicks, A. Carbognani, B. D. Warner, F. Vachier, F. Marchis, and J. T. Pollock. Physical modeling of triple near-Earth Asteroid (153591) 2001 SN_{263} from radar and optical

light curve observations. *Icarus*, 248:499–515, 2015.

R. Behrend, L. Bernasconi, R. Roy, A. Klotz, F. Colas, P. Antonini, R. Aoun, K. Augustesen, E. Barbotin, N. Berger, H. Berrouachdi, E. Brochard, A. Cazenave, C. Cavadore, J. Coloma, V. Cotrez, S. Deconihout, C. Demeautis, J. Dorseuil, G. Dubos, R. Durkee, E. Frappa, F. Hormuth, T. Itkonen, C. Jacques, L. Kurtze, A. Laffont, M. Lavayssière, J. Lecacheux, A. Leroy, F. Manzini, G. Masi, D. Matter, R. Michelsen, J. Nomen, A. Oksanen, P. Pääkkönen, A. Peyrot, E. Pimentel, D. Pray, C. Rinner, S. Sanchez, K. Sonnenberg, S. Sposetti, D. Starkey, R. Stoss, J.-P. Teng, M. Vignand, and N. Waelchli. Four new binary minor planets: (854) Frostia, (1089) Tama, (1313) Berna, (4492) Debussy. *Astron. Astrophys.*, 446:1177–1184, February 2006.

M. Belton, C. Chapman, P. Thomas, M. Davies, R. Greenberg, K. Klaasen, D. Byrnes, L. D'Amario, S. Synnott, W. Merline, J.-M. Petit, A. Storrs, and B. Zellner. The bulk density of asteroid 243 Ida from Dactyl's orbit. *Nature*, 374:785–788, 1995.

L. A. M. Benner, J. L. Margot, M. C. Nolan, J. D. Giorgini, M. Brozovic, D. J. Scheeres, C. Magri, and S. J. Ostro. Radar Imaging and a Physical Model of Binary Asteroid 65803 Didymos. In *Bull. Am. Astron. Soc.*, volume 42, 2010.

J. Berthier, F. Vachier, F. Marchis, J. Ďurech, and B. Carry. Physical and dynamical properties of the main belt triple Asteroid (87) Sylvia. *Icarus*, 239:118–130, 2014.

R. P. Binzel and T. C. van Flandern. Minor planets - The discovery of minor satellites. *Science*, 203:903–905, 1979.

M. Birlan, O. Vaduvescu, A. Tudorica, A. Sonka, A. Nedelcu, A. Galad, F. Colas, F. Pozo N., A. Barr D., R. Toma, I. Comsa, P. Rocher, V. Lainey, D. Vidican, D. Asher, C. Opriseanu, C. Vancea, J. P. Colque, C. P. Soto, R. Rekola, and E. Unda-Sanzana. More than 160 near Earth asteroids observed in the EURONEAR network. *Astron. Astrophys.*, 511:A40, 2010.

M. Birlan, D. A. Nedelcu, M. Popescu, P. Vernazza, F. Colas, and A. Kryszczyńska. Spectroscopy and surface properties of (809) Lundia. *Mon. Not. R. Astron. Soc.*, 437:176–184, 2014.

W. F. Bottke and H. J. Melosh. The formation of asteroid satellites and doublet craters by planetary tidal forces. *Nature*, 381:51–53, 1996a.

W. F. Bottke and H. J. Melosh. Binary asteroids and the formation of doublet craters. *Icarus*, 124:372–391, 1996b.

W. F. Bottke, D. Vokrouhlický, D. P. Rubincam, and M. Brož. The Effect of Yarkovsky Thermal Forces on the Dynamical Evolution of Asteroids and Meteorids. In W. F. Bottke, A. Cellino, P. Paolicchi, and R. P. Binzel, editors, *Asteroids III*, pages 395–408. Univ. of Arizona Press, 2002.

W. F. Bottke, David Vokrouhlický, David P Rubincam, and David Nesvorný. The Yarkovsky and Yorp Effects: Implications for Asteroid Dynamics. *Annual Review of Earth and Planetary Sciences*, 34:157–191, 2006.

F. Braga-Ribas, B. Sicardy, J. L. Ortiz, C. Snodgrass, F. Roques, R. Vieira-Martins, J. I. B. Camargo, M. Assafin, R. Duffard, E. Jehin, J. Pollock, R. Leiva, M. Emilio, D. I. Machado, C. Colazo, E. Lellouch, J. Skottfelt, M. Gillon, N. Ligier, L. Maquet, G. Benedetti-Rossi, A. R. Gomes, P. Kervella, H. Monteiro, R. Sfair, M. El Moutamid, G. Tancredi, J. Spagnotto, A. Maury, N. Morales, R. Gil-Hutton, S. Roland, A. Ceretta, S.-H. Gu, X.-B. Wang, K. Harpsøe, M. Rabus, J. Manfroid, C. Opitom, L. Vanzi, L. Mehret, L. Lorenzini, E. M. Schneiter, R. Melia, J. Lecacheux, F. Colas, F. Vachier, T. Widemann, L. Almenares, R. G. Sandness, F. Char, V. Perez, P. Lemos, N. Martinez, U. G. Jørgensen, M. Dominik, F. Roig, D. E. Reichart, A. P.

Lacluyze, J. B. Haislip, K. M. Ivarsen, J. P. Moore, N. R. Frank, and D. G. Lambas. A ring system detected around the Centaur (10199) Chariklo. *Nature*, 508:72–75, 2014.

H. E. Brooks. Orbits of Binary Near-Earth Asteroids from Radar Observations. In *Bull. Am. Astron. Soc.*, volume 38, 2006.

M. Brozović, L. A. M. Benner, P. A. Taylor, M. C. Nolan, E. S. Howell, C. Magri, D. J. Scheeres, J. D. Giorgini, J. T. Pollock, P. Pravec, A. Galád, J. Fang, J. L. Margot, M. W. Busch, M. K. Shepard, D. E. Reichart, K. M. Ivarsen, J. B. Haislip, A. P. Lacluyze, J. Jao, M. A. Slade, K. J. Lawrence, and M. D. Hicks. Radar and optical observations and physical modeling of triple near-Earth Asteroid (136617) 1994 CC. *Icarus*, 216:241–256, 2011.

M. W. Buie, C. B. Olkin, W. J. Merline, B. Timerson, D. Herald, W. M. Owen, H. B. Abramson, K. J. Abramson, D. C. Breit, D. B. Caton, S. J. Conard, M. A. Croom, R. W. Dunford, J. A. Dunford, D. W. Dunham, C. K. Ellington, Y. Liu, P. D. Maley, A. M. Olsen, R. Royer, A. E. Scheck, C. Sherrod, L. Sherrod, T. J. Swift, L. W. Taylor, and R. Venable. Shape and Size of Patroclus and Menoetius from a Stellar Occultation. In *Bull. Am. Astron. Soc.*, volume 46, 2014.

M. W. Busch. ALMA and asteroid science. *Icarus*, 200:347–349, 2009.

M. W. Busch, S. J. Ostro, L. A. M. Benner, M. Brozovic, J. D. Giorgini, J. S. Jao, D. J. Scheeres, C. Magri, M. C. Nolan, E. S. Howell, P. A. Taylor, J. L. Margot, and W. Brisken. Radar observations and the shape of near-Earth asteroid 2008 EV_5. *Icarus*, 212:649–660, 2011.

B. Carry. *Asteroids physical properties from high angular-resolution imaging*. PhD thesis, Observatoire de Paris, 2009.

B. Carry. Density of asteroids. *Planet. Space Sci.*, 73:98–118, 2012.

B. Carry, M. Kaasalainen, W. J. Merline, T. G. Müller, L. Jorda, J. D. Drummond, J. Berthier, L. O'Rourke, J. Ďurech, M. Küppers, A. Conrad, P. Tamblyn, C. Dumas, H. Sierks, and Osiris Team. Shape modeling technique KOALA validated by ESA Rosetta at (21) Lutetia. *Planet. Space Sci.*, 66:200–212, 2012.

B. Carry, A. Matter, P. Scheirich, P. Pravec, L. Molnar, S. Mottola, A. Carbognani, E. Jehin, A. Marciniak, R. P. Binzel, F. E. DeMeo, M. Birlan, M. Delbo, E. Barbotin, R. Behrend, M. Bonnardeau, F. Colas, P. Farissier, M. Fauvaud, S. Fauvaud, C. Gillier, M. Gillon, S. Hellmich, R. Hirsch, A. Leroy, J. Manfroid, J. Montier, E. Morelle, F. Richard, K. Sobkowiak, J. Strajnic, and F. Vachier. The small binary asteroid (939) Isberga. *Icarus*, 248:516–525, 2015.

A. Cellino, R. Pannunzio, V. Zappala, P. Farinella, and P. Paolicchi. Do we observe light curves of binary asteroids? *Astron. Astrophys.*, 144: 355–362, 1985.

C. R. Chapman, J. Veverka, P. C. Thomas, K. Klaasen, M. J. S. Belton, A. Harch, A. McEwen, T. V. Johnson, P. Helfenstein, M. E. Davies, W. J. Merline, and T. Denk. Discovery and Physical Properties of Dactyl a Satellite of Asteroid 243 Ida. *Nature*, 374: 783+, 1995.

S. R. Chesley, D. Farnocchia, M. C. Nolan, D. Vokrouhlický, P. W. Chodas, A. Milani, F. Spoto, B. Rozitis, L. A. M. Benner, W. F. Bottke, M. W. Busch, J. P. Emery, E. S. Howell, D. S. Lauretta, J. L. Margot, and P. A. Taylor. Orbit and bulk density of the OSIRIS-REx target Asteroid (101955) Bennu. *Icarus*, 235: 5–22, 2014.

A. R. Conrad, W. M. Keck Observatory, W. J. Merline, J. D. Drummond, P. M. Tamblyn, C. Dumas, B. X. Carry, R. D. Campbell, R. W. Goodrich, W. M. Owen, and C. R. Chapman. S/2008 (41) 1. *IAU Circ.*, 8930, 2008.

D. Cotto-Figueroa, T. S. Statler, D. C. Richardson, and P. Tanga. Killing the YORP Cycle: A Stochastic and Self-Limiting YORP Effect. In *Bull. Am. Astron. Soc.*, volume 45, 2013.

M. Ćuk. Formation and Destruction of Small Binary Asteroids. *Astrophys. J. Lett.*, 659:L57–L60, 2007.

M. Ćuk and J. A. Burns. Effects of thermal radiation on the dynamics of binary NEAs. *Icarus*, 176:418–431, 2005.

M. Ćuk and D. Nesvorný. Orbital evolution of small binary asteroids. *Icarus*, 207:732–743, 2010.

M. Delbo, S. Ligori, A. Matter, A. Cellino, and J. Berthier. First VLTI-MIDI Direct Determinations of Asteroid Sizes. *Astrophys. J.*, 694: 1228–1236, 2009.

M. Delbo, K. Walsh, M. Mueller, A. W. Harris, and E. S. Howell. The cool surfaces of binary near-Earth asteroids. *Icarus*, 212:138–148, 2011.

F. E. DeMeo, B. Carry, F. Marchis, M. Birlan, R. P. Binzel, S. J. Bus, P. Descamps, A. Nedelcu, M. Busch, and H. Bouy. A spectral comparison of (379) Huenna and its satellite. *Icarus*, 212:677–681, 2011.

P. Descamps, F. Marchis, T. Michalowski, F. Vachier, F. Colas, J. Berthier, M. Assafin, P. B. Dunckel, M. Polinska, W. Pych, D. Hestroffer, K. P. M. Miller, R. Vieira-Martins, M. Birlan, J.-P. Teng-Chuen-Yu, A. Peyrot, B. Payet, J. Dorseuil, Y. Léonie, and T. Dijoux. Figure of the double Asteroid 90 Antiope from adaptive optics and lightcurve observations. *Icarus*, 187:482–499, 2007.

P. Descamps, F. Marchis, J. Pollock, J. Berthier, F. Vachier, M. Birlan, M. Kaasalainen, A. W. Harris, M. H. Wong, W. J. Romanishin, E. M. Cooper, K. A. Kettner, P. Wiggins, A. Kryszczynska, M. Polinska, J.-F. Coliac, A. Devyatkin, I. Verestchagina, and D. Gorshanov. New determination of the size and bulk density of the binary Asteroid 22 Kalliope from observations of mutual eclipses. *Icarus*, 196:578–600, 2008.

P. Descamps, F. Marchis, T. Michalowski, J. Berthier, J. Pollock, P. Wiggins, M. Birlan, F. Colas, F. Vachier, S. Fauvaud, M. Fauvaud, J.-P. Sareyan, F. Pilcher, and D. A. Klinglesmith. A giant crater on 90 Antiope? *Icarus*, 203:102–111, 2009.

P. Descamps, F. Marchis, J. Berthier, J. P. Emery, G. Duchêne, I. de Pater, M. H. Wong, L. Lim, H. B. Hammel, F. Vachier, P. Wiggins, J.-P. Teng-Chuen-Yu, A. Peyrot, J. Pollock, M. Assafin, R. Vieira-Martins, J. I. B. Camargo, F. Braga-Ribas, and B. Macomber. Triplicity and physical characteristics of Asteroid (216) Kleopatra. *Icarus*, 211:1022–1033, 2011.

A. Doressoundiram, P. Paolicchi, A. Verlicchi, and A. Cellino. The formation of binary asteroids as outcomes of catastrophic collisions. *Planet. Space Sci.*, 45:757–770, 1997.

S R Duddy, Stephen C Lowry, S D Wolters, A Christou, Paul R Weissman, Simon F Green, and B. Rozitis. Physical and dynamical characterisation of the unbound asteroid pair 7343-154634. *Astron. Astrophys.*, 539:A36, 2012.

S. R. Duddy, S. C. Lowry, A. Christou, S. D. Wolters, B. Rozitis, S. F. Green, and P. R. Weissman. Spectroscopic observations of unbound asteroid pairs using the WHT. *Mon. Not. R. Astron. Soc.*, 429:63–74, 2013.

D. W. Dunham. Recently-observed planetary occultations. *Occultation Newsletter, International Occultation Timing Association (IOTA)*, 2:139–143, 1981.

D. D. Durda. The formation of asteroidal satellites in catastrophic collisions. *Icarus*, 120: 212–219, 1996.

D. D. Durda, W. F. Bottke, B. L. Enke, W. J. Merline, E. Asphaug, D. C. Richardson, and Z. M. Leinhardt. The formation of asteroid satellites

in large impacts: results from numerical simulations. *Icarus*, 170:243–257, 2004.

J. P. Emery, D. P. Cruikshank, and J. Van Cleve. Thermal emission spectroscopy (5.2 38 μm) of three Trojan asteroids with the Spitzer Space Telescope: Detection of fine-grained silicates. *Icarus*, 182:496–512, 2006.

E. G. Fahnestock and D. J. Scheeres. Simulation and analysis of the dynamics of binary near-Earth Asteroid (66391) 1999 KW4. *Icarus*, 194:410–435, 2008.

E. G. Fahnestock and D. J. Scheeres. Binary asteroid orbit expansion due to continued YORP spin-up of the primary and primary surface particle motion. *Icarus*, 201:135–152, 2009.

J. Fang and J. L. Margot. Binary Asteroid Encounters with Terrestrial Planets: Timescales and Effects. *Astron. J.*, 143:25, 2012a.

J. Fang and J. L. Margot. The Role of Kozai Cycles in Near-Earth Binary Asteroids. *Astron. J.*, 143:59, 2012b.

J. Fang and J. L. Margot. Near-Earth Binaries and Triples: Origin and Evolution of Spin-Orbital Properties. *Astron. J.*, 143:24, 2012c.

J. Fang, J. L. Margot, M. Brozovic, M. C. Nolan, L. A. M. Benner, and P. A. Taylor. Orbits of near-Earth asteroid triples 2001 SN_{263} and 1994 CC: Properties, origin, and evolution. *Astron. J.*, 141:154, 2011.

J. Fang, J. L. Margot, and P. Rojo. Orbits, Masses, and Evolution of Main Belt Triple (87) Sylvia. *Astron. J.*, 144:70, 2012.

J. Frouard and A. Compère. Instability zones for satellites of asteroids: The example of the (87) Sylvia system. *Icarus*, 220:149–161, 2012.

P. Goldreich and R. Sari. Tidal Evolution of Rubble Piles. *Astrophys. J.*, 691:54–60, 2009.

J. Hanuš, J. Ďurech, M. Brož, B. D. Warner, F. Pilcher, R. Stephens, J. Oey, L. Bernasconi, S. Casulli, R. Behrend, D. Polishook, T. Henych, M. Lehký, F. Yoshida, and T. Ito. A study of asteroid pole-latitude distribution based on an extended set of shape models derived by the lightcurve inversion method. *Astron. Astrophys.*, 530:A134, 2011.

A. W. Harris, E. G. Fahnestock, and P. Pravec. On the shapes and spins of rubble pile asteroids. *Icarus*, 199:310–318, 2009.

J. L. Hilton. Asteroids Masses and Densities. In W. F. Bottke, A. Cellino, P. Paolicchi, and R. P. Binzel, editors, *Asteroids III*, pages 103–112. Univ. of Arizona Press, 2002.

K. A. Holsapple. Spin limits of Solar System bodies: From the small fast-rotators to 2003 EL61. *Icarus*, 187(2):500–509, 2007.

R. S. Hudson. Three-Dimensional Reconstruction of Asteroids from Radar Observations. *Remote Sensing Reviews*, 8:195–203, 1993.

S. A. Jacobson and D. J. Scheeres. Long-term Stable Equilibria for Synchronous Binary Asteroids. *Astrophys. J. Lett.*, 736:L19, 2011a.

S. A. Jacobson and D. J. Scheeres. Dynamics of rotationally fissioned asteroids: Source of observed small asteroid systems. *Icarus*, 214(1): 161–178, 2011b.

S. A. Jacobson, F. Marzari, A. Rossi, D. J. Scheeres, and Donald R Davis. Effect of rotational disruption on the size-frequency distribution of the Main Belt asteroid population. *Mon. Not. R. Astron. Soc.*, page L15, 2014a.

S. A. Jacobson, D. J. Scheeres, and J. McMahon. Formation of the Wide Asynchronous Binary Asteroid Population. *Astrophys. J.*, 780:60, 2014b.

W. R. Johnston. Binary Minor Planets V7.0. *NASA Planetary Data System*, 219, 2014.

A. Kryszczyńska, F. Colas, P. Descamps, P. Bartczak, M. Polińska, T. Kwiatkowski, J. Lecacheux, R. Hirsch, M. Fagas,

K. Kamiński, T. Michałowski, and A. Marciniak. New binary asteroid 809 Lundia. I. Photometry and modelling. *Astron. Astrophys.*, 501:769–776, 2009.

C. Laver, I. de Pater, F. Marchis, M. Ádámkovics, and M. H. Wong. Component-resolved near-infrared spectra of the (22) Kalliope system. *Icarus*, 204:574–579, December 2009.

H. F. Levison, W. F. Bottke, M. Gounelle, A. Morbidelli, D. Nesvorný, and K. Tsiganis. Contamination of the asteroid belt by primordial trans-Neptunian objects. *Nature*, 460:364–366, 2009.

C. Magri, S. J. Ostro, D. J. Scheeres, M. C. Nolan, J. D. Giorgini, L. A. M. Benner, and J. L. Margot. Radar observations and a physical model of Asteroid 1580 Betulia. *Icarus*, 186:152–177, 2007.

F. Marchis, P. Descamps, D. Hestroffer, and J. Berthier. Discovery of the triple asteroidal system 87 Sylvia. *Nature*, 463:822–824, 2005a.

F. Marchis, P. Descamps, D. Hestroffer, J. Berthier, M. E. Brown, and J. L. Margot. Satellites of (87) Sylvia. *IAU Circ.*, 8582, 2005b.

F. Marchis, D. Hestroffer, P. Descamps, J. Berthier, A. H. Bouchez, R. D. Campbell, J. C. Y. Chin, M. A. van Dam, S. K. Hartman, E. M. Johansson, R. E. Lafon, D. Le Mignant, I. de Pater, P. J. Stomski, D. M. Summers, F. Vachier, P. L. Wizinovich, and M. H. Wong. A low density of 0.8 g cm^{-3} for the Trojan binary asteroid 617 Patroclus. *Nature*, 439:565–567, 2006a.

F. Marchis, M. H. Wong, J. Berthier, P. Descamps, D. Hestroffer, F. Vachier, D. Le Mignant, W. M. Keck Observatory, and I. de Pater. S/2006 (624) 1. *IAU Circ.*, 8732, 2006b.

F. Marchis, M. Baek, P. Descamps, J. Berthier, D. Hestroffer, and F. Vachier. S/2004 (45) 1. *IAU Circ.*, 8817, 2007.

F. Marchis, P. Descamps, M. Baek, A. W. Harris, M. Kaasalainen, J. Berthier, D. Hestroffer, and F. Vachier. Main belt binary asteroidal systems with circular mutual orbits. *Icarus*, 196:97–118, 2008a.

F. Marchis, P. Descamps, J. Berthier, and J. P. Emery. S/2008 (216) 1 and S/2008 (216) 2. *IAU Circ.*, 8980, 2008b.

F. Marchis, P. Descamps, J. Berthier, D. Hestroffer, F. Vachier, M. Baek, A. W. Harris, and D. Nesvorný. Main belt binary asteroidal systems with eccentric mutual orbits. *Icarus*, 195: 295–316, 2008c.

F. Marchis, J. Pollock, P. Pravec, M. Baek, J. Greene, L. Hutton, P. Descamps, D. E. Reichart, K. M. Ivarsen, J. A. Crain, M. C. Nysewander, A. P. Lacluyze, J. B. Haislip, and J. S. Harvey. (3749) Balam. *IAU Circ.*, 8928, 2008d.

F. Marchis, B. Macomber, J. Berthier, F. Vachier, and J. P. Emery. S/2009 (93) 1 and S/2009 (93) 2. *IAU Circ.*, 9069, 2009.

F. Marchis, V. Lainey, P. Descamps, J. Berthier, M. Van Dam, I. de Pater, B. Macomber, M. Baek, D. Le Mignant, H. B. Hammel, M. Showalter, and F. Vachier. A dynamical solution of the triple asteroid system (45) Eugenia. *Icarus*, 210:635–643, 2010.

F. Marchis, J. E. Enriquez, J. P. Emery, J. Berthier, P. Descamps, and F. Vachier. The origin of (90) Antiope from component-resolved near-infrared spectroscopy. *Icarus*, 213:252–264, 2011.

F. Marchis, J. E. Enriquez, J. P. Emery, M. Mueller, M. Baek, J. Pollock, M. Assafin, R. Vieira Martins, J. Berthier, F. Vachier, D. P. Cruikshank, L. F. Lim, D. E. Reichart, K. M. Ivarsen, J. B. Haislip, and A. P. LaCluyze. Multiple asteroid systems: Dimensions and

thermal properties from Spitzer Space Telescope and ground-based observations. *Icarus*, 221:1130–1161, 2012.

F. Marchis, J. Durech, J. Castillo-Rogez, F. Vachier, M. Cuk, J. Berthier, M. H. Wong, P. Kalas, G. Duchene, M. A. van Dam, H. Hamanowa, and M. Viikinkoski. The Puzzling Mutual Orbit of the Binary Trojan Asteroid (624) Hektor. *Astrophys. J. Lett.*, 783:L37, 2014.

J. L. Margot. S/2003 (379) 1. *IAU Circ.*, 8182, 2003.

J. L. Margot. Recent observations of binary and multiple systems. In *Second Workshop on Binaries in the Solar System*, Wasowo, Poland, 2010.

J. L. Margot and M. E. Brown. Discovery and characterization of binary asteroids 22 Kalliope and 87 Sylvia. In *Bull. Am. Astron. Soc.*, volume 33, 2001.

J. L. Margot and M. E. Brown. A low density M-type asteroid in the main belt. *Science*, 300 (5627):1939–1942, 2003.

J. L. Margot, M. C. Nolan, L. A. M. Benner, S. J. Ostro, R. F. Jurgens, J. D. Giorgini, M. A. Slade, and D. B. Campbell. Binary asteroids in the near-earth object population. *Science*, 296:1445–8, 2002.

J. L. Margot, P. Pravec, M. C. Nolan, E. S. Howell, L. A. M. Benner, J. D. Giorgini, R. F. Jurgens, S. J. Ostro, M. A. Slade, C. Magri, P. A. Taylor, P. D. Nicholson, and D. B. Campbell. Hermes as an exceptional case among binary near-earth asteroids. In *IAU General Assembly*, 2006.

F. Marzari, A. Rossi, and D. J. Scheeres. Combined effect of YORP and collisions on the rotation rate of small Main Belt asteroids. *Icarus*, 214(2):622–631, 2011.

J. McMahon and D. Scheeres. Secular orbit variation due to solar radiation effects: a detailed model for BYORP. *Cel. Mech. Dyn. Astr.*, 106: 261–300, 2010a.

J. McMahon and D. Scheeres. Detailed prediction for the BYORP effect on binary near-Earth Asteroid (66391) 1999 KW4 and implications for the binary population. *Icarus*, 209:494–509, 2010b.

W. J. Merline, L. M. Close, C. Dumas, C. R. Chapman, F. Roddier, F. Menard, D. C. Slater, G. Duvert, C. Shelton, and T. Morgan. Discovery of a moon orbiting the asteroid 45 Eugenia. *Nature*, 401:565+, 1999.

W. J. Merline, L. M. Close, J. C. Shelton, C. Dumas, F. Menard, C. R. Chapman, and D. C. Slater. Satellites of Minor Planets. *IAU Circ.*, 7503, 2000.

W. J. Merline, L. M. Close, N. Siegler, D. Potter, C. R. Chapman, C. Dumas, F. Menard, D. C. Slater, A. C. Baker, M. G. Edmunds, G. Mathlin, O. Guyon, and K. Roth. S/2001 (617) 1. *IAU Circ.*, 7741, 2001.

W. J. Merline, L. M. Close, N. Siegler, C. Dumas, C. Chapman, F. Rigaut, F. Menard, W. M. Owen, and D. C. Slater. S/2002 (3749) 1. *IAU Circ.*, 7827, 2002a.

W. J. Merline, P. M. Tamblyn, C. Dumas, L. M. Close, C. R. Chapman, F. Menard, W. M. Owen, D. C. Slater, and J. Pepin. S/2002 (121) 1. *IAU Circ.*, 7980, 2002b.

W. J. Merline, S. J. Weidenschilling, D. D. Durda, J. L. Margot, P. Pravec, and A.D. Storrs. Asteroids Do Have Satellites. In W. F. Bottke, A. Cellino, P. Paolicchi, and R. P. Binzel, editors, *Asteroids III*, pages 289–312. Univ. of Arizona Press, 2002c.

W. J. Merline, L. M. Close, P. M. Tamblyn, F. Menard, C. R. Chapman, C. Dumas, G. Duvert, W. M. Owen, D. C. Slater, and M. F. Sterzik. S/2003 (1509) 1. *IAU Circ.*, 8075, 2003a.

W. J. Merline, P. M. Tamblyn, C. R. Chapman, D. Nesvorny, D. D. Durda, C. Dumas, A. D. Storrs, L. M. Close, and F. Menard. S/2003 (22899) 1. *IAU Circ.*, 8232, 2003b.

W. J. Merline, P. M. Tamblyn, C. Dumas, L. M. Close, C. R. Chapman, and F. Menard. S/2003 (130) 1. *IAU Circ.*, 8183, 2003c.

W. J. Merline, P. M. Tamblyn, C. Dumas, F. Menard, L. M. Close, C. R. Chapman, G. Duvert, and N. Ageorges. S/2004 (4674) 1. *IAU Circ.*, 8297, 2004.

W. J. Merline, P. M. Tamblyn, J. D. Drummond, J. C. Christou, A. R. Conrad, W. M. Keck Observatory, B. Carry, C. R. Chapman, C. Dumas, D. D. Durda, W. M. Owen, and B. L. Enke. S/2009 (317) 1. *IAU Circ.*, 9099, 2009.

W. J. Merline, P. M. Tamblyn, B. D. Warner, P. Pravec, J. P. Tamblyn, C. Neyman, A. R. Conrad, W. M. Owen, B. Carry, J. D. Drummond, C. R. Chapman, B. L. Enke, W. M. Grundy, C. Veillet, S. B. Porter, C. Arcidiacono, J. C. Christou, D. D. Durda, A. W. Harris, H. A. Weaver, C. Dumas, D. Terrell, and P. Maley. S/2012 (2577) 1. *IAU Circ.*, 9267, 2013.

T. Michałowski, P. Bartczak, F. P. Velichko, A. Kryszczyńska, T. Kwiatkowski, S. Breiter, F. Colas, S. Fauvaud, A. Marciniak, J. Michałowski, R. Hirsch, R. Behrend, L. Bernasconi, C. Rinner, and S. Charbonnel. Eclipsing binary asteroid 90 Antiope. *Astron. Astrophys.*, 423:1159–1168, 2004.

A. Morbidelli, H. F. Levison, K. Tsiganis, and R. Gomes. Chaotic capture of Jupiter's Trojan asteroids in the early Solar System. *Nature*, 435:462–465, 2005.

N. A. Moskovitz. Colors of dynamically associated asteroid pairs. *Icarus*, 221(1):63–71, 2012.

M. Mueller, F. Marchis, J. P. Emery, A. W. Harris, S. Mottola, D. Hestroffer, J. Berthier, and M. di Martino. Eclipsing binary Trojan asteroid Patroclus: Thermal inertia from Spitzer observations. *Icarus*, 205:505–515, 2010.

S. P. Naidu and J. L. Margot. Near-Earth Asteroid Satellite Spins Under Spin-Orbit Coupling. *Astron. J.*, 149:80, 2015.

S. P. Naidu, J. L. Margot, M. W. Busch, P. A. Taylor, M. C. Nolan, E. S. Howell, J. D. Giorgini, L. A. M. Benner, M. Brozovic, and C. Magri. Dynamics of binary near-Earth asteroid system (35107) 1991 VH. In *Bull. Am. Astron. Soc.*, volume 43, 2012.

S. P. Naidu, J. L. Margot, P. A. Taylor, M. C. Nolan, M. W. Busch, L. A. M. Benner, M. Brozovic, J. D. Giorgini, J. S. Jao, and C. Magri. Radar Imaging and Characterization of the Binary Near-Earth Asteroid (185851) 2000 DP107. *Astron. J.*, 150:54, 2015.

D. Nesvorný, A. N. Youdin, and D. C. Richardson. Formation of Kuiper Belt Binaries by Gravitational Collapse. *Astron. J.*, 140:785–793, 2010.

M. C. Nolan, A. A. Hine, E. S. Howell, L. A. M. Benner, and J. D. Giorgini. 2003 SS_{84}. *IAU Circ.*, 8220, 2003.

M. C. Nolan, E. S. Howell, T. M. Becker, C. Magri, J. D. Giorgini, and J. L. Margot. Arecibo Radar Observations of 2001 SN263: A Near-Earth Triple Asteroid System. In *Bull. Am. Astron. Soc.*, volume 40, 2008.

M. C. Nolan, C. Magri, E. S. Howell, L. A. M. Benner, J. D. Giorgini, C. W. Hergenrother, R. S. Hudson, D. S. Lauretta, J. L. Margot, S. J. Ostro, and D. J. Scheeres. Shape model and surface properties of the OSIRIS-REx target Asteroid (101955) Bennu from radar and lightcurve observations. *Icarus*, 226:629–640, 2013.

K. S. Noll, W. M. Grundy, E. I. Chiang, J. L. Margot, and S. D. Kern. Binaries in the Kuiper Belt. In A. Barucci, M. Boehnhardt, D. Cruikshank, and A. Morbidelli, editors, *The Solar*

System Beyond Neptune, pages 345–363. Univ. of Arizona Press, 2008.

S. J. Ostro, J. L. Margot, L. A. M. Benner, J. D. Giorgini, D. J. Scheeres, E. G. Fahnestock, S. B. Broschart, J. Bellerose, M. C. Nolan, C. Magri, P. Pravec, P. Scheirich, R. Rose, R. F. Jurgens, E. M. De Jong, and S. Suzuki. Radar Imaging of Binary Near-Earth Asteroid (66391) 1999 KW4. *Science*, 314:1276–1280, 2006.

H. B. Perets and S. Naoz. Kozai Cycles, Tidal Friction, and the Dynamical Evolution of Binary Minor Planets. *Astrophys. J. Lett.*, 699: L17–L21, 2009.

D. Polishook. Spin axes and shape models of asteroid pairs: Fingerprints of YORP and a path to the density of rubble piles. *Icarus*, 241:79–96, 2014.

D. Polishook and N. Brosch. Photometry and spin rate distribution of small-sized main belt asteroids. *Icarus*, 199:319–332, 2009.

D. Polishook, N. Brosch, and D. Prialnik. Rotation periods of binary asteroids with large separations - Confronting the Escaping Ejecta Binaries model with observations. *Icarus*, 212: 167–174, 2011.

D. Polishook, N. Moskovitz, R. P. Binzel, F. E. DeMeo, D. Vokrouhlický, J. Žižka, and D. Oszkiewicz. Observations of "fresh" and weathered surfaces on asteroid pairs and their implications on the rotational-fission mechanism. *Icarus*, 233:9–26, 2014a.

D. Polishook, N. Moskovitz, F. E. DeMeo, and R. P. Binzel. Rotationally resolved spectroscopy of asteroid pairs: No spectral variation suggests fission is followed by settling of dust. *Icarus*, 243:222–235, 2014b.

P. Pravec and G. Hahn. Two-Period Lightcurve of 1994 AW_1: Indication of a Binary Asteroid? *Icarus*, 127:431–440, 1997.

P. Pravec and A. W. Harris. Fast and Slow Rotation of Asteroids. *Icarus*, 148:12–20, 2000.

P. Pravec and A. W. Harris. Binary asteroid population. 1. Angular momentum content. *Icarus*, 190:250–259, 2007.

P. Pravec and D. Vokrouhlický. Significance analysis of asteroid pairs. *Icarus*, 204:580–588, 2009.

P. Pravec, M. Wolf, and L. Šarounová. How many binaries are there among the near-Earth asteroids? In J. Svoren, E. M. Pittich, and H. Rickman, editors, *IAU Colloq. 173: Evolution and Source Regions of Asteroids and Comets*, page 159, 1999.

P. Pravec, P. Scheirich, P. Kušnirák, L. Šarounová, S. Mottola, G. Hahn, P. Brown, G. Esquerdo, N. Kaiser, Z. Krzeminski, D. P. Pray, B. D. Warner, A. W. Harris, M. C. Nolan, E. S. Howell, L. A. M. Benner, J. L. Margot, A. Galád, W. Holliday, M. D. Hicks, Y. N. Krugly, D. Tholen, R. Whiteley, F. Marchis, D. R. Degraff, A. Grauer, S. Larson, F. P. Velichko, W. R. Cooney, R. Stephens, J. Zhu, K. Kirsch, R. Dyvig, L. Snyder, V. Reddy, S. Moore, Š. Gajdoš, J. Világi, G. Masi, D. Higgins, G. Funkhouser, B. Knight, S. Slivan, R. Behrend, M. Grenon, G. Burki, R. Roy, C. Demeautis, D. Matter, N. Waelchli, Y. Revaz, A. Klotz, M. Rieugné, P. Thierry, V. Cotrez, L. Brunetto, and G. Kober. Photometric survey of binary near-Earth asteroids. *Icarus*, 181:63–93, 2006.

P. Pravec, A. W. Harris, and B. D. Warner. NEA rotations and binaries. In *IAU Symposium*, volume 236, pages 167–176, 2007.

P. Pravec, A. W. Harris, D. Vokrouhlický, B. D. Warner, P. Kušnirák, K. Hornoch, D. P. Pray, D. Higgins, J. Oey, A. Galád, Š. Gajdoš, L. Kornoš, J. Világi, M. Husárik, Y. N. Krugly, V. Shevchenko, V. Chiorny, N. Gaftonyuk, W. R. Cooney, J. Gross, D. Terrell, R. D. Stephens, R. Dyvig, V. Reddy, J. G. Ries, F. Colas, J. Lecacheux, R. Durkee, G. Masi,

R. A. Koff, and R. Goncalves. Spin rate distribution of small asteroids. *Icarus*, 197:497–504, 2008.

P. Pravec, D. Vokrouhlický, D. Polishook, D. J. Scheeres, A. W. Harris, A. Galád, O. Vaduvescu, F. Pozo, A. Barr, P. Longa, F. Vachier, F. Colas, D. P. Pray, J. Pollock, D. Reichart, K. Ivarsen, J. Haislip, A. Lacluyze, P. Kušnirák, T. Henych, F. Marchis, B. Macomber, S. A. Jacobson, Y. N. Krugly, A. V. Sergeev, and A. Leroy. Formation of asteroid pairs by rotational fission. *Nature*, 466:1085–1088, 2010.

P. Pravec, P. Scheirich, D. Vokrouhlický, A. W. Harris, P. Kušnirák, K. Hornoch, D. P. Pray, D. Higgins, A. Galád, J. Világi, Š. Gajdoš, L. Kornoš, J. Oey, M. Husárik, W. R. Cooney, J. Gross, D. Terrell, R. Durkee, J. Pollock, D. E. Reichart, K. Ivarsen, J. Haislip, A. LaCluyze, Y. N. Krugly, N. Gaftonyuk, R. D. Stephens, R. Dyvig, V. Reddy, V. Chiorny, O. Vaduvescu, P. Longa-Peña, A. Tudorica, B. D. Warner, G. Masi, J. Brinsfield, R. Gonçalves, P. Brown, Z. Krzeminski, O. Gerashchenko, V. Shevchenko, I. Molotov, and F. Marchis. Binary asteroid population. 2. Anisotropic distribution of orbit poles of small, inner main-belt binaries. *Icarus*, 218: 125–143, 2012.

P. Pravec, P. Kusnirak, K. Hornoch, A. Galad, Y. N. Krugly, V. Chiorny, R. Inasaridze, O. Kvaratskhelia, V. Ayvazian, O. Parmonov, J. Pollock, S. Mottola, J. Oey, D. Pray, J. Zizka, J. Vrastil, I. Molotov, D. E. Reichart, K. M. Ivarsen, J. B. Haislip, and A. LaCluyze. (8306) Shoko. *IAU Circ.*, 9268, 2013.

P. Rojo and J. L. Margot. S/2007 (702) 1. *CBET*, 1016, 2007.

A. Rossi, F. Marzari, and D. J. Scheeres. Computing the effects of YORP on the spin rate distribution of the NEO population. *Icarus*, 202(1): 95–103, 2009.

B. Rozitis, E. Maclennan, and J. P. Emery. Cohesive forces prevent the rotational breakup of rubble-pile asteroid (29075) 1950 DA. *Nature*, 512:174–176, 2014.

D. P. Rubincam. Radiative Spin-up and Spin-down of Small Asteroids. *Icarus*, 148(1):2–11, 2000.

D. P. Sánchez and D. J. Scheeres. Simulating Asteroid Rubble Piles with A Self-gravitating Soft-sphere Distinct Element Method Model. *Astrophys. J.*, 727(2):120, 2011.

D. P. Sánchez and D. J. Scheeres. The strength of regolith and rubble pile asteroids. *Meteoritics & Planetary Science*, 49(5):788–811, 2014.

D. J. Scheeres. Stability of Binary Asteroids. *Icarus*, 159:271–283, October 2002.

D. J. Scheeres. Rotational fission of contact binary asteroids. *Icarus*, 189:370–385, 2007.

D. J. Scheeres. Stability of the planar full 2-body problem. *Cel. Mech. Dyn. Astr.*, 104:103–128, 2009a.

D. J. Scheeres. Minimum energy asteroid reconfigurations and catastrophic disruptions. *Planetary and Space Science*, 57(2):154–164, 2009b.

D. J. Scheeres, E. G. Fahnestock, S. J. Ostro, J. L. Margot, L. A. M. Benner, S. B. Broschart, J. Bellerose, J. D. Giorgini, M. C. Nolan, C. Magri, P. Pravec, P. Scheirich, R. Rose, R. F. Jurgens, E. M. De Jong, and S. Suzuki. Dynamical Configuration of Binary Near-Earth Asteroid (66391) 1999 KW4. *Science*, 314:1280–1283, 2006.

P. Scheirich and P. Pravec. Modeling of lightcurves of binary asteroids. *Icarus*, 200: 531–547, 2009.

P. Scheirich, P. Pravec, S. A. Jacobson, J. Ďurech, P. Kušnirák, K. Hornoch, S. Mottola, M. Mommert, S. Hellmich, D. Pray, D. Polishook, Y. N. Krugly, R. Y. Inasaridze,

O. I. Kvaratskhelia, V. Ayvazian, I. Slyusarev, J. Pittichová, E. Jehin, J. Manfroid, M. Gillon, A. Galád, J. Pollock, J. Licandro, V. Alí-Lagoa, J. Brinsfield, and I. E. Molotov. The binary near-Earth Asteroid (175706) 1996 FG_3 - An observational constraint on its orbital evolution. *Icarus*, 245:56–63, 2015.

M. K. Shepard, J. L. Margot, C. Magri, M. C. Nolan, J. Schlieder, B. Estes, S. J. Bus, E. L. Volquardsen, A. S. Rivkin, L. A. M. Benner, J. D. Giorgini, S. J. Ostro, and M. W. Busch. Radar and infrared observations of binary near-Earth Asteroid 2002 CE26. *Icarus*, 184:198–210, 2006.

A. Springmann, P. A. Taylor, E. S. Howell, M. C. Nolan, L. A. M. Benner, M. Brozović, J. D. Giorgini, and J. L. Margot. Radar shape model of binary near-Earth asteroid (285263) 1998 QE_2. In *Lunar and Planetary Science Conference*, volume 45, 2014.

Y. Takahashi, M. W. Busch, and D. J. Scheeres. Spin State and Moment of Inertia Characterization of 4179 Toutatis. *Astron. J.*, 146:95, 2013.

P. M. Tamblyn, W. J. Merline, C. R. Chapman, D. Nesvorny, D. D. Durda, C. Dumas, A. D. Storrs, L. M. Close, and F. Menard. S/2004 (17246) 1. *IAU Circ.*, 8293, 2004.

P. Tanga and M. Delbo. Asteroid occultations today and tomorrow: toward the GAIA era. *Astron. Astrophys.*, 474:1015–1022, 2007.

P. A. Taylor and J. L. Margot. Tidal evolution of close binary asteroid systems. *Cel. Mech. Dyn. Astr.*, 108:315–338, 2010.

P. A. Taylor and J. L. Margot. Binary asteroid systems: Tidal end states and estimates of material properties. *Icarus*, 212:661–676, 2011.

P. A. Taylor and J. L. Margot. Tidal end states of binary asteroid systems with a nonspherical component. *Icarus*, 229:418–422, 2014.

P. A. Taylor, J. L. Margot, M. C. Nolan, L. A. M. Benner, S. J. Ostro, J. D. Giorgini, and C. Magri. The shape, mutual orbit, and tidal evolution of binary near-Earth asteroid 2004 DC. In *Asteroids, Comets, Meteors Conference*, volume 1405, page 8322, 2008.

P. A. Taylor, E. S. Howell, M. C. Nolan, and A. A. Thane. The shape and spin distributions of near-Earth asteroids observed with the Arecibo radar system. In *Bull. Am. Astron. Soc.*, volume 44, 2012a.

P. A. Taylor, M. C. Nolan, and E. S. Howell. 5143 Heracles. *CBET*, 3176, 2012b.

P. A. Taylor, M. C. Nolan, E. S. Howell, L. A. M. Benner, M. Brozovic, J. D. Giorgini, J. L. Margot, M. W. Busch, S. P. Naidu, C. Nugent, C. Magri, and M. K. Shepard. 2004 FG_{11}. *CBET*, 3091, 2012c.

P. A. Taylor, E. S. Howell, M. C. Nolan, A. Springmann, M. Brozovic, L. M. Benner, J. S. Jao, J. D. Giorgini, J. Margot, J. Fang, T. M. Becker, Y. R. Fernandez, R. J. Vervack, P. Pravec, P. Kusnirak, L. Franco, A. Ferrero, A. Galad, D. P. Pray, B. D. Warner, and M. D. Hicks. Physical characterization of binary near-Earth asteroid (153958) 2002 AM_{31}. In *Bull. Am. Astron. Soc.*, volume 45, 2013.

P. A. Taylor, B. D. Warner, C. Magri, A. Springmann, M. C. Nolan, E. S. Howell, K. J. Miller, L. F. Zambrano-Marin, J. E. Richardson, M. Hannan, and P. Pravec. The smallest binary asteroid? The discovery of equal-mass binary 1994 CJ_1. In *Bull. Am. Astron. Soc.*, volume 46, 2014.

E. F. Tedesco. Binary asteroids - Evidence for their existence from lightcurves. *Science*, 203: 905–907, 1979.

B. Timerson, J. Brooks, S. Conard, D. W. Dunham, D. Herald, A. Tolea, and F. Marchis. Occultation evidence for a satellite of the Trojan asteroid (911) Agamemnon. *Planetary and Space Science*, 87:78–84, 2013.

D. Vokrouhlický. (3749) Balam: A Very Young Multiple Asteroid System. *Astrophys. J. Lett.*, 706:L37–L40, 2009.

D. Vokrouhlický and D. Nesvorný. Pairs of Asteroids Probably of a Common Origin. *Astron. J.*, 136:280–290, 2008.

K. J. Walsh, D. C. Richardson, and P. Michel. Rotational breakup as the origin of small binary asteroids. *Nature*, 454:188–191, 2008.

S. J. Weidenschilling. Hektor - Nature and origin of a binary asteroid. *Icarus*, 44:807–809, 1980.

S. J. Weidenschilling, P. Paolicchi, and V. Zappalà. Do asteroids have satellites? In R. P. Binzel, T. Gehrels, and M. S. Matthews, editors, *Asteroids II*, pages 643–660. University of Arizona Press, 1989.

S. J. Weidenschilling, F. Marzari, D. R. Davis, and C. Neese. Origin of the Double Asteroid 90 Antiope: A Continuing Puzzle. In *Lunar and Planetary Science Conference*, volume 32, page 1890, 2001.

S. D. Wolters, P. R. Weissman, A. Christou, S. R. Duddy, and S. C. Lowry. Spectral similarity of unbound asteroid pairs. *Mon. Not. R. Astron. Soc.*, 439:3085–3093, 2014.

D. K. Yeomans, P. G. Antreasian, A. Cheng, D. W. Dunham, R. W. Farquhar, R. W. Gaskell, J. D. Giorgini, C. E. Helfrich, A. S. Konopliv, J. V. McAdams, J. K. Miller, W. M. Owen, Jr., P. C. Thomas, J. Veverka, and B. G. Williams. Estimating the mass of asteroid 433 Eros during NEAR spacecraft flyby. *Science*, 285:560–561, 1999.

This 2-column preprint was prepared with the AAS LaTeX macros v5.2.

Planetary and Space Science 73 (2012) 98–118

Contents lists available at SciVerse ScienceDirect

Planetary and Space Science

journal homepage: www.elsevier.com/locate/pss

Density of asteroids

B. Carry *

European Space Astronomy Centre, ESA, P.O. Box 78, 28691 Villanueva de la Cañada, Madrid, Spain

ARTICLE INFO

Article history:
Received 23 August 2011
Received in revised form
1 March 2012
Accepted 6 March 2012
Available online 3 April 2012

Keywords:
Minor planets
Mass
Volume
Density
Porosity

ABSTRACT

The small bodies of our solar system are the remnants of the early stages of planetary formation. A considerable amount of information regarding the processes that occurred during the accretion of the early planetesimals is still present among this population. A review of our current knowledge of the density of small bodies is presented here. Density is indeed a fundamental property for the understanding of their composition and internal structure. Intrinsic physical properties of small bodies are sought by searching for relationships between the dynamical and taxonomic classes, size, and density. Mass and volume estimates for 287 small bodies (asteroids, comets, and transneptunian objects) are collected from the literature. The accuracy and biases affecting the methods used to estimate these quantities are discussed and best-estimates are strictly selected. Bulk densities are subsequently computed and compared with meteorite density, allowing to estimate the macroporosity (*i.e.*, amount of voids) within these bodies. Dwarf-planets apparently have no macroporosity, while smaller bodies (<400 km) can have large voids. This trend is apparently correlated with size: C- and S-complex asteroids tend to have larger density with increasing diameter. The average density of each Bus-DeMeo taxonomic classes is computed (DeMeo et al., 2009; Icarus 202). S-complex asteroids are more dense on average than those in the C-complex that in turn have a larger macroporosity, although both complexes partly overlap. Within the C-complex asteroids, B-types stand out in albedo, reflectance spectra, and density, indicating a unique composition and structure. Asteroids in the X-complex span a wide range of densities, suggesting that many compositions are included in the complex. Comets and TNOs have high macroporosity and low density, supporting the current models of internal structures made of icy aggregates. Although the number of density estimates sky-rocketed during last decade from a handful to 287, only a third of the estimates are more precise than 20%. Several lines of investigation to refine this statistic are contemplated, including observations of multiple systems, 3-D shape modeling, and orbital analysis from Gaia astrometry.

1. Small bodies as remnants of planetesimals

The small bodies of our solar System are the left-overs of the building blocks that accreted to form the planets, some 4.6 Gyr ago. They represent the most direct witnesses of the conditions that reigned in the proto-planetary nebula (Bottke et al., 2002a). Indeed, terrestrial planets have thermally evolved and in some cases suffered erosion (*e.g.*, plate tectonic, volcanism) erasing evidence of their primitive composition. For most small bodies, however, their small diameter limited the amount of radiogenic nuclides in their interior, and thus the amount of energy for internal heating. The evolution of small bodies is therefore mainly exogenous, through eons of collisions, external heating, and bombardment by high energy particles.

A detailed study of the composition of small bodies can be achieved in the laboratory, by analyzing their terrestrial counterparts: meteorites. The distribution of elements, isotopes in meteorites, together with the level of heating and aqueous alteration they experienced tell us about the temperature, elemental abundance, and timescales during the accretion stages (*e.g.*, Halliday and Kleine, 2006). The connection of this information with specific locations in the Solar System constrains the formation scenarios of our Solar System. This requires the identification of links between the meteorites and the different populations of small bodies.

Indeed, if meteorites are samples from the Solar System, several questions are raised. Is this sampling complete? Is this sampling homogeneous? Some of the identified asteroid types (see Section 2) lack of a terrestrial analog. The most flagrant examples are the O-type asteroids (3628) Božněmcová and (7472) Kumakiri that appear unlike any measured meteorite assemblage (Burbine et al., 2011). Coupled mineralogical and dynamical studies have shown that meteorites come from specific locations.

* Tel.: +34 91 81 31 233.
E-mail address: benoit.carry@esa.int

0032-0633/$ - see front matter © 2012 Elsevier Ltd. All rights reserved.
http://dx.doi.org/10.1016/j.pss.2012.03.009

Other regions of the Solar System may therefore be unrepresented in our meteorite collection (see the discussions in, Burbine et al., 2002; Bottke et al., 2002b; Vernazza et al., 2008, for instance).

Additionally, the current orbits of small bodies may be different from the place they originally formed. For instance, it has been suggested that the giant planets migrated to their current orbits (the Nice model, see, Tsiganis et al., 2005), injecting material from the Kuiper Belt into the inner Solar System (Levison et al., 2009). Similarly, gravitational interaction among planetary embryos may have caused outward migration of planetesimals from Earth's vicinity into the main belt (Bottke et al., 2006). Current distribution of small bodies may therefore not reflect the original distribution of material in the Solar System. It however tells us about the dynamical processes that occurred over history. Analysis of the composition of meteorites in the laboratory, of small bodies from remote-sensing, and of their distribution in the Solar System are therefore pre-requisites to understanding the formation and evolution of our Solar System.

2. Linking small bodies with meteorites

Most of our knowledge on the mineralogy of asteroids has been derived by the analysis of their reflectance spectra in the visible and near-infrared (VNIR). The shape of these spectra has been used to classify the asteroids into broad groups, following several classification schemes called taxonomies. In what follows, I refer to the taxonomy by DeMeo et al. (2009), based on the largest wavelength range (0.4−2.4 μm). It encloses 15 classes grouped into three *complexes* (C, S, and X), with nine additional classes called *end-members* (see, DeMeo et al., 2009, for a detailed description of the classes). Mineralogical interpretations and links with meteorites have been proposed for several classes.

Asteroids belonging to the S-complex (S, Sa, Sq, Sr, and Sv) and to the Q class have been successfully linked to the most common meteorites, the ordinary chondrites (OCs). This link had been suggested for years based on the presence of two deep absorption bands in their spectra, around 1 and 2 μm, similar to that of OCs and characteristic of a mixture of olivines and pyroxenes (see for instance, Chapman, 1996; Brunetto et al., 2006, among many others). The analysis of the sample from the S-type asteroid Itokawa returned by the Hayabusa spacecraft confirmed this link (Yurimoto et al., 2011). The two end-member classes A and V have a mineralogy related to the S-complex. A-types are asteroids made of almost pure olivine, which possible analogs are the achondrite meteorites of the Brachinite and Pallasite groups (see, *e.g.*, Bell et al., 1989; de León et al., 2004). In opposition, V-types are made of pure pyroxenes and are related to the HED achondrite meteorites (*e.g.*, McCord et al., 1970). A- and V-types are believed to correspond to the mantle and the crust of differentiated parent bodies (Burbine et al., 1996).

The link between the hydrated carbonaceous chondrites (CCs) CI and CM and the asteroids in the C-complex seems well established (Cloutis et al., 2011a,b). The anhydrous CV/CO carbonaceous chondrites have also been linked with B-types (Clark et al., 2010). The scarcity and low contrast of absorption features in the VNIR prevent a detailed description of the mineralogy and association with meteorites of these asteroid types (B, C, Cb, Cg, Cgh, Ch). Spectroscopy in the 2.5−4 μm wavelength range, however, revealed the presence of hydration features (Lebofsky, 1978; Jones et al., 1990; Rivkin et al., 2002). These features were interpreted as evidences for aqueous alteration, similar to that experienced by CI/CM parent bodies (Cloutis et al., 2011a,b). Due to their similar composition to that of the solar photosphere, CI meteorites are often considered the most primitive material in the Solar System (see, Weisberg et al., 2006, for an overview of meteorite classes). This has made the compositional study of these so-called *primitive asteroids* a primary goal in planetary science.

The VNIR spectra of asteroids in the X-complex are devoid of strong absorption bands. However, several weak features (*e.g.*, around 0.9 μm) have been identified and used to discriminate subclasses (Clark et al., 2004; Ockert-Bell et al., 2010; Fornasier et al., 2011). Proposed meteorite analogs for X, Xc, Xe, and Xk asteroids virtually cover the entire meteorite collection: the anhydrous CV/CO carbonaceous chondrites (Barucci et al., 2005, 2012), enstatite chondrites and aubrites (Vernazza et al., 2009b, 2011b; Ockert-Bell et al., 2010), mesosiderites (Vernazza et al., 2009b), stony-iron (Ockert-Bell et al., 2010), and iron meteorites (Fornasier et al., 2011). The mineralogy represented in the X-complex is therefore probably more diverse than in the S- and C-complexes, due to the limits of the taxonomy based on spectral features only. It is worth noting that in former taxonomies (*e.g.*, Tholen and Barucci, 1989), the X-complex was divided into three main groups, E, M, and P, distinguished by albedo.

L-types have been suggested to be the most ancient asteroids that currently exist. From the comparison of their VNIR spectra with laboratory material, a fraction of 30 ± 10% of calcium- and aluminum-rich inclusions was proposed (Sunshine et al., 2008). This value is significantly higher than that of meteorites. This suggests a very early accretion together with a low degree of alteration while crossing the entire history of the Solar System. With a similar spectral shape, K-types have often be described as intermediates between S- and C-like material (DeMeo et al., 2009). Most of the K-type are associated with the Eos dynamical family in the outer Main Belt. They have been tentatively linked with the anhydrous CO, CV, and CK, and hydrated but metal-rich CR carbonaceous chondrites meteorites (Bell et al., 1989; Doressoundiram et al., 1998; Clark et al., 2009).

The mineralogy of the remaining end-members classes is more uncertain, owing to the apparent absence of strong spectral features (D and T) or to the mismatch of features with any known material (O and R). It has been suggested that T-types contain a high fraction of metallic contents, and may be related to the iron cores of differentiated asteroids, hence iron meteorites (Britt et al., 1992). D-types are among the reddest objects in the Solar System, not unlike that of comet nuclei and some transneptunian objects (Barucci et al., 2008). Their emission spectra in the mid-infrared indeed show striking similarities with that of comet nuclei (Emery et al., 2006, 2011). Both O and R classes were defined to describe the spectral shape of a single object, (3628) Božněmcová and (349) Dembowska respectively. Both types display broad absorption bands around 1 and 2 μm. These bands are however unlike those of S-types or any type of pyroxenes and olivines in our sample collection (Burbine et al., 2011).

Comets and transneptunian objects (TNOs) are volatile-rich bodies. These two populations are dynamically linked, the latter being one of the reservoir of periodic comets (Jewitt, 2004). Several compositional groups have been identified among TNOs: water ice dominated spectra, methane-rich spectra, and featureless spectra similar to that of comet nuclei (Barucci et al., 2008). There is no evidence for a meteorite sample from these dynamic classes, although the delivery from Kuiper Belt material to Earth should be possible (Gounelle et al., 2008).

As seen from this short summary, asteroid–meteorites connections and detailed mineralogy remain open questions in many cases: only about half of the 24 classes defining the taxonomy by DeMeo et al. (2009) have a mineralogical interpretation. Expanding the taxonomy toward longer wavelengths (2–5 and 5−40 μm range) will help in that respect (*e.g.*, Rivkin et al., 1995, 2002; Emery et al., 2006). Additional constraints must however be used to refine current mineralogy interpretations, especially for objects

with featureless spectra. Visible and radar albedos, thermal inertia, and density provide valuable constraints on the composition of these objects (*e.g.*, Fornasier et al., 2011). Among these, the most fundamental property to understand the composition and internal structure is perhaps the density (Britt et al., 2002; Consolmagno et al., 2008).

3. The density: a fundamental property

As described above, from the analysis of the surface properties such as reflectance spectra or albedo, it is possible to make inferences on composition. These observables however tell us about surface composition only, which may or may not be reflective of the bulk composition of the body (Elkins-Tanton et al., 2011). For instance, the surface of Earth, the *Blue Planet*, is covered by water while its overall composition is totally different. Earth's density is indeed indicative of a rocky composition with a core of denser material. Densities of small bodies are much more subtle, but still contain critical information.

From the compilation of the density of about 20 asteroids, Britt et al. (2002) already showed that differences are visible among that population. In a more recent review including 40 small bodies, Consolmagno et al. (2008) highlighted four trends in macroporosity (hereafter $\mathcal{P}$). The macroporosity reflects the amount of voids larger than the typical micrometer-sized cracks of meteorites. The largest asteroids (mass above 10^{20} kg) are apparently compact bodies without any macroporosity. This contrasts strongly with all the other less massive small bodies that have 20% or more macroporosity. The fraction of voids increases dramatically for icy bodies (comets and TNOs). Finally, *primitive* C-type asteroids tends to have larger macroporosity than the *basaltic* S-type.

Macroporosity, if present to a large extend, may have strong consequences on certain physical properties such as gravity field, thermal diffusivity, seismic velocity, and of course on collisional lifetimes (see the review by Britt et al., 2002). Macroporosity can also help in understanding the collisional history: intact bodies are expected to have low-to-no macroporosity, while heavily impacted objects may have large cracks, fractures (*i.e.*, moderate $\mathcal{P}$), or be gravitational re-accumulation of material (*i.e.*, rubble-piles, characterized by high values of $\mathcal{P}$).

4. Determination of density

Direct measurement of the *bulk* density (ρ) involves the independent measures of the mass (M) and volume (V): $\rho = M/V$. Indirect determination of the density are also possible by modeling the mutual eclipses of a binary system (*e.g.*, Behrend et al., 2006) or the non-gravitational forces on a comet nucleus (*e.g.*, Davidsson et al., 2007). This study aims at deriving constraints on the intrinsic physical properties of small bodies by searching for relationships between the dynamical and taxonomic classes, size, and density. An extensive compilation of the mass, volume, and resulting density estimates available in the literature is therefore presented here.

There are 994 published mass estimates for 267 small bodies (Section 4.1). For each object, the volume determinations are also compiled here, resulting in 1454 independent estimates (Section 4.2). Finally, the density of 24 small bodies has also been indirectly determined (Section 4.3). In total, 287 density estimates are available, for small bodies pertaining to all the dynamical classes: 17 near-Earth asteroids (NEAs), 230 Main-Belt (MBAs) and Trojan asteroids, 12 comets, and 28 transneptunian objects (TNOs). There is however a large spread among the independent estimates of the mass and volume estimates of these objects. Additionally, several estimates lead to obvious non-physical densities such as 0.05 or 20, the respective densities of Aerogel and Platinum. A rigorous selection of the different estimates is therefore needed. Some specifics of mass and diameter estimates are discussed below, together with selection criteria.

4.1. Mass estimates

The determination of the mass of a minor planet relies on the analysis of its gravitational effects on other objects (see the review by Hilton (2002), for instance). The 994 mass estimates for 267 small bodies listed in Appendix A can be divided into four categories, owing to the gravitational effects that were analyzed:

1. *Orbit deflection during close encounters*: The mass of small bodies is several order of magnitude lower than that of planets. Asteroids can nevertheless slightly influence the orbit of other smaller asteroids (*e.g.*, Michalak, 2000, 2001) and of Mars (*e.g.*, Pitjeva, 2001; Mouret et al., 2009) during *close* encounters. This method has been widely used, resulting in 547 mass estimates. An accuracy of few percent can be reached for the most massive asteroids such as (1) Ceres, (2) Pallas, or (4) Vesta (*e.g.*, Konopliv et al., 2006; Zielenbach, 2011). The accuracy however drops for smaller asteroids, and about a third have uncertainties cruder than 100% (see, for instance, Somenzi et al., 2010; Zielenbach, 2011, and Fig. 1a).
2. *Planetary ephemeris*: Numerical models have been developed to describe and predict the position of planets and minor planets around the Sun. In addition to the Sun and the planets, the gravitational influence of several asteroids must be taken into account to properly describe the observed position of planets, satellites, and spacecrafts (see, Baer and Chesley, 2008; Baer et al., 2011; Fienga et al., 2008, 2009, 2010; Folkner et al., 2009, for details). In that respect, this method is similar to the analysis of close encounters. There is however a strong philosophical difference between these two methods: analysis of close encounters consists of considering N times a 1-to-1 gravitational interaction, while planetary ephemeris are conceptually closer to an N-to-1 interaction. Similar to the results obtained from close encounters, the best accuracy is achieved for largest asteroids and becomes cruder for smaller

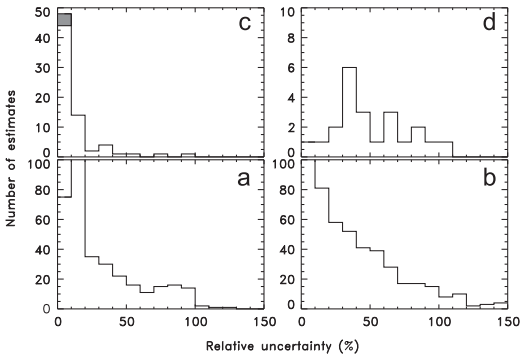

Fig. 1. Distribution of the relative accuracy of mass estimates obtained with four different methods (see text): (a) orbit deflection during close encounters, (b) planetary ephemeris, (c) orbit of natural satellites or spacecrafts (gray bar), and (d) indirect determination of density (Section 4.3) converted into mass.

objects. The mean accuracy is of 45%, but values are distributed up to 100% (Fig. 1b).

3. *Spacecraft tracking*: The Doppler shifts of the radio signals sent by spacecraft around an asteroid can be used to determine its orbit or the deflection of its trajectory during a flyby. These frequency shifts are imposed by the gravitational perturbation and are related to the mass of the asteroid (Yeomans et al., 1997, 2000; Fujiwara et al., 2006; Pätzold et al., 2011). It is by far the most precise technique with a typical accuracy of a couple of percent (Fig. 1c). It will however remain limited to a handful of small bodies (only four to date).
4. *Orbit of a satellite*: From optical or radar images of the components of the system, their mutual orbit can be determined and the mass derived with Kepler's third law (see, for instance, Petit et al., 1997; Merline et al., 1999, 2002; Margot et al., 2002, Marchis et al., 2005, 2008a,b, Brown et al., 2005, 2010; Carry et al., 2011; Fang et al., 2011). The 28 mass estimates available for TNOs were derived from optical imaging with the Hubble space telescope or large ground-based telescopes equipped with adaptive-optics cameras (*e.g.*, Grundy et al., 2009; Dumas et al., 2011). Similarly, the 17 mass estimates for NEAs were all derived from radar (*e.g.*, Ostro et al., 2006; Shepard et al., 2006), with the exception of Itokawa which was the target of the Hayabusa sample-return mission (Fujiwara et al., 2006). Additionally, the mass of 26 MBAs was determined by optical imaging. In total, 68 mass estimates have been derived by analyzing the orbit of a satellite. It is the second most-precise technique with a typical accuracy of about 10–15% (Fig. 1c). It is the most productive method of accurate mass determinations. With currently more than 200 known binaries, many mass estimates are still to come.

Based on these considerations and a close inspection of the different mass estimates available (*e.g.*, Fig. 2), the following criteria for selecting mass estimates were applied: Mass estimates derived from either the third or the fourth method (spacecraft or satellite) prevail upon the first two methods (deflection and ephemeris). Mass estimates leading to non-physical densities are discarded. Mass estimates that do not agree within uncertainties with the range drawn by the weighted average and standard deviation are discarded. The weighted average and standard deviation are subsequently recomputed. The 994 mass estimates are provided in Appendix A together with bibliographic references and notes on selection.

A summary of the precision achieved on mass estimates is presented in Fig. 3. The contribution provided here is illustrated by the difference between the cumulative distribution of relative precision before (dashed line) and after (solid line) the selection (about 20% of the estimates were discarded). For estimates with a relative uncertainty below 50%, the selection of estimates slightly improves the final accuracy, increasing the number of accurate estimates by 5–10%. The apparent *degradation* introduced by the selection for low-precision estimates is due to a rejection of about 10% of these estimates. In other words, these estimates lead to unrealistic densities and should not be considered. Furthermore, the distribution presented in Fig. 3 is based on the uncertainties reported by the different authors. The discrepancy between estimates however often reaches disconcerting levels. For instance, the estimates M_{28} (Krasinsky et al., 2001), M_{72} (Baer et al., 2008), M_{80} (Fienga et al., 2009), and M_{86} (Folkner et al., 2009) of the mass of (52) Europa fall within the range drawn by the weighted mean and deviation (Fig. 2). They nevertheless strongly disagree: the different values are between 4 and 11 σ one from each other.

Such differences are indicative of underestimated uncertainties. Accuracy is often reported as the formal standard deviation (σ), which in some cases may be small compared to systematics. The uncertainties on the mass determinations should therefore be considered as lower limits, to which some systematics could be added. As a result, the cumulative distribution of the relative precision presented in Fig. 3 is optimistic and gives an upper limit to the amount of accurate estimates. Therefore, even with mass estimates available for more than 250 small bodies, our knowledge is still very limited: Only about half of the estimates are more accurate than 20%, and no more than 70% of the estimates are more accurate than 50% (higher uncertainties preventing any firm conclusion).

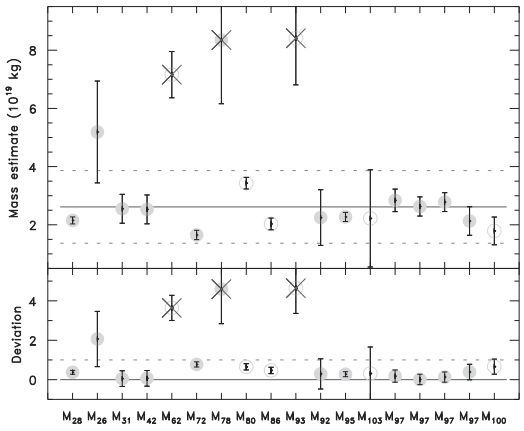

Fig. 2. The 18 mass estimates for (52) Europa (see Appendix D for the references). **Top:** The different mass estimates M_i, in 10^{19} kg. Symbols indicate the method used to determine the mass: deflections (gray disk) or planetary ephemeris (open circle). Crossed estimates were discarded from the analysis (see text). Horizontal solid and dashed lines are respectively the weighted average (μ) and standard deviation (σ) of the mass estimates before selection. **Bottom:** Same as above, but plotted as a function of the distance to the average value, in units of deviation: $(M_i-\mu)/\sigma$. Similar plots for each of the 140 small bodies with multiple mass estimates are provided in Appendix A.

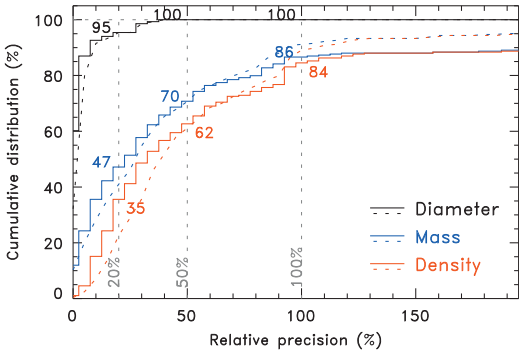

Fig. 3. Cumulative distribution of the accuracy on the diameter (black), mass (blue), and density (red) estimates. Dashed and solid lines represent the distributions before and after selection of best estimates (see text for details). Three reference levels for the relative accuracy are drawn: 20%, 50% and 100%, with the fraction of targets with a better accuracy reported for each estimate (after selection only). (For interpretation of the references to color in this figure caption, the reader is referred to the web version of this article.)

4.2. Volume estimates

As already noted by several authors, the most problematic part of determining the density of a small body is to measure any mass at all (*e.g.*, Merline et al., 2002; Consolmagno et al., 2008). The number of density estimates presented here is limited by the number of mass estimates, and not by the number of volume estimates (generally reported as volume-equivalent diameter, hereafter ϕ). Many different observing techniques and methods of analysis have been used to evaluate the diameter of small bodies (see the review by Carry et al., 2012). The 1454 diameter estimates listed in Appendix B were derived with 15 different methods, that can be grouped into four categories:

1. *Absolute magnitude*: It could almost be considered an *absence* of size estimate. It is the crudest method to evaluate the diameter of a small body (Fig. 4a). From the absolute magnitude H and an *assumed* geometric albedo p, the diameter is given by $\phi(\mathrm{km}) = 1329 p^{-0.5} 10^{-0.2H}$ (Pravec and Harris, 2007, and references therein). The diameter of 29 small bodies presented here were derived using their absolute magnitude, in the absence of any other estimates. This particularly applies to TNOs.
2. *Thermal modeling of mid-infrared radiometry*: It is by far the main provider of diameter estimates: 1233 diameter estimates out of the 1454 listed in Appendix B (*i.e.*, ≈85%). Asteroids are indeed among the brightest sources in the sky at mid-infrared wavelengths (5−20 μm), so infrared satellites (IRAS, ISO, AKARI, Spitzer, and WISE) have been able to acquire observations of a vast number of these objects (see, Tedesco et al., 2002; Ryan and Woodward, 2010; Usui et al., 2011; Masiero et al., 2011; Mueller et al., 2011). The diameter and albedo of the colder TNOs have also been studied at longer wavelengths with Spitzer and Herschel (*e.g.*, Stansberry et al., 2008; Müller et al., 2009). As visible in Fig. 4b, the typical uncertainty is of only few percent. In many case, however, the different estimates from thermal modeling disagree above their respective quoted uncertainty (see Table 3 in Delbo and Tanga (2009), illustrating the issue). For instance, in the case of Europa (Fig. 5), both diameter estimates ϕ_{64} (Ryan and Woodward, 2010) were based on the same data, but used two different thermal modeling, and disagree at more than 6σ. Such differences are again indicative of underestimated uncertainties. Accuracy is often reported as the formal standard deviation (σ), which in some cases may be small compared to systematics. In the present case, the simplified standard thermal model (Lebofsky et al., 1986) and near-Earth asteroid thermal model (Harris, 1998) widely used do not take into account the spin and shape of the small body into account, and can therefore be strongly biased. A more realistic level of accuracy is about 10% (Lim et al., 2010), at which these estimates are still highly valuable given the huge number of small bodies that have been studied that way.
3. *Direct measurements of a single geometry*: Stellar occultations or disk-resolved images can provide an extremely precise measure of the apparent size and shape of a small body (*e.g.*, Brown and Trujillo, 2004; Brown et al., 2006; Marchis et al., 2006, 2008a; Dunham et al., 2011). When these direct measurements are limited to a single geometry, however, the evaluation of the diameter may be biased. The volume is 3-D while a single geometry only provides 2-D constraints. The typical accuracy of 5% (Fig. 4c) may therefore be optimistic. Nevertheless, these estimates are highly valuable, being based on direct measurements.
4. *Shape modeling based on several geometries:* The least numerous but most precise diameter estimates are derived when the spin and 3-D shape of the objects are modeled, thus limiting the 2-D to 3-D related biases (Fig. 4d). Small bodies can be modeled as smooth tri-axial ellipsoids (*e.g.*, Thomas et al., 2005; Schmidt et al., 2009; Drummond et al., 2009, 2010), convex shapes (Descamps et al., 2007; Ďurech et al., 2011), or realistic 3-D shapes (Veverka et al., 2000; Ostro et al., 2006, 2010; Carry et al., 2010a, 2010b; Sierks et al., 2011). In particular, spacecraft encounters with (25 143) Itokawa and (21) Lutetia have shown that multi-data approaches provide

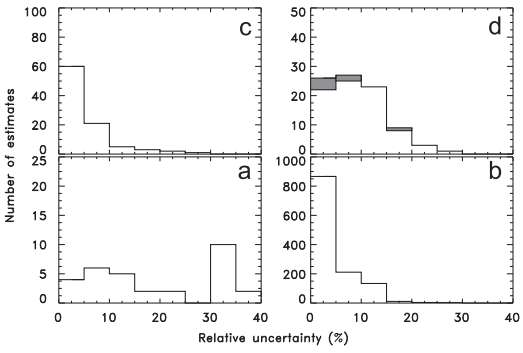

Fig. 4. Distribution of the relative accuracy of diameter estimates obtained with four classes of different methods (see text): (a) crude estimates from absolute magnitude, (b) thermal radiometry, (c) direct measurement limited to a single geometry, and (d) shape modeling based on several geometries (gray bars represent the diameters derived from spacecraft encounters). Although estimates in sub-plot (d) are expected to be the most precise, it is not reflected in their relative uncertainty distribution. The possible underestimation of biases in other techniques may be the cause (see text).

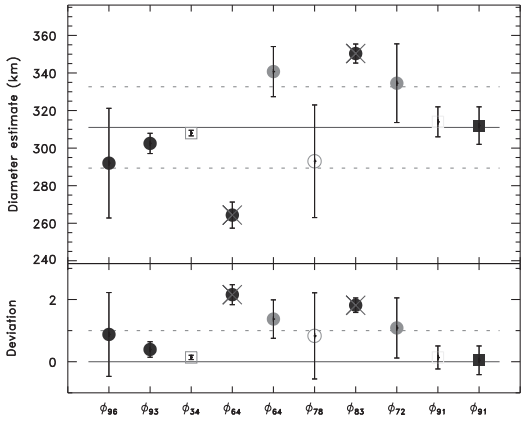

Fig. 5. The 10 diameter estimates for (52) Europa (see Appendix D for the references). **Top:** The different diameter estimates ϕ_i, in km. Symbols indicate the method used to determine the diameter: mid-infrared radiometry modeled using the Standard Thermal Model (STM: ϕ_{96}, ϕ_{93}, ϕ_{64}, and ϕ_{83}) and the near-Earth asteroid thermal model (NEATM: ϕ_{64} and ϕ_{72}), disk-resolved imaging on a single epoch (ϕ_{34}), combination of lightcurves and stellar occultations (ϕ_{78}), or shape modeling (ϕ_{91}). See Appendix B for a complete description of the symbols. Crossed estimates were discarded from the analysis (see text). Horizontal solid and dashed lines are respectively the weighted average (μ) and standard deviation (σ) of the diameter estimates before selection. **Bottom:** Same as above, but plotted as a function of the distance to the average value, in units of deviation: $(\phi_i - \mu)/\sigma$. Similar plots for each of the 258 small bodies with multiple diameter estimates are provided in Appendix B.

reliable and precise diameter estimates: *e.g.*, lightcurve-derived shape model with thermal radiometry (Mueller et al., 2006) or combined inversion of disk-resolved imaging and lightcurves (Kaasalainen, 2011; Carry et al., 2010b, 2012).

As visible in Figs. 3 and 4, the diameter estimates are generally intrinsically much more precise than the mass determination: all the estimates are known to better than 50% relative precision, and a large majority to better than 10%. Diameter estimates from different techniques moreover generally agree, suggesting that systematics are commensurable with formal uncertainties. The same selection criteria than for mass estimates were applied here, and about 15% of the estimates were discarded. Paradoxically, once the mass is determined, the uncertainty on the volume ($\delta V/V$) often becomes the major source of uncertainty on the density (ρ). Indeed,

$$\frac{\delta\rho}{\rho}=\sqrt{\left(\frac{\delta M}{M}\right)^2+\left(\frac{\delta V}{V}\right)^2}=\sqrt{\left(\frac{\delta M}{M}\right)^2+9\left(\frac{\delta\phi}{\phi}\right)^2} \quad (1)$$

The contribution of the uncertainty on the diameter ($\delta\phi/\phi$) therefore easily overwhelms that of the mass ($\delta M/M$) . In the compilation presented here, however, the mass is the limiting factor for 61% of the objects, contributing to $\approx$ 72% of the density uncertainty. This is mainly due to the high number of non-precise mass estimates (Fig. 3). If only the density estimates with a relative precision better than 20% are considered, then the situation is reversed: the diameter is the limiting factor for 75% of the objects, contributing to $\approx$68% of the density uncertainty. For these reasons, the mass should therefore be considered the limiting factor in most of the cases. As already discussed elsewhere, however, when a reliable mass estimate is available (*i.e.*, usually from the presence of a satellite), the precision on the volume generally limits the accuracy on the density (Merline et al., 2002; Britt et al., 2002; Consolmagno et al., 2008).

4.3. Indirect density estimates

For small bodies with diameters of a few to tens of kilometers the methods to estimate their mass listed above (Section 4.1) cannot be used. The gravitational influence of these very small bodies is too tiny to be measured. Even in the case of binary systems, their angular extent is generally too small to be imaged with current technology. The only exception are the small binary NEAs that can be imaged with radar during close approaches with Earth. Yet, a large fraction of the currently known binaries are small-sized systems discovered by studying their lightcurves (86 out of 207, *e.g.*, Mottola and Lahulla (2000); Pravec et al. (2002, 2006)). Indeed, photometric observations of the mutual eclipses of a system provide many constraints, for instance, on the ratio between the diameters of the two components or between the primary diameter and the orbit semi-major axis (see, Scheirich and Pravec, 2009).

Nevertheless, these parameters are dimensionless from lightcurve observations only. The *absolute* scale, hence semi-major axis and thus mass, cannot be derived. Usually, both components are *assumed* to have the same bulk density to bypass this restriction (*e.g.*, Scheirich and Pravec, 2009). These estimates are indirect, being derived without measuring the mass nor the size. The accuracy reached greatly depends on each system, and ranges from a few percent to 100% (Fig. 1d). It is worth noting that if small-sized binaries are formed by rotational breakup (Walsh et al., 2008) as suggested by the fast rotations of the primaries (Pravec et al., 2002, 2006, 2010), the porosity, hence density, of the components may be significantly different. These density estimates may therefore be biased, in the absence of an independent measure of the scale of the systems.

Measuring the mass of comets is another challenge. With diameters typically smaller than 10 km, comets have very small masses. In the absence of a satellite, studying their gravitational effect on other objects is hopeless. The activity of their nucleus however provides an indirect way to estimate their mass. Indeed, the forces resulting from the gas jets slowly change the orbit of the nucleus around the Sun. Modeling this non-gravitational effect provides the mass of the nucleus (*e.g.*, Davidsson and Gutiérrez, 2004, 2005, 2006; Davidsson et al., 2007; Sosa and Fernández, 2009). The masses of 11 comets have been derived using this approach. Richardson et al. (2007) have also studied the expansion of ejecta created by the Deep Impact experiment on the comet 9P/Tempel1. This is the most direct measurement of the mass of a comet, independent of the non-gravitational effect.

A summary of the mass, volume-equivalent diameter and bulk density of the 287 small bodies compiled here is provided in Table 1. The values listed are the weighted average and standard deviation of all the selected estimates (see Appendixes A–C). The density is given normalized to that of liquid water (1000 kg m^{-3}), *i.e.*, dimensionless. The estimates have been ranked from A to E, owing to the level of relative accuracy achieved on the density: B better than 20%, C between 20 and 50%, D between 50 and 100%, and E cruder than 100%. A stands for reliable estimates (more precise than 20%), based on more than five mass estimates and five diameter estimates, or a spacecraft encounter. Irrelevant densities are tagged with a cross (✗). Only about a third of the 287 density estimates have a relative precision better than 20% (Fig. 3), and two third better than 50%, above which level nothing relevant can be derived.

The fraction of volume occupied by voids, the macroporosity $\mathcal{P}$, is also reported, computed as:

$$\mathcal{P}(\%)=100\left(1-\frac{\rho}{\rho_m}\right) \quad (2)$$

with ρ the asteroid bulk density and ρ_m the bulk density of the associated meteorite (Table 2). The macroporosity is the least constrained of all the quantities discussed here. Indeed, it is affected by the uncertainties and possible biases on the diameter and mass estimates and also from the possible ambiguous links with meteorites (Section 2 and Table 3). Depending on the meteorite association, the macroporosity may change by 30–40%. For instance, while (16) Psyche was the most porous asteroid listed by Britt et al. (2002) and Consolmagno et al. (2008) with a macroporosity of about 70%, it stands in the low macroporosity range (about 18%). A low macroporosity is actually more consistent with the link between Psyche and iron meteorites than the very high value of $\sim$75% found previously.

5. Density and macroporosity of small bodies

The density and macroporosity of small bodies and their relationships with asteroid taxonomy, dynamical class, and diameter are discussed here.

For asteroids, the distribution of density estimates over taxonomic classes is presented in Fig. 6. The taxonomy is based on a limited sample (371 objects, see, DeMeo et al., 2009) and the relative part represented by each class in the whole population may be substantially different (Bus, 1999) but this discussion is beyond the scope of present analysis. Density estimates are available for the three complexes: 109 for C-complex, and 50 for both S- and X-complexes. End-members are less represented: only 15 density estimates are available, although end-members represent about 20% of the asteroids. For density estimates with

Table 1
Compilation of the average mass (M) and volume-equivalent diameter (ϕ) estimates (see Appendixes A–C), and resulting bulk density (ρ) and macroporosity ($\mathcal{P}$) for 287 objects, with their associated uncertainties. For each object, the dynamical class is listed (Dyn.), together with the taxonomic class (Tax., for asteroids only) and associated meteorite (Met.). The density estimates are ranked A–E, owing to the level of confidence at which they are determined (see text). Unrealistic density estimates are marked with a cross (✗) and uncertainties on the macroporosity larger than 100% are listed as ∞. **References**: (1) Clark et al. (2010), (2) Ockert-Bell et al. (2010), and (3) Fornasier et al. (2011). An electronic version of this table is available at https://genoide.imcce.fr/tools/public/densities.php.

Designation		Classification			Masses (kg)			Diameter (km)			Density		Porosity		Rank
#	Name	Dyn.	Tax.	Met.	M	δM	Fig.	ϕ	$\delta\phi$	Fig.	ρ	$\delta\rho$	$\mathcal{P}$	$\delta\mathcal{P}$	
1	Ceres	MBA	C	CM	9.44	$\pm 0.06\times10^{20}$	A.1	944.79	± 22.99	B.1	2.13	±0.15	4	± 1	A
2	Pallas	MBA	B	CK[1]	2.04	$\pm 0.04\times10^{20}$	A.2	514.41	± 19.12	B.2	2.86	±0.32	0	± 11	A
3	Juno	MBA	Sq	OC	2.73	$\pm 0.29\times10^{19}$	A.3	241.79	± 10.58	B.3	3.68	±0.62	0	± 16	A
4	Vesta	MBA	V	HED	2.63	$\pm 0.05\times10^{20}$	A.4	519.33	± 6.84	B.4	3.58	±0.15	0	± 4	A
5	Astraea	MBA	S	OC	2.64	$\pm 0.44\times10^{18}$	A.5	113.41	± 3.53	B.5	3.45	±0.66	0	± 19	B
6	Hebe	MBA	S	OC	1.39	$\pm 0.10\times10^{19}$	A.6	190.92	± 7.15	B.6	3.81	±0.50	0	± 13	A
7	Iris	MBA	S	OC	1.29	$\pm 0.21\times10^{19}$	A.7	225.89	± 25.94	B.7	2.14	±0.81	35	± 38	C
8	Flora	MBA	S	OC	9.17	$\pm 1.75\times10^{18}$	A.8	139.12	± 2.26	B.8	6.50	±1.28	0	± 19	✗
9	Metis	MBA	S	OC	8.39	$\pm 1.67\times10^{18}$	A.9	164.46	± 7.67	B.9	3.60	±0.87	0	± 24	C
10	Hygiea	MBA	C	CM	8.63	$\pm 0.52\times10^{19}$	A.10	421.60	± 25.69	B.10	2.19	±0.42	2	± 19	A
11	Parthenope	MBA	Sq	OC	5.91	$\pm 0.45\times10^{18}$	A.11	151.07	± 5.11	B.11	3.27	±0.41	1	± 12	A
12	Victoria	MBA	L	CO	2.45	$\pm 0.46\times10^{18}$	A.12	124.09	± 8.31	B.12	2.45	±0.67	19	± 27	C
13	Egeria	MBA	Ch	CM	8.82	$\pm 4.25\times10^{18}$	A.13	214.73	± 11.53	B.13	1.70	±0.86	24	± 50	D
14	Irene	MBA	S	OC	2.91	$\pm 1.88\times10^{18}$	A.14	147.75	± 5.03	B.14	1.72	±1.12	48	± 65	D
15	Eunomia	MBA	K	CV	3.14	$\pm 0.18\times10^{19}$	A.15	256.63	± 1.04	B.15	3.54	±0.20	0	± 5	B
16	Psyche	MBA	Xk	Ata[2]	2.72	$\pm 0.75\times10^{19}$	A.16	248.45	± 17.13	B.16	3.38	±1.16	15	± 34	C
17	Thetis	MBA	S	OC	1.33	$\pm 0.12\times10^{18}$	A.17	82.76	± 8.79	B.17	4.48	±1.48	0	± 33	C
18	Melpomene	MBA	S	OC	3.22	$\pm 1.28\times10^{18}$	A.18	141.72	± 4.86	B.18	2.15	±0.88	35	± 41	C
19	Fortuna	MBA	Ch	CM	8.60	$\pm 1.46\times10^{18}$	A.19	206.90	± 6.49	B.19	1.85	±0.35	17	± 19	A
20	Massalia	MBA	S	OC	5.00	$\pm 1.04\times10^{18}$	A.20	136.99	± 8.82	B.20	3.71	±1.05	0	± 28	C
21	Lutetia	MBA	Xk	EH[2]	1.70	$\pm 0.01\times10^{18}$	A.21	98.00	± 5.00	B.21	3.44	±0.52	0	± 15	A
22	Kalliope	MBA	X	Ata[2]	7.96	$\pm 0.31\times10^{18}$	A.22	170.23	± 10.46	B.22	3.08	±0.58	23	± 18	B
23	Thalia	MBA	S	OC	1.96	$\pm 0.09\times10^{18}$	A.23	106.81	± 3.23	B.23	3.07	±0.31	7	± 10	B
24	Themis	MBA	C	CM[1]	5.89	$\pm 1.91\times10^{18}$	A.24	183.84	± 11.40	B.24	1.81	±0.67	19	± 37	C
25	Phocaea	MBA	S	OC	5.99	$\pm 0.60\times10^{17}$	A.25	80.19	± 4.66	B.25	2.21	±0.44	33	± 20	C
26	Proserpina	MBA	S	OC	7.48	$\pm 8.95\times10^{17}$		89.63	± 3.55	B.26	1.98	±2.38	40	± ∞	E
27	Euterpe	MBA	S	OC	1.67	$\pm 1.01\times10^{18}$	A.26	105.80	± 7.23	B.27	2.69	±1.71	19	± 63	D
28	Bellona	MBA	S	OC	2.62	$\pm 0.15\times10^{18}$	A.27	108.10	± 11.49	B.28	3.95	±1.28	0	± 32	C
29	Amphitrite	MBA	S	OC	1.29	$\pm 0.20\times10^{19}$	A.28	217.59	± 10.71	B.29	2.38	±0.51	28	± 21	C
30	Urania	MBA	S	OC	1.74	$\pm 0.49\times10^{18}$	A.29	94.48	± 5.37	B.30	3.92	±1.29	0	± 32	C
31	Euphrosyne	MBA	C	CM	1.27	$\pm 0.65\times10^{19}$	A.30	272.92	± 8.85	B.31	1.18	±0.61	47	± 52	D
33	Polyhymnia	MBA	S	OC	6.20	$\pm 0.74\times10^{18}$		53.98	± 0.91		75.28	±9.71	0	± 12	✗
34	Circe	MBA	Ch	CM	3.66	$\pm 0.03\times10^{18}$	A.31	113.02	± 4.90	B.32	4.83	±0.63	0	± 13	✗
36	Atalante	MBA	C	CM	4.32	$\pm 3.80\times10^{18}$		110.14	± 4.38	B.33	6.17	±5.48	0	± 88	E
38	Leda	MBA	Cgh	CM	5.71	$\pm 5.47\times10^{18}$		115.41	± 1.33	B.34	7.09	±6.79	0	± 95	E
39	Laetitia	MBA	S	OC	4.72	$\pm 1.14\times10^{18}$	A.32	153.80	± 4.14	B.35	2.47	±0.63	25	± 25	C
41	Daphne	MBA	Ch	CM	6.31	$\pm 0.11\times10^{18}$	A.33	181.05	± 9.60	B.36	2.03	±0.32	9	± 16	B
42	Isis	MBA	S	OC	1.58	$\pm 0.52\times10^{18}$	A.34	102.73	± 2.73	B.37	2.78	±0.93	16	± 33	C
43	Ariadne	MBA	Sq	OC	1.21	$\pm 0.22\times10^{18}$	A.35	63.61	± 4.66	B.38	8.99	±2.57	0	± 28	✗
45	Eugenia	MBA	C	CM	5.79	$\pm 0.14\times10^{18}$	A.36	201.81	± 14.77	B.39	1.34	±0.29	40	± 22	C
46	Hestia	MBA	Xc	Mes	5.99	$\pm 0.49\times10^{18}$	A.37	125.29	± 5.21	B.40	5.81	±0.87	0	± 14	E
47	Aglaja	MBA	B	CV	3.25	$\pm 1.68\times10^{18}$	A.38	141.90	± 8.72	B.41	2.17	±1.19	22	± 55	D
48	Doris	MBA	Ch	CM	6.12	$\pm 2.96\times10^{18}$	A.39	211.67	± 10.85	B.42	1.23	±0.62	45	± 50	D
49	Pales	MBA	Ch	CM	4.22	$\pm 2.15\times10^{18}$	A.40	150.82	± 3.81	B.43	2.35	±1.21	0	± 51	D
50	Virginia	MBA	Ch	CM[3]	2.31	$\pm 0.70\times10^{18}$	A.41	99.42	± 0.46	B.44	4.49	±1.35	0	± 30	E
51	Nemausa	MBA	Ch	CM	2.48	$\pm 0.86\times10^{18}$	A.42	148.85	± 3.56	B.45	1.43	±0.50	36	± 35	C
52	Europa	MBA	C	CM	2.38	$\pm 0.58\times10^{19}$	A.43	310.21	± 10.34	B.46	1.52	±0.39	32	± 26	C
53	Kalypso	MBA	C	CM	5.63	$\pm 5.00\times10^{18}$		109.06	± 7.27	B.47	8.28	±7.54	0	± 91	✗
54	Alexandra	MBA	Cgh	CM	6.16	$\pm 3.50\times10^{18}$	A.44	149.68	± 9.85	B.48	3.50	±2.11	0	± 60	D
56	Melete	MBA	Xk	Mes	4.61	$\pm 0.00\times10^{18}$	A.45	113.63	± 8.27	B.49	6.00	±1.31	0	± 21	C

57	Mnemosyne	MBA	S	OC	1.26	$\pm 0.24 \times 10^{19}$	A.46	113.01	± 4.46	B.50	16.62	± 3.73	0	± 22	✗
59	Elpis	MBA	B	CV	3.00	$\pm 0.50 \times 10^{18}$	A.47	163.61	± 6.50	B.51	1.30	± 0.26	53	± 20	C
60	Echo	MBA	S	Ec	3.15	$\pm 0.32 \times 10^{17}$	A.48	60.00	± 1.33	B.52	2.78	± 0.33	16	± 12	B
61	Danae	MBA	S	OC	2.89	$\pm 2.78 \times 10^{18}$		82.52	± 2.73	B.53	9.81	± 9.49	0	± 96	D
63	Ausonia	MBA	S	OC	1.53	$\pm 0.15 \times 10^{18}$	A.49	94.45	± 7.15	B.54	3.46	± 0.86	0	± 24	C
65	Cybele	MBA	Xk	Mes	1.36	$\pm 0.31 \times 10^{19}$	A.50	248.29	± 17.59	B.55	1.70	± 0.52	59	± 30	C
67	Asia	MBA	S	OC	1.03	$\pm 0.10 \times 10^{18}$		60.99	± 2.41	B.56	8.66	± 1.32	0	± 15	✗
68	Leto	MBA	S	OC	3.28	$\pm 1.90 \times 10^{18}$	A.51	124.96	± 6.42	B.57	3.21	± 1.92	3	± 60	D
69	Hesperia	MBA	Xk	Mes	5.86	$\pm 1.18 \times 10^{18}$	A.52	136.69	± 4.71	B.58	4.38	± 0.99	0	± 22	C
70	Panopaea	MBA	Cgh	CM	4.33	$\pm 1.09 \times 10^{18}$		133.43	± 7.58	B.59	3.48	± 1.05	0	± 30	C
72	Feronia	MBA	D	CM	3.32	$\pm 8.49 \times 10^{18}$		83.95	± 4.02	B.60	10.71	± 27.44	0	± ∞	✗
74	Galatea	MBA	C	CM	6.13	$\pm 5.36 \times 10^{18}$		120.67	± 7.15	B.61	6.66	± 5.94	0	± 89	D
76	Freia	MBA	C	CM	1.97	$\pm 4.20 \times 10^{18}$	A.53	167.87	± 8.73	B.62	0.79	± 1.69	64	± CO	E
77	Frigga	MBA	Xe	EH[2]	1.74	$\pm 0.68 \times 10^{18}$		66.97	± 1.28	B.63	11.05	± 4.34	0	± 39	✗
78	Diana	MBA	Ch	CM	1.27	$\pm 0.13 \times 10^{18}$	A.54	123.63	± 4.57	B.64	1.28	± 0.19	42	± 14	B
81	Terpsichore	MBA	Cb	CM	6.19	$\pm 5.31 \times 10^{18}$		121.77	± 2.34	B.65	6.54	± 5.62	0	± 85	D
84	Klio	MBA	Ch	CM	5.47	$\pm 4.06 \times 10^{17}$		79.40	± 1.95	B.66	2.08	± 1.55	7	± 74	D
85	Io	MBA	Cb	CM	2.57	$\pm 1.48 \times 10^{18}$	A.55	155.00	± 6.00	B.67	1.31	± 0.77	41	± 58	D
87	Sylvia	MBA	X	CV	1.48	$\pm 0.00 \times 10^{19}$	A.56	278.14	± 10.75	B.68	1.31	± 0.15	52	± 11	B
88	Thisbe	MBA	B	CV	1.53	$\pm 0.31 \times 10^{19}$	A.57	204.04	± 9.12	B.69	3.44	± 0.84	0	± 24	C
89	Julia	MBA	X	CV	6.71	$\pm 1.82 \times 10^{18}$	A.58	147.57	± 8.32	B.70	3.98	± 1.27	0	± 31	C
90	Antiope	MBA	C	CM	8.30	$\pm 0.20 \times 10^{17}$	A.59	122.15	± 2.77	B.71	0.86	± 0.06	61	± 7	B
92	Undina	MBA	Xk	Mes	4.43	$\pm 0.25 \times 10^{18}$	A.60	124.44	± 3.25	B.72	4.39	± 0.42	0	± 9	B
93	Minerva	MBA	C	CM	3.50	$\pm 0.40 \times 10^{18}$		149.79	± 8.08	B.73	1.98	± 0.39	11	± 19	B
94	Aurora	MBA	C	CM	6.23	$\pm 3.64 \times 10^{18}$	A.61	186.35	± 8.84	B.74	1.83	± 1.10	18	± 60	D
96	Aegle	MBA	T	Ata	6.48	$\pm 6.26 \times 10^{18}$	A.62	167.92	± 5.49	B.75	2.61	± 2.53	34	± 97	D
97	Klotho	MBA	Xc	Ata[2]	1.33	$\pm 0.13 \times 10^{18}$		84.79	± 3.13	B.76	4.16	± 0.62	0	± 14	B
98	Ianthe	MBA	Ch	CM	8.93	$\pm 1.99 \times 10^{17}$	A.63	106.16	± 3.76	B.77	1.42	± 0.35	36	± 24	C
105	Artemis	MBA	Ch	CM	1.53	$\pm 0.54 \times 10^{18}$	A.64	119.10	± 6.78	B.78	1.73	± 0.67	23	± 38	C
106	Dione	MBA	Cgh	CM	3.06	$\pm 1.54 \times 10^{18}$	A.65	147.17	± 3.34	B.79	1.83	± 0.92	18	± 50	D
107	Camilla	MBA	X	CV	1.12	$\pm 0.03 \times 10^{19}$	A.66	210.68	± 8.89	B.80	2.28	± 0.29	18	± 12	B
111	Ate	MBA	Ch	CM	1.76	$\pm 0.44 \times 10^{18}$	A.67	142.85	± 5.94	B.81	1.15	± 0.32	48	± 27	C
112	Iphigenia	MBA	Ch	CM	1.97	$\pm 6.78 \times 10^{18}$		71.07	± 0.52	B.82	10.48	± 36.06	0	± ∞	✗
117	Lomia	MBA	X	CV	6.08	$\pm 0.63 \times 10^{18}$	A.68	146.78	± 3.96	B.83	3.67	± 0.48	0	± 13	B
121	Hermione	MBA	Ch	CM	4.97	$\pm 0.33 \times 10^{18}$	A.69	195.36	± 10.62	B.84	1.27	± 0.22	43	± 17	B
126	Velleda	MBA	S	OC	0.47	$\pm 5.79 \times 10^{18}$		44.79	± 1.33	B.85	10.00	± 123.00	0	± ∞	✗
127	Johanna	MBA	Ch	CM	3.08	$\pm 1.35 \times 10^{18}$	A.70	116.14	± 3.93	B.86	3.75	± 1.68	0	± 44	C
128	Nemesis	MBA	C	CM	5.97	$\pm 2.56 \times 10^{18}$	A.71	184.19	± 5.19	B.87	1.82	± 0.79	18	± 43	C
129	Antigone	MBA	X	Ste[2]	2.65	$\pm 0.89 \times 10^{18}$	A.72	119.44	± 3.91	B.88	2.96	± 1.04	29	± 35	C
130	Elektra	MBA	Ch	CM	6.60	$\pm 0.40 \times 10^{18}$	A.73	189.62	± 6.81	B.89	1.84	± 0.22	17	± 12	B
132	Aethra	MBA	Xe	EH	0.41	$\pm 2.71 \times 10^{18}$		35.83	± 6.59	B.90	17.09	± 112.83	0	± ∞	✗
135	Hertha	MBA	Xk	Ata[2]	1.21	$\pm 0.16 \times 10^{18}$	A.74	76.12	± 3.29	B.91	5.23	± 0.96	0	± 18	B
137	Meliboea	MBA	C	CM	7.27	$\pm 3.07 \times 10^{18}$	A.75	145.92	± 3.58	B.92	4.46	± 1.91	0	± 42	E
138	Tolosa	MBA	S	OC	4.93	$\pm 2.59 \times 10^{17}$		51.86	± 3.07	B.93	6.74	± 3.74	0	± 55	E
139	Juewa	MBA	X	CV	5.54	$\pm 2.20 \times 10^{18}$	A.76	161.43	± 7.38	B.94	2.51	± 1.05	9	± 41	C
141	Lumen	MBA	Ch	CM	8.25	$\pm 5.77 \times 10^{18}$		131.35	± 5.21	B.95	6.95	± 4.93	0	± 70	✗
144	Vibilia	MBA	Ch	CM	5.30	$\pm 1.20 \times 10^{18}$	A.77	141.34	± 2.76	B.96	3.58	± 0.84	0	± 23	C
145	Adeona	MBA	Ch	CM	2.08	$\pm 0.57 \times 10^{18}$	A.78	149.50	± 5.45	B.97	1.18	± 0.34	47	± 29	C
147	Protogeneia	MBA	C	CM	1.23	$\pm 0.05 \times 10^{19}$		118.44	± 10.45	B.98	14.13	± 3.78	0	± 26	✗
148	Gallia	MBA	S	OC	4.89	$\pm 1.67 \times 10^{18}$		83.45	± 5.07	B.99	16.06	± 6.22	0	± 38	✗
150	Nuwa	MBA	C	CM	1.62	$\pm 0.20 \times 10^{18}$	A.79	146.54	± 9.15	B.100	0.98	± 0.22	56	± 22	C
152	Atala	MBA	S	OC	5.43	$\pm 1.24 \times 10^{18}$		60.03	± 3.01	B.101	47.92	± 13.10	0	± 27	✗
154	Bertha	MBA	Cb	CM	9.19	$\pm 5.20 \times 10^{18}$	A.80	186.85	± 1.83	B.102	2.69	± 1.52	0	± 56	D
156	Xanthippe	MBA	Ch	CM	6.49	$\pm 3.71 \times 10^{18}$		116.34	± 4.14	B.103	7.86	± 4.57	0	± 58	✗
163	Erigone	MBA	Ch	CM	2.01	$\pm 0.68 \times 10^{18}$		72.70	± 1.95	B.104	9.99	± 3.45	0	± 34	✗
164	Eva	MBA	X	Ev	9.29	$\pm 7.76 \times 10^{17}$		101.77	± 3.61	B.105	1.68	± 1.41	39	± 84	D
165	Loreley	MBA	C	CM	1.91	$\pm 0.19 \times 10^{19}$	A.81	164.92	± 8.14	B.106	8.14	± 1.46	0	± 17	✗
168	Sibylla	MBA	Ch	CM	3.92	$\pm 1.80 \times 10^{18}$	A.82	149.06	± 4.29	B.107	2.26	± 1.05	0	± 46	C
173	Ino	MBA	X	CV	4.79	$\pm 3.11 \times 10^{18}$	A.83	160.07	± 6.04	B.108	2.23	± 1.47	20	± 65	D
179	Klytaemnestra	MBA	S	OC	2.49	$\pm 1.19 \times 10^{17}$		75.02	± 3.21	B.109	1.12	± 0.55	66	± 49	C

Table 1 (*continued*)

Designation		Classification			Masses (kg)			Diameter (km)			Density		Porosity		Rank
#	Name	Dyn.	Tax.	Met.	M	δM	Fig.	ϕ	$\delta\phi$	Fig.	ρ	$\delta\rho$	$\mathcal{P}$	$\delta\mathcal{P}$	
185	Eunike	MBA	C	CM	3.56	$\pm$ 2.61 $\times 10^{18}$	A.84	160.61	$\pm$ 5.00	B.110	1.64	$\pm$1.21	27	$\pm$74	D
187	Lamberta	MBA	Ch	CM	1.80	$\pm$ 0.85 $\times 10^{18}$	A.85	131.31	$\pm$ 1.08	B.111	1.51	$\pm$0.71	32	$\pm$47	C
189	Phthia	MBA	Sa	OC	3.84	$\pm$ 0.81 $\times 10^{16}$		40.91	$\pm$ 1.36	B.112	1.07	$\pm$0.25	67	$\pm$23	C
192	Nausikaa	MBA	S	OC	1.79	$\pm$ 0.42 $\times 10^{18}$	A.86	90.18	$\pm$ 2.80	B.113	4.64	$\pm$1.17	0	$\pm$25	C
194	Prokne	MBA	Ch	CM	2.68	$\pm$ 0.29 $\times 10^{18}$	A.87	170.33	$\pm$ 6.92	B.114	1.03	$\pm$0.16	53	$\pm$16	B
196	Philomela	MBA	S	OC	4.00	$\pm$ 1.53 $\times 10^{18}$	A.88	145.29	$\pm$ 7.71	B.115	2.48	$\pm$1.02	25	$\pm$41	C
200	Dynamene	MBA	Ch	CM	1.07	$\pm$ 0.16 $\times 10^{19}$		130.71	$\pm$ 3.01	B.116	9.14	$\pm$1.51	0	$\pm$16	✗
204	Kallisto	MBA	S	OC	0.60	$\pm$ 1.81 $\times 10^{18}$		50.36	$\pm$ 1.69	B.117	8.98	$\pm$27.07	0	$\pm\infty$	✗
209	Dido	MBA	Xc	Mes	4.59	$\pm$ 7.42 $\times 10^{18}$		140.35	$\pm$ 10.12	B.118	3.17	$\pm$5.17	25	$\pm\infty$	E
210	Isabella	MBA	Cb	CM	3.41	$\pm$ 1.09 $\times 10^{18}$		73.70	$\pm$ 8.47	B.119	16.26	$\pm$7.65	0	$\pm$47	✗
211	Isolda	MBA	Ch	CM	4.49	$\pm$ 2.43 $\times 10^{18}$	A.89	149.81	$\pm$ 6.10	B.120	2.54	$\pm$1.41	0	$\pm$55	D
212	Medea	MBA	D	CM	1.32	$\pm$ 0.10 $\times 10^{19}$		144.13	$\pm$ 7.23	B.121	8.41	$\pm$1.43	0	$\pm$17	✗
216	Kleopatra	MBA	Xe	Ata[2]	4.64	$\pm$ 0.20 $\times 10^{18}$	A.90	127.47	$\pm$ 8.44	B.122	4.27	$\pm$0.86	0	$\pm$20	C
217	Eudora	MBA	X	CV	1.52	$\pm$ 0.06 $\times 10^{18}$		68.62	$\pm$ 1.41	B.123	8.98	$\pm$0.65	0	$\pm$7	✗
221	Eos	MBA	K	CV	5.87	$\pm$ 0.34 $\times 10^{18}$		103.52	$\pm$ 5.60	B.124	10.10	$\pm$1.74	0	$\pm$17	✗
230	Athamantis	MBA	S	OC	1.89	$\pm$ 0.19 $\times 10^{18}$		110.17	$\pm$ 4.57	B.125	2.69	$\pm$0.43	19	$\pm$15	B
234	Barbara	MBA	L	CO	0.44	$\pm$ 1.45 $\times 10^{18}$		45.62	$\pm$ 1.93	B.126	8.84	$\pm$29.17	0	$\pm\infty$	✗
238	Hypatia	MBA	Ch	CM	4.90	$\pm$ 1.70 $\times 10^{18}$	A.91	146.13	$\pm$ 2.66	B.127	2.99	$\pm$1.05	0	$\pm$35	C
240	Vanadis	MBA	C	CM	1.10	$\pm$ 0.92 $\times 10^{18}$	A.92	94.03	$\pm$ 5.37	B.128	2.53	$\pm$2.15	0	$\pm$84	D
241	Germania	MBA	Cb	CM	0.86	$\pm$ 5.00 $\times 10^{18}$		178.60	$\pm$ 7.84	B.129	0.28	$\pm$1.67	87	$\pm\infty$	✗
243	Ida	MBA	S	OC	3.78	$\pm$ 0.20 $\times 10^{16}$		31.29	$\pm$ 1.20	B.130	2.35	$\pm$0.29	29	$\pm$12	A
253	Mathilde	MBA	Cb	CM	1.03	$\pm$ 0.04 $\times 10^{17}$	A.93	53.00	$\pm$ 2.59	B.131	1.32	$\pm$0.20	41	$\pm$15	A
259	Aletheia	MBA	X	CV	7.79	$\pm$ 0.43 $\times 10^{18}$	A.94	190.05	$\pm$ 6.82	B.132	2.16	$\pm$0.26	22	$\pm$12	B
266	Aline	MBA	Ch	CM	4.15	$\pm$ 0.42 $\times 10^{18}$		107.95	$\pm$ 6.62	B.133	6.29	$\pm$1.32	0	$\pm$20	E
268	Adorea	MBA	X	CV	3.25	$\pm$ 2.26 $\times 10^{18}$	A.95	140.31	$\pm$ 3.34	B.134	2.24	$\pm$1.56	19	$\pm$69	D
283	Emma	MBA	C	CM[3]	1.38	$\pm$ 0.03 $\times 10^{18}$	A.96	132.74	$\pm$ 10.13	B.135	1.12	$\pm$0.25	49	$\pm$23	C
304	Olga	MBA	Xc	Mes	1.15	$\pm$ 1.12 $\times 10^{18}$		70.30	$\pm$ 2.32	B.136	6.31	$\pm$6.18	0	$\pm$97	D
306	Unitas	MBA	S	OC	5.33	$\pm$ 5.77 $\times 10^{17}$		52.88	$\pm$ 3.48	B.137	6.88	$\pm$7.57	0	$\pm\infty$	E
322	Phaeo	MBA	D	CM	1.86	$\pm$ 0.04 $\times 10^{18}$		71.88	$\pm$ 4.32	B.138	9.56	$\pm$1.73	0	$\pm$18	✗
324	Bamberga	MBA	Cb	CM	1.03	$\pm$ 0.10 $\times 10^{19}$	A.97	234.67	$\pm$ 7.80	B.139	1.52	$\pm$0.20	32	$\pm$13	A
328	Gudrun	MBA	S	OC	3.16	$\pm$ 0.46 $\times 10^{18}$	A.98	122.59	$\pm$ 3.72	B.140	3.27	$\pm$0.55	1	$\pm$17	B
334	Chicago	MBA	C	CM	5.06	$\pm$ 5.63 $\times 10^{18}$	A.99	167.26	$\pm$ 7.27	B.141	2.06	$\pm$2.31	8	$\pm\infty$	E
337	Devosa	MBA	Xk	Hex3	1.08	$\pm$ 0.16 $\times 10^{18}$	A.100	63.87	$\pm$ 3.14	B.142	7.91	$\pm$1.65	0	$\pm$20	✗
344	Desiderata	MBA	C	CM	1.39	$\pm$ 0.48 $\times 10^{18}$	A.101	129.20	$\pm$ 3.37	B.143	1.22	$\pm$0.43	45	$\pm$35	C
345	Tercidina	MBA	Ch	CM	2.68	$\pm$ 1.18 $\times 10^{18}$	A.102	98.78	$\pm$ 2.63	B.144	5.30	$\pm$2.37	0	$\pm$44	C
346	Hermentaria	MBA	S	OC	6.33	$\pm$ 0.18 $\times 10^{18}$		93.27	$\pm$ 3.05	B.145	14.89	$\pm$1.52	0	$\pm$10	✗
349	Dembowska	MBA	R	OC	3.58	$\pm$ 1.03 $\times 10^{18}$	A.103	145.23	$\pm$ 17.21	B.146	2.23	$\pm$1.01	33	$\pm$45	C
354	Eleonora	MBA	A	Pal	7.18	$\pm$ 2.57 $\times 10^{18}$	A.104	154.34	$\pm$ 5.65	B.147	3.73	$\pm$1.39	21	$\pm$37	C
356	Liguria	MBA	Ch	CM	7.83	$\pm$ 1.50 $\times 10^{18}$		134.76	$\pm$ 5.17	B.148	6.10	$\pm$1.36	0	$\pm$22	✗
365	Corduba	MBA	Ch	CM	5.84	$\pm$ 0.95 $\times 10^{18}$		104.51	$\pm$ 2.42	B.149	9.76	$\pm$1.73	0	$\pm$17	✗
372	Palma	MBA	X	CV	5.15	$\pm$ 0.64 $\times 10^{18}$	A.105	191.12	$\pm$ 2.68	B.150	1.40	$\pm$0.18	49	$\pm$13	B
375	Ursula	MBA	Xc	Mes	8.45	$\pm$ 5.26 $\times 10^{18}$	A.106	191.65	$\pm$ 4.01	B.151	2.29	$\pm$1.43	46	$\pm$62	D
379	Huenna	MBA	C	CM[1]	3.83	$\pm$ 0.20 $\times 10^{17}$		87.28	$\pm$ 5.70	B.152	1.10	$\pm$0.22	51	$\pm$20	C
381	Myrrha	MBA	X	CV	9.18	$\pm$ 0.80 $\times 10^{18}$		123.41	$\pm$ 6.30	B.153	9.32	$\pm$1.64	0	$\pm$17	✗
386	Siegena	MBA	Ch	CM	8.14	$\pm$ 1.58 $\times 10^{18}$	A.107	170.35	$\pm$ 8.40	B.154	3.14	$\pm$0.76	0	$\pm$24	C
387	Aquitania	MBA	L	CO	1.90	$\pm$ 0.64 $\times 10^{18}$	A.108	103.51	$\pm$ 2.23	B.155	3.27	$\pm$1.11	0	$\pm$34	C
404	Arsinoe	MBA	B	CV	3.42	$\pm$ 3.03 $\times 10^{18}$		96.97	$\pm$ 3.01	B.156	7.16	$\pm$6.38	0	$\pm$89	D
405	Thia	MBA	Ch	CM	1.38	$\pm$ 0.14 $\times 10^{18}$		122.14	$\pm$ 7.69	B.157	1.44	$\pm$0.30	35	$\pm$21	C
409	Aspasia	MBA	Xc	Mes	1.18	$\pm$ 0.23 $\times 10^{19}$	A.109	176.33	$\pm$ 4.50	B.158	4.10	$\pm$0.84	3	$\pm$20	C
410	Chloris	MBA	Ch	CM	6.24	$\pm$ 0.30 $\times 10^{18}$	A.110	115.55	$\pm$ 8.22	B.159	7.72	$\pm$1.69	0	$\pm$21	✗
416	Vaticana	MBA	S	OC	3.27	$\pm$ 3.10 $\times 10^{18}$		87.10	$\pm$ 2.57	B.160	9.44	$\pm$8.99	0	$\pm$95	D
419	Aurelia	MBA	Cb	CM[1]	1.72	$\pm$ 0.34 $\times 10^{18}$	A.111	124.47	$\pm$ 3.08	B.161	1.70	$\pm$0.35	24	$\pm$21	C
420	Bertholda	MBA	X	CV	1.48	$\pm$ 0.09 $\times 10^{19}$		141.54	$\pm$ 2.08	B.162	9.96	$\pm$0.75	0	$\pm$7	✗
423	Diotima	MBA	C	CM	6.91	$\pm$ 1.93 $\times 10^{18}$	A.112	211.64	$\pm$ 16.02	B.163	1.39	$\pm$0.50	38	$\pm$35	C

433	Eros	NEA	S	OC	6.69	$\pm$ 0.00 $\times$ 10^{15}		16.85	$\pm$ 0.07	B.164	2.67	$\pm$0.03	1	$\pm$1	A
442	Eichsfeldia	MBA	Ch	CM	1.95	$\pm$ 0.20 $\times$ 10^{17}		65.58	$\pm$ 1.70	B.165	1.32	$\pm$0.16	41	$\pm$12	B
444	Gyptis	MBA	C	CM	1.06	$\pm$ 0.28 $\times$ 10^{19}	A.113	164.63	$\pm$ 2.60	B.166	4.55	$\pm$1.23	0	$\pm$27	C
445	Edna	MBA	Ch	CM	3.47	$\pm$ 0.78 $\times$ 10^{18}		88.60	$\pm$ 4.10	B.167	9.52	$\pm$2.50	0	$\pm$26	✗
449	Hamburga	MBA	C	CM	1.57	$\pm$ 1.40 $\times$ 10^{18}		66.76	$\pm$ 4.82	B.168	10.07	$\pm$9.24	0	$\pm$91	E
451	Patientia	MBA	Cb	CM	1.09	$\pm$ 0.53 $\times$ 10^{19}	A.114	234.42	$\pm$ 10.17	B.169	1.60	$\pm$0.80	28	$\pm$50	D
455	Bruchsalia	MBA	Xk	Mes	1.19	$\pm$ 0.12 $\times$ 10^{18}		88.13	$\pm$ 6.89	B.170	3.32	$\pm$0.84	21	$\pm$25	C
469	Argentina	MBA	Xk	Mes	4.53	$\pm$ 1.76 $\times$ 10^{18}	A.115	126.00	$\pm$ 4.91	B.171	4.32	$\pm$1.75	0	$\pm$40	C
471	Papagena	MBA	S	OC	3.05	$\pm$ 1.73 $\times$ 10^{18}	A.116	124.55	$\pm$ 8.77	B.172	3.01	$\pm$1.82	9	$\pm$60	D
481	Emita	MBA	Ch	CM	5.78	$\pm$ 1.45 $\times$ 10^{18}		107.23	$\pm$ 4.71	B.173	8.95	$\pm$2.53	0	$\pm$28	C
485	Genua	MBA	S	OC	1.36	$\pm$ 0.44 $\times$ 10^{18}		56.31	$\pm$ 4.15	B.174	14.53	$\pm$5.68	0	$\pm$39	✗
488	Kreusa	MBA	Ch	CM	2.48	$\pm$ 1.14 $\times$ 10^{18}	A.117	162.32	$\pm$ 9.54	B.175	1.10	$\pm$0.54	50	$\pm$49	C
490	Veritas	MBA	Ch	CM	5.99	$\pm$ 2.23 $\times$ 10^{18}	A.118	110.96	$\pm$ 3.80	B.176	8.37	$\pm$3.23	0	$\pm$38	C
491	Carina	MBA	X	CV	4.82	$\pm$ 1.95 $\times$ 10^{18}		97.36	$\pm$ 3.18	B.177	9.97	$\pm$4.15	0	$\pm$41	C
503	Evelyn	MBA	Ch	CM	2.85	$\pm$ 0.34 $\times$ 10^{18}		87.58	$\pm$ 3.58	B.178	8.10	$\pm$1.38	0	$\pm$17	✗
505	Cava	MBA	Xk	LL1	3.99	$\pm$ 3.84 $\times$ 10^{18}		101.51	$\pm$ 1.83	B.179	7.28	$\pm$7.02	0	$\pm$96	D
508	Princetonia	MBA	X	CV	2.99	$\pm$ 0.65 $\times$ 10^{18}	A.119	139.69	$\pm$ 3.40	B.180	2.09	$\pm$0.47	25	$\pm$22	C
511	Davida	MBA	C	CM	3.38	$\pm$ 1.02 $\times$ 10^{19}	A.120	298.28	$\pm$ 11.92	B.181	2.43	$\pm$0.79	0	$\pm$32	C
516	Amherstia	MBA	X	CV	1.43	$\pm$ 1.33 $\times$ 10^{18}		69.84	$\pm$ 4.38	B.182	8.01	$\pm$7.60	0	$\pm$94	D
532	Herculina	MBA	S	OC	1.15	$\pm$ 0.28 $\times$ 10^{19}	A.121	217.49	$\pm$ 5.10	B.183	2.12	$\pm$0.53	36	$\pm$25	C
536	Merapi	MBA	X	CV	2.61	$\pm$ 0.47 $\times$ 10^{19}	A.122	155.17	$\pm$ 3.53	B.184	13.36	$\pm$2.59	0	$\pm$19	✗
554	Peraga	MBA	Ch	CI1	6.59	$\pm$ 0.66 $\times$ 10^{17}	A.123	96.46	$\pm$ 1.68	B.185	1.40	$\pm$0.15	12	$\pm$11	B
582	Olympia	MBA	S	OC	0.43	$\pm$ 1.17 $\times$ 10^{18}		43.39	$\pm$ 1.49	B.186	10.00	$\pm$27.35	0	$\pm\infty$	✗
584	Semiramis	MBA	S	OC	8.23	$\pm$ 5.77 $\times$ 10^{17}		51.78	$\pm$ 2.15	B.187	11.31	$\pm$8.06	0	$\pm$71	✗
602	Marianna	MBA	Ch	CM	1.02	$\pm$ 0.05 $\times$ 10^{19}		127.95	$\pm$ 2.86	B.188	9.29	$\pm$0.76	0	$\pm$8	✗
604	Tekmessa	MBA	Xc	Mes	1.45	$\pm$ 0.28 $\times$ 10^{18}		64.42	$\pm$ 3.01	B.189	10.35	$\pm$2.46	0	$\pm$23	✗
617	Patroclus	MBA	X	CV	1.36	$\pm$ 0.11 $\times$ 10^{18}		143.14	$\pm$ 8.37	B.190	0.88	$\pm$0.17	68	$\pm$19	B
624	Hektor	MBA	X	CV	9.95	$\pm$ 0.12 $\times$ 10^{18}		226.68	$\pm$ 15.15	B.191	1.63	$\pm$0.32	41	$\pm$20	C
626	Notburga	MBA	Cb	CM	3.24	$\pm$ 1.30 $\times$ 10^{18}	A.124	96.84	$\pm$ 4.67	B.192	6.81	$\pm$2.90	0	$\pm$42	E
654	Zelinda	MBA	Ch	CM	1.35	$\pm$ 0.14 $\times$ 10^{18}		127.83	$\pm$ 5.23	B.193	1.23	$\pm$0.19	45	$\pm$15	B
665	Sabine	MBA	X	CV	6.98	$\pm$ 3.98 $\times$ 10^{17}		52.71	$\pm$ 0.72	B.194	9.10	$\pm$5.20	0	$\pm$57	E
675	Ludmilla	MBA	S	OC	1.20	$\pm$ 0.24 $\times$ 10^{19}		67.66	$\pm$ 0.94		73.99	$\pm$15.05	0	$\pm$20	✗
679	Pax	MBA	L	CO	7.14	$\pm$ 1.99 $\times$ 10^{17}		64.88	$\pm$ 3.64	B.195	4.99	$\pm$1.62	0	$\pm$32	C
680	Genoveva	MBA	X	CV	2.69	$\pm$ 0.04 $\times$ 10^{18}		84.69	$\pm$ 1.71	B.196	8.45	$\pm$0.52	0	$\pm$6	✗
690	Wratislavia	MBA	B	CV	1.28	$\pm$ 0.03 $\times$ 10^{19}		146.21	$\pm$ 11.02	B.197	7.81	$\pm$1.77	0	$\pm$22	✗
702	Alauda	MBA	B	CV	6.06	$\pm$ 3.60 $\times$ 10^{18}	A.125	191.65	$\pm$ 8.22	B.198	1.64	$\pm$0.99	41	$\pm$60	D
704	Interamnia	MBA	B	CI1	3.28	$\pm$ 0.45 $\times$ 10^{19}	A.126	317.19	$\pm$ 4.65	B.199	1.96	$\pm$0.28	0	$\pm$14	A
720	Bohlinia	MBA	Sq	OC	5.97	$\pm$ 0.80 $\times$ 10^{16}	A.127	34.64	$\pm$ 1.81	B.200	2.74	$\pm$0.56	17	$\pm$20	C
735	Marghanna	MBA	Ch	CM	2.15	$\pm$ 0.68 $\times$ 10^{18}		72.27	$\pm$ 2.22	B.201	10.87	$\pm$3.56	0	$\pm$32	✗
739	Mandeville	MBA	Xc	Mes	1.16	$\pm$ 1.07 $\times$ 10^{18}		105.53	$\pm$ 1.68	B.202	1.88	$\pm$1.74	55	$\pm$92	D
747	Winchester	MBA	B	CV	3.81	$\pm$ 2.22 $\times$ 10^{18}	A.128	170.07	$\pm$ 6.70	B.203	1.47	$\pm$0.87	47	$\pm$59	D
751	Faina	MBA	Ch	CM	3.27	$\pm$ 0.58 $\times$ 10^{18}	A.129	107.31	$\pm$ 1.48	B.204	5.05	$\pm$0.92	0	$\pm$18	B
758	Mancunia	MBA	X	CV	9.31	$\pm$ 0.80 $\times$ 10^{17}		87.08	$\pm$ 1.31	B.205	2.69	$\pm$0.26	3	$\pm$9	B
760	Massinga	MBA	S	OC	1.33	$\pm$ 1.32 $\times$ 10^{18}		70.82	$\pm$ 0.92	B.206	7.15	$\pm$7.10	0	$\pm$99	D
762	Pulcova	MBA	Cb	CM[1]	1.40	$\pm$ 0.10 $\times$ 10^{18}	A.130	138.40	$\pm$ 5.96	B.207	1.00	$\pm$0.14	55	$\pm$14	B
769	Tatjana	MBA		CM	6.31	$\pm$ 0.64 $\times$ 10^{16}		106.27	$\pm$ 4.02	B.208	10.03	$\pm$1.52	0	$\pm$15	✗
776	Berbericia	MBA	Cgh	CM	2.20	$\pm$ 2.71 $\times$ 10^{18}	A.131	152.29	$\pm$ 4.25	B.209	1.18	$\pm$1.46	47	$\pm\infty$	E
784	Pickeringia	MBA	C	CM	3.74	$\pm$ 0.32 $\times$ 10^{18}		82.52	$\pm$ 7.18	B.210	12.70	$\pm$3.49	0	$\pm$27	✗
786	Bredichina	MBA	C	CM	2.82	$\pm$ 2.79 $\times$ 10^{18}		98.34	$\pm$ 6.00	B.211	5.66	$\pm$5.69	0	$\pm\infty$	E
790	Pretoria	MBA	X	Cv	4.58	$\pm$ 0.28 $\times$ 10^{18}	A.132	160.98	$\pm$ 11.16	B.212	2.09	$\pm$0.45	24	$\pm$21	C
804	Hispania	MBA	C	CM	5.00	$\pm$ 1.78 $\times$ 10^{18}	A.133	148.25	$\pm$ 4.08	B.213	2.93	$\pm$1.06	0	$\pm$36	C
809	Lundia	MBA	V	HED	9.27	$\pm$ 3.09 $\times$ 10^{14}		10.26	$\pm$ 0.07		1.64	$\pm$0.10	49	$\pm$6	B
854	Frostia	MBA	V	HED	1.06	$\pm$ 0.95 $\times$ 10^{15}		8.39	$\pm$ 1.27	B.214	0.88	$\pm$0.13	72	$\pm$14	B
895	Helio	MBA	B	CV	9.87	$\pm$ 6.05 $\times$ 10^{18}	A.134	148.43	$\pm$ 5.02	B.215	5.76	$\pm$3.58	0	$\pm$62	D
914	Palisana	MBA	Ch	CM	2.35	$\pm$ 0.24 $\times$ 10^{18}		81.27	$\pm$ 5.34	B.216	8.36	$\pm$1.85	0	$\pm$22	✗
949	Hel	MBA	Xk	Mes	1.73	$\pm$ 0.62 $\times$ 10^{18}		63.56	$\pm$ 4.01	B.217	12.86	$\pm$5.19	0	$\pm$40	✗
1013	Tombecka	MBA	Xk	Mes	0.17	$\pm$ 1.43 $\times$ 10^{18}		35.18	$\pm$ 2.24	B.218	7.50	$\pm$62.74	0	$\pm\infty$	E
10^{15}	Christa	MBA	Xc	Mes	4.77	$\pm$ 0.68 $\times$ 10^{18}		99.77	$\pm$ 2.46	B.219	9.17	$\pm$1.46	0	$\pm$15	✗
10^{21}	Flammario	MBA	Cb	CM	5.14	$\pm$ 0.12 $\times$ 10^{18}		99.27	$\pm$ 3.27	B.220	10.03	$\pm$1.02	0	$\pm$10	✗
1036	Ganymed	NEA	S	OC	1.67	$\pm$ 3.18 $\times$ 10^{17}		34.28	$\pm$ 1.38	B.221	7.91	$\pm$15.10	0	$\pm\infty$	✗

Table 1 (*continued*)

Designation		Classification			Masses (kg)			Diameter (km)			Density		Porosity		Rank
#	Name	Dyn.	Tax.	Met.	M	δM	Fig.	ϕ	$\delta\phi$	Fig.	ρ	$\delta\rho$	$\mathcal{P}$	$\delta\mathcal{P}$	
1089	Tama	MBA	S	OC	8.90	$\pm$ 3.20 $\times$ 10^{14}		13.44	$\pm$ 0.61	B.222	2.52	$\pm$ 0.29	24	$\pm$ 11	B
1171	Rusthawelia	MBA	X	CV	1.81	$\pm$ 0.20 $\times$ 10^{18}		70.98	$\pm$ 2.42	B.223	9.66	$\pm$ 1.45	0	$\pm$ 15	✗
1313	Berna	MBA	S	OC	2.25	$\pm$ 2.00 $\times$ 10^{15}		13.93	$\pm$ 0.64	B.224	1.21	$\pm$ 0.14	63	$\pm$ 11	B
1669	Dagmar	MBA	ag	CM	3.98	$\pm$ 0.80 $\times$ 10^{16}	A.135	42.99	$\pm$ 2.86	B.225	0.95	$\pm$ 0.27	57	$\pm$ 28	C
1686	De Sitter	MBA		CM	6.76	$\pm$ 3.18 $\times$ 10^{18}		30.60	$\pm$ 1.41	B.226	450.51	$\pm$ 220.97	0	$\pm$ 49	✗
3169	Ostro	MBA	Xe	EH	1.86	$\pm$ 0.62 $\times$ 10^{14}		5.15	$\pm$ 0.08		2.59	$\pm$ 0.20	25	$\pm$ 7	B
3671	Dionysus	NEA	Cb	CM	8.38	$\pm$ 2.79 $\times$ 10^{11}		0.92	$\pm$ 0.05	B.227	1.60	$\pm$ 0.60	28	$\pm$ 37	C
3749	Balam	MBA	S	OC	5.09	$\pm$ 0.20 $\times$ 10^{14}		6.99	$\pm$ 3.00	B.228	2.83	$\pm$ 3.64	14	$\pm\infty$	E
4492	Debussy	MBA		CM	3.33	$\pm$ 3.00 $\times$ 10^{14}		15.78	$\pm$ 1.91	B.229	0.90	$\pm$ 0.10	60	$\pm$ 11	B
5381	Sekhmet	NEA	S	OC	1.04	$\pm$ 0.35 $\times$ 1012		1.00	$\pm$ 0.10		1.98	$\pm$ 0.65	40	$\pm$ 32	C
25143	Itokawa	NEA	S	OC	3.50	$\pm$ 0.10 $\times$ 1010		0.32	$\pm$ 0.01	B.230	1.91	$\pm$ 0.21	42	$\pm$ 11	A
26308	1998 SM165	TNO		Ice	6.78	$\pm$ 2.40 $\times$ 10^{18}		284.37	$\pm$ 5.07	B.231	0.56	$\pm$ 0.20	43	$\pm$ 35	C
35107	1991 VH	NEA	Sq	OC	1.40	$\pm$ 0.14 $\times$ 1012		1.13	$\pm$ 0.01	B.232	1.50	$\pm$ 0.50	54	$\pm$ 33	C
42355	Typhon	TNO		Ice	9.49	$\pm$ 0.52 $\times$ 10^{17}		181.70	$\pm$ 5.10	B.233	0.30	$\pm$ 0.03	69	$\pm$ 10	B
47171	1999 TC36	TNO		Ice	1.42	$\pm$ 0.02 $\times$ 10^{19}	A.136	402.46	$\pm$ 9.40	B.234	0.41	$\pm$ 0.03	58	$\pm$ 7	B
50000	Quaoar	TNO		Ice	1.60	$\pm$ 0.30 $\times$ 10^{21}		946.58	$\pm$ 137.26	B.235	3.60	$\pm$ 1.70	0	$\pm$ 47	C
58534	Logos	TNO		Ice	2.70	$\pm$ 0.30 $\times$ 10^{17}		110.00	$\pm$ 40.00		0.38	$\pm$ 0.42	61	$\pm\infty$	E
65489	Ceto	TNO		Ice	5.41	$\pm$ 0.42 $\times$ 10^{18}		250.58	$\pm$ 28.70	B.236	0.65	$\pm$ 0.23	34	$\pm$ 35	C
65803	Didymos	NEA		CM	5.24	$\pm$ 0.52 $\times$ 10^{11}		0.80	$\pm$ 0.08		1.90	$\pm$ 0.53	15	$\pm$ 28	C
66063	1998 RO1	NEA	S	OC	3.60	$\pm$ 1.80 $\times$ 10^{11}		0.68	$\pm$ 0.11	B.237	2.79	$\pm$ 1.47	15	$\pm$ 52	D
66391	1999 KW4	NEA	S	OC	2.35	$\pm$ 0.10 $\times$ 1012		1.31	$\pm$ 0.03		1.80	$\pm$ 0.29	45	$\pm$ 16	B
66652	Borasisi	TNO		Ice	3.75	$\pm$ 0.40 $\times$ 10^{18}		447.00	$\pm$ 90.00		0.08	$\pm$ 0.04	91	$\pm$ 61	D
88611	2001 QT297	TNO		Ice	2.36	$\pm$ 0.01 $\times$ 10^{18}	A.137	225.00	$\pm$ 75.00		0.39	$\pm$ 0.39	60	$\pm\infty$	E
90482	Orcus	TNO		Ice	6.34	$\pm$ 0.03 $\times$ 10^{20}	A.138	915.50	$\pm$ 42.58	B.238	1.57	$\pm$ 0.22	0	$\pm$ 13	B
134340	Pluto	TNO		Ice	1.30	$\pm$ 0.01 $\times$ 10^{22}		2390.00	$\pm$ 10.00		1.81	$\pm$ 0.02	0	$\pm$ 1	A
134860	2000 OJ67	TNO		Ice	2.14	$\pm$ 0.11 $\times$ 10^{18}		190.00	$\pm$ 65.00		0.59	$\pm$ 0.61	40	$\pm\infty$	E
136108	Haumea	TNO		Ice	4.01	$\pm$ 0.04 $\times$ 10^{21}	A.139	1244.99	$\pm$ 92.39	B.239	3.96	$\pm$ 0.88	0	$\pm$ 22	C
136199	Eris	TNO		Ice	1.66	$\pm$ 0.02 $\times$ 10^{22}		2357.83	$\pm$ 75.19	B.240	2.41	$\pm$ 0.23	0	$\pm$ 9	B
136617	1994 CC	NEA		CM	2.59	$\pm$ 0.13 $\times$ 10^{11}		0.62	$\pm$ 0.06		2.07	$\pm$ 0.61	7	$\pm$ 29	C
153591	2001 SN263	NEA		CM	9.17	$\pm$ 0.02 $\times$ 1012		2.59	$\pm$ 0.20		0.99	$\pm$ 0.22	55	$\pm$ 23	C
164121	2003 YT1	NEA		CM	1.27	$\pm$ 0.39 $\times$ 1012		1.08	$\pm$ 0.01	B.241	1.90	$\pm$ 0.59	15	$\pm$ 31	C
175706	1996 FG3	NEA	C	CM	4.27	$\pm$ 1.42 $\times$ 1012		1.75	$\pm$ 0.06	B.242	1.36	$\pm$ 0.65	39	$\pm$ 47	C
185851	2000 DP107	NEA		CM	4.60	$\pm$ 0.50 $\times$ 10^{11}		1.63	$\pm$ 0.35		0.95	$\pm$ 1.04	57	$\pm\infty$	E
276049	2002 CE26	NEA	C	CM	1.95	$\pm$ 0.25 $\times$ 10^{13}		3.46	$\pm$ 0.35		0.89	$\pm$ 0.29	60	$\pm$ 32	C
311066	2004 DC	NEA		CM	3.57	$\pm$ 0.36 $\times$ 1010		0.34	$\pm$ 0.03		1.73	$\pm$ 0.49	22	$\pm$ 28	C
1999	OJ4	TNO		Ice	3.91	$\pm$ 0.22 $\times$ 10^{17}		130.00	$\pm$ 45.00		0.33	$\pm$ 0.35	66	$\pm\infty$	E
2000	CF105	TNO		Ice	1.85	$\pm$ 0.12 $\times$ 10^{17}		188.00	$\pm$ 38.00		0.05	$\pm$ 0.03	94	$\pm$ 60	✗
2000	QL251	TNO		Ice	3.11	$\pm$ 0.05 $\times$ 10^{18}		150.00	$\pm$ 50.00		1.75	$\pm$ 1.76	0	$\pm\infty$	E
2000	UG11	NEA		CM	9.35	$\pm$ 1.59 $\times$ 10^{9}		0.30	$\pm$ 0.10		0.66	$\pm$ 0.67	70	$\pm\infty$	E
2001	QC298	TNO		Ice	1.08	$\pm$ 0.07 $\times$ 10^{19}		244.00	$\pm$ 55.00		1.41	$\pm$ 0.96	0	$\pm$ 67	D
2001	QW322	TNO		Ice	2.15	$\pm$ 0.18 $\times$ 10^{18}		128.00	$\pm$ 3.00		1.00	$\pm$ 1.00	0	$\pm\infty$	✗
2001	XR254	TNO		Ice	4.00	$\pm$ 0.17 $\times$ 10^{18}		225.00	$\pm$ 75.00		0.67	$\pm$ 0.67	32	$\pm\infty$	E
2003	QY90	TNO		Ice	1.01	$\pm$ 0.78 $\times$ 10^{18}		150.00	$\pm$ 50.00		0.57	$\pm$ 0.72	42	$\pm\infty$	E
2003	TJ58	TNO		Ice	2.25	$\pm$ 0.15 $\times$ 10^{17}		75.00	$\pm$ 25.00		1.01	$\pm$ 1.02	0	$\pm\infty$	E
2003	UN284	TNO		Ice	1.31	$\pm$ 0.26 $\times$ 10^{18}		124.00	$\pm$ 8.00		1.00	$\pm$ 1.00	0	$\pm\infty$	✗
2004	PB108	TNO		Ice	9.68	$\pm$ 0.57 $\times$ 10^{18}		140.00	$\pm$ 50.00		6.73	$\pm$ 7.22	0	$\pm\infty$	E
2005	EO304	TNO		Ice	2.10	$\pm$ 0.08 $\times$ 10^{18}		152.00	$\pm$ 2.00		1.00	$\pm$ 1.00	0	$\pm\infty$	✗
2006	BR284	TNO		Ice	5.70	$\pm$ 0.19 $\times$ 10^{17}		89.80	$\pm$ 0.90		1.00	$\pm$ 1.00	0	$\pm\infty$	✗
2006	JZ81	TNO		Ice	1.18	$\pm$ 0.51 $\times$ 10^{18}		122.00	$\pm$ 16.00		1.00	$\pm$ 1.00	0	$\pm\infty$	✗
2006	CH69	TNO		Ice	8.30	$\pm$ 2.75 $\times$ 10^{17}		99.99	$\pm$ 11.00		1.00	$\pm$ 1.00	0	$\pm\infty$	✗
2007	TY430	TNO		Ice	7.90	$\pm$ 2.10 $\times$ 10^{17}		50.00	$\pm$ 20.00		0.75	$\pm$ 1.00	25	$\pm\infty$	✗
	1P/Halley	COM		Ice	3.20	$\pm$ 1.20 $\times$ 10^{14}		10.39	$\pm$ 2.00		0.54	$\pm$ 0.37	45	$\pm$ 68	D
	2P/Encke	COM		Ice	9.20	$\pm$ 5.80 $\times$ 10^{13}		4.71	$\pm$ 0.81	B.243	1.67	$\pm$ 1.36	0	$\pm$ 81	D
	6P/dArest	COM		Ice	2.80	$\pm$ 0.80 $\times$ 10^{12}		1.70	$\pm$ 0.20		1.08	$\pm$ 0.49	0	$\pm$ 45	C

9P/Tempel1	COM	Ice	5.48	$\pm 0.56 \times 10^{13}$	A.140	6.00	± 0.20	B.244	0.48	± 0.06	51	± 14	B
10P/Tempel2	COM	Ice	3.50	$\pm 1.50 \times 10^{14}$		9.60	± 1.39		0.75	± 0.46	24	± 61	D
19P/Borrely	COM	Ice	2.70	$\pm 2.10 \times 10^{12}$		4.80	± 0.40		0.12	± 0.09	87	± 77	x
22P/Kopff	COM	Ice	5.30	$\pm 2.20 \times 10^{12}$		3.59	± 0.40		0.21	± 0.11	78	± 53	D
45P/H-M-P	COM	Ice	1.90	$\pm 3.50 \times 10^{11}$		0.66	± 0.20		1.26	± 2.59	0	$\pm \infty$	E
46P/Wirtanen	COM	Ice	3.30	$\pm 2.30 \times 10^{11}$		1.15	± 0.06		0.40	± 0.28	59	± 71	D
67P/C-G	COM	Ice	1.50	$\pm 0.60 \times 10^{13}$		2.96	± 0.10	B.245	0.43	± 0.37	56	± 85	D
81P/Wild2	COM	Ice	8.10	$\pm 0.81 \times 10^{12}$		2.08	± 0.06	B.246	0.10	± 0.10	30	± 14	B
SL9	COM	Ice	1.53	$\pm 0.15 \times 10^{12}$		1.79	± 0.18		0.50	± 0.05	50	± 10	B

Table 2
Average bulk density (ρ) measured on $\mathcal{N}_s$ sample of $\mathcal{N}_m$ meteorites used in Table 1: Ordinary chondrites (OC: H, L, and LL), Carbonaceous chondrites (CC: CI, CM, CR, CO, CV, and CK), Enstatites chondrites (EH and EL), Achondrites HED (*i.e.*, average of Howardites, Eucrites, and Diogenites), Stony-Iron (Pallasites, Mesosiderites, and Steinbach), and Iron meteorites (Ataxites and Hexahedrites). Terrestrial weathering has a strong effect on the porosity of found OCs with respect to fallen OCs (Consolmagno et al., 2008). Only measurements on falls are therefore used here. For the other meteorite classes, both finds and falls are used. The density of liquid water of 1.00 ± 0.10 is used as a proxy for the volatiles that compose icy bodies. **References**: (1) Consolmagno and Britt (1998). (2) Britt and Consolmagno (2003), (3) Consolmagno et al. (2008), (4) Macke et al. (2010), and (5) Macke et al. (2011).

Meteorite		ρ	$\mathcal{N}_s$	$\mathcal{N}_m$	Refs.
Ord. chondrites	H	3.42 ± 0.18	265	157	2,3
Ord. chondrites	L	3.36 ± 0.16	277	160	2,3
Ord. chondrites	LL	3.22 ± 0.22	149	39	2,3
Carb. Chondrites	CI	1.60 ± 0.03	14	4	2,3
Carb. Chondrites	CM	2.25 ± 0.08	33	18	2,3
Carb. Chondrites	CR	3.10	7	3	2
Carb. Chondrites	CO	3.03 ± 0.19	22	8	2,3
Carb. Chondrites	CV	2.79 ± 0.06	51	10	2,3
Carb. Chondrites	CK	2.85 ± 0.08	3	3	3
Enstatites	EH	3.47 ± 0.21	16	9	4
Enstatites	EL	3.46 ± 0.32	25	14	4
Achondrites	HED	3.25 ± 0.26	96	56	5
Stony-Iron	Pal	4.76 ± 0.10	10	5	2
Stony-Iron	Mes	4.35 ± 0.02	8	3	2
Stony-Iron	Ste	4.18 ± 0.10	2	1	2
Iron	Ata	4.01 ± 0.04	1	1	1
Iron	Hex	7.37 ± 0.14	2	2	1
Iron	Oct	7.14 ± 0.13	5	5	1

relative accuracy better 20% only, the statistic is however based on low-numbers (see Table 3). The situation is particularly dramatic for end-members: only K-type and V-types have reliable estimates. The number of density estimates for comets and TNOs also drops with increasing levels of relative precision (Table 3).

The density estimates are plotted in Fig. 7, regrouped into six categories: TNOs, comets, and four asteroid groups: S-, C-, and X-complexes, and end-members. Macroporosity estimates (Eq. (2)) are similarly plotted in Fig. 8. Several trends can be observed:

- Asteroids in the S-complex are more dense than those in the C-complex (confirming Britt et al. (2002) findings).
- Asteroids in the C-complex seem to have larger macroporosity than those in the S-complex.
- The density of asteroids from both the S-complex and the C-complex seems to increase with the mass, apparently resulting from a decreasing macroporosity.
- In both C- and S-complexes, NEAs seem to have a lower density than MBAs, following the trend between mass and density observed for MBAs.
- At comparable sizes, B-types appear significantly denser ($\rho \sim 2.4$) than the other types of the C-complex that gather around $\rho \sim 1.4$.
- The density of the X-complex asteroids covers a large range, from the most dense Xc-types with $\rho \sim 4.9$ to X-types with $\rho \sim 1.8$.
- Comets have very low densities ($\rho \sim 0.5$), low even considering their volatile-rich composition (in agreement with spacecraft observations, see, Richardson et al., 2007).
- The density of TNOs covers a large range, from comet-like ($\rho \sim 0.5$) to the rocky (50 000) Quaoar ($\rho \sim 3.6$).
- Dwarf-planets apparently have no macroporosity, contrary to small bodies whose masses are inferior to $\approx 10^{20}$ kg.
- For each type of small body, the dispersion in density and macroporosity is huge.

Table 3
Average density ρ_i for each asteroid taxonomic type (DeMeo et al., 2009), based on $\mathcal{N}_i$ estimates. The *i* indices stand for the level of accuracy considered: more accurate than 20%, 50%, and no restriction on precision (∞). For each class, the associated meteorite (Met., see Table 2) and number of asteroids observed by DeMeo et al. (2009) with the corresponding fraction represented by the class are reported. The average density for transneptunian objects and comets are also reported.

Type	Met.	Taxonomy		Average density for each class					
		(#)	(%)	$\mathcal{N}_\infty$	ρ_∞	$\mathcal{N}_{50}$	ρ_{50}	$\mathcal{N}_{20}$	ρ_{20}
S	OC	144	38	50	2.66 ± 1.29	28	2.70 ± 0.69	11	2.72 ± 0.54
Sa	OC	2	<1	1	1.07 ± 0.25	1	1.07 ± 0.25		–
Sq	OC	29	7	5	2.78 ± 0.85	4	2.78 ± 0.81	2	3.43 ± 0.20
Sr	OC	22	5		–		–		–
Sv	OC	2	<1		–		–		–
B	CV	4	1	10	2.19 ± 1.00	4	2.15 ± 0.74	2	2.38 ± 0.45
C	CM	13	3	33	1.57 ± 1.38	19	1.41 ± 0.69	5	1.33 ± 0.58
Cb	CM	3	<1	13	1.88 ± 2.09	6	1.43 ± 0.74	3	1.25 ± 0.21
Cg	CM	1	<1	1	0.96 ± 0.27	1	0.96 ± 0.27		–
Cgh	CM	10	2	5	2.64 ± 1.35	1	3.48 ± 1.06		–
Ch	CM	18	4	47	1.96 ± 1.65	27	1.70 ± 1.10	9	1.41 ± 0.29
X	CV	4	1	26	2.87 ± 2.59	15	1.99 ± 0.99	8	1.85 ± 0.81
Xc	Mes	3	<1	9	4.96 ± 2.39	3	4.63 ± 0.76	2	4.86 ± 0.81
Xe	EH	7	1	4	2.94 ± 0.85	2	2.91 ± 0.65	1	2.60 ± 0.20
Xk	Mes	18	4	13	3.85 ± 1.27	9	3.79 ± 1.18	3	4.22 ± 0.65
D	CM	16	4	3	9.56 ± 0.22		–		–
K	CV	16	4	2	4.25 ± 2.03	1	3.54 ± 0.21	1	3.54 ± 0.21
L	CO	22	5	4	3.24 ± 1.03	3	3.22 ± 0.97		–
T	Ata	4	1	1	2.61 ± 2.54		–		–
A	Pal	6	1	1	3.73 ± 1.40	1	3.73 ± 1.40		–
O	OC	1	<1		–		–		–
Q	OC	8	2		–		–		–
R	OC	1	<1	1	2.23 ± 1.02	1	2.23 ± 1.02		–
V	HED	17	4	3	1.93 ± 1.07	3	1.93 ± 1.07	3	1.93 ± 1.07
Transneptunian objects				22	0.77 ± 0.80	10	1.06 ± 0.80	6	1.06 ± 0.75
Comets				12	0.47 ± 0.25	4	0.56 ± 0.14	3	0.54 ± 0.09

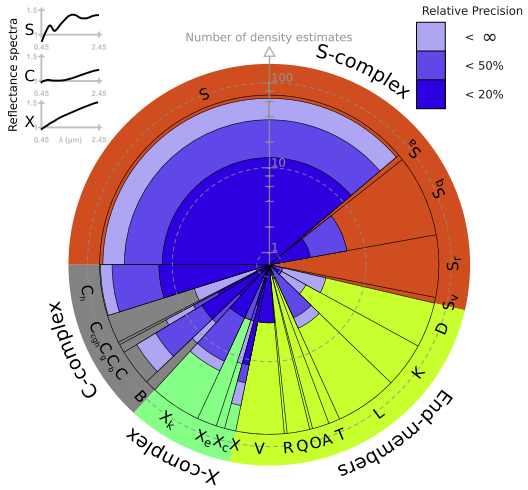

Fig. 6. Pie chart showing the fraction of asteroids within each class of the taxonomy by DeMeo et al. (2009), based on 371 objects. Complexes (C, S, and X) and end-members are displayed in gray, red, green and yellow respectively. Typical reflectance spectra of the complexes are also reported (top left). For each class, the number of density estimates, with a relative precision better than 20%, 50%, and regardless to the precision (∞), are drawn in blue wedges. (For interpretation of the references to color in this figure caption, the reader is referred to the web version of this article.)

These trends are discussed below. The large dispersion of values is however attributed to observational and methodological biases, rather than to genuine physical effects. Indeed, when considering different levels of accuracy, the distributions narrow with precision. In other words, biased estimates artificially spread the density distribution, hence the need for *realistic* evaluation of uncertainties.

5.1. C-complex and sub-groups

Most of the asteroids in the C-complex have densities ranging from the highly porous (253) Mathilde ($\rho \sim 1.3$) to the dense (2) Pallas ($\rho \sim 2.9$). This interval overlaps with CCs meteorites, and the structure of these asteroids ranges from large, compact, bodies ($\mathcal{P} \sim 0\%$) to rubble-piles ($\mathcal{P} \sim 40{-}60\%$). This trend for large bodies to present a zero macroporosity can be explained by the high pressure of their interiors. Following Britt et al. (2002), and references therein, silicate grains start to fracture when the pressure reaches $\sim 10^7$ Pa. This threshold is reached within the first few kilometers from the surface of large bodies, allowing a thin layer only to host macroporosity. Because large-scale *grains* (*i.e.*, rubble) are expected to grind at much smaller pressures, the transition from compact to fractured bodies is expected to be smooth.

Indeed, these different structures are apparently correlated with the mass of the asteroids (Fig. 9). The correlation coefficient between density and diameter is 68% and this trend seems real although the sample is still size-limited. From this trend (the linear regression in Fig. 9), the mass of hypothetical asteroids made of each type of CCs meteorites, without macroporosity, are all within $10^{19}{-}10^{20}$ kg, corresponding to the observed transition between compact and fractured asteroids. This suggests that large C-complex asteroids ($\phi \geq 300$ km) have intact structures, while smaller asteroids have porous interiors because the internal pressure never reaches the threshold for silicate compaction. This is consistent with the current vision of the dynamical history of the Main Belt: large asteroids survived intact throughout the history of the Solar System, while most of the material was removed or grinded into pieces (Morbidelli et al., 2009). This is

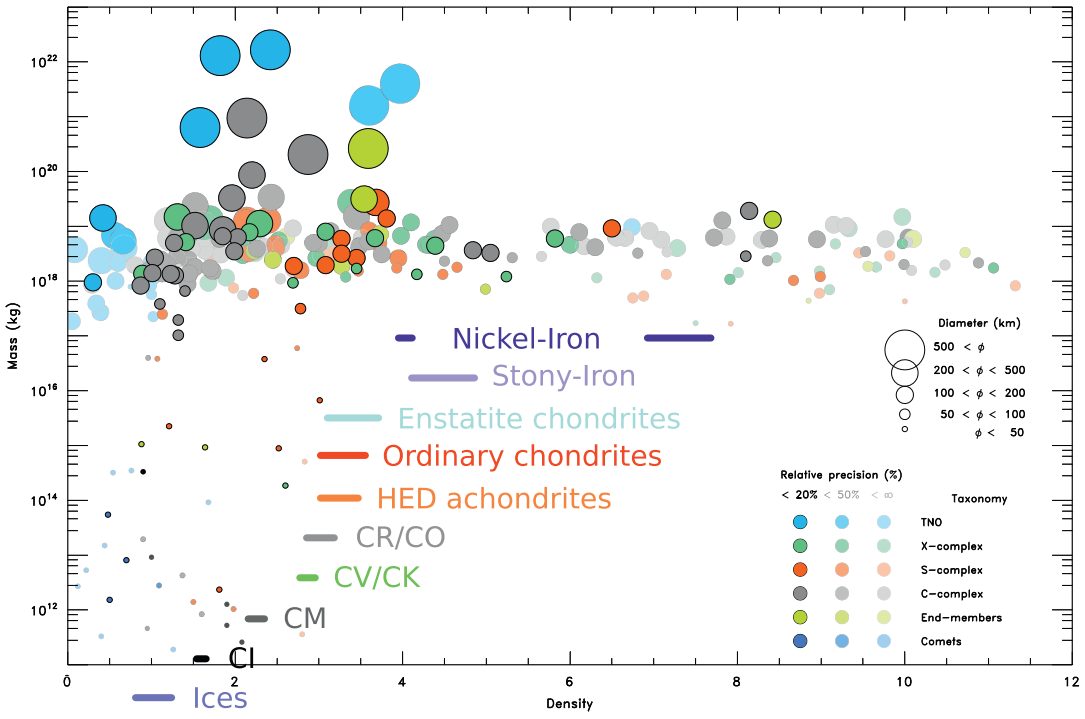

Fig. 7. Density vs. Mass. Small bodies are divided into six categories: TNOs (light blue), comets (blue), and asteroids (all dynamic class together) divided into four taxonomic groups: S-complex in red, C-complex in grey, X-complex in green, and end-members in yellow (similar to Fig. 6). Asteroids which taxonomy is unknown are plotted in black. The size of the symbols is a function of the object diameters, and the three different levels of contrast correspond to three cuts of relative accuracy: $<20\%$, $<50\%$, and regardless to the precision ($<\infty$). The density of the different class of meteorites is also drawn, at arbitrary masses (Table 2). (For interpretation of the references to color in this figure caption, the reader is referred to the web version of this article.)

also supported by the apparent lower density of about 1.2 for the 7 NEAs, with respect to about 2 for the 53 MBAs.

Among the C-complex, B-types have distinct surface properties: negative spectral slope in the visible and higher albedo (see the compilation of albedo per taxonomic class from Ryan and Woodward (2010); Usui et al. (2011); Masiero et al. (2011)). From a comprehensive comparison of 22 C-complex asteroids with laboratory spectra of meteorites, Clark et al. (2010) indeed found that spectra of C-types were best matched by aqueous-altered CI/CM carbonaceous chondrites while those of B-types by other CCs sub-groups (mainly CO, CV, but also CK and CR). This is supported by the density estimates (Table 3): B-types are significantly denser ($\rho \sim 2.4$) than the other types of the C-complex, following the trend observed in meteorites. Although only two B-types have density estimates more accurate than 20%, (2) Pallas and (704) Interamnia, this trend of a larger density is constantly found at different levels of precision (Table 3) and diameters (Table 1). B-types are thus intrinsically more dense than the other C-types, independently from the mass-density trend observed among C-complex asteroids (see above). Therefore, in addition to albedo and reflectance spectra that point toward different surface properties/composition, density suggests that there are fundamental differences in the composition and internal structures of B-types. The recent recovery of the Almahata Sitta meteorite, originating from the impact of asteroid 2008 TC_3 on Earth in October 2008, indeed indicated that B-type could be associated with unusual Ureilite achondrites (Jenniskens et al., 2009). Based on a comparison of the densities of (1) Ceres and (2) Pallas (used as archetypes for the definition of C and B taxonomic classes), Carry et al. (2010a) had suggested that B-types were less hydrated than C-types; a hypothesis supported by the lack of signature of organic or icy material in their spectra (Jones et al., 1990).

Finally, the three D-types have density estimates of around 9. These estimates were discarded from the analysis, as their uncertainty range does not overlap with meteorites, even the highly dense iron hexahedrites (Table 2).

5.2. S-complex and related end-members

The density of S-complex asteroids is distributed in a narrow interval (about 2 to 3), slightly below the density of their associated meteorites, the ordinary chondrites. The resulting macroporosity is generally smaller than 30%, *i.e.*, these asteroids may present cracks and fractures but are still coherent (not rubble-piles). This highlights intrinsic differences with the C-complex. The higher density is revelatory of the difference in composition: *basaltic* ordinary chondrites vs. *primitive* CI/CM carbonaceous chondrites. The lower macroporosity suggests a difference in formation and response to shocks. S-complex asteroids are made of *igneous* rocks, *i.e.*, they experienced a stage of high temperatures and were partly or entirely melted. If S-types acquired some cohesion in the process, subsequent impacts would have either not enough energy to overpass this cohesion barrier, leaving them with cracks and fractures only, or enough energy to break their

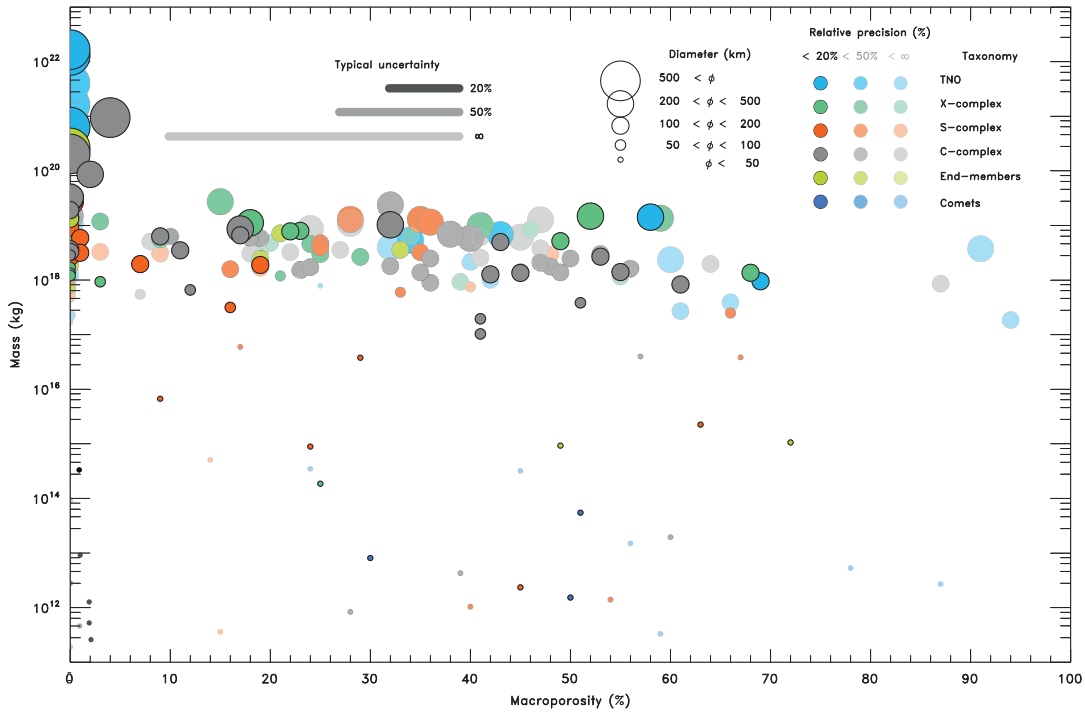

Fig. 8. Macroporosity vs. Mass. The color and size of the symbols are similar to Fig. 7. Macroporosity is obtained from Eq. (2) and the asteroid–meteorite links listed in Table 3. The typical uncertainty in macroporosity for three precision level on density are displayed (20%, 50%, and regardless to the precision: ∞). Additionally, an erroneous asteroid–meteorite link can shift any value by 30–40%. (For interpretation of the references to color in this figure caption, the reader is referred to the web version of this article.)

structure and destroy them ("battered to bits": Burbine et al. (1996)). The current S-complex asteroids would therefore be the few remnants of an originally much larger population (Morbidelli et al., 2009).

There are only four density estimates of asteroids belonging to the A and V classes. The only A-type, (354) Eleonora, has a density of 3.7 $\pm$ 1.4, much higher than S-types. This value is in agreement with the density of terrestrial olivines and stony-iron Pallasites meteorites (Section 2 and Table 2), although the rough relative accuracy allows a wide range of possibilities. Average density of the three V-types is surprisingly low: $\approx$1.9. A close inspection however reveals that (4) Vesta has a high density of 3.6 while the two 10 km-sized (809) Lundia and (854) Frostia have low densities of 1.6 and 0.9 respectively. These density measurements are hardly comparable. Vesta is a differentiated asteroid with a pyroxene-rich crust, analog to the HED meteorites, and a denser olivine-rich mantle (*e.g.*, McCord et al., 1970; Binzel et al., 1997). The low density of Lundia and Frostia implies a high macroporosity, above 50%, in the rubble-pile regime. Owing to their small size, they are the product of the collisional disruption of a larger parent body, and such a porous structure is not so surprising.

5.3. X-complex, or X melting pot?

The large spread in density and macroporosity of asteroids in the X-complex does not reduce with increasing levels of accuracy, contrary to the other groups of small bodies. This suggests that multiple compositions are present in the complex. This is supported by the many different proposed analog meteorites (see Section 2) and wider distribution of albedo with respect to C- and S-complexes (Figure 9 by Ryan and Woodward, 2010). The current definition of the X-complex (DeMeo et al., 2009) indeed encompass the former E, M, and P groups that were distinguished owing to their albedo (Tholen and Barucci, 1989).

Both Xc and Xk class have densities above 4, in the range of stony-iron and iron meteorites (Table 2). The density of X-types and Xe-types is lower, at about 1.8 and 2.6 respectively, closer to the proposed CV carbonaceous chondrites and enstatite chondrites meteorites. These asteroids have been grouped together in the taxonomy by DeMeo et al. (2009) owing to their spectra similarity. Given the low-contrast of their reflectance spectra, however, this grouping may be artificial. Many different compositions are likely to be represented among the X-complex. Further understanding and classification of these asteroids will benefit using a larger wavelength range (*e.g.*, Vernazza et al., 2011b) and albedo (*e.g.*, Ockert-Bell et al., 2010; Fornasier et al., 2011).

5.4. Dwarf-planets and small bodies

There are only eight small bodies more massive than 10^{20} kg: Ceres, Pallas, Vesta, Quaoar, Orcus, Pluto, Haumea, and Eris. These objects have diameters larger than 500 km and can be considered dwarf-planets. Their density is high, between 2 and 4, above that of their analog meteorites. This population particularly stands out in Fig. 8, where the dwarf-planets ($M \geq 10^{20}$ kg) are all packed near the $\mathcal{P} \approx 0$ axis, and the other small bodies below 10^{20} kg are

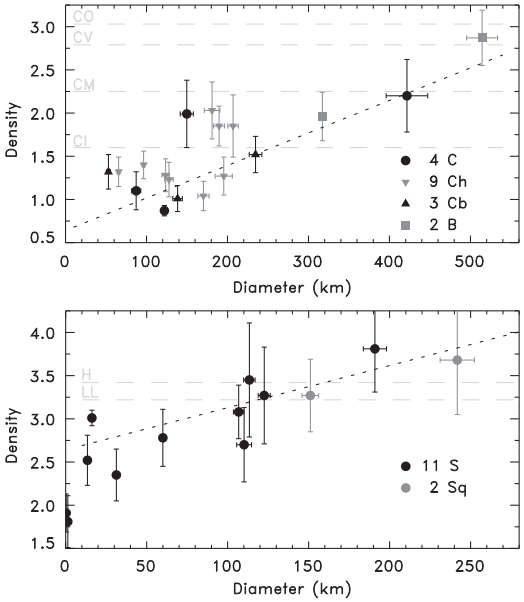

Fig. 9. Density *vs.* diameter. **Top:** The 18 asteroids in the C-complex (20% relative precision only, without Ceres). Average density for the CI, CM, CV, and CV carbonaceous chondrites is also reported (light grey horizontal dashed lines). The oblique dotted line is a linear regression on this sample with a correlation coefficient of 68%. **Bottom:** The 13 asteroids in the S-complex (20% relative precision only). Average density for the LL and H ordinary chondrites are also reported (light grey horizontal dashed lines). The oblique dotted line is a linear regression on this sample with a correlation coefficient of 51%.

spread over the entire graph. This suggests that these bodies are differentiated, with the presence of higher density material below the surface, *e.g.*, silicate or iron cores (Fraser and Brown, 2010; Castillo-Rogez and McCord, 2010).

The majority (75%) of the small bodies in the sample compiled here are main-belt and Trojan asteroids with masses between 10^{17} and 10^{20} kg. These asteroids have diameters between 50 and 400 km, densities between 0.9 and 5.8, and macroporosities up to 70%, from the highly porous (90) Antiope to the very compact asteroid (46) Hestia. The pressure inside an object with a mass lower than $\approx 10^{20}$ kg never reaches 10^7 Pa (the threshold for silicate grain compaction, see Section 5.1, Fig. 9, and Consolmagno et al., 2008). These high levels of macroporosity are therefore not unexpected. The broad range of densities is more surprising. It is partly due to different compositions of these objects, but also to the often large biases affecting the density estimates. Indeed, the fraction of asteroids with densities lower than 4 decreases from 56% to 16% by considering the estimates more precise than 20% only. Said differently, most of the small bodies with a density larger than ≈ 4 suffer from low-precision estimates with underestimated volume and/or overestimated mass.

This is supported by the distribution of density and macroporosity among NEAs ($M \leq 10^{17}$ kg). If the macroporosity of NEA also spans a similar range up to 70%, the most dense NEA is (433) Eros, with $\rho \sim 3$ *only*. By opposition to MBAs, all the mass estimates available for NEA were derived from a spacecraft encounter or from the orbit of a satellite, the most-precise techniques (Fig. 1). The accuracy on their density is therefore limited by the relative precision of their volume-equivalent diameters, which is generally less affected by biases (Section 4). The distribution of density among NEAs may therefore be more representative of the *real* density distribution than what we now observe for main-belt asteroids. Because NEAs only represent 6% of the sample presented here, strong efforts to improve the mass estimates of MBAs must be undertaken.

5.5. Transneptunian objects

This population includes a wide range of sizes, from dwarf-planets such as Pluto with diameters above 2000 km down to small bodies of a few tens of kilometers. All of the 28 TNOs listed in Table 1 have satellites and the main source of uncertainty is the precision on volume estimates, similar to NEAs. The situation is however worse for TNOs. Indeed, volume estimates from thermal radiometry (*e.g.*, Lellouch et al., 2010), stellar occultation (*e.g.*, Sicardy et al., 2011) or direct imaging (*e.g.*, Fraser and Brown, 2010) are available for the few larger TNOs only. The diameter of 11 TNOs was roughly estimated from their apparent magnitude. Given the lack of knowledge on their albedo and the 20% uncertainty affecting albedo estimates (see, Lim et al., 2010), only crude diameter estimates can be derived (Fig. 4a). The diameters of seven additional TNOs have been estimated from an *assumed* density of 1.0 (Parker et al., 2011; Sheppard et al., 2012). Only 10 density estimates were therefore determined from *direct* measurements. Of these, only five have a relative precision better than 20%: 1999 TC_{36}, Typhon, Orcus, Pluto, and Eris.

The five TNOs larger than ≈ 1000 km have densities above 1.5, indicating differentiated interiors as described before (Section 5.4). On the contrary, the five other 100 km-sized TNOs have densities around 0.5, indicative of highly porous structures ($\mathcal{P} \geq 50\%$). The increase in macroporosity for smaller objects is similar to that observed for asteroids. Current asteroid and TNO populations are the result of collisions over History and such similarities are therefore expected.

5.6. Comets

The comets are the least massive objects listed here, from 10^{14} to 10^{17} kg. With a diameter of typically a few hundred meters to a couple of kilometers and a very bright coma with respect to the nucleus itself as soon as they are active, observations of comet nuclei are very difficult. Current knowledge of the physical properties of comet nuclei is therefore still limited (Lamy et al., 2004).

The comets have a very low density: nine of the 12 comets listed here have a density below 1. The weighted average density of all 12 comets is 0.47 ± 0.25 only, marginally below the limit value of 0.6 inferred from rotation properties (*e.g.*, Lamy et al., 2004; Snodgrass et al., 2006). The resulting macroporosity is generally high ($\mathcal{P} \geq 30-50\%$), consistent with our current understanding of the structure of a comet nucleus: a highly porous assemblage of ices and silicates (see, Weissman et al., 2004, for a review). These values of density and macroporosity are consistent with those of the small-sized TNOs (Section 5.5). This is reassuring given that TNOs are thought to be the reservoir of Jupiter-family comets (Jewitt, 2004).

6. Perspectives

Our knowledge on the density and macroporosity of small bodies has seen a revolution in the last 10 years, from 17 objects listed by Britt et al. (2002), to 40 by Consolmagno et al. (2008), to 287 here. If the sample has increased by about an order of magnitude, only a third of the density estimates have a relative

precision better than 20%. Improving the accuracy of mass and volume estimates is therefore necessary. Several lines of investigations are still required to improve our understanding of asteroids composition and internal structure.

6.1. Asteroid-meteorite link

As briefly described in Section 2, only half of the 24 classes of the asteroid taxonomy have mineralogy interpretations (DeMeo et al., 2009). Together with the dynamic of asteroids, it is one of the fundamental knowledge required to constrain the models of planetary formation (*e.g.*, Morbidelli et al., 2005; Walsh et al., 2011). Efforts to determine the surface properties must be continued. Irradiation experiments in the laboratory have allowed to understand the space weathering processes on the surfaces of olivines- and pyroxenes-rich S-complex asteroids (see, Chapman, 1996; Strazzulla et al., 2005; Vernazza et al., 2006, 2009a, among many others), including the related end-members A- and V-types (Brunetto et al., 2007; Fulvio et al., 2012). The influence of the space weathering on the reflectance spectra of most meteorite types is however still unknown, apart from some experiments on enstatite chondrites and mesosiderites (Vernazza et al., 2009b).

Mid-infrared spectroscopy (2–5 and 5−40 μm range) will also help refining the mineralogy (*e.g.*, Rivkin et al., 2002; Emery et al., 2006), providing the regolith packing can be reproduced in the laboratory (*e.g.*, Vernazza et al., 2010, 2011a; King et al., 2011). Albedo measurements should also be used (Fornasier et al., 2011), although the typical uncertainty of about 20% that can be expected from simple thermal models (Lim et al., 2010) may preclude strong conclusions for the time being. Density can also greatly help in that respect. The comparison of bulk density resulting from the possible composition with the asteroid bulk density may confirm or invalidate the composition (Sierks et al., 2011). Refining the asteroid–meteorite links will allow to secure the macroporosity estimates, hence our knowledge of the interior of small bodies.

6.2. Accurate mass estimates

Estimating any mass at all is the limiting factor in determining the density of small bodies (*e.g.*, Consolmagno et al., 2008). Furthermore, in most of the cases, the density accuracy is hampered by the large uncertainty of mass estimates (Section 4.2). Improving the number and accuracy of mass estimates is therefore required.

The study of binary systems is highly relevant in that respect. It is the most productive method to determine accurate mass estimates (Fig. 1c). However, only a third of the 200 known binaries have a mass estimate (Section 4.1). Most of the binaries were indeed discovered from lightcurves, and their angular separation is too small to be resolved. Upcoming facilities such as the ALMA interferometer or the E-ELT will provide the angular resolution required to resolve these systems, and many more accurate mass determinations should be available in few years. Additional optical and radar imaging observations, together with lightcurves of mutual events of known binaries, will also help improving the current mass estimates (*e.g.*, Descamps et al., 2008).

In parallel, the astrometry observations by Gaia will provide additional mass determinations. Around 350 000 small bodies are expected to be observed during the 5 years mission, with an average of 50 to 60 epochs on each (Mignard et al., 2007). The micro-arcsecond precision of Gaia's astrometry will allow to refine the accuracy on the orbit of asteroids by several orders of magnitude. Such a precision will have a snowball effect on subsequent mass estimates from planetary ephemeris and orbit deflections. Close encounters between asteroids will also be observed during the mission and the mass of about 50 asteroids with an expected relative precision better than 10% will be determined (Mouret et al., 2007). Although most of these objects are most likely already listed in Appendix A, the mass estimates are expected to be less affected by biases, owing to the unprecedented completeness of Gaia catalog. The number of mass estimates and their level of accuracy is therefore expected to improve significantly at the 2020 horizon.

6.3. Accurate volume estimates

As described in Section 4, the contributions of the mass and diameter uncertainties to the density uncertainty are not even. The precision on the diameter is indeed the limiting factor of the most accurate density estimates (see also Fig. 3). Relative precision on the *volume* below 10–15% is required to take advantage of any mass determination. The accuracy on the *diameter* should therefore be of a few percent at most. Thanks to improved observing facilities and from improved methods of analysis, our understanding of the physical properties of asteroids as seen a revolution in last decade, making such a goal achievable.

Many different observing techniques and methods of analysis can be used to evaluate the diameter of small bodies. In particular, multi-data approaches have been proven successful in determining the 3-D shape, size, and spin axis of small bodies (see Section 4.2). The recent flyby of asteroid (21) Lutetia by the ESA Rosetta mission showed that the diameter estimate derived before the flyby from optical lightcurves and disk-resolved images was accurate to 2% (using the KOALA 3-D shape modeling algorithm, see, (Kaasalainen, 2011; Carry et al., 2010b, 2012). Besides, 3-D shape models offer the possibility to analyze thermal radiometry data with more advanced thermal models (*e.g.*, Lagerros, 1996, 1997; Müller et al., 2005; Mueller et al., 2006; Delbo and Tanga, 2009; Rozitis and Green, 2011; O'Rourke et al., 2012). Such models allow to derive several surface properties such as the albedo and thermal inertia. These quantities can in turn be used to help constraining the asteroid–meteorite links (Section 6.1). Large observing programs (*e.g.*, lightcurves, adaptive-optics disk-resolved images on large telescopes, stellar occultation campaigns) to derive 3-D shape models of all the small bodies listed in Table 1 have therefore far-reaching implications.

7. Conclusion

An extensive review of current knowledge on the density and macroporosity of small bodies is presented. The density estimates of 287 small bodies are presented, computed from 994 mass estimates, 1454 volume-equivalent diameter estimates, and 24 indirect density estimates. All the dynamical classes are represented in the sample: 17 near-Earth asteroids, 230 Main-Belt and Trojan asteroids, 12 comets, and 28 transneptunian objects. The accuracy and biases affecting mass and diameter estimates are discussed and best-estimates are strictly selected. Bulk densities are computed and compared with meteorite density, allowing to estimate the macroporosity. Although the sample still suffers from large uncertainties and often biases (Sections 4 and 5), several trends can be identified:

1. Dwarf-planets apparently have no macroporosity, contrary to small bodies whose mass is inferior to $\approx 10^{20}$ kg.
2. Asteroids in the S-complex are more dense than those in the C-complex that in turn present a larger macroporosity.

3. There is a trend of increasing density with mass for asteroids in both S- and C-complexes. This trends is also visible from the lower density of NEAs with respect to MBAs.
4. B-types seem structurally different from other C-complex asteroids (albedo, reflectance spectra, density).
5. The X-complex encompasses many different compositions and should be revised using additional data (*e.g.*, albedo).
6. Comets and TNOs have similar low density and high macroporosity, consistent with a structure of porous icy agglomerates.

Several lines of investigations to improve the number and accuracy of density estimates are discussed. The search for binary asteroids and subsequent orbital analysis, together with detailed 3-D shape modeling from multi-data inversion techniques stand out as key programs.

Acknowledgments

A big thank you to P. Tanga and D. Hestroffer for poking me about coming to the Gaia GREAT meeting in Pisa, without them I wouldn't have started this painful (but fruitful!) task of compiling masses. Dankeschön, merci to T. Müller, F. Marchis and A. Fienga for sharing their results ahead of publication. Thanks to F. DeMeo for constructive discussions. Thank you to the two anonymous referees for their constructive comments. As a result, the present manuscript includes a significantly higher amount of material in the introductory sections. Gracias R. Soja and E. Treguier for all our discussions about this topic and for the fun in the office. This research made heavy use of NASA's Astrophysics Data System Abstract Service (ADS) and Data Archive, thanks to the developers and maintainers.

Appendix A. Supplementary material

Supplementary data associated with this article can be found in the online version at doi:http://dx.doi.org.10.1016/j.pss.2012.03.009.

References

Baer, J., Chesley, S.R., 2008. Astrometric masses of 21 asteroids, and an integrated asteroid ephemeris. Celestial Mechanics and Dynamical Astronomy 100, 27–42.
Baer, J., Chesley, S.R., Matson, R.D., 2011. Astrometric masses of 26 asteroids and observations on asteroid porosity. Astronomical Journal 141, 143–155.
Baer, J., Milani, A., Chesley, S.R., Matson, R.D., 2008. An observational error model, and application to asteroid mass determination. Bulletin of the American Astronomical Society 141, 493.
Barucci, A., Belskaya, I., Fornasier, S., Fulchignoni, M., Clark, B.E., Coradini, A., Capaccioni, F., Dotto, E., Birlan, M., Leyrat, C., Sierks, H., Thomas, N., Vincent, J.B., 2012. Overview of Lutetia's surface composition. Planetary and Space Science 66 (1), 23–30.
Barucci, M.A., Brown, M.E., Emery, J.P., Merlin, F., 2008. Composition and surface properties of transneptunian objects and centaurs. The Solar System Beyond Neptune, 143–160.
Barucci, M.A., Fulchignoni, M., Fornasier, S., Dotto, E., Vernazza, P., Birlan, M., Binzel, R.P., Carvano, J.M., Merlin, F., Barbieri, C., Belskaya, I.N., 2005. Asteroid target selection for the new Rosetta mission baseline. 21 Lutetia and 2867 Steins. Astronomy and Astrophysics 430, 313–317.
Behrend, R., Bernasconi, L., Roy, R., Klotz, A., Colas, F., Antonini, P., Aoun, R., Augustesen, K., Barbotin, E., Berger, N., Berrouachdi, H., Brochard, E., Cazenave, A., Cavadore, C., Coloma, J., Cotrez, V., Deconihout, S., Demeautis, C., Dorseuil, J., Dubos, G., Durkee, R., Frappa, E., Hormuth, F., Itkonen, T., Jacques, C., Kurtze, L., Laffont, A., Lavayssière, M., Lecacheux, J., Leroy, A., Manzini, F., Masi, G., Matter, D., Michelsen, R., Nomen, J., Oksanen, A., Pääkkönen, P., Peyrot, A., Pimentel, E., Pray, D.P., Rinner, C., Sanchez, S., Sonnenberg, K., Sposetti, S., Starkey, D., Stoss, R., Teng, J.P., Vignand, M., Waelchli, N., 2006. Four new binary minor planets: (854) Frostia, (1089) Tama, (1313) Berna, (4492) Debussy. Astronomy and Astrophysics 446, 1177–1184.
Bell, J.F., Davis, D.R., Hartmann, W.K., Gaffey, M.J., 1989. Asteroids—The big picture. Asteroids II, 921–945.
Binzel, R.P., Gaffey, M.J., Thomas, P.C., Zellner, B.H., Storrs, A.D., Wells, E.N., 1997. Geologic mapping of Vesta from 1994 Hubble space telescope images. Icarus 128, 95–103.
Bottke Jr., W.F., Cellino, A., Paolicchi, P., Binzel, R.P., 2002a. An overview of the asteroids: the asteroids III perspective. Asteroids III, 3–15.
Bottke Jr., W.F., Nesvorný, D., Grimm, R.E., Morbidelli, A., O'Brien, D.P., 2006. Iron meteorites as remnants of planetesimals formed in the terrestrial planet region. Nature 439, 821–824.
Bottke Jr., W.F., Vokrouhlický, D., Rubincam, D.P., Broz, M., 2002b. The effect of Yarkovsky thermal forces on the dynamical evolution of asteroids and meteoroids. Asteroids, 395–408.
Britt, D.T., Bell, J.F., Haack, H., Scott, E.R.D., 1992. The reflectance spectrum of troilite and the T-type asteroids. Meteoritics 27, 207.
Britt, D.T., Consolmagno, G.J., 2003. Stony meteorite porosities and densities: a review of the data through 2001. Meteoritics and Planetary Science 38, 1161–1180.
Britt, D.T., Yeomans, D.K., Housen, K.R., Consolmagno, G.J., 2002. Asteroid density, porosity, and structure. Asteroids III 1, 485–500.
Brown, M.E., Bouchez, A.H., Rabinowitz, D.L., Sari, R., Trujillo, C.A., vanDam, M.A., Campbell, R.D., Chin, J.C.Y., Hartman, S.K., Johansson, E.M., Lafon, R.E., LeMignant, D., Stomski Jr., P.J., Summers, D.M., Wizinowich, P.L., 2005. Keck observatory laser guide star adaptive optics discovery and characterization of a satellite to the large Kuiper belt pbject 2003 EL_{61}. Astrophysical Journal 632, L45–L48.
Brown, M.E., Ragozzine, D., Stansberry, J., Fraser, W.C., 2010. The size, density, and formation of the Orcus–Vanth system in the Kuiper belt. Astronomical Journal 139, 2700–2705.
Brown, M.E., Schaller, E.L., Roe, H.G., Rabinowitz, D.L., Trujillo, C.A., 2006. Direct measurement of the size of 2003 UB313 from the Hubble space telescope. Astrophysical Journal 643, L61–L63.
Brown, M.E., Trujillo, C.A., 2004. Direct measurement of the size of the large Kuiper belt object (50000) Quaoar. Astronomical Journal 127, 2413–2417.
Brunetto, R., de León, J., Licandro, J., 2007. Testing space weathering models on A-type asteroid (1951) Lick. Astronomy and Astrophysics 472, 653–656.
Brunetto, R., Vernazza, P., Marchi, S., Birlan, M., Fulchignoni, M., Orofino, V., Strazzulla, G., 2006. Modeling asteroid surfaces from observations and irradiation experiments: the case of 832 Karin. Icarus 184, 327–337.
Burbine, T.H., Duffard, R., Buchanan, P.C., Cloutis, E.A., Binzel, R.P., 2011. Spectroscopy of O-type asteroids. In: Lunar and Planetary Institute Science Conference Abstracts, p. 2483.
Burbine, T.H., McCoy, T.J., Meibom, A., Gladman, B., Keil, K., 2002. Meteoritic parent bodies: their number and identification. Asteroids III, 653–667.
Burbine, T.H., Meibom, A., Binzel, R.P., 1996. Mantle material in the main belt: battered to bits? Meteoritics and Planetary Science 31, 607–620.
Bus, S.J., 1999. Compositional Structure in the Asteroid Belt: Results of a Spectroscopic Survey. Ph.D. Thesis, Massachusetts Institute of Technology.
Carry, B., Dumas, C., Kaasalainen, M., Berthier, J., Merline, W.J., Erard, S., Conrad, A.R., Drummond, J.D., Hestroffer, D., Fulchignoni, M., Fusco, T., 2010a. Physical properties of (2) Pallas. Icarus 205, 460–472.
Carry, B., Hestroffer, D., DeMeo, F.E., Thirouin, A., Berthier, J., Lacerda, P., Sicardy, B., Doressoundiram, A., Dumas, C., Farrelly, D., Müller, T.G., 2011. Integral-field spectroscopy of (90482) Orcus–Vanth. Astronomy and Astrophysics 534, A115.
Carry, B., Kaasalainen, M., Leyrat, C., Merline, W.J., Drummond, J.D., Conrad, A.R., Weaver, H.A., Tamblyn, P.M., Chapman, C.R., Dumas, C., Colas, F., Christou, J.C., Dotto, E., Perna, D., Fornasier, S., Bernasconi, L., Behrend, R., Vachier, F., Kryszczynska, A., Polinska, M., Fulchignoni, M., Roy, R., Naves, R., Poncy, R., Wiggins, P., 2010b. Physical properties of the ESA Rosetta target asteroid (21) Lutetia. II. Shape and flyby geometry. Astronomy and Astrophysics 523, A94.
Carry, B., Kaasalainen, M., Merline, W.J., Müller, T.G., Jorda, L., Drummond, J.D., Berthier, J., O'Rourke, L., Ďurech, J., Küppers, M., Conrad, A.R., Dumas, C., Sierks, H., the OSIRIS Team, 2012. KOALA shape modeling technique validated at (21) Lutetia by ESA Rosetta mission. Planetary and Space Science 66 (1), 200–212.
Castillo-Rogez, J.C., McCord, T.B., 2010. Ceres: evolution and present state constrained by shape data. Icarus 205, 443–459.
Chapman, C.R., 1996. S-type asteroids, ordinary chondrites, and space weathering: the evidence from Galileo's fly-bys of Gaspra and Ida. Meteoritics and Planetary Science 31, 699–725.
Clark, B.E., Bus, S.J., Rivkin, A.S., Shepard, M.K., Shah, S., 2004. Spectroscopy of X-type asteroids. Astronomical Journal 128, 3070–3081.
Clark, B.E., Ockert-Bell, M.E., Cloutis, E.A., Nesvorny, D., Mothé-Diniz, T., Bus, S.J., 2009. Spectroscopy of K-complex asteroids: parent bodies of carbonaceous meteorites? Icarus 202, 119–133.
Clark, B.E., Ziffer, J., Nesvorný, D., Campins, H., Rivkin, A.S., Hiroi, T., Barucci, M.A., Fulchignoni, M., Binzel, R.P., Fornasier, S., DeMeo, F., Ockert-Bell, M.E., Licandro, J., Mothé-Diniz, T., 2010. Spectroscopy of B-type asteroids: subgroups and meteorite analogs. Journal of Geophysical Research (Planets) 115, E06005.
Cloutis, E.A., Hiroi, T., Gaffey, M.J., Alexander, C.M.O., Mann, P., 2011a. Spectral reflectance properties of carbonaceous chondrites: 1. CI chondrites. Icarus 212, 180–209.
Cloutis, E.A., Hudon, P., Hiroi, T., Gaffey, M.J., Mann, P., 2011b. Spectral reflectance properties of carbonaceous chondrites: 2. CM chondrites. Icarus 216, 309–346.
Consolmagno, G., Britt, D., Macke, R., 2008. The significance of meteorite density and porosity. Chemie der Erde/Geochemistry 68, 1–29.

Consolmagno, G.J., Britt, D.T., 1998. The density and porosity of meteorites from the Vatican collection. Meteoritics and Planetary Science 33, 1231–1241.

Davidsson, B.J.R., Gutiérrez, P.J., 2004. Estimating the nucleus density of Comet 19P/Borrelly. Icarus 168, 392–408.

Davidsson, B.J.R., Gutiérrez, P.J., 2005. Nucleus properties of Comet 67P/Churyumov Gerasimenko estimated from non-gravitational force modeling. Icarus 176, 453–477.

Davidsson, B.J.R., Gutiérrez, P.J., 2006. Non-gravitational force modeling of Comet 81P/Wild 2.I. A nucleus bulk density estimate. Icarus 180, 224–242.

Davidsson, B.J.R., Gutiérrez, P.J., Rickman, H., 2007. Nucleus properties of Comet 9P/Tempel 1 estimated from non-gravitational force modeling. Icarus 187, 306–320.

de León, J., Duffard, R., Licandro, J., Lazzaro, D., 2004. Mineralogical characterization of A-type asteroid (1951) Lick. Astronomy and Astrophysics 422, L59–L62.

Delbo, M., Tanga, P., 2009. Thermal inertia of main belt asteroids smaller than 100 km from IRAS data. Planetary and Space Science 57, 259–265.

DeMeo, F.E., Binzel, R.P., Slivan, S.M., Bus, S.J., 2009. An extension of the Bus asteroid taxonomy into the near-infrared. Icarus 202, 160–180.

Descamps, P., Marchis, F., Michalowski, T., Vachier, F., Colas, F., Berthier, J., Assafin, M., Dunckel, P.B., Polinska, M., Pych, W., Hestroffer, D., Miller, K.P.M., Vieira-Martins, R., Birlan, M., Teng-Chuen-Yu, J.P., Peyrot, A., Payet, B., Dorseuil, J., Léonie, Y., Dijoux, T., 2007. Figure of the double Asteroid 90 Antiope from adaptive optics and lightcurve observations. Icarus 187, 482–499.

Descamps, P., Marchis, F., Pollock, J., Berthier, J., Vachier, F., Birlan, M., Kaasalainen, M., Harris, A.W., Wong, M.H., Romanishin, W.J., Cooper, E.M., Kettner, K.A., Wiggins, P., Kryszczynska, A., Polinska, M., Coliac, J.F., Devyatkin, A., Verestchagina, I., Gorshanov, D., 2008. New determination of the size and bulk density of the binary Asteroid 22 Kalliope from observations of mutual eclipses. Icarus 196, 578–600.

Doressoundiram, A., Barucci, M.A., Fulchignoni, M., Florczak, M., 1998. EOS Family: A Spectroscopic Study. Icarus 131, 15–31.

Drummond, J.D., Christou, J.C., Nelson, J., 2009. Triaxial ellipsoid dimensions and poles of asteroids from AO observations at the Keck-II telescope. Icarus 202, 147–159.

Drummond, J.D., Conrad, A., Merline, W.J., Carry, B., Chapman, C.R., Weaver, H.A., Tamblyn, P.M., Christou, J.C., Dumas, C., 2010. Physical properties of the ESA Rosetta target asteroid (21) Lutetia. I. The triaxial ellipsoid dimensions, rotational pole, and bulk density. Astronomy and Astrophysics 523, A93.

Dumas, C., Carry, B., Hestroffer, D., Merlin, F., 2011. High-contrast observations of (136108) Haumea. A crystalline water-ice multiple system. Astronomy and Astrophysics 528, A105.

Dunham, D.W., Herald, D., Frappa, E., Hayamizu, T., Talbot, J., Timerson, B., 2011. Asteroid Occultations. NASA Planetary Data System. EAR-A-3-RDR-OCCULTATIONS-V9.0.

Ďurech, J., Kaasalainen, M., Herald, D., Dunham, D., 2011. Combining asteroid models derived by lightcurve inversion with asteroidal occultation silhouettes. Icarus 214, 652–670.

Elkins-Tanton, L.T., Weiss, B.P., Zuber, M.T., 2011. Chondrites as samples of differentiated planetesimals. Earth and Planetary Science Letters 305, 1–10.

Emery, J.P., Burr, D.M., Cruikshank, D.P., 2011. Near-infrared spectroscopy of trojan asteroids: evidence for two compositional groups. Astronomical Journal 141, 25.

Emery, J.P., Cruikshank, D.P., van Cleve, J., 2006. Thermal emission spectroscopy (5.2 38 μm) of three trojan asteroids with the Spitzer Space Telescope: detection of fine-grained silicates. Icarus 182, 496–512.

Fang, J., Margot, J.L., Brozovic, M., Nolan, M.C., Benner, L.A.M., Taylor, P.A., 2011. Orbits of near-earth asteroid triples 2001 SN263 and 1994 CC: Properties, Origin, and Evolution. Astronomical Journal 141, 154–169.

Fienga, A., Laskar, J., Morley, T., Manche, H., Kuchynka, P., Le Poncin-Lafitte, C., Budnik, F., Gastineau, M., Somenzi, L., 2009. INPOP08, a 4-D planetary ephemeris: from asteroid and time-scale computations to ESA Mars Express and Venus Express contributions. Astronomy and Astrophysics 507, 1675–1686.

Fienga, A., Manche, H., Kuchynka, P., Laskar, J., Gastineau, M., 2010. INPOP10a. Scientific Notes.

Fienga, A., Manche, H., Laskar, J., Gastineau, M., 2008. INPOP06: a new numerical planetary ephemeris. Astronomy and Astrophysics 477, 315–327.

Folkner, W.M., Williams, J.G., Boggs, D.H., 2009. The planetary and lunar ephemeris de 421. IPN Progress Report 42, pp. 1–34.

Fornasier, S., Clark, B.E., Dotto, E., 2011. Spectroscopic survey of X-type asteroids. Icarus 214, 131–146.

Fraser, W.C., Brown, M.E., 2010. Quaoar: a rock in the Kuiper belt. Astrophysical Journal 714, 1547–1550.

Fujiwara, A., Kawaguchi, J., Yeomans, D.K., Abe, M., Mukai, T., Okada, T., Saito, J., Yano, H., Yoshikawa, M., Scheeres, D.J., Barnouin-Jha, O.S., Cheng, A.F., Demura, H., Gaskell, G.W., Hirata, N., Ikeda, H., Kominato, T., Miyamoto, H., Nakamura, R., Sasaki, S., Uesugi, K., 2006. The rubble-pile asteroid Itokawa as observed by Hayabusa. Science 312, 1330–1334.

Fulvio, D., Brunetto, R., Vernazza, P., Strazzulla, G., 2012. Space weathering of Vesta and V-type asteroids: new irradiation experiments on HED meteorites. Astronomy and Astrophysics 537, L11.

Gounelle, M., Morbidelli, A., Bland, P.A., Spurny, P., Young, E.D., Sephton, M., 2008. Meteorites from the outer solar system? The Solar System Beyond Neptune, 525–541.

Grundy, W.M., Noll, K.S., Buie, M.W., Benecchi, S.D., Stephens, D.C., Levison, H.F., 2009. Mutual orbits and masses of six transneptunian binaries. Icarus 200, 627–635.

Halliday, A.N., Kleine, T., 2006. Meteorites and the timing, mechanisms, and conditions of terrestrial planet accretion and early differentiation. Meteorites and the Early Solar System II, 775–801.

Harris, A.W., 1998. A thermal model for near-Earth asteroids. Icarus 131, 291–301.

Hilton, J.L., 2002. Asteroid masses and densities. Asteroids III, 103–112.

Jenniskens, P., Shaddad, M.H., Numan, D., Elsir, S., Kudoda, A.M., Zolensky, M.E., Le, L., Robinson, G.A., Friedrich, J.M., Rumble, D., Steele, A., Chesley, S.R., Fitzsimmons, A., Duddy, S., Hsieh, H.H., Ramsay, G., Brown, P.G., Edwards, W.N., Tagliaferri, E., Boslough, M.B., Spalding, R.E., Dantowitz, R., Kozubal, M., Pravec, P., Borovicka, J., Charvat, Z., Vaubaillon, J., Kuiper, J., Albers, J., Bishop, J.L., Mancinelli, R.L., Sandford, S.A., Milam, S.N., Nuevo, M., Worden, S.P., 2009. The impact and recovery of asteroid 2008 TC_3. Nature 458, 485–488, http://dx.doi.org/10.1038/nature07920.

Jewitt, D.C., 2004. From cradle to grave: the rise and demise of the comets, pp. 659–676.

Jones, T.D., Lebofsky, L.A., Lewis, J.S., Marley, M.S., 1990. The composition and origin of the C, P and D asteroids: water as tracer of thermal evolution in the outer belt. Icarus 88, 172–193.

Kaasalainen, M., 2011. Maximum compatibility estimates and shape reconstruction with boundary curves and volumes of generalized projections. Inverse Problems and Imaging 5, 37–57.

King, P.L., Izawa, M.R.M., Vernazza, P., McCutcheon, W.A., Berger, J.A., Dunn, T., 2011. Salt: a critical material to consider when exploring the solar system. Lunar and Planetary Institute Science Conference Abstracts 42, p. 1985.

Konopliv, A.S., Yoder, C.F., Standish, E.M., Yuan, D.N., Sjogren, W.L., 2006. A global solution for the Mars static and seasonal gravity, Mars orientation, Phobos and Deimos masses, and Mars ephemeris. Icarus 182, 23–50.

Krasinsky, G.A., Pitjeva, E.V., Vasiliev, M.V., Yagudina, E.I., 2001. Estimating masses of asteroids. In: Communications of IAA of RAS.

Lagerros, J.S.V., 1996. Thermal physics of asteroids. I. Effects of shape, heat conduction and beaming. Astronomy and Astrophysics 310, 1011–1020.

Lagerros, J.S.V., 1997. Thermal physics of asteroids. III. Irregular shapes and albedo variegations. Astronomy and Astrophysics 325, 1226–1236.

Lamy, P.L., Toth, I., Fernandez, Y.R., Weaver, H.A., 2004. The sizes, shapes, albedos, and colors of cometary nuclei. Comets II, 223–264.

Lebofsky, L.A., 1978. Asteroid 1 Ceres—evidence for water of hydration. Monthly Notices of the Royal Astronomical Society 182, 17–21.

Lebofsky, L.A., Sykes, M.V., Tedesco, E.F., Veeder, G.J., Matson, D.L., Brown, R.H., Gradie, J.C., Feierberg, M.A., Rudy, R.J., 1986. A refined 'standard' thermal model for asteroids based on observations of 1 Ceres and 2 Pallas. Icarus 68, 239–251.

Lellouch, E., Kiss, C., Santos-Sanz, P., Müller, T.G., Fornasier, S., Groussin, O., Lacerda, P., Ortiz, J.L., Thirouin, A., Delsanti, A., Duffard, R., Harris, A.W., Henry, F., Lim, T., Moreno, R., Mommert, M., Mueller, M., Protopapa, S., Stansberry, J., Trilling, D., Vilenius, E., Barucci, A., Crovisier, J., Doressoundiram, A., Dotto, E., Gutiérrez, P.J., Hainaut, O.R., Hartogh, P., Hestroffer, D., Horner, J., Jorda, L., Kidger, M., Lara, L.M., Rengel, M., Swinyard, B.M., Thomas, N., 2010. 'TNOs are cool': a survey of the trans-neptunian region. II. The thermal lightcurve of (136108) Haumea. Astronomy and Astrophysics 518, L147.

Levison, H.F., Bottke, W.F., Gounelle, M., Morbidelli, A., Nesvorný, D., Tsiganis, K., 2009. Contamination of the asteroid belt by primordial trans-Neptunian objects. Nature 460, 364–366.

Lim, T.L., Stansberry, J., Müller, T.G., Mueller, M., Lellouch, E., Kiss, C., Santos-Sanz, P., Vilenius, E., Protopapa, S., Moreno, R., Delsanti, A., Duffard, R., Fornasier, S., Groussin, O., Harris, A.W., Henry, F., Horner, J., Lacerda, P., Mommert, M., Ortiz, J.L., Rengel, M., Thirouin, A., Trilling, D., Barucci, A., Crovisier, J., Doressoundiram, A., Dotto, E., Gutiérrez Buenestado, P.J., Hainaut, O.R., Hartogh, P., Hestroffer, D., Kidger, M., Lara, L.M., Swinyard, B.M., Thomas, N., 2010. TNOs are Cool: a survey of the trans-Neptunian region. III. Thermophysical properties of 90482 Orcus and 136472 Makemake. Astronomy and Astrophysics 518, L148.

Macke, R.J., Britt, D.T., Consolmagno, G.J., 2011. Density, porosity, and magnetic susceptibility of achondritic meteorites. Meteoritics and Planetary Science 46, 311–326.

Macke, R.J., Consolmagno, G.J., Britt, D.T., Hutson, M.L., 2010. Enstatite chondrite density, magnetic susceptibility, and porosity. Meteoritics and Planetary Science 45, 1513–1526.

Marchis, F., Descamps, P., Baek, M., Harris, A.W., Kaasalainen, M., Berthier, J., Hestroffer, D., Vachier, F., 2008a. Main belt binary asteroidal systems with circular mutual orbits. Icarus 196, 97–118.

Marchis, F., Descamps, P., Berthier, J., Hestroffer, D., Vachier, F., Baek, M., Harris, A.W., Nesvorný, D., 2008b. Main belt binary asteroidal systems with eccentric mutual orbits. Icarus 195, 295–316.

Marchis, F., Hestroffer, D., Descamps, P., Berthier, J., Laver, C., de Pater, I., 2005. Mass and density of Asteroid 121 Hermione from an analysis of its companion orbit. Icarus 178, 450–464.

Marchis, F., Kaasalainen, M., Hom, E.F.Y., Berthier, J., Enriquez, J., Hestroffer, D., Le Mignant, D., de Pater, I., 2006. Shape, size and multiplicity of main-belt asteroids. Icarus 185, 39–63.

Margot, J.L., Nolan, M.C., Benner, L.A.M., Ostro, S.J., Jurgens, R.F., Giorgini, J.D., Slade, M.A., Campbell, D.B., 2002. Binary asteroids in the near-Earth object population. Science 296, 1445–1448.

Masiero, J.R., Mainzer, A.K., Grav, T., Bauer, J.M., Cutri, R.M., Dailey, J., Eisenhardt, P.R.M., McMillan, R.S., Spahr, T.B., Skrutskie, M.F., Tholen, D., Walker, R.G., Wright, E.L., DeBaun, E., Elsbury, D., Gautier IV, T., Gomillion, S., Wilkins, A.,

2011. Main belt asteroids with WISE/NEOWISE. I. Preliminary albedos and diameters. Astrophysical Journal 741, 68.
McCord, T.B., Adams, J.B., Johnson, T.V., 1970. Asteroid Vesta: spectral reflectivity and compositional implications. Science 168, 1445–1447.
Merline, W.J., Close, L.M., Dumas, C., Chapman, C.R., Roddier, F., Ménard, F., Slater, D.C., Duvert, G., Shelton, C., Morgan, T., 1999. Discovery of a moon orbiting the asteroid 45 Eugenia. Nature 401, 565–568.
Merline, W.J., Weidenschilling, S.J., Durda, D.D., Margot, J.L., Pravec, P., Storrs, A.D., 2002. Asteroids do have satellites. Asteroids III, 289–312.
Michalak, G., 2000. Determination of asteroid masses—I. (1) Ceres, (2) Pallas and (4) Vesta. Astronomy and Astrophysics 360, 363–374.
Michalak, G., 2001. Determination of asteroid masses. II. (6) Hebe, (10) Hygiea, (15) Eunomia, (52) Europa, (88) Thisbe, (444) Typtis, (511) Davida and (704) Interamnia. Astronomy and Astrophysics 374, 703–711.
Mignard, F., Cellino, A., Muinonen, K., Tanga, P., Delbo, M., Dell'Oro, A., Granvik, M., Hestroffer, D., Mouret, S., Thuillot, W., Virtanen, J., 2007. The Gaia mission: expected applications to asteroid science. Earth Moon and Planets 101, 97–125.
Morbidelli, A., Bottke, W.F., Nesvorný, D., Levison, H.F., 2009. Asteroids were born big. Icarus 204, 558–573.
Morbidelli, A., Levison, H.F., Tsiganis, K., Gomes, R., 2005. Chaotic capture of Jupiter's Trojan asteroids in the early Solar System. Nature 435, 462–465.
Mottola, S., Lahulla, F., 2000. Mutual eclipse events in asteroidal binary system 1996 FG_3: observations and a Numerical Model. Icarus 146, 556–567.
Mouret, S., Hestroffer, D., Mignard, F., 2007. Asteroid masses and improvement with GAIA. Astronomy and Astrophysics 472, 1017–1027.
Mouret, S., Simon, J.L., Mignard, F., Hestroffer, D., 2009. The list of asteroids perturbing the Mars orbit to be seen during future space missions. Astronomy and Astrophysics 508, 479–489.
Mueller, M., Delbo, M., Hora, J.L., Trilling, D.E., Bhattacharya, B., Bottke, W.F., Chesley, S., Emery, J.P., Fazio, G., Harris, A.W., Mainzer, A., Mommert, M., Penprase, B., Smith, H.A., Spahr, T.B., Stansberry, J.A., Thomas, C.A., 2011. ExploreNEOs. III. Physical characterization of 65 potential spacecraft target asteroids. Astronomical Journal 141, 109.
Mueller, M., Harris, A.W., Bus, S.J., Hora, J.L., Kassis, M., Adams, J.D., 2006. The size and albedo of Rosetta fly-by target 21 Lutetia from new IRTF measurements and thermal modeling. Astronomy and Astrophysics 447, 1153–1158.
Müller, T.G., Lellouch, E., Böhnhardt, H., Stansberry, J., Barucci, A., Crovisier, J., Delsanti, A., Doressoundiram, A., Dotto, E., Duffard, R., Fornasier, S., Groussin, O., Gutiérrez, P.J., Hainaut, O.R., Harris, A.W., Hartogh, P., Hestroffer, D., Horner, J., Jewitt, D.C., Kidger, M., Kiss, C., Lacerda, P., Lara, L.M., Lim, T., Mueller, M., Moreno, R., Ortiz, J.L., Rengel, M., Santos-Sanz, P., Swinyard, B., Thomas, N., Thirouin, A., Trilling, D., 2009. TNOs are cool: a survey of the transneptunian region. Earth Moon and Planets 105, 209–219.
Müller, T.G., Sekiguchi, T., Kaasalainen, M., Abe, M., Hasegawa, S., 2005. Thermal infrared observations of the Hayabusa spacecraft target asteroid 25143 Itokawa. Astronomy and Astrophysics 443, 347–355.
Ockert-Bell, M.E., Clark, B.E., Shepard, M.K., Isaacs, R.A., Cloutis, E.A., Fornasier, S., Bus, S.J., 2010. The composition of M-type asteroids: synthesis of spectroscopic and radar observations. Icarus 210, 674–692.
O'Rourke, L., Müller, T.G., Valtchanov, I., Altieri, B., Gonz Ailez-Garcia, B., Bhattacharya, B., Jorda, L., Carry, B., Küppers, M., Groussin, O., Altwegg, K., Barucci, A., Bockelée-Morvan, D., Crovisier, J., Dotto, E., Garcia-Lario, P., Kidger, M., Llorente, A., Llorente, R., Marstona, A.P., Sanchez Portal, M., Schulz, R., Sierra, M., Teyssiera, D., Vavreka, R., 2012. Thermal & shape properties of Asteroid (21) Lutetia from Herschel observations around the Rosetta flyby. Planetary and Space Science 66 (1), 192–199.
Ostro, S.J., Magri, C., Benner, L.A.M., Giorgini, J.D., Nolan, M.C., Hine, A.A., Busch, M.W., Margot, J.L., 2010. Radar imaging of asteroid 7 Iris. Icarus 207, 285–294.
Ostro, S.J., Margot, J.L., Benner, L.A.M., Giorgini, J.D., Scheeres, D.J., Fahnestock, E.G., Broschart, S.B., Bellerose, J., Nolan, M.C., Magri, C., Pravec, P., Scheirich, P., Rose, R., Jurgens, R.F., De Jong, E.M., Suzuki, S., 2006. Radar imaging of binary near-Earth asteroid (66391) 1999 KW4. Science 314, 1276–1280.
Parker, A.H., Kavelaars, J.J., Petit, J.M., Jones, L., Gladman, B., Parker, J., 2011. Characterization of seven ultra-wide trans-neptunian binaries. Astrophysical Journal 743, 1.
Pätzold, M., Andert, T., Asmar, S.W., Anderson, J.D., Barriot, J.P., Bird, M.K., Husler, B., Hahn, M., Tellmann, S., Sierks, H., Lamy, P., Weiss, B.P., 2011. Asteroid 21 Lutetia: low mass, high density. Science 334, 491.
Petit, J.M., Durda, D.D., Greenberg, R., Hurford, T.A., Geissler, P.E., 1997. The long-term dynamics of Dactyl's orbit. Icarus 130, 177–197.
Pitjeva, E.V., 2001. Progress in the determination of some astronomical constants from radiometric observations of planets and spacecraft. Astronomy and Astrophysics 371, 760–765.
Pravec, P., Harris, A.W., 2007. Binary asteroid population. 1. Angular momentum content. Icarus 190, 250–259.
Pravec, P., Harris, A.W., Michalowski, T., 2002. Asteroid rotations. Asteroids III, 113–122.
Pravec, P., Scheirich, P., Kušnirák, P., Šarounová, L., Mottola, S., Hahn, G., Brown, P.G., Esquerdo, G.A., Kaiser, N., Krzeminski, Z., Pray, D.P., Warner, B.D., Harris, A.W., Nolan, M.C., Howell, E.S., Benner, L.A.M., Margot, J.L., Galád, A., Holliday, W., Hicks, M.D., Krugly, Y.N., Tholen, D.J., Whiteley, R.J., Marchis, F., Degraff, D.R., Grauer, A., Larson, S., Velichko, F.P., Cooney, W.R., Stephens, R., Zhu, J., Kirsch, K., Dyvig, R., Snyder, L., Reddy, V., Moore, S., Gajdoš, Š., Világi, J., Masi, G., Higgins, D., Funkhouser, G., Knight, B., Slivan, S.M., Behrend, R., Grenon, M., Burki, G., Roy, R., Demeautis, C., Matter, D., Waelchli, N., Revaz, Y., Klotz, A., Rieugné, G., Thierry, P., Cotrez, V., Brunetto, L., Kober, G., 2006. Photometric survey of binary near-Earth asteroids. Icarus 181, 63–93.
Pravec, P., Vokrouhlický, D., Polishook, D., Scheeres, D.J., Harris, A.W., Galád, A., Vaduvescu, O., Pozo, F., Barr, A., Longa, P., Vachier, F., Colas, F., Pray, D.P., Pollock, J., Reichart, D., Ivarsen, K., Haislip, J., Lacluyze, A., Kušnirák, P., Henych, T., Marchis, F., Macomber, B., Jacobson, S.A., Krugly, Y.N., Sergeev, A.V., Leroy, A., 2010. Formation of asteroid pairs by rotational fission. Nature 466, 1085–1088.
Richardson, J.E., Melosh, H.J., Lisse, C.M., Carcich, B., 2007. A ballistics analysis of the Deep Impact ejecta plume: determining Comet Tempel 1's gravity, mass, and density. Icarus 190, 357–390.
Rivkin, A.S., Howell, E.S., Britt, D.T., Lebofsky, L.A., Nolan, M.C., Branston, D.D., 1995. Three-micron spectrometric survey of M- and E-class asteroids. Icarus 117, 90–100.
Rivkin, A.S., Howell, E.S., Vilas, F., Lebofsky, L.A., 2002. Hydrated minerals on asteroids: the astronomical record. Asteroids III, 235–253.
Rozitis, B., Green, S.F., 2011. Directional characteristics of thermal-infrared beaming from atmosphereless planetary surfaces—a new thermophysical model. Monthly Notices of the Royal Astronomical Society 415, 2042–2062.
Ryan, E.L., Woodward, C.E., 2010. Rectified asteroid albedos and diameters from IRAS and MSX Photometry Catalogs. Astronomical Journal 140, 933–943.
Scheirich, P., Pravec, P., 2009. Modeling of lightcurves of binary asteroids. Icarus 200, 531–547.
Schmidt, B.E., Thomas, P.C., Bauer, J.M., Li, J., McFadden, L.A., Mutchler, M.J., Radcliffe, S.C., Rivkin, A.S., Russell, C.T., Parker, J.W., Stern, S.A., 2009. The shape and surface variation of 2 Pallas from the Hubble space telescope. Science 326, 275–278.
Shepard, M.K., Margot, J.L., Magri, C., Nolan, M.C., Schlieder, J., Estes, B., Bus, S.J., Volquardsen, E.L., Rivkin, A.S., Benner, L.A.M., Giorgini, J.D., Ostro, S.J., Busch, M.W., 2006. Radar and infrared observations of binary near-Earth Asteroid 2002 CE26. Icarus 184, 198–210.
Sheppard, S.S., Ragozzine, D., Trujillo, C., 2012. 2007 TY430: A Cold Classical Kuiper belt type binary in the Plutino population. Astronomical Journal 143 (3), Article ID 58, http://dx.doi.org/10.1088/0004-6256/143/3/58.
Sicardy, B., Ortiz, J.L., Assafin, M., Jehin, E., Maury, A., Lellouch, E., Hutton, R.G., Braga-Ribas, F., Colas, F., Hestroffer, D., Lecacheux, J., Roques, F., Santos-Sanz, P., Widemann, T., Morales, N., Duffard, R., Thirouin, A., Castro-Tirado, A.J., Jelínek, M., Kubánek, P., Sota, A., Sánchez-Ramírez, R., Andrei, A.H., Camargo, J.I.B., da Silva Neto, D.N., Gomes, A.R., Martins, R.V., Gillon, M., Manfroid, J., Tozzi, G.P., Harlingten, C., Saravia, S., Behrend, R., Mottola, S., Melendo, E.G., Peris, V., Fabregat, J., Madiedo, J.M., Cuesta, L., Eibe, M.T., Ullán, A., Organero, F., Pastor, S., de Los Reyes, J.A., Pedraz, S., Castro, A., de La Cueva, I., Muler, G., Steele, I.A., 2011. A Pluto-like radius and a high albedo for the dwarf planet Eris from an occultation. Nature 478, 493–496.
Sierks, H., Lamy, P., Barbieri, C., Koschny, D., Rickman, H., Rodrigo, R., A'Hearn, M.F., Angrilli, F., Barucci, A., Bertaux, J.L., Bertini, I., Besse, S., Carry, B., Cremonese, G., Da Deppo, V., Davidsson, B., Debei, S., De Cecco, M., De Leon, J., Ferri, F., Fornasier, S., Fulle, M., Hviid, S.F., Gaskell, G.W., Groussin, O., Gutierrez, P.J., Jorda, L., Kaasalainen, M., Keller, H.U., Knollenberg, J., Kramm, J.R., Kührt, E., Küppers, M., Lara, L.M., Lazzarin, M., Leyrat, C., Lopez Moreno, J.L., Magrin, S., Marchi, S., Marzari, F., Massironi, M., Michalik, H., Moissl, R., Naletto, G., Preusker, F., Sabau, L., Sabolo, W., Scholten, F., Snodgrass, C., Thomas, N., Tubiana, C., Vernazza, P., Vincent, J.B., Wenzel, K.P., Andert, T., Pätzold, M., Weiss, B.P., 2011. Images of asteroid (21) Lutetia: a remnant planetesimal from the early Solar System. Science 334, 487–490.
Snodgrass, C., Lowry, S.C., Fitzsimmons, A., 2006. Photometry of cometary nuclei: rotation rates, colours and a comparison with Kuiper belt objects. Monthly Notices of the Royal Astronomical Society 373, 1590–1602.
Somenzi, L., Fienga, A., Laskar, J., Kuchynka, P., 2010. Determination of asteroid masses from their close encounters with Mars. Planetary and Space Science 58, 858–863.
Sosa, A., Fernández, J.A., 2009. Cometary masses derived from non-gravitational forces. Monthly Notices of the Royal Astronomical Society 393, 192–214.
Stansberry, J., Grundy, W., Brown, M.E., Cruikshank, D.P., Spencer, J.R., Trilling, D., Margot, J.L., 2008. Physical properties of Kuiper belt and centaur objects: constraints from the Spitzer space telescope. The Solar System Beyond Neptune, 161–179.
Strazzulla, G., Dotto, E., Binzel, R.P., Brunetto, R., Barucci, M.A., Blanco, A., Orofino, V., 2005. Spectral alteration of the Meteorite Epinal (H5) induced by heavy ion irradiation: a simulation of space weathering effects on near-Earth asteroids. Icarus 174, 31–35.
Sunshine, J.M., Connolly, H.C., McCoy, T.J., Bus, S.J., La Croix, L.M., 2008. Ancient asteroids enriched in refractory inclusions. Science 320, 514.
Tedesco, E.F., Noah, P.V., Noah, M.C., Price, S.D., 2002. The supplemental IRAS minor planet survey. Astronomical Journal 123, 1056–1085.
Tholen, D.J., Barucci, M.A., 1989. Asteroid taxonomy. Asteroids II, 298–315.
Thomas, P.C., Parker, J.W., McFadden, L.A., Russell, C.T., Stern, S.A., Sykes, M.V., Young, E.F., 2005. Differentiation of the asteroid Ceres as revealed by its shape. Nature 437, 224–226.
Tsiganis, K., Gomes, R., Morbidelli, A., Levison, H.F., 2005. Origin of the orbital architecture of the giant planets of the solar system. Nature 435, 459–461.
Usui, F., Kuroda, D., Müller, T.G., Hasegawa, S., Ishiguro, M., Ootsubo, T., Ishihara, D., Kataza, H., Takita, S., Oyabu, S., Ueno, M., Matsuhara, H., Onaka, T., 2011. Asteroid catalog using Akari: AKARI/IRC mid-infrared asteroid survey. Publications of the Astronomical Society of Japan 63, 1117–1138.

Vernazza, P., Binzel, R.P., Rossi, A., Fulchignoni, M., Birlan, M., 2009a. Solar wind as the origin of rapid reddening of asteroid surfaces. Nature 458, 993–995.
Vernazza, P., Binzel, R.P., Thomas, C.A., DeMeo, F.E., Bus, S.J., Rivkin, A.S., Tokunaga, A.T., 2008. Compositional differences between meteorites and near-Earth asteroids. Nature 454, 858–860.
Vernazza, P., Brunetto, R., Binzel, R.P., Perron, C., Fulvio, D., Strazzulla, G., Fulchignoni, M., 2009b. Plausible parent bodies for enstatite chondrites and mesosiderites: Implications for Lutetia's fly-by. Icarus 202, 477–486.
Vernazza, P., Brunetto, R., Strazzulla, G., Fulchignoni, M., Rochette, P., Meyer-Vernet, N., Zouganelis, I., 2006. Asteroid colors: a novel tool for magnetic field detection? The case of Vesta. Astronomy and Astrophysics 451, 43–46.
Vernazza, P., Carry, B., Emery, J.P., Hora, J.L., Cruikshank, D.P., Binzel, R.P., Jackson, J., Helbert, J., Maturilli, A., 2010. Mid-infrared spectral variability for compositionally similar asteroids: implications for asteroid particle size distributions. Icarus 207, 800–809.
Vernazza, P., King, P.L., Izawa, M.R.M., Maturilli, A., Helbert, J., Cruikshank, D., Brunetto, R., Marchis, F., Binzel, R.P., Flemming, R.L., 2011a. Opening the mid-IR window on asteroid physical properties. In: Lunar and Planetary Institute Science Conference Abstracts, vol. 42, p. 1344.
Vernazza, P., Lamy, P., Groussin, O., Hiroi, T., Jorda, L., King, P.L., Izawa, M.R.M., Marchis, F., Birlan, M., Brunetto, R., 2011b. Asteroid (21) Lutetia as a remnant of earth's precursor planetesimals. Icarus 216, 650–659.
Veverka, J., Robinson, M., Thomas, P., Murchie, S., Bell, J.F., Izenberg, N., Chapman, C., Harch, A., Bell, M., Carcich, B., Cheng, A., Clark, B., Domingue, D., Dunham, D., Farquhar, R., Gaffey, M.J., Hawkins, E., Joseph, J., Kirk, R., Li, H., Lucey, P., Malin, M., Martin, P., McFadden, L., Merline, W.J., Miller, J.K., Owen, W.M., Peterson, C., Prockter, L., Warren, J., Wellnitz, D., Williams, B.G., Yeomans, D.K., 2000. NEAR at eros: imaging and spectral results. Science 289, 2088–2097.
Walsh, K.J., Morbidelli, A., Raymond, S.N., O'Brien, D.P., Mandell, A.M., 2011. A low mass for Mars from Jupiter's early gas-driven migration. Nature 475, 206–209.
Walsh, K.J., Richardson, D.C., Michel, P., 2008. Rotational breakup as the origin of small binary asteroids. Nature 454, 188–191.
Weisberg, M.K., McCoy, T.J., Krot, A.N., 2006. Systematics and evaluation of meteorite classification. Meteorites and the Early Solar System II, 19–52.
Weissman, P.R., Asphaug, E., Lowry, S.C., 2004. Structure and density of cometary nuclei. Comets II, 337–357.
Yeomans, D.K., Antreasian, P.G., Barriot, J.P., Chesley, S.R., Dunham, D.W., Farquhar, R.W., Giorgini, J.D., Helfrich, C.E., Konopliv, A.S., McAdams, J.V., Miller, J.K., Owen, W.M., Scheeres, D.J., Thomas, P.C., Veverka, J., Williams, B.G., 2000. Radio science results during the NEAR-shoemaker spacecraft rendezvous with eros. Science 289, 2085–2088.
Yeomans, D.K., Barriot, J.P., Dunham, D.W., Farquhar, R.W., Giorgini, J.D., Helfrich, C.E., Konopliv, A.S., McAdams, J.V., Miller, J.K., Owen Jr., W.M., Scheeres, D.J., Synnott, S.P., Williams, B.G., 1997. Estimating the mass of asteroid 253 Mathilde from tracking data during the NEAR flyby. Science 278, 2106.
Yurimoto, H., Abe, K.i., Abe, M., Ebihara, M., Fujimura, A., Hashiguchi, M., Hashizume, K., Ireland, T.R., Itoh, S., Katayama, J., Kato, C., Kawaguchi, J., Kawasaki, N., Kitajima, F., Kobayashi, S., Meike, T., Mukai, T., Nagao, K., Nakamura, T., Naraoka, H., Noguchi, T., Okazaki, R., Park, C., Sakamoto, N., Seto, Y., Takei, M., Tsuchiyama, A., Uesugi, M., Wakaki, S., Yada, T., Yamamoto, K., Yoshikawa, M., Zolensky, M.E., 2011. Oxygen isotopic compositions of asteroidal materials returned from Itokawa by the Hayabusa mission. Science 333, 1116–1118.
Zielenbach, W., 2011. Mass Determination Studies of 104 Large Asteroids. Astronomical Journal 142, 120–128.

Scheeres D. J., Britt D., Carry B., and Holsapple K. A. (2015) Asteroid interiors and morphology. In *Asteroids IV* (P. Michel et al., eds.), pp. 745–766. Univ. of Arizona, Tucson, DOI: 10.2458/azu_uapress_9780816532131-ch038.

Asteroid Interiors and Morphology

D. J. Scheeres
The University of Colorado Boulder

D. Britt
University of Central Florida

B. Carry
Institut de Mécanique Céleste et de Calcul des Éphémérides

K. A. Holsapple
University of Washington

The geophysical study of asteroids has moved from the realm of speculation and constraint to a more data rich environment where observations can be directly used to understand and probe the physical nature of these bodies. While many broad questions were posed in the *Asteroids III* chapter on asteroid interiors, in the current setting we are now able to probe more deeply into these questions, taking advantage of many different observations of asteroids across their entire size scale. The current chapter will take a very broad survey of what constraints currently exist in this area, what progress has been made in understanding these bodies analytically and through simulations, and what current theories can inform and guide future observations and tests of our understanding. The following topics are covered in this chapter: the strength of asteroid materials as inferred from meteors and meteorites, the density and porosity of asteroids as inferred from remote observations, global constraints on asteroid strength and morphology based on ground- and spacebased observations, analytical theories of asteroid strength and evolution, and the current state of numerical simulation techniques of asteroid interiors and morphology.

1. INTRODUCTION

The past decade has seen an astonishing array of advances across a wide spectrum of important inputs to the problem and mystery of asteroid interiors. These include the development of a large database concerning asteroid component strengths, as evidenced by meteors and meteorites (section 2); the compilation of extensive densities and inferred porosities for asteroids based on groundbased observations (section 3); the development of new computational techniques for the simulation of how asteroid rubble piles deform and fission or shed mass when subject to extreme rotation rates (section 4); and the development of crucial insights into the unique geophysics of specific asteroidal bodies (section 6). This chapter will review these different areas of advancements in an attempt to unify these disparate topics and show where future progress can be made in this field.

Knowledge about asteroid interiors is a crucial aspect for understanding these bodies, as it provides clues about their evolutionary history, in turn providing strong constraints on the history of the solar system. Unlike asteroid surfaces, it is impossible to peer directly within or easily take a sample measurement from within a body. Thus the study of asteroid interiors must rely on a combination of measurement and theory to develop constraints on the interior environment. Given these restrictions, previous investigations have studied observable characteristics that may be related to the nature of their interiors. This being said, there are measurement techniques that can probe the interior properties of bodies, in particular through seismic and radar sounding measurements. These are discussed in section 5 and represent a potential source for future advancements in this field.

The most accessible features of an asteroid that are related to their interior structure are the mass, density, shape, and spin. These are strongly constrained by the interior structure, and by the strength and mechanical properties of that structure. By focusing on these specific observables, we can start to answer basic questions about these bodies: How strong are they? What is the nature of that strength? Are the interiors rubble piles full of voids at various size scales, or are they solid coherent structures? How do these properties depend on composition, shape, spin, size, or location?

Important steps in answering the above questions have occurred since the publication of the *Asteroids III* volume

(e.g., *Asphaug et al.,* 2002; *Britt et al.,* 2002). These advances are related to the accumulation of fundamental data on these bodies through meteor falls and groundbased observations, analytical studies of the shapes of rubble piles, and ever more precise numerical simulations that probe the mechanics of rubble-pile interactions. We do note that our discussion will be more focused on the smaller asteroid bodies and rubble-pile structures, as this is where much of the progress has occurred in the last decade. This is not to discount the important results from the European Space Agency (ESA) Rosetta mission to asteroid (21) Lutetia or the NASA Dawn mission to asteroid (4) Vesta; however, we refer the interested reader to the chapters in this volume by Russell et al. and Barucci et al. for a detailed discussion of those scientific results.

The topic of asteroid interiors has been dealt with previously in the *Asteroids III* chapter by *Asphaug et al.* (2002). That chapter serves as a fundamental starting point for the current survey, and we assume that the interested reader is familiar with that work. The current chapter takes a different approach from that earlier work, reflecting the current thinking about what aspects of observations can be directly applied to understanding asteroid interiors. Another important resource from the *Asteroids III* book is the chapter on gravitational aggregates by *Richardson et al.* (2002). The current chapter extends that descriptive chapter in the direction of geophysics, striving to link the possible granular nature of asteroids with fundamental physical processes that occur for aggregates. The goal of that chapter was to distinguish the different ways in which a shattered body could exist, from a random assemblage to a coherent collection of components shattered in place from an initial monolithic body. The current chapter does not deal much with this distinction, although its implications do arise when discussing observations of macroporosity. What is new in the current chapter, with regard to gravitational aggregates, is the realization that such assemblages may have a small level of cohesion, which changes the dynamical evolution of these bodies in a significant and observable way. Additionally, not considered in that chapter was the size distribution of the particles of these aggregates, which has now been theorized to be a crucial aspect of their geophysics (*Sánchez and Scheeres,* 2014). Observations have not conclusively identified which of the many types of gravitational aggregates discussed in *Richardson et al.* (2002) might in fact exist in nature; however, many different observations (as discussed in this chapter) seem to fit best with their definition of "rubble pile," stated verbatim as: *"This structure is literally a pile of rubble, with the organization that you might expect from a bunch of rocks dumped from a truck. A body that has been completely shattered and reassembled may fit into this category."*

The outline of the chapter is as follows. In section 2 we focus on what we know about the fundamental strength and mechanical properties of the constituent pieces of asteroids as represented in the meteorite collection and meteor observations. From this study we find that there remain interesting and significant disconnects between the measured strength of meteorites and the inferred strength that they have based on the altitude at which they fail, which is expected to be related to their possible rubble-pile structure. This data provides insights into bodies up to several meters in size, but not beyond this limit.

In section 3 we use groundbased observations, and some spacecraft observations, to develop a wide range of constraints on how the constituent components of asteroids are assembled by computing their density and porosity. The implications are that some asteroids are highly porous bodies, in general, supporting the idea that these can be rubble piles. From this data there is also a clear progression of larger bodies having lower porosities, indicating the importance of gravitational compression. From this data we gain insight into the structure of bodies at the larger scale, ranging up to several hundreds of kilometers in size.

Section 4 applies and interprets the size-spin data for insight and motivation into an understanding of asteroid morphology and strength. From this data we can place constraints on the properties of the asteroid population and expose areas of uncertainty and ambiguity. Linking these observations with modeling and theories of asteroid strength has provided new insights and constraints on the global strength of asteroids, and provided clues as to their internal morphology. Theory and data from this section also help address the gap between the insights from meteorites on smaller bodies and from the groundbased studies of larger bodies.

Section 5 discusses the insights that can be inferred on asteroid interiors using the visible geology of asteroid surfaces, constraints on the transmission of seismic energy, and by an improved understanding of the rate of dissipation that may occur in asteroids. These methods indicate a potential pathway for better probing and determining the unique geophysical environment within small rubble-pile bodies.

Finally, section 6 focuses on a number of specific asteroids that have been observed with some level of precision since *Asteroids III,* with the exception of (4) Vesta. These include the targets of spacecraft missions, (433) Eros and (25143) Itokawa; the unique case of 2008 TC_3, which was analyzed both with groundbased observations and on the ground with meteorite falls; and a number of ground observed asteroids including (216) Kleopatra, (29075) 1950 DA, (66391) 1999 KW_4; and two active asteroids, P/2013 P5 and P/2013 R3. Many of these bodies are discussed in detail elsewhere in this book, but our discussions are focused specifically on what these bodies tell us about asteroid interiors and strength. Finally, overall conclusions are drawn and future areas where additional research and observations are needed are highlighted.

2. MATERIAL CONSTRAINTS

Meteorites and meteors are samples of materials from small bodies in near-Earth space, albeit transported from all regions of the solar system (see the chapter by Binzel et al. in this volume). Note that a meteorite and a meteor can be just different manifestations of the same object; a meteor is the visual and sonic phenomena of the small body transit-

ing Earth's atmosphere, while a meteorite is the surviving material that can be collected on the surface of Earth. As small bodies encounter Earth, their interaction with Earth's atmosphere, their mass loss on entry, the characteristics of their fall, and analysis of recovered fragments all provide clues about the structure, cohesion, and mineralogical homogeneity of the parent small bodies. This subsection is focused on summarizing and collecting in one place information on the strength of these bodies, both as individual components and as agglomerations when they first enter the atmosphere. For more information, see also the chapters by Borovička et al. and Jenniskens in this volume.

2.1. Meteorite Strength

An individual recovered meteorite is a direct sample of the material properties and strength of the components of small bodies. However, the samples that survive the stress of deceleration and atmospheric entry are necessarily biased toward the strongest and most coherent materials in the parent object. Weak and volatile-rich material tends to be destroyed on entry. Shown in Table 1 are the compressive strengths of a number of meteorites along with common materials for comparison [taken from *Popova et al.* (2011); see also *Kimberley and Ramesh* (2011) for additional data].

Natural materials can be very strong, such as individual crystals of quartz (1100 MPa). Single mineral strengths derive from the inherent strength of the crystal structure. Rocks are collections of minerals and their strength derives from a mixture of their mineral crystal strengths, their formation conditions, and the nature of the bonding between minerals. Igneous rocks like granite, for example (100–140 MPa), are composed of a substantial amount of quartz, but as a whole the bonding between their minerals makes the rock much less strong than the individual minerals. Unreinforced concrete at 20 MPa compressive strength is a good comparison standard.

Like rocks, there are substantial variations in the inherent strength of meteorites. Most ordinary chondrites (the most abundant type of meteorite fall) are much stronger than concrete. Volatile-rich carbonaceous chondrites are much weaker, and in some cases, e.g., the Tagish Lake meteorite (meteorites are named for the localities where they are recovered and in this chapter they will be often referred to by their meteorite name), their measured strengths are on the order of weakly consolidated soils (dirt clods).

Why are ordinary chondrites so strong? In general, they are conglomerates of chondrules (millimeter-sized spheres of minerals formed in the solar nebula), chondrule fragments, dusty matrix, and iron-nickel metal that have been welded together by varying levels of grain-boundary melting. In addition to welding in the silicates, the metal in ordinary chondrites provides a natural reinforcing mesh that is often interconnected in some ordinary chondrites that have been subjected to higher temperatures and thus have undergone some degree of remelting and metamorphic processing referred to as having higher metamorphic grades. As a result, high-metamorphic-grade ordinary chondrites can have many of the strength properties and reactions to stress of steel-reinforced concrete. However, there are some very weak ordinary chondrites. The Holbrook meteorite (Table 1) is a high-metamorphic-grade ordinary chondrite but is very weak and friable. Weston is also a high-grade chondrite but the individual chondrules are so poorly cemented that it falls apart with handling. The best analogy for this sample is a loosely glued collection of millimeter-sized spheres. However, the individual chondrules that are weakly held in Weston are individually quite strong.

The major exception to the story of relatively weak ordinary chondrite bolides is the large and well-studied Chelyabinsk

TABLE 1. Meteorite and material strength.

Material	Meteorite Type	Compressive Strength (MPa)	Tensile Strength (MPa)
Concrete — Unreinforced	Typical sidewalk	20	
Quartz	Single crystal	1100	55
Granite		100–140	
Medium dirt clod		0.2–0.4	
Holbrook, Arizona	L6 (OC)	6.2	
La Lande, New Mexico	L5 (OC)	373.4	
Tsarev	L5 (OC)	160–420	16–62
Covert	H5 (OC)	75.3	
Kunashak	L5 (OC)	265	49
Elenovka	L5 (OC)	20	2
Krymka	LL3 (OC)	160	22
Seminole	H4 (OC)	173	22.5
Plutusk	H5 (OC)	21.3	31
Hoba	Iron — ataxite	700	
Sikhote-Alin	Iron — octahedrite	410	44
Tagish Lake	C2 (CC)	0.25–1.2	
Murchison bolides	CM (CC)	~50	0.1–1

OC = ordinary chondrite; CC = carbonaceous chondrite. Data from *Popova et al.* (2011).

bolide and meteorite (*Borovička et al.,* 2013). While its first breakup was at high altitude (~45 km and 0.7 MPa), it underwent a series of fragmentation events. This included 11 fragmentations between 39 and 29 km under atmospheric dynamic pressure loads of 1–5 MPa and several boulders breaking off at 26–24 km under loads of 10–13 MPa. Interestingly, the main body remained relatively intact down to 22 km until its massive disaggregation at 18 MPa. This is probably due to the heterogeneities and highly shocked nature of the Chelyabinsk meteorite and the presence of extensive melt veins that welded portions of the meteorite.

Volatile-rich materials like the Tagish Lake meteorite are much different than the ordinary chondrite bolides. In this case the strength of the individual cobbles is roughly what is seen in the atmospheric breakup phenomena and this is the only case where the maximum compressive strength inferred in the atmosphere is greater than the compressive strength of the measured meteorite. This may be due to the presence of ice surviving in Tagish Lake. Recovered samples often expressed significant amounts of water when brought above freezing temperatures (*Brown et al.,* 2002), and samples of Tagish Lake that have been kept at freezing temperatures show lower porosity than samples that have been allowed to warm (*Ralchenko et al.,* 2014). It may be that ice-filled pore space within the meteorite provided extra strength for the bolide during atmospheric entry.

The meteorites listed in Table 1 are samples of hand- and cobble-sized survivors of atmospheric entry, which are the strongest and most coherent materials of the original small body. The vast majority of bolides do not survive entry as anything other than widely dispersed ablation dust. Typically the minority of small bodies that do survive entry lose approximately >95% of their preatmospheric mass (*Popova et al.,* 2011). Only a handful of bolides have been tracked to delivering material to the surface with that material recovered. Shown in Table 2 are bolides with recovered meteorites (*Popova et al.,* 2011).

TABLE 2. Select bolides with recovered meteorites (*Popova et al.,* 2011; *Borovička et al.,* 2013).

Meteorite (type)	Compressive Strength (MPa)		
	Range for Met. Type	First Breakup	Max.
Pribram (H5)	77–247	0.9	
Lost City (H5)	77–247	0.7	2.8
Innisfree (L5)	20–450	0.1	3
Chelyabinsk (LL5)	0.7	18	
Tagish Lake (C2)	0.25–1.2	0.3	2.2
Moravka (H5–6)	77–327	<0.9	5
Neuschwanstein (EL6)	3.6	9.6	
Park Forest (L5)	20–450	0.03	7
Villalbeto de la Pena (L6)	63–98	5.1	
Bunburra Rockhole (Ach)	0.1	0.9	
Almahata Sitta (Ure, OC)	0.2–0.3	1	
Jesenice (L6)	63–98	0.3	3.9
Grimsby (H4–6)	77–327	0.03	3.6

2.2. Bolides and Boulders

A bolide is roughly defined as a large, bright meteor that is typically brighter than the full Moon during its brief peak brightness. The physical phenomena are the result of a small body entering the atmosphere at hypersonic speeds [in the case of near-Earth asteroids (NEAs), velocities are in the range of ~12–20 km s^{-1}) and rapidly shedding their orbital kinetic energy into visible and thermal energy from friction with the atmosphere. As the body comes apart the initially compact mass fragments, exposing a larger surface area to rapid deceleration. This is seen as bright flashes within the bolide as smaller fragments rapidly heat, ablate, and decelerate. This typically occurs at altitudes ranging over 70–23 km and the small body's response to the atmospheric ram pressure can be used to estimate the body's coherent strength under compression (*Popova et al.,* 2011). These bolides are typically recorded on specialized optical tracking networks, but for the brightest objects security cameras and even dashcams are a valuable source of data (*Brown et al.,* 2002). Table 2 shows strength data from bolides with recovered meteorites. This permits a direct comparison of the strength of the surviving fragments with the strength estimated during the breakup of the small body on atmospheric entry.

Several points are readily apparent from Table 2. While most recovered meteorites are very strong, the initial breakup of the entering small body occurs at very low compressive stress. Initial breakup altitudes can be very high, as much as 70 km in some cases for the weakest bodies in Table 2, and the maximum compressive stress in Table 2 may occur at what are also substantial altitudes typically in the range of 35–20 km. For the initial breakup, these altitudes represent relatively low stresses, creating failures within weakly bound materials.

A question that has yet to be fully addressed is whether these stresses are consistent with some small asteroids being rubble piles, potentially held together by weak cohesive forces (see section 4.5). Examples of low-coherent-strength objects from Table 2 would include the Grimsby and Park Forest meteorites. However, while the first breakup provides insight into the strength of the entering body, the bolide phenomenon continues as the individual large pieces of the body break up under rising compressive stresses. Essentially these are the cobbles and boulders within the body shattering under rising stresses, and represent the state of fracturing and cohesion within individual components of the small body. For example, Park Forest started to fail under low compressive stress of 0.03 MPa, but the last major breakup was at more than 2 orders of magnitude greater stress. One possible explanation would be that the weak breakup occurred for a boulder within the rubble pile that failed along zones of preexisting weakness. While the basic material of ordinary chondrites is very strong, these objects are often pervasively fractured from a long impact and shock history and would be much weaker along their existing fractures. Indeed, that is the primary reason for multiple observations that large bodies are globally much weaker than smaller ones. However,

not all entering bolides fail under the stress of atmospheric entry. There are a number of examples of coherent "boulders" impacting the ground with little or no apparent fragmentation during entry. A recent example was the meter-sized boulder Carancas (H4–5) that created a 13-m-wide crater near Lake Titicaca in 2007 (*Borovička and Spurný,* 2008).

2.3. Meteorite Showers

While coherent boulders occasionally do survive atmospheric entry, a much more typical case is the meteorite shower. These are small bodies that break up in the atmosphere similarly to the observed bolides. Table 3 includes a list of selected large meteorite falls (meteorites that were observed to fall from space) and finds (meteorites that were found some time after they fell). The discussion of atmospheric breakup and observed bolides has focused on stony meteorites, since so far no iron meteorite falls have been instrumentally recorded. On the other hand, irons are much stronger under compression and tension than stones and recovered irons are typically much larger than stones. Most of the recovered mass of meteorites are irons and the 15 largest meteorites are all irons. There are strong positive selection effects in finding irons since they are clearly unusual in the terrestrial environment. That said, note that of the largest irons, only two are single bodies. The largest meteorite in total mass is Campo del Cielo, which fell in at least 30 fragments. Most of the fragments are buried so the mass and fragment count is a rough estimate. The largest single body to reach the ground is either Hoba, which was found in a single mass, or Sikhote-Alin, which fragmented on impact (producing a 60-m-diameter crater and more than 9000 fragments).

For stony meteors, almost all the large mass meteorites are showers. Some of the more famous showers are listed in Table 3. With stones, the entry phenomena make it more likely that they will shatter in the atmosphere, producing a literal shower of rocky fragments. These fragments tend to be largely homogeneous. Investigations of several showers have, with one notable exception, not found significant mineralogical variation within the shower (*Consolmagno et al.,* 2008). The major exception is the Almahata Sitta fall, which was primarily ureilite material with a significant component of ordinary chondrite (see the chapter by Jenniskens in this volume). Heterogeneity within meteorites is not unknown and it is not uncommon to find xenoliths (different meteorite types, literally "foreign rock") incorporated into meteorite breccias (*Brearley and Jones,* 1998); however, the level of heterogeneity is typically pretty small. Xenoliths are usually confined to single or a few clasts within a much larger homogeneous matrix. The shower data suggests that an Almahata Sitta level of heterogeneity is rare. For discussion about Kaidun, see the chapter by Borovička et al. in this volume.

TABLE 3. Selected large meteorites and showers (*Grady,* 2000).

Meteorite	Date (dd/mm/yyyy)	Mass (kg)	No. Fragments
Campo del Cielo (IAB Iron)	Find	100,000	30
Sikhote-Alin (IIAB Iron)	12/02/1947	70,000	9000
Hoba (IVB Iron)	Find	60,000	1
Cape York (IIIAB Iron)	Find	58,000	8
Willamette (IIIAn Iron)	Find	14,500	1
Pultusk (H5)	30/01/1868	8863	70,000
Allende (CV3)	08/02/1969	5000	1000
Jilin City (H5)	08/03/1976	4000	100
Tsarev (L5)	06/12/1922	1132	40
Knyahinya (L5)	09/06/1866	500	1000
Mocs (L6)	03/02/1882	300	3000
Homestead (L5)	12/02/1875	230	
Holbrook (L/LL6)	09/06/1866	218	14,000
Forest City (H5)	02/05/1890	122	2000

2.4. Summative Discussion

The data presented here on meteorites, bolides, and showers provides some basic insights on the structure of meteorite parent bodies up to several meters in size. For stony bodies of even a few meters in diameter, rubble piles seem to be the norm. The relatively low stresses on breakup seen in most of the bolides and the prevalence of showers for large stones point to a rubble-pile structure being very common. The individual components of these aggregates can be very strong, ranging up to an order of magnitude stronger than concrete, but the overall body is very weak. Volatile-rich bodies are both individually and collectively very weak.

Mineralogical homogeneity seems to be the general rule in small bodies. While there are significant exceptions and xenoliths are not uncommon, the shower data point to largely homogenous small bodies. Finally, for small bodies, irons are easily the strongest and most-coherent materials. Their large compressive and tensile strengths and apparent relatively low fracturing result in irons being by far the largest meteorites that survive atmospheric entry. However, they are relatively rare in the fall population, and the selection effects of their large strength suggest they are overrepresented in the fall population relative to their share of the NEA population.

3. ASTEROID BULK PROPERTIES

The next section probes the interiors of asteroids through a different approach, based on determining their bulk densities and bulk porosities. This takes us beyond the strength of the individual components of asteroidal bodies, either determined by measurements on meteorite falls or through inferred strengths in the upper atmosphere. The bulk densities are found by comparing mass estimates to volume or size estimates for these bodies. Bulk porosities are estimated by comparing the bulk densities to the asteroid spectral type, to determine likely grain densities and hence bulk porosities

The fundamental data compiled here concerning asteroid densities and macroporosities are presented in Figs. 1 and 2. Details on how the data were compiled are given in *Carry* (2012), and are not repeated here. While the previous section

was focused on meter-sized bodies, the focus in this section is necessarily on the other end of the scale, with most of the reliable data on densities and porosity existing for larger bodies, up to hundreds of kilometers. Only in a few situations are there good data on smaller bodies.

The first evidence on asteroid interiors was derived from meteorites, with identification of differentiated and nondifferentiated internal structures (see section 2). Dynamical families, originating from catastrophic disruptive collisions, provide another way to study asteroid interiors. Clumps of asteroids identified dynamically (e.g., *Bendjoya and Zappalà,* 2002) also share common surface properties, which are in turn used to discriminate genuine family members from the background population (*Parker et al.,* 2008; *Carruba*

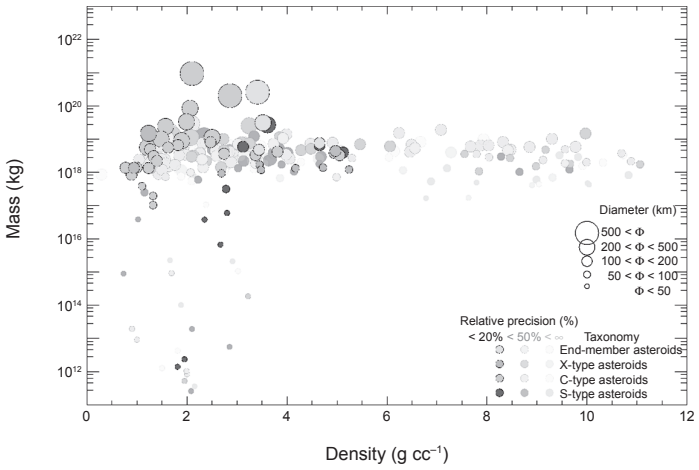

Fig. 1. See Plate 24 for color version. Density vs. mass. Asteroids are divided into four taxonomic groups (from *DeMeo et al.,* 2009): S-complex in red, C-complex in gray, X-complex in green, and end members in yellow. The size of the symbols indicates the asteroid diameter, below 50 km, between 50 and 100 km, 100 and 200 km, 200 and 500 km, and above 500 km. The three different levels of contrast correspond to three cuts of relative accuracy: <20%, <50%, and regardless of precision (<∞).

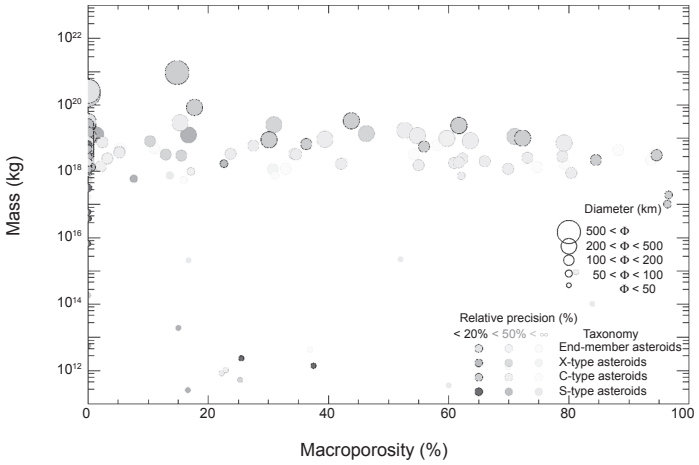

Fig. 2. See Plate 25 for color version. Macroporosity vs. mass. See Fig. 1 for the explanation of symbols.

et al., 2013). Such similarities are suggestive of a homogeneous interior for the parent bodies of these families (see the chapter by Michel et al. in this volume).

3.1. Density

Density is perhaps the most fundamental property for discriminating the composition and internal structure of asteroids (*Britt et al.,* 2002). It is also extremely difficult to measure, and the number of precisely measured asteroid densities is still very limited. This is because both mass and volume are required to determine the density of an asteroid.

Estimating any mass at all is a challenge, owing to the relatively low mass of asteroids as compared to other planetary objects. The exception is for binary asteroids, for which the total mass can be easily estimate (see the chapter by Margot et al. in this volume). The number of mass determinations thus limits the number of density estimates. The precision of these estimates is, however, limited by the uncertainty on asteroid diameters (*Carry,* 2012).

Any determination of the mass relies on measurements of the gravitational interaction between the target asteroids and other objects. The most accurate estimates (at a few percent accuracy) are derived from radio science experiments during spacecraft encounters [orbit or flyby (e.g., *Yeomans et al.,* 2000; *Abe et al.,* 2006; *Pätzold et al.,* 2011)] and studies of binary asteroids (see the chapter by Margot et al.). The vast majority of asteroids, however, have never been visited by spacecraft nor possess satellites [only a handful of large asteroids possess satellites, albeit the fraction is higher at smaller size; about 15% of near- Earth asteroids have satellites (*Margot et al.,* 2002)]. It is nevertheless possible to determine their mass from the gravitational pull they exert on other planetary objects: asteroids, planets and their satellites, and interplanetary spacecrafts (see, e.g., *Hilton,* 2002; *Fienga et al.,* 2008; *Kuchynka and Folkner,* 2013; *Goffin,* 2014).

Methods based on long-range influence rely heavily on the modeling of all relevant gravitational effects and interactions in the solar system (e.g., asteroid ephemerides, planets, general relativity) and are therefore more prone to systematic errors, and current precision is still limited to date [often above 50%, see the dispersion of estimates, together with the discussion on the accuracy and biases affecting mass estimates, in *Carry* (2012)]. Current samples of asteroid masses are therefore strongly biased. First, the best determinations are for binaries, but there may be differences between binary and single asteroid internal structures and thus extrapolating the density determined from binary asteroids to the whole population may introduce biases. Second, only large asteroids are massive enough to perturb the orbits of other objects. Thus this sample is mainly limited to asteroids larger than 100 km, while there is evidence for a size-dependence of the density owing to a different level of macroporosity [see Fig. 2 below and Fig. 9 in *Carry* (2012)].

The situation for diameter estimates is less dramatic. There are many techniques to measure the apparent size or surface area of an asteroid, and diameter estimates are available for tens of thousands of objects (e.g., *Masiero et al.,* 2011). Although diameter estimates are less prone to systematics than mass estimates [values generally agree to within measurement uncertainties (see *Carry,* 2012)], their contribution to the density uncertainty overwhelms that of mass. Diameter determinations have to be as accurate as 2–3% to allow density estimates to be more precise than 20%, a level over which density estimates hardly provide constraints. While simple modeling can have systematics above this level, realistic descriptions of asteroids, including knowledge of spin and three-dimensional shape, can provide this level of accuracy (see the chapter by Durech et al. in this volume).

Despite these limitations, the field of asteroid density has seen a revolution since the time of *Asteroids III* (*Britt et al.,* 2002). There has been a tenfold improvement in sample numbers (from 20 to 320), spanning many different taxonomic classes (and hence composition), diameters, and heliocentric distance (*Carry,* 2012). The upcoming decade will certainly provide many more determinations with a high level of accuracy. First, the stellar catalog at the microarcsecond level provided by the ESA Gaia mission should improve the precision on asteroid astrometry by an order of magnitude. Mass determinations from orbital perturbations should therefore become more precise. The observation of asteroids by Gaia will also allow the determination of the mass of about 150 asteroids with a relative precision better than 50%. It is even expected that 50 of these determinations will be more precise than 10% (*Mouret et al.,* 2007). The number of known binaries is also constantly increasing, adding to the number of high accuracy density estimates (see the chapter by Margot et al.).

3.2. Macroporosity

A density estimate by itself can restrict the list of possible components of an asteroid's composition. For example, a low-density asteroid such as (617) Patroclus [$\rho \approx 1$ g cm^{-3} (*Marchis et al.,* 2006; *Mueller et al.,* 2010)] cannot host large fractions of dense material or even silicates. The internal structure can be constrained using a comparison of the asteroid bulk density (ρ_A) with the grain density of its most likely constituents (ρ_C), as determined from study of the surface composition (see the chapter by Reddy et al. in this volume).

If $\rho_A \ll \rho_C$, the asteroid is underdense. This points toward large-scale voids or the presence of low-density material (i.e., volatiles) in its interior. While this is a typical case for comets, many asteroids are also seen to have porous internal structure. The porosity p, i.e., the fraction of volume occupied by empty space ($p = 1–\rho_A/\rho_C$), provides a measure of these structures. Because meteorites have microporosity (empty spaces at the grain-size scale, noted p_m), the macroporosity $\mathcal{P}$ has been defined as the fraction of volume occupied by large voids, i.e., $\mathcal{P} = p–p_m$. The question of the distribution of these volatiles or voids inside the asteroid remains open (*Britt et al.,* 2002). Following the terminology of *Richardson et al.* (2002), we can ask whether they are the results of cracks within a shattered monolith,

or interstices of a rubble pile formed through gravitational reagglomeration after a disruptive collision.

If $\rho_A \gg \rho_C$, the asteroid is overdense, and some high-density material must be present in its interior. This could be due to gravitational self-compression, differentiation (e.g., *Russell et al.,* 2012), or the result of the collision between two bodies of different densities. Most asteroids with a mass above 10^{19} kg are overdense, while the majority of asteroids below that threshold present some level of macroporosity. This is consistent with large bodies having enough internal energy from accretion and radioactive decay to differentiate.

If $\rho_A \approx \rho_C$, no clear conclusions can be made. However, given the comparable spectral properties observed among members of dynamical families, it may be reasonable to assume that the body is homogeneous.

3.3. What Can Be Concluded

Based on the data presented in Table 4 and Figs. 1 and 2, and more fully discussed in *Carry* (2012), there are a number of overall conclusions that can be drawn from these compilations, listed below.

- Asteroids in the S-complex are on average more dense than those in the C-complex.
- Asteroids in the C-complex seem to have larger macroporosity than those in the S-complex, hinting at a looser structure.
- The density of asteroids from both the S-complex and the C-complex seems to increase with the mass, apparently resulting from a decreasing macroporosity.
- In both the C and S-complex, NEAs (with masses from 10^{11} to 10^{16} kg) seem to have a lower density than main-belt asteroids, following the trend between mass and density observed for large asteroids.
- At comparable sizes, B-types appear significantly denser ($\rho \sim 2.4$ g cm^{-3}) than the other types of the C-complex that gather around $\rho \sim 1.4$ g cm^{-3}.
- While asteroids in both C- and S-complexes have narrow density ranges (with a few exceptions), asteroids in the X-complex covers a larger range, from the most dense Xc-types with $\rho \sim 4.9$ g cm^{-3} to X-types with $\rho \sim 1.8$ g cm^{-3}.
- Dwarf-planets (with masses above 10^{20} kg) apparently have little macroporosity, contrary to small bodies whose masses are inferior to $\approx 10^{20}$ kg (*Consolmagno et al.,* 2008).
- With the exception of NEAs, the dispersion in density and macroporosity is huge.

3.4. Future Prospects

As discussed above, the accuracy and reliability of density estimates have seen dramatic improvement since the time of *Asteroids III*. Even though many estimates still suffer from mild inaccuracy, the techniques are constantly being refined, and the next decade will provide more, increasingly reliable density measurements. A major issue still to be resolved is, how certain are the link between asteroids and meteorites? Based on their spectral properties, asteroids are classed within taxonomies (e.g., *Tholen and Barucci,* 1989; *Tedesco et al.,* 1989; *Bus and Binzel,* 2002). The latest to date by *DeMeo et al.* (2009) defines 26 classes, but analog minerals and meteorites have been identified for only 50% of them (see the chapters in this volume by DeMeo et al. and Reddy et al.). In other words, we have no reference density for half the taxonomic classes among asteroids. Discovering this meteorite-asteroid link is crucial for future interpretations of asteroid interiors.

4. ASTEROID STRENGTH AND FAILURE LIMITS

In addition to the constraints on asteroid density and porosity that can be determined from the population of ob-

TABLE 4. Average density, porosity, and macroporosity for the 12 (out of 26) taxonomic classes where density determinations more accurate than 20% are available ($\mathcal{N}$ determinations).

Class	Met.	$\mathcal{N}$	Density (g cm^{-3})	Porosity (%)	Macroporosity (%)
S	OC	11	2.72 ± 0.54	30.88 ± 8.76	25.28 ± 31.67
Sq	OC	2	3.43 ± 0.20	3.79 ± 0.35	–1.81 ± 2.16
B	CV	2	2.38 ± 0.45	38.66 ± 10.63	16.86 ± 6.81
C	CI	5	1.33 ± 0.58	84.96 ± 52.43	49.96 ± 43.61
Cb	CI	3	1.25 ± 0.21	96.80 ± 23.11	61.80 ± 20.86
Ch	CI	9	1.41 ± 0.29	74.47 ± 21.73	39.47 ± 16.29
X	EL	8	1.85 ± 0.81	90.81 ± 56.70	86.91 ± 147.58
Xc	Mes	2	4.86 ± 0.81	–9.47 ± 2.49	–14.47 ± 28.74
Xe	EH	1	2.60 ± 0.20	40.00 ± 4.42	36.20 ± 47.49
Xk	Mes	3	4.22 ± 0.65	4.27 ± 1.05	–0.73 ± 1.46
K	CV	1	3.54 ± 0.21	–6.78 ± 0.72	–28.58 ± 5.31
V	HED	3	1.93 ± 1.07	68.39 ± 53.72	57.39 ± 71.55

The analog meteorite of each class is listed. A negative porosity is indicative of an "overdense" structure. Table adapted from *Carry* (2012).

served asteroids, there are also significant constraints that can been gleaned from the combined data on asteroid spin rates, spin states, morphology, and sizes, filling the gap between meter-sized meteors (section 2) and kilometer-sized asteroids (section 3). The significant data for these inferences are summarized in Fig. 3, which shows asteroid diameters and spin rates taken from the database described by *Warner et al.* (2009). Also indicated on this figure are those asteroids that are tumbling or are binary asteroids, and a number of spin-limit curves as a function of different cohesive strength theories (all to be discussed later). Over the last few decades these observations have accumulated to the point where useful inferences on asteroid morphology can be made. In Fig. 3 we only show those bodies that have a quality measure of 2^- or higher, meaning that these observations are deemed reliable. It is interesting to note that there are a number of unconfirmed observations of spin periods (i.e., of quality measured less than 2^- and thus not shown in the figure) that could be significant if shown to be true. These are discussed later, in the hopes of motivating additional observations.

This data has motivated several different theories for the strength and morphology of asteroids. Significant among these is a better understanding that the spin limits do not require the rubble-pile hypothesis for almost all asteroids, the cohesion hypothesis in rubble-pile bodies, and the existence of tidal dissipations within such bodies. In the following subsections we discuss these issues in more detail, trying to integrate the physical and mathematical theories used to explain certain aspects of this data alongside a discussion of the data itself.

The precursor to these studies was given almost 20 years ago by *Harris* (1996), in which he noted that no asteroid had a spin period shorter than about 2.2 h and that the spin periods of objects in a given size range abruptly truncate at that value. He noted that this limit is essentially the spin rate $\omega_s = \sqrt{4\pi G\rho/3}$, where G is the gravitational constant and $\rho \sim 2.2$ is the bulk density, at which internal tensile stresses would be present within a spherical, constant density object (the actual spin rate for a body also depends strongly on its elongation). This spin rate also corresponds to local circular speed at the surface of the body, at which centrifugal forces equal the gravitational attraction of the body. From that connection he concluded that all or most asteroids must have a rubble-pile structure, as defined earlier, although that is not

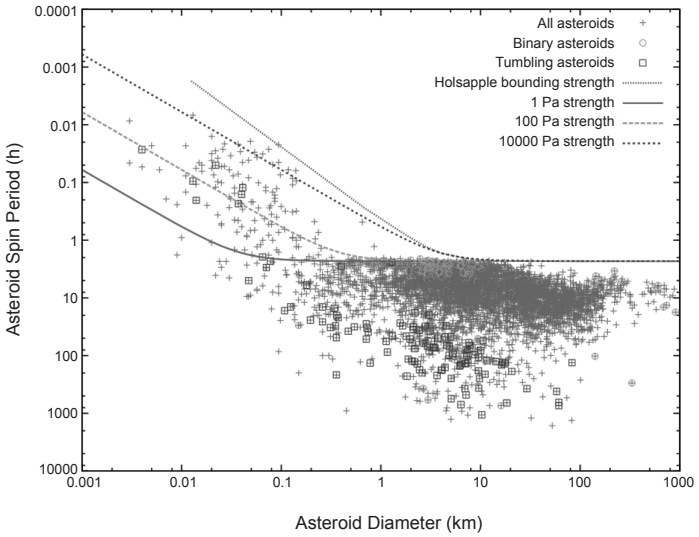

Fig. 3. See Plate 26 for color version. Asteroid size vs. spin period, with binaries and tumblers called out specifically. All others are assumed to be single, uniform rotators. Only bodies with periods deemed to be reliable (see *Warner et al.,* 2009) are shown. The plot shows distinct structures. No object larger than a kilometer in diameter spins faster than an ~2.4-h period, now known as the gravity spin barrier and that is understood to not be an indicator of cohesionless material by itself. Instead it is simply that at these size scales the gravity effects dominate any strength effect. A number of smaller bodies spin faster; those must experience tensile stress and must have some cohesive strength to hold together. Typically, the observed maximum spins are larger for smaller sizes. Also plotted are spin limits as a function of diameter for levels of asteroid strength. Data shown is as of August 2014.

the current interpretation. In addition, he also predicted that asteroids could spin faster than this limit if they had some strength, although no such asteroids were known at that time. He suggested there would be two regimes for spin, a gravity-dominated regime for larger asteroids and a strength-dominated regime for smaller asteroids. He suggested that in the strength regime their spin could increase inversely proportional to the diameter of the object. Since that paper, these ideas have been essentially verified and expanded, but with clarifications and new interpretations. A number of "fast spinners" have been found with shorter periods; however, they are all less than 1 km in diameter. And there have been detailed modeling studies deriving the relation between asteroid shape, maximum spin, and internal properties.

4.1. Analytical and Numerical Models of Rubble Piles

We first provide a brief review of current and past methods used to model asteroids, their interiors, and their morphologies. Studies of relations between shape, density, and spin of isolated self-gravitational bodies dates back several centuries, but mainly in application to fluid bodies. In those cases, the nature of the bodies was assumed to be fluid, the spin was known, and the goal was to determine the permissible shape. In 1687, Isaac Newton determined that the shape of a fluid Earth with gravitational and rotational forces is a slightly oblate spheroid. In 1742, Colin Maclaurin extended the work to discover the existence of equilibrium oblate spheroidal shapes with large ellipticity for rotating bodies with self-gravity, now called the "Maclaurin spheroids." *Jacobi* (1834) discovered the "Jacobi ellipsoids": equilibrium ellipsoidal shapes with three unequal axes. *Roche* (1850) added tidal forces during an orbit around a parent body and determined that there is a limit to the orbit radius, the famous Roche limit, inside of which there are no equilibrium solutions. *Poincaré* (1885) discovered other pear-shaped, non-ellipsoidal possibilities for equilibrium. *Chandrasekhar* (1969) gives a complete exposition of these classical works. A number of authors have used those fluid limits to infer limits on the mass density or density distribution of solar system bodies, although the mass density dependence can be swamped by other factors, the most important of which is the nonfluid composition. A separate approach to analyzing the internal stress properties of a nonfluid gravitating ellipsoid was given by *Chree* (1895), using linear elastic response from an initial stress-free state to model the mechanics of a self-gravitating body. This approach has motivated some modern study as well, discussed later.

Just as for a fluid, an ideal rubble-pile body can be assumed to have no tensile strength. But that does not mean that it behaves as a fluid. Consider an idealized rubble-pile body consisting of dry sand. Sand is an assemblage of relatively rigid, angular, submillimeter-sized grains that must interact during deformations. In a shearing deformation, the grains must move up and over adjacent grains. That motion is suppressed if the sand is subjected to a compressive pressure such as from gravity. That simple physical idea is the basis for the standard continuum soil mechanics models of failure, the Mohr-Coulomb and the Drucker-Prager criteria. In those models, the shearing strength is strongly increased by a compressive pressure in a relation that is assumed to be linear. The coefficient of that linear form is called the "angle of friction," although its presence is due to the interlocking of grains, not surface friction. These criterion have similar results, although Mohr-Coulomb is considered to be more accurate while Drucker-Prager is easier to handle analytically. It is the basis for the important difference between the behavior of water and the behavior of sand. The shearing resistance of water is independent of the confining pressure so that the angle of friction is zero. From this example it is clear that a material with no tensile strength can certainly have other strengths, including shear strength.

For that reason, the classical fluid theories relating shape and spin do not apply to rubble-pile, asteroid objects. *Holsapple* (2001, 2004) presented a comprehensive study of the relations between shape, spin, and internal properties for rubble-pile objects as a direct generalization of the historical fluid theories, and includes them as special cases. He assumed constant mass density, a general ellipsoidal shape, and in *Holsapple* (2001) a Mohr-Coulomb and in *Holsapple* (2004) a Drucker-Prager failure model. He was able to derive specific algebraic relations for the maximum spin allowable as a function of internal density, ellipsoidal shape, and angle of friction. *Sharma et al.* (2009) and *Sharma* (2013) analyze the problem following a somewhat different methodology and find similar results. Other studies on the stability of a continuum model of asteroids have also been made more in line with the classical approach developed by *Chree* (1895). In particular, *Dobrovolskis* (1982) studied internal stresses in Phobos; *Washabaugh and Scheeres* (2002) study the energetics of nonfluid, self-gravitating ellipsoids using a linear elastic model with a Young's modulus and Poisson ratio; and *Kadish et al.* (2005, 2008) studied stresses in bodies grown by accretion.

In the analytical realm Scheeres has also pursued the understanding of how a collection of self-gravitating rigid bodies evolves when subject to increasing spin rates. These studies have mainly focused on the dynamical stability of fissioned bodies (*Scheeres,* 2002a, 2009b), conditions for when bodies will transition from resting to orbiting configurations (*Scheeres,* 2002b, 2009a), and identification of different possible resting states that bodies may have when in contact (*Scheeres,* 2002b, 2012). These analyses are, by default, somewhat simple, although there are a few general results that can be discerned.

Over this same time period a number of researchers have pursued the modeling of cohesionless asteroid rubble piles using numerical methods, primarily with discrete element method (DEM)-based approaches. There have been two major modeling directions that have been used, the so-called hard-sphere DEM (HSDEM) and soft-sphere DEM (SSDEM) models. An HSDEM code models all particle interactions as impulsive, and thus does not directly determine or track forces. This is a computational simplification that allows for relatively rapid combined dynamical and interaction

computations, but makes it difficult to track or determine interior stress states or conditions. An SSDEM code allows for particle deformation (using an analytical model), and thus directly computes contact forces between the grains. This provides a more natural and realistic way for computing rubble piles in a condensed phase, as the grains are then allowed to come to complete rest with each other (which is impossible in an HSDEM as it only models two-body interactions), form force chains, and enable the internal stress state of the modeled body to be computed. The chapter by Murdoch et al. in this volume provides a more detailed discussion of HSDEM and SSDEM codes as applied to asteroids.

Some representative initial studies in this area for modeling asteroids were done by Richardson's group using an HSDEM code (*Richardson et al.,* 1998, 2005; *Walsh and Richardson,* 2006). They studied the ability of a collection of same-sized grains with a given level of spin to form a stable configuration, with the use of classical Jacobi or Maclaurin ellipsoids used as a measure of stability, and explored how such bodies would deform and fission following a planetary flyby or when subject to a rapid rotation rate. The mechanical properties of the grains are not directly controlled in these studies; in particular, the friction angle is simulated by having the grains either fall into a crystalline-packed matrix or through the use of a bimodal grain size distribution to promote a loss of friction (*Walsh et al.,* 2012).

Sánchez and Scheeres introduced a self-gravitating SSDEM model for describing the global behavior of rubble-pile bodies (*Sánchez and Scheeres,* 2011, 2012), in part to overcome such limitations. These models used grains with a size dispersion to avoid crystallization. The friction angle of the rubble pile is controlled by surface friction and interlocking. With this approach it becomes possible to track the internal stress and failure conditions using a granular mechanics code. Relevant results are given below.

An additional approach to the modeling of asteroid rubble piles was introduced in *Hirabayashi and Scheeres* (2014) and applied in *Hirabayashi* (2014) and *Hirabayashi and Scheeres* (2015). In this approach a detailed asteroid shape model can be used and the interior stress states computed by using commercial finite-element-analysis methods. This approach has the significant capability of being able to develop detailed models for the failure of asteroids when subject to gravitational and inertial forces. The use of a general approach enables the detailed analysis of plastic deformation modes and inclusion of detailed continuum model parameters such as Poisson ratio, cohesion, and angle of friction.

4.2. Rubble-Pile Shapes

Using the methods outlined above, the most fundamental question to be asked is what the expected shape of a rubble pile should be. Some insight can be gained by observing the surface slopes of asteroids, as these can indicate if there are regions that are clearly beyond the angle of repose for geological granular material; however, this cannot always be clearly linked to the internal processes. A number of different asteroid slopes have been computed in the past for specific shapes, and a recent analysis by *Richardson and Bowling* (2014) shows that most asteroids with known shapes have the majority of their surfaces beneath a typical angle of repose for granular material of ~35°. While there are some specific bodies that have significant regions of their surface that are clearly beyond these angles, such as (6489) Golevka (*Hudson et al.,* 2000) and (4179) Toutatis (*Hudson et al.,* 2003), such situations have not been commonly found in the estimated asteroid shapes described to date.

There have been some attempts at approaching the stability of rubble-pile asteroids through analysis of their shapes alone. *Harris et al.* (2009) and *Minton* (2008) approached the problem by analyzing the expected shapes of an asteroid where the surface slopes are constrained to be less than or equal to a certain limit. These analyses were used to explore the likely surface environment of rotationally symmetric, spheroidal asteroids commonly found to be the primaries of binary systems. The poster child of such asteroid shapes is (66391) 1999 KW_4–Alpha, which exhibits many peculiar features that are indicative of this body to be at or near its failure limit. More recently, *Scheeres* (2015) has studied these bodies using an approach that is fundamentally motivated by the surface slopes and combines some of the methodology from *Harris et al.* (2009) along with orbital dynamics considerations.

Such analyses are limited, however, in that they do not consider the totality of the mechanical principles that must be accommodated in order to say with certainty whether a given shape is stable or not. Indeed, it is possible for a given shape to have low slopes across its surface (even zero slope, and much less than the angle of repose), yet be structurally unstable as viewed from a mechanics point of view, which also considers its internal stress field and common failure theories. The necessary approach for that sort of analysis requires the development of a stress field within the body that accounts for all internal forces and that vanishes at the surface. The development of such stress fields is not in general unique. However, if one assumes linear elasticity, an ideal ellipsoidal shape, and a stress-free initial state, then a unique stress field can be derived. Given such a stress field, it is then possible to evaluate it against a failure theory, with the most commonly used ones being the Mohr-Coulomb or Drucker-Prager theory. For a cohesionless body these are simply specified as a function of their interior stress field for a given internal friction angle. Furthermore, there is only one stress state that is in equilibrium and also at the failure limit at each interior point. That occurs at a higher spin than for the elastic solutions, and provides the maximum possible spins among all possible stress fields.

In a series of papers, *Holsapple* (2001, 2004) applied this basic approach and evaluated the limit spins as a function of the ellipsoidal shape of a large range of asteroids modeled as ellipsoids of axes $a \geq b \geq c$. A representative result is given in Fig. 4, which depicts the maximum equilibrium spin as a function of the aspect ratio b/a, for a prolate object ($a > b = c$), along with data for a number of asteroids. The limit

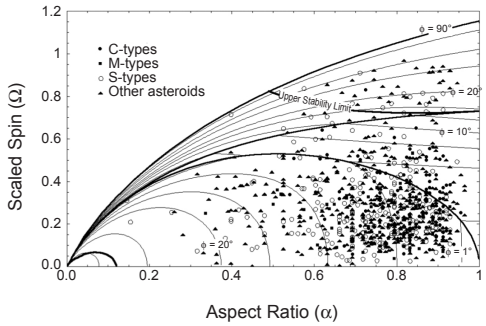

Fig. 4. Maximum equilibrium spin limits (Ω) for a prolate rubble pile body as a function of its aspect ratio defined as its polar extent over its total length, (α = c/a). The spin limit is normalized to be independent of density and depends upon the angle of friction, (ϕ), and for each angle of friction there is an upper spin limit and a lower spin limit. At the upper limit equilibrium cannot be achieved for a larger spin and at the lower limit equilibrium cannot be achieved for a smaller spin. Under the dictates of the theory all the asteroid objects plotted, even if not exactly ellipsodidal, must have some nonzero angle of friction arising from a particulate structure. See *Holsapple* (2001) for a more complete discussion of this figure.

spin is found to depend explicitly on the angle of friction, as is shown in the curves, which for most soils is on the order of 35°. (A fluid body with spin cannot be exactly prolate, but instead must have a Jacobi shape. Therefore it does not appear on this figure.)

Spherical asteroids are represented at the right abscissa of Fig. 4. As an example computation, assume a 35° angle of friction and a mass density of 2.5 g cm^{-3}. From this analysis the body cannot have a period shorter than 2.5 h before it begins to deform. However, the period at which a loose surface particle would spin off that spherical object is p_s = $2\pi = (\omega_s 3600) = 2.08$ h, the case noted by Harris (note that the surface speed for escape from a spherical asteroid is a factor of $\sqrt{2}$ faster than the spin-off speed, so a particle would not escape after spin-off unless the spin period was shorter than 1.5 hr). Between these limits loose particles spun off could remain around the asteroid for some period of time. A similar elongated ellipsoidal object with an aspect ratio of 0.5 has a deformation spin period limit of 4.2 h and the particle spin-off limit of 2.9 h.

These theoretical results add detail to the basic idea that rubble-pile asteroids cannot spin faster than some well-defined limit, with specific results about the dependence of that limit spin on the actual shape, density, and internal strength of an object. For the idealized ellipsoidal case, elongation lowers the spin limit, but not as much as the linear decrease as suggested in *Harris* (1996).

On a case-by-case basis these analyses can be compared to calculations with numerical codes. A particle-based analysis of equilibrium shape was presented by *Richardson et al.* (2005) using an HSDEM code with 1000 total particles. They considered a spinup of an initial shape and the subsequent reformation to an equilibrium shape. Those reformed equilibrium shapes were roughly consistent with the Holsapple continuum limits discussed above, but for an angle of friction of ~40°. Subsequent analysis by *Walsh et al.* (2012) indicated that the effective friction angle of their stacked hard-spheres was on the order of 40°, leading to consistency with this result. It is also relevant to note that *Washabaugh and Scheeres* (2002) showed that the total energy of ellipsoidal shapes at a given level of angular momentum was minimized in a broad region in the vicinity of the Jacobi and Maclaurin ellipsoids. While not providing specific failure conditions, their analysis did include the effect of Poisson's ratio in their stress field, accounting for a non-incompressible condition that has been associated with granular materials. In another study, *Tanga et al.* (2009) demonstrate the ability of rubble piles modeled with HSDEM to evolve toward the fluid equilibrium shapes of Jacobi and Maclaurin ellipsoids when subject to intermittent "shaking" due to relatively small impacts.

4.3. Deformation of Rubble Piles

A natural follow-on question regards the expected shape deviation of a rubble-pile body when subject to a changing angular momentum. For asteroids such changes in angular momentum are known to occur for smaller bodies due to the Yarkovsky-O'Keefe-Radzievskii-Paddack (YORP) effect (see the chapter by Vokrouhlický et al. in this volume) and for larger bodies due to impacts. The outcomes of such evolutionary questions can only be addressed through theory and simulation; however, such studies are important as they provide predictions for what may occur in actual asteroid systems.

This question of the fate of an object as its spin limit is slowly subjected to additional angular momentum was analyzed using a continuum model in *Holsapple* (2010). Such an object must globally change shape once it reaches the limiting failure condition outlined above in order to remain stable. Holsapple assumed that the body transitions through a sequence of evolving ellipsoidal shapes. The dynamical theory leads to an ordinary differential equation for the axis ratios of the ellipsoid (*Holsapple,* 2010, equation (45)), which can be numerically integrated. A typical result is presented in Fig. 5, which plots the axis ratios along level sets of solutions to the differential equations.

For an object starting in the upper right corner of this figure, which represents a slightly oblate initial shape, the body will flatten, becoming more oblate. It can ideally approach a very flat shape with thickness only a fraction of its diameter before then deforming to a prolate shape. For a body initially at a shape near the center of this plot, it will become more prolate, eventually approaching a very long shape, with a/c of 5.1 or more. As it deforms, although its angular momentum increases, in most cases its spin decreases because its moment of inertia increases. The implication of this is important for

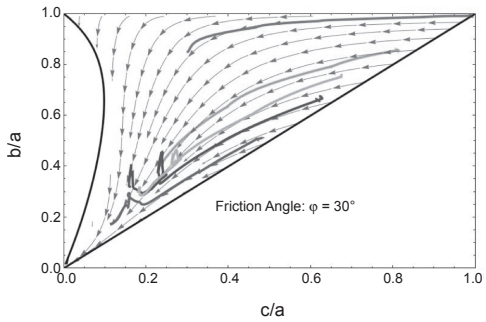

Fig. 5. Figure showing the deformation path of the semi-major axis ratios of an ellipsoid as its angular momentum is increased. An object with the angle of friction of 30° can be at its limit spin at any point along one of the curves in this figure. If the angular momentum is slowly increased, e.g., by YORP, the object deforms and traces a path in the direction indicated along the curves shown. The overlain lines show results of numerical simulations using a SSDEM model. From *Sánchez and Scheeres* (2012). These curves terminate when the body fissions, which is not modeled in the analytical theory.

interpreting the spin limit in Fig. 3. It predicts that bodies that lie at the minimum spin period line may not necessarily be at the limit of their angular momentum, but may be starting to go through a deformation that may actually decrease their spin rate as their angular momentum increases.

These deformational dynamics have also been seen in numerical simulations. *Walsh et al.* (2008) analyzed the effect of spinup on initially spheroidal rubble piles modeled with an HSDEM code. They found that as spin increased, components of the body would migrate to the equator, both causing a bulge to form and leading to loss of components into orbit about the body. These studies indicated a link between the expected shape deformation from YORP spinup and with these bodies being linked to binary formation. *Sánchez and Scheeres* (2012) also analyzed such spinup deformations using an SSDEM code. Their numerically computed deformations are plotted in Fig. 5 and are seen to closely follow the analytical curves derived by *Holsapple* (2010). However, we note that these simulations are only started in ellipsoidal shapes and are not constrained to be ellipsoidal (unlike the Holsapple computations). Thus as the angular momentum becomes large enough, the collections of grains are seen to undergo deformation beyond the classical ellipsoid shape. This is seen as the sequence of ideal ellipsoid deformations end once they become unstable and sensitive to collapse, which occurs at extreme elongations. The manner in which such systems fail range from surface shedding to fission, and is largely driven by the morphology of the mass distribution. Specifically, in the *Sánchez and Scheeres* (2012) simulations, initially ellipsoidal bodies are found to separate due to fission while initially spherical bodies are seen to shed material from their surface. Another possible outcome of deformation is a change in the body's YORP coefficient, which can cause a body's spin evolution to change sign, as initially noted in *Scheeres et al.* (2007) and recently studied in detail in *Statler* (2009) and *Cotto-Figueroa et al.* (2015).

Strongly oblate shapes have been found in several asteroids, some of which are fast rotating, such as (66391) 1999 KW_4, (341843) 2008 EV_5, (367943) Duende (formerly 2012 DA_{14}), (101955) Bennu (formerly 1999 RQ_{36}), (65803) Didymos, (2867) Šteins, and others. The equators of these objects generally protrude outside the equivalent oblate ellipsoidal shape, and therefore loose particles at their equator can spin off (*Scheeres,* 2015). Such shed particles are found to eventually escape (*Jacobson and Scheeres,* 2011a), although if sufficient numbers are shed in a short period, they may also form into a secondary (*Walsh et al.,* 2008, 2012). Analytical studies of such spunup shapes have been published by *Harris et al.* (2009), *Minton* (2008), and most recently *Scheeres* (2015). These studies seek to tie surface deformation to the overall shape of the body, with a particular focus on the oblate, fast-spinning shapes that have been associated with primaries of binary asteroids.

4.4. Evidence for Fission

One predicted outcome for rapidly spinning bodies is that they can undergo a shape bifurcation and separation into multiple components. This outcome is to be compared to the loss of material directly from the surface — a distinction that has been studied to some extent in *Walsh et al.* (2008), *Hirabayashi and Scheeres* (2014), and *Hirabayashi* (2014). Analytical methods applied to simplified studies have been able to model such fission mechanics. In *Scheeres* (2009a) it was shown that the first components to fission in a non-uniform body will be those whose mass centers are the furthest from each other. For simple models of ellipsoids resting on each other, this corresponds to the distinct bodies fissioning first. Under this assumption, it is possible to show that the dynamical evolution of a fissioned body can be directly related to the relative mass fraction between the components (*Scheeres,* 2007, 2009b). Specifically, if the mass ratio between the bodies is less than ~0.2, the resulting system has positive total energy and can escape [albeit not immediately (*Jacobson and Scheeres,* 2011a)], while for mass ratios larger than this the bodies are gravitationally bound and cannot escape without exogenous forcing.

This theory was specifically supported with the observations from *Pravec et al.* (2010) on asteroid pairs, which are asteroids that have had an extremely close passage to each other at an extremely slow speed (<1 m s^{-1}) at some point in the past (*Vokrouhlický and Nesvorný,* 2008). In the Pravec survey the relative sizes of asteroid pairs were determined and the spin period of the primary measured (see Fig. 6). This survey showed the predicted relation between mass ratio and formation of asteroid pairs, as there is a cut-off in asteroid pairs for mass ratios larger than ~0.2. As a secondary confirmation, the analysis also showed that the spin rates of

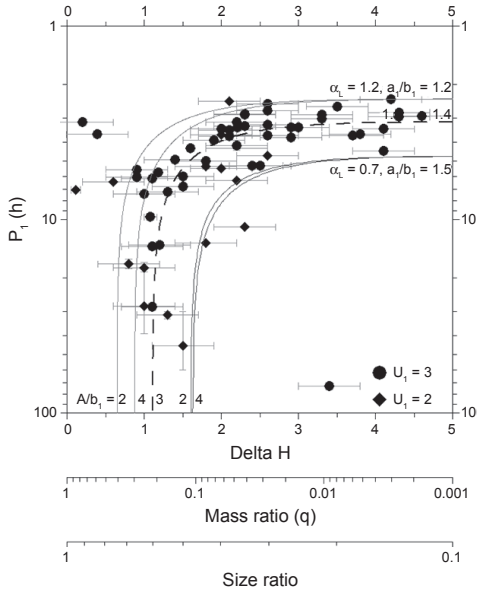

Fig. 6. Asteroid pairs showing the mass ratio and spin period of the primary with data through September 2014 (*Pravec,* 2014). There are a few significant outliers that do not fit with the theory, although the majority of added pairs is consistent with the initial interpretation in *Pravec et al*. (2010), where the parameters and detailed models used are described.

primaries decrease as the mass ratio limit is approached, which is the predicted mechanism for ejection, where energy for escape is taken from the spin rate of the primary. Additional observations of asteroid pairs have largely been consistent, although there are a few bodies that do not follow this rule and thus may be asteroid pairs formed by another mechanism (cf. *Vokrouhlický and Nesvorný,* 2008). There have also been spectroscopic studies of these asteroid pairs by *Polishook et al.* (2014), which have also been interpreted to support the fission hypothesis. This is significant as it has direct bearing on the manner in which rubble-pile bodies fail, even though there is not much detail. The implications of such fissioning have been investigated in *Jacobson and Scheeres* (2011a), which is described more fully in the chapter by Walsh and Jacobson in this volume.

4.5. Spin Limits for Cohesive Objects

Since *Asteroids III,* a significant number of small asteroids spinning above the limits derived for a cohesionless rubble pile have been discovered. Those objects, whose existence was predicted in *Harris* (1996), must have sufficient internal strength to withstand their internal tensile stresses. The question these bodies raise is what physics provide the source of that strength, what magnitude of strength is needed, and whether these can still be thought of as rubble-pile bodies.

That question was first addressed in *Holsapple* (2007), where the rubble-pile analysis outlined above was expanded to include strength models with cohesive strength, and it was found that the limit spins could be substantially faster if the internal material was capable of withstanding some level of tensile stress. However, that is true only for smaller asteroids, as can be seen in Fig. 3, as all the strength-limit curves fall back to the nominal spin limit for increasing size (which is the reason why the gravity spin limit does not necessarily imply cohesionless rubble piles). Holsapple derived specific limit curves for two strength cases. First, for a constant strength it is found that the maximum spin rate decreases linearly as the asteroid diameter increases, as noted in *Harris* (1996). Second, it was assumed that the strength of meter- to kilometer-sized objects will decrease with increasing size, to the –1/2 power, and in this way accounting for increasing planes of weakness in a larger body. Then the limits of spin vs. size decrease with the power of –5/4. The resulting curve is the upper, bounding curve plotted in Fig. 3. This curve furnishes an upper bound to all the present data and is for a material that has a tensile strength of only 100 kPa in a 10-cm specimen, and then decreasing as $1\sqrt{r}$ with size r. That value is more than an order of magnitude less than measured for typical meteorites (see section 2). Therefore, whether these data are really constrained by a strength limit or not remains an open question, as the limit may only indicate a lack of mechanism to further increase spin rates. A related question is also whether this represents the strength of individual components.

Sánchez and Scheeres (2014) have investigated the question of what minimum level of strength could exist between rubble-pile components. It is an important distinction that they are not considering the strength of all components, but are probing for the presence of possible cohesive strength between rubble-pile components. Their theory notes that van der Waals attractions between the finest material present in the rubble pile (in sufficient quantities to form an underlying matrix of material) should hold larger components in place, in the same way that cement holds rocks within a matrix. Using data from the Apollo lunar experiments and samples, and information on size distributions inferred from observations and samples from Itokawa, they predict the possible strength of this regolith to be on the order of 100 Pa, with their preferred value stated as 25 Pa (it should be noted that this value depends on an assumed density, angle of friction, and other shape parameters). This model probes the lower end of the strength envelope to determine whether there is any evidence for such cohesive strength in rubble-pile asteroids.

Sánchez and Scheeres (2014) point to a few aspects of the asteroid size, spin, and morphology database represented in Fig. 3, in addition to some specific asteroids, as evidence for their theory. First they note that cohesive strength between rubble-pile components greater than ~100 Pa should

lead to a more filled-in population below the strength line in the intermediate size range of 0.1–1 km. However, only when total effective strength (which is actually a function of density and shape assumptions as well) falls below the 100-Pa limit is the visual gap less significant. Another prediction from this theory is that binaries should not form when less than a certain size, as the spin rate required for fission to overcome cohesion would cause the resulting fragments to separate at speeds in excess of their mutual gravitational escape speed. They use this to explain the sharp drop-off in binaries below a few hundred meters, which has been shown to be statistically significant (see the chapter by Margot et al. in this volume). Finally, the presence of small and rapidly spinning tumbling asteroids at the strength limit is also consistent with the failure of rubble-pile asteroids with cohesion, as such a failure will generally induce tumbling in the separated bodies, which will also immediately escape from each other (*Scheeres et al.,* 2010). There are also a few specific bodies that provide additional support for this weak level of strength being present in a rubble-pile body. These are P/2013 R3, (29075) 1950 DA, and 2008 TC_3, which are discussed in the final section.

Before continuing it is important to note that the apparent gap between strengths greater than 100 Pa and the observed bodies in the 0.1–1-km range has been challenged by a number of observations that show the existence of objects that fill in the region beneath the upper bound. These are noted in *Holsapple* (2007) and reported in *Masiero et al.* (2009), *Chang et al.* (2014), and *Urakawa et al.* (2014). These observations have not been deemed sufficiently reliable in the lightcurve database (*Warner et al.,* 2009) to include in the confirmed cases. It is important that these objects be viewed in future apparitions to confirm them. Confirmation of these bodies' size and spin rates would have a significant impact on our understanding of the possible strength of asteroids.

5. PROBING ASTEROID INTERIORS

Although the previous models and interpretations take the interior properties of asteroids into account, they do not directly sense or constrain the interior properties or geophysics. This is because they still rely on external measures of the asteroid stability state, such as its shape, size, and spin. This section discusses approaches that are currently being developed to probe the interior properties of an asteroid, taking advantage of fundamental geophysical properties and observable effects. There are three main recent advances in this area, the first of which is the classical interpretation of surface geological structures to make inferences on the interior of an asteroid. Second is the analysis of the interior seismic properties of rubble-pile bodies. Third is the analysis of tidal dissipation effects within small rubble-pile bodies. A fourth advance that can be mentioned in passing is the use of radar to probe the interior of a rubble-pile body. However, there have not been definitive analyses of this approach for asteroidal bodies, although such analyses will be performed for the first time at a comet by the Rosetta spacecraft.

5.1. Geological Interpretation

The classical approach to interpreting the interior structure of an asteroid was pioneered at the asteroid (433) Eros, although it has also been applied to interpret the interior of Phobos (see the chapter by Marchi et al. in this volume). The underlying theory is outlined in *Prockter et al.* (2002) and interprets surface features as expressions of subsurface strength. The key focus was on the lineaments and global structures such as Rahe Dorsum on Eros. *Buczkowski et al.* (2008) studied the lineaments across Eros to determine whether there was clear evidence for internal strength or structures. While certain correlations seem to exist, along with evidence for some subsurface structure, it is also difficult to independently confirm what these structures may be, whether they arise from the mechanical properties of the regolith itself, or how they could be uniquely estimated (*Robinson et al.,* 2002). The approach has also had limited use at (25143) Itokawa, where there are no specific global geographic features that could be used to make interior interpretations other than the component shapes themselves. On the other hand, such an approach can be very valuable at a larger body such as (4) Vesta, which has many global features that could be used as constraints on the interior of the body (reviewed in the chapter by Russell et al. in this volume).

5.2. Seismic Effects

The importance of seismic effects was underlined by the Near Earth Asteroid Rendezvous (NEAR) observations of Eros. While craters were present on that body, they became more sparse at smaller sizes, with the surface dominated by a thick layer of regolith (*Chapman et al.,* 2002). This was explained using a statistical and global analysis of crater erasure due to seismic shaking as a result of impacts on Eros (*Richardson et al.,* 2004). In a subsequent analysis, *Thomas and Robinson* (2005) were able to positively correlate the erasure of small craters with a single large impact, thus linking the transmission of seismic energy from an impact to the surface motion of regolith and not due to regolith created in the impact itself. The chapter by Marchi et al. in this volume reviews this material in more detail.

Motivated by, and contemporaneous with, this physical correlation there were many different studies of the effects of impacts on the redistribution of regolith. These include the use of particle hydrodynamic codes for simulating impacts (*Nolan et al.,* 2001), coupled models of seismic transmission and granular motion (*Richardson et al.,* 2004; *Richardson and Bowling,* 2014), and the application of Earth geophysical models of seismic-energy transmission to rubble-pile bodies (*Martin et al.,* 2008; *Blitz,* 2009).

A culmination of these analyses is the realization that the mechanical properties of a rubble-pile body can be linked with the observed crater distributions and levels of erasure. *Asphaug* (2008) proposes a methodology to directly estimate the attenuation of seismic energy within a rubble pile using the observed largest crater on that body. This basic idea has

also migrated beyond the use of naturally occurring impacts to include the application of controlled and induced cratering blasts or impacts on the surface of a rubble-pile asteroid. By controlling the energy and deposition of the blast, it is possible to infer the seismic transmission of energy at distal points of a rubble-pile body by comparing before and after images of the surface. This can be enhanced by the deployment of instrumented devices across the surface, where they can record the sensed seismic energy or, in the extreme case if they are lofted from the surface, determine the strength of the seismic wave by tracking the length of their ballistic phase. Such ideas were proposed in *Scheeres et al.* (2003) and have subsequently appeared as a concept in a number of space science missions, with the combination of calibrated blasts and sensing measuring devices proposed in the Discovery mission Binary Asteroid In-Situ Explorer (BASiX) (*Robert et al.,* 2010). Similar concepts have also been subsequently proposed in the mission concepts of MarcoPolo-R (*Michel et al.,* 2014) and Asteroid Impact and Deflection Assessment (AIDA) (*Galvez et al.,* 2013). This approach to seismic inference will be realized with the currently planned Hayabusa-2 mission to primitive asteroid 1999 JU_3. This mission concept calls for using an explosive device to accelerate an impactor into the surface of the body, creating a crater and seismic energy source that can then be tracked by observing modifications of the surface (*Tsuda et al.,* 2013).

5.3. Tidal Dissipation

Another measure that can used to peer into the interior of a rubble-pile body is related to energy dissipation due to tidal deformations. There are two main ways in which rubble-pile bodies can dissipate excess kinetic energy via this method. One occurs if the body is in a non-uniform rotation state, as this induces traveling waves of alternating accelerations, which can cause stress and strains that dissipate energy. This effect has been linked to the fact that the vast majority of asteroids are in or near a rotation state about their maximum moment of inertia (*Burns and Safronov,* 1973). *Harris* (1994) showed that the vast majority of known tumbling asteroids had an overall slow rotation rate, meaning that the time for them to relax to uniform rotation could be long, although these estimates depend on assuming that the geophysical properties of larger planetary bodies and satellites are similar to rubble-pile bodies.

To better constrain and understand how the observed tumblers should be interpreted in terms of their internal geophysics of tidal dissipation, there have been several analytical and numerical studies of how asteroids could enter complex rotation states and what the frequency of them entering such states should be. This would allow for the comparison of the population with different dissipation rates. The trend of tumbling with greater spin period implicitly indicates that asteroids are dissipative bodies. The degree of dissipation is not fully understood, and depends on the assumed parameters of rigidity, μ, which measures the stiffness of the body; the quality factor, Q, which is inversely proportional to the rate of energy dissipation due to non-uniform deformations; and the rate at which tumblers are created. We note that tumblers can be created in several ways: catastrophic disruptions (*Asphaug and Scheeres,* 1999; *Scheeres et al.,* 2000b), planetary flybys (*Scheeres et al.,* 2000b, 2005; *Pravec et al.,* 2014), YORP-induced fission (*Sánchez and Scheeres,* 2014), and, potentially, YORP spindown effects either in isolation (*Vokrouhlický et al.,* 2007) or in combination with impacts (*Marzari et al.,* 2011; *Henych and Pravec,* 2013).

On the other hand, the application of standard planetary theory geophysics to rubble-pile asteroids made in earlier studies may not be appropriate. This has motivated researchers to develop improved mathematical models and to carry out geophysical analyses that are relevant for this environment. *Efroimsky and Williams* (2009) considered the effect of frequency dependent terms in tidal dissipation, while *Sharma et al.* (2005) and *Breiter et al.* (2009) have developed novel mathematical expressions for tidal dissipation. Perhaps most fundamental, however, is the study by *Goldreich and Sari* (2009), which shows that rubble-pile bodies are expected to behave distinctively relative to the classical planetary satellite theory. In their analysis they show that the functional relationship between the quality factor, Q, and the Love number of an object, k (related to the rigidity of the body and how the shape responds to tidal stress), should follow a variation where $Q/k \propto r$, the radius of the body, which is distinctly different than the classical relationship. Specifically, they show that the effective dimensionless rigidity of a rubble pile is smaller than that of a monolithic body of the same size, with the reduction arising from the concentration of stresses due to the presence of voids. Using this result they show that it is likely that a rubble-pile secondary in a binary asteroid system should circularize, which cannot be necessarily concluded if the secondary is monolithic and follows the classical planetary relation. The implications of their analysis for the relaxation time for tumbling asteroids has not been made as of yet.

The Goldreich and Sari analysis has been applied to develop a more detailed model for the expected evolution of binary asteroid systems. In *Jacobson and Scheeres* (2011b) they analyze the joint evolutionary dynamics of tidal dissipation and the binary YORP (BYORP) effect (see the chapter by Vokrouhlický et al. in this volume) in light of the Goldreich and Sari theory for tidal dissipation. They find that there should exist a so-called BYORP and tide equilibrium where a contractive BYORP effect acting on the synchronous secondary is balanced by an expansive tidal effect due to dissipation in the rapidly rotating primary. The existence of this equilibrium is significant for a number of reasons, described elsewhere in this volume in the chapters by Walsh and Jacobson and Vokrouhlický et al. In the context of this chapter the significance is that this provides a direct way in which to constrain and indirectly measure the rigidity of the primary in a rubble-pile binary asteroid. Once a binary asteroid is known or suspected to lie in such an equilibrium, it also provides a way to evaluate the functional relationship between a body's size and its quality factor and tidal

Love number. The existence of this equilibrium has been recently validated for binary asteroid 1996 FG_3 (*Scheirich et al.,* 2015). From that study there is an inferred value of rigidity times quality factor of $\mu Q \sim 2.7 \times 10^9$ Pa, which is orders of magnitude less than that expected for a monolithic body and for what has been bounded in the past for binary asteroids (*Margot et al.,* 2002). This result is significant, as it is the first "measured" value of this parameter for a rubble-pile body, albeit there are a number of significant sources of uncertainty that are discussed in that paper.

A significant next step in analysis will be to start to blend these results to better understand the dissipation rate within rubble-pile bodies. This will require additional theoretical, observational, and ultimately numerical computations to fully understand. It also provides motivation for a space science mission to a binary asteroid in a BYORP-tide equilibrium, since obtaining a precise estimate of the rigidity requires that the secondary body be fully mapped.

6. SPECIFIC ASTEROID OBSERVATIONS

In addition to the insights obtained by analyzing the asteroid population database, there have been significant insights from analyzing specific asteroids. There have been a number of dramatic and unprecedented observations of single bodies that provide deep insight into the morphology and, in some cases, the mechanical properties of these asteroids. In the following we discuss some of the more significant of these bodies. As some of these bodies are discussed in more detail elsewhere, in some cases we only draw on a few aspects of the analysis and indicate the appropriate chapter for more details. Instead of grouping these bodies by how they were observed, which could be done, we just list them in order of their alphabetical names and designations.

6.1. (433) Eros

At the time the *Asteroids III* book was being completed, significant, but incomplete, data on asteroid (433) Eros taken by the NEAR-Shoemaker spacecraft was already included. The definitive analysis of the gravity field of this asteroid had not been published, however, and is what we focus on here. Initial data indicated that the asteroid's gravity field was homogeneous at the few-kilometers scale (*Asphaug et al.,* 2002). Subsequent analysis of the gravity field was made and reported in two papers (*Miller et al.,* 2002; *Konopliv et al.,* 2002). Both papers included a comparison between the measured gravity field and a homogenous gravity field computed from the shape with a constant density assumption. Density variations can be detected through the comparisons of measured and computed gravity field coefficients (cf. *Scheeres et al.,* 2000a; *Takahashi and Scheeres,* 2014). Gravity field comparisons in both papers showed differences at the relative level of less than 10^{-3} through the 6th degree-and-order gravity terms. At higher degree and order the uncertainty in the gravity-field coefficients was greater than this relative level, meaning that at these higher levels the differences were indistinguishable from noise. This provides a strong constraint on the density homogeneity within this asteroid. We also note that the bulk density of this body was determined to be 2.67 ± 0.03 g cm^{-3} (*Miller et al.,* 2002), indicating a relatively low level of macroporosity of approximately 20% assuming the S-type asteroid had a grain density of ordinary chondrites (*Yeomans et al.,* 2000). The *Miller et al.* (2002) paper also made an accurate rotation-state estimate for the body, and was unable to observe any complex rotation except that driven by solar torques. This indicates that the body had fully relaxed to principle-axis rotation.

6.2. (25143) Itokawa

The asteroid (25143) Itokawa was visited by the Hayabusa spacecraft in 2005 (see the chapter by Yoshikawa et al. in this volume). The greatest achievement of that mission was the collection of a small but valuable sample of regolith from the surface. However, several important observations and measurements of the asteroid were also taken during the few months that the spacecraft was in close proximity to that body. There were several important determinations with regard to the geophysics of this asteroid. These include the total bulk density of the body, measured to be 1.9 ± 0.13 g cm^{-3}, corresponding to a macroporosity of 41% for this S-type asteroid (*Fujiwara et al.,* 2006). As the spacecraft never spent significant time in ballistic motion close to the asteroid, the gravity field determination was not able to progress beyond the total mass. Subsequent to the mission it has been speculated that the density distribution within the body is heterogeneous. This idea was first proposed in *Scheeres and Gaskell* (2008) to explain the apparent disconnect between the predicted YORP torque (which was computed to be negative based on several different computations) and the lack of a detected change in its spin. This theory predicted that either the head or neck region of the body should have a greater density. *Lowry et al.* (2014) were able to detect a measurable acceleration in the spin rate of Itokawa. Based on the theory outlined in *Scheeres and Gaskell* (2008) and *Breiter et al.* (2009) it was determined that the density disparity between the head and body would need to be 2.85 and 1.75 g cm^{-3}, respectively, for this effect alone to account for the disparity. Such a drastic disparity between densities, 62%, is not out of the question given that the secondary and primary of (66391) 1999 KW_4 have a large density disparity, although for that body it is only 42% for the nominal values (see below). However, as discussed in the chapter by Vokrouhlický et al. in this volume, there are other effects besides a density disparity that could have caused the acceleration of Itokawa, making the result somewhat uncertain.

Beyond the mass, bulk density, macroporosity, and possible density heterogeneity, important information was obtained regarding the size distribution of rocks, boulders, and grains on Itokawa. Based on images taken while in close proximity to the body, the size distribution of boulders and rocks across its surface was measured and found to follow a size distribution with an exponent of -3.1 ± 0.1 down to

5 m (*Michikami et al.,* 2008). A more recent paper revisits the Itokawa data and focuses on the difference between the head and body of this asteroid, as well as discussing several possible hypotheses for its formation (*Mazrouei et al.,* 2013). They find a somewhat steeper size distribution down to 6 m, albeit changing depending on where on the body one looks. Ultimately their general conclusions on the distribution of larger blocks are consistent with *Michikami et al.* (2008). Using the returned samples, a size-distribution analysis was also made by *Tsuchiyama et al.* (2011). Across the grain sizes ranging from 0.5 to 100 μm they found a size distribution with an exponent between –2.8 and –2 (steeper at the smaller sizes). While these two size distributions (from the observations and the samples) cannot be easily combined, they do present some insight into the size distribution of grains and boulders within a rubble-pile asteroid. Tscuchiyama et al. present the hypothesis that the size distribution may break to a shallower level at millimeter- to centimeter-sized grains, which may explain why they were viewed as the dominant grain size on the body [at least in the Muses-Sea region (*Yano et al.,* 2006)]. These measurements of size distribution are important as they speak directly to the presumed size distributions that all rubble-pile bodies may have. Also, the recent theory on cohesive strength in rubble piles (*Sánchez and Scheeres,* 2014) depends explicitly on the presence of fine regolith grains for its physical realization.

6.3. (216) Kleopatra

The asteroid (216) Kleopatra is a strangely shaped main-belt asteroid with a total length on the order of 250 km and with a very narrow "neck" (*Ostro et al.,* 2000). This asteroid has already been distinguished by its rapid rotation and odd shape. *Descamps et al.* (2011) reported the discovery of two satellites about this asteroid, enabling a precise mass of the asteroid to be determined. However, while their observations were also consistent with the *Ostro et al.* (2000) radar-based shape, they reported finding a significantly larger size for this body, approximately 25% larger in mean diameter than the Ostro et al. radar shape. A different set of observations by *Marchis et al.* (2012) reported an even larger size, raising the interesting situation of knowing the mass and shape of the body but not its size and hence density. The rapid rotation of this object and its shape mean that the stability of this body is highly sensitive to its bulk density and size. *Hirabayashi and Scheeres* (2014) took advantage of this size ambiguity to probe the stability of this body across a range of sizes, from the *Ostro et al.* (2000) size to the *Marchis et al.* (2012) size. Based on an averaged stress analysis, essentially applying the averaging method of Holsapple to a non-ideal shape, they were able to determine that the *Descamps et al.* (2011) size requires the lowest angle of friction to keep the body stable. This analysis has also been confirmed using a finite-element plastic-deformation analysis that shows that the smaller *Ostro et al.* (2000) size will tend to collapse, the larger *Marchis et al.* (2012) size will tend to separate, and the *Descamps et al.* (2011) size seems to be the most stable again, and is only susceptible to surface failures that could be related to inaccuracies in the detailed shape of the body (*Hirabayashi,* 2014). This analysis is listed here as it represents a unique use of continuum and failure theory to help resolve an inconsistency in measurements.

6.4. (29075) 1950 DA

The asteroid (29075) 1950 DA is well known as one of the most hazardous bodies for Earth in the solar system, due to its relatively high impact probability of 1 in 4000 (albeit in the year 2880) and its relatively large size, on the order of 1 km (see the chapter by Harris et al. in this volume). In *Rozitis et al.* (2014) the body's density is determined by using the measured Yarkovsky acceleration of the body and analyzing the thermal inertia. This allowed them to infer that the body was a rubble pile, that the rotation of the body was retrograde, and that the corresponding shape model for this rotation pole could be used (*Busch et al.,* 2007). Based on these measurements, *Rozitis et al.* (2014) determined that the body was spinning beyond the failure limit at which both loose material would be shed from its surface and it would undergo global deformation. Due to this they concluded that the body required cohesion to stay intact, and applied basic techniques (*Holsapple,* 2001) to determine the level of cohesive strength needed. Based on a Drucker-Prager failure model they were able to identify a minimum necessary strength of approximately 65 Pa for the body to hold together, which they note is comparable to the level of strength for rubble-pile bodies hypothesized in *Sánchez and Scheeres* (2014). A detailed finite-element analysis was performed by *Hirabayashi and Scheeres* (2015) that confirmed this strength as a lower bound and found that for uniform strength, the center of the body should fail prior to the surface. They note that should this occur, it could result in a less-dense core, which could be detected with an orbiting spacecraft.

6.5. (66391) 1999 KW_4

The binary asteroid (66391) 1999 KW_4 was observed with range-Doppler radar at a number of epochs, enabling a detailed model of the shapes of each of its components and their relative orbital and rotational dynamics *(Ostro et al.,* 2006; *Scheeres et al.,* 2006). These papers provided the first, and to date most accurate, insight into the morphology of a binary asteroid system, and it is of interest to briefly review the results here. First, it is important to note that in the nominal model the primary rotates just shy of where loose material should be shed from its surface, implying that its interior may also be close to a failure limit. At the lower end of density for the primary the surface may require cohesive strength to stay together. Thus this body exhibits and showcases the traits of the rapidly rotating oblate bodies discussed earlier in this chapter and has been used as the motivating example of this class of body (*Harris et al.,* 2009; *Scheeres,* 2015).

The primary has an obliquity of about 3° with respect to the orbit plane of the binary and the secondary has relative

librations of several degrees. Thus the system is not in a fully relaxed state. Based on the shape of the secondary we note that the predicted BYORP coefficient is positive, meaning that this system could be undergoing expansion (the system is currently being monitored for BYORP expansion, as described in the chapter by Vokrouhlický et al. in this volume). As this system has not settled into a fully relaxed state it introduces the interesting possibility that it could be tracked over longer time periods to possibly determine or detect effects associated with either tidal relaxation or with BYORP expansion.

There is a large density disparity between the primary and secondary body. The primary density is determined to be 1.97 ± 0.24 g cm^{-3} and the secondary to be $2.81^{+0.82}_{-0.63}$ g cm^{-3}, a relative factor of 42%. Possible reasons for such a disparity are discussed in *Scheeres et al.* (2006), and involve the compaction of the secondary by continuous shaking and the expansion of the primary due to the extremely rapid rotation rate.

6.6. 2008 TC_3

Now we consider asteroid 2008 TC_3, which became the Almahata Sitta meteorite (*Jenniskens et al.,* 2009). This asteroid was observed prior to entering Earth's atmosphere during the brief period after its discovery. Lightcurve observations of this body showed that it was spinning with a period of 100 s and also was in a tumbling rotation state (*Scheirich et al.,* 2010). It can be found on Fig. 3, where it is the smallest known tumbler and only requires approximately 100 Pa of cohesive strength to withstand disruption. Based on analysis of the meteorite fall, this body consisted of several different mineralogical types that constituted separate components in the parent asteroid (see the chapter by Jenniskens in this volume), with one possible interpretation being that it could be described as a rubble pile (*Jenniskens et al.,* 2009). Analysis of the preentry observations and the meteorite falls also indicate that the body had significant macroporosity (*Kohout et al.,* 2011). The meteor was observed to break up high in the atmosphere, indicating a weak body (*Borovička and Charvat,* 2009; *Popova et al.,* 2011). Furthermore, *Borovička and Charvat* (2009) note the presence of an abundance of micrometer- and larger-sized dust associated with the meteor, consistent with this dust composing a "substantial part" of the total mass of the object. These disparate observations related to this asteroid were linked together in the recent theory proposed in *Sánchez and Scheeres* (2014), and described earlier in section 4.5, although there remain questions about that interpretation (see discussion in the chapter by Borovička et al. in this volume).

6.7. P/2013 P5

Body P/2013 P_5 was initially catalogued as a comet, yet now seems to more properly identified as an asteroid (see the chapter by Jewitt et al. in this volume; *Jewitt et al.,* 2013; *Hainaut et al.,* 2014). This body has exhibited periodic shedding over a number of different observational epochs. Material shed from its surface has been seen to consist of fine grains down to 10 μm in size at least. A clear explanation for its periodic shedding has not been found, although some initial analysis of this phenomenon has occurred (*Scheeres,* 2015).

6.8. P/2013 R3

Finally, we mention another active asteroid, P/2013 R_3 (*Jewitt et al.,* 2014). This body was seen to fail in an entirely different morphological fashion, splitting repeatedly into smaller components that escaped from each other. *Hirabayashi et al.* (2014) analyzed the main components of this body and estimated the initial spin rate of the protobody by mapping estimates of size and speed backward to the inferred epoch of disruption. Based on this analysis they predicted a range of possible strengths for the progenitor rubble-pile body prior to breakup, from 40 to 200 Pa, with the range of values accounting for uncertainties in size, density, and relative speed.

7. CONCLUSIONS

In this chapter we bring together disparate material on the strength, mechanics, and morphology of asteroids based on meteors and meteorites, groundbased observations, spacebased observations, analysis, and numerical simulation. While there has been significant progress on all fronts since *Asteroids III*, many new issues and questions have been exposed as well. A main issue that arises is the wide variation in strength determinations of asteroids and their constituents. While direct comparisons of meteor strengths as parameterized by dynamic pressure and strength parameterized by spin rate cannot be naively made, there must be some underlying connection between these. Elucidation of this should be a priority, as it would enable a clear application of meteor data to the interpretation of strength of rubble-pile bodies. Another area that is ripe for progress is an improved theory of tidal dissipation within rubble-pile bodies, coupled with new ways in which the fundamental parameters of rubble piles can be estimated. This involves a better understanding of how asteroids are made to tumble, modified theories for tidal dissipation of rubble-pile bodies, and estimation of improved values for rigidity, tidal Love number, and quality factors of rubble piles. Finally, the continued advancement in analytical and numerical simulation tools will be essential for continued progress in this difficult and fundamental issue of asteroid mechanics.

Acknowledgments. D.J.S. acknowledges support from the NASA Near Earth Object Observations Program through grant NNX14AL16G. The authors appreciate the thorough reviews from two expert referees.

REFERENCES

Abe S., Mukai T., Hirata N., et al. (2006) Mass and local topography measurements of Itokawa by Hayabusa. *Science, 312,* 1344–1347.

Asphaug E. (2008) Critical crater diameter and asteroid impact seismology. *Meteoritics & Planet. Sci., 43,* 1075–1084.

Asphaug E. and Scheeres D. J. (1999) Deconstructing Castalia: Evaluating a postimpact state. *Icarus, 139(2),* 383–386.

Asphaug E., Ryan E. V., and Zuber M. T. (2002) Asteroid interiors. In *Asteroids III* (W. F. Bottke Jr. et al., eds.), pp. 463–484. Univ. of Arizona, Tucson.

Bendjoya P. and Zappalà V. (2002) Asteroid family identification. In *Asteroids III* (W. F. Bottke Jr. et al., eds.), pp. 613–618. Univ. of Arizona, Tucson.

Blitz C. (2009) Modélisation de la propagation des ondes sismiques et des ejecta dans les astéroides : Application à lérosion des cratères de lastéroide (433) Eros. Ph.D. thesis, Institut de Physique du Globe de Paris, Paris.

Borovicka J. and Charvat Z. (2009) Meteosat observation of the atmospheric entry of 2008 TC3 over Sudan and the associated dust cloud. *Astron. Astrophys., 507(2),* 1015.

Borovička J. and Spurnỳ P. (2008) The Carancas meteorite impact — Encounter with a monolithic meteoroid. *Astron. Astrophys., 485(2),* L1–L4.

Borovička J., Spurnỳ P., Brown P., et al. (2013) The trajectory, structure and origin of the Chelyabinsk asteroidal impactor. *Nature, 503,* 235–237.

Brearley A. J. and Jones R. H. (1998) Chondritic meteorites. *Rev. Mineral. Geochem., 36(1),* 3–1.

Breiter S., Bartczak P., Czekaj M., et al. (2009) The YORP effect on 25143 Itokawa. *Astron. Astrophys., 507(2),* 1073.

Britt D. T., Yeomans D. K., Housen K. R., and Consolmagno G. J. (2002) Asteroid density, porosity, and structure. In *Asteroids III* (W. F. Bottke Jr. et al., eds.), pp. 485–500. Univ. of Arizona, Tucson.

Brown P. G., Revelle D. O., Tagliaferri E., and Hildebrand A. R. (2002) An entry model for the Tagish Lake fireball using seismic, satellite and infrasound records. *Meteoritics & Planet. Sci., 37(5),* 661–675.

Buczkowski D. L., Barnouin-Jha O. S., and Prockter L. M. (2008) 433 Eros lineaments: Global mapping and analysis. *Icarus, 193(1),* 39–52.

Burns J. A. and Safronov V. S. (1973) Asteroid nutation angles. *Mon. Not. R. Astron. Soc., 165,* 403.

Bus S. J. and Binzel R. P. (2002) Phase II of the Small Main-Belt Asteroid Spectroscopic Survey: A feature-based taxonomy. *Icarus, 158,* 146–177.

Busch M. W., Giorgini J. D., Ostro S. J., et al. (2007) Physical modeling of near-Earth asteroid (29075) 1950 DA. *Icarus, 190(2),* 608–621.

Carruba V., Domingos R. C., Nesvorný D., et al. (2013) A multidomain approach to asteroid families' identification. *Mon. Not. R. Astron. Soc., 433,* 2075–2096.

Carry B. (2012) Density of asteroids. *Planet. Space Sci., 73,* 98–118.

Chandrasekhar S. (1969) *Ellipsoidal Figures of Equilibrium.* Dover, New York.

Chang C.-K., Waszczak A., Lin H.-W., et al. (2014) A new large super-fast rotator: (335433) 2005 UW163. *Astrophys. J. Lett., 791(2),* L35.

Chapman C. R., Merline W. J., Thomas P. C., et al. (2002) Impact history of Eros: Craters and boulders. *Icarus, 155(1),* 104–118.

Chree C. (1895) The equilibrium of an isotropic elastic solid ellipsoid under the action of normal surface forces of the second degree, and bodily forces derived from a potential of the second degree. *Q. J. Pure Appl. Math., 27,* 338–353.

Consolmagno G. J., Britt D. T., and Macke R. J. (2008) The significance of meteorite density and porosity. *Chem. Erde–Geochem., 68(1),* 1–29.

Cotto-Figueroa D., Statler T. S., Richardson D. C., and Tanga P. (2015) Coupled spin and shape evolution of small rubble-pile asteroids: Self-limitation of the YORP effect. *Astrophys. J., 803,* 25.

DeMeo F. E., Binzel R. P., Slivan S. M., and Bus S. J. (2009) An extension of the Bus asteroid taxonomy into the near-infrared. *Icarus, 202,* 160–180.

Descamps P., Marchis F., Berthier J., et al. (2011) Triplicity and physical characteristics of asteroid (216) Kleopatra. *Icarus, 211(2),* 1022–1033.

Dobrovolskis A. R. (1982) Internal stresses in Phobos and other triaxial bodies. *Icarus, 52(1),* 136–148.

Efroimsky M. and Williams J. G. (2009) Tidal torques: A critical review of some techniques. *Cel. Mech. Dyn. Astron., 104(3),* 257–289.

Fienga A., Manche H., Laskar J., and Gastineau M. (2008) INPOP06: A new numerical planetary ephemeris. *Astron. Astrophys., 477(1),* 315–327.

Fujiwara A., Kawaguchi J., Yeomans D. K., et al. (2006) The rubble-pile asteroid Itokawa as observed by Hayabusa. *Science, 312,* 1330–1334.

Galvez A., Carnelli I., Michel P., et al. (2013) AIDA: The asteroid impact and deflection assessment mission. In *European Planetary Science Congress, 8,* EPSC2013-1043. *Available online at http://meetings. copernicus. org/epsc2013*.

Grady M. M. (2000) *Catalogue of Meteorites, 5th edition.* Cambridge Univ., Cambridge.

Goffin E. (2014) Astrometric asteroid masses: A simultaneous determination. *Astron. Astrophys., 565,* A56.

Goldreich P. and Sari R. (2009) Tidal evolution of rubble piles. *Astrophys. J., 691,* 54–60.

Hainaut O. R., Boehnhardt H., Snodgrass C., et al. (2014) Continued activity in P/2013 P5 PanSTARRS. Unexpected comet, rotational break-up, or rubbing binary asteroid? *Astron. Astrophys., 563,* 75.

Harris A. W. (1994) Tumbling asteroids. *Icarus, 107(1),* 209–211.

Harris A. W. (1996) The rotation rates of very small asteroids: Evidence for 'rubble pile' structure. *Lunar Planet. Sci. XXVII,* p. 493. Lunar and Planetary Institute, Houston.

Harris A. W., Fahnestock E. G., and Pravec P. (2009) On the shapes and spins of rubble pile asteroids. *Icarus, 199(2),* 310–318.

Henych T. and Pravec P. (2013) Asteroid rotation excitation by sub-catastrophic impacts. *Mon. Not. R. Astron. Soc., 432(2),* 1623–1631.

Hilton J. M. (2002) Asteroid masses and densities. In *Asteroids III* (W. F. Bottke Jr. et al., eds.), pp. 103–112. Lunar and Planetary Institute, Houston.

Hirabayashi M. (2014) Structural stability of asteroids. Ph.D. thesis, University of Colorado, Boulder.

Hirabayashi M. and Scheeres D. J. (2014) Analysis of asteroid (216) Kleopatra using dynamical and structural constraints. *Astrophys. J., 780(2),* 160.

Hirabayashi M. and Scheeres D. J. (2015) Stress and failure analysis of rapidly rotating asteroid (29075) 1950 DA. *Astrophys. J. Lett., 798,* L8.

Hirabayashi M., Scheeres D. J., Sánchez D. P., and Gabriel T. (2014) Constraints on the physical properties of main belt Comet P/2013 R3 from its breakup event. *Astrophys. J. Lett., 789,* L12.

Holsapple K. A. (2001) Equilibrium configurations of solid cohesionless bodies. *Icarus, 154(2),* 432–448.

Holsapple K. A. (2004) Equilibrium figures of spinning bodies with self-gravity. *Icarus, 172(1),* 272–303.

Holsapple K. A. (2007) Spin limits of solar system bodies: From the small fast-rotators to 2003 EL61. *Icarus, 187,* 500–509.

Holsapple K. A. (2010) On YORP-induced spin deformations of asteroids. *Icarus, 205(2),* 430–442.

Housen K. R., Holsapple K. A., and Voss M. E. (1999) Compaction as the origin of the unusual craters on the asteroid Mathilde. *Nature, 402,* 155–157.

Hudson R. S., Ostro S. J., Jurgens R. F., et al. (2000) Radar observations and physical model of asteroid 6489 Golevka. *Icarus, 148(1),* 37–51.

Hudson R. S., Ostro S. J., and Scheeres D. J. (2003) High-resolution model of asteroid 4179 Toutatis. *Icarus, 161,* 346–355.

Jacobi C. G. J. (1834) Ueber die figur des gleichgewichts. *Ann. Phys., 109(8–16),* 229–233.

Jacobson S. A. and Scheeres D. J. (2011a) Dynamics of rotationally fissioned asteroids: Source of observed small asteroid systems. *Icarus, 214,* 161–178.

Jacobson S. A. and Scheeres D. J. (2011b) Long-term stable equilibria for synchronous binary asteroids. *Astrophys. J. Lett., 736(1),* L19.

Jenniskens P., Shaddad M. H., Numan D., et al. (2009) The impact and recovery of asteroid 2008 TC3. *Nature, 458(7237),* 485–488.

Jewitt D., Agarwal J., Weaver H., et al. (2013) The extraordinary multi-tailed main-belt comet P/2013 P5. *Astrophys. J. Lett., 778(1),* L21.

Jewitt D., Agarwal J., Li J., et al. (2014) Disintegrating asteroid P/2013 R3. *Astrophys. J. Lett., 784(1),* L8.

Kadish J., Barber J. R., and Washabaugh P. D. (2005) Stresses in rotating spheres grown by accretion. *Intl. J. Solids Structures, 42(20),* 5322–5334.

Kadish J., Barber J. R., Washabaugh P. D. and Scheeres D. J. (2008) Stresses in accreted planetary bodies. *Intl. J. Solids Structures, 45(2),* 540–550.

Kimberley J. and Ramesh K. T. (2011) The dynamic strength of an ordinary chondrite. *Meteoritics & Planet Sci., 46(11),* 1653–1669.

Kohout T., Kiuru R., Montonen M., et al. (2011) Internal structure and physical properties of the asteroid 2008 TC3 inferred from a study of the Almahata Sitta meteorites. *Icarus, 212(2),* 697–700.

Konopliv A. S., Miller J. K., Owen W. M., et al. (2002) A global solution for the gravity field, rotation, landmarks, and ephemeris of Eros. *Icarus, 160,* 289–299.

Kuchynka P. and FolknerW. M. (2013) A new approach to determining asteroid masses from planetary range measurements. *Icarus, 222,* 243–253.

Lowry S. C.,Weissman P. R., Duddy S. R., et al. (2014) The internal structure of asteroid (25143) Itokawa as revealed by detection of YORP spin-up. *Astron. Astrophys., 562,* 48.

Marchis F., Hestroffer D., Descamps P., et al. (2006) A low density of 0.8 g cm^{-3} for the Trojan binary asteroid 617 Patroclus. *Nature, 439,* 565–567.

Marchis F., Enriquez J. E., Emery J. P., et al. (2012) Multiple asteroid systems: Dimensions and thermal properties from Spitzer Space Telescope and ground-based observations. *Icarus, 221(2),* 1130–1161.

Margot J. L., Nolan M. C., Benner L. A. M., et al. (2002) Binary asteroids in the near-Earth object population. *Science, 296(5572),* 1445–1448.

Martin R., Komatitsch D., Blitz C., and Le Goff N. (2008) Simulation of seismic wave propagation in an asteroid based upon an unstructured mpi spectral-element method: Blocking and non-blocking communication strategies. In *High Performance Computing for Computational Science — VECPAR 2008* (J. M. Laginha et al., eds.), pp. 350–363. Springer-Verlag, Berlin.

Marzari F., Rossi A., and Scheeres D. J. (2011) Combined effect of YORP and collisions on the rotation rate of small main belt asteroids. *Icarus, 214(2),* 622–631.

Masiero J., Jedicke R., Ďurech J., et al. (2009) The thousand asteroid light curve survey. *Icarus, 204(1),* 145–171.

Masiero J. R., Mainzer A. K., Grav T., et al. (2011) Main belt asteroids with WISE/NEOWISE. I. Preliminary albedos and diameters. *Astrophys. J., 741,* 68.

Mazrouei S., Daly M. G., Barnouin O. S., et al. (2013) Block distributions on Itokawa. *Icarus, 229,* 181–189.

Michel P., Barucci M. A., Cheng A. F., et al. (2014) MarcoPolo-R: Near-Earth asteroid sample return mission selected for the assessment study phase of the ESA program cosmic vision. *Acta Astronaut., 93,* 530–538.

Michikami T., Nakamura A. M., Hirata N., et al. (2008) Size-frequency statistics of boulders on global surface of asteroid 25143 Itokawa. *Earth Planets Space, 60(1),* 13–20.

Miller J. K., Konopliv A. S., Antreasian P. G., et al. (2002) Determination of shape, gravity, and rotational state of asteroid 433 Eros. *Icarus, 155,* 3–17.

Minton D. A. (2008) The topographic limits of gravitationally bound, rotating sand piles. *Icarus, 195(2),* 698–704.

Mouret S., Hestroffer D., and Mignard F. (2007) Asteroid masses and improvement with Gaia. *Astron. Astrophys., 472,* 1017–1027.

Mueller M., Marchis F., Emery J. P., et al. (2010) Eclipsing binary Trojan asteroid Patroclus: Thermal inertia from Spitzer observations. *Icarus, 205,* 505–515.

Nolan M. C., Asphaug E., Greenberg R., and Melosh H. J. (2001) Impacts on asteroids: Fragmentation, regolith transport, and disruption. *Icarus, 153(1),* 1–15.

Ostro S. J., Scott R., Nolan M. C., et al. (2000) Radar observations of asteroid 216 Kleopatra. *Science, 288(5467),* 836–839.

Ostro S. J., Margot J. -L., Benner L. A. M., et al. (2006) Radar imaging of binary near-Earth asteroid (66391) 1999 KW4. *Science, 314,* 1276–1280.

Parker A., Ivezić Ž., Jurić M., et al. (2008) The size distributions of asteroid families in the SDSS Moving Object Catalog 4. *Icarus, 198,* 138–155.

Pätzold M., Andert T., Asmar S. W., et al. (2011) Asteroid 21 Lutetia: Low mass, high density. *Science, 334,* 491.

Poincaré H. (1885) Sur l'équilibre d'une masse fluide animée d'un mouvement de rotation. *Acta Mathemat., 7(1),* 259–380.

Polishook D., Moskovitz N., Binzel R. P., et al. (2014) Observations of fresh and weathered surfaces on asteroid pairs and their implications on the rotational-fission mechanism. *Icarus, 233,* 9–26.

Popova O., Borovička J., Hartmann W. K., et al. (2011) Very low strengths of interplanetary meteoroids and small asteroids. *Meteoritics & Planet. Sci., 46(10),* 1525–1550.

Pravec P. (2014) Asteroid spin-up fission systems. In *Asteroids, Comets, Meteors 2014, Book of Abstracts* (K. Muinonen et al., eds.), p. 451. University of Helsinki, Finland.

Pravec P., Vokrouhlickỳ D., Polishook D., et al. (2010) Formation of asteroid pairs by rotational fission. *Nature, 466(7310),* 1085–1088.

Pravec P., Scheirich P., Ďurech J., et al. (2014) The tumbling spin state of (99942) Apophis. *Icarus, 233,* 48–60.

Prockter L., Thomas P., Robinson M., et al. (2002) Surface expressions of structural features on eros. *Icarus, 155(1),* 75–93.

Ralchenko M., Britt D. T., Samson C. et al. (2014) Bulk physical properties of the Tagish Lake meteorite frozen pristine fragments. *Lunar Planet. Sci. XLV,* Abstract #1021. Lunar and Planetary Institute, Houston.

Richardson J. E. and Bowling T. J. (2014) Investigating the combined effects of shape, density, and rotation on small body surface slopes and erosion rates. *Icarus, 234,* 53–65.

Richardson D. C., Bottke W. F., Love S. G., et al. (1998) Tidal distortion and disruption of Earth-crossing asteroids. *Icarus, 134(1),* 47–76.

Richardson D. C., Leinhardt Z. M., Melosh H. J., et al. (2002) Gravitational aggregates: Evidence and evolution. In *Asteroids III* (W. F. Bottke Jr. et al., eds.), pp. 501–515. Univ. of Arizona, Tucson.

Richardson J. E., Melosh H. J., and Greenberg R. (2004) Impact-induced seismic activity on asteroid 433 Eros: A surface modification process. *Science, 306(5701),* 1526–1529.

Richardson D. C., Elankumaran P., and Sanderson R. E. (2005) Numerical experiments with rubble piles: Equilibrium shapes and spins. *Icarus, 173(2),* 349–361.

Robert O., Lognonne P., Scheeres D. J., et al. (2010) Seismology on a small body: Expected results for the BASiX Discovery mission proposal. Abstract U51B-0044 presented at 2010 Fall Meeting, AGU, San Francisco, California, 13–17 Dec.

Robinson M. S., Thomas P. C., Veverka J., et al. (2002) The geology of 433 Eros. *Meteoritics & Planet. Sci., 37(12),* 1651–1684.

Roche E. (1850) La figure dune masse fluide soumise lattraction dun point loign. *Acad. Sci. Montpellier,1,* 1847–1850.

Rozitis B., MacLennan E., and Emery J. P. (2014) Cohesive forces prevent the rotational breakup of rubble-pile asteroid (29075) 1950 DA. *Nature, 512(7513),* 174–176.

Russell C. T., Raymond C. A., Coradini A., et al. (2012) Dawn at Vesta: Testing the protoplanetary paradigm. *Science, 336,* 684–686.

Sánchez P. and Scheeres D. J. (2011) Simulating asteroid rubble piles with a self-gravitating soft-sphere distinct element method model. *Astrophys. J., 727,* 120.

Sánchez P. and Scheeres D. J. (2012) DEM simulation of rotation-induced reshaping and disruption of rubble-pile asteroids. *Icarus, 218,* 876–894.

Sánchez P. and Scheeres D. J. (2014) The strength of regolith and rubble pile asteroids. *Meteoritics & Planet. Sci., 49(5),* 788–811.

Scheeres D. J. (2002) Stability in the full two-body problem. *Cel. Mech. Dyn. Astron., 83(1),* 155–169.

Scheeres D. J. (2007) Rotational fission of contact binary asteroids. *Icarus, 189,* 370–385.

Scheeres D. J. (2009a) Minimum energy asteroid reconfigurations and catastrophic disruptions. *Planet. Space Sci., 57(2),* 154–164.

Scheeres D. J. (2009b) Stability of the planar full 2-body problem. *Cel. Mech. Dyn. Astron., 104(1),* 103–128.

Scheeres D. J. (2012) Minimum energy configurations in the n-body problem and the celestial mechanics of granular systems. *Cel. Mech. Dyn. Astron., 113(3),* 291–320.

Scheeres D. J. (2015) Landslides and mass shedding on spinning spheroidal asteroids. *Icarus, 247,* 1–17.

Scheeres D. J. and Gaskell R. W. (2008) Effect of density inhomogeneity on YORP: The case of Itokawa. *Icarus, 198(1),* 125–129.

Scheeres D. J., Khushalani B., and Werner R. A. (2000a) Estimating asteroid density distributions from shape and gravity information. *Planet. Space Sci., 48,* 965–971.

Scheeres D. J., Ostro S. J., Werner R. A., et al. (2000b) Effects of gravitational interactions on asteroid spin states. *Icarus, 147(1),* 106–118.

Scheeres D. J., Asphaug E. I., Colwell J., et al. (2003) Asteroid surface science with pods. *Lunar Planet. Sci. XXXIV,* Abstract #1444. Lunar and Planetary Institute, Houston.

Scheeres D. J., Benner L. A. M., Ostro S. J., et al. (2005) Abrupt alteration of asteroid 2004 MN4's spin state during its 2029 Earth flyby. *Icarus, 178(1),* 281–283.

Scheeres D. J., Fahnestock E. G., Ostro S. J., et al. (2006) dynamical configuration of binary near-Earth asteroid (66391) 1999 KW4. *Science, 314,* 1280–1283.

Scheeres D. J., Abe M., Yoshikawa M., et al. (2007) The effect of YORP on Itokawa. *Icarus 188,* 425–429.
Scheeres D. J., Hartzell C. M., Sánchez P., and Swift M. (2010) Scaling forces to asteroid surfaces: The role of cohesion. *Icarus, 210,* 968-984.
Scheirich P., Urech J. D., Pravec P., et al. (2010) The shape and rotation of asteroid 2008 TC3. *Meteoritics & Planet. Sci., 45(10–11),* 1804–1811.
Scheirich P., Pravec P., Jacobson S. A., et al. (2015) The binary near-Earth asteroid (175706) 1996 FG3 — an observational constraint on its orbital stability. *Icarus, 245,* 56–63.
Sharma I. (2013) Structural stability of rubble-pile asteroids. *Icarus, 223,* 367–382.
Sharma I., Burns J. A., and Hui C. -Y. (2005) Nutational damping times in solids of revolution. *Mon. Not. R. Astron. Soc., 359(1),* 79–92.
Sharma I., Jenkins J. T., and Burns J. A. (2009) Dynamical passage to approximate equilibrium shapes for spinning, gravitating rubble asteroids. *Icarus, 200(1),* 304–322.
Statler T. S. (2009) Extreme sensitivity of the YORP effect to small-scale topography. *Icarus, 202(2),* 502–513.
Tanga P., Comito C., Paolicchi P., et al. (2009) Rubble-pile reshaping reproduces overall asteroid shapes. *Astrophys. J. Lett., 706(1),* L197.
Takahashi Y. and Scheeres D. J. (2014) Morphology driven density distribution estimation for small bodies. *Icarus, 233,* 179–193.
Tedesco E. F., Williams J. G., Matson D. L., et al. (1989) Three-parameter asteroid taxonomy classifications. In *Asteroids II* (R. P. Binzel et al., eds.), pp. 1151–1161. Univ. of Arizona, Tucson.
Tholen D. J. and Barucci M. A. (1989) Asteroid taxonomy. In *Asteroids III* (R. P. Binzel et al., eds.), pp. 298–315. Univ. of Arizona, Tucson.
Thomas P. C. and Robinson M. S. (2005) Seismic resurfacing by a single impact on the asteroid 433 Eros. *Nature, 436,* 366–369.
Tsuchiyama A., Uesugi M., Matsushima T., et al. (2011) Three-dimensional structure of Hayabusa samples: Origin and evolution of Itokawa regolith. *Science, 333(6046),* 1125–1128.
Tsuda Y., Yoshikawa M., Abe M., Minamino H., and Nakazawa S. (2013) System design of the Hayabusa 2 asteroid sample return mission to 1999 JU3. *Acta Astronaut., 91,* 356–362.
Urakawa S., Ohtsuka K., Abe S., Ito T., and Nakamura T. (2014) Fast rotation of a subkilometer-sized near-Earth object 2011 XA3. *Astron. J., 147(5),* 121.
Vokrouhlický D. and Nesvorný D. (2008) Pairs of asteroids probably of a common origin. *Astron. J., 136(1),* 280.
Vokrouhlický D., Breiter S., Nesvorný D., and Bottke W. F. (2007) Generalized YORP evolution: Onset of tumbling and new asymptotic states. *Icarus, 191(2),* 636–650.
Walsh K. J. and Richardson D. C. (2006) Binary near-Earth asteroid formation: Rubble pile model of tidal disruptions. *Icarus, 180(1),* 201–216.
Walsh K. J., Richardson D. C., and Michel P. (2008) Rotational breakup as the origin of small binary asteroids. *Nature, 454(7201),* 188–191.
Walsh K. J., Richardson D. C., and Michel P. (2012) Spinup of rubble-pile asteroids: Disruption, satellite formation, and equilibrium shapes. *Icarus, 220(2),* 514–529.
Warner B. D., Harris A. W., and Pravec P. (2009) The asteroid lightcurve database. *Icarus, 202(1),* 134–146.
Washabaugh P. D. and Scheeres D. J. (2002) Energy and stress distributions in ellipsoids. *Icarus, 159(2),* 314–321.
Yano H., Kubota T., Miyamoto H., et al. (2006) Touchdown of the Hayabusa spacecraft at the Muses Sea on Itokawa. *Science, 312(5778),* 1350–1353.
Yeomans D. K., Antreasian P. G., Barriot J.-P., et al. (2000) Radio science results during the NEAR-Shoemaker spacecraft rendezvous with Eros. *Science, 289,* 2085–2088.

A&A 528, A105 (2011)
DOI: 10.1051/0004-6361/201015011

Astronomy & Astrophysics

High-contrast observations of (136108) Haumea

A crystalline water-ice multiple system⋆

C. Dumas[1], B. Carry[2,3], D. Hestroffer[4], and F. Merlin[2,5]

[1] European Southern Observatory. Alonso de Córdova 3107, Vitacura, Casilla 19001, Santiago de Chile, Chile
e-mail: cdumas@eso.org
[2] LESIA, Observatoire de Paris, CNRS, 5 place Jules Janssen, 92195 Meudon Cedex, France
e-mail: benoit.carry@sciops.esa.int
[3] European Space Astronomy Centre, ESA, PO Box 78, 28691 Villanueva de la Cañada, Madrid, Spain
[4] IMCCE, Observatoire de Paris, CNRS. 77, Av. Denfert-Rochereau, 75014 Paris, France
e-mail: hestro@imcce.fr
[5] Universit Paris 7 Denis Diderot, 4 rue Elsa Morante, 75013 Paris, France
e-mail: frederic.merlin@obspm.fr

Received 18 May 2010 / Accepted 6 January 2011

ABSTRACT

Context. The trans-Neptunian region of the Solar System is populated by a wide variety of icy bodies showing great diversity in orbital behavior, size, surface color, and composition. One can also see there are dynamical families and binary systems. One surprising feature detected in the spectra of some of the largest trans-Neptunians is the presence of crystalline water-ice. This is the case for the large TNO (136 108) Haumea (2003 EL_{61}).
Aims. We seek to constrain the state of the water ice of Haumea and its satellites and to investigate possible energy sources that maintain the water ice in its crystalline form.
Methods. Spectro-imaging observations in the near infrared were performed with the integral field spectrograph SINFONI mounted on UT4 at the ESO Very Large Telescope. The spectra of both Haumea and its larger satellite Hi'iaka were analyzed. Relative astrometry of the components was also measured, providing a check of the orbital solutions and equinox seasons.
Results. We describe the physical characteristics of the crystalline water-ice present on the surface of Haumea and its largest satellite Hi'iaka and analyze possible sources of heating to maintain water in a crystalline state: tidal dissipation in the system components vs. radiogenic source. The surface of Hi'iaka appears to be covered by large grains of water ice, almost entirely in its crystalline form. Under some restricted conditions, both radiogenic heating and tidal forces between Haumea and Hi'iaka could provide the energy needed to maintain the ice in its crystalline state.

Key words. Kuiper belt objects: individual: (136108) Haumea – techniques: high angular resolution – techniques: imaging spectroscopy – methods: observational – infrared: planetary systems

1. Introduction

The planetesimals orbiting beyond Neptune, the trans-Neptunian objects (TNOs), are remnants of the Solar System's formation in its outer part. They are thought to be among the most pristine objects in our solar system, although their outer surface layers have been altered by irradiation and collisions over the age of the solar system. Currently, the TNOs population accounts for ∼1300 known objects, which are difficult to observe owing to their extreme heliocentric distances and relatively small size. Our knowledge of their physical characteristics is limited for now to studying the few largest and brightest objects, which still reveal that this population displays a large number of binary and multiple systems when compared to other small solar system bodies such as main belt asteroids (e.g., Noll et al. 2008). Transneptunian binaries can be found as gravitationally bound systems with similar mass components, but systems harboring smaller moons, which are by definition harder to detect, have also been discovered around (134 340) Pluto, (136 108) Haumea (2003 EL_{61}), (50 000) Quaoar, (90 482) Orcus, etc. (Noll et al. 2008). Thanks to their binary nature, the total mass of these systems can be inferred, which provides a valuable tool for characterizing their surface and internal physical properties when combined with spectroscopy and radiometric sizes.

Haumea is the largest member of a TNO family, which is likely the outcome of a collision (Brown et al. 2007; Ragozzine & Brown 2007; Schaller & Brown 2008; Rabinowitz et al. 2008; Snodgrass et al. 2010). Here we report spectro-imaging observations of all three components of the Haumea system performed in 2007 at the ESO Very Large Telescope. Our data and related compositional modeling show that the surface of the outer satellite Hi'iaka is mostly coated with crystalline water ice, as in the case of the central body Haumea (Trujillo et al. 2007; Merlin et al. 2007; Pinilla-Alonso et al. 2009). We also discuss the effects of tidal torques as a possible source of energy that is responsible for the crystalline state of the water-ice of Hi'iaka.

2. Observations and data reduction

Haumea was observed in *H* and *K* bands on 2007 March 15 UT, using the laser guide-star facility (LGSF) and the SINFONI

⋆ Based on observations collected at the European Southern Observatory, Paranal, Chile - 60.A-9235.

instrument (Spectrograph for INtegral Field Observations in the Near Infrared), both installed at the 8 m "Yepun" unit of the ESO Very Large Telescope. The use of SINFONI for the observations of the large TNOs Haumea and Eris has been described in earlier papers (Merlin et al. 2007; Dumas et al. 2007), and more information about this instrument can be found in Eisenhauer et al. (2003) and Bonnet et al. (2004). In a nutshell, SINFONI is an integral field spectrometer working in the [1.0−2.5] μm range, which is also equipped with an adaptive optics (AO) system with Natural Guide Star (NGS) and Laser Guide Star (LGS) channels. While our previous published observations were obtained in non-AO mode (seeing-limited), the results presented in this paper made use of the AO system and the LGS facility. The laser produces an artificial visible-light star of $R_{\rm mag} \sim 13.4$ in the line of sight of Haumea ($V_{\rm mag} \sim 17.4$), thus returning a gain of four magnitudes for characterizing the higher orders of the wavefront in comparison to non-laser observations. Haumea itself was used as a reference source for the tip-tilt, delivering optimal correction by the AO-LGS system. The atmospheric conditions were extremely good during the observations, with an uncorrected seeing varying between 0.5 and 0.6″. On 2007 March 15, between 6h34 UT and 7h24 UT, six exposures of 300 s each were obtained on Haumea (total integration time of 0.5 h), interspaced by 3 exposures of 300 s to record the sky background. We used the H+K spectral grating (spectral resolution of ∼1500) covering both H and K bands simultaneously, and a plate scale of 100 mas/spaxel (3″ × 3″ total field). Calibrations to correct our spectra from the solar response and telluric absorption features were obtained immediately after Haumea by observing the local telluric standard HD 142093 ($V_{\rm mag} \sim 7.3$, G2V) in NGS mode at similar airmass and with the same instrumental setting.

The data (science target and telluric standard) were mainly reduced using the ESO pipeline 1.9.3 (Modigliani et al. 2006). We first corrected all raw frames from the noise pattern of dark and bright horizontal lines introduced when reading the detector. We then used the ESO pipeline to produce all master files needed by the data reduction, such as the badpixel masks, master darks and flats, and the wavelength and distortion calibration files, which respectively associate a wavelength value to each pixel and reconstruct the final image cubes. Each object frame was subtracted from the sky frame recorded closest in time and the quality of the sky subtraction was improved by enabling the correction of sky residuals in the pipeline, i.e. by subtracting the median value of each image slice in the reconstructed, sky-corrected, spectro-image cube.

Figure 1 shows two H+K-band images of Haumea obtained in seeing-limited and LGS modes. The improvement in contrast returned by the LGS is immediately apparent, as the two satellites of Haumea are visible in the LGS image, allowing us to carry out a detailed spectroscopic and astrometric study of the components of this system.

We thus were able to extract the spectra of Haumea and its brighter satellite Hi'iaka separately. The faintest satellite Namaka could not be spectrophotometrically isolated from Haumea owing to its too close proximity at the time of these observations. Nevertheless, we could neglect the contribution of the satellite to the overall spectrum as its H magnitude is ∼24.9 (Fraser & Brown 2009), i.e., within the noise level for a given wavelength bin of our data cube. The individual spectra were then corrected from the remaining bad pixels, combined, and finally divided by the spectrum of the local telluric standard HD 142093. A detailed analysis of the cube and subsequent modeling of the spectra revealed that division of our spectra by the solar analog had the effect of introducing a small artifact in the spectrum of Haumea in the [1.65−1.8] μm range. This particular feature came from the contamination of our spectra by a faint background object within the close vicinity of the standard star. We characterized the impact of the contaminant by dividing our spectrum of HD 142093 by the spectrum of a good solar analog, HD 11532 ($V_{\rm mag} \sim 9.7$, G5) used by our ESO Large Program (Prog. ID 179.C-0171, PI: Barucci) and obtained with a similar setup and airmass ($\Delta_{\rm airmass} \sim 0.03$). We then applied correction to our final spectra of Haumea and Hi'iaka by dividing both of them by the relative response of the two telluric standard stars over the [1.65−1.8] μm range.

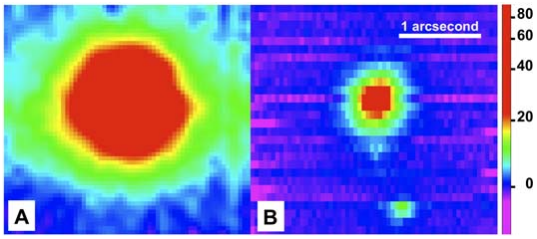

Fig. 1. Comparison of H+K band SINFONI images of Haumea obtained under similar conditions but in seeing-limited observations (A, *left*) and LGS-AO corrected mode (B, *right*). The spatial and intensity scales are similar and the intensity is given in ADU. The improved contrast and spatial resolution of the AO image (B) is apparent in comparison to the non-AO image (A), making possible the detection of the two faint satellites: Namaka (faintest, just below Haumea) and Hi'iaka (brightest, bottom of image). The images were obtained by summing all the slices of our data-cube to produce the equivalent of a broad H+K band image.

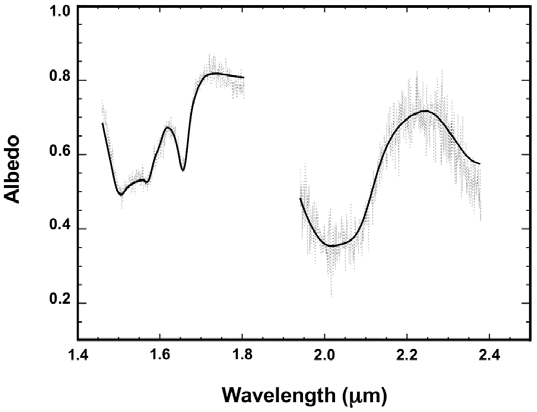

Fig. 2. Spectrum of Haumea (thin dashed line) obtained with the SINFONI instrument using LGS-AO assisted observations, and our spectral model (solid line, see text).

3. Structure of the water ice

3.1. Spectral behavior

Our spectra of Haumea (Fig. 2) and of its brightest satellite (Fig. 3) reveal clear absorption bands of water ice as reported by Barkume et al. (2006) around 1.5 and 2.0 μm. Previous reports (e.g. Trujillo et al. 2007; Merlin et al. 2007) had also shown

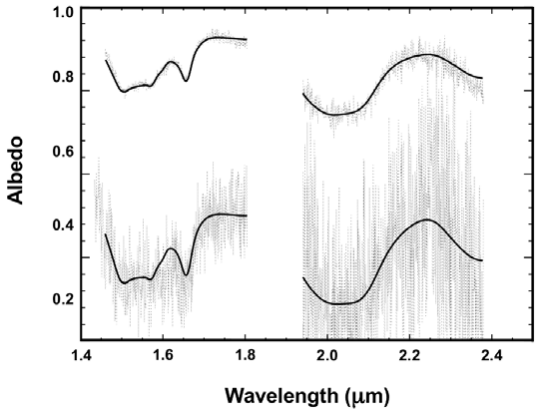

Fig. 3. Spectra of Haumea (*top*, offsetted by +1 unit for clarity) and of Hi'iaka (*bottom*), the largest of Haumea's satellites. The spectrum of the satellite (thin dashed line) was extracted from the same data set as in Fig. 2. Our spectral model (solid line) is described in the text.

Table 1. Depth of the water ice absorption bands in the spectra of Haumea and its outermost satellite Hi'iaka.

Absorption band	Band depth (Primary)	Band depth (Satellite)
1.50 μm	0.36 ± 0.05	0.53 ± 0.25
1.65 μm	0.24 ± 0.04	0.54 ± 0.25
2.00 μm	0.55 ± 0.05	0.72 ± 0.35

that the spectrum of Haumea displays the clear signature of crystalline water ice at 1.65 μm. Here, these LGS-assisted VLT observations clearly show that water ice in its crystalline state is similarly present on the brightest of the satellites. The crystalline ice on Hi'iaka was also reported previously by Takato et al. (unpublished) from seeing-limited observations carried out at Subaru under very good atmospheric conditions, while this paper reports LGS-assisted observations of Haumea's satellite and Hapke modeling of its reflectance spectrum. The primary object spectrum does not display other major absorption bands in the 1.45−2.35 μm range. We can suspect a couple of absorption bands around 2.21 μm and 2.25 μm in the spectrum of Haumea, which, if real, might be explained by the presence of $NH_3{\cdot}H_2O$ and, tentatively, $NH4^+$, on the surface, with the latter the likely product of irradiation of ammonia hydrate (Cook et al. 2009). Better data are needed to confirm these bands. The spectrum of Hi'iaka is still too noisy to search for the signature of any additional compounds.

The crystalline water ice band (at 1.65 μm) is very deep in the spectrum of both objects. This behavior is similar to those of pure crystalline water ice at low temperatures (see Grundy & Schmitt 1998). Considering the high albedo of the primary object (Stansberry et al. 2008), we can assume that crystalline water ice is the major compound on the surface of Haumea and Hi'iaka (and likely Namaka as well). For both spectra, we analyzed the relative depth of the water ice absorption bands at 1.5 μm, 1.65 μm, and 2.0 μm in comparison to the continuum flux estimated at each band center. This continuum was first removed from our measured spectrum before estimating the depth of each band. The results are given in Table 1.

The absorption bands of the spectrum of the satellite are deeper than those of the spectrum of Haumea by a factor ∼1.5 for the wide absorption bands (1.5 and 2 μm) and more than 2.5 for the finer 1.65 μm band. This implies a larger grain size for the water ice on the surface of the satellite. Concerning the depth of the absorption band at 1.65 μm, we can suggest that the surface of the satellite has suffered less from the irradiation processes than the surface of Haumea (see Merlin et al. 2007, for a discussion about the shape and location of the 1.65 μm band).

3.2. Spectral modeling

To investigate the surface properties of Haumea and Hi'iaka, we ran a radiative transfer model, based on Hapke theory (Hapke 1981). We computed the geometric albedo at a zero phase angle from Eq. (44) of Hapke (1981). The phase function, which describes the angular distribution of light scattered from a body, is represented by a single Henyey-Greenstein function (Henyey & Greenstein 1941) with an asymmetry parameter of $v = -0.4$. The backscattering parameter is $B = 0.7$. These values are close to those used by Verbiscer & Helfenstein (1998) for the icy satellites of the giant planets, which exhibit similar strong water ice features. We follow the formalism of Emery & Brown (2004) to compute the geometric albedo from different compounds, assuming a salt and pepper or an intimate mixture. The free parameters of our models are the grain size and the relative amount of each chemical compound. The lowest reduced χ^2 values between the observed spectra and our synthetic spectra were reached using the Marqvardt-Levenberg algorithm, although it is important to note that our model results are not unique and only show the most probable surface composition from our initial set of probable chemical analogs (see Barucci et al. 2008a, on a discussion of the limits of this model).

To perform our spectral modeling, we used optical constants for the several ices at low temperature (close to 40 K) that are suspected to be present on the surface of these icy bodies, including pure and amorphous water ice (Grundy & Schmitt 1998), as well as pure methane ice (Quirico & Schmitt 1997). We also used optical constants of dark compounds, such as amorphous black carbon (Zubko et al. 1996) and Titan Tholin (Khare et al. 1986), which reproduce the low albedo of a large portion of these objects (Stansberry et al. 2008).

Our best result, obtained by assuming an albedo of 0.6 (normalized over the 1.6−1.7 μm region of the spectrum), includes 73% (particle size of 9 μm) of crystalline water ice, 25% (particle size of 10 μm) of amorphous water ice, and 2% (particle size of 10 μm) of Titan Tholin. No other major compound seem to be present on the surface of Haumea. The albedo value in the near infrared was determined from its V albedo (Stansberry et al. 2008), its $V - J$ color and the reflectance ratio reported between the CH_4 band at 1.6 μm (CH4s) and J band (Lacerda et al. 2008). We normalized our spectra by convolving them with the response curve of the CH4s filter used by Lacerda et al. (2008) in the H-band region. For the satellite, we treated its albedo as a free parameter in our model, and the best fit was obtained for an albedo of 0.4 in CH4s band and a composition made of 100% of crystalline water ice (particle size of 20 μm). The results of our spectral modeling are given in Figs. 2 and 3.

3.3. Discussion

Our observations and modeling results clearly show that crystalline water ice is present on the surface of the largest satellite, and probably more abundantly than on the surface of the central body (larger particle size and greater amount). Even though our

results would require an independent determination of Hi'iaka's albedo, it is highly probable that the surface of the satellite is completely covered by crystalline water ice, especially if the exact albedo in the CH4s band is close to, or even larger than, the value of 40%. The presence of crystalline water ice on the surface of Hi'iaka demonstrates that crystalline ice can be present on the surface of very small bodies. Indeed, if we adopt a 1600 km diameter for the primary (Rabinowitz et al. 2006), a similar visible albedo between the two bodies, and a magnitude difference of 3.3 (Brown et al. 2005), we derive a diameter of 170 km for the largest satellite.

Mastrapa & Brown (2006) and Zheng et al. (2008) show that the crystalline water ice feature almost disappears after irradiation over a time span of only several Myr to several hundred Myr, so the life time of the crystalline state of water ice is expected to be small on outer solar system objects, especially for low-temperature surfaces. Also, crystalline water ice can only be formed from amorphous water ice after episodes of sufficient heating, since this mechanism is very efficient above 100 K (Jewitt & Luu 2004), but still possible at lower temperatures. Based on this, some competitive mechanisms must be involved to explain that water ice is found mostly in its crystalline state over planet satellites and TNOs, including those of small size. As shown here, our spectral modeling results show that crystalline water ice is dominant and "fresh" (less than several Myr) on the surface of Haumea and its largest satellite. Zheng et al. (2008) shows that the amorphization of crystalline ice by irradiation becomes less efficient with increasing temperature, with the effect of "thermal recrystallization" even becoming dominant at higher temperatures than 40 K. This could partly explain why crystalline ice is still found on small outer solar system bodies. Several authors have also proposed cryovolcanic processes to explain the observation of crystalline water ice (e.g. Jewitt & Luu 2004; Cook et al. 2007). From observations, this assumption could be possible for a few objects where ammonia ice has been detected; for instance: Charon (Brown & Calvin 2000; Buie & Grundy 2000; Dumas et al. 2001; Cook et al. 2007), Quaoar (Jewitt & Luu 2004), or Orcus (Barucci et al. 2008b). Ammonia depresses the melting point and could cause liquid to be compressed and pressurized enough at high depths to reach the surface (Cook et al. 2007). However, the presence of absorption bands due to ammonia is not definitive in our spectra.

Brown et al. (2007) reports the probable discovery of a family of Kuiper belt objects with surface properties and orbits that are nearly identical to those of Haumea, most likely ejected fragments of the parent body's ice mantle. Recent simulations performed by Ragozzine & Brown (2007) seem to confirm this hypothesis even if the epoch found for the collision seems too ancient (1 Gyr) to conserve the fresh mantle of these bright objects. From photometry, Rabinowitz et al. (2008) show that the members of this family have a common phase curve and have the bluest color among all the TNOs. These observations suggest a high albedo for all of the objects and assume very fresh surfaces. Barkume et al. (2008) show that all observed members of this family show clear absorption features of crystalline water ice, which are not observed in other small TNOs (diameter smaller than ~1000 km), although the number of putative family members has recently been lowered by Snodgrass et al. (2010). Still, the hypothesis of an energetic collisional event could provide a scenario that explains the presence of nearly pure crystalline water ice on the surface of Hi'iaka, especially if we consider that the largest Haumea satellite is still too small to reach the melting point of H_2O at any depth. The next section below investigates the possibility of maintaining interior temperatures high enough by involving other scenarios: radiogenic heating and tidal effects between Haumea and Hi'iaka.

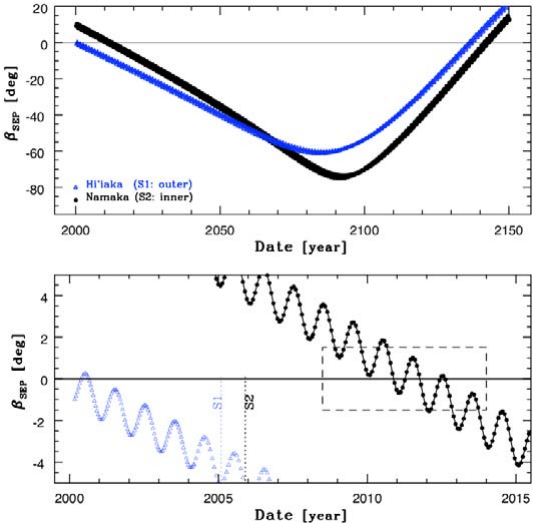

Fig. 4. Prediction of the Earth's elevation (sub-Earth point's latitude: SEP_β) above the orbital plane for each of the two satellites. Open triangles (blue) indicate the outer satellite S1 Hi'iaka discovered in 2005, filled circles (black) the recently discovered inner satellite S2 Namaka.

4. Orbits of Haumea's satellites

Taking advantage of the imaging capabilities of SINFONI, we extracted the relative astrometric positions of (136 108) Haumea and its two satellites by fitting Gaussian profiles on each of the components. We found the brighter satellite (S1: Hi'iaka) at ($-0\farcs277^{\pm.01}$ E, $-1\farcs318^{\pm.01}$ N) from (136 108) Haumea, and the faintest satellite (S2: Namaka) at ($+0\farcs026^{\pm.02}$ E, $-0\farcs528^{\pm.03}$ N). The large error bars along the SN direction are due to the non-squared shape of SINFONI spaxels, which is twice as large in the SN direction than along the EW direction.

These positions agree with orbits recently determined by Ragozzine & Brown (2009), emphasizing the astrometric quality of the data obtained with SINFONI at the VLT. These orbits lead to mutual events (eclipses) between Haumea and its satellite Namaka within the period ≈2008−2011 (see Fig. 4). There are two equinox seasons during one orbital period of the system around the Sun, hence approximately one each 130 years. Such events are of prime importance because their photometric follow-up can lead directly to a direct determination of the real size of the components, and hence their bulk density, with high accuracy. These events have been indeed predicted by Fabrycky et al. (2008) based on HST and Keck observations. The characteristic modulation of the curves (which depend only on the inclination of the orbit) in Fig. 4 is the effect of the parallax, leading to several favorable opportunities to observe transits and occultation phenomena. It is worth noting that some symmetric solutions for the orbit orientation, although less likely, cannot strictly be ruled out, which would have strong consequences on the prediction of the equinox seasons. Because of scarcity of such occultation events within the transneptunian region, it is important to gather additional astrometric data on the position of

Table 2. Orbital and physical parameters of the Haumea system.

	Mass (m^a) (kg)	Size (r^a) (km)	Si^b (%)	$E_{Si}{}^c$ (W)	$E_{Tides}{}^d$ (W)	δT^e (K s^{-1})
Haumea	4.00×10^{21}	690	88–97	$\approx 10^{10}$	$\approx 5 \times 10^9$	6×10^{-16}
Hi'iaka	1.8×10^{19}	195	≤ 10	$\approx 10^7$	$\approx 10^7$	3×10^{-16}
Namaka	2×10^{18}	100	≤ 10	$\approx 10^6$	$\approx 10^7$	6×10^{-15}

Notes. [(a)] Ragozzine & Brown (2009), [(b)] silicate content in mass (Si) estimated from the body's density, [(c)] subsequent radiogenic energy, [(d)] the total energy available from tidal dissipation, [(e)] resulting temperature rate.

the inner satellite for better constraining its orbit orientation, and consequently the prediction of the mutual events.

5. Discussion

This paper shows that crystalline ice is not only present on the largest body of the Haumea multiple system, which could be explained by the long-lived effect of radiogenic heating, but also on the external satellite Hi'iaka (and hence likely on the inner satellite Namaka). Several mechanisms to explain the widespread presence of crystalline ice among primitive small solar system objects have already been proposed (Jewitt & Luu 2004; Grundy et al. 2006; Cook et al. 2007), and all require that some earlier heating events above 80–90 K (Schmitt et al. 1988) might have occurred at large heliocentric distances. In the following, we explore the efficiency of radiogenic heating and tidal dynamical effects as possible heat sources for maintaining water ice in its crystalline state over Hi'iaka.

The radiogenic heating still present in such bodies comes from long-period unstable elements such as ^{40}K, ^{232}Th, and ^{238}U. The heating depends on the volume/surface ratio of the body and mostly the total mass of silicates (for rocks it is 4.5×10^{-12} W kg^{-1} overall). Assuming a two-layer model for the internal structure of Haumea with a silicate core (density of 3500 kg m^{-3}) and a water ice surface (density of 900 kg m^{-3}), we find that the rock fraction should represent between 88% and 97% of the mass of Haumea ($4.00 \pm 0.04 \times 10^{21}$ kg) (Ragozzine & Brown 2009) to comply with the possible density range (2600 to 3300 kg m^{-3}) reported by Rabinowitz et al. (2006). The radiogenic energy presently available is thus on the order of 10^{10} W, about 10 times what is expected for the asteroid (1) Ceres. In the perspective of a high-impact scenario, the fraction of rock in the satellites should be lower. Still, a 10% rock fraction for the satellites would provide radiogenic energy on the order of 10^6 W for Namaka, and 10^7 W for Hi'iaka, which is comparable to the icy satellite of Saturn Tethys (although it is understood that for Tethys, resurfacing processes to maintain water ice in its crystalline state differ and invoke the action of particle bombardment from both the nearby E-ring and Saturn's magnetosphere).

Assuming now that all the energy involved from the tidal flexure is dissipated, an *upper-bound* to the crystalline-ice production can be obtained. The amount of thermal energy dissipated in the body is the residual of the transfer of orbital and rotational energy of the deformed body $\dot{E}_{th} = |\dot{W}_{tide} + \dot{W}_{rot}|$. Here we have to consider the more general case of inclined and eccentric orbits, elongated primary (the large lightcurve amplitude observed in Rabinowitz et al. (2006) and Lellouch et al. (2010) is clearly associated to the shape effect, although the object displays albedo markings, see Lacerda et al. (2008)), and non synchronous rotation. However, for the upper-bound computation derived here, we neglect the effect of eccentricity, obliquity, and shape, according to the considerations proposed by Ferraz-Mello et al. (2008) for fast rotators[1]. As a result, the energy released by the effect of tides can be expressed as

$$\dot{E}_{th} = \frac{3}{2} \mathcal{G} m^2 \frac{r^5}{a^6} \Omega \, k_d . \epsilon, \quad (1)$$

where a is the semi-major axis of the orbit; Ω, m, and r Haumea's spin rate, mass, and equivalent radius; k_d the Love dynamical number, ϵ the phase lag of the tide and $\mathcal{G}$ the constant of gravitation.

Considering the rheology of the material (viscosity, elasticity, and rigidity) and response to forced periodic oscillations through $k_d \cdot \epsilon$, only a fraction of this energy will be dissipated. For a typical icy body, one can assume $Q \approx 30$–100, which also depends on the temperature of the ice. The Love number scales linearly with the body's size, and one can assume $k_d \cdot \epsilon \propto 10^{-2}$ for Haumea and $\propto 10^{-3}$ for its satellites. Thus, the total energy dissipated inside the outer satellite Hi'iaka (from the tides raised by the central body) can approach 10^7 W. Conversely, taking the mass, sizes, and different Love numbers into account, the energy dissipated from tides raised by the satellites on Haumea is about 5×10^9 W (somewhat lower than the expected radiogenic energy available).

In comparison, the energy needed to crystallize 95% of amorphous ice (starting from an equilibrium temperature of $\approx$50 K) corresponds to an increase in temperature of about 40–50 K (with corresponding characteristic times of about 10^8 and 10^5 years, respectively) (Schmitt et al. 1988). Taking the water-ice heat capacity ($C = 2 \times 10^3$ J K^{-1} kg^{-1}) and the energy found previously, one finds a temperature increase rate $\delta T = 3 \times 10^{-16}$ K s^{-1} for a 10^{19} kg satellite and $\delta T = 6 \times 10^{-16}$ K s^{-1} for the $\sim 10^{20}$ kg of water ice composing Haumea's crust. These values lead to an increase of 50 K in two and five Gyrs for Haumea and Hi'iaka respectively.

This scenario is valid for an energy equally distributed inside the whole volume. If, for some reason, the energy is mostly dissipated in some fraction of the mass or conducted to the surface, then the increase in temperature can be even greater. This could be the case if the surface displays cracks in the ice, where the heating could be more concentrated from the friction occurring during the tides. Possible cryovolcanism with a liquid subsurface (Desch et al. 2009) can also be favored by such tidal flexions.

Compared to other systems like Io or Enceladus, the amount of energy involved is very low. However, given the uncertainty of our order of magnitude calculations, it would still be possible, but only under particular conditions, that tides contribute to the generation of crystalline ice on the satellites surface. Knowledge of the spin vector coordinates of Haumea is required to proceed

[1] This simplification is based on the following consideration: if the very elongated primary is a fast rotator, the tides it will generate will have high frequencies (see Ferraz-Mello et al. 2008, for more detailed information).

with more specific computations for modeling the tidal effect, the dissipation, heat transfer, and ice crystallization. Besides, if the tides are efficient at producing crystallisation on the outer satellite, one also expects to have crystalline ice on the inner satellite Namaka.

6. Conclusion

We presented spectro-imaging observations of (136 108) Haumea obtained in the near infrared [1.6–2.4 μm] with the integral-field spectrograph SINFONI at the ESO VLT. The presence of crystalline water ice is confirmed on the surfaces of Haumea and Hi'iaka, the largest of the two satellites. Analysis of the spectral bands of water ice and Hapke modeling of our data show that the surface of Hi'iaka is mainly coated with "fresh" ice with larger particles (20 μm), supporting a less altered surface than on Haumea.

Energy sources responsible for the crystallization of the water ice were discussed, and we conclude that radiogenic heating, as well as – under very specific conditions – tidal heating, could explain this observational result.

Improved spectrophotometry of the individual components of the system, and better constraints on Haumea size, shape, and spin state, as well as more detailed modeling of the tidal heating, are now required to proceed in this investigation.

Acknowledgements. The authors wish to thank the referee Josh Emery, for the pertinent comments that improved the manuscript. We thank H. Hussman (DLR, Berlin), N. Rambaux, and V. Lainey (IMCCE) for fruitful discussions about the general treatment of the tides, as well as the whole ESO-Garching commissioning team for the SINFONI LGS system, in particular Stefan Stroebele, Ronald Donaldson, Sylvain Oberti, and Enrico Fedrigo.

References

Barkume, K. M., Brown, M. E., & Schaller, E. L. 2006, ApJ, 640, 87
Barkume, K. M., Brown, M. E., & Schaller, E. L. 2008, AJ, 135, 55
Barucci, M. A., Merlin, F., Guilbert, A., et al. 2008a, A&A, 479, L13
Barucci, M. A., Brown, M. E., Emery, J. P., & Merlin, F. 2008b, in The Solar System Beyond Neptune (Tucson: University of Arizona Press), 143
Bonnet, H., Abuter, R., Baker, A., et al. 2004, The ESO Messenger, 117, 17
Brown, M. E., & Calvin, W. M. 2000, Science, 287, 107
Brown, M. E., Bouchez, A. H., Rabinowitz, D., et al. 2005, ApJ, 632, L45
Brown, M. E., Barkume, K. M., Ragozzine, D., & Schaller, E. L. 2007, Nature 446, 294
Buie, M. W., & Grundy, W. M. 2000, Icarus, 148, 324
Cook, J. C., Desch, S. J., Roush, T. L., Trujillo, C. A., & Geballe, T. R. 2007, ApJ, 663, 1406
Cook, J. C., Olkin, C. B., Desch, S. J., et al. 2009, LPSC, 2222
Desch, S., Cook, J., Doggett T., & Porter, S. B. 2009, Icarus, 202, 694
Dumas, C., Smith, B. A., & Terrile, R. J. 2001, AJ, 126, 1080
Dumas, C., Merlin, F., Barucci, M. A., et al. 2007, A&A, 471, 331
Eisenhauer, F., Abuter, R., Bickert, K., et al. 2003, SPIE, 4841, 1548
Emery, J. P., & Brown, R. H. 2004, Icarus, 170, 131
Fabrycky, D. C., Ragozzine, D., Brown, M. E., & Holman, M. J. 2008, IAU Circ., 8949, 1
Ferraz-Mello, S., Rodríguez, A., & Hussmann, H. 2008, Celest. Mech. Dyn. Astron., 101, 171
Fraser, W. C., & Brown, M. E. 2009, ApJ, 695, 1
Grundy, W. M., & Schmitt, B. 1998, JGR, 103, 25809
Grundy, W. M., Young, L. A., Spencer, J. R., et al. 2006, Icarus, 184, 543
Hapke, B. 1981, JGR, 86, 3039
Henyey, L. G., & Greenstein, J. L. 1941, ApJ, 93, 70
Jewitt, D. C., & Luu, J. 2004, Nature, 432, 731
Khare, B. N., Sagan, C., Ogino, H., et al. 1986, Icarus, 67, 176
Lacerda, P., Jewitt, D., & Peixinho, N. 2008, AJ, 135, 1749
Lellouch, E., Kiss, C., Santos-Sanz, P., et al. 2010, A&A, 518, A147
Mastrapa, R. M. E., & Brown, R. H. 2006, Icarus, 183, 207
Merlin, F., Guilbert, A., Dumas, C., et al. 2007, A&A, 466, 1185
Modigliani, A., Hummel, W., Abuter, R., et al. 2006, Proceedings of ADA-4 Conference: Astronomical Data Analysis 4, Marseilles, France, 18−20 Sep.
Noll, K. S., Grundy, W. M., Chiang, E. I., Margot, J. L., & Kern, S. D. 2008, in The Solar System Beyond Neptune, 345
Pinilla-Alonso, N., Brunetto, R., Licandro, J., et al. 2009, A&A, 496, 547
Quirico, E., & Schmitt, B. 1997, Icarus, 127, 354
Rabinowitz, D. L., Barkume, K., Brown, M. E., et al. 2006, ApJ, 639, 1238
Rabinowitz, D. L., Schaefer, B. E., Schaefer, M., & Tourtellotte, S. W. 2008, AJ, 136, 1502
Ragozzine, D., & Brown, M. E. 2007, AJ, 134, 2160
Ragozzine, D., & Brown, M. E. 2009, AJ, 137, 4766
Schaller, E. L., & Brown, M. E. 2008, ApJ, 68, 107
Schmitt, B., Grim, R., & Greenberg, R. 1988, Eslab Symposium on Infrared Spectroscopy in Astronomy
Snodgrass, C., Carry, B., Dumas, C., & Hainaut, O. 2010, A&A, 511, A72
Stansberry, J., Grundy, W., Brown, M., et al. 2008, in The Solar System Beyond Neptune, ed. M. A. Barucci, H. Boehnhardt, D. P. Cruikshank, & A. Morbidelli (Tucson: University of Arizona Press), 161
Trujillo, C. A., Brown, M. E., Barkume, K. M., Schaller, E. L., & Rabinowitz, D. L. 2007, ApJ, 655, 1172
Verbiscer, A., & Helfenstein, P. 1998, in Solar System Ices (Dordrecht: Kluwer Academic Publishers), ASSL, 227, 157
Zheng, W., Jewitt, D., & Kaiser, R. I. 2009, ApJS, 181, 53
Zubko, V. G., Mennella, V., Colangeli, L., & Bussoletti, E. 1996, MNRAS, 282, 1321

A&A 534, A115 (2011)
DOI: 10.1051/0004-6361/201117486

Astronomy & Astrophysics

Integral-field spectroscopy of (90482) Orcus-Vanth⋆

B. Carry[1,2,3,4], D. Hestroffer[4], F. E. DeMeo[2,5], A. Thirouin[6], J. Berthier[4], P. Lacerda[7], B. Sicardy[2,8,9], A. Doressoundiram[2], C. Dumas[10], D. Farrelly[11], and T. G. Müller[12]

[1] European Space Astronomy Centre, ESA, PO Box 78, 28691 Villanueva de la Cañada, Madrid, Spain
e-mail: benoit.carry@esa.int
[2] LESIA, Observatoire de Paris, CNRS, 5 place Jules Janssen, 92190 Meudon, France
[3] Université Paris 7 Denis-Diderot, 5 rue Thomas Mann, 75205 Paris Cedex, France
[4] IMCCE, Observatoire de Paris, UPMC, CNRS, 77 Av. Denfert Rochereau 75014 Paris, France
[5] Department of Earth, Atmospheric, and Planetary Sciences, MIT, 77 Massachusetts Avenue, Cambridge, MA 02139, USA
[6] Instituto de Astrofísica de Andalucía, CSIC, Apt 3004, 18080 Granada, Spain
[7] Queen's University, Belfast, County Antrim BT7 1NN, Ireland
[8] Université Pierre et Marie Curie, 4 place Jussieu, 75252 Paris Cedex 5, France
[9] Institut Universitaire de France, 103 Bld Saint Michel, 75005 Paris, France
[10] Alonso de Córdova 3107, Vitacura, Casilla 19001, Santiago de Chile, Chile
[11] Utah State University, 0300 Old Main Hill, Logan, UT 84322, USA
[12] Max-Planck-Institut für extraterrestrische Physik (MPE), Giessenbachstrasse, 85748 Garching, Germany

Received 15 June 2011 / Accepted 27 August 2011

ABSTRACT

Aims. We seek to constrain the surface composition of the trans-Neptunian object (90482) Orcus and its small satellite Vanth, as well as their mass and density.
Methods. We acquired near-infrared spectra (1.4−2.4 μm) of (90482) Orcus and its companion Vanth using the adaptive-optics-fed integral-field spectrograph SINFONI mounted on Yepun/UT4 at the European Southern Observatory Very Large Telescope. We took advantage of a very favorable appulse (separation of only 4″) between Orcus and the UCAC2 29643541 star (m_R = 11.6) to use the adaptive optics mode of SINFONI, allowing both components to be spatially resolved and Vanth colors to be extracted independently from Orcus.
Results. The spectrum of Orcus we obtain has the highest signal-to-noise ratio to date, and we confirm the presence of H_2O ice in crystalline form, together with the presence of an absorption band at 2.2 μm. We set an upper limit of about 2% to the presence of methane, and 5% for ethane. Since the methane alone cannot account for the 2.2 μm band, the presence of ammonia is suggested to the level of a couple of percent. The colors of Vanth are found to be slightly redder than those of Orcus, but the large measurement uncertainties prevent us from drawing any firm conclusions about the origin of the pair (capture or co-formation). Finally, we reset the orbital phase of Vanth around Orcus, and confirm the orbital parameters derived by Brown and collaborators.

Key words. techniques: high angular resolution – techniques: imaging spectroscopy – Kuiper belt objects: individual: (90482) Orcus – methods: observational

1. Introduction

Moons in the solar system are of high importance because they provide the most direct and precise way to derive the mass of the minor planets they orbit around (see Hilton 2002). Combined with volume estimates, their densities can be calculated, providing information about their composition and interior (e.g., Merline et al. 2002; Britt et al. 2002). They can subsequently help us to constrain the characteristics of the most pristine material of the solar system, and further our understanding of planetary system formation and dynamical evolution. In this valuable context, the trans-Neptunian binary (TNB) Orcus/Vanth system is of particular interest for the following reasons:

1. With an estimated albedo of ~27% (Lim et al. 2010), Orcus is among the brightest known trans-Neptunian objects (TNOs), and has a diameter of about 850 km.
2. Near-infrared spectroscopy of Orcus has revealed a surface rich in water ice in crystalline form (Fornasier et al. 2004; de Bergh et al. 2005; Trujillo et al. 2005; Barucci et al. 2008b; DeMeo et al. 2010). Moreover, Trujillo et al. (2005), Barucci et al. (2008b), and Delsanti et al. (2010) detected a weak band around 2.2 μm that might be associated with either methane (CH_4) or ammonia (NH_3). The long-term stability of all ices are affected by high energy photon bombardment (causing photodissociation and sputtering), micrometeorite impacts, radioactive decay, and sublimation. Both methane and ammonia are expected to be destroyed by solar irradiation on short timescales (Strazzulla & Palumbo 1998; Cooper et al. 2003; Cottin et al. 2003). Ammonia's presence, if confirmed, would thus require an active process to resupply the surface with ammonia, such as impact gardening or, more favorably, cryovolcanism (the ammonia lowers the melting temperature of water ice and hence favors such mechanism as highlighted by Cook et al. 2007). Bodies in the outer solar system that have methane on

⋆ Based on observations collected at the European Southern Observatory Very Large Telescope (programs ID: 284.C-5044 and 384.C-0877).

their surface have retained their atmospheres, which has important implications for its discovery on the surface of Orcus.

3. Recent radiometric measurements from ESA *Herschel* (as part of the key program "TNOs are Cool!"; see Müller et al. 2009) have been used to refine the size estimate of Orcus to 850 ± 90 km (Lim et al. 2010). The diameter estimate will potentially be improved from the stellar occultations expected for upcoming years. Thus the improvement in the accuracy to which Vanth's orbit is known (based on the solution by Brown et al. 2010) will help us to determine the bulk density of Orcus.

We present here new spectro-imaging data obtained in 2010 that provide constraints on the composition of Orcus and the orbit of Vanth. We describe in Sect. 2 the observations, list in Sect. 3 the data reduction and spectral extraction steps, present in Sect. 4 the analysis of the colors and spectra of Orcus and Vanth, and detail in Sect. 5 the orbit computation and stellar occultation prediction.

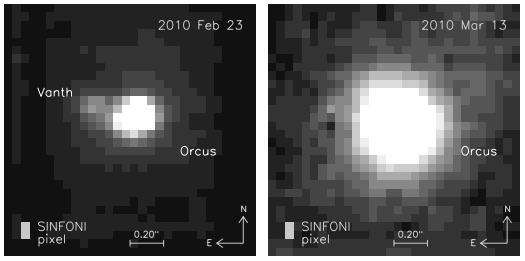

Fig. 1. Two images of the Orcus-Vanth system, obtained by summing all individual observations and stacking the resulting cube for the whole range of wavelengths. *Left*: our 2010 February 23 UT observations using the appulse NGS AO correction, representing a total integration time of 4050 s. Both Orcus and Vanth are easily separable in the image. *Right*: our 2010 March 13 UT observations using the LGS AO correction, without TTS reference (see text), corresponding to a total integration time of 5400 s. The angular resolution provided in that mode forbids the detection of Vanth, whose flux, spread over many pixels, is hidden within the background noise.

2. Observations

The brightness contrast ($\Delta m_V \sim 2.6$) and small apparent angular separation (~0.2″) between Orcus and its satellite Vanth require the use of a high angular-resolution camera/spectrograph to spatially resolve the system. This means observations have to be conducted in the visible from the *Hubble* Space Telescope (e.g., Brown et al. 2010), or in the near-infrared with ground-based telescopes equipped with adaptive optics (AO) modules. The latter is of great interest for cold objects such as TNOs because many ices display strong absorption bands in the near-infrared (see Barucci et al. 2008a).

However, because adaptive-optics systems require a bright ($m_V \leq 15$) reference source (a natural guide star: NGS) to correct the incident wavefront from the deformations induced by the atmospheric turbulence, study of TNOs from the ground with AO is generally limited to the brightest objects (e.g., Pluto or Haumea). The extension of these studies to fainter targets is possible thanks to two techniques. First, a laser beam can be projected into the atmosphere to create an artificial star of magnitude $m_R \sim 13.4$, called a laser guide star (LGS). However, because the laser beam is deflected on its way up by the atmospheric turbulence, the LGS position moves on the plane of the sky in a random pattern (corresponding to low orders of the turbulence, called tip-tilt). Hence, a natural close-by star must be monitored to correct the wavefront for the motion of the LGS. Because the requirement on these reference stars (called tip-tilt star: TTS) are less strict (angular distance and brightness) than for NGS, several TNOs have already been observed this way (e.g., Brown et al. 2006; Dumas et al. 2011).

The second technique consists of computing close encounters (separations smaller than about 30″) on the plane of the sky between the object of interest and a star suitable as a NGS (e.g., Berthier & Marchis 2001). These events are called *appulses*. On 2010 February 23 UT, Orcus had a particularly favorable appulse with the star UCAC2 29643541 ($m_R = 11.6$) at an angular separation of only 4″. We thus observed it in Service Mode (program ID: 284.C-5044) at the European Southern Observatory (ESO) Very Large Telescope (VLT) with the near-infrared integral-field spectrograph SINFONI (Eisenhauer et al. 2003; Bonnet et al. 2004). Observations were realized simultaneously in the atmospheric H and K bands (1.45−2.45 μm) using the $H + K$ grating of SINFONI, providing a spectral resolving power R of about 1500. We used a plate scale of 50 × 100 mas/pixel, associated with a 3″ × 3″ field of view. We alternated observations of Orcus and the nearby sky in a jitter pattern to allow optimal sky subtraction, being cautious to avoid the NGS (4″).

Unfortunately, the AO module of SINFONI had not been designed to offer differential tracking (i.e., NGS fixed on the plane of the sky, field of view following a target with non-sidereal motion). We thus had to set the duration of integrations as a compromise between the slew of Orcus on the detector plane and the count level reached on Vanth ($m_V \sim 21.6$). We used individual exposures of 150 s to theoretically[1] achieve an average signal-to-noise ratio (S/N) of 1 on Vanth over H band. In return, during a single exposure, Orcus moved by −0.109″ in right ascension and 0.039″ in declination, distorting its apparent shape, which was thus elongated along the SE-NW direction as is clearly visible in Fig. 1.

Atmospheric conditions at the time of the observations were very good, with an average seeing of 0.8″ and a coherence time ranging from 7 to 20 ms. Orcus was close to zenith during the observations with an airmass ranging from 1.05 to 1.4. This allowed the AO system to provide an optimal correction, resulting in a spatial resolution close to the diffraction limit of the telescope (the full width at half maximum (*FWHM*) of Orcus was 85 × 100 mas in K-band).

We also report here on some test observations of Orcus performed on 2010 March 13 UT at the ESO VLT (prog. ID: 384.C-0877) in the so-called "*seeing enhancer*" mode. This mode consists of closing the AO loop on a LGS, but without providing any TTS, Orcus itself being too faint ($m_V \sim 19.7$) to be used as a TTS (as opposed to targets such as Haumea, see Dumas et al. 2011, for instance). Hence, only the higher orders of the atmospheric turbulence are corrected (i.e., there is no tip-tilt correction). The advantage of this mode is that we can perform differential tracking and therefore take longer exposures (600 s). The instrument settings and observing strategy were otherwise similar to those for February observations.

Atmospheric conditions were worse during March observations, with an average seeing of 0.9″, and coherence time of about 3 ms. However, the quality of the correction provided by the AO in that mode is intrinsically lower than for the

[1] Computation made using ESO Exposure Time Calculator.

appulse: the *FWHM* of Orcus was 0.38″ (still representing an improvement by a factor of ≈2 with respect to seeing-limited observations). Despite the shape of Orcus being elongated by its apparent displacement in February, the quality of the data was superior (with a shorter exposure time) to the March data, where the spread of its light is directly related to the lower AO correction achieved. This highlights the advantage of searching for favorable appulses for faint moving targets to use bright NGS as reference for the adaptive-optics correction.

3. Data reduction and analysis

We used the SINFONI pipeline (Modigliani et al. 2007) version 2.0.5 to perform the basic data reduction: bad pixel removal, flat fielding correction, subtraction of the sky background from the jittered observations, and wavelength calibration with Xenon-Argon-Krypton lamps (see Guilbert et al. 2009, for a complete description of the procedure on other faint TNOs). Default parameters were used, except for in the "*jitter*" recipe where we set the parameters *scales.sky* to true and *density* to three to achieve optimal sky-background correction. This provided us with 27 and 9 individual cubes (two spatial plus one spectral dimensions) of Orcus/Vanth for February and March observations, respectively.

We then computed the average centroid position of Orcus for each individual observation by stacking the cubes along wavelength. We used this information to shift and add all the cubes into a single one for each date, corresponding to equivalent exposure times of 4050 s and 5400 s. We then re-aligned all the wavelength slices of the cube because the centroid position of Orcus was not constant with wavelength but rather experienced a slow drift caused by the differential atmospheric refraction as described in Carry et al. (2010).

We then extracted the respective spectra of Orcus and Vanth by adjusting (using `MPFIT` least square algorithm of Markwardt 2009), for each wavelength, a model $\mathcal{I}$ composed of a linear background and two Moffat functions describing both components

$$\mathcal{I}(x, y) = \mathcal{F}_{\rm o}(x, y) + \mathcal{F}_{\rm v}(x, y) + ax + by + c, \quad (1)$$

where $\mathcal{F}_i$ are the two Moffat functions, representing Orcus ($\mathcal{F}_{\rm o}$) and Vanth ($\mathcal{F}_{\rm v}$), defined by

$$\mathcal{F}_i(x, y) = f_i. \left[1 + \left((x - x_i^c) \frac{\cos\theta}{\sigma_x} - (y - y_i^c) \frac{\sin\theta}{\sigma_y} \right)^2 + \left((x - x_i^c) \frac{\sin\theta}{\sigma_x} + (y - y_i^c) \frac{\cos\theta}{\sigma_y} \right)^2 \right]^{-\alpha}, \quad (2)$$

where x, y are the frame spatial dimensions, f_i is the peak level of each Moffat function centered on the coordinates (x_i^c, y_i^c). σ_x, σ_y are the half-width at half maximum (HWHM) along two perpendicular directions, making an angle θ with the detector x direction, and α is the power-law index of the Moffat functions. The final spectrum was cleaned for bad points using a 3σ median smoothing procedure.

The advantage of this method is to provide the spectra of both components as well as their relative astrometry. We discuss both points in the subsequent sections.

4. Spectral analysis

4.1. The surface composition of Orcus

Figure 2 compares our new spectrum of Orcus to that of Barucci et al. (2008b). The overall spectral shape reveals the presence of water ice, dominated by the crystalline form as already addressed in previous work (Fornasier et al. 2004; de Bergh et al. 2005; Trujillo et al. 2005; Barucci et al. 2008b; Guilbert et al. 2009; Delsanti et al. 2010; DeMeo et al. 2010).

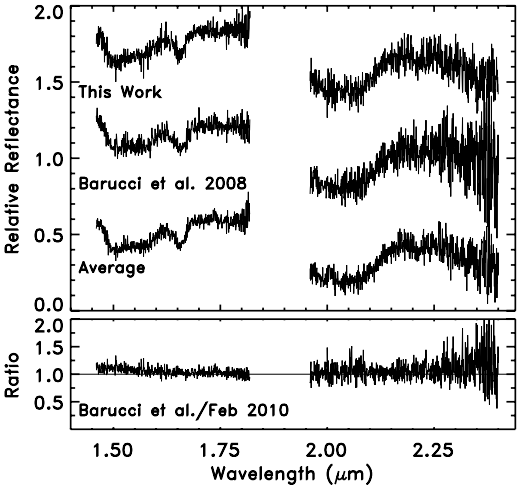

Fig. 2. *Upper panel*: spectra of Orcus in the *H* and *K* bands from this work (*top*) and Barucci et al. (2008b) (*middle*). The bottom spectrum is an average of the two. The spectra are normalized to 1.0 at 1.75 μm and are shifted by +0.65, 0, and −0.4. The spectrum taken in March 2010 was significantly noisier than the two shown here so we neither plot it nor use it in our analysis. *Lower panel*: the ratio of the Barucci et al. data to data from this work, which shows little difference between the spectra apart from a small flux difference shortward of 1.65 μm.

The ratio of these two spectra, shown in the bottom part of Fig. 2, reveals their similarity, although we note a difference in the overall flux level (∼10%) shortward of ∼1.65 μm. This difference does not appear to be related to any variation in H_2O (amount or grain size) because it is present shortward of 1.5 μm. Potential explanations include instrumental effects or differences of the standard stars.

We confirm the detection of a feature near 2.2 μm with a band center located at 2.209 ± 0.002 μm and a band depth of 9 ± 2% that previous works have attributed to CH_4, NH_3, or NH_4^+. We combined the Barucci et al. spectrum with ours to slightly increase the overall S/N. We did not include the spectra of both Delsanti et al. (2010) or DeMeo et al. (2010) because the quality of these data were significantly lower. This average spectrum is used for all of the analysis reported in this section.

Current volatile retention models (e.g., Schaller & Brown 2007; Levi & Podolak 2009) predict that CH_4 is unstable on Orcus' surface over its lifetime, although Orcus' intermediate size among TNOs place it closer to the retention boundary than most other objects and provide us with an opportunity to test these models and perhaps place some constraints on the assumptions therein. An important step in understanding Orcus' surface composition is thus a search for weak bands hidden in the spectrum near the detection limit. While many species could potentially exist in small quantities on the surface, the lack of multiple strong bands makes their identification difficult. Here we focus on searching for methane bands in the spectrum primarily because of the abundance of strong bands in the appropriate wavelength regime, but also because of the important implications

A&A 534, A115 (2011)

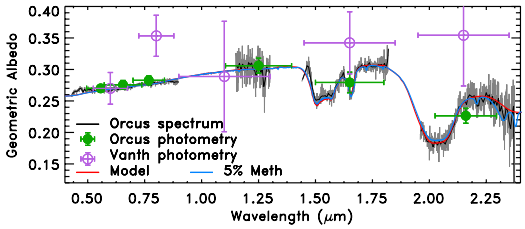

Fig. 3. Plotted here is the average spectrum of Orcus from our work and Barucci et al. together with the visible data from DeMeo et al. (2009), scaled to the visible albedo estimated by Lim et al. (2010). Overplotted are the basic model in red (#1 in Table 1) and model with additional 5% methane in blue (#2, *ibid*). Also shown in purple are the visible and near-infrared colors of Vanth. The *V*, *I*, and *J* band measurements are from Brown et al. (2010). The colors of Vanth are normalized to Orcus' spectrum at 0.6 microns.

Table 1. Material present in the models of surface composition.

	Material	Amount (%)	Grain size (μm)
Model 1	Crystalline H_2O	60	18
	Amorphous H_2O	10.5	18
	Titan tholins	2	10
	Triton tholins	6	10
	Blue compound	22.5	10
Model 2	Crystalline H_2O	60	18
	Amorphous H_2O	5.5	18
	Titan tholins	2	10
	Triton tholins	6	10
	Blue compound	22.5	10
	Methane	5	100

Table 2. Parameters for weak bands.

Species	λ_e (μm)	λ_m (μm)	$\Delta\lambda$ (nm)	Depth (%)
CH_4	1.670	1.654 ± 0.004	8 ± 5	4.1 ± 1.9
CH_4	1.724	–	–	<2
CH_4	2.208	2.209 ± 0.002	6 ± 2	9.5 ± 2.3
C_2H_6	2.274	–	–	<2
C_2H_6	2.314	–	–	<2

Notes. Band centers (λ_e) of the strongest CH_4 bands from Quirico & Schmitt (1997). We list the band center (λ_m), width ($\Delta\lambda$), and depth, from the Gaussian fit to our data at these wavelengths if detected.

a detection would have on our understanding of the surface conditions of these bodies and the criteria for volatile retention.

First, to remove the dominant signature of the crystalline water ice from the spectrum we model the composition of Orcus using a code based on radiative transfer theory (Hapke 1993) using optical constants of laboratory materials for inputs. We use optical constants of H_2O ice in both crystalline and amorphous form (at 40 K and 38 K from Grundy & Schmitt 1998; and Schmitt et al. 1998, respectively) and Titan and Triton tholin (Khare et al. 1984, 1993). The temperature of the H_2O optical constants are appropriate because the blackbody temperature at 39 AU is about 43 K and Pluto's surface temperature (with a similar semi-major axis) is measured to be 40 ± 2 K (Tryka et al. 1994). Triton and Titan tholins are used as representative material that aid in fitting the spectrum, because optical constants are available for these materials. However, they could be replaced with different materials, such as other organics that have similar spectral properties. The models we present here (see Table 1 and Fig. 3) are based on the recent analysis by DeMeo et al. (2010) but differ slightly because they are based on the recent reevaluation of the albedo of Orcus from 0.20 ± 0.03 (Stansberry et al. 2008) to 0.27 ± 0.06 by Lim et al. (2010). We reduced the fraction of amorphous water ice to about 10%, increasing the crystalline H_2O by the same amount to provide a closer fit of the 1.65 μm band and adjusted the cosine asymmetry factor (Hapke 1993) to properly fit the data's higher albedo. The spectrum was then divided by the model #1, without methane (Table 1). We created a program in IDL designed to fit Gaussians to potential features in designated wavelength regions. The program was set to search in the regions near 1.67, 1.72, and 2.2 μm, where methane absorbs strongly (Quirico & Schmitt 1997). We did not search for the band near 1.80 μm because of poor telluric correction in this wavelength range, nor the bands near 2.32 μm and 2.43 μm owing to a decreasing S/N at wavelengths longer than ≈2.3 μm from low detector sensitivity. A least squares minimization (Markwardt 2009) was used to find the best-fit center, width, and depth of the bands.

The results of the Gaussian fits are listed in Table 2, and plots of the fits are shown in Fig. 4. We find a Gaussian fit near the 1.67 μm feature, although the center is at 1.654 μm indicating that it is residual crystalline H_2O that was not removed by the division of the data by the model. We do not find a band at 1.67 μm nor at 1.72 μm. The depth of the 2.209 μm Gaussian fit is 9.5 ± 2.3%. While we do not fit a Gaussian to the 2.32 μm feature, we do note that the reflectance of the data is lower in this region with respect to the model that excludes CH_4 (#1) suggesting there is a compound absorbing in this region, though not necessarily CH_4.

The question that remains is "can the band at 2.2 μm be produced by methane even though we do not detect any other bands?" The relative band depths of the 1.67 and 1.72 μm features compared to the 2.2 μm feature are 95% and 88%, respectively, assuming a grain size of 200 μm (the relative depths do not change significantly with variations in grain size of ±100 μm). We should clearly be able to detect all three bands, if the 2.2 μm feature were due to methane only (as visible in Fig. 3 by comparing the spectrum of Orcus with model #2, including 5% of methane to account for the 2.2 μm feature), thus we place a limit of a maximum fraction of about 2% for methane at the surface. Our constraint of 2% is lower than the constraint set in DeMeo et al. (2010) partly because of the higher quality of our data, but also because the bands predicted by the 5% methane model at the higher albedo are weaker than for the lower albedo model. The majority (or all) of the 2.2 μm absorption must therefore be due to either hydrated ammonia, ammonium, as suggested in previous works, or another yet unknown compound that absorbs in this region. Since H_2O:NH_3 and NH_4^+ do not have any other distinguishing features in the wavelength range of our data we can neither confirm nor exclude their presence.

We also search for bands at 2.274 and 2.314 μm, the positions of the strongest bands of ethane (Quirico & Schmitt 1997). Ethane is a by-product of methane and its potential presence on Orcus was suggested by models fitted to data by Delsanti et al. (2010). We do not find any bands at the locations of ethane absorption within the limits of the quality of our data (which is the best to date). Either there is no ethane (less than about 5%,

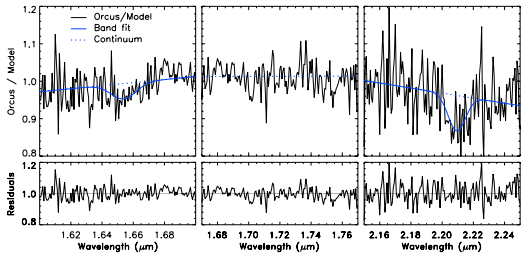

Fig. 4. Gaussian fits to the data to search for weak bands. Two bands of approximately 4% and 9% are detected around 1.65 and 2.2 μm, respectively (see Table 2). No band with any depth weaker than about 2% is detectable around 1.72 μm.

Table 3. Relative magnitude difference of Orcus and Vanth.

Filter	Orcus[1]	Δmag	Flux ratio	Refs.
V	19.36 ± 0.05	2.61 ± 0.10	9.0 ± 0.9	1
I	18.63 ± 0.05	2.31 ± 0.10	8.6 ± 2.9	1
J	20.64 ± 0.04	2.66 ± 0.34	11.5 ± 0.5	1
H	21.65 ± 0.03	2.34 ± 0.12	11.6 ± 1.3	2
Ks	–	2.07 ± 0.24	14.9 ± 3.2	2

References. (1) Brown et al. (2010); (2) this work.

depending on grain size, within the limits of detection with our data) on Orcus' surface or, less likely, there is a concentration of ethane on the part of the surface observed by Delsanti et al. that we did not observe. We also check for the possible presence of other volatile compounds: CO_2 (three narrow features near 2 μm), CO (1.578 μm, we do not search at 2.352 μm because of the poor quality of the data), N_2 (2.15 μm), and methanol (2.27 μm). We do not detect any of these features in our data.

4.2. The colors of Vanth

The spectrum of Vanth that we extracted had a very low S/N, hence we drastically reduced its spectral resolution and we only report in Table 3 its magnitude differences from Orcus in H- and K-band. Figure 3 compares the visible and near-infrared colors of Vanth to those of Orcus, scaled to the visible albedo of Orcus from Lim et al. (2010). Although the errors are large, the colors indicate that Vanth is slightly redder in both the visible wavelength regime as reported by Brown et al. (2010) and the near-infrared as indicated by our data. While the colors of Vanth do not suggest that there is a strong presence of water ice similar to that seen on Orcus, the possibility cannot be ruled out within the uncertainty of the data. As already addressed by Brown et al., it is impossible to draw any conclusions about the origin of this color difference to distinguish between a capture or collision formation scenario. Even if Vanth was indeed found to have colors inconsistent with water ice, this might may not exclude a collision formation scenario.

5. Orbital characterization

The relative orbit of the Orcus/Vanth system was previously determined by Brown et al. (2010) from observations conducted using the *Hubble* Space Telescope (HST), mainly with the high resolution channel of the Advanced Camera for Surveys (ACS), over the period 2005−2007. Three years after, the uncertainty in the orbital period leads to a position uncertainty for Vanth along its orbit of about 15°, corresponding to 2000 km (Fig. 5). With one additional point for the relative position of the components after three years, corresponding to some 2000 revolutions of the pair, it is possible to refine the orbit, especially the orbital period, which in turn allows us to refine the position prediction for future observations, in particular stellar occultations.

In this section we present the relative astrometry measurements, the subsequent orbit computation, and the consequences for the predictions of stellar occultations.

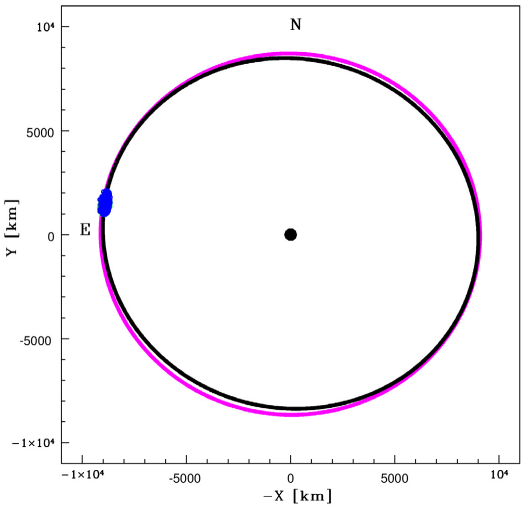

Fig. 5. Predicted position of Vanth relative to Orcus on 2010 Feb. 23.237, from the extrapolation of the initial 2004−2007 data by Brown et al. (2010). The two curves reprensent two possible solutions with symmetric pole solutions. The dots in the Eastern part of the frame correspond to the predicted positions at the time of the SINFONI observation for all retained orbital solutions given in Fig. 6.

5.1. Astrometry measurements

To extract the relative astrometry of Orcus and Vanth, we first stacked the spectrocubes along the wavelength dimension to obtain two frames of higher SNR, one at each epoch. We then used the image model $\mathcal{I}$ presented in Sect. 3, the astrometry being defined by the relative position of the Moffat function centers.

As visible in Fig. 1, Vanth is easily separable from Orcus on the image obtained in February, and we estimate the accuracy of its position to be about 25 mas, corresponding to a fourth of a pixel on the SINFONI detector. However, our observing date, which was imposed by the stellar appulse, was not optimal for taking full advantage of the parallactic effect and removing the ambiguity in the relative orbit inclination (see the two curves in Fig. 5). On the other hand, the moderate spatial resolution (*FWHM* of 380 mas) achieved in March did not allow the localization of Vanth, whose flux was spread over a large area and diluted by the background noise (Fig. 1).

We also use the astrometric measurements given in Brown et al. (2010), although, after analyzing the public HST data, it is clear that the dates given in Brown et al. (2010) are wrong by a constant offset of half a day (as confirmed by D. Ragozzine

Table 4. Astrometric data for the relative position of Orcus/Vanth used to reconstruct their mutual orbit.

Date[†] (JD)	ΔX[‡] ($''$)	ΔY[‡] ($''$)	Δ (AU)	r (AU)	α (°)	δ (°)	Instr.
2 453 687.66400	0.206	–0.147	47.811	47.702	144.039	–4.356	ACS
2 454 040.36900	0.226	–0.111	48.075	47.752	144.813	–4.729	ACS
2 454 044.36600	–0.258	–0.005	48.013	47.752	144.839	–4.766	ACS
2 454 051.57900	–0.006	–0.243	47.898	47.753	144.871	–4.828	ACS
2 454 056.08900	–0.036	0.240	47.824	47.754	144.882	–4.865	ACS
2 454 066.14600	0.053	0.240	47.659	47.755	144.882	–4.938	ACS
2 454 080.33600	–0.030	–0.244	47.433	47.757	144.824	–5.019	ACS
2 454 416.29300	–0.263	–0.024	47.968	47.801	145.703	–5.304	NICMOS3
2 454 439.78000	0.245	0.078	47.585	47.804	145.696	–5.473	WFPC2
2 455 250.73686	0.260	0.052	46.954	47.895	146.287	–6.396	SINFONI

Notes. [(†)] The first block is reproduced from Brown et al. (2010) with the corrected values for the dates (see text). The second bloc corresponds to our appulse observation on 2010 February 23. [(‡)] Positions are positive through east and north.

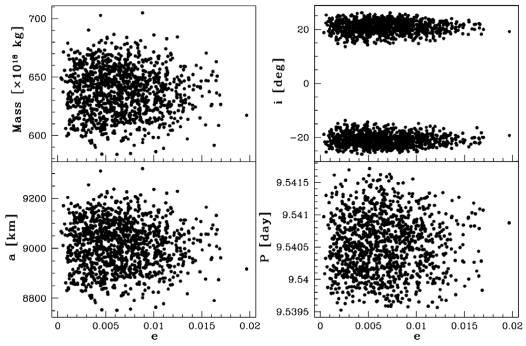

Fig. 6. Elliptical orbital elements: system mass ($\mathcal{M}$), semi-major axis (a), inclination (i), and period (P), plotted as a function of the eccentricity (e). Each point represents a different orbital solution that fits the astrometry measurements in Table 4. See Table 5 for a summary of the orbital elements.

Table 5. Orbital elements and physical parameters for the Orcus/Vanth system.

Qty.	Value	Uncert.	Description	
a	9030	89	km	Semi-major axis
e	0.007	0.003	–	Eccentricity
i	(±)21	2	deg.	Inclination[1]
Ω	144	63	deg.	Ascending node[1]
n	37.732	0.002	deg/day	Mean motion
P	9.5406	0.0004	day	Orbital period
P_A	(321, –2)	3	deg.	Pole A coordinates[2]
P_B	(340, +38)	3	deg.	Pole B coordinates[2]
$\mathcal{M}$	641	19	10^{18} kg	Total mass
$\mathcal{D}$	850	90	km	Diameter[3]
D_o	807 or 761	100	km	Orcus diameter[4]
D_v	267 or 378	100	km	Vanth diameter[4]
ρ	2250 or 2470	885	kg m^{-3}	Bulk density

Notes. Uncertainties are the formal 1σ confidence intervals (from Fig. 6) and do not account for possible systematics (that arise from model incompleteness, e.g., neglecting Orcus J_2 which is unknown). [(1)] In the tangent plane. [(2)] Pole coordinates are given in the ecliptic J2000 reference frame. [(3)] Volume-equivalent from radiometry (see Lim et al. 2010). [(4)] Assuming alternatively $p_v = p_o$, or $p_o = 0.27$ and $p_v = 0.12$.

and M. Brown, personal communication). All the astrometric measurements are reproduced in Table 4, along with the observation circumstances: heliocentric distance (Δ) and range to observer (r), right ascencion (α), and declination (δ).

5.2. Orbit improvement

With our additional astrometric data, we can improve the orbital parameters, reset the orbital phase of Vanth, and, taking advantage of the time leverage, provide tighter constrains than possible before of the orbital period. We computed an improved Keplerian orbit using a statistical inversion algorithm (Hestroffer et al. 2005), which allows us to probe a large portion of the orbital parameter space. We show in Fig. 6 all the solutions that are consistent with the observations, within the measurement uncertainties, and list the resulting improved orbital and physical parameters in Table 5.

As mentioned before, the position of Vanth in its orbit on 2010 Feb. 23 (see Fig. 5) did not allow us to remove the ambiguity of the inclination of the orbit (±21° with respect to the average plane-of-the-sky). However, the orbital pole solution that is almost perpendicular to the ecliptic (P_A, corresponding to $i = +21°$), coordinates ECJ2000 (321°, −2°), is statistically more probable given the observable data (see Fig. 6), although the other solution (P_B) inclined at about 52° from the ecliptic, coordinates ECJ2000 (340°, +38°), provides very similar residuals and cannot yet be ruled out.

All the possible solutions that we find have low eccentricities ($e \leq 0.02$). Brown et al. (2010) previously highlighted the nearly circular nature of Vanth's orbit around Orcus, although we find here several solutions with higher eccentricities than the upper limit they reported (0.0036, 1σ deviation to the data). Similarly, we determine an average orbital period that is longer than the value of Brown et al. (2010) (consistent with Ortiz et al. 2011, however), their shorter period being still possible, although less likely. These differences might originate from the circular assumption about the orbit of Vanth used by Brown et al. In any case, since the eccentricity of the orbit is small, it suggests that the tides have circularized the orbit, and subsequently that the satellite is also in synchronous rotation. The time for the

circularisation of the orbit of a satellite in such a system can be short, on the order of $\tau_c \sim (a/R_2)^5\, n^{-1} \sim 10^6$ years (Ferraz-Mello et al. 2008). Another reasonable consequence of such a tidal evolution is that the orbital plane is aligned to the equator of the primary. In this case, we would currently see Orcus under a small aspect angle (roughly 10° and 30° for P_A and P_B, respectively).

The circular orbit might also be caused, independently of tidal effects, by a Kozai resonance ($\sqrt{1-e^2}\,\cos i = \text{const.}$, Kozai 1962), in which case the inclination of Vanth's orbit with respect to Orcus' equator can be large. This also means that the direction of the spin for the primary is unconstrained and that its aspect angle can be much larger. We favor here the first solution (P_A) as it is slightly more probable statistically, and is consistent with the low amplitude of the variations present in the optical lightcurve of Orcus (0.04 mag, see Thirouin et al. 2010, and references therein).

The total mass $\mathcal{M}$ is derived to high precision from Kepler's third law, considering that this dynamical system is quite isolated over the observational timescale, supported by the two-body fit. The recent size determined using ESA *Herschel* data by Lim et al. (2010) allows us to evaluate the volume, hence density, of the components. Because the components are not resolved by the thermal infrared pixels, one can only derive a radiometric volume-equivalent diameter $\mathcal{D}$ for the system, and subsequently model-dependent values for the density. This effective diameter can be simply related to the volume-equivalent diameter of each component by considering their projected apparent surface $\mathcal{D}^2 = D_o^2 + D_v^2$. If we assume that the two components are of similar density, one eventually gets a rough estimate of the bulk density

$$\rho = \frac{6\,\mathcal{M}}{\pi\,\mathcal{D}^3}\,\frac{(1+\mathcal{R}^2)^{3/2}}{(1+\mathcal{R}^3)}, \tag{3}$$

where the size ratio of the bodies $\mathcal{R} \equiv D_v/D_o = \sqrt{\frac{p_o}{p_v}}\,10^{-0.2\,\Delta m}$ essentially depends on their apparent magnitude difference ($\Delta m \approx 2.4 \pm 0.4$, see Table 3), modulated by their unknown albedo ratio. Following Brown et al. (2010), we consider two possible albedos for Vanth: firstly 0.27 (i.e., equal to that of Orcus, corresponding to co-formation mechanisms, as described in Sect. 5.3), and secondly 0.12, typical of TNOs exempt of water ice (for capture mechanisms, as in Sect. 5.3). We find mass ratios of 30 and 8, for the equal-albedo and different-albedo assumptions respectively, close to the estimates of Brown et al. (2010) and Ortiz et al. (2011). On the basis of the refined volume-equivalent diameter of the Orcus/Vanth system by Lim et al. (2010), which is 10% smaller than the estimate of Brown et al. (2010), we find a density of about 2.3 ± 0.8 g/cc. In any case, the uncertainty in the bulk density is dominated by the uncertainty in the size determination, which cannot be more accurate than about 10% (Lim et al. 2010). The relative precision in the bulk density cannot therefore be smaller than about 30%. More accurate knowledge of the spin properties of Orcus, and of its shape are now required to improve its size, hence volume, estimate.

5.3. Formation mechanism

Trans-Neptunian binaries can be used to impose constraints on various models of solar system formation evolution, e.g., to constrain Neptune's migration history (Murray-Clay & Schlichting 2011). Several formation mechanisms have been proposed and each leads to different predictions for the physical and orbital properties of TNBs. These formation mechanisms can, broadly, be broken down into four classes: collision (Weidenschilling 2002), rotational fission (Ortiz et al. 2011), capture (e.g., Goldreich et al. 2002; Funato et al. 2004; Astakhov et al. 2005; Lee et al. 2007; Gamboa Suárez et al. 2010), and gravitational collapse (Nesvorný et al. 2010).

In the collision model of Weidenschilling (2002), two objects collide inside the Hill sphere of a third object. These objects then fuse into a single object thereby producing a binary. The capture models of Goldreich et al. (2002) rely on two objects interpenetrating their mutual Hill sphere and then being stabilized either through dynamical friction (the L^2 mechanism) or through a scattering event with a third, similarly sized, object (the L^3 mechanism). Funato et al. (2004) proposed a hybrid collision-capture mechanism. Initially two objects collide to produce a binary whose components (as is usual for a collision) have quite different masses. Subsequently, exchange "reactions" with larger third bodies displace the secondary and so ramp up the mass ratio. This eventually leads to binaries with similarly sized partners. However, this mechanism appears to lead to orbital properties (in particular, ellipticities) dissimilar to those actually observed (e.g., Noll 2003; Astakhov et al. 2005).

An additional capture scenario, chaos-assisted capture (CAC, see Astakhov et al. 2005; Lee et al. 2007), was originally proposed to explain the capture of irregular moons at the giant planets (e.g., Astakhov et al. 2003). The scenario for the formation of TNBs is as follows: two objects initially become caught up in very long-living, yet ultimately unstable, chaotic orbits within their mutual Hill sphere. During this phase, the binary may be permanently captured and subsequently hardened through multiple scattering encounters with relatively small "intruder" bodies. The CAC model predicts similarly sized binary components whose mutual orbits are in good agreement with observations. It has been indeed proposed that the propensity to form similarly sized binary partners is a direct fingerprint of chaos-assisted capture. A further specific prediction of the CAC mechanism concerns the distribution of retrograde and prograde mutual orbits, i.e., mutual orbit inclinations (Astakhov et al. 2005; Lee et al. 2007). In particular, retrograde mutual orbits are predicted to be relatively common. The CAC mechanism was criticized by Schlichting & Sari (2008) who argue, e.g., that formation via transient, chaotic binaries is not as important as the L^2 and L^3 mechanisms. These objections are addressed in some detail by Gamboa Suárez et al. (2010).

Finally, Nesvorný et al. (2010) proposed a model in which TNBs formed during gravitational collapse. Angular momentum considerations in the planetesimal disk explain the formation of binaries rather than condensation into a single object. This gravitational instability model predicts identical compositions and colors for TNB partners and also inclinations of generally $i \leq 50°$, i.e., retrograde mutual orbits are predicted to be rare. Unfortunately, true inclinations of mutual TNB orbits is currently available for a handful of systems only (see Grundy et al. 2011). For example, Table 5 and Figs. 5 and 6 show that only knowledge of the true inclination of the mutual orbit (i.e., that obtained by making further observations to remove the symmetry ambiguity) will help us determine whether the mutual orbit of the Orcus/Vanth system is either prograde or retrograde.

We note that the CAC model also allows for the direct formation of almost circular orbits similar to that of Orcus/Vanth. This mechanism was proposed as a possible origin of the apparently almost circular orbit of the TNB 2001 QW_{322} (Petit et al. 2008; Gamboa Suárez et al. 2010). It is conceivable that the Orcus/Vanth system was produced in a similar manner.

Table 6. Relative positions (δx, δy) of Vanth with respect to Orcus for future occultation events (δx positive through East).

Date	δx (km)	δy (km)
2012 Mar 21	–6977	–5259
2012 Nov 16	–8937	347

Notes. Uncertainty on position draws an ellipse of ±450 × 120 km on Earth, around the reported positions (see text for details).

In summary, determining the colors and compositions, as well as the true mutual orbital inclinations of TNBs (Schlichting & Sari 2008) remain important quests. Knowledge of these properties will provide important information to constrain, and to distinguish between, the variously proposed TNB formation models.

5.4. Stellar occultations

Observations of stellar occultation phenomena are of great interest for deriving, in a direct and most precise way, the size of the occulting body. When several chords are gathered, one can derive the projected shape contour (see Millis & Dunham 1989, for a extensive summary). Moreover, these observations help us to ascertain whether there is a teneous atmosphere, and then derive its pressure profile (e.g., Sicardy et al. 2003).

In the case of a binary system, it is also important to be able to predict the path of each component more than the one of the center of gravity (Assafin et al. 2010). Given the large separation of Vanth from Orcus (~9000 km), the prediction of an event by the secondary can be either deplaced in time by several minutes when the binary system is oriented in the direction of apparent motion, or fully decoupled from the one of the primary otherwise. The occultation path of the primary might indeed be invisible from Earth while that of the secondary could be visible.

Owing to the current uncertainty in TNO ephemerides, a precise prediction of occultation requires "last-minute" astrometry measurements relative a to background star to obtain reliable predictions of the occultation track on Earth. In addition, the position of the secondary relative to the primary is needed to a precision of approximately 100 km to enable useful observational campaigns to be established. Given the improvement in the period estimate, and the orbital phase reset provided by our astrometric point obtained in 2010, we can derive more accurate prediction for the location of the secondary and subsequently for the track of stellar occultations by Vanth. Given the possible mass-ratio range, the path on the Earth of the primary can also be shifted from the position of the center-of-mass. Assuming that the components have the same albedo, the mass ratio is on the order of $\approx 0.02^{+0.07}_{-0.02}$, corresponding to a shift of 180^{+630}_{-180} km. We list in Table 6 the relative position of Vanth around Orcus for upcoming stellar occultations. The relative positions in Table 6 corresponds to the nominal values; the associated error distribution is not exactly Gaussian, but an ellipse curved and stretched along the trajectory (similar to Fig. 5). The one σ uncertainty is large, approximately ±450 km along the secondary's nominal trajectory (about ±120 km across), for both occultations. Depending on the occultation occurence (motion relative to the star and orientation of this uncertainty ellipse), it can correspond to a shift of the occultation path on Earth (or miss) or a shift in time. Updates are available online[2].

[2] http://www.lesia.obspm.fr/perso/bruno-sicardy/

6. Conclusion

On the basis of spectro-imaging measurements of the Orcus-Vanth system, we have been able to obtain a spectrum of Orcus, measure the H and K magnitudes of Vanth, and determine their mutual relative positions. We have searched for possible weak bands in the spectrum of Orcus, limiting the possible amount of CH_4 to no more than ~2%, and ethane to ~5%. The presence of other compound(s) is required to explain the depth of the absorption band detected at 2.2 μm. Presence of hydrated ammonia, or ammonium, could explain the observed band, but the lack of distinguishable features for these species in the observed wavelength range forbid any strong conclusion to be drawn.

Vanth has been found to be slightly redder than Orcus in the visible to near-infrared wavelength range, although uncertainties in the measurements are large. While this suggests that Vanth's composition, or age, is different from Orcus, it does not constrain formation scenarios (collision, co-formation, or capture). By detecting Vanth at another position three years after previous orbit calculations by Brown et al. (2010), we have been able to reset the phase of the orbit, allowing predictions of Vanth's track on Earth during future stellar occultation events.

Acknowledgements. We thank the staff of ESO's Paranal observatory for their assistance in obtaining this data. This research used the VO tool Miriade (Berthier et al. 2008) developed at IMCCE, and NASA's Astrophysics Data System. We acknowledge support from the Faculty of the European Space Astronomy Centre (ESAC) for F.D. visit. P.L. is grateful for the financial support of a Michael West Fellowship and of the Royal Society in the form of a Newton Fellowship. We thank our anonymous referee for their constructive comments.

References

Assafin, M., Camargo, J. I. B., Vieira Martins, R., et al. 2010, A&A, 515, A32
Astakhov, S. A., Burbanks, A. D., Wiggins, S., & Farrelly, D. 2003, Nature, 423, 264
Astakhov, S. A., Lee, E. A., & Farrelly, D. 2005, MNRAS, 360, 401
Barucci, M. A., Brown, M. E., Emery, J. P., & Merlin, F. 2008a, The Solar System Beyond Neptune, 143
Barucci, M. A., Merlin, F., Guilbert, A., et al. 2008b, A&A, 479, L13
Berthier, J., & Marchis, F. 2001, BAAS, 33, 1049
Berthier, J., Hestroffer, D., Carry, B., et al. 2008, LPI Contributions, 1405, 8374
Bonnet, H., Abuter, R., Baker, A., et al. 2004, The Messenger, 117, 17
Britt, D. T., Yeomans, D. K., Housen, K. R., & Consolmagno, G. J. 2002, Asteroids III, 485
Brown, M. E., van Dam, M. A., Bouchez, A. H., et al. 2006, ApJ, 639, 43
Brown, M. E., Ragozzine, D., Stansberry, J., & Fraser, W. C. 2010, AJ, 139, 2700
Carry, B., Vernazza, P., Dumas, C., & Fulchignoni, M. 2010, Icarus, 205, 473
Cook, J. C., Desch, S. J., Roush, T. L., Trujillo, C. A., & Geballe, T. R. 2007, ApJ, 663, 1406
Cooper, J. F., Christian, E. R., Richardson, J. D., & Wang, C. 2003, Earth Moon and Planets, 92, 261
Cottin, H., Moore, M. H., & Bénilan, Y. 2003, ApJ, 590, 874
de Bergh, C., Delsanti, A., Tozzi, G. P., et al. 2005, A&A, 437, 1115
Delsanti, A., Merlin, F., Guilbert-Lepoutre, A., et al. 2010, A&A, 520, A40
DeMeo, F. E., Fornasier, S., Barucci, M. A., et al. 2009, A&A, 493, 283
DeMeo, F. E., Barucci, M. A., Merlin, F., et al. 2010, A&A, 521, A35
Dumas, C., Carry, B., Hestroffer, D., & Merlin, F. 2011, A&A, 528, A105
Eisenhauer, F., Abuter, R., Bickert, K., et al. 2003, SPIE, 4841, 1548
Ferraz-Mello, S., Rodríguez, A., & Hussmann, H. 2008, Celest. Mech. Dyn. Astron., 101, 171
Fornasier, S., Dotto, E., Barucci, M. A., & Barbieri, C. 2004, A&A, 422, L43
Funato, Y., Makino, J., Hut, P., Kokubo, E., & Kinoshita, D. 2004, Nature, 427, 518
Gamboa Suárez, A., Hestroffer, D., & Farrelly, D. 2010, Celest. Mech. Dyn. Astron., 106, 245
Goldreich, P., Lithwick, Y., & Sari, R. 2002, Nature, 420, 643
Grundy, W. M., & Schmitt, B. 1998, J. Geophys. Res., 103, 25809
Grundy, W. M., Noll, K. S., Nimmo, F., et al. 2011, Icarus, 213, 678
Guilbert, A., Alvarez-Candal, A., Merlin, F., et al. 2009, Icarus, 201, 272

Hapke, B. 1993, Theory of reflectance and emittance spectroscopy (Cambridge University Press)
Hestroffer, D., Vachier, F., & Balat, B. 2005, Earth Moon and Planets, 97, 245
Hilton, J. L. 2002, Asteroids III, 103
Khare, B. N., Sagan, C., Arakawa, E. T., et al. 1984, Icarus, 60, 127
Khare, B. N., Thompson, W. R., Cheng, L., et al. 1993, Icarus, 103, 290
Kozai, Y. 1962, AJ, 67, 591
Lee, E. A., Astakhov, S. A., & Farrelly, D. 2007, MNRAS, 379, 229
Levi, A., & Podolak, M. 2009, Icarus, 202, 681
Lim, T. L., Stansberry, J., Müller, T. G., et al. 2010, A&A, 518, L148
Markwardt, C. B. 2009, in ASP Conf. Ser. 411, ed. D. A. Bohlender, D. Durand, & P. Dowler, 251
Merline, W. J., Weidenschilling, S. J., Durda, D. D., et al. 2002, Asteroids III, 289
Millis, R. L., & Dunham, D. W. 1989, Asteroids II, 148
Modigliani, A., Hummel, W., Abuter, R., et al. 2007 [arXiv:astro-ph/0701297]
Müller, T. G., Lellouch, E., Böhnhardt, H., et al. 2009, Earth Moon and Planets, 105, 209
Murray-Clay, R. A., & Schlichting, H. E. 2011, ApJ, 730, 132
Nesvorný, D., Youdin, A. N., & Richardson, D. C. 2010, AJ, 140, 785
Noll, K. S. 2003, Earth Moon and Planets, 92, 395
Ortiz, J. L., Cikota, A., Cikota, S., et al. 2011, A&A, 525, A31
Petit, J.-M., Kavelaars, J. J., Gladman, B. J., et al. 2008, Science, 322, 432
Quirico, E., & Schmitt, B. 1997, Icarus, 127, 354
Schaller, E. L., & Brown, M. E. 2007, ApJ, 659, L61
Schlichting, H. E., & Sari, R. 2008, ApJ, 673, 1218
Schmitt, B., Quirico, E., Trotta, F., & Grundy, W. M. 1998, in Solar System Ices, ed. B. Schmitt, C. de Bergh, & M. Festou, Astrophys. Space Sci. Libr., 227, 199
Sicardy, B., Widemann, T., Lellouch, E., et al. 2003, Nature, 424, 168
Stansberry, J., Grundy, W., Brown, M. E., et al. 2008, The Solar System Beyond Neptune, 161
Strazzulla, G., & Palumbo, M. E. 1998, Planet. Space Sci., 46, 1339
Thirouin, A., Ortiz, J. L., Duffard, R., et al. 2010, A&A, 522, A93
Trujillo, C. A., Brown, M. E., Rabinowitz, D. L., & Geballe, T. R. 2005, ApJ, 627, 1057
Tryka, K. A., Brown, R. H., Chruikshank, D. P., et al. 1994, Icarus, 112, 513
Weidenschilling, S. J. 2002, Icarus, 160, 212

A&A 511, A72 (2010)
DOI: 10.1051/0004-6361/200913031

Astronomy & Astrophysics

Characterisation of candidate members of (136108) Haumea's family⋆

C. Snodgrass[1,2], B. Carry[1,3], C. Dumas[1], and O. Hainaut[4]

[1] European Southern Observatory, Alonso de Córdova 3107, Vitacura, Casilla 19001, Santiago de Chile, Chile
[2] Max Planck Institute for Solar System Research, Max-Planck-Strasse 2, 37191 Katlenburg-Lindau, Germany
e-mail: snodgrass@mps.mpg.de
[3] LESIA, Observatoire de Paris-Meudon, 5 place Jules Janssen, 92195 Meudon Cedex, France
[4] European Southern Observatory, Karl-Schwarzschild-Strasse 2, 85748 Garching bei München, Germany

Received 31 July 2009 / Accepted 14 December 2009

ABSTRACT

Context. Ragozzine & Brown presented a list of candidate members of the first collisional family to be found among the trans-Neptunian objects (TNOs), the one associated with (136108) Haumea (2003 EL_{61}).
Aims. We aim to identify which of the candidate members of the Haumea collisional family are true members, by searching for water ice on their surfaces. We also attempt to test the theory that the family members are made of almost pure water ice by using optical light-curves to constrain their densities.
Methods. We use optical and near-infrared photometry to identify water ice, in particular using the $(J - H_S)$ colour as a sensitive measure of the absorption feature at 1.6 μm. We use the CH_4 filter of the new Hawk-I instrument at the VLT as a short H-band (H_S) for this as it is more sensitive to the water ice feature than the usual H filter.
Results. We report colours for 22 candidate family members, including NIR colours for 15. We confirm that 2003 SQ_{317} and 2005 CB_{79} are family members, bringing the total number of confirmed family members to 10. We reject 8 candidates as having no water ice absorption based on our Hawk-I measurements, and 5 more based on their optical colours. The combination of the large proportion of rejected candidates and time lost to weather prevent us from putting strong constraints on the density of the family members based on the light-curves obtained so far; we can still say that none of the family members (except Haumea) require a large density to explain their light-curve.

Key words. Kuiper Belt: general – methods: observational – techniques: photometric – infrared: planetary systems – Kuiper Belt objects: individual: (136108) Haumea

1. Introduction

The trans-Neptunian object (TNO) (136108) Haumea (2003 EL_{61}) was discovered by Santos-Sanz et al. (2005) and quickly attracted a lot of attention as a highly unusual body. It is one of the largest TNOs (Rabinowitz et al. 2006; Stansberry et al. 2008) and yet is a fast rotator (period ∼3.9 h) with a highly elongated shape (Rabinowitz et al. 2006). Its surface was shown to be dominated by water ice by Near Infra-Red (NIR) spectroscopy (Tegler et al. 2007; Trujillo et al. 2007; Merlin et al. 2007; Pinilla-Alonso et al. 2009), yet has a high density of 2.5–3.3 g cm^{-3} (Rabinowitz et al. 2006). It was found to have two satellites (Brown et al. 2005a, 2006), which also have water ice surfaces (Barkume et al. 2006; Fraser & Brown 2009). Lacerda et al. (2008) found that Haumea presents hemispherical colour heterogeneity, with a dark red "spot" on one side, using high precision photometry.

Brown et al. (2006) and Barkume et al. (2006) postulated that the density, shape and water ice surface could be explained by a large collision early in the history of the Solar System. Brown et al. (2007b) then identified a family of 6 TNOs (1995 SM_{55}, 1996 TO_{66}, 2002 TX_{300}, 2003 OP_{32} and 2005 RR_{43}), in addition to Haumea and its satellites, with orbits that could be linked to Haumea and water ice surfaces, which were also attributed to coming from this massive collision. This theory required that the proto-Haumea was a very large body (radius ∼830 km) that had already differentiated early in the formation of the Solar System, and that the collision stripped nearly all of the outer (water ice) mantle (∼20% of the total mass of the original body). This left the dense core as Haumea with a thin coating of water ice and created a family of re-accumulated lumps of almost pure water ice. Ragozzine & Brown (2007) find that the collision must have taken place in the early Solar System (with an age of at least 1 Gyr), although the lack of weathering on the surfaces may imply young bodies (Rabinowitz et al. 2008). The existence of such a family has implications for the dynamics of the Kuiper Belt (Levison et al. 2008).

Ragozzine & Brown (2007) performed a dynamical study and identified two further family members (2003 UZ_{117} and 1999 OY_3) with strong dynamical links to the family and colours consistent with water ice, and also published a list of candidate family members that had orbital elements consistent with this dynamical family, totalling 35 objects including the known members. Most of these candidates lacked the NIR spectra that could identify water ice on their surfaces though, so they remained only potential family members. The diffusion time and interaction with resonances make it possible for interlopers to appear close to the family dynamically, so it is essential to

⋆ Based on observations collected at the European Southern Observatory, La Silla & Paranal, Chile – 81.C-0544 & 82.C-0306.

A&A 511, A72 (2010)

have both dynamical and physical properties characterisation to confirm family membership (Cellino et al. 2002). Some could be ruled out by either existing NIR spectra (Makemake has a methane ice surface; Dumas et al. 2007; Brown et al. 2007a) or by very red optical colours (1996 RQ_{20}, 1999 CD_{158}, 1999 KR_{16}, 2002 AW_{197}, 2002 GH_{32}; see Table 4 for references) or a strong red slope in optical spectra (2005 UQ_{513}; Pinilla-Alonso et al. 2008). Schaller & Brown (2008) subsequently published NIR spectra which confirmed 2003 UZ_{117} and 2005 CB_{79} as family members, and rejected 2004 SB_{60}. We observed 13 of the 18 remaining candidate objects (along with some of the already characterised objects) with the goal of providing this physical information, to identify those with water ice surfaces and also to test the idea that these family members could be made of nearly pure water ice. We describe our observations, the results from them, and their implications in the following sections.

2. Observations and data reduction

The best method to test for water ice on the surface of a Solar System body is through NIR spectroscopy, as water ice has strong absorption bands at ∼1.6 and ∼2.0 μm, but this is only possible for the brightest TNOs ($K \lesssim 18$). Still, it is possible to get an indication of the presence or absence of water ice for fainter bodies using photometry, which can be performed on smaller (fainter) TNOs.

We conducted the observations at the European Southern Observatory (program IDs: 81.C-0544 & 82.C-0306), on both the La Silla and Paranal (VLT) sites. Observations in the visible wavelengths (*BVRi* filters) were performed using the EFOSC2 instrument (Buzzoni et al. 1984) mounted on the NTT (since April 2008; Snodgrass et al. 2008). This is a focal reducing imager and spectrograph with a single CCD. The near-infrared observations (J, CH_4 bands) were performed using the newly commissioned wide-field camera Hawk-I (Pirard et al. 2004; Casali et al. 2006). We had three observing runs scheduled with each instrument, as detailed in Table 1. This table lists all objects we attempted to observe, although not all were detected and some time was lost to poor weather conditions. In particular the June 17th Hawk-I run (run B) was very badly affected by clouds, with only 1999 KR_{16} reliably detected in both bands. Exposure times were generally 300–600 s in the optical, while in the NIR we took sequences of J-CH_4-J to give an average J magnitude at the time of the CH_4 observations, and to confirm identification of the object based on its motion between the two sets of J-band images. The CH_4 filter observations took the largest part of the time; between 15 min for the brightest objects to a few hours for the faintest ones, each split into short individual exposures and dithered due to the bright NIR sky. Note that due to the long effective exposure times any variation (due to shape or albedo variation across the surface) is smeared out, and cannot be detected in our NIR data.

The advantage of using Hawk-I is that the CH_4 band filter is a medium width filter with a wavelength range that is entirely within the broad water ice absorption between 1.4 and 1.75 μm. The standard H-band is broader and covers a range that is part in and part out of this band[1] . We therefore use the CH_4 filter as a short H filter (henceforth H_S) which gives a colour measurement ($J - H_S$) that is very sensitive to water ice absorption. All of the filters used in this work are listed in Table 2.

[1] See http://www.eso.org/sci/facilities/paranal/instruments/hawki/inst for transmission curves.

Table 1. Observational circumstances.

Object (#)	Object (Designation)	r^a (AU)	Δ^b (AU)	α^c (°)	Run^d	Epochs^e B	V	R	i
	1996 RQ 20	39.6	39.0	1.1	C			4	
20161	1996 TR 66	40.3	40.0	1.4	E	2	2	2	2
	1998 HL 151	38.9	38.2	1.0	A	2	2	2	2
181855	1998 WT 31	38.0	37.3	1.0	E	2	2	10	2
	1999 CD 158	47.6	46.5	0.6	E	1	1	24	1
40314	1999 KR 16	36.3	35.6	1.2	B				
	1999 OH 4	39.1	39.6	1.3	A	1	1	1	1
	”	39.1	38.2	0.6	C	2	2	2	2
	1999 OK 4	46.4	45.8	1.1	A	1	1	1	1
86047	1999 OY 3	40.1	39.7	1.3	A			11	
”	”	40.2	39.5	1.1	B				
”	”	40.2	39.4	0.8	D				
86177	1999 RY 215	35.8	34.8	0.2	C			21	
”	”	35.8	34.8	0.3	D				
	2000 CG 105	46.8	46.1	0.8	E	2	2	22	2
130391	2000 JG 81	34.8	33.8	0.5	A	1	1	1	1
	2001 FU 172	31.8	30.9	1.0	A	1	1	1	1
	2001 QC 298	40.6	39.6	0.3	C			17	
	”	40.6	39.6	0.2	D				
55565	2002 AW 197	46.6	45.8	0.7	F				
	2002 GH 32	43.1	42.2	0.7	A	3	3	18	3
	”	43.1	42.4	1.0	B				
55636	2002 TX 300	41.4	40.6	0.8	D				
136108	Haumea	51.1	50.6	1.0	A	1	1	1	1
”	”	51.1	50.8	1.1	B				
”	”	51.1	51.1	1.1	F				
	2003 HA 57	32.7	32.0	1.3	A	1	1	1	1
	”	32.7	32.2	1.6	B				
	2003 HX 56	46.5	45.9	1.0	A	2	2	2	2
120178	2003 OP 32	41.4	40.6	0.6	D				
	2003 QX 91	33.6	32.6	0.5	C			4	
	2003 SQ 317	39.3	38.3	0.6	C			15	
	”	39.3	38.3	0.4	D				
	2003 TH 58	36.0	35.1	0.5	E	2	2	23	2
	”	36.0	35.1	0.7	F				
136199	Eris	96.7	95.9	0.4	D				
	2003 UZ 117	39.4	38.9	1.3	D				
	2004 PT 107	38.3	37.9	1.4	A	4	4	24	4
	”	38.3	37.7	1.3	B				
	”	38.3	37.4	0.7	D				
120347	2004 SB 60	44.0	43.1	0.6	C			16	
	2005 CB 79	40.1	39.3	0.9	E	1	1	2	1
	”	40.0	39.2	0.8	F				
	2005 GE 187	30.8	29.9	0.9	A	3	3	33	3
	”	30.8	30.1	1.3	B				
	”	30.8	31.1	1.7	C			17	
	”	30.8	31.3	1.6	D				
202421	2005 UQ 513	48.8	48.1	0.8	C			10	
”	”	48.8	48.0	0.7	D				

Notes. [a] Heliocentric distance. [b] Geocentric distance. [c] Phase angle. [d] Runs: A = 2008 June 3rd–5th, EFOSC2; B = 2008 June 17th, Hawk-I; C = 2008 August 30th–September 1st, EFOSC2; D = 2008 September 9th, Hawk-I; E = 2008 December 29th–31st, EFOSC2; F = 2009 January 4th, Hawk-I. [e] Number of epochs observed in each filter (for EFOSC2 runs).

The data were reduced in the normal manner (bias subtraction, flat fielding, sky subtraction etc. as appropriate). For the EFOSC2 data the objects were generally visible in individual frames and aperture photometry was performed directly on each, using the optimum aperture based on the measured stellar FWHM in each frame and an average aperture correction measured using the field stars (see Snodgrass et al. 2005). Where

Table 2. Filters used in this study.

Filter	Instrument	λ_c μm	$\Delta\lambda$ μm
B	EFOSC2	0.440	0.094
V	EFOSC2	0.548	0.113
R	EFOSC2	0.643	0.165
i	EFOSC2	0.793	0.126
J	Hawk-I	1.258	0.154
H_S (CH4)	Hawk-I	1.575	0.112

Notes. λ_c = Central Wavelength, $\Delta\lambda$ = Bandwidth.

multiple epochs were obtained we then report a weighted mean magnitude. This approach allowed us to look for variation in the *R*-band magnitude for those objects where we obtained a light-curve. For fainter objects the images were shifted based on the predicted motion of each object and combined to give a deep image per filter. We also produced equivalent combined images of the star fields (no shifts) in which we could measure the brightness of field stars for photometric calibration. For Hawk-I all data were shifted and combined as the individual exposures were short because of the high sky background in the NIR.

The EFOSC2 data were calibrated in the normal way, via observations of standard stars from the Landolt (1992) catalogue. The EFOSC2 *i*-band data was calibrated directly onto the Landolt scale; this filter is very close to the standard Cousins *I*-band used by Landolt. Data from non-photometric nights were calibrated via observation of the same fields on later photometric nights, to calibrate the field stars as secondary standard stars.

Calibration of the Hawk-I data was a more involved process as it contained the non-standard filter H_S. The *J* and *H* band magnitudes of all available stars in each field were taken from the 2MASS point source catalogue (Skrutskie et al. 2006). We then generated theoretical colours $(H_{2M} - H_S)$ for stars of all spectral types (O-M) by convolving the response of the 2MASS *H* and the Hawk-I H_S with spectra from the libraries of Pickles (1998) and Ivanov et al. (2004)[2]. For stars the resulting difference is linearly related to the 2MASS $(J - H)$ colour (Fig. 1):

$$(H_{2M} - H_S) = -0.097(J - H)_{2M} - 0.019. \quad (1)$$

We used this relation to generate the expected colour, and therefore H_S magnitude, for each 2MASS star in each field, which were then used to give the calibrated H_S magnitude for the TNOs. We also used the same approach to derive the colour term for the difference between 2MASS and Hawk-I *J* bands, and found that the Hawk-I *J* does not significantly differ from the 2MASS band, as expected. We note that the spectral types further from the linear trend fall into two groups; those below the trend at $(J - H)_{2M} \approx 0$ are B stars that do not feature in our NIR images, while the "tail" that curves away from the line at the red end is made up of M giants, with M8-10 being significant away from the linear relation. These are separable from the rest of the sample though as giants have a very red 2MASS $(J - K)$ colour; Brown (2003) show that stars with $(J - K) \geq 0.5$ are most likely giants, while we find that using limit of $(J - K) \leq 1.26$ removes the M8-10iii stars that do not fit the linear trend while keeping other stars. Having said this, we note that the exclusion or inclusion of these stars made no significant difference to our calibration as there were very few late M giant stars within our sample.

[2] These libraries can be downloaded from the ESO web pages at http://www.eso.org/sci/observing/tools/standards/IR_spectral_library_new/

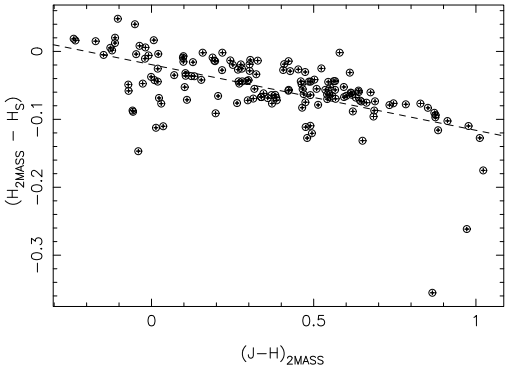

Fig. 1. Theoretical difference between 2MASS *H* and Hawk-I H_S for different stellar spectra, as a function of 2MASS $(J - H)$.

The colours of the 2MASS stars in the fields observed were approximately normally distributed around a mean $(J-H)_{2M} = 0.6$ with a standard deviation of 0.2.

3. Colours

We report the resulting photometry in Table 3, where we give the mean magnitude in each band at each epoch and also an indication of the variation seen in the *R*-band where we obtained light-curves. In Table 4 we give the average colours of all family members that have published photometry, including our own results, taking a weighted mean where multiple measurements exist. From these average colours we calculate reflectances by comparing them to the Solar colours. To calculate the reflectance in the H_S band we used a theoretical $(J - H_S)$ colour for the Sun generated by convolving the response of these filters with the Solar spectrum. We subsequently confirmed this value by observing a Solar analogue star with Hawk-I: the theoretical $(J - H_S)_\odot = 0.273$, while the value measured for the Solar twin S966 (taken from the catalogue of Solar twins in M 67 by Pasquini et al. 2008) is $(J - H_S)_\odot = 0.288 \pm 0.007$. These are consistent at the level of the uncertainty on our TNO colour measurements. We also report the visible slope for each object (%/100 nm) in Table 4, calculated from the reflectances via a linear regression over the full *BVRI* range when it is available, or whichever measurements exist in other cases.

The reflectance "spectra" of the TNOs from this photometry are shown in Fig. 2, for all objects with photometry in at least three bands. The combined visible and NIR spectrum of Haumea from Pinilla-Alonso et al. (2009) is shown for comparison to the photometry. The large TNOs Eris (not a family member; observed for comparison) and Makemake (dynamically a family member candidate) are known to have methane ice surfaces from NIR spectroscopy (Dumas et al. 2007; Brown et al. 2007a) and clearly differ from the Haumea spectrum. Note that those objects marked with an asterisk in the figure have their reflectance normalised to the *R*-band, as no *V*-band photometry was available. For Haumea-like neutral spectra this makes no difference, but this could give an offset in the case of red slopes; these four spectra should not be directly compared with the others in the figure, but can be compared with the Haumea spectrum.

Table 3. Photometry. Mean apparent magnitudes for each object at each epoch.

	Object	Run[a]	B	V	R	I	J	H_S	Δm_R[b]
	1996 RQ 20	C	–	–	22.95 ± 0.05	–	–	–	–
	1998 HL 151	A	25.37 ± 0.28	24.25 ± 0.12	23.87 ± 0.13	23.08 ± 0.17	–	–	–
181855	1998 WT 31	E	24.52 ± 0.15	23.81 ± 0.11	23.24 ± 0.06	22.69 ± 0.14	–	–	<0.1
	1999 CD 158	E	23.08 ± 0.07	22.31 ± 0.06	21.68 ± 0.01	21.20 ± 0.06	–	–	0.6
40314	1999 KR 16	B	–	–	–	–	20.02 ± 0.07	19.47 ± 0.10	–
	1999 OH 4	C	25.01 ± 0.22	22.39 ± 0.09	22.19 ± 0.10	21.76 ± 0.32	–	–	–
86047	1999 OY 3	A,D	–	–	22.26 ± 0.03	–	21.78 ± 0.10	22.04 ± 0.35	<0.1
86177	1999 RY 215	C,D	–	–	22.16 ± 0.01	–	21.19 ± 0.14	20.66 ± 0.17	<0.1
	2000 CG 105	E	24.14 ± 0.09	22.60 ± 0.04	22.62 ± 0.02	22.52 ± 0.09	–	–	0.45
	2001 FU 172	A	26.71 ± 1.52	23.80 ± 0.15	23.13 ± 0.12	22.66 ± 0.19	–	–	–
	2001 QC 298	C,D	–	–	22.18 ± 0.03	–	21.16 ± 0.08	20.65 ± 0.12	0.4
55565	2002 AW 197	F	–	–	–	–	18.50 ± 0.05	18.11 ± 0.06	–
	2002 GH 32	A	23.91 ± 0.09	21.87 ± 0.05	21.87 ± 0.02	19.96 ± 0.09	–	–	0.75
55636	2002 TX 300	D	–	–	–	–	18.67 ± 0.07	19.14 ± 0.10	–
136108	Haumea	F	–	–	–	–	16.46 ± 0.07	17.06 ± 0.08	–
	2003 HX 56	A	25.25 ± 0.36	24.03 ± 0.16	23.68 ± 0.16	23.42 ± 0.43	–	–	–
120178	2003 OP 32	D	–	–	–	–	19.08 ± 0.05	19.58 ± 0.06	–
	2003 QX 91	C	–	–	23.66 ± 0.12	–	–	–	–
	2003 SQ 317	C,D	–	–	22.05 ± 0.02	–	21.59 ± 0.05	22.04 ± 0.19	1.0
	2003 TH 58	E	23.50 ± 0.05	22.89 ± 0.04	22.51 ± 0.02	22.03 ± 0.04	21.73 ± 0.09	20.45 ± 0.18	<0.1
	2003 UZ 117	D	–	–	–	–	20.24 ± 0.07	20.86 ± 0.10	–
	2004 PT 107	A,D	–	–	21.66 ± 0.01	–	20.41 ± 0.14	19.87 ± 0.18	0.05
120347	2004 SB 60	C	–	–	20.21 ± 0.01	–	–	–	0.2
	2005 CB 79	E,F	21.45 ± 0.02	20.71 ± 0.03	20.36 ± 0.02	19.98 ± 0.03	19.67 ± 0.07	20.18 ± 0.16	–
	2005 GE 187	A	23.76 ± 0.10	22.78 ± 0.09	22.02 ± 0.01	21.47 ± 0.11	–	–	<0.1
	"	C,D	–	–	22.13 ± 0.03	–	20.84 ± 0.08	20.18 ± 0.12	0.5
202421	2005 UQ 513	C,D	–	–	20.30 ± 0.01	–	18.89 ± 0.07	18.59 ± 0.10	0.3
136199	Eris	D	–	–	–	–	17.73 ± 0.07	17.49 ± 0.09	

Notes. [a] Runs A-F as listed in Table 1. [b] Δm_R is the variation in R-band magnitude seen for objects where (partial) light-curves were obtained. The uncertainty on each is ∼0.1 mag.

4. Discussion

4.1. Family membership

We first wish to determine which candidates are actually family members, and which are dynamical interlopers with different surface properties. We find that the $(J - H_S)$ colour is a good diagnostic of the presence or absence of the water ice absorption feature at 1.6 μm, as expected: For Haumea we measure $(J - H_S) = -0.60 \pm 0.11$, and the colour is also significantly negative for the other known family members observed, while for the methane ice dominated comparison TNO Eris we find $(J - H_S) = 0.25 \pm 0.11$. The colours for all objects are given in Table 4, along with the visible slopes, and these are also plotted in Fig. 3. In the figure there is a clear separation between the family members with negative $(J - H_S)$ at the bottom and the other objects at the top, and also a tendency for those with water ice to have blue/neutral surfaces (shallower slopes). While those without water ice have a large range of slopes from neutral to very red, there are no bodies in the lower right of the figure (water ice and red slope). We use this separation to make a rough assessment of the family membership for candidates with only optical colours; we can rule out membership for objects with very red slopes, but cannot use a blue slope to confirm membership.

We confirm two more family members in addition to those listed by Ragozzine & Brown (2007); 2003 SQ_{317} and 2005 CB_{79}. These have $(J - H_S) = -0.45 \pm 0.20$ and -0.50 ± 0.17 respectively. 2005 CB_{79} has since been confirmed as a family member by NIR spectroscopy (Schaller & Brown 2008). For 2003 SQ_{317} the lack of optical colours as supporting evidence and the relatively large uncertainty on $(J - H_S)$ makes the water ice detection preliminary, and spectroscopy or further photometry would be worthwhile, but the evidence is certainly as strong as for some previous spectroscopic water ice "detections" so we choose to regard this as a confirmed family member for the purposes of this paper. This brings the total number of confirmed family members to 10, of the 35 candidate objects. We are far more efficient at rejecting candidates though; 8 objects have $(J - H_S)$ colours inconsistent with water ice, and cannot be true family members. These are 1999 KR_{16}, 1999 RY_{215}, 2001 QC_{298}, 2002 AW_{197}, 2003 TH_{58}, 2004 PT_{107}, 2005 GE_{187} and 2005 UQ_{513}. This is in agreement with Pinilla-Alonso et al. (2008), who rejected 2005 UQ_{513} on the basis of a very red slope in an optical spectrum. We also find that 1998 WT_{31} and 2001 FU_{172} have strongly red visible slopes, and can probably be rejected as family members without Hawk-I data. Including also Makemake and 2004 SB_{60}, which have been shown to lack water ice on their surfaces by NIR spectroscopy (Brown et al. 2007a; Schaller & Brown 2008) and the others listed in the introduction which have previously been found to have very red optical colours, this gives a total of 15 of the 35 candidates that are shown not to belong to the family. Finally, we also observed 1998 HL_{151}, 1999 OH_4, 2000 CG_{105} and 2003 HX_{56} in the optical, but all of these were too faint to put meaningful constraints on their family membership. We summarise which objects we believe to be family members, which we can rule out, and which we do not yet have enough information on in the last column of Table 4.

Given the high rate of rejection of candidates, we consider the likelihood that this is a true family from a statistical point of view, or whether the ∼30% of water ice bodies within the

Table 4. Average colours in $BVRIJH_S$ for all candidates (and Eris), and assessment of likely membership based on these colours.

Object[a] #	Designation	$(B-V)$ (mag)	$(V-R)$ (mag)	$(R-I)$ (mag)	$(R-J)$ (mag)	$(J-H_S)$ (mag)	Vis. slope (%/100 nm)	Ref.[b]	Family?
24835	1995 SM 55†	0.65 ± 0.01	0.39 ± 0.01	0.36 ± 0.02	0.65 ± 0.03	–	2.0 ± 0.8	1–8	Y
	1996 RQ 20	0.96 ± 0.13	0.46 ± 0.05	0.71 ± 0.12	–	–	22.4 ± 6.8	9, 10	N
19308	1996 TO 66†	0.68 ± 0.02	0.39 ± 0.01	0.37 ± 0.02	0.61 ± 0.10	–	2.9 ± 0.5	1, 10–14	Y
	1998 HL 151	0.67 ± 0.18	0.42 ± 0.16	0.79 ± 0.31	–	–	18.1 ± 16.9	15, 16, 32	?
181855	1998 WT 31	0.76 ± 0.32	0.51 ± 0.25	0.60 ± 0.28	–	–	16.6 ± 5.2	32	N
	1999 CD 158	0.83 ± 0.06	0.51 ± 0.05	0.54 ± 0.06	1.38 ± 0.09	–	15.8 ± 0.6	6, 32	N
40314	1999 KR 16	1.07 ± 0.03	0.75 ± 0.02	0.74 ± 0.02	1.56 ± 0.08[c]	0.56 ± 0.13	40.9 ± 6.2	9, 16–18, 32	N
	1999 OH 4	2.99 ± 0.48	0.21 ± 0.20	0.44 ± 0.47	–	–	20.2 ± 35.6	32	?
86047	1999 OY 3†	0.75 ± 0.03	0.26 ± 0.03	0.33 ± 0.04	0.80 ± 0.12	−0.26 ± 0.36	−0.5 ± 5.3	3, 32	Y
86177	1999 RY 215	–	–	–	0.99 ± 0.18	0.52 ± 0.22	–	28	N
	2000 CG 105	1.11 ± 0.25	0.39 ± 0.13	0.21 ± 0.22	–	–	6.7 ± 17.5	32	?
	2001 FU 172	2.91 ± 1.53	0.66 ± 0.19	0.53 ± 0.22	–	–	39.8 ± 27.9	32	N
	2001 QC 298	0.66 ± 0.07	0.37 ± 0.07	0.63 ± 0.07	1.06 ± 0.21	0.52 ± 0.14	9.7 ± 10.0	19, 32	N
55565	2002 AW 197	0.93 ± 0.03	0.62 ± 0.02	0.55 ± 0.02	1.16 ± 0.04	0.39 ± 0.08	22.8 ± 3.5	20–22, 32	N
	2002 GH 32	0.91 ± 0.06	0.66 ± 0.06	0.56 ± 0.05	–	–	24.8 ± 4.7	19, 23	N
55636	2002 TX 300†	0.66 ± 0.02	0.36 ± 0.02	0.32 ± 0.03	–	−0.47 ± 0.13	0.2 ± 1.1	21, 23, 32	Y
136108	Haumea†	0.64 ± 0.01	0.33 ± 0.01	0.34 ± 0.01	0.88 ± 0.01	−0.60 ± 0.11	−0.6 ± 0.9	21, 24, 25, 32	Y
	2003 HX 56	1.27 ± 1.37	-0.26 ± 2.07	1.28 ± 2.10	–	–	18.4 ± 32.7	32	?
120178	2003 OP 32†	0.70 ± 0.05	0.39 ± 0.06	0.37 ± 0.05	–	−0.51 ± 0.08	3.4 ± 1.1	9, 26, 32	Y
	2003 SQ 317	–	–	–	0.43 ± 0.04	−0.45 ± 0.20	–	32	Y
	2003 TH 58	0.58 ± 0.12	0.29 ± 0.13	0.59 ± 0.15	-0.13 ± 0.15	1.29 ± 0.20	3.6 ± 11.4	32	N
	2003 UZ 117†	–	–	–	–	−0.62 ± 0.12	1.1 ± 0.7[d]	22, 27, 28, 32	Y
	2004 PT 107	0.82 ± 0.21	0.65 ± 0.10	0.68 ± 0.10	1.15 ± 0.16	0.54 ± 0.22	27.9 ± 8.4	32	N
	2005 CB 79	0.73 ± 0.04	0.37 ± 0.05	0.36 ± 0.05	0.71 ± 0.08	−0.50 ± 0.17	3.1 ± 2.5	32	Y
136472	Makemake	0.83 ± 0.02	0.5 ± 0.1[e]	0.3 ± 0.1[e]	–	–	7.7 ± 8.8	21, 29	N
	2005 GE 187	–	–	–	1.22 ± 0.19	0.65 ± 0.14	–	32	N
145453	2005 RR 43†	0.77 ± 0.06	0.41 ± 0.04	0.29 ± 0.08	0.48 ± 0.04	–	3.3 ± 6.0	8, 22, 26	Y
202421	2005 UQ 513	–	–	–	1.39 ± 0.08	0.30 ± 0.12	18.1 ± 2.0[d]	27, 28, 30, 32	N
136199	Eris	0.78 ± 0.01	0.45 ± 0.03	0.33 ± 0.02	0.52 ± 0.02	0.25 ± 0.11	5.9 ± 5.6	21, 22, 31, 32	–

Notes. [(a)] There are no published colours for candidates 1996 TR_{66}, 1997 RX_9, 1999 OK_4, 2000 JG_{81}, 2003 HA_{57}. For 2003 QX_{91} and 2004 SB_{60} we measured R-band photometry, but not colours. None of these candidates are included in the table.
[(b)] References: [1] Boehnhardt et al. (2001); [2] Gil-Hutton & Licandro (2001); [3] Doressoundiram et al. (2002); [4] McBride et al. (2003); [5] Tegler & Romanishin (2003); [6] Delsanti et al. (2004); [7] Doressoundiram et al. (2007); [8] Rabinowitz et al. (2008); [9] Jewitt & Luu (2001); [10] Tegler & Romanishin (1998); [11] Jewitt et al. (1998); [12] Barucci et al. (1999); [13] Davies et al. (2000); [14] Hainaut et al. (2000); [15] Hainaut & Delsanti (2002); [16] Trujillo & Brown (2002); [17] Sheppard & Jewitt (2002); [18] Delsanti et al. (2006); [19] Santos-Sanz et al. (2009); [20] Doressoundiram et al. (2005a); [21] Rabinowitz et al. (2007); [22] DeMeo et al. (2009); [23] Doressoundiram et al. (2005b); [24] Rabinowitz et al. (2006); [25] Lacerda et al. (2008); [26] Perna et al. (2010); [27] Pinilla-Alonso et al. (2007); [28] Alvarez-Candal et al. (2008); [29] Ortiz et al. (2007); [30] Fornasier et al. (2009); [31] Brown et al. (2005b); [32] This work. Where colours for a given object are published by multiple authors, we quote a weighted mean.
[(c)] $(R-J)$ calculated from near simultaneous R and J observations by [17] and [18] respectively. No correction is made to this (or any other colour in the table) for possible differences due to changes in rotational phase, although [17] show 1999 KR_{16} to have a light-curve amplitude of $\Delta m = 0.18$ mag.
[(d)] Although no photometry is published, measurements of the spectral slope for these objects (derived from optical spectra) can be found in Table 2 of Fornasier et al. (2009). We give a weighted mean for each object, and list the references to the original papers in the table.
[(e)] The colours for Makemake are calculated from the BVI photometry from [21] along with the R-band photometry from [26]. We use a phase function of $\beta = 0.05$ mag deg^{-1} to correct the R-band photometry to zero phase angle, as [21] show that β is approximately constant at this value between the V and I bands. The uncertainty is dominated by the uncertainty on the R-band photometry.
[(†)] These objects listed as confirmed family members by Ragozzine & Brown (2007).

candidates could just reflect the proportion within the TN region in general. Based on the TNO taxonomy proposed by Fulchignoni et al. (2008), the confirmed family members all belong to the BB class, while the rejected candidates come from all 4 of the groups (the majority of the newly rejected ones are from the red classes RR and IR, since they were mostly rejected due to their red slopes). The BB class makes up only 20% of the whole TNO population; the proportion of BB within the candidates (≡ confirmed family members / candidates ≈30%) is high but not so unusual given the small numbers of objects involved. If instead of taxonomic classes we consider the proportion of TNOs with water ice detections (from IR spectroscopy), then in the case of the general population we find ∼50% (from Table 1 of Barucci et al. 2008), making the proportion of bodies with water ice in the candidates lower than the general population, although this number contains significant biases as the spectroscopy only covers the brightest bodies. We can conclude that we do not see a significantly larger number of water ice bodies in the candidate list than in the general population, but this ignores grouping in orbital element space.

In Fig. 4 we show the candidates in terms of their orbital parameters semi-major axis, inclination and eccentricity. The confirmed family members cluster tightly around the centre of the distribution in both plots, where the original orbit of the pre-collision Haumea was (Haumea itself now has a higher eccentricity than the centre of the family due to interaction with

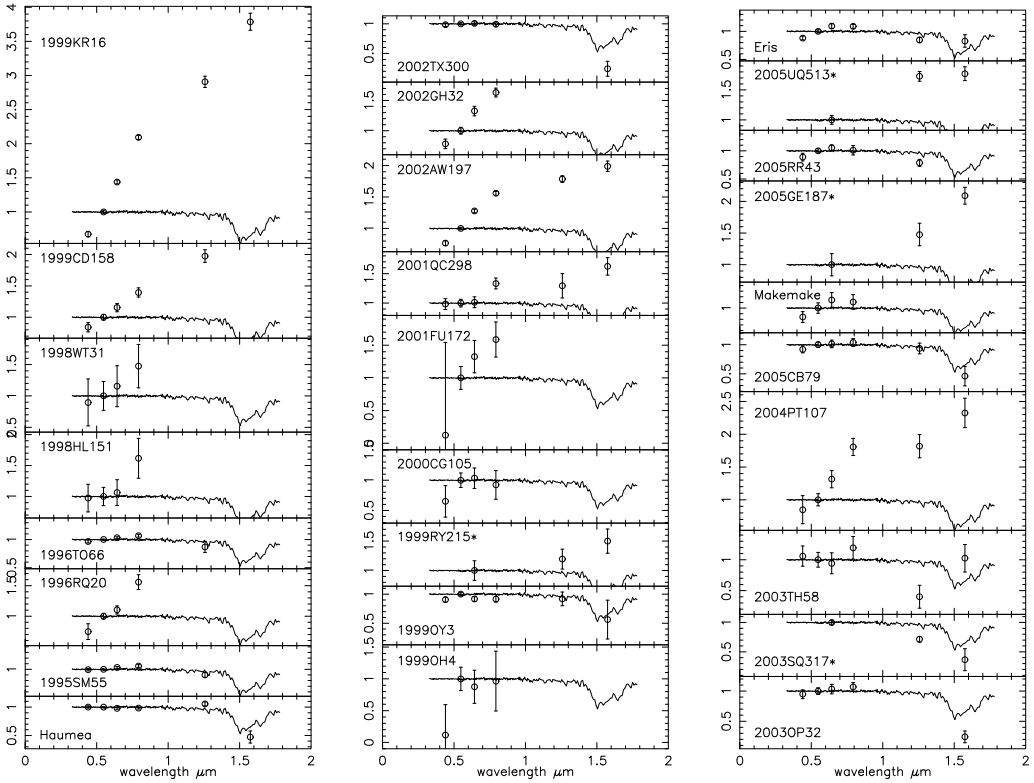

Fig. 2. Visible and NIR photometry for all candidate family members with observations in at least three bands. The data are normalized at 0.55 μm (V filter), except in the four cases where no V-band photometry exists. These data are normalised to the R-band, and are indicated by an asterisk next to the designation. The spectrum of Haumea is shown for comparison in each; this is taken from Pinilla-Alonso et al. (2009). The photometry of the large TNO Eris is also shown for comparison; it is not associated with the family, and has a spectrum dominated by methane ice (Dumas et al. 2007).

Neptune through orbital resonance, see Ragozzine & Brown 2007). This suggests that the family hypothesis is a valid one, but that the spread in orbital elements since the collision is less than the range investigated by Ragozzine & Brown (2007). Taking the required collision velocities from that paper ($\delta v_{\rm min}$; the minimum ejection velocity required including the effects of eccentricity and inclination diffusion in mean-motion resonances) we find that the largest velocity required by any confirmed family member is 123.3 m/s (for 1995 SM_{55}), while candidates are listed with $\delta v_{\rm min}$ up to 250 m/s. If we restrict the candidate list to those with $\delta v_{\rm min} \leq 150$ m/s, we find that the proportion of confirmed water ice detections rises to 53%, and goes up to 64% if we look only at those with lower $\delta v_{\rm min}$ than 1995 SM_{55}, so the grouping is statistically significant compared with the general population of bodies with water ice surfaces within the TN region. It should be noted though that there are rejected candidates spread evenly across the phase space, including 2005 UQ_{513} and 1999 CD_{158} near to the centre of the family distribution, which demonstrates the importance of physical studies of the candidates to confirm membership. The remaining unknown objects near to the centre of the distribution are 1999 OK_4 and 2003 QX_{91} (although the latter has high eccentricity and a high $\delta v_{\rm min}$ of 222 m/s) which should be high priority targets for further study to measure candidate family member surface properties, along with 1997 RX_9 which has a low $\delta v_{\rm min}$ of 86.8 m/s.

It is noticeable that the confirmed members remain the larger bodies, even though this photometric method is sensitive to water ice absorption on bodies too small for NIR spectroscopy. We tested the idea that retention of a water ice surface could be a property of only the larger TNOs by looking for a correlation between absolute magnitude and the $(J - H_S)$ index, but found that no such correlation exists. It is likely that there are smaller water ice covered family members, however they have yet to be discovered or confirmed. We also tested for any correlation of the colour with orbital elements and found none; we are dealing with a family clustered in dynamical element space, not a consequence of any correlation of, for example, the presence of water ice with semi-major axis.

4.2. Light-curves

This work aimed to test both the membership of the candidate family members and also the hypothesis that the family members apart from Haumea itself are composed of almost pure water ice, being made of the reassembled fragments of the outer layers

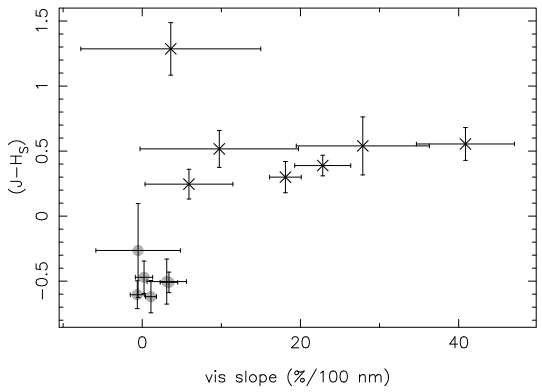

Fig. 3. ($J - H_S$) colour against visible slope (%/100 nm) for all candidates (and Eris) and where both measurements have been made. Filled circles are confirmed family members, crosses show rejected candidates. Haumea itself is the point in the very bottom left.

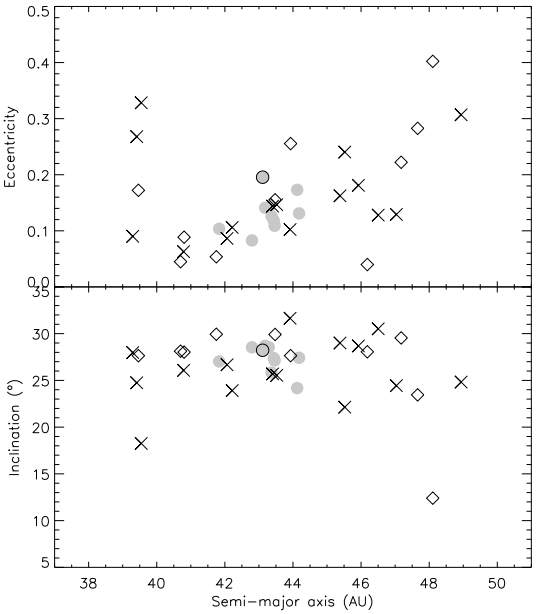

Fig. 4. Confirmed family members (grey filled circles), rejected candidates (crosses) and those with unknown surface properties (open diamonds) plotted in terms of the orbital parameters semi-major axis, inclination and eccentricity. Haumea itself is shown as a grey circle with a black outline.

of the differentiated proto-Haumea (Brown et al. 2007b). This can be probed by testing the density of the family members; Haumea is known to have a rock-like density of 2.5–3.3 g cm^{-3} (the value found from combining the size from Stansberry et al. 2008; and mass from Ragozzine & Brown 2009; agrees with the value from the light-curve model of Rabinowitz et al. 2006) but the other family members should have densities at or below the density of water ice, ∼1 g cm^{-3}. To test this we sought to apply the technique of measuring rotation rate and elongations using light-curves, which then constrain the density of a strengthless body to be

$$\rho \geq \frac{10.9}{P_{\rm rot}^2}\frac{a}{b} \text{ g cm}^{-3}, \quad (2)$$

where a/b is the axial ratio for an ellipsoid and the rotation period $P_{\rm rot}$ is in hours (Pravec & Harris 2000). We can reasonably expect the recombined fragments from a collision to be a loosely packed "rubble pile" and therefore strengthless. This method only gives a lower limit to the density as the object does not need to be spinning at its break up velocity, but must be below it, and also that the light-curve amplitude Δm only gives a lower limit on the elongation, $a/b \geq 10^{0.4\Delta m}$. Despite this, when studying a population a cut off in minimum densities becomes apparent, which can be used as a reasonable measurement of the bulk density of the bodies in the population. This has been clearly demonstrated for asteroids (Pravec et al. 2002), where there are many ($N > 1000$) light-curves available, and also used to derive a low bulk density for cometary nuclei (Snodgrass et al. 2006), in agreement with the results found by the *Deep Impact* mission (Richardson et al. 2007), despite the relatively low number of light-curves available for nuclei.

We measured partial light-curves for 13 of the candidates using EFOSC2, however poor weather during these runs prevented us from building up the number of light-curves required to study the density of these bodies by this statistical technique. This was further hampered by the large proportion of the candidates which were eventually rejected as non-family members. For 1998 WT$_{31}$ and 1999 OY$_3$ we have less than 10 points spread over three and two nights respectively and there is no significant variation. 1999 RY$_{215}$ and 2003 TH$_{58}$ also show no significant variation despite larger data sets. For 1999 CD$_{158}$, 2000 CG$_{105}$, 2002 GH$_{32}$ and 2005 UQ$_{513}$ the light-curves show significant variation, with ranges of $\Delta m = 0.6$, 0.45, 0.75 and 0.3 mag, but no period could be determined. For 2001 QC$_{298}$ there is possibly a maximum each night in the data, with $\Delta m = 0.4$, but there can be other periods beyond the ∼12 h best fit. 2003 SQ$_{317}$ gives a good fit with single peak light-curve of 3.7 h, while a double peaked light-curve at 7.5 h also looks reasonable. 2004 PT$_{107}$ shows a possible slight variation (0.05 mag), but not a very convincing one, with a suggested long period (∼20 h). We obtained data on 2004 SB$_{60}$ on two nights which show a variation of $\Delta m = 0.2$, but no clear periodicity. There is a possible solution at around 17.5 h, but it is not convincing. 2005 GE$_{187}$ has a reasonably convincing single peak light-curve with a 6.1 h period and $\Delta m = 0.5$.

The only light-curve in this set of relevance to the density of the family members is that of 2003 SQ$_{317}$, shown in Fig. 5. The period of 3.7 h and the range of $\Delta m = 1.0$ mag implies a high density, $\rho \geq 2.0$ g cm^{-3}, however this is for a single peaked light-curve as would be caused by albedo variations and not shape. The light-curves of Solar System minor bodies are more likely to be caused by shape than albedo patterns (Jewitt 2008; Sheppard et al. 2008). Assuming that this single peak light-curve shows half of the period of the true shape controlled light-curve, the implied density is $\rho \geq 0.5$ g cm^{-3}, which is a weak constraint. Given the sparse light-curve coverage there are also other possible periods. We cannot rule out a low density and therefore an entirely ice composition for this body.

Of the other family members 5 of the large bodies with confirmed water ice surfaces also have light-curves (not including Haumea itself). 1995 SM$_{55}$ has a rotation period of 8.08 h and $\Delta m = 0.19$ (Sheppard & Jewitt 2003) (implying

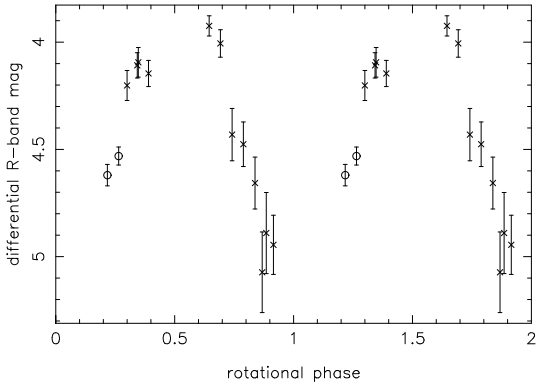

Fig. 5. Light-curve for 2003 SQ_{317}, with data taken on two nights (circles from the night of August 30th 2008 and crosses from August 31st) folded onto a 3.74 h period.

$\rho \geq 0.20$ g cm^{-3}). 1996 TO_{66} has $P_{\rm rot} = 7.9$ h, $\Delta m = 0.26$ (Sheppard & Jewitt 2003) ($\rho \geq 0.22$), but both the period and amplitude of the light-curve are seen to change (Hainaut et al. 2000). 2002 TX_{300} has a period between 8 and 12 h and a low amplitude of $\Delta m = 0.08$ (Sheppard & Jewitt 2003) ($\rho \geq 0.18$). Perna et al. (2009) find that 2005 RR_{43} has $P_{\rm rot} = 5.08$ h, $\Delta m = 0.12$ ($\rho \geq 0.47$). Observations from the same group find no obvious periodicity for 2003 UZ_{117}. None of these light-curves require high densities, although for these very large objects it is also likely that the rubble pile assumption will be invalidated due to compaction by self gravity, in which case finding the density from the light-curve involves assuming fluid like behaviour (see Lacerda & Jewitt 2007).

5. Summary

We have presented optical and/or near infrared colours for 22 of the 35 candidate members of Haumea's collisional family that were listed by Ragozzine & Brown (2007). We make use of a unique capability of the new Hawk-I instrument at the VLT to evaluate the depth of the 1.6 μm water ice absorption band using NIR photometry on objects too faint for spectroscopy. We find:

1. Of the 15 candidates observed with Hawk-I, 7 were found to be family members. Most (6) of these were already known family members, including Haumea itself, whose confirmation proves the validity of the photometric technique used. In addition to the confirmed family members listed by Ragozzine & Brown (2007) we confirm the identification by Schaller & Brown (2008) of water ice on 2005 CB_{79}, and identify 2003 SQ_{317} and as a probable new family member.
2. We reject the other 8 candidates observed with Hawk-I as interlopers which lack water ice absorption. In general the rejected bodies are relatively far from the centre of the family in orbital parameter space.
3. We present optical colours for 10 candidates and also collect all available colour information from the literature for the full set. Of the 20 candidates not yet observed with Hawk-I there are optical colours for 13. We find that all objects where the NIR colour indicates water ice have neutral or blue slopes, and consequently we can reject the possibility of water ice on the surface of the very red objects in this sample with a reasonable degree of confidence. In this way we rule out family membership for a further 5 of the candidates, in addition to 2 candidates which are already known to have no water ice on their surface from NIR spectroscopy.
4. Of the 35 family member candidates this gives totals of 10 confirmed members (29%), 15 non-members (43%) and 10 that still have to have their surfaces characterised. It appears that the family members all fall within the centre of the dynamical region searched by Ragozzine & Brown (2007), so we expect that most of the remaining bodies will also be rejected.
5. We obtained partial *R*-band light-curves for 13 of the candidates, only two of which were subsequently confirmed as a family members. Of these 1999 OY_3 showed no significant variation in the short sequence we were able to obtain on it, while 2003 SQ_{317} shows variations consistent with a 3.74 h single peak light-curve, but other periods are possible in the sparse data. Neither this nor the existing light-curves in the literature for other family members provide strong constraints on the density of these bodies, so we cannot yet determine whether or not they are "pure" water ice bodies formed from the outer layers of the pre-collision Haumea.

Acknowledgements. We thank the dedicated staff of ESO's La Silla and Paranal observatories for their assistance in obtaining this data, and in particular Giovanni Carraro for providing us with the Hawk-I observations of the Solar analogue. We are grateful to Noemi Pinilla-Alonso for providing the spectrum of Haumea and Davide Perna for providing us with his results in advance of their publication. We thank Pedro Lacerda and Franck Marchis for helpful suggestions. We also thank the referee, David Rabinowitz, for constructive comments that improved the paper.

References

Alvarez-Candal, A., Fornasier, S., Barucci, M. A., de Bergh, C., & Merlin, F. 2008, A&A, 487, 741
Barkume, K. M., Brown, M. E., & Schaller, E. L. 2006, ApJ, 640, L87
Barucci, M. A., Doressoundiram, A., Tholen, D., Fulchignoni, M., & Lazzarin, M. 1999, Icarus, 142, 476
Barucci, M. A., Brown, M. E., Emery, J. P., & Merlin, F. 2008, in The Solar System Beyond Neptune, ed. M. A. Barucci, H. Boehnhardt, D. P. Cruikshank, & A. Morbidelli (University of Arizona Press), 143
Boehnhardt, H., Tozzi, G. P., Birkle, K., et al. 2001, A&A, 378, 653
Brown, M. E., Bouchez, A. H., Rabinowitz, D. L., et al. 2005a, ApJ, 632, L45
Brown, M. E., Trujillo, C. A., & Rabinowitz, D. L. 2005b, ApJ, 635, L97
Brown, M. E., van Dam, M. A., Bouchez, A. H., et al. 2006, ApJ, 639, 4346
Brown, M. E., Barkume, K. M., Blake, G. A., et al. 2007a, AJ, 133, 284
Brown, M. E., Barkume, K. M., Ragozzine, D., & Schaller, E. L. 2007b, Nature, 446, 294
Brown, T. M. 2003, ApJ, 593, L125
Buzzoni, B., Delabre, B., Dekker, H., et al. 1984, The Messenger, 38, 9
Casali, M., Pirard, J.-F., Kissler-Patig, M., et al. 2006, SPIE, 6269
Cellino, A., Bus, S. J., Doressoundiram, A., & Lazzaro, D. 2002, Asteroids III, 633
Davies, J. K., Green, S., McBride, N., et al. 2000, Icarus, 146, 253
Delsanti, A., Hainaut, O., Jourdeuil, E., et al. 2004, A&A, 417, 1145
Delsanti, A., Peixinho, N., Boehnhardt, H., et al. 2006, AJ, 131, 1851
DeMeo, F. E., Fornasier, S., Barucci, M. A., et al. 2009, A&A, 493, 283
Doressoundiram, A., Peixinho, N., de Bergh, C., et al. 2002, AJ, 124, 2279
Doressoundiram, A., Barucci, M. A., Tozzi, G. P., et al. 2005a, Planetary and Space Science, 53, 1501
Doressoundiram, A., Peixinho, N., Doucet, C., et al. 2005b, Icarus, 174, 90
Doressoundiram, A., Peixinho, N., Moullet, A., et al. 2007, AJ, 134, 2186
Dumas, C., Merlin, F., Barucci, M. A., et al. 2007, A&A, 471, 331
Fornasier, S., Barucci, M. A., de Bergh, C., et al. 2009, A&A, 508, 457
Fraser, W. C., & Brown, M. E. 2009, ApJ, 695
Fulchignoni, M., Belskaya, I., Barucci, M. A., de Sanctis, M. C., & Doressoundiram, A. 2008, in The Solar System Beyond Neptune, ed. M. A. Barucci, H. Boehnhardt, D. P. Cruikshank, & A. Morbidelli (University of Arizona Press), 181

Gil-Hutton, R., & Licandro, J. 2001, Icarus, 152, 246
Hainaut, O. R., Delahodde, C. E., Boehnhardt, H., et al. 2000, A&A, 356, 1076
Hainaut, O. R., & Delsanti, A. C. 2002, A&A, 389, 641
Ivanov, V. D., Rieke, M. J., Engelbracht, C. W., et al. 2004, ApJS, 151, 387
Jewitt, D. C. 2008, Small Bodies in Planetary Systems
Jewitt, D. C., & Luu, J. X. 2001, AJ, 122, 2099
Jewitt, D., Luu, J., & Trujillo, C. 1998, AJ, 115, 2125
Lacerda, P., & Jewitt, D. C. 2007, AJ, 133, 1393
Lacerda, P., Jewitt, D., & Peixinho, N. 2008, AJ, 135, 1749
Landolt, A. U. 1992, AJ, 104, 340
Levison, H. F., Morbidelli, A., Vokrouhlický, D., & Bottke, W. F. 2008, AJ, 136, 1079
McBride, N., Green, S. F., Davies, J. K., et al. 2003, Icarus, 161, 501
Merlin, F., Guilbert, A., Dumas, C., et al. 2007, A&A, 466, 1185
Ortiz, J. L., Santos Sanz, P., Gutiérrez, P. J., Duffard, R., & Aceituno, F. J. 2007, A&A, 468, L13
Pasquini, L., Biazzo, K., Bonifacio, P., Randich, S., & Bedin, L. R. 2008, A&A, 489, 677
Perna, D., Dotto, E., Barucci, M. A., et al. 2009, A&A, 508, 451
Perna, D., Barucci, M. A., Fornasier, S., et al. 2010, A&A, 510, A53
Pickles, A. J. 1998, PASP, 110, 863
Pinilla-Alonso, N., Licandro, J., Gil-Hutton, R., & Brunetto, R. 2007, A&A, 468, L25
Pinilla-Alonso, N., Licandro, J., & Lorenzi, V. 2008, A&A, 489, 455
Pinilla-Alonso, N., Brunetto, R., Licandro, J., et al. 2009, A&A, 496, 547
Pirard, J.-F., Kissler-Patig, M., Moorwood, A. F. M., et al. 2004, SPIE, 5492, 1763
Pravec, P., & Harris, A. W. 2000, Icarus, 148, 12
Pravec, P., Harris, A. W., & Michałowski, T. 2002, in Asteroids III, ed. W. F. Bottke, A. Cellino, P. Paolicchi, & R. P. Binzel (University of Arizona Press), 113
Rabinowitz, D. L., Barkume, K. M., Brown, M. E., et al. 2006, ApJ, 639, 1238
Rabinowitz, D. L., Schaefer, B. E., & Tourtellotte, S. W. 2007, AJ, 133, 26
Rabinowitz, D. L., Schaefer, B. E., Schaefer, M., & Tourtellotte, S. W. 2008, AJ, 136, 1502
Ragozzine, D., & Brown, M. E. 2007, AJ, 134, 2160
Ragozzine, D., & Brown, M. E. 2009, AJ, 137, 4766
Richardson, J. E., Melosh, H. J., Lisse, C. M., & Carcich, B. 2007, Icarus, 190, 357
Santos-Sanz, P., Ortiz, J. L., Aceituno, F. J., Brown, M. E., & Rabinowitz, D. 2005, IAU Circ., 8577, 2
Santos-Sanz, P., Ortiz, J. L., Barrera, L., & Boehnhardt, H. 2009, A&A, 494, 693
Schaller, E. L., & Brown, M. E. 2008, ApJ, 684, L107
Sheppard, S. S., & Jewitt, D. C. 2002, AJ, 124, 1757
Sheppard, S. S., & Jewitt, D. C. 2003, Earth Moon and Planets, 92, 207
Sheppard, S. S., Lacerda, P., & Ortiz, J. L. 2008, in The Solar System Beyond Neptune, ed. M. A. Barucci, H. Boehnhardt, D. P. Cruikshank, & A. Morbidelli (University of Arizona Press), 129
Skrutskie, M. F., Cutri, R. M., Stiening, R., et al. 2006, AJ, 131, 1163
Snodgrass, C., Fitzsimmons, A., & Lowry, S. C. 2005, A&A, 444, 287
Snodgrass, C., Lowry, S. C., & Fitzsimmons, A. 2006, MNRAS, 373, 1590
Snodgrass, C., Saviane, I., Monaco, L., & Sinclaire, P. 2008, The Messenger, 132, 18
Stansberry, J., Grundy, W., Brown, M., et al. 2008, in The Solar System Beyond Neptune, ed. M. A. Barucci, H. Boehnhardt, D. P. Cruikshank, & A. Morbidelli (University of Arizona Press), 161
Tegler, S. C., & Romanishin, W. 1998, Nature, 392, 49
Tegler, S. C., & Romanishin, W. 2003, Icarus, 161, 181
Tegler, S. C., Grundy, W. M., Romanishin, W., et al. 2007, AJ, 133, 526
Trujillo, C. A., & Brown, M. E. 2002, ApJ, 566, L125
Trujillo, C. A., Brown, M. E., Barkume, K. M., Schaller, E. L., & Rabinowitz, D. L. 2007, ApJ, 655, 1172

Astronomy & Astrophysics manuscript no. main
July 27, 2012

Characterisation of candidate members of (136108) Haumea's family ⋆

II. Follow-up observations

Benoît Carry[1,2,3,4], Colin Snodgrass[5,6], Pedro Lacerda[7], Olivier Hainaut[8], and Christophe Dumas[6]

[1] European Space Astronomy Centre, ESA, P.O. Box 78, 28691 Villanueva de la Cañada, Madrid, Spain
[2] IMCCE, Observatoire de Paris, UPMC, CNRS, 77 Av. Denfert Rochereau 75014 Paris, France
[3] LESIA, Observatoire de Paris-Meudon, 5 place Jules Janssen, 92195 Meudon Cedex, France
[4] Université Paris 7 Denis-Diderot, 5 rue Thomas Mann, 75205 Paris CEDEX, France
[5] Max Planck Institute for Solar System Research, Max-Planck-Strasse 2, 37191 Katlenburg-Lindau, Germany
[6] European Southern Observatory, Alonso de Córdova 3107, Vitacura, Casilla 19001, Santiago de Chile, Chile
[7] Queen's University, Belfast, County Antrim BT7 1NN, Northern Ireland
[8] European Southern Observatory, Karl-Schwarzschild-Strasse 2, D-85748 Garching bei München, Germany

Received / Accepted

ABSTRACT

Context. From a dynamical analysis of the orbital elements of transneptunian objects (TNOs), Ragozzine & Brown reported a list of candidate members of the first collisional family found among this population, associated with (136 108) Haumea (a.k.a. 2003 EL_{61}).
Aims. We aim to distinguish the true members of the Haumea collisional family from interlopers. We search for water ice on their surfaces, which is a common characteristic of the known family members. The properties of the confirmed family are used to constrain the formation mechanism of Haumea, its satellites, and its family.
Methods. Optical and near-infrared photometry is used to identify water ice. We use in particular the CH_4 filter of the Hawk-I instrument at the European Southern Observatory Very Large Telescope as a short H-band (H_S), the $(J - H_S)$ colour being a sensitive measure of the water ice absorption band at 1.6 μm.
Results. Continuing our previous study headed by Snodgrass, we report colours for 8 candidate family members, including near-infrared colours for 5. We confirm one object as a genuine member of the collisional family (2003 UZ_{117}), and reject 5 others. The lack of infrared data for the two remaining objects prevent any conclusion from being drawn. The total number of rejected members is therefore 17. The 11 confirmed members represent only a third of the 36 candidates.
Conclusions. The origin of Haumea's family is likely to be related to an impact event. However, a scenario explaining all the peculiarities of Haumea itself and its family remains elusive.

Key words. Kuiper Belt; Methods: observational; Techniques: photometric; Infrared: solar system

1. Introduction

The dwarf planet (136 108) Haumea (Santos-Sanz et al. 2005) is among the largest objects found in the Kuiper Belt (Rabinowitz et al. 2006, Stansberry et al. 2008), together with Pluto, Eris, and Makemake. It is a highly unusual body with the following characteristics:

1. It has a very elongated cigar-like shape (Rabinowitz et al. 2006, Lellouch et al. 2010).
2. It is a fast rotator ($P_{rot} \sim 3.9$ h, Rabinowitz et al. 2006).
3. It has two non-coplanar satellites (Brown et al. 2006, Ragozzine & Brown 2009, Dumas et al. 2011).
4. It is the largest member of a dynamical family (Brown et al. 2007, Ragozzine & Brown 2007), whose velocity dispersion is surprisingly small (Schlichting & Sari 2009, Leinhardt et al. 2010).
5. Its surface composition is dominated by water ice (Tegler et al. 2007, Trujillo et al. 2007, Merlin et al. 2007, Pinilla-Alonso et al. 2009, Dumas et al. 2011), yet it has a high density of 2.5-3.3 g cm^{-3} (Rabinowitz et al. 2006).
6. It surface has a hemispherical colour heterogeneity, with a dark red "spot" on one side (Lacerda et al. 2008, Lacerda 2009).

Brown et al. (2007) proposed that Haumea suffered a giant collision that ejected a large fraction of its ice mantle, which formed both the two satellites and the dynamical family and left Haumea with rapid rotation. A number of theoretical studies have since looked at the family formation in more detail (see Sect. 5).

A characterisation of the candidate members (35 bodies listed by Ragozzine & Brown 2007, including Haumea itself) however showed that only 10 bodies out of 24 studied share their surface properties with Haumea (Snodgrass et al. 2010), and can thus be considered genuine family members. Moreover, these confirmed family members cluster in the orbital elements space (see Fig. 4 in Snodgrass et al. 2010), and the highest velocity found was ~123 m s^{-1} (for 1995 SM_{55}).

Send offprint requests to: B. Carry, e-mail: benoit.carry@esa.int
⋆ Based on observations collected at the European Southern Observatory, La Silla & Paranal, Chile - 81.C-0544 & 82.C-0306 & 84.C-0594

We report on follow-up observations to Snodgrass et al. (2010) of 8 additional candidate members of Haumea's family. We describe our observations in Sect. 2, the colour measurements in Sect. 3, the lightcurve analysis and density estimates in Sect. 4, and we discuss in Sect. 5 the family memberships of the candidates and the implication of these for the characteristics of the family.

2. Observations and data reduction

We performed our observations at the European Southern Observatory (ESO) La Silla and Paranal Very Large Telescope (VLT) sites (programme ID: 84.C-0594). Observations in the visible wavelengths (*BVRi* filters) were performed using the EFOSC2 instrument (Buzzoni et al. 1984) mounted on the NTT (since April 2008; Snodgrass et al. 2008); while near-infrared observations (J, CH_4 filters) were performed using the wide-field camera Hawk-I (Pirard et al. 2004, Casali et al. 2006, Kissler-Patig et al. 2008) installed on the UT4/Yepun telescope. We use the medium-width CH_4 filter as a narrow H band (1.52–1.63 μm, hereafter H_S) to measure the J-H_S colour as a sensitive test for water ice (see Snodgrass et al. 2010, for details). We list the observational circumstances in Table 1.

We reduced the data in the usual manner (*i.e.*, bias subtraction, flat fielding, sky subtraction, as appropriate). We refer readers to Snodgrass et al. (2010) for a complete description of the instruments and the methods we used to detect the targets, and both measure and calibrate their photometry.

For each frame, we used the SkyBoT cone-search method (Berthier et al. 2006) to retrieve all known solar system objects located in the field of view. We found 3 main-belt asteroids, and the potentialy hazardeous asteroid (29 075) 1950 DA (*e.g.* Giorgini et al. 2002, Ward & Asphaug 2003), in our frames. We report the circumstances of their serendipitous observations in Table 1 and their apparent magnitude in Table 2, together with the family candidates and our back-up targets.

Table 1. Observational circumstances.

(#)	Object (Designation)	Δ^a (AU)	r^b (AU)	α^c (°)	Runs[d]
	1999 CD 158	47.5	46.5	0.5	B
	1999 OK 4	46.5	45.5	0.3	⋆
	2000 CG 105	45.8	46.8	0.1	A,B
	2001 FU 172	32.2	32.0	1.7	A
	2002 GH 32	43.2	42.9	1.2	B
	2003 HA 57	32.7	32.3	1.6	A
	2003 UZ 117	39.4	39.4	1.4	A
	2004 FU 142	33.5	33.2	0.0	A
	2005 CB 79	39.9	39.0	0.4	A
	2005 GE 187	30.3	30.2	1.9	A
24	Themis	3.4	4.0	12.0	B
10 199	Chariklo	13.8	13.6	4.1	B
29 075	1950 DA	0.8	1.0	62.7	A
158 589	Snodgrass	3.5	3.1	15.5	A
104 227	2000 EH 125	3.0	2.5	18.5	A
202 095	2004 TQ 20	2.2	1.9	2.4	A
	2010 CU 19	1.3	1.6	0.6	A

Notes. [a] Heliocentric distance. [b] Geocentric distance. [c] Phase angle. [d] Runs: A = 2010 February 15–17, EFOSC2; B= 2010 February 22, Hawk-I. ⋆ Observed on 2009 July 24 with EFOSC2.

3. Colours

We report the photometry of all the objects in Table 2, where we give the apparent magnitude in each band, averaged over all the observations. We used a common sequence of filters (RBViR) to observe all the objects. This limits the influence of the shape-related lightcurve on the colour determination. In Table 3, we report the average colours of all the family candidates observed here, and refer to Snodgrass et al. (2010) for a complete review of the published photometry.

From these average colours, we calculate reflectances by comparing them to the solar colours. We also report the visible slope for each object (%/100 nm) in Table 3, calculated from the reflectances via a linear regression over the full *BVRi* range. The reflectance "spectra" of the candidates from this photometry are shown in Fig. 1. The reflectance spectrum of (136 108) Haumea from Pinilla-Alonso et al. (2009) is shown for comparison to the photometry. For all the objects but 1999 CD_{158} (Delsanti et al. 2004), the link between the visible and near-infrared wavelengths was made by extrapolating the visible spectral slope to the J-band, owing to a lack of simultaneous observations. Among these objects, 2002 GH_{32} has a distinctive spectral behaviour. It displays a slight dip at 1.5 μm despite a red slope, as its ($J - H_S$) colour (0.18 ± 0.19) is slightly bluer than that of the Sun (0.28; Snodgrass et al. 2010). Given the uncertainty in this point, and the red optical slope, we do not believe that this is evidence of strong water ice absorption.

From the visible and near-infrared colours that we report here, we confirm that 2003 UZ_{117} is a genuine family member, in agreement with Ragozzine & Brown (2007) and Snodgrass et al. (2010), and reject 1999 CD_{158}, 2000 CG_{105}, 2001 FU_{172}, 2002 GH_{32}, and 2005 GE_{187}. The TNO 1999 OK_4 remains a possible candidate, as it has a neutral slope in the visible, but the poor signal-to-noise ratio of the data for this faint target does not allow us to draw a stronger conclusion. In any case, a neutral slope by itself does not confirm family membership without near-infrared observations. This object is dynamically very near to the centre of the family and remains worthy of further investigation. 2003 HA_{57} has a red slope, but not a very strong one. It is further from the centre of the distribution, with $\delta v > 200\,\mathrm{m\,s^{-1}}$, so it is unlikely to be a family member (see below). We cannot firmly conclude anything about the membership of 1999 OK_4 and 2003 HA_{57}. The current number of confirmed family members is 11 over 36 (including Haumea and an additional dynamical candidate (2009 YE_7) that was found and directly confirmed by Trujillo et al. (2011)), or 31%. The number of rejected candidates is 17 over 36, hence 47% of the population, and there are only 8 objects whose status remains unknown.

4. Rotation and density

To constrain the density of family members, and therefore test the hypothesis that they are formed of almost pure water ice, we investigated their rotational lightcurves. In the February 2010 observing run, we performed a time series of R-band photometry on 2005 CB_{79}, which was demonstrated to be a family member by Schaller & Brown (2008) and Snodgrass et al. (2010). We measured 69 points over the course of three nights, with a typical uncertainty in each measurement of 0.03 magnitudes. We observed a variation of around 0.15 magnitudes, but found no convincing periodicity. Thirouin et al. (2010) found a period of 6.76 hours and a similar magnitude range.

A total of 8 family members have published lightcurve measurements (Table 4). These can be used to estimate the density by

Table 2. Mean apparent magnitudes for each object.

Object	B	V	R	i	J	CH_4
1999 CD 158	–	–	–	–	20.79 ± 0.08	20.44 ± 0.10
1999 OK 4	24.90 ± 0.16	24.54 ± 0.17	23.95 ± 0.14	23.64 ± 0.20	–	–
2000 CG 105	24.32 ± 0.14	23.62 ± 0.10	23.15 ± 0.05	22.61 ± 0.07	21.89 ± 0.10	21.64 ± 0.14
2001 FU 172	23.40 ± 0.05	21.73 ± 0.04	20.82 ± 0.03	19.99 ± 0.03	–	–
2002 GH 32	–	–	–	–	21.49 ± 0.12	21.31 ± 0.15
2003 HA 57	24.37 ± 0.09	23.48 ± 0.09	22.96 ± 0.05	22.69 ± 0.12	–	–
2003 UZ 117†	21.86 ± 0.09	21.34 ± 0.08	21.09 ± 0.08	20.67 ± 0.07	–	–
2003 UZ 117⋆	22.04 ± 0.10	21.32 ± 0.06	21.01 ± 0.06	20.62 ± 0.06	–	–
2005 CB 79	–	–	20.29 ± 0.01	–	–	–
2005 GE 187	23.73 ± 0.14	22.91 ± 0.12	22.23 ± 0.09	21.49 ± 0.06	–	–
1950 DA	19.59 ± 0.07	19.15 ± 0.06	18.82 ± 0.02	18.56 ± 0.04	–	–
2000 EH 125	21.58 ± 0.03	20.78 ± 0.02	20.37 ± 0.02	20.05 ± 0.03	–	–
2004 TQ 20	21.93 ± 0.06	21.23 ± 0.07	21.19 ± 0.08	20.73 ± 0.07	–	–
2010 CU 19	–	19.26 ± 0.04	–	–	–	–
Chariklo	–	–	–	–	16.98 ± 0.02	16.86 ± 0.02
Themis	–	–	–	–	12.38 ± 0.02	12.25 ± 0.02
Snodgrass	22.40 ± 0.14	21.61 ± 0.10	21.20 ± 0.05	20.69 ± 0.08	–	–

Notes. † First night, ⋆ Second night.

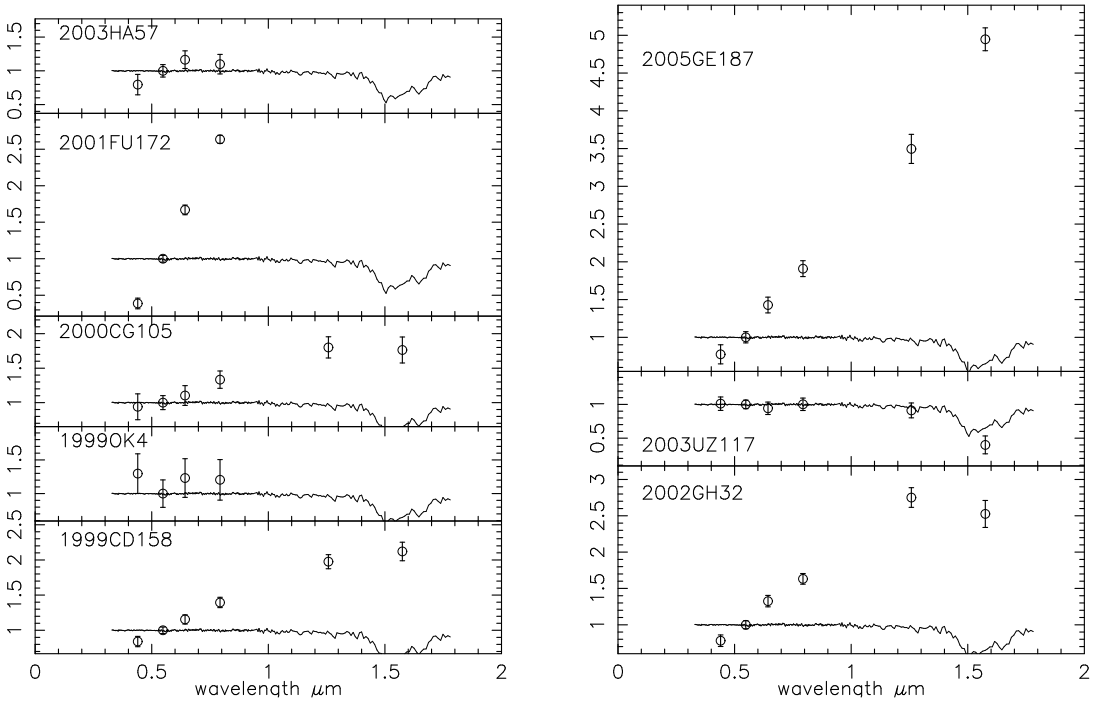

Fig. 1. Visible and near-infrared photometry for the candidate family members (see Table 3). The data are normalized at 0.55 μm (V filter). The spectrum of Haumea (taken from Pinilla-Alonso et al. 2009) is shown for comparison in each.

two methods. By either balancing gravitational and centrifugal forces for an assumed strengthless (rubble pile) body, as applied to asteroids (Pravec et al. 2002) and comets (Snodgrass et al. 2006), or by assuming a fluid equilibrium shape (*i.e.*, a Jacobi ellipsoid), which may be more appropriate for large icy bodies such as TNOs (Lacerda & Jewitt 2007). The densities of TNOs derived from lightcurves was reviewed by Duffard et al. (2009) and Thirouin et al. (2010). Of particular interest is the high value of 2.38 g cm^{-3} determined for 2003 OP$_{32}$, which is a large confirmed family member with a strong water-ice spectrum (Brown et al. 2007). The quoted value is considerably higher than that of water ice, and close to the value determined for

Table 3. Average colours in $BVRiJH_S$, and assessment of likely membership based on these colours.

Object Designation	$(B-V)$ (mag.)	$(V-R)$ (mag.)	$(R-i)$ (mag.)	$(R-J)$ (mag.)	$(J-H_S)^\star$ (mag.)	Vis. slope (%/100nm)	Ref.	Family?
1999 CD 158	0.83 ± 0.06	0.51 ± 0.05	0.54 ± 0.06	1.38 ± 0.09	0.35 ± 0.12	15.8 ± 0.6	1,5,8	N
1999 OK 4	0.36 ± 0.23	0.58 ± 0.22	0.32 ± 0.24	–	–	1.4 ± 18.1	8	?
2000 CG 105	0.71 ± 0.17	0.56 ± 0.11	0.77 ± 0.29	–	0.25 ± 0.17	11.3 ± 4.3	5,8	N
2000 JG 81	–	0.50 ± 0.11	0.33 ± 0.12	–	–	5.6 ± 21.6	6	?
2001 FU 172	1.67 ± 0.06	0.91 ± 0.05	0.83 ± 0.03	–	–	64.2 ± 4.3	5,8	N
2002 GH 32	0.91 ± 0.06	0.66 ± 0.06	0.56 ± 0.05	–	0.18 ± 0.19	24.8 ± 4.7	5,8	N
2003 HA 57	0.89 ± 0.13	0.52 ± 0.10	0.27 ± 0.12	–	–	8.7 ± 11.6	8	?
2003 UZ 117	0.52 ± 0.12	0.25 ± 0.11	0.42 ± 0.11	–	-0.74 ± 0.16	-0.5 ± 3.7	2-5,7,8	Y
2005 GE 187	0.81 ± 0.18	0.69 ± 0.14	0.74 ± 0.11	1.22 ± 0.19	0.65 ± 0.14	32.8 ± 12.3	5,8	N
Haumea	0.64 ± 0.01	0.33 ± 0.01	0.34 ± 0.01	0.88 ± 0.01	-0.60 ± 0.11	-0.6 ± 0.9	5	Y

References. [1] Delsanti et al. (2004); [2] DeMeo et al. (2009); [3] Pinilla-Alonso et al. (2007); [4] Alvarez-Candal et al. (2008); [5] Snodgrass et al. (2010, and references therein); [6] Benecchi et al. (2011); [7] Trujillo et al. (2011); [8] This work. Where colours for a given object are published by multiple authors, we quote a weighted mean.

Notes. * In the present study, H_s correspond to Hawk-I CH_4 filter

Table 4. Rotational periods (SP: single peak, DP: double peak) of family candidates.

#	Object Designation	H	$d^\dagger$ (km)	Δm	Period SP (h)	Period DP (h)	Ref.	$\rho_m^\star$ (g cm^{-3})
24835	1995 SM 55	4.8	174	0.19	4.04 ± 0.03	8.08 ± 0.03	2	0.60
19308	1996 TO 66	4.5	200	0.32	3.96 ± 0.04	7.92 ± 0.04	2	0.63
						11.9	5	
						6.25 ± 0.03	1	
86047	1999 OY 3	6.74	71					
55636	2002 TX 300	3.2	364	0.08	8.16		8	0.16
					8.12 ± 0.08	16.24 ± 0.08	3	
					12.10 ± 0.08	24.20 ± 0.08	3	
					7.89 ± 0.03	15.78 ± 0.03	4	
136108	Haumea	0.01	1313	0.28		3.9154 ± 0.0001	6,8,10	2.56
120178	2003 OP 32	3.95	258	0.13	4.05		8	0.59
	2003 SQ 317	6.3	87	1.00	3.74 ± 0.10	7.48 ± 0.10	9	0.5
	2003 UZ 117	5.3	138	0.20	~6		7	0.27
	2005 CB 79	4.7	182	0.04	6.76		8	0.21
145453	2005 RR 43	4.0	252	0.12	7.87		8	0.38
					5.08 ± 0.03		7	
	2009 YE 7	4.4	209					

References. [1] Hainaut et al. (2000); [2] Sheppard & Jewitt (2002); [3] Sheppard & Jewitt (2003); [4] Ortiz et al. (2004); [5] Belskaya et al. (2006); [6] Lacerda et al. (2008); [7] Perna et al. (2010); [8] Thirouin et al. (2010); [9] Snodgrass et al. (2010); [10] Lellouch et al. (2010)

Notes. † Diameter computed using an assumed geometric albedo of 0.7, with the exception of Haumea, whose diameter is taken from Lellouch et al. (2010). 2002 TX_{300} has a diameter measurement of 286 km and albedo of 88% (Elliot et al. 2010), but these are inconsistent with the given H magnitude.
* Density computed assuming a Jacobi ellipsoid shape with a DP rotation period (see text for details).

Haumea itself (2.61 g cm^{-3}, Thirouin et al. 2010), and is therefore inconsistent with this body being a pure water-ice fragment from the original Haumea's outer mantle. However, this (minimum) density is derived assuming that the best-fit single peaked period of 4.05 hours is the correct spin rate, which can only be true if the variation is due to an albedo patch on a spheroidal body, *i.e.*, a Maclaurin spheroid rather than a Jacobi ellipsoid. If the true rotation period is instead twice this value (*i.e.*, the double peaked lightcurve is due to shape instead of albedo features), then the required minimum density is 0.59 g cm^{-3}, which provides a far weaker constraint. No other family member (aside from Haumea itself) has a reported rotation rate fast enough to require a high density (Table 4 and Fig. 2).

Instead of considering individual rotation periods, we consider the family as a whole. Fig. 2 compares all confirmed family members (black points) with all other TNO lightcurve measurements (open circles) taken from the compilation of Duffard et al. (2009). The rotation period plotted assumes a double-peaked period for all objects (*i.e.*, shape-controlled lightcurve), and the curved lines show densities calculated based on the assumption of hydrostatic equilibrium (Jacobi ellipsoids). Rotation rates from the Duffard et al. (2009) table are taken at face value (no further attempt has been made to judge the reliability of the determined periods), with the exception of two very short rotation periods (1996 TP_{66} and 1998 XY_{95}, with single peak periods of 1.96 and 1.31 hours respectively; Collander-Brown et al. 1999,

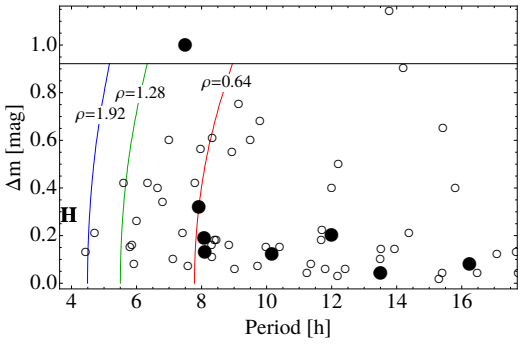

Fig. 2. Lightcurve amplitude (Δm) as a function of the rotation period (in hours) for the TNOs in the vicinity of Haumea. Filled and open circles stand for confirmed family members and background population (from Duffard et al. 2009, Thirouin et al. 2010), respectively. The letter H shows the position of Haumea. Vertical blue, red, and green curves are the limit for stability, assuming the objects are in hydrostatic equilibrium, *i.e.*, stable objects left of a line are denser than the number in the label (in g cm^{-3}). Objects above the black line ($\Delta m \sim 0.9$ mag) are unstable (under the hydrostatic equilibrium assumption), and are likely contact binaries.

2001) that appear in the table despite the original authors stating that these were unrealistic (and statistically insignificant) mathematical best fits. We removed these values and regard the rotation periods of these two objects as unknown. For all other objects where there are both multiple period determinations and no preferred period in Duffard et al., we take the shortest period to give the highest possible minimum density.

Seven of the eight family members fall into the relatively long-period (low-density) area of this plot, with $\rho \leq 0.64$ g cm^{-3}. The exception is 2003 SQ$_{317}$, which has a large lightcurve amplitude (Snodgrass et al. 2010), implying that it is likely to be a contact binary (therefore the Jacobi ellipsoid model does not hold, Lacerda & Jewitt 2007).

A direct comparison between the densities of family members and other TNOs is not straightforward since analysis of the rotational properties based on hydrostatic equilibrium can in general only set lower limits on the densities of the objects. We can, however, use the observed lightcurve properties (Fig. 2) to assess the probability that the family members and other TNOs were drawn from the same 2-D distribution in spin period vs. Δm. To do so, we use the 2-D Kolmogorov-Smirnov (K-S) test (Peacock 1983). The 2-D K-S test uses the Z statistic (the maximum absolute difference between the cumulative distributions of the samples) to quantify the dissimilarity between the distributions of two samples. The larger the value of Z, the more dissimilar the distributions.

We exclude Haumea and objects with $\Delta m > 0.9$ mag from this calculation: Haumea is not representative of the densities of its family, and objects with very large Δm obey a different relationship between rotational properties and bulk density (Lacerda & Jewitt 2007). Considering the two populations made of the 7 family members and the 64 background TNOs, we obtain a value of $Z = 1.276$. The corresponding probability that the P vs. Δm distributions of family members and other TNOs would differ by more than they do is $P_{>Z} = 0.040$. If we furthermore discard objects with $\Delta m < 0.1$ mag that are unlikely to be Jacobi ellipsoids, the populations are made of 5 and 42 TNOs respectively, and the K-S probability lowers to $P_{>Z} = 0.014$. These low values of $P_{>Z}$ suggest that the family members have different rotational properties from other TNOs, although the current data are still insufficient to quantitatively compare the densities of family members and other TNOs.

We note that the small numbers of objects and rather uncertain rotation periods for many, make such an analysis approximate at best, *i.e.*, this is not yet a statistically robust result. Furthermore, many of the larger objects with long rotation periods and low lightcurve amplitudes are likely to be spheroidal rather than ellipsoidal bodies, with single peak lightcurves due to albedo features (Pluto is an example), and we have made no attempt to separate these from the shape controlled bodies in Fig. 2. In addition, no restriction on orbit type (*e.g.*, classicals, scattered disk) is imposed on the objects in Fig. 2, as the total number of TNOs with lightcurves in the Duffard et al. (2009) compilation is still relatively low (67 objects included in Fig. 2).

5. Family membership and formation scenario

5.1. Orbital elements

We show in Fig. 3 the orbital parameters (semi-major axis, inclination and eccentricity) of the candidates. As already noted by Snodgrass et al. (2010), the confirmed family members cluster tightly around the centre of the distribution in both plots, at the supposed location of the pre-collision Haumea (Haumea itself having now a higher eccentricity, owing to its interaction with Neptune through orbital resonance, see Ragozzine & Brown 2007). Water ice has been detected on all the objects within the isotropic δv limit of 150 m s^{-1} defined for a collision-formation scenario by Ragozzine & Brown (2007), while only 14% of the objects with a larger velocity dispersion harbour water ice surfaces. Even assuming that all the as-yet uncharacterised candidates have water ice on their surfaces brings this number to only 32%, which significantly differs from the proportion inside the 150 m s^{-1} region. The probability of randomly selecting the single most clustered set of 11 out of a sample of 36 is only 10^{-9}. The clustering of water-bearing objects around the position of the proto-Haumea in orbital parameter space is therefore real, with a very high statistical significance. Wider photometric surveys of the trans-Neptunian region (Trujillo et al. 2011, Fraser & Brown 2012) find no further bodies with the strong water-ice spectrum characteristic of the family, which appears to be a unique cluster of objects.

5.2. Mass of the family

We discuss below how current observations can constraint the formation scenario of Haumea and its family. We first evaluate the mass of the family by summing over all confirmed members. We evaluate the mass M of each object from its absolute magnitude H, from

$$M = \frac{\pi\rho}{6}\left(\frac{1329}{\sqrt{p_V}}\right)^3 10^{-0.6H}, \quad (1)$$

where p_V is the geometric albedo (assumed to be 0.7 for family members), and ρ their density (assumed to be 0.64 g cm^{-3}, the largest found for a family member, see Fig. 2, and consistent with the typical density of TNOs, see Carry 2012). The 11

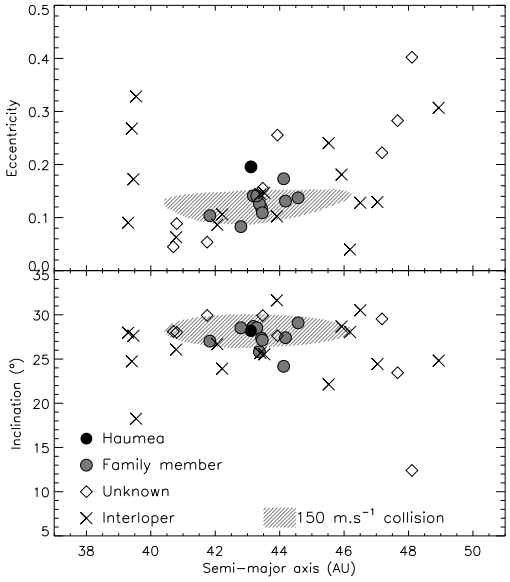

Fig. 3. Confirmed family members (grey filled circles with a black outline), rejected candidates: interlopers (crosses), and those with unknown surface properties (open diamonds) plotted in terms of the orbital osculating parameters semi-major axis, inclination and eccentricity. Haumea itself is shown as a black disk. We also drawn the area corresponding to a simulation of ejected particules from a nominal collision with an isotropic Δv of 150 m s^{-1} (Ragozzine & Brown 2007).

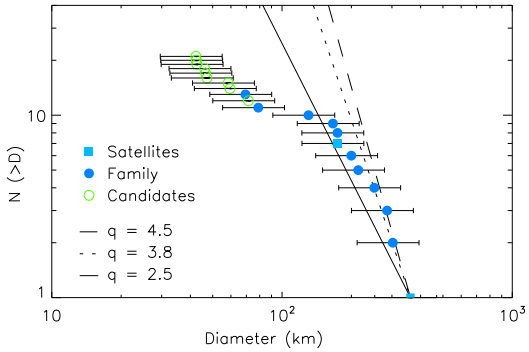

Fig. 4. Cumulative size distribution for confirmed (filled blue circles) and remaining candidate (open green circles) family members, compared with three power law models (see text). The models have $q = 2.5$ (solid line), $q = 3.8$ (dashed line) and $q = 4.5$, approximating the model of Leinhardt et al. (2010), (dotted line). The satellites of Haumea, Hi'iaka and Namaka, are represented by blue squares.

confirmed family members account for only 1% of the mass of Haumea (4×10^{21} kg, Ragozzine & Brown 2009), raising to 1.4% when also considering Hi'iaka and Namaka, the two satellites of Haumea, as family members. Including all the 8 remaining candidates adds only another 0.01%.

This mass fraction is however a lower limit, as more icy family members can be expected to be found. The area encompassed by the confirmed family member in orbital element space (Fig. 3) is wide (6 AU). Given the small fraction of known TNOs (a couple of percent, for TNOs of 100 km diameter, see Trujillo 2008), many more objects are still to be discovered in the vicinity of Haumea. To estimate how much mass has yet to be discovered, we compare the observed cumulative size-distribution of family members with three simple models, described by power laws of the form $N(> r) \propto r^{-q}$ (Fig. 4). The observed distribution includes the satellites of Haumea (namely Hi'aka and Namaka) which have 0.29 and 0.14 times Haumea's diameter of 1250 km (Fraser & Brown 2009, Ragozzine & Brown 2009, Carry 2012), and is based on the observed distribution of absolute magnitudes H and an assumed Haumea-like albedo of 0.7 (Table 4), with the exception of 2002 TX_{300}, which has a diameter determined by stellar occultation (Elliot et al. 2010). We also include the remaining candidates (open circles) that have not yet been ruled out, which are nearly all smaller (fainter) than the confirmed family members. The first model is based on the classical distribution for collisional fragments, with $q = 2.5$ (Dohnanyi 1969). The second takes the size distribution for large TNOs measured by Fraser & Kavelaars (2009), $q = 3.8$. The third is a simplification of the model presented by Leinhardt et al. (2010), with the mass distribution shown in their Fig. 3 approximated by a $q_M = 1.5$ power law, which corresponds to a very steep size distribution of $q = 4.5$. We normalise the distribution to the largest object, Hi'iaka, on the assumption that there are no more family members with $H \approx 3$ ($D \approx 400$ km) to be found.

The $q = 2.5$ model predicts that the largest object still to be discovered has a diameter of around 140 km, or $H \approx 5$. This corresponds to an apparent magnitude at opposition fainter than 21, which is below the detection limits of wide area TNO surveys to date (Trujillo & Brown 2003). Extrapolating this model to small sizes predicts a total mass of the family of ~2% of Haumea's mass, with nearly all of that mass in the already discovered large fragments. Models 2 and 3 predict the largest family members still to be discovered of diameters ~220 km and 250 km respectively, objects at least a magnitude brighter, which would have had a chance of being found by existing surveys, depending on where in their orbits they currently are. These models cannot be extrapolated (model 2 is based on the observed TNO size distribution, which has a different slope at smaller sizes, and model 3 is a coarse approximation to the simulations by Leinhardt et al. (2010), which give a total family mass of ~7% of Haumea), but they do allow there to be considerable missing mass in these large undetected bodies. These models show that in the case of a collisional size distribution we already know of all the large bodies, and all the significant mass, while steeper distributions can be observationally tested as they imply missing members with large diameters that should easily be found by new surveys (*e.g.*, Pan-STARRS, LSST).

5.3. Family formation models

The clustering of Haumea's family, with a low δv between fragments, may be its most peculiar property (Marcus et al. 2011), and can be used as a strong constraint on formation models. Additionally, the models must explain the spin of

Haumea and the mass and velocity dispersion of its fragments, keeping in mind that some of the original mass has been lost over time (TNO region is thought to be far less populous today than it was in the early solar system, see, *e.g.*, Morbidelli et al. 2008). None of the models below studied the long-term stability of the satellites or the fate of ejected fragment formed during the collision/fission, but Lykawka et al. (2012) found that about 25% of the fragments would not survive over 4 Gyr, the first Gyr being when most of the dynamical evolution took place.

The model by Schlichting & Sari (2009), which describes the cataclysmic disruption of a large icy satellite around Haumea, reproduces the velocity distribution of the family, and gives an original mass of the family of around 1% of Haumea. The spin period of Haumea, however, is expected to be longer than observed, based on considerations on physics of impacts and tides in the system (see arguments by Leinhardt et al. 2010, Ortiz et al. 2012, and reference therein). The rotational fission scenario presented by Ortiz et al. (2012) does reproduce Haumea's spin period, but predicts a velocity distribution several times higher than observed. a peculiar kind of *graze and merge* impact can explain Haumea's shape and spin, and a family of icy objects with low δv, that have a total original mass $\sim$ 7% of the proto-Haumea. This mass is higher than that observed, but may be consistent with objects lost from the family by dynamical interactions.

Cook et al. (2011) suggested an alternative solution, that bodies without the unique strong water ice signature could also be family members but from different layers in a differentiated proto-Haumea. This *black sheep* hypothesis has fewer observational constraints, as currently too few objects are known to be able to identify the family by dynamics alone (*i.e.*, without spectral information), so it is possible to imagine a higher mass and larger velocity dispersion. However, as discussed above, the clustering of family members with icy surfaces suggests that the true family members have a small velocity dispersion. Further modelling is required to tell whether a low δv population of pure ice bodies can come from a population of a mixture of higher-velocity collisional fragments.

6. Conclusions

We have presented optical and near-infrared colours for 8 of the 36 candidate members of Haumea's collisional family (Ragozzine & Brown 2009), in addition to the 22 objects we already reported (Snodgrass et al. 2010). We confirmed the presence of water ice on the surface of 2003 UZ_{117}, confirming its link with Haumea, and rejected 5 other candidates (following our prediction that most of the remaining objects would be interlopers, Snodgrass et al. 2010).

Of the 36 family member candidates including Haumea, only 11 (30%) have been confirmed on the basis of their surface properties, and a total of 17 have been rejected (47%). All the confirmed members are tightly clustered in orbital elements, the largest velocity dispersion remaining 123.3 m s^{-1} (for 1995 SM_{55}). These fragments, together with the two satellites of Haumea, Hi'iaka and Namaka, account for about 1.5% of the mass of Haumea.

The current observational constraints on the family formation can be summarised as:

1. A highly clustered group of bodies with unique spectral signatures.
2. An elongated and fast-rotating largest group member.
3. A velocity dispersion and total mass lower than expected for a catastrophic collision with a parent body of Haumea's size, but a size distribution consistent with a collision.

Various models have been proposed to match these unusual constraints, although so far none of these match the full set of constraints.

Acknowledgements. We thank the dedicated staff of ESO's La Silla and Paranal observatories for their assistance in obtaining this data. Thanks to Blair and Alessandro for sharing their *jarabe* during observations at La Silla. This research used VO tools SkyBoT (Berthier et al. 2006) and Miriade (Berthier et al. 2008) developed at IMCCE, and NASA's Astrophysics Data System. A great thanks to all the developers and maintainers. Thanks to an anonymous referee for his comments and careful checks of all our tables and numbers. We acknowledge support from the Faculty of the European Space Astronomy Centre (ESAC) for granting the visit of C. Snodgrass. P. Lacerda is grateful for financial support from a Michael West Fellowship and from the Royal Society in the form of a Newton Fellowship. The research leading to these results has received funding from the European Union Seventh Framework Programme (FP7/2007-2013) under grant agreement no. 268421.

References

Alvarez-Candal, A., Fornasier, S., Barucci, M. A., de Bergh, C., & Merlin, F. 2008, Astronomy and Astrophysics, 487, 741
Belskaya, I. N., Ortiz, J. L., Rousselot, P., et al. 2006, Icarus, 184, 277
Benecchi, S. D., Noll, K. S., Stephens, D. C., Grundy, W. M., & Rawlins, J. 2011, Icarus, 213, 693
Berthier, J., Hestroffer, D., Carry, B., et al. 2008, LPI Contributions, 1405, 8374
Berthier, J., Vachier, F., Thuillot, W., et al. 2006, in Astronomical Society of the Pacific Conference Series, Vol. 351, Astronomical Data Analysis Software and Systems XV, ed. C. Gabriel, C. Arviset, D. Ponz, & S. Enrique, 367
Brown, M. E., Barkume, K. M., Ragozzine, D., & Schaller, E. L. 2007, Nature, 446, 294
Brown, M. E., van Dam, M. A., Bouchez, A. H., et al. 2006, Astrophysical Journal, 639, 4346
Buzzoni, B., Delabre, B., Dekker, H., et al. 1984, The Messenger, 38, 9
Carry, B. 2012, Planetary and Space Science, in press
Casali, M., Pirard, J.-F., Kissler-Patig, M., et al. 2006, SPIE, 6269
Collander-Brown, S. J., Fitzsimmons, A., Fletcher, E., Irwin, M. J., & Williams, I. P. 1999, Monthly Notices of the Royal Astronomical Society, 308, 588
Collander-Brown, S. J., Fitzsimmons, A., Fletcher, E., Irwin, M. J., & Williams, I. P. 2001, Monthly Notices of the Royal Astronomical Society, 325, 972
Cook, J. C., Desch, S. J., & Rubin, M. 2011, in Lunar and Planetary Inst. Technical Report, Vol. 42, Lunar and Planetary Institute Science Conference Abstracts, 2503
Delsanti, A., Hainaut, O. R., Jourdeuil, E., et al. 2004, Astronomy and Astrophysics, 417, 1145
DeMeo, F. E., Fornasier, S., Barucci, M. A., et al. 2009, Astronomy and Astrophysics, 493, 283
Dohnanyi, J. S. 1969, Journal of Geophysical Research, 74, 2531
Duffard, R., Ortiz, J. L., Thirouin, A., Santos-Sanz, P., & Morales, N. 2009, Astronomy and Astrophysics, 505, 1283
Dumas, C., Carry, B., Hestroffer, D., & Merlin, F. 2011, Astronomy and Astrophysics, 528, A105
Elliot, J. L., Person, M. J., Zuluaga, C. A., et al. 2010, Nature, 465, 897
Fraser, W. C. & Brown, M. E. 2009, Astrophysical Journal, 695, L1
Fraser, W. C. & Brown, M. E. 2012, Astrophysical Journal, 749, 33
Fraser, W. C. & Kavelaars, J. J. 2009, Astronomical Journal, 137, 72
Giorgini, J. D., Ostro, S. J., Benner, L. A. M., et al. 2002, Science, 296, 132
Hainaut, O. R., Delahodde, C. E., Boehnhardt, H., et al. 2000, Astronomy and Astrophysics, 356, 1076
Kissler-Patig, M., Pirard, J., Casali, M., et al. 2008, Astronomy and Astrophysics, 491, 941
Lacerda, P. 2009, Astronomical Journal, 137, 3404
Lacerda, P. & Jewitt, D. C. 2007, Astronomical Journal, 133, 1393
Lacerda, P., Jewitt, D. C., & Peixinho, N. 2008, Astronomical Journal, 135, 1749
Leinhardt, Z. M., Marcus, R. A., & Stewart, S. T. 2010, Astrophysical Journal, 714, 1789
Lellouch, E., Kiss, C., Santos-Sanz, P., et al. 2010, Astronomy and Astrophysics, 518, L147
Lykawka, P. S., Horner, J., Mukai, T., & Nakamura, A. M. 2012, Monthly Notices of the Royal Astronomical Society, 421, 1331
Marcus, R. A., Ragozzine, D., Murray-Clay, R. A., & Holman, M. J. 2011, Astrophysical Journal, 733, 40

Merlin, F., Guilbert, A., Dumas, C., et al. 2007, Astronomy and Astrophysics, 466, 1185
Morbidelli, A., Levison, H. F., & Gomes, R. 2008, The Solar System Beyond Neptune, 275
Ortiz, J. L., Sota, A., Moreno, R., et al. 2004, Astronomy and Astrophysics, 420, 383
Ortiz, J. L., Thirouin, A., Campo Bagatin, A., et al. 2012, Monthly Notices of the Royal Astronomical Society, 419, 2315
Peacock, J. A. 1983, Monthly Notices of the Royal Astronomical Society, 202, 615
Perna, D., Barucci, M. A., Fornasier, S., et al. 2010, Astronomy and Astrophysics, 510, A53
Pinilla-Alonso, N., Brunetto, R., Licandro, J., et al. 2009, Astronomy and Astrophysics, 496, 547
Pinilla-Alonso, N., Licandro, J., Gil-Hutton, R., & Brunetto, R. 2007, Astronomy and Astrophysics, 468, L25
Pirard, J.-F., Kissler-Patig, M., Moorwood, A. F. M., et al. 2004, SPIE, 5492, 1763
Pravec, P., Harris, A. W., & Michalowski, T. 2002, Asteroids III, 113
Rabinowitz, D. L., Barkume, K. M., Brown, M. E., et al. 2006, Astrophysical Journal, 639, 1238
Ragozzine, D. & Brown, M. E. 2007, Astronomical Journal, 134, 2160
Ragozzine, D. & Brown, M. E. 2009, Astronomical Journal, 137, 4766
Santos-Sanz, P., Ortiz, J. L., Aceituno, F. J., Brown, M. E., & Rabinowitz, D. L. 2005, IAU Circular, 8577, 2
Schaller, E. L. & Brown, M. E. 2008, Astrophysical Journal, 684, L107
Schlichting, H. E. & Sari, R. 2009, Astrophysical Journal, 700, 1242
Sheppard, S. S. & Jewitt, D. C. 2002, Astronomical Journal, 124, 1757
Sheppard, S. S. & Jewitt, D. C. 2003, Earth Moon and Planets, 92, 207
Snodgrass, C., Carry, B., Dumas, C., & Hainaut, O. R. 2010, Astronomy and Astrophysics, 511, A72
Snodgrass, C., Lowry, S. C., & Fitzsimmons, A. 2006, Monthly Notices of the Royal Astronomical Society, 373, 1590
Snodgrass, C., Saviane, I., Monaco, L., & Sinclaire, P. 2008, The Messenger, 132, 18
Stansberry, J., Grundy, W., Brown, M. E., et al. 2008, The Solar System Beyond Neptune, 161
Tegler, S. C., Grundy, W. M., Romanishin, W. J., et al. 2007, Astronomical Journal, 133, 526
Thirouin, A., Ortiz, J. L., Duffard, R., et al. 2010, Astronomy and Astrophysics, 522, A93
Trujillo, C. A. 2008, Future Surveys of the Kuiper Belt, ed. Barucci, M. A., Boehnhardt, H., Cruikshank, D. P., Morbidelli, A., & Dotson, R., 573–585
Trujillo, C. A. & Brown, M. E. 2003, Earth Moon and Planets, 92, 99
Trujillo, C. A., Brown, M. E., Barkume, K. M., Schaller, E. L., & Rabinowitz, D. L. 2007, Astrophysical Journal, 655, 1172
Trujillo, C. A., Sheppard, S. S., & Schaller, E. L. 2011, Astrophysical Journal, 730, 105
Ward, S. N. & Asphaug, E. 2003, Geophysical Journal International, 153, 6

LETTER

doi:10.1038/nature09453

A collision in 2009 as the origin of the debris trail of asteroid P/2010 A2

Colin Snodgrass[1,2], Cecilia Tubiana[1], Jean-Baptiste Vincent[1], Holger Sierks[1], Stubbe Hviid[1], Richard Moissl[1], Hermann Boehnhardt[1], Cesare Barbieri[3], Detlef Koschny[4], Philippe Lamy[5], Hans Rickman[6,7], Rafael Rodrigo[8], Benoît Carry[9], Stephen C. Lowry[10], Ryan J. M. Laird[10], Paul R. Weissman[11], Alan Fitzsimmons[12], Simone Marchi[3] & the OSIRIS team*

The peculiar object P/2010 A2 was discovered[1] in January 2010 and given a cometary designation because of the presence of a trail of material, although there was no central condensation or coma. The appearance of this object, in an asteroidal orbit (small eccentricity and inclination) in the inner main asteroid belt attracted attention as a potential new member of the recently recognized[2] class of main-belt comets. If confirmed, this new object would expand the range in heliocentric distance over which main-belt comets are found. Here we report observations of P/2010 A2 by the Rosetta spacecraft. We conclude that the trail arose from a single event, rather than a period of cometary activity, in agreement with independent results[3]. The trail is made up of relatively large particles of millimetre to centimetre size that remain close to the parent asteroid. The shape of the trail can be explained by an initial impact ejecting large clumps of debris that disintegrated and dispersed almost immediately. We determine that this was an asteroid collision that occurred around 10 February 2009.

P/2010 A2 orbits much closer to the Sun (its semi-major axis is 2.29 astronomical units, AU) than the previously discovered main-belt comets, the activity of which seems to be driven by episodic ice sublimation[2]. The discovery of a parent body a few arcseconds (~1,500 km) away from the trail[4,5] implied that it was debris from a recent collision rather than the tail of a comet, although Earth-based observations alone are consistent with a comet model[6]. It was suggested that the trail formed between January and August 2009, and was comprised of relatively large (diameter >1 mm) grains[7]. Here we use the term 'trail' to describe a tail made up of large particles, rather than dust from a currently active comet. Hubble Space Telescope observations refine the diameter of the parent body to 120 m and the date to February/March 2009 (ref. 3).

We obtained an improved three-dimensional description of the trail geometry by observing it with the OSIRIS Narrow Angle Camera[8] on board the European Space Agency's Rosetta spacecraft on 16 March 2010. Rosetta was approaching the asteroid belt for its July 2010 fly-by of asteroid 21 Lutetia, and at the time of observation was 1.8 AU from the Sun and 10° out of P/2010 A2's orbital plane. From this vantage point the separation between the anti-velocity (orbit) angle and the anti-Sun (comet tail) direction was much larger than was possible to observe from Earth. We also obtained reference images of P/2010 A2 from Earth using the 3.6 m New Technology Telescope (NTT) at the European Southern Observatory's La Silla observatory and the 200″ Hale telescope at Palomar Mountain. Figure 1 displays images of P/2010 A2 at four epochs, from the Earth and from Rosetta. We measured the position angle of the trail and extracted the flux profile along the trail axis at each epoch (Fig. 2).

We simulate the shape of the observed trail at each epoch by modelling the trajectories of dust grains, as is commonly done for comet tails[9,10]. The motion depends on the grains' initial velocity and the ratio β between solar radiation pressure and solar gravity, which is related to the size of the grains[11]. Owing to the small phase angle as viewed from Earth it is not possible to find a unique solution for the dust ejection epochs from the ground-based observations alone: the best estimate indicates that particles must have been emitted before August 2009, and should be of at least millimetre size to account for the low dispersion and their apparent position close to the projected anti-velocity vector. The higher phase angle of the OSIRIS observations allows a more precise simulation of the trail, and consequently we obtained a very narrow time frame for the emission of the dust. The grains must have been released around 10 February 2009, plus or minus 5 days, with the uncertainty being due to the measurement of the position angle of the faint trail in the OSIRIS images. To account for the position angle and the length of the trail, we must consider grains ranging from millimetre to centimetre size and larger. The particle sizes from this model, together with the brightness profile shown in Fig. 2, allow us to measure the size distribution of grains, and from this derive a total mass of the ejecta of 3.7×10^8 kg, or approximately 16% of a parent body of diameter 120 m, assuming a density of 2,500 kg m^{-3} and an albedo of 15% for both the asteroid and the grains.

The shape of the trail cannot be reproduced with a traditional comet-tail model, even when considering a longer timescale for the event. Cometary models all produce tail geometries in the OSIRIS image with a fan that reaches a point at the nucleus and becomes wider farther from it (see Supplementary Information for examples). All images of P/2010 A2 show a distinctive broad edge at the 'nucleus' end and then a trail with parallel edges. From the Rosetta observing geometry this edge is even broader than it is from Earth. This shape can be reproduced by a number of parallel synchrones: contours in the model that show the location of dust produced at the same time. In this model, an initial dust cloud is formed (presumably by a collision) in February 2009, which initially does not spread much (less than 1,000 km) but over a year solar gravity and radiation pressure expand this small trail to its observed width and length, respectively. Higher-resolution images from the Hubble Space Telescope[3] show the presence of parallel striae in the trail, very well aligned with the synchrone representing the original event as estimated from our simulations. These striae indicate that some areas of higher densities existed in the original cloud: larger clumps of material that fragmented and dispersed as they were ejected. The width of the broad front end of the trail from these different geometries can be used to constrain the speed of particles in the original ejecta cloud to less than 1 m s^{-1}. Impact

[1]Max-Planck-Institut für Sonnensystemforschung, Max-Planck-Strasse 2, 37191 Katlenburg-Lindau, Germany. [2]European Southern Observatory, Alonso de Córdova 3107, Casilla 19001, Santiago 19, Chile. [3]University of Padova, Department of Astronomy, Vicolo dell'Osservatorio 3, 35122 Padova, Italy. [4]Research and Scientific Support Department, European Space Agency, Keplerlaan 1, Postbus 229, 2201 AZ Noordwijk ZH, The Netherlands. [5]Laboratoire d'Astrophysique de Marseille, UMR61 10 CNRS/Université Aix-Marseille, 38 rue Frédéric Joliot-Curie, 13388 Marseille cedex 13, France. [6]Department of Astronomy and Space Physics, Uppsala University, Box 516, 75120 Uppsala, Sweden. [7]PAS Space Research Center, Bartycka 18A, 00-716 Warszawa, Poland. [8]Instituto de Astrofísica de Andalucía, CSIC, Box 3004, 18080 Granada, Spain. [9]LESIA, Observatoire de Paris—Meudon, 5 place Jules Janssen, 92195 Meudon cedex, France. [10]Centre for Astrophysics and Planetary Science, University of Kent, Canterbury CT2 7NH, UK. [11]Jet Propulsion Laboratory, 4800 Oak Grove Drive, MS 183-301, Pasadena, California 91101, USA. [12]Astrophysics Research Centre, Queen's University Belfast, BT7 1NN, UK. *Lists of participants and affiliations appear at the end of the paper.

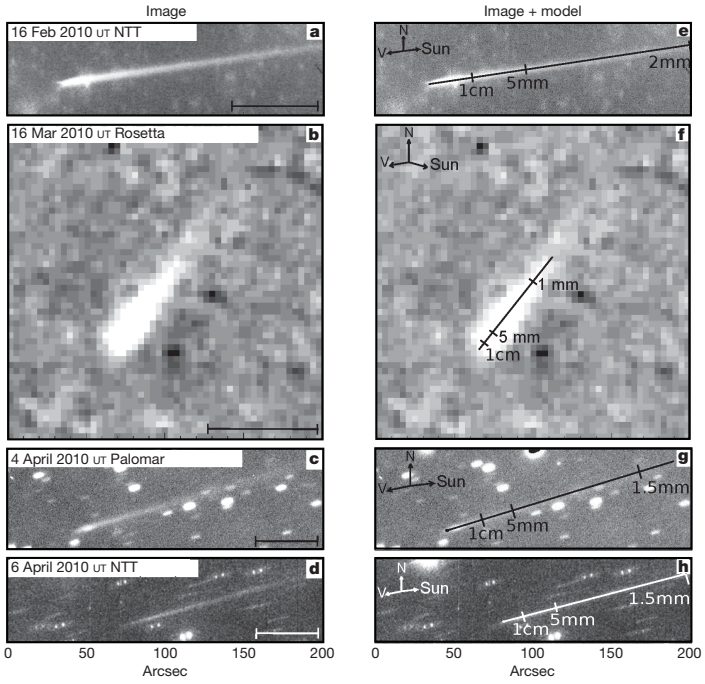

Figure 1 | Images of P/2010 A2 at four epochs. These are, from top to bottom, from the NTT (February), Rosetta (March), Palomar (April) and the NTT (April), respectively. The scale bars in the lower right of **a**–**d** show a projected distance of 5×10^4 km. When possible, we median-combined images centred on the object to increase the signal-to-noise ratio (relative to a single exposure) of the trail and remove background stars. To isolate the faint dust trail in the OSIRIS data we first subtracted an image of the background star field from each frame before shifting the frame on the basis of the motion of the object and then median-combining. On the right we show the same images overlaid with synchrones generated from the Finson–Probstein model. Numbers indicate estimates of the particle size distribution along the synchrones, derived from the model. The orientation of the images is North up, East left. The compass in the top left of panels **e** to **h** shows the direction of the heliocentric velocity vector (orbit) V and the direction to the Sun. The advantage of the Rosetta observing geometry is clear, with the broad head of the trail and obvious difference between the observed position angle and the anti-velocity vector apparent in the OSIRIS image. Models based on a period of cometary activity (rather than a single event) or smaller particle sizes produce a significantly different pattern of synchrones in **f** (see Supplementary Figs 2–4) that does not fit the observations. The same models all produce similar synchrones to those in the impact model for **e**, **g** and **h**, and therefore cannot be ruled out on the basis of Earth-based data alone.

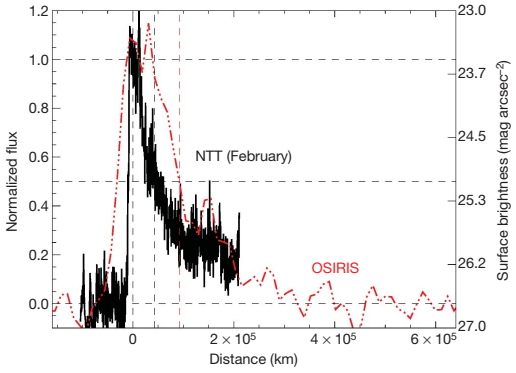

Figure 2 | Flux profiles along the trail. The normalized profiles for the February NTT (solid black line) and the OSIRIS data sets (dot-dashed red line) are shown. The *x* axis is in kilometres along the trail, with the conversion from the projected scale in arcseconds on sky based on the geometry derived from our model. The vertical dashed lines indicate the half-maximum of the profiles, used to measure the scale length of the trails in these images with different sensitivities. The two profiles have scale lengths of 4.3×10^4 and 9.3×10^4 km along the trail. The right *y* axis shows the calibrated surface brightness of the NTT profile in R-band magnitudes per square arcsecond. The flux profiles from the other Earth-based observations match the NTT one, but are omitted for clarity because they have higher noise owing to the shorter integration times. We derive a size distribution using the NTT flux profile and the size of particles as a function of distance along the trail from the Finson–Probstein model. This is done by converting the total flux across the trail at each distance to a reflecting area (assuming an albedo of 15%), and finding the corresponding number of particles of the appropriate size. The resulting cumulative size distribution is shown in Supplementary Fig. 6, and has a slope that matches the prediction for a population of collisional remnants[24].

experiments[12] find that such a low velocity implies a parent body of low strength and high porosity, although recent computer simulations suggest that impacts on such a small asteroid will lead to low-velocity ejecta independently of porosity[13].

Previously, asteroid collision models have been used to explain the dust trails associated with main-belt comets[14], but the longer-lasting dust production and repeated activity of comet Elst–Pizarro at each perihelion[15,16] rule out recent (within the past few years) collisions. Collisions inferred from asteroid families[17] or large-scale denser regions in the zodiacal dust cloud[18] have ages of 10^4 to 10^9 years. Our observations show direct evidence for a collision that is recent in observational terms, with a debris trail that is still evolving. From estimates of the population of the main asteroid belt[19,20] and an estimated impactor diameter of 6–9 m (ref. 21), we expect roughly one impact of this size every 1.1 billion years for a parent body of diameter 120 m, or approximately one every 12 years somewhere in the asteroid belt. This is in agreement with a single detection by the LINEAR survey; we expect that more small collisions will be detected by next-generation surveys. Collisions of this size therefore contribute around 3×10^7 kg yr^{-1} of dust to the zodiacal cloud, which is negligible compared with comets and the total required to maintain a steady state[22], in agreement with recent models[23].

Received 4 May; accepted 25 August 2010.

1. Birtwhistle, P., Ryan, W. H., Sato, H., Beshore, E. C. & Kadota, K. Comet P/2010 A2 (LINEAR). *IAU Circ.* **9105** (2010).
2. Hsieh, H. H. & Jewitt, D. A population of comets in the main asteroid belt. *Science* **312,** 561–563 (2006).
3. Jewitt, D., Weaver, H., Agarwal, J., Mutchler, M. & Drahus, M. A recent disruption of the main-belt asteroid P/2010 A2. *Nature* doi: 10.1038/nature09456 (this issue).
4. Licandro, J., Tozzi, G. P., Liimets, T., Haver, R. & Buzzi, L. Comet P/2010 A2 (LINEAR). *IAU Circ.* **9109** (2010).
5. Jewitt, D., Annis, J. & Soares-Santos, M. Comet P/2010 A2 (LINEAR). *IAU Circ.* **9109** (2010).
6. Moreno, F. *et al.* Water-ice driven activity on main-belt comet P/2010 A2 (LINEAR)? *Astrophys. J.* **718,** L132–L136 (2010).

RESEARCH LETTER

7. Sekanina, Z. Comet P/2010 A2 (LINEAR). *IAU Circ.* **9110** (2010).
8. Keller, H. U. *et al.* OSIRIS, the scientific camera system onboard Rosetta. *Space Sci. Rev.* **128,** 433–506 (2007).
9. Finson, M. & Probstein, R. A theory of dust comets. 1. Model and equations. *Astrophys. J.* **154,** 327–380 (1968).
10. Beisser, K. & Boehnhardt, H. Evidence for the nucleus rotation in streamer patterns of comet Halley's dust tail. *Astrophys. Space Sci.* **139,** 5–12 (1987).
11. Burns, J. A., Lamy, P. L. & Soter, S. Radiation forces on small particles in the solar system. *Icarus* **40,** 1–48 (1979).
12. Michikami, T., Moriguchi, K., Hasegawa, S. & Fujiwara, A. Ejecta velocity distribution for impact cratering experiments on porous and low strength targets. *Planet. Space Sci.* **55,** 70–88 (2007).
13. Jutzi, M., Michel, P., Benz, W. & Richardson, D. C. Fragment properties at the catastrophic disruption threshold: the effect of the parent body's internal structure. *Icarus* **207,** 54–65 (2010).
14. Lien, D. J. Asteroid debris trails: evidence for recent collisions in the asteroid belt. *Bull. Am. Astron. Soc.* **30,** 1035 (1998).
15. Hsieh, H. H., Jewitt, D., Lacerda, P., Lowry, S. C. & Snodgrass, C. The return of activity in main-belt comet 133P/Elst-Pizarro. *Mon. Not. R. Astron. Soc.* **403,** 363–377 (2010).
16. Bagnulo, S., Tozzi, G. P., Boehnhardt, H., Vincent, J.-B. & Muinonen, K. Polarimetry and photometry of the peculiar main-belt object 7968 = 133P/Elst-Pizarro. *Astron. Astrophys.* **514,** A99 (2010).
17. Nesvorný, D., Bottke, W. F., Dones, L. & Levison, H. F. The recent breakup of an asteroid in the main-belt region. *Nature* **417,** 720–771 (2002).
18. Nesvorný, D. *et al.* Candidates for asteroid dust trails. *Astron. J.* **132,** 582–595 (2006).
19. Bottke, W. F. *et al.* Linking the collisional history of the main asteroid belt to its dynamical excitation and depletion. *Icarus* **179,** 63–94 (2005).
20. Marchi, S. *et al.* The cratering history of asteroid (2867) Steins. *Planet. Space Sci.* **58,** 1116–1123 (2010).
21. Holsapple, K. A. & Housen, K. R. A crater and its ejecta: an interpretation of deep impact. *Icarus* **187,** 345–356 (2007).
22. Sykes, M. V., Grün, E., Reach, W. T. & Jenniskens, P. in *Comets II* (eds Festou, M. C., Keller, H. U. & Weaver, H. A.) 677–693 (Univ. Arizona Press, 2004).
23. Nesvorný, D. *et al.* Cometary origin of the zodiacal cloud and carbonaceous micrometeorites. implications for hot debris disks. *Astrophys. J.* **713,** 816–836 (2010).
24. Dohnanyi, J. W. Collisional model of asteroids and their debris. *J. Geophys. Res.* **74,** 2531–2554 (1969).

Supplementary Information is linked to the online version of the paper at www.nature.com/nature.

Acknowledgements We thank R. Schulz and the Rosetta operations team for enabling these 'target of opportunity' observations to be performed. OSIRIS is funded by the national space agencies ASI, CNES, DLR, the Spanish Space Program (Ministerio de Educacion y Ciencia), SNSB and the ESA. The ground-based observations were collected (in part) at the European Southern Observatory, Chile, under programmes 084.C-0594(A) and 185.C-1033(A).

Author Contributions C.S. and C.T. led this project and performed the data reduction and analysis, J.-B.V. did the modelling and led the interpretation, H.S., S.H. and R.M. were responsible for the planning and execution of the OSIRIS observations, H.B. contributed to the modelling and interpretation. C.B., D.K., P.L., H.R. and R.R. are the Lead Scientists of the OSIRIS project. The OSIRIS team built and run this instrument and made the observations possible. B.C., S.C.L., R.J.M.L., P.R.W. and A.F. were the observers who provided the ground-based observations. S.M. provided calculations of the collision probability.

Author Information Reprints and permissions information is available at www.nature.com/reprints. The authors declare no competing financial interests. Readers are welcome to comment on the online version of this article at www.nature.com/nature. Correspondence and requests for materials should be addressed to C.S. (snodgrass@mps.mpg.de).

The OSIRIS team

M. A'Hearn[13], F. Angrilli[14], A. Barucci[9], J.-L. Bertaux[15], G. Cremonese[16], V. Da Deppo[17], B. Davidsson[6], S. Debei[14], M. De Cecco[18], S. Fornasier[9], P. Gutiérrez[8], W.-H. Ip[19], H. U. Keller[20], J. Knollenberg[21], J. R. Kramm[1], E. Kuehrt[21], M. Kueppers[22], L. M. Lara[8], M. Lazzarin[3], J. J. López-Moreno[8], F. Marzari[23], H. Michalik[20], G. Naletto[24], L. Sabau[25], N. Thomas[26] & K.-P. Wenzel[4]

[13]University of Maryland, Department of Astronomy, College Park, Maryland 20742-2421, USA. [14]Department of Mechanical Engineering—University of Padova, Via Venezia 1, 35131 Padova, Italy. [15]LATMOS, CNRS/UVSQ/IPSL, 11 Boulevard d'Alembert, 78280 Guyancourt, France. [16]INAF—Osservatorio Astronomico di Padova, Vicolo dell'Osservatorio 5, 35122 Padova, Italy. [17]CNR-IFN UOS Padova LUXOR, Via Trasea 7, 35131 Padova, Italy. [18]UNITN, Università di Trento, Via Mesiano 77, 38100 Trento, Italy. [19]National Central University, Institute of Astronomy, 32054 Chung-Li, Taiwan. [20]Institut für Datentechnik und Kommunikationsnetze der TU Braunschweig, Hans-Sommer-Strasse 66, 38106 Braunschweig, Germany. [21]DLR Institute for Planetary Research, Rutherfordstrasse 2, 12489 Berlin, Germany. [22]ESA-ESAC, Camino bajo del Castillo S/N, 28691 Villanueva de la Cañada, Madrid, Spain. [23]Department of Physics—University of Padova, Via Marzolo 8, 35131 Padova, Italy. [24]Department of Information Engineering—University of Padova, Via Gradenigo, 6/B I, 35131 Padova, Italy. [25]Instituto Nacional de Tecnica Aeroespacial, Carretera de Ajalvir, p.k. 4, 28850 Torrejon de Ardoz, Madrid, Spain. [26]Physikalisches Institut, Abteilung Weltraumforschung und Planetologie, Universität Bern, Sidlerstrasse 5, 3012 Bern, Switzerland.

REPORTS

Images of Asteroid 21 Lutetia: A Remnant Planetesimal from the Early Solar System

H. Sierks,[1]* P. Lamy,[2] C. Barbieri,[3,32] D. Koschny,[4] H. Rickman,[5,31] R. Rodrigo,[6] M. F. A'Hearn,[7] F. Angrilli,[8,32] M. A. Barucci,[9] J.-L. Bertaux,[10] I. Bertini,[32] S. Besse,[7] B. Carry,[11] G. Cremonese,[12,32] V. Da Deppo,[13,32] B. Davidsson,[5] S. Debei,[8,32] M. De Cecco,[14] J. De Leon,[6] F. Ferri,[32] S. Fornasier,[9,33] M. Fulle,[15] S. F. Hviid,[1] R. W. Gaskell,[16] O. Groussin,[2] P. Gutierrez,[6] W. Ip,[17] L. Jorda,[2] M. Kaasalainen,[18] H. U. Keller,[19] J. Knollenberg,[20] R. Kramm,[1] E. Kührt,[20] M. Küppers,[11] L. Lara,[6] M. Lazzarin,[3] C. Leyrat,[9] J. J. Lopez Moreno,[6] S. Magrin,[3] S. Marchi,[21,32] F. Marzari,[22,32] M. Massironi,[23,32] H. Michalik,[24] R. Moissl,[1,11] G. Naletto,[25,32] F. Preusker,[20] L. Sabau,[26] W. Sabolo,[6] F. Scholten,[20] C. Snodgrass,[1] N. Thomas,[27] C. Tubiana,[1] P. Vernazza,[2] J.-B. Vincent,[1] K.-P. Wenzel,[4] T. Andert,[28] M. Pätzold,[29] B. P. Weiss[30]

Images obtained by the Optical, Spectroscopic, and Infrared Remote Imaging System (OSIRIS) cameras onboard the Rosetta spacecraft reveal that asteroid 21 Lutetia has a complex geology and one of the highest asteroid densities measured so far, 3.4 ± 0.3 grams per cubic centimeter. The north pole region is covered by a thick layer of regolith, which is seen to flow in major landslides associated with albedo variation. Its geologically complex surface, ancient surface age, and high density suggest that Lutetia is most likely a primordial planetesimal. This contrasts with smaller asteroids visited by previous spacecraft, which are probably shattered bodies, fragments of larger parents, or reaccumulated rubble piles.

The European Space Agency's Rosetta mission flew by asteroid Lutetia on 10 July 2010, with a closest approach distance of 3170 km. Lutetia was chosen because of its size and puzzling surface spectrum (*1*, *2*). The Optical, Spectroscopic, and Infrared Remote Imaging System (OSIRIS) on board Rosetta (*3*) took 462 images, in 21 broad- and narrowband filters extending from 240 to 1000 nm, through both its narrow-angle camera (NAC) and wide-angle camera (WAC). These images covered more than 50% of the asteroid surface, mostly of the northern hemisphere (figs. S1 and S2). The resolved observations started 9 hours 30 min before the closest approach (CA) and finished 18 min after CA. At CA, the asteroid filled the field of view of the NAC with a spatial scale of ~60 m per pixel. The observations reveal a morphologically diverse surface, indicating a long and complex history.

We modeled the global shape of Lutetia, combining two techniques: stereophotoclinometry (*4*) using 60 NAC and WAC images, and inversion of a set of 50 photometric light curves and of contours of adaptive optics images (*5*, *6*). The asteroid's overall dimensions are (121 ± 1) × (101 ± 1) × (75 ± 13) km^3 along the principal axes of inertia. The north pole direction is defined by a right ascension of 51.8° ± 0.4° and a declination of +10.8° ± 0.4°, resulting in an obliquity of 96°. From the global shape model, we derived a volume of (5.0 ± 0.4) × 10^5 km^3. The volume error is well constrained by (i) the dynamical requirement of principal-axis rotation, (ii) the existence of ground-based adaptive optics images from viewing directions other than that of the flyby, and (iii) the pre-flyby Knitted Occultation, Adaptive-optics and Lightcurves Approach (KOALA) model (*5*), which matched the shape model of the imaged part within 5%, giving us confidence that this model is accurate at this level for the southern hemisphere of Lutetia not seen during the flyby. The volume-equivalent diameter of Lutetia is 98 ± 2 km. Combining our volume estimate with the mass of (1.700 ± 0.017) × 10^{18} kg measured by the Radio Science Investigation (*7*), we obtained a density of 3.4 ± 0.3 g/cm^3. This value is higher than that found for most nonmetallic asteroids, whose bulk densities are in the range from 1.2 to 2.7 g/cm^3, well below the average grain density of their likely meteoritic analogs. Such low densities imply large macroporosities (*8*) that are associated with "rubble pile" asteroids (*9*).

Using crater density, cross-cutting and overlapping relationships, and the presence of deformational features such as faults, fractures, and grooves, we have identified five major regions on the surface observed during CA. Two regions (Pannonia and Raetia) imaged at lower resolution were defined on the basis of sharp morphological boundaries as crater walls and ridges [Fig. 1 and see the supporting online material (SOM) for details]. The surface is covered in regolith, with slopes below the angle of repose for talus almost everywhere, but large features reveal the underlying structure. A cluster of craters close to the pole in the Baetica region is one of the most prominent features of the northern hemisphere. The most heavily cratered, and therefore oldest, regions (Noricum and Achaia) are separated by the Narbonensis region, which is defined by a crater ~55 km in diameter (Fig. 2). This crater (Massilia) contains several smaller units and is deformed by grooves and pit chains, indicating modifications that took place after its initial formation. Another large impact crater is seen close to the limb (Raetia region). A subparallel ridge formation is seen close to the terminator. A number of scarps and linear features (grooves, fractures, and faults) transecting several small craters (Fig. 2 and fig. S3) are organized along systems characterized by specific orientations for each region and with no obvious relationships with the major craters. However, in the Noricum region, a prominent scarp bounds a local topographic

[1]Max-Planck-Institut für Sonnensystemforschung, Max-Planck-Strasse 2, 37191 Katlenburg-Lindau, Germany. [2]Laboratoire d'Astrophysique de Marseille, CNRS and Université de Provence, 38 Rue Frédéric Joliot-Curie, 13388 Marseille, France. [3]University of Padova, Department of Astronomy, Vicolo dell'Osservatorio 3, 35122 Padova, Italy. [4]Research and Scientific Support Department, European Space Agency (ESA), 2201 Noordwijk, Netherlands. [5]Department of Physics and Astronomy, Uppsala University, 75120 Uppsala, Sweden. [6]Instituto de Astrofísica de Andalucía, Consejo Superior de Investigaciones Científicas (CSIC), 18080 Granada, Spain. [7]Department of Astronomy, University of Maryland, College Park, MD 20742–2421, USA. [8]Department of Mechanical Engineering, University of Padova, Via Venezia 1, 35131 Padova, Italy. [9]Laboratoire d'Etudes Spatiales et d'Instrumentation en Astrophysique, Observatoire de Paris, 5 Place Jules Janssen, 92195 Meudon, France. [10]LATMOS, CNRS/UVSQ/IPSL, 11 Boulevard d'Alembert, 78280 Guyancourt, France. [11]European Space Astronomy Centre, ESA, Villanueva de la Cañada, Madrid, Spain. [12]Istituto Nazionale di Astrofisica, Osservatorio Astronomico di Padova, Vicolo dell'Osservatorio 5, 35122 Padova, Italy. [13]CNR-IFN UOS Padova LUXOR, Via Trasea 7, 35131 Padova, Italy. [14]UNITN, Università di Trento, Via Mesiano, 77, 38100 Trento, Italy. [15]Osservatorio Astronomico de Trieste, 34014 Trieste, Italy. [16]Planetary Science Institute, 1700 East Fort Lowell, Suite 106, Tucson, AZ 85719, USA. [17]Institute for Space Science, National Central University, 32054 Chung-Li, Taiwan. [18]Department of Mathematics, Tampere University of Technology, 33101 Tampere, Finland. [19]Institute for Geophysics and Extraterrestrial Physics, Technische Universität Braunschweig, 38106 Braunschweig, Germany. [20]Institut für Planetenforschung, Deutsches Zentrum fuer Luft- und Raumfahrt, Rutherfordstrasse 2, 12489 Berlin, Germany. [21]Universite de Nice–Sophia Antipolis, Observatoire de la Cote d'Azur, CNRS, 06304 Nice, France. [22]Department of Physics, University of Padova, Via Marzolo 8, 35131 Padova, Italy. [23]Dipartimento di Geoscienze, Università di Padova, Via Gradenigo 6, 35131 Padova, Italy. [24]Institut für Datentechnik und Kommunikationsnetze, 38106 Braunschweig, Germany. [25]Department of Information Engineering, University of Padova, Via Gradenigo 6, 35131 Padova, Italy. [26]Instituto Nacional de Técnica Aeroespacial, 28850 Torrejon de Ardoz, Spain. [27]Physikalisches Institut der Universität Bern, Sidlerstrasse 5, 3012 Bern, Switzerland. [28]Institut für Raumfahrttechnik, Universität der Bundeswehr München, Neubiberg, Germany. [29]Rheinisches Institut für Umweltforschung, Abteilung Planetenforschung, Universität zu Köln, Cologne, Germany. [30]Department of Earth, Atmospheric, and Planetary Sciences, Massachusetts Institute of Technology, Cambridge, MA, USA. [31]Polish Academy of Sciences Space Research Center, Bartycka 18A, 00-716 Warsaw, Poland. [32]Centro Interdipartimentale di Studi e Attività Spaziali (CISAS)–G. Colombo, Università di Padova, Via Venezia 15, 35131 Padova, Italy. [33]Universite Paris Diderot, Sorbonne Paris Cité, 4 Rue Elsa Morante, 75205 Paris, France.

*To whom correspondence should be addressed. E-mail: sierks@mps.mpg.de

high where lineaments run almost parallel to the scarp itself and to the rims of the crater cluster in Baetica. High-resolution topography models produced by stereo image processing (*10*) show that one long (>10 km) groove in the Noricum region (Fig. 2C and fig. S4) is roughly 100 m deep and on a local topographic high. The linear features are similar in appearance to those on the martian moon Phobos, which are commonly interpreted as resulting from a large impact (*11*). On 433 Eros, the existence of similar grooves has been interpreted as evidence of competent rock below the regolith, although this asteroid is thought to be heavily fractured (*12*–*14*). Recent work suggests that cracks can be supported in very low-strength material on a body as small as Eros (*15*). The pattern of grooves on Lutetia suggests strain structures or fractures within a body of considerable strength.

Lutetia is heavily cratered, although the crater spatial density varies considerably across the imaged hemisphere. We have identified more than 350 craters with diameters between 600 m and 55 km, which allowed us to determine Lutetia's crater retention age by measuring the crater size-frequency distribution (SFD). We chose to perform the crater count on the Achaia region because it is a remarkably flat area imaged with uniform illumination conditions. In this region, we counted 153 craters over an area of 2800 km^2. We compared Achaia's SFD with those for asteroids 253 Mathilde and 243 Ida (Fig. 3). At large crater sizes (>10 km), the crater SFD of Achaia is quite similar to that of Ida, whereas Mathilde is only slightly less cratered. There are about two or three times fewer craters at a diameter of 1 km than on Ida or Mathilde, respectively. At very small sizes (<1 km), there is a strong depletion of craters. Asteroids as large as Lutetia can be globally affected by seismic shaking; this argument has been used to explain the depletion of <200-m-diameter craters on Eros (*13*, *16*) but cannot explain the observed paucity of craters with diameters up to 5 to 8 km (*17*). The apparent break in the SFD at this size range is statistically significant: According to the Kolmogorov-Smirnov test, the probability that the observed crater SFD (for diameter > 0.8 km) is consistent with a simple hard rock scaling law model (for an approximately linear crater SFD, see Fig. 3C) is only ~3%.

Small crater obliteration by Massilia crater ejecta seems unlikely given that the Achaia region does not show a systematic decrease in crater density with increasing distance to Massilia. A possible explanation for the break is a transition in the physical properties of the target. Small craters, which affect only the upper layers, form in shattered material. Larger craters, able to excavate to greater depth, form in competent rock.

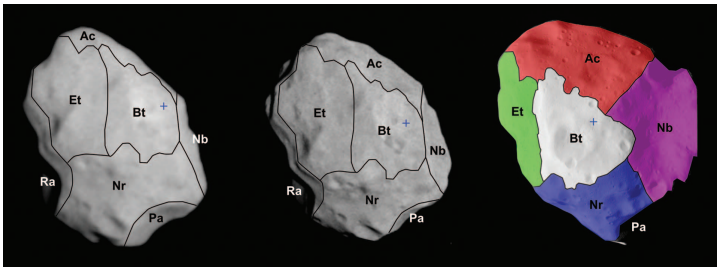

Fig. 1. Regions on Lutetia. Three images taken at −60, −30, and −3 min before CA (left to right) showing the different regions: Bt, Baetica; Ac, Achaia; Et, Etruria; Nb, Narbonensis; Nr, Noricum; Pa, Pannonia; and Ra, Raetia. The images were taken at distances of 53, 27, and 3.5 × 10^6 m and phase angles of 8°, 4°, and 52°. The resolutions of each image are approximately 1000, 500, and 60 m per pixel; Lutetia has been scaled to appear approximately the same size in each panel. The north pole is indicated by the blue cross.

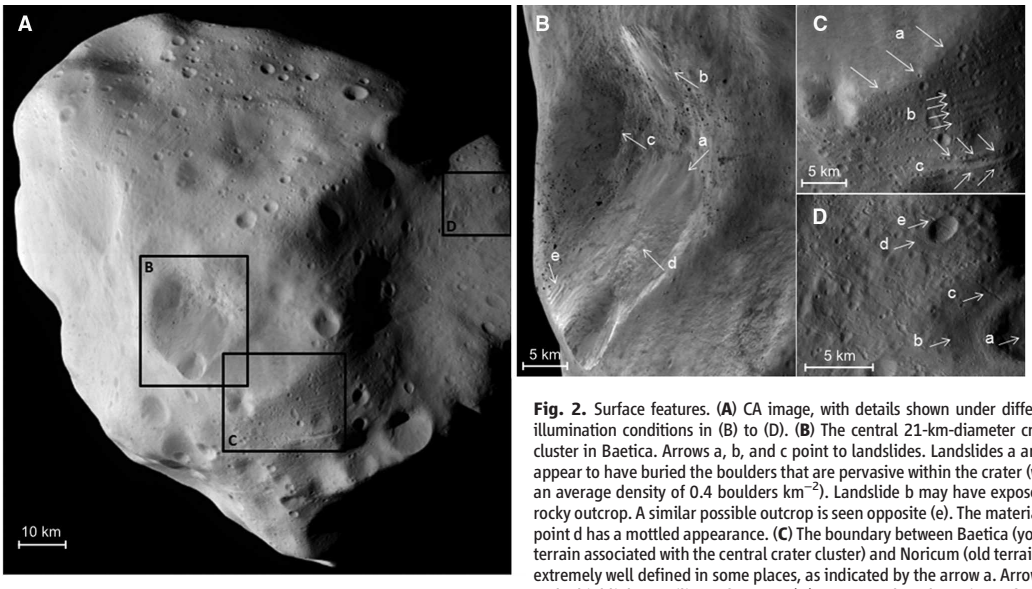

Fig. 2. Surface features. (**A**) CA image, with details shown under different illumination conditions in (B) to (D). (**B**) The central 21-km-diameter crater cluster in Baetica. Arrows a, b, and c point to landslides. Landslides a and b appear to have buried the boulders that are pervasive within the crater (with an average density of 0.4 boulders km^{-2}). Landslide b may have exposed a rocky outcrop. A similar possible outcrop is seen opposite (e). The material at point d has a mottled appearance. (**C**) The boundary between Baetica (young terrain associated with the central crater cluster) and Noricum (old terrain) is extremely well defined in some places, as indicated by the arrow a. Arrows b and c highlight curvilinear features. (**D**) Arrows c, d, and e point to further curvilinear features on the surface of Lutetia. In the Narbonensis region, most curvilinear features show this orientation. The curvilinear features cut the crater and its rim. Feature c cuts through the debris apron (b) of the crater (a). This implies that these linear features are younger than the craters or impact into an area with existing large-scale cracks and subsequent regolith movement.

We therefore modeled a gradual transition in the crater scaling law as strength and density increase with depth in a fractured layer (*18*). We determined the depth of this layer by fitting the model to the observed crater SFD (*19*, *20*) (Fig. 3C). For typical rock properties (SOM text), the depth of the fractured layer is ~3 km. Based on this model, and using the lunar chronology as calibration (*20*), we find a crater retention age of 3.6 ± 0.1 billion years for Achaia.

Scaling laws (*21*) and hydrocode simulations performed with the iSALE (impact Simplified Arbitrary Lagrangian Eulerian code) (*22*) show that the impactor that produced Massilia had a diameter ~ 8 km. According to the simulation, this impact heavily fractured but did not completely shatter Lutetia. The current main-belt impact rate suggests that such an impact occurs every ~9 billion years; therefore, the impact may have occurred relatively early in Solar System history, when the collisional environment in the asteroid belt was more intense. The early occurrence of such an impact is in agreement with the crater retention age for Lutetia.

The Baetica region is partially covered by smooth material that is interpreted as ejecta from the 21-km-diameter crater cluster. The images show evidence that older, smaller craters were partially buried by the ejecta. The depth of the ejecta blanket is estimated to be up to ~600 m, based on the depth-to-diameter ratios of these buried craters. The asymmetric shape of the 21-km crater cluster may be the result of internal inhomogeneity. Preexisting planes of weakness in bedrocks may control final crater shapes and facilitate the detachment of blocks and their emplacement within ejecta deposits (*23*). The crater interior (Fig. 2B) shows a great variety of deposits: smooth and fine deposits with boulders, gravitational taluses, and landslide accumulations. Ejecta blocks have been recorded on other asteroids (*13*) and Phobos (*24*). On Lutetia, approximately 200 blocks of up to 300 m in dimension were found around the central crater region alone. Their steep size distribution (a power law equation with an exponent of –5) is comparable to that seen on Eros (*13*). The presence of boulders adjacent to another impact site in the Pannonia region suggests that boulder generation is a common feature of large impacts on Lutetia, and points to excavation of shattered bedrock. The landslides appear to have been emplaced after the boulders and may have been triggered by further impacts.

To investigate the reflectance properties of the surface, OSIRIS obtained images (including several color sequences) at different asteroid rotational phases and over a range of phase angles from 0.15° to 156°. The slope of the phase curve (fig. S5) for phase angles between 5° and 30° is 0.030 mag/° for the 631-nm filter. The Lutetia disk-integrated geometric albedo was measured to be 0.194 ± 0.006 at 631 nm and 0.169 ± 0.009 at 375 nm, giving an average value in the V band (550 nm) of 0.19 ± 0.01 and a Bond albedo of 0.073 ± 0.002.

We computed disk-resolved reflectivity maps at 10° solar phase angle using the three-dimensional shape model and light-scattering theory (*25*) in order to remove the effect of variation in illumination conditions due to the topography (Fig. 4). We detected variations of the surface reflectivity at 647 nm wavelength. The most important variegations are located inside the crater cluster in the Baetica region (Fig. 4A), where reflectivity varies up to 30% between the darkest and brightest areas. Small spatial variations in reflectivity are also present on surrounding terrain (Fig. 4B) but with a much lower contrast. In Baetica, a clear correlation is found with the local surface slope. Landslide flows or possible rock outcrops appear much brighter than the accumulation areas or surrounding cratered terrains. This suggests either a different texture of regolith or that space weathering modified the surface of the oldest areas, whereas young surfaces have been less exposed to solar radiation. Similar variations of reflectivity have been already observed on Eros, where a strong correlation between the spectral slope and the downslope movement of regolith was found (*13*). Disk-integrated spectrophotometry obtained 1 hour before CA reveals a flat and featureless spectrum, with a moderate spectral slope in the visible range (3%/10^3 Å between 536 and 804 nm), in agreement with spectra obtained from the Rosetta Visible InfraRed Thermal Imaging Spectrometer (VIRTIS) (*26*) and ground-based spectra taken at a similar phase angle (fig. S6). These data are consistent with both particular types of carbonaceous chondrite meteorites, namely CO3 and CV3 (*1*, *27*), and enstatite chondrites (ECs) (*28*). Average bulk densities (*8*, *29*) range from 2.96 to 3.03 g/cm^3 for CO and CV meteorites and 3.55 g/cm^3 for ECs. If Lutetia were composed purely of EC material, this would imply a bulk asteroid macroporosity of ~0 to 13% (given the uncertainty range on Lutetia's density). The low densities of COs and CVs preclude the possibility of

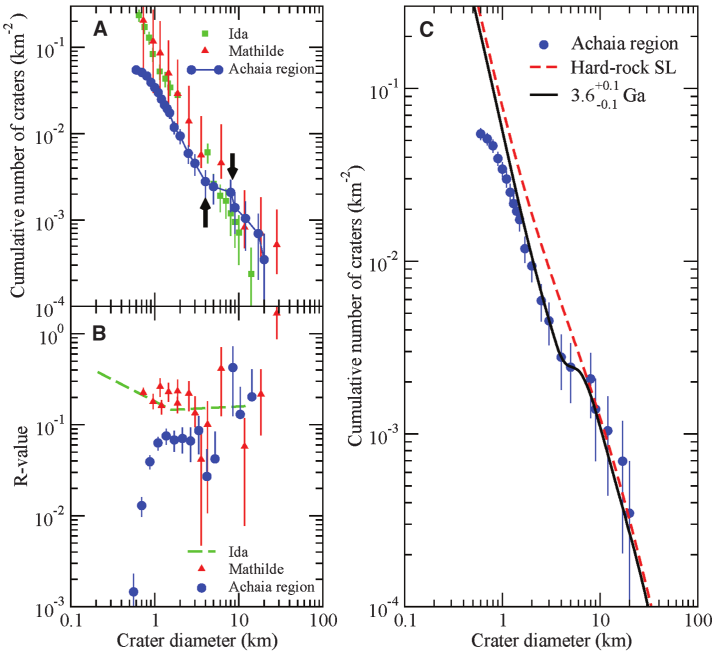

Fig. 3. Crater SFD. (**A**) Cumulative crater SFD of the Achaia region compared with those for Ida and Mathilde, the second- and third-largest asteroids imaged by spacecraft so far, respectively [data from (*17*)]. The arrows indicate the suggested break at 5 to 8 km in the Achaia crater SFD. (**B**) SFD shown in (A) expressed in terms of relative (*R*) values (cumulative crater SFD normalized to a power law with exponent –2). *R* values for Ida are not published, but the overall trend (dashed line) was computed from the published cumulative distribution. (**C**) Achaia crater SFD model fit. The dashed red curve represents a fit of the largest craters of the distribution (diameter > 10 km) obtained using current models for the main-belt asteroid size distribution (*35*) and the crater scaling law (SL) for hard rock (*21*). The black curve is the best fit achieved by a two-layer (fractured material over competent rock) model, which gives a crater retention age of 3.6 ± 0.1 billion years.

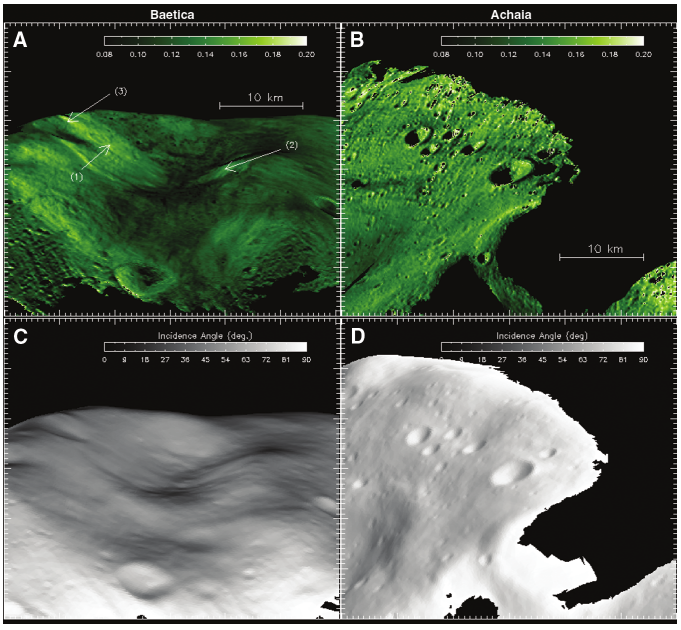

Fig. 4. Slope-corrected reflectivity maps (**A** and **B**) and incidence angle maps (**C** and **D**). These are images at 647 nm of parts of the Baetica [(A) and (C)] and Achaia [(B) and (D)] regions that have been photometrically corrected with Hapke bidirectional reflectance theory (*25*) to remove the effect of different angles of incidence and emission for different local slopes, leaving variations in brightness due only to local albedo variations (resolution, 60 m per pixel). During the photometric correction, the Hapke model parameters describing the single scattering albedo, the coherent backscattering, the shadow hiding, the surface roughness, and the asymmetric factor were all fixed to the value that best reproduced the overall surface reflectivity. The images are corrected to a solar phase angle of 10° for both Baetica and Achaia (the original phase angles for these regions were ~70° to 95°). This phase angle was arbitrarily chosen to avoid the opposition effect that may affect the reflectivity near 0° phase angle. Large variations are visible in the younger Baetica region, whereas the older Achaia region is more uniform (aside from a dark streak associated with a crater in the left of the image). The landslide indicated by 1 and possible outcrops 2 and 3 in Baetica have a reflectivity up to 30% brighter than the accumulation area.

a pure composition of either meteorite group. If Lutetia's surface were made of these materials, this would suggest that the interior may be differentiated (*30*).

These macroporosities for Lutetia clearly exclude a rubble-pile structure, which typically have macroporosities >25 to 30% (*9*). Such a high porosity structure is also inconsistent with the extensive ejecta blankets observed around the large craters (*31*). If Lutetia is undifferentiated, these porosities would also exclude a completely shattered but coherent structure (total porosity in the range of 15 to 25%) (*32*). Partial differentiation (*30*) could permit much higher grain densities in the interior and therefore higher porosity and a heavily fractured body. It is therefore likely that Lutetia has survived the age of the Solar System with its primordial structure intact; i.e., it has not been disrupted by impacts. This interpretation is consistent with the current view that the collisional lifetime against catastrophic destruction of bodies with diameters ≥100 km exceeds the age of the Solar System (*33*). The network of curvilinear features, the crater morphology, and the crater SFD discussed above both indicate that Lutetia's interior has considerable strength and relatively low porosity as compared to that expected for primordial aggregates of fine dust. One possibility is that Lutetia is partially differentiated, with a fractured but unmelted chondritic surface overlaying a higher-density sintered or melted interior (*30*). In any case, Lutetia is closer to a small planetesimal than to the smaller asteroids seen by previous missions, which are thought to be shattered or rubble-pile minor bodies.

References and Notes

1. M. A. Barucci, M. Fulchignoni, in *Rosetta: ESA's Mission to the Origin of the Solar System*, R. Schulz, C. Alexander, H. Boehnhardt, K.-H. Glassmeier, Eds. (Springer, New York, 2009), pp. 55–68.
2. M. Lazzarin *et al.*, *Mon. Not. R. Astron. Soc.* **408**, 1433 (2010).
3. H. U. Keller *et al.*, *Space Sci. Rev.* **128**, 433 (2007).
4. R. W. Gaskell *et al.*, *Meteorit. Planet. Sci.* **43**, 1049 (2008).
5. B. Carry *et al.*, *Astron. Astrophys.* **523**, A94 (2010).
6. M. Kaasalainen, *Inverse Problem and Imaging* **5**, 37 (2011).
7. M. Pätzold *et al.*, *Science* **334**, 491 (2011).
8. G. Consolmagno, D. Britt, R. Macke, *Chemie der Erde Geochemistry* **68**, 1 (2008).
9. We use rubble pile to mean a "strengthless aggregate held together by gravity only," following the definition of (*34*)
10. J. Oberst *et al.*, *Icarus* **209**, 230 (2010).
11. P. Thomas, J. Veverka, A. Bloom, T. Duxbury, *J. Geophys. Res.* **84**, 8457 (1979).
12. J. Veverka *et al.*, *Science* **289**, 2088 (2000).
13. R. J. Sullivan, P. C. Thomas, S. L. Murchie, M. S. Robinson, in *Asteroid III*, W. F. Bottke Jr., A. Cellino, P. Paolicchi, R. P. Binzel, Eds. (Univ. of Arizona Press, Tucson, AZ, 2002), pp. 331–350.
14. A. F. Cheng, in *Asteroid III*, W. F. Bottke Jr., A. Cellino, P. Paolicchi, R. P. Binzel, Eds. (Univ. of Arizona Press, Tucson, AZ, 2002), pp. 351–366.
15. E. Asphaug, *Annu. Rev. Earth Planet. Sci.* **37**, 413 (2009).
16. J. E. Richardson Jr., H. J. Melosh, R. J. Greenberg, D. P. O'Brien, *Icarus* **179**, 325 (2005).
17. D. P. O'Brien, R. Greenberg, J. E. Richardson, *Icarus* **183**, 79 (2006).
18. S. Marchi, M. Massironi, E. Martellato, L. Giacomini, L. M. Prockter, *Planet. Space Sci.*, available at http://arxiv.org/abs/1105.5272.
19. S. Marchi *et al.*, *Planet. Space Sci.* **58**, 1116 (2010).
20. S. Marchi, S. Mottola, G. Cremonese, M. Massironi, E. Martellato, *Astron. J.* **137**, 4936 (2009).
21. K. A. Holsapple, K. R. Housen, *Icarus* **187**, 345 (2007).
22. K. Wünnemann, G. S. Collins, H. J. Melosh, *Icarus* **180**, 514 (2006).
23. H. J. Melosh, in *Impact Cratering—A Geological Process* (Oxford Univ. Press, New York, 1989), p. 84.
24. P. C. Thomas *et al.*, *J. Geophys. Res.* **105**, 15091 (2000).
25. B. Hapke, *Icarus* **157**, 523 (2002).
26. A. Coradini *et al.*, *Science* **334**, 492 (2011).
27. M. A. Barucci *et al.*, *Astron. Astrophys.* **477**, 665 (2008).
28. P. Vernazza *et al.*, *Icarus* **202**, 477 (2009).
29. R. J. Macke, G. J. Consolmagno, D. T. Britt, M. L. Hutson, *Meteorit. Planet. Sci.* **45**, 1513 (2010).
30. L. T. Elkins-Tanton, B. P. Weiss, M. T. Zuber, *Earth Planet. Sci. Lett.* **305**, 1 (2011).
31. K. R. Housen, K. A. Holsapple, *Icarus* **163**, 102 (2003).
32. D. T. Britt, D. Yeomans, K. Housen, G. Consolmagno, in *Asteroid III*, W. F. Bottke Jr., A. Cellino, P. Paolicchi, R. P. Binzel, Eds. (Univ. of Arizona Press, Tucson, AZ, 2002), pp. 485–500.
33. A. Morbidelli, W. F. Bottke, D. Nesvorný, H. F. Levison, *Icarus* **204**, 558 (2009).
34. S. L. Wilkison *et al.*, *Icarus* **155**, 94 (2002).
35. W. F. Bottke Jr. *et al.*, *Icarus* **175**, 111 (2005).

Acknowledgments: OSIRIS was built by a consortium of the Max-Planck-Institut für Sonnensystemforschung, Katlenburg-Lindau, Germany; CISAS–University of Padova, Italy; the Laboratoire d'Astrophysique de Marseille, France; the Instituto de Astrofísica de Andalucia, CSIC, Granada, Spain; the Research and Scientific Support Department of the ESA, Noordwijk, Netherlands; the Instituto Nacional de Técnica Aeroespacial, Madrid, Spain; the Universidad Politéchnica de Madrid, Spain; the Department of Physics and Astronomy of Uppsala University, Sweden; and the Institut für Datentechnik und Kommunikationsnetze der Technischen Universität Braunschweig, Germany. The support of the national funding agencies of Germany (DLR), France (CNES), Italy (ASI), Spain (MEC), Sweden (SNSB), and the ESA Technical Directorate is gratefully acknowledged. We thank the Rosetta Science Operations Centre and the Rosetta Mission Operations Centre for the successful flyby of 21 Lutetia.

Supporting Online Material

www.sciencemag.org/cgi/content/full/334/6055/487/DC1
SOM Text
References (*36*, *37*)

21 April 2011; accepted 21 September 2011
10.1126/science.1207325

LETTER

doi:10.1038/nature12918

Localized sources of water vapour on the dwarf planet (1) Ceres

Michael Küppers[1], Laurence O'Rourke[1], Dominique Bockelée-Morvan[2], Vladimir Zakharov[2], Seungwon Lee[3], Paul von Allmen[3], Benoît Carry[1,4], David Teyssier[1], Anthony Marston[1], Thomas Müller[5], Jacques Crovisier[2], M. Antonietta Barucci[2] & Raphael Moreno[2]

The 'snowline' conventionally divides Solar System objects into dry bodies, ranging out to the main asteroid belt, and icy bodies beyond the belt. Models suggest that some of the icy bodies may have migrated into the asteroid belt[1]. Recent observations indicate the presence of water ice on the surface of some asteroids[2–4], with sublimation[5] a potential reason for the dust activity observed on others. Hydrated minerals have been found[6–8] on the surface of the largest object in the asteroid belt, the dwarf planet (1) Ceres, which is thought to be differentiated into a silicate core with an icy mantle[9–11]. The presence of water vapour around Ceres was suggested by a marginal detection of the photodissociation product of water, hydroxyl (ref. 12), but could not be confirmed by later, more sensitive observations[13]. Here we report the detection of water vapour around Ceres, with at least 10^{26} molecules being produced per second, originating from localized sources that seem to be linked to mid-latitude regions on the surface[14,15]. The water evaporation could be due to comet-like sublimation or to cryo-volcanism, in which volcanoes erupt volatiles such as water instead of molten rocks.

We observed Ceres with the Heterodyne Instrument for the Far Infrared (HIFI)[16] on the European Space Agency's Herschel Space Observatory[17] on four occasions between November 2011 and March 2013 (Extended Data Table 1) as part of the MACH-11 ('Measurements of 11 asteroids and comets with Herschel') guaranteed time programme (principal investigator L.O'R.) and of a follow-up Director's Discretionary Time Program. We used HIFI to search for water vapour directly, because it is more sensitive to water concentrated in the near-Ceres environment than previous instruments used to search for hydroxyl (OH). We observed the water ground-state line at a frequency of 556.936 GHz. The angular diameter of Ceres was <1 arcsec for all observations, compared to the beam width of HIFI, which was approximately 40 arcsec at the frequency of the water line. Although we cannot resolve Ceres spatially, we can derive information about the longitudinal distribution of the water sources on the surface from the variation of the absorption over the rotation of Ceres. Details of observations and data reduction are provided in the Supplementary Information and in Extended Data Table 1.

Figure 1 shows time-averaged spectra taken in October 2012 and on 6 March 2013, normalized to the thermal continuum of Ceres (measured with the expected brightness, see Extended Data Table 2). At the frequency of the water line, absorption in the thermal continuum of Ceres is clearly visible in the late 2012 observations, whereas in the 2013 data it is next to a weaker emission line detected at the 3σ level. The low outflow velocity (0.3–0.7 km s^{-1}) determined from the offset of the absorption line is comparable to the escape velocity of Ceres (about 0.52 km s^{-1}; ref. 18), showing that a fraction of the evaporated water does not escape from Ceres. For line strengths and offset information, see Extended Data Table 3.

The strength of the absorption is variable on short timescales (hours; Fig. 2) as well as on longer timescales (weeks and months; Extended Data Fig. 1 and Extended Data Table 3). We interpret the short-term variation in terms of localized sources on Ceres rotating into and out of the hemisphere visible by Herschel. Figure 2 shows the correlation of the strength of the absorption line with the position of features on the

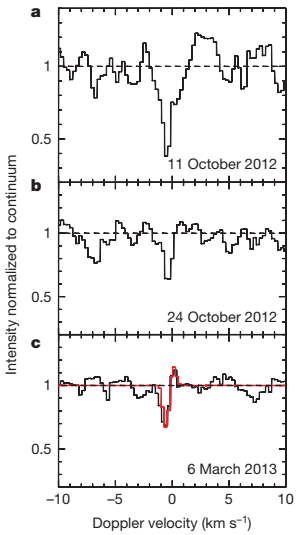

Figure 1 | Submillimetre water absorption line from the dwarf planet (1) Ceres. The spectra of the ground-state transition line 1_{10}–1_{01} of ortho-water at 556.939 GHz were obtained on 11.83–11.92 October 2012 UT (**a**), 24.84–24.96 October 2012 UT (**b**) and 6.13–6.55 March 2013 UT (**c**), with HIFI's Wide-Band Spectrometer. The spectra, which are the averages of the linear H and V polarizations, were divided by the Ceres continuum thermal emission. The abscissa represents the Doppler velocity in the Ceres frame, after correction for the relative motion between Ceres and Herschel. The spectral resolution is 1.1 MHz (0.5 km s^{-1}) with 0.6 MHz sampling. The water line is seen in absorption against the thermal emission of Ceres. Material moving towards the observer causes the absorption line to be blue-shifted. In the 6 March spectrum (**c**), a redshifted emission line is visible next to the blue-shifted absorption line, showing that the exosphere of Ceres extends towards the limbs. The possible polarization of this line is discussed in the Supplementary Information. Overplotted on the 6 March spectrum is a model of the spectrum of the water line for two active spots 60 km in diameter situated on the surface of Ceres (red spectrum in **c**). The simulation takes into account the variation of the sub-observer point longitude during the 10-hour-long observation. The model spectrum is adjusted to the depth of the observed spectrum. The relative strengths of the redshifted and blue-shifted peaks are correctly reproduced.

[1]European Space Agency, European Space Astronomy Centre, PO Box 78, Villanueva de la Cañada 28691, Spain. [2]Laboratoire d'études spatiales et d'instrumentation en astrophysique, Observatoire de Paris, CNRS, Université Pierre et Marie Curie (UPMC), Université Paris-Diderot, 5 Place Jules Janssen, 92195 Meudon, France. [3]Jet Propulsion Laboratory, Pasadena, 4800 Oak Grove Drive, La Cañada Flintridge, California 91011, USA. [4]Institut de Mécanique Céleste et de Calcul des Éphémérides, Observatoire de Paris, Unité Mixte de Recherche (UMR) 8028. CNRS, 77 Avenue Denfert Rochereau, 75014 Paris, France. [5]Max-Planck-Institut für extraterrestrische Physik (MPE), Giessenbachstrasse 1, 85748 Garching, Germany.

RESEARCH LETTER

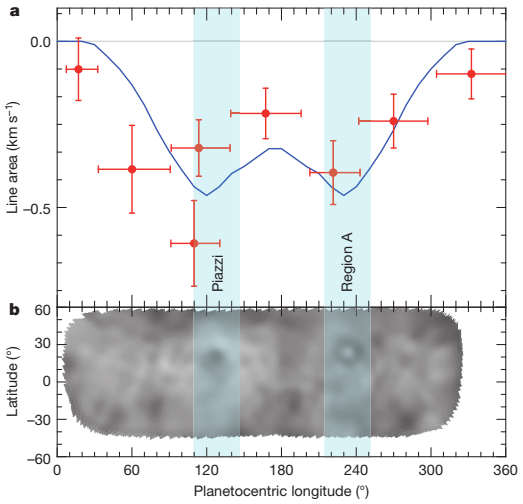

Figure 2 | Variability of water absorption on 6 March 2013. a, Line area of the water absorption line (normalized to the continuum emission of Ceres) at 557 GHz as a function of the longitude of the sub-observer point. Measurements are shown as red dots; error bars on the intensity are 1σ and the horizontal bars show the range of sub-observer longitudes covered by individual measurements. The two conflicting data points at sub-observer point longitude $\Lambda \approx 110°$ were taken within a time interval of 9 hours (corresponding to the rotation period of Ceres), and suggest temporal variability at the regional scale. Vertical bands indicate the planetocentric longitude of the dark regions: Piazzi (longitude, 123°, latitude +21°) and Region A (longitude 231°, latitude +23°)[14,15,19]. The curve in blue is the result of a gas-kinetic model of the exosphere of Ceres[21] (see Supplementary Information). Water is released from localized sources 60 km in diameter situated at the longitudes and latitudes of regions Piazzi and Region A, with a total production rate of 10^{26} molecules per second for each source. The surface temperature of Ceres varies from 235 K (subsolar, that is, when the Sun is at zenith) to 168 K (morning and evening). The excitation and radiative transfer models of the water 1_{10}–1_{01} line include excitation of the vibrational bands by the Sun's infrared radiation, excitation of the rotational lines by thermal radiation from Ceres, collisions with water and self-absorption effects[22] (see Supplementary Information). **b**, A map of Ceres from near-infrared adaptive-optics imaging observations[14]. Piazzi and Region A are seen as dark regions, with a bright centre within Region A.

Ceres surface that are known from ground-based[14,15] and Hubble Space Telescope[19] observations. In all observations that detected water vapour from Ceres, the absorption line strength is strongly correlated with the visibility of surface areas identified as dark regions (about 5% darker than the average surface) in near-infrared observations. We identify those regions as the likely source of most of the evaporating water. A bright region known from observations in the visible region of the spectrum does not appear to contribute. Possibly, the dark regions are warmer than the average surface, resulting in efficient sublimation of small water-ice reservoirs.

Although the small number of observations does not allow a unique interpretation of the long-term variation, the lack of detection of the water line at 2.94 astronomical units (AU; where 1 AU is the mean distance from Earth to the Sun) in November 2011 and its first detection at 2.72 AU are consistent with the steep increase of water-ice sublimation between 3 AU and 2.5 AU (ref. 20). In addition, the larger absorption strength on 11 October 2012 compared to the observations two weeks later and five months later suggests sporadic changes in the water evaporation. Given that the spin axis of Ceres is nearly perpendicular to its orbital plane[14], we expect seasonal variations driven by spin-axis obliquity to contribute little to the variability.

We analysed the water exosphere of Ceres with a gas kinetic Direct Simulation Monte Carlo[21] model (Extended Data Fig. 2) that considers water vapour to be ejected from localized sources, and then to slow down in Ceres' gravity field. To simulate water spectra, we use a state-of-the-art two-dimensional excitation model[22], which considers excitation by radiation from Ceres and the Sun and collisional excitation (see details in Supplementary Information). The temporal variation of the absorption line observed on 6 March 2013 is well described by a model that considers outgassing from two sources coincident with dark regions Piazzi and Region A (Fig. 2). Modelling predicts line emission at positive velocities (Fig. 1), caused by gas expansion from dense to more rarefied regions. The resulting total production rate of about 2×10^{26} molecules (or 6 kg) per second of water requires only a tiny fraction of the Ceres surface to be covered by water ice. The surface of Ceres receives on average a solar input power of approximately 50 W m^{-2} (a quarter of the total solar power at the heliocentric distance of Ceres, with the factor 1/4 being the ratio between the cross-section of Ceres and its surface area). Because Ceres is located in the transition range between the outer Solar System, where most of the solar energy will be re-emitted as thermal radiation, and the inner Solar System, where most of the energy will go into sublimation of the ice, we assume that half of the energy will be used for sublimation. With a latent heat of sublimation of 2.5×10^6 J kg^{-1}, the corresponding sublimation rate is 10^{-5} kg m^{-2} s^{-1}. To sublimate 6 kg s^{-1} of water ice, Ceres must have a surface area covered with water ice of 0.6 km^2, or approximately 10^{-7} of its total surface area. If the activity is restricted to areas with a radius of about 100 km (the approximate size of the identified source regions), the active surface fraction required within those areas is still very small ($<10^{-5}$ of the surface area of the identified source regions).

An unexpected aspect of the data is that the absorption line appears to be strongly linearly polarized in October 2012, whereas no significant polarization was seen in March 2013. See Extended Data Table 3, Extended Data Fig. 3, and Supplementary Information for further analysis.

The measured water production is two orders of magnitudes higher than is predicted from a model of sublimation maintained from water supplied from the interior of Ceres[23]. In addition, the water activity is most probably not concentrated on polar regions, where water ice would be most stable. We propose two mechanisms for maintaining the observed water production on Ceres. The first is cometary-type sublimation of (near) surface ice. In this case the sublimating ice drags near-surface dust with it and in this way locally removes the surface layer and exposes fresh ice. Transport from the interior is not required. The second mechanism is geysers or cryovolcanoes, for which an interior heat source is needed. For Jupiter's satellite Io and Saturn's moon Enceladus the source of activity is dissipation of tidal forces from the planet[24,25]. That can be excluded for Ceres, but some models suggest that a warm layer in the interior heated by long-lived radioisotopes may maintain cryovolcanism on Ceres at the present time (ref. 26 and references therein).

One way of distinguishing between the two mechanisms is to analyse the variation of the water activity of Ceres over its orbit. Taking the activity of main-belt comets as a reference, cometary activity is expected to be concentrated at the perihelion passage[5]. On the other hand, cryovolcanism receives its energy from the interior and so no dependence on heliocentric distance would be seen, although sporadic variations of activity are likely. The currently available data appear to be consistent with the cometary hypothesis, but more observations are needed to distinguish between these possibilities (see Fig. 3).

Although ground- and space-based observations may further map the behaviour of Ceres over its orbit, the Dawn spacecraft mission[27] arriving to orbit Ceres in early 2015 is expected to be key in providing a long-term follow-up on the water outgassing behaviour of Ceres. In particular, it will provide long-term monitoring of the water outgassing concentration and stability of the activity in the dark regions where we suggest that the water-ice mantle of Ceres may reach the surface. Two of the instruments on Dawn—the near-infrared spectrometer (VIR)

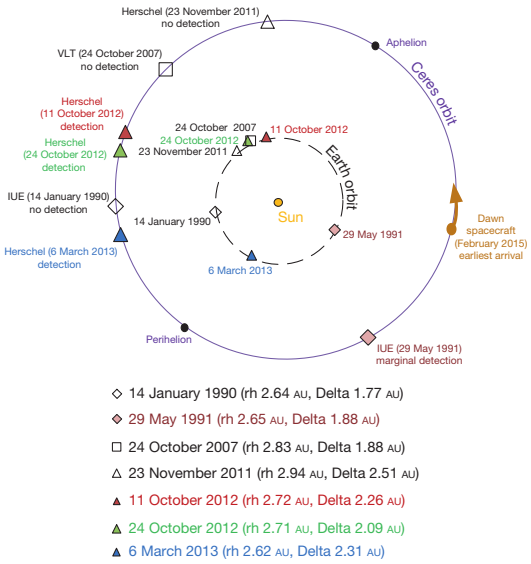

Figure 3 | Water production of Ceres versus position on its orbit. Searches for water activity on Ceres were performed with the International Ultraviolet Explorer (IUE), the Very Large Telescope (VLT), and Herschel. The inner orbit is that of Earth, the outer orbit that of Ceres. rh is the heliocentric distance of Ceres and Delta is the distance between Ceres and the observer. If cometary activity is the source of water on Ceres we would expect the onset of activity to appear well before perihelion before becoming much weaker at some time after perihelion. The pre-perihelion data are consistent with that picture. No activity was detected by VLT and Herschel at less than 2.83 AU; then Herschel detected activity in all observations within 2.72 AU. The non-detection by IUE at almost the same orbital position as one of the Herschel observations three orbital periods earlier can be explained by the higher sensitivity of Herschel for near-equatorial sources. The single observation postperihelion (a marginal detection by IUE) does not allow us to draw conclusions about the behaviour when Ceres is receding from the Sun. Dawn will visit Ceres on the postperihelion arc. The water absorption was strongest in the first Herschel detection on 11 October 2012, well before passing perihelion. To first order this is not what we would expect for cometary activity. It may have been caused by an analogue of a cometary outburst. Alternatively, it could have been a volcanic eruption. In that case, the correlation of the detectability with heliocentric distance may be coincidental. Additional observations are required to distinguish better between different mechanisms for the water activity.

and the gamma ray and neutron detector (GRaND)—may contribute significantly to this task. Although no observations of water are available for the orbital position of Ceres at the time of its arrival (Fig. 3) and the heliocentric distances in the spacecraft's initial few months around Dawn of 2.85–2.95 AU appear to be unfavourable for detecting activity, it may be that the post-perihelion activity is maintained to larger distances.

The identification of more than one water source on Ceres suggests outgassing from a small ice fraction near the surface as opposed to sporadic activity triggered by a singular event like a recent large impact. This supports the idea that Ceres possesses an icy mantle, and it also implies that we have detected water activity in the asteroid main belt. If the water is from cometary sublimation, it demonstrates that activity driven by water sublimation is not limited to classical comets, but is present in the asteroid belt as well. This supports the new vision of our Solar System with a continuum in composition and ice content between asteroid and comet populations[28].

Online Content Any additional Methods, Extended Data display items and Source Data are available in the online version of the paper; references unique to these sections appear only in the online paper.

Received 23 August; accepted 26 November 2013.

1. Walsh, K. J., Morbidelli, A., Raymond, S. N., O'Brien, D. P. & Mandell, A. M. A low mass for Mars from Jupiter's early gas-driven migration. *Nature* **475,** 206–209 (2011).
2. Campins, H. *et al.* Water ice and organics on the surface of the asteroid 24 Themis. *Nature* **464,** 1320–1321 (2010).
3. Rivkin, A. S. & Emery, J. P. Detection of ice and organics on an asteroidal surface. *Nature* **464,** 1322–1323 (2010).
4. Licandro, J. *et al.* (65) Cybele: detection of small silicate grains, water-ice, and organics. *Astron. Astrophys.* **525,** A34 (2011).
5. Jewitt, D. The active asteroids. *Astron. J.* **143,** 66 (2012).
6. Lebofsky, L. A., Feierberg, M. A., Tokunaga, A. T., Larson, H. P. & Johnson, J. R. The 1.7- to 4.2-micron spectrum of asteroid 1 Ceres: evidence for structural water in clay minerals. *Icarus* **48,** 453–459 (1981).
7. King, T. V. V., Clark, R. N., Calvin, W. M., Sherman, D. M. & Brown, R. H. Evidence for ammonium-bearing minerals on Ceres. *Science* **255,** 1551–1553 (1992).
8. Milliken, R. E. & Rivkin, A. S. Brucite and carbonate assemblages from altered olivine-rich materials on Ceres. *Nature Geosci.* **2,** 258–261 (2009).
9. Thomas, P. C. *et al.* Differentiation of the asteroid Ceres as revealed by its shape. *Nature* **437,** 224–226 (2005).
10. McCord, T. B. & Sotin, C. Ceres: evolution and current state. *J. Geophys. Res.* **110,** E05009 (2005).
11. Castillo-Rogez, J. C. & McCord, T. B. Ceres' evolution and present state constrained by shape data. *Icarus* **205,** 443–459 (2010).
12. A'Hearn, M. F. & Feldman, P. D. Water vaporization on Ceres. *Icarus* **98,** 54–60 (1992).
13. Rousselot, P. *et al.* A search for water vaporization on Ceres. *Astron. J.* **142,** 125 (2011).
14. Carry, B. *et al.* Near-infrared mapping and physical properties of the dwarf-planet Ceres. *Astron. Astrophys.* **478,** 235–244 (2008).
15. Carry, B. *et al.* The remarkable surface homogeneity of the Dawn mission target (1) Ceres. *Icarus* **217,** 20–26 (2012).
16. de Graauw, Th *et al.* The Herschel-Heterodyne Instrument for the Far-Infrared (HIFI). *Astron. Astrophys.* **518,** L6 (2010).
17. Pilbratt, G. L. *et al.* Herschel Space Observatory. An ESA facility for far-infrared and submillimetre astronomy. *Astron. Astrophys.* **518,** L1 (2010).
18. Carry, B. Density of asteroids. *Planet. Space Sci.* **73,** 98–118 (2012).
19. Li, J.-Y. *et al.* Photometric analysis of 1 Ceres and surface mapping from HST observations. *Icarus* **182,** 143–160 (2006).
20. Biver, N. *et al.* The 1995–2002 long-term monitoring of comet C/1995 O1 (Hale–Bopp) at radio wavelength. *Earth Moon Planets* **90,** 5–14 (2002).
21. Crifo, J. F., Loukianov, G. A., Rodionov, A. V. & Zakharov, V. V. Comparison between Navier–Stokes and direct Monte-Carlo simulations of the circumnuclear coma I. Homogeneous, spherical sources. *Icarus* **156,** 249–268 (2002).
22. Zakharov, V., Bockelée-Morvan, D., Biver, N., Crovisier, J. & Lecacheux, A. Radiative transfer simulation of water rotational excitation in comets. Comparison of the Monte Carlo and escape probability methods. *Astron. Astrophys.* **473,** 303–310 (2007).
23. Fanale, F. P. & Salvail, J. R. The water regime of asteroid (1) Ceres. *Icarus* **82,** 97–110 (1989).
24. Peale, S. J., Cassen, P. & Reynolds, R. T. Melting of Io by tidal dissipation. *Science* **203,** 892–894 (1979).
25. Howett, C. J. A., Spencer, J. R., Pearl, J. & Segura, M. High heat flow from Enceladus' south polar region measured using 10–600 cm-1 Cassini/CIRS data. *J. Geophys. Res.* **116,** E03003 (2011).
26. McCord, T. B., Castillo-Rogez, J. & Rivkin, A. Ceres: its origin, evolution and structure and *Dawn's* potential contribution. *Space Sci. Rev.* **163,** 63–76 (2011).
27. Russell, C. T. & Raymond, C. A. The Dawn mission to Vesta and Ceres. *Space Sci. Rev.* **163,** 3–23 (2011).
28. Gounelle, M. *et al.* in *The Solar System Beyond Neptune* (eds Barucci, M. A., Boehnhardt, H., Cruikshank, D. P. & Morbidelli, A.) 525–541 (Univ. Arizona Press, 2008).

Supplementary Information is available in the online version of the paper.

Acknowledgements Herschel is an ESA space observatory with science instruments provided by European-led principal investigator consortia and with important participation by NASA. The HIFI was designed and built by a consortium of institutes and university departments from across Europe, Canada and the United States under the leadership of SRON, the Netherlands Institute for Space Research, and with major contributions from Germany, France and the USA. This development was supported by national funding agencies: CEA, CNES, CNRS (France); ASI (Italy); and DLR (Germany). Additional funding support for some instrument activities was provided by the ESA. We thank the team at the Herschel Science Centre for their flexibility in scheduling the observations. We thank the Herschel Project Scientist and the Time Allocation Committee for the allocation of Director Discretionary Time. B.C. acknowledges support from the faculty of the European Space Astronomy Centre (ESAC). We thank A. Pollock for proofreading the final text.

Author Contributions M.K. proposed the observations of Ceres with HIFI as part of L.O'R.'s MACH-11 Guaranteed Time Program. M.K., L.O'R., D.B.-M., B.C., D.T. and A.M. planned the observations. M.K., D.B.-M., B.C., D.T., R.M. and J.C. contributed to the data analysis. The modelling was performed by D.B.-M., V.Z., S.L., P.v.A. and T.M. The manuscript was written by M.K., L.O'R., D.B.-M., B.C. and M.A.B. All authors discussed the results and reviewed the manuscript.

Author Information Reprints and permissions information is available at www.nature.com/reprints. The authors declare no competing financial interests. Readers are welcome to comment on the online version of the paper. Correspondence and requests for materials should be addressed to M.K. (michael.kueppers@sciops.esa.int).

Icarus 226 (2013) 723–741

Contents lists available at SciVerse ScienceDirect

Icarus

journal homepage: www.elsevier.com/locate/icarus

The taxonomic distribution of asteroids from multi-filter all-sky photometric surveys

F.E. DeMeo [a,*], B. Carry [b,c]

[a] Department of Earth, Atmospheric and Planetary Sciences, MIT, 77 Massachusetts Avenue, Cambridge, MA 02139, USA
[b] Institut de Mécanique Céleste et de Calcul des Éphémérides, Observatoire de Paris, UMR8028 CNRS, 77 Avenue Denfert-Rochereau, 75014 Paris, France
[c] European Space Astronomy Centre, ESA, P.O. Box 78, 28691 Villanueva de la Cañada, Madrid, Spain

ARTICLE INFO

Article history:
Received 6 April 2013
Revised 4 June 2013
Accepted 24 June 2013
Available online 4 July 2013

Keywords:
Asteroids, Surfaces
Asteroids, Composition
Spectrophotometry

ABSTRACT

The distribution of asteroids across the main belt has been studied for decades to understand the current compositional distribution and what that tells us about the formation and evolution of our Solar System. All-sky surveys now provide orders of magnitude more data than targeted surveys. We present a method to bias-correct the asteroid population observed in the Sloan Digital Sky Survey (SDSS) according to size, distance, and albedo. We taxonomically classify this dataset consistent with the Bus and Binzel (Bus, S.J., Binzel, R.P. [2002]. Icarus 158, 146–177) and Bus–DeMeo et al. (DeMeo, F.E., Binzel, R.P., Slivan, S.M., Bus, S.J. [2009]. Icarus 202(July), 160–180) systems and present the resulting taxonomic distribution. The dataset includes asteroids as small as 5 km, a factor of three in diameter smaller than in previous work such as by Mothé-Diniz et al. (Mothé-Diniz, T., Carvano, J.M.Á., Lazzaro, D. [2003]. Icarus 162(March), 10–21). Because of the wide range of sizes in our sample, we present the distribution by number, surface area, volume, and mass whereas previous work was exclusively by number. While the distribution by number is a useful quantity and has been used for decades, these additional quantities provide new insights into the distribution of total material. We find evidence for D-types in the inner main belt where they are unexpected according to dynamical models of implantation of bodies from the outer Solar System into the inner Solar System during planetary migration (Levison, H.F., Bottke, W.F., Gounelle, M., Morbidelli, A., Nesvorný, D., Tsiganis, K. [2009]. Nature 460(July), 364–366). We find no evidence of S-types or other unexpected classes among Trojans and Hildas, albeit a bias favoring such a detection. Finally, we estimate for the first time the total amount of material of each class in the inner Solar System. The main belt's most massive classes are C, B, P, V and S in decreasing order. Excluding the four most massive asteroids, (1) Ceres, (2) Pallas, (4) Vesta and (10) Hygiea that heavily skew the values, primitive material (C-, P-types) account for more than half main-belt and Trojan asteroids by mass, most of the remaining mass being in the S-types. All the other classes are minor contributors to the material between Mars and Jupiter.

1. Introduction

The current compositional makeup and distribution of bodies in the asteroid belt is both a remnant of our early Solar System's primordial composition and temperature gradient and its subsequent physical and dynamical evolution. The distribution of material of different compositions has been studied based on photometric color and spectroscopic studies of ~2,000 bodies in visible and near-infrared wavelengths (Chapman et al., 1971, 1975; Gradie and Tedesco, 1982; Gradie et al., 1989; Bus, 1999; Bus and Binzel, 2002a; Mothé-Diniz et al., 2003). These data were based on all available spectral data at the time the work was performed including spectral surveys such as Tholen (1984), Zellner et al. (1985), Barucci et al. (1987), Xu et al. (1995), Bus and Binzel (2002a), Lazzaro et al. (2004).

The first in-depth study showing the significance of global trends across the belt looked at surface reflectivity (albedo) and spectrometric measurements of 110 asteroids. It was then that the dominant trend in the belt was found: S-types are more abundant in the part of the belt closer to the Sun and the C-types further out (Chapman et al., 1975). Later work by Gradie and Tedesco (1982) and Gradie et al. (1989) revealed clear trends for each of the major classes of asteroids, concluding that each group formed close to its current location.

The Small Main-belt Asteroid Spectroscopic Survey (SMASSII, Bus and Binzel, 2002b) measured visible spectra for 1447 asteroids and the Small Solar System Objects Spectroscopic Survey (S3OS2) observed 820 asteroids (Lazzaro et al., 2004). The conclusion of

* Corresponding author.
E-mail address: fdemeo@mit.edu (F.E. DeMeo).

0019-1035/$ - see front matter © 2013 Elsevier Inc. All rights reserved.
http://dx.doi.org/10.1016/j.icarus.2013.06.027

these major spectral surveys brought new discoveries and views of the main belt. Bus and Binzel (2002b) found the distribution to be largely consistent with Gradie and Tedesco (1982), however they noted more finer detail within the S and C complex distributions, particularly a secondary peak for C-types at 2.6 AU and for S-types at 2.85 AU. Mothé-Diniz et al. (2003) combined data from multiple spectral surveys looking at over 2000 asteroids with H magnitudes smaller than 13 ($D \sim 15$ km for the lowest albedo objects). Their work differed from early surveys finding that S-types continued to be abundant at further distances, particularly at the smaller size range covered in their work rather than the steep dropoff other surveys noted.

Only in the past decade have large surveys at visible and mid-infrared wavelengths been available allowing us to tap into the compositional detail of the million or so asteroids greater than 1 km that are expected to exist in the belt (Bottke et al., 2005). The results of these surveys (including discovery surveys), however, are heavily biased toward the closest, largest, and brightest of asteroids. This distorts our overall picture of the belt and affects subsequent interpretation.

In this work we focus on the data from the Sloan Digital Sky Survey Moving Object Catalog (SDSS, MOC, Ivezić et al., 2001, 2002) that observed over 100,000 unique asteroids in five photometric bands over visible wavelengths. These bands provide enough information to broadly classify these objects taxonomically (e.g., Carvano et al., 2011). In this work we refer to the SDSS MOC as SDSS for simplicity. We classify the SDSS data and determine the distribution of asteroids in the main belt. We present a method to correct for the survey's bias against the dimmest, furthest bodies.

Traditionally, the asteroid compositional distribution has been shown as the number objects of each taxonomic type as function of distance. While the number distribution is important for size–frequency distributions and understanding the collisional environment in the asteroid belt, the concern with this method is that objects of very different sizes are weighted equally. For example, objects with diameters ranging from 15 km to greater than 500 km were assigned equal importance in previous works. This is particularly troublesome for SDSS and other large surveys because the distribution by number further misrepresents the amount of material of each class by equally weighting objects that differ by two orders of magnitude in diameter and by six orders of magnitude in volume. To create a more realistic and comprehensive view of the asteroid belt we provide the taxonomic distribution according to number, surface area, volume, and mass. New challenges are presented when attempting to create these distributions including the inability to account for the smallest objects (below the efficiency limit of SDSS), the incompleteness of SDSS even at size ranges where the survey is efficient, and incomplete knowledge of the exact diameters, albedos and densities of each object. We attempt to correct for as many of these issues as possible in the present study.

The distribution according to surface area is perhaps the most technically correct result because only the surfaces of these bodies are measured. We only have indirect information about asteroid interiors, mainly derived from the comparison of their bulk density with that of their surface material, suggesting differentiation in some cases, and presence of voids in others (e.g., Consolmagno et al., 2008; Carry, 2012). The homogeneity in surface reflectance and albedo of asteroids pertaining to dynamical families (e.g., Ivezić et al., 2002; Cellino et al., 2002; Parker et al., 2008; Carruba et al., 2013) however suggest that most asteroids have an interior composition similar to their surface composition. Nevertheless, recent models find that large bodies even though masked with fairly primitive surfaces could actually have differentiated interiors (Elkins-Tanton et al., 2011; Weiss et al., 2012). The distribution of surface area is relevant for dust creation from non-catastrophic collisions (e.g. Nesvorný et al., 2006, 2008) and from a resource standpoint such as for mining materials on asteroid surfaces. The volume of material provides context for the total amount of material in the asteroid belt with surfaces of a given taxonomic class. While we do not know the actual composition or properties of the interiors we can at least account for the material that exists.

The most ideal case is to determine the distribution of *mass*. This view accounts for all of the material in the belt, corrects for composition and porosity of the interior and properly weights the relative importance of each asteroid according to size and density. While the field is a long way away from having perfectly detailed shape and density measurements for every asteroid, by applying estimated sizes and average densities per taxonomic class to a large, statistical sample, we provide in this work the first look at the distribution of classes in the asteroid belt according to mass, and estimate the total amount of material each class represents in the inner Solar System.

Section 2 introduces the data used for this work. We overview observing biases and our correction method in Sections 3 and 4. We describe our classification method for our sample in Section 5. We then explain in Section 6 our method for building the compositional distribution and application of our dataset to all asteroids in the main belt. Finally, we present in Section 7 the bias-corrected taxonomic distribution of asteroid material across the main belt according to number, surface area, volume, and mass, and discuss the results in Section 8.

2. The dataset

2.1. Selection of high quality measurements from SDSS

The Sloan Digital Sky Survey (SDSS) is an imaging **and spectroscopy** survey dedicated to observing galaxies and quasars (Ivezić et al., 2001). The images are taken in five filters, u′, g′, r′, i′, and z′, from 0.3 to 1.0 μm. The survey also observed over 400,000 moving objects in our Solar System of which over 100,000 are unique objects linked to known asteroids. The current release of the Moving Object Catalogue (SDSS MOC 4, Ivezić et al., 2002) includes observations through March 2007.

We restrict our sample from the SDSS MOC database according to the following criteria. First, we keep only objects assigned a number or a provisional designation, i.e., those for which we can retrieve the orbital elements. We then remove observations that are deemed unreliable: with any apparent magnitudes greater than 22.0, 22.2, 22.2, 21.3, 20.5 for each filter (5.9% of the SDSS MOC4), which are the limiting magnitudes for 95% completeness (Ivezić et al., 2001), or any photometric uncertainty greater than 0.05 (excluding the u′ filter, explained below). These constraints remove a very large portion of the SDSS dataset (about 87% of all observations), largely due to the greater typical error for the z′ filter. While there is only a small subset of the sample remaining (Fig. 1), we are assured of the quality of the data. Additionally, for higher errors, the ambiguity among taxonomic classes possible for an object becomes so great that any classification becomes essentially meaningless. We exclude the u′ filter from this work primarily because of the significantly higher errors in this filter compared to the others (Fig. 2), and secondarily because neither the Bus nor Bus–DeMeo taxonomies (that we use as reference for classification consistency, Bus and Binzel, 2002a; DeMeo et al., 2009) covered that wavelength range.

The fourth release of the MOC contains non-photometric nights in the dataset. The SDSS provides data checks that indicate

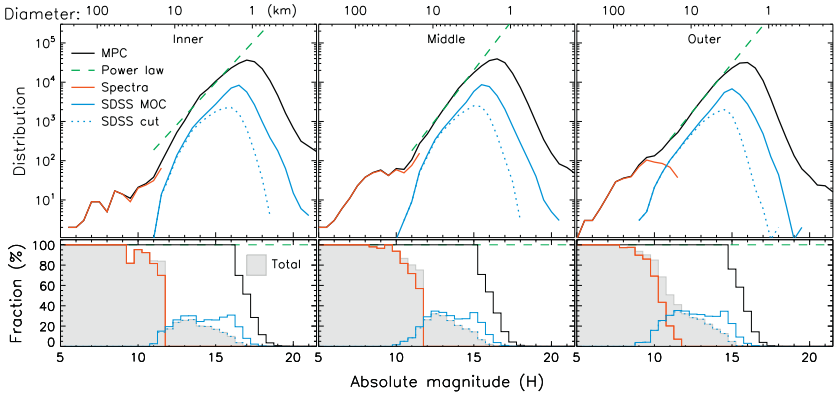

Fig. 1. Number (top) and fraction (bottom) of all asteroids discovered (solid black) and observed by spectroscopic surveys (red), or SDSS MOC (blue) in each zone of the main belt. The subset of SDSS MOC we used here (with cuts applied to photometry, see Section 2.1) is shown in dotted blue. The completeness of discovered asteroids at each size range is determined by extrapolating the expected population using a power law fit (dashed green) to the MPC list of discovered asteroids (solid black). The power law indices calculated in this work (see Section 6.3) for the IMB, MMB, and OMB (determined over the H magnitude range 14–16, 13–15, and 12–14.5) are −2.15, −2.57, and −2.42, respectively. In the bottom panel the total fraction of the sample (before bias correction) is shaded in gray. (For interpretation of the references to color in this figure legend, the reader is referred to the web version of this article.)

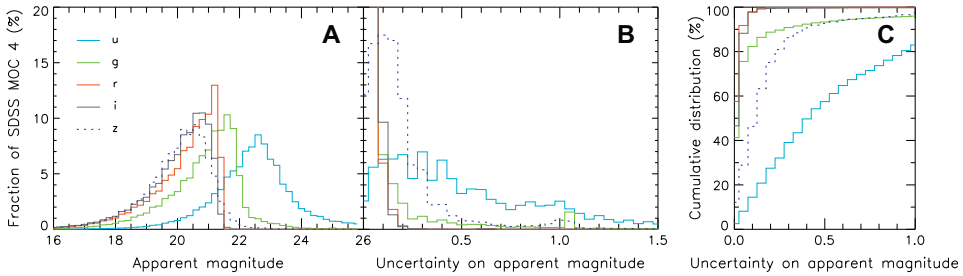

Fig. 2. Distribution of the apparent magnitude (A) and associated uncertainty (B) for all the SDSS MOC4 observations (471,569). The larger uncertainty affecting the observations in the u′ filter (C) precludes any reliable classification information to be retrieved from this filter.

potential problems with the measurements,[1] and we thus remove observations with flags relevant to moving objects and good photometry: `edge`, `badsky`, `peaks too close`, `not checked`, `binned4`, `nodeblend`, `deblend degenerate`, `bad moving fit`, `too few good detections`, and `stationary`. These flags note issues such as data where objects were too close to the edge of the frame, the peaks from two objects were too close to be deblended, the object was detected only in a 4 × 4 binned frame, or the object was not detected as moving. Further details of the flags are provided on the websites in the footnotes. The presence of these flags does not necessary imply problematic data, but because the observations removed due to these flags represent a small percentage of the total objects that fall within the magnitude and photometric error constraints (∼2%), we prefer to slightly restrict the sample than to contaminate it. Of the 471,569 observations in MOC4 we have a sample of 58,607 observations after applying the selection criteria. We keep observations that are flagged as having interpolation (37% of our sample), including `psf flux interp` (26% of our sample) which indicates that over 20% of the point spread function flux is interpolated. We also include observations corrected for cosmic rays (6.5%) and those that might have a cosmic ray but are uncorrected (1.5%). Anyone wishing to use the SDSS data or classification results to analyze particular objects rather than large populations is cautioned to note all flags associated with an observation.

[1] http://www.sdss.org/dr4/products/catalogs/flags.html, http://www.sdss.org/dr4/products/catalogs/flags_detail.html, http://www.sdss.org/dr7/tutorials/flags/index.html, http://www.astro.washington.edu/users/ivezic/sdssmoc/moving_flags.txt.

2.2. Average albedo of each taxonomic class

There have been recent efforts to determine average albedos per taxonomic class (Ryan et al., 2010; Usui et al., 2011; Masiero et al., 2011). These results can be used to more accurately estimate the diameter of a body of a given taxonomic class. In some cases, however, the results disagree by more than the reported uncertainties (e.g., B-types, see Table 1). We calculate mean values, weighted by the number of albedos determined and their accuracy, for each taxonomic class for this work based on averages reported from previously published results (Ryan et al., 2010; Usui et al., 2011; Masiero et al., 2011). See Table 1 for a summary of published values and the averages we use in this work. It must also be noted that the average albedo per class does not necessarily represent the actual albedo for any particular

Table 1
Summary of albedo determination for asteroids listed in DeMeo et al. (2009) based on radiometry, using data from IRAS (Ryan et al., 2010), AKARI (Usui et al., 2011), and WISE (Masiero et al., 2011) infrared satellites. The two columns for IRAS correspond to two different thermal models applied to the data set (STM and NEATM, see Ryan et al., 2010, for details). The mean albedo (last column) is obtained by averaging all the determinations, weighted by their accuracy and number.

Class	IRAS			AKARI		WISE		Average
	#	a_{STM}	a_{NEATM}	#	a	#	a	a
A	4	0.26 ± 0.12	0.18 ± 0.04	6	0.23 ± 0.06	5	0.19 ± 0.03	0.20 ± 0.03
B	2	0.26 ± 0.13	0.08 ± 0.09	3	0.14 ± 0.03	2	0.12 ± 0.02	0.14 ± 0.04
C	42	0.08 ± 0.02	0.06 ± 0.01	44	0.06 ± 0.03	32	0.06 ± 0.03	0.06 ± 0.01
D	11	0.08 ± 0.03	0.07 ± 0.03	14	0.06 ± 0.03	13	0.05 ± 0.03	0.06 ± 0.01
K	12	0.16 ± 0.07	0.12 ± 0.04	14	0.14 ± 0.04	11	0.13 ± 0.06	0.14 ± 0.02
L	12	0.14 ± 0.04	0.11 ± 0.04	16	0.12 ± 0.04	19	0.15 ± 0.07	0.13 ± 0.01
Q	1	0.51 ± 0.10	0.41 ± 0.08	1	0.28 ± 0.01	1	0.15 ± 0.03	0.27 ± 0.08
S	50	0.26 ± 0.06	0.20 ± 0.06	104	0.23 ± 0.05	121	0.22 ± 0.07	0.23 ± 0.02
V	1	0.37 ± 0.08	0.35 ± 0.07	1	0.34 ± 0.01	8	0.36 ± 0.10	0.35 ± 0.01

object because albedo may vary greatly among each class (e.g., Masiero et al., 2011).

The X class is divided into three classes, E, M, and P, distinguished solely by their albedo ($P < 0.075$, $0.075 < M < 0.30$, $E > 0.30$). We calculate average albedo in each class from the roughly 2,000 objects in our sample that have WISE, AKARI, or IRAS albedos. We find average albedos of 0.45, 0.14, and 0.05 for E, M, and P, respectively. Because the average albedo for a given class is calculated solely using objects with spectral data, and the spectral measurements are biased toward brighter, higher albedo objects, this average could consequently be biased toward higher albedos.

2.3. Average density of each taxonomic class

To convert from number of objects to mass, the average density for each class is crucial. Recently, an order of magnitude improvement of the sample of **asteroid** density estimates to 287 allowed the computation of the average density for each taxonomic class (Carry, 2012). In that work, multiple average densities are reported depending on the cutoff quality of measurements included. For the densities used in this work we chose the average densities using only the highest quality measurements (despite the smaller sample size). While these values are certainly an improvement over assuming the same density for all asteroids, there is still significant uncertainty in the real densities for any single object, and there is likely a correlation between density and size particularly due to differences in macroporosity (see Carry (2012) for details). Because we use such a large sample, the differences between any single asteroid and the average should have only a minor effect on the outcome.

For E, M, and P class objects no average density was reported in Carry (2012). In this work we take all objects with densities in each of those classes and calculate average densities for each class. We find densities of $\rho_E = 2.8 \pm 1.2, \rho_M = 3.5 \pm 1.0$, and $\rho_P = 2.7 \pm 1.6$ g/cm^3. The density of M-types is the highest which is consistent with the current interpretation for their composition. Some objects in that class are thought to be metallic, and to contain significant amounts of dense iron (e.g., Gaffey et al., 1989; Lipschutz et al., 1989; Bell et al., 1989). However, the M-class is degenerate in both visible spectrum and geometric albedo because multiple kinds of asteroids are known to fall in that category each having different composition and density (see Rivkin et al., 2000; Shepard et al., 2008; Ockert-Bell et al., 2010 among others.) Not enough data are available to confidently distinguish the distributions of the different objects falling in the M-class so we group them together in this work. Additionally, as no density measurements are available for the D class, we assign an average density of 1 g/cm^3, a density consistent with comets and transneptunian objects from the outer Solar System (Carry, 2012).

3. Observing biases

Asteroid observations over visible wavelengths are subject to multiple biases, and the SDSS dataset is no exception. Detection biases for automatic surveys (relevant to discovery surveys as well as SDSS) are due to properties of the asteroid (such as size, albedo, and distance), the physical equipment (such as telescope size and CCD quality), the scan pattern of the sky, and the software's automatic detection algorithm. For a thorough description of asteroid observing biases see Jedicke et al., 2002.

Efforts to correct the observed asteroid distribution from observing biases have been undertaken for decades (Chapman et al., 1971; Kiang, 1971; Gradie and Tedesco, 1982; Gradie et al., 1989; Bus, 1999; Stuart et al., 2004). One of the most significant is a bias toward observing objects with the highest apparent brightness (objects that are larger, closer, or have a higher surface albedo). This bias is particularly important for the smallest asteroids, where the incompleteness of observed versus as-yet undiscovered asteroids is considerable for any magnitude-limited survey.

The basis of relating the information in the given dataset to the entire suite of asteroids done here is fundamentally the same as in most previous work, however, it is executed slightly differently. In previous work (e.g., Kiang, 1971; Chapman et al., 1971, 1975; Gradie and Tedesco, 1982; Zellner et al., 1985; Bus, 1999; Bus and Binzel, 2002b; Mothé-Diniz et al., 2003) the asteroid belt is broken up into bins based on orbital elements (typically semi-major axis but some works include inclination as well) and brightness (earlier works used the apparent magnitude in V but later works used the absolute magnitude H). A correction factor is calculated as the total discovered numbered objects in each bin divided by the total number of objects in each bin in the given dataset. Each object in the dataset is then multiplied by the appropriate correction factor.

In this work we determine the fraction of each taxonomic class in each bin from our dataset and apply those fractions to the total number of discovered objects. These methods are most accurate if the original dataset is essentially an unbiased dataset and assume the relative fractions in each bin in the given dataset represent the actual relative fractions of all asteroids. We describe in this work many steps to both minimize bias in the dataset and to most accurately compare objects of similar size. These include using the average albedo per taxonomic class to move from an H magnitude-limited to diameter -limited sample and correcting for discovery incompleteness at large H magnitudes. This work accounts for both the sensitivity difference between the inner and outer parts of the belt and uses a dataset sensitive enough to probe to very small sizes.

Many of the previous spectroscopic surveys were subject to a target selection bias. These surveys focused more heavily on objects within asteroid families making the sample weighted more

strongly toward these objects. Previous work included a correction for these biases (e.g., Bus and Binzel, 2002a; Mothé-Diniz et al., 2003). However, because the SDSS is an **automated** survey that does not specifically target any type of objects or region of the belt it does not have the bias of many of the asteroid spectroscopic surveys that targeted specific regions.

It is also arguable that, even after correcting for this selection bias, counting family members overweights the importance of the original parent body in terms of overall compositional distribution. Even with an ideal, unbiased dataset, if one counts each asteroid with an equal weight (for example, by number) the compositional distribution will be heavily weighted toward the asteroid families even though all the family members are essentially of the same composition and originate from the same body. This is fine for studies of number distributions, but not for the distribution of total material. A way to mitigate this oversampling of families is to explore the distribution in terms of volume or mass as explained in the introduction. In this case we are counting all contributed material of the family; in essence we are putting the ejected fragments back together again and accounting for the total amount of material.

Accounting for the bias amongst the smallest asteroids is common to many datasets. Unique to SDSS compared to previous spectroscopic work is the bias against observing the largest, brightest asteroids because they saturated the SDSS detector. Any study of the SDSS sample would need to correct for the missing large asteroids.

4. Defining the least-biased subset

4.1. Corrections for the largest, brightest asteroids

SDSS did not have the capability to measure the largest, brightest asteroids. Conveniently, past spectroscopic surveys are nearly complete at these sizes and fill in that gap (Fig. 1).

We include the taxonomic classes for 1488 asteroids with an absolute magnitude H < 12 determined using spectroscopic measurements in the visible wavelengths (Zellner et al., 1985; Bus and Binzel, 2002b; Lazzaro et al., 2004; DeMeo et al., 2009), available on the Planetary Data System (Neese, 2010). We keep only the large objects from these surveys where spectroscopic sampling is nearly complete (>90%). The smaller objects in the spectroscopic surveys (H > 12) were not included in this work because they are more subject to observing biases and selection criteria (Mothé-Diniz et al., 2003). If an object was observed both in the spectroscopic surveys and the SDSS dataset, we use the data and classification from the spectroscopic surveys.

4.2. Corrections for the smallest, dimmest asteroids

Rather than extrapolating into regions in which we have no data that could misrepresent reality, we instead remove the biased portions of the data. We determine the size of the smallest, dark asteroid at a far distance (in this case, the outer belt) at which the SDSS survey is highly efficient. This number is based on the magnitude limits given by Ivezić et al. (2001) and the turnover in objects detected in the survey as a function of size (described in the next paragraph). We then remove any asteroids from the sample that are smaller than that limit. In essence, we create a sample restricted by a physical rather than an observable quantity: a diameter-limited instead of an apparent magnitude-limited sample.

Taking the SDSS sample, we determine the largest absolute magnitude (H) at which the survey is sensitive for each zone. We present in Fig. 1 the number of objects and fraction of the sample covered by the spectroscopic surveys as well as the fraction the SDSS covers relative to all discovered and undiscovered asteroids for a large range of absolute magnitudes. The peak of the black solid line in Fig. 1 represents the limit of discovery efficiency for zones of the main belt. The cutoff magnitudes are roughly 17.2, 16.5, 15.5, 14.5, and 12.5 for the inner (IMB), middle (MMB), and outer main belt (OMB), Cybeles and Hildas, and Trojans, respectively.

We use these absolute magnitude limits to define the asteroid size range for which a distribution study can be reasonably confident. The smallest size sampled among all asteroid types is limited by the darkest, farthest objects (P-type, see Table 2). For our sample we use the outer main belt to determine our size cutoff. It would be preferable to use the Hilda or Trojan regions, because then we explore the same size range from the main belt out to the Trojans. However, this would drastically limit our sample size. It is thus important to recognize that our results do not contain Hildas and Trojans down to as small sizes as in the main belt. In our sample, the number of Hildas and Trojans is severely biased toward larger sizes, however, because these populations contain asteroids all with similarly low albedos (Grav et al., 2011, 2012a,b) there is no significant bias on the relative number of bodies of each taxonomic class. For this reason we include the Hildas and Trojans in the present work.

The smallest P-type asteroids the SDSS surveyed in the OMB have H = 15.5 which represents a diameter of ~5 km. While we sample, for example, S-types in the outer belt and C-types in the inner belt with diameters of ~2 km and S- and V-types in the inner belt to 1 km or less, including these smaller objects in our sample would bias the results in terms of number toward these smaller objects that are not sampled in the outer belt. Instead we include in our sample only objects that are 5 km or larger. This size is equivalent to a different H magnitude for each class. The ratio of each taxonomic class' albedo (a_i, where i is the taxonomic class) with the P-type albedo (a_P) can be used to determine the magnitude difference between same-size objects of different taxonomic classes using the equation

$$H_i - H_P = 2.5 \log \frac{a_P}{a_i} \quad (1)$$

We cut the sample of each taxonomic class according to these H magnitude limits, which are listed in Table 2. The average albedo for each class was determined by taking the average of the albedo determined for each class from IRAS, AKARI, and WISE (Ryan et al., 2010; Usui et al., 2011; Masiero et al., 2011, see Section 2.2). Using a different H magnitude for each taxonomic class is critical. If we cut our sample at H = 15.5 for all objects we would be comparing, for example, 5 km P-types to 2 km S-types, which are much more numerous owing to the steep size–frequency distribution of the asteroid population.

Table 2
Cuts on the absolute magnitude for each taxonomic class. These cutoffs were determined by the limiting case of P-type asteroids in the outer belt. Average density (in g/cm^3, from Carry, 2012) and albedo (see Section 2.2) are also reported. We choose a density of D-types of 1 g/cm^3, consistent with an outer Solar System origin because no D-type densities have been accurately measured.

Class	H_{cut}	Density	Albedo
A	13.99	3.73 ± 1.40	0.20 ± 0.03
B	14.38	2.38 ± 0.45	0.14 ± 0.04
C	15.30	1.33 ± 0.58	0.06 ± 0.01
D	15.30	1.00 ± 1.00	0.06 ± 0.01
K	14.38	3.54 ± 0.21	0.14 ± 0.02
L	14.46	3.22 ± 0.97	0.13 ± 0.01
S	13.84	2.72 ± 0.54	0.23 ± 0.02
V	13.39	1.93 ± 1.07	0.35 ± 0.01
E	13.12	2.67 ± 1.20	0.45 ± 0.21
M	14.49	3.49 ± 1.00	0.13 ± 0.05
P	15.50	2.84 ± 1.60	0.05 ± 0.01

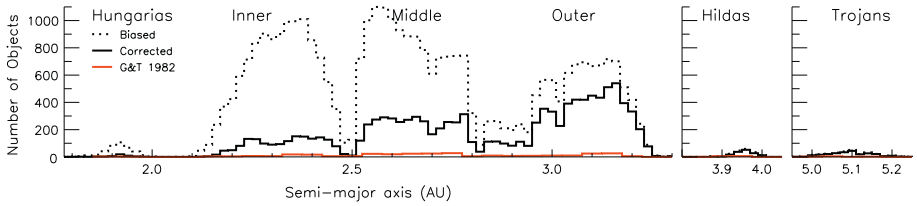

Fig. 3. Number of asteroids as a function of heliocentric distance for three different samples: our original sample made of spectroscopic surveys and SDSS photometry (34,503 asteroids, dashed line), our bias-corrected sample (13,211 solid line), and the sample of 656 taxonomically classified asteroids from Gradie and Tedesco (1982).

The size of the SDSS sample before and after the bias-correction selection is shown in Fig. 3,, together with the number of objects presented in the preceding work by Gradie and Tedesco (1982). It is clear that a vast number of objects are removed from the inner and middle sections of the belt because they are below the critical size limit. To give an estimate on the importance of this size correction, there are ~5000 5 km asteroids in the middle belt, however there are about ~40,000 2 km ones known, nearly a factor of 10 greater.

5. Taxonomic classification

The SDSS asteroid data has been grouped and classified according to their colors by many authors. Ivezić et al. (2002) classified the C, S, and V groups using the z′–i′ color and the first principal component of the r′–i′ versus r′–g′ colors. Nesvorný et al. (2005) used the first two principal components of u′, g′, r′, i′, z′ colors and distinguished between the C, X, and S-complexes. Carvano et al. (2011) converted colors to reflectance values and created a probability density map of previously classified asteroids and synthetic spectra to classify the SDSS dataset.

In this work we seek to maximize the taxonomic detail contained in the dataset and strive to keep the class definitions as consistent as possible with previous spectral taxonomies that were based on higher spectral resolution and larger wavelength coverage data sets, specifically Bus (Bus and Binzel, 2002a) and Bus–DeMeo (DeMeo et al., 2009) taxonomies.

5.1. Motivation for manually defined class boundaries

The best way to mine the most information out of such a large dataset could be to perform an analysis of the variation and clustering. Methods such as Principal Component Analysis or Hierarchical Clustering could separate and highlight groups within the data. The advantage to automated methods is they are unbiased by human intervention and can efficiently characterize large datasets, which are the motivations for many unsupervised classifications.

However, because most of our understanding of asteroid mineralogy comes from relating asteroid spectral taxonomic classes to meteorite classes and comparing absorption bands, we find it more relevant to connect this low-resolution data to already defined and well-studied asteroid taxonomic classes (that were based on Principal Component Analysis). This facilitates putting the SDSS results in context with the findings from other observations that have accumulated over decades. To classify the data we started with the class centers and standard deviations (based on data used to create the Bus–DeMeo taxonomy converted to SDSS colors) to calculate the distance of each object to the class center.

Considering the above, while we still use the class centers and calculated deviations as a guide, we choose to fix boundaries for each class and manually tweak them (as described below) according to the data to best capture the essence of each class. A negative consequence of fixed boundaries is that near the boundary objects exist on either side that may have very similar characteristics though are classified differently (as opposed to methods which assign a probability for each object to be in a certain class). Additionally, a human bias is added. The advantage, however, is we are forced to carefully evaluate the motivation for the definition of each class to group objects according to the most diagnostic spectral parameters (particularly considering the much wider spread of the SDSS dataset), consistency with previous classifications, and potential compositional interpretation. Additionally, fixing the boundary allows us to more easily use the classifications as a tool. We can use these classifications to determine the fraction of objects in each class and the mass of each taxonomic type across the Solar System.

5.2. Defining the class boundaries

We transform the apparent magnitudes from SDSS to reflectance values to directly compare with taxonomic systems based on reflectance data. We then subtract solar colors in each filter and calculate reflectance values using the following equation:

$$R_f = 10^{-0.4[(M_f - M_g) - (M_{f,\odot} - M_{g,\odot})]} \quad (2)$$

where (M_f) and $(M_{f,\odot})$ are the magnitudes of the object and Sun in a certain filter f, respectively, at the central wavelength of the filter. The equation is normalized to unity at the central wavelength of filter g using (M_g) and $(M_{g,\odot})$: the g magnitudes of the object and Sun, respectively. Solar colors used in this work are r′–g′ = −0.45 ± 0.02, i′–g′ = −0.55 ± 0.03, and z′–g′ = −0.61 ± 0.04 from Holmberg et al. (2006). Note that because we use solar colors in the Sloan filters we do not convert from the g′, r′, i′, z′ filters (central wavelengths: g′ = 0.4686, r′ = 0.6166, i′ = 0.7480, z′ = 0.8932 μm) to standard g, r, i, z filters. As mentioned in Section 2.1, we do not use the u′ filter because of the very large errors for this datapoint.

The classification of the dataset is based on two dimensions: spectral slope over the g′, r′, and i′ reflectance values (hereafter gri-slope), representing the slope of the continuum, and z′–i′ color, representing band depth of a potential 1 μm band. We restrict the evaluation of the spectral slope to g′, r′, and i′ filters only, excluding the z′ filter because it may be affected by the potential 1 μm band. These two parameters (slope and band depth) are the most characteristic spectral distinguishers in all major taxonomies beginning with Chapman et al. (1975) because they account for the largest amount of meaningful and readily interpretable variance in the system.

We choose not to use a^* defined by Ivezić et al. (2002) or the first Principal Component (PC1) defined by Nesvorný et al. (2005) used in other works. a^* is the first principal component of the r′–i′ versus g′–r′ colors and PC1 is the first principal component of the measured fluxes of all five filters. To most effectively use Principal Component Analysis, the dimension with the greatest variance, slope in this case, should be removed before running PCA

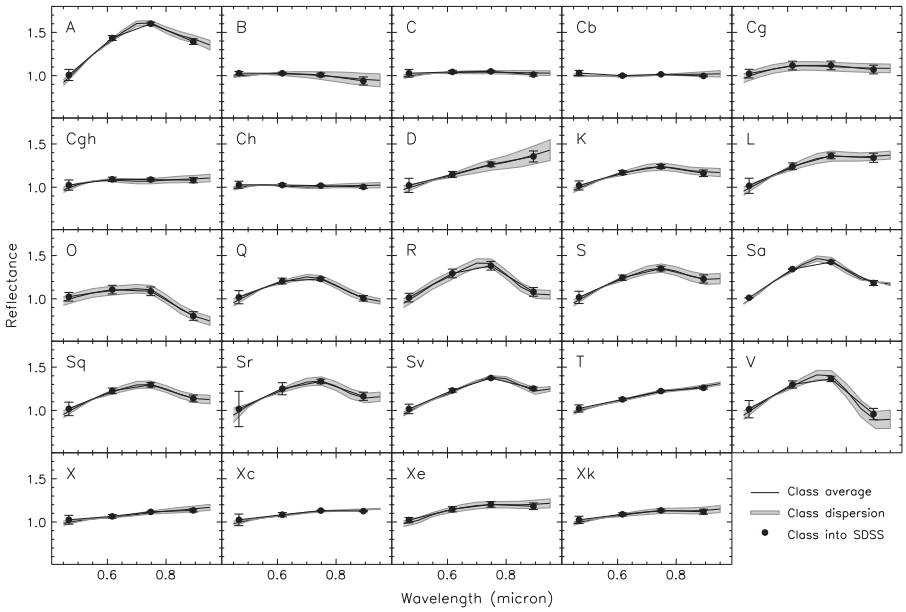

Fig. 4. Average Bus–DeMeo (DeMeo et al., 2009) spectra converted to SDSS colors used to define the classification boundaries. The black dots (with 1 standard deviation from the mean plotted) represent the average Bus–DeMeo spectra converted into SDSS colors. The u′ filter is extrapolated from the data because the spectra do not cover those wavelengths (the u′ filter is not used in the classification of SDSS data, however). The gray background plots the average spectrum plus one sigma for comparison with the colors. Because the Cg, O, and R classes are defined by a single object the standard deviation is set to 0.1. (For interpretation of the references to color in this figure legend, the reader is referred to the web version of this article.)

to increase sensitivity to more subtle variation (see discussion in Bus (1999)). We also disfavor the inclusion of the u′ filter (used for PC1) as it adds significant noise to the data (Fig. 2). We find our slope parameter is reasonably well-correlated with $a^{\star}$ but not well-correlated with PC1, as expected from the use of u′ photometry in PC1.

We base the classification on the 371 spectra used to create the Bus–DeMeo taxonomy (DeMeo et al., 2009), whose classes are very similar those of the Bus taxonomy (Bus and Binzel, 2002a), with a few classes removed. The variation among the reflectance spectra of the 371 asteroids used to define the Bus–DeMeo classes helped guide the boundary conditions of the present SDSS taxonomy. We convert all the spectra into SDSS reflectance values by convolving them with the SDSS filter transmission curves,[2] thus providing the average SDSS colors and standard deviation per class (see Fig. 4).

Because the SDSS data have a spectral resolution significantly lower than the Bus–DeMeo data set (see Fig. 4) and subtle spectral details are lost, we combine certain classes into their broader complex. The C-complex encompasses the region including C-, Cb-, Cg-, Cgh-, and Ch-types. The S-complex encompasses the S-, Sa-, Sq-, Sr-, and Sv-types. The X-complex includes X-, Xc-, Xe-, Xk-, and T-types. The classes that are maintained individually are A, B, D, L, K, Q, and V. While we distinguish all these classes based on the SDSS colors here, we slightly modify our use of some of these classes for this work (see Section 6.1). We do not classify the rare R- or O-type in this work, because there is significant overlap between O-types or R-types and other classes in the visible wavelength range, and they are particularly rare classes. The R class would overlap the V class essentially spanning the shallower z′–i′ "band depth" region. We tested separating the R class, but the majority of the objects classified as R were located in the Vesta family.

While the Bus–DeMeo class averages are very useful as a guide, the system was based on a sample size three orders of magnitude smaller than present SDSS sample. The SDSS dataset therefore shows a much more continuous range of reflectance characteristics. To compare the two datasets, we plot the distribution of SDSS objects in z′–i′ color and gri-slope, with the 371 objects from the Bus–DeMeo taxonomy (Fig. 5). Furthermore, the figure shows the boundaries for each class defined in this work. We drew boundaries that best separated each class based on the position of the class centers and standard deviations based on the 371 spectra dataset. We visually inspected each boundary by plotting the spectral data on each side of the boundary and comparing them with the designated class to tweak the position of the line and best separate each class.

We strove to preserve the uniqueness of the more exotic classes, restricting A- and D-types to the outliers with the largest slopes, and Q- and V-types with the deepest bands. The B-type was defined to have both a large, negative gri-slope and a negative z′-i′ value. A list of all the boundaries is provided in Table 3. Classification is performed in decision tree form, where the gri-slope and z′–i′ value of the asteroid is compared with each region in the following order: C, B, S, L, X, D, K, Q, V, A. If the object falls in more than one class, it is designated to the last class in which it resides. As can be seen in Fig. 5, there are a handful of objects that reside outside the defined classes. We give these objects the designation "U", historically used to mark unusual objects in a sample that do not fall near any class. We do not include these objects in

[2] http://www.sdss.org/dr7/instruments/imager/.

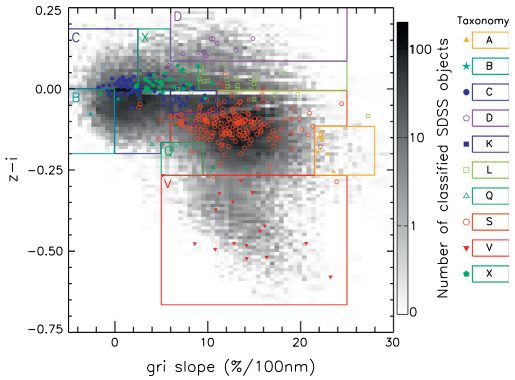

Fig. 5. Boundaries used to classify SDSS data into taxonomic classes. The colored points are the spectra from the Bus–DeMeo taxonomy (DeMeo et al., 2009) converted to SDSS colors. In the background, the density of the number of objects from MOC4 are plotted to show the dispersion of the SDSS data. (For interpretation of the references to color in this figure legend, the reader is referred to the web version of this article.)

Table 3
Table of classification boundaries. The classification is performed following the order: C, B, S, L, X, D, K, Q, V, A.

Class	Slope (%/100 nm)		z′–i′	
	(min)	(max)	(min)	(max)
A	21.5	28.0	−0.265	−0.115
B	−5.0	0.0	−0.200	0.000
C	−5.0	6.0	−0.200	0.185
D	6.0	25.0	0.085	0.335
K	6.0	11.0	−0.075	−0.005
L	9.0	25.0	−0.005	0.085
Q	5.0	9.5	−0.265	−0.165
S	6.0	25.0	−0.265	−0.005
V	5.0	25.0	−0.665	−0.265
X	2.5	9.0	−0.005	0.185

our study. Most of these extreme behaviors are likely due to problems with the data even though no flags were assigned (see details in Section 2.1). Follow-up observations could determine whether the objects really are unique.

5.3. Determining a single classification for multiple observations

Of the many observations in the SDSS MOC that remained after we applied cuts on the photometric precision (58,607, see Section 2.1), many were actually the same object observed more than once. The number of unique objects in our sample is 34,503. For some of these objects, not all observations fell into the same class. Because we seek to categorize each object with a unique class, we use the following criteria to choose a single class for any object that has multiple observations that fall under multiple classifications (5401 asteroids, i.e., 15.7% of the sample):

- The class with the majority number of classifications is assigned (2619 asteroids, i.e., 7.6% of the sample)
- If two classes have equal frequency and one of them is C, S, or X we assign the object to C, S, or X, continuing the philosophy of remaining conservative when assigning a more rare class (1867 asteroids, i.e., 5.4% of the sample)
- If the two majority classes are C/S, X/C, S/X (or three competing classes of C/S/X) we assign it to the U class and disregard those objects in the distribution work (919 asteroids, i.e., 2.6% of the sample). We prefer to keep the sample smaller, rather than contaminate it with objects that we have randomly chosen a classification among C, S, or X and thus possibly bias the sample.
- For objects that are assigned multiple classes but none is either the majority or C, S, or X is assigned to the U class.

Among the largest asteroids, particularly those between H magnitudes of 9 and 12, several asteroids observed by the SDSS had taxonomic classes from previous spectroscopic measurements. The classification based on SDSS and previous work were generally consistent, but in cases that differed, we assigned the asteroid to the class determined by spectroscopic measurements.

5.4. Caution on taxonomic interpretation

One must be careful when interpreting the classifications presented here. First, the resolution of the SDSS data are significantly lower than the spectra to which they are compared. Second, the fact that we find multiple classifications for multiply observed objects suggests there is a larger uncertainty in the data than expected. Third, for many classes (particularly L, S, Q, A), the visible data can only suggest the presence of a 1 μm band, but do not actually predict the depth or shape of that band (for more detail see DeMeo et al., 2009; DeMeo, 2010). This is important because, for example, a spectrum might look closer to a K- or an L-type in the visible range, but near-infrared data could place them more confidently in the S-class (or vice versa).

Each class is meant to be representative of a certain spectral characteristic, but with limited wavelength coverage and limited resolution, there is some degeneracy. For example, the Q-class defined here represents objects with a low slope and moderate 1 μm band depth. We do not suppose that all objects classified as a Q-type are young, fresh surfaces as is typically associated with the Q class. Careful follow-up observations are important to make such a claim.

Defining boundaries for C, X, and D-types is not easy because they are distinguished only by slope and there is a continuous gradient of slope characteristics. This problem is not unique to the SDSS dataset. The boundary between each type is somewhat arbitrary. The difference between a C-type of slope zero and a D-type with a high slope is meaningful, however we do not yet know how to interpret the significance of these spectral differences. It is likely that there is some contamination between C- and X-types with our classification scheme, though it is unlikely that much contamination exists for example between C- and D-types that are more easily distinguished.

5.5. Verification of our classifications

With a unique class assigned to each object in our dataset we can now evaluate the robustness of our classifications. First, we compare the classification of each asteroid with the results of Carvano et al. (2011) available on the Planetary Data System (Hasselmann et al., 2011). Because their classification is based on the same dataset, it is not an entirely independent check. However, their classification method is different so consistency between the two supports both methods. Fig. 6 graphically compares the two classifications. We list the classification differences that are generally compatible but represent the different choices each method made. We find the two classifications quite consistent. Of the major classification differences between the two methods we suspect some are due to boundary condition differences and others are due to Carvano's inclusion of the u′ filter, which we exclude in our work (see Section 2.1).

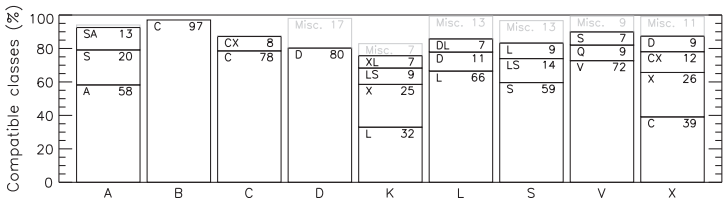

Fig. 6. Comparison of classifications in this work to those of Carvano et al. (2011). For each class in our work a bar represents how those objects are classified in the Carvano system. Some objects were given two letters by Carvano given in the PDS archive (Hasselmann et al., 2011). We categorize according to the most numerous classes assigned by Carvano compared to this work. All "compatible" classes are shown since they are relatively in agreement based on classes that border others. These highlight the small but compatible differences between the classifications. Miscellaneous includes other classes we feel are compatible but make up a small percentage of the sample. All B-types in our work are classified as C-type by Carvano because they do not make a distinction between the two. The small unlabeled fraction represents mismatches where our work and Carvano's get significantly different results. The right side of each bar labels the percent of the total each Carvano class represents.

Second, we retrieved the albedo of the asteroids as determined from IRAS, AKARI, and WISE data (Tedesco et al., 2002; Ryan et al., 2010; Usui et al., 2011; Masiero et al., 2011, 2012; Grav et al., 2011, 2012a,b). We found 17,575 asteroids (out of 34,503, i.e., 51%) with albedo determinations. We present in Fig. 7 the distribution of albedo for each class, and the average values in Table 4. The agreement between the average albedo per Bus–DeMeo class from previous work (see Table 1) and of the asteroids classified from SDSS colors gives confidence in our capability to assign a relevant class to these asteroids. One of the greatest differences is the albedo of the B class.

We have separated the spectra of objects with negative slopes into the B class using SDSS colors as has traditionally been done in taxonomic systems. This separation can be a useful indicator of spectral differences between B and C classes. The average albedo for B-types classified from spectroscopic samples is significantly higher than for C-types (see Table 1) suggesting a compositional difference. However, the average albedo of B-types in our SDSS sample is similar to that for C-types so we caution that the B-types classified from spectroscopic surveys may not be fully representative of the B-types in our sample.

6. Building the compositional distribution

6.1. Additional taxonomic modifications

Keeping in mind the cautions mentioned in Section 5.4, for the taxonomic distribution work presented here we apply slight modifications to the classes. First, we note a significant over abundance of S-types in the Eos family. This is due to the similarity of S- and K-type spectra using only a few color points and the visible-only wavelength range. We thus reclassify all S-type objects to K-type within the Eos family (defined by the family's current orbital elements $a \in [2.95, 3.1]$, $i \in [8°, 12°]$, and $e \in [0.01, 0.13]$). Reviewing this change shows that the background of S-types is now evenly distributed, no longer showing a concentration within the Eos family. Additionally, for this study we group Q-types with the S-types because they are compositionally similar (Binzel et al., 2010; Nakamura et al., 2011).

In the previous section we discussed the albedo differences between B-types in our sample and B-types from other work. While future work may want to focus specifically on objects with negative slopes, in this we choose to merge B-types with C-types classified by the SDSS dataset.

Our SDSS observations classify some Hildas and Trojans as K- and L-types. Careful examination reveals that for the K- and L- type objects that are near the border the X and D classes, the spectra could also be consistent with X and D. These Hilda and Trojan K- and L-types that have multiple observations are also classified X and D. For example, the Centaur (8405) Asbolus has a very red visible spectral slope (Barucci et al., 1999), categorizing it as a D-type. Eight SDSS observations place this object in the L class and four in the D class. This difficulty is partially due to the degeneracy of the visible wavelength data. The Bus Ld class that is intermediate between the L and D classes does not remain an intact definable class when near-infrared data are available (DeMeo et al., 2009). There are four SDSS L-type Hildas and Trojans with albedos all of which are below 0.08 further suggesting that these objects are not characterized by what the K and L classes are compositionally meant to represent. We therefore choose the more conservative option to reclassify the Hilda and Trojan K- and L-types. The K-types that have slopes more consistent with the X class are relabeled as X, while the L-types have slopes more consistent with D-type and are relabeled as D.

Among the Hungarias, a population of small ($H > 13$) C-types is seen. Upon closer inspection, all (8) of the small C-types with WISE data have extremely high albedos (0.4–0.9), suggesting they are actually E-types (the high albedo group of X-types). This is unsurprising, as the Hungaria region is known to contain a large population of high albedo E-type asteroids. We thus correct our Hungaria sample by assuming all small C-types are incorrectly classified, and remove those with H magnitudes greater than the E-type cutoff from our sample. We expect some overlap between C-types and X-types (E, M, P) in other regions of the belt as well (as addressed in Section 5.4) although the classification of X v. C should be more balanced.

While we make these modifications for the objects in the SDSS sample we do not make changes to the large objects classified spectroscopically from previous work.

6.2. Discovery completeness

While we select the subset of SDSS data where the survey is efficient, the dataset not complete. The information from the SDSS dataset must be applied to all existing asteroids in the same size range. The Minor Planet Center (MPC) catalogues all asteroid discoveries. Here we asses discovery completeness.

In Fig. 8, we plot the cumulative number of discoveries in the outer belt for every two years of the past 10 years (to 2013–01-01). We derive a limiting magnitude for the completeness of the MPC database of H = 16, 15 and 14.5 (diameter of about 2, 3, and 4 km) for the inner, middle, and outer belt, respectively. We determine the completeness of small asteroids in each section of the main belt by extrapolating the size of the population using a power law fit to each region of the main belt (shown in Fig. 1). The difference between the currently observed populations and the extrapolated populations derived from these power laws provide the expected number of asteroids to be discovered at each

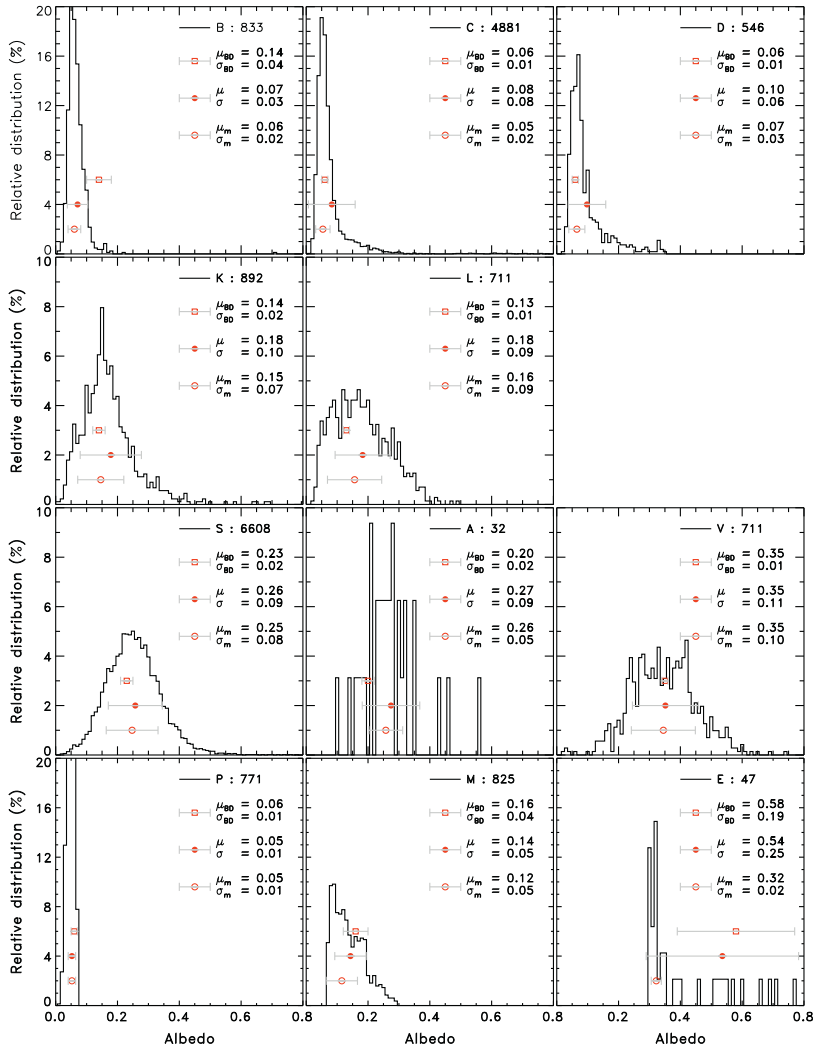

Fig. 7. Relative distribution of albedo for each class. For each class, we report the number of asteroids with albedo estimates, and the average albedo with its standard deviation (μ, σ, open circle), together with the mode of the histogram (μ_m, σ_m, filled circles). We also report the average albedo of the asteroids in the Bus–DeMeo sample (μ_{BD}, σ_{BD}, square symbol, see Table 1).

size range. The power law indices we find for the IMB, MMB, and OMB (determined over the H magnitude range 14–16, 13–15, and 12–14.5) are −2.15, −2.57, and −2.42, respectively. These power law indices agree with other fits to the observations (Gladman et al., 2009) as well as with the theoretical index calculated assuming a collision-dominated environment (Dohnanyi, 1969).

For almost all H magnitudes in our sample we are nearly discovery complete. For the smallest size we use a power law function to determine completeness. In the H = 15–16 magnitude range, we are 100%, 85%, and 60% complete in the IMB, MMB, and OMB respectively. When applying the taxonomic fractions to the MPC sample of known asteroids we add a correction factor to account the 15% and 40% of objects that have not been discovered in the middle and outer belt in the H = 15–16 range. For Cybeles, Hildas, and Trojans we do not extrapolate to determine sample completeness because there is far too much uncertainty in the size distribution of those populations due to fewer discoveries. We have not corrected these populations. The completeness of our dataset can be evaluated on Fig. 1.

There are undoubtedly still many objects yet to be discovered, especially at sizes smaller than we cover in this work. For reference, we explore the total mass these undiscovered objects are expected to represent. The largest objects represent the overwhelming majority of the mass in the main belt. In fact, the asteroids from the spectral surveys (particularly H < 10) represent

Table 4
Average albedo of each class based on the 17,575 objects in our SDSS dataset that had calculated albedos (51% of our dataset). The results are consistent with previous albedo averages (Tables 1 and 2) strengthening the robustness of this work.

Class	$N_{objects}$	Average	Mode
A	32	0.274 ± 0.093	0.258 ± 0.055
B	833	0.071 ± 0.033	0.061 ± 0.021
C	4881	0.083 ± 0.076	0.054 ± 0.023
D	546	0.098 ± 0.061	0.065 ± 0.026
K	892	0.178 ± 0.099	0.146 ± 0.075
L	711	0.183 ± 0.089	0.157 ± 0.088
S	6565	0.258 ± 0.087	0.247 ± 0.084
V	711	0.352 ± 0.107	0.345 ± 0.104
E	47	0.536 ± 0.247	0.322 ± 0.016
M	825	0.143 ± 0.051	0.115 ± 0.051
P	771	0.053 ± 0.012	0.053 ± 0.012

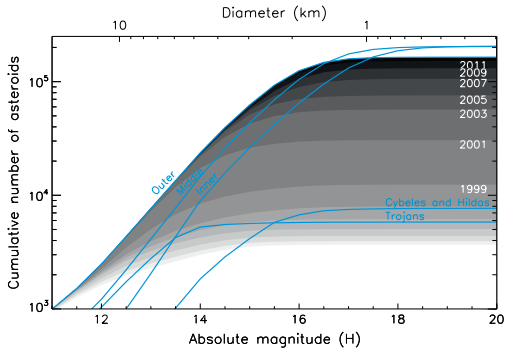

Fig. 8. Discovery completeness through 2013. For the outer belt, we plot the cumulative distribution as function of time up to 2013 January 01 (shades of gray), showing the evolution of the completeness limit to smaller (higher H) objects. We derive a limiting magnitude for the completeness of the MPC database of H = 16, 15 and 14.5 (diameter of about 2, 3, and 4 km) for the inner, middle, and outer belt, respectively.

97% of the mass (assuming a mass of 30×10^{20} kg for the entire main belt, Kuchynka et al., 2013).

We calculate the undiscovered mass (assuming a general density of 2.0 g/cm^3 and an albedo of 0.18, 0.14, and 0.09 for the inner, mid, and outer main belt, based on WISE measurements, see Mainzer et al., 2011) up to H magnitude of 22 to be 5.7×10^{12}, 4.8×10^{13}, and 1.6×10^{14} kg for the IMB, MMB, and OMB, that each contain a total mass (with the same generic albedo and density assumptions) of 6.2×10^{20}, 1.3×10^{21}, and 7.1×10^{20} kg, with a total of 26×10^{20} kg. Therefore, although hundreds of thousands of asteroids will still be discovered and they will provide valuable information about asteroids at small size scales, their expected contribution in terms of mass is minuscule (below the part per million level).

6.3. Applying the SDSS distribution to all asteroids

After applying data quality cutoffs, H-magnitude cutoffs, and taxonomic classifications, we can now calculate the number of SDSS objects in each class according to size and distance. We use H magnitude bins of 1 magnitude ranging from 3 to 16 (though each class has its appropriate H magnitude cutoff listed in Table 2). The semi-major axis bins applied are 0.02 AU wide ranging from 1.78 to 5.40 AU. Only asteroids among Hungarias, the main belt, Cybeles, Hildas and Trojans are included in this study covering the distances 1.78–2.05, 2.05–3.27, 3.27–3.7, 3.7–4.2, and 5.05–5.40 AU, respectively. Near-Earth objects, comets, Centaurs, transneptunian objects and any other objects outside the mentioned zones were excluded. We calculate the number of objects in each bin and the fraction of each class in each bin (F_i, where i is the taxonomic class). For example, for objects with H magnitudes between 13 and 14 and semi-major axes between 2.30 and 2.32 AU, we might find 60% of the objects are S-type ($F_s = 0.6$), 20% are C-type ($F_c = 0.2$), 20% are X-type ($F_x = 0.2$). Figs. 9 and 10 show the bias-corrected and biased fraction of objects. The biased view of the asteroid belt shows a dominance of S-types (by number) out to nearly 3 AU because of the inclusion of the abundant smaller, higher albedo bodies (whose small, dark counterparts, the C-types, were not observed). The bias-corrected version demonstrates that instead, the S-types and C-types alternate dominating by number throughout the belt. Asteroid families play an important role in these figures since they contribute large numbers of taxonomically similar objects.

Albedo data enable the separation of X-types into three sub groups: E, M, P (Tholen, 1984). Since albedo data are not available for every single spectral X-type, we calculate the fraction of E, M, and P for each region: Hungaria, Inner, Middle, Outer, Cybele, Hilda, Trojan. This fraction is calculated based on ~2000 X-type objects in our sample with albedo measurements (from a total of 2500 X-types) from IRAS, AKARI, and WISE (Ryan et al., 2010; Usui et al., 2011; Masiero et al., 2011). See Fig. 11 for the bias-corrected distribution of the E, M, and P types across the main belt that was used to extrapolate the X-type EMP fraction for our entire dataset. Among Hungarias the sample is entirely E-type as expected. There are an insignificant number of E-types among the other regions (though we note a bias against observing high visible albedo objects in mid-infrared wavelength ranges). The fraction of all bias-corrected X-types that are M in each region are: 0.00, 0.58, 0.44, 0.35, 0.28, 0.08, and 0.17, respectively. The fraction for P-types is thus one minus the M-type fraction, except for the Hungaria region where it is also zero. Among Trojans we find that 0.17 (1 out of 6) X-types have an M-type albedo, however because of large uncertainty due to a small sample we assume the same fraction for Trojans as Hildas (0.08).

We now know the relative abundance of each taxonomic type at each size range and distance determined from the SDSS dataset with and adjustment for the division of E, M, and P types from the X class. However, at many size ranges the SDSS only observed ~30% of the total asteroids that exist at that size and distance. As long as we only use a size range in which asteroid discovery is essentially complete or make a correction for discovery incompleteness, we can apply these fractions to the entire set of known asteroids at these sizes from the Minor Planet Center to determine the distribution of taxonomic type across the main belt according to number, surface area, volume, and mass.

When calculating the number of objects, surface area, volume, or mass at each size range and distance we use two different methods. For the largest asteroids with H < 10 where our SDSS sample is complete, we calculate the surface area, volume, or mass for each asteroid using that body's H magnitude, albedo (or average albedo for its taxonomic class when not available), and average density (Carry, 2012) for that taxonomic class.

For objects with 10 < H < 13, where our sampling is not complete, we use the following method. The surface area, volume, or mass is calculated for an object using the H magnitude, average albedo and average density for that class. That value is multiplied by the number of objects of that class in that bin (N_i) which is the total number of known asteroids in that (size and distance) bin, N_{bin}, and by the fraction (F_i) of objects of that class from SDSS: $N_i = N_{bin} \times F_i$.

For objects with H > 13 we have the added complication that we cannot directly apply our fraction to the total number of known objects because our fraction of each type at each size from SDSS

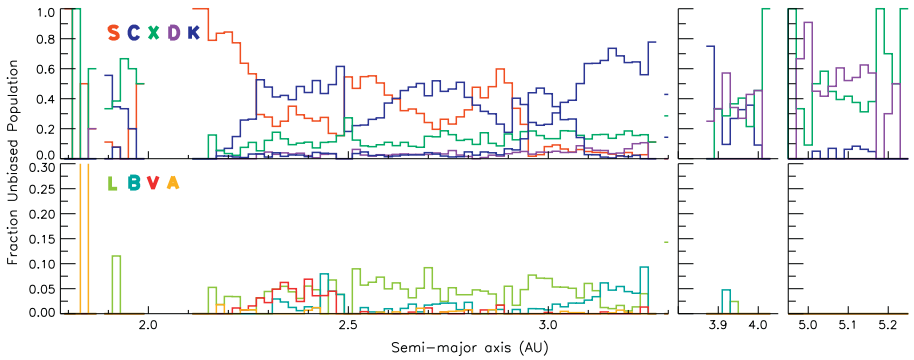

Fig. 9. The bias-corrected fraction of each class in each 0.02 AU bin according to SDSS data (each bin summing over all classes equals 100%). All objects are 5 km or larger. The distribution in this figure is dominated by smaller objects (H of 13–15.5). Because we are plotting by number of asteroids, the collisional families play an important role in this figure (e.g., the Vestoids in the inner belt).

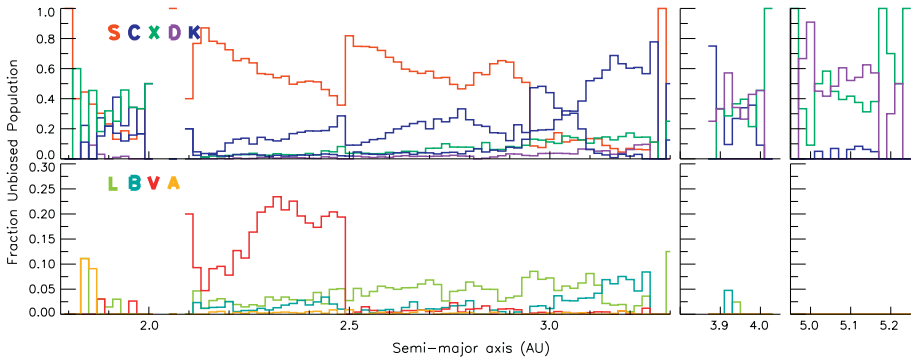

Fig. 10. The observed fraction of each class in each bin according to SDSS data (each bin summing over all classes equals 100%). In this case we did not cut the sample at a particular size range. The smaller, brighter S-types are more prevalent everywhere, and small, bright V-types make up nearly 20% of the second half of the inner belt. In this case we are plotting S-types smaller than 5 km whereas we are not sampling the darker C-types of similar size. The difference between this figure and Fig. 9 demonstrates the importance of correcting a sample for observational biases.

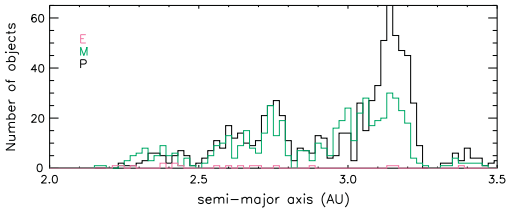

Fig. 11. The bias-corrected distribution of E, M, and P-type asteroids across the main belt based on the 1500 X-types in our sample (including spectral surveys and SDSS) with WISE, AKARI, or IRAS albedo determinations (Ryan et al., 2010; Usui et al., 2011; Masiero et al., 2011). These objects are used to determine the relative fraction of M to P types among X class objects in each zone of the belt. Because only a subset of our SDSS X-types had albedos available we applied the fraction of M/P in each region to our entire X-type dataset. In the area near 3.0 AU we remove all SDSS objects classified as X-type in the Eos family. Because of the spectral similarity between X and K-types in SDSS colors, many K-types Eos family objects were classified as X (see Section 6.1 for discussion on classification ambiguity).

is calculated with certain (higher albedo) classes removed. We thus must also calculate the fraction of objects in the SDSS database that were kept, F_{kept}, (i.e., those that were not removed because they are smaller than ∼5 km) for H magnitude bins H = 13, 14, and 15. For all other size bins F_{kept} is equal to 1. The number of objects of a certain class (N_i) can be determined by the total number of discovered objects in that bin (N_{bin}) multiplied by the fraction of objects in that class (F_i) and by the fraction of objects in that bin that are kept (F_{kept}), thus $N_i = N_{bin} \times F_i \times F_{kept}$.

Previously in this section, we calculated the bias-corrected fraction of E, M, and P types in each zone, although, as above, we cannot apply this true (bias-corrected) correction factor to the observed (biased) MPC dataset. For the H bins 14 and 15 where some M-types were removed due to size we calculate the fraction of (M + P)-types kept in each region. The fraction for H = 14 is 0.60, 0.67, 0.64, 0.79, for the IMB, MMB, OMB, and Cybeles and 0.22, 0.39, 0.41, 0.70 for H = 15. There are no small objects in our sample to be removed in the Hilda and Trojan regions so the fraction kept is unity.

Finally, if we simply assume an average H magnitude for each bin (say 12.5 for the H = 12 bin) we could potentially over- or underestimate the surface area, volume, or mass, depending on the H magnitude distribution of objects in that bin. We thus calculate the number of objects in each 0.1 H magnitude sub-bin and apply the same class fractions to each for accuracy.

7. The compositional makeup of the main belt

7.1. Motivation for number, surface area, volume, and mass

Previous work calculated compositional distribution based on the number of objects at each distance (e.g. Chapman et al., 1975; Gradie and Tedesco, 1982; Gradie et al., 1989; Mothé-Diniz et al., 2003). This was not unreasonable because those datasets included only the largest objects, often greater than 50 km in diameter.

If we restrict our study to the number of asteroids, our views would be strongly influenced by the small asteroids. There are indeed more asteroids of small size than large ones. This is the result of eons of collisions, grinding the asteroids down from larger to smaller. The size–frequency distribution of asteroids (Fig. 1) can be approximated by a power-law, and for any diameter below 20 km, there are about 10 times more asteroids with half the diameter. The amount of material (i.e., the volume) of the two size ranges is however similar: if there are n asteroids of a given diameter D, there are about $10n$ asteroids with a diameter of $D/2$, each with a volume 8 times smaller, evening out the apparently dominating importance of the smaller sizes. Ceres alone contains about a third of the mass in the entire main belt using a mass of 30×10^{20} kg for the main belt (Kuchynka et al., 2013), and 9×10^{20} kg for Ceres (from a selection of 28 estimates, see Carry, 2012)), and yet it is negligible (1 out of 600,000) when accounted for in a distribution by number. Therefore, the relative importance of Ceres in the main belt can change by orders of magnitude depending on how we look at the distribution.

The study of the compositional distribution by number is perfectly valid and is useful for size–frequency distribution studies and collisional evolution. For studies of the distribution of the amount of material, it puts too much emphasis on the small objects compared to the largest. A simple way to balance the situation is to consider each object weighted by its diameter. This opens new views on asteroids: we can study how much surface area of a given composition is accessible for sampling or mining purposes (Section 7.2), or how much material accreted in the early Solar System has survived in the Belt (Sections 7.3 and 7.4 for the distributions by volume and mass).

7.2. Asteroid distribution by surface area

To estimate the surface area of each asteroid, we need first to estimate its diameter D. For that we use the following equation from Pravec et al. (2007, and references therein):

$$D = \frac{1329}{\sqrt{a}} 10^{-0.2H} \quad (3)$$

where H is the absolute magnitude (determined by the SDSS survey) and a is the albedo. For the largest asteroids ($H < 10$) we use the object's calculated albedo from WISE, AKARI, or IRAS. For small asteroids, and large ones for which no albedo is available, we use the average albedo for that object's taxonomic class, see Section 2.2. The equation above provides a crude estimation of the diameter only. Evaluation for a particular target should be considered with caution, the absolute magnitude and albedo being possibly subject to large uncertainties and biases (e.g., Romanishin et al., 2005; Mueller et al., 2011; Pravec et al., 2012). We can nevertheless make good use of this formula for statistical purposes: the precision on the diameters is indeed rough but seemingly unbiased (Carry, 2012). With a diameter D determined for each asteroid, we estimated their individual surface area $\mathcal{S}$ by computing the area of a sphere of the same diameter: $\mathcal{S} = \pi D^2$. The surface area distribution is presented in Fig. 12.

The total surface area per bin ranges from 10^3 km^2 in the Hungarias to 10^6 in the main belt. Viewing the distribution with respect to surface area we can immediately notice the relative importance of larger bodies. Ceres and Pallas are represented by the blue peak near 2.75 AU and Vesta by the red peak near 2.35 AU. Additionally the E-types in pink, distributed throughout the main belt, are each only one or two asteroids.

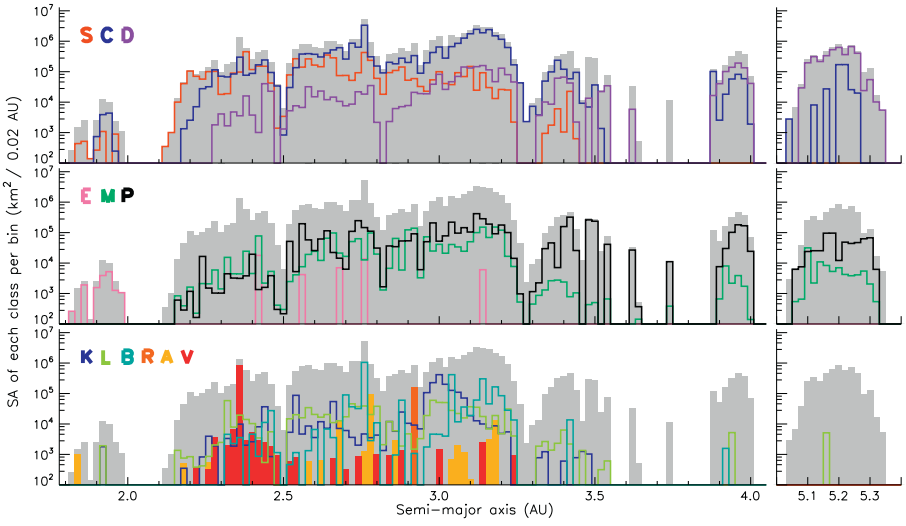

Fig. 12. The surface area (km^2) of each taxonomic class in each 0.02 AU. The y-axis scale is logarithmic to include all classes on the same scale. All objects are 5 km or larger. While we do not classify R-types in our SDSS dataset, the one R-type in this plot is (349) Dembowska, from the spectroscopic surveys.

7.3. Asteroid distribution by volume

While the real value we seek is mass, because the density contributes significant uncertainty to the mass calculation we also present the distribution according to volume of material which gives similar results but is not affected by density uncertainties.

To evaluate the amount of material in the main belt, for each taxonomic class, we estimate the volume $\mathcal{V}$ of all the asteroids by computing the volume of a sphere of the same diameter: $\mathcal{V} = \pi D^3/6$. We use the same method to calculate the total volume distribution by applying SDSS taxonomic fractions to the MPC dataset as described in Section 6.3. By looking at the compositional distribution in terms of volume instead of numbers, most of the issues described in Section 7.1 are addressed. Indeed, if there are about 2500 asteroids with a diameter of 10 km in the main belt, their cumulated volume is 300 times smaller than that of Ceres, re-establishing the proportions. The conversion from numbers to volume also corrects our sample for an overrepresentation of the contribution by collisional families (when viewed by number). Indeed, a swarm of fragments is released during every cataclysmic disruptive event, "artificially" increasing the relative proportion of a given taxonomic class locally (e.g., the Vestoids in the inner belt, see Fig. 10). Here, we are accounting for all the material of the family as if put back together again.

We present the distribution of taxonomic class by volume in Fig. 13. The distribution is the same as for surface area, but with the *y*-axis stretched because volume is proportional to diameter cubed while surface area is proportional to diameter squared. Asteroid distributions by volume were first presented by Consolmagno et al. (2012).

7.4. Asteroid distribution by mass

Ultimately, the mass is the physical parameter we seek that provides insights on the distribution of material in the Solar System. To precisely measure the mass of each asteroid we would need a fleet of missions to fly by each asteroid. Barring that as an option in the foreseeable future, to *estimate* the mass of each asteroid we need an approximate density together with the estimated volume determined above. The density is the least well-constrained value used in this work because these measurements are extremely difficult to obtain (see discussion in Britt et al., 2002, 2006; Carry, 2012). Nevertheless, the study of meteorites tells us that the available range for asteroid density is narrower than it may seem. Indeed, no meteorite denser than 7.7 g/cm^3 has ever been found, and most of the meteorites cluster in a tight range, from 2 to 5 g/cm^3 (see Consolmagno and Britt, 1998; Consolmagno et al., 2008; Britt and Consolmagno, 2003; Macke et al., 2010, 2011, and references therein), with the exception of iron meteorites above 7 g/cm^3 (see the summary table in Carry (2012)). This range may be wider, especially at the lower end, for asteroids due to the possible presence of voids in their interiors, such as the low density of 1.3 g/cm^3 found for Asteroid (253) Mathilde (Veverka et al., 1997). However, even if we assign an incorrect density to an asteroid, the impact on its mass will remain contained within a factor of 4 at the very worst. The impact may even be smaller as the typical densities of the most common asteroid classes (i.e., C and S) are known with better accuracy (Carry, 2012).

The uncertainty on the density will therefore affect the distribution in a much lesser extent than equal weighting of bodies according to number. Of course, any uncertainty on any of the parameters will sum up in the total uncertainty. However, we are confident that the trends we discuss below are real: both the discovery completeness, diameter estimates, and average albedo and density per taxonomic class have become more and more numerous and reliable over the last decade.

To calculate the distribution by mass we apply the average density of each class (Table 2, Section 2.3) and multiply that by the volume determined in the previous Section. For Ceres, Vesta, Pallas, and Hygiea, the four most massive asteroids we include their measured masses (9.44, 2.59, 2.04, and 0.86×10^{20} kg, from Carry (2012), Russell et al. (2012)) each accounting for about 31%, 9%, 7% and 3% of the mass of the main belt, respectively (using a total mass of the belt of 30×10^{20} kg, Kuchynka et al. (2013)).

The distribution of mass is presented in Fig. 14 The fractional distribution of each class throughout the belt is given in Fig. 15.

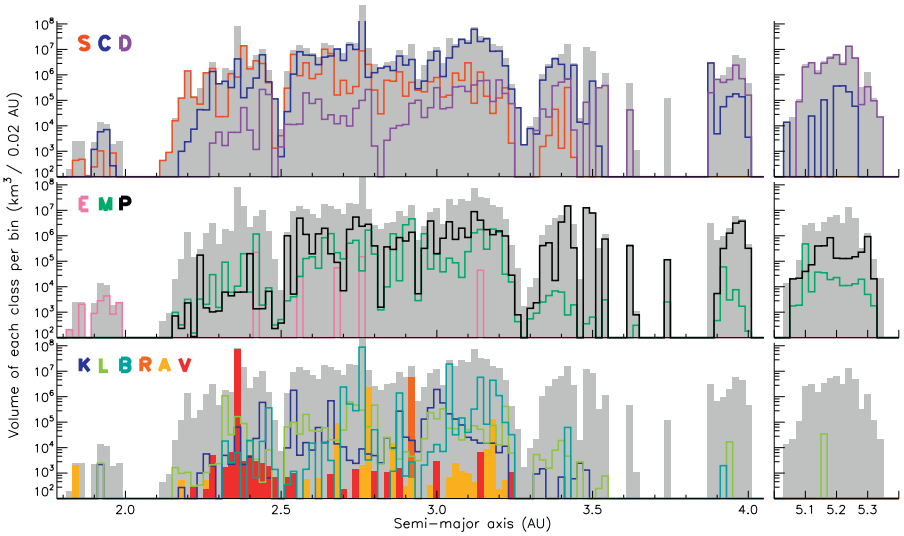

Fig. 13. The volume (km^3) of each taxonomic class in each 0.02 AU. The *y*-axis scale is logarithmic to include all classes on the same scale. All objects are 5 km or larger.

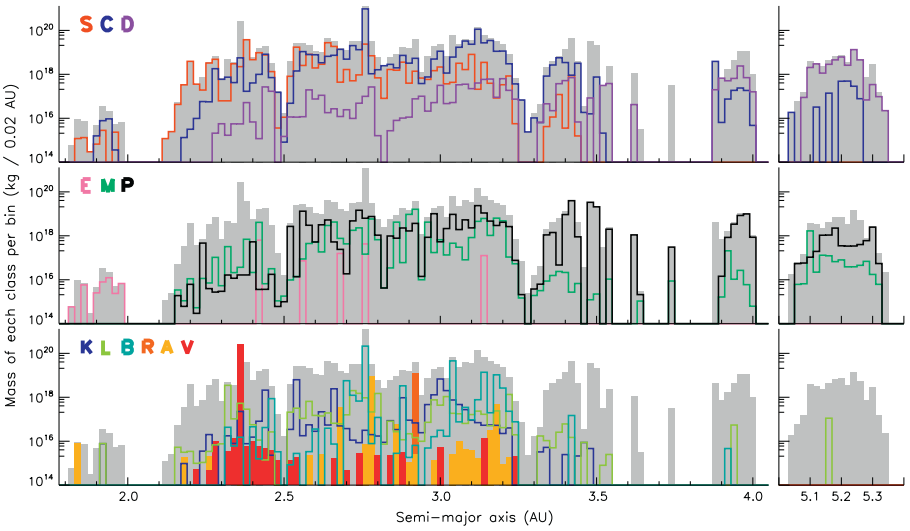

Fig. 14. The mass (kg) of each taxonomic class in each 0.02 AU bin. All objects are 5 km or larger.

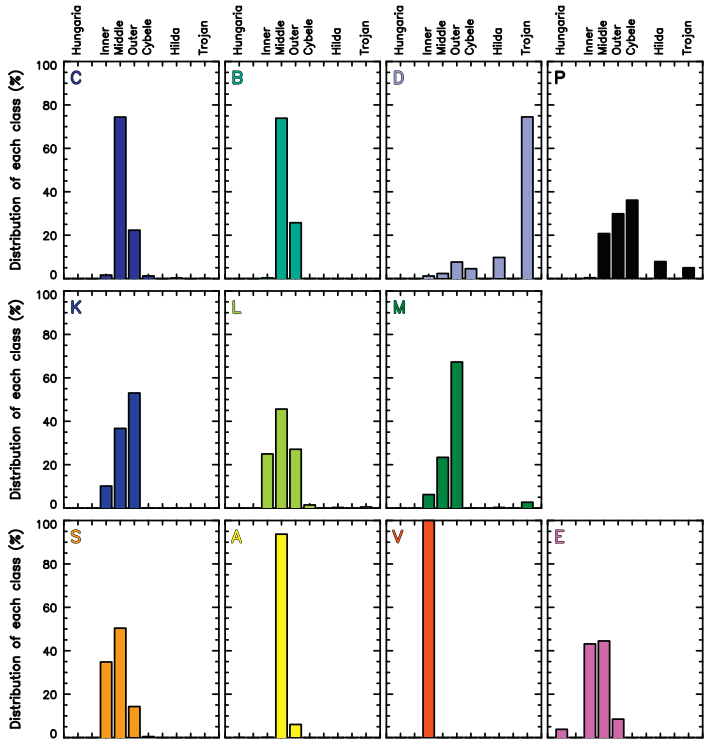

Fig. 15. The fractional mass distribution of each class across the belt. The total of each class across all zones sums to 100%.

Again, we find the general trends to be similar to volume and surface area. The difference in the case of mass is that the relative abundance of the taxonomic types have changed. Because S-types are generally denser than C-types by a factor of roughly 2 we see S-type material is more abundant relative to C than in our previous plots. Because in many cases the relative abundance of different taxonomic types already vary by an order of magnitude or more, we do not see drastic relative abundance changes. For example, C-types contribute more mass to the outer belt than S-types even though their relative abundance by mass is closer than by volume.

7.5. Search for S-types among Hildas and Trojans

We note a sharp cliff at the edge of the outer belt delineating the limit of S-type asteroids. Mothé-Diniz et al. (2003) were the first to show the presence of S-types out to 3 AU in their dataset of asteroids 15 km and greater. We find that almost no S-types exist among Cybeles, and they are entirely absent beyond 3.5 AU.

Despite the bias toward discovering S-types (they reflect five times more light than C-, D-, and P- type bodies of the same size) and their abundance in the main belt, we find no convincing evidence for S-type asteroids among Hildas and Trojans. Ten asteroids among Hildas and Trojans have at least one SDSS measurement classified as S-type. Half of those objects have another observation that does not suggest an S-like composition (the second observation is typically classified D). Visual inspection suggests the quality of the data for two of them are poor. Only one object has an albedo measurement, but the low value of 0.07 is very unlikely to represent an S-type composition. One object among each of the Hildas and Trojans remains. While we cannot rule out these objects, given the other mis-categorized data and our caution against interpreting single objects, we do not find any convincing evidence from this dataset of S-types among Hildas or Trojans (or any other high albedo classes). We reach conclusions similar to the many authors who have investigated the compositions of these regions (Emery and Brown, 2003; Emery and Brown, 2004; Emery et al., 2011; Fornasier et al., 2004; Fornasier et al., 2007; Yang and Jewitt, 2007, 2011; Roig et al., 2008; Gil-Hutton and Brunini, 2008; Grav et al., 2011, 2012a,b). The wider range of albedos found among the smallest Trojans (Fernández et al., 2009; Grav et al., 2012b) which are not well-sampled in this work should prompt further follow up investigation of these targets to determine their taxonomic class. While it is possible this albedo difference with size is due to the younger age of the smaller bodies (Fernández et al., 2009), finding a wider variety of classes would prove interesting in the context of current dynamical theories such as by Morbidelli et al. (2005).

7.6. Evidence for D-types in the inner belt

We find evidence for D-types in the inner and mid belt from SDSS colors. The potential presence of D-types was also seen by Carvano et al. (2011). Here we take a scrutinizing look at the SDSS data to be certain the data are reliable.

While D-types typically have a low albedo, Bus–DeMeo D-types have been measured to have albedos as high as 0.12 (Bus and Tholen D-types have maximum albedos of 0.25). We compare the median albedo of D-types in the inner, middle, and outer belt. For samples of 35, 81 and 108 we find medians of 0.13, 0.13, and 0.08. The median albedos in the inner and middle belt suggest that there is more contamination from other asteroid classes, however, there is still a large portion of the sample with low albedos. Next we inspect the data for all SDSS D-types in the inner belt including those without albedos. We find that 9 out of the 65 objects were observed more than once and that they all remain consistent with a D classification, all objects observed twice were twice classified as D, objects with more observations were classified as D for at least half the observations. Additionally, we check if any of the 65 D-types are members of families. We find two objects associated with the Nysa-Polana family. Because there are many C- and X-types in that family it could indicate those two objects were misclassified, however, they represent a small fraction of our sample. Because many these objects have low albedos, are not associated with C- or X-type families and have been observed multiple times and remain consistent with the D class, we have confidence in the existence of D-types in the inner belt. The orbital elements of inner belt D-types are scattered; we find no clustering of objects. The presence of D-type asteroids in the inner belt might not be entirely consistent with the influx of primitive material from migration in the Nice model. Levison et al. (2009) find that D-type and P-type material do not come closer than 2.6 AU in their model, however, their work focused on bodies with diameters greater than 40 km.

8. Overall view

We find a total mass of the main belt of 2.7×10^{21} kg which is in excellent agreement with the estimate by Kuchynka et al. (2013) of 3.0×10^{21} kg. The main belt's most massive classes are C, B, P, V and S in decreasing order (all B-types come from the spectroscopic sample, not the SDSS sample, see Section 6.1). The total mass of each taxonomic class and respective percentage of the total main belt mass is listed in Table 5. The overall mass distribution is heavily skewed by the four most massive asteroids, (1) Ceres, (2) Pallas, (4) Vesta and (10) Hygiea, together accounting for more than half of the mass of the entire main belt. Ceres, Pallas, Vesta, Hygiea are roughly 35%, 10%, 8%, and 3% respectively of the mass of the main belt (based on the total mass from this work). If we remove the four most massive bodies as shown in Table 5, the most massive classes are then C, P, S, B and M in decreasing order. The mass of the C class is six times the mass of the S class, and with Ceres and Hygeia removed, the S-types are about 1/3 and C-types/3 of their combined mass.

The distribution of each class by total mass percentage in each zone of the main belt is shown in Table 6. As we expect, E-types dominate the Hungaria region both by mass percentage and also in total number of objects, and C and S-types are the next most abundant by mass in the Hungaria region. Most of the mass of the inner belt is in Vesta, and S-types account for 4 times more mass in the inner belt than C-types (~20 and ~5% of the total mass, respectively). In the middle belt Ceres and Pallas once again make up the majority of the mass. When excluding these two bodies, C-types and S-types each make up ~30% of the mass of the middle

Table 5
Total mass of each taxonomic type. We present the total mass and fractional mass of each type. The last column is the percentage with the four most massive asteroids (Ceres, Pallas, Vesta, and Hygiea) removed. The 5 most massive classes are in bold. While we list the values two 2 decimal places as the mathematical result we do not claim accuracy to that level.

Class	Mass (kg)	Fraction (%)	Largest removed (%)
A	9.93×10^{18}	0.37	0.37
B	3.00×10^{20}	**11.10**	**3.55**
C	1.42×10^{21}	**52.53**	**14.41**
D	5.50×10^{19}	2.03	2.03
K	2.56×10^{19}	0.95	0.95
L	1.83×10^{19}	0.68	0.68
S	2.27×10^{20}	**8.41**	**8.41**
V	2.59×10^{20}	**9.59**	**0.01**
E	1.46×10^{18}	0.05	0.05
M	8.82×10^{19}	3.26	3.26
P	2.98×10^{20}	**11.02**	**11.02**
Total	2.70×10^{21}	100	45

Table 6
Percentage of mass distributed through each zone. The total for each zone summed over all classes equals 100%. In some zones there were very few (<20) objects of a certain class. We note these here to be aware of possible uncertainties do to small number statistics: A-types in all zones, B-types in Hildas, C-types in Trojans, D-, K-, L-, and S-types in Cybeles, V-types in the middle and outer belt, and X-types in Trojans.

Zone	A	B	C	D	K	L	S	V	E	M	P	Total
Hungaria	7	0	21	1	5	7	9	0	50	0	0	100
Inner	0	<1	6	<1	1	1	21	69	<1	1	<1	100
Middle	<1	15	70	<1	1	1	8	0	<1	1	4	100
Outer	<1	13	52	1	2	1	5	0	<1	10	15	100
Cybele	0	<1	13	2	<1	<1	1	0	0	<1	84	100
Hilda	0	0	14	15	0	<1	0	0	0	1	71	100
Trojan	0	0	2	67	0	<1	0	0	0	4	26	100

Table 7
Percentage of mass distribution for each class in each zone. The percentage for each class summed over all zones equals 100%.

Zone	A	B	C	D	K	L	S	V	E	M	P
Hungaria	<1	0	0	0	<1	<1	0	0	3	0	0
Inner	<1	<1	1	1	10	25	35	100	44	6	<1
Middle	94	74	74	2	37	47	51	0	45	23	21
Outer	6	26	22	8	53	27	14	0	8	67	30
Cybele	0	<1	1	5	<1	1	<1	0	0	<1	36
Hilda	0	0	<1	10	0	<1	0	0	0	<1	8
Trojan	0	0	<1	74	0	<1	0	0	0	3	5
Total	100	100	100	100	100	100	100	100	100	100	100

belt, P-types ~20% and B- and M-types ~5%. The outer belt is heavily weighted toward C-types including or excluding the most massive body, (10) Hygiea. A shift to an abundance of P-types occurs in the Cybeles. Both the Cybeles and Hildas are predominantly P-type by mass. The majority of Trojans are D-type asteroids. Based on these findings, we can confirm and recreate the general trend of E, S, C, P, and D-type asteroids with increasing distance from the Sun as established by Gradie and Tedesco (1982) and Gradie et al. (1989).

Previous work reports the distribution as relative frequency in each semi-major axis bin. Thus the results reported so far can be compared to previous work, however, previous fractions were reported by number and not by mass. This view ignores the relative importance of each semi-major axis zone. The results must be weighted according to how much mass each region holds. The Hungarias only contain about 0.02% of the mass of the inner belt for example. The total mass of each region increases moving outward, peaks in the middle belt and decreases thereafter, though the Trojans hold more mass than the Hildas. Excluding the 4 most massive objects the total mass peaks in the outer belt.

A relative weighting by mass allows us to more accurately see how each class is distributed across the belt (see Table 7). For example there have been differing views about S-type abundances. S-types are typically thought of being most abundant in the inner belt where their relative frequency is greatest (Gradie et al., 1989; Bus and Binzel, 2002a). Mothé-Diniz et al. (2003) find S-types distributed evenly across the main belt. We report that one third of the mass of all S-types is in the inner belt, one half is actually in the middle, belt and ~15% of S-type mass is in the outer belt.

Another example of the importance of relative weighting is the E-types. E-types are typically associated with the Hungaria region. The numerous E-types (Tholen, 1984; Clark et al., 2004) found in this region are thought to be a part of the Hungaria asteroid family (Warner et al., 2009; Milani et al., 2010), the largest being (434) Hungaria after which this region is named. However, Hungarias only account for 3% of the mass of E-types. Nearly 90% of the mass of E-types resides in the inner and middle belt split among a few large asteroids.

While the large majority of V-type mass is contained within Vesta (although one must keep in mind this is a differentiated body and thus has differing composition as a function of distance from the center, only the surface layer is V-type), aside from Vesta nearly 20% of the mass of V-types is in the outer belt, due to (1459) Magnya. A careful study of the distribution of V-types across the belt with follow-up observations of SDSS candidates was performed by (Moskovitz et al., 2008).

Most of the mass of C- and B-types lies in the middle belt, however, if Ceres and Pallas are excluded, the majority lies in the outer belt. While most of the mass of C-types is in the middle and outer belt, the inner belt and Cybeles contain roughly the same amount of C-type material (1%). P-types are actually relatively evenly distributed throughout the middle, outer, and Cybele regions and the Hildas and Trojans only account for a small mass (<15%) although this number is biased because discoveries among Hildas and Trojans are incomplete.

Tables 5–7 provide the total amount of material for each asteroid class present in the inner Solar System and how they are distributed. The composition of each body was set at an early stage of the Solar System formation when the asteroids accreted. The subsequent dynamical history of the Solar System may have shifted their positions and greatly reduced their numbers (e.g., Gomes et al., 2005; Morbidelli et al., 2005; Tsiganis et al., 2005; Minton et al., 2009). The masses listed in Table 5 can be directly compared to the output of numerical simulations using assumptions on the original formation location of each class.

9. Conclusion

In this work we present the bias-corrected taxonomic distribution of asteroids down to 5 km. We present a method to connect the broad-band photometry of the Sloan Digital Sky Survey to previous asteroid taxonomies, based on spectra with high spectral resolution and similar wavelength range. Such a method could be applied to other multi-filter surveys. We then present a bias-correction method relevant to large datasets whereby we select the least-biased subset to account for regions and sizes adequately sampled by the SDSS survey and include a correction for discovery incompleteness of the MPC at the smallest sizes. The color-based taxonomy and bias-correction is used to study the distribution of

material in the asteroid belt for the first time according to a variety of new parameters (surface area, volume, and mass) rather than number to more accurately represent the total material. These quantities add a new perspective that was previously unachievable by studying solely the distribution by number. For instance, the E-types, are often described as unique to the Hungarias yet 90% of E-type mass is in the main belt. Additionally, the primary residence of S-types is typically thought to be the inner belt, yet we find half the mass of S-types is in the middle belt.

We confirm many trends seen in previous works with S- and V-type asteroids accounting for most of the inner belt, and C-, P-, and D-type asteroids dominating the outer belt to the Trojans. We find this view of the compositional distribution of the largest bodies determined in the early 1980s is still robust. We confirm the presence of S-types in the outer parts of the main belt as seen by Mothé-Diniz et al. (2003) as well as the scarcity of S-type among Hildas and Trojans noted by many authors. We find evidence for numerous D-types in the inner belt that were previously expected to be nonexistent in that region, and in possible contradiction with the dynamical models of implementation of trans-neptunian objects in the outer belt during planetary migration.

The main belt's most massive classes are C, B, P, V and S in decreasing order. Excluding the four most massive asteroids, (1) Ceres, (2) Pallas, (4) Vesta and (10) Hygiea that heavily skew the values, primitive material (C-, P-types) account for more than half main-belt and Trojan asteroids, most of the remaining mass being in the S-types. All the other classes are minor contributors to the material between Mars and Jupiter.

Acknowledgments

We thank Rick Binzel, Tom Burbine, and Andy Rivkin for useful discussions and clarifications. We thank two anonymous referees for helpful comments. We acknowledge support from the Faculty of the European Space Astronomy Centre (ESAC) for F.D.'s visit. This material is based upon work supported by the National Science Foundation under Grant 0907766 and by the National Aeronautics and Space Administration under Grant No. NNX12AL26G. Any opinions, findings, and conclusions or recommendations expressed in this material are those of the authors and do not necessarily reflect the views of the National Science Foundation or the National Aeronautics and Space Administration.

Funding for the SDSS and SDSS-II has been provided by the Alfred P. Sloan Foundation, the Participating Institutions, the National Science Foundation, the U.S. Department of Energy, the National Aeronautics and Space Administration, the Japanese Monbukagakusho, the Max Planck Society, and the Higher Education Funding Council for England. The SDSS Web Site is http://www.sdss.org/.

This publication makes use of data products from the Wide-field Infrared Survey Explorer, which is a joint project of the University of California, Los Angeles, and the Jet Propulsion Laboratory/California Institute of Technology, funded by the National Aeronautics and Space Administration.

References

Barucci, M.A., Capria, M.T., Coradini, A., Fulchignoni, M., 1987. Classification of asteroids using G-mode analysis. Icarus 72 (November), 304–324.
Barucci, M.A., Lazzarin, M., Tozzi, G.P., 1999. Compositional surface variety among the Centaurs. Astron. J. 117 (April), 1929–1932.
Bell, J.F., Davis, D.R., Hartmann, W.K., Gaffey, M.J., 1989. Asteroids: The big picture. Asteroids II, 921–948.
Binzel, R.P. et al., 2010. Earth encounters as the origin of fresh surfaces on near-Earth asteroids. Nature 463 (January), 331–334.
Bottke, W.F., Durda, D.D., Nesvorný, D., Jedicke, R., Morbidelli, A., Vokrouhlický, D., Levison, H., 2005. The fossilized size distribution of the main asteroid belt. Icarus 175 (May), 111–140.
Britt, D.T., Consolmagno, G.J., 2003. Stony meteorite porosities and densities: A review of the data through 2001. Meteorit. Planet. Sci. 38 (August), 1161–1180.
Britt, D.T., Yeomans, D.K., Housen, K.R., Consolmagno, G.J., 2002. Asteroid density, porosity, and structure. Asteroids III, 485–500.
Britt, D.T., Consolmagno, G.J., Merline, W.J., 2006. Small body density and porosity: New data, new insights. In: Mackwell, S., Stansbery, E., (Eds.), 37th Annual Lunar and Planetary Science Conference, vol. 37, March. Lunar and Planetary Inst. Technical Report, p. 2214.
Bus, S.J., 1999. Compositional Structure in the Asteroid Belt: Results of a Spectroscopic Survey. Ph.D. Thesis, Massachusetts Institute of Technology (January).
Bus, S.J., Binzel, R.P., 2002a. Phase II of the Small Main-Belt Asteroid Spectroscopic Survey: A feature-based taxonomy. Icarus 158 (July), 146–177.
Bus, S.J., Binzel, R.P., 2002b. Phase II of the Small Main-Belt Asteroid Spectroscopic Survey: The observations. Icarus 158 (July), 106–145.
Carruba, V., Domingos, R.C., Nesvorný, D., Roig, F., Huaman, M.E., Souami, D., 2013. A multi-domain approach to asteroid families identification. Mon. Not. R. Astron. Soc., in press.
Carry, B., 2012. Density of asteroids. Planet. Space Sci. 73 (Decembe), 98–118.
Carvano, J.M., Hasselmann, H., Lazzaro, D., Mothé-Diniz, T., 2011. SDSS-based taxonomic classification and orbital distribution of main belt asteroids. Astron. Astrophys. 510, 1–12.
Cellino, A., Bus, S.J., Doressoundiram, A., Lazzaro, D., 2002. Spectroscopic properties of asteroid families. Asteroids III, 633–643.
Chapman, C.R., Johnson, T.V., McCord, T.B., 1971. A review of spectrophotometric studies of asteroids. NASA Spec. Publ. 267, 51–65.
Chapman, C.R., Morrison, D., Zellner, B.H., 1975. Surface properties of asteroids – A synthesis of polarimetry, radiometry, and spectrophotometry. Icarus 25 (May), 104–130.
Clark, B.E., Bus, S.J., Rivkin, A.S., Shepard, M.K., Shah, S., 2004. Spectroscopy of X-type asteroids. Astron. J. 128 (December), 3070–3081.
Consolmagno, G.J., Britt, D.T., 1998. The density and porosity of meteorites from the Vatican collection. Meteorit. Planet. Sci. 33 (November), 1231–1241.
Consolmagno, G., Britt, D., Macke, R., 2008. The significance of meteorite density and porosity. Chemie der Erde/Geochemistry 68 (April), 1–29.
Consolmagno, G., Macke, R.J., Britt, D.T., 2012. The evidence in asteroids for chemical and physical trends in the solar nebula. In: AAS Division for Planetary Sciences Meeting Abstracts, vol. 44, October, p. 110.20 (abstracts).
DeMeo, F., 2010. Ph.D. Thesis, Observatoire de Paris.
DeMeo, F.E., Binzel, R.P., Slivan, S.M., Bus, S.J.., 2009. An extension of the Bus asteroid taxonomy into the near-infrared. Icarus 202 (July), 160–180.
Dohnanyi, J.S., 1969. Collisional model of asteroids and their Debris. J. Geophys. Res. 74 (May), 2431–2554.
Elkins-Tanton, L.T., Weiss, B.P., Zuber, M.T., 2011. Chondrites as samples of differentiated planetesimals. Earth Planet. Sci. Lett. 305, 1–10.
Emery, J.P., Brown, R.H., 2003. Constraints on the surface composition of Trojan asteroids from near-infrared (0.8–4.0 μm) spectroscopy. Icarus 164 (July), 104–121.
Emery, J.P., Brown, R.H., 2004. The surface composition of Trojan asteroids: Constraints set by scattering theory. Icarus 170 (July), 131–152.
Emery, J.P., Burr, D.M., Cruikshank, D.P., 2011. Near-infrared spectroscopy of Trojan asteroids: Evidence for two compositional groups. Astron. J. 141 (January), 25, 1–18.
Fernández, Y.R., Jewitt, D., Ziffer, J.E., 2009. Albedos of small jovian Trojans. Astron. J. 138 (July), 240–250.
Fornasier, S., Dotto, E., Marzari, F., Barucci, M.A., Boehnhardt, H., Hainaut, O., de Bergh, C., 2004. Visible spectroscopic and photometric survey of L5 Trojans: Investigation of dynamical families. Icarus 172 (November), 221–232.
Fornasier, S., Dotto, E., Hainaut, O., Marzari, F., Boehnhardt, H., de Luise, F., Barucci, M.A., 2007. Visible spectroscopic and photometric survey of Jupiter Trojans: Final results on dynamical families. Icarus 190 (October), 622–642.
Gaffey, M.J., Bell, J.F., Cruikshank, D.P., 1989. Reflectance spectroscopy and asteroids surface mineralogy. Asteroids II, 98–127.
Gil-Hutton, R., Brunini, A., 2008. Surface composition of Hilda asteroids from the analysis of the Sloan Digital Sky Survey colors. Icarus 193 (February), 567–571.
Gladman, B.J., Davis, D.R., Neese, C., Jedicke, R., Williams, G., Kavelaars, J.J., Petit, J.-M., Scholl, H., Holman, M., Warrington, B., Esquerdo, G., Tricarico, P., 2009. On the asteroid belt's orbital and size distribution. Icarus 202 (July), 104–118.
Gomes, R., Levison, H.F., Tsiganis, K., Morbidelli, A., 2005. Origin of the cataclysmic Late Heavy Bombardment period of the terrestrial planets. Nature 435 (May), 466–469.
Gradie, J., Tedesco, E., 1982. Compositional structure of the asteroid belt. Science 216 (June), 1405–1407.
Gradie, J.C., Chapman, C.R., Tedesco, E.F., 1989. Distribution of taxonomic classes and the compositional structure of the asteroid belt. Asteroids II, 316–335.
Grav, T. et al., 2011. WISE/NEOWISE observations of the jovian Trojans: Preliminary results. Astrophys. J. 742 (November), 40, 1–10.
Grav, T. et al., 2012a. WISE/NEOWISE observations of the Hilda population: Preliminary results. Astrophys. J. 744 (January), 197, 1–15.
Grav, T., Mainzer, A.K., Bauer, J.M., Masiero, J.R., Nugent, C.R., 2012b. WISE/NEOWISE observations of the jovian Trojan population: Taxonomy. Astrophys. J. 759 (November), 49, 1–10.
Hasselmann, P.H., Carvano, J.M., Lazzaro, D., 2011. SDSS-based asteroid taxonomy V1.0. NASA Planet. Data Syst. (June).
Holmberg, J., Flynn, C., Portinari, L., 2006. The colours of the Sun. Mon. Not. R. Astron. Soc. 367 (April), 449–453.

Ivezić, Ž. et al., 2001. Solar System objects observed in the Sloan Digital Sky Survey Commissioning Data. Astron. J. 122 (November), 2749–2784.

Ivezić, Ž. et al., 2002. Color confirmation of asteroid families. Astron. J. 124 (November), 2943–2948.

Jedicke, R., Larsen, J., Spahr, T., 2002. Observational selection effects in asteroid surveys. Asteroids III, 71–87.

Kiang, T., 1971. The distribution of asteroids in the direction perpendicular to the Ecliptic plane. NASA Spec. Publ. 267, 187–195.

Kuchynka, P., Folkner, W.M., 2013. A new approach to determining asteroid masses from planetary range measurements. Icarus 222 (January), 243–253.

Lazzaro, D., Angeli, C.A., Carvano, J.M., Mothé-Diniz, T., Duffard, R., Florczak, M., 2004. S^3OS^2: The visible spectroscopic survey of 820 asteroids. Icarus 172 (November), 179–220.

Levison, H.F., Bottke, W.F., Gounelle, M., Morbidelli, A., Nesvorný, D., Tsiganis, K., 2009. Contamination of the asteroid belt by primordial trans-neptunian objects. Nature 460 (July), 364–366.

Lipschutz, M.E., Gaffey, M.J., Pellas, P., 1989. Meteoritic parent bodies: Nature, number, size and relation to present-day asteroids. Asteroids II, 740–777.

Macke, R.J., Consolmagno, G.J., Britt, D.T., Hutson, M.L., 2010. Enstatite chondrite density, magnetic susceptibility, and porosity. Meteorit. Planet. Sci. 45 (September), 1513–1526.

Macke, R.J., Britt, D.T., Consolmagno, G.J., 2011. Density, porosity, and magnetic susceptibility of achondritic meteorites. Meteorit. Planet. Sci. 46 (February), 311–326.

Mainzer, A. et al., 2011. Preliminary results from NEOWISE: An enhancement to the wide-field infrared survey explorer for Solar System science. Astrophys. J. 731 (April), 53–66.

Masiero, J.R. et al., 2011. Main belt asteroids with WISE/NEOWISE. I. Preliminary albedos and diameters. Astrophys. J. 741 (November), 68, 1–20.

Masiero, J.R. et al., 2012. Preliminary analysis of WISE/NEOWISE 3-band cryogenic and post-cryogenic observations of main belt asteroids. Astrophys. J. 759 (November), 1–5, L8.

Milani, A., Knežević, Z., Novaković, B., Cellino, A., 2010. Dynamics of the Hungaria asteroids. Icarus 207 (June), 769–794.

Minton, D.A., Malhotra, R., 2009. A record of planet migration in the main asteroid belt. Nature 457 (February), 1109–1111.

Morbidelli, A., Levison, H.F., Tsiganis, K., Gomes, R., 2005. Chaotic capture of Jupiter's Trojan asteroids in the early Solar System. Nature 435 (May), 462–465.

Moskovitz, N.A., Jedicke, R., Gaidos, E., Willman, M., Nesvorný, D., Fevig, R., Ivezić, Ž., 2008. The distribution of basaltic asteroids in the main belt. Icarus 198 (November), 77–90.

Mothé-Diniz, T., Carvano, J.M.Á., Lazzaro, D., 2003. Distribution of taxonomic classes in the main belt of asteroids. Icarus 162 (Mar.), 10–21.

Mueller, M. et al., 2011. ExploreNEOs III physical characterization of 65 potential spacecraft target asteroids. Astron. J. 141 (April), 109, 1–9.

Nakamura, T. et al., 2011. Itokawa dust particles: A direct link between S-type asteroids and ordinary chondrites. Science 333 (August), 1113–1115, <http://adsabs.harvard.edu/abs/2011Sci...333.1113N>.

Neese, C., 2010. Asteroid Taxonomy. NASA Planetary Data System, eAR-A-5-DDR-TAXONOMY-V6.0.

Nesvorný, D., Jedicke, R., Whiteley, R.J., Ivezić, Ž., 2005. Evidence for asteroid space weathering from the Sloan Digital Sky Survey. Icarus 173 (January), 132–152.

Nesvorný, D., Vokrouhlický, D., Bottke, W.F., Sykes, M., 2006. Physical properties of asteroid dust bands and their sources. Icarus 181 (March), 107–144.

Nesvorný, D., Bottke, W.F., Vokrouhlický, D., Sykes, M., Lien, D.J., Stansberry, J., 2008. Origin of the near-Ecliptic circumsolar dust band. Astrophys. J. 679 (June), L143–L146.

Ockert-Bell, M.E., Clark, B.E., Shepard, M.K., Isaacs, R.A., Cloutis, E.A., Fornasier, S., Bus, S.J., 2010. The composition of M-type asteroids: Synthesis of spectroscopic and radar observations. Icarus 210 (December), 674–692.

Parker, A., Ivezić, Ž., Jurić, M., Lupton, R., Sekora, M.D., Kowalski, A., 2008. The size distributions of asteroid families in the SDSS Moving Object Catalog 4. Icarus 198 (November), 138–155.

Pravec, P., Harris, A.W., 2007. Binary asteroid population. 1. Angular momentum content. Icarus 190 (September), 250–259.

Pravec, P., Harris, A.W., Kušnirák, P., Galád, A., Hornoch, K., 2012. Absolute magnitudes of asteroids and a revision of asteroid albedo estimates from WISE thermal observations. Icarus 221 (September), 365–387.

Rivkin, A.S., Howell, E.S., Lebofsky, L.A., Clark, B.E., Britt, D.T., 2000. The nature of M-class asteroids from 3-micron observations. Icarus 145 (June), 351–368.

Roig, F., Ribeiro, A.O., Gil-Hutton, R., 2008. Taxonomy of asteroid families among the Jupiter Trojans: comparison between spectroscopic data and the Sloan Digital Sky Survey colors. Astron. Astrophys. 483 (June), 911–931.

Romanishin, W., Tegler, S.C., 2005. Accurate absolute magnitudes for Kuiper belt objects and Centaurs. Icarus 179 (December), 523–526.

Russell, C.T. et al., 2012. Dawn at Vesta: Testing the protoplanetary paradigm. Science 336 (May), 684–686.

Ryan, E.L., Woodward, C.E., 2010. Rectified asteroid albedos and diameters from IRAS and MSX photometry catalogs. Astron. J. 140 (October), 933–943.

Shepard, M.K., Clark, B.E., Nolan, M.C., Howell, E.S., Magri, C., Giorgini, J.D., Benner, L.A.M., Ostro, S.J., Harris, A.W., Warner, B.D., Pray, D.P., Pravec, P., Fauerbach, M., Bennett, T., Klotz, A., Behrend, R., Correia, H., Coloma, J., Casulli, S., Rivkin, A.S., 2008. A radar survey of M- and X-class asteroids. Icarus 195 (May), 184–205.

Stuart, J.S., Binzel, R.P., 2004. Bias-corrected population, size distribution, and impact hazard for the near-Earth objects. Icarus 170 (August), 295–311.

Tedesco, E.F., Noah, P.V., Noah, M.C., Price, S.D., 2002. The supplemental IRAS minor planet survey. Astron. J. 123 (February), 1056–1085.

Tholen, D.J., 1984. Asteroid Taxonomy from Cluster Analysis of Photometry. Ph.D. Thesis, Arizona Univ., Tucson.

Tsiganis, K., Gomes, R., Morbidelli, A., Levison, H.F., 2005. Origin of the orbital architecture of the giant planets of the Solar System. Nature 435 (May), 459–461.

Usui, F. et al., 2011. Asteroid catalog using Akari: AKARI/IRC mid-infrared asteroid survey. Publ. Astron. Soc. Jpn. 63 (June), 1117–1138.

Veverka, J. et al., 1997. NEAR's flyby of 253 Mathilde: Images of a C asteroid. Science 278, 2109–2114.

Warner, B.D., Harris, A.W., Vokrouhlický, D., Nesvorný, D., Bottke, W.F., 2009. Analysis of the Hungaria asteroid population. Icarus 204 (November), 172–182.

Weiss, B.P. et al., 2012. Possible evidence for partial differentiation of Asteroid Lutetia from Rosetta. Planet. Space Sci. 66 (June), 137–146.

Xu, S., Binzel, R.P., Burbine, T.H., Bus, S.J., 1995. Small Main-Belt Asteroid Spectroscopic Survey: Initial results. Icarus 115 (May), 1–35.

Yang, B., Jewitt, D., 2007. Spectroscopic search for water ice on jovian Trojan asteroids. Astron. J. 134 (July), 223–228.

Yang, B., Jewitt, D., 2011. A near-infrared search for silicates in jovian Trojan asteroids. Astron. J. 141 (Mar.), 95, 1–8.

Zellner, B., Tholen, D.J., Tedesco, E.F., 1985. The eight-color asteroid survey – Results for 589 minor planets. Icarus 61 (March), 355–416.

REVIEW

doi:10.1038/nature12908

Solar System evolution from compositional mapping of the asteroid belt

F. E. DeMeo[1,2] & B. Carry[3,4]

Advances in the discovery and characterization of asteroids over the past decade have revealed an unanticipated underlying structure that points to a dramatic early history of the inner Solar System. The asteroids in the main asteroid belt have been discovered to be more compositionally diverse with size and distance from the Sun than had previously been known. This implies substantial mixing through processes such as planetary migration and the subsequent dynamical processes.

Although studies of exoplanetary systems have the advantage of numbers[1] to answer the question of how planetary systems are built, our Solar System has the advantage of detail. For nearly two centuries since their first discovery, asteroids have been viewed as remnants of planetary formation. Located between Mars and Jupiter in the main asteroid belt (Fig. 1), they were thought to have formed essentially where they now are[2].

Early measurements showed asteroids in the inner part of the main asteroid belt were more reflective and appear subtly 'redder' than the outer, 'bluer' ones[3–6]. In the 1980s, distinct colour groupings of major asteroid compositional types were discovered as a function of distance from the Sun[2]. In the classic theory, this was interpreted as the remnant of a thermal gradient across the main belt at the time the Solar System formed[2,7–9]. An understanding of that gradient promised to hold clues to the initial conditions during planet formation.

Yet, over the course of the discovery of over half a million asteroids since the 1980s, the idea of a static Solar System history has dramatically shifted to one of great dynamic change and mixing. Driving this view was the effect on the main asteroid belt of planetary migration models that aimed to recreate the structure of the rest of the Solar System, such as the orbits of the giant planets, Pluto and the transneptunian objects, and the Jupiter Trojan asteroids (which reside in the L4 and L5 Lagrange points of Jupiter's orbit)[10–13].

As the planetary migration models evolved, so also new compositional characteristics of the main belt were uncovered through observation that were increasingly inconsistent with the classic theory. At first, just a few rogue asteroids were found to be contaminating the distinct groupings[14–16]. Now, with tens of thousands of asteroids to analyse for which we have compositional measurements[17,18], we can see that this mixing of asteroid types is more of the rule, rather than the exception, across the main belt[19].

Today, all the newly revealed aspects of the main asteroid belt, including its orbital and compositional structure and the dynamical processes that sculpt it, contribute to a more coherent story. In modern dynamical models, the giant planets are thought to have migrated over substantial distances, shaking up the asteroids—which formed throughout the Solar System—like flakes in a snow globe, and transporting some of them to their current locations in the asteroid belt (Fig. 2). The main asteroid belt thus samples the conditions across the entire Solar System. Yet, at the same time, the Hilda asteroids (located 4 AU from the Sun between the main belt and Jupiter (one astronomical unit is approximately the Earth–Sun distance); see Fig. 1) and the Jupiter Trojans appear distinctly homogeneous, challenging us to untangle the various events of the Solar System's evolution. Our Solar System's path to creating the arrangement of the planets today and the conditions that made life on Earth possible will set the context for understanding the myriad of exoplanetary systems.

Send in the rogues

Their generally redder-to-bluer colour and compositional trend implied that asteroids tend to preserve their initial formation environment: the temperature and compositional gradient in that part of the disk at the time of planetesimal formation[2,9]. From what astronomers understood at the time (the 1980s), guided by comparison with meteorites, the reddish (with a positive slope from ultraviolet-to-visible wavelengths) ones filling the inner main belt were melted igneous bodies[20], and the bluish (with a neutral slope from the ultraviolet-to-visible) ones in the outer main belt had undergone little thermal alteration[6]. The goal of the next decade (the 1990s) was to explain how the thermal gradient could be so steep, creating such wildly different outcomes, from melted to primitive over a distance of just 1 AU (ref. 21).

That original interpretation of the compositions of reddish and bluish asteroids was wrong. In fact, direct sampling (by spacecraft[22]) of the reddish asteroid (25143) Itokawa definitively showed that it did experience some heating but was relatively primitive, compared with the previous interpretation of a melted body[23–27]. Although it was still a challenge to explain the asteroids' compositional and thermal trend from warm to cold, it was not as drastic a gradient as had been supposed.

Such compositional measurements for the largest asteroids seemed to explain the gradient better, but the few measurements becoming available for smaller objects were beginning to reveal the misfits. First was (1459) Magnya, a basaltic fragment discovered among the cold, bluish bodies[14]. Then, a handful more of these rogue igneous asteroids were found dispersed across the main asteroid belt[16,28,29]. Iron asteroids present in the main belt should have formed much closer to the Sun[15]. Primitive asteroids were discovered in the inner belt[30], and furthermore, the reddish objects occurred throughout the outer belt[31–33]. Other asteroids that appeared to be dry asteroids were discovered to contain volatiles on or just below the surface, suggesting that they formed beyond the snowline (the distance from the Sun at which the temperature is low enough for water to be ice)[34–38]. At first, these observations seemed to represent 'contamination' by individual, unusual asteroids, but gradually it has become clear that even the core groups of reddish and bluish asteroids were more broadly distributed, further challenging the classic theory of a static Solar System.

[1]Harvard-Smithsonian Center for Astrophysics, 60 Garden Street, MS-16, Cambridge, Massachusetts 02138, USA. [2]Department of Earth, Atmospheric and Planetary Sciences, Massachusetts Institute of Technology (MIT), 77 Massachusetts Avenue, Cambridge, Massachusetts 02139, USA. [3]Institut de Mécanique Céleste et de Calcul des Éphémérides, Observatoire de Paris, UMR8028 CNRS, 77 avenue Denfert-Rochereau, 75014 Paris, France. [4]European Space Astronomy (ESA) Centre, PO Box 78, Villanueva de la Cañada 28691, Madrid, Spain.

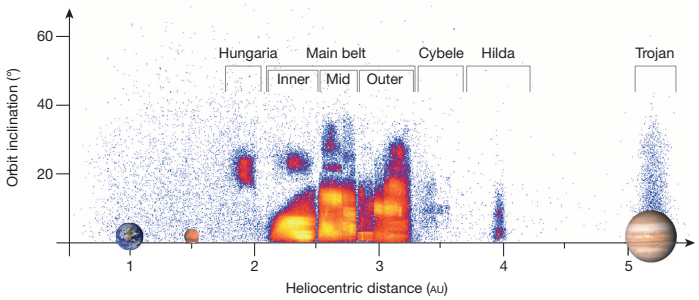

Figure 1 | The asteroid belt in context with the planets. This plot shows the location of the main belt with respect to the planets and the Sun as well as the orbital structure of asteroid inclinations and number density of objects (yellow represents the highest number density, blue the lowest). Asteroids have much higher orbital eccentricities and inclinations than do the planets. The structure of the main belt is divided by unstable regions, seen most prominently at 2.5 AU and 2.8 AU (locations where an asteroid's orbit is 'in resonance' with Jupiter's orbit), that separate the inner, middle and outer sections of the main belt. The Hungaria asteroids are located closer to the Sun than is the main belt and have orbital inclinations centred near 20 degrees. The Hildas are located near 4 AU and the Jupiter Trojans are in the L4 and L5 Lagrange points of Jupiter's orbit.

The compositional medley of asteroids

Equipped with an abundance of visible-wavelength colours and surface-brightness measurements from recent surveys[17,18] we can now reveal a new map of the distribution of asteroids down to diameters of 5 km (ref. 19) (Fig. 3). Traditionally, the distribution has been presented as the relative fraction of asteroid classes as a function of distance[2,9,31,32]. Now we compare bodies ranging from 5 km to 1,000 km in diameter, so an equal weighting would distort the view. By transforming the map of the asteroid belt to the distribution of mass[19,39], we are able to account for each asteroid type accurately, rather than the frequency or number of types (Fig. 3). Furthermore, we can now explore the change in distribution as a function of size (Fig. 4).

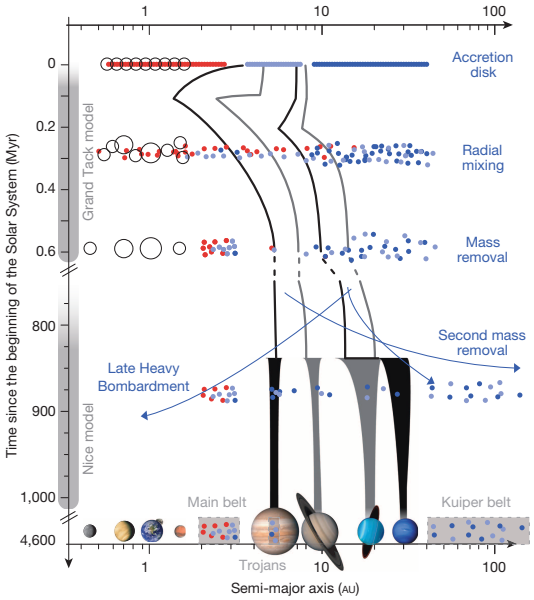

Figure 2 | Cartoon of the effects of planetary migration on the asteroid belt. This figure captures some major components of the dynamical history of small bodies in the Solar System based on models[11,12,51,54]. These models may not represent the actual history of the Solar System, but are possible histories. They contain periods of radial mixing, mass removal and planet migration—ultimately arriving at the current distribution of planets and small-body populations.

This is what we have found. The rarer asteroid types, such as the crust and mantle remnants of fully heated and melted bodies, are seen in all regions of the main belt[14,16]. We do not yet know whether this means that the locations of their respective parent bodies were ubiquitous in the inner Solar System or whether they were created close to the Sun and later injected into the main belt[15,40].

Asteroids that look compositionally Trojan-like (D-types; see Fig. 3) are detected in the inner belt, where they are not predicted to exist by dynamical models[19,41,42]. Their presence so close to the Sun demands an explanation for how they arrived there and whether they are really linked to the Trojan asteroids at all.

The Hungaria region is typically associated with its eponymous and brightest member, (434) Hungaria, and similarly super-reflective asteroids[2,8] (E-types; see Fig. 3). Despite this, most of the mass of this region is contained within a few reddish and bluish objects, which are also common elsewhere in the main belt[43–45].

The relative mass contribution of each asteroid class changes as a function of size in each region of the main belt. Most dramatic is the increase of bluish objects (C-types; see Fig. 3) as size decreases in the inner belt. Although these bluish objects are notoriously rare in the inner belt at large sizes[2,32], where they comprise only 6% of the total mass, half of the mass is bluish at the smallest sizes.

In the outer belt, reddish asteroids (S-types; see Fig. 3) make up a small fraction of the total there, yet their actual mass is still quite significant. In fact, we now find more than half of the mass of reddish objects outside the inner belt[19].

Just over a decade ago, astronomers still clung to the concept of an orderly compositional gradient across the main asteroid belt[46]. Since then the trickle of asteroids discovered in unexpected locations has turned into a river. We now see that all asteroid types exist in every region of the main belt (see Box 1 for a discussion of Hildas and Trojans). The smorgasbord of compositional types of small bodies throughout the main belt contrasts with the compositional groupings at large sizes. All these features demanded major changes in the interpretation of the history of the current asteroid belt and, in turn, of the Solar System.

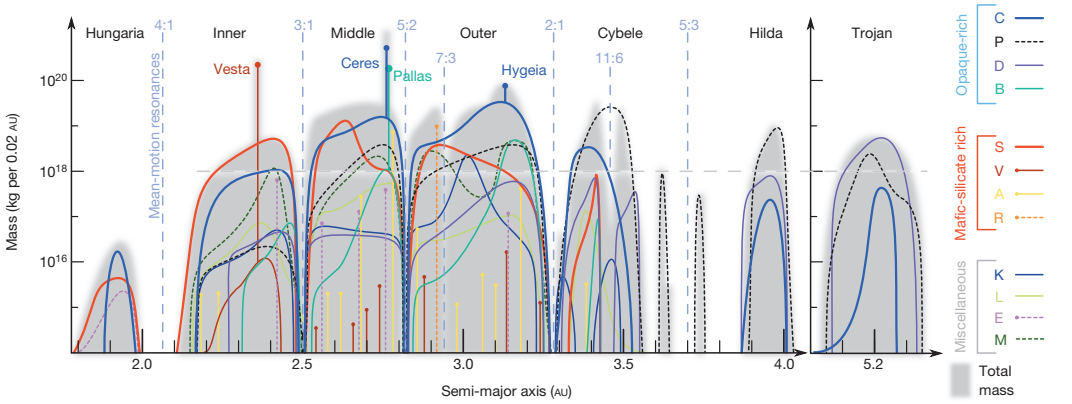

Figure 3 | The compositional mass distribution throughout the asteroid belt out to the Trojans. The grey background is the total mass within each 0.02-AU bin. Each colour represents a unique spectral class of asteroid, denoted by a letter in the key. The horizontal line at 10^{18} kg is the limit of the work from the 1980s[2,8,9]. The upper portion of the plot remains consistent with that work, but immense detail is now revealed at the lower mass range[19].

Cracking the 'compositional code' of the map

Earlier planetesimal-formation theories that explained the history of the asteroid belt invoked turbulence in the nebula, radial decay of material due to gas drag, sweeping resonances and scattered embryos[47,48]. Individually, each mechanism was, however, insufficient, and even together, although many of these mechanisms could deplete, excite and partially mix the main belt, they could not adequately reproduce the current asteroid belt[49].

The concept of planetary migration—whereby the planets change orbits over time owing to gravitational effects from the surrounding dust, gas or planetesimals—was not new, but its introduction as a major driver of the history of the asteroid belt came only recently. Migration models began by explaining the orbital structure and mass distribution of the outer Solar System, including the Kuiper belt past Neptune[50]. Individual models could successfully recreate specific parts, but we still sought to define a consistent set of events that would explain all aspects of the outer Solar System. Every action of the planets causes a reaction in the asteroid belt, so these models also needed to be consistent with the compositional framework within the main belt that we see today.

The Nice model was the first comprehensive solution that could simultaneously explain many unique structural properties of the Solar System[11–13,51,52],

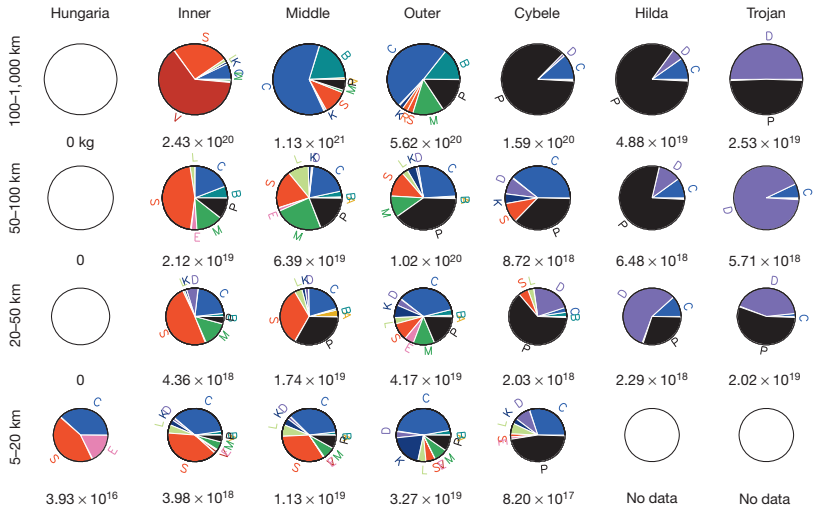

Figure 4 | The compositional mass distribution as a function of size throughout the main belt out to the Trojans. The mass is calculated for each individual object with a diameter of 50 km and greater, using its albedo to determine size and the average density[39] for that asteroid's taxonomic class. For the smaller sizes we determine the fractional contribution of each class at each size and semi-major axis, and then apply that fraction to the distribution of all known asteroids from the Minor Planet Center (http://minorplanetcenter.org/) including a correction for discovery incompleteness at the smallest sizes in the middle and outer belt[19]. Asteroid mass is grouped according to objects within four size ranges, with diameters of 100–1,000 km, 50–100 km, 20–50 km and 5–20 km. Seven zones are defined as in Fig. 1: Hungaria, inner belt, middle belt, outer belt, Cybele, Hilda and Trojan. The total mass of each zone at each size is labelled and the pie charts mark the fractional mass contribution of each unique spectral class of asteroid. The total mass of Hildas and Trojans are underestimated because of discovery incompleteness. The relative contribution of each class changes with both size and distance.

RESEARCH REVIEW

BOX 1

The Hilda and Trojan asteroids

The Hilda and Jupiter Trojan asteroids are located beyond the main asteroid belt at 4 AU and 5.2 AU, respectively (Fig. 1). The asteroid types in these regions are physically distinct from the main belt and from each other: the largest Hildas are dominated by spectral P-type asteroids and the largest Trojans are dominated by D-types[2] (Fig. 3). Despite interlopers of all types becoming more common throughout the main belt, the Hildas and Trojans remained curiously distinct and homogeneous.

Continued observations find that bright objects among Hildas and Trojans are scarce even at the small size scales[78–85]. It was recently and unexpectedly discovered, however, that the smallest bodies in these regions break rank (Fig. 4): most of the small Hildas have physical properties more similar to Trojans (D-type) and the makeup of the Trojans also changes with size with differing fractions of D-types and Hilda-like P-types[19,86,87]. Migration scenarios can now explain why the Hildas and Trojans look so different from the main belt, but they cannot yet explain the important details of why they look distinct from each other at the largest sizes (in relative fraction of the D-type and P-type asteroids) and are also different at the smaller sizes.

such as the locations of the giant planets and their orbital eccentricities[11], capture of the irregular satellites of Saturn[53], and the orbital properties of the Trojans[12] (Fig. 2). In the original model, Jupiter moves inward while the other giant planets migrate outward. As Jupiter and Saturn cross their 1:2 mean motion resonance, the system is destabilized[11]. In the most recent version of this model, the interaction between the giant planets and a massive, distant Kuiper disk causes the system to destabilize[13]. At that point, the primordial Jupiter Trojan region is emptied. Bodies that were scattered inward from beyond Neptune then repopulate this region. By reproducing the Trojans' orbital distributions and mass, the Nice model also naturally explains the why the Trojan region is compositionally distinct from the main belt: it would be populated solely by outer Solar System bodies and would not contain locally formed asteroids.

Missing from the Nice model, however, was an explanation of the large-scale mixing of reddish and bluish material in the asteroid belt that was becoming increasingly prominent. The Grand Tack model[54] showed that during the time of terrestrial planet formation (before the events of the Nice model would have taken place), Jupiter could have migrated as close to the Sun as Mars is today. Jupiter would have moved right through the primordial asteroid belt, emptying it and then repopulating it with scrambled material from both the inner and outer Solar System as Jupiter then reversed course and headed back towards the outer Solar System. Once the details of the resulting distribution in the Grand Tack model have been closely compared to the emerging observational picture, it will become clear whether this model can crack the asteroid belt's 'compositional code'.

Planetary migration ends well within the first billion years of our Solar System's 4.5-billion-year history. The asteroid belt, however, is still dynamic today. Collisions between asteroids are continuously grinding the bodies down to smaller and smaller sizes. The smaller ones (<40 km) are then subject to the Yarkovsky effect, according to which uneven diurnal heating and cooling of the body alters its orbit[55–59]. The Yarkovsky effect thoroughly mixes small bodies within each section of the main belt, but once they reach a major resonance—such as the 3:1 and 5:2 mean motion resonances at the locations where the orbital periods of an asteroid and of Jupiter are related by integers—they are swiftly ejected from the main belt[57–59]. Current observations[60,61] and models[28,62–64] indicate that the strong resonances with Jupiter inhibit the crossing of material from one region to another. These processes continue to mould the asteroid belt, erasing some of its past history and creating new structures in this complex system.

New observational evidence that reveals a greater mixing of bodies supports the idea of a Solar System that was and continues to be in a state of evolution and flux. Indeed, dynamical models have been leading us step-by-step to interpret the asteroid belt as a melting pot of bodies arriving from diverse backgrounds. Dynamical models have come a long way, but they have yet to explain the dichotomy between the orderly trend among the largest asteroids and the increased mixing of asteroid types at smaller sizes. Particularly noticeable are the scatter of igneous bodies and the existence of asteroids that look physically similar to Trojans in the inner belt. These details promise to teach us how our Solar System was built, providing context for other planetary systems.

The future

The ultimate goal of asteroid studies is to complete the picture of where these bodies formed and how they relate to the current chemistry and volatile abundance on Earth. No longer is our Solar System just an isolated example, and with only a minimal speculative extrapolation, asteroid-like building blocks seem likely to have influenced countless terrestrial-like planetary systems. The ongoing hunt for Earth-like planets has as its corollary the hunt for possible signatures of asteroid-like zones and an assessment of their uniqueness or commonality in all planetary systems.

Even though we now know the asteroid distributions in the Solar System down to 5 km, we are still literally only scratching the surface of what can be known about them. Asteroid interiors are the *terra incognita* for the next generation of asteroid researchers. At present we are frustrated by the inability of most physical measurements to provide any information on the interior of an asteroid. An asteroid's interior reveals its thermal history, which constrains the initial conditions of the protoplanetary disk during planetesimal formation. NASA's Dawn spacecraft mission recently provided a glimpse inside Vesta, determining the core mass fraction of this large asteroid from shape and gravity measurements[65]. When Dawn visits Ceres, we will learn to what extent this large asteroid differentiated into an ice mantle and rocky core[66–68]. Increased measurements of asteroid densities, provided mainly by the study of binary asteroids, will help us to infer their interior structure[39].

Each of our broad asteroid classes probably encompasses a wide variety of surface compositions[69,70]. Our meteorite collection has provided significant detail about the range of asteroid compositions, but to make firm links between the asteroids and meteorites, we need to observe an asteroid in space and then measure the same body in a laboratory. This will be achieved by asteroid sample return missions that are already under way[71–73], as well as 'free sample return' by meteorite falls such as the serendipitously discovered Almahata Sitta meteorite (formerly asteroid 2008 TC_3)[74,75].

Finally, the next step in distribution trends is to complement a refined understanding of asteroid compositions with physical measurements capable of detecting that detail on a large scale. The compositional trends discussed up to now cover broad taxonomic classes and combine objects into just a few major groups that do not accurately reflect the complexity of the asteroids' original and current compositions. Higher-spectral-resolution large-scale surveys at visible[76,77] and near- to mid-infrared wavelengths combined with the already available albedo information for hundreds of thousands of asteroids would be the most realistic data set to attain over the next decade or two.

Received 10 July; accepted 22 November 2013.

1. Wright, J. T. *et al.* The Exoplanet Orbit Database. *Publ. Astron. Soc. Pacif.* **123,** 412–422 (2011).
2. Gradie, J. & Tedesco, E. Compositional structure of the asteroid belt. *Science* **216,** 1405–1407 (1982).
This is a comprehensive view of the compositional trends of the asteroid belt that served for decades as the backbone for interpretations of the main belt.
3. Fischer, H. Farbmessungen an kleinen planeten. *Astron. Nachr.* **272,** 127–147 (1941).
4. Wood, X. H. J. & Kuiper, G. P. Photometric studies of asteroids. *Astrophys. J.* **137,** 1279–1285 (1963).
5. Chapman, C. R., Johnson, T. V. & McCord, T. B. in *Proc. IAU Colloq. 12* (ed. Gehrels, T.) SP 267, 1–47 (National Aeronautics and Space Administration, 1971).
6. Chapman, C. R., Morrison, D. & Zellner, B. Surface properties of asteroids—a synthesis of polarimetry, radiometry, and spectrophotometry. *Icarus* **25,** 104–130 (1975).

7. Zellner, B., Tholen, D. J. & Tedesco, E. F. The eight-color asteroid survey—results for 589 minor planets. *Icarus* **61,** 355–416 (1985).
8. Gradie, J. C., Chapman, C. R. & Tedesco, E. F. in *Asteroids II* (eds Binzel, R. P., Gehrels, T. & Matthews, M. S.) 316–335 (Univ. Arizona Press, 1989).
9. Bell, J. F., Davis, D. R., Hartmann, W. K. & Gaffey, M. J. in *Asteroids II* (eds Binzel, R. P., Gehrels, T. & Matthews, M. S.) 921–945 (Univ. Arizona Press, 1989).
10. Malhotra, R. The origin of Pluto's peculiar orbit. *Nature* **365,** 819–821 (1993).
11. Tsiganis, K., Gomes, R., Morbidelli, A. & Levison, H. F. Origin of the orbital architecture of the giant planets of the Solar System. *Nature* **435,** 459–461 (2005).
12. Morbidelli, A., Levison, H. F., Tsiganis, K. & Gomes, R. Chaotic capture of Jupiter's Trojan asteroids in the early Solar System. *Nature* **435,** 462–465 (2005).
13. Levison, H. F., Morbidelli, A., Tsiganis, K., Nesvorny, D. & Gomes, R. Late orbital instabilities in the outer planets induced by interaction with self-gravitating planetesimal disk. *Astron. J.* **142,** 152 (2011).
14. Lazzaro, D. *et al.* Discovery of a basaltic asteroid in the outer main belt. *Science* **288,** 2033–2035 (2000).
15. Bottke, W. F., Nesvorny, D., Grimm, R. E., Morbidelli, A. & O'Brien, D. P. Iron meteorites as remnants of planetesimals formed in the terrestrial planet region. *Nature* **439,** 821–824 (2006).
16. Moskovitz, N. A. *et al.* The distribution of basaltic asteroids in the main belt. *Icarus* **198,** 77–90 (2008).
17. Ivezić, Z. *et al.* Solar System objects observed in the Sloan Digital Sky Survey commissioning data. *Astron. J.* **122,** 2749–2784 (2001).
This is the original article on asteroid measurements from the Sloan Digital Sky Survey (SDSS), which provided multi-filter photometry in the visible spectrum for over 100,000 asteroids.
18. Mainzer, A. *et al.* Preliminary Results from NEOWISE: an enhancement to the Wide-field Infrared Survey Explorer for Solar System science. *Astrophys. J.* **731,** 53 (2011).
This is the original article on asteroid measurements from the Wide-field Infrared Survey Explorer (WISE), which provides diameters and albedos (surface brightness) for over 100,000 asteroids.
19. DeMeo, F. E. & Carry, B. The taxonomic distribution of asteroids from multi-filter all-sky photometric surveys. *Icarus* **226,** 723–741 (2013).
This work created a new framework to quantify the compositional makeup of the asteroid belt by looking at the distribution by mass rather than numbers.
20. McCord, T. B. & Gaffey, M. J. Asteroids—surface composition from reflection spectroscopy. *Science* **186,** 352–355 (1974).
21. Grimm, R. E. & McSween, H. Y. Heliocentric zoning of the asteroid belt by aluminum-26 heating. *Science* **259,** 653–655 (1993).
22. Nakamura, T. *et al.* Itokawa dust particles: a direct link between S-type asteroids and ordinary chondrites. *Science* **333,** 1113–1116 (2011).
23. Chapman, C. R. S-type asteroids, ordinary chondrites, and space weathering: the evidence from Galileo's fly-bys of Gaspra and Ida. *Meteorit. Planet. Sci.* **31,** 699–725 (1996).
24. Sasaki, S. *et al.* Production of iron nanoparticles by laser irradiation in a simulation of lunar-like space weathering. *Nature* **410,** 555–557 (2001).
25. Chapman, C. R. Space weathering of asteroid surfaces. *Annu. Rev. Earth Planet. Sci.* **32,** 539–567 (2004).
26. Brunetto, R. *et al.* Space weathering of silicates simulated by nanosecond pulse UV excimer laser. *Icarus* **180,** 546–554 (2006).
27. Binzel, R. P., Rivkin, A. S., Bus, S. J., Sunshine, J. M. & Burbine, T. H. MUSES-C target asteroid (25143) 1998 SF36: a reddened ordinary chondrite. *Meteorit. Planet. Sci.* **36,** 1167–1172 (2001).
28. Roig, F., Ribeiro, A. O. & Gil-Hutton, R. Taxonomy of asteroid families among the Jupiter Trojans: comparison between spectroscopic data and the Sloan Digital Sky Survey colors. *Astron. Astrophys.* **483,** 911–931 (2008).
29. Carvano, J. M., Hasselmann, H., Lazzaro, D. & Mothé-Diniz, T. SDSS-based taxonomic classification and orbital distribution of main belt asteroids. *Astron. Astrophys.* **510,** A43 (2010).
30. Clark, B. E., Bell, J. F., Fanale, F. P. & O'Connor, D. J. Results of the seven-color asteroid survey: infrared spectral observations of ~50-km size S-, K-, and M-type asteroids. *Icarus* **113,** 387–402 (1995).
31. Bus, S. J. & Binzel, R. P. Phase II of the Small Main-Belt Asteroid Spectroscopic Survey: a feature-based taxonomy. *Icarus* **158,** 146–177 (2002).
32. Mothé-Diniz, T., Carvano, J. & Lazzaro, D. Distribution of taxonomic classes in the main belt of asteroids. *Icarus* **162,** 10–21 (2003).
This was the first extensive look at asteroid compositional distributions at smaller sizes; it indicates that the distribution differs from that in ref. 2.
33. Lazzaro, D. *et al.* S3OS2: the visible spectroscopic survey of 820 asteroids. *Icarus* **172,** 179–220 (2004).
34. Hsieh, H. & Jewitt, D. A population of comets in the main asteroid belt. *Science* **312,** 561–563 (2006).
35. Campins, H. *et al.* Water ice and organics on the surface of the asteroid 24 Themis. *Nature* **464,** 1320–1321 (2010).
36. Rivkin, A. S. & Emery, J. P. Detection of ice and organics on an asteroidal surface. *Nature* **464,** 1322–1323 (2010).
37. Licandro, J. *et al.* (65) Cybele: detection of small silicate grains, water-ice, and organics. *Astron. Astrophys.* **525,** A34 (2011).
38. Jewitt, D. The active asteroids. *Astron. J.* **143,** 66 (2012).
39. Carry, B. Density of asteroids. *Planet. Space Sci.* **73,** 98–118 (2012).
This work conducted a detailed analysis of 994 mass estimates and 1,500 volume determinations of 300 asteroids, demonstrating density trends per asteroid taxonomic class.
40. Elkins-Tanton, L. T., Weiss, B. P. & Zuber, M. T. Chondrites as samples of differentiated planetesimals. *Earth Planet. Sci. Lett.* **305,** 1–10 (2011).
41. DeMeo, F. E., Binzel, R. P., Carry, B., Polishook, D. & Moskovitz, N. A. Unexpected D-type interlopers in the inner main belt. *Icarus* **229,** 392–399 (2014).
42. Levison, H. *et al.* Contamination of the asteroid belt by primordial trans-Neptunian objects. *Nature* **460,** 364–366 (2009).
43. Carvano, J. M., Lazzaro, D., Mothé-Diniz, T., Angeli, C. A. & Florczak, M. Spectroscopic survey of the Hungaria and Phocaea dynamical groups. *Icarus* **149,** 173–189 (2001).
44. Assandri, M. C. & Gil-Hutton, R. Surface composition of Hungaria asteroids from the analysis of the Sloan Digital Sky Survey colors. *Astron. Astrophys.* **488,** 339–343 (2008).
45. Warner, B., Harris, A. W., Vokrouhlicky, D., Nesvorny, D. & Bottke, W. F. Analysis of the Hungaria asteroid population. *Icarus* **204,** 172–182 (2009).
46. Meibom, A. & Clark, B. E. Evidence for the insignificance of ordinary chondritic material in the asteroid belt. *Meteorit. Planet. Sci.* **34,** 7–24 (1999).
47. Ruzmaikina, T. V., Safronov, V. S. & Weidenschilling, S. J. in *Asteroids II* (eds Binzel, R. P., Gehrels, T. & Matthews, M. S.) 681–700 (Univ. Arizona Press, 1989).
48. Petit, J. M., Chambers, J., Franklin, F. & Nagasawa, M. in *Asteroids III* (eds Bottke, W. F., Cellino, A., Paolicchi, P. & Binzel, R. P.) 711–723 (Univ. Arizona Press, 2002).
49. O'Brien, D. P., Morbidelli, A. & Bottke, W. F. The primordial excitation and clearing of the asteroid belt—revisited. *Icarus* **191,** 434–452 (2007).
50. Gomes, R. The origin of the Kuiper Belt high-inclination population. *Icarus* **161,** 404–418 (2003).
51. Gomes, R., Levison, H. F., Tsiganis, K. & Morbidelli, A. Origin of the cataclysmic Late Heavy Bombardment period of the terrestrial planets. *Nature* **435,** 466–469 (2005).
52. Morbidelli, A., Tsiganis, K., Crida, A., Levison, H. F. & Gomes, R. Dynamics of the giant planets of the solar system in the gaseous protoplanetary disk and their relationship to the current orbital architecture. *Astron. J.* **134,** 1790–1798 (2007).
53. Nesvorny, D., Vokrouhlický, D. & Morbidelli, A. Capture of irregular satellites during planetary encounters. *Astron. J.* **133,** 1962 (2007).
54. Walsh, K. J., Morbidelli, A., Raymond, S. N., O'Brien, D. P. & Mandell, A. M. A low mass for Mars from Jupiter's early gas-driven migration. *Nature* **475,** 206–209 (2011).
55. Chesley, S. R. *et al.* Direct detection of the Yarkovsky effect by radar ranging to asteroid 6489 Golevka. *Science* **302,** 1739–1742 (2003).
56. Bottke, W. F., Vokrouhlický, D., Rubincam, D. P. & Nesvorný, D. The Yarkovsky and YORP effects: implications for asteroid dynamics. *Annu. Rev. Earth Planet. Sci.* **34,** 157–191 (2006).
57. Gladman, B. J. *et al.* Dynamical lifetimes of objects injected into asteroid belt resonances. *Science* **277,** 197–201 (1997).
58. Farinella, P., Vokrouhlicky, D. & Hartmann, W. K. Meteorite delivery via Yarkovsky orbital drift. *Icarus* **132,** 378–387 (1998).
59. Bottke, W. F., Vokrouhlicky, D., Broz, M., Nesvorny, D. & Morbidelli, A. Dynamical spreading of asteroid families by the Yarkovsky effect. *Science* **294,** 1693–1696 (2001).
60. Parker, A. *et al.* The size distributions of asteroid families in the SDSS Moving Object Catalog 4. *Icarus* **198,** 138–155 (2008).
61. Masiero, J. R. *et al.* Asteroid family identification using the hierarchical clustering method and WISE/NEOWISE physical properties. *Astrophys. J.* **770,** 7 (2013).
62. Wetherill, G. W. Steady state populations of Apollo-Amor objects. *Icarus* **37,** 96–112 (1979).
63. Wisdom, J. Chaotic behavior and the origin of the 3/1 Kirkwood gap. *Icarus* **56,** 51–74 (1983).
64. Nesvorný, D. *et al.* Fugitives from the Vesta family. *Icarus* **193,** 85–95 (2008).
65. Russell, C. T. *et al.* Dawn at Vesta: testing the protoplanetary paradigm. *Science* **336,** 684–686 (2012).
66. Thomas, P. C. *et al.* Differentiation of the asteroid Ceres as revealed by its shape. *Nature* **437,** 224–226 (2005).
67. Carry, B. *et al.* Near-infrared mapping and physical properties of the dwarf-planet Ceres. *Astron. Astrophys.* **478,** 235–244 (2008).
68. Castillo-Rogez, J. Ceres—neither a porous nor salty ball. *Icarus* **215,** 599–602 (2011).
69. Gaffey, M. J. *et al.* Mineralogical variations within the S-type asteroid class. *Icarus* **106,** 573–602 (1993).
70. Tholen, D. J. & Barucci, M. A. in *Asteroids II* (eds Binzel, R. P., Gehrels, T. & Matthews, M. S.) 1139–1150 (Univ. Arizona Press, 1989).
71. Lauretta, D. S. *et al.* OSIRIS-REx—exploration of asteroid (101955) 1999 RQ36. *AGU Fall Meet. Abstr.* P21E–01 (2011).
72. Yano, H. *et al.* Hayabusa's follow-on mission for surface and sub-surface sample return from a C-type NEO. In *38th COSPAR Scientific Assembly* 635; http://adsabs.harvard.edu/abs/2010cosp...38..635Y (2010).
73. Barucci, M. A. *et al.* MarcoPolo-R near earth asteroid sample return mission. *Exp. Astron.* **33,** 645–684 (2012).
74. Jenniskens, P. *et al.* The impact and recovery of 2008 TC_3. *Nature* **458,** 485–488 (2009).
75. Brown, P. *et al.* The fall of the Grimsby meteorite—I: Fireball dynamics and orbit from radar, video, and infrasound records. *Meteorit. Planet. Sci.* **46,** 339–363 (2011).
76. Mignard, F. *et al.* The Gaia Mission: expected applications to asteroid science. *Earth Moon Planets* **101,** 97–125 (2007).
77. Jones, R. L. *et al.* Solar System science with LSST. *Earth Moon Planets* **105,** 101–105 (2009).
78. Emery, J. P. & Brown, R. H. Constraints on the surface composition of Trojan asteroids from near-infrared (0.8–4.0 μm) spectroscopy. *Icarus* **164,** 104–121 (2003).
79. Emery, J. P. & Brown, R. H. The surface composition of Trojan asteroids: constraints set by scattering theory. *Icarus* **170,** 131–152 (2004).

RESEARCH REVIEW

80. Emery, J. P., Burr, D. M. & Cruikshank, D. P. Near-infrared spectroscopy of Trojan asteroids: evidence for two compositional groups. *Astron. J.* **141,** 25 (2011).
81. Yang, B. & Jewitt, D. Spectroscopic search for water ice on Jovian Trojan asteroids. *Astron. J.* **134,** 223–228 (2007).
82. Yang, B. & Jewitt, D. A near-infrared search for silicates in Jovian Trojan asteroids. *Astron. J.* **141,** 95 (2011).
83. Fornasier, S. *et al.* Visible spectroscopic and photometric survey of L5 Trojans: investigation of dynamical families. *Icarus* **172,** 221–232 (2004).
84. Fornasier, S. *et al.* Visible spectroscopic and photometric survey of Jupiter Trojans: final results on dynamical families. *Icarus* **190,** 622–642 (2007).
85. Gil-Hutton, R. & Brunini, A. Surface composition of Hilda asteroids from the analysis of the Sloan Digital Sky Survey colors. *Icarus* **193,** 567–571 (2008).
86. Grav, T. *et al.* WISE/NEOWISE observations of the Hilda population: preliminary results. *Astrophys. J.* **744,** 197 (2012).
87. Grav, T., Mainzer, A. K., Bauer, J. M., Masiero, J. R. & Nugent, C. R. WISE/NEOWISE observations of the Jovian Trojan population: taxonomy. *Astrophys. J.* **759,** 49 (2012).

Acknowledgements We are grateful to R. Binzel for help in shaping this review, and to K. Walsh, W. Bottke, N. Moskovitz, D. Polishook, T. Burbine, J. Wisdom and A. Morales for discussions. We thank C. Chapman for a review. We acknowledge support from the ESAC faculty for F.E.D.'s visit. This material is based upon work supported by the National Science Foundation under grant number 0907766 and by the National Aeronautics and Space Administration (NASA) under grant number NNX12AL26G. Any opinions, findings and conclusions or recommendations expressed in this material are those of the authors and do not necessarily reflect the views of the National Science Foundation or NASA. Support for this work was provided by NASA through the Hubble Fellowship grant HST-HF-51319.01-A, awarded by the Space Telescope Science Institute, which is operated by the Association of Universities for Research in Astronomy, Inc., for NASA, under contract NAS 5-26555. F.E.D. is a Hubble Fellow.

Author Contributions Both authors worked jointly on the scientific analysis that resulted in Figs 3 and 4. F.E.D. led the manuscript writing effort and B.C. created the figures.

Author Information Reprints and permissions information is available at www.nature.com/reprints. The authors declare no competing financial interests. Readers are welcome to comment on the online version of the paper. Correspondence and requests for materials should be addressed to F.E.D. (fdemeo@cfa.harvard.edu).

Icarus 268 (2016) 340–354

Contents lists available at ScienceDirect

Icarus

journal homepage: www.journals.elsevier.com/icarus

Spectral properties of near-Earth and Mars-crossing asteroids using Sloan photometry

B. Carry [a,b,*], E. Solano [c,d], S. Eggl [a], F.E. DeMeo [e,f]

[a] IMCCE, Observatoire de Paris, PSL Research University, CNRS, Sorbonne Universités, UPMC Univ Paris 06, Univ. Lille, France
[b] European Space Astronomy Centre, ESA, P.O. Box 78, 28691 Villanueva de la Cañada, Madrid, Spain
[c] Centro de Astrobiologia (INTA-CSIC), Departamento de Astrofísica, P.O. Box 78, E-28691 Villanueva de la Cañada, Madrid, Spain
[d] Spanish Virtual Observatory, Spain
[e] Department of Earth, Atmospheric and Planetary Sciences, MIT, 77 Massachusetts Avenue, Cambridge, MA, 02139, USA
[f] Harvard-Smithsonian Center for Astrophysics, 60 Garden Street, MS-16, Cambridge, MA, 02138, USA

ARTICLE INFO

Article history:
Received 28 October 2015
Revised 11 December 2015
Accepted 25 December 2015
Available online 15 January 2016

Keywords:
Near-Earth objects
Asteroids, composition
Photometry

ABSTRACT

The nature and origin of the asteroids orbiting in near-Earth space, including those on a potentially hazardous trajectory, is of both scientific interest and practical importance. We aim here at determining the taxonomy of a large sample of near-Earth and Mars-crosser asteroids and analyze the distribution of these classes with orbit. We use this distribution to identify the source regions of near-Earth objects and to study the strength of planetary encounters to refresh asteroid surfaces. We measure the photometry of these asteroids over four filters at visible wavelengths on images taken by the Sloan Digital Sky Survey (SDSS). These colors are used to classify the asteroids into a taxonomy consistent with the widely used Bus-DeMeo taxonomy (DeMeo et al. [2009]. Icarus 202, 160–180) based on visible and near-infrared spectroscopy. We report here on the taxonomic classification of 206 near-Earth and 776 Mars-crosser asteroids determined from SDSS photometry, representing an increase of 40% and 663% of known taxonomy classifications in these populations. Using the source region mapper by Greenstreet et al. (Greenstreet, S., Ngo, H., Gladman, B. [2012]. Icarus, 217, 355–366), we compare for the first time the taxonomic distribution among near-Earth and main-belt asteroids of similar diameters. Both distributions agree at the few percent level for the inner part of the main belt and we confirm this region as a main source of near-Earth objects. The effect of planetary encounters on asteroid surfaces are also studied by developing a simple model of forces acting on a surface grain during planetary encounter, which provides the minimum distance at which a close approach should occur to trigger resurfacing events. By integrating numerically the orbit of the 519 S-type and 46 Q-type asteroids in our sample back in time for 500,000 years and monitoring their encounter distance with Venus, Earth, Mars, and Jupiter, we seek to understand the conditions for resurfacing events. The population of Q-type is found to present statistically more encounters with Venus and the Earth than S-types, although both S- and Q-types present the same amount of encounters with Mars.

1. Introduction

Asteroids are the leftovers of the building blocks that accreted to form the planets in the early Solar System. They are also the progenitors of the constant influx of meteorites falling on the planets, including the Earth. Apart from the tiny sample of rock from asteroid (25,143) Itokawa brought back by the Hayabusa spacecraft (Nakamura et al., 2011), these meteorites represent our sole possibility to study in details the composition of asteroids. Identifying their source regions is crucial to determine the physical conditions and abundances in elements that reigned in the protoplanetary nebula around the young Sun (see, e.g., McSween et al., 2006). From the analysis of a bolide trajectory, it is possible to reconstruct its heliocentric orbit and to find its parent body (e.g., Gounelle et al., 2006), but such determinations have been limited to a few objects only (Rudawska et al., 2012).

Among the different dynamical classes of asteroids, the near-Earth and Mars-crosser asteroids (NEAs and MCs), whose orbits cross that of the telluric planets, form a transient population. Their typical lifetime is of a few million years only (Bottke et al., 2002;

* Corresponding author at: IMCCE, Observatoire de Paris, PSL Research University, CNRS, Sorbonne Universités, UPMC Univ Paris 06, Univ. Lille, France.
E-mail address: benoit.carry@oca.eu (B. Carry).

http://dx.doi.org/10.1016/j.icarus.2015.12.047
0019-1035/

Morbidelli et al., 2002) before being ejected from the Solar System, falling into the Sun, or impacting a planet. These populations are therefore constantly replenished by asteroids from the main asteroid belt, the largest reservoir of known small bodies, between Mars and Jupiter.

The resonances between the orbits of asteroids and that of Jupiter have been long thought (Wetherill, 1979; Wisdom, 1983) to provide the kick in eccentricity necessary to place asteroids on planet-crossing orbits. It was later found that the secular resonance ν_6, delimiting the inner edge of the main belt, and the 3:1 mean-motion resonance (MMR) with Jupiter, separating the inner from the middle belt, were the most effective, compared to the 5:2 resonance, for instance, which tends to eject asteroids from the Solar System (see Morbidelli et al., 2002 for a review). The major role played by the ν_6 resonance was confirmed by the comparison between the reflectance spectra of the most common meteorites, the ordinary chondrites (OCs, 80% of all meteorite falls), the dominant class in the near-Earth space, the S-type asteroids (about 65% of the observed population, Binzel et al., 2004), and the dynamical family of S-types asteroids linked with (8) Flora in the inner belt (Vernazza et al., 2008).

The NEAs also represent ideal targets for space exploration owing to their close distance from Earth. This proximity is quantified by the energy required to set a spacecraft on a rendezvous trajectory and is often expressed as Δv (in km/s), the required change in speed. This is the reason why the first mission to an asteroid targeted the Amor (433) Eros (Veverka et al., 2000), why all the targets of sample-return missions were selected among NEAs: (25,143) Itokawa for JAXA Hayabusa (Fujiwara et al., 2006), (101,955) Bennu for NASA OSIRIS-REx (Origins-Spectral Interpretation-Resource Identification-Security-Regolith Explorer, Lauretta et al., 2011), (162,173) Ryugu for JAXA Hayabusa2 (Yano et al., 2010), and (175,706) 1996 FG3 and (341,843) 2008 EV5 for the former ESA M3/M4 candidate MarcoPolo-R (Barucci et al., 2012) and ARM (Asteroid Redirect Mission, Abell et al., 2015), and why the recent proposition for a demonstration project of an asteroid deflection by ESA, AIDA (Asteroid Impact & Deflection Assessment, Murdoch et al., 2012), targets the NEA (65,803) Didymos. This latter point, the protection from asteroid hazard, is certainly the most famous aspect of the asteroid research known to the general public, and has triggered many initiatives leading to breakthroughs in NEA discovery and characterization of their surface and physical properties (see, e.g., Binzel, 2000; Stokes et al., 2000; Ostro et al., 2002; Binzel et al., 2004; Jedicke et al., 2007; Mainzer et al., 2011a; Mueller et al., 2011 among others).

In both attempting to link NEAs and MCs transient populations with their source regions and meteorites and designing a protection strategy, the study of their composition is key. Indeed, dynamical studies allows to determine relative probabilities of the origin of asteroids belonging to those populations (e.g., Bottke et al., 2002; Greenstreet et al., 2012). These links are however not sufficient, and must be ascertained by compositional similarities (Vernazza et al., 2008; Binzel et al., 2015; Reddy et al., 2015). Moreover, different compositions yield different densities and internal structure/cohesion (Carry, 2012), and an asteroid on a impact trajectory with Earth of a given size will require a different energy to be deflected or destroyed according to its nature (Jutzi and Michel, 2014).

Here, we aim at classifying a large number of near-Earth and Mars-crosser asteroids into broad compositional groups by using imaging archival data. We present in Section 2 the procedure we used to retrieve the photometry at visible wavelengths from the publicly available images of the Sloan Digital Sky Survey (SDSS). We describe in Section 3 how we use the SDSS photometry to classify the objects into the commonly-used Bus-DeMeo taxonomy of asteroids (DeMeo et al., 2009), following the work by DeMeo and Carry (2013). We present the results of the classification in Section 4 before discussing their implications for source regions in Section 5 and for surface rejuvenation processes in Section 6.

2. Visible photometry for the Sloan Digital Sky Survey

2.1. The Sloan Digital Sky Survey

The Sloan Digital Sky Survey (SDSS) is a wide-field imaging survey dedicated to observing galaxies and quasars at different wavelengths. From 1998 to 2009, the survey covered over 14,500 square degrees in 5 filters: u', g', r', i', z' (centered on 355.1, 468.6, 616.5, 748.1 and 893.1 nm), with estimated limiting magnitude of 22.0, 22.2, 22.2, 21.3, and 20.5 for 95% completeness (Ivezić et al., 2001).

2.2. The Moving Object Catalog

In the course of the survey, 471,569 moving objects were identified in the images and listed in the Moving Object Catalogue (SDSS MOC, currently in its 4th release, including observations through March 2007). Among these, 220,101 were successfully linked to 104,449 unique objects corresponding to known asteroids (Ivezić et al., 2001). The remaining 251,468 moving objects listed in the MOC corresponded to unknown asteroids at the time of the release (August 2008).

First, we keep objects assigned a number or a provisional designation only, i.e., those for which we can retrieve the orbital elements. Among these, we select the near-Earth and Mars-crossers asteroids according to the limits on their semi-major axis, perihelion, and aphelion listed in Table 1, resulting in 2071 observations of 1315 unique objects. We then remove observations that are deemed unreliable: with any apparent magnitudes greater than the limiting magnitudes reported above (Section 2.1), or any photometric uncertainty greater than 0.05. These constraints remove a large portion of the dataset (about 75%), primarily due to the larger typical error for the z' filter. While there is only a small subset of the sample remaining, we are assured of the quality of the data (see DeMeo and Carry, 2013 for additional information on the definition of photometric cuts). Additionally, for higher errors, the ambiguity among taxonomic classes possible for an object becomes so large that the classification (Section 3) becomes essentially meaningless. In this selection process, we kept 588 observations of 353 individual asteroids from the SDSS MOC4, as listed in Table 1.

2.3. Identifying unknown objects in the MOC4

As mentioned above, more than half of the MOC4 entries had not been linked with known asteroids. At the time of the release (August 2008), about 460,000 asteroids had been discovered and 350,000 were numbered (i.e., had well-constrained orbits allowing easy cross-matching with SDSS detected sources). The current number of discovered asteroids has now risen above 700,000, with more than 370,000 numbered objects. We therefore use the improved current knowledge on the asteroid population to link unknown MOC sources to known objects.

We use the Virtual Observatory (VO) SkyBoT cone-search service (Berthier et al., 2006), hosted at IMCCE,[1] for that purpose. SkyBoT pre-computes weekly the ephemeris of all known Solar System objects for the period 1889–2060, and stores their heliocentric positions with a time step of 10 days, allowing fast computation of positions at any time. The cone-search tool allows to request the list of known objects within a field of view at any given epoch as seen from

[1] http://vo.imcce.fr/webservices/skybot/.

Table 1
Definition of the dynamical classes of near-Earth and Mars-crosser asteroids used in present study, based on the semi-major axis (a), perihelion (q), and aphelion (Q) of their orbit. All the objects have a perihelion inward of Mars aphelion ($Q_{\mathcal{J}}$) at 1.666 AU. The number of objects listed in the SDSS MOC4 (Section 2.2), identified in SDSS MOC4 using SkyBoT (SVO-MOC, Section 2.3), and by the SVO NEA project (Section 2.4) are also listed. See Fig. 1 for the distribution of these objects in the orbital element space.

Class	a (AU)		q (AU)		Q (AU)	MOC4	SVO-MOC	SVO_{griz}	SVO_{gri}
	min	max	min	max	min				
Atens	–	1.0	–	$Q_{\mathcal{J}}$	0.983	–	–	10	1
Apollos	1.0	–	–	1.017	–	14	18	82	70
Amors	–	–	1.017	1.3	–	29	73	111	40
Mars-crosser	–	–	–	$Q_{\mathcal{J}}$	–	310	383	622	567
Total	–	–	–	–	–	353	474	825	678

Earth in typically less than 10 s. We send 251,468 requests to SkyBoT, corresponding to the 251,468 unknown objects in the MOC4, centered on the MOC4 object's coordinates, at the reported epoch of observation, within a circular field of view of 30 arcsec. Although many asteroids among the 700,000 known have position uncertainty larger than this value (as derived from their orbital parameter uncertainty), this cut ensures that we only keep objects with a high probability to be linked with the MOC sources.

To further restrict the number of false-positive associations, we compare the position, apparent motion, and apparent magnitude of the MOC sources to that predicted from ephemeris provided by SkyBoT, based on the database of orbital elements AstOrb.[2] We consider successful association of SDSS sources with SkyBoT entry if the positions are closer than 30″, the apparent V-Johnson magnitudes do not differ by more than 0.5, and the apparent motions are co-linear (difference in $d\alpha\cos(\delta)/dt$ and $d\delta/dt$ of less than 3″/h). However, neither SkyBoT nor MOC4 provide estimates on the uncertainty in the apparent velocity. The only information is the uncertainty in the velocity components parallel and perpendicular to the SDSS scanning direction. The mean value of this error (both in the parallel and in the perpendicular direction) is of 1″/h. We are taking this value as one standard deviation to set the cut above.

Of the 251,468 unidentified MOC sources, SkyBoT provides known asteroids within 30 arcsec for 68,497 (27%), corresponding to 41,055 unique asteroids. We trim this value to 57,646 (36,730 asteroids) for which the association can be considered certain. The vast majority of these now-identified asteroids have orbits within the main belt (35,404, corresponding to 96%), but some are NEAs (48, 0.1%), or MCs (73, 0.2%). Their respective numbers are reported in Table 1. The complete list of MOC entries associated to known asteroids (277,747 entries associated to 141,388 asteroids) is freely accessible.[3]

2.4. The SVO near-Earth Asteroids Recovery Program

In addition, we search the images of the SDSS for NEAs and MCs that were either not identified as moving objects by the automatic SDSS pipeline, rejected by the MOC data selection,[4] or imaged after the latest compilation of the SDSS MOC4 (i.e., observed after March 2007). Indeed, only moving objects with an apparent motion between 0.05 and 0.050 deg/day were included in the MOC, leaving a significant fraction of NEAs un-cataloged (Solano et al., 2013).

We use the resources of the citizen-science project "Near-Earth Asteroids Recovery Program" of the Spanish Virtual Observatory (SVO) which was originally designed for this very purpose: to identify and measure the astrometry of NEAs in archival imaging data (Solano et al., 2013). For each Aten, Amor, Apollo, and Mars-crosser listed by the Minor Planet Center[5] (MPC), its ephemeris are computed over the period of operation of the SDSS imaging survey (1998–2009) and compared to the footprints of the images of the survey. The images possibly containing an object brighter than the SDSS limiting magnitude ($V = 22$) are then proposed to the public for identification through a web portal.[6] Since the beginning of the project in 2011, over 2500 astrometry measurements of about 600 NEAs not identified in the MOC have been reported to the MPC (see Solano et al., 2013 for details on the project).

To compute the photometry of the NEAs measured by the users we first searched in the photometric catalog of the 8th SDSS Data Release.[7] If no photometry associated with the NEA was found, we ran SExtractor on the corresponding images and calibrated the SExtractor magnitudes by comparing them with the SDSS magnitudes of the sources identified in the image.

Owing to the more stringent limiting magnitude in the z' filter, many asteroids are identified over three bands ($g'r'i'$) only. We also report these objects here, although deriving a taxonomic classification is of course less accurate. Overall, we collect 1194 four bands ($g'r'i'z'$) photometry measurements of 825 unique asteroids and 976 three-bands ($g'r'i'$) photometry measurements of 678 distinct asteroids (Table 1). We present in Fig. 2 a comparison of our measurements with the magnitudes reported in the SDSS MOC4 for the common asteroids in both sets, showing excellent agreement (values agree with a standard deviation of 0.05 mag).

3. Taxonomic classification

The SDSS photometry has been used to classify asteroids according to their colors by many authors (e.g., Ivezić et al., 2002; Nesvorný et al., 2005; Parker et al., 2008; Carvano et al., 2010). One key advantage of the survey was the almost simultaneous acquisition of all filters (5 min in total), hence limiting the impact of geometry-related lightcurve on the apparent magnitude. Here we follow the work by DeMeo and Carry (2013, 2014) in which the class definitions are set to be as consistent as possible with previous spectral taxonomies based on higher spectral resolution and larger wavelength coverage data sets, specifically Bus and Bus-DeMeo taxonomies (Bus and Binzel, 2002; DeMeo et al., 2009). We present concisely the classification scheme below and refer to DeMeo and Carry (2013) for a complete description.

3.1. From SDSS to Bus-DeMeo taxonomy

First, we convert the photometry into reflectance (using solar colors from Holmberg et al., 2006) and normalize them to unity in filter g'. Second, we compute the slope of the continuum over the g', r', and i' filters (hereafter gri-slope), and the z'–i' color (hereafter zi-color), representing the band depth of a potential 1 μm band, because they are the most characteristic spectral

[2] http://asteroid.lowell.edu/.
[3] http://svo2.cab.inta-csic.es/vocats/svomoc.
[4] http://www.astro.washington.edu/users/ivezic/sdssmoc/sdssmoc.html.
[5] http://minorplanetcenter.org/.
[6] http://www.laeff.cab.inta-csic.es/projects/near/main/.
[7] http://cdsarc.u-strasbg.fr/vizbin/Cat?II/306.

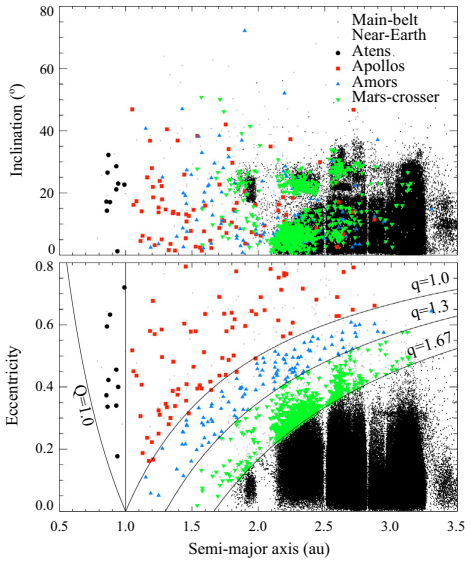

Fig. 1. Distribution of the NEAs and Mars-crossers studied here as a function of their osculating elements (semi-major axis, eccentricity, and inclination). The black dots represent the first 10,000 main-belt asteroids, the grey dots the 532 NEAs with spectral classification from the literature (see Section 3.2), and the black circles, red squares, blue triangle, and green stars the Atens, Apollos, Amors, and Mars-crossers we classify from SDSS. (For interpretation of the references to color in this figure legend, the reader is referred to the web version of this article.)

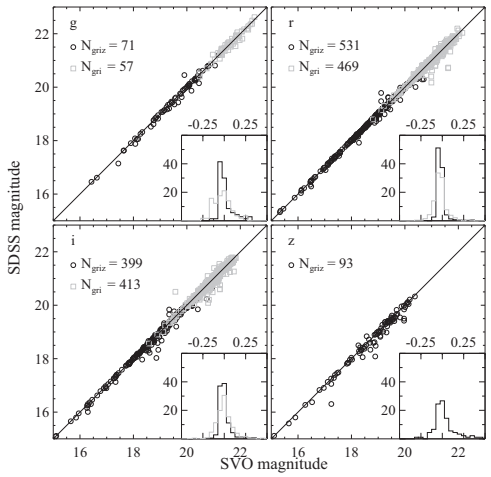

Fig. 2. Comparison of the apparent magnitude measured by our system (SVO magnitude) with that reported in the SDSS MOC4 (SDSS magnitude) for the four g', r', i', and z' filters. For each, the number of common objects is reported, for both four-bands (black circles) and three-bands (grey squares) sets. The inserted histograms show the distribution of the magnitude difference (MOC-SVO).

distinguishers in all major taxonomies (beginning with Chapman et al., 1975). The classification into the taxonomy is then based on these two parameters.

As a results of the limited spectral resolution and range of SDSS photometry, we group together certain classes into broader complexes (see correspondences in Table 2). For asteroids with multiple observations that fall under multiple classifications, we use the tree-like selection to assign a final class (see DeMeo and Carry (2013) for details and DeMeo et al. (2014a) for an example of a spectroscopic confirmation campaign of the SDSS classification used here). We successfully classify 982 asteroids from the sample of 1015 near-Earth and Mars-crosser asteroids with four-bands photometry (i.e., 97% of the sample).

For objects with three-bands photometry only, we set their z' magnitude to the limiting magnitude of 20.5 (Ivezić et al., 2001) as an upper limit for their brightness. We then classify these asteroids using the scheme presented above. Because the magnitude of 20.5 in z' is an upper limit, the actual zi-color for these asteroids may be overestimated. The classification can therefore be degenerated, all the classes with similar gri-slope and lower zi-color being possible. We assign tentative classification to 254 asteroids from the sample of 678 near-Earth and Mars-crosser asteroids with three-bands photometry (i.e., 37% of the sample).

In all cases, we mark objects with peculiar spectral behavior with the historical notation "U" (for unclassified), and discard them from the analysis. There are 33 and 424 asteroids in the four-bands and three-bands photometry samples respectively for which we cannot assign a class. These figures highlight the ambiguity raised by the lack of information on the presence or absence of an absorption band around one micron, to which the z' filter is sensitive.

3.2. Gathering classifications from past studies

Many different authors have reported on the taxonomic classification of NEAs. We gather here the results of Dandy et al. (2003), Binzel et al. (2004), Lazzarin et al. (2005), de León et al. (2006, 2010), Thomas and Binzel (2010), Popescu et al. (2011), Ye (2011), Reddy et al. (2011), Polishook et al. (2012), Sanchez et al. (2013), DeMeo et al. (2014b). These authors used different taxonomic schemes to classify their observations, using either broad-band filter photometry or spectroscopy, at visible wavelengths only or also in the near infrared. We therefore transpose the classes of these different schemes (Tholen, 1984; Tholen and Barucci, 1989; Bus and Binzel, 2002; DeMeo et al., 2009) into the single, consistent, set of 10 classes we already use for the SDSS data. Here also, we attribute the historical "U" designation for objects with apparently contradictory classifications (e.g., QX or STD in Ye, 2011). These pathological cases represent 15% of the objects with

Table 2
Correspondence between the classes from different taxonomies (e.g., Tholen and Barucci, 1989; Bus and Binzel, 2002) found in the literature, used to classify the SDSS photometry (in bold), and their equivalence in the reduced version of the taxonomy by DeMeo et al. (2009) adopted here, following the work by DeMeo and Carry (2013). We strive to preserve the most extreme classes (like A, B) and we convert the tentative classification (e.g., RS) into their broader, safer, complex (S). We also consider as unknown (U) any data of insufficient quality.

SDSS & literature	Bus-DeMeo
A, AR, AS	A
B	B
C, C:, Cb, Cg, Ch	C
D, DT	D
K, K:	K
L, Ld	L
Q, Q/R, R, RQ	Q
O, Q/R/S, R, RS	S
S, S:, S(I → V), Sa, Sk, Sl, Sq, Sq:, Sr	S
V, V:	V
E, M, P, **X**, X:, XT, Xc, Xe, Xk	X
U, C(u), R(u), S(u), ST, STD, QX	U

multiple class determinations. In total, we gather 1022 classifications for 648 objects listed in the literature.

4. Results

We list in Table B.1 the photometry and the taxonomy of all 982 near-Earth and Mars-crossers asteroids with four-bands photometry. The 254 asteroids with three-bands photometry are listed separately in Table B.2, because their taxonomic classification is less robust. In many cases, the upper limit of 20.5 for their z' magnitude provides a weak constraint on their taxonomy, and classes with high zi-color (mainly V-types) are more easily identified. This sample based on three-bands photometry only is therefore biased, but it can be used as a guideline for selecting targets for spectroscopic follow-ups. We concentrate below on the sample based on four-bands photometry.

The 206 NEAs presented here have absolute magnitudes between 12 and 23. Our sample fully overlaps with the size range of the 523 NEAs characterized by visible/near-infrared spectroscopy published to date and represents an increase of ≈40% of the current sample size (Fig. 3). A significant fraction (46%) of the NEA population with $H < 16$ (about 2 km diameter for an albedo of 0.20) has a taxonomic classification. For smaller diameters, the fraction drops quickly to 10% and less. The sub-kilometer population of NEAs is therefore still poorly categorized.

The absolute magnitude of the 776 MCs reported here ranges from 11 to 19. Our sample represents the first classification of sub-kilometric Mars-crossers, and a sixfold increase to the sample of 117 MCs from spectroscopy (Fig. 3). Similarly to NEAs, about 40% of the MC population with $H < 14$ (about 5 km diameter for an albedo of 0.20) now has a taxonomic classification, and the fraction drops quickly to 10% for smaller diameters.

4.1. Taxonomy and orbital classes

We present in Fig. 4 how the different classes distribute among the orbital populations. As already reported by Binzel et al. (2004),

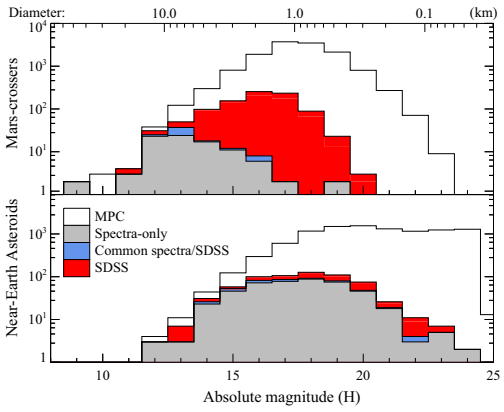

Fig. 3. Distribution of the known taxonomy for near-Earth and Mars-crosser asteroids as a function of their absolute magnitude H. The white histogram corresponds to the total number of discoveries (listed in AstOrb), the grey to the taxonomic classification found in the literature, the blue to the overlap between literature and present study, and the red the four-bands set. An approximative conversion to diameter is also reported, using $D = 1329 \times p_v^{-0.5} \times 10^{-0.2H}$, with the geometric albedo p_v taken as 0.2 (the majority, ≈60%, of the objects classified here being S-types). (For interpretation of the references to color in this figure legend, the reader is referred to the web version of this article.)

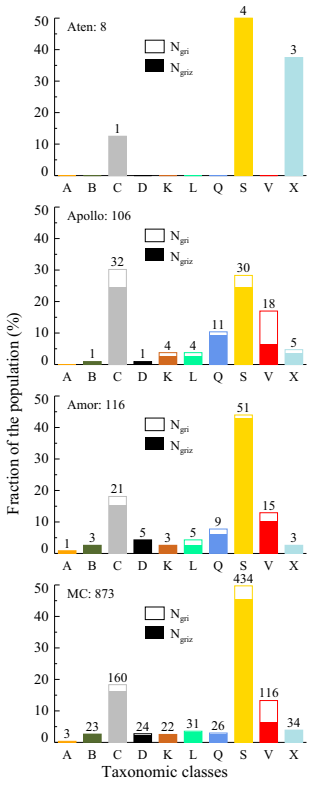

Fig. 4. Distribution of the taxonomic classes for each dynamical group: Aten, Apollo, Amor, and Mars-crosser. The number of object with four-band photometry in each class is reported. Empty and filled bars stands for the three and four band photometry samples respectively.

the broad S- (including Q-types), C-, X-complexes, and V-types dominate the NEA population, the minor classes (A, B, D, K, L) accounting for a few percents only, similarly to what is found in the inner main belt (DeMeo and Carry, 2013, 2014). We find that the S-complex encompasses twice as many objects as the C- and X-complexes, compared to the threefold difference reported by Binzel et al. (2004).

The distribution of taxonomic classes among MCs is similar to that of Apollos and Amors (with only 8 Atens, our sample suffers from low-number statistics). Our findings of V-types accounting for roughly 5% of all MCs may therefore seem puzzling considering the lack of V-types among the ≈100 classified MCs highlighted by Binzel et al. (2004). It is, however, an observation selection effect. Indeed, Mars-crossers are inner-main belt (IMB) asteroids which eccentricity has been increased by numerous weak mean-motion resonances ("chaotic diffusion", see Morbidelli and Nesvorný, 1999). The IMB hosting the largest reservoir of V-types in the Solar System (Vestoids, Binzel and Xu, 1993), V-types were expected in MC space.

The size distribution of known Vestoids however peaks at $H = 16$ (about 1.5 km diameter), and the largest members have an absolute magnitude of 14 (we use the list of Vestoids from Nesvorný, 2012). All the V-types identified here have an absolute magnitude above 14, and so does (31,415) 1999 AK23 ($H = 14.4$),

Table 3
List of NEAs with a low δv, hence potential targets for space missions. For each NEA, the taxonomic class determined here is reported, together with the dynamical class, the absolute magnitude and the orbital elements. The targets of the asteroid-deflection mission AIDA (Didymos) and of the return-sample missions Hayabusa (Itokawa), OSIRIS-REx (Bennu), and Hayabusa2 (Ryugu) are also included for comparison.

Designation	Type	Class	δv (km/s)	H	s (%/100 nm)	$z-i$	a (AU)	e	i (°)
2004 EU22	X	Apollo	4.420	23.00	0.78	0.044	1.175	0.162	5.3
1996 XB27	D	Amor	4.750	22.00	0.85	0.123	1.189	0.058	2.5
2000 TL1	C	Apollo	4.870	22.00	−0.09	0.002	1.338	0.300	3.6
2001 QC34	Q	Apollo	4.970	20.00	0.69	−0.228	1.128	0.187	6.2
1999 FN19	S	Apollo	5.020	22.00	0.96	−0.135	1.646	0.391	2.3
2000 SL10	Q	Apollo	5.080	21.00	0.86	−0.189	1.372	0.339	1.5
1994 CN2	S	Apollo	5.150	16.00	1.12	−0.073	1.573	0.395	1.4
2002 LJ3	S	Amor	5.280	18.00	1.07	−0.258	1.462	0.275	7.6
2004 UR	C	Apollo	5.320	22.00	0.13	−0.025	1.559	0.406	2.4
2006 UP	S	Amor	5.350	23.00	1.43	−0.074	1.586	0.301	2.3
1994 CC	S	Apollo	5.370	17.00	0.99	−0.210	1.638	0.417	4.7
2010 WY8	K	Amor	5.670	21.00	0.92	−0.042	1.385	0.136	6.0
2002 XP40	S	Amor	5.720	19.00	1.63	−0.092	1.645	0.296	3.8
1993 QA	D	Apollo	5.740	18.00	1.02	0.174	1.476	0.315	12.6
2004 RK9	C	Amor	5.760	21.00	0.14	−0.050	1.837	0.426	6.2
2001 FC7	C	Amor	5.780	18.00	0.16	−0.034	1.436	0.115	2.6
1977 VA	C	Amor	5.940	19.20	0.34	−0.010	1.866	0.394	3.0
2001 WL15	C	Amor	6.000	18.00	0.34	−0.179	1.989	0.475	6.9
2000 XK44	L	Amor	6.080	18.00	1.24	0.020	1.724	0.385	11.2
2003 BH	V	Apollo	6.090	20.00	1.79	−0.273	1.456	0.356	13.1
2000 NG11	X	Amor	6.130	17.00	0.27	0.089	1.881	0.368	0.8
2000 RW37	C	Apollo	6.150	20.00	0.45	−0.166	1.248	0.250	13.8
2001 FD90	V	Amor	6.200	19.00	0.75	−0.419	2.046	0.478	7.3
2002 PG80	S	Amor	6.210	18.00	1.09	−0.225	2.013	0.438	4.4
2004 VB	S	Apollo	6.260	20.00	1.04	−0.200	1.458	0.409	10.9
1993 DQ1	S	Amor	6.270	16.00	1.20	−0.207	2.036	0.493	10.0
2000 YG4	Q	Amor	6.300	20.00	0.61	−0.155	2.211	0.503	2.6
2004 KD1	C	Amor	6.330	17.00	0.13	−0.110	1.720	0.331	10.1
2004 RS25	C	Amor	6.410	20.00	0.39	−0.057	2.128	0.479	6.7
2004 QZ2	S	Amor	6.470	18.00	−5.74	−0.227	2.260	0.495	1.0
2001 FY	S	Amor	6.530	18.00	1.36	−0.132	1.886	0.327	4.7
2009 OC	S	Amor	6.540	20.00	0.85	−0.153	2.137	0.446	4.6
2004 XM35	S	Amor	6.560	19.00	1.13	−0.111	1.837	0.301	5.4
2005 QG88	K	Apollo	6.560	20.00	0.99	−0.056	1.728	0.493	11.3
1999 KX4	V	Amor	6.580	16.00	1.60	−0.432	1.457	0.293	16.6
2002 TY57	S	Amor	6.600	19.00	0.86	−0.154	1.922	0.327	3.5
Itokawa	S	Apollo	4.632	19.20			1.324	0.280	1.6
Bennu	C	Apollo	5.087	20.81			1.126	0.204	6.0
Ryugu	B	Apollo	4.646	19.17			1.189	0.190	5.9
Didymos	X	Apollo	5.098	17.94			1.644	0.384	3.4

the first V-type among MCs reported recently by Ribeiro et al. (2014). Only 33 MCs had been characterized with this absolute magnitude or higher to date, and the previous lack of report of V-types among MCs is consistent with our findings.

4.2. Low-δv as space mission targets

Within the 206 NEA serendipitously observed by the SDSS, we identify 36 potential targets for space missions based on their accessibility. We select all the NEA with a δv below 6.5 km/s. As a matter of comparison, the required δv to reach the Moon and Mars are of 6.0 and 6.3 km/s (e.g., Abell et al., 2012). We list in Table 3 the basic characteristics of these potential targets, together with the targets already, or planned to be, visited by spacecraft.

Among the list of low-δv objects, we find a large majority of S-types, following their dominance in the sample presented here of about 60%. We, however, note the presence of potential D-, L-, and K-types. To date, of the 24 taxonomic classes, only C- (Mathilde, Ceres), S- (Ida, Eros, Gaspra, Itokawa, and Toutatis), Xe- (Steins), Xk- (Lutetia), and V-types (Vesta) have been visited by spacecraft. These potential D-, L-, and K-types targets may represent good opportunities for exploration. Data in the visible can only suggest the presence of an absorption band at 1 μm, and near-infrared data is required to confirm these potential classifications.

5. Source regions

The population of NEAs being eroded on short timescale (<10 My) by planetary collisions and dynamical ejections, new objects must be injected in the NEA space to explain the current observed population. We use our sample of 982 NEAs and MCs to identify possible source regions. For that, we use the source region mapper[8] by Greenstreet et al. (2012), built on the result of numerical simulations of the orbital evolution of test particules in the five regions defined by Bottke et al. (2002): ν_6 secular resonance, 3:1 mean-motion resonance with Jupiter, Mars-crossers (MC), Outer Belt (OB), and Jupiter Family Comet (JFC).

For each object, we compute its probability $\mathcal{P}_i$ to originate from the ith source region. We then normalize all $\mathcal{P}_i$ for each source region. The sum of the normalized $\mathcal{P}_i$ over a given taxonomic class therefore represents the fraction of objects (by number) of this class in the source region (Table 4). Uncertainties are computed from the source region mapper uncertainties, quadratically added with the margin of error (at 95% confidence level) to account for the sample size. We can then compare these predicted fractions to the observed distribution of taxonomic classes for each source region.

[8] Updated by S. Greenstreet from the original mapper to include the probability of the source regions of the MCs themselves.

Table 4
Relative fraction of each taxonomic class (by number of objects) from each source region defined by Bottke et al. (2002) and Greenstreet et al. (2012), compared with the distribution of taxonomic types among 3–5 km inner main belt (IMB) asteroids (where Q-types are merged with S-types, see DeMeo and Carry, 2013).

Class	Source regions					$IMB_{3-5\ km}$	
	MC	ν_6	$MMR_{3:1}$	OB	JFC	(#)	(%)
A	0.4 ± 5.9	0.5 ± 6.3	0.3 ± 5.5	0.0 ± 3.0	0.0 ± 3.0	9	0.4
B	2.4 ± 5.8	1.7 ± 5.4	2.9 ± 6.1	6.1 ± 7.5	0.4 ± 4.3	34	1.5
C	15.7 ± 5.2	20.5 ± 5.4	22.7 ± 5.6	38.6 ± 6.6	47.3 ± 10.6	589	25.7
D	2.5 ± 5.7	2.3 ± 5.6	2.5 ± 5.8	5.8 ± 7.2	9.7 ± 8.5	20	0.9
K	2.8 ± 5.9	2.5 ± 5.8	2.4 ± 5.7	4.8 ± 6.9	1.8 ± 7.3	57	2.5
L	3.8 ± 5.9	3.4 ± 5.7	4.4 ± 6.1	1.9 ± 5.1	0.4 ± 4.2	73	3.2
Q	3.6 ± 5.6	4.3 ± 5.8	6.3 ± 6.4	3.8 ± 5.8	2.4 ± 5.5	0	0.0
S	52.8 ± 4.6	44.5 ± 4.6	42.0 ± 4.8	23.8 ± 4.8	23.4 ± 6.9	1145	50.0
V	13.0 ± 5.5	15.6 ± 5.7	12.5 ± 5.5	7.0 ± 5.0	3.0 ± 4.7	247	10.8
X	3.2 ± 5.5	4.7 ± 6.0	4.0 ± 5.8	8.1 ± 7.2	11.7 ± 10.3	117	5.1

The vast majority of NEAs with taxonomic classification sustain diameters of less than 5 km (absolute magnitude above 14). Because the distribution of taxonomic classes in the main belt varies with diameter (DeMeo and Carry, 2014), we need to compare the predicted fraction of Table 4 with objects with $H > 14$ in each source region. For the first time, thanks to the large dataset of asteroids provided by the Sloan Digital Sky Survey (SDSS), such information is available for the inner part of the main belt (DeMeo and Carry, 2013, 2014) and is reported in Table 4 (3–5 km diameter range).

The comparison of the ν_6 and 3:1 source regions (delimiting the inner belt) with the observations in Fig. 5 shows a very good match of the distributions (correlation coefficient of 0.99, maximum difference of 5%). This validates the dynamical path from the inner belt to the near-Earth space as described in the model by Greenstreet et al. (2012). Although the inner belt is widely accepted as a major source for NEAs and meteorites (e.g., Bottke et al., 2002; Binzel et al., 2004; Vernazza et al., 2008; Binzel et al., 2015), the relative contribution of the different source regions particularly with respect to asteroid size is still a matter of debate. For the first time, we compare here populations of the same size range.

Unfortunately, there is no similar data set for the other source regions (MC, OB, and JFC) to be compared with our prediction. We can still note the overall trend of increasing fraction of C/D/X-types in OB and JFC compared with the inner regions, as expected. The fraction of K-types peaks in the outer belt, place of the Eos family, also as expected, although a steady distribution of K-types across source regions is also consistent within uncertainties. We also note a strong correlation between MC and small inner-belt asteroid populations (correlation coefficient 0.97), which is not related to the origin of NEAs, but of MC themselves, via chaotic diffusion from the inner belt (see Morbidelli and Nesvorný, 1999; Michel et al., 2000).

A peculiar feature of Table 4 is the high fraction of S-type in all source regions. Based on present set of NEAs and the dynamical model by Greenstreet et al. (2012), one asteroid below 5 km diameter out of four should be an S-type in the outer belt and the same applies to Jupiter family comets. Although the census of composition in this size range (3–5 km) is far from being complete in these regions, there is a bias toward detecting S-types due to their high albedo (≈0.20) compared to that of the C/P/D-types found there (around 0.05, see Mainzer et al., 2011b; DeMeo and Carry, 2013 for albedo averages over taxonomic classes) S-types are minor contributors to the outer belt for diameters above 5 km (DeMeo and Carry, 2014) and searches for S-type material have been unsuccessful among Cybeles, Hildas, and Trojans (see Emery and Brown, 2003, 2004; Emery et al., 2011; Fornasier et al., 2004, 2007; Yang and Jewitt, 2007, 2011; Roig et al., 2008; Gil-Hutton and Brunini, 2008; Marsset et al., 2014). However, only 4% of the sample (42 objects) are predicted to originate from the OB and JFC source regions. The results for these regions is, thus, based on small number statistics. The large fraction of S-types in these source regions suggests nevertheless that dynamical models may require further refinements.

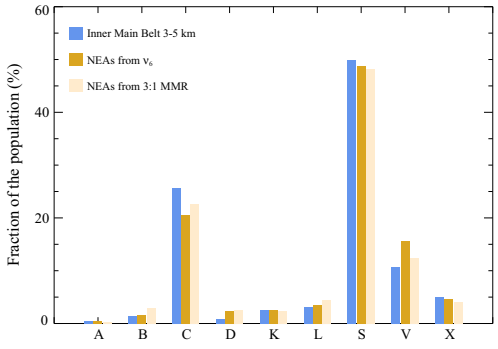

Fig. 5. Relative fractions (by number) of taxonomic classes for asteroids in the inner part of the main-belt (2.0–2.5 AU) with diameter between 3 and 5 km (computed from DeMeo and Carry, 2013, 2014) compared with the predicted fractions originating from ν_6 and 3:1 resonances (see Section 5).

6. Spectral slope and space weathering

6.1. Size dependence of spectral slope

A size dependency of the spectral characteristics of S-type asteroids has been detected early on (e.g., Gaffey et al., 1993) and a correlation between size and spectral slope among NEAs and MCs was shown by Binzel et al. (2004) based on a sample of 187 S- and 20 Q-types. Independently of the other reddening effects due to grain size (see, e.g., Cloutis et al., 2015) and solar phase angle (Bell et al., 2002; Sanchez et al., 2012; Reddy et al., 2015), this trend has been associated with space weathering, causing the spectrum of Q-types, i.e., that of ordinary chondrites made of assemblage of olivine and pyroxenes, to redden into S-type spectra under the action of solar wind ions (see Sasaki et al., 2001; Strazzulla et al., 2005 among many others). Even if the timescale of this reddening is still debated (from $<10^6$ yrs by, e.g., Vernazza et al. (2009) to more than 10^9 yrs by, e.g., Willman and Jedicke (2011)), it is shorter than the age of the Solar System (see also

Jedicke et al., 2004; Nesvorný et al., 2005; Willman et al., 2008, 2010; Dell'Oro et al., 2011; Marchi et al., 2010, 2012). Some regolith refreshing mechanisms must therefore be invoked to explain non- and less-weathered surfaces.

Because the collisional lifetime decreases with size, the surface is expected to be younger at smaller sizes. Smaller asteroids should therefore have a shallower spectral slope than larger bodies on average, albeit with a larger dispersion as collisions are a stochastic process (Binzel et al., 2004). This trend has been found recently for the small (diameter below 5 km) members of the Koronis family in the main belt (≈400 objects, Rivkin et al., 2011; Thomas et al., 2011, 2012). We present in Fig. 6 the spectral slope of 467 S-types plotted against their absolute magnitude. This sample is almost 3 times bigger than that of Binzel et al. (2004), and although we cannot directly compare the values of the spectral slope due to the different definitions and normalization wavelength, we note that we observe the same linear trend from 5 to 1 km (also visible in Thomas et al., 2012). However, we do not observe an increase of the standard deviation toward smaller diameters nor a "saturation" regime below 1 km as visible in their Fig. 7. If this trend seems to persist below 1 km, the statistical relevance of this information decreases, however, as the number of objects drops dramatically, both here and in Binzel et al. (2004).

We interpret the difference between our findings and those reported by Binzel et al. (2004) as the effect of the larger sample, in which the signal to noise ratio of the data is roughly constant over the entire size range: contrarily to the spectral observations, generally noisier for small objects, the limiting factor of the present SDSS data is the apparent z' magnitude. Objects with four-bands photometry were brighter than magnitude 20 at the time of their observations, that is 2 magnitudes brighter than the limiting magnitude in g', r', and i', over which the spectral slope is computed.

Perhaps not surprisingly, a similar trend is visible for the 38 Q-types displayed in Fig. 6. These represent the youngest surfaces of their size range. Following the argument above, larger asteroids are refreshed less often than smaller objects, and this also applies to Q-types on their path to redden into S-types, independently of the mechanism that originally reset their surface.

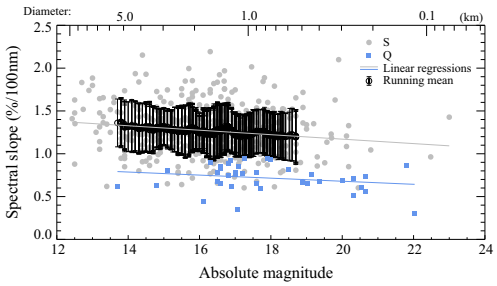

Fig. 6. Spectral slope of 467 S- and 38 Q-types against their absolute magnitude (H). An approximative conversion to diameter is also reported (see Fig. 3). For both, a linear regression is presented, together with a running-window average (window size 50) for the sample of S-types.

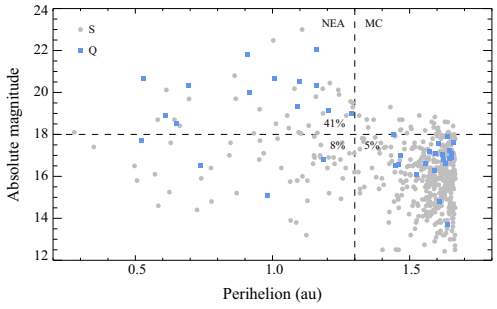

Fig. 7. Absolute magnitude of S- and Q-types asteroids against perihelion distance. Below $H = 18$ (95% of our MC sample), the Q/S fraction among NEAs and MCs is roughly similar (5–8%). The Q/S fraction rapidly increase for smaller diameters ($H > 18$) among NEAs, and many Q-types will be discovered in the sub-kilometer population of MCs.

6.2. Planetary encounters refresh surfaces

If collisions play a stochastic role in modulating the spectral slope of silicate-rich asteroids (S-, A-, V-, Q-types), the question on the main rejuvenating process is still open. Binzel et al. (2010) and DeMeo et al. (2014b) have recently provided observational support to the mechanism proposed by Nesvorný et al. (2005) of close encounters with terrestrial planets. The tidal stress during the close encounters has been proposed to reveal fresh material (responsible for the Q-type appearance) via landslides and regolith shaking.

Both Binzel et al. (2010) and DeMeo et al. (2014b) investigated the orbital history[9] of two samples of near-Earth Q- and S-type asteroids, searching for planetary encounters "close enough" (up to a few lunar distances) to reset space weathering effect. As a results, all the Q-types they tracked had small MOID with either the Earth or Mars in the past 500,000 years, a time at which some level of space weathering should have already developed (see Section 6.1 above). A significant fraction of S-types had also small MOIDs with terrestrial planets. However, the MOID measures the distance between two orbits, and not between two bodies, and a small MOID does not necessarily implies encounters. The authors concluded that planetary encounters, with Mars and the Earth, could explain the presence of Q-types among NEAs (while they are rare among main-belt asteroids). They derived a putative range $r^\star$ of 16 Earth radii at which the resurfacing could be felt by asteroids.

Independently, Nesvorný et al. (2010) used the sample by Binzel et al. (2010), using a different approach. By tracking[10] test particles from NEA source regions (similar to Bottke et al., 2002 in a way) to NEA space and using a simple step-function model for space weathering, they explored the possible range of planetary distances and space weathering timescales that would result in the amount and orbital distribution of the Q/S ratio. They concluded on a smaller sphere of influence of planets, with $r^\star$ between 5 and 10 Earth radii. Contrarily to Binzel et al. (2010), who only addressed Earth encounters, they found encounters with Venus were as effective as those with the Earth. They finally found that encounters with Mars were less important, and predicted a very small fraction of Q-types among Mars-crossers ($\lesssim 1\%$).

The 23 Q-types candidates we identified among Mars-crossers (Section 4) account for about 2.5% of the sample (and the Q/S ratio is about 5%). This ratio is smaller than for NEAs where it reaches 20% (the total fraction of Q-types among NEAs is 8%), but it is a lower limit. The Q/S fraction is indeed strongly diameter-dependent as illustrated in Fig. 7. When comparing similar size range ($H < 18$, corresponding to 95% of the MC sample here), the

[9] Trajectories of 6 clones per asteroid with a difference of 10^{-6} AU/yr in initial velocity in each direction were integrated with SWIFT3 RMVS (Levison and Duncan, 1994) over 500 kyr, with a time step of 3.65 days. Minimum Orbital Insertion Distance (MOID) were averaged over 50 years.

[10] Trajectories of 100 clones per asteroid, spread along the line of variation, were integrated also with SWIFT3 RMVS over 1 Myr, with a time step of 1 days.

Q/S fraction is roughly similar for NEAs and MCs, around 5–8%. The ratio jumps to 40% for sub-kilometric NEAs, and many more Q-types could be discovered among sub-kilometric MCs. Because of this high fraction of Q-types among MCs, challenging the prediction by Nesvorný et al. (2010), we first derive the theoretical radius of influence during an planetary encounter by studying the forces acting on surface grains (Sections 6.2.1–6.2.4) and then study the dynamical history of all the S- and Q-types asteroids presented here, recording their close encounters with massive bodies (Section 6.2.5).

6.2.1. Resurfacing model

While resurfacing of asteroids by planetary encounters has already been studied (Nesvorný et al., 2005, 2010; Binzel et al., 2010; DeMeo et al., 2014b), the physics of the surface was not given much attention in the aforementioned articles. The velocity and duration of the encounter, the object's shape, internal structure, surface gravity, local slopes, rotation rate and orientation, and the nature of the pre-existing regolith and its cohesion, were listed as possible parameters dictating the distance at which an encounter can resurface the asteroid.

In the following we are interested in finding the mean processes responsible for resurfacing and the minimum close encounter distances at which it would occur. We thus consider a simple force balance equation describing the accelerations a surface particle is likely to experience at the moment of closest approach. A particle on the asteroid's surface is subject to the following forces during a flyby (e.g., Hartzell and Scheeres, 2011):

$$F_{td} + F_{cf} + F_{es} + F_{lt} = F_{ga} + F_{co} + F_{sp} \quad (1)$$

On the left-hand side of Eq. (1) we have summed all the forces that can displace the particle: F_{td} are the tidal forces due to the planetary encounter, F_{cf} is the centrifugal pseudo force due to the asteroid's rotation, F_{es} is a repulsive electrostatic force that originates from the electric charging of surface particles, and F_{lt} is the displacement force acting when the asteroid's rotation state changes (librational transport, see Yu et al., 2014). The right-hand side contains forces that can keep a particle in place: F_{ga} is the self-gravity of the asteroid, F_{co} is the cohesion between surface particles, and F_{sp} is the solar radiation pressure. We describe the force model in detail in Appendix A and show in Fig. 8 their absolute magnitude as function of the diameter of surface grains.

To determine the minimum planet-to-asteroid distances that would result in the resurfacing of the asteroid, we consider two limiting cases (see Fig. 9). *Easy* and *hard* cases are defined based on whether the conditions for resurfacing are favorable or not, respectively. By doing so, we aim at deriving limits to distinguish regions in the parameter space where resurfacing is practically guaranteed, from regions that will leave the asteroid's surface untouched.

6.2.2. Easy resurfacing conditions

If the asteroid has a rotation rate close to the spin-barrier and it passes the planet with its spin axis perpendicular to the orbital plane of the hyperbolic encounter, i.e., with zero obliquity with respect to the planet, resurfacing is more likely. Since fast rotators are stable with regard to perturbations of the spin state, we can assume that the initial spin vector remains constant and librational transport will not play a role. Low self-gravity is also conducive to resurfacing. The effect of solar radiation pressure can be neglected, because it is orders of magnitude weaker than the other contributions.

Considering the high porosity of the first layers of asteroid surfaces Vernazza et al. (2012) that could originate from the electrostatic charging of the surface particles, we deem cohesion between surface particles to be negligible in this case. Since electrostatic inter-particle repulsion is already incorporated in the assumption of a highly porous upper layer of regolith, no additional electrostatic forces shall be considered. As a consequence of the above assumptions that yield the best case scenario in terms of resurfacing an asteroid, Eq. (1) simplifies to

$$F_{td} + F_{cf}^{\max} = F_{ga}^{\min} \quad (2)$$

Inserting the forces discussed in Appendix A into Eq. (2), we find the distance $r^\star$ between the asteroid and the planet where all accelerations cancel. In other words, $r^\star$ is the largest planet-to-asteroid distance at which a particle is no longer bound to the asteroid. If we assume the asteroid to be a tri-axial ellipsoid defined by $R_a \geqslant R_b \geqslant R_c$, rearranging its surface can take place at a planetary distance of

$$r^\star_{easy} = \left(\frac{6\mathcal{G}M}{4\pi\mathcal{G}\beta\rho - 3\omega_{sb}^2} \right)^{1/3} \quad (3)$$

where $\beta = R_b R_c / R_a^2$ is a shape factor relating the three principle axes. Eq. (3) describes a particle that is on the point of the surface farthest away from the center of rotation. It is easy to see that for any sort of ellipsoid shape the denominator in Eq. (3) shrinks. Therefore, ellipsoid shapes have extended resurfacing distances compared to

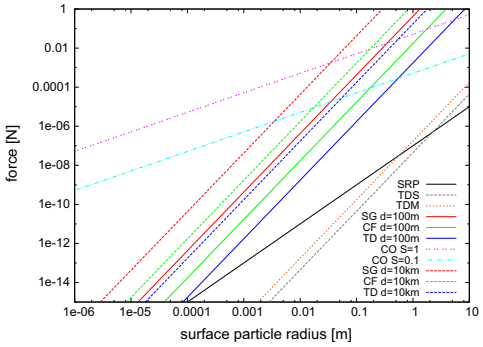

Fig. 8. Comparison of the forces acting on surface particles as function of their diameter during an encounter with the Earth at a 10 Earth-radii distance. The different lines represent the absolute magnitude of the following forces: self gravity (SG), cohesion (CO), centrifugal forces (CF), solar radiation pressure (SRP) for two different asteroid diameters, 100 m and 10 km, with the same bulk density (1900 kg m^{-3}) and rotation period (P = 10 h). Tidal accelerations due to the Moon (TDM) and the Sun (TDS) are only visible for the asteroid with a 100 m diameter. The range of likely cohesive forces is represented by the choice of cleanliness parameters between 0.1 and 1 (Perko et al., 2001; Scheeres et al., 2010; Hartzell and Scheeres, 2011; Sánchez and Scheeres, 2014). One can see that cohesion dominates all other forces for particle sizes below 10^{-3} m.

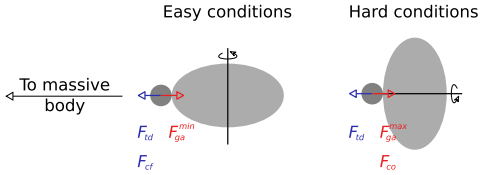

Fig. 9. Schematic view of the easy (Section 6.2.2) and hard (Section 6.2.3) conditions for resurfacing. The forces acting on a surface particles are: F_{td} are the tidal forces due to the planetary encounter, F_{cf} is the centrifugal force due to the asteroid's rotation, F_{ga} is the self-gravity of the asteroid, and F_{co} is the cohesion between surface particles.

spherical shapes (in which $\beta = 1$). Also, $r^{\star}_{easy}$ can become arbitrarily large when $\omega = \omega_{sb} = \sqrt{4\pi G\beta\rho/3}$ (with ρ the asteroid bulk density), i.e., when the asteroid's spin reaches the spin barrier (e.g., Pravec et al., 2006). Since an asteroid is expected to have shed most of its surface material at the spin barrier (Holsapple, 2007a), resurfacing will become impossible. Therefore, we will only consider rotation states slightly below this limit ($2\pi/\omega = P \sim 2.5$ h).

6.2.3. Hard resurfacing conditions

Resurfacing becomes most difficult, on the other hand, if the asteroid has basically no rotation or an obliquity close to 90° during its flyby. Then, there is no centrifugal acceleration that facilitates the collapse of rubble pile columns or lifts particles off the surface. Resurfacing is also more difficult if the asteroid mass is high, enhancing its self gravity. If electric charges of surface aggregates are feeble, the particles may settle and interlock in dense configurations that are dominated by cohesion rather than by electrostatic repulsion (Scheeres et al., 2010). Finally, for non-rotating bodies a change in the asteroid rotation is likely to occur due to the dynamical instability of a non-rotating configuration during flybys. Hence, librational transport could, in principle, occur. Yet, since we are interested in the case where resurfacing is most difficult, we will neglect its contribution regardless. The equation describing a scenario when resurfacing is most difficult thus writes:

$$F_{td} = F_{ga}^{\max} + F_{co} \tag{4}$$

Following the same approach as for easy resurfacing and using Eq. (4) to derive $r^{\star}_{hard}$ leads to planetary distances that are far below the asteroid's disruption regime. Indeed, cohesive forces are dominating all other contributions for particle sizes below 10^{-3} m, as visible in Fig. 8, since 99% of the particles that cover the surface have radii below 10^{-4} m (Appendix A.4). Consequently Eq. (4) is not a good estimator for the resurfacing limit. Since resurfacing is guaranteed when the asteroid enters the deformation or even disruption regime, we can simply use asteroid's Roche limit as a proxy for the conservative resurfacing distance. If we assume a perfectly spherical asteroid without rotation we have the following force equilibrium

$$F_{ga} = F_{td} \tag{5}$$

and consequently

$$r^{\star}_{hard} = R\left(\frac{2M}{m}\right)^{1/3} \approx \left(\frac{3M}{2\pi\rho}\right)^{1/3}, \tag{6}$$

where once again, R is the asteroid's (maximum) radius, and m and M are the asteroid and the planet masses. The simple spherical Roche limit serves as a proxy for $r^{\star}_{hard}$, as it would hold as a lower boundary should the asteroid be an ellipsoid.

6.2.4. Planet to NEA distance for resurfacing

We use the two relations determined above for easy and hard resurfacing to evaluate the minimum distance at which a planetary encounter can displace surface particles. We compute the easy and hard cases for the following parameters: an absolute magnitude of 20 (corresponding to diameter of 200 and 600 m for albedo of 0.5 and 0.05 respectively), a bulk density of 1.9 and 2.7 g cm^{-3}, and a shape factor β of 0.21. We show these threshold distances for Venus, Earth, and Mars, as function of the asteroid rotation period in Fig. 10.

First, the difference between the easy and hard resurfacing distances is substantial, especially for fast rotator. Then, we find distances ranging from a couple of planetary radii up to 10 planetary radii in extreme cases, when the rotation period is close to the spin barrier. This is fully compatible, yet slightly lower, than the estimates of 5–10 planetary radii from Nesvorný et al. (2010) derived independently. This implies that resurfacing through planetary encounters is not common, as the encounters have to be very close.

However, one might ask whether it is permissible to simply ignore the effect of cohesion, as has been done in Eq. 5. In fact, Fig. 8 shows that cohesion dominates other forces up to millimeter

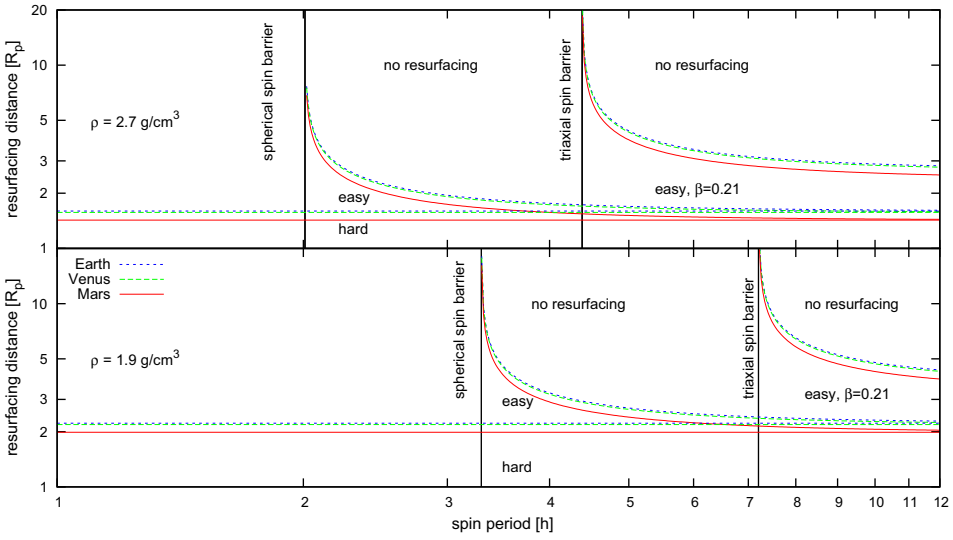

Fig. 10. Best case ($r^{\star}_{easy}$) and worst case ($r^{\star}_{hard}$) resurfacing distances in planetary radii for an asteroid (see text for details) that has close encounters with Mars, Venus and the Earth. Resurfacing is possible for close encounter distances below the respective lines. Note that forces scale with asteroid diameter and this picture is therefore valid for any NEA size.

sized particles. However, for larger particles this is no longer the case. If the asteroid comes close enough during its approach, tidal forces will then be strong enough to lift decimeter- to meter-sized objects on the surface of the asteroid. While objects of this size do not contribute significantly to the overall surface of the asteroid (Sánchez and Scheeres, 2014), they can refresh the surface if displaced by triggering landslides for instance.

A similar line of thought can be used to argue that we may be able to ignore cohesive and tensile effects in the case of non-spherical objects, since the internal stresses decay rapidly towards the surface (Holsapple, 2007b; Sánchez and Scheeres, 2014). Such an approach would not be permissible, if we were searching for criteria to describe global deformation or complete asteroid failure. There, one would have to account for internal cohesion and material stresses (Sharma et al., 2006). Yet, as we are merely interested in whether the combination of forces acting during a close encounter can displace any sort of particle on the surface of the asteroid, we argue that our simplified approach is valid.

6.2.5. Dynamical simulations

We investigate the hypothesis of resurfacing by planetary encounters developed above by testing whether there is a significant difference in the number of potential resurfacing events between Q- and S-type asteroid samples. We probe the dynamical history of each asteroid by propagating its position together with a sample of 96 clones 0.5 Myrs into the past using a symplectic integrator based on Yoshida's T + V split (Yoshida, 1990) with General Relativity (GR) correction (Lubich et al., 2010). Symplectic integrators have the advantage that the error in the mean anomaly, i.e., the position on the planet on its orbit, does not grow as quickly as with standard propagators (Eggl and Dvorak, 2010 and references therein). Using an 8th order integrator with a stepsize of 1 day in the drift in mean anomaly over 0.5 Myrs is less than 0.015° in the two-body problem Sun-Earth, corresponding to a total along track displacement of less than 6 Earth radii. As for close encounters, the propagator is able to resolve all close encounters lasting more than 6 h reasonably well. The limit resolution is reached for encounters lasting three hours. While the integration algorithm is not regularized, care has been taken to avoid losing accuracy due to imprecise calculation of accelerations and the accumulation of round off errors (e.g., via the use of Kahan summation).

Each simulation contained the following massive perturbers: the 8 planets, the barycenter of the Pluto system as well the major asteroids (1) Ceres, (2) Pallas, (4) Vesta and (10) Hygiea, henceforth referred to as the massive bodies. Initial conditions for the massive bodies were taken from JPL DE405 ephemerides at the epoch J2000. The initial conditions for the asteroids were constructed using the open source software `OrbFit`[11] (Milani et al., 2008), taking all observations up to April 2014 into account. Asteroid orbits were fit to the non-relativistic dynamical system containing all planets and the Pluto system. No asteroid perturbers were taken into account during the fitting process. Given the timescales involved in the orbit fitting and differential correction, the discrepancies arising from neglecting GR and the major perturbing asteroids on the investigated asteroids can be considered small compared to the orbit uncertainties.

The uncertainty covariance matrix resulting from the orbital fit was then sampled along the line of variation (Milani et al., 2000) from -3σ to $+3\sigma$ with 96 clones per asteroid. The 96 clones were then propagated together with the nominal orbit in order to see the dispersion in phase space. All close encounters, with the Earth, Venus, Mars, Jupiter and the main perturbing asteroids were cataloged for each clone in form of close minimum encounter distance (MED) and time histograms. The following limit distances were used to trigger a close encounter log: Jupiter: 2.56956 AU, Venus, Earth and Mars: 0.256956 AU, the main perturbing asteroids: 0.0256956 AU. These values correspond to approximately 7 Hill's radii for Jupiter, 25 for the Earth and Venus, 35 Hill's radii for Mars and 35–70 Hill's radii for the perturbing asteroids. Minimum encounter distances and velocities were calculated using cubic spline interpolation of the asteroid's orbit during its close encounter. Global minimum and average encounter distances together with their variances were also saved. In addition, minimum orbit intersection distances (MOIDs) were calculated every 800 days. Similarly to the MED values, MOID histograms, averages and variances were cataloged.

It should be mentioned that results stemming from integrating NEA orbits backwards in time need to be interpreted with care. Similarly to forward propagation NEAs on chaotic trajectories with the terrestrial planets have a relatively short horizon that limits an accurate prediction of their dynamical evolution (see, e.g., Michel, 1997). In such cases even robust ensemble statistics will not yield reliable estimates on close encounter distances since the divergence of nearby solution becomes exponential. As a consequence, we decided to exclude those NEAs from the statistics as soon as the spread in clone encounter distances becomes large. In our dynamical study, we also excluded the Yarkovsky effect for the following reasons. First, the spin state and orientation of the chosen targets are largely unknown. While this could be remedied using a statistical distribution of drift parameters among the clones of each NEA as proposed, for instance, by Spoto et al. (2014), this would only lead to an artificially increased spread in 96 clones making it harder to determine which NEAs are on chaotic orbits and which are not. Second, close encounters can change the spin state, making self-consistent predictions very difficult. That being said, Yarkovsky drift rates of our targets range between 10^{-4} and 10^{-3} AU/Myr. The cross-track error that results from neglecting the Yarkovsky drift alone can range between 2 and 20 Earth radii over 0.5 Myrs, and along track position errors are much larger.

Regardless of the simplifications of our dynamical model, we find that all the Q-types have a minimum MOID allowing a close encounter with the Earth (18% of the sample), or Mars (100%) in the past 500,000 years (we use the median values from all the clones here). A large fraction of the S-type sample also present a minimum MOID that could have led to a close encounter with one of the terrestrial planets (12.9%, 6.7%, and 95.4% for the Earth, Venus, and Mars respectively), similarly to the situation presented by Binzel et al. (2010) and DeMeo et al. (2014b). However, a small MOID does not necessary imply a close encounter: the MOID provides a measure of the distance between the orbits, not between the bodies. The typical example would be a Trojan asteroid, for which the MOID is small by definition, but that would never encounter the planet.

To overcome this issue, we also study the minimum encounter distance (MED) of the asteroids and their clones: that is the real distance between the particles and the massive bodies. However, even with a symplectic integrator, the drift in mean anomaly steadily increases with ephemeris time, and reach the level of a few planetary radii, at which the resurfacing is deemed to occur (see Section 6.2.4 above). Results for MED therefore potentially suffer from an underestimation of the number of close encounters, especially for the closest. The total number of detected MED resurfacing events is much less than the theoretically favorable number of configurations given by the encounter numbers using MOIDs. However, MEDs share the same trends with our MOID results.

The analysis using the median properties of each asteroid with its 96 clones seems therefore not conclusive: based on MED values,

[11] http://adams.dm.unipi.it/orbfit/.

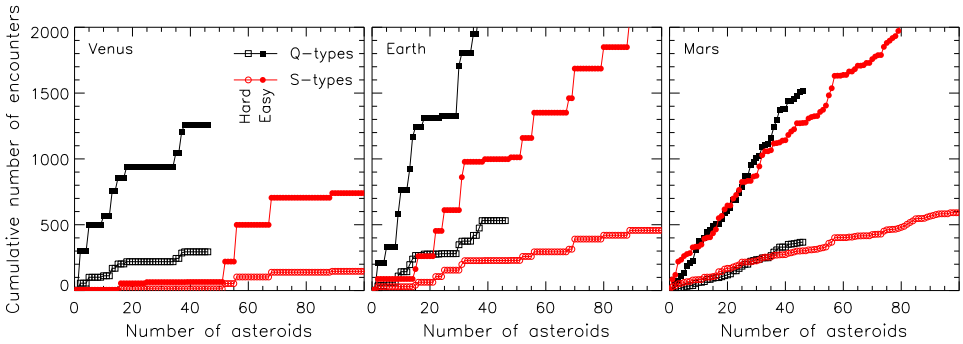

Fig. 11. Comparison of the number of close encounters for the easy and hard resurfacing cases (filled and open symbols) for the samples of Q- and S-type asteroids (in black squares and red circles). (For interpretation of the references to color in this figure legend, the reader is referred to the web version of this article.)

the planetary encounters are not expected to play any role in rejuvenating the surface of the Q-types, and based on MOID values, there should be more fresh surfaces (i.e., less S-types) as the vast majority of our sample present small MOID with Mars. We therefore study the populations of S- and Q-types statistically. We present in Fig. 11 the cumulative number of close encounters reaching the planetary distance for easy and hard resurfacing scenarios (see Sections 6.2.2 and 6.2.3) between our sample of asteroids and Venus, the Earth, and Mars. There is a clear difference in the number of encounters experienced by the population of Q-types compared to the S-types sample for both Venus and the Earth. That is, the asteroids presenting a fresh surface, similar to ordinary chondrites and exempt of signature from space weathering, tend to have more close encounters with massive bodies that those asteroids with space-weathered surface. Significant resurfacing would thus occur from the stress during repetitive close encounters with planets. The distribution of encounters for both the Earth and Venus clearly highlights the sample of Q-types among the NEAs sample presented here (and somewhat provides an *a posteriori* validation of our classification into S- and Q-types, the two groups being apparently dynamically different).

Conversely, the encounter distribution with Mars is similar for both taxonomic classes, as both could theoretically have numerous encounters with Mars, within the expected distance suitable for resurfacing to occur. Among all the parameters recorded during the dynamical simulation, none showed a significant difference between the two populations and we are therefore limited to speculations. Because the sample of MCs studied here exhibit larger diameters than the NEAs encountering the Earth, they are deemed to be older. Their surface may therefore have reached the saturation state introduced by Marchi et al. (2012), where rejuvenation is inefficient. The frequent encounters with Mars would then no longer turn the S-type surfaces into Q-types. Another possibility is that the limit for easy resurfacing being tight to the rotation period and obliquity during the close encounter, only a small fraction of close encounters do trigger resurfacing events, with a preference for fast-spinning asteroids. A survey of rotation period of Q-types among NEAs and MCs population could address this point.

7. Conclusion

In this work, we report on the dynamical and surface properties of near-Earth asteroids (NEAs) and Mars-crosser asteroids (MCs), based on the analysis of their colors in the visible. Our sample includes:

- 43 NEAs and 310 MCs listed in the Moving Object Catalogue (MOC4) of the Sloan Digital Sky Survey (SDSS);
- 206 NEAs and 776 MCs, in publicly available images of the SDSS, using our citizen-science project "Near-Earth Asteroids Recovery Program" of the Spanish Virtual Observatory (SVO, Solano et al., 2013) measured in four filters (g', r', i', and z');
- 678 NEAs and MCs asteroids measured in three filters (g', r', and i') also from our citizen-science project, for 254 of which we assign tentative taxonomic classification.

In total we have determined the taxonomic class of these 982 NEAs and MCs using the DeMeo-Carry taxonomy for SDSS colors (DeMeo and Carry, 2013), that is compatible with the Bus-DeMeo taxonomy based on V+NIR spectra (DeMeo et al., 2009).

The sample of taxonomic classes presented here correspond to an increase of known classes by 40% and 600% for NEA and MC populations, respectively. Among those, 36 NEAs can be considered potential targets for space missions, owing to their low δv. Some candidates for rare taxonomic classes such as D-, L-, and K-types are present within this sample and would benefit from further spectral investigations.

We then use the sample of asteroids with taxonomic classes based on four-filter observations to study their source regions and the effect of planetary encounters on their surface properties. To this end,

- we compare the distribution of taxonomic classes between our sample of NEAs and MCs and the source regions, using the predictions resulting from the dynamical model presented by Greenstreet et al. (2012). The population of 2–5 km diameter asteroids in the main belt (DeMeo and Carry, 2014) match closely the predictions from the sample presented here, supporting that the ν_6 secular resonance and the 3:1 mean-motion resonance with Jupiter are the primary sources of kilometer-size NEAs;
- we analyze the dependence of spectral slope on diameter for asteroids in the S-complex. A linear trend of shallower slope toward higher absolute magnitude is found;
- we develop a simple force model on surface grains during a planetary encounter;
- we investigate the planetary distance at which a resurfacing event is expected to occur, by considering two extreme cases to the simple force model, when the conditions are the most or conversely the least conducive to favorable resurfacing event. This distance is found to be a function of the rotation period and density of the asteroid, and of the spin obliquity during the

encounters. It ranges from 2 to ≈10 planetary radii for Venus, the Earth, and Mars. Such values are consistent with previous estimates by Binzel et al. (2010) and Nesvorný et al. (2010);
- we study the dynamical history of the sample of S- and Q-type by propagating their positions backward in time for 0.5 Myrs, together with 96 clones, using a symplectic post-Newtonian integrator. The population of Q-type presents statistically more encounters with Venus and the Earth at distance where resurfacing should occur than S-types. However, both populations present a high number of encounters with Mars and are indistinguishable.

Acknowledgments

We thanks S. Greenstreet for providing the source region mapper extended to include Mars-crosser space. We acknowledge support from the Faculty of the European Space Astronomy Centre (ESAC) for B. Carry's visit. S. Eggl would like to acknowledge the support of the European Commission H2020-PROTEC-2014 Grant No. 640351 (NEOShield-2). This publication makes use of the NEAs Precovery Service, developed under the Spanish Virtual Observatory project (Centro de Astrobiologia, INTA-CSIC) supported from the Spanish MICINN through grants AyA2008-02156 and AyA2011-24052. This work was granted access to the HPC resources of MesoPSL financed by the Region Ile de France and the project Equip@Meso (reference ANR-10-EQPX-29-01) of the programme Investissements dAvenir supervised by the Agence Nationale pour la Recherche. This material is based upon work supported, in part, by the National Science Foundation under Grant 0907766. Any opinions, findings, and conclusions or recommendations expressed in this material are those of the authors and do not necessarily reflect the views of the National Science Foundation.

This publication makes use of data products from the Wide-field Infrared Survey Explorer, which is a joint project of the University of California, Los Angeles, and the Jet Propulsion Laboratory/California Institute of Technology, funded by the National Aeronautics and Space Administration. Funding for the creation and distribution of the SDSS Archive has been provided by the Alfred P. Sloan Foundation, the Participating Institutions, the National Aeronautics and Space Administration, the National Science Foundation, the U.S. Department of Energy, the Japanese Monbukagakusho, and the Max Planck Society. The SDSS Web site is http://www.sdss.org/.

Appendix A. Forces model

In the following we will briefly discuss the force models used in Eqs. (2) and (4).

A.1. Self gravity of the asteroid

On the surface of the asteroid a particle of mass μ will experience the following gravitational pull towards the asteroid's center of mass:

$$F_{ga} = \mathcal{G}\mu m/R^2 \tag{A.1}$$

where $\mathcal{G}$ is the gravitational constant, m the mass and R the local radius of the asteroid.

A.2. Forces due to the rotating frame

In a rotating frame of reference, surface particles are subject to a centrifugal force F_{cf}. It will suffice to consider principle axis rotation as we are primarily interested in best and worst case scenarios. Therefore, the particle feeling the maximum centrifugal acceleration then is located farthest from the axis of rotation and we have

$$F_{cf} = \mu R\omega^2 \cos\phi \tag{A.2}$$

Here, ω is the spin rate and ϕ the angle between the asteroid's spin axis and the vector $\vec{r}$ connecting the centers of gravity of the planet and the asteroid. In other words ϕ is the asteroids obliquity with respect to is planetocentric orbit. Consequently, $F_{cf}^{\max} = \mu R^{\max}\omega_{sb}^2$. This corresponds to a particle on the equator of a spherical asteroid with maximum radius $R^{\max}$ and a rotation rate close to the spin barrier ω_{sb}. As we assume that the particles are at rest on the surface, no Coriolis forces will have to be accounted for.

A.3. Tidal acceleration

Asteroid that have close encounters with other massive bodies will experience tidal forces. Towards an asteroid's surface the tidal acceleration becomes stronger compared to volume elements that are closer to the center of gravity. Consequently surface particles are pulled away more easily than say boulders close to the center of the asteroid. A simple model for the tidal force acting on a particle with mass μ is:

$$F_{td} = 2R\mathcal{G}\mu M/D^3 \tag{A.3}$$

where M is the mass of the planet and D the distance between the asteroid and the planet. In principle, there are additional tidal contributions from the Sun, and the Moon if the Earth is approached. Those are, however, small compared to the contribution of the Earth itself and shall, therefore, be neglected.

A.4. Particle Cohesion

The role of cohesion in rubble pile asteroids has been studied extensively over the past years (Scheeres et al., 2010; Hartzell and Scheeres, 2011; Sánchez and Scheeres, 2014). It is currently understood that particle cohesion plays and important role in determining limits for rubble-pile asteroid failures, fission, and for the survival of contact binaries. The standard cohesion model as presented in Hartzell and Scheeres (2011) is based on van der Waals interaction in granular materials. The inter particle force can be modeled as:

$$F_{co} = CS^2\sigma \tag{A.4}$$

where $C = 5.14 \times 10^{-2}$ kg/s^2 is a material constant related to the Hamaker constant, $S \sim 1$ is the so-called cleanliness ratio, a qualitative factor indicating the impurity of granular surface coatings and σ is the radius of the particles on the asteroid's surface. For a detailed discussion of Eq. (A.4) see e.g. Hartzell and Scheeres (2011). As it is harder to free larger particles or rocks from the surface, we will increase the particle radius that shall be lifted against cohesion. Eq. (A.4) illustrates that the larger the particles and the cleaner the surface, the larger the cohesive force. Let us now determine the approximate size of the largest particles that will be relevant for our resurfacing considerations. For this purpose we assume an $N \propto (2\sigma)^{-3}$ distribution of the number of particles N on the asteroid's surface. Using Eq. (36) in Sánchez and Scheeres (2014) we can calculate the particle diameter up to which smaller particles cover 99% of the surface. This is $\sigma = 100r_0$, where we furthermore assume that r_0 is of the order of the smallest particle radii that could be detected on Itokawa ($r_0 \simeq 10^{-6}$ m). Hence, practically all of the asteroid's surface is covered by particles smaller than 0.1 mm.

Appendix B. Supplementary material

Supplementary data associated with this article can be found, in the online version, at http://dx.doi.org/10.1016/j.icarus.2015.12.047.

References

Abell, P. et al., 2012. The near-Earth object human space flight accessible targets study (NHATS) list of near-Earth asteroids: Identifying potential targets for future exploration. In: AAS/Division for Planetary Sciences Meeting Abstracts, vol. 44.

Abell, P. et al., 2015. NASA's Asteroid Redirect Mission (ARM). In: AAS/Division for Planetary Sciences Meeting Abstracts, vol. 47, p. 312.06.

Barucci, M.A. et al., 2012. MarcoPolo-R near Earth asteroid sample return mission. Exp. Astron. 33, 645–684.

Bell, J.F. et al., 2002. Near-IR reflectance spectroscopy of 433 Eros from the NIS instrument on the NEAR mission. I. Low phase angle observations. Icarus 155, 119–144.

Berthier, J. et al., 2006. SkyBoT, a new VO service to identify Solar System objects. In: Gabriel, C. et al., (Eds.), Astronomical Data Analysis Software and Systems XV, Astronomical Society of the Pacific Conference Series, vol. 351. p. 367.

Binzel, R.P., 2000. The Torino impact hazard scale. Planet. Space Sci. 48, 297–303.

Binzel, R.P., Xu, S., 1993. Chips off of Asteroid 4 Vesta: Evidence for the parent body of basaltic achondrite meteorites. Science 260 (5105), 186–191.

Binzel, R.P. et al., 2004. Observed spectral properties of near-Earth objects: Results for population distribution, source regions, and space weathering processes. Icarus 170, 259–294.

Binzel, R.P. et al., 2010. Earth encounters as the origin of fresh surfaces on near-Earth asteroids. Nature 463, 331–334.

Binzel, R., Reddy, V., Dunn, T., 2015. The near-Earth object population: Connections to comets, main-belt asteroids, and meteorites. Asteroids IV.

Bottke, W.F. et al., 2002. Debiased orbital and absolute magnitude distribution of the near-Earth objects. Icarus 156, 399–433.

Bus, S.J., Binzel, R.P., 2002. Phase II of the small main-belt asteroid spectroscopic survey: A feature-based taxonomy. Icarus 158, 146–177.

Carry, B., 2012. Density of asteroids. Planet. Space Sci. 73, 98–118.

Carvano, J.M. et al., 2010. SDSS-based taxonomic classification and orbital distribution of main belt asteroids. Astron. Astrophys. 510, A43.

Chapman, C.R., Morrison, D., Zellner, B.H., 1975. Surface properties of asteroids – A synthesis of polarimetry, radiometry, and spectrophotometry. Icarus 25, 104–130.

Cloutis, E.A. et al., 2015. Olivine-metal mixtures: Spectral reflectance properties and application to asteroid reflectance spectra. Icarus 252, 39–82.

Dandy, C.L., Fitzsimmons, A., Collander-Brown, S.J., 2003. Optical colors of 56 near-Earth objects: Trends with size and orbit. Icarus 163, 363–373.

de León, J. et al., 2006. Spectral analysis and mineralogical characterization of 11 olivine pyroxene rich NEAs. Adv. Space Res. 37, 178–183.

de León, J. et al., 2010. Observations, compositional, and physical characterization of near-Earth and Mars-crosser asteroids from a spectroscopic survey. Astron. Astrophys. 517, A23.

Dell'Oro, A., Marchi, S., Paolicchi, P., 2011. Collisional evolution of near-Earth asteroids and refreshing of the space-weathering effects. Mon. Not. R. Astron. Soc. 416, L26–L30.

DeMeo, F., Carry, B., 2013. The taxonomic distribution of asteroids from multi-filter all-sky photometric surveys. Icarus 226, 723–741.

DeMeo, F.E., Carry, B., 2014. Solar System evolution from compositional mapping of the asteroid belt. Nature 505, 629–634.

DeMeo, F.E. et al., 2009. An extension of the Bus asteroid taxonomy into the near-infrared. Icarus 202, 160–180.

DeMeo, F.E. et al., 2014a. Unexpected D-type interlopers in the inner main belt. Icarus 229, 392–399.

DeMeo, F.E., Binzel, R.P., Lockhart, M., 2014b. Mars encounters cause fresh surfaces on some near-Earth asteroids. Icarus 227, 112–122.

Eggl, S., Dvorak, R., 2010. An introduction to common numerical integration codes used in dynamical astronomy. In: Dynamics of Small Solar System Bodies and Exoplanets. Springer, pp. 431–480.

Emery, J.P., Brown, R.H., 2003. Constraints on the surface composition of Trojan asteroids from near-infrared (0.8–4.0 μm) spectroscopy. Icarus 164, 104–121.

Emery, J.P., Brown, R.H., 2004. The surface composition of Trojan asteroids: Constraints set by scattering theory. Icarus 170, 131–152.

Emery, J.P., Burr, D.M., Cruikshank, D.P., 2011. Near-infrared spectroscopy of Trojan asteroids: Evidence for two compositional groups. Astron. J. 141, 25.

Fornasier, S. et al., 2004. Visible spectroscopic and photometric survey of L5 Trojans: Investigation of dynamical families. Icarus 172, 221–232.

Fornasier, S. et al., 2007. Visible spectroscopic and photometric survey of Jupiter Trojans: Final results on dynamical families. Icarus 190, 622–642.

Fujiwara, A. et al., 2006. The rubble-pile asteroid itokawa as observed by Hayabusa. Science 312, 1330–1334.

Gaffey, M.J. et al., 1993. Mineralogical variations within the S-type asteroid class. Icarus 106, 573–602.

Gil-Hutton, R., Brunini, A., 2008. Surface composition of Hilda asteroids from the analysis of the Sloan Digital Sky Survey colors. Icarus 193, 567–571.

Gounelle, M., Spurný, P., Bland, P.A., 2006. The orbit and atmospheric trajectory of the Orgueil meteorite from historical records. Meteoritics Planet. Sci. 41, 135–150.

Greenstreet, S., Ngo, H., Gladman, B., 2012. The orbital distribution of near-Earth objects inside Earth's orbit. Icarus 217, 355–366.

Hartzell, C.M., Scheeres, D.J., 2011. The role of cohesive forces in particle launching on the Moon and asteroids. Planet. Space Sci. 59, 1758–1768.

Holmberg, J., Flynn, C., Portinari, L., 2006. The colours of the Sun. Mon. Not. R. Astron. Soc. 367, 449–453.

Holsapple, K.A., 2007a. Spin limits of Solar System bodies: From the small fast-rotators to 2003 EL61. Icarus 187 (2), 500–509.

Holsapple, K.A., 2007b. Spin limits of Solar System bodies: From the small fast-rotators to 2003 EL61. Icarus 187, 500–509.

Ivezić, Ž. et al., 2001. Solar System objects observed in the Sloan Digital Sky Survey commissioning data. Astron. J. 122, 2749–2784.

Ivezić, Ž. et al., 2002. Color confirmation of asteroid families. Astron. J. 124, 2943–2948.

Jedicke, R. et al., 2004. An age-colour relationship for main-belt S-complex asteroids. Nature 429, 275–277.

Jedicke, R. et al., 2007. The next decade of Solar System discovery with Pan-STARRS. In: Valsecchi, G.B., Vokrouhlický, D., Milani, A. (Eds.), IAU Symposium, vol. 236. pp. 341–352.

Jutzi, M., Michel, P., 2014. Hypervelocity impacts on asteroids and momentum transfer I. Numerical simulations using porous targets. Icarus 229, 247–253.

Lauretta, D.S., Drake, M.J., Team, O., 2011. OSIRIS-REx – Exploration of Asteroid (101955) 1999 RQ36. American Geophysical Union (Fall) (abstracts).

Lazzarin, M. et al., 2005. Spectroscopic investigation of near-Earth objects at Telescopio Nazionale Galileo. Mon. Not. R. Astron. Soc. 359, 1575–1582.

Levison, H.F., Duncan, M.J., 1994. The long-term dynamical behavior of short-period comets. Icarus 108, 18–36.

Lubich, C., Walther, B., Brügmann, B., 2010. Symplectic integration of post-newtonian equations of motion with spin. Phys. Rev. D 81 (10), 104025.

Mainzer, A. et al., 2011a. NEOWISE observations of near-Earth objects: Preliminary results. Astrophys. J. 743, 156.

Mainzer, A. et al., 2011b. NEOWISE studies of spectrophotometrically classified asteroids: Preliminary results. Astrophys. J. 741, 90.

Marchi, S. et al., 2010. On the puzzle of space weathering alteration of basaltic asteroids. Astrophys. J. 721, L172–L176.

Marchi, S., Paolicchi, P., Richardson, D.C., 2012. Collisional evolution and reddening of asteroid surfaces – I. The problem of conflicting time-scales and the role of size-dependent effects. Mon. Not. R. Astron. Soc. 421, 2–8.

Marsset, M. et al., 2014. Similar origin for low- and high-albedo jovian Trojans and Hilda asteroids? Astron. Astrophys. 568, L7.

McSween, H.Y., Lauretta, D.S., Leshin, L.A., 2006. Meteorites and the timing, mechanisms, and conditions of terrestrial planet accretion and early differentiation. Meteorites Early Solar Syst. II, 53–66.

Michel, P., 1997. Effects of linear secular resonances in the region of semimajor axes smaller than 2 {AU}. Icarus 129 (2), 348–366.

Michel, P. et al., 2000. The population of Mars-crossers: Classification and dynamical evolution. Icarus 145, 332–347.

Milani, A., Chesley, S.R., Valsecchi, G.B., 2000. Asteroid close encounters with Earth: Risk assessment. Planet. Space Sci. 48, 945–954.

Milani, A. et al., 2008. Topocentric orbit determination: Algorithms for the next generation surveys. Icarus 195 (1), 474–492.

Morbidelli, A., Nesvorný, D., 1999. Numerous weak resonances drive asteroids toward terrestrial planets orbits. Icarus 139, 295–308.

Morbidelli, A. et al., 2002. Origin and evolution of near-Earth objects. Asteroids III, 409–422.

Mueller, M. et al., 2011. ExploreNEOs. III. Physical characterization of 65 potential spacecraft target asteroids. Astron. J. 141, 109.

Murdoch, N. et al., 2012. Asteroid Impact & Deflection Assessment (AIDA) mission. Tech. Rep., European Space Agency.

Nakamura, T. et al., 2011. Itokawa dust particles: A direct link between S-type asteroids and ordinary chondrites. Science 333, 1113–1115.

Nesvorný, D., 2012. Nesvorny HCM asteroid families v2.0. NASA Planetary Data System, eAR-A-VARGBDET-5-NESVORNYFAM-V2.0.

Nesvorný, D. et al., 2005. Evidence for asteroid space weathering from the Sloan Digital Sky Survey. Icarus 173, 132–152.

Nesvorný, D. et al., 2010. Do planetary encounters reset surfaces of near Earth asteroids? Icarus 209, 510–519.

Ostro, S.J. et al., 2002. Asteroid radar astronomy. Asteroids III, 151–168.

Parker, A. et al., 2008. The size distributions of asteroid families in the SDSS Moving Object Catalog 4. Icarus 198, 138–155.

Perko, H.A., Nelson, J.D., Sadeh, W.Z., 2001. Surface cleanliness effect on lunar soil shear strength. J. Geotechn. Geoenviron. Eng. 127 (4), 371–383.

Polishook, D. et al., 2012. Spectral and spin measurement of two small and fast-rotating near-Earth asteroids. Icarus 221, 1187–1189.

Popescu, M. et al., 2011. Spectral properties of eight near-Earth asteroids. Astron. Astrophys. 535, A15.

Pravec, P. et al., 2006. Photometric survey of binary near-Earth asteroids. Icarus 181, 63–93.

Reddy, V., Nathues, A., Gaffey, M.J., 2011. First fragment of Asteroid 4 Vesta's mantle detected. Icarus 212, 175–179.

Reddy, V. et al., 2015. Mineralogy and surface composition of asteroids. Asteroids IV, na.

Ribeiro, A.O. et al., 2014. The first confirmation of V-type asteroids among the Mars crosser population. Planet. Space Sci. 92, 57–64.
Rivkin, A.S. et al., 2011. Ordinary chondrite-like colors in small Koronis family members. Icarus 211, 1294–1297.
Roig, F., Ribeiro, A.O., Gil-Hutton, R., 2008. Taxonomy of asteroid families among the Jupiter Trojans: Comparison between spectroscopic data and the Sloan Digital Sky Survey colors. Astron. Astrophys. 483, 911–931.
Rudawska, R., Vaubaillon, J., Atreya, P., 2012. Association of individual meteors with their parent bodies. Astron. Astrophys. 541, A2.
Sanchez, J.A. et al., 2012. Phase reddening on near-Earth asteroids: Implications for mineralogical analysis, space weathering and taxonomic classification. Icarus 220, 36–50.
Sanchez, J.A. et al., 2013. Surface composition and taxonomic classification of a group of near-Earth and Mars-crossing asteroids. Icarus 225, 131–140.
Sánchez, P., Scheeres, D.J., 2014. The strength of regolith and rubble pile asteroids. Meteorit. Planet. Sci. 49, 788–811.
Sasaki, S. et al., 2001. Production of iron nanoparticles by laser irradiation in a simulation of lunar-like space weathering. Nature 410, 555–557.
Scheeres, D.J. et al., 2010. Scaling forces to asteroid surfaces: The role of cohesion. Icarus 210, 968–984.
Sharma, I., Jenkins, J.T., Burns, J.A., 2006. Tidal encounters of ellipsoidal granular asteroids with planets. Icarus 183, 312–330.
Solano, E. et al., 2013. Precovery of near-Earth asteroids by a citizen-science project of the Spanish Virtual Observatory. Astron. Nachr. 335, 142–149.
Spoto, F. et al., 2014. Nongravitational perturbations and virtual impactors: The case of Asteroid (410777) 2009 FD. Astron. Astrophys. 572, A100.
Stokes, G.H. et al., 2000. Lincoln near-Earth asteroid program (LINEAR). Icarus 148, 21–28.
Strazzulla, G. et al., 2005. Spectral alteration of the Meteorite Epinal (H5) induced by heavy ion irradiation: A simulation of space weathering effects on near-Earth asteroids. Icarus 174, 31–35.
Tholen, D.J., 1984. Asteroid Taxonomy from Cluster Analysis of Photometry. Ph.D. Thesis, Arizona Univ., Tucson.
Tholen, D.J., Barucci, M.A., 1989. Asteroid taxonomy. Asteroids II, 298–315.
Thomas, C.A., Binzel, R.P., 2010. Identifying meteorite source regions through near-Earth object spectroscopy. Icarus 205, 419–429.
Thomas, C.A. et al., 2011. Space weathering of small Koronis family members. Icarus 212, 158–166.
Thomas, C.A., Trilling, D.E., Rivkin, A.S., 2012. Space weathering of small Koronis family asteroids in the SDSS Moving Object Catalog. Icarus 219, 505–507.
Vernazza, P. et al., 2008. Compositional differences between meteorites and near-Earth asteroids. Nature 454, 858–860.
Vernazza, P. et al., 2009. Solar wind as the origin of rapid reddening of asteroid surfaces. Nature 458, 993–995.
Vernazza, P. et al., 2012. High surface porosity as the origin of emissivity features in asteroid spectra. Icarus 221, 1162–1172.
Veverka, J. et al., 2000. NEAR at Eros: Imaging and spectral results. Science 289, 2088–2097.
Wetherill, G.W., 1979. Steady state populations of Apollo-Amor objects. Icarus 37, 96–112.
Willman, M., Jedicke, R., 2011. Asteroid age distributions determined by space weathering and collisional evolution models. Icarus 211, 504–510.
Willman, M. et al., 2008. Redetermination of the space weathering rate using spectra of Iannini asteroid family members. Icarus 195, 663–673.
Willman, M. et al., 2010. Using the youngest asteroid clusters to constrain the space weathering and gardening rate on S-complex asteroids. Icarus 208, 758–772.
Wisdom, J., 1983. Chaotic behavior and the origin of the 3/1 Kirkwood gap. Icarus 56, 51–74.
Yang, B., Jewitt, D., 2007. Spectroscopic search for water ice on jovian Trojan asteroids. Astron. J. 134, 223–228.
Yang, B., Jewitt, D., 2011. A near-infrared search for silicates in jovian Trojan asteroids. Astron. J. 141, 95.
Yano, H. et al., 2010. Hayabusa's follow-on mission for surface and sub-surface sample return from a C-type NEO. In: 38th COSPAR Scientific Assembly, COSPAR Meeting, vol. 38. p. 635.
Ye, Q.-z., 2011. BVRI photometry of 53 unusual asteroids. Astron. J. 141, 32.
Yoshida, H., 1990. Construction of higher order symplectic integrators. Phys. Lett. A 150 (5), 262–268.
Yu, Y. et al., 2014. Numerical predictions of surface effects during the 2029 close approach of Asteroid 99942 Apophis. Icarus 242, 82–96.

A&A 609, A113 (2018)
DOI: 10.1051/0004-6361/201730386

Astronomy & Astrophysics

Solar system science with ESA *Euclid*

B. Carry[1,2]

[1] Université Côte d'Azur, Observatoire de la Côte d'Azur, CNRS, Lagrange, 06304 Nice, France
[2] IMCCE, Observatoire de Paris, PSL Research University, CNRS, Sorbonne Universités, UPMC Univ. Paris 06, Univ. Lille, France
e-mail: benoit.carry@oca.eu

Received 2 January 2017 / Accepted 3 November 2017

ABSTRACT

Context. The ESA *Euclid* mission has been designed to map the geometry of the dark Universe. Scheduled for launch in 2020, it will conduct a six-year visible and near-infrared imaging and spectroscopic survey over 15 000 deg^2 down to $V_{AB} \sim 24.5$. Although the survey will avoid ecliptic latitudes below 15°, the survey pattern in repeated sequences of four broadband filters seems well-adapted to detect and characterize solar system objects (SSOs).
Aims. We aim at evaluating the capability of *Euclid* of discovering SSOs and of measuring their position, apparent magnitude, and spectral energy distribution. We also investigate how the SSO orbits, morphology (activity and multiplicity), physical properties (rotation period, spin orientation, and 3D shape), and surface composition can be determined based on these measurements.
Methods. We used the current census of SSOs to extrapolate the total amount of SSOs that will be detectable by *Euclid*, that is, objects within the survey area and brighter than the limiting magnitude. For each different population of SSO, from neighboring near-Earth asteroids to distant Kuiper-belt objects (KBOs) and including comets, we compared the expected *Euclid* astrometry, photometry, and spectroscopy with the SSO properties to estimate how *Euclid* will constrain the SSOs dynamical, physical, and compositional properties.
Results. With the current survey design, about 150 000 SSOs, mainly from the asteroid main-belt, should be observable by *Euclid*. These objects will all have high inclination, which is a difference to many SSO surveys that focus on the ecliptic plane. *Euclid* may be able to discover several 10^4 SSOs, in particular, distant KBOs at high declination. The *Euclid* observations will consist of a suite of four sequences of four measurements and will refine the spectral classification of SSOs by extending the spectral coverage provided by *Gaia* and the LSST, for instance, to 2 microns. Combined with sparse photometry such as measured by *Gaia* and the LSST, the time-resolved photometry will contribute to determining the SSO rotation period, spin orientation, and 3D shape model. The sharp and stable point-spread function of *Euclid* will also allow us to resolve binary systems in the Kuiper belt and detect activity around Centaurs.
Conclusions. The depth of the *Euclid* survey ($V_{AB} \sim 24.5$), its spectral coverage (0.5 to 2.0 μm), and its observation cadence has great potential for solar system research. A dedicated processing for SSOs is being set up within the *Euclid* consortium to produce astrometry catalogs, multicolor and time-resolved photometry, and spectral classification of some 10^5 SSOs, which will be delivered as Legacy Science.

Key words. methods: statistical – minor planets, asteroids: general – Kuiper belt: general – comets: general

1. Introduction

The second mission in ESA's Cosmic Vision program, *Euclid* is a wide-field space mission dedicated to the study of dark energy and dark matter through mapping weak gravitational lensing (Laureijs et al. 2011). It is equipped with a silicon-carbide 1.2 m aperture Korsch telescope and two instruments: a VISible imaging camera, and a Near Infrared Spectrometer and Photometer (VIS and NISP; see Cropper et al. 2014; Maciaszek et al. 2014). The mission design combines a large field of view (FoV, 0.57 deg^2) with high angular resolution (pixel scales of 0.1″ and 0.3″ for VIS and NISP, corresponding to the diffraction limit at 0.6 and 1.7 μm).

Scheduled for a launch in 2020 and operating during six years from the Sun-Earth Lagrange L2 point, *Euclid* will carry out an imaging and spectroscopic survey of the extragalactic sky of 15 000 deg^2 (the Wide Survey), avoiding galactic latitudes lower than 30° and ecliptic latitudes below 15° (Fig. 1), totaling 35 000 pointings. A second survey, two magnitudes deeper and located at very high ecliptic latitudes, will cover 40 deg^2 spread across three areas (the Deep Survey). Additionally, 7000 observations of 1200 calibration fields, mainly located at −10° and +10° galactic latitude, will be acquired during the course of the mission to monitor the stability of the telescope point-spread function (PSF), and assess the photometric and spectroscopic accuracy of the mission.

Euclid imaging detection limits are required at $m_{AB} = 24.5$ (10σ on a 1″ extended source) with VIS, and $m_{AB} = 24$ (5σ point source) in the Y, J, and H filters with NISP. Spectroscopic requirements are to cover the same near-infrared wavelength range at a resolving power of 380 and to detect at 3.5σ an emission line at 3×10^{-16} erg cm^{-1} s^{-1} (on a 1″ extended source). The NISP implementation consists of two grisms, *red* (1.25 to 1.85 μm) and *blue* (0.92 to 1.25 μm, usage of which will be limited to the Deep Survey), providing a continuum sensitivity to $m_{AB} \approx 21$. To achieve these goals, the following survey operations were designed:

1. The observations will consist of a step-and-stare tiling mode, in which both instruments target the common 0.57 deg^2 FOV before the telescope slews to other coordinates.
2. Each tile will be visited only once, with the exception of the Deep Survey, in which each tile will be pointed at 40 times,

A&A 609, A113 (2018)

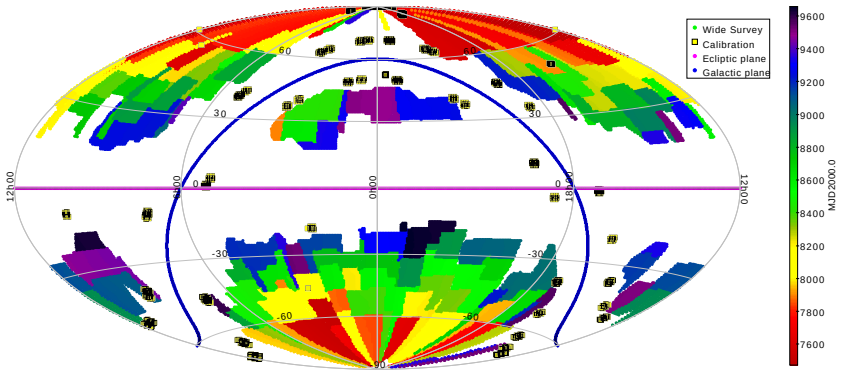

Fig. 1. Expected coverage of the *Euclid* Wide Survey (called the reference survey), color-coded by observing epoch, in an Aitoff projection of ecliptic coordinates. The horizontal gap corresponds to low ecliptic latitudes (the cyan line represents the ecliptic plane), and the circular gap to low galactic latitudes (the deep blue line stands for the galactic plane). The black squares filled with yellow are the calibration fields, which are to be repeatedly observed during the six years of the mission, to assess the stability and accuracy of the *Euclid* PSF, photometry, and spectroscopy.

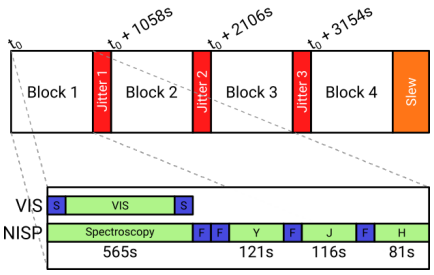

Fig. 2. Observation sequence for each pointing. The observing block, composed of a simultaneous VIS and NISP/spectroscopy exposure and three NISP/imaging exposures (Y, J, H), is repeated four times, with small jitters ($100'' \times 50''$). The blue boxes F and S stand for overheads that are due to the rotation of the filter wheel and shutter opening/closure. Figure adapted from Laureijs et al. (2011).

and the calibration fields, which will be observed 5 times each on average.

3. The filling pattern of the survey will follow the lines of ecliptic longitude at quadrature. Current survey planning foresees a narrow distribution of the solar elongation of $\Psi = 91.0 \pm 1.5°$ only; the range of solar elongation available to the telescope is limited to 87°–110°.
4. The observation of each tile will be subdivided into four observing blocks that differ by only small jitters ($100'' \times 50''$). These small pointing offsets will allow to fill the gaps between the detectors that make up the focal plane of each instrument. In this way, 95% of the sky will be covered by three blocks, and 50% by four blocks.
5. In each block, near-infrared slitless spectra will be obtained with NISP simultaneously with a visible image with VIS, with an integration time of 565 s. This integration time implies a saturation limit of $V_{AB} \approx 17$ for a point-like source. Then, three NISP images will be taken with the Y, J, and H near-infrared filters, with integration times of 121, 116, and 81 s, respectively (Fig. 2).

All these characteristics make the *Euclid* survey a potential prime data set for legacy science. In particular, the access to the near-infrared sky, about seven magnitudes fainter than the DENIS and 2MASS (Epchtein et al. 1994; Skrutskie et al. 2006) surveys, and two to three magnitudes fainter than the current ESO VISTA Hemispherical Survey (VHS; McMahon et al. 2013), makes *Euclid* suitable for a surface characterization of solar system objects (SSOs), especially in an era rich in surveys that only operate in visible wavelengths, such as the Sloan Digital Sky Survey (SDSS), Pan-STARRS, ESA *Gaia*, and the Large Synoptic Sky Survey (LSST) (Abazajian et al. 2003; Jewitt 2003; Gaia Collaboration 2016; LSST Science Collaboration et al. 2009).

We discuss here the potential of the *Euclid* mission for solar system science. In the following, we consider the following populations of SSOs, defined by their orbital elements (Appendix A):

- near-Earth asteroids (NEAs), including the Aten, Apollo, and Amor classes, whose orbits cross the orbits of terrestrial planets;
- Mars-crossers (MCs), a transitory population between the asteroid main belt and near-Earth space;
- main-belt asteroids (MBA) in the principal reservoir of asteroids in the solar system, between Mars and Jupiter, split into Hungarian, inner main-belt (IMB), middle main-belt (MMB), outer main-belt (OMB), Cybele, and Hilda;
- Jupiter trojans (Trojans), orbiting the Sun at the Lagrange L4 and L5 points of the Sun-Jupiter system;
- Centaurs whose orbits cross the orbits of giant planets;
- Kuiper-belt objects (KBOs) farther away than Neptune, divided into detached, resonant, and scattered-disk objects (SDO), and inner, main, and outer classical belt (ICB, MCB, and OCB); and
- comets from the outskirts of the solar system on highly eccentric orbits that are characterized by activity (coma) at short heliocentric distances.

The discussion is organized as follows: the expected number of SSO observations is presented in Sect. 2, and the difficulties we expect for these observations are described in Sect. 3. The problems of source identification and the contribution to astrometry and orbit determination are discussed in Sect. 4. Then the potential for spectral characterization from VIS and NISP photometry is detailed in Sect. 5, and the same is done for

B. Carry: Solar system science with ESA *Euclid*

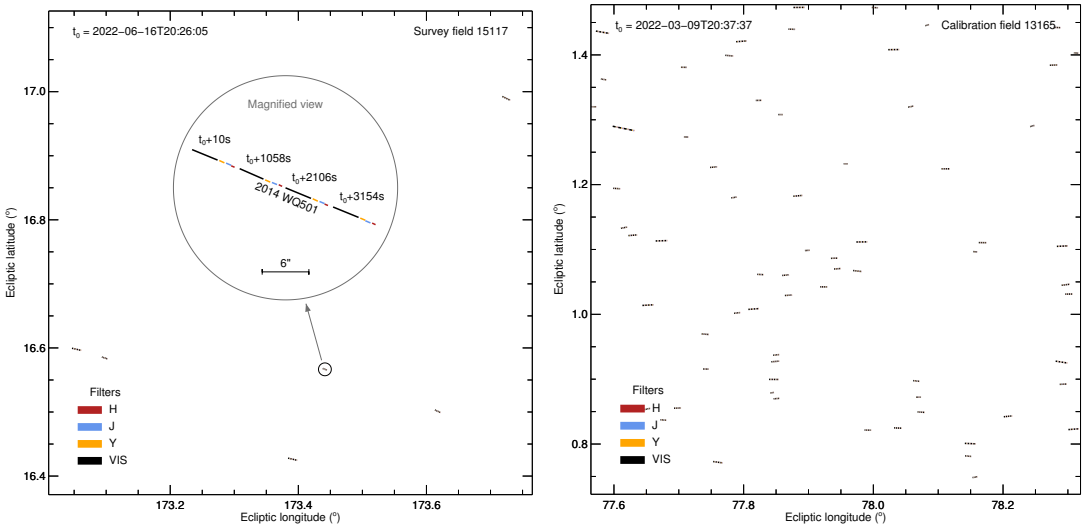

Fig. 3. Examples of the contamination of *Euclid* FOV by SSOs. *Left*: survey field 15117 centered on (RA, Dec) = (167.218°, +12.740°) and starting on 2022 June 16 at 20:26:05 UTC. The successive trails impressed by the 6 known SSOs during the *Euclid* hour-long sequence of VIS-NISP imaging observations are drawn in different colors, one for each filter (VIS, *Y*, *J*, and *H*). We can expect about a hundred times more SSOs at the limiting magnitude of *Euclid* (e.g., Fig. 4). The inset is a magnified view of 2014 WQ501, a main-belt asteroid, illustrating the highly elongated shape of an SSO in *Euclid* frames. The scale bar of 6″ corresponds to 60 pixels in VIS frames and 20 pixels in NISP. The timings reported are the starting time of the VIS exposures. The slitless spectra will be acquired by NISP simultaneously with the VIS images. *Right*: calibration field 13 165 centered on (RA, Dec) = (76.785°, +23.988°) and starting on 2022 March 9 at 20:37:37 UTC. There are 117 known SSOs in the field, and here also, a hundred times more SSOs will be detected at the limiting magnitude of *Euclid*.

NISP spectroscopy in Sect. 6. The *Euclid* capabilities for directly imaging satellites and SSO activity are presented in Sect. 7, and the contribution of *Euclid* to the 3D shape and binarity modeling from light curves is described in Sect. 8.

2. Expected number of SSO observations

Although the *Euclid* Wide survey will avoid the ecliptic plane (Fig. 1), its observing sequence is by chance well adapted to detect moving objects. As described above, each FoV will be imaged 16 times in one hour in four repeated blocks. Given the pixel scale of the VIS and NISP cameras of 0.1″ and 0.3″, any SSO with an apparent motion higher than ≈0.2″/h should therefore be detected by its trailed appearance and/or motion across the different frames (Fig. 3).

To estimate the number of SSOs that might be detected by *Euclid*, we first built the cumulative size distribution (CSD) of each population. We used the absolute magnitude H as a proxy for the diameter D. The relation between these two is $D(\mathrm{km}) = 1329 p_V^{-1/2} 10^{-0.2H}$ (e.g., Bowell et al. 1989), where p_V is the surface albedo in V, which quantifies its capability of reflecting light. Minor planets, especially asteroids, tend to be very dark, and their albedo is generally very low, from a few percents to ≈30% (see, e.g., Mainzer et al. 2011).

We retrieved the absolute magnitude from the `astorb` database (Bowell et al. 1993), with the exception of comets, which are not listed in `astorb`, and for which we used the compiled data by Snodgrass et al. (2011). The challenge was then to extrapolate the observed distributions (shown as solid lines in Fig. 4) to smaller sizes. Most are close to power-law distributions (Dohnanyi 1969) in the form $\mathrm{d}N/\mathrm{d}H \propto 10^{\gamma H}$, with different slopes γ. We model each population below and represent them with dashed lines in Fig. 4:

- NEAs: we used the synthetic population by Granvik et al. (2016), which is very similar to the population used by Harris & D'Abramo (2015). However, we took a conservative approach and increased the uncertainty of the model to encompass both estimates.
- MCs: no dedicated study of the CSD of MCs is available. We therefore took the NEA model above, scaled by a factor of three, to match the currently known MC population. The upper estimate was taken as a power-law fit to the current population with $\gamma = 0.41$, and the lower estimate is that of the scaled NEA model by Granvik et al. (2016), reduced by a factor of two.
- MBAs: we used the knee distribution by Gladman et al. (2009), in which large objects ($H \in [11, 15]$) follow a steep slope ($\gamma \sim 0.5$), while smaller asteroids follow a shallower slope of $\gamma = 0.30 \pm 0.02$ in the range $H \in [15, 18]$, after which no constraint is available. This model is scaled to 25 954 asteroids at $H = 15$. These authors found the CSD to be very smooth in this absolute magnitude range compared to earlier works (Jedicke & Metcalfe 1998; Ivezić et al. 2001; Wiegert et al. 2007). We modified their model only slightly by changing the slope at $H = 15.25$ instead of $H = 15$: the shallower slope does no longer fit the observed data below $H = 15.25$. The observing strategy by Gladman et al. (2009) was indeed aimed at constraining the faint end of the CSD, and the constraints on large bodies was weak (only a small sky area had been targeted).
- Trojans: we used the model of Jewitt et al. (2000), with $\gamma = 0.4 \pm 0.06$. More recently, Grav et al. (2011) found

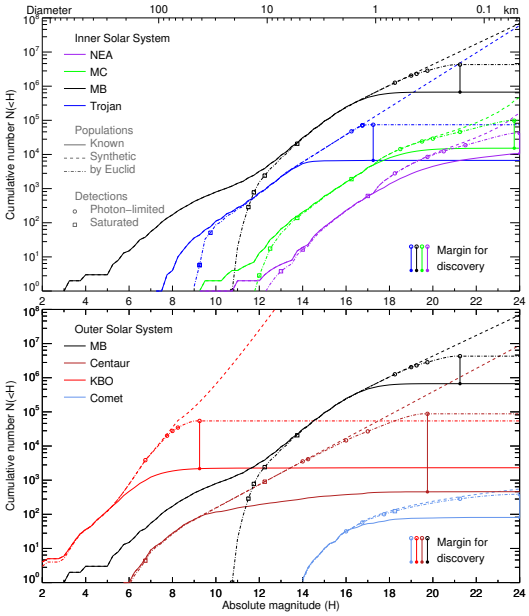

Fig. 4. Cumulative size distribution of each SSO population for current census (solid lines) and synthetic populations (average estimates represented by the dashed lines, upper and lower estimate not plotted for clarity). The number of known objects that is observable at the limiting apparent magnitude of *Euclid* over the entire celestial sphere is represented by the dot-dashed lines. The open squares and circles represent the 0, 25, 50, 75, and 100% marks of the $(H-V)$ cumulative probability function at the saturation and photon-starving ends. The total number of objects expected on the sky is marked by the filled circles. The difference between these filled circles and the current census represents the margin for discovery.

a similar γ, but restricted their study to Trojans with $D >$ 10 km. We scaled their model to the number of 310 known Trojans at $H = 12.5$. The steeper slope (i.e., $\gamma = 0.46$) seems to reproduce the currently observed population more accurately. The baseline numbers for Trojans presented here may therefore be underestimated, and the upper estimate might represent the real Trojan population better. Finally, we did not use the knee model by Yoshida & Nakamura (2005), who predicted a change in slope at $D \approx 5$ km, because their model no longer fits the known population.

– Centaurs: we used the $\gamma = 0.34 \pm 0.04$ from Bauer et al. (2013), which is close to the 0.4 estimate from Jedicke et al. (2002). We scaled the power law to correspond to the cumulative population (7) at $H = 8.25$.
– KBOs: first, we built the CSD of the resonant population using a single power law of index $\gamma = 0.9^{+0.2}_{-0.4}$, scaled to a total of 22 000 objects a $H = 8.66$, as proposed by Volk et al. (2016) based on the early results of the Outer Solar System Origins Survey (OSSOS; Bannister et al. 2016), which is consistent with the earlier work by Gladman et al. (2012) based on the Canada-France Ecliptic Plane Survey (CFEPS). Then, we built the CSD of the scattered-disk objects using the *divot* distribution by Shankman et al. (2016): large objects follow a steep slope ($\gamma \sim 0.9$), scaled to a total of 6500 objects a $H = 8$, which changes at $H = 8.0$ to a shallower $\gamma = 0.50^{+0.15}_{-0.08}$. The differential size distribution presents a drop at $H = 8.0$ where the slope changes, the smaller objects being less numerous by a factor of 5.6 (see Shankman et al. 2016, for details). Finally, we took the CSD of objects in the classical belt from Petit et al. (2016), who proposed a knee distribution: $\gamma = 1.02$, scaled to a total of 1800 objects at $H = 7$, until $H = 7.0$ (in agreement with Adams et al. 2014), where it switches to $\gamma = 0.65 \pm 0.05$. The CSD for the entire KBO population is the sum of the three aforementioned CSD.
– Comets: we used the knee CSD from Snodgrass et al. (2011). Largest comets follow a $\gamma = 0.38^{+0.06}_{-0.04}$ until $H = 17$ (converted from the turnover radius of 1.25 km using an albedo of 0.04), after which the CSD is shallower, although less constrained, and we assumed the average slope found by Snodgrass et al. (2011) with arbitrary uncertainties: $\gamma = 0.04^{+0.06}_{-0.02}$.

The question is then which range of absolute magnitudes will be accessible to *Euclid* for each population, considering it will observe in the range $V_{AB} = 17$–24.5. This conversion from apparent to absolute magnitude only depends on the geometry of observation (Bowell et al. 1989) through the heliocentric distance (Δ), range to the observer (r), and phase angle (α, the angle between the target-Sun and target-observer vectors):

$$H = V + 2.5\log\left(r^2\Delta^2\right) - 2.5\log\left((1-G)\phi_1 + G\phi_2\right), \quad (1)$$

with the phase functions approximated by

$$\phi_1 = \exp\left(-3.33\tan\left(\frac{\alpha}{2}\right)^{0.63}\right), \quad (2)$$

$$\phi_2 = \exp\left(-1.87\tan\left(\frac{\alpha}{2}\right)^{1.22}\right). \quad (3)$$

Although a more accurate model (with two phase slopes G_1 and G_2) of the phase dependence has been developed recently (Muinonen et al. 2010), the differences in the predicted magnitudes between the two systems are minor for our purpose. We therefore use the former and simpler H–G system in the following, assuming the canonic value of $G = 0.15$.

The three geometric parameters (r, Δ, α) are tied together by the solar elongation Ψ, which is imposed by the spacecraft operations ($\Psi = 91.0 \pm 1.5°$). In practice, it is sufficient to estimate the range of heliocentric distances at which *Euclid* will observe an SSO from a given population to derive the two other geometric quantities, and hence the $(H-V)$ index:

$$r = \cos\Psi + \sqrt{\cos^2\Psi - 1 + \Delta^2}. \quad (4)$$

$$\alpha = \left|\mathrm{asin}\left(\frac{\sin\Psi}{\Delta}\right)\right|. \quad (5)$$

We thus computed the probability density function (PDF) of the heliocentric distance of each population. For this, we computed the 2D distribution of the semimajor axis *vs* eccentricity of each population using bins of 0.05 in AU and eccentricity. For each bin, we computed the PDF of the heliocentric distance from Kepler's second law. We then summed individual PDFs from each bin, normalized by the number of SSOs in each bin divided by the entire population.

We then combined the distribution of the solar elongation from the reference survey and the PDF of the heliocentric distance of each population in Eqs. (4) and (5) to obtain a PDF of the (H–V) index (Eq. (1)). The fraction of populations to be observed by *Euclid* at each magnitude is estimated by multiplying

Table 1. Expected number of SSOs observed by *Euclid* for each population.

Population		All-sky	f_W	f_C	*Euclid*		Absolute magnitude limits		
Name	N_{now}	N_S	(%)	(%)	$N_{E,d}$	$N_{E,o}$	H_{100}	H_{50}	H_1
NEA	16062	$1.9^{+1.1}_{-0.6} \times 10^5$	7.2 ± 0.4	0.8 ± 0.1	$1.4^{+1.0}_{-0.5} \times 10^4$	$1.5^{+1.0}_{-0.6} \times 10^4$	22.75	23.75	26.50
MC	15488	$1.2^{+1.6}_{-0.8} \times 10^5$	9.0 ± 0.6	0.6 ± 0.1	$1.0^{+1.7}_{-0.8} \times 10^4$	$1.2^{+1.7}_{-0.8} \times 10^4$	21.00	21.25	22.75
MB	674981	$4.3^{+1.0}_{-0.9} \times 10^6$	1.5 ± 0.0	0.7 ± 0.0	$8.2^{+2.5}_{-2.2} \times 10^4$	$9.7^{+2.5}_{-2.2} \times 10^4$	19.50	20.00	21.25
Trojan	6762	$1.3^{+0.9}_{-0.7} \times 10^5$	5.1 ± 1.5	0.5 ± 0.4	$7.1^{+9.3}_{-4.9} \times 10^3$	$7.5^{+9.5}_{-5.0} \times 10^3$	17.00	17.25	18.25
Centaur	470	$1.8^{+1.4}_{-1.0} \times 10^4$	12.2 ± 0.9	0.6 ± 0.4	$2.2^{+2.1}_{-1.4} \times 10^3$	$2.2^{+2.1}_{-1.4} \times 10^3$	14.75	15.50	18.25
KBO	2331	$9.8^{+2.2}_{-1.9} \times 10^4$	4.9 ± 0.2	0.6 ± 0.1	$5.3^{+1.6}_{-1.3} \times 10^3$	$5.5^{+1.6}_{-1.3} \times 10^3$	8.25	8.75	10.00
Comet	1301	$185.2^{+15.4}_{-13.5}$	19.5 ± 0.5	1.0 ± 0.3	$21.5^{+4.2}_{-3.6}$	$38.2^{+4.9}_{-4.3}$	18.25	19.00	22.00
Total	717395	$4.9^{+1.4}_{-1.2} \times 10^6$	2.1 ± 0.1	0.7 ± 0.0	$1.2^{+0.7}_{-0.4} \times 10^5$	$1.4^{+0.7}_{-0.4} \times 10^5$			

Notes. For the whole celestial sphere, we report the current number of known SSOs (N_{now}, at the time of the writing on 2017 June 28), the expected number of observable objects (N_S) at the limiting apparent magnitude of *Euclid* ($V_{AB} < 24.5$), and the solar elongation ($\Psi = 91.0 \pm 1.5°$). Using the fraction of known SSOs within the area of the *Euclid* Wide survey (f_W) and calibration frames (f_C), we estimate the total number of discoveries ($N_{E,d}$) and observations ($N_{E,o}$) by *Euclid*. The absolute magnitude corresponding to a probability of 100%, 50%, and 1% that SSOs will be within the detection envelop of *Euclid* are also reported.

the CSD of the synthetic populations with the cumulative distribution of the (H−V) index at either end of the magnitude range of *Euclid* (V_{AB} = 17−24.5, see the dot-dashed lines in Fig. 4). The number of observable SSOs on the entire celestial sphere (N_S) can be read from this graph, and they are reported in Table 1. The difference between synthetic and observed population also provides an estimate of the potential number of objects to be discovered by *Euclid* down to V_{AB} = 24.5.

We then estimated how many of these objects will be observed by *Euclid*. For this, we computed the position of all known SSOs every six months for the entire duration of the *Euclid* operations (2020 to 2026) using the Virtual Observatory (VO) web service SkyBot 3D[1] (Berthier et al. 2008). This allows computing the fraction of known SSOs within the area covered by the *Euclid* surveys (f_W, f_D, and f_C for the Wide and Deep Surveys, and calibration frames). We report these fractions in Table 1, except for f_D, which is negligible (on the order of 1−10 ppm) because only very few SSOs on highly inclined orbits are known (although there is a clear bias against discovering such objects in the current census of SSOs, see Petit et al. 2017; Mahlke et al. 2017). These figures are roughly independent of the epoch for all populations but for the Trojans, which are confined around the Lagrangian L4 and L5 points on Jupiter's orbit and therefore cover a limited range in right ascension at each epoch.

Overall, about 150 000 SSOs are expected to be observed by *Euclid* in a size range that is currently unexplored by large surveys. This estimate may be refined once dedicated studies of the detection envelop of moving objects will be performed on simulated data. *Euclid* could discover thousands of outer SSOs and tens of thousands of sub-kilometric main-belt, Mars-crosser, and near-Earth asteroids (see the typical absolute magnitudes probed by *Euclid* in Table 1). Nevertheless, the Large Synoptic Survey Telescope (LSST, LSST Science Collaboration et al. 2009) is expected to see scientific first-light in 2021. The LSST will repeatedly image the sky down to $V \approx 24$ over a wide range of solar elongations, and will be a major discoverer of faint SSOs. Assuming a discovery rate of 10 000 NEAs, 10 000 MCs, 550 000 MBAs, 30 000 Trojans, 3000 Centaurs, 4000 KBOs, and 1000 comets per year (LSST Science Collaboration et al. 2009), most of the SSOs that are potentially available for discovery are expected to be discovered by the LSST in the southern hemisphere. The exploration of small KBOs in the northern hemisphere will be reserved for *Euclid*, however.

[1] http://vo.imcce.fr/webservices/skybot3d/

3. Specificity of the SSO observations with *Euclid*

The real challenge of SSO observations with *Euclid* will be the astrometry and photometry of highly elongated sources (as indicated in Fig. 3). We present in Fig. 5 and Table 2 a summary of the apparent non-sidereal rate of the different SSO populations. With the exception of the most distant populations of KBOs, Centaurs, and comets, all SSOs will present rates above 10″/h. This implies a motion of hundreds of pixels between the first and last VIS frame. During a single exposure, each SSO will move and produce a trailed signature, a streak, whose length will typically range from 1 to 50 pixels for VIS. The situation will be more favorable for NISP because of the shorter integration times and larger pixel scale, and most SSOs will not trail, or will only trail across a few pixels (Table 2).

Some recent developments have been made to detect streaks, motivated by the optical detection and tracking of artificial satellites and debris on low orbits around the Earth. Dedicated image processing for trails can be set up to measure the astrometry and photometry of moving objects within a field of fixed stars, without an a priori knowledge of their apparent motion (e.g., Virtanen et al. 2016). The success rate in detecting these trails has been shown to reach up to 90%, even in the regime with low signal-to-noise ratio (≈1). These algorithms are currently being tested on simulated *Euclid* data of SSOs (M. Granvik, priv. comm.).

4. Source identification, astrometry, and dynamics

As established in Sect. 2, *Euclid* will observe about 150 000 SSOs, even if its nominal survey avoids ecliptic latitudes below 15°, with the notable exception of the calibration fields (Fig. 1).

The design of the surveys, with hour-long sequences of observation of each field, will preclude orbit determination for newly discovered objects, however. This hour-long coverage is nevertheless sufficient to distinguish between NEAs, MBAs, and

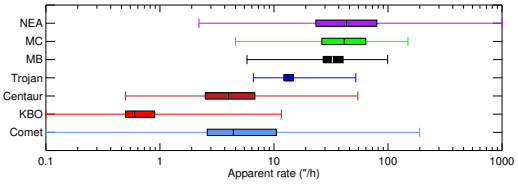

Fig. 5. Five-number summary (minimum, maximum, median, 25%, and 75% quartiles) of the apparent rate of each SSO population. The *Euclid* mode of observation at quadrature reduces the apparent rate compared to opposition, for example.

Table 2. Apparent motion and trailing of SSOs observed by *Euclid*.

Population	Rate ($''$/h)	VIS (pix)	NISP (pix)	Y (pix)	J (pix)	H (pix)
NEA	$43.3^{+36.5}_{-19.9}$	67.9	22.6	4.8	4.6	3.2
MC	$41.3^{+22.6}_{-14.9}$	64.8	21.6	4.6	4.4	3.1
MB	$32.5^{+7.9}_{-5.5}$	51.0	17.0	3.6	3.5	2.4
Trojan	$13.3^{+1.4}_{-1.1}$	20.9	7.0	1.5	1.4	1.0
Centaur	$4.0^{+2.9}_{-1.5}$	6.2	2.1	0.4	0.4	0.3
KBO	$0.6^{+0.3}_{-0.1}$	1.0	0.3	0.1	0.1	0.0
Comet	$4.4^{+6.2}_{-1.8}$	6.9	2.3	0.5	0.5	0.3

Notes. For each main population of SSOs, we report the apparent rate and its 25% and 75% quartile variations (i.e., half the population is within these two values), and the length of the trails on the detector during the simultaneous VIS imaging and NISP spectroscopic 565 s exposure, and the following NISP Y, J, and H imaging exposures of 121, 116, and 81 s.

KBOs (Spoto et al. 2017). The situation will be very similar to that of the SDSS Moving Object Catalog (MOC), in which many SSO sightings corresponded to unknown objects at the time of the release (still about 53% at the time of the fourth release, Ivezić et al. 2001, 2002). Attempts at identification will have to be regularly performed a posteriori when the number of known objects, hence orbits, will increase, in the same way as we did for the SDSS MOC, where we identified 27% of the unknown sources (Carry et al. 2016) using the SkyBoT Virtual Observatory tool (Berthier et al. 2006, 2016). The success rate for an a posteriori identification of SSOs detected by *Euclid* is expected to be even higher than in this last study, as the LSST will be sensitive to the same apparent magnitude range.

Compared with tens of points over many years provided by the LSST, the astrometry by *Euclid* will probably contribute little to the determination of SSO orbits, with the following exceptions. First, the objects in the outer solar system (Centaurs and KBOs) in the northern hemisphere will not be observed by the LSST. In this respect, the Deep Survey will allow us to study the population of highly inclined Centaurs and KBOs (e.g., Petit et al. 2017) through repeated observations of the northern Ecliptic cap (about 40 times). Second, the parallax between the Earth and the Sun-Earth L2 point is large, from about a degree for asteroids in the inner belt to a few tens of arcseconds for KBOs. Simultaneous observation of the same field from the two locations thus provides the distance of the SSO, which drastically reduces the possible orbital parameter space (Eggl 2011). Thus, an interesting synergy between the LSST and *Euclid* will lie in planning these simultaneous observations (see Rhodes et al. 2017). The practical implementation may be difficult, however, as the observations by *Euclid* at a solar elongation Ψ of $91.0 \pm 1.5°$ impose observations close to sunset or sunrise from the LSST.

5. Photometry and spectral classification

In this section we study the effect of *Euclid* on the spectral classification of SSOs through determining their spectral energy distribution (SED; see Appendix B) over a wide wavelength range, from the visible with VIS ($0.5\,\mu$m) to the near-infrared with NISP ($2\,\mu$m). While colors in the visible have been and will be obtained for several 10^6 SSOs through surveys such as ESA *Gaia* and the LSST (Gaia Collaboration 2016; LSST Science Collaboration et al. 2009), a collection of near-infrared photometry is lacking. The only facility currently operating from which near-infrared colors for numerous SSOs have been obtained is the ESO VISTA telescope (Popescu et al. 2016). As described above, the upcoming ESA *Euclid* mission (and also the NASA WFIRST mission, which shares many specifications with *Euclid*, see Green et al. 2012; Holler et al. 2017) may radically change this situation.

At first order, SSOs display a G2V spectrum at optical wavelength because the light of the Sun is reflected by their surface. Depending on their surface composition, regolith packing, and degree of space weathering, their spectra are modulated by absorption bands and slope effects, however. Historically, SSOs spectra have always been studied in reflectance, that is, their recorded spectrum divided by the spectrum of the Sun, approximated by a G2V star observed with the same instrument setting as the scientific target. The colors and low resolution ($R \approx 300-500$) of asteroids have been used for decades to classify them in a scheme called taxonomy, which only uses the visible range or only the near-infrared, or both (see Chapman et al. 1975; Barucci et al. 1987; Bus & Binzel 2002b,a; DeMeo et al. 2009). For KBOs, broadband colors and medium resolution ($R \approx 3000-5000$) have been used to characterize their surface composition (e.g., Snodgrass et al. 2010; Carry et al. 2011, 2012), although current taxonomy is based on broadband colors alone (Fulchignoni et al. 2008).

Information on the taxonomic class has been derived for about 4000 asteroids based on their low-resolution spectra (mainly from the SMASS, SMASSII, and S^3OS^2 surveys, see Bus & Binzel 2002b,a; Lazzaro et al. 2004). Using the broadband photometry from the Sloan Digital Sky Survey (SDSS), many studies have classified tens of thousands of asteroids (e.g., Ivezić et al. 2001, 2002; Nesvorný et al. 2005; Carvano et al. 2010; DeMeo & Carry 2013). These studies opened a new era in the study of asteroid families (Carruba et al. 2013), space weathering (Nesvorný et al. 2005; Thomas et al. 2012), in the distribution of material in the inner solar system (DeMeo & Carry 2014; DeMeo et al. 2014), and in the origins of near-Earth asteroids (Carry et al. 2016). The ongoing survey ESA *Gaia* will provide low-resolution spectra ($R \approx 35$) for 300 000 asteroids with high photometric accuracy, and the taxonomic class will be determined for each SSO (Delbo et al. 2012).

Nevertheless, any classification based on SDSS, *Gaia*, or the LSST (which will use a filter set comparable to that of SDSS), suffers from a wavelength range limited to only the visible. It is known, however, that several classes are degenerate over this spectral range, and only near-infrared colors/spectra can distinguish them (Fig. 6 and DeMeo et al. 2009). The near-infrared photometry provided by *Euclid* will therefore be highly valuable, similar to that reported from the 2MASS (Sykes et al. 2000) or ESO VISTA VHS (McMahon et al. 2013; Popescu et al. 2016) surveys.

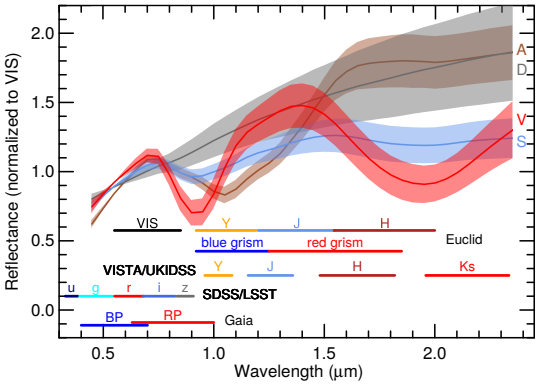

Fig. 6. Examples of asteroid classes (A, D, S, and V) that are degenerate over the visible wavelength range. For reference, the wavelength coverage of each photometric filter and grism on board *Euclid* is shown, together with the filter sets of SDSS and LSST (*u*, *g*, *r*, *i*, *z*; Ivezić et al. 2001), VISTA and UKIDSS (*Y*, *J*, *H*, *Ks*; Hewett et al. 2006), and the *Gaia* blue and red photometers (BP, RP) that will produce low-resolution spectra (resolving power of a few tens; Delbo et al. 2012).

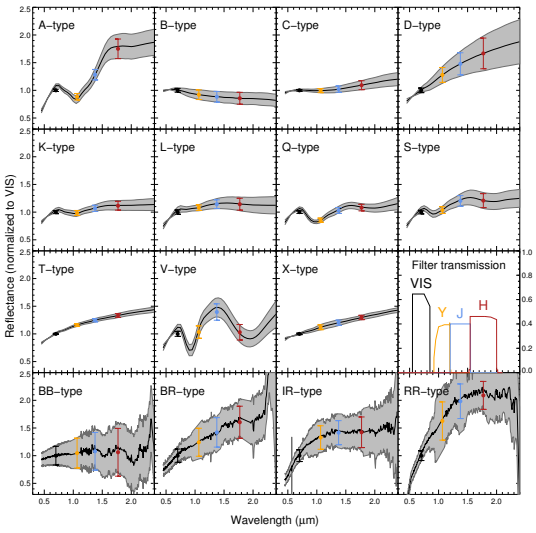

Fig. 7. Eleven asteroid (A- to X-type) and four KBO (BB, BR, IR, RR) spectral classes considered here, converted into photometry for the classification simulation (see text). The transmission curves of the VIS and NISP filters are also plotted for reference.

To estimate the potential of the *Euclid* photometry for a spectral classification of asteroids, we simulated data using the visible and near-infrared spectra of the 371 asteroids that were used to create the Bus-DeMeo taxonomy (DeMeo et al. 2009), and of 43 KBOs with known taxonomy (Merlin et al. 2017). We converted their reflectance spectra into photometry (Fig. 7), taking the reference VIS and NISP filter transmission curves[2].

[2] Available at the Geneva university *Euclid* pages.

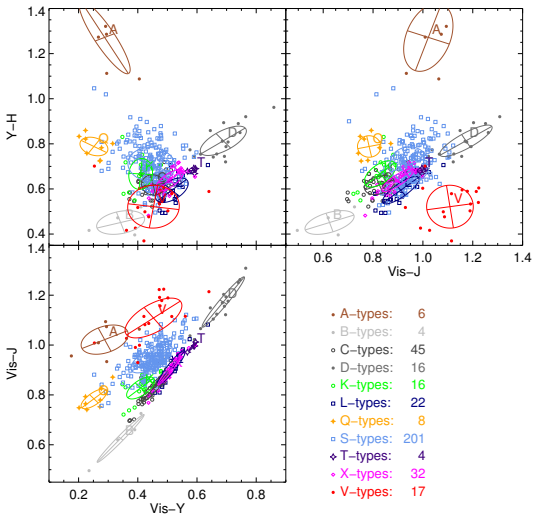

Fig. 8. Classification results for the 371 asteroids from Bus-DeMeo taxonomy, presented in three filter combinations: VIS-Y, VIS-J, and Y-H. Several extreme classes, such as A, B, D, V, and T, can be easily discarded thanks to the large wavelength coverage of *Euclid*.

One key aspect of the *Euclid* operations in determining the SSO colors is the repetition of the four-filter sequence during an hour. Thus, each filter will be bracketed by other filters in time. This will allow determining magnitude difference between each pair of filters without the biases that are otherwise introduced by the intrinsic variation of the target (Appendix B). For a detailed discussion of this effect, see Popescu et al. (2016).

For each class and filter combination, we computed the average color, dispersion, and covariance. This allowed us to classify objects based on their distance to all the class centers, normalized by the typical spread of the class (Pajuelo 2017). This learning sample is of course limited in number, and all classes are not evenly represented. It nevertheless allowed us to estimate the *Euclid* capabilities by applying the classification scheme to the same sample. This is presented in Fig. 8. The leverage provided by the long wavelength coverage allowed us to clearly identify several classes: A, B, D, V, Q, and T (DeMeo et al. 2009). The main classes in the asteroid belt, the C, S, and X (DeMeo & Carry 2014), are more clumped, and our capabilities to classify them will depend on the exact throughput of the optical path of *Euclid*.

For KBOs, their spectral behavior from the blue-ish BB to the extremely red RR will place them in these graphs along a line that extends from the C, T, and D types (whose colors are close to those of the BB, BR, and IR classes). The RR types will be even farther from the central clump than the D types. Identifying the different KBO spectral classes should therefore be straightforward with the filter set of *Euclid*.

In all cases, a spectral characterization using *Euclid* colors will benefit from the colors and spectra in the visible observed by *Gaia* and the LSST (Delbo et al. 2012; LSST Science Collaboration et al. 2009), the visible albedo (from IRAS, AKARI, WISE, and Herschel observations; e.g., Tedesco et al. 2002; Müller et al. 2009; Masiero et al. 2011; Usui et al. 2011), and solar phase function parameters (see

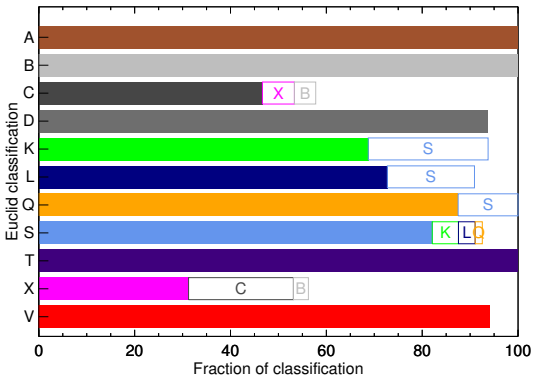

Fig. 9. Percentage of correct (solid bar) and compatible (open bar) classification for each Bus-DeMeo taxonomic classes. The *Euclid* photometry alone allows to classify asteroids into 11 classes.

Oszkiewicz et al. 2012, for an example of using the phase function for taxonomy). The success rate of a classification based on *Euclid* photometry therefore only represents a lower estimate.

We present in Fig. 9 the success rate of a classification of the 371 asteroids from the Bus-DeMeo taxonomy. The classes are generally recovered with a success rate above 60%, and when misclassified, asteroids are sorted into spectrally similar (compatible) classes with a success rate closer to 90%, except for the C and X classes. We did not repeat the exercise for KBOs because the available sample is limited. Because their spectral classes are very similar to those of the C, T, and D-type asteroids, and because they are even redder, we expect that it will be straightforward to identify them with the filter set of *Euclid*.

In summary, the VIS and NISP photometry that will be measured by *Euclid* seems very promising to classify SSOs into their historical spectral classes.

6. Near-infrared spectroscopy with NISP

Euclid will also acquire near-infrared low-resolution (resolving power of 380) spectra for many SSOs, down to $m_{\rm AB} \approx 21$, which is similar to the limiting magnitude of *Gaia*. Simultaneously to the four VIS exposures, NISP will acquire four slitless spectra of the same FOV. In the Wide Survey, only the *red* grism (1.25 to 1.85 μm) will be used, the usage of the *blue* grism (0.92 to 1.25 μm) being limited to the Deep Survey. The *red* grism will cover typical absorption bands of volatile compounds (e.g., water or methane ices) such as are found on distant KBOs. The main diagnostic features of asteroids (NEAs, MBAs) are located within the blue arm at 1 μm and at 2 μm, however, which is outside the spectral range of the *red* grism.

Because there is no slit, many sources will be blended. To decontaminate each slitless spectrum from surrounding sources, the exposures will be taken with three different grism orientations, 90° apart. For exposures whose spectral dispersion is aligned with the ecliptic, that is, which are parallel to the typical SSO motion, each SSO will blend with itself. For the remaining orientations, SSOs will often blend with background sources, which degrades both spectra. This may be a problem for the wide survey in its lowermost ecliptic latitude range, where many sources will be blended with G2V spectra from SSOs.

The apparent motion of outer SSOs being limited (Table 2), their spectra may be extracted by the *Euclid* consortium tools, which are designed to work on elongated sources (typically 1″). Near-infrared spectra for thousands of Centaurs and KBOs could thus be produced by *Euclid*. It may be challenging to extract the spectra for objects in the inner solar system, and an in-depth assessment of the feasibility of such measurements is beyond the scope of this paper. In both cases, these spectra will be very similar to the low-resolution spectra that were used to define the current asteroid taxonomy (DeMeo et al. 2009) and diagnostic of the KBO class as defined by (Fulchignoni et al. 2008).

7. Multiplicity and activity of SSOs

With a very stable PSF and a pixel scale of 0.1″ and 0.3″ for VIS and NISP, which is close to the diffraction limit of *Euclid*, the source morphology can be studied. This is indeed one of the main goals of the cosmological survey (Laureijs et al. 2011). We first assess how *Euclid* might detect satellites around SSOs, and then consider their activity, that is, their dust trails.

7.1. Direct imaging of multiple systems with Euclid

In the two decades since the discovery of the first asteroid satellite, Dactyl around (243) Ida, by the Galileo mission (Chapman et al. 1995), direct imaging has been the main source of discovery and characterization of satellites around large SSOs in the main belt (e.g., Merline et al. 1999; Berthier et al. 2014), among Jupiter Trojans (Marchis et al. 2006, 2014), and KBOs (e.g., Brown et al. 2005, 2006, 2010; Carry et al. 2011; Fraser et al. 2017). This is particularly evident for KBOs, for which 65 of the 80 known binary systems where discovered by the *Hubble* Space Telescope, and the other 14 by large ground-based telescopes, often supported by adaptive optics (see, e.g., Parker et al. 2011; Johnston 2015; Margot et al. 2015). The situation is different for NEAs and small MBAs, for which most discoveries and follow-up observations were made with optical light curves and radar echoes (e.g., Pravec & Harris 2007; Pravec et al. 2012; Fang et al. 2011; Brozović et al. 2011).

To estimate the capabilities of *Euclid* to angularly resolve a multiple system, we used the compilation of system parameters by Johnston (2015). We computed the magnitude difference between components Δm from their diameter ratio, and their typical separation Θ from the ratio of the binary system semimajor axis to its heliocentric semimajor axis (Table 3).

The angular resolution of *Euclid* will thus allow us to detect satellites of KBOs and large MBAs, but not those around NEAs, MCs, and small MBAs. The case of KBOs is straightforward, owing to the very little smearing of their PSF from their apparent motion (Table 2). Based on the expected number of observations of KBOs (Table 1) and their binarity fraction, *Euclid* is expected to observe 300 ± 200 multiple KBO systems, which is a four-fold increase.

The case of MBAs is more complex. First, there are only 25 large MBAs with an inclination higher than 15°, which will make them potentially observable by *Euclid*. Second, the fraction and properties of multiple systems for MBAs with a diameter of between 10 and 100 km is terra incognita. The reason are observational biases: detection by light curves is more efficient on close-by components, and direct imaging, especially from ground-based telescopes using adaptive optics, focused on bright, hence large, primaries. If most binaries around small asteroids (D < 10 km) are likely formed by rotational fission

Table 3. Typical magnitude difference (Δm) and angular separation (Θ) between components of multiple SSO systems.

Population	Δm (mag)	Θ ($''$)	f (%)
NEA and MC	$1.8^{+2.0}_{-1.8}$	$0.01^{+0.01}_{-0.01}$	15 ± 5
MBA ($D < 10$ km)	$2.5^{+0.9}_{-0.9}$	$0.01^{+0.01}_{-0.01}$	15 ± 5
MBA ($D > 100$ km)	$5.4^{+2.7}_{-2.7}$	$0.30^{+0.25}_{-0.25}$	3 ± 2
KBO	$1.5^{+2.0}_{-1.5}$	$0.43^{+0.60}_{-0.43}$	6 ± 4

Notes. NEA and MCs share similar characteristics, and so do large MBAs and Trojans. We split MBAs into two categories according to the diameter D of the main component. Estimates on the binary frequency in each populations are based on the reviews by Noll et al. (2008) and Margot et al. (2015). We only consider high-inclination KBOs here because the binary fraction in the cold belt is closer to 30% (Fraser et al. 2017).

caused by YORP spin-up (Walsh et al. 2008; Pravec et al. 2010; Walsh & Jacobson 2015), satellites of larger bodies are the result of reaccumulation of ejecta material after impacts (Michel et al. 2001; Durda et al. 2004). Some satellites around medium-sized MBAs are therefore to be expected, but with unknown frequency. Considering a ratio of ≈5 between the semimajor axis of binary system and the diameter of the main component (typical of large MBAs; see Margot et al. 2015) and the size distribution of high-inclination MBAs, only a handful of potential systems would have separations that are angularly resolvable by *Euclid*. Finally, the apparent motion of MBAs implies highly elongated PSFs, which diminishes the fraction of detectable systems even further.

For these reasons, *Euclid* will contribute little if anything at all to the characterization of multiple systems among asteroids. The prospects for discovering KBO binaries are very promising, however.

7.2. Detection of activity

The distinction between comets and other types of small bodies in our solar system is by convention based on the detection of activity, that is, of unbound atmosphere that is also called coma. Comets cannot be distinguished based only on their orbital elements (Fig. A.1). The picture was blurred further with the discovery of comae around Centaurs and even MBAs, which are called active asteroids (see Jewitt 2009; Jewitt et al. 2015, for reviews).

The cometary-like behavior of these objects was discovered either by sudden surges in magnitude or by diffuse non-point-like emission around them. There are currently 18 known active asteroids and 12 known active Centaurs, corresponding to 25 ppm and 13% of their host populations, respectively. The property of the observed comae is typically 1 to 5 mag fainter than the nucleus within a 3″ radius (although this large aperture was chosen to avoid contamination from the nucleus PSF, which extended to about 2″ due to atmospheric seeing, Jewitt 2009).

With much higher angular resolution and its very stable PSF as required for its primary science goal (Laureijs et al. 2011), *Euclid* has the capability of detecting activity like this. Based on the expected number of observations (Table 1) and on the aforementioned fraction of observed activity, *Euclid* may observe several active asteroids and about 300^{+300}_{-200} active Centaurs. As in the case of multiple systems, however, the detection capability will be diminished by the trailed appearance of SSOs. This will be dramatic for MBAs, but limited for Centaurs (Table 2): the typical motion will be of six pixels, that is, 0.6″, while typical comae extend over several arcseconds.

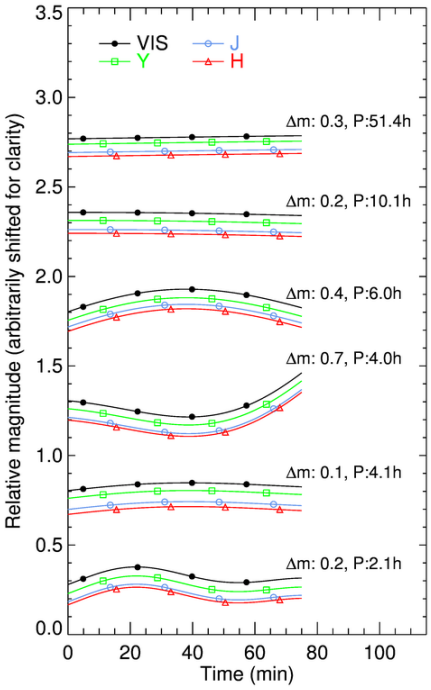

Fig. 10. Examples of simulated SSO multi-filter light curves as observed by *Euclid* VIS and NISP. For each light curve, the amplitude (Δm) and rotation period (P) is reported. For each, the four light curves corresponding to the different filters are printed (with a magnitude difference reduced by a factor 10 for clarity), together with the photometry at the cadence of *Euclid*.

8. Time-resolved photometry

The observations of each field in four repeated sequences of VIS and NISP photometry will provide hour-long light curves sampled by 4×4 measurements, or a single light curve made of 16 measurements by converting all magnitudes based on the knowledge of the SED (Fig. 10, Appendix B).

For decades, optical light curves have been the prime data set for 3D shape modeling and the study of SSO multiplicity from mutual eclipses (see the reviews by Margot et al. 2015; Ďurech et al. 2015). Taken alone, a single light curve, such as those that *Euclid* will provide, does not provide many constraints. Shape and dynamical modeling both require multiple Sun-target-observer geometries, which can only be achieved by accumulating data over many years and oppositions.

8.1. Period, spin, and 3D shape modeling

Traditionally, the period, spin orientation, and 3D shape of asteroids were determined using many light curves that were

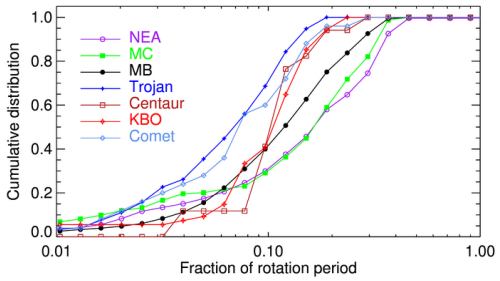

Fig. 11. Cumulative distribution of the rotation fraction covered by one hour of observations, computed on the 5759 entries with a quality code 2 or 3 from the Planetary Data System archive (Harris et al. 2017), and the 25 comets from Samarasinha et al. (2004) and Lowry et al. (2012).

taken over several apparitions (e.g., Kaasalainen & Torppa 2001; Kaasalainen et al. 2001). It has been show later on that photometry measurements, sparse in time[3], convey the same information and can be use alone or in combination with dense light curves (Kaasalainen 2004). Large surveys such as *Gaia* and the LSST will deliver sparse photometry for several 10^{5-6} SSOs (Mignard et al. 2007; LSST Science Collaboration et al. 2009).

In assessing the effect of PanSTARRS and *Gaia* data on shape modeling, Ďurech et al. (2005) and Hanuš & Ďurech (2012) showed, however, that searching for the rotation period with sparse photometry alone may result in many ambiguous solutions. The addition of a single dense light curve often removes many aliases and harmonics in a periodogram and removes the ambiguous solutions; the effect of the single light curve depends on the fraction of the period it covers (J. Durech, pers. comm.).

The rotation periods of SSOs range from a few minutes to several hundred hours. The bulk of the distribution, however, is confined to between 2.5 h (which is called the spin barrier, see e.g., Scheeres et al. 2015) and 10–15 h. This implies that *Euclid* light curves will typically cover between 5–10 and 40% of the SSO rotation periods (Fig. 11). *Euclid* light curves will cover more than a quarter of the rotation (the maximum change in geometry over a rotation, used here as a baseline) for 35% of NEAs, 28% of MCs, and 16% of MBAs, and only a handful of outer SSOs. The hour-long light curves provided by *Euclid* will thus be valuable for 3D shape modeling of thousands of asteroids ($5.25^{+3.50}_{-2.10} \times 10^3$ NEAs, $3.36^{+4.76}_{-2.24} \times 10^3$ MCS, and $1.55^{+0.40}_{-0.35} \times 10^4$ MBAs).

8.2. Mutual events and multiplicity

Binary asteroids represent about 15 ± 5% of the population of NEAs that are larger than 300 m (Sect. 7; Pravec et al. 2006), and a similar fraction is expected among MCs and MBAs with a diameter smaller than 10 km (Table 3; Margot et al. 2015). Most of these multiple systems were discovered by light-curve observations that recorded mutual eclipsing and occulting events (140 of the 205 binary asteroid systems known to date, the remaining are mostly binary NEAs discovered by radar echoes; see Johnston 2015).

These systems have orbital periods of 24 ± 10 h and a diameter ratio of 0.33 ± 0.17, which implies a magnitude drop of $0.11^{+0.13}_{-0.08}$ during mutual eclipses and occultations (computed from the compilation of binary system properties by Johnston 2015). The hour-long light curves provided by *Euclid* will thus typically cover 4^{+3}_{-1}% of the orbital period. When we consider that the systems are in mutual events for about 20% of the orbital period at the high phase angle probed by *Euclid* (e.g., Pravec et al. 2006; Carry et al. 2015), there is a corresponding probability of ≈(5 ± 2)% to witness mutual events. Hence, *Euclid* could record mutual events for 900^{+700}_{-450} NEAs, MCs, and MBAs, which will help to characterize these systems in combination with other photometric data sets, such as those provided by *Gaia* and the LSST.

9. Conclusion

We have explored how the ESA mission *Euclid* might contribute to solar system science. The operation mode of *Euclid* is by chance well designed for the detection and identification of moving objects. The deep limiting magnitude ($V_{AB} \sim 24.5$) of *Euclid* and large survey coverage (even though low ecliptic latitudes are avoided) promise about 150 000 observations of SSOs in all dynamical classes, from near-Earth asteroids to distant Kuiper-belt objects, including comets.

The spectral coverage of *Euclid* photometry, from the visible to the near-infrared, complements the spectroscopy and photometry obtained in the visible alone by *Gaia* and the LSST; this will allow a spectral classification. The hour-long sequence of observations can be used to constrain the rotation period, spin orientation, 3D shape, and multiplicity of SSOs when combined with the sparse photometry of *Gaia* and the LSST. The high angular resolution of *Euclid* is expected to allow the detection of several hundreds of satellites around KBOs and activity for the same number of Centaurs.

The exact number of observations of SSOs, the determination of the astrometric, photometric, and spectroscopic precision as a function of apparent magnitude and rate, and the details of data treatments will have to be refined when the instruments are fully characterized. The exploratory work presented here aims at motivating further studies on each aspect of SSO observations by *Euclid*.

In summary, against all odds, a survey explicitly avoiding the ecliptic promises great scientific prospects for solar system research, which could be delivered as Legacy Science for Euclid. A dedicated SSO processing is currently being developed within the framework of the *Euclid* data analysis pipeline. The main goal of the mission will benefit from this addition through the identification of blended sources (e.g., stars and galaxies) with SSOs.

Furthermore, any extension of the survey to lower latitude would dramatically increase the figures reported here: there are twice as many SSOs for every 3° closer to the ecliptic. Any observation at low ecliptic latitude, such as calibration fields, during idle time of the main survey or after its completion, or dedicated to a solar system survey would provide thousands of SSOs each time, allowing us to study the already-known dark matter of our solar system: the low-albedo minor planets.

Acknowledgements. The present study made a heavy use of the Virtual Observatory tools SkyBoT[4] (Berthier et al. 2006, 2016), SkyBoT 3D[5] (Berthier et al. 2008), TOPCAT[6], and STILTS[7] (Taylor 2005). Thanks to the developers for their development and reaction to my requests, in particular,

[3] Light curves whose sampling is typically longer than the period are called sparse photometry, as opposed to dense light curves, whose period is sampled by many measurements (see, e.g., Hanuš et al. 2016).

[4] SkyBoT: http://vo.imcce.fr/webservices/skybot/
[5] SkyBoT 3D: http://vo.imcce.fr/webservices/skybot3d/
[6] TOPCAT: http://www.star.bris.ac.uk/~mbt/topcat/
[7] STILTS: http://www.star.bris.ac.uk/~mbt/stilts/

J. Berthier. The present article benefits from many discussions and comments I received, and I would like to thank L. Maquet and C. Snodgrass for our discussions regarding comet properties, the ESA *Euclid* group at ESAC B. Altieri, P. Gomez, H. Bouy, and R. Vavrek for our discussions on *Euclid* and SSO, in particular P. Gomez for sharing the Reference Survey with me. Of course, I would not have had these motivating experiences without the support of the ESAC faculty (ESAC-410/2016). Thanks to F. Merlin for creating and sharing the KBO average spectra for this study. Thanks also to R. Laureijs and T. Müller for their constructive comments on an early version of this article, and to S. Paltani and R. Pello for providing the transmission curves of the VIS and NISP filters.

References

Abazajian, K., Adelman-McCarthy, J. K., Agüeros, M. A., et al. 2003, AJ, 126, 2081
Adams, E. R., Gulbis, A. A. S., Elliot, J. L., et al. 2014, AJ, 148, 55
Bannister, M. T., Kavelaars, J. J., Petit, J.-M., et al. 2016, AJ, 152, 70
Barucci, M. A., Capria, M. T., Coradini, A., & Fulchignoni, M. 1987, Icarus, 72, 304
Bauer, J. M., Grav, T., Blauvelt, E., et al. 2013, ApJ, 773, 22
Berthier, J., Vachier, F., Thuillot, W., et al. 2006, in Astronomical Data Analysis Software and Systems XV, eds. C. Gabriel, C. Arviset, D. Ponz, & S. Enrique, ASP Conf. Ser., 351, 367
Berthier, J., Hestroffer, D., Carry, B., et al. 2008, LPI Contributions, 1405, 8374
Berthier, J., Vachier, F., Marchis, F., Ďurech, J., & Carry, B. 2014, Icarus, 239, 118
Berthier, J., Carry, B., Vachier, F., Eggl, S., & Santerne, A. 2016, MNRAS, 458, 3394
Bowell, E., Hapke, B., Domingue, D., et al. 1989, Asteroids II, 524
Bowell, E., Muinonen, K. O., & Wasserman, L. H. 1993, in Asteroids, Comets, Meteors 1993, LPI Contributions, 810, 44
Brown, M. E., Bouchez, A. H., Rabinowitz, D. L., et al. 2005, ApJ, 632, L45
Brown, M. E., van Dam, M. A., Bouchez, A. H., et al. 2006, ApJ, 639, 43
Brown, M. E., Ragozzine, D., Stansberry, J., & Fraser, W. C. 2010, AJ, 139, 2700
Brozović, M., Benner, L. A. M., Taylor, P. A., et al. 2011, Icarus, 216, 241
Bus, S. J., & Binzel, R. P. 2002a, Icarus, 158, 146
Bus, S. J., & Binzel, R. P. 2002b, Icarus, 158, 106
Carruba, V., Domingos, R. C., Nesvorný, D., et al. 2013, MNRAS, 433, 2075
Carry, B., Hestroffer, D., DeMeo, F. E., et al. 2011, A&A, 534, A115
Carry, B., Snodgrass, C., Lacerda, P., Hainaut, O., & Dumas, C. 2012, A&A, 544, A137
Carry, B., Matter, A., Scheirich, P., et al. 2015, Icarus, 248, 516
Carry, B., Solano, E., Eggl, S., & DeMeo, F. E. 2016, Icarus, 268, 340
Carvano, J. M., Hasselmann, H., Lazzaro, D., & Mothé-Diniz, T. 2010, A&A, 510, A43
Chang, C.-K., Ip, W.-H., Lin, H.-W., et al. 2014, ApJ, 788, 17
Chapman, C. R., Morrison, D., & Zellner, B. H. 1975, Icarus, 25, 104
Chapman, C. R., Veverka, J., Thomas, P. C., et al. 1995, Nature, 374, 783
Cropper, M., Pottinger, S., Niemi, S.-M., et al. 2014, in Space Telescopes and Instrumentation 2014: Optical, Infrared, and Millimeter Wave, SPIE, 9143, 91430J
Delbo, M., Gayon-Markt, J., Busso, G., et al. 2012, Planet. Space Sci., 73, 86
DeMeo, F., & Carry, B. 2013, Icarus, 226, 723
DeMeo, F. E., & Carry, B. 2014, Nature, 505, 629
DeMeo, F. E., Binzel, R. P., Slivan, S. M., & Bus, S. J. 2009, Icarus, 202, 160
DeMeo, F. E., Binzel, R. P., Carry, B., Polishook, D., & Moskovitz, N. A. 2014, Icarus, 229, 392
Dohnanyi, J. S. 1969, J. Geophys. Res., 74, 2531
Durda, D. D., Bottke, W. F., Enke, B. L., et al. 2004, Icarus, 170, 243
Ďurech, J., Grav, T., Jedicke, R., Denneau, L., & Kaasalainen, M. 2005, Earth Moon Planets, 97, 179
Ďurech, J., Carry, B., Delbo, M., Kaasalainen, M., & Viikinkoski, M. 2015, Asteroid Models from Multiple Data Sources (Univ. Arizona Press), 183
Eggl, S. 2011, Celes. Mech. Dyn. Astron., 109, 211
Epchtein, N., de Batz, B., Copet, E., et al. 1994, Astrophys. Space Sci., 217, 3
Fang, J., Margot, J.-L., Brozovic, M., et al. 2011, AJ, 141, 154
Fraser, W. C., Bannister, M. T., Pike, R. E., et al. 2017, Nature Astron., 1, 0088
Fulchignoni, M., Belskaya, I., Barucci, M. A., De Sanctis, M. C., & Doressoundiram, A. 2008, The Solar System Beyond Neptune, 181
Gaia Collaboration (Prusti, T., et al.) 2016, A&A, 595, A1
Gladman, B., Marsden, B. G., & Vanlaerhoven, C. 2008, Nomenclature in the Outer Solar System (Univ. Arizona Press), 43
Gladman, B. J., Davis, D. R., Neese, C., et al. 2009, Icarus, 202, 104
Gladman, B., Lawler, S. M., Petit, J.-M., et al. 2012, AJ, 144, 23
Granvik, M., Morbidelli, A., Jedicke, R., et al. 2016, Nature, 530, 303
Grav, T., Mainzer, A. K., Bauer, J., et al. 2011, AJ, 742, 40
Green, J., Schechter, P., Baltay, C., et al. 2012, Wide-Field InfraRed Survey Telescope (WFIRST) Final Report, Tech. Rep.
Hanuš, J., & Ďurech, J. 2012, Planet. Space Sci., 73, 75
Hanuš, J., Ďurech, J., Oszkiewicz, D. A., et al. 2016, A&A, 586, A108
Harris, A. W., & D'Abramo, G. 2015, Icarus, 257, 302
Harris, A. W., Warner, B. D., & Pravec, P. 2017, NASA Planetary Data System
Hewett, P. C., Warren, S. J., Leggett, S. K., & Hodgkin, S. T. 2006, MNRAS, 367, 454
Holler, B. J., Milam, S. N., Bauer, J. M., et al. 2017, ArXiv e-prints [arXiv:1709.02763]
Ivezić, Ž., Tabachnik, S., Rafikov, R., et al. 2001, AJ, 122, 2749
Ivezić, Ž., Lupton, R. H., Jurić, M., et al. 2002, AJ, 124, 2943
Jedicke, R., & Metcalfe, T. S. 1998, Icarus, 131, 245
Jedicke, R., Larsen, J., & Spahr, T. 2002, Asteroids III, 71
Jewitt, D. 2003, Earth Moon Planets, 92, 465
Jewitt, D. 2009, AJ, 137, 4296
Jewitt, D. C., Trujillo, C. A., & Luu, J. X. 2000, AJ, 120, 1140
Jewitt, D., Hsieh, H., & Agarwal, J. 2015, The Active Asteroids (Univ. Arizona Press), 221
Johnston, W. 2015, Binary Minor Planets V8.0, NASA Planetary Data System, eAR-A-COMPIL-5-BINMP-V8.0
Kaasalainen, M. 2004, A&A, 422, L39
Kaasalainen, M., & Torppa, J. 2001, Icarus, 153, 24
Kaasalainen, M., Torppa, J., & Muinonen, K. 2001, Icarus, 153, 37
Laureijs, R., Amiaux, J., Arduini, S., et al. 2011, ArXiv e-prints [arXiv:1110.3193]
Lazzaro, D., Angeli, C. A., Carvano, J. M., et al. 2004, Icarus, 172, 179
Lowry, S., Duddy, S. R., Rozitis, B., et al. 2012, A&A, 548, A12
LSST Science Collaboration, Abell, P. A., Allison, J., et al. 2009, ArXiv e-prints [arXiv:0912.0201]
Maciaszek, T., Ealet, A., Jahnke, K., et al. 2014, in Space Telescopes and Instrumentation 2014: Optical, Infrared, and Millimeter Wave, SPIE, 9143, 91430K
Mahlke, M., Bouy, H., Altieri, B., et al. 2017, A&A, in press, DOI: 10.1051/0004-6361/201730924
Mainzer, A., Grav, T., Masiero, J., et al. 2011, ApJ, 741, 90
Marchis, F., Hestroffer, D., Descamps, P., et al. 2006, Nature, 439, 565
Marchis, F., Durech, J., Castillo-Rogez, J., et al. 2014, ApJ, 783, L37
Margot, J.-L., Pravec, P., Taylor, P., Carry, B., & Jacobson, S. 2015, Asteroid Systems: Binaries, Triples, and Pairs, eds. P. Michel, F. E. DeMeo, & W. F. Bottke (Univ. Arizona Press), 355
Masiero, J. R., Mainzer, A. K., Grav, T., et al. 2011, ApJ, 741, 68
McMahon, R. G., Banerji, M., Gonzalez, E., et al. 2013, The Messenger, 154, 35
Merlin, F., Hromakina, T., Perna, D., Hong, M. J., & Alvarez-Candal, A. 2017, A&A, 604, A86
Merline, W. J., Close, L. M., Dumas, C., et al. 1999, Nature, 401, 565
Michel, P., Benz, W., Tanga, P., & Richardson, D. C. 2001, Science, 294, 1696
Mignard, F., Cellino, A., Muinonen, K., et al. 2007, Earth Moon and Planets, 101, 97
Muinonen, K., Belskaya, I. N., Cellino, A., et al. 2010, Icarus, 209, 542
Müller, T. G., Lellouch, E., Böhnhardt, H., et al. 2009, Earth Moon Planets, 105, 209
Nesvorný, D., Jedicke, R., Whiteley, R. J., & Ivezić, Ž. 2005, Icarus, 173, 132
Noll, K. S., Grundy, W. M., Chiang, E. I., Margot, J.-L., & Kern, S. D. 2008, Binaries in the Kuiper Belt, eds. M. A. Barucci, H. Boehnhardt, D. P. Cruikshank, A. Morbidelli, & R. Dotson, 345
Oszkiewicz, D. A., Bowell, E., Wasserman, L. H., et al. 2012, Icarus, 219, 283
Pajuelo, M. 2017, Ph.D. Thesis, Observatoire de Paris
Parker, A. H., Kavelaars, J. J., Petit, J.-M., et al. 2011, ApJ, 743, 1
Petit, J.-M., Bannister, M. T., Alexandersen, M., et al. 2016, in AAS/Division for Planetary Sciences Meeting Abstracts, 48, 120.16
Petit, J.-M., Kavelaars, J. J., Gladman, B. J., et al. 2017, AJ, 153, 236
Polishook, D., Ofek, E. O., Waszczak, A., et al. 2012, MNRAS, 421, 2094
Popescu, M., Licandro, J., Morate, D., et al. 2016, A&A, 591, A115
Pravec, P., & Harris, A. W. 2007, Icarus, 190, 250
Pravec, P., Scheirich, P., Kušnirák, P., et al. 2006, Icarus, 181, 63
Pravec, P., Vokrouhlický, D., Polishook, D., et al. 2010, Nature, 466, 1085
Pravec, P., Scheirich, P., Vokrouhlický, D., et al. 2012, Icarus, 218, 125
Rhodes, J., Nichol, B., Aubourg, E., et al. 2017
Russell, C. T., Raymond, C. A., Coradini, A., et al. 2012, Science, 336, 684
Samarasinha, N. H., Mueller, B. E. A., Belton, M. J. S., & Jorda, L. 2004, Rotation of cometary nuclei (Univ. Arizona Press), 281
Scheeres, D. J., Britt, D., Carry, B., & Holsapple, K. A. 2015, Asteroid Interiors and Morphology, eds. P. Michel, F. E. DeMeo, & W. F. Bottke (Univ. Arizona Press), 745
Shankman, C., Kavelaars, J., Gladman, B. J., et al. 2016, AJ, 151, 31
Sierks, H., Lamy, P., Barbieri, C., et al. 2011, Science, 334, 487

Skrutskie, M. F., Cutri, R. M., Stiening, R., et al. 2006, AJ, 131, 1163
Snodgrass, C., Carry, B., Dumas, C., & Hainaut, O. R. 2010, A&A, 511, A72
Snodgrass, C., Fitzsimmons, A., Lowry, S. C., & Weissman, P. 2011, MNRAS, 414, 458
Spoto, F., Del Vigna, A., Milani, A., Tomei, G., & Tanga, P. 2017, A&A, submitted
Sykes, M. V., Cutri, R. M., Fowler, J. W., et al. 2000, Icarus, 146, 161
Szabó, G. M., Ivezić, Ž., Jurić, M., Lupton, R., & Kiss, L. L. 2004, MNRAS, 348, 987
Taylor, M. B. 2005, in Astronomical Data Analysis Software and Systems XIV, eds. P. Shopbell, M. Britton, & R. Ebert, ASP Conf. Ser., 347, 29
Tedesco, E. F., Noah, P. V., Noah, M. C., & Price, S. D. 2002, AJ, 123, 1056
Thomas, C. A., Trilling, D. E., & Rivkin, A. S. 2012, Icarus, 219, 505
Usui, F., Kuroda, D., Müller, T. G., et al. 2011, PASJ, 63, 1117
Veverka, J., Robinson, M., Thomas, P., et al. 2000, Science, 289, 2088
Virtanen, J., Poikonen, J., Säntti, T., et al. 2016, Adv. Space Res., 57, 1607
Volk, K., Murray-Clay, R., Gladman, B., et al. 2016, AJ, 152, 23
Walsh, K. J., & Jacobson, S. A. 2015, Formation and Evolution of Binary Asteroids, eds. P. Michel, F. E. DeMeo, & W. F. Bottke, 375
Walsh, K. J., Richardson, D. C., & Michel, P. 2008, Nature, 454, 188
Waszczak, A., Chang, C.-K., Ofek, E. O., et al. 2015, AJ, 150, 75
Wiegert, P., Balam, D., Moss, A., et al. 2007, AJ, 133, 1609
Yoshida, F., & Nakamura, T. 2005, AJ, 130, 2900

Appendix A: Definition of small-body populations

We describe here the boundaries in orbital elements to define the population we used thoroughout the article. The boundaries for NEA classes are taken from Carry et al. (2016), and the boundary of the outer solar system is adopted from Gladman et al. (2008).

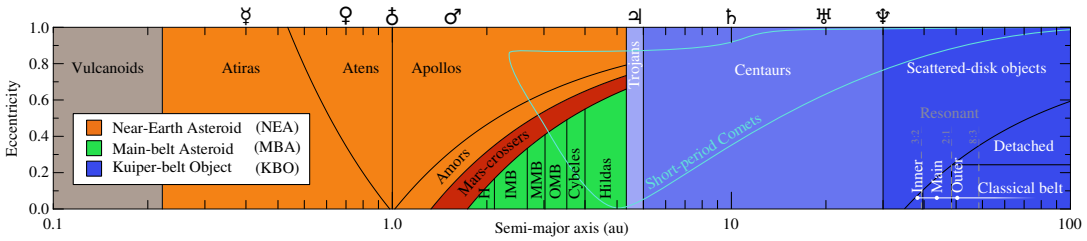

Fig. A.1. Different classes of SSOs used thoroughout the article. H stands for Hungarias, and IMB, MMB, and OMB for inner, middle, and outer belt, respectively. Comet orbital elements formally overlap with other classes because their classification is based on the presence of a coma at short heliocentric distance.

Table A.1. Definition of all the dynamical populations use here as a function of their semimajor axis, eccentricity, perihelion, and aphelion (using the definitions in Carry et al. 2016; Gladman et al. 2008).

Class	Semimajor axis (au)		Eccentricity		Perihelion (au)		Aphelion (au)	
	min.	max.	min.	max.	min.	max.	min.	max.
NEA	–	–	–	–	–	1.300	–	–
Atira	–	$a_{\oplus}$	–	–	–	–	–	$q_{\oplus}$
Aten	–	$a_{\oplus}$	–	–	–	–	$q_{\oplus}$	–
Apollo	$a_{\oplus}$	4.600	–	–	–	$Q_{\oplus}$	–	–
Amor	$a_{\oplus}$	4.600	–	–	$Q_{\oplus}$	1.300	–	–
MC	1.300	4.600	–	–	1.300	$Q_{\mars}$	–	–
MBA	$Q_{\mars}$	4.600	–	–	$Q_{\mars}$	–	–	–
Hungaria	–	$J_{4:1}$	–	–	$Q_{\mars}$	–	–	–
IMB	$J_{4:1}$	$J_{3:1}$	–	–	$Q_{\mars}$	–	–	–
MMB	$J_{3:1}$	$J_{5:2}$	–	–	$Q_{\mars}$	–	–	–
OMB	$J_{5:2}$	$J_{2:1}$	–	–	$Q_{\mars}$	–	–	–
Cybele	$J_{2:1}$	$J_{5:3}$	–	–	$Q_{\mars}$	–	–	–
Hilda	$J_{5:3}$	4.600	–	–	$Q_{\mars}$	–	–	–
Trojan	4.600	5.500	–	–	–	–	–	–
Centaur	5.500	$a_{\neptune}$	–	–	–	–	–	–
KBO	$a_{\neptune}$	–	–	–	–	–	–	–
SDO	$a_{\neptune}$	–	–	–	–	37.037	–	–
Detached	$a_{\neptune}$	–	0.24	–	37.037	–	–	–
ICB	37.037	$N_{2:3}$	–	0.24	37.037	–	–	–
MCB	$N_{2:3}$	$N_{1:2}$	–	0.24	37.037	–	–	–
OCB	$N_{1:2}$	–	–	0.24	37.037	–	–	–

Notes. See Fig. A.1 for the distribution of these populations in the semimajor axis – eccentricity orbital element space. The numerical value of the semimajor axes a, perihelion q, aphelion Q, and mean-motion resonances (indices $_{i:j}$) are for the Earth $a_{\oplus}$, $q_{\oplus}$, and $Q_{\oplus}$ at 1.0, 0.983, and 1.017 AU; for Mars $Q_{\mars}$ at 1.666 AU; for Jupiter $J_{4:1}$, $J_{3:1}$, $J_{5:2}$, $J_{2:1}$, and $J_{5:3}$ at 2.06, 2.5, 2.87, 3.27, 3.7 AU; and for Neptune $a_{\neptune}$, $N_{2:3}$, and $N_{1:2}$ at 30.07, 47.7, and 39.4 AU. The somewhat arbitrary limit of 37.037 AU corresponds to the innermost perihelion that is accessible to detached KBOs (semimajor axis of $N_{1:2}$ and eccentricity of 0.24).

A&A 609, A113 (2018)

Appendix B: *Euclid* colors and SSO light curves

Owing to the ever-changing Sun-SSO-observer geometry and the rotating irregular shape of SSOs, the apparent magnitude of SSOs is constantly changing. Magnitude variations in multi-filter time series are thus a mixture of low-frequency geometric evolution, high-frequency shape-related variability, and intrinsic surface colors.

The slow geometric evolution can easily be taken into account (Eq. (1)), but we need to separate the intrinsic surface colors from the shape-related variability to build the SED (Sect. 5) and to obtain a dense light curve (Sect. 8). Often, only the simplistic approach of taking the pair of filters closest in time can be used to determine the color (e.g., Popescu et al. 2016), while hoping the shape-related variability will not affect the color measurements (Fig. 10, Szabó et al. 2004).

The sequence of observations by *Euclid* in four repeated blocks, each containing all four filters (Fig. 2), allows a more subtle approach, however. For any given color, that is, for each filter pair, each filter will be bracketed in time three times by the other filter. The reference magnitudes provided by the bracketing filter allow us to estimate the magnitude at the observing time of the other filter. For instance, to determine the (VIS-Y) index, we can use the first two measurements in VIS to estimate the VIS magnitude at the time the *Y* filter was acquired (by simple linear interpolation for instance). This corrects, although only partially, for the shape-related variability. Hence, any colors will be evaluated six times over an hour, although not entirely independently each time.

The only notable assumption here is that the SED is constant over rotation, meaning that the surface composition and properties are homogeneous on the surface, which is a soft assumption based on the history of spacecraft rendezvous with asteroids (i.e., Eros, Gaspra, Itokawa, Mathilde, Ida, Šteins, Lutetia, and Ceres, with the only exception of the Vesta, see e.g., Veverka et al. 2000; Sierks et al. 2011; Russell et al. 2012).

We tested this approach by simulating observation sequences by *Euclid*. For each of the 371 asteroids of the DeMeo et al. (2009), we simulated 800 light curves made of Fourier series of the second order, with random coefficients to produce a light curve amplitude between 0 and 1.6 mag and a random rotation period between 1 and 200 h. These ≈300 000 light curves span the observed range of amplitude and period parameter space, estimated from the 5759 entries with a quality code 2 or 3 from the Planetary Data System archive (Fig. B.1; Harris et al. 2017). We limited the simulation to second-order Fourier series as dense light curves for about a thousand asteroids from the Palomar Transient Factory showed that is was sufficient to reproduce most asteroid light curves (Polishook et al. 2012; Chang et al. 2014; Waszczak et al. 2015). For each light curve, we determined the 4×4 apparent magnitude measurements using the definition of the observing sequence of *Euclid* (Fig. 2) and the SSO color (from Sect. 5), and we added a random Gaussian noise of 0.02 mag.

We then analyzed these 4×4 measurements with the method described above. For each SSO and each light curve, we determined all the colors (VIS-Y, VIS-J, VIS-H, Y-J, Y-H, and J-H) and compared them with the input of the simulation, hereafter called the residuals. For each color, we also recorded the estimate dispersion.

The accuracy on each color was found to be at the level of the single measurement uncertainty (Fig. B.1). This is due to the availability of multiple estimates of each color, which improves the resulting signal-to-noise ratio. The residuals are found to be very close to zero: offsets below the millimagnitude (mmag) with a standard deviation below 0.01, that is, smaller than individual measurement uncertainty (about a factor of five). We repeated the analysis with higher levels of Gaussian noise on individual measurements (0.05 and 0.10 mag, the latter corresponding to the expected precision at the limiting magnitude of *Euclid*), adding 600 000 simulated light curves to the exercise, and found similar results: the color uncertainty remains at the level of the uncertainty on individual measurement and the residuals remain close to zero, with a dispersion following the individual measurement uncertainty reduced by a factor of about five. The colors determined with this technique are therefore precise and reliable.

The processing described here is a simple demonstration that the SED can be precisely determined from *Euclid* multi-filter time series. As a corollary, a single light curve of 16 measurements can be reconstructed from the 4×4 measurements. These will be the root of the spectral classification (Sect. 5) and time-resolved photometry analysis (Sect. 8). The technique will be further refined for the data processing: we considered here each color, that is, each pair of filters, independently. No attempt for a multi-pair analysis was made for this simple demonstration of the technique, while a combined analysis is expected to reduce the residuals, that is, potential biases, even more.

B. Carry: Solar system science with ESA *Euclid*

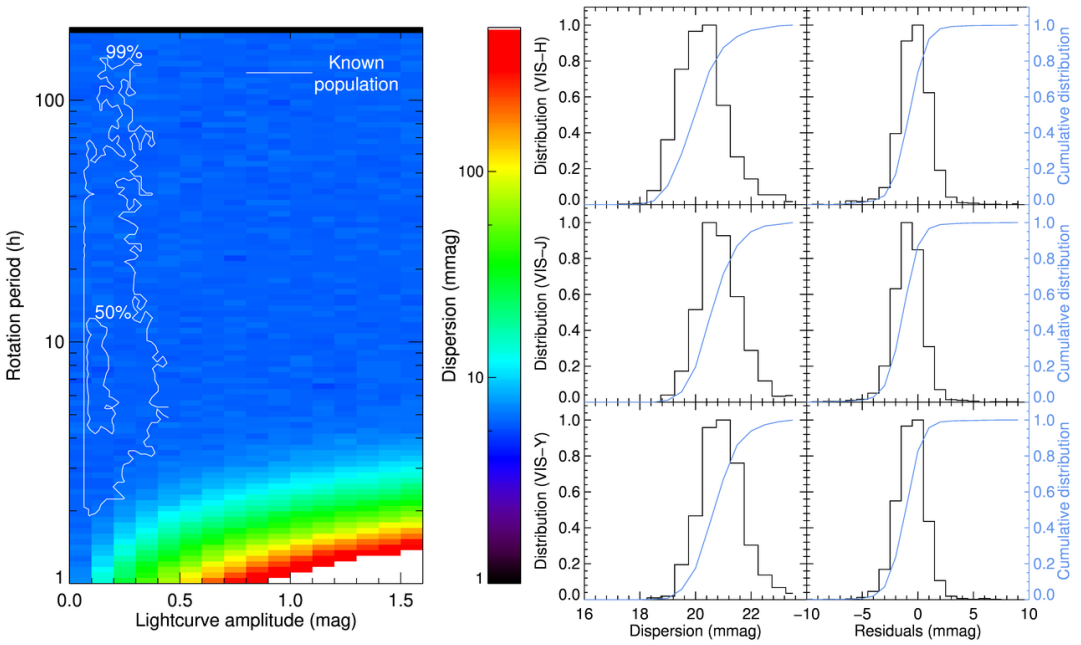

Fig. B.1. *Left*: distribution of the dispersion of color measurement in period-amplitude space. The white contours represent the regions encompassing 50% and 99% of the population with known rotation period and amplitude, respectively. The largest uncertainties are found for high-amplitude short rotation-period light curves, which is outside the typical space sampled by SSOs. *Right*: distribution of the dispersion and residuals of color determination in VIS-Y, VIS-J, and VIS-H colors (the remaining colors are a combination of these three). The dispersion is typically at the level of the individual measurement uncertainty (here 0.020 mag). Residuals are much smaller, close to zero, and with a dispersion below 0.01 mag.

Planetary and Space Science 123 (2016) 87–94

Contents lists available at ScienceDirect

Planetary and Space Science

journal homepage: www.elsevier.com/locate/pss

The daily processing of asteroid observations by Gaia

Paolo Tanga [a,*], François Mignard [a], Aldo Dell'Oro [f], Karri Muinonen [c,b], Thierry Pauwels [h], William Thuillot [d], Jérôme Berthier [d], Alberto Cellino [e], Daniel Hestroffer [d], Jean-Marc Petit [g], Benoit Carry [d], Pedro David [d], Marco Delbo' [a], Grigori Fedorets [c], Laurent Galluccio [a], Mikael Granvik [c,b], Christophe Ordenovic [a], Hanna Pentikäinen [c]

[a] Laboratoire Lagrange, UMR7293/CNRS, UNS, Observatoire de la Côte d'Azur, route de l'Observatoire, CS34229, F-06304 Nice Cedex 4, France
[b] Finnish Geospatial Research Institute, Geodeetinrinne 2, FI-02430 Masala, Finland
[c] Department of Physics, Gustaf Hällströmin katu 2a, FI-00014 University of Helsinki, Finland
[d] Observatoire de Paris, IMCCE, Institut de mécanique céleste et de calcul des éphémérides, Unité Mixte de Recherche UMR-CNRS 8028, 77 avenue Denfert-Rochereau, F-75014 Paris, France
[e] INAF - Osservatorio Astrofisico di Torino, Strada Osservatorio 20, 10025 Pino Torinese, Italy
[f] INAF - Osservatorio Astrofisico di Arcetri, Largo E. Fermi 5, 50125 Firenze, Italy
[g] Observatoire de Besançon, UMR CNRS 6213, 41 bis avenue de l'Observatoire, F-25000 Besançon, France
[h] Observatoire Royal de Belgique, Avenue Circulaire 3, B-1180 Bruxelles, Belgique

ARTICLE INFO

Article history:
Received 24 April 2015
Received in revised form
6 October 2015
Accepted 12 November 2015
Available online 27 November 2015

Keywords:
Gaia mission
Astrometry
Asteroids

ABSTRACT

The Gaia mission started its regular observing program in the summer of 2014, and since then it is regularly obtaining observations of asteroids. This paper draws the outline of the data processing for Solar System objects, and in particular on the daily "short-term" processing, from the on-board data acquisition to the ground-based processing. We illustrate the tools developed to compute predictions of asteroid observations, we discuss the procedures implemented by the daily processing, and we illustrate some tests and validations of the processing of the asteroid observations. Our findings are overall consistent with the expectations concerning the performances of Gaia and the effectiveness of the developed software for data reduction.

1. Introduction: Gaia and Solar System objects

The European mission Gaia observes the whole sky from the Lagrangian point L2, where the required thermal stability is guaranteed (details and capabilities are described in detail by Prusti (2012), De Brujine, 2012, and references therein). The satellite operates in continuous scanning mode, its spin being of 6 h. Two lines of sight separated on the scanning plane by 106.5° (the basic angle), are simultaneously imaging the sky on the same focal plane. This feature, reducing the measurements of large angular separations to small distances on the focal plane, is the essential principle allowing Gaia to have a homogeneous all-sky astrometric accuracy, without zonal errors. The slow change in the orientation of the scanning plane, steered by a 62.97-days precession and by the 1-year revolution around the Sun, determines a rather homogenous coverage of the sky resulting, over 5 years of nominal mission duration, in 80–100 observations for an average direction, slightly less on the ecliptic (60–70).

The images formed on the focal plane, consisting of a large giga-pixel array of 106 CCDs, are electronically tracked on the CCD itself by a displacement of the charge (Time Delay Integration mode, TDI) at the same pace as the image drifts due to the spacecraft rotation.

The CCDs are organized in the order of crossing by the drifting images. First, there are two CCD strips devoted to source detection (one for each of the two lines of sight); they constitute the instrument called Sky Mapper (SM). Then, 9 strips of astrometric CCDs follow (Astrometric Field, AF). Next, other CCD strips are devoted to low resolution spectro-photometry (red and blue photometer, RP/BP) and high resolution spectroscopy (Radial Velocity Spectrometer, RVS). RVS is not considered for asteroid studies, due to its narrow range of wavelength.

Each source that enters the field of view of Gaia will produce a signal on one SM CCD. If bright enough ($V < 20.7$ is the current threshold) and nearly point-like (about < 600 mas diameter) its position is then recorded by the on-board Video Processing Unit (VPU). The VPU automatically assigns a "window" around each object detected by the SM, and propagates these windows to the other CCDs in the direction of the image drift. Only these very small windows (the smallest, but more common ones spanning

* Corresponding author.
E-mail address: Paolo.Tanga@oca.eu (P. Tanga).

http://dx.doi.org/10.1016/j.pss.2015.11.009
0032-0633/

6 pixels only) are transmitted to Earth, in such a way that the telemetry does not exceed the possible downlink rate. Due to this windowing strategy, two point-like sources separated by more than ~300 mas (6 pixels) are detected as two different images and processed separately.

Due to its orbital motion, a Solar System object (SSO) may leave the transmitted window before arriving at the last CCD. As a consequence, each "observation" consists of a maximum of 10 positions (AF and SM instruments), distributed over 50 s (the duration of a transit).

One should note that the cut–off at magnitude $V = 20.7$ is not dictated by a threshold on the minimum, acceptable signal-to-noise ratio, as at this brightness level very accurate astrometry can still be obtained. Rather, the limit is imposed by constraints on the data downlink rate, especially in the densest areas of the Milky Way.

All source identifications and further processing are done on the ground and are part of the activities of the Data Processing and Analysis Consortium (DPAC). Also, DPAC is in charge of running the Astrometric Global Iterative Solution (AGIS), a highly optimized software system that looks for the best-fitting self-consistent attitude and astrometric solution on the sphere, taking into account all measurements and instrument calibration parameters. The astrometry based on the best AGIS result is used for the preparation of each intermediate release.

Starting from 2006, DPAC of Gaia was charged by ESA for implementing the data processing pipelines that will deliver the first-level analysis of Gaia observations. The Gaia outcome – in fact – will consist not only of the individual measurements, but also of calibrated data (fluxes, positions, spectra), global statistics, and the results of the exploration of the bulk properties of the sources (classification, distributions etc).

In this context, the Coordination Unit 4 (CU4) has the task of performing the analysis of objects deserving a specific treatment, namely multiple stellar systems, exoplanets (PI: D. Pourbaix, Brussels Univ.), Solar System objects (PI: P. Tanga) and extended sources (Ch. Ducourant, Obs. Bordeaux, France).

All the software produced within DPAC runs at Data Processing Centers; the Data Processing Center CNES (DPCC) in Toulouse, France, is in charge of Solar System data, among others. Essentially, the processing will proceed blindly for the whole DPAC community. This approach, along with the absence of any proprietary period, ensures that the data products of Gaia will be available to the whole scientific community (including the DPAC scientists) at the same time, as established by the ESA-DPAC agreement.

Gaia will obtain during its 5-year operation ~70 observations per object, on average, for about 350,000 asteroids.

We recall here that the scientific community was made aware of unexpected technical difficulties (in particular, the presence of stray-light) discovered during commissioning. Recent studies of these issues reveal that they will not affect the revolutionary potential of Gaia, with a very modest degradation in the expected performance (De Bruijne et al., 2006).

The DPAC CU4 has implemented two pipelines for Solar System processing (Tanga et al., 2007; Mignard et al., 2007):

- SSO-ST: the "Solar System short-term processing" is devoted to alert a ground-based network (Gaia-FUN-SSO, steered by IMCCE, Observatoire de Paris) in case a new asteroid is discovered. This pipeline will be running daily at DPCC (CNES in Toulouse) and is also used to verify and monitor the quality of the data received by Gaia.
- SSO-LT: the "Solar System long-term processing" will run for the data releases and perform a more sophisticated data reduction with the best possible astrometric solution and the advanced instrument calibrations. Also, it will eventually perform the global data reduction by executing tasks that require the largest possible set of observations.

The fist intermediate data release is planned for mid-2016, and is expected to provide data for not less than 90% of the sources observed by Gaia.

The SSO-ST chain is currently running at CNES for the validation of the data processing. This implies that the observations being processed are concerning – for the time being – known asteroids. This situation offers several opportunities for validating the performances of Gaia on asteroid detection, and for tuning the SSO-ST pipeline.

The goal of this paper is to illustrate the main processing steps of SSO-ST. First of all, we explain the approach and the performance of the software that we developed for predicting the observations by Gaia (Section 2), an essential validation tool. Then we review the SSO-ST pipeline step by step, starting from asteroid identification (Section 3). The processing continues with the measurement of asteroid positions on the focal plane (Section 4) and the subsequent coordinate transformations (Section 5) toward the sky reference. The observations of a target are grouped together and an orbital solution is determined. As the goal of SSO-ST is to provide a first, approximate orbit for the recovery of new objects from the ground, a statistical approach is adopted (Section 6). We conclude by describing the ground-based follow-up activities (Section 7).

2. Prediction of Solar System observations

To define more precisely the quality of the observations with respect to expectations, we can exploit the simulations produced by a software developed by F. Mignard and P. Tanga at Laboratoire Lagrange (OCA, Nice). This unique tool exploits the very stable scanning law and the full orbital data set from the Minor Planet Center to predict when and how often a source will be seen by Gaia. The accuracy of the predictions and crossing times, compared to real Gaia data, are excellent, so that reliable statistics can be built.

The transit predictor has been developed within the CU4/SSO in order to be able to compute in advance the observations of Solar System objects to be seen by Gaia during its operations.

The software is an outgrowth of a detection simulator used and maintained over the years, since the very preliminary studies on Gaia, based on similar overall principles, but aiming at accurate individual transit data instead of an overall statistical relevance. In the earlier phase some approximations were acceptable (such as the 2-body Keplerian motion). The same liberty was used for the Gaia orbit about L2, in absence of other constraints before launch.

Moving to a predictor of what actually happens during the real mission implied a more rigourous modelling of the mission environment and of the dynamical modelling of the planetary motion. With the predictor the use of an exact Gaia scanning law is mandatory to reproduce the actual pointing of each FOV. Similarly, the Gaia orbit should be as close as possible to the true path of Gaia on its Lissajous orbit. Finally, the orbital elements of the asteroids must be taken to full accuracy at a reference epoch and then the position and velocity must be propagated with planetary perturbations and numerical integration instead of the simplified 2-body problem.

The program essentially solves for any ith asteroid and for each Field Of View F over an interval of time $[T_b, T_e]$, the following equation in t

$$\mathbf{G}_F(t) = \mathbf{U}_i(t) \tag{1}$$

where $\mathbf{U}_i(t)$ is the unit vector of the asteroid proper direction at time t and $\mathbf{G}_F(t)$ stands for the pointing direction of Gaia FOV F. The

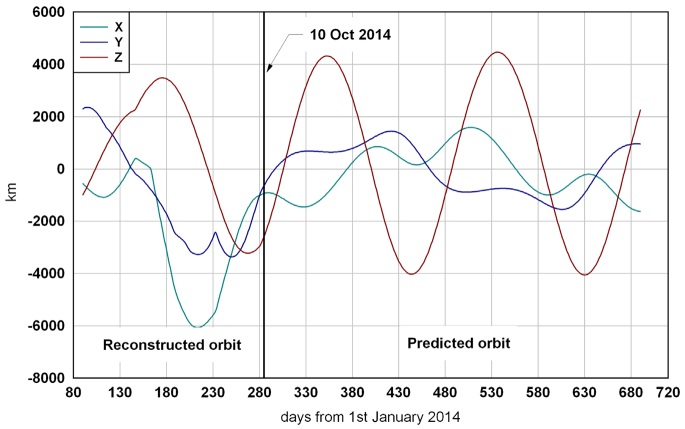

Fig. 1. Difference between the MOC orbit by the Gaia Mission Operation Center of ESA (MOC) provided on 14 October 2014, compared to the first post-launch predicted orbit of 30 December 2013. The colors represents the differences along the (X,Y,Z) cartesian coordinates. Until 10 October 2014 the comparison is between the reconstructed and the predicted orbits, while after this is between the two predicted orbits. The large difference (still within the requirements) is due to the origin of the predicted orbit, starting 80 days before the origin of the plot. On the short term (a few days after the prediction) the situation is better and the divergence builds up gradually. (For interpretation of references to color in this figure legend, the reader is refered to the web version of this article.)

left-hand-side is the Gaia attitude model, here the Nominal Scanning Law, while the right-hand-side resulted from the integration of the planetary motion.

The adopted position of Gaia is provided by the Gaia Mission Operation Center, as reconstructed from telemetry over the past epochs. Afterwards, the targeted orbit is used, which is always within 7000 km of the actual orbit.

Over a certain interval of time the program finds all the roots $t_1, t_2, \ldots, t_{r_k}$ of Eq. (1). The solutions are found with an iterative process to locate a first approximation within a spin period and then accurately compute the solution with a Newton–Raphson method. The software has been strongly optimized for speed and allows to run a prediction for ~500,000 asteroids over 5 years in less than one hour of CPU time on a desk-computer, with output files reaching 1 GB.

The positions and velocity of the asteroids are computed by a numerical integration from the osculating epoch, using gravitational perturbations from the 8 planets (Mercury to Neptune) with the main component of the relativistic contribution.

The solar term with relativistic effect is computed as

$$\frac{d\mathbf{v}}{dt} = -\frac{GM_\odot \mathbf{r}}{r^3} + \frac{GM_\odot}{c^2 r^3}\left(4GM_\odot \frac{\mathbf{r}}{r} - v^2\mathbf{r} + 4(\mathbf{r}\cdot\mathbf{v})\mathbf{v}\right) \quad (2)$$

with $\mathbf{r} = \mathbf{r}_p - \mathbf{r}_\odot$ for the heliocentric position vector of the asteroid.

The planetary perturbations are given by

$$\sum_k GM_k \left[\frac{\mathbf{r}_k - \mathbf{r}}{|\mathbf{r}_k - \mathbf{r}|^3} - \frac{\mathbf{r}_k}{r_k^3}\right] \quad (3)$$

where $\mathbf{r}_k$ is the heliocentric position vector of the kth planet. Solar System ephemerides are taken from INPOP10e expressed in the barycentric frame with ICRF orientation and using TCB as independent variable.

There are at least three sources of uncertainty to consider:

- The computational accuracy.
- The position of the asteroid on the sky, including its orbit uncertainty.
- The position on the Gaia Focal Plane Assembly and the associated transit times.

This refers to the numerical solution of the transit equation (Eq. (1)) and to the numerical integration of the planetary dynamical equations, assuming all other parameters are exactly known. Convergence to the transit time is achieved to better than 1 ms. Other computations have the accuracy permitted by the numerical representation of numbers, which, apart from the epoch, is not a source of concern. The numerical integration of the asteroid motion over an interval of time that could reach 5 years is also compatible with a sub-mas astrometric accuracy. This is fully sufficient for the purpose of the transit predictor.

The quality of the prediction of the gaiacentric position is primarily determined by the knowledge of the osculating elements, rather than by the dynamical model, and by the predicted Gaia orbit. It is not easy to figure out how good the osculating elements are for every asteroid. As a rule of thumb for numbered asteroids (those with an IAU definitive number) the proper position is generally better than 0.5″ and often better than 0.2″.

The uncertainty stemming from the Gaia orbit itself can be easily estimated. As mentioned above, there is a requirement that the actual Gaia orbit is always within 7000 km of the predicted orbit, dictated by the optimization of the scanning law for the relativistic experiments of light deflection. Assuming an asteroid at 2.5 au, this uncertainty in the Gaia barycentric position translates into 4″ for the asteroid Gaiacentric direction.

Comparisons of successive releases of the Gaia orbits indicate that the 7000 km requirement is met as shown in Fig. 1, where the first predicted orbit is compared to the actual orbit until 10 October 2014 and to the most recent predicted orbit afterwards. One may assume that in 2015 the difference between the actual Gaia orbit and the one used in this version of the software will be similar giving then a maximum uncertainty as large as 4″ in the predicted Gaiacentric direction of the asteroids, but only 1.5″ RMS. For the numbered asteroids with good orbital elements, the uncertainty in the Gaia orbit could be the largest single factor in the overall uncertainty of the proper direction.

The main source of uncertainty here is the use of the Nominal Scanning Law of Gaia to compute the satellite attitude instead of the true attitude (not known in fact for the future!). Comparisons between daily attitude solution to the nominal scanning law have

shown that the actual attitude does not differ from the targeted scanning by more than 30″ and that it is very often less than 15″.

This gives an error ~0.5 s in the crossing time and 100–200 pixels in the direction perpendicular to the scan. Comparisons to true Gaia observations processed by the Initial Data Treatment (IDT, implementing the first, approximate astrometric reduction) show that the difference is almost always less than 100 pixels across-scan (corresponding to 0.4 s). Limited test trials with the daily attitude have reduced this difference to few pixels and 0.03 s in the transit time, thus producing a additional validation of the implementation.

During the ACM2014 meeting, the detection of the asteroid (4997) Ksana has been presented as a validation of the capabilities of Gaia and of the accuracy of the predictor. The sky position of this specific asteroid was within 2″ from the prediction. Further tests with a larger population of asteroids show that – when a multi-opposition, good quality orbit is available, the discrepancy is more of the order of ~200 mas.

3. Identification of asteroids in the data flow

The identification of Solar System objects in the data exploits the position and brightness of the source as reconstructed by the "Initial Data Treatment" (IDT) on the ground, which uses the daily attitude to perform a first, quick astrometric reduction with a very short delay from the observation. IDT considers data packets containing variable amounts of data, and for each packet performs the so-called cross-matching. This complex procedure identifies stars in the data packet by matching the position of the sources, to previously catalogued detections.

As the asteroid moves with a substantial displacement from one observation to the other, cross-matching fails to match its positions. Un-matched sources are provided to CU4 as candidate moving objects.

Within the SSO-ST pipeline, receiving the IDT output, a search algorithm (Berthier et al., 2006) attempts to match the position and the (approximate) magnitude of each observed source to the ephemerides of each asteroid. The principles for computing the theoretical position of the asteroid are similar to those illustrated in Section 2, but the details are different, as more stringent requirements for the computation of speed are present. Also, the sources of some ancillary data required for the computation are different, as for instance the IDT data flow itself contains the position of Gaia at the epoch of each observation. Eventually, the equatorial coordinates of the observation computed by IDT are used, as they can be directly compared to the ephemerides, instead of predicting focal plane coordinates (a process that adds further uncertainties).

The source of orbital elements is the commonly used ASTORB database maintained at Lowell observatory (Flagstaff, AZ, USA). As for un-numbered asteroids the discrepancy between prediction and observation can be rather high, a probabilistic approach is adopted to identify the most likely candidate for each source. In practice, when the ephemeris uncertainty contained in ASTORB (called CEU, "Current Ephemeris Uncertainty") is of the order of a few arc-seconds or less, it is highly probable that only a single candidate asteroid can be associated to the prediction. Conversely, increasing orbital uncertainties result in higher and higher ambiguity of identification, as the object can fall into the overlapping uncertainty areas of several known sources. In such a situation the possible object identities are rated according to each orbital uncertainty and to the distance from the detected position. A "probability of identification" is assigned based on this criteria. The top element of the list, having the highest probability, is considered to be the most plausible candidate. If that match is wrong, the anomaly will be identified further downstream in the processing (for example it can exhibit a high residual when orbital fitting is attempted) and the alternative identities can be tested.

Failing the identification with respect to the data base of a moving object – i.e. low probability of identification – reveals the possible presence of a new asteroid and may result in the triggering of ground-based follow up. However, up to now (summer 2015), a high number of "contaminants" (i.e. unmatched sources that are not asteroids), due to the non perfect efficiency of IDT in the stellar cross-matching, prevents the use of SSO-ST for the original goal of alert triggering on unknown targets. A strategy to overcome this problem has been identified and is being tested. Only when the influence of contaminants will be negligible, SSO-ST will release the alerts to the community.

4. Analysis of the asteroid signals

The processing of the astrometry starts in a first module ("CCD processing") with the analysis of the CCD counts in order to determine the relevant parameters of the signals of the asteroids. In SSO-ST such parameters are the mean position (centroid) of the observed source for each CCD, and the associated flux.

Centroid coordinates are raw quantities defined only in the space of the CCD window samples collected by the Gaia instrument. In short-term processing, centroids are computed by assuming a star-like PSF, that is by assuming, as a first approximation, that the source is not smeared by proper motion and not extended. While angular extension has an impact depending upon the size of the asteroid, smearing due to motion is nearly always present. In fact, the TDI mode of the CCD assumes that the source is moving across the field of view only due to the satellite rotation (i.e. as a fixed source, a star does). The asteroid proper motion relative to stars induces an image smearing. By fitting this signal with a model not taking motion into account, a deterioration of the astrometry is present. However, this approximation is fully acceptable and consistent with the accuracy requirements in short-term processing, as much higher uncertainty sources (in particular the attitude, see Section 5) are present.

As an example, we can consider a typical Main Belt, moving at ~10 mas/s relative to stars. While crossing a single CCD (in 4.4 s) in the AF instrument, the image smearing can reach 44 mas, i.e. 73% of the pixel size. The error on the centroiding due to the assumption of a fixed source, will be a fraction of that quantity. However, the error on the attitude (Section 5) will be much larger in the short-term processing (typically 100 mas) fully dominating the statistics (Section 5).

On the other hand, despite the fact that centroids are accurate enough, we cannot expect that the *goodness of fit*, expressed in terms of the reduced χ^2 of the difference between the observed signal and the PSF model, is the same we would have if the uncertainty was dominated only by mere photon noise statistics. Fig. 2

Fig. 3 shows the analysis of the distribution of the χ^2 for a sample of ~300 real asteroid signals provided for validation tests, for two window classes, corresponding to objects fainter than $V < 16$ and for objects $13 < V < 16$ (6-pixels and 12-pixels width windows, respectively). The difference between the observed (red) and theoretical (black) distribution is mainly due to smearing by source motion.

A quality control of the data has been performed by simulating the distribution of the χ^2. Our simulation takes into account both the distribution of the magnitudes of the observed sample and the distribution of the along-scan motion. The distribution of the along-scan motions of the asteroids is generated by a Gaussian

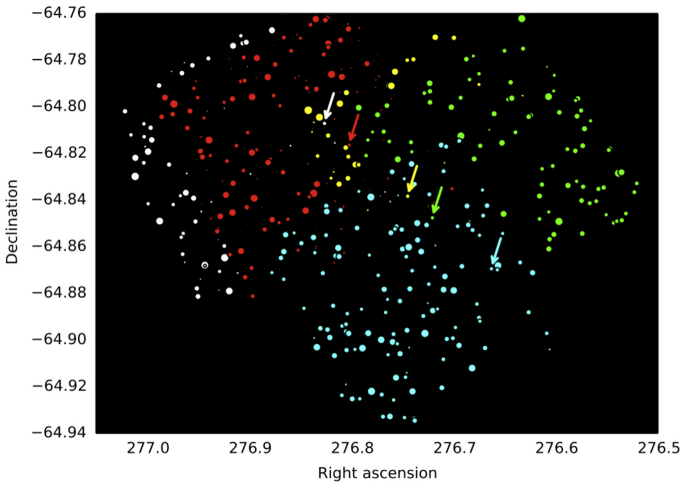

Fig. 2. Each dot in this plot represents a source observed by Gaia, with the size representing different magnitudes. Five consecutive scans (each lasting 6 s) have been used to search for the asteroid (4997) Ksana, based on its predicted position. The arrows indicate the positions of the asteroid (4997) Ksana at each different scan, starting from the first (upper left) to the last one (lower right). The different colors are used to identify the different scans. Courtesy ESA/Gaia/DPAC/Airbus DS. (For interpretation of references to color in this figure legend, the reader is refered to the web version of this article.)

distribution, with null average, reproducing rather well the simulated velocities.

Simulations on long time intervals (5 years of nominal mission) exhibit a standard deviation of the along-scan motion of about 10 mas/s for Main Belt asteroids, and 30 mas/s for Near Earth Objects. Our analysis matches a velocity dispersion of about 15 mas/s which might also be biased, with respect to predictions, by the narrow interval of time considered. As a consequence we naturally assume that the distribution of the velocities of such a subset cannot match exactly the expected distribution of the whole population and for the entire duration of the mission.

On the other hand, this result shows that the expectations on the centroiding accuracy are completely realistic and correspond to the real performance of Gaia.

5. Astrometric data reduction

The positions of the asteroids derived from the signal acquired by Gaia are expressed in pixel coordinates on the CCDs. The transformation from pixel coordinates on each CCD to right ascension–declination pairs in the Barycentric Reference System (BCRS) is the task of an appropriate software module. In the same way the timings, given initially in OBMT, On-Board Mission Timeline (a technical timescale of Gaia) are converted to Barycentric Coordinate Time, TCB, the time-like coordinate of BCRS.

This coordinate transformation is heavily dependent on the framework set up by the core CUs of DPAC, and in particular on the results obtained by Initial Data Treatment (IDT), First Look (FL), One-Day Astrometric Solution (ODAS) and Astrometric Global Iterative Solution (AGIS), and on the software produced by the core CUs, made available to the Gaia community through an appropriate library.

Accurate transformations from CCD coordinates to sky coordinates, as computed by AGIS, are not available before many months after the observations, so in SSO-ST the low-precision ODAS solution is adopted to convert CCD coordinates to positions in the sky. Since in the course of one day, Gaia is mainly scanning along a great circle in the sky, reasonable accuracy in the transformation is available in the so-called along-scan direction, but in the perpendicular direction, across-scan, the transformation is less well constrained.

On the average there will be a delay of one to two days between the epoch of observation, and its ground-based processing. This delay in producing an alert is critical for the recovery of the asteroids and all the efforts are spent to keep it below 3 days.

Ancillary tasks of this software module are dedicated to select the appropriate positions for further processing. For instance, an asteroid may, due to its motion in the sky, leave the transmitted window before reaching the last CCD. In that case a spurious centroiding, not corresponding to the object, can be computed by the “CCD processing”. As a consequence, the positions in the sky will no longer follow a linear motion, which should be the case in the course of one regular transit (about one minute). By fitting a linear motion to the positions, it is possible to reject such outliers.

Also, by the same procedure, a so-called “average” transit position and a transit speed are derived. These transit positions and speeds are not intended for publication but can be used to link together observations, separated in time, of a same (unknown) asteroid. Orbits, however, will be computed from the individual positions for each CCD.

Such individual positions of the new asteroids will be sent to the Minor Planet Center. In SSO-ST this is done as quickly as possible, with short batches of a few positions. It should be noted that timings sent to the Minor Planet Center will not be in TCB (as will be in the output catalogue), but rather converted to the more user-friendly UTC.

Finally, an important task is the validation of the data. Both in the simulation phase and with real data, a number of checks are done to see whether the data produced corresponds to the expectations. The most important check is that within a transit (about one minute) the different positions of an SSO show a linear motion in the sky within the quoted uncertainties. To this end, the software collects statistics of all objects processed, and generates user-defined plots to visualize these statistics, but also generates plots of single transits, to check whether a given SSO exhibits the expected linear motion or not.

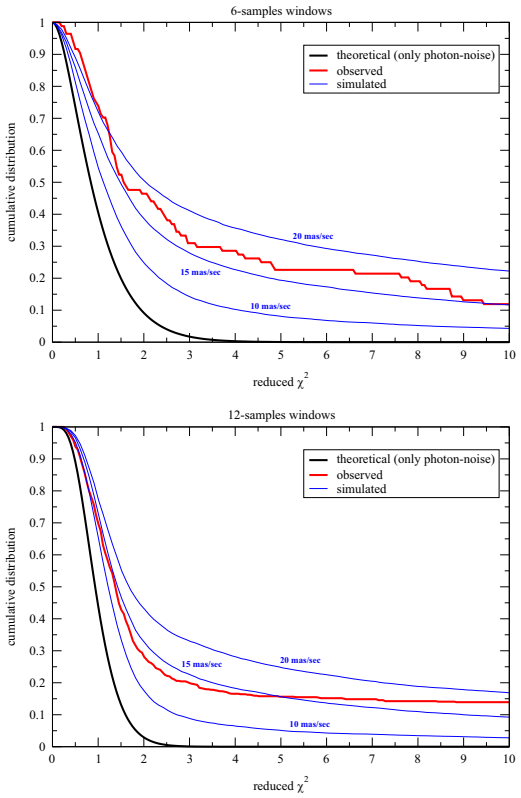

Fig. 3. Cumulative distribution of the χ^2, that is the fraction of centroids with χ^2 larger than the values in abscissa. The red line is the distribution of the observed χ^2, while the black line is the theoretical distribution of the signal with simulated photon noise included. Blue lines represent simulations with three different values of the proper motion dispersion (10, 15 and 20 mas/s). Top panel: 6-pixels window; bottom panel: 12-pixels window. The black line represents the theoretical curve in presence of photon noise. (For interpretation of references to color in this figure legend, the reader is refered to the web version of this article.)

The example in Fig. 4 shows a possible result from single-transit analysis. Not all the details shown in this plot are fully understood at present, such as the "corkscrew motion" around the average displacement, that could be partially related to the lower resolution (a factor 3) in the across-scan direction (horizontal axis) and to a preliminary geometric calibration of the focal plane.

The final uncertainty on each position represented by the dashed circles (50–100 mas in radius) is consistent with the low accuracy of the daily attitude solution, independent from the object magnitude, that will collapse in the global astrometric solution. At the end of mission, the expected single-epoch accuracy for a $V=20$ asteroid with a "slow" proper motion (at the level of an average Main Belt) will be around 1.5 mas, while at $V=15$ it will approach 0.1 mas.

As a consequence, there is a huge difference between the precision of the observations released on a daily basis, and the final ones. Incidentally, we can anticipate that asteroid positions reduced with accurate astrometric solutions will probably be released periodically in the planned Gaia Data Releases, and sent to MPC at the same time. Further details on the expected final accuracy can be found in Tanga and Mignard (2012).

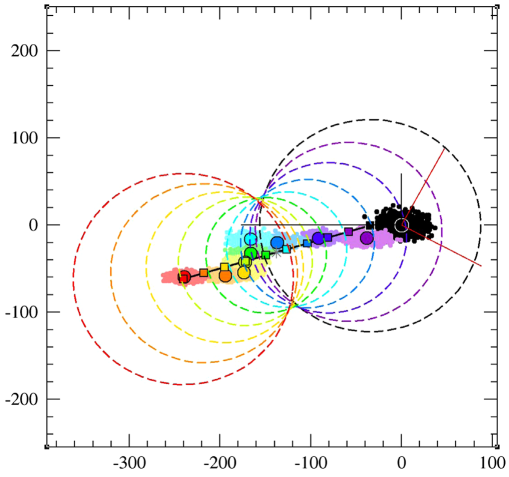

Fig. 4. Validation plot for the analysis of a single transit. It is a representation of a small portion of the sky showing the different derived positions for a bright asteroid. The figure is oriented in such a way that the scan direction is vertical. The axis values are in mas. There are 10 positions, corresponding to the SM CCD (black, arbitrarily chosen as origin) and all 9 AF CCDs (rainbow colors from violet to red). The picture is supposed to show the motion in the sky of an SSO over ~one minute (the duration of a transit). The colored circles (with solid contours) represent the measured positions converted to sky coordinates. Each of them is surrounded by a compact cloud of dots (lighter color) representing the scattering on the positions as derived from the centroiding uncertainty. The colored squares represent a fit of a linear motion to the derived positions. The dashed circles represent an error budget containing the uncertainties on the fit plus the errors on the daily attitude. Rather than showing a linear motion, the derived positions (solid circles) show a path more resembling a corkscrew motion, which deviates significantly from a linear motion, if one considers the errors on the fit of the PSF to the images alone. But if one considers also the errors on the attitude, the deviations are still well within the uncertainties. It is not clear what the origin of the corkscrew motion is, but it may imply that there is a rotational residual in the attitude with a period of the order of 1 minute and an amplitude of the order of a few tens of mas. (For interpretation of references to color in this figure legend, the reader is refered to the web version of this article.)

6. Orbital inversion

For all candidate "new" asteroids seen by Gaia, a short-arc initial orbit is required, for ground-based recovery.

Within Gaia DPAC CU4 object processing, initial orbital inversion is carried out for Solar System objects using random-walk statistical ranging (Muinonen et al., 2015, a newly developed method based on Markov chain Monte Carlo (MCMC). Random-walk ranging derives from a number of earlier ranging methods (Virtanen et al., 2001; Muinonen et al., 2001) and the MCMC ranging method by Oszkiewicz et al. (2009). They start from the selection of a pair of astrometric observations, whereafter the gaiacentric ranges and angular deviations in Right Ascension (R.A.) and Declination (Decl.) are randomly sampled. Orbital elements then follow from the two Cartesian positions, obtaining probabilistic weights on the basis of the specific ranging method in question.

We describe the six osculating orbital elements of an asteroid at a given epoch t_0 by the vector $\boldsymbol{P}$. For Cartesian elements, $\boldsymbol{P}=(X,Y,Z,\dot{X},\dot{Y},\dot{Z})^T$, where, in a given reference frame, the vectors $(X,Y,Z)^T$ and $(\dot{X},\dot{Y},\dot{Z})^T$ denote the position and velocity, respectively. Let $p_{\rm p}$ be the orbital–element probability density function (p.d.f.). Within the Bayesian framework, $p_{\rm p}$ is proportional to the a priori and observational error p.d.f.s $p_{\rm pr}$ and p_{ϵ}, the latter being evaluated for the sky-plane ("Observed-Computed") residuals $\Delta\boldsymbol{\psi}$

$(\boldsymbol{P})$ (Muinonen and Bowell, 1993),

$$p_p(\boldsymbol{P}) \propto p_{pr}(\boldsymbol{P}) p_\epsilon(\Delta\boldsymbol{\psi}(\boldsymbol{P})),$$
$$\Delta\boldsymbol{\psi}(\boldsymbol{P}) = \boldsymbol{\psi} - \boldsymbol{\Psi}(\boldsymbol{P}), \quad (4)$$

where $\boldsymbol{\psi}$ and $\boldsymbol{\Psi}$ denote the observations and the computed positions. p_ϵ is typically assumed to be Gaussian. The final a posteriori p.d.f. is then

$$p_p(\boldsymbol{P}) \propto \exp[-\tfrac{1}{2}\chi^2(\boldsymbol{P})],$$
$$\chi^2(\boldsymbol{P}) = \Delta\boldsymbol{\psi}^T(\boldsymbol{P}) \Lambda^{-1} \Delta\boldsymbol{\psi}(\boldsymbol{P}). \quad (5)$$

The random-walk ranging method for sampling the a posteriori probability density is implemented in the "short-arc orbit determination" package DPAC CU4 software at CNES, Toulouse, France. The input consists of individual astrometric positions for an object. The orbital computation results (i.e., 2000 sample orbits computed by random-walk ranging) are passed through to the rest of the chain for ephemeris prediction to be diffused to the ground-based follow-up network Gaia-FUN-SSO.

As an example to illustrate the performance of the approach, we compute the orbital distribution of a single anonymous object observed by Gaia around November 8, 2014. The data consist of 55 observations over 19 h 55.2 min.

The initial guess for the range is 2.5 ± 0.2 AU using the Gaussian probability distribution, based on the assumption that the majority of the observed asteroids are main-belt objects. The algorithm, however, also takes into consideration other possible orbital types, by changing the initial guess for the range into uniform sampling of ranges, should the initial guess fail during the first 50 attempts. In Fig. 5 we illustrate the results using Keplerian orbital elements.

We have also observed the so-called phase transition (e.g., Muinonen et al., 2006) to occur around the 12-h observational time interval. After the phase transition, corresponding to a substantially smaller region in the orbital parameter space, the ephemeris prediction is constrained into a relatively small portion of the sky, which is a major aid for follow-up observations. However, the tentative conclusion has been reached on the basis of only several tens of observations, and therefore additional data are required for confirmation. The length of the observational time interval varies with different asteroid orbital type and may be used as an indirect means to distinguish between different orbit types also in the Gaia data set.

7. Ground-based follow up

The ground-based Follow-Up network for the Solar System Objects observed by Gaia (Gaia-FUN-SSO) is coordinated within DPAC, but relies on a network of that is completely external to the DPAC itself.

Nominally, it is designed to operate on newly discovered asteroids, but since SSO-ST is not yet operating in discovery mode, the network was mainly activated on test target, with training goals. Gaia-FUN-SSO is entirely managed at IMCCE, Paris, where a new web interface for registering the users, automatically disseminating the alerts and collecting the observations, was implemented (https://gaiafunsso.imcce.fr/).

The Gaia-FUN-SSO network has been set up on a volunteering base and gathers 56 observing sites equipped with 80 telescopes ensuring a good geographical coverage on Earth and some redundancy for overcoming bad meteorological conditions. This coverage, could be improved by expanding further to the southern hemisphere and North America. Nevertheless, such a big number of participants ensures a good potential when alerts are triggered.

Within the network almost 30 telescopes (those with diameter larger than 0.8 m) are capable of tracking the Gaia discoveries close to the mission limit in brightness ($V=20$).

8. Conclusions

We presented a quick overview of the main steps for Solar System processing of Gaia data. Despite the fact that these analysis are still very preliminary, we can say that the results obtained on

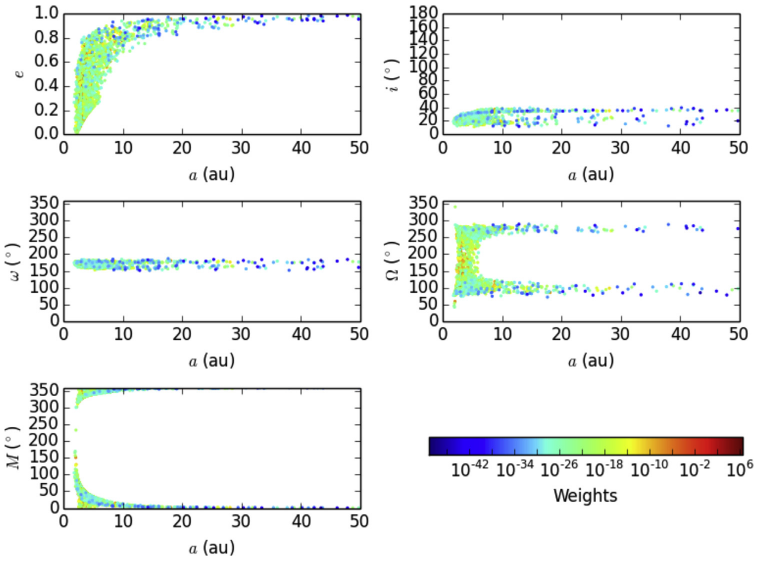

Fig. 5. Keplerian orbital elements from random-walk ranging for one of the objects with 55 Gaia observations from two different transits. The asteroid is likely to be a Main Belt object, and the weights already indicate a preferred phase-space regime.

validation data, extracted from the large volume of Gaia observations, appear to be consistent with the expectations. In particular, the single-epoch astrometric positions of asteroids on the sky are well within a dispersion of ~70 mas, as allowed by the properties of the approximate, daily attitude. In future months Gaia observations will be used to trigger alerts on objects of special interest, and the long-term pipeline, implementing more accurate solutions, will also be tested, in the attempt to produce astrometry to be published in one of the first intermediate releases of Gaia.

Acknowledgements

We gratefully acknowledge the Gaia team at CNES (Toulouse, France) where the Solar System data are processed. This research is funded, in part, by the Academy of Finland (KM's project 1257966). GF acknowledges the support of the Magnus Ehrnrooth Foundation. ADO and AC acknowledge financial support from the Italian Space Agency (ASI), under the contracts 'Gaia Mission - The Italian Participation to DPAC', 2014-025-R.0. TP is supported by Prodex. PT acknowledges support from CNES, and the Action Spécifique Gaia.

References

Berthier, J., Vachier, F., Thuillot, W., Fernique, P., Ochsenbein, F., Genova, F., Lainey, V., Arlot, J.-E., 2006. Astronomical Data Analysis Software and Systems XV 351, 367.

De Bruijne, J.H.J., Rygl, K.L.J., Antoja, T., 2015. Gaia Astrometric Science Performance – Post-launch Predictions. arXiv:1502.00791 [astro-ph].

Mignard, F., Cellino, A., Muinonen, K., Tanga, P., Delbò, M., Dell'Oro, A., Granvik, M., Hestroffer, D., Mouret, S., Thuillot, W., Virtanen, J., 2007. The Gaia mission: expected applications to asteroid science. Earth, Moon, Planets 101 (3-4), 97–125.

Muinonen, K., Bowell, E., 1993. Asteroid orbit determination using Bayesian probabilities. Icarus 104, 255–279.

Muinonen, K., Virtanen, J., Bowell, E., 2001. Collision probability for Earth-crossing asteroids using orbital ranging. Celestial Mech. Dyn. Astron. 81, 93–101.

Muinonen, K., Virtanen, J., Granvik, M., Laakso, T., 2006. Asteroid orbits using phase-space volumes of variation. MNRAS 368, 809–818.

Muinonen, K., Fedorets, G., Pentikäinen, H., Pieniluoma, T., Oszkiewicz, D., Granvik, M., Virtanen, J., Tanga, P., Mignard, F., Berthier, J., Dell'Oro, A., Carry, B., and Thuillot, W. 2015. Asteroid orbits with Gaia using random-walk statistical ranging. Planet. Space Sci., (submitted for publication).

Oszkiewicz, D., Muinonen, K., Virtanen, J., Granvik, M., 2009. Asteroid orbital ranging using Markov-chain Monte Carlo. Meteorit. Planet. Sci. 44 (12), 1897–1904.

Prusti, T., 2012. The promises of Gaia. Astronomische Nachrichten 333, 453.

Tanga, P., Delbo', M., Hestroffer, D., Cellino, A., Mignard, F., 2007. Gaia observations of Solar System objects: Impact on dynamics and ground-based observations. Adv. Space Res. 40, 209–214.

Tanga, P., Mignard, F., 2012. The Solar System as seen by Gaia: the asteroids and their accuracy budget. Planet. Space Sci. 73 (1), 5–9.

Virtanen, J., Muinonen, K., Bowell, E., 2001. Statistical ranging of asteroid orbits. Icarus 154, 412–431.

Telescopes and Instrumentation

Automatic Removal of Fringes from EFOSC Images

Colin Snodgrass[1]
Benoît Carry[2]

[1] Max Planck Institute for Solar System Research, Katlenburg-Lindau, Germany
[2] L'Institut de Mécanique Céleste et de Calcul des Éphémérides (IMCCE), Observatoire de Paris, France

EFOSC, in common with many instruments with older CCDs, shows a fringe pattern in images taken at red wavelengths. These fringes are difficult to remove without significant manual adjustment for each individual frame, which is a time-consuming exercise, but necessary for reliable photometry of faint objects across the whole field of view. We present a simple technique to automatically remove fringes from CCD images, and provide scripts (available on the ESO website) to apply this to EFOSC data, or to any other images.

Fringing in CCD images

Astronomical charge-coupled device (CCD) images are often affected by fringe patterns (Figure 1a). These fringes are created by the interference of monochromatic light within the CCD. Narrowband filters are typically affected, as well as broadband filters containing strong sky emission lines. Lines due to atmospheric OH affect bandpasses at the red end of the CCD wavelength range ($\lambda > 700$ nm), i.e., *R*-, *I*- and *Z*-bands. The problem is discussed in more detail in the broad introduction to CCD data reduction by Gullixson (1992) and Howell (2006), and in the recent paper by Howell (2012). While the latest generation of CCDs does not suffer from this problem, there are many instruments still in active use (such as EFOSC2 at the New Technology Telescope [NTT]; Buzzoni et al., 1984) that employ older CCDs. Given the increasing popularity of ESO's archival data in publications, removal of fringes from images remains a necessary reduction step for many users.

Fringes are a cosmetic problem — obvious to the human eye when a typical "z-scale" algorithm is used to display astronomical images — but add only a small additional flux to the image. For shorter exposure images they are hardly noticeable and attempts to remove them can be more trouble than they are worth (even a good fringe map has some associated noise, and it is worth remembering that all reduction steps add noise to the image; Newberry [1991]). However, for longer exposures, and especially when dealing with photometry of multiple or extended objects, or of moving targets, it can be critical to remove the fringes to provide properly uniform photometry across the field. As calibrations (biases, flats) are taken during the day, or during twilight, they do not show the faint night sky-emission fringes and cannot be used for correcting the fringe patterns. Therefore, fringes are not removed by the standard data-processing techniques (bias subtraction, bad pixel masking, and flat-fielding). Fringe removal requires an extra step, where a description of the fringe pattern is scaled and subtracted from each image. This has traditionally been a rather labour-intensive step, typically requiring careful manual adjustments for each science image, as the intensity of the fringes is highly variable, depending on atmospheric conditions.

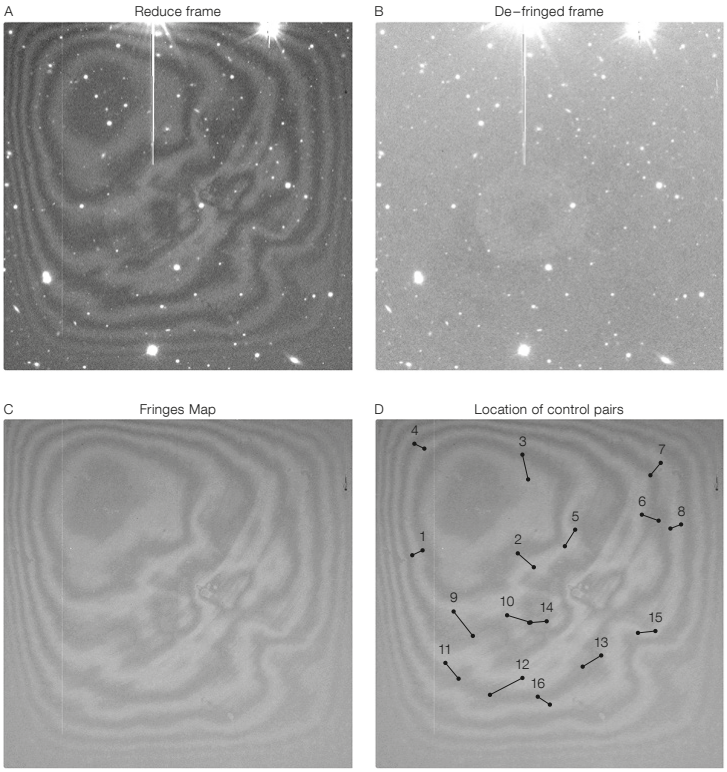

Figure 1. a) *R*-band EFOSC2 frame presenting a strong fringe pattern (following standard reduction steps: bias subtraction and flat fielding); b) same as a, but after application of the defringing method presented here; c) the fringe map used in the correction; d) location of the control pairs used to scale the fringe map (see text).

Properties of the fringes

The location of the fringes in the images is determined by changes in the thickness of the CCD. Hence, the pattern of the fringes on the detector is globally stable with time. The intensity of the fringes

depends on the amount of incoming monochromatic light, either from the sky emission lines or selected by a narrow-band filter. The fringes can therefore present large intensity variations from image to image, even during a single night of observation, reaching up to several percent of the noise level from the sky background. This variability presents the largest challenge in correcting for fringing, as care has to be taken to scale the fringe pattern to the correct intensity for each image individually before subtraction.

The stability of the fringe pattern means that a single high signal-to-noise (S/N) fringe map can be used to describe the pattern. These are generally created through a combination of frames taken of the night sky (under moonless conditions, as a bright sky background can mask the faint fringes). When data are taken of a given target with a significant jitter pattern — i.e., movement of the telescope in a random fashion between each image, so that sources do not fall on the same pixels in multiple images — then the data frames themselves can be median-combined to leave only the fringe pattern. Alternatively, images of a deliberately selected "empty" field can be used, but this uses a significant amount of good observing time for calibration. Howell (2012) describes a new method of constructing a fringe map using neon lamp illumination during daytime calibrations, which has the advantage that very high S/N can be achieved without wasting any time during the night. For EFOSC, a pre-prepared fringe map is available for download[1]. Fringe maps for EFOSC have been measured through different filters and at different times (including before and after moving the instrument from the 3.6-metre telescope to the NTT — see Snodgrass et al. [2008]), and demonstrate the stability of the fringe pattern and the fact that it is almost identical in different passbands.

Once a fringe map is obtained, by any of the above methods, it has to be scaled to the intensity of the fringe pattern in each science frame, and then subtracted from the data. Note that the fringe pattern is additional flux, so it is subtracted from the data, unlike flat-field variations, which are corrected by division. Here lies the difficulty in the operation, as the intensity of the fringe pattern is highly variable on short timescales. In general it increases with increasing exposure time (longer exposures are more significantly affected), so to first order the pattern can be scaled by the length of each exposure. This is the approach used by the fringe removal option within the widely used *ccdproc* task in IRAF (part of the core *ccdred* package — Valdes [1988]), but this method can considerably over- or under-correct due to the intrinsic variations of the night sky-emission lines, which are not correlated to exposure time. The *ccdproc* task also gives the option of specifying additional scaling factors via image headers, but this requires considerable manual iteration to get a satisfactory result. It is worth noting that the same IRAF package also includes the *mkfringecor* task, which is used to combine frames to construct a good fringe map.

A second approach implemented within IRAF is to scale the fringe map to globally minimise the difference between the map and object frames, which is used by the *rmfringe* and *irmfringe* tasks in the *mscred* package (Valdes, 1998). This approach works better, but requires careful masking of sources, bad pixels and cosmic rays to avoid these affecting the minimisation. It therefore needs some preparatory work, and can be time consuming when dealing with many frames (especially where these are of different fields).

Automatic de-fringing method

Here we describe a method that allows frames to be processed simply and automatically, with minimal preparation beyond the construction of the fringe map. We take advantage of the stability of the shape of the fringe pattern to clean it from the scientific frames, by using knowledge of the pattern to define areas of each image to perform automatic scaling. We describe the fringe pattern in terms of "dark" and "bright" areas, corresponding to the background sky and the fringes themselves (see Figure 1c). The precise choice of areas is not important, providing they sample the variation in the fringe pattern well (in practice, any sufficiently large number of random points will work).

To estimate the amplitude of the fringe pattern, we measure the flux difference between bright and dark areas. Practically, we use a series of "control pairs", each consisting of a couple of reference locations, taken in and out of the fringe pattern (Figure 1d). For each pair *i*, we measure the flux difference on the frame between the bright and dark area, $\delta F_i = F_{\rm bright} - F_{\rm dark}$, and, at the same position on the fringe map, the flux difference between the bright and dark areas, δM_i. The scale factor to be applied to the fringe map is then taken as the median of all the ratios, $\delta F_i / \delta M_i$. Theoretically, a single control pair would be enough to scale the fringe map. However, the presence of any astronomical source (star, galaxy, nebulosity, etc.) close to one of the ends of the control pair would bias the scale factor. Therefore we select several control pairs (typically 5 to 20) spread across the full field. Experimentation with the number and position of the pairs has shown that the quality of the subtraction is hardly affected by these factors.

The list of control pairs is based on the constant fringe pattern, so it can be fixed for a given instrument, and does not need to be modified for different datasets — with a sufficient number of pairs the occasional overlap of a pair with a source doesn't affect the scaling. This allows highly automated de-fringing — once a fringe map and a suitable set of pairs are defined for a given instrument, the de-fringing operation does not require further human intervention. As the measurement of each pair is a simple operation, a large number can be used without any concerns about computing time. The scripting of this operation is relatively straightforward — we provide implementations in two popular systems used for astronomical data reduction, IDL and IRAF. A table of control points for EFOSC is provided with the code[2].

The same approach has been applied as part of the Elixir pipeline for data from the MegaCam instrument at the Canada-France-Hawaii Telescope (Magnier & Cuillandre, 2004; Regnault et al., 2009). The scripts we provide implement a more general solution, designed to work with EFOSC, but applicable to all imaging data with no modification.

Example: photometry of trans-Neptunian objects

As an example of the method presented here, we present an image taken from a photometric survey of faint trans-Neptunian objects; members of a dynamical family related to the dwarf planet (136108) Haumea (Snodgrass et al. 2010; Carry et al. 2012). We measured visible colours (in *BVRi* bands) and rotational light curves (*R*-band) of 30 targets with *V* magnitudes between approximately 20 and 24, using EFOSC. All the targets were moving relative to the comparison field stars, alternatively coming in and out of the fringe pattern (Figure 1a), and were therefore affected by it at a level that could have a significant influence on the photometry, especially for the faintest targets. We removed the fringe pattern using the method described here, and present the cleaned version of an example frame in Figure 1b. In this particular example, a faint circle is visible near the centre of the image, which is not part of the fringe pattern but a ghost reflection due to the bright star just off of the top of the frame. Such a faint structure is nearly impossible to identify in the original frame due to the fringes. Jitter patterns were employed to allow new fringe frames to be created, and with many moving targets observed over three multi-night runs, a large number of different fields were observed, including some relatively dense star fields. All were automatically processed via this method with no manual adjustments required. Our method has also been successfully applied to EFOSC images of extended sources (active comets) by Lacerda (2013).

References

Buzzoni, B. et al. 1984, The Messenger, 38, 9
Carry, B. et al. 2012, A&A, 544, A137
Gullixson, C. A. 1992, in ASP Conference Series, Vol. 23, *Astronomical CCD Observing and Reduction Techniques*, ed. S. B. Howell, 130
Howell, S. B. 2006, Cambridge observing handbooks for research astronomers, Vol. 5, *Handbook of CCD Astronomy*, eds. R. Ellis, J. Huchra, S. Kahn, G. Rieke & P. B. Stetson, (Cambridge: Cambridge University Press)
Howell, S. B. 2012, PASP, 124, 263
Lacerda, P. 2013, MNRAS, 428, 1818
Magnier, E. A. & Cuillandre, J.-C. 2004, PASP, 116, 449
Newberry, M. V. 1991, PASP, 103, 122
Regnault, N. et al. 2009, A&A, 506, 999
Snodgrass, C. et al. 2010, A&A, 511, A72
Snodgrass, C. et al. 2008, The Messenger, 132, 18
Valdes, F. 1988, in *Instrumentation for Ground-Based Optical Astronomy*, ed. L. B. Robinson, 417
Valdes, F. G. 1998, in ASPacific Conference Series, Vol. 145, *Astronomical Data Analysis Software and Systems VII*, eds. R. Albrecht, R. N. Hook, & H. A. Bushouse, 53

Links

[1] Pre-prepared EFOSC fringe image from: http://www.eso.org/sci/facilities/lasilla/instruments/efosc/inst/fringing.html
[2] Scripts for defringing EFOSC images in IDL and IRAF available from:

Telescopes and Instrumentation

A Simpler Procedure for Specifying Solar System Objects in Phase 2

Benoît Carry[1,2]
Jérôme Berthier[1]

[1] IMCCE, Observatoire de Paris, PSL Research University, CNRS, Sorbonne Universités, UPMC Univ Paris 06, Université Lille, France
[2] Laboratoire Lagrange, Université de Nice Sophia Antipolis, CNRS, Observatoire de la Côte d'Azur, France

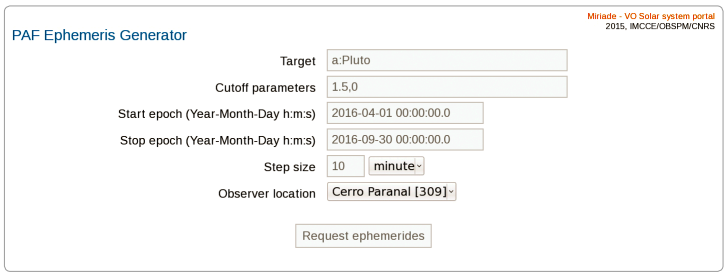

Figure 1. The PAF query form, hosted at IMCCE and ESO. Here, ephemerides are requested for (134340) Pluto, from Paranal, for the entire Period 97, with a time step of 10 minutes. The PAF parameters refer to the cut-off on the target airmass (≤ 1.5) and the Sun's elevation (≤ 0 degrees) for displaying ephemerides.

Observations of Solar System objects in Service Mode require a special procedure. Observers preparing Observing Blocks must submit a detailed ephemerides file for each target for the whole duration of the observability period, which can sometimes be the entire ESO Period. These ephemerides files are ASCII files and follow a strict format, compatible with the VLT parameter file format. We present a simple web service that is now available to replace the former two-step process.

ESO ephemerides requirements

As with many other telescopes, Very Large Telescope (VLT) observations done at a non-sidereal tracking rate require a special procedure at the VLT. In Visitor Mode (VM), each visiting astronomer is responsible for updating both the coordinates and the apparent motion of the target at the time of execution of an Observing Block (OB), prepared with the Phase 2 Proposal Preparation tool (P2PP). In this case, the choice of source of ephemerides, and its format, is at the discretion of the visiting astronomer.

The situation is different in Service Mode (SM), where the staff at Paranal execute OBs prepared weeks in advance by remote astronomers. The procedure set by ESO for Phase 2 preparation in the case of moving targets thus includes the submission of an ephemerides file together with each OB. Both the content and format of these ephemerides files are strictly defined. The ESO Phase 2 web pages[1] document these requirements thoroughly. We limit the description here to the core of these files.

For each OB, the ephemerides file lists the successive coordinates and apparent motion of the target, for the whole duration of its observability period. The apparent displacement of the target cannot exceed 30 arcseconds between two consecutive entries (3 arcseconds in the case of SINFONI, due to its much smaller acquisition field of view). As a result, such files may contain up to several thousand entries.

The coordinates are requested as topocentric astrometric equatorial coordinates, at J2000 equinox (International Celestial Reference Frame). The VLT telescope control system corrects for precession, nutation, annual aberration and atmospheric refraction, and coordinates should not be submitted as apparent coordinates.

Ephemerides computation at IMCCE

The Bureau des longitudes, created during the French Revolution by the law of Messidor 7, year 3 by the Convention Nationale, is the academy responsible for the definition of the French national ephemerides. The practical realisation of these ephemerides is entrusted to the Institut de mécanique céleste et de calcul des éphémérides (IMCCE). Aside from the official astronomical and nautical ephemerides publications[2], the IMCCE releases ephemerides computations through its website.

The ephemerides of planets and small Solar System objects (SSOs) are computed in a quasi-inertial reference frame, taking into account post-Newtonian approximations. The geometric positions of the major planets and the Moon are provided by Intégrateur Numérique Planétaire de l'Observatoire de Paris (INPOP) planetary theory (Fienga et al., 2014). Those of small SSOs (asteroids, comets, Centaurs, trans-Neptunian objects) are calculated by numerical integration of the *N*-body perturbed problem (Gragg–Bulirsch–Stoer algorithm: Bulirsch & Stoer, 1966; Stoer & Bulirsch, 1980), with the exception of the natural satellites, for which positions are obtained from dedicated solutions of their motion, e.g., Lainey et al. (2007; 2004a, b) for Mars and Jupiter, Vienne & Duriez (1995) for Saturn, Laskar & Jacobson (1987) for Uranus, and Le Guyader (1993) for Neptune. The typical accuracy of asteroid and comet ephemerides are at the level of tens of milliarcseconds, mainly due to the accuracy of their osculating elements.

In 2005, the IMCCE started to implement Virtual Observatory (VO) compliant interfaces in its ephemerides services (Thuillot et al., 2005). A web portal[3] describes the various services, such as Solar System object identification (SkyBoT: Berthier et al., 2006), or general ephemerides computation (Miriade: Berthier et al., 2009). All our services are accessible via web services (based on the SOAP and HTTP POST method) which allows interaction between the application and the services via HTTP request and web forms, and are integrated in several VO-compliant software packages, such as the widespread Aladin Sky Atlas (Bonnarel et al., 2000). We describe below an extension of the Miriade ephemerides

generator to simply and quickly generate ephemerides files compliant with ESO Phase 2 requirements.

A simple solution for Phase 2 preparation

We have implemented the strict VLT parameter file format (PAF) as one of the possible outputs of the Miriade VO ephemerides generator. This makes it easy to generate a fully PAF-compliant ephemerides file by setting the *–pafParams* option within the Miriade web service.

In order to reduce the final number of entries, the service includes a test on two parameters: the target airmass and the Sun's elevation above the horizon. Only entries satisfying both conditions (target above a threshold airmass, and Sun below a threshold elevation) are reported by the service. The default thresholds are an airmass of 2.6 and an elevation of 0 degrees, i.e., sunset and sunrise.

We have also developed a simple query form, hosted on both the IMCCE[4] and ESO[5] websites, in which users need only fill in the target (helped by the auto-completion Application Program Interface [API] of our SsODNet[6] service), the observatory (Paranal or La Silla), the time span and time interval of the ephemerides entries, and, optionally, the thresholds for entry selection (see Figure 1). The code source of this query form can be provided upon request[7], and copy-pasted into any web page, the computations being carried out at IMCCE.

References

Berthier, J. et al. 2009, European Planetary Science Congress 2009, 676

Berthier, J. et al. 2006, ADASS, ASP Conference Series, 351, ed. Gabriel, C., Ponz, D. & Enrique, S., 367

Bonnarel, F. et al. 2000, A&AS, 143, 33

Bulirsch, R. & Stoer, J. 1966, Numerische Mathematik, 8, 1

Fienga, A. et al. 2014, Scientific notes

Lainey, V., Arlot, J. E. & Vienne, A. 2004, A&A, 427, 371

Lainey, V., Dehant, V. & Patzold, M. 2007, A&A, 465, 1075

Lainey, V., Duriez, L. & Vienne, A. 2004, A&A, 420, 1171

Laskar, J. & Jacobson, R. A. 1987, A&A, 188, 212

Le Guyader, C. 1993, A&A, 272, 687

Stoer, J. & Bulirsch, R. 1980, *Introduction to numerical analysis*, (New York: Springer)

Thuillot, W. et al. 2005, BAAS, 37, 638

Vienne, A. & Duriez, L. 1995, A&A, 297, 588

Links

[1] Moving targets in Phase 2: https://www.eso.org/sci/observing/phase2/SMSpecial/MovingTargets.html

[2] Publications of IMCCE: http://www.imcce.fr/en/publications/publications_officielles.html

[3] IMCCE VO Web Portal: http://vo.imcce.fr/

[4] IMCCE ephemerides query form: http://vo.imcce.fr/webservices/miriade/?forms

[5] ESO Phase 2 ephemerides query form: http://www.eso.org/sci/observing/phase2/SMSpecial/MovingTargets.html

[6] SsODNet target name autocompletion: http://vo.imcce.fr/webservices/ssodnet/

[7] Query form source code: http://vo.imcce.fr/webservices/miriade/?clients

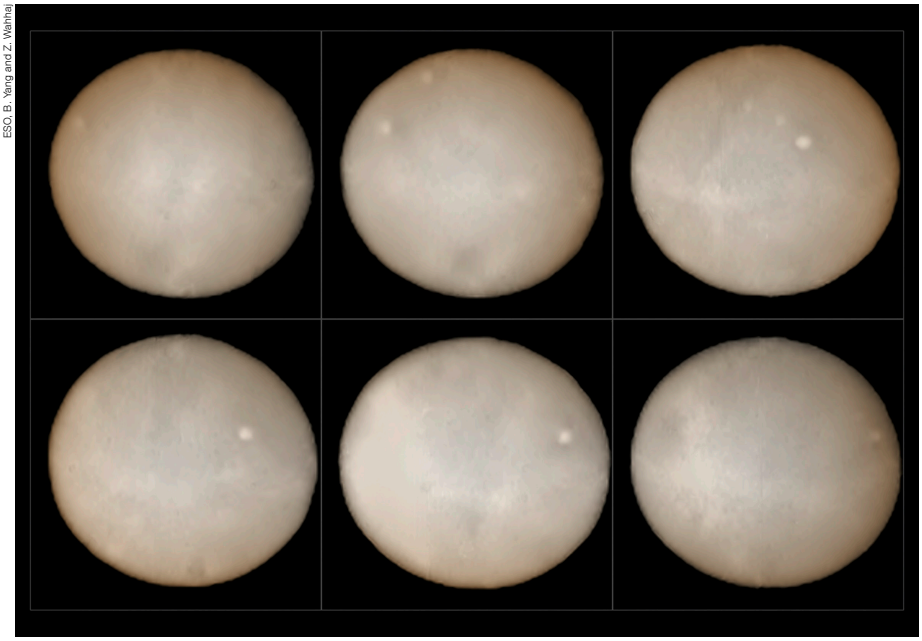

ESO, B. Yang and Z. Wahhaj

The two hemispheres of the dwarf planet Ceres are visible in this series of images, taken two weeks apart, made by the Spectro-Polarimetric High-contrast Exoplanet REsearch (SPHERE) instrument. Several transitory bright spots are seen, whose nature is not yet well understood. The NASA *Dawn* satellite is currently in orbit around Ceres. See Picture of the Week potw1536 for more detail.

Monthly Notices of the ROYAL ASTRONOMICAL SOCIETY

MNRAS **458,** 3394–3398 (2016) doi:10.1093/mnras/stw492
Advance Access publication 2016 March 2

Prediction of transits of Solar system objects in *Kepler*/K2 images: an extension of the Virtual Observatory service SkyBoT

J. Berthier,[1⋆] B. Carry,[1,2⋆] F. Vachier,[1] S. Eggl[1] and A. Santerne[3⋆]

[1] *IMCCE, Observatoire de Paris, PSL Research University, CNRS, Sorbonne Universités, UPMC Univ Paris 06, Univ Lille, France*
[2] *Laboratoire Lagrange, Université de Nice-Sophia Antipolis, CNRS, Observatoire de la Côte d'Azur, France*
[3] *Instituto de Astrofísica e Ciências do Espaço, Universidade do Porto, CAUP, Rua das Estrelas, P-4150-762 Porto, Portugal*

Accepted 2016 February 26. Received 2016 February 23; in original form 2016 February 4

ABSTRACT

All the fields of the extended space mission *Kepler*/K2 are located within the ecliptic. Many Solar system objects thus cross the K2 stellar masks on a regular basis. We aim at providing to the entire community a simple tool to search and identify Solar system objects serendipitously observed by *Kepler*. The sky body tracker (SkyBoT) service hosted at Institut de mécanique céleste et de calcul des éphémérides provides a Virtual Observatory compliant cone search that lists all Solar system objects present within a field of view at a given epoch. To generate such a list in a timely manner, ephemerides are pre-computed, updated weekly, and stored in a relational data base to ensure a fast access. The SkyBoT web service can now be used with *Kepler*. Solar system objects within a small (few arcminutes) field of view are identified and listed in less than 10 s. Generating object data for the entire K2 field of view (14°) takes about a minute. This extension of the SkyBoT service opens new possibilities with respect to mining K2 data for Solar system science, as well as removing Solar system objects from stellar photometric time series.

Key words: virtual observatory tools – ephemerides – planetary systems.

1 INTRODUCTION

The NASA Discovery mission *Kepler* was launched in 2009, with the aim of detecting exoplanets from the photometric signature of their transit in front of their host star (Borucki et al. 2009). Following the second failure of a reaction wheel in 2013 May, the original field of view (FoV) in Cygnus could not be fine pointed anymore. An extension of the mission, dubbed K2 (Howell et al. 2014), was designed to be a succession of 3-month long campaigns, where the spacecraft's FoV scans the ecliptic plane. This mode of operations implies that many Solar system objects (SSOs) cross the subframes centred on K2 mission targets. Following a visual inspection of the K2 engineering FoV, Szabó et al. (2015) reported that SSOs had crossed half of the 300 stars monitored over the 9 d of engineering observations.

Owing to the large number of stellar targets in each K2 campaign, the likelihood of observing SSOs at any single epoch is indeed high. Given a typical mask size around each target of 15 × 15 pixels or 1 × 1 arcmin for between 10 000 and 30 000 stellar targets, the filling factor[1] of K2 entire FoV ranges from 3 per cent to 10 per cent (Table 1). A corresponding fraction of the SSOs that cross K2 FoVs are within a target mask at each instant, from a few tens of minutes for a near-Earth object to approximately 6 h for a main-belt asteroid, and up to several days for a Trojan or a transneptunian object. Over a whole campaign, the cumulative probability to observe these SSOs get close to one, as the different target masks, stacked over ecliptic longitude, almost fill entirely the range of ecliptic latitudes within K2 FoVs (Table 1). Each SSO has thus only a few per cent chance to dodge all the target masks as it crosses K2 FoV (Table 1). Several programmes dedicated to planetary science have been already carried out by K2, like characterization of the rotation period of transneptunian objects (Pál et al. 2015). The giant planet Neptune and its satellites were also observed in C3, and Uranus will be in C8.

Considering the typical magnitude of K2 stellar targets (80 per cent of the stars have a $V \leq 15$–16), and the typical K2 photometric precision of a few hundreds ppm, many SSOs will be imaged together with the stars. At any instant several thousands of SSOs with $V \leq 20$ lay within K2 entire FoV (e.g. Fig. 1). An asteroid of 20th magnitude will contribute to the star signal at a level of 1000 ppm, and is, therefore, easily detectable.

There is a twofold interest in having a simple tool to predict *encounters* between stars and SSOs:

(i) The K2 community profits from identifying any encounters that add undesirable signals, hence photon noise, to stellar light curves, at non-negligible levels.

⋆ E-mail: berthier@imcce.fr (JB); benoit.carry@oca.eu (BC); alexandre.santerne@astro.up.pt (AS)

[1] The fraction of the K2 FoV that is actually downlinked.

Table 1. Number of K2 stellar targets, fraction of the total field of view downlinked to Earth, filling fraction of ecliptic latitudes (β_f), expected average number and standard deviation of stellar encounters for each SSO (μ_e and σ_e), for each campaign (up to C7).

Campaign	Targets	Area (per cent)	β_f (per cent)	μ_e	σ_e
C0	7756	2.90	94.16	4.3	2.7
C1	21 647	8.09	98.25	11.8	5.4
C2	13 401	5.01	96.53	7.4	4.4
C3	16 375	6.12	97.94	9.1	4.8
C4	15 781	5.90	98.18	8.7	4.2
C5	25 137	9.40	98.68	13.8	6.3
C6	27 289	10.20	98.91	14.9	6.2
C7	13 261	4.96	96.74	7.3	4.9

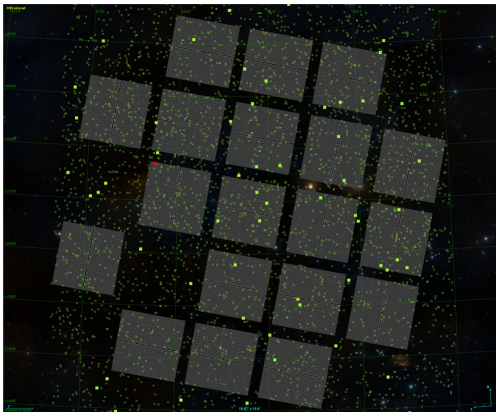

Figure 1. K2 full frame image taken on 2014 March 11, at 23:27:23.77 UTC (mid-exposure), overplotted on the DSS coloured view, displayed by Aladin. All the 3136 known SSOs brighter than $V \leq 20$ (among 9702) present within the FoV reported by SkyBoT are represented, by the green circles for asteroids (and solid squares for $V \leq 16.5$), and by the red dot for a comet (84P, $V = 18.8$).

(ii) The Solar system community profits, as each encounter provides a short light curve (typical a couple of hours) of an SSO with excellent photometric accuracy. On average, 10 encounters per campaign can be expected (Table 1).

To cater to those demands, we present an extension of our Virtual Observatory (VO) tool sky body tracker (SkyBoT) (Berthier et al. 2006), hosted at Institut de mécanique céleste et de calcul des éphémérides (IMCCE). This tool is web based, open-access, and provides a simple way to identify all the SSOs present within a FoV at a given epoch. This paper is organized as following: in Section 2, we describe the SkyBoT service, its algorithm and access, and we show a pair of examples in Section 3.

2 SKYBOT: THE VO SKY BODY TRACKER

The typical queries to astronomical catalogues are so-called *cone searches*, in which all targets within a given FoV are returned. This is mostly adapted to objects with fixed coordinates, such as stars and galaxies, their parallax and proper motion being much smaller than the FoV. But the coordinates of objects in our Solar system constantly change and cone searches cannot use pre-defined catalogues. As a result, most tools for source identification fail to associate the observed SSO with a known source. The SkyBoT service provides a solution by pre-computing ephemerides of all the known SSOs, and storing them in a relational data base for rapid access upon request.

2.1 Ephemerides computation and SkyBoT algorithm

Among other services, the IMCCE produces the French national ephemerides under the supervision of the Bureau des longitudes. The development and maintenance of ephemerides tools for the astronomical community is also a part of its duties. As such, the institute offers online computation of SSO ephemerides through a set of web services.[2]

The ephemerides of planets and small SSOs are computed in the ICRF quasi-inertial reference frame taking into account perturbations of the eight planets, and post-Newtonian corrections. The geometric positions of the major planets and the Moon are provided by INPOP planetary theory (Fienga et al. 2014). Those of small SSOs (asteroids, comets, Centaurs, transneptunian objects) are calculated by numerical integration of the *N*-body perturbed problem (Gragg–Bulirsch–Stoer algorithm, see Bulirsch & Stoer 1966; Stoer & Bulirsch 1980), using the latest published osculating elements, from the `astorb` (Bowell, Muinonen & Wasserman 1993) and `cometpro` (Rocher & Cavelier 1996) data bases. The overall accuracy of asteroid and comet ephemerides provided by our services are at the level of tens of milliarcseconds, mainly depending on the accuracy of the minor planet's osculating elements. The positions of natural satellites are obtained thanks to dedicated solutions of their motion, e.g. Lainey, Duriez & Vienne (2004a), Lainey, Arlot & Vienne (2004b), Lainey, Dehant & Pätzold (2007) for Mars and Jupiter, Vienne & Duriez (1995) for Saturn, Laskar & Jacobson (1987) for Uranus, and Le Guyader (1993) for Neptune's satellites.

The ephemerides of all the known objects of our Solar system are recomputed on a weekly basis, for a period which extends from the end of the 19th century (1889 November 13) to the first half of the 21st century (2060 March 21), and stored with a time step of 10 d in a hierarchical tree structure supported by nodes based on geocentric equatorial coordinates. For each cone search, this data base is queried, and all the targets expected to be within the FoV are listed. Their topocentric ephemerides for the exact requested time are then computed on the fly.

The apparent topocentric celestial coordinates (i.e. relative to the true equator and equinox of the date) are computed by applying light aberration, precession, and nutation corrections to the observer–target vector. The coordinates of the topocentre can either be provided directly by users (longitude, latitude, altitude), or by using the observatory code provided by IAU Minor Planet Center[3] for listed observatories.

The SkyBoT service was released in 2006 (Berthier et al. 2006). It is mostly used to identify moving objects in images (e.g. Conrad et al. 2009; Delgado, Delmotte & Vuong 2011; Carry et al. 2012; Bouy et al. 2013), and data mining of public archives (e.g. Vaduvescu et al. 2009, 2011, 2013; Carry et al. 2016). It responds to about 80 000 requests every month (more than 18 millions in 7 yr),

[2] http://vo.imcce.fr/webservices/
[3] http://www.minorplanetcenter.net/iau/lists/ObsCodesF.html

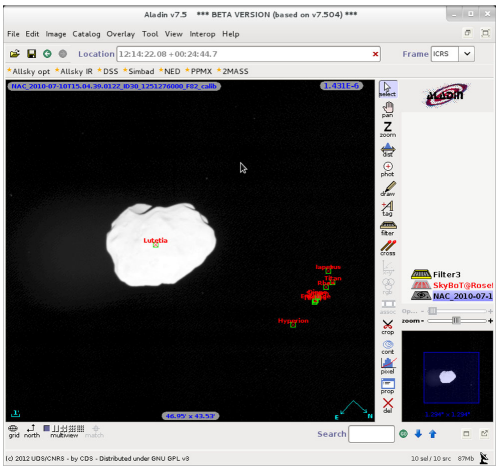

Figure 2. OSIRIS NAC image taken during the flyby of asteroid (21) Lutetia by ESA *Rosetta* space mission, on 2010 July 10, at 15:04:30 UTC (Sierks et al. 2011), displayed in Aladin. A SkyBoT cone-search query correctly lists Lutetia, together with Saturn and its satellites imaged in the background. Considering their dramatic difference of distance to *Rosetta* (36 000 km and 6.8 au, respectively), this example validates the SkyBoT upgrade to space missions.

and has a typical response time of less than 10 s for 95 per cent of requests.

2.2 An extension to non-Earth-bound geometries

Owing to the large number of known SSOs (currently 700 000), and the extended period of time that needs to be covered (from the first photographic plates to the present), pre-computations are the key to a timely service. As the data base of pre-computed ephemerides was ordered in a tree based on equatorial coordinates (RA/Dec.) to allow quick identification of potential targets within a FoV, the service was limited to a single geometry. The large parallax presented by objects within the Solar system indeed implies different equatorial coordinates depending on the position of the observer. The first releases of SkyBoT were thus limited to Earth geocentre, topocentres, and low-orbit satellites such as the *Hubble Space Telescope* or the International Space Station.

In 2010, we started a new phase of the SkyBoT development to allow the use of its cone-search method from other geometries. This was motivated by availability of wide-field ($2^\circ \times 2^\circ$ and $10^\circ \times 10^\circ$) images taken by the OSIRIS camera on-board the ESA *Rosetta* mission, which is on an interplanetary trajectory crossing the asteroid main-belt, between Mars and Jupiter. The great distance between the probe and the Earth, combined with the proximity of SSOs implied observing geometries so different that the Earth-bound data base could not be used to search for and identify targets correctly. This challenge was recently solved. An example validating the corresponding update of the SkyBoT service is presented in Fig. 2.

To preserve the fast response time of the service, a switch was set in place, to redirect queries to different data bases, one for each space probe. These data bases have smaller time coverage, corresponding only to the mission lifetimes. The weekly computation of ephemerides is, therefore, not as CPU intensive as for the main (Earth) data base. There are currently two space probes available: *Rosetta* and *Kepler*. The architecture of SkyBoT after the update is such that we can add more space probes upon request: any space mission located on a Earth leading or trailing orbit (e.g. *Herschel*), or at L2 point (e.g. JWST, *Euclid*), or on an interplanetary trajectory (e.g. *Cassini*, JUNO) could be added, if desired by the community.

2.3 Access to the service

There are several ways to use the SkyBoT web service. Users who may want to discover the service can use a simple query form on the IMCCE's VO SSO portal[4] or the well-established Aladin Sky Atlas (Bonnarel et al. 2000). The service is also fully compliant with VO standards, and thus, can be scripted in two different ways: (i) by writing a client to send requests to the SkyBoT server and to analyse the response, or (ii) by using a command-line interface and a data transfer program such as CURL or WGET.

In all cases, three parameters must be passed to SkyBoT: the pointing direction (RA/Dec.), the epoch of observation, and the size of the FoV. The typical response time for request from K2 point of view are of a few seconds for small FoV (target mask), and of about 1 min for the entire FoV of *Kepler* of about 14°.

3 SOME EXAMPLES

We now present a couple of examples of the typical usage of the SkyBoT service for K2. In Fig. 1, we show a full frame image from C0, together with the result of a SkyBoT request: among the 9702 SSOs located in the FoV at that time, 3136 are brighter than $V \leq 20$, and about 50 are brighter than $V \leq 16$, thus potentially observable by K2. In Fig. 3, we present the light curve of the star EPIC 201872595 ($K_p = 12.2$) from Campaign #1, in which each surge of flux is caused by the transit of a different SSO within the target mask. The stellar flux is clearly contaminated by the SSOs. This is an obvious case of transits by SSOs, each being barely less bright ($V \sim 14$–15) than the target star. Fainter SSOs ($V \sim 18$–19) still affect stellar light curves, without being easily identifiable by naked eye. Using the SkyBoT service, it is easy to check any suspicious point in a stellar light curve, by performing a cone search, centred on the star, at the time of the corresponding photometry measurement, with a narrow FoV of a few arcseconds corresponding to the apparent size of the stellar mask.

The service also allow us to hunt for photometric data of SSOs. One can use SkyBoT to get the list of all the SSOs within the K2 entire FoV for each campaign, and compute their encounters with target stars to extract their photometry. For the fast generation of detailed ephemerides for each target, we recommend the use of our Miriade service (Berthier et al. 2009). Requesting SkyBoT cone search for the entire FoV, with a time step of 30 min during a whole campaign, is more CPU intensive than computing the same ephemerides for only the identified targets with Miriade.

In Fig. 4, we present 10 light curves of asteroid (484) Pittsburghia (apparent magnitude ∼15) we measured in K2 Campaign #0. The light curves have been constructed following the steps described above: a global SkyBoT request, followed by a Miriade generation of ephemerides every 30 min for Pittsburghia, and finally a check of whenever the asteroid was within one of the stellar masks. The synthetic light curve was generated using the 3D shape model of Pittsburghia by Durech et al. (2009) and Hanuš et al. (2011) is

[4] http://vo.imcce.fr

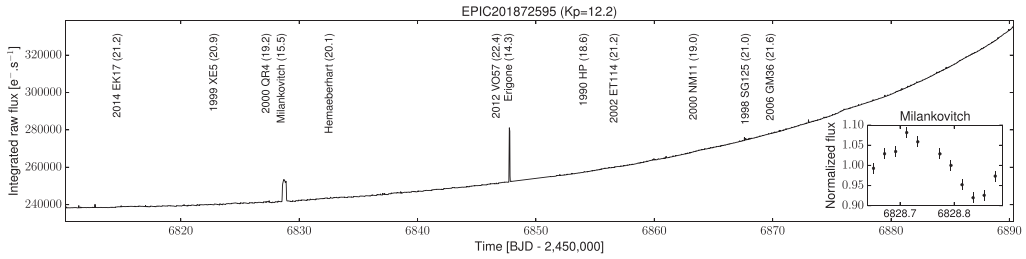

Figure 3. K2 raw light curve integrated overall pixels of the target EPIC 201872595 ($K_p = 12.2$) observed during Campaign #1. The increase in flux along the campaign is a systematic effect. The predicted transits of known SSOs down to a magnitude of 22.5 are indicated together with their expected V magnitude. The transit of two relatively bright SSOs, (1605) Milankovitch and (163) Erigone, are clearly visible. The fainter SSOs also imprint a significant increase in the observed flux as they pass into the target imagette. The inset in the bottom right is a zoom on the transit of (1605) Milankovitch. It displays the target-corrected and normalized flux of the SSO, and highlights the phase rotation of the SSO.

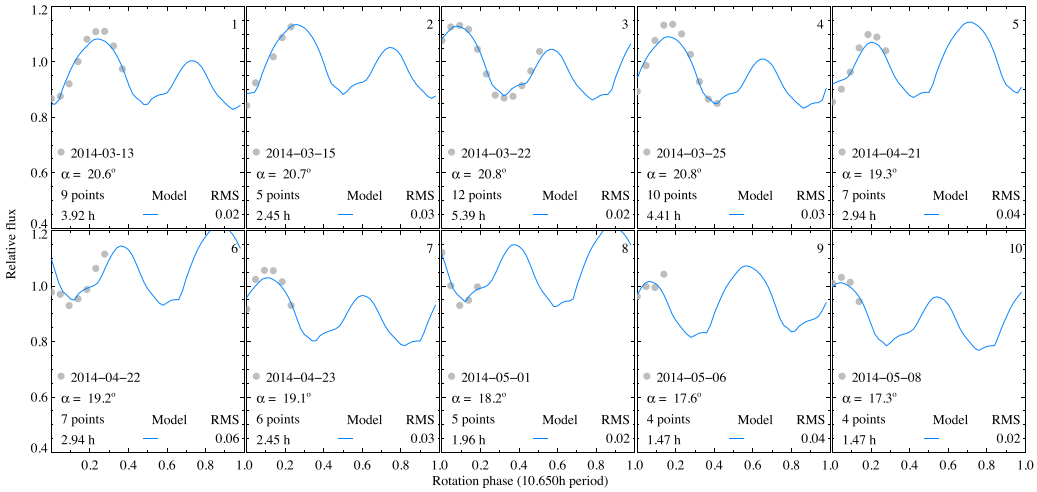

Figure 4. Example of asteroid light curves retrieved from K2 images. The grey dots represent the measured photometry of (484) Pittsburghia, and the blue curves stand for the synthetic light curves obtained from the 3D shape model of the asteroid by Durech et al. (2009) and Hanuš et al. (2011). The residuals between observed and modelled points are of 0.03 mag on average, as reported on each graph.

overplotted to the data. The excellent match of the photometry measured on K2 frames with the shape models illustrate the interest of data mining K2 data archive for SSO period determination and shape modelling.

4 CONCLUSION

We present a new version of the VO web service SkyBoT. Its cone-search method allow us to list all the SSOs present within a given FoV at a given epoch, as visible from the Earth, the ESA *Rosetta* mission, and now the NASA *Kepler* telescope. More space missions can be added upon request, if desired by the community. Typical queries over limited FoVs take less than 10 s, while queries over extended FoV such as *Rosetta*/OSIRIS camera or *Kepler* full CCD array take about a minute. Possible applications of SkyBoT for K2 data are presented, and the results illustrate the interest of K2 for studying asteroids spin, period, and shapes from the light curves which can be extracted from K2 data. Their analysis and interpretation will be presented in a forthcoming paper (Carry et al., in preparation).

ACKNOWLEDGEMENTS

We acknowledges support of the ESAC Faculty for J. Berthier's visit. This research has received funding from the European Union's H2020-PROTEC-2014 – Protection of European assets in and from space project no. 640351 (NEOShield-2). A. Santerne is supported by the European Union under a Marie Curie Intra-European Fellowship for Career Development with reference FP7-PEOPLE-2013-IEF, number 627202. He also acknowledges the support from the Fundação para a Ciência e Tecnologia, FCT (Portugal) in the form of the grants UID/FIS/04434/2013 (POCI-01-0145-FEDER-007672)

and POPH/FSE (EC) by FEDER funding through the program 'Programa Operacional de Factores de Competitividade – COMPETE'.

REFERENCES

Berthier J., Vachier F., Thuillot W., Fernique P., Ochsenbein F., Genova F., Lainey V., Arlot J.-E., 2006, in Gabriel C., Arviset C., Ponz D., Enrique S., eds, ASP Conf. Ser. Vol. 351, Astronomical Data Analysis Software and Systems XV. Astron. Soc. Pac., San Francisco, p. 367
Berthier J. et al., 2009, European Planetary Science Congress. p. 676 (Available at: http://meetings.copernicus.org/epsc2009)
Bonnarel F. et al., 2000, A&AS, 143, 33
Borucki W. J. et al., 2009, Science, 325, 709
Bouy H., Bertin E., Moraux E., Cuillandre J.-C., Bouvier J., Barrado D., Solano E., Bayo A., 2013, A&A, 554, A101
Bowell E., Muinonen K. O., Wasserman L. H., 1993, Proc. IAU Symp. 160, Asteroids, Comets, Meteors. Lunar and Planetary Institute, Houston, TX, p. 44
Bulirsch R., Stoer J., 1966, Numer. Math., 8, 1
Carry B., Snodgrass C., Lacerda P., Hainaut O., Dumas C., 2012, A&A, 544, A137
Carry B., Solano E., Eggl S., DeMeo F. E., 2016, Icarus, 268, 340
Conrad A. R., Goodrich R. W., Campbell R. D., Merline W. J., Drummond J. D., Dumas C., Carry B., 2009, Earth Moon Planets, 105, 115
Delgado A., Delmotte N., Vuong M., 2011, in Evans I. N., Accomazzi A., Mink D. J., Rots A. H., eds, ASP Conf. Ser. Vol. 442, Astronomical Data Analysis Software and Systems XX. Astron. Soc. Pac., San Francisco, p. 111
Durech J. et al., 2009, A&A, 493, 291
Fienga A., Manche H., Laskar J., Gastineau M., Verma A., 2014, Scientific Notes, preprint (arXiv:1405.0484)
Hanuš J. et al., 2011, A&A, 530, A134
Howell S. B. et al., 2014, PASP, 126, 398
Lainey V., Duriez L., Vienne A., 2004a, A&A, 420, 1171
Lainey V., Arlot J. E., Vienne A., 2004b, A&A, 427, 371
Lainey V., Dehant V., Pätzold M., 2007, A&A, 465, 1075
Laskar J., Jacobson R. A., 1987, A&A, 188, 212
Le Guyader C., 1993, A&A, 272, 687
Pál A., Szabó R., Szabó G. M., Kiss L. L., Molnár L., Sárneczky K., Kiss C., 2015, ApJ, 804, L45
Rocher P., Cavelier C., 1996, in Ferraz-Mello S., Morando B., Arlot J.-E., eds, Proc. IAU Symp. 172, Dynamics, Ephemerides, and Astrometry of the Solar System. Kluwer, Dordrecht, p. 357
Sierks H. et al., 2011, Science, 334, 487
Stoer J., Bulirsch R., 1980, Introduction to Numerical Analysis. Springer-Verlag, New York
Szabó R. et al., 2015, AJ, 149, 112
Vaduvescu O., Curelaru L., Birlan M., Bocsa G., Serbanescu L., Tudorica A., Berthier J., 2009, Astron. Nachr., 330, 698
Vaduvescu O., Tudorica A., Birlan M., Toma R., Badea M., Dumitru D., Opriseanu C., Vidican D., 2011, Astron. Nachr., 332, 580
Vaduvescu O. et al., 2013, Astron. Nachr., 334, 718
Vienne A., Duriez L., 1995, A&A, 297, 588

This paper has been typeset from a TEX/LATEX file prepared by the author.